
SILICON CARBIDE - MATERIALS, PROCESSING AND APPLICATIONS IN ELECTRONIC DEVICES

Edited by **Moumita Mukherjee**

INTECHWEB.ORG

Silicon Carbide - Materials, Processing and Applications in Electronic Devices

Edited by Moumita Mukherjee

Published by InTech

Janeza Trdine 9, 51000 Rijeka, Croatia

Copyright © 2011 InTech

All chapters are Open Access articles distributed under the Creative Commons Non Commercial Share Alike Attribution 3.0 license, which permits to copy, distribute, transmit, and adapt the work in any medium, so long as the original work is properly cited. After this work has been published by InTech, authors have the right to republish it, in whole or part, in any publication of which they are the author, and to make other personal use of the work. Any republication, referencing or personal use of the work must explicitly identify the original source.

Statements and opinions expressed in the chapters are these of the individual contributors and not necessarily those of the editors or publisher. No responsibility is accepted for the accuracy of information contained in the published articles. The publisher assumes no responsibility for any damage or injury to persons or property arising out of the use of any materials, instructions, methods or ideas contained in the book.

Publishing Process Manager Dragana Manestar

Technical Editor Teodora Smiljanic

Cover Designer Jan Hyrat

Image Copyright Only Fabrizio, 2011. Used under license from Shutterstock.com

First published September, 2011

Printed in Croatia

A free online edition of this book is available at www.intechopen.com
Additional hard copies can be obtained from orders@intechweb.org

Silicon Carbide - Materials, Processing and Applications in Electronic Devices,
Edited by Moumita Mukherjee

p. cm.
978-953-307-968-4

INTECH OPEN ACCESS
PUBLISHER

INTECH open

free online editions of InTech
Books and Journals can be found at
www.intechopen.com

Contents

Preface IX

Part 1 Silicon Carbide: Theory, Crystal Growth, Defects, Characterization, Surface and Interface Properties 1

- Chapter 1 **Mechanical Properties of Amorphous Silicon Carbide 3**
Kun Xue, Li-Sha Niu and Hui-Ji Shi
- Chapter 2 **SiC Cage Like Based Materials 23**
Patrice Mélinon
- Chapter 3 **Metastable Solvent Epitaxy of SiC, the Other Diamond Synthetics 53**
Shigeto R. Nishitani, Kensuke Togase, Yosuke Yamamoto, Hiroyasu Fujiwara and Tadaaki Kaneko
- Chapter 4 **The Formation of Silicon Carbide in the SiC_x Layers (x = 0.03–1.4) Formed by Multiple Implantation of C Ions in Si 69**
Kair Kh. Nussupov and Nurzhan B. Beisenkhanov
- Chapter 5 **SiC as Base of Composite Materials for Thermal Management 115**
J.M. Molina
- Chapter 6 **Bulk Growth and Characterization of SiC Single Crystal 141**
Lina Ning and Xiaobo Hu
- Chapter 7 **SiC, from Amorphous to Nanosized Materials, the Exemple of SiC Fibres Issued of Polymer Precursors 161**
Philippe Colomban
- Chapter 8 **Micropipe Reactions in Bulk SiC Growth 187**
M. Yu. Gutkin, T. S. Argunova, V. G. Kohn, A. G. Sheinerman and J. H. Je

- Chapter 9 **Thermal Oxidation of Silicon Carbide (SiC) – Experimentally Observed Facts** 207
Sanjeev Kumar Gupta and Jamil Akhtar
- Chapter 10 **Creation of Ordered Layers on Semiconductor Surfaces: An ab Initio Molecular Dynamics Study of the SiC(001)-3×2 and SiC(100)-c(2×2) Surfaces** 231
Yanli Zhang and Mark E. Tuckerman
- Chapter 11 **Optical Properties and Applications of Silicon Carbide in Astrophysics** 257
Karly M. Pitman, Angela K. Speck, Anne M. Hofmeister and Adrian B. Corman
- Chapter 12 **Introducing Ohmic Contacts into Silicon Carbide Technology** 283
Zhongchang Wang, Susumu Tsukimoto, Mitsuhiro Saito and Yuichi Ikuhara
- Chapter 13 **SiC-Based Composites Sintered with High Pressure Method** 309
Piotr Klimczyk
- Part 2 Silicon Carbide: Electronic Devices and Applications** 335
- Chapter 14 **SiC Devices on Different Polytypes: Prospects and Challenges** 337
Moumita Mukherjee
- Chapter 15 **Recent Developments on Silicon Carbide Thin Films for Piezoresistive Sensors Applications** 369
Mariana Amorim Fraga, Rodrigo Sávio Pessoa, Homero Santiago Maciel and Marcos Massi
- Chapter 16 **Opto-Electronic Study of SiC Polytypes: Simulation with Semi-Empirical Tight-Binding Approach** 389
Amel Laref and Slimane Laref
- Chapter 17 **Dielectrics for High Temperature SiC Device Insulation: Review of New Polymeric and Ceramic Materials** 409
Sombel Diahm, Marie-Laure Locatelli and Zarel Valdez-Nava
- Chapter 18 **Application of Silicon Carbide in Abrasive Water Jet Machining** 431
Ahsan Ali Khan and Mohammad Yeakub Ali

- Chapter 19 **Silicon Carbide Filled Polymer Composite for Erosive Environment Application: A Comparative Analysis of Experimental and FE Simulation Results** 453
Sandhyarani Biswas, Amar Patnaik and Pradeep Kumar
- Chapter 20 **Comparative Assessment of Si Schottky Diode Family in DC-DC Converter** 469
Nor Zaihar Yahaya
- Chapter 21 **Compilation on Synthesis, Characterization and Properties of Silicon and Boron Carbonitride Films** 487
P. Hoffmann, N. Fainer, M. Kosinova, O. Baake and W. Ensinger

Preface

Silicon Carbide (SiC) and its polytypes have been a part of human civilization for a long time; the technical interest of this hard and stable compound has been realized in 1885 and 1892 by *Cowless* and *Acheson* for grinding and cutting purpose, leading to its manufacture on a large scale. The fundamental physical limitations of Si operation at higher temperature and power are the strongest motivations for switching to wide bandgap (WBG) semiconductors such as SiC for these applications. The high output power density of WBG transistors allows the fabrication of smaller size devices with the same output power. Higher impedance, due to the smaller size, allows easier and lower loss matching in amplifiers. The operation at high voltage, due to its high breakdown electric field, not only reduces the need for voltage conversion, but also provides the potential to obtain high efficiency, which is a critical parameter for amplifiers. The wide bandgap enables it to operate at elevated temperatures. These attractive features in power amplifier enabled by the superior properties make these devices promising candidates for microwave power applications. Especially military systems such as electrically steered antennas (ESA) could benefit from more compact, broadband and efficient power generation.

Another application area is robust front end electronics such as low noise amplifiers (LNAs) and mixers. A higher value of saturation velocity in SiC will allow higher current and hence higher power from the devices. Heat removal is a critical issue in microwave power transistors. The thermal conductivity of SiC is substantially higher than that of GaAs and Si. The large bandgap and high temperature stability of SiC and GaN also makes them possible to operate devices at very high temperatures. At temperatures above 300 °C, SiC has much lower intrinsic carrier concentrations than Si and GaAs. This implies that devices designed for high temperatures and powers should be fabricated from WBG semiconductors, to avoid effects of thermally generated carriers. When the ambient temperature is high, the thermal management to cool down crucial hot sections introduces additional overhead that can have a negative impact relative to the desired benefits when considering the overall system performance.

The potential of using SiC in semiconductor electronics has been already recognized half a century ago. Despite its well-known properties, it has taken a few decades to overcome the exceptional technological difficulties of getting SiC material to reach device quality and travel the road from basic research to commercialization.

SiC exists in a large number of cubic (C), hexagonal (H) and rhombohedral (R) polytype structures. It varies in the literature between 150 and 250 different ones. For microwave and high temperature applications the 4H is the most suitable and popular polytype. Its carrier mobility is higher than in the 6H-SiC polytype, which is also commercially available. SiC as a material is thus most suited for applications in which high-temperature, high-power, and high-frequency devices are needed. To that end, this book is a good compendium of advances made since the early 1990s at numerous reputable international institutions by top authorities in the field.

Sequence of chapters is arranged to cover a wide array of activities in a fairly coherent and effective manner. In 21 chapters of the book, special emphasis has been placed on the “materials” aspects and developments thereof. To that end, about 70% of the book addresses the theory, crystal growth, defects, surface and interface properties, characterization, and processing issues pertaining to SiC. The remaining 30% of the book covers the electronic device aspects of this material. Overall, this book will be valuable as a reference for SiC researchers for years to come.

This book prestigiously covers our current understanding of SiC as a semiconductor material in electronics. Its physical properties make it more promising for high-powered devices than silicon. The volume is devoted to the material and covers methods of epitaxial and bulk growth. Identification and characterization of defects is discussed in detail. The contributions help the reader to develop a deeper understanding of defects by combining theoretical and experimental approaches. Apart from applications in power electronics, sensors, and NEMS, SiC has recently gained new interest as a substrate material for the manufacture of controlled graphene. SiC and graphene research is oriented towards end markets and has high impact on areas of rapidly growing interest like electric vehicles.

Dr. Moumita Mukherjee,
Scientist-B, Senior Asst. Professor
Centre for Millimeter-wave Semiconductor Devices and Systems (CMSDS),
Institute of Radio Physics and Electronics,
University of Calcutta,
India

Part 1

Silicon Carbide: Theory, Crystal Growth, Defects, Characterization, Surface and Interface Properties

Mechanical Properties of Amorphous Silicon Carbide

Kun Xue¹, Li-Sha Niu² and Hui-Ji Shi²

¹State Key Laboratory of Explosion Science and Technology,
Beijing Institute of Technology

²School of Aerospace, FML, Department of Engineering Mechanics,
Tsinghua University, Beijing,
China

1. Introduction

Excellent physical and chemical properties make silicon carbide (SiC) a prominent candidate for a variety of applications, including high-temperature, high-power, and high-frequency and optoelectronic devices, structural component in fusion reactors, cladding material for gas-cooled fission reactors, and an inert matrix for the transmutation of Pu (Katoh, Y. et al., 2007; Snead, L. L. et al., 2007). Different poly-types of SiC such as 3C, 6H of which 6H have been researched the most. There has been a considerable interest in fabricating 3C-SiC/6H-SiC hetero p-n junction devices in recent years. Ion implantation is a critical technique to selectively introduce dopants for production of Si-based devices, since conventional methods, such as thermal diffusion of dopants, require extremely high temperatures for application to SiC. There is, however, a great challenge with ion implantation because it inevitably produces defects and lattice disorder, which not only deteriorate the transport properties of electrons and holes, but also inhibit electrical activation of the implanted dopants (Benyagoub, A., 2008; Bolse, W., 1999; Jiang, W. et al., 2009; Katoh, Y. et al., 2006). Meanwhile the swelling and mechanical properties of SiC subjected to deslative neutron irradiation are of importance in nuclear applications. In such irradiations the most dramatic material and microstructural changes occur during irradiation at low temperatures. Specifically, at temperatures under 100°C volumetric swelling due to point defect induced strain has been seen to reach 3% for neutron irradiation doses of ~0.1-0.5. At these low temperatures, amorphization of the SiC is also possible, which would lead to a substantial volumetric expansion of ~15%, along with decreases in mechanical properties such as hardness and modulus (Snead, L. L. et al., 1992; Snead, L. L. et al., 1998; Snead, L. L., 2004; Weber, W. J. et al., 1998).

Intensive experimental and theoretical efforts have been devoted to the dose and temperature dependence of the properties of irradiation-amorphized SiC (a-SiC) (Weber, W. J. et al., 1997). Heera *et al.* (Heera, V. et al., 1997) found that the amorphization of SiC induced by 2 MeV Si⁺ implantation is accompanied by a dramatic and homogeneous volume swelling until a critical dose level dependent on the temperature. Afterwards the volume tends to saturate and the density of a-SiC is about 12% less than that of the crystalline

material. The experimental values of the elastic modulus and hardness of *a*-SiC estimated from measurements of surface and buried amorphous layers show a large degree of variability. In general, the hardness and elastic modulus in *a*-SiC are observed to decrease 20%-60% and 25%-40%, respectively. Weber *et al.* (Weber, W. J. *et al.*, 1998) performed nanoindentation experiments with Berkovich indenter on the Ar⁺ beam induced *a*-SiC. The results suggest that the elastic modulus decreases ~24%, from 550 to 418 GPa. Snead *et al.* (Snead, L. L. *et al.*, 1992) reported that the elastic modulus in SiC, irradiated with C⁺ at low temperatures, decrease from 400 GPa in the virgin region to about 275 GPa in the amorphized region; whereas the hardness was observed to decrease from 41 to 32 GPa. The mechanical properties of *a*-SiC irradiated by neutron have also been investigated (Snead, L. L. *et al.*, 1998). A density decrease of 10.8% from the crystalline to amorphous (c-a) state is revealed along with a decrease in hardness from 38.7 to 21.0 GPa and a decrease in elastic modulus from 528 to 292 GPa.

The varying amorphous nature of *a*-SiC depending on the damage accumulation could justify the wide range of experimental measurements of mechanical properties of *a*-SiC. Thus of particular fundamental and technological interest has been developing the models capable of describing the various physical properties of SiC as a function of microstructural changes, specifically from c-a. Gao and Weber (Gao, F. & Weber, W. J., 2004) investigated the changes in elastic constants, the bulk and elastic moduli of SiC as a function of damage accumulation due to cascade overlap using molecular dynamics (MD) simulation. The results indicate a rapid decrease of these properties with increasing dose but the changes begin to saturate at doses greater than 0.1 MD-dpa. Given that fully amorphous state is reached at a dose of about 0.28 MD-dpa, they suggested that point defects and small cluster may contribute more significantly to the changes of elastic constants than the topological disorder associated with amorphization.

Although the inherent correlation between the mechanical properties and the disordered microstructures of *a*-SiC has been widely accepted, there still lacks a comprehensive description of this correlation given the intricate nature of *a*-SiC. Thus based on detailed examinations of an extensive series of simulated *a*-SiC models with varying concentration of defects, this chapter first attempts to characterize the structure of *a*-SiC with a range of underpinning parameters, whereby substantiates the correlation between the amorphous structure of SiC and a variety of mechanical properties. MD simulations are used to simulate the mechanical responses of varied disordered SiC microstructures subject to two typical loadings, namely axial tension and nanoindentation, which are critical for measures of strength and ductility of bulk *a*-SiC and hardness of *a*-SiC film. The role of these simulations is not necessarily to reproduce exact experimental behaviors, but rather to identify possible atomistic mechanisms associated with a variety of disordered SiC structures, especially from c-a.

Amorphous materials often exhibit unique deformation mechanisms distinct from their crystalline counterparts. The coexistence of brittle grains and soft amorphous grain boundaries (GBs) consisting in nanocrystalline SiC (nc-SiC) results in unusual deformation mechanisms. In the simulation of nanoindentation (Szlufarska, I. *et al.*, 2005), as the indenter depth increases, the deformation dominated by the crystallization of disordered GBs which “screen” the crystalline grains from deformation switches to the deformation dominated by disordering of crystalline grains. Plastic flow along grain boundaries can also effectively

suppresses the cavity nucleation, leading to increased ductility and toughness without compromising its strength (Mo, Y. & Szlufarska, I., 2007).

Because amorphous materials lack a topologically ordered network, analysis of deformations and defects presents a formidable challenge. Conventional computational techniques used for crystalline solids, such as the modulus of slip vector (Rodríguez de la Fuente, O. et al., 2002), centrosymmetry, and local crystalline order, fail to identify the deformation defects in disordered materials. Various models have been proposed to describe defects in such structures. The prevailing theory of plasticity in metallic glasses involves localized flow events in shear transformation zones (STZ) (Shi, Y. & Falk, M. L., 2005). An STZ is a small cluster of atoms that can rearrange under applied stress to produce a unit of plastic deformation. It is worth noting that most of these theories are based on the observations of metallic glasses. Whereas covalently bonded amorphous solids differ from their metallic counterparts due to their directed stereochemical bonds in forms of well-defined coordination polyhedral, e.g. $[\text{SiX}_4]$ or $[\text{CX}_4]$ tetrahedra in SiC. Thanks to the short range order retained in the amorphous covalent materials, plastic deformation tends to be more pronounced localized than in the case of metallic glasses (Szlufarska, I. et al., 2007). Moreover for amorphous alloys like *a*-SiC, the degree of chemical order has been always under the debates, although the consensus from these recent experimental studies of *a*-SiC seems to be in favor of the existence of C-C homonuclear bonds (Bolse, W., 1998; Ishimaru, M. et al., 2002; Ishimaru, M. et al., 2006; Snead, L. L. & Zinkle, S. J., 2002). The presence of dual disorder, namely chemical and topological disorder, in *a*-SiC definitely complicates the analysis of amorphous structure and the underlying atomic mechanisms.

In general a truly atomistic model of plastic flow in amorphous covalent materials is still lacking. Instead of starting with complete *a*-SiC where widespread inhomogeneities frozen into the entire material, we rather begin with a perfect 3C-SiC, then proceed to gradually increase the concentration of damage until a complete amorphous state is reached. Being a link between perfect crystalline and complete amorphous SiC, partially disordered SiC presents a favorable prototype to discern the role of isolated or clustered defects in the evolution of atomic mechanism, where the deformation defects are comparatively readily to identify.

In this chapter, we first outline the studies concerning the c-a transition of irradiation-amorphized SiC, laying the basis for the analysis of SiC amorphous. Then a complete topological description of simulated SiC structures ranging from c-a is presented in both the short- and medium-range with a special focus on the correlation between chemical disorder and the topology of *a*-SiC. Simulated tensile testing and nanoindentation are carried out on the varying *a*-SiC to examine the variations of mechanical response with varying concentration of defects. The correlation between some key mechanical properties of *a*-SiC, such as Young's modulus, strength, hardness, and the microstructure are quantified by virtue of chemical disorder, an characteristics underpinning the c-a transition. A crossover of atomic mechanisms from c-a are also discussed. This crossover is also embodied in the switch of the fracture.

2. Amorphization mechanism of irradiation-amorphized SiC

With regard to the characterization of the varying disordered microstructures of *a*-SiC, the mechanisms controlling the c-a transformation have been of particular interest. By simulating the accumulation of irradiation damages due to the low energy recoils, Malerba

and Perlado (Malerba, L. & Perlado, J. M., 2001) argued that both Frenkel pairs and antisite defects play significant roles in the amorphization process and that the coalescence and growth of defect clusters account for the amorphization of SiC. Antisite defects were found to be less numerous than Frenkel defects, whose accumulation has been instead primarily supposed to trigger amorphization. However Frenkel pairs have strong correlation with antisites. The MD simulation of the disordering and amorphization processes in SiC irradiated with Si and Au ions reveals much higher concentration of antisites in complete amorphous areas where are supposed to comprise large amount of Frenkel pairs than other disordered domains (Gao, F. & Weber, W. J., 2001). Furthermore where is significant overlap of antisite coordination shells, where there are a significant number of Frenkel pairs that are accommodated. If completely excluding antisites, Frenkel defects would become extremely unstable, leading to difficulties of amorphization. Rong *et al.* (Rong, Z. et al., 2007) simulated the recovery of point defects created by a single cascade during the thermo annealing via dynamic lattice MD technique. The results suggest that a large number of irradiation induced Frenkel pairs are formed in metastable configurations, and majority of close pairs would recombine during the annealing at 200 K and 300 K. Contrasting with the dramatic annihilation of Frenkel defects upon annealing, the number of antisite largely remains constant even increases somewhat due to the recombination of interstitials from one sublattice with vacancies on the other. Therefore the role of antisite in the amorphization of SiC is of equal essence.

Basically both Frenkel and antisite defects could give rise to dual disorder, namely topological and chemical disorder. Homonuclear bonds (C-C, Si-Si) are likely to form when antisite or Frenkel defects are introduced, producing a certain degree of chemical disorder. The homonuclear bond ratio R_{hnb} , defined for SiC as the ratio of number of homonuclear bonds to twice the number of heteronuclear bonds, provides a full homonuclear bond analysis. Chemical disorder χ (Terstoff, J., 1994), defined as the ratio of C-C bonds to C-Si bonds, $N_{\text{C-C}}/N_{\text{Si-C}}$, is not a full homonuclear bond analysis and is specified only for C atoms. The argument for using χ instead of R_{hnb} derives mostly from the practical uncertainty of enumerating Si-Si bonds in amorphous structures for which Si atoms have no clearly defined first coordination shell. In practice, χ is quite a good approximation to R_{hnb} and the deviation is proportional to the coordination number difference between Si and C.

The topological disorder of α -SiC manifests itself in variations of the short- and medium-range. Short-range order (SRO), as its name implies, concerns structural order involving nearest-neighbour coordination shell. This is easiest to discuss in the case of covalently bonded amorphous solids since the presence of their directed stereochemical bonds simplifies the description considerably. For example, in the case of SiC, SRD is defined in terms of well defined local coordination tetrahedra. The parameters which are sufficient to describe topological SRO in stereochemical systems are the (coordination) number, N_{ij} , of nearest neighbors of type j around an origin atom of type i , the nearest-neighbour bond length R_{ij} , the bond angle subtended at atom i , θ_{jik} (when the atom of type k is different from j). The connectivity of polyhedral dictates the type and extent of medium-range order (MRO). Shortest-path ring (Rino, J. P. et al., 2004), defined as a shortest path consisting of nearest-neighboring atoms, and local cluster primitive ring (Yuan, X. & Hobbs, L. W., 2002) are among often used means to characterize the MRO. Because Frenkel pairs and antisites have overlapping effects on the amorphization of SiC, and exclusively focusing on the formal Frenkel pairs and antisite configuration themselves has ignored the multiplier effects

on the immediate coordination of a much larger number of atoms, hierarchical parameters signifying SRO and MRO seem to be more appropriate to describe the c-a transition and varying microstructures of *a*-SiC. The c-a transition is accordingly described in terms of the variations in the chemical disorder χ and other topological parameters. The correlation between them would be clarified in the next section.

3. Characterization of the structures of *a*-SiC

Considerable investigations, including experimental and MD simulation studies, indicate a strong correlation between chemical and topological disorder. The x-ray absorption and Ramann spectroscopy performed by Bolse(Bolse, W., 1998) on Na⁺ irradiated SiC clearly showed that a large fraction of the [SiC₄] tetrahedra is destroyed only after the removal of chemical order. The inspection of MD simulated melt-quenched *a*-SiC Has also revealed that chemical disorder determines the short- and medium-range topological order in *a*-SiC(Xue, K. et al., 2008). Therein an extended tetrahedron model only dependent on the composition and chemical disorder χ was developed to predict the probabilities of various local coordination tetrahedra, namely, Si-Si_{4-n}C_n and C-Si_{4-n}C_n ($n = 0-4$), reflecting the local spatial distribution of homonuclear bonds.

(χ)	C4	Si4	l_{C-C}	l_{Si-C}	l_{Si-Si}	Density ($\times 10^3$ Kg/m ³)	Potential Energy (eV/atom)
0.0	100.	100.	N	1.896	N	3.217	-6.39279
0.045	99.9	99.6	1.662	1.862	2.185	3.213	-6.32738
0.133	99.5	98.9	1.661	1.867	2.191	3.148	-6.21825
0.24	98.4	97.8	1.648	1.872	2.225	3.087	-6.10155
0.39	96.1	95.1	1.646	1.877	2.258	3.063	-5.99751
0.422	96.3	92.1	1.635	1.880	2.28	3.058	-5.9726
0.54	96.2	84.1	1.610	1.885	2.337	3.053	-5.88191
0.7	94.2	83.5	1.585	1.904	2.379	3.049	-5.81427

Table 1. Structural characteristics and potential energies of chemical disordered SiC with varying χ . Notations: X4 (X = C or Si), the percentage of four-fold coordinated X atoms; l_{X-Y} (X, Y = C or Si), the average bond length of X-Y bond. In our calculations the cut-off distances of the C-C, Si-C, and C-C interactions are 1.75 Å, 2.0 Å and 2.5 Å, respectively.

The inspection of MD simulated irradiation-induced *a*-SiC has investigated the changes of topological order as a function of chemical disorder and suggested that some threshold chemical disorder should be one requirement for amorphization(Xue, K. & Niu, L.-S., 2009; Yuan, X. & Hobbs, L. W., 2002). Herein interatomic interactions were modeled using the 1994 Tersoff potential improved by Tang and Yip(Tang, M. & Yip, S., 1995; Tersoff, J., 1994). Devanathan et al.(Devanathan, R. et al., 2007) compared the structures of modeled melt-quenched *a*-SiC obtained from three different potentials, namely Tersoff, Brenner, and ionic potentials, with the results of a tight-binding MD (TBMD) simulation and an *ab initio* study. They found that the structural features of *a*-SiC given by Tersoff potential appear to be in better agreement with *ab initio* and TBMD results. In order to explore the role of chemical disorder in the changes of SiC topology, varying chemical disorder ranging from 0 to 0.7 are imposed on a set of 3C-SiC perfect crystal models by swapping pairs of random sites.

The SRO and MRO of all SiC assemblies with varying imposed chemical disorder are examined in terms of a variety of parameters, such as coordination number, pair correlation functions $g_{\alpha\beta}(r)$ and local cluster primitive ring statistics. Table 1 summaries the variations of some important SRO indicators of α -SiC with varying χ . The number of four-fold coordinated C and Si atoms declines with increasing χ especially for the case of Si atom, which is in accordance with the argument in Sec. 2 that more interstitials (vacancies) are accommodated in the areas abundant in antisites. Another feature worth noting is the significant lengthening of C-C bond and the shortening of Si-Si and Si-C bonds, the trend being more pronounced for small χ .

The two body structural correlations of the amorphous materials are analyzed by pair correlations functions $g_{\alpha\beta}(r)$. The evolution of MRO can be traced in terms of the local cluster primitive (LC) ring content, defined as a closed circuit passing through a given atom of the network which cannot be decomposed into two smaller circuits. The LCs have been shown to uniquely characterize the topologies of all compact crystalline silica, Si_3N_4 and SiC polymorphs (Hobbs, L. W. et al., 1999). In the case of crystalline α - or β -SiC, the LCs comprises 12 6-rings (as in Si).

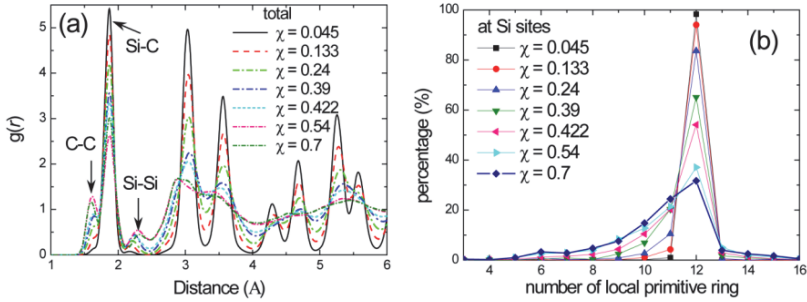


Fig. 1. (a) Total pair correlation function $g_{\alpha\beta}(r)$ and (b) distribution of local cluster ring number at Si sites for α -SiC samples with varying chemical disorder (Xue, K. & Niu, L.-S., 2009).

Fig. 1(a) shows the $g_{\alpha\beta}(r)$ for the SiC assemblies with increasing χ . The C-Si peak substantially declines as χ increases accompanying the enhancement of the C-C and Si-Si peaks. Any appreciable changes of $g_{\alpha\beta}(r)$ could barely be identified after $\chi \sim 0.5$, in a sense meaning the saturation of short-range disordering. Fig. 1(b) demonstrates that the majority of the LCs for $\chi < 0.24$ consist of 12 6-SiC as in 3C-SiC, significant changes of LCs contents occur within the range of $0.24 < \chi < 0.54$, and afterwards the changes tend to saturate. The chemical disorder dependences of SRO and MRO depict the same picture: perfect topological order in 3C-SiC structure is energetically stable until chemical disorder reaches beyond the $\chi = 0.24 - 0.42$ range; for $\chi \geq 0.54$, topological perfection appears impossible to maintain and a stable amorphous structure is achieved.

4. Tensile testing simulation of α -SiC

4.1 Variations in elastic properties of SiC from crystalline to amorphous

Gao and Weber (Gao, F. & Weber, W. J., 2004) calculated the changes of elastic constants, C_{11} , C_{12} , C_{44} , the bulk modulus, B , and averaged elastic modulus, E as a function of dose for cascade-amorphized SiC by imposing moderate strain ($<1\%$) along the MD cell axes. All

elastic constants and elastic modulus show expected softening behavior under irradiation for the dose range of interest. Fig. 2 shows their typical results with regard to the variations of elastic modulus, E and bulk modulus B . These elastic properties decrease rapidly at doses less than 0.1 MD-dpa, and the decrease becomes smaller at the high dose levels. On account of the dose dependence of the formation and coalescence of point defects and small clusters, they concluded that point defects and small clusters contribute much greater than topological disorder to the degradation of elastic properties of a -SiC.

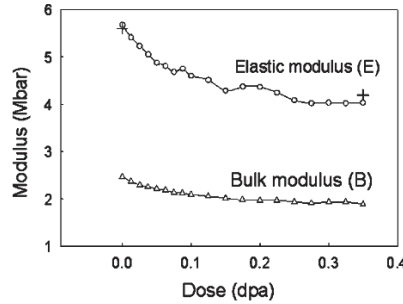


Fig. 2. variation of elastic modulus, E , and bulk modulus, B , as a function of dose (Rino, J. P. et al., 2004)

4.2 Tensile mechanical response of a -SiC

Point defects, small clusters and topological disorder as forms of defect accumulation could somehow indicate the dependence of mechanical properties of a -SiC on the disordered microstructure. However it is difficult to enumerate these damages due to the ambiguous definitions of their complicated configurations. Bearing in mind that chemical disorder χ is of essence to trigger the c - a transition as elucidated in Sec.3, chemical disorder χ is able to distinguish varying disordered SiC structures. Thus formulating the correlation between a variety of mechanical properties and chemical disorder χ provide a favorable alternative to quantify the microstructure dependence of mechanical properties.

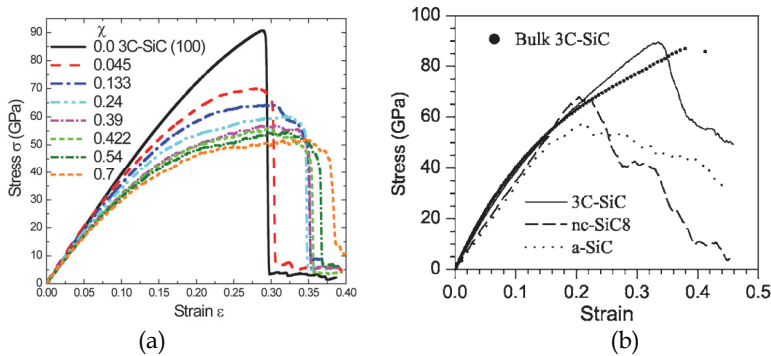


Fig. 3. (a) stress vs strain curves for a -SiC samples with varying chemical disorder at a strain rate of 10^8 s^{-1} (Xue, K. & Niu, L.-S., 2009); (b) stress vs strain curves for 3C-SiC, nc-SiC and melt-quenched a -SiC with an extension rate of 100 m/s (Ivashchenko, V. I. et al., 2007)

Simulated axial tensile testing is carried out on a set of SiC assemblies with varying chemical disorder χ , representing a range of disordered structures from crystalline to complete amorphous. The full stress-strain dependences for different SiC assemblies with varying χ are shown in Fig. 3. The stress-strain curve for 3C-SiC features a linear elastic stage ending up with an abrupt drop of the stress, while the presence of negligible chemical disorder χ ($\chi=0.045$) gives rise to a noticeable deviation beyond $\varepsilon \approx 0.13$ from what would be expected from extrapolation of the linear elastic region. Meanwhile an appreciable softening of the material after the stress reaches σ_{\max} can be observed, evidenced by the weak decrease of the stress before the rupture. This plasticlike behavior becomes increasingly evident with increasing χ , pronounced plastic flow plateau covering a major part of the whole mechanical response. Such plasticlike behavior is reproduced in the tension of simulated melt-quenched a -SiC with a drastic reduction in the number of tetrahedrally coordinated atoms (Ivashchenko, V. I. et al., 2007).

4.3 Mechanical properties of a -SiC as a function of chemical disorder χ

The chemical disorder dependence of the mechanical response of a -SiC is likewise embodied in the variations of the Young's modulus and strength of a -SiC with varying chemical disorder [Fig. 4]. Young's modulus and strength generally exhibit monotonic decrease with increasing χ while in distinct manners until χ reaches 0.54, afterwards tend to saturate regardless of the further increase of χ . Young's modulus E_Y shows negative linear dependence on χ within the range of $0 < \chi < 0.54$ as follows:

$$E_Y = 0.9994E_{Y0} - 0.316 \times \chi \times E_{Y0} \quad (1)$$

where E_{Y0} is Young's modulus along the [100] direction of 3C-SiC (~ 413 GPa). Young's modulus of complete a -SiC is around ~ 321.4 GPa, agreeing well with the value calculated for the melt-quenched a -SiC which stands at ~ 327 GPa (Ivashchenko, V. I. et al., 2007). In contrast with the consistent reduction of E_Y with increasing χ before $\chi < 0.54$, a dramatic decrease of 23.2% for strength occurs at $\chi = 0.045$, decreasing from ~ 90.8 GPa ($\chi = 0$) to ~ 69.7 GPa ($\chi = 0.045$). Whereas strength almost linearly declines afterwards with increasing χ as the following relation until $\chi = 0.54$,

$$S = 0.745S_0 - 0.328 \times \chi \times S_0 \quad (2)$$

where S_0 is the strength of 3C-SiC (~ 90.8 GPa). When χ is beyond 0.54, a complete amorphous state is reached, Young's modulus and strength tend to be constant, which is in line with the saturation of Elastic moduli of a -SiC at high doses (Gao, F. & Weber, W. J., 2004).

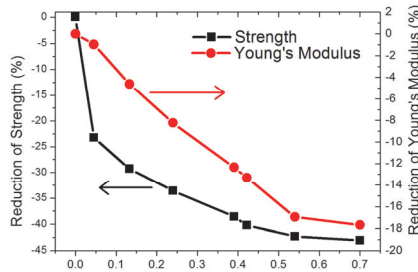


Fig. 4. Variations of Young's modulus and strength as a function of chemical disorder (Xue, K. & Niu, L.-S., 2009)

4.4 Deformation mechanisms

In order to gain further insights into the chemical disorder dependence of Young's modulus and strength, the knowledge of the deformation mechanisms of varying disordered structures is necessary. Young's modulus of the covalent network is closely related with the ability of the topological network to homogeneously elastic deform to accomodate the small strain. Despite of the presence of moderate chemical disorder χ , the almost intact connection of fundamental tetrahedral units, as well as their relative orientation, ensure the homogeneously collective deformation of these units at small χ . Thus no appreciable decrease of Young's modulus could be detected for the SiC assembly with $\chi = 0.045$. As χ increases, the topological order gradually decays, resulting in the reduced stiffness of the network and The ensuing decrease of Young's modulus until a complete amorphous state is reached. Actually the linear elastic region of mechanical response of *a*-SiC gradually diminishes with the increasing χ .

Although a handful of homonuclear bonds introduced by a negligible chemical disorder ($\chi = 0.045$) barely affect the topological order and the Young's modulus, they account for a substantial decline of strength. Due to the atom size difference, the C-C bonds in the undeformed system have been stretched with a bond length increase of $\sim 7\%$ contrasting to the contraction of Si-C and Si-Si bonds. With the strain processes, these stretched C-C bonds are expected to break prior Si-C and Si-Si bonds. The premature breakage of C-C bonds disconnects the neighboring tetrahedral network where the stress builds up. More decohesions of atomic bonds therein conversely take place due to the localized stress. As a results, Localized softened clusters around the initial chemical disorder sites are formed, where atomic rearrangements dominate the confined plastic flow. Fig. 5 (a) illustrates the atomic slipping occurring in these softened regions. With the increased χ , the enhanced topological disorder gives rise to the prevalence of softening regions. Thus the localized plastic flow evolves into percolating flow through the entire system [Fig. 5(b)].

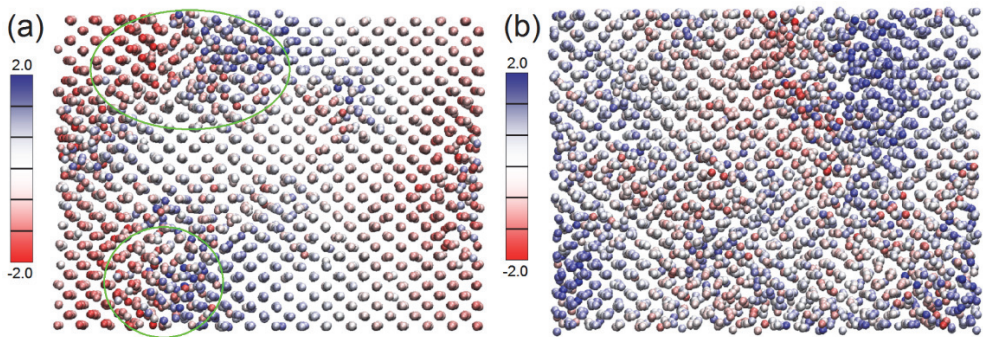


Fig. 5. Atomic configurations for (a) the $\chi = 0.045$ and (b) the $\chi = 0.39$ assemblies at $\epsilon = 0.27$. Atoms are colored according to their motion relative to the homogeneous deformation. Blue atoms have moved towards right relative to what would be expected if the deformation had been homogeneous and elastic; red atoms have moved towards left. The scale indicates how the atoms have moved (in angstroms)(Xue, K. & Niu, L.-S., 2009).

4.5 Fracture modes

When the disordered SiC undergoes c-a transition with the increasing chemical disorder χ , the main deformation mechanism evolves from elastic deformation to localized atomic rearrangement, and then to percolating plastic flow. This crossover is also manifested itself in the switch of the fracture mechanism. At a slight chemical disorder ($\chi = 0.045$), localized softened clusters are embedded in the rigid topological ordered lattice which strongly suppresses the nucleation of nanocavities inside the disordered clusters. Thus the failure of ligaments between softened clusters rather than the percolation of nanocavities leads to the final brittle fracture, which is supported by the sudden drop of cavity density at $\epsilon \sim 0.3$ [Fig.6]. Increased chemical disorder substantially alters the atomistic picture of fracture mechanisms. In the fully amorphous system ($\chi = 0.54$), extensive plastic flow nucleates a large number of nanocavities, their coalescence and percolation through the system leading to the final fracture. This argument is consistent with the slow decline of cavity density after $\epsilon \sim 0.23$ for the $\chi = 0.54$ assembly [Fig. 6]. For *a*-SiC with moderate chemical disorder ($0 < \chi < 0.54$), we can expect a competition of brittle and ductile fracture mechanism, dominated by lattice instability and coalescence of nanocavities, respectively.

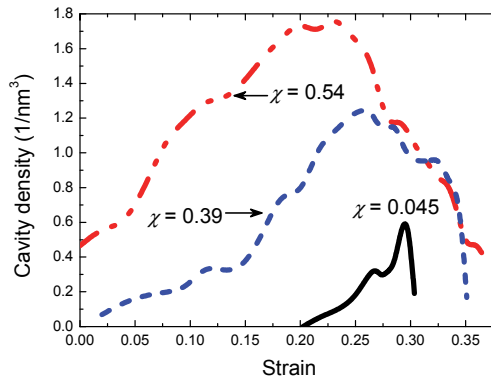


Fig. 6. Cavity densities as a function of strain (a) for different *a*-SiC samples with varying chemical disorder at a strain rate of 10^8 s^{-1} and (b) for the $\chi = 0.54$ ensemble at different strain rates (Xue, K. & Niu, L.-S., 2009).

Recently special efforts have been made to reveal the possible crossover of fracture modes during c-a transition. Glassy materials are considered up to now as the archetype of pure brittle materials, the brittle fracture of which proceeds solely by decohesion of atomic bonds at the crack tip. However, AFM and high scanning electron microscopy (SEM) studies have generated considerable controversy about the nature of fracture mechanism in brittle amorphous solids (Celarie, F. et al., 2003). Xi *et al.* (Xi, X. K. et al., 2005) found a dimple structure at the fracture surface of Mg-based bulk metallic glass by high resolution SEM, indicating that the fracture in brittle metallic glassy materials might also proceed through the softening mechanism but at nanometer scale. Chen *et al.* (Chen, Y.-C. et al., 2007) further investigates the interaction of voids in silica glass by means of multimillion-to-billion-atom MD simulation, unveiling the mechanism of nanocavities nucleation. These findings are in line with the ductile fracture observed in *a*-SiC with $\chi \geq 0.54$ mediated by coalescence of cavities similar to metal materials, although taking place at different length scales.

5. Nanoindentation simulations of *a*-SiC

5.1 P-h curves of *a*-SiC

Nanoindentation is a widely used technique for probing mechanical properties and stability, especially of surfaces and thin films. From the shape of load-indentation displacement (P - h) curves, one can extract information about elastic moduli or hardness. Atomistic computer simulations have been found very helpful in unraveling the processes underlying the nanoindentation responses. For example, MD simulations of indentation of 3C-SiC have shown that the p - h curve [Fig.7(b)] is correlated with the nucleation and coalescence of dislocations under an indenter (Szlufarska, I. et al., 2005).

Amorphous materials lack a long-range order of topological network and hence there is no clear notion of dislocations. Thus understanding atomistic processes during nanoindentation in amorphous materials presents a great challenge. A few atomistic simulations have been performed to tackle this problem. Szlufarska *et al.* (Szlufarska, I. et al., 2007) undertook the difficult task of simulating nanoindentation of melt-quenched *a*-SiC with a diamond indenter. The simulation reveals a noticeable localization of damage in the vicinity of the indenter, however the localization is less pronounced than in the case of 3C-SiC. As shown in Fig. 7(a), the P - h curve for *a*-SiC exhibits irregular, discrete load drops similar to 3C-SiC [Fig. 7(b)]. Here, the load drops correspond to braking of the local arrangements of atoms, in analogy to the slipping of atomic layers in 3C-SiC. Simulations also show that, even at indentation depth h smaller than those at which the material yields plastically, the material's response is not entirely elastic. Instead, the amorphous structure, which is metastable by nature, supports a small inelastic flow related to relaxation of atoms through short migration distances.

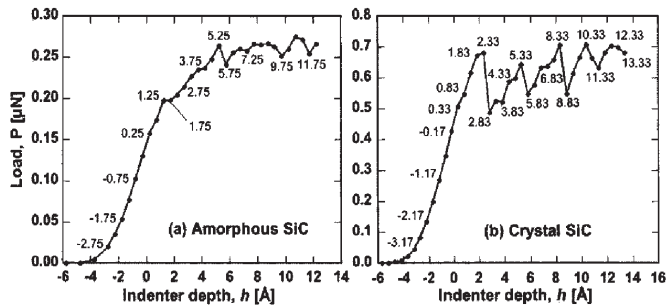


Fig. 7. Load-displacement (P - h) responses for (a) *a*-SiC and (b) 3C-SiC (Szlufarska, I. et al., 2007)

As aforementioned imposing increasing chemical disorder χ on 3C-SiC is able to produce a series of disordered SiC structures ranging from perfect crystalline to complete amorphous, providing favorable prototypes to observe the dependence of hardness on the damage accumulation. More importantly, this means could allow us to identify possible atomistic mechanisms in the early stages of plastic deformation as a function of microstructure. A set of disordered SiC assemblies with varying chemical disorder χ are established as the substrates in the means introduced in Sec.2. The Geometrical setup of the indenter and the substrate is detailed in ref (Xue, K. & Niu, L.-S., 2010). In the case of 3C-SiC, the x , y , z directions correspond to the $[110]$, $[001]$ and $[110]$ crystallographic directions, respectively.

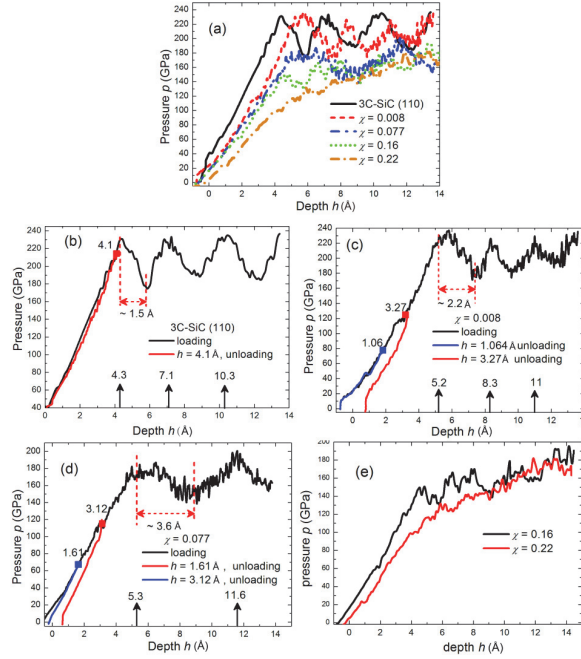


Fig. 8. Pressure-depth (p - h) response: (a) comparison of loading curves for 3C-SiC and a -SiC with varying chemical disorder. (b) Loading and unloading curves from $h = 4.1$ Å (red) for 3C-SiC. (c) Loading and unloading curves from $h = 1.06$ Å (blue) and $h = 3.27$ Å (red) for the $\chi = 0.008$ assembly. (d) Loading and unloading curves from $h = 1.61$ Å (blue) and $h = 3.12$ Å (red) for the $\chi = 0.077$ assembly. (e) Loading curves for the $\chi = 0.16$ and the $\chi = 0.22$ assemblies (Xue, K. & Niu, L.-S., 2010).

Fig.8 shows the computed p - h curves for varying SiC assemblies. Here the pressure (p) defined as the load P divided by actual contact is plotted as a function of depth h . For (110) surface of 3C-SiC, p - h curve displays a linear elastic region followed by a series of sudden load drops occurring at depths equally spaced by ~ 3 Å, resembling the simulated P - h curve of 3C-SiC modeled using an interatomic potential developed by Vashishta *et al.* (Szlufarska, I. et al., 2005). The p - h curves of the $\chi = 0.008$ assembly is similar to the case of 3C-SiC featuring roughly equally spaced peaks after the yield. Whereas the position of the first peak at which the maximum pressure is achieved is significantly deferred accompanying noticeable broadening of peaks. The alteration becomes increasingly pronounced with increasing χ . For the $\chi = 0.077$ assembly, pressure peaks enveloping numerous small serrations are considerably broadened with a much larger separation of ~ 6 Å. Meanwhile the intensity (peak pressure) and magnitude (the amount of load drop) of peaks are substantially reduced. Given that the disordered atoms just account for $\sim 3.5\%$ and $\sim 5\%$ of total atoms for the $\chi = 0.008$ and $\chi = 0.077$ assembly, respectively, the changes of the p - h response seem striking. The defined peak structures of the p - h curves evolves into irregularly spaced fluctuations for the $\chi = 0.16$ assembly and small oscillations in the $\chi = 0.22$ assembly. These substantial changes of the p - h response with increasing χ suggest a crossover of underlying atomistic mechanisms, as we will discuss later.

5.2 Hardness

The hardness (H) is usually defined as equal to the peak force applied during indentation divided by the projected contact area. The calculated values of hardness here are estimated by yield strength. For 3C-SiC and a -SiC with low or moderate chemical disorder ($\chi \leq 0.16$), yield strength is taken as the pressure of the first peak maximum signifying the onset of structural instability. However, the monotonically ascent p - h curve for the $\chi = 0.22$ assembly displays a kink rather than distinguishable load peaks, so the pressure at the kink is picked up as the measure of calculated hardness. It's worth noting that the contact pressure derived from nanoindentation simulations is usually several times greater than the experimental hardness (Mulliah, D. et al., 2006; Noreyan, A. et al., 2005). One major reason is the fact that the indenter size used in the MD simulations is always smaller by two or three orders of magnitude than the indenter used in experiments. According to a relation between contact pressure (p) and the indenter size at the onset of the nucleation of dislocation (Liu, X. M., 2008), we can readily convert the calculated yield strength into the equivalent hardness.

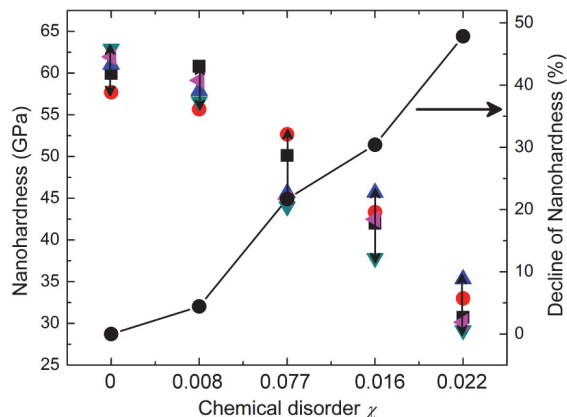


Fig. 9. Calculated hardness of disordered SiC with increasing chemical disorder (Xue, K. & Niu, L.-S., 2010)

The calculated hardness values for different SiC assemblies are plotted in Fig. 9. A remarkable reduction of hardness can be observed for the $\chi = 0.077$ assembly. For the complete a -SiC assembly with $\chi = 0.22$, the hardness value is ~50% less than in 3C-SiC which agrees with the reduction of hardness in a -SiC observed in the experiments (Khakani, M. A. E. & al, e., 1994).

5.3 Atomistic mechanisms

The distinctive characteristics of the p - h curves of SiC from c-a could be understood in light of the corresponding atomistic mechanisms, which entail the detailed analysis of the evolution of the associated microstructures with the increasing indent depth h . The shortest path ring distribution has been widely used to identify the subsurface defects during the nanoindentation (Szulafarska, I. et al., 2004). The presence of nonthreefold rings marks the occurrence of structural deformation, most likely the presence of dislocations.

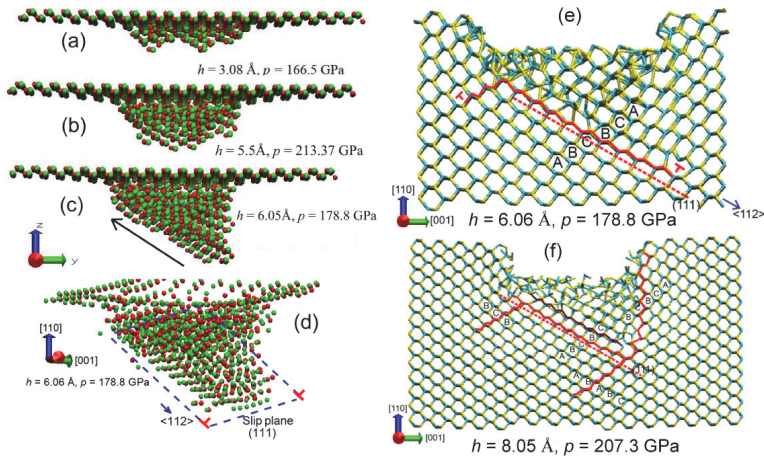


Fig. 10. $(\bar{1}10)$ projections of indentation damages in 3C-SiC composed by disordered atoms with non-threefold rings at different depths. (a) $h = 3.08 \text{ \AA}$, (b) $h = 5.5 \text{ \AA}$, (c) $h = 6.05 \text{ \AA}$. (d) shows the (111) slip plane along which the slip of atomic layers occur at $h = 6.05 \text{ \AA}$. (e) and (f) illustrate the $(\bar{1}10)$ projections of 3C-SiC structure beneath the indenter after the first slip and the second slip of atomic layers, respectively. A stack fault along the red line (e) exists in (111) plane, which is terminated with a Shockley partial dislocation along the $[110]$ direction with Burgers vector $1/6[112]$. A second outburst of dislocations occurs on next (111) plane just below the first (111) plane (f). (Xue, K. & Niu, L.-S., 2010)

The atomistic mechanisms of 3C-SiC during indentations have been elaborated in quite a few of publications (Chen, H.-P. et al., 2007; Szlufarska, I. et al., 2004, 2005; Xue, K. & Niu, L.-S., 2010). Herein some basic deformation mechanisms related to the nanoindentation of 3C-SiC (110) surface with the cuboidal indenter are to be laid out in order to how the atomistic deformation determines the mechanical response, namely p - h curves. Basically the series of equally spaced sudden load drops can be attributed to the dissipation of accumulated stress by subsequent breaking of atomic layers of the substrate whose separation in the indentation (z) direction (here that is $[110]$ crystallographic direction). Fig. 10 (a)-(d) demonstrates the atomic configurations which contain only nonthreefold rings before and after the onset of plastic yield. Fig. 10 (b) and (c) clearly shows the bending and slipping in (111) plane of sequent atomic layers under the indenter, corresponding to the accumulation and release of the load, respectively. The first dislocation emits from the corners of the indenter after the slip and resides in the (111) plane [Fig.10 (e)]. The following dislocation arising from the second slip of atomic layers initiates on the next below (111) plane [Fig. 10(f)]. Two stack faults existing on the neighboring $\{111\}$ planes can be identified after the second load drop [Fig.01(f)], forming a thin layer of hexagonal (wurtzite) structure in the face-centered cubic (zinc-blende) structure of crystalline grains. Similar type of defect has been observed in the indentation of nc-SiC (Szlufarska, I. et al., 2005).

A negligible degree of chemical disorder ($\chi = 0.008$) just disorders $\sim 3.5\%$ of total atoms, barely affecting the topological order. Whereas these small fraction of defects prone to cluster effectively hinders the symmetrical bending of atomic layers under the indenter [Fig.

11(a)], more energy being dissipated in the atomic rearrangement of disordered clusters rather than the bending of atomic layers. As the result the onset of plastic yield occurs at much deeper depth than 3C-SiC. The slipping of atomic layers upon the critical strain is alike arrested by these embedded disordered clusters [Fig.11(b)], evidenced by the prematurely terminated dislocation propagating a relatively shorter distance compared with ones in perfect lattice [Fig.11(c)]. Further penetration of the indenter motivates the pinned dislocation which resumes propagation again as seen in Fig. 10(d). These intermittent slipping of atomic layers accounts for a slower release of accumulated stress, corresponding to the broadened and serrated peaks in the $\chi = 0.008$ assembly. A second breaking of atomic layers triggers a following dislocation located in (111) plane with a separation of several atomic layers below the first sliding plane [Fig.11(d)]. Afterwards the bending of atomic layers overlaps with the unfolding of the previous incomplete slip. Therefore the accumulation of stress offsets partial release of load, leading to less pronounced load drop after the first peak.

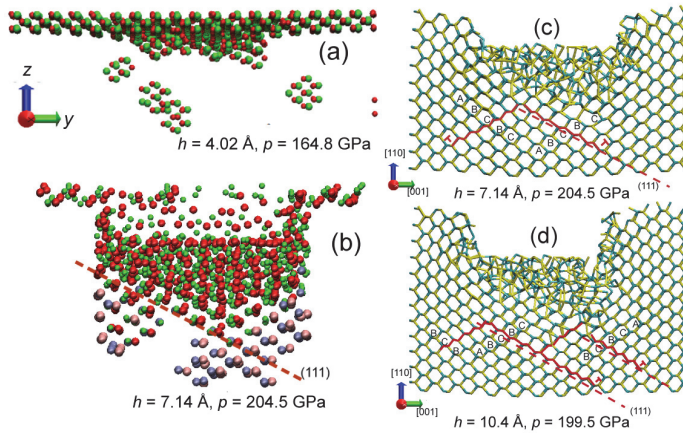


Fig. 11. The $(\bar{1}10)$ projections of indentation damages for the $\chi = 0.008$ assembly before (a) and after (b) the first slip of atomic layers. The pink and light blue atoms refer to the chemical disordered atoms. (c) and (d) illustrate the $(\bar{1}10)$ projections of the $\chi = 0.008$ assembly beneath the indenter after the first slip and the second slip of atomic layers, respectively. (Xue, K. & Niu, L.-S., 2010)

With increased chemical disorder ($\chi = 0.077$), extended disordered clusters penetrating the atomic layers contribute to the substantial decay of the elastic resistance of the network. The atomic rearrangement confined in these softened regions emerges as a major energy dissipation mode complementary to the bending and slipping of atomic layers. The release of stress through localized plastic flow accounts for the remarkable reduction of hardness for the $\chi = 0.077$ assembly. Moreover, as the continuous atomic layers are dissolved into discrete but coupled fragments cemented by disordered clusters, the discrete motions of atomic layer fragments become prevalent, which are correlated but inconsistent, for the topological environment varies from one fragment to another. Therefore one load drop in the p - h curve of the $\chi = 0.077$ assembly envelops a number of correlated but uncooperative

slips of atomic layer fragments. Furthermore, the spacing between two load peaks is also no longer correlated with the separation of atomic layers in z directions.

Further increase of chemical disorder produces a percolating disordered zone through the network. The proportion of disordered atoms in the $\chi = 0.16$ assembly exceeds 17%. Then the a -SiC can be considered as a mixture of two coexisting phases: hard crystalline fragments and soft amorphous regions. Henceforth the discrete motion of a fragment are decoupled from those of the neighboring fragments, giving rise to the irregular fluctuations in the p - h curve for the $\chi = 0.16$ assembly. Both uncorrelated deformation of atomic layer fragments and enhanced plastic flow in amorphous regions contribute to the significant reduction of hardness in $\chi = 0.16$ assembly. Nevertheless, the localized plastic flow plays a dominant role in the $\chi = 0.22$ assembly, since there are no distinguishable peaks rather than small oscillations detected in the p - h curve for the $\chi = 0.22$ assembly.

6. Discussion

This chemical disorder based model make an initiative to quantify the correlation between mechanical properties and irradiation-amorphized SiC, while gaining valuable insights for understanding the variations of mechanical responses from the perspective of atomistic mechanisms. However we should be aware of the limitations in the conclusion drawn. The main assumption of this model is that chemical disorder underpins the changes of topological order and then determines the c-a transition of SiC. This assumption is justified by the investigation into the topological structures of a range of SiC with varying imposed level of chemical disorder. Whereas the current experimental observation could just support the existence of C-C and Si-Si homonuclear bonds, rather than provide the accurate degree of chemical disorder. Also it is agreed that the total amorphization is attained at critical threshold in deposited nuclear energy loss which is a function of ion energy and temperature (Benyagoub, A., 2008; Bolse, W., 1998). Whether the experimental measured threshold of deposited nuclear energy loss corresponds to the simulated chemical disorder is still an open question.

Incapable of describing the configuration of the defects also limits the ability of chemical order χ to characterize the structure of a -SiC, especially in the case involving moderate χ . For example, two a -SiC assemblies with identical chemical disorder may well feature distinct configurations of defects, say, one having dispersed isolated chemical disordered defects while the defects in another network tend to cluster. It is impossible to distinguish them only via chemical disorder χ . Actually, SiC exhibits different amorphization behavior in response to ion beam irradiation depending on the ion energy and ion mass. The irradiation with ions of medium mass (such as C, Si, etc) having energies of a few hundreds keV primarily produce interstitials, vacancies, antisite and small defect cluster (Gao, F. & Weber, W. J., 2001). The growth and coalescence of these point defects and small clusters correspond to partial or total amorphization. In contrast, heavy impinging ion (such as Au, etc) creates, within its displacement cascade, an amorphous zone surrounded by a defective crystalline region which in turn becomes amorphous after subsequent ion impacts, either directly by defect accumulation or indirectly by the growing of already existing amorphous zones. Therefore the c-a transition process for 3C-SiC undergoes different path depending on ion mass. Complementary to chemical disorder, additional parameter(s) containing the information about the defects configuration are necessary to describe the c-a transition.

Another issue concerning the chemical disorder based model is that it somehow underestimates the effects of Frenkel pair and vacancy clusters on the irradiation induced

amorphization. Although increased chemical disorder could simultaneously produce interstitials, vacancies and interstitial/vacancy clusters, the concentration of these defects is far from the level observed in the irradiation experiments. The current model only involving chemical disorder should be accordingly modified to take into consideration the concentrations of other defects while eliminating the overlapping effects arising from these two major defects.

7. Summary

Chemical disorder χ , a measure of the likelihood of forming homonuclear bonds in SiC controls the c-a transition occurring in the irradiation induced amorphization of SiC. A chemical disorder based model is proposed to describe the variations of different mechanical properties of SiC during the c-a transition as a function of microstructures. Elasticity and stiffness related mechanical properties of disordered SiC depend on the chemical disorder in distinct manners, which can be attributed to the different evolution stages of topological order with increasing chemical disorder. MD simulations reveal the atomistic mechanisms of varying α -SiC in response to tension and nanoindentation. A crossover of atomistic mechanism with damage accumulation is found in both cases, which is responsible for the evolution of mechanical responses when SiC varies from crystalline to fully amorphous. This crossover also manifests itself in the switch of fracture mode varying from brittle fracture to nano-ductile failure due to the coalescence of nanocavities.

8. Acknowledgment

The authors are grateful for funding from National Basic Research Program of China No. 2010CB631005 and State Key Laboratory of Explosion Science and Technology No. QNKT10-10 and No. ZDKT09-02.

9. References

- Benyagoub, A. (2008). Irradiation Effects Induced in Silicon Carbide by Low and High Energy Ions. *Nuclear Instruments and Methods in Physics Research B*, Vol. 266, No., pp. 2766-71, 0168-583X
- Bolse, W. (1998). Formation and Development of Disordered Networks in Si-Based Ceramics under Ion Bombardment. *Nuclear Instruments and Methods in Physics Research Section B: Beam Interactions with Materials and Atoms*, Vol. 141, No. 1-4, pp. 133-39, 0168-583X
- Bolse, W. (1999). Amorphization and Recrystallization of Covalent Tetrahedral Networks. *Nuclear Instruments and Methods in Physics Research Section B: Beam Interactions with Materials and Atoms*, Vol. 148, No. 1-4, pp. 83-92, 0168-583X
- Celarie, F.; Prades, S.; Bonamy, D.; Ferrero, L.; Bouchaud, E.; Guillot, C. & Marliere, C. (2003). Glass Breaks Like Metal, but at the Nanometer Scale. *Physical Review Letters*, Vol. 90, No. 7, pp. 075504,
- Chen, H.-P.; Kalia, R. K.; Nakano, A. & Vashishta, P. (2007). Multimillion-Atom Nanoindentation Simulation of Crystalline Silicon Carbide: Orientation Dependence and Anisotropic Pileup. *Journal of Applied Physics*, Vol. 102, No. 6, pp. 063514,

- Chen, Y.-C.; Lu, Z.; Nomura, K.-i.; Wang, W.; Kalia, R. K.; Nakano, A. & Vashishta, P. (2007). Interaction of Voids and Nanoductility in Silica Glass. *Physical Review Letters*, Vol. 99, No. 15, pp. 155506,
- Devanathan, R.; Gao, F. & Weber, W. J. (2007). Atomistic Modeling of Amorphous Silicon Carbide Using a Bond-Order Potential. *Nuclear Instruments and Methods in Physics Research Section B: Beam Interactions with Materials and Atoms*, Vol. 255, No. 1, pp. 130-35, 0168-583X
- Gao, F. & Weber, W. J. (2001). Computer Simulation of Disordering and Amorphization by Si and Au Recoils in 3c--SiC. *Journal of Applied Physics*, Vol. 89, No. 8, pp. 4275-81,
- Gao, F. & Weber, W. J. (2004). Mechanical Properties and Elastic Constants Due to Damage Accumulation and Amorphization in SiC. *Physical Review B*, Vol. 69, No. 22, pp. 224108,
- Heera, V.; Prokert, F.; Schell, N.; Seifarth, H.; Fukarek, W.; Voelskow, M. & Skorupa, W. (1997). Density and Structural Changes in SiC after Amorphization and Annealing. *Applied Physics Letters*, Vol. 70, No. 26, pp. 3531-33,
- Hobbs, L. W.; Jesurum, C. E. & Berger, B. (1999). *Rigidity Theory and Applications* Kluwer/Plenum, New York
- Ishimaru, M.; Bae, I.-T.; Hirotsu, Y.; Matsumura, S. & Sickafus, K. E. (2002). Structural Relaxation of Amorphous Silicon Carbide. *Physical Review Letters*, Vol. 89, No. 5, pp. 055502,
- Ishimaru, M.; Bae, I.-T.; Hirata, A.; Hirotsu, Y.; Valdez, J. A. & Sickafus, K. E. (2006). Chemical Short-Range Order in Ion-Beam-Induced Amorphous SiC: Irradiation Temperature Dependence. *Nuclear Instruments and Methods in Physics Research Section B: Beam Interactions with Materials and Atoms*, Vol. 242, No. 1-2, pp. 473-75, 0168-583X
- Ivashchenko, V. I.; Turchi, P. E. A. & Shevchenko, V. I. (2007). Simulations of the Mechanical Properties of Crystalline, Nanocrystalline, and Amorphous SiC and Si. *Physical Review B* Vol. 75, No. 8, pp. 085209,
- Jiang, W.; Weber, W. J.; Lian, J. & Kalkhoran, N. M. (2009). Disorder Accumulation and Recovery in Gold-Ion Irradiated 3c-SiC. *Journal of Applied Physics*, Vol. 105, No. 1, pp. 013529,
- Katoh, Y.; Hashimoto, N.; Kondo, S.; Snead, L. L. & Kohyama, A. (2006). Microstructural Development in Cubic Silicon Carbide During Irradiation at Elevated Temperatures. *Journal of Nuclear Materials* Vol. 351, No., pp. 228-40, 0022-3115
- Katoh, Y.; Snead, L. L.; Henager Jr, C. H.; Hasegawa, A.; Kohyama, A.; Riccardi, B. & Hegeman, H. (2007). Current Status and Critical Issues for Development of SiC Composites for Fusion Applications. *Journal of Nuclear Materials*, Vol. 367-370, No. Part 1, pp. 659-71, 0022-3115
- Khakani, M. A. E. & al, e. (1994). Hardness and Young's Modulus of Amorphous a-SiC Thin Films Determined by Nanoindentation and Bulge Tests. *Journal of Materials Research*, Vol. 9, No. 1, pp. 96-103,
- Liu, X. M. "Research on Plastic Behavior of Nano-Material Based on Dislocation Mechanism." Ph.D thesis, University of Tsinghua, 2008.
- Malerba, L. & Perlado, J. M. (2001). Molecular Dynamics Simulation of Irradiation-Induced Amorphization of Cubic Silicon Carbide. *Journal of Nuclear Materials*, Vol. 289, No. 1-2, pp. 57-70, 0022-3115

- Mo, Y.&Szlufarska, I. (2007). Simultaneous Enhancement of Toughness, Ductility, and Strength of Nanocrystalline Ceramics at High Strain-Rates. *Applied Physics Letters*, Vol. 90, No. 18, pp. 181926,
- Mulliah, D.;Kenny, S. D.;McGee, E.;Smith, R.;Richter, A.&Wolf, B. (2006). Atomistic Modelling of Ploughing Friction in Silver, Iron and Silicon. *Nanotechnology*, Vol., No. 8, pp. 1807, 0957-4484
- Noreyan, A.;Amar, J. G.&Marinescu, I. (2005). Molecular Dynamics Simulations of Nanoindentation of -Sic with Diamond Indenter. *Materials Science and Engineering B*, Vol. 117, No. 3, pp. 235-40, 0921-5107
- Rino, J. P.;Ebbsj, I.;Branicio, P. S.;Kalia, R. K.;Nakano, A.;Shimojo, F.&Vashishta, P. (2004). Short- and Intermediate-Range Structural Correlations in Amorphous Silicon Carbide:A Molecular Dynamics Study. *Physical Review B*, Vol. 70, No. 4, pp. 045207,
- Rodriuez de la Fuente, O.;Zimmerman, J. A.;Gonzalez, M. A.;de la Figuera, J.;Hamilton, J. C.;Pai, W. W.&Rojo, J. M. (2002). Dislocation Emission around Nanoindentations on a (001) Fcc Metal Surface Studied by Scanning Tunneling Microscopy and Atomistic Simulations. *Physical Review Letters*, Vol. 88, No. 3, pp. 036101,
- Rong, Z.;Gao, F.;Weber, W. J.&Hobler, G. (2007). Monte Carlo Simulations of Defect Recovery within a 10 Kev Collision Cascade in 3c--Sic. *Journal of Applied Physics*, Vol. 102, No. 10, pp. 103508,
- Shi, Y.&Falk, M. L. (2005). Strain Localization and Percolation of Stable Structure in Amorphous Solids. *Physical Review Letters*, Vol. 95, No. 9, pp. 095502,
- Snead, L. L.;Steiner, D.&Zinkle, S. J. (1992). Measurement of the Effect of Radiation Damage to Ceramic Composite Interfacial Strength. *Journal of Nuclear Materials*, Vol. 191-194, No. Part 1, pp. 566-70, 0022-3115
- Snead, L. L.;Zinkle, S. J.;Hay, J. C.&Osborne, M. C. (1998). Amorphization of Sic under Ion and Neutron Irradiation. *Nuclear Instruments and Methods in Physics Research Section B: Beam Interactions with Materials and Atoms*, Vol. 141, No. 1-4, pp. 123-32, 0168-583X
- Snead, L. L.&Zinkle, S. J. (2002). Structural Relaxation in Amorphous Silicon Carbide. *Nuclear Instruments and Methods in Physics Research Section B: Beam Interactions with Materials and Atoms*, Vol. 191, No. 1-4, pp. 497-503, 0168-583X
- Snead, L. L. (2004). Limits on Irradiation-Induced Thermal Conductivity and Electrical Resistivity in Silicon Carbide Materials. *Journal of Nuclear Materials*, Vol. 329-333, No., pp. 524-29, 0022-3115
- Snead, L. L.;Nozawa, T.;Katoh, Y.;Byun, T.-S.;Kondo, S.&Petti, D. A. (2007). Handbook of Sic Properties for Fuel Performance Modeling. *Journal of Nuclear Materials*, Vol. 371, No., pp. 329-77, 0022-3115
- Szlufarska, I.;Kalia, R. K.;Nakano, A.&Vashishta, P. (2004). Nanoindentation-Induced Amorphization in Silicon Carbide. *Applied Physics Letters*, Vol. 85, No. 3, pp. 378-80,
- Szlufarska, I.;Kalia, R. K.;Nakano, A.&Vashishta, P. (2005). Atomistic Mechanisms of Amorphization During Nanoindentation of Sic: A Molecular Dynamics Study. *Physical Review B*, Vol. 71, No. 17, pp. 174113,
- Szlufarska, I.;Nakano, A.&Vashishta, P. (2005). A Crossover in the Mechanical Response of Nanocrystalline Ceramics. *Science*, Vol. 309, No. 5736, pp. 911-14,

- Szlufarska, I.;Kalia, R. K.;Nakano, A.&Vashishta, P. (2007). A Molecular Dynamics Study of Nanoindentation of Amorphous Silicon Carbide. *Journal of Applied Physics*, Vol. 102, No. 2, pp. 023509,
- Tang, M.&Yip, S. (1995). Atomistic Simulation of Thermomechanical Properties of Beta -Sic. *Physical Review B*, Vol. 52, No. 21, pp. 15150,
- Tersoff, J. (1994). Chemical Order in Amorphous Silicon Carbide. *Physical Review B*, Vol. 49, No. 23, pp. 16349,
- Weber, W. J.;Yu, N.;Wang, L. M.&Hess, N. J. (1997). Temperature and Dose Dependence of Ion-Beam-Induced Amorphization in [Alpha]-Sic. *Journal Of Nuclear Materials*, Vol. 244, No. 3, pp. 258-65, 0022-3115
- Weber, W. J.;Wang, L. M.;Yu, N.&Hess, N. J. (1998). Structure and Properties of Ion-Beam-Modified (6h) Silicon Carbide. *Materials Science and Engineering A*, Vol. 253, No. 1-2, pp. 62-70, 0921-5093
- Xi, X. K.;Zhao, D. Q.;Pan, M. X.;Wang, W. H.;Wu, Y.&Lewandowski, J. J. (2005). Fracture of Brittle Metallic Glasses: Brittleness or Plasticity. *Physical Review Letters*, Vol. 94, No. 12, pp. 125510,
- Xue, K.;Niu, L.-S.&Shi, H.-J. (2008). Effects of Quench Rates on the Short- and Medium-Range Orders of Amorphous Silicon Carbide: A Molecular-Dynamics Study. *Journal of Applied Physics*, Vol. 104, No. 5, pp. 053518,
- Xue, K.&Niu, L.-S. (2009). Understanding the Changes in Mechanical Properties Due to the Crystalline-to-Amorphization Transition in Sic. *Journal of Applied Physics*, Vol. 106, No. 6, pp. 083505,
- Xue, K.&Niu, L.-S. (2010). A Crossover in the Mechanical Response of Silicon Carbide Due to the Accumulation of Chemical Disorder. *Journal of Applied Physics*, Vol. 107, No. 8, pp. 083517,
- Yuan, X.&Hobbs, L. W. (2002). Modeling Chemical and Topological Disorder in Irradiation-Amorphized Silicon Carbide. *Nuclear Instruments and Methods in Physics Research Section B: Beam Interactions with Materials and Atoms*, Vol. 191, No. 1-4, pp. 74-82, 0168-583X

SiC Cage Like Based Materials

Patrice Mélinon
*University of Lyon and CNRS
 France*

1. Introduction

SiC is a compound of silicon and carbon with a chemical formula SiC. Silicon carbide(SiC) as a material is the most promising for applications in which high-temperature, high-power, and high-frequency devices, catalyst support, high irradiation environments are needed. Naturally occurring SiC is found only in poor quantities that explains the considerable effort made in the industrial SiC engineering. At a first glance, silicon and carbide are close but a careful inspection reveals different properties leading to brothers at odds behavior. In well ordered stoichiometric compounds SiC adopts a tetrahedral bonding like observed in common semiconductors (zincblende and wurtzite are the most populars). The difference of electronegativities induces a ionicity which is not enough to promote NaCl or CsCl structures but enough to induce multipolar effects. These multipolar effects are responsible to the huge number of polytypes. This polytypism has numerous applications including quantum confinement effects and graphene engineering. In this chapter, special emphasis has been placed on the non stoichiometric compounds. Silicon architectures are based from sp^3 or more dense packing while carbon architectures cover a large spread of hybridization from sp to sp^3 , the sp^2 graphite-like being the stable structure in standard conditions. When we gather silicon and carbon together one of the basic issue is: what is the winner? When silicon and carbon have the same concentration (called stoichiometric compound), the answer is trivial: "the sp^3 " lattice since both the elements share this hybridization in bulk phase. In rich silicon phases, the sp^3 hybridization is also a natural way. However, a mystery remains when rich carbon compounds are synthesized. Silicon sp^2 lattice is definitively unstable while carbon adopts this structure. One of the solution is the cage-like structure (the fullerenes belongs to this family) where the hybridization is intermediate between sp^2 and sp^3 . Other exotic structures like buckydiamonds are also possible. Special architectures can be built from the elemental SiC cage-like bricks, most of them are not yet synthesized, few are experimentally reported in low quantity. However, these structures are promising as long the electronic structure is quite different from standard phase and offer new areas of research in fuel cells (catalysis and gas storage), superconductivity, thermoelectric, optical and electronic devices...Moreover, the cage like structure permits endohedrally doping opening the way of heavily doped semiconductors strain free. Assembling elemental bricks lead to zeolite-like structures. We review the properties of some of these structures and their potential applications.

1.1 Carbon

Carbon has six electrons. Two of them will be found in the $1s$ orbital close to the nucleus forming a compact core, the next two going into the $2s$ orbital. The remaining ones will be in two separate $2p$ orbitals. The electronic structure of carbon is normally written $1s^2 2s^2 2p^2$. Contrary to silicon, germanium and tin, the unlikely promotion of an outer shell electron in a d state avoids the formation of compact structures. This clearly indicates that most of the chemical bonding involves valence electrons with sp character. In order to form two, three or four hybrid orbitals, the corresponding number of atomic orbitals has to be mixed within the framework of "hybridization concept". When the s orbital and all three p orbitals are mixed, the hybridization is sp^3 . The geometry that achieves this is the tetrahedral geometry T_d , where any bond angle is 109.47° (see fig. 1).

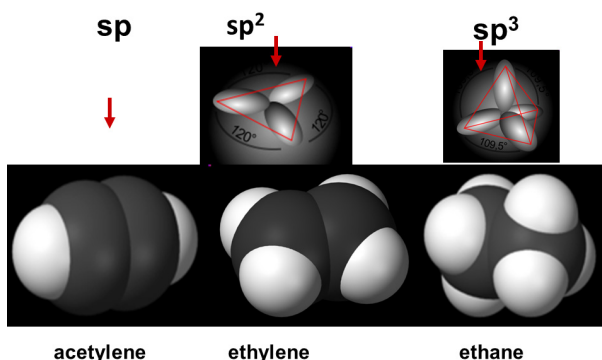


Fig. 1. elementary molecules corresponding to the three possible types of bonding. Acetylene C_2H_2 (sp bonding), ethylene C_2H_4 (sp^2 bonding) and ethane C_2H_6 (sp^3 bonding).

1.1.1 sp hybridization

When the s orbital and one p orbital are mixed, the hybridization is sp . The geometry is now linear, with the bond angle between the hybrid orbitals equal to 180° . The additional p electrons which do not participate to the σ bonding (strong bond resulting from the overlap of hybrid orbitals) form the π bond, each orbital being perpendicular to the basal plane containing the σ bond. The sp carbon chains can present alternating single and triple bonds (polyynes)[α -carbyne] or only double bonds (polycumulene)[β -carbyne]; polyynes being more stable owing to the Peierls distortion (Kavan et al., 1995) which lifts the symmetry: double-double bond to simple-triple bond. The existence of carbyne is a subject of controversy and strictly speaking cannot be classified as a carbon allotrope. The existence of long linear chains becomes unlikely as soon as the length grows up. Crystalline carbyne must be unstable against virulent graphitization (sp to sp^2 transition) under normal conditions (Baughman, 2006). Up to date, the largest synthesized carbyne chain was $HC_{16}H$ (Lucotti et al., 2006) where terminated hydrogen ensures the stabilization of the carbyne. Even though, carbyne is the best prototype of the 1D network, the purity of the samples and the low chemical stability are the major hindrance for applications.

1.1.2 sp^2 hybridization

When the s orbital and two of the p orbitals for each carbon are mixed, the hybridization for each carbon is sp^2 . The resulting geometry is the trigonal (hexagonal) planar geometry, with the bond angle between the hybrid orbitals equal to 120° , the additional p electron is at the origin of the π band.

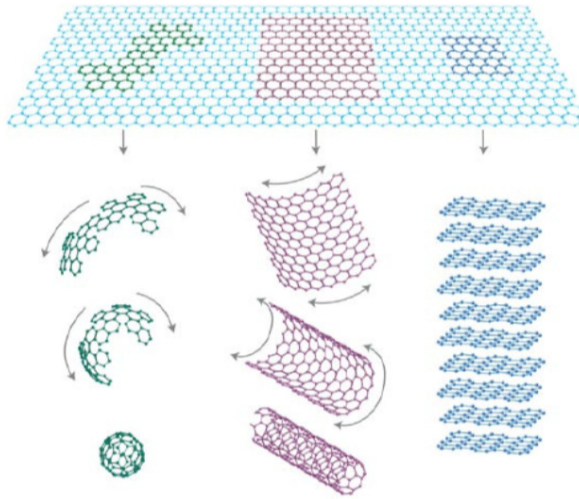


Fig. 2. how to build up graphite, nanotube or fullerene from a graphene sheet (after the original figure from Geim *et al* (Geim and Novoselov, 2007))

Graphene is of importance both for its unusual transport properties and as the mother for fullerene and nanotube families (figure 2). Graphene can be defined as an infinite periodic arrangement of (only six-member carbon ring) polycyclic aromatic carbon. It can be looked at as a fullerene with an infinite number of atoms. Owing the theoretical unstability of 2D networks, graphene sheets are stable over several microns enough for applications. Graphene has a two atom basis (A and B) per primitive cell arranged in a perfect hexagonal honeycomb. Except the center of the Brillouin zone Γ , the structure can be entirely described by symmetry with the particular setpoints \mathbf{M} , \mathbf{K} and \mathbf{K}' related by the relationship $\mathbf{K} = -\mathbf{K}'$. For each atom, three electrons form tight bonds with neighbor atoms in the plane, the fourth electron in the p_z orbital does not interact with them leading to zero p_z orbital energy $E_z = 0$. It can be easily seen that the electron energy is zero at \mathbf{K} and \mathbf{K}' , graphene being a semiconductor with a zero bandgap. The most striking result is the linear relationship for the dispersion curve near \mathbf{K} and \mathbf{K}' . Since the effective mass is related to the second derivation of the energy, this implies a zero mass for the two electrons (one by site A and B). As a consequence, the classical picture of the Schrödinger equation must be replaced by the Dirac equation where Dirac spinors (two component wave function) are required in the mathematical description of the quantum state of the relativistic electron. This linear dispersion involving a multi degenerated states at the intersecting cones is broken by several ways: impurities, defects, interaction with two or

many graphene sheets (Partoens and Peeters, 2006)(Charlier et al., 1991), confinement effect (Nakada et al., 1996)(Son et al., 2006). After the degeneracy splitting, the dispersion tends to be parabolic with a "classical" effective mass. 3D graphite is formed by the stacking of graphene layers (Chung, 2002). The space group is $P6_3mmc - D_{6h}^{14}$ (number 194) with four atoms in the unit cell, two in position 2b at $\pm(00\frac{1}{4})$, and two in position 2d at $(\frac{2}{3}\frac{1}{3}\frac{1}{4})$. The two planes are connected by a translation $\mathbf{t} = (\mathbf{a}_1 + \mathbf{a}_2)/3 + \mathbf{a}_3/2$ or by a C_6 rotation about the sixfold symmetry axis followed by a translation $\mathbf{a}_3/2$ (\mathbf{a}_i are the graphite lattice vectors)(fig. 3). This geometry permits the overlap of the π electrons leading to the π bonding. The electrons participating in this π -bonding seem able to move across these π -bonds from one atom to the next. This feature explains graphite's ability to conduct electricity along the sheets of carbon atom parallel to the (0001) direction just as graphene does.

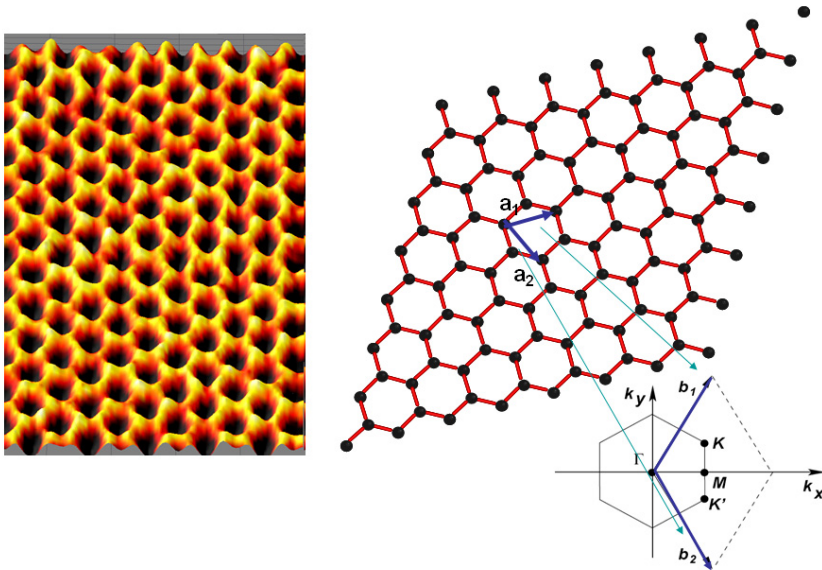


Fig. 3. left panel: Image of a single suspended sheet of graphene taken with a transmission electron microscope, showing individual carbon atoms (yellow) on the honeycomb lattice (after Zettl Research Group Condensed Matter Physics Department of Physics University of California at Berkeley). Right panel: ball and stick representation with unit vectors \mathbf{a}_1 and \mathbf{a}_2 . The first 2D Brillouin zone is shown with the irreducible points (for further details about the figure see (Melinon and Masenelli, 2011)).

1.1.3 sp^3 hybridization

The most popular form is the cubic diamond (called diamond C-2), the second allotrope of carbon where each atom joined to four other carbons in regular tetrahedrons. The crystal structure is a face-centered cubic lattice with two atoms in the primitive cell. All the

C_2 units are in the staggered mode. The space group is $Fd\bar{3}m - O_h^7$ (number 227) with eight atoms in the conventional unit cell (two in the primitive cell). The two atoms are in position a (0,0,0) and (1/4,1/4,1/4) respectively with the coordinates of equivalent positions (0,0,0;0,1/2,1/2;1/2,0,1/2;1/2,1/2,0). The lattice constant is $a=3.5669\text{\AA}$ and the interatomic distance 1.5445\AA (see figure 14). Contrary to graphite, the lack of the delocalized π band ensures an insulator character. Diamond is indeed a wide indirect band gap material with the $\Gamma'_{25} - \Gamma_{15}$ transition of 7.3 eV and the indirect band gap of 5.45 eV. A (metastable) hexagonal polymorph of diamond (lonsdaleite) is also reported. The crystallographic description of this structure is $P6_3/mmc - D_{6h}^4$ (number 194) with four atoms per unit cell in position $4f \pm(1/3,2/3,1/16; 2/3,1/3,9/16)$. The lattice parameters are $a=2.522\text{\AA}$ and $c=4.119\text{\AA}$, respectively. The main difference between the hexagonal structure and that of diamond is that in one quarter of the C_2 units the bonds are eclipsed. Other stacking sequence allows polytypism.

1.2 Silicon

Silicon has 14 electrons. Ten of them will be found in the $1s$, $2s$ and $2p$ orbitals close to the nucleus, the next two going into the $3s$ orbital. The remaining ones will be in two separate $3p$ orbitals. The electronic structure of silicon is written in the form $1s^2 2s^2 2p^6 3s^2 3p^2$. Because of this configuration, Si atoms most frequently establish sp^3 bonds (hybridization of a s orbital and three p orbitals) leading to tetrahedrally coordinated phases.

1.2.1 sp^3

The most stable phase in silicon is the cubic diamond. The structure is identical to the one discussed for carbon. The lattice constant is $a=5.43\text{\AA}$. Each silicon is linked to the four neighboring atoms by 2.3515\AA bond. Silicon diamond is an indirect band gap material. The $\Gamma'_{25} - \Gamma_{15}$ transition is at 3.5 eV and the indirect band gap at 1.17 eV. As in carbon polytypism in hexagonal phase is also reported (combining eclipsed and staggered modes). Recently, a new metastable form has been isolated: the clathrate II (fig. 4). In the clathrates, the tetrahedra are mainly stacked in eclipsed mode while diamond is formed by stacking them in the staggered mode. Clathrate II is built by the coalescence of two Si_{28} and four Si_{20} per unit cell. It belongs to the same space group than the cubic diamond structure $Fd\bar{3}m$. Using the crystallographic notation, clathrate II is labeled Si-34 since we have $1/4(2 \times 28 + 4 \times 20) = 34$ atoms in the primitive cell. Such a structure is obtained by template one Si atom in the Si_5 basic sp^3 tetrahedron with Si_{28} cage, this latter having T_d point group symmetry. Si_{28} has four hexagons and share these hexagons with its four Si_{28} neighboring cages. The space filling needs additional silicon atoms in a tetrahedral symmetry forming Si_{20} cages. 85,7% of the membered rings are pentagons, implying that the electronic properties are sensitive to the frustration effect (contrary to bonding states, antibonding states contain one bonding node in odd membered rings). The difference in energy within DFT between Si-34 and Si-2 is of 0.06 eV per bond compared to 0.17 eV in the first metastable beta-tin structure. Clathrate II (Si-34) is obtained by heating the $NaSi_2$ silicide under vacuum or using a high pressure belt. Note that carbon clathrate is not yet synthesized as long as the precursor does not exist while the competition between clathrate and graphite (the most stable) phase operates. Several authors mentioned the Si clathrate potentiality for applications in optoelectronic devices. First of all, the wide band gap opening (around 1.9 eV) (Gryko et al., 2000; Melinon et al., 1998 ; Connetable et al., 2003; Connetable, 2003a ; Adams et al., 1994) ensures electronic transition

in the visible region and offers new potentialities in "all silicon" optoelectronic devices. Endohedrally doping is also possible. The Fermi level can be tailored by varying both the concentration and the type of atom inside the cage up to large concentration (>10%) without stress, vacancy-containing centers or misfits. For example, Fermi level easily lies at 0.5 eV above the conduction band minimum in n-doped clathrate (see fig. 13). Doped semiconducting clathrates (Tse et al., 2000) as candidates for thermoelectric power since endohedral atoms can effectively rattle around the cages.

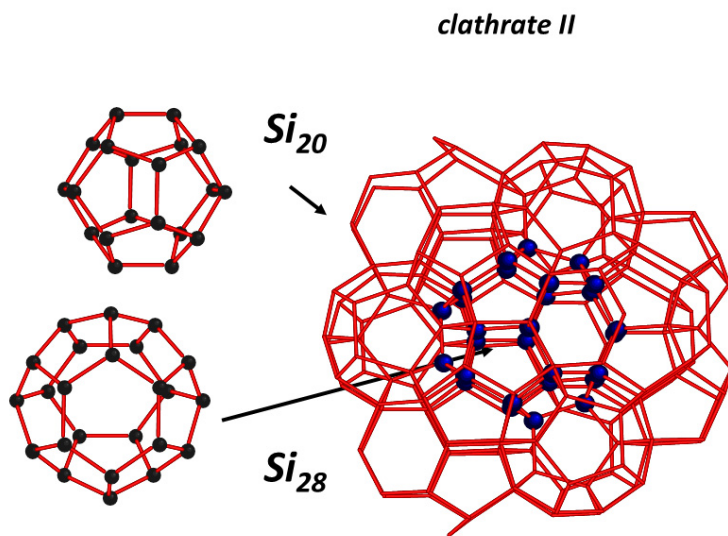


Fig. 4. a piece of clathrate II reported in silicon with a combination of Si_{28} and Si_{20} .

1.2.2...and beyond

Contrary to carbon, the first transition observed in the excited state allows *spd* hybridizations. This is out of scope of this paper. *spd* hybridizations are reported in very small silicon clusters or in bulk phase at high pressure/temperature.

1.2.3 The case of sp^2

The elements with a principal quantum number equal to or greater than three are not capable of forming multiple bonds because of the considerable Pauli repulsion between the electrons of the inner shells. This golden rule summarizes the absence of π bonding in silicon. "Silicon graphite" is less stable than its diamond phase by 0.71 eV per atom (Yin and Cohen, 1984).

1.3 Silicon carbide

SiC is a compound of silicon and carbon with the net formula SiC. The first thing to note is that, from a bond point of view, chemical ordering is energetically favored: a Si-C bond (6.34 eV/atom (Kackell, 1994a;b)) is more stable by -0.35 eV/atom than the average of a Si-Si (4.63 eV/atom (Alfe et al., 2004)) and a C-C bond (7.35 eV/atom (Yin and Cohen, 1984)). The

applications are numerous (Choyke, 2004; Feng, 2004)) including the hardness (almost as hard as diamond), the extreme resistance to chemicals and radiation, a refractory compound, a tuning (wide) bandgap with high electron mobility, high breakdown electric field and good thermal conductivity. This is also a safe bio compatible compound.

Then, starting from a crystal with a perfect chemical order, introducing some disorder will cost two energetic contributions: a chemical enthalpy ΔH_{chem} , which is about 0.35 eV/atom in the ordered phase (Martins and Zunger, 1986) as mentioned above, and a strain enthalpy ΔH_{size} . Indeed, the large atomic size difference introduces a microscopic strain by incorporating C-C or Si-Si bonds while an ordered crystal is intrinsically strain free (we neglect the small variations in the atomic positions in polytypes). ΔH_{size} is of the same order of magnitude than the chemical contribution ($\Delta H_{size} \simeq 0.4$ eV/atom (Terstoff, 1994)). With a simple Arrhenius' law giving the measure of disorder, we can check that the occurrence of Si-Si and/or C-C bonds is negligible over a large range of temperature. This differs from other compounds, such as SiGe where the chemical contribution is almost zero (a few meV negative (Martins and Zunger, 1986), meaning that Si-Ge bonds are slightly less favorable than Si-Si and Ge-Ge bonds and since Si and Ge have a comparable atomic size ($d_{Si-Si} = 2.35$ Å, $d_{Ge-Ge} = 2.445$ Å), the gain in strain energy is low enough to allow a significant chemical disorder.

1.4 The bottleneck: ionicity in SiC crystal

There is a charge transfer from Si to C in relation with the electronegativity difference between Si and C atoms (Zhao and Bagayoko, 2000). This charge transfer 0.66 |e| (Segall et al., 1996) is affected by the d orbitals in silicon. The ionicity can be defined according to empirical laws stated by Pauling and Phillips or more accurate model within the calculated valence-charge asymmetry (Garcia and Cohen, 1993). Pauling made use of thermochemical arguments based from the electronegativities to determine the ionicity $f_i = 0.11$. Another standard picture based from the dielectric model first introduced by Phillips gives $f_i = 0.177$. However, Phillips' or Pauling's models do not take into account the crystal structure. This can be done in the simple static model where the ionicity parameter is defined in terms of the symmetric and antisymmetric parts of the atomic valence-charge density (Garcia and Cohen, 1993). According to the considered polytype, the static ionicity values f_i are 0.4724 (2H), 0.4718 (3C), 0.4720 (4H), and 0.4719 (6H). They do not change much from one polytype to another but they strongly differ from Pauling's ionicity (Wellenhofer et al., 1996). One possible consequence of the ionicity, depending on the structure, is the appearance of a spontaneous polarization.

1.5 Clathrate

No information about a SiC clathrate is available. Moriguchi *et al* (Moriguchi et al., 2000) and Wang *et al* (Wang et al., 2008) investigated the theoretical Si_xGe_{1-x} type II clathrate (see chapter 4). To minimize the homonuclear bonding Si-Si or Ge-Ge in pentagonal rings, non stoichiometric compounds ($x=1/17, 4/17, 5/17, 12/17, 13/17, 16/17$) have been investigated. Some of these clathrate alloys with an ideal $Fd\bar{3}m$ symmetry are found to have direct band gap at the $\pi/a(111)$ L point in the Brillouin zone which could be important for optoelectronic devices. However, the clathrate lattice needs a set of Si-Si, Si-Ge and Ge-Ge bonds which are close in distance values. This will be not the case in the SiC clathrate and questions the existence of such lattices in SiC.

1.6 Polytypism

name	space group	a	c	x	y	z	Wyckoff
3C-SiC	$F43m$ 216	4.368	-	(Si)0	0	0	4a
				(C)3/4	3/4	3/4	4d
3C-SiC	$P6_3mc$ 186	3.079	7.542	(Si)0	0	0	2a
				(C)0	0	1/4	2a
				(Si)1/3	2/3	1/3	2b
				(C)1/3	2/3	7/12	2b
				(Si)2/3	1/3	2/3	2b
				(C)2/3	1/3	11/12	2b
2H-SiC	$P6_3mc$ 186	3.079	5.053	(Si) 1/3	2/3	0	2b
				(C) 1/3	2/3	3/8	2b
4H-SiC	$P6_3mc$ 186	3.079	10.07	(Si) 0	0	0	2a
				(C) 0	0	3/16	2a
				(Si) 1/3	2/3	1/4	2b
				(C) 1/3	2/3	7/16	2b
6H-SiC	$P6_3mc$ 186	3.079	15.12	(Si) 0	0	0	2a
				(C) 0	0	1/8	2a
				(Si) 1/3	2/3	1/6	2b
				(C) 1/3	2/3	7/24	2b
				(Si) 2/3	1/3	1/3	2b
				(C) 2/3	1/3	11/24	2b

Table 1. The space group, unit cell lattice parameters (a and c), carbon and silicon fractional coordinates (x, y, z), multiplicities and Wyckoff positions of the sites for selected polytypes. A refinement of the positions is given by Bauer *et al* (Bauer *et al.*, 1998)

Polytypism occurs when a structural change occurs within the same hybridization. In the case of SiC, we have some degrees of freedom in the way individual layers are stacked within a crystal structure, the driving force being the conservation of the chemical ordering. Silicon carbide exhibits a pronounced polytypism, the most simple polytypes are zinc-blende SiC (3C-SiC) and wurtzite (2H-SiC), the two structures correspond to the cubic and hexagonal diamonds when all the atoms are Si or C (see figure 5). The crystallographic data for selected polytypes are displayed in table 1

A single Si-C bilayer can be viewed as a planar sheet of silicon atoms coupled with a planar sheet of carbon atoms. The plane formed by a Si-C bilayer is known as the basal plane, while the crystallographic c-axis direction, also known as the stacking direction or the [0001] direction in the hexagonal lattice, is defined normal to the Si-C bilayer plane. All the SiC polytypes are classified following the arrangements of cubic or hexagonal SiC bilayers, stacking along the cubic [111] or the equivalent hexagonal [0001] direction.

The differences of cohesive energy in polytypes range in a few 0.01 eV (see table 2), state of the art *ab initio* calculations are not straightforward and out of range. Simple empirical potential (Ito and Kangawa, 2002; Ito *et al.*, 2006), which incorporates electrostatic energies due to bond charges and ionic charges or Ising's model (Heine *et al.*, 1992a) are reliable as depicted in table 2. According to Heine *et al* Heine *et al.* (1992a) one defines

$$\Delta E_{ANNI,2H-SiC} = 2J_1 + 2J_3 \quad (1)$$

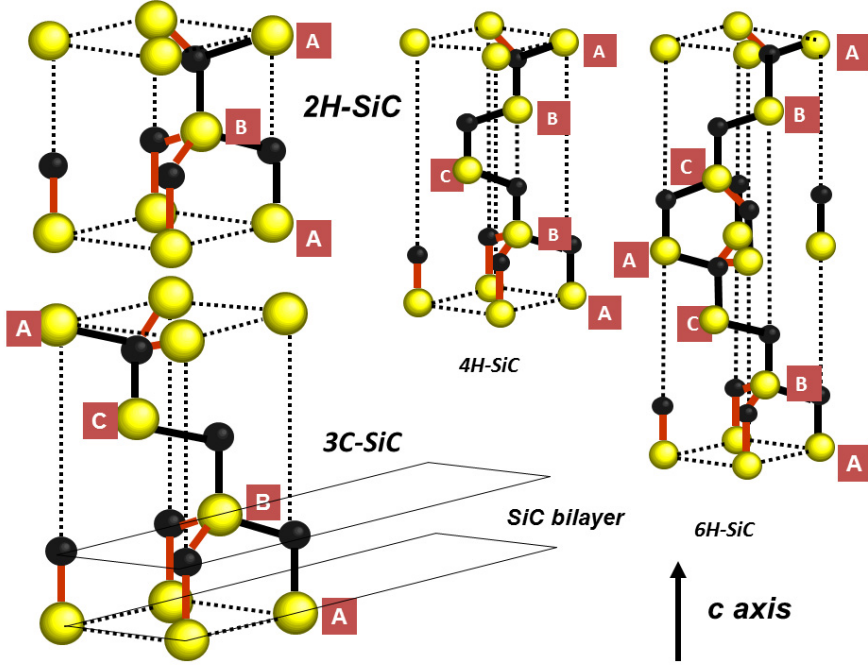


Fig. 5. ball and stick representation in three dimensional perspective of the first polytypes 2H-SiC, 4H-SiC and 6H-SiC compared to 3C-SiC. The chains structures which defined the stacking sequence are in dark color while selected Si-C bonds are in red color. The SiC bilayer is also shown. (Kackell, 1994a) after the original figure in reference (Melinon and Masenelli, 2011)

$$\Delta E_{ANNNI,4H-SiC} = J_1 + 2J_2 + J_3 \quad (2)$$

$$\Delta E_{ANNNI,6H-SiC} = \frac{2}{3}J_1 + \frac{4}{3}J_2 + 2J_3 \quad (3)$$

1.7 Application of the polytypism: quantum wells

Multi quantum wells first introduced by Esaki (Esaki and Chang, 1974) are potential wells that confine particles periodically, particles which were originally free to move in three dimensions. Esaki (Esaki and Chang, 1974) has defined a multi quantum well structure (MQWS) as a periodic variation of the crystal potential on a scale longer than the lattice constant, the most popular heterostructure being GaAs/AlAs superlattice (Sibille et al., 1990). MQWS devices are of prime importance in the development of optoelectronic devices. Unfortunately, these MQWS use elements which are not compatible with the basic "silicon" technology. This limits the integration of optoelectronic devices in complex chips. MQWS SiC based materials are under consideration keeping at mind that the stacking (a combination of eclipsed and staggered modes) of tetrahedra cell CSi_4 or SiC_4 strongly modify the bandgap value. This can be achieved controlling the stacking mode (polytypism assimilated to stacking

model	3C-SiC	2H-SiC	4H-SiC	6H-SiC	J_1	J_2	J_3
empirical ^a	0	2.95×10^{-3}	1.47×10^{-3}	0.92×10^{-3}	1.52	0.0	-0.05
DFT-GGA ^a	0	2.95×10^{-3}	-0.09×10^{-3}	-0.16×10^{-3}	1.55	-0.78	-0.08
DFT-LDA ^b	0	4.35×10^{-3}	-0.39×10^{-3}	-0.60×10^{-3}	4.85	-2.56	-0.50
DFT-LDA ^c	0	1.80×10^{-3}	-2.5×10^{-3}	-1.80×10^{-3}	2.00	-3.40	-0.20
DFT-LDA ^d	0	0.9×10^{-3}	-2.0×10^{-3}	-1.45×10^{-3}	1.08	-2.45	-0.18
FP-LMTO ^e	0	2.7×10^{-3}	-1.2×10^{-3}	-1.05×10^{-3}	3.06	-2.57	-0.35
DFT-LDA ^f	0	2.14×10^{-3}	-1.24×10^{-3}	-1.09×10^{-3}	2.53	-2.31	-0.40
DFT-LDA ^g	0	2.32×10^{-3}	-1.27×10^{-3}	-1.10×10^{-3}	2.71	-2.43	-0.39
DFT-GGA ^g	0	3.40×10^{-3}	-0.35×10^{-3}	-0.45×10^{-3}	3.72	-20.5	-0.33

Table 2. calculated energy difference (in eV) for selected polytypes within different models.

^a from reference (Ito et al., 2006)

^b from reference (Cheng et al., 1988)

^c from reference (Park et al., 1994)

^d from reference (Kackell, 1994a)

^e from reference (Limpijumnong and Lambrecht, 1998)

^f from reference (Lindelfelt et al., 2003)

^g from reference (Liu and Ni, 2005)

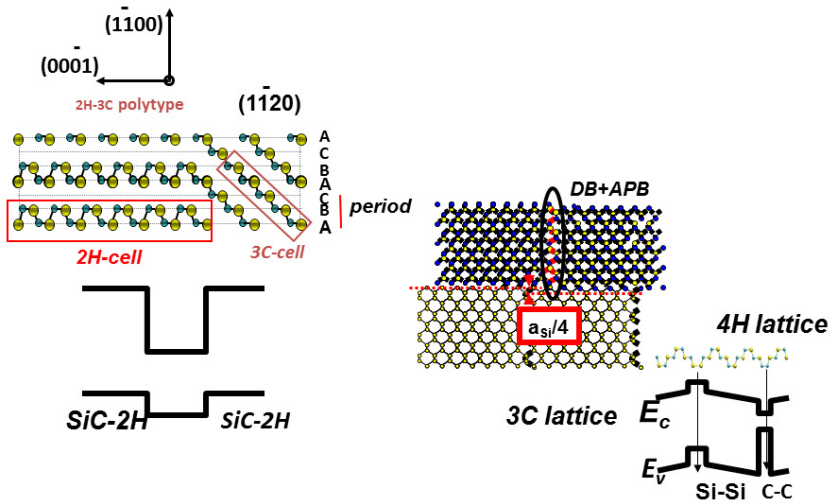


Fig. 6. left panel: illustration of the quantum well formed by the polytypism. Right panel: illustration of the quantum well formed by antiphase boundary (after the original figures in reference (Melinon and Masenelli, 2011) and references therein)

faults) or introduced extended defects such as antiphase boundary APB. The maximum value modulation in the potential corresponds with the bandgap difference between 3C-SiC and 2H-SiC $\Delta E_{max} = E_{g(3C-SiC)} - E_{g(2H-SiC)} \approx 1\text{eV}$ (see fig. 6).

1.7.1 Antiphase boundary

In the APBs (see fig. 6), the crystallographic direction remains unchanged but each side of the boundary has an opposite phase. For example, in 3C-SiC described by ABCABCABC layers, one or two layer interruption in the stacking sequence gives the following sequence ABCABABCAB which is the alternance of *fcc/hcp/fcc* layers. The chemical ordering is disrupted with the appearance of Si-Si and C-C bonds. The associated bandgap modulation depends to several: the difference in valence, the difference in size of the atoms and the electrostatic repulsion in the Si-Si and C-C bond near the interface. APB formation is obtained when 3C-SiC grows epitaxially on (100) silicon clean substrate (Pirouz et al., 1987). Deak *et al.* (Deak et al., 2006) reported a theoretical work where the expected tuning of the effective band gap ranges around 1 eV.

1.7.2 Cubic/hexagonal stacking

As mentioned above (fig. 6), MQWS can be built from the stacking of different crystal structures of the same material as in wurtzite/zincblende heterostructures (Sibille et al., 1990).

1.8 Amorphous phase

1.8.1 Carbon

The maximum disorder can be observed in carbon where a large spread in hybridization and bonds coexist. Amorphous carbon can be rich in sp^2 bonding (vitreous carbon) or rich in sp^3 bonding (tetrahedral amorphous carbon and diamond like carbon). The properties of amorphous carbon films depend on the parameters used during the deposition especially the presence of doping such as hydrogen or nitrogen. Note that hydrogen stabilizes the sp^3 network by the suppression of dangling bonds.

1.8.2 Silicon

Since Si adopts a sp^3 hybridization, the amorphous state will be a piece of sp^3 network. The most popular model is the continuous random network (CRN) first introduced by Polk and Boudreaux (Polk and Boudreaux, 1973). As a consequence, five or seven-membered rings are introduced in the initial diamond lattice to avoid the occurrence of a long range order. Finally, dangling bonds are created at the surface and a spread in bond lengths and bond angles was observed (within 1% and 10%, respectively). Elemental a-Si cannot be used practically because of the dangling bonds, whose energy levels appear in the bandgap of silicon. Fortunately, this problem is solved by hydrogen incorporation which passivates the dangling bonds and participates to the relaxation of the stress in the matrix (a-Si:H). CRN models are hand-built models. A more rigorous approach is done by classical, semi empirical or *ab initio* calculations using molecular dynamics algorithms where a cluster of crystalline Si is prepared in a liquid state and rapidly quenched.

1.8.3 Silicon carbon

The major question is the extent of chemical disorder present in amorphous SiC network. There is not a consensus in the a-SiC network because of the huge number of parameters (chemical ordering, carbon hybridization, spread in angles and bonds, odd membered rings, dangling bonds ...). The control of the chemical ordering in amorphous phase is the key point for applications in optoelectronics devices.

2. Cage-like molecules

2.1 Carbon: a rapid survey

2.1.1 Size range

Due to the high flexibility of the carbon atom, numerous isomers can be expected exhibiting complex forms such as linear chains (sp hybridization), rings, fused planar cycles (sp^2 hybridization), compact (sp^3 hybridization) and fullerene structures. We focus on particular structures in relation with complex architectures (zeolites) in bulk phase. From this point of view, fullerenes play an important role (Melinon et al., 2007).

2.1.2 Empty cages (fullerenes)

Starting with a piece of graphene (fully sp^2 hybridized), the final geometry is given by a subtle balance between two antagonistic effects. One is the minimization of the unpaired electrons at the surface of the apex, the other is the strain energy brought by the relaxation due to this minimization. The suppression of unpaired electrons is given by the standard topology (Euler's theorem). It is stated that (Melinon and Masenelli, 2011; Melinon and San Miguel, 2010) (and references therein)

$$2N_4 + N_5 = 12 \quad (4)$$

where N_i is the number of i membered-rings. The first case is $N_4 = 0$. This is achieved introducing at least and no more twelve pentagons ($N_5 = 12$), the number of hexagons (the elemental cell of the graphene) being $N_6 = 2i$ where i is an integer. Chemists claim that adjacent pentagons are chemically reactive and then introduce the concept of pentagonal rule (Kroto, 1987). Inspecting the Euler's relationship clearly indicates that the first fullerene with isolated pentagons is C_{60} with I_h symmetry. The mean hybridization is given by the π -Orbital Axis Vector Analysis

$$n = \frac{2}{1 - \frac{4\pi}{\sqrt{3}N}} \quad (5)$$

then taking graphene as reference for energy, the difference in energy writes

$$\Delta E = -3.1 \times 10^{-3} \left(\theta_{\pi\sigma} - \frac{\pi}{2} \right)^2 \quad (6)$$

where

$$\sin\left(\theta_{\pi\sigma} - \frac{\pi}{2}\right) = \frac{2\pi^{1/2}N^{-1/2}}{3^{3/4}} \quad (7)$$

$\theta_{\pi\sigma}$ is the angle between π and σ orbitals.

The first ($n=3$, $N_6 = 0$) is the popular dodecahedron with I_h symmetry. Equation 5 gives a fully sp^3 hybridization. C_{20} is an open shell structure with a zero HOMO-LUMO separation. This structure is not stable as long as the pentagons are fused and the strain energy maximum. Prinzbach *et al* (Prinzbach et al., 2000) prepared the three isomers according to different routes for the synthesis. The determination of the ground state in C_{20} is a subject of controversy as depicted in table 3 despite state of the art calculations.

method	geometry	$E_{ring} - E_{bowl}$	$E_{ring} - E_{cage}$	rank
^a MP2/TZVd	optimized	2.08	0.03	bowl-cage-ring
^a MP2/TZV2d	optimized	2.06	-0.66	cage-bowl-ring
^a MP2/TZV2d1f	optimized	2.10	-0.54	cage-bowl-ring
^a MP2/TZV2d1f	HF/6-31G*	2.61	0.69	bowl-cage-ring
^a MR-MP2/TZV2d	MP2/TZV2d1f	2.42	-0.02	cage-bowl-ring
^a MR-MP2/TZV2d1f	MP2/TZV2d1f	2.53	0.19	bowl-cage-ring
^a MR-MP2/TZV2d1f	HF/6-31G*	3.00	1.27	bowl-cage-ring
^b QMC	HF/6-31G*	1.1	2.10	bowl-ring-cage
^a LDA/TZV2df//MP2/TZV2df		2.00	-1.0	cage-bowl-ring
^c DFT B3LYP/6-311G*//B3LYP/6-311G*		0.4	1.9	ring-bowl-cage

Table 3. energy difference in eV (± 0.5 eV) between the ring (expected ground state), bowl and cage against several methods which different treatments of correlation and polarization effects. The last column indicates the rank in stability

^a after reference (Grimme and Muck-Lichtenfeld, 2002)

^b after reference (Sokolova et al., 2000)

^c after reference (Allison and Beran, 2004)

The *HOMO* state in $I_h C_{20}$ has a G_u state occupied by two electrons, the closed-shell electronic structure occurs for C_{20}^{2+} . These high degeneracies are lifted by a Jahn Teller effect which distorts the cage (Parasuk and Almlof, 1991). Indeed after relaxation, the degeneracies can be removed lowering the total energy (-1.33eV in D_{2h} with respect to I_h (Wang et al., 2005)) and opening a *HOMO LUMO* separation (Sawtarie et al., 1994). It has been stated that dodecahedrane $C_{20}H_{20}$ first synthesized by Paquette's group (Ternansky et al., 1982) is stable with a heat of formation about 18.2 kcal/mol (Disch and Schulman, 1996). The dodecahedron is characterized by a 7.3 eV *HOMO* (h_u) *LUMO* a_g separation (Zdetsis, 2007). However, the *HOMO-LUMO* separation does not increases monotonically with the hydrogen content indicating particular stable structures such as $I_h C_{20}H_{10}$ with the same *HOMO-LUMO* separation than the fully saturated $I_h C_{20}H_{20}$ (Milani et al., 1996). Coming back to the equation 4. Another solution is $N_5 = 0$ giving $N_4 = 6$ (square rings as reported in in cyclobutane where the strain is maximum). The first polyhedron (equivalent to C_{60}) where isolated square rule is achieved is the hexagonal cuboctahedron with O_h symmetry (24 atoms) (the first Brillouin zone in fcc lattice, see fig. 15). However, the strain energy gained in squares is too large to ensure the stability as compared to $D_6 C_{24}$ fullerene with (Jensen and Toftlund, 1993). C_{24} with $N_5 = 12$ is the first fullerene with hexagonal faces which presents in the upper symmetry a D_{6d} structure compatible with the translational symmetry (D_6 after relaxation). This is a piece of clathrate I described later (see fig. 13). Another fullerene $T_d C_{28}$ has a ground state with $a^5 A_2$ high-spin open-shell electronic state, with one electron in the a_1 molecular orbital and three electrons in the t_2 orbital (Guo et al., 1992) (see fig. 7). The close shell structure needs four electrons with a particular symmetry, three of them will be distributed on the t_2 orbital (*p-like* character) the last in the a_1 orbital (*s-like* character). This is the template of the carbon atom

making a sp^3 network. The four unpaired electrons make C_{28} behave like a sort of hollow superatom with an effective valence of 4. Introducing four hydrogen atoms outside in the T_d symmetry induces a close shell structure with the filling of the t_2 and a_1 states is checked by a *HOMO LUMO* separation of about 2.5 eV (Pederson and Laouini, 1993). $C_{28}H_4$ is the template of CH_4 leading to the hyperdiamond lattice. A closed shell structure is also done by the transfer of four electrons from a tetravalent embryo inside the cage. Since the size of C_{28} is low, this can be realized by incorporating one "tetravalent" atom inside the cage ($X=Ti, Zr, Hf, U, Sc$)(Guo et al., 1992)(Pederson and Laouini, 1993)(Makurin et al., 2001) (figure 7).

2.2 Silicon

2.2.1 Surface reconstruction

Theoretical determination of the ground-state geometry of Si clusters is a difficult task. One of the key point is the massive surface reconstruction applied to a piece of diamond (Kaxiras, 1990). The surface reconstruction was first introduced by Haneman (Haneman, 1961). The presence of a lone pair (dangling bond) destabilizes the network. One of the solution is the pairing. Since the surface is flat, this limits the possibility of curvature as reported in fullerenes. However, the surface relaxation is possible introducing pentagons (see for example references (Pandey, 1981; Himpsel et al., 1984; Lee and Kang, 1996; Xu et al., 2004; Ramstad et al., 1995)). This the key point to understand the stuffed fullerenes.

2.2.2 Stuffed fullerenes

Even though, the hybridization is fully sp^3 as in crystalline phase, $I_h Si_{20}$ is not a stable molecule, the ground state for this particular number of Si atoms corresponding to two Si_{10} clusters (Sun et al., 2002; Li and Cao, 2000). Si_{20} cage -like structure is a distorted icosahedron with an open-shell electronic configuration as reported in C_{20} fullerene. Likewise, $T_d Si_{28}$ fullerene is not a stable molecule. Starting from the T_d symmetry, a relaxation leads to a distorted structure which is a local minimum. Contrary to C_{28} (see above), the *HOMO* in $T_d Si_{28}$ is formed by the t_2 symmetry level and the a_1 symmetry level for *LUMO* (Gao and Zheng, 2005). Si in Si_{28} is more atomic like than C in C_{28} (Gong, 1995). Except these discrepancies, Si_{28} can be stabilized by four additional electrons coming from four hydrogen atoms outside or a tetravalent atom inside. However the cage diameter is too big for an efficient coupling with one tetravalent atom, even for the bigger known (uranium). Consequently, a single metal atom cannot prevent the $T_h Si_{28}$ cage from puckering and distortion. This problem can be solved introduced a molecule which mimics a giant tetravalent atom, the best being $T_d Si_5$ referred to Si_5H_{12} which has a perfect T_d symmetry (figure 7). $T_d Si_5$ has a completely filled twofold degenerated level at the *HOMO* state (Gao and Zheng, 2005). The final cluster $Si_5@Si_{28}$ is noted Si_{33} . Si_{33} has two classes of network: one corresponding to the fullerene family which exhibits T_d symmetry and can be deduced from a piece of clathrate, and one corresponding to the surface reconstruction of the Si crystal having a T_{d1} space group (Kaxiras, 1990). The difference is the exact position of Si_5 inside the Si_{28} cage. Since the total energy in the two isomers are very close, this emphasizes the concept of "superatom" with a large isotropy. The hybridization picture is not the good approach and a charge transfer picture seems more appropriate. Stuffed fullerene Si_{33} is found to be unreactive in agreement with the *HOMO LUMO* separation.

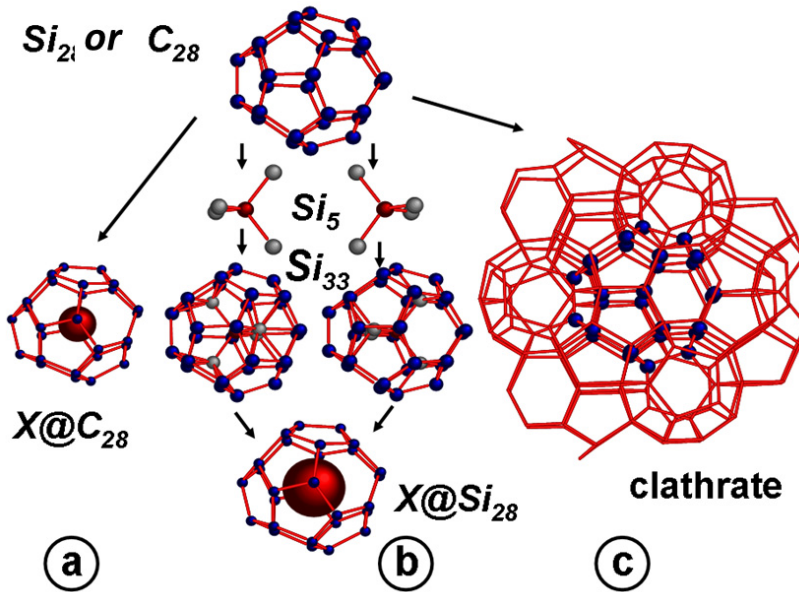


Fig. 7. scenario the an efficient doping in C_{28} and Si_{28} cage. Contrary to carbon , silicon needs a giant tetravalent atom. (a) endohedrally doped C_{28} cage stable for a tetravalent atom (uranium for example). (b) endohedral doping in Si_{28} cage by incorporation of two Si_5 clusters. The two isomers have roughly the same cohesive energy within DFT-GGA framework. (after the original figure in reference (Melinon and Masenelli, 2009))

2.3 Silicon carbon

The driving force in bulk is the chemical ordering. Inspecting equation 4 gives two possibilities: fullerene or cuboctahedron families. The first leads to non chemical ordering, the second to chemical ordering with a large stress because of four fold rings.

2.3.1 Quasi chemical ordering: buckydiamond

Starting from a spherically truncated bulk diamond structure, relaxation gives (Yu et al., 2009) a buckydiamond structure where the facets are reconstructed with the same manner as Si or C surfaces (figure 8). The inner shells have a diamond-like structure and the cluster surface a fullerene-like structure. Even though, the chemical ordering is not strictly achieved at the surface, the ratio of C-C and Si-Si bonds due to pentagons decreases as the cluster size increases. The reconstruction presents some striking features with the surface reconstruction in bulk phase.

2.3.2 Non chemical ordering: core shell structure

Most of the experiments done in SiC nanoclusters indicate a phase separation which does not validate a buckyball structure even though the buckyball is expected stable. The kinetic pathway plays an important role and the final state strongly depends to the synthesis: route

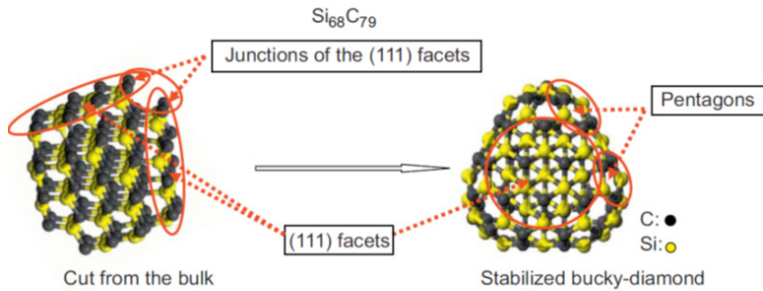


Fig. 8. A piece of β – SiC (truncated octahedron with (111) facets) and the final geometry after relaxation. The more spherical shape indicates a massive reconstruction of the surface. The inner shell remains sp^3 hybridized with a nearly T_d symmetry while the surface presents a set of pentagons and hexagons which is common in fullerenes. The original figure is in reference (Yu et al., 2009)

chemical or physical. The key point is the stoichiometry. When carbon and silicon are in the same ratio, one observes a complete phase separation with a core shell structure for the corresponding clusters.

2.3.3 Non chemical ordering: amorphous structure

Figure 9 displays the structure of the cluster starting with a core shell structure. It is found that for Si core ($Si_n@C_m$, $Si_m@C_n$), Si atoms are dragged to the exterior and the relaxation process leads to a strong distortion, with some Si and C atoms bonded. The spread in angles indicate a complexity in the hybridization close to the amorphous state. One of the key point is the phase separation in small nanoclusters as depicted on figure 9 where Si-Si, C-C bonds coexist with Si-C bonds at the interface of Si- and C-rich regions, respectively.

3. SiC cage like

For a low percentage of silicon, carbon adopts a geometry close to the fullerene where a few Si-atoms (less than twelve) are substituted to carbon atoms in the fullerene structure (Ray et al., 1998; Pellarin et al., 1999). The effect of the stoichiometry can be studied by selective laser evaporation. One takes advantage of the difference in cohesive energy (bonding) between Si-Si and C-C bonds within a parent SiC stoichiometric cluster. As a function of time during laser irradiation, sequential evaporation of Si atoms (or molecules) yield is more efficient than carbon evaporation leading to pure carbon clusters after total evaporation of silicon atoms. Inspecting the different size distributions deduced from a time of flight mass spectrometer against time reveals sequentially different structures: stoichiometric

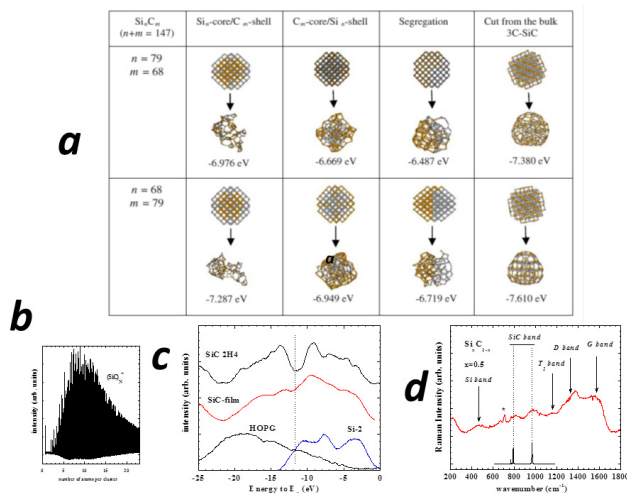


Fig. 9. (a) Relaxation of different hypothetical structures. from left to right: ($Si_n@C_m$, $Si_m@C_n$) showing the complex "amorphous structure" and the lack of the spherical shape, $C_n@Si_m$, $C_m@Si_n$ showing the C-rich region in the core, the spherical shape being preserved, the non chemical ordering phase showing the strong relaxation and the incomplete chemical ordering due to the large barriers in the diffusion and the buckyball structure. The cohesive energy per atom is also displayed. The original figure is in reference (Yu et al., 2009). (b) size distribution of SiC nanoparticles prepared in a laser vaporization source. A cluster assembled film is subsequently prepared by low energy cluster beam deposition. (c) valence band spectra deduced from XPS spectroscopy and (d) Raman band spectra showing silicon- and carbon-rich local phases. To guide the eye, the Raman modes and their symmetries in the crystal are given. The Raman spectrum of a 2H-SiC is also displayed. the spread in bond lengths and bond angles due to the multiple hybridization is well illustrated by the broad bands in Raman and XPS spectra. In a crude approximation, these bands reflect the p -DOS in the infinite lattice. The original figure is in reference (Melinon et al., 1998a)

clusters, heterofullerenes ($C_{2N} - nSi_n$) and C_{2N} fullerenes, respectively. The figure 10 displays the landscape of the phase transition between a pure fullerene like structure up to a piece of adamantane, the stoichiometry being the tuning parameter.

Figure 11 displays the symbolic ball and stick models for two heterofullerenes with one silicon atom, respectively, C_{60} being the mother. Inspecting the region near the gap (HOMO-LUMO region) shows the analogy with doped semiconductors by substitution. HOMO-LUMO separation in heterofullerenes are weakly affected by Si atoms compared to pure C_{60} fullerenes. The Si-related orbitals (dashed lines) can be described in terms of defect levels. Because Si and C belong to the same column, Si atom plays the role of co doping with two acceptor-like and donor-like levels. For two Si atoms substituted in C_{60} , the mechanism is the same excepted the splitting of each donor level in two levels.

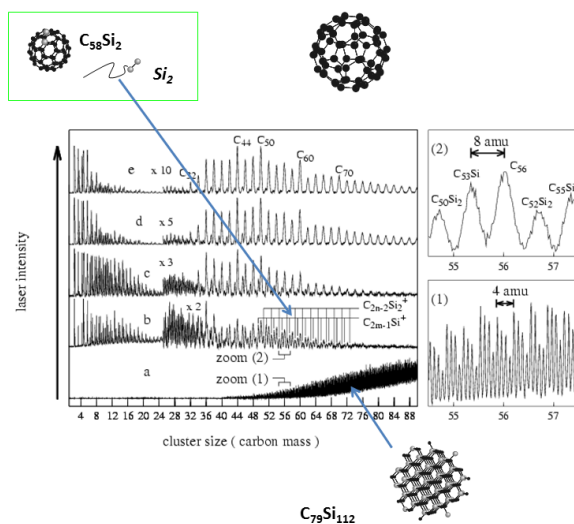


Fig. 10. Photoionization mass spectra of initial stoichiometric SiC clusters for increasing laser fluences. The time of flight mass spectrometer can be equipped with a reflectron device. Experimental details are given in the reference (Pellarin et al., 1999). The horizontal scale is given in equivalent number of carbon atoms. (a) High resolution one-photon ionization mass spectrum obtained in the reflectron configuration. (b) to (e) Multiphoton ionization mass spectra obtained at lower resolution without the reflectron configuration to avoid blurring from possible unimolecular evaporation in the time of flight mass spectrometer. The right part of the spectra (b) to (e) have been magnified for a better display. In (b) the heterofullerene series with one and two silicon atoms are indicated. Insets (1) and (2) give a zoomed portion of spectra 3(a) and 3(b). The 4 a.m.u. separation between Si_nC_m mass clumps is shown in (1) and the composition of heterofullerenes (8 a.m.u. apart) is indicated in (2). The mass resolution in (2) is too low to resolve individual mass peaks as in (1) (after the original figure (Pellarin et al., 1999)).

3.1 C_{60} functionalized by Si

Because of the closed shell structure, C_{60} packing forms a Van der Waals solid. Many research have been done to functionalize the C_{60} molecules without disrupt the π - π conjugation (Martin et al., 2009). Most of the methods are derived from chemical routes. Silicon atom can be also incorporated between two C_{60} molecules (Pellarin et al., 2002) by physical route. Bridging C_{60} is evidenced in free phase by photofragmentation experiments (Pellarin et al., 2002) and in cluster assembled films by EXAFS spectroscopy performed at the Si K edge (Tournus et al., 2002). Such experiments are compatible with a silicon atom bridging two C_{60} molecules. Different geometries are tested and the best configuration for the fit corresponds to a silicon atom bridging two C_{60} . Figure 11 displays the configuration where two nearest C_{60} face the silicon atom with a pentagonal face. In this case, we have ten neighbors located at 2.52\AA as compared to four neighbors located at 1.88\AA in SiC carbide. The geometry around silicon suggests an unusual bonding close to intercalated graphite rather than a sp^3 basic set.

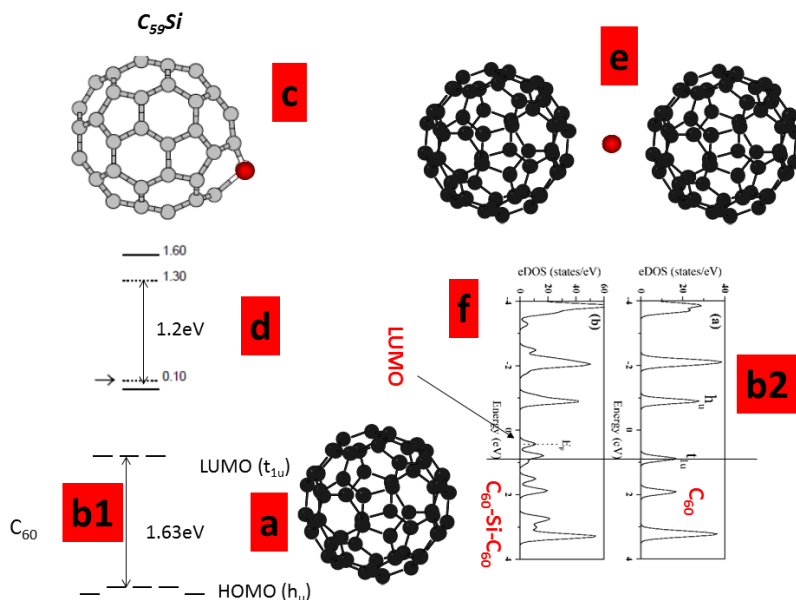


Fig. 11. a: symbolic ball and stick representation of C_{60} . b1,2: selected energy levels near the HOMO-LUMO C_{60} region. c: symbolic ball and stick representation of SiC_{59} , the geometries are deduced from DFT-LDA calculations and relaxed following the standard conjugate gradient scheme (see reference (Ray et al., 1998)). The red sphere is the silicon atom. d: selected energy levels near the SiC_{59} HOMO-LUMO region. Full lines and dotted lines indicate the carbon- and silicon-related orbitals, respectively. Taking only carbon-related orbitals, the HOMO-LUMO separation is respectively 1.68 eV, 1.60 eV for C_{60} , $C_{59}Si$ and respectively. The arrow gives the HOMO LUMO separation. In this way, the HOMO-LUMO separation is 1.2 eV in $C_{59}Si$. e: ball and stick representation of $C_{60}-Si-C_{60}$ (after reference (Tournus et al., 2002)). f: selected energy levels near the HOMO-LUMO $C_{60}-Si-C_{60}$ region

4. Zeolites: expanded-volume phases of SiC

There is an entanglement between empty or stuffed fullerenes and zeolite lattices. The interest on these nanocage based materials has been impelled by their potentialities in different domains from which we mention the optoelectronic engineering, integrated batteries, thermoelectric power, hard materials or superconductivity. These expanded-volume phases 12 are formed by triplicate arrangement of a combination of these elemental cages (fullerenes for example). The doped expanded-volume phases offer new advantages

i) A large flexibility in the nature and the strength of the coupling between the guest atom and the host cage following the valence and the size of the guest atom.

ii) a large flexibility in doping (n or p) as long no significant stress is observed for a very large concentration (up to 10%). Two kinds of open structures are under consideration. The first is the Kelvin's lattice (named bitruncated cubic honeycomb or "sodalite" in zeolite language formed by a regular stacking of truncated octahedra which are Archimedean solids with 14

faces (8 regular hexagons and 6 squares), 36 edges, and 24 vertices leading to the net formula $(AB)_{12}$ ($A=C, Si$, $B=C, Si$) the second the clathrate formed by a stacking of fullerenes. From a topological point of view, the clathrate is the best candidate to the complex mathematical problem of minimal partitioning of space into equal volumes is given by the Weaire-Phelan conjecture. However, SiC is not stable in clathrate structure because of the odd parity in five fold rings.

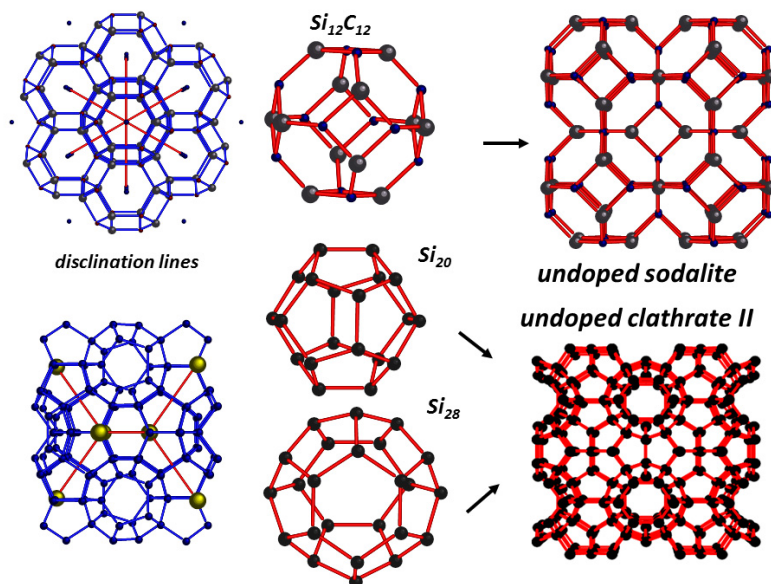


Fig. 12. sodalite structure compared to clathrate II. Both lattices are expanded volume phases but sodalite presents even membered rings allowing a chemical ordering. The "disclination lines" (for the definition see (Melinon and San Miguel, 2010)) display the lattice formed by endohedral atoms in the case of doped structures.

4.1 Clathrates: a survey

Clathrates are 3D periodic networks of dodecahedral fullerenes with either X_{24} or X_{28} polyhedral cage-like nanoclusters respectively. In type-I clusters, only X_{20} and X_{24} can be found, while the so-called type-II phases contain X_{20} and X_{28} . The silicon clusters are sharing faces, giving rise to full sp^3 -based networks of slightly distorted tetrahedra.

4.2 Endohedral doping

Elemental electronic devices need n and p doping. n-type doping of diamond is one of the most important issues for electronic application of diamond and remains a great challenge. This is due to the fact that the solubility of donor impurities in the diamond lattice is predicted to be low. Highly conductive silicon obtained by heavy doping is limited by the maximum solubility of the dopants provided it can be kept in solid solution. Beyond this limit precipitates or vacancy-containing centers are reported. Endohedral doping is one of the solution as long as the Fermi level can be tailored by varying both the concentration

and the type of atom inside the cage. This is well illustrated in clathrate Si-46, $\text{Na}_8\text{@Si} - 46$ and $\text{Ba}_8\text{@Si} - 46$ (see figure 13) (the notation $\text{Ba}_8\text{@Si} - 46$ indicates eight barium atoms for

name	space group	a	x	y	z	Wyckoff
X-34	$Fd\bar{3}m$ origin at center $\bar{3}m$	a	1/8	1/8	1/8	8a
			0.782	0.782	0.782	32e
			0.817	0.817	0.629	96g
X-46	$Pm\bar{3}m$ origin at $4\bar{3}m$	a	1/4	0	1/2	6c
			0.1847	0.1847	0.1847	16i
			0	0.3088	0.1173	24k
sodalite	$Pm\bar{3}n$	b	1/4	0	1/2	6c
			1/4	1/2	0	6d

Table 4. The space group, unit cell lattice parameters (a and c) in Å, carbon and silicon fractional coordinates (x, y, z), multiplicities and Wyckoff positions of the sites for selected clathrates I and II and sodalite.

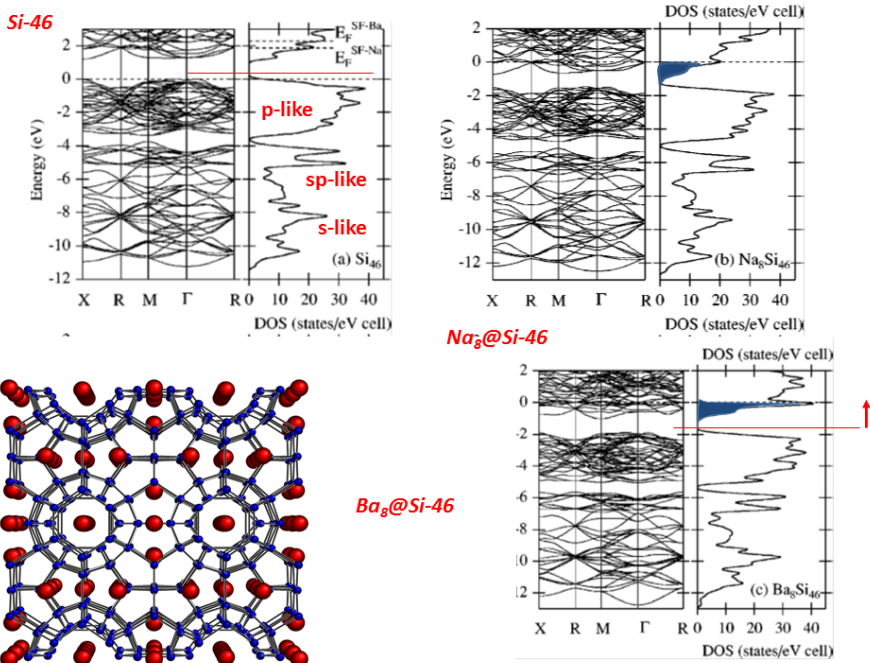


Fig. 13. Band structures and density of states for (a) Si-46, (b) $\text{Na}_8\text{@Si} - 46$, and (c) $\text{Ba}_8\text{@Si} - 46$. The ball and stick representation displays the $\text{X}_8\text{@Si} - 46$ lattice (X=Na,Ba). Density of states are calculated using 0.1 eV Gaussian broadening of the band structure. Energy is measured from the top of the valence band or the Fermi level, which is denoted by horizontal broken lines. The blue filled region displays the occupied states in the conduction band. Note the strong hybridization of the Barium states responsible of the high density of states at E_F in $\text{Ba}_8\text{@Si} - 46$. This sample is superconductor with a $T_c = 8\text{K}$. (after the original figure from (Moriguchi et al., 2000a)).

46 silicon atoms corresponding to the number of Si atoms in the primitive cell, in this case all the cages Si_{20} and Si_{24} are occupied. Note that the decoupling between the host lattice (the clathrate) and the guest lattice (doping atoms) is the key point for thermoelectric power generation and superconductivity applications in cage-like based materials. Moreover, the cage-like based materials present an interesting feature due to the great number of the atoms inside the elemental cell. This is well illustrated in the figure showing two $\{111\}$ cleavage planes in a diamond lattice. The first (labeled "diamond") displays the well known honeycomb lattice with a nice "open" structure. The second corresponds to the clathrate with a more complex structure. This partially explained why the cage-like structures contrary to diamond (unlike hardness, which only denotes absolute resistance to scratching) the toughness is high and no vulnerable to breakage (Blase et al., 2004)(fig. 14).

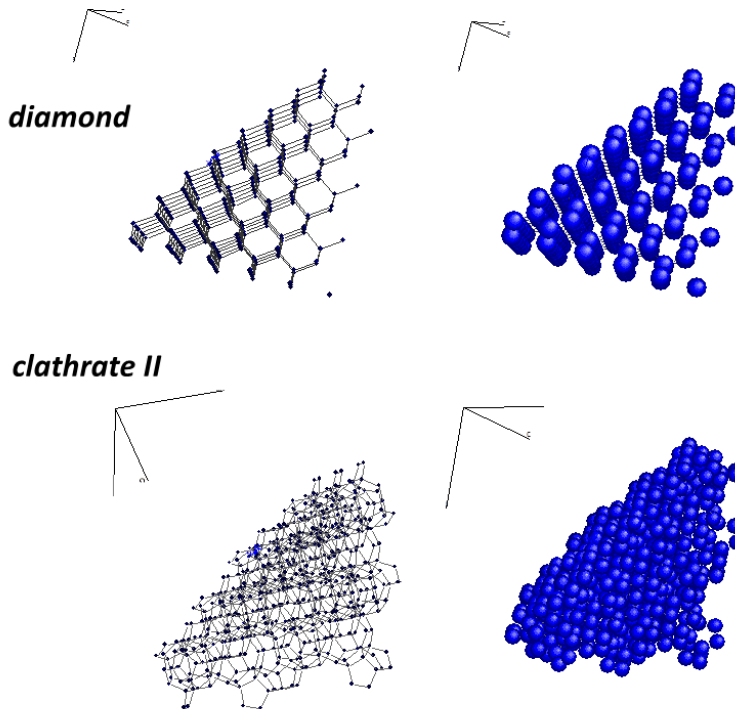


Fig. 14. cleavage plane along 111 projection in diamond and clathrate structures showing the large difference in atomic density. The toughness is high and no vulnerable to breakage in clathrate despite a weaker bonding (10% lower than in diamond phase). For more details see reference (Blase et al., 2004).

4.3 Carbon clathrate

The carbon clathrate synthesis is a major challenge since no precursor exists except intercalated graphite and doped fullerites. The competition between $sp - sp^2$ and sp^3 phases avoids the natural formation of carbon clathrate at high pressure and/or temperature. Numerous authors have attempted the synthesis without success.

4.4 Silicon clathrate

In the absence of angle-resolved photoemission data, the band structure of clathrates has been discussed on the basis of tight-binding (Adams et al., 1994) and *ab-initio* density functional (Hohenberg and Kohn, 1964; Kohn, 1999) (DFT) calculations (Melinon et al., 1998 ; Moriguchi et al., 2000; Saito and Oshiyama, 1995; Adams et al., 1994). In particular, DFT studies within the local density approximation (Kohn and Sham, 1965) (LDA) predict (Moriguchi et al., 2000a; Adams et al., 1994) that the Si-34 phase displays a "nearly-direct" band gap which is ~ 0.7 eV larger than the one of bulk Si-2 diamond. Such a large band gap has been attributed to the presence of pentagons which frustrates the formation of completely bonding states between Si- $3p$ orbitals at the top of the valence bands, thus reducing the p -band width.

4.5 Silicon carbon: topology

As mentioned above, chemical ordering is the driving force and expanded volume phases as candidates need odd parity in rings. No clathrate lattice excepted may be non stoichiometric compounds are expected.

4.6 Sodalite and other simple phases

The Atlas of Zeolite Framework Types (Ch. Baerlocher, L.B. McCusker and D.H. Olson, Elsevier, Amsterdam, 2007) contains 176 topological distinct tetrahedral TO_4 frameworks, where T may be Si. Some examples are illustrated in figure 15. The crystallographic data are given in table 5. From a theoretical point of view, the SiO_4 unit cell can be replaced by SiC_4 or CSi_4 . The most compact is the sodalite mentioned above. Within DFT-LDA calculations, the difference in energy between the sodalite and the cubic 3C-SiC is 0.6 eV per SiC units (16.59 eV per SiC in 3C-SiC within the DFT-LDA framework (Hapiuk et al., 2011)). Among the huge family of structures, ATV is more stable with a net difference of 0.52 eV per SiC units (see table 6). This energy is small enough to take in consideration cage-like SiC based materials and the potentiality for its synthesis. This opens a new field in doping as long the elements located at the right side in the periodic table induce a p-like doping while elements at the left side induce a n-like doping. Moreover, one can takes advantage to the wide band opening in expanded-volume phases. Inspecting the table reveals a direct gap in ATV structure within DFT-LDA level. This structure is the most stable and presents interesting features for optical devices in near UV region. Even though DFT/LDA has the well-known problem of band-gap underestimation, it is still capable of capturing qualitatively important aspects by comparison between 3C- and other structures. Open structures have a promising way as long as the structures could be synthesized by chemists.

name	space group	a	x	y	z	Wyckoff
ATV	$ABm2$ [number 39]	a=5.788 b=9.236 c=5.007				
	Si		0.849	.25	0.692	4c
	Si		0.651	0.099	0.192	8d
	C		0.849	0.25	0.308	4c
	C		0.651	0.0.099	0.808	8d
AFI	$P6cc$ [number 184]	a=8.4669 b=a c=5.003				
	Si		0.455	0.122	0.192	12d
	C		0.545	0.878	0.808	12d
LTA	$Fm\bar{3}c$ [number 226]	a=b=c=10.2129				
	Si		0	0.0924	0.1848	96i
	C		0	0.1848	0.0924	96i
VFI	$P6_3cm$ [number 185]	a=b=11.6075 c=5.0307				
	Si	0.4227	0	0.063	6c	
	Si		0.1786	0.512	0.563	12d
	C		0.5773	0	0.937	6c
	C		0.8214	0.488	0.437	12d
ATO	$R\bar{3}$ [number 148]	a=b=12.942 c=3.0284				
	Si		0.1992	0.251	0.250	18f
	C		0.0518	0.251	0.250	18f

Table 5. The space group, unit cell lattice parameters (a and c) in Å, carbon and silicon fractional coordinates (x, y, z), multiplicities and Wyckoff positions of the sites for selected zeolites. 3C-SiC and sodalite are displayed in tables 1 and 4 respectively. The lattice parameters are deduced from DFT-LDA calculations within SIESTA code and standard procedure (Hapiuk et al., 2011). The coordinates are in reference (Demkov et al., 1997).

name	energy difference per SiC units	bandgap	type	d _{SiC}
3C-SiC	0	1.376	indirect	1.88
ATV	0.524	1.949	direct $\Gamma - \Gamma$	(1.842-1.923)
sodalite	0.598	1.718	indirect	1.881
VFI	1.065	1.063	indirect	(1.889-1.904)
LTA	1.126	1.586	indirect	(1.883-1.887)
ATO	1.210	1.035	indirect	(1.908-2.104)

Table 6. energy difference to the ground state per SiC in eV, LDA bandgap, transition and neighboring distance at the DFT-LDA level. Calculations were done within the density functional theory DFT in the local density approximation . The Perdew-Zunger parametrization of the Ceperley-Alder homogeneous electron gas exchange-correlation potential was used. The valence electrons were treated explicitly while the influence of the core electrons and atomic nuclei was replaced by norm-conserving Trouiller-Martins pseudo potentials factorized in Kleinman-Bylander form. For the doping elements, pseudo potentials were generated including scalar relativistic effects and a nonlinear core correction was used to mimic some of the effects of the d shell on the valence electrons. We employed the SIESTA program package which is a self-consistent pseudo potential code based on numerical pseudo atomic orbitals as the basis set for decomposition of the one-electron wave functions (Hapiuk et al., 2011).

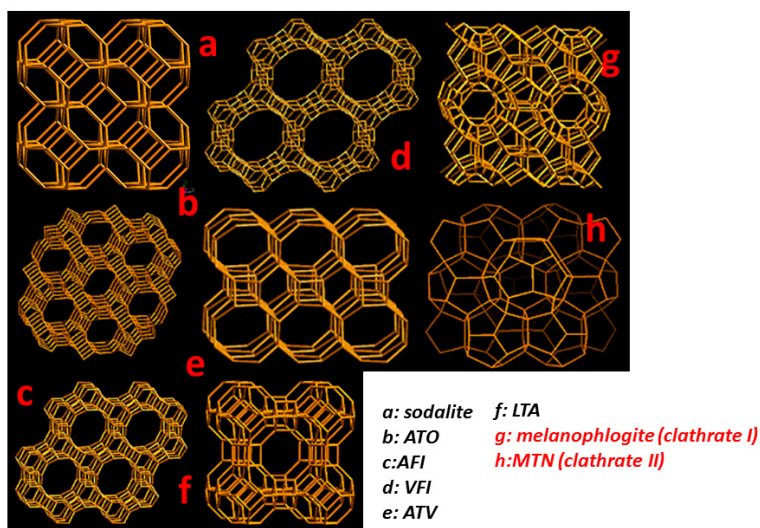


Fig. 15. selected zeolites forms. (a) sodalite with single 6-rings in ABC sequence with single 4-rings or 6-2 rings. (b) ATO with single 4- or 6-rings. (c) AFI with single 4- or 6-rings. (d) VFI with single 6-rings. (e) ATV with single 4-rings. (f) LTA with double 4-rings, (single 4-rings), 8-rings or 6-2 rings. (g) melanophlogite with 5-rings (clathrate I see above). (h) MTN with 5-rings (clathrate II see text). The two clathrate forms are unlikely because the breakdown of the chemical ordering. For more details see the "Commission of the International Zeolite Association (IZA-SC)" <http://izasc-mirror.la.asu.edu/fmi/xsl/IZA-SC/ft.xml>

5. Conclusion: future research

Most of the SiC forms are nearly sp^3 hybridized. Inspecting the new architectures based from cage-like cells do not reveal anyway another hybridization. The silicon make one's mark, other hybridizations are definitively discarded. However, the topology of the open-structures like zeolites is still interesting since its offer a set of unique features: low density, tunable bandgap (direct or indirect), endohedral doping hydrogen storage ... This is enough to promote a renewable interest and some efforts for their synthesis. In addition, all the properties attributed to the open structures in cage-like based materials are universal since the driving force is the topology, namely the symmetry of the cage and the symmetry of the whole lattice. Same features are observed in other binary compounds such as GaAs or ZnO. In addition, the inspection of the bulk and molecular phases underlines the prominent role of the pentagons where the chemical ordering is broken. This is the striking difference between C₃Si and SiC.

6. References

- Kavan, L., Hlavatý, J., Kastner, J. and Kuzmany, H. (1995) *Electrochemical carbyne from perfluorinated hydrocarbons: synthesis and stability studied by Raman scattering*, *Carbon* 33, 1321–1329.
- Baughman, R.H. (2006) *Dangerously Seeking Linear Carbon* *Science* 312, 1009–1110.
- Lucotti, A., Tommasini, M., Zoppo, M., Del Castiglioni, C., Zerbi, G., Cataldo, F., Casari, C.S., Bassi, A., Li Russo, V., Bogana, M. and Bottani, C.E. (2006). *Raman and SERS investigation of isolated sp carbon chains*, *Chemical Physics Letters* 417, p78–82.
- Geim, A.K. and Novoselov, K.S. (2007) *The rise of graphene*, *Nature Materials* 6, 183–191.
- Partoens, B. and Peeters, F.M. (2006) *From graphene to graphite: Electronic structure around the K point*, *Phys. Rev. B* 74, 075404 1–11.
- Charlier, J.C., Michenaud, J.P., Gonze, X. and Vigneron, J.P. (1991) *Tight-binding model for the electronic properties of simple hexagonal graphite*, *Phys. Rev. B* 44, 13237–13249.
- Nakada, K., Fujita, M., Dresselhaus, G. and Dresselhaus, M.S. (1996) *Edge state in graphene ribbons: Nanometer size effect and edge shape dependence*, *Phys. Rev. B* 54, 17954–17961.
- Son, Y.W., Cohen, M.L. and Louie, S.G. (2006) *Energy Gaps in Graphene Nanoribbons*, *Phys. Rev. Lett.* 97, 216803 1–4.
- Chung, D.D.L. (2002) *Review Graphite*, *J. of Mat. Sci.* 37, 1475–1489.
- Melinon, P. and Masenelli B., *From Small Fullerenes to Superlattices: Science and Applications*, Pan Stanford Publishing Pte Ltd (2011)
- Gryko, J., McMillan, P., Marzke, R., Ramachandran, G., Patton, D., Deb, S. and Sankey, O. (2000) *Low-density framework form of crystalline silicon with a wide optical band gap* *Phys. Rev. B* 62, R7707–R7710.
- Adams, G.B., O'Keeffe, M., Demkov, A.A., Sankey, O.F. and Huang, Y. (1994) *Wide-band-gap Si in open fourfold-coordinated clathrate structures*, *Phys. Rev. B* 49, 8048–8053.
- Melinon, P., Keghelian, P., Blase, X., Le Brusq, J., and Perez, A. (1998). *Electronic signature of the pentagonal rings in silicon clathrate phases: Comparison with cluster-assembled films* *Phys. Rev. B* 58, 12590–12593.
- Connetable, D., Timoshevskii, V., Masenelli, B., Beille, J., Marcus, J., Barbara, B., Saitta, A., Rignanese, G., Melinon, P., Yamanaka, S. and Blase, X. (2003) *Superconductivity in Doped sp³ Semiconductors: The Case of the Clathrates* *Phys. Rev. Lett.* 91, 247001 1–4.

- Connetable, D. (2003) *Ph.D. thesis, Universite of Lyon, LPMCN batiment Brillouin Do maine de la Doua 69622 Villeurbanne France*
- Tse, J.S. Uehara, K. Rousseau, R. Ker, A. Ratcliffe, C.L. White, M.A. and Mackay, G. *Structural principles and amorphouslike thermal conductivity of Na-doped silicon clathrates* *Phys. Rev. Lett.* 85, 114–117.
- Yin, M.T. and Cohen, M.L. (1974) *Structural theory of graphite and graphitic silicon*, *Phys. Rev. B* 29, 6996–6998.
- Kackell, P. and Wenzien, B. and Bechstedt, F. *Electronic properties of cubic and hexagonal SiC polytypes from ab initio calculations* *Phys. Rev. B* 50, 10761–10768.
- Kackell, P. and Wenzien, B. and Bechstedt, F. (1994) *Influence of atomic relaxations on the structural properties of SiC polytypes from ab initio calculations* *Phys. Rev. B* 50, 10761–10768.
- Alfe, D.; and Gillan, M.J. and Towler, M.D. and Needs, R.J. (2004) *Diamond and β -tin structures of Si studied with quantum Monte Carlo calculations* *Phys. Rev. B* 70, 214102 1–8.
- W. J. Choyke, Hiroyuki Matsunami, G. Pensl *Silicon Carbide: recent major advances* Springer Verlag, Berlin Heidelberg (2004). *Phys. Rev. B* 44, 17037–17046.
- Zhe Chuan Feng, *SiC power materials: Devices and applications*, Springer Verlag, Berlin Heidelberg (2004). *Phys. Rev. B* 44, 17037–17046.
- Martins, J. L. and Zunger, A. (1986) *Stability of ordered bulk and epitaxial semiconductor alloys* *Phys. Rev. Lett.* 56, 1400–1404.
- Tersoff, J. (1994) *Chemical order in amorphous silicon carbide* *Phys. Rev. B* 49, 16349–16352.
- G L Zhao and D Bagayoko (2000) *Electronic structure and charge transfer in 3C and 4H-SiC* *New Journal of physics* 2, 16 1–12.
- Segall, M. D., Shah, R., Pickard, C. J. and Payne. *Population analysis of plane-wave electronic structure calculations of bulk materials* *Phys. Rev. B* 54, 16317–16320.
- Garcia, A. and Cohen, M.L. (1993) *First-principles ionicity scales. I. Charge asymmetry in the solid state* *Phys. Rev. B* 47, 4215–4220.
- Wellenhofer, G. and Karch, K. and Pavone, P. and Rossler, U. and Strauch, D. (1996) *Pressure dependence of static and dynamic ionicity of SiC polytypes* *Phys. Rev. B* 53, 6071–6075.
- Moriguchi, K.; and Munetoh, S. and Shintani, A. (2000) *First-principles study of $\text{Si}_{34-x}\text{Ge}_x$ clathrates: Direct wide-gap semiconductors in Si-Ge alloys* *Phys. Rev. B* 62, 7138–7143.
- Wang, H. and Chu, W. and Jin, H. and Xiong, Y. (2008) *Atomistic simulation of SiGe clathrate alloys* *Chem. Phys.* 344, 299–308.
- Ito, T. and Kangawa, Y. (2002). *An empirical potential approach to wurtzite zinc blende structural stability of semiconductors* *Journal of Crystal Growth* 235, 149–153.
- Ito, T., Sano, K., Akiyama, T. and Nakamura, K. (2006). *A simple approach to polytypes of SiC and its application to nanowires* *Thin Solid Films* 508, 243–246.
- Heine, V., Cheng, C. and Needs, R. (1992a). *Computational study into the origin of SiC polytypes* *Materials Science and Engineering, B: Solid-State Materials for Advanced Technology* B11, 55–60.
- Esaki, L. and Chang, L. (1974). *New Transport Phenomenon in a Semiconductor Superlattice* *Phys. Rev. Lett.* 33, 495–498.
- Bauer, A., Kraulich, J., Dressler, L., Kuschnerus, P., Wolf, J., Goetz, K., Kackell, P., Furthmüller, J. and Bechstedt, F. (1998) *High-precision determination of atomic positions in crystals: The case of 6H- and 4H-SiC* *Phys. Rev. B* 57, 2647–2650.
- Sibille, A., Palmier, J., Wang, H. and Mollot, F. (1990). *Observation of Esaki-Tsu Negative Differential Velocity in GaAs/AlAs Superlattices* *Phys. Rev. Lett.* 64, 52–55.

- Polk, D. and Boudreaux, D. (1973). *Tetrahedrally Coordinated Random-Network Structure* *Phys. Rev. Lett.* 31,92–95.
- Pirouz, P., Chorey, C. and Powell, J. (1987). *Antiphase boundaries in epitaxially grown β -SiC* *Appl. Phys. Lett.* 4,221–223.
- Deak, P., Buruzs, A., Gali, A. and Frauenheim, T. (2006). *Strain-Free Polarization Superlattice in Silicon Carbide: A Theoretical Investigation* *Phys. Rev. Lett.* 96,236803 1–4.
- Cheng, C., Needs, R. and Heine, V. (1988). *Inter-layer interactions and the origin of SiC polytypes* *J. Phys. C: Solid State Phys.* 21,1049–1063.
- Park, C., Cheong, B., Lee, K. and Chang, K. (1994). *Structural and electronic properties of cubic, 2H 4H and 6H SiC* *Phys. Rev. B* 49,4485–4493.
- Limpijumong, S. and Lambrecht, W. (1998). *Total energy differences between SiC polytypes revisited* *Phys. Rev. B* 57,12017–12022.
- Lindelfelt, U., Iwata, H., Oberg, S. and Briddon, P. (2003). *Stacking faults in 3C-, 4H-, and 6H-SiC polytypes investigated by an ab initio supercell method* *Phys. Rev. B* 67,157204 1–12.
- Liu, Z. and Ni, J. (2005). *Layered growth modelling of epitaxial growth processes for SiC polytypes* *J. Phys.: Condens. Matter* 17,5355–5366.
- Melinon, P., Masenelli, B., Tournus, F. and Perez, A. (2007). *Playing with carbon and silicon at the nanoscale* *Nature Materials* 6,479–490.
- P.Melinon and A. San Miguel (2010). *From silicon to carbon clathrates : nanocage materials Chapter in the vol. "Clusters and Fullerenes" The HANDBOOK OF NANOPHYSICS* Taylor & Francis. (K.Sattler guest editor). ISBN: 9781420075540.
- Kroto, H. (1987). *The stability of the fullerenes C_n , with $n = 24, 28, 32, 36, 50, 60$ and 70* *Nature* 329,529–531.
- Prinzbach, H., Weiler, A., Landenberger, P., Wahl, F., Worth, J., Scott, L., Gelmont, M., Olevano, D. and Issendorf, B. (2000). *Gas-phase production and photoelectron spectroscopy of the smallest fullerene, C_{20}* *Nature* 407,60–63.
- Parasuk, V. and Almlof, J. (1991). *C_{20} : the smallest fullerene?* *Chem. Phys. Lett.* 184,187–190.
- Wang, Z., Lian, K., Pan, S. and Fan, X. (2005b). *A Path from I_h to C_1 Symmetry for C_{20} Cage Molecule* *Journal of Computational Chemistry* 26,1279–1283.
- Grimme, S. and Muck-Lichtenfeld, C. (2002). *Structural isomers of C_{20} Revisited: The Cage and Bowl are Almost Isoenergetic* *CHEMPHYSICHEM* 2,207–209.
- Sokolova, S., Luchow, A. and Anderson, J. (2000). *Energetics of carbon clusters C_{20} from all-electron quantum monte carlo calculations* *Chemical Physics Letters* 323,2229–233.
- Allison, C. and Beran, K. (2004). *Energetic analysis of 24 C_{20} isomers*, *Journal of Molecular Structure Theochem* 680,59–63.
- Sawtarie, M., Menon, M. and Subbaswamy, K. (1994). *Structure of C_{20} : Bicyclic ring versus cage* *Phys. Rev. B* 49,7739–7743.
- Ternansky, R., Balogh, D. and Paquette, L. (1982). *Dodecahedrane* *J. Am. Chem. Soc.* 104,4503–4504.
- Disch, R. and Schulman, J. (1996). *Heat of Formation of Dodecahedrane* *J. Phys. Chem.* 100,3504–3506.
- Zdetsis, A. (2007). *High-symmetry high-stability silicon fullerenes: A first-principles study* *Phys. Rev. B* 76,075402 1–5.
- Milani, C., Giambelli, C., Roman, H., Alasia, F., Benedek, G., Broglia, R., Sanguinetti, S. and Yabana, K. (1996). *The valence of small fullerenes* *Chemical Physics Letters* 258,554–558.

- Jensen, F. and Toftlund, H. (1993). *Structure and stability of C₂₄ and B₁₂N₁₂ isomers* *Chemical Physics Letters* 201,89–96.
- Guo, T., Diener, M., Chai, Y., Alford, M., Hauer, R., McClure, S., Ohno, T., Weaver, J., Scuseria, G. and Smalley, R. *Uranium stabilization of C₂₈: A Tetravalent Fullerene* *Science New Series* 257,1661–1664.
- Pederson, M. and Laouini, M. (1993). *Covalent container compound: Empty, endohedral and exohedral C₂₈ complexes* *Phys. Rev. B* 48,2733–2737.
- Makurin, Y., Sofronov, A., Gusev, A. and Ivanovsky, A. (2001). *Electronic structure and chemical stabilization of C₂₈ fullerene* *Chem. Phys.* 270,293–308.
- Haneman, D. (1961) *Surface Structures and Properties of Diamond-structure Semiconductors*, *Phys. Rev.* 121,1093–1100.
- Kaxiras, E. (1990). *Effect of surface reconstruction on stability and reactivity of Si clusters*, *Phys. Rev. Lett.* 64,551–554.
- Pandey, K.C. (1981) *New π -bonded Chain Model for Si(111) 2×1 Surface*, *Phys. Rev. Lett.* 47,1913–1917.
- Himpsel, F.J. and Marcus, P.M. and Tromp, R. and Batra, P. and Cook, M.R. and Jona, F. and Liu, H. (1984) *Structure analysis of Si(111) 2×1 with low-energy electron diffraction*, *Phys. Rev. B* 30,2257–2259.
- Lee, S. and Kang, M. (1996). *Model-dependent electronic structure of the Si(111) (2X1) surface* *Phys. Rev. B* 54,1482–1485.
- Xu, G. and Deng, B. and Yu, Z. and Tong, S.Y. and Van Hove, M.A. and Jona, F. and Zasada, I. (2004) *Atomic structure of the cleaved Si(111)-(2 \times 1) surface refined by dynamical LEED*, *Phys. Rev. B* 70,045307–045313.
- Ramstad, A., Brocks, G. and Kelly, P. (1995). *Theoretical study of the Si (100) surface reconstruction* *Phys. Rev. B* 51,14504–14522.
- Sun, Q., Wang, Q., Briere, T., Kumar, V. and Kawazoe, Y. (2002a). *First-principles calculations of metal stabilized Si₂₀ cages* *Phys. Rev. B* 65,235417 1–5.
- Li, B. and Cao, P. (2000). *Stable structures for si₂₀ clusters* *Phys. Rev. A* 62,023201 1–5.
- Gao, Y. and Zeng, X. (2005). *M₄@Si₂₈ (M=Al,Ga) Metal-encapsulated tetrahedral silicon fullerene* *The J. of Chem. Phys.* 123,204325 1–4.
- Gong, X. (1995). *Stability and electronic properties of nanoscale silicon clusters* *Phys. Rev. B* 52,14677–14681.
- Kaxiras, E. Zeger, L.M. Antonelli, A. and Juan, Y.M. (1994) *Electronic properties of a cluster-based solid form of carbon: C₂₈ hyperdiamond*, *Phys. Rev. B* 49,8446 –8453.
- Yu, M. and Wu, S.Y. and Jayanthi, C.S. (2009) *A self-consistent and environment-dependent Hamiltonian for large-scale simulations of complex nanostructures* *Physica E* 42,1–16.
- Ray, C., Pellarin, M., Lerme, J., Vialle, J., Broyer, M., Blase, X., Melinon, P., Keghelian, P. and Perez, A. (1998). *Synthesis and structure of silicon-doped heterofullerenes* *Phys. Rev. Lett.* 80,5365–5368.
- Pellarin, M., Ray, C., Lerme, J., Vialle, J. L., Broyer, M., Blase, X., Keghelian, P., Melinon, P. and Perez, A. (1999). *Photolysis experiments on SiC mixed clusters: From silicon carbide clusters to silicon-doped fullerenes* *J. of Chem. Phys.* 110,6927–6938.
- Martin, N. Giacalone, F. and Prato, M. editors (2009). *Fullerene Polymers: Synthesis, Properties and Applications* Wiley .

- M. Pellarin, E. Cottancin, J. Lerme, J.L. Vialle, M. Broyer, F. Tournus, B. Masenelli, P. Melinon (2002). *Coating and polymerization of C60 with carbon : A gas phase photodissociation study* *J. Chem. Phys.* 117,3088–3097.
- Melinon, P., Keghelian, P., Perez, A., Ray, C., Lerme, J., Pellarin, M., Broyer, M., Boudeulle, M., Champagnon, B. and Rousset, J. *Nanostructured SiC films obtained by neutral-cluster depositions* *Phys. Rev. B* 58,16481–16490.
- F. Tournus, B. Masenelli, P. Melinon, X. Blase, A. Perez, M. Pellarin, M. Broyer, A.M. Flanck, P. Lagarde (2002). *Bridging C60 by silicon : towards non-van der Waals C60-based materials* *Phys. Rev. B* 65,165417 1–6.
- Blase,X. Gillet,P. San Miguel,A. and Melinon,P. (2004). *Exceptional Ideal Strength of Carbon Clathrates* *Phys. Rev. Lett.* 65,215505 1–4.
- Hohenberg,P. and Kohn,W. *Inhomogeneous Electron Gas* *Phys. Rev. B* 136,864–871.
- Hohenberg,P. and Kohn,W. (1999). *Electronic structure of matter* *Rev. Mod. Phys.* 71,1253–1266.
- Saito,S. and Oshiyama,A. (1995). *Electronic structure of Si46 and Na2Ba6Si46* *Phys. Rev. B* 51,2628–2631.
- Moriguchi, K., Yonemura, M., Shintani, A. and Yamanaka, S. (2000a). *Electronic structures of Na8Si46 and Ba8Si46* *Phys. Rev. B* 61,9859–9862.
- Kohn, W. and Sham, L. (1965). *Self-Consistent Equations Including Exchange and Correlation Effects* *Phys. Rev.* 140,A1133–A1138.
- to be published
- Demkov,A.A. Sankey,O.F. Gryko,J. and McMillan,P.F. (1997) *Theoretical predictions of expanded-volume phases of GaAs* *Phys. Rev. B* 55,6904–6913.
- P.Melinon and A. San Miguel (2010). *From silicon to carbon clathrates : nanocage materials Chapter in the vol. "Clusters and Fullerenes" The HANDBOOK OF NANOPHYSICS* Taylor & Francis. (K.Sattler guest editor). ISBN: 9781420075540.
- Adams, G., O'Keekke, M., Demkov, A., Sankey, O. and Huang, Y. (1994). *Wide-band gap Si in open fourfold-coordinated clathrate structures* *Phys. Rev. B* 49,8048–8053.
- Melinon, P. and Masenelli,B. (2009) . *Cage-like based materials with carbon and silicon* *ECS transaction* 13.

Metastable Solvent Epitaxy of SiC, the Other Diamond Synthetics

Shigeto R. Nishitani¹, Kensuke Togase¹, Yosuke Yamamoto¹,
Hiroyasu Fujiwara², and Tadaaki Kaneko³

¹*Kwansei Gakuin University, Department of Informatics,*

²*(Late) Kyoto University, Department of Energy Science,*

³*Kwansei Gakuin University, Department of Physics,
Japan*

1. Introduction

Professor W. Shockley, a Nobel prize winner and the ‘father’ of the transistor, predicted in the 1950s that SiC would soon replace Si in devices because of its superior material properties (Cited from Choyke, 1960). His prediction, however, has not yet come true because of the high cost of manufacturing SiC wafers. The current price of 2-inch SiC wafers is close to that of diamond jewellery rather than to that of Si wafers. Nevertheless, owing to its promising physical properties for high-power devices and for achieving significant reductions in CO₂ emission, many researchers and companies are purchasing many SiC wafers (Madar, 2004; Nakamura et al., 2004). Very recently, the present authors reported a novel process for fabricating epitaxial SiC (Nishitani & Kaneko, 2008). This process has the potential to cost less and to provide SiC wafers with high crystalline quality. Here we present a new synthesis process for manufacturing SiC. In this process, the driving force for crystal growth is elucidated by considering a similarity—the coexistence of the stable and metastable phases—with the diamond synthesis process reported by Bonenkirk et al. (1959) of General Electric.

In this review, the authors introduce the experimental procedures and the results of this novel process of making stable phase of SiC at first. Then they will show the speculated mechanism from the thermodynamical point of view, especially the concept of the double phase diagram and the concentration profile. In the end, understanding the phase stability of many polytypes of SiC, the reported phase diagrams, the difficulty of the equilibrium state achievement, and the results of the first principles calculations will be discussed.

2. Experimental results

2.1 Conventional methods

While SiC was first synthesized by Acheson at the end of the 19th century (Acheson, 1896), single-crystal wafers of SiC became commercially available only in the early 1990s. Boules of other important semiconductors such as Si, GaAs and InP are manufactured through a liquid process, while those of SiC are produced through a vapor process. Owing to the

peritectic reaction of SiC at above 2500 °C as shown in the phase diagram of Fig. 1, growth from a stoichiometric melt is not possible at normal pressure. The incongruent compounds are usually produced by the solution method. The low carbon solubility in liquid Si leads to insufficient mass transport of C, and this in turn results in the crystal growth in the Si-C solution method being quite slow (Hofmann & Müller, 1999). The solution method provides crystals with better crystallinity and a smaller defect density as compared to vapor methods. Thus, the solution method is preferred for preparing SiC (Hofmann & Müller, 1999). Many attempts have been made to increase the carbon solubility in liquid Si, especially by the addition of metallic elements or the application of high pressures. Nevertheless, the productivity of such methods does not exceed that of the vapor methods (Casady & Johnson, 1996; Chaussende et al., 2007; Hofmann & Müller, 1999; Wesch, 1996).

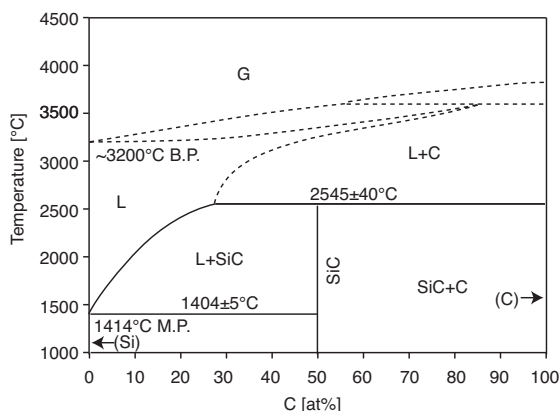


Fig. 1. Phase diagram of Si-C binary system (Olesinski & Abbaschian, 1996).

Among the vapor processes, the sublimation process, which is schematically illustrated in Fig. 2a and which was first proposed Tairov & Tsvetkov (1978), is the standard process used for the commercial manufacture of SiC. In this process, the source powder and a seed crystal are placed in a graphite crucible. SiC powder is then heated to typically 2400 °C and allowed to sublime. Si and C vapors are transferred in an inert gas, and they recrystallize on a slightly cooler single-crystal seed. The temperature dependency of the crucible is schematically shown in the left-hand panel of Fig. 2a. The main drawback of this method is that the obtained boules contain many types of grown-in defects, such as micropipes, step bunching, dislocations and stacking faults. For the reduction of these defects, the operation parameters such as the growth temperature, gas flow rate and total pressure should be controlled quite steadily for a long operation time. This long and sensitive operation performed at a high temperature and involving a temperature gradient makes SiC wafers expensive. Researches on alternative processes such as chemical vapor deposition and the vapor-liquid-solid process are continuing with the objective of improving the growth rate and crystal quality (Chaussende et al., 2007).

2.2 Metastable solvent epitaxial method

Our proposed method employs the solution growth technique. A schematic drawing of the apparatus is presented in Fig. 2b. In this method, C is transferred through liquid Si instead of Ar gas, which is used in the conventional method. Poly-crystalline 3C-SiC source and single-crystalline 4H-SiC plate are placed in a TaC crucible and liquid Si solvent is sandwiched

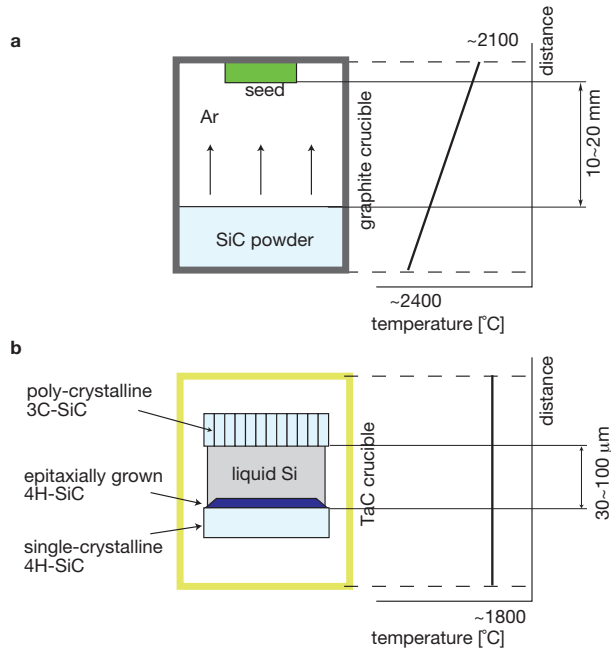


Fig. 2. Schematic illustrations of **a** the conventional sublimation method and **b** the new solvent method for the preparation of SiC. Their setups are similar and comprise the sources (SiC powder and polycrystalline 3C-SiC), transfer media (Ar and liquid Si), produced crystals (the seed and 4H-SiC fine particles) and crucibles (graphite and TaC). The characteristic differences are in the thicknesses and the temperature profiles of the transfer media, as illustrated in the panels on the right-hand side.

between them. The solvent is a very thin layer with a thickness of 30~100 μm . The temperature inside the crucible is held constant.

After holding at the growth temperature of 1800°C for 10 min, the newly grown 4H-SiC layer is observed on the original 4H-SiC single-crystalline plate as shown in Fig. 3 (Nishitani & Kaneko, 2008). The scanning electron microscopy image shows the transverse section of a sample with the sandwiched structure of SiC and Si layers. Because the substrate of 4H-SiC is n-doped, the newly grown 4H-SiC layer is easily distinguished from the original substrate. The feed of polycrystalline 3C-SiC was dense before the operation. Its boundaries dissolve preferentially, and it becomes porous during the operation. The wave dispersion X-ray (WDX) profile of carbon in Fig. 3 shows a concentration of 50% in the SiC layers and almost zero in the Si solvent. Upon reversing the configuration of 3C- and 4H-SiC plates, 4H-SiC grew epitaxially again, which indicates that no unintentional temperature gradient occurs in the crucible; thus, the temperature gradient cannot be the driving force of the solvent movement.

In the case of replacing the single-crystalline 4H-SiC to polycrystalline 3C-SiC in the configuration of Fig. 2b, many fine particles with diameters of 30~300 μm are observed to be produced on the both sides of polycrystalline 3C-SiC source plates, as shown in Fig. 4a. Multifaceted crystals grow like mushrooms and no grain boundaries are observed in them.

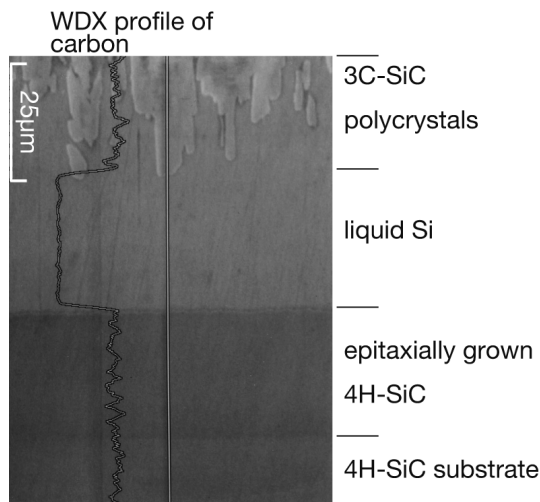


Fig. 3. Scanning electron microscopy image and wave dispersion X-ray (WDX) profile of carbon of epitaxially grown 4H-SiC in the transverse section of a sample with the sandwiched structure of SiC and Si layers(Nishitani & Kaneko, 2008).

Figure 4c shows the Raman spectra of the fine crystalline particles and the polycrystalline 3C-SiC substrate obtained using a 488-nm excitation laser at room temperature. The spectra of the substrate show broad peaks at around 768 cm^{-1} and 797 cm^{-1} , which are typical of 3C-SiC with randomly distributed stacking faults(Rohmfeld et al., 1998-I). On the other hand, the fine particles show a sharp peak at 776 cm^{-1} , which is typical of 4H-SiC. Thus, we conclude that fine single-crystal 4H-SiC particles are crystallized from polycrystalline 3C-SiC in the absence of a temperature gradient. 4H-SiC crystals grow without a temperature gradient nor a concentration difference between sources and products of SiC.

3. Speculated mechanism

3.1 Solution method

The origin of the driving force for crystal growth is the same as that in the case of diamond synthesis from a solvent of a metal-carbon binary system. Both the diamond synthesis method and the proposed method for SiC synthesis are solution growth methods; a typical example of a solution growth method is the method used for the growth of alum crystals, which is very familiar as a topic frequently dealt with in science classes, even in primary schools. Thus, a review of the growth process of alum crystals would be a good starting point for explaining as well as understanding the growth of diamond and SiC crystals. Large alum single crystals can be obtained as follows. First, alum powder is dissolved in hot water. Next, a seed tied to a long thread is inserted into the solution, and the solution is cooled and left to stand. A crystal starts growing from the seed and develops into a large single crystal.

Figure 5a shows schematic representations of the alum deposition process. The upper panel represents the dissolution of alum in water at a high temperature and the lower panel represents the deposition of alum on the seed at a low temperature. In the system shown in Fig. 5b, the source and seed are sandwiching the water solution; a temperature gradient is applied in the water solution. This is the setup in the so-called solvent zone technique,

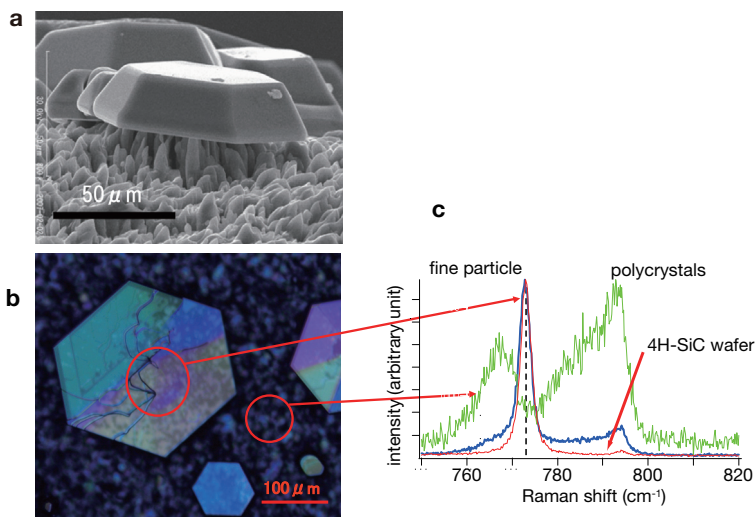


Fig. 4. **a** Side view and **b** top view of fine particles on the polycrystalline 3C-SiC source plate and **c** Raman spectra of the regions in **b** indicated by the circles. **a** is a scanning electron microscopy image and **b** is an optical microscopy image. The spectrum of the single-crystal 4H-SiC wafer is also shown in **c** as a standard.

where dissolution and deposition occur simultaneously. The driving force for crystal growth is supersaturation, which can be schematically explained by considering the solubility limit of alum or the so-called phase diagram of an alum-water system.

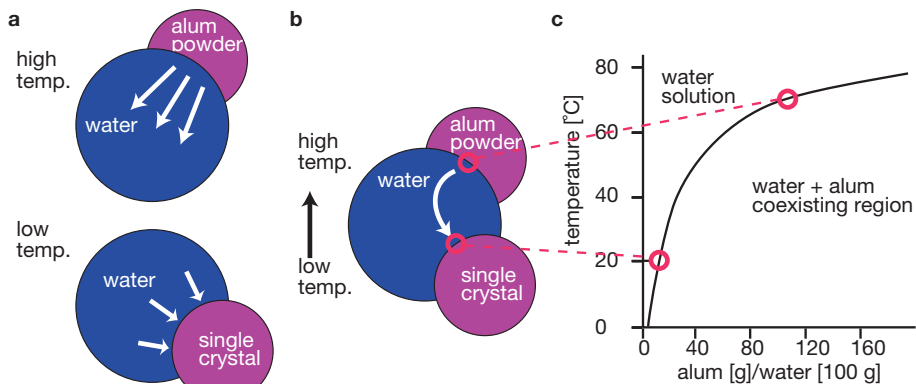


Fig. 5. Schematic drawings of **a** alum deposition and **b** the solvent zone technique in which a temperature gradient is present; **c** the phase diagram of the potassium alum-water system. In **a** and **b**, the vertical positions of the alum powder (source), water (solvent) and single crystal (seed) represent their relative energies or chemical potentials.

The solubility of potassium alum in water is measured as shown in Fig. 5c. The solubility limit, or liquidus of alum, separates the water solution region from the region where water and alum

coexist. As the temperature increases, the solubility limit shifts to higher alum contents. At 80 °C, 321 g of potassium alum dissolves in 100 g of water. Such a solution can be cooled to a temperature where the solubility limit is considerably low, and it is called a supersaturated solution. At lower temperatures around the seed crystal, the small solubility limit facilitates the deposition of alum on the seed crystal. As marked in Fig. 5c, the temperature gradient between the source and the seed alum results in different solubility limits around them; this difference is the driving force for the dissolution and deposition of alum.

3.2 Double phase diagram

Although diamond synthesis in a metal-carbon system at high pressures is slightly complex, it is based on the same mechanism as that of alum deposition. The initial materials used for diamond synthesis in the original General Electric process were graphite and group VIII transition metals (Bonenkirk et al., 1959). At a high pressure and a high temperature, metal melts and comes into contact with graphite. The liquid metal was initially thought to function as a catalyst by the workers at General Electric, but was later clarified to act as a transport medium by Giardini and Tydings (Giardini & Tydings, 1962). Similar to Fig. 5b, a schematic drawing of a diamond synthesis system is shown in Fig. 6a. The liquid metal that is commonly used in diamond synthesis is Ni; the Ni-C phase diagram at 54 Kbar is shown in Fig. 6b (Strong & Hanneman, 1967). Although the graphite phase is the only stable phase at normal pressure, at 54 Kbar, the diamond phase is stable below 1740 K. Liquid Ni coexists with the diamond phase between 1667 K and 1728 K. Thus, the solution growth of diamond from liquid Ni is possible in this temperature range. The true trick in diamond synthesis is not the 'stability' of the diamond phase, but the 'metastability' of the graphite phase, as indicated by the dashed lines in Fig. 6b. The synthetic capsule in high-pressure anvils is small and it is very difficult to manage sensitive temperature gradients. Thus, each process of crystal growth, i.e. the melting of metastable graphite in liquid Ni, carbon transfer within the solvent and crystallization of stable diamond on the seed, occurs in a very small temperature range. The driving forces for these reactions cannot be obtained from the temperature gradient, but can be obtained from the difference in the stability between graphite and diamond. For example in Fig. 6b, at 1700 K, the solubility of metastable graphite in liquid Ni represented by the dashed line is higher than that of stable diamond denoted by the solid line. The driving force for the crystal growth of the alum shown in Fig. 5 is generated when there is a spatial or temporal temperature difference, but that in diamond synthesis can be produced even at a constant temperature.

Figure 6b shows the so-called double phase diagram that is well known in metallurgy, e.g. the Fe-C system (Hansen & Anderko, 1958), and that is commonly observed for the systems containing metastable phases (Ishihara et al., 1984-5). The mechanism of crystal growth in the presence of a solubility difference between the stable and metastable phases, which is discussed in the present study, can be observed in the work of Van Lent (1961) on the transformation of mercury/white tin amalgams to gray tin, and it was first elucidated by Hurler et al. (1967) using the so-called thin alloy zone (TAZ) crystallization.

3.3 Ostwald ripening and concentration profile

The solution growth is easily understood by the phase diagrams, but the simultaneous growth and dissolution processes of polytypes are hardly recognized. Such a puzzling process can be observed in the Ostwald ripening, which is shown schematically in Figs. 7. Ostwald ripening, also called coarsening, which occurs at the late stage of the precipitation,

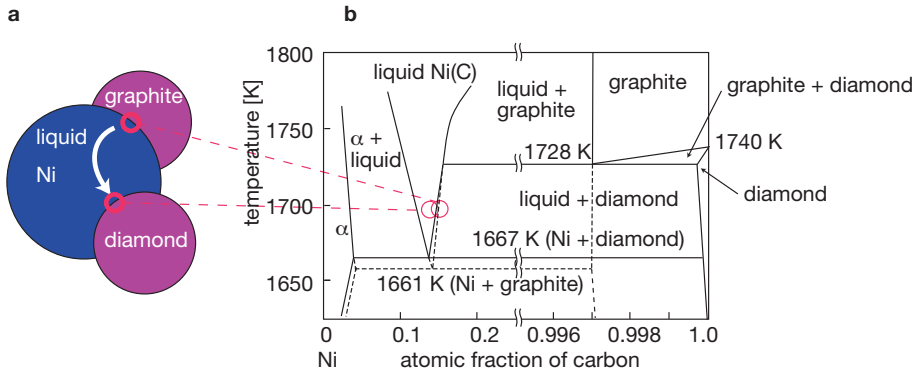


Fig. 6. Schematic drawings of **a** diamond synthesis and **b** enlarged sections of the Ni-C phase diagram at 54 Kbar. In **a**, graphite, liquid Ni and diamond are the source, solvent and seed, respectively. In **b**, the stable Ni-diamond and metastable Ni-graphite reactions are represented by solid and dashed lines, respectively (Strong & Hanneman, 1967).

is driven spontaneously by the diffusion between small (S) and large (L) precipitates due to Gibbs-Thomson effect. In this section, the matrix and precipitate phases are represented as α and β , respectively. The precipitates show the same composition of x_β but different pressures of small and large radii, which makes the different free energies, G_β^s and G_β^L , as shown in free-energy vs. concentration diagram of Fig. 7a. The common tangents of free-energy curves between matrix solution and precipitates show different angles and touch at the different concentrations x_α^L and x_α^S of the free energy curve of the matrix solution. This concentration difference of matrix appears at the interfaces of the precipitates. Fig. 7b shows the schematic diagram of the solute concentration profile of the system of α matrix and small(S) and large(L) β precipitates. The matrix concentration equilibrating with the small precipitates should be higher than that with the large precipitates. This difference drives the solute diffusion and thus the simultaneous growth and dissolution of precipitates.

3.4 Direct melting of metastable phases

Ostwald ripening is the reaction in a solid solutions, which means the life time of metastable phase may be longer at lower temperatures and lower diffusivity. Does such a metastable phase directly melt in liquid?

The typical example of the behavior of the coexistence of stable and metastable phases is observed in the Fe-C system. As mentioned before, the double phase diagram of Fe-C and Fe-Fe₃C systems is well studied and established. The melting behavior of metastable Fe₃C phase has investigated in detail by Okada et al. (1981). They measured the differential thermal analysis (DTA) curves for the white, gray and mixture cast irons at the eutectic temperature and composition region. Fig. 8 shows the summarized results of DTA curves as well as the schematic double phase diagram. The endothermic temperatures shift due to the kinetic reason of the measuring apparatus, but the corrected temperatures show the stable and metastable eutectic temperatures of 1426K and 1416K, respectively. The specimens of gray cast iron contains stable phases of graphite and fcc-Fe(austenite), where they all melt only

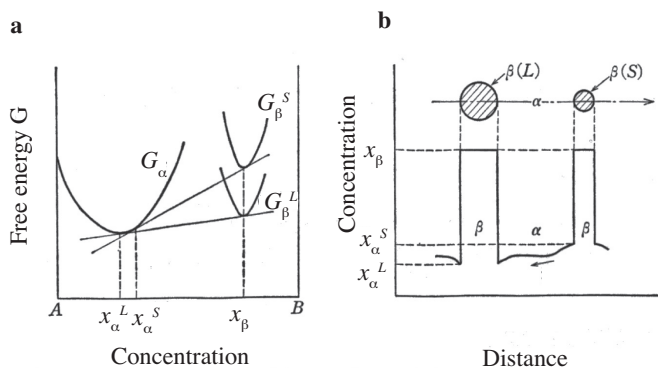


Fig. 7. Schematic drawings of **a** free energy vs. concentration diagram and **b** concentration profile of the Ostwald ripening.

at the stable eutectic temperature of 1426K. On the other hand, the specimens of white cast iron shows the double peaks of endothermic reactions at the slow heating rates. Okada et al. (1981) found that at the first peak the metastable Fe_3C melts but soon graphite solidifies and then remelt at the second peak. At the faster heating rates, only the melting of the metastable Fe_3C phase occurs. For the specimens of mixture cast iron, the reactions are complicated but the melting and solidifying occur simultaneously. These experimental results indicate that the metastable phase is so stable that can melt directly.

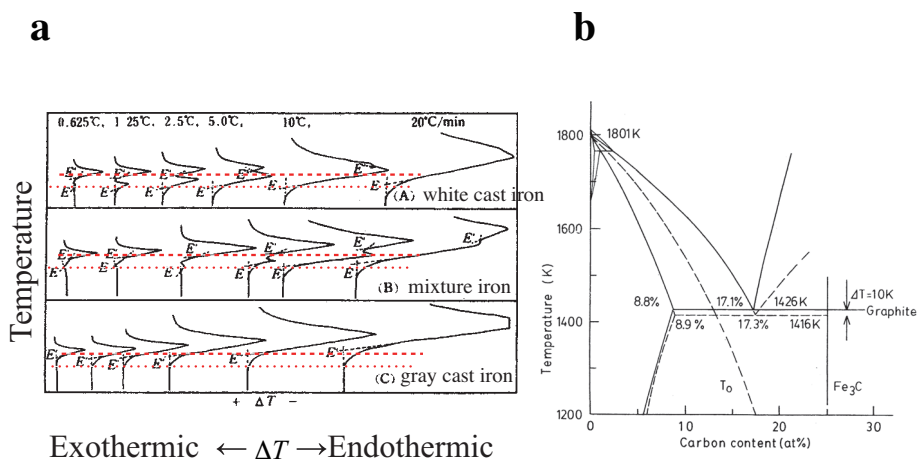


Fig. 8. **a** DTA curves of cast irons (Okada et al., 1981) and **b** the double phase diagram of equilibrium Fe-Graphite and metastable Fe- Fe_3C systems.

3.5 Speculated mechanism

From the experimental result shown in Fig. 4, 4H-SiC is expected to be more stable than 3C-SiC. The Si-C system should show a double phase diagram, as schematically shown in Fig. 9a. The corresponding free-energy vs. concentration diagram is also illustrated in Fig. 9b.

The solubility limit of each phase is determined by the tangent common to the free-energy curves of the coexisting phases. At the temperature indicated by the dotted line, the solubility limit of metastable 3C-SiC is x_1^{3C} , which corresponds to the dashed line of the liquidus in Fig. 9a. The solubility limit of stable 4H-SiC is x_1^{4H} , which corresponds to the solid line of the liquidus. The concentration gradient in the layers consisting of 3C-SiC and 4H-SiC and a very thin layer of liquid Si in between is obtained. The schematic carbon concentration profile in the liquid Si layer is shown in Fig. 9c. The concentration gradient at the metastable solubility limit of 3C-SiC leads to the extraction of C from the source plates. This concentration gradient also causes carbon diffusion across the liquid Si solvent and to the interface of the seed, where C is deposited due to the supersaturation of 4H-SiC. Although the small solubility limit of C in liquid Si, which is the cause of the slow growth of SiC in the conventional liquid method, still remains, the small thickness of the Si solvent in the new method leads to a sufficient concentration gradient for the growth of 4H-SiC crystals.

4. Phase stability of SiC polytypes

4.1 Phase diagram assessment of Si-C system

The key data in order to rationalize this novel process is the phase stability or the hierarchy of SiC polytypes. The reported phase diagrams, however, are somewhat conflicting. The standard data book Chase (1998) shows the standard formation enthalpies for α and β phases, as follows:

$$\Delta_f H(\alpha - \text{SiC}, 298.15\text{K}) = -71.546 \pm 6.3\text{kJ/mol}$$

$$\Delta_f H(\beta - \text{SiC}, 298.15\text{K}) = -73.220 \pm 6.3\text{kJ/mol}.$$

Although the data shows that the β (cubic) phase is more stable than the α (hexagonal) phase at 298.15K, the difference of the measured values are within the measurement errors. The α (hexagonal) phase indicated in Chase (1998) is 6H, but also mentioned that the many polytypes have not been adequately differentiated thermodynamically. The heat capacity and Gibbs free energy are also reported as shown in Fig. 10. The measured values and the adapted functions in Chase (1998) suggest that α (hexagonal) phase is less stable up to 2000K, and they concluded unlikely the transformation to β (cubic) phase at about 2300K.

The most widely adapted phase diagram should be that by Olesinski & Abbaschian (1996) as shown in Fig. 1, where the β (cubic) phase is more stable than the α (hexagonal) phase at any temperatures below the periodic temperature of the decomposition of SiC, 2545°C. Although the evaluators of Olesinski & Abbaschian (1996) mentioned nothing on the types of α (hexagonal) phase, the same authors reported the co-existence of polytypes of α phases, 6H, 15R, and 4H(Olesinski & Abbaschian, 1984). Furthermore, it also mentioned on the report of Verma & Krishna (1966), the existence of α stability above 2000°C. On the other hand, Fromm & Gebhardt (1976) reported the different type of phase diagram as shown in Fig. 11, where the phase transition from β to α phases occurs at around 2000°C.

Solubilities of carbon in liquid silicon measured by Hall (1958), Scace & Slack (1959), Dash (1958), Dolloff (1960), Nozaki et al. (1970), Oden & McCune (1987), Suhara et al. (1989), Kleykamp & Schumacher (1993), Iguchi & Narushima (1993), Ottem (1993), and Yanabe et al. (1997) are summarized as in Figs. 12. Two reported phase diagrams as shown in Fig. 1 and Fig. 11 are based on the data given by Dolloff (1960). Dolloff (1960)'s data, however, are distinctively different from the others, where the solubility limits are larger than the others.

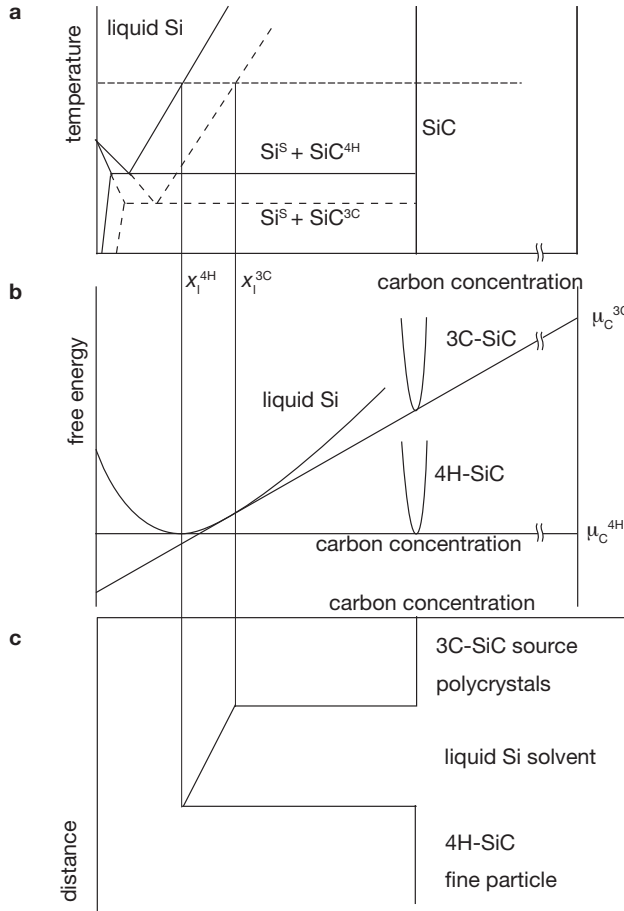


Fig. 9. Schematic drawings of **a** the predicted Si-C double phase diagram, **b** related free-energy vs. concentration diagram and **c** carbon concentration profile in the liquid Si solvent between the 3C-SiC source and the 4H-SiC fine particles. The metastable eutectic temperature of the reaction $\text{liquid Si} \rightarrow \text{Si}^{\text{S}} + \text{SiC}^{3\text{C}}$ is lower than the stable eutectic temperature of the reaction $\text{liquid Si} \rightarrow \text{Si}^{\text{S}} + \text{SiC}^{4\text{H}}$, where Si^{S} denotes solid Si. The chemical potentials of C, μ_c , are given by the intersections of the common tangents with the pure-carbon line in **b**, and are spatially different in the liquid Si solvent contacting with 3C-SiC and 4H-SiC in **c**. The configuration of **c** is related to that of the panel on the left-hand side in Fig. 2b.

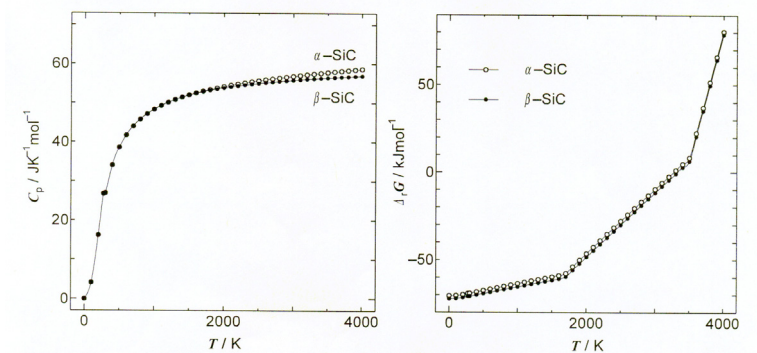


Fig. 10. Heat capacity and Gibbs energy of SiC(Chase, 1998).

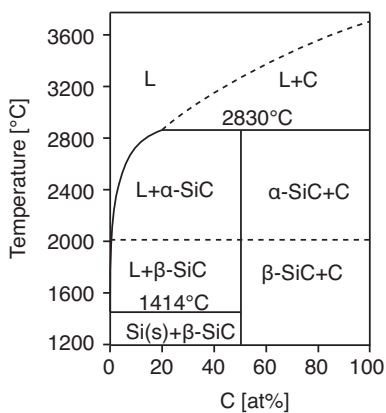


Fig. 11. Phase diagram of Si-C binary system including the phase transition from β to α phase around 2000°C(Fromm & Gebhardt, 1976).

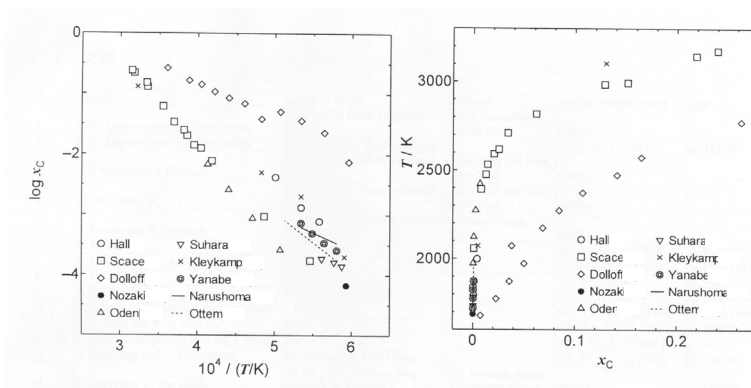


Fig. 12. Solubility of carbon in liquid silicon.

The reported phase stability between α (hexagonal) and β (cubic) might be 6H and 3C. If this assumption is true, 4H stability has not been shown experimentally. Furthermore, the distinct difference of solubility limits indicates that the coexistence of stable and metastable phases.

4.2 Difficulty of the equilibrium state

Although the conflicts of phase diagrams shown above remain, there have been many attempts of experimental and theoretical researches on the kinetic process of crystal growth of SiC polytypes. Famous stability diagrams of SiC polytypes proposed by Knippenberg (1963) and Inomata et al. (1968) show that the crystalized phases are controlled both by the temperature and growth rate of the operations.

The limit to slow growth rate of kinetic processes or results of long period holding should be equal to static results. But it is very difficult to dissolve whole amount of SiC crystals due to small solubility limit of SiC in liquid Si. If there remain seeds of metastable phases during the previous processes, it is difficult to remove all of them. The metastable phase also grows due to the co-existence of less stable phases as shown in Ostwald ripening, or from super-saturated liquid Si. Furthermore, the required high temperature and inert environment make the static conditions very difficult.

Inomata et al. (1969) performed careful experimental observations on the relationship between the polytypes of SiC and the supersaturation of the solution at 1800°C with the solution method, and have shown the following results;

1. β -SiC crystallizes from highly supersaturated solution. The crystals obtained at the condition of low supersaturation, however, consist of mainly α -SiC such as 4H, 15R and 6H.
2. Relative amount of 4H increased markedly with decreasing the supersaturation.
3. From the results stated above, it is concluded that 4H is the most stable structure at 1800°C among the basic polytypes of SiC, 3C, 4H, 15R and 6H.

Those results indicate that the difference between 4H and 6H is crucial for determining the hierarchy of SiC polytypes.

Izhevskiy et al. (2000) summarized not only the kinetic observations, but also pointed out the impurity effects, especially nitrogen affects the transformations among 6H, 3C and 4H SiCs. Not only through the contamination of the higher temperature operations, but also from the starting materials made by Acheson method, specimens contain non-negligible nitrogen. Very recent improvements on materials and apparatuses make it possible to avoid nitrogen inclusions and get the hierarchy of pure SiC polytypes experimentally soon.

4.3 First principles calculations

For some cases of hardly measuring experimental value, the first principles calculations give some hints of the puzzles, and have been applied on the topic of the hierarchy of SiC polytypes. Liu & Ni (2005) have summarized the results of the first principles calculations of SiC. All calculations show that β -SiC is less stable than α -SiCs of 2H, 4H and 6H. The hierarchy between 4H and 6H is subtle; two of nine calculations shows that 6H SiC is most stable, but the majority of the results indicates that 4H SiC is most stable. Of course the calculating results should be judged by the precisions, the energy differences, however, are too small from 0.2 to 2 meV/Si-C pair to identify. Although the reliability of the first principles calculations of the hierarchy of SiC polytypes are insufficient, it is important that the calculating results show against the experimental results. Those are ground state results, which means that is

only reliable at low temperatures. For including the finite temperature effect, the vibrational entropy effect is crucial, because the configurational entropies should be similar among these SiC polytypes due to the similar local configurations of tetrahedrons. One calculating result including the vibrational effect is shown by Nishitani et al. (2009) as in Fig. 13.

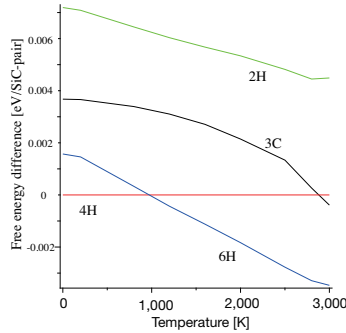


Fig. 13. First principles calculations of temperature dependency of free energy difference of 6H, 3C, and 2H against 4H SiC (Nishitani et al., 2009). Finite temperature effects are included through the vibrational free energy calculated by Phonon codes (Medea-phonon, n.d.; Parlinski et al., 1997).

These first principles calculations were carried out using the Vienna Ab initio Simulation Package (VASP) code (Kresse & Furthmüller, 1996a;b; Kresse & Hafner, 1993; 1994). The interaction between the ions and valence electrons was described by a projector augmented-wave (PAW) method (Kresse & Joubert, 1999). A plane-wave basis set with a cutoff of 400 eV was used. The exchange-correlation functional was described by the generalized gradient approximation (GGA) of the Perdew-Wang91 form (Perdew & Wang, 1992). Phonon calculation was performed by a commercial pre-processor of Medea-phonon (Medea-phonon, n.d.) with the direct method developed by Parlinski et al. (1997). The volumes and/or c/a ratios were fitted to the most stable point at each temperature.

Fig. 13 shows the temperature dependencies of free energy of 6H, 3C, and 2H SiC polytypes measured from 4H SiC. 4H SiC is most stable at low temperatures, but 6H SiC is most stable at higher temperatures. 3C SiC is less stable against 4H or 6H SiC except at very high temperature region. Those results are consistent with the other speculations but the precisions of the calculations are not enough. Although the more precise calculations will alter the results of hierarchy of polytypes, their result pointed out the possibility of the phase transition in the Si-C system from the first principles calculations.

5. Conclusions

We have utilized a new method for manufacturing SiC from liquid Si; in this method, single crystals of 4H-SiC are obtained from polycrystalline 3C-SiC source in the absence of a temperature gradient. The origin of the driving force for crystal growth is the same as that in the case of diamond synthesis from a metal-carbon solvent, and it is elucidated by considering the stable-metastable double phase diagrams. This similarity in the growth mechanism indicates that the methods developed for diamond synthesis can be directly used for growing large-size SiC crystals from a metastable solvent of Si.

6. References

- Acheson, A. G. (1896). Production of artificial crystalline carbonaceous materials, *U.S. Patent Number 492767*.
- Bonenkirk, H. P., Bundy, F. P., Hall, H. T., Strong, H. M. & Wentorf, R. H. (1959). Preparation of diamond, *Nature* 184: 1094–1098.
- Casady, J. B. & Johnson, R. W. (1996). Status of silicon carbide (SiC) as a wide-bandgap semiconductor for high-temperature applications: A review, *Solid-State Electronics* 39: 1409–1422.
- Chase, M. W. J. (1998). *NIST-JANAF Thermochemical Tables, 4th ed.*, ACS, AIP and NIST, New York, pp. 648–9.
- Chaussende, D., Wellmann, P. J. & Pons, M. (2007). Status of SiC bulk growth processes, *J. Phys. D: Appl. Phys.* 40: 6150–6158.
- Cited from Choyke, W. J. (1960). *Silicon carbide — a high temperature semiconductor*, Pergamon Press, Oxford, p. xviii.
- Dash, W. C. (1958). Silicon crystals free of dislocations, *J. Appl. Phys.* 29: 736.
- Dolloff, R. T. (1960). *WADD Tech. Report 60-143*: 1–22.
- Fromm, E. & Gebhardt, E. (1976). *Gase und Kohlenstoff in Metallen, II Daten*, Springer-Verlag, pp. 730–33.
- Giardini, A. A. & Tydings, J. E. (1962). Diamond synthesis: Observations on the mechanism of formation, *American Mineralogist* 47: 1393–1421.
- Hall, R. N. (1958). Electrical contacts to silicon carbide, *J. Appl. Phys.* 29(6): 914–917.
- Hansen, M. & Anderko, K. (1958). *Constitution of binary alloys, 2nd Ed.*, McGraw-Hill, New York, pp. 353–365.
- Hofmann, D. H. & Müller, M. H. (1999). Prospects of the use of liquid phase techniques for the growth of bulk silicon carbide crystals, *Mater. Sci. and Eng. B* 61-62: 29–39.
- Hurle, D. T. J., Mullin, J. B. & Pike, E. R. (1967). Thin alloy zone crystallisation, *J. Mater. Sci.* 2: 46–62.
- Iguchi, Y. & Narushima, T. (1993). *1st. Int. Conf. on Processing Materials for Properties*, The Minerals, Metals & Materials Society, pp. 437–440.
- Inomata, Y., Inona, A., Mitomo, M. & Sudzuki, H. (1968). Relation between growth temperature and the structure of SiC crystals grown by sublimation method, *Yogyo-Kyokai-Shi* 76(9): 313–319.
- Inomata, Y., Inoue, Z., Mitomo, M. & Tanaka, H. (1969). Polytypes of SiC crystals grown from molten silicon, *Yogyo-Kyokai-Shi* 77(3): 83–88.
- Ishihara, K. N., Nishitani, S. R., Miyake, H. & Shingu, P. H. (1984-5). Rapid solidification and the metastable phase diagrams of the Fe-C, Co-C and Ni-C systems, *Int. J. Rapid Solidification* 1: 51–58.
- Izhevskiy, V. A., Genova, L. A., Bressiani, J. C. & Bressiani, A. H. A. (2000). Review article: silicon carbide. structure, properties and processing, *Cerâmica* 46: 4 – 13.
- Kleykamp, H. & Schumacher, G. (1993). The constitution of the silicon-carbon system, *Ber. Bunsenges. Phys. Chem.* 97(6): 799–805.
- Knippenberg, W. F. (1963). Growth phenomena in silicon carbide, *Philips Research Reports* 18: 161–274.
- Kresse, G. & Furthmüller, J. (1996a). Efficiency of ab-initio total energy calculations for metals and semiconductors using a plane-wave basis set, *Comput. Mat. Sci.* 6: 15–50.
- Kresse, G. & Furthmüller, J. (1996b). Efficient iterative schemes for ab initio total-energy calculations using a plane-wave basis set, *Phys. Rev. B* 54(16): 11169–11186.

- Kresse, G. & Hafner, J. (1993). Abinitio molecular-dynamics for liquid-metals, *Phys. Rev. B* 47(1): 558–561.
- Kresse, G. & Hafner, J. (1994). Ab-initio molecular-dynamics simulation of the liquid-metal amorphous-semiconductor transition in germanium, *Phys. Rev. B* 49(20): 14251–14269.
- Kresse, G. & Joubert, D. (1999). From ultrasoft pseudopotentials to the projector augmented-wave method, *Phys. Rev. B* 59(3): 1758–1775.
- Liu, Z. & Ni, J. (2005). Layered growth modelling of epitaxial growth processes for SiC polytypes, *J. Phys.: Condens. Matter* 17: 5355–5366.
- Madar, R. (2004). Silicon carbide in contention, *Nature* 430: 974–975.
- Medea-phonon (n.d.). <http://www.materialsdesign.com/medea-phonon.htm>.
- Nakamura, D., Gunjishima, I., Yamaguchi, S., Ito, T., Okamoto, A., Kondo, H., Onda, S. & Takatori, K. (2004). Ultra high-quality silicon carbide single crystals, *Nature* 430: 1009–1012.
- Nishitani, S. R. & Kaneko, T. (2008). Metastable solvent epitaxy of SiC, *J. Crystal Growth* 210: 1815–1818.
- Nishitani, S. R., Takeda, R., Ishii, H., Yamamoto, Y. & Kaneko, T. (2009). First principles calculations of vibrational free energy estimated by the quasi-harmonic approximation, *J. Japan Inst. Metals* 72(9): 566–70.
- Nozaki, T., Yatsurugi, Y. & Akiyama, N. (1970). Concentration and behavior of carbon in semiconductor silicon, *J. Electrochem. Soc.* 117(12): 1566–1568.
- Oden, L. L. & McCune, R. A. (1987). Phase-equilibria in the al-si-c system, *Metall. Trans. A* 18A(12): 2005–2014.
- Okada, A., Miyake, H. & Ozaki, R. (1981). Structural changes of cast iron during heating at constant rate in the region of eutectic temperature and differential thermal analysis, *J. Jpn. Foundrymen's Soc.* 53(1): 9–14.
- Olesinski, R. W. & Abbaschian, G. J. (1984). The c-si(carbon-silicon) system, *Bulletin of Alloy Phase Diagrams* 5(5): 486–489.
- Olesinski, R. W. & Abbaschian, G. J. (1996). *Binary Alloy Phase Diagrams, 2nd ed.*, ASM International, Materials Park, Ohio, pp. 882–3.
- Ottem, L. (1993). *SINTEF Report STF34 F93027*.
- Parlinski, K., Li, Z. Q. & Kawazoe, Y. (1997). First-principles determination of the soft mode in cubic ZrO_2 , *Phys. Rev. Lett.* 78(21): 4063 – 4066.
- Perdew, J. P. & Wang, Y. (1992). Accurate and simple analytic representation of the electron-gas correlation-energy, *Phys. Rev. B* 45(23): 13244–13249.
- Rohmfeld, S., Hundhausen, M. & Ley, L. (1998-I). Raman scattering in polycrystalline 3C-SiC: Influence of stacking faults, *Phys. Rev. B* 58: 9858–9862.
- Scace, R. I. & Slack, G. A. (1959). *J. Chem. Phys.* 30(6): 1551–1555.
- Strong, H. M. & Hanneman, R. E. (1967). Crystallization of diamond and graphite, *J. Chem. Phys.* 46: 3668–3676.
- Suhara, S., Yuge, N., Fukai, M. & Aratani, F. (1989). *ZAIRYO TO PROCESS (Materials and Processes)* 2(4): 1341.
- Tairov, Y. M. & Tsvetkov, V. F. (1978). Investigation of growth processes of ingots of silicon carbide single crystals, *J. Cryst. Growth* 43: 209–212.
- Van Lent, P. H. (1961). The position of gray tin in the tin-mercury system, *Acta Metallurgica* 9: 125–128.

- Verma, A. R. & Krishna, P. (1966). *Polymorphism and polytypism in Crystal*, John Wiley and Sons, New York.
- Wesch, W. (1996). Silicon carbide: Synthesis and processing, *Nuclear Inst. Methods Phys. Res. B* 116: 305–321.
- Yanabe, K., Akasaka, M., Takeuchi, M., Watanabe, M., Narushima, T. & Iguchi, Y. (1997). *Materials Trans. JIM* 38(11): 990–994.

The Formation of Silicon Carbide in the SiC_x Layers (x = 0.03–1.4) Formed by Multiple Implantation of C Ions in Si

Kair Kh. Nussupov and Nurzhan B. Beisenkhanov
*Kazakh-British Technical University
 Kazakhstan*

1. Introduction

Promising application of thin-film technology is the synthesis of SiC, possessing such valuable properties as high hardness (33400 Mn/m²), chemical resistance, high melting point (2830°C), wide bandgap (2.3–3.3 eV), etc (Lindner, 2003). Unfortunately, since it is still difficult to grow SiC material of crystalline quality to meet requirements for a large scale industrial application, small-size and high-cost SiC wafers severely limit their applications at present (Liangdeng et al., 2008). Doped with different impurities, silicon carbide is used in semiconductor technology (Yan et al., 2000; Chen et al., 2003). Field-effect transistors, diodes and other electronic devices based on SiC have several advantages compared to similar silicon devices. Among them, the opportunity to work at temperatures up to 600°C, high speed and high radiation resistance. A large number of polytypes of SiC makes it possible to create heteropolytype structures (Lebedev et al., 2001, 2002a, 2005) to form a defect-free, near-perfect contacts with unusual electronic properties (Fissel et al., 2001; Lebedev et al., 2002b; Semenov et al., 2010). Diode structures have been established (Lebedev et al., 2002b), in which the value of uncompensated donors $N_d - N_a$ was $(1.7-2) \times 10^{17} \text{ cm}^{-3}$ in the layer (n) 6H-SiC and acceptors $N_a - N_d \sim 3 \times 10^{18} \text{ cm}^{-3}$ in the layer (p) 3C-SiC. In the spectrum of the electroluminescence of diodes revealed two bands with maxima $h\nu_{\text{max}} \approx 2.9 \text{ eV}$ (430 nm) and 2.3 eV (540 nm), close the band gaps of 6H- and 3C-SiC. Currently, using the methods of vacuum sublimation (Savkina et al., 2000), molecular beam epitaxy (Fissel et al., 1996), the epitaxial and heteropolytype layers based on the cubic 3C-SiC and two hexagonal 6H-SiC, 4H-SiC on substrates of SiC, are grown. By chemical vapor deposition (CVD) (Nishino et al., 2002) are grown heteroepitaxial layers of 3C-SiC on substrates of Si. At the temperatures below 1200°C there are conditions for the growth of both poly- and nanocrystalline SiC with different degrees of crystallinity and structure of the cubic polytype 3C-SiC. Such conditions were realized in the magnetron sputtering (Kerdiles et al., 2000; Sun et al., 1998), laser ablation (Spillman et al., 2000) and plasma deposition (Liao et al., 2005), plasma-enhanced chemical vapor deposition (George et al., 2002; Pajagopalan et al., 2005), molecular beam epitaxy (Fissel et al., 2000). At temperatures below 1500°C in the direct deposition of carbon and silicon ions with an energy of $\sim 100 \text{ eV}$, the growth of nanocrystalline films with a consistent set of the polytypes 3C, 21R, 27R, 51R, 6H is possible (Semenov et al., 2008, 2009, 2010). Photoluminescence spectrum from the front surface of the nanocrystalline film

containing cubic 3C and rhombohedral 21R, has a band emission with three peaks at 2.65, 2.83, 2.997 eV (469, 439, 415 nm), the shoulder of 2.43 eV (511 nm) and a weak peak at 3.366 eV (369 nm) (Semenov et al., 2010).

Of particular interest is the synthesis of SiC layers in silicon by ion implantation (Lindner, 2003; Liangdeng et al., 2008; Kimura et al., 1982, 1984) due to the possibilities to obtain the films of a given thickness and composition, nanolayers of chemical compounds and multilayer structures, as well as the insulating layers in the manufacture of integrated circuits. Silicon structures with a hidden layer of silicon carbide can be used as a SOI-structure (silicon-on-insulator), which have advantages over structures with a hidden layer of SiO₂, obtained by the SIMOX (Separation by IMplantation of OXYgen). Crystalline films of high-quality β -SiC on SiO₂ can be obtained by multiple ion implantation of C in Si and selective oxidation of the top layer of Si (Serre et al., 1999).

High-dose carbon implantation into silicon in combination with subsequent or in situ thermal annealing has been shown to be able to form polycrystalline or epitaxial cubic SiC (β -SiC) layers in silicon (Liangdeng et al., 2008; Kantor et al., 1997; Durupt et al., 1980; Calcagno et al., 1996). To create a SiC-Si heterojunctions were among the first used the method of ion implantation the authors of (Borders et al., 1971; Baranova et al., 1971), in which the synthesis of silicon carbide was carried out by implantation of ¹²C⁺ ions ($E = 200$ кэВ, $D = \sim 10^{17}$ см⁻² (Borders et al., 1971) or $E = 40$ кэВ, $D > 10^{17}$ ион/см² (Baranova et al., 1971)) into a silicon substrate. From the position of the IR absorption band (700–725 см⁻¹), reducing its half-width after annealing and displacement in the region at 800 см⁻¹, corresponding to transverse optical phonons of SiC, it was found that the formation of crystalline SiC phase occurs in the temperature range near 850°C (Borders et al., 1971) and 900°C (Baranova et al., 1971). Silicon carbide was identified using transverse optical phonon spectra in most of the above work on ion implantation, as well as in (Gerasimenko et al., 1974, Wong et al., 1998, Akimchenko et al., 1977a, 1980; Chen et al., 1999, Kimura et al., 1981). The detection of longitudinal optical vibrations of lattice atoms (LO phonons) and their changes during film annealing give additional information on the crystallization processes (Akimchenko et al., 1977b, 1979).

Difficulties associated with the problem of synthesis of a crystalline silicon carbide prevent the wide use of SiC in microelectronics. The Si-C mixture, after implantation of large doses of carbon, is assumed to be amorphous (Lindner, 2003; Liangdeng et al., 2008; Kimura et al., 1981). Carbon atom diffusion in the implanted layer is restricted by the strong Si-C bonds (Liangdeng et al., 2008). A negative influence of stable C- and C-Si-clusters (Yan et al., 2000, Chen et al., 2003; Kimura et al., 1982, 1984; Durupt et al., 1980, Calcagno et al., 1996; Borders et al., 1971) on the crystallization of SiC in the implanted silicon layers with different concentration of the implanted carbon, was found. Heat treatment up to 1200°C does not lead to complete disintegration of the clusters and the release of C and Si atoms to form the Si-C-bonds with tetrahedral orientation which is characteristic of the crystalline SiC phase (Khokhlov et al., 1987). However intensively developing area is the formation in SiO₂ by ion implantation of nanostructured systems with inclusions of nanocrystals and clusters of Si, SiC and C, providing the expense of size effects luminescence virtually the entire visible spectrum (Zhao et al., 1998; Tetelbaum et al., 2009; Perez-Rodriguez et al., 2003; Gonzalez-Varona et al., 2000; Belov et al., 2010). This makes it necessary to study the mechanisms of formation of nanocrystals Si, SiC, carbon nanoclusters and amorphous SiC precipitates during the implantation and

annealing. It is of considerable interest to study the effect of the concentration component, nanoclusters, the phase composition of SiC films and their heat or plasma treatment on the crystallization processes and clustering, the size of nanocrystals and, consequently, the physical properties of the films.

A number of studies have shown that the implantation of ions with multiple different energies is the most suitable for obtaining a uniform layer of carbon and silicon atoms to form SiC (Liangdeng et al., 2008, Calcagno et al., 1996, Srikanth et al., 1988, Rothmund&Fritzsche, 1974, Reeson et al., 1990, Lindner et al., 1996; Martin et al., 1990). By carefully selecting the values of implantation energy and corresponding doses of carbon ions, a rectangular carbon concentration profile can be achieved for the buried β -SiC layer using this approach.

Implantation of carbon ions at temperatures of silicon substrate well above room temperature by in-situ annealing helps to form SiC crystalline layers immediately during implantation or after annealing at lower temperatures (Durupt et al., 1980; Frangis et al., 1997; Edelman et al., 1976; Simon et al., 1996; Preckwinkel et al., 1996). High temperature of the substrate can be achieved also by using beams with high current density of carbon ions (Reeson et al., 1990; Alexandrov et al., 1986). Treatment of carbon implanted silicon layers by power ion (Liangdeng et al., 2008; Bayazitov et al., 2003), electron (Theodossiu et al., 1999) or laser (Bayazitov et al., 2003a, 2003b) beams like thermal annealing also leads to the formation of a polycrystalline β -SiC layer.

In this paper, the composition and structure of homogeneous SiC_{1.4}, SiC_{0.95}, SiC_{0.7}, SiC_{0.4}, SiC_{0.12} and SiC_{0.03} layers, received by multiple high-dose implantation of carbon ions with energies of 40, 20, 10, 5 and 3 keV are investigated. The influence of decay of carbon- and carbon-silicon clusters during thermal annealing or hydrogen glow discharge plasma processing on the formation of tetrahedral Si-C-bonds and crystallization processes in silicon layers with high and low concentrations of carbon, is studied.

2. Experimental

Single-crystal (100) silicon wafers of sizes 7×12×0.4 mm³ with an electrical resistivity 4–5 Ω -cm were implanted by ¹²C⁺ ions with energies of 40, 20, 10, 5, and 3 keV at room temperature in vacuum reached by fully oil-free pumping. To prevent sample heating, the ion current density was kept below 4 μ A/cm².

The SiC_x films structure was investigated by X-ray diffraction using a narrow collimated (0.05×1.5 mm²) monochromatic (CuK α) X-ray beam directed at an angle of 5° to the sample surface. The average crystallite size was estimated from the width of X-rays lines by Jones method. The surface of the layers was analyzed by Atomic force microscopy (JSPM 5200, Jeol, Japan) using AFM AC technique. The investigation of morphology and structure of the SiC_x layers was carried out by transmission electron microscopy (JEM-100CX, JEOL, Japan). The IR transmission spectra were recorded in differential regime on double-beam infrared spectrometer UR-20 (400–5000 cm⁻¹). The spectra both at perpendicular incidence of infrared rays on the sample surface and at an angle of 73° with respect to the normal to the sample surface were measured. The composition of the layers was examined by Auger electron spectroscopy. The parameters were as follows: incident electron beam of diameter 1 μ m, energy 10 keV, angle of incidence 45°, diameter of scanning region 300 μ m, vacuum 1.33 ×10⁻⁸ Pa, angle of Ar⁺ beam incidence 45°.

The glow discharge hydrogen plasma was generated at a pressure of 6.5 Pa with a capacitive coupled radio frequency (r.f.) power (27.12 MHz) of about 12.5 W. The temperature of processing did not exceed 100°C and it was measured by thermocouple. The processing time was 5 min.

3. Results and discussion

3.1 Depth profiles of multiple-energy implanted carbon in Si

To produce a rectangular profile of the distribution of carbon atoms in silicon five energies and doses have been chosen in such a way (Table 1) that the concentration ratio of C and Si atoms to a depth (up to ~120 nm) was equal to the values of $N_C/N_{Si} = 1.0, 0.8, 0.5, 0.3, 0.1$ and 0.03 . The calculated profiles N_C (Burenkov) are the sums of the distributions (Figs. 1 and 2), constructed for the chosen values of energies (E) and doses (D) of carbon ions using the values of the ion mean projective range, $R_p(E)$, and the root-mean-square deviation, $\Delta R_p(E)$, (Table 1) and moment $S_k(E_0)$, according to Burenkov et al. (1985). On these figures are presented the calculated profiles N_C (Gibbons), which are the sums of Gaussian distributions constructed by using values of $R_p(E)$ and $\Delta R_p(E)$ according to Gibbons et al. (1975) (LSS):

$$N(x) = \frac{D}{\Delta R_p(2\pi)^{1/2}} \exp\left[-\frac{(x - R_p)^2}{2\Delta R_p^2}\right], \quad (1)$$

where x is the distance from the surface.

Figs. 1 and 2 also show the experimental profiles $N_C(20^\circ\text{C})$, $N_C(1250^\circ\text{C})$ and $N_O(1250^\circ\text{C})$, obtained by Auger electron spectroscopy, which show the concentration ratio of carbon and oxygen atoms (N_C/N_{Si} and N_O/N_{Si}) over the sample depth after implantation and annealing at 1250°C for 30 min in an argon atmosphere with low oxygen content. Fig. 1 shows that the average concentrations of carbon and oxygen were: a) $N_C/N_{Si} = 1.4$ and $N_O/N_{Si} \approx 2.6$; b) $N_C/N_{Si} = 0.95$ and $N_O/N_{Si} \approx 2.33$; c) $N_C/N_{Si} = 0.7$ and $N_O/N_{Si} \approx 3.0$; and as follows from Fig. 2: a) $N_C/N_{Si} = 0.4$; b) $N_C/N_{Si} = 0.12$.

Thus, the average carbon concentration over the depth exceeded the corresponding calculated values ($N_C/N_{Si} = 0.1; 0.3; 0.5; 0.8$ and 1.0) and led to the formation of layers $SiC_{0.12}$, $SiC_{0.4}$, $SiC_{0.7}$, $SiC_{0.95}$ and $SiC_{1.4}$ (Table 2). The average value of the ratio of N_O/N_{Si} exceeded the stoichiometric value for SiO_2 ($N_O/N_{Si} = 2$), indicating on the saturation of the surface layer by oxygen. In high-temperature annealing a desorption of carbon atoms from the surface and an adsorption of oxygen atoms are occurred. There are clear interfaces $SiO_{3.0}:SiC_{0.7}$, $SiO_{2.33}:SiC_{0.95}$ and $SiO_{2.6}:SiC_{1.4}$ suggesting the interconnectedness of these processes. The mechanism of desorption of carbon may be associated with a diffusion process along the grain boundaries of counter flow of oxygen molecules O_2 into deep layer and molecules of CO and CO_2 from the layer toward the surface.

Penetration of oxygen deep into the implanted layer until the substrate was also shown in (Chen et al., 2003). The mechanism of instability of silicon carbide films during high-temperature annealing in the presence of oxygen is of special interest (Singh et al., 2002).

Process can occur in accordance with the expression $2SiC + 3O_2 \xrightarrow{950-1700^\circ\text{C}} 2SiO_2 + 2CO$.

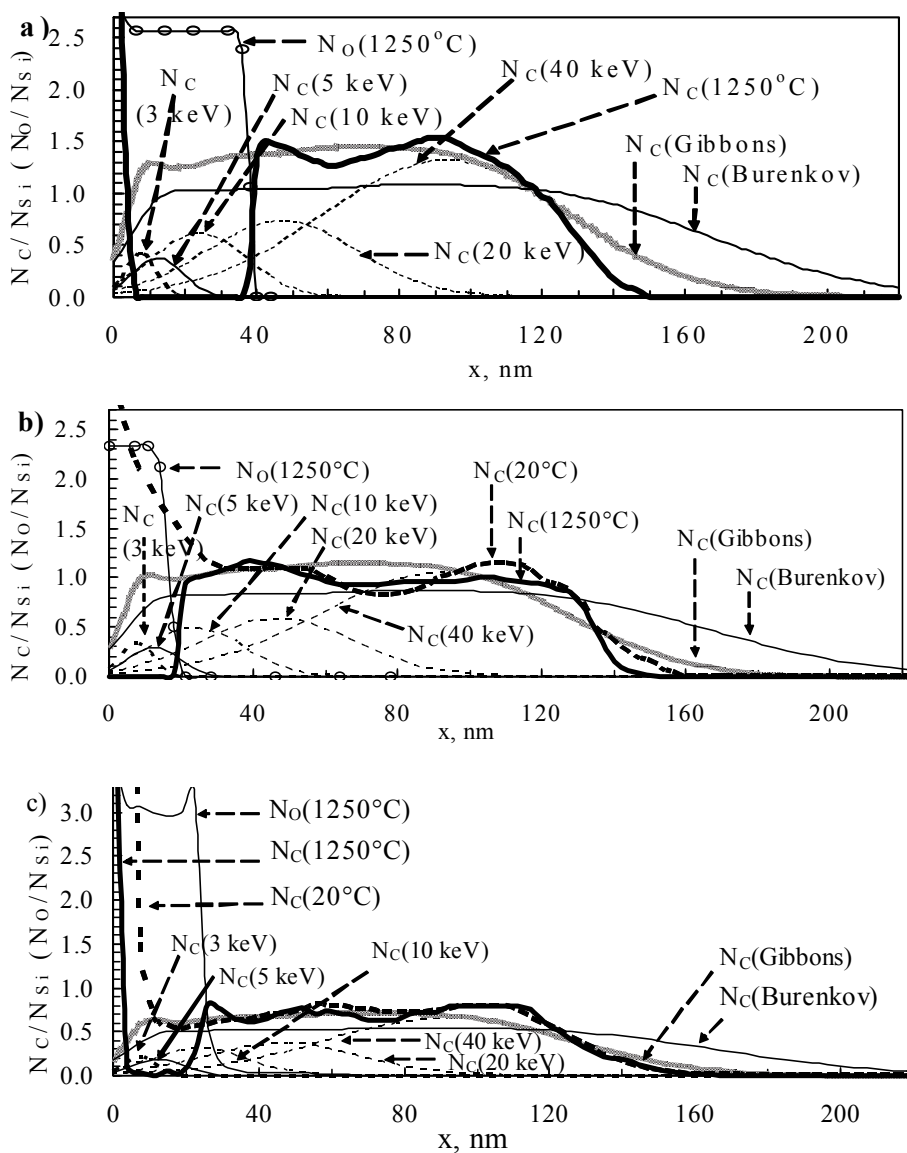


Fig. 1. ^{12}C distribution profiles in Si produced by ion implantation (see table 1). (a) $\text{SiC}_{1.4}$; (b) $\text{SiC}_{0.95}$; (c) $\text{SiC}_{0.7}$. $N_c(\text{Burenkov})$ and $N_c(\text{Gibbons})$ are the profiles calculated according to Burenkov et al. (1985) and Gibbons et al. (1975), respectively, where $N_c(\text{Gibbons}) = N_c(40 \text{ keV}) + N_c(20 \text{ keV}) + N_c(10 \text{ keV}) + N_c(5 \text{ keV}) + N_c(3 \text{ keV})$. $N_c(20^\circ\text{C})$, $N_c(1250^\circ\text{C})$ and $N_o(1250^\circ\text{C})$ are the Auger profiles of carbon and oxygen, respectively, in a layer after high-dose implantation and annealing at $T = 1250^\circ\text{C}$ for 30 min.

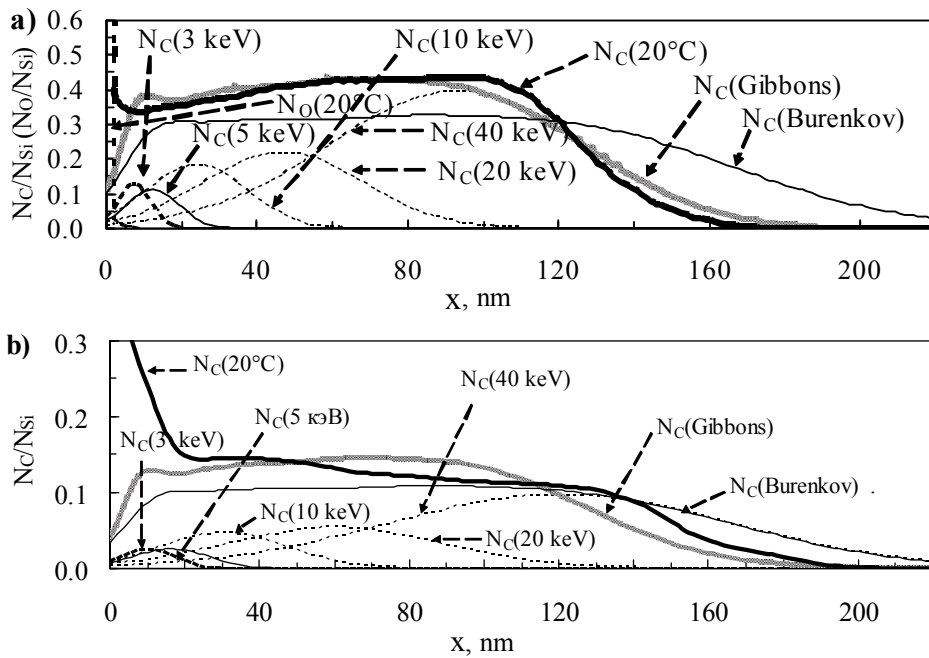


Fig. 2. ^{12}C distribution profiles in Si produced by ion implantation (see table 1). (a) $SiC_{0.4}$; (b) $SiC_{0.12}$. $N_C(\text{Burenkov})$ and $N_C(\text{Gibbons})$ are the profiles calculated according to Burenkov et al. (1985) and Gibbons et al. (1975), respectively, where $N_C(\text{Gibbons}) = N_C(40\text{ keV}) + N_C(20\text{ keV}) + N_C(10\text{ keV}) + N_C(5\text{ keV}) + N_C(3\text{ keV})$. $N_C(20^\circ C)$ and $N_O(20^\circ C)$ are the Auger profiles of carbon and oxygen, respectively, in a layer after high-dose implantation.

E, keV		40	20	10	5	3
$D(SiC_{1.0}), 10^{17}\text{ cm}^{-2}$		5.60	1.92	0.990	0.330	0.230
$D(SiC_{0.8}), 10^{17}\text{ cm}^{-2}$		4.48	1.54	0.792	0.264	0.184
$D(SiC_{0.5}), 10^{17}\text{ cm}^{-2}$		2.80	0.96	0.495	0.165	0.115
$D(SiC_{0.3}), 10^{17}\text{ cm}^{-2}$		1.68	0.576	0.297	0.099	0.069
$D(SiC_{0.1}), 10^{17}\text{ cm}^{-2}$		0.56	0.192	0.099	0.033	0.023
$D(SiC_{0.03}), 10^{17}\text{ cm}^{-2}$		0.168	0.058	0.030	0.010	0.007
N _C (Burenkov) profile (Burenkov et al., 1985)	$R_p(E)$, nm	120.4	60.0	30.3	16.1	10.5
	$\Delta R_p(E)$, nm	46.0	28.3	16.9	10.2	7.2
N _C (Gibbons) profile (Gibbons et al., 1975)	$R_p(E)$, nm	93.0	47.0	24.0	12.3	7.5
	$\Delta R_p(E)$, nm	34.0	21.0	13.0	7.00	4.3

Table 1. Values of energy, E , dose, D , projected range, $R_p(E)$, and straggling, $\Delta R_p(E)$, for $^{12}C^+$ ions in Si, used for constructing a rectangular distribution profile

In (Mandal et al., 2001) reported 100% conversion of SiC into SiO₂ in accordance with the expression of $\text{SiC} + \text{O}_2 = \text{SiO}_2 + \text{CO/CO}_2$.

In the case of high concentrations of carbon (SiC_{1.4}, SiC_{0.95}, SiC_{0.7} and SiC_{0.4}) the experimentally obtained profiles of the carbon atoms were almost rectangular (Figs. 1 and 2) and close in concentration value to the calculated concentration profile according Gibbons et al. (1975), while for layers with low carbon concentration SiC_{0.12} is closer to the calculated profile according Burenkov et al. (1985) (Fig. 2). Factors contributing to the excess concentration of carbon in the surface silicon layer in comparison with the calculated values by (Burenkov et al., 1985) at high-dose ¹²C ion implantation can be considered sputtering the surface in conjunction with a decrease in the values of R_p due to the presence of strong Si-C- and C-clusters, double and triple Si-C- and C-C-bonds.

Depth range, nm	40–110	20–120	25–120	10–120	20–120
SiC _x (Burenkov)	SiC _{1.0}	SiC _{0.8}	SiC _{0.5}	SiC _{0.3}	SiC _{0.1}
SiC _x (Gibbons)	SiC _{1.38}	SiC _{1.06}	SiC _{0.67}	SiC _{0.40}	SiC _{0.13}
SiC _x (AES)	SiC _{1.4}	SiC _{0.95}	SiC _{0.7}	SiC _{0.4}	SiC _{0.12}

Table 2. Average values of carbon concentration $x = N_C/N_{\text{Si}}$ in the SiC_x layers calculated according Burenkov et al. (1985) and Gibbons et al. (1975) and experimentally obtained by Auger electron spectroscopy

3.2 Investigation of the structure by electron microscopy

By transmission electron microscopy structural features of the SiC_{1.4}, SiC_{0.95} and SiC_{0.7} films, formed in the surface layer of single crystal Si wafers using multiple ion implantation, after annealing at 1200°C for 30 minutes were investigated. Figure 3 schematically shows a section of the objects. The investigated area can be divided into three sections: section 1 consists of a layer SiC_x; section 2 includes a [transition layer "Si-SiC_x" + layer SiC_x]; section 3 is a three-layer structure [layer-Si + transition layer "Si-SiC_x" + layer SiC_x].

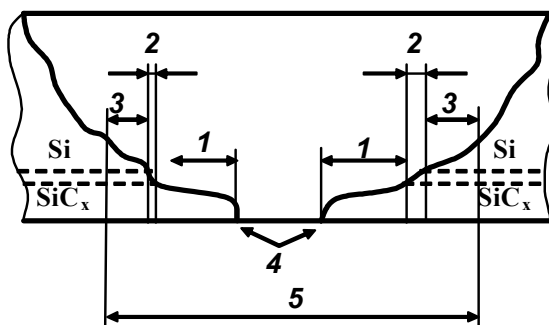


Fig. 3. Schematic cross section of the sample under study: (1) SiC_x regions, (2) regions of an intermediate Si-SiC_x layer, (3) double-diffraction regions, (4) a through hole, and (5) the area to be analyzed by transmission electron microscopy.

The layers SiC_{1.4}, SiC_{0.95} and SiC_{0.7} are solid, homogeneous, fine polycrystalline films (Figs. 4a-c, 5a, b and 6a, b, light areas, respectively). Some electron diffraction patterns contain superimposed point (c-Si) and ring (SiC) electron diffraction patterns (Fig.4b, c, 5b and 6b).

These patterns were recorded from areas 3 where the objects were presented together with single- and polycrystalline structures (for example Si + SiC_{1.4}). In Figs. 4b, 5b and 6b the microstructure of sections 1 (light area), 2 (intermediate region) and 3 (dark area) are shown.

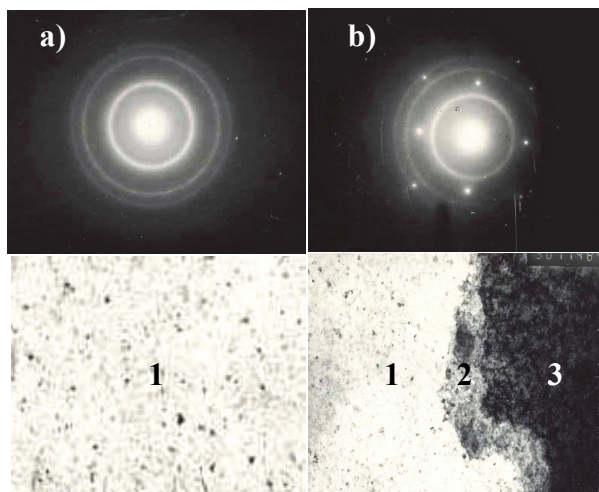


Fig. 4. Electron diffraction patterns and microstructure ($\times 50000$) of the SiC_{1.4} layer after annealing at temperature 1200°C for 30 min: rings – SiC, point reflections – Si, bright regions – SiC_{1.4} layer, dark regions – c-Si. a) SiC_{1.4} region; b) SiC_{1.4} regions + intermediate Si– SiC_{1.4} layer + c-Si: (1) SiC_{1.4} regions, (2) regions of an intermediate Si– SiC_{1.4} layer, (3) double-diffraction regions.

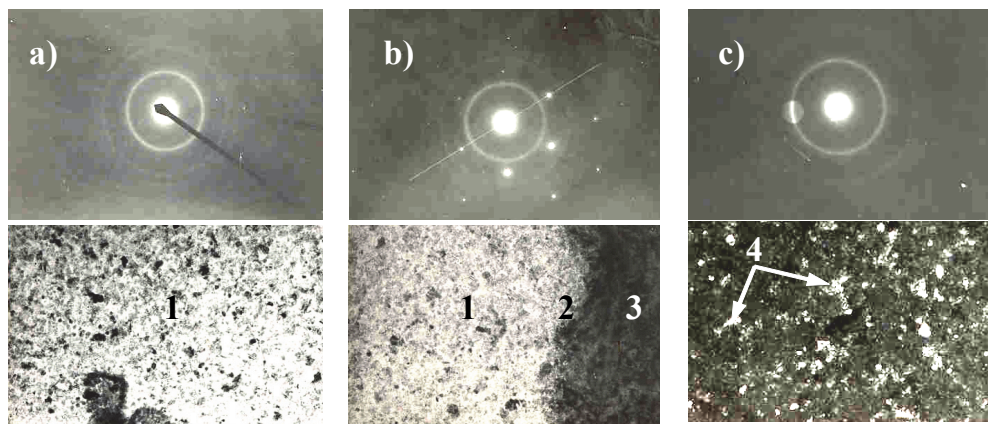


Fig. 5. Electron diffraction patterns and microstructure ($\times 50000$) of the SiC_{0.95} layer after annealing at temperature 1200°C for 30 min: rings – SiC, point reflections – Si, bright regions – SiC_{0.95} layer, dark regions – c-Si. a) SiC_{0.95} region; b) SiC_{0.95} regions + intermediate Si– SiC_{0.95} layer + c-Si, c) SiC crystallites in dark-field image regime: (1) SiC_{0.95} regions, (2) regions of an intermediate Si–SiC_{0.95} layer, (3) double-diffraction regions, (4) SiC crystallites.

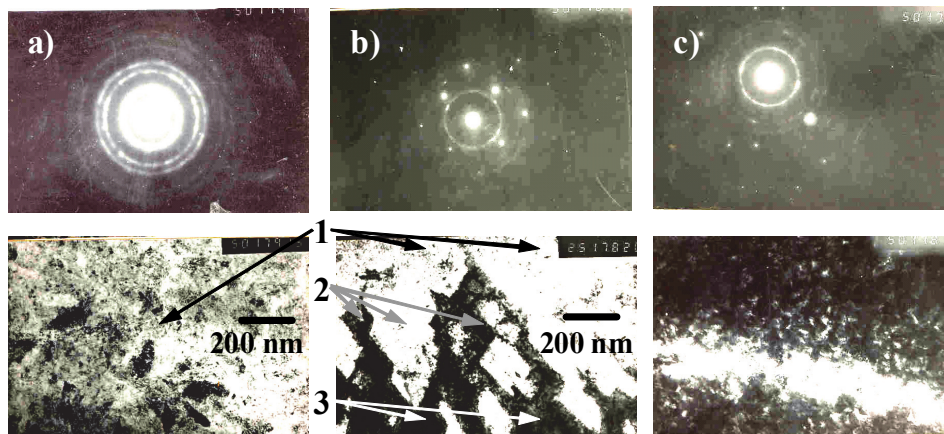


Fig. 6. Electron diffraction patterns and microstructure ($\times 50000$) of the $\text{SiC}_{0.7}$ layer after annealing at temperature 1200°C for 30 min: rings – SiC , point reflections – Si , bright regions – $\text{SiC}_{0.7}$ layer, dark regions – c-Si . a) $\text{SiC}_{0.7}$ region; b) $\text{SiC}_{0.7}$ regions + intermediate $\text{Si-SiC}_{0.7}$ layer + c-Si , c) SiC crystallites in dark-field image regime: (1) $\text{SiC}_{0.7}$ regions, (2) regions of an intermediate $\text{Si-SiC}_{0.7}$ layer, (3) double-diffraction regions

The value of $D \cdot d$ of device, calculated from the point patterns of the silicon lattice, was equal $D \cdot d = (3.53 \pm 0.01) \text{ nm} \cdot \text{mm}$. The diameters D of the most intensive rings of $\text{SiC}_{1.4}$ pattern were 10.4, 14.0, 22.9 and 26.9 mm, corresponding to the (002) plane of graphite ($d = 0.338 \text{ nm}$) and silicon carbide $\beta\text{-SiC}(111)$, $\beta\text{-SiC}(220)$, $\beta\text{-SiC}(311)$ (Fig. 4), respectively. The absence of some rings on the patterns is caused by their weak intensity. The diameters of the most intensive rings of $\text{SiC}_{0.95}$ were also 14.0, 22.9 and 26.9 mm and correspond to $\beta\text{-SiC}(111)$, $\beta\text{-SiC}(220)$, $\beta\text{-SiC}(311)$ (Fig. 5). The diameters of rings of $\text{SiC}_{0.7}$ diffraction pattern were 14.0, 22.9, 26.9, 28.0, 35.3, 39.7 mm (Fig. 6) and agree well with the calculated values of the diameters of 1, 3, 4, 5, 7 and 9 of the silicon carbide rings, corresponding to a system of planes $\beta\text{-SiC}(111)$, $\beta\text{-SiC}(220)$, $\beta\text{-SiC}(311)$, $\beta\text{-SiC}(222)$, $\beta\text{-SiC}(331)$, $\beta\text{-SiC}(422)$, ($d = 0.2518 \text{ nm}$, 0.1542 nm , 0.1311 nm , 0.1259 nm , 0.1000 nm , 0.0890 nm , respectively). Graphite rings in the electron diffraction patterns of $\text{SiC}_{0.7}$ and $\text{SiC}_{0.95}$ are not explicitly observed, which may be due to the absence of excess carbon.

In dark-field image regime the individual grains are visible as bright light spots. For a layer $\text{SiC}_{0.95}$ (Fig. 5c), as well as for the layer $\text{SiC}_{1.4}$, the presence of small and large grains of size from 10 to 80 nm was observed. The crystallites have various shapes - globular or plate-like. For a layer $\text{SiC}_{0.7}$ (Fig. 6c) crystallites were globular, needle or plate-like and had sizes from 10 to 400 nm after annealing at 1200°C . Small crystallites have a globular shape. These data differ from the X-ray diffraction data which was 5–10 nm (Akimchenko et al., 1977, 1980, Calcagno et al., 1996). It should be noted that by X-ray diffraction the average crystallite size was determined. In the layer $\text{SiC}_{0.7}$ due to the high concentration of carbon atoms one can expect a large number of stable clusters that hinder the crystallization process. In this case a significant prevalence of nanocrystals of a few nanometers sizes can be expected that are making a major contribution to the value of the average grain size. Small nanocrystals should give a reflection of the size in hundredths and tenths of a millimeter on the pattern, it is difficult to distinguish them and they are observed as a bright diffuse background between the larger crystallites (Fig. 6c).

Transition layer with a lower concentration of carbon between the Si substrate and $\text{SiC}_{0.7}$ is not uniform. It can be assumed that excess silicon atoms that are between the large SiC grains, in the process of recrystallization are combined with the substrate, forming a sawtooth SiC-Si structure (Fig. 6b).

3.3 Investigation of the structure by X-ray diffraction

After annealing of the $\text{SiC}_{1.4}$ layer in vacuum 10^{-4} Pa at temperatures 1200 and 1400°C in the X-ray diffraction patterns the intensive lines of polycrystalline silicon carbide are observed (Fig. 7a, b). There are also weak lines of polycrystalline silicon, apparently, from the transition layer “Si-SiC_{1.4}”, where presents excess silicon, forming in the annealing process the Si crystallites. The integrated intensity of SiC lines after annealing at 1400°C was significantly lower than after annealing at 1200°C. This may occur because of the disintegration of silicon carbide and desorption of carbon from the layer at temperatures above 950°C (see section 3.1). The decrease in phase volume of nanocrystalline SiC at temperatures above 1200°C can also occur due to evaporation of silicon in a vacuum, the melting point (1423°C) of which is less than the sublimation temperature of carbon (Semenov et al., 2009).

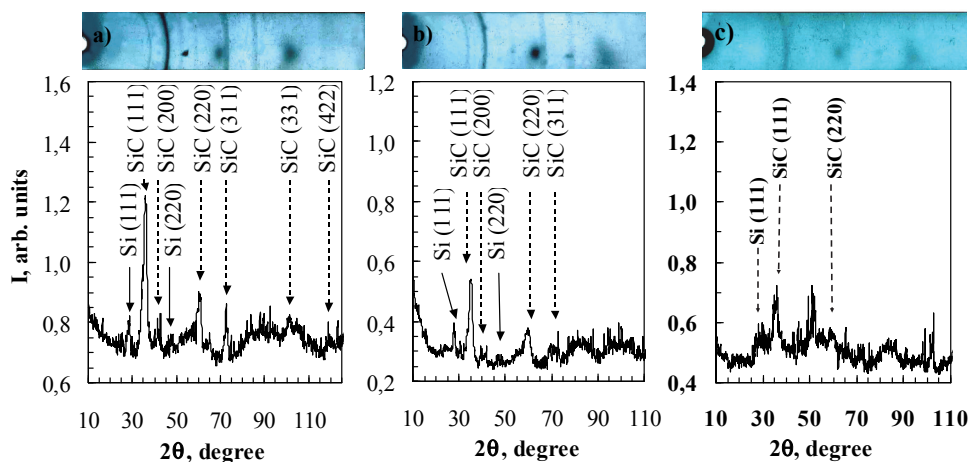


Fig. 7. X-ray diffraction patterns of the $\text{SiC}_{1.4}$ layer annealed for 30 min at (a) 1200 °C, (b) 1400°C, (c) after annealing at 1400°C and processing by glow discharge hydrogen plasma for 5 min.

An absence of SiC crystallites and the corresponding X-ray lines at high annealing temperatures 900–1100°C indicates a low ability of atoms to diffusion in the layer $\text{SiC}_{1.4}$. This may be caused by high concentrations of stable double and triple bonds like $\text{Si}=\text{C}$, $\text{Si}\equiv\text{C}$, $\text{C}=\text{C}$, $\text{C}\equiv\text{C}$, $\text{Si}=\text{Si}$, $\text{Si}\equiv\text{Si}$ and strong clusters that prevent the diffusion of atoms in the layer and are decomposed at temperatures of 1200°C and above. An attempt was made to use processing by the hydrogen glow discharge plasma for the modification of the structural properties of the SiC_x films. For this purpose, the $\text{SiC}_{1.4}$ layer annealed at 1400°C was treated by the hydrogen glow discharge plasma (27.12 MHz, 12.5 W, 6.5 Pa, 100°C, 5 min).

After treatment by H-plasma is not taken place the complete destruction of the SiC crystallites (Fig. 7c). However, the intensity of X-ray lines of SiC decreased in comparison with the corresponding lines on the diffraction pattern before treatment (Fig. 7b). This demonstrates the

destructive effect of plasma on the structure of the β -SiC crystallites, although the capacity of plasma was only 12,5 W, and SiC on the hardness scale, according to Knoop holds a high place (SiC, 2480) after diamond (C, 7000), boron carbide (B₄C, 2750), and aluminum boride (AlB, 2500). In addition, the processing by H-plasma for 5 minutes led to complete disappearance of the lines Si(111) and Si(220), reflected by the crystallites of silicon in the transition layer "film-substrate" ("SiC-Si"). It follows that the effect of hydrogen plasma propagates on the entire depth of the implanted layer (200 nm) and involves a intensive penetration of hydrogen ions through the solid film. Thus, the characteristics of the hydrogen glow discharge plasma and treatment (27.12 MHz, 12.5 W, 6.5 Pa, 100°C, 5 min) were sufficient to break the Si-Si and Si-C tetrahedral bonds and can be used to decay the stable carbon and carbon-silicon clusters.

Immediately after implantation and annealing of the SiC_{0.95} layer at 1100°C and below (Fig. 8a) on the diffraction patterns not seen any lines of polycrystalline phases. A weak line of β -SiC(111) after annealing at 1150°C is observed, which becomes more pronounced after annealing at 1250°C (Fig. 8b). In contrast to the layers SiC_{1.4} and SiC_{0.95}, the diffraction pattern of the SiC_{0.7} layer (Fig. 8c) demonstrates the presence of β -SiC(111) line and weak Si(111) line after annealing at relatively low temperature of 1000°C for 30 minutes, due to the decrease of carbon concentration and, consequently, the concentration of stable carbon clusters. Annealing at 1100°C led to an increase in the intensity of the β -SiC(111) and Si(111) lines (Fig. 8d) and to an appearance of β -SiC(200), β -SiC(220), β -SiC(311) и Si(220) lines, which indicates an improvement in the crystallite structure. Line intensity from the SiC_{0.7} layer shows a preferred content of polycrystalline β -SiC phase after annealing in comparison with the phase content of poly-Si, which is caused by a relatively high concentration of carbon. The average crystallite size of β -SiC and Si was about 3–7 nm in the planes: β -SiC(111) ~ 3 nm, β -SiC(220) ~ 6.5 nm, Si(111) ~ 4.5 nm.

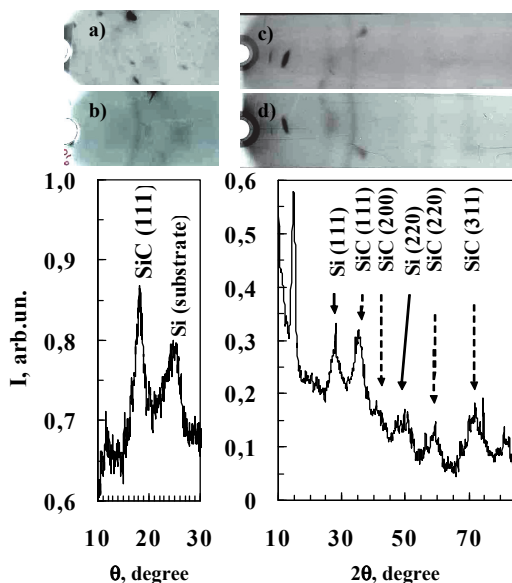


Fig. 8. X-ray diffraction patterns of the SiC_{0.95} layer annealed at (a) 1100°C, (b) 1250°C and of the SiC_{0.7} layer annealed at (c) 1000°C, (d) 1100°C, for 30 min obtained using X-ray chambers RKD (a, b) and RKU-114M1 (c, d). Intensity curves correspond to X-ray patterns (b, d).

In the layer $\text{SiC}_{0.4}$ the presence of polycrystalline phases of SiC and Si after implantation and annealing at 1000, 1100 and 1250°C are revealed. High intensity peaks of SiC after annealing at 1100°C (Fig. 9a) indicates on intensive process of crystallization of β -SiC due to lower content of stable clusters in comparison with the layers $\text{SiC}_{1.4}$, $\text{SiC}_{0.95}$ and $\text{SiC}_{0.7}$. High amplitude of β -SiC peaks after annealing at 1250°C confirms this assertion. In diffraction pattern of $\text{SiC}_{0.12}$ layer after implantation a broad diffuse line of amorphous silicon Si(111) ($\theta = 14.3^\circ$) is observed (Fig.10a). After annealing at 800°C a narrowing of this line, at 900°C - a sharp narrowing of the line Si(111) and the appearance of Si(220) and Si(311) lines of polycrystalline Si phase, as well as two weak lines of β -SiC, at 1250°C - a decrease of the integrated intensity of Si lines, are observed.

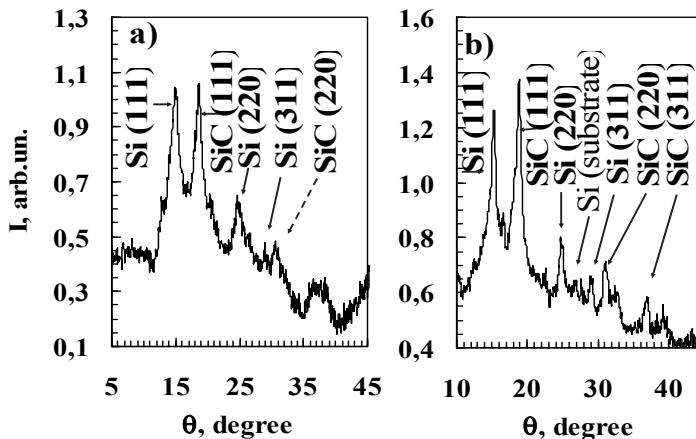


Fig. 9. X-ray diffraction patterns of the $\text{SiC}_{0.4}$ layer annealed for 30 min at (a) 1100°C and (b) 1250°C.

The implantation of carbon causes the formation of weakly ordered set of randomly oriented Si regions of size ~ 1.5 nm. Temperature dependence of the average crystallite size Si (Fig. 11a, curve 1) and SiC (curve 2) in plane (111) shows that at low temperatures the curve 1 is characterized by slow growth in the size of weakly ordered Si nanocrystals. Their transformation into well ordered Si crystallites at 800°C is taken place. Average size of Si crystallites is 47 nm after annealing at 1250°C. The formation of β -SiC crystallites prevent a complete recrystallization of layer at this temperature.

The integrated intensity curve of Si(111) line, which is proportional to the phase volume, has three sections in the temperature ranges of 20–800°C, 800–900°C and 900–1250°C (Fig. 11b). In the range of 20–800°C I_{int} decreases, indicating a decrease in the total volume of nanocrystals Si, although their sizes increase up to 2.2 nm. The growth of weak ordered Si crystallites is accompanied by the displacement of carbon atoms in the surrounding space, which no longer contribute to the intensity of the Si (111) line due to increased concentration of carbon. In addition, there is recrystallization of silicon near the substrate. It is assumed that, after annealing at 800°C (Figs. 11b and 12) approximately $k_{800} \approx [I_{\text{int}}(800^\circ\text{C})/I_{\text{int}}(20^\circ\text{C})] \times 100\% = 72\%$ of silicon atoms in the layer is incorporated into crystallites of Si. The remaining atoms of Si (28%) are in an amorphous mixture of Si and C atoms, or reunited with the substrate.

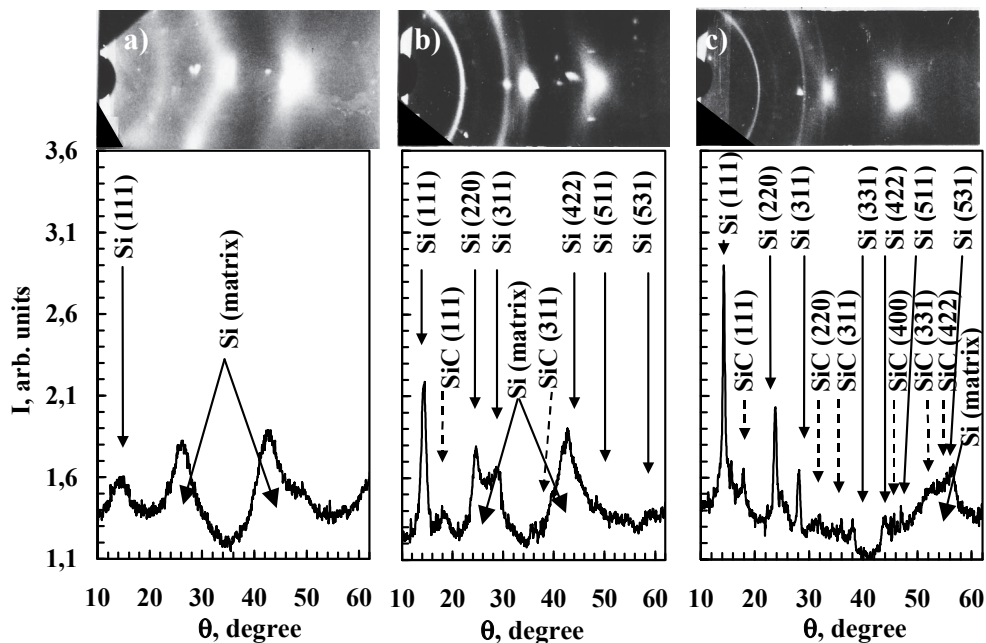


Fig. 10. X-ray diffraction patterns of the $\text{SiC}_{0.12}$ layer (a) before and after annealing for 30 min at (b) 1100°C and (c) 1250°C.

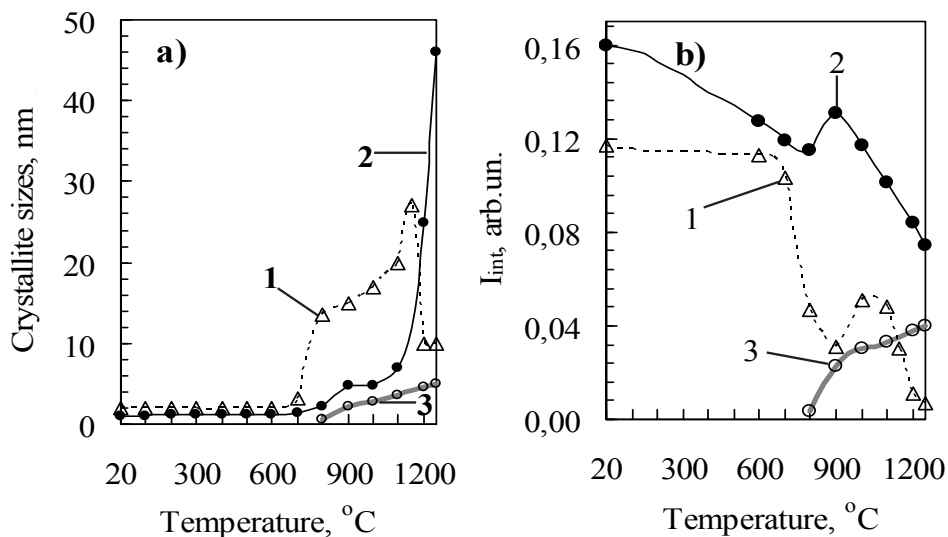


Fig. 11. Average sizes (a) of Si and SiC crystallites in the (111) plane and (b) the integrated intensities of the Si(111) and SiC(111) lines after implantation of carbon ions in silicon and annealing. 1 – Si (for layer $\text{SiC}_{0.03}$), 2 – Si (for layer $\text{SiC}_{0.12}$), 3 – SiC (for layer $\text{SiC}_{0.12}$).

Fig. 12 schematically shows the variation of the structure of the layer, its phase composition and phase volume, as well as the average grain size as a function of annealing temperature (a) and scheme of Si and SiC crystallite formation in this layer (b). The diagram is based on the curves in Fig. 11a, b for $\text{SiC}_{0.12}$. Regions "amorphous Si-C mixture" and "c-Si" are formed adhering to the relation: "amorphous Si-C mixture" + "c-Si" = 100% - ("poly-SiC" + "poly-Si" + "amorphous -Si").

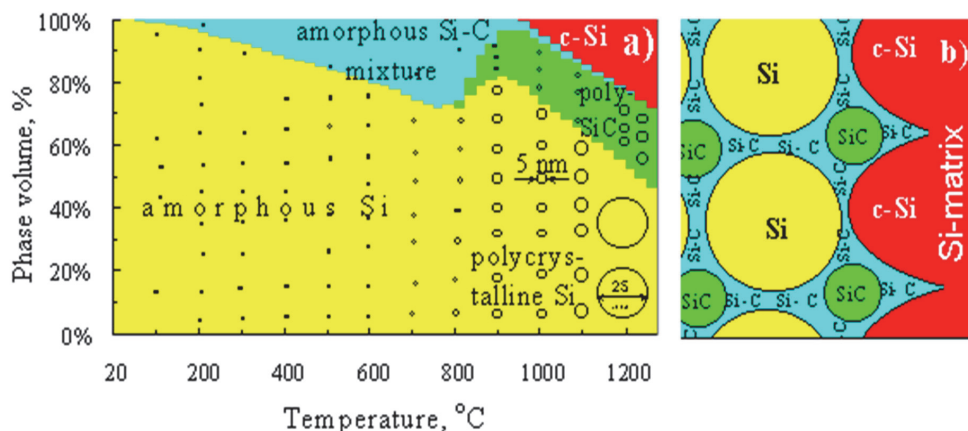


Fig. 12. Crystallization of the $\text{SiC}_{0.12}$ layer: (a) the phase volumes at various annealing temperatures and (b) the formation of crystalline Si and SiC crystallites in the temperature range 900–1000 °C.

In the range of 800–900 °C the increase in both size crystallites Si (from 2.2 to 4.7 nm) and the volume of polycrystalline phase of Si (Fig. 11a and 12) is observed. This is due to the formation of SiC crystallites at 900 °C in the regions of carbon accumulation and the joining of excess silicon atoms to Si crystallites. So, k is increased: $k_{900} \approx 82\%$. This leads to a decrease in Si-C-mixture volume (Fig. 12). After annealing at 1000 °C and 1250 °C, an increase in the phase volume and crystallite sizes of β -SiC as well as a decrease in k due to recrystallization of regions near the Si substrate, are taken place: $k_{1000} \approx 73\%$ and $k_{1250} \approx 46\%$. Si crystallite sizes increased almost 10 times (up to 47 nm). Probably, there is destruction of defective silicon crystallites and the uniting of their atoms into crystallites with a perfect structure or with the substrate. As can be seen from the diagram, after annealing at 1200 °C in the layer $\text{SiC}_{0.12}$ ~50% of silicon atoms are incorporated into Si crystallites with an average size of 25 nm, 25% of Si atoms are included into β -SiC crystallite with size of 5 nm and 25% are joined with Si substrate. Since the unit cell volume for Si is twice more than the cell volume for SiC, the volume of the surface layer of Si after implantation and annealing of carbon should not change appreciably, and the above relations can be regarded as a volume ratio of phases.

During annealing at 1400 °C there is the destruction of most of the silicon crystallites and connection of their atoms to the substrate. The intensity of the lines Si was significantly lower than the intensities of β -SiC lines (Fig. 13). It is assumed that recrystallized Si layer with ingrained in him crystallites of β -SiC and Si on a silicon substrate was obtained.

During a growth of the crystallite size is manifested basic thermodynamic law: in an isolated system, the processes occurring with increasing free energy, is prohibited. Combining the

two grains is taken place, if it is accompanied by a gain in energy which is greater than its costs for the destruction of the crystallites. In this case, the redistribution of atoms with a change in chemical bond lengths and angles between them is taken place, in order to select a more favorable energy state, which is the states with tetrahedral oriented bonds, characteristic of crystalline phases of Si and SiC.

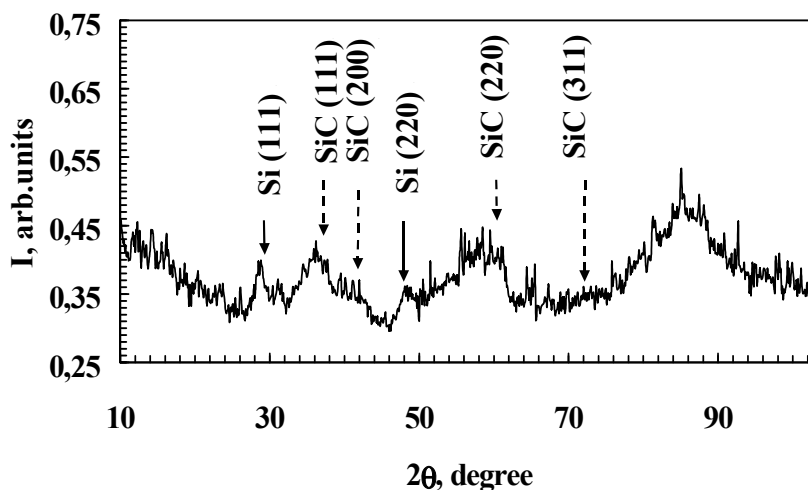


Fig. 13. X-ray diffraction pattern of the SiC_{0.12} layer after annealing at 1400°C for 30 min.

The X-ray diffraction results are in accordance with the data of Auger electron spectroscopy, whereby the concentration of carbon atoms in a layer is $N_C/N_{Si} = 0.12/1$ (Fig. 2). Then the maximum possible ratio of atoms, forming part of SiC and Si, will be: $N_{SiC}/N_{Si} = 0.24/0.88 = 0.27$. As seen in Figure 11b, the maximum quantity of poly-SiC, obtained at 1250°C, was $I_{int}(SiC) = 0.040$, and poly-Si was $I_{int}(Si) = 0.131$ at 900°C, i.e., $I_{int}(SiC)/I_{int}(Si) = 0.040/0.131 = 0.30$, which is comparable with the data of Auger electron spectroscopy.

Similar features are observed for a layer with a lower carbon concentration SiC_{0.03}. Immediately after the implantation the same broad diffuse line of amorphous silicon Si(111) at $\theta = 14.3^\circ$ is observed (Fig. 14). Increase of annealing temperature above 800°C causes narrowing of this line, increasing the number and amplitude of the line intensity which reaches its maximum at 1100°C. However, in the X-ray diffraction patterns of SiC_{0.03} layer no lines of polycrystalline silicon carbide in the whole temperature range are observed due to insufficient concentration of the carbon atoms to form a large number of SiC crystallites. Annealing at temperatures above 1100° C reduces the intensity of Si lines and results their disappearance after annealing at 1250°C due to recrystallization of the layer.

For comparison, in Table 3 the grain sizes of silicon and silicon carbide in plane (111) in layers Si(111) and β -SiC(111) are given. Dimensions of weakly ordered regions in SiC_{0.03} layer, contributing to the intensity of the Si(111) line, exceed the same values for SiC_{0.12}. This is associated with a lower concentration of carbon and larger volume of Si regions with extremely low concentrations of carbon. At temperatures of 1200 and 1250°C a decrease in the average crystallite size up to 10 nm is observed, which is associated with the process of recrystallization near the substrate.

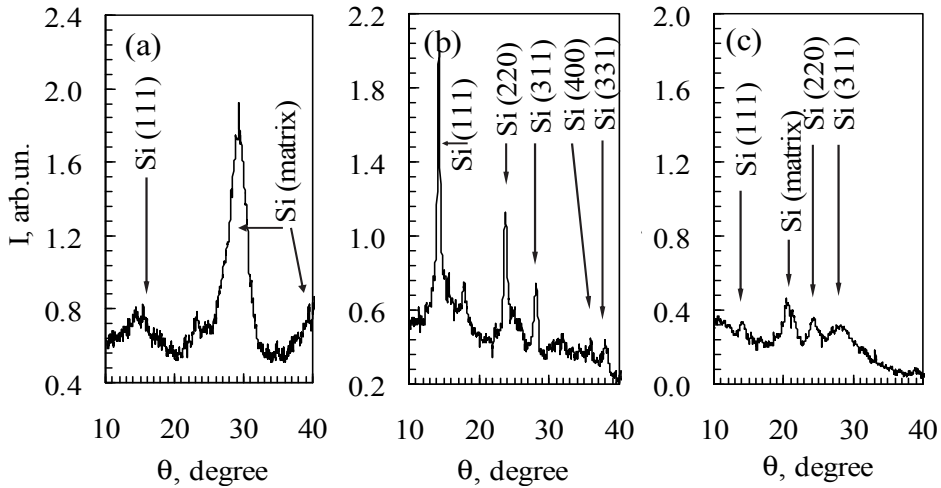


Fig. 14. X-ray diffraction of $\text{SiC}_{0.03}$ layer after implantation of carbon ions in Si (a) and annealing at 1100°C (b) and 1200°C (c) for 30 min.

Temperature ($^\circ\text{C}$)	ϵ (nm)					
	$\text{SiC}_{0.03}$		$\text{SiC}_{0.12}$		$\text{SiC}_{0.4}$	
	Si	β -SiC	Si	β -SiC	Si	β -SiC
20	2	-	1.1	-	-	-
700	3	-	1.3	-	-	-
800	13	-	2	-	-	-
900	15	-	4.5	2		
1000	17	-	5	3	4	3
1100	20	-	7	3.5	4	3
1150	27	-	12	4		
1200	10	-	25	4.5		
1250	10	-	46	5	9	4.5

Table 3. Average size (ϵ) of Si- and β -SiC crystallites in SiC_x layers

Temperature dependences of the integrated intensity of Si(111) line (Fig. 15) for the $\text{SiC}_{0.03}$ and $\text{SiC}_{0.12}$ layers are similar in nature. A lower carbon concentration in $\text{SiC}_{0.03}$ layer results more intensive decrease in the phase volume of poly-Si at temperatures above 700°C due to more intensive recrystallization near the substrate. The value of k were: $k_{800} \approx 40\%$, $k_{900} \approx 27\%$, $k_{1000} \approx 44\%$, $k_{1100} \approx 41\%$, $k_{1250} \approx 6\%$. Growth of k up to 44% at 1000°C for $\text{SiC}_{0.03}$ layer due to accession of excess silicon atoms from the carbon-rich Si-C-mixture to the Si crystallite is taken place. For a layer $\text{SiC}_{0.12}$, that is observed at a temperature of 100°C below due to a higher concentration of carbon, therefore the carbon rich region is formed at lower temperatures and does not require significant movements of atoms. Annealing at 1250°C results in uniting of $\text{SiC}_{0.03}$ layer with single-crystal substrate ($K_{1250} \times 100\% = [0,007/0,116] \times 100\% = 6\%$) and the decrease in the average size of residual crystallites up to 10 nm.

3.4 Investigations by infrared spectroscopy

The influence of carbon concentration in the SiC_x layers and annealing temperature on the parameters of the spectra of infrared spectroscopy was investigated. For this purpose, using two-beam infrared spectrometer UR-20 the IR transmission spectra of $\text{SiC}_{1.4}$, $\text{SiC}_{0.95}$, $\text{SiC}_{0.7}$, $\text{SiC}_{0.4}$, $\text{SiC}_{0.12}$ and $\text{SiC}_{0.03}$ layers before and after isochronous annealing in vacuum at temperature range $200\text{--}1400^\circ\text{C}$ were measured (Figs. 16–21).

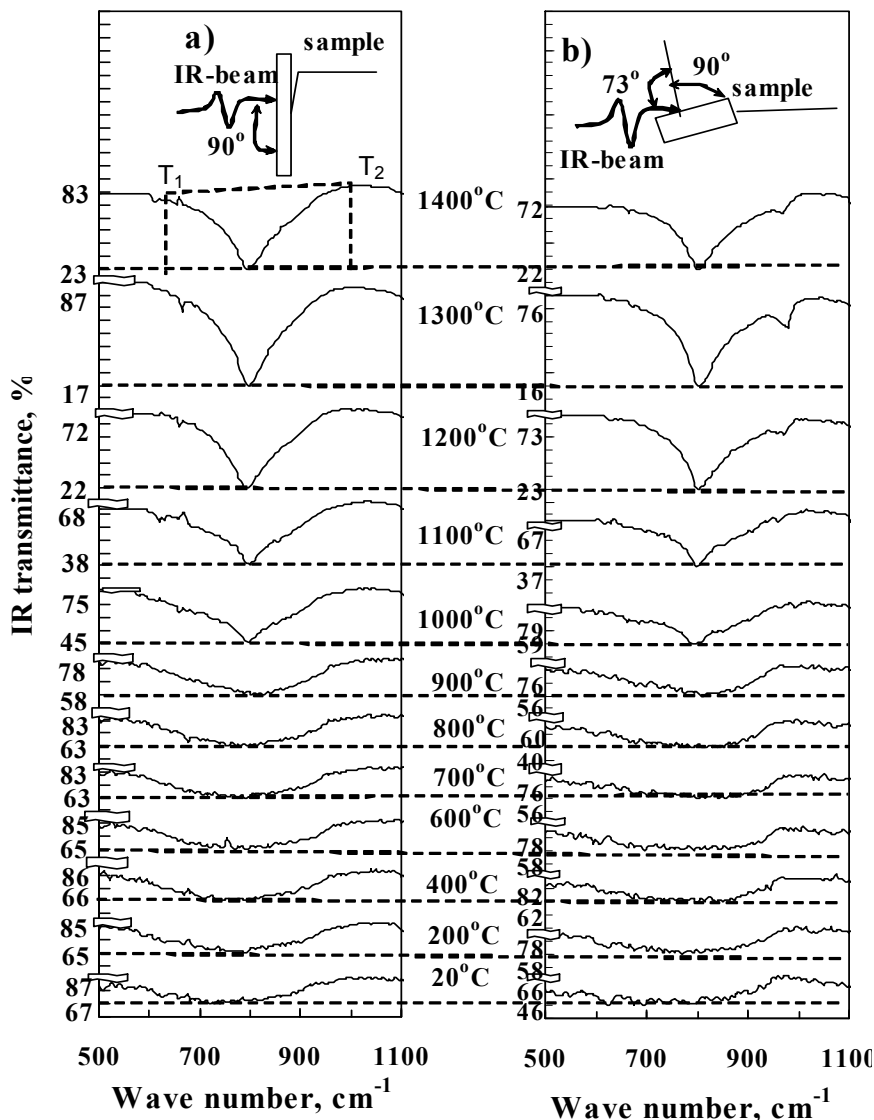


Fig. 16. IR transmission spectra of the $\text{SiC}_{1.4}$ layer recorded (a) under normal incidence of IR radiation on the sample and (b) at an angle of 73° to the normal to the sample surface.

At respecting certain condition, one can observe not only the transverse optical oscillations of atoms (TO-phonons), as well as longitudinal optical lattice oscillations (LO-phonons). For this purpose, we measured IR transmittance spectra of the implanted layers both at normal incidence of radiation on the sample, and at 73° to the normal to the surface (Figs. 16–21a, b). For a visual comparison of spectra from the SiC_x layers in Fig. 22 series of spectra of these layers before and after annealing at 600, 1000 and 1300°C measured at normal incidence of radiation on the sample, are presented. It is seen that among these layers a SiC-peak of the IR transmittance for the $\text{SiC}_{0.7}$ layer has maximum value of amplitude and minimum half-width after annealing at 1300°C . This implies a maximum number of tetrahedral oriented Si-C-bonds and high crystallinity of this layer, although the carbon concentration below the stoichiometric SiC. This phenomenon requires an explanation. For this purpose, an analysis of dependence of SiC-peak parameters on both annealing temperature and concentration of carbon for SiC_x layers was carried out.

It is well known that the spectral range $500\text{--}1100\text{ cm}^{-1}$ considered here includes the absorption bands corresponding to valence oscillations (in which the lengths of bonds vary predominantly) of the Si-C, C-C, and C-O-bonds, as well as deformation vibrations (in which the angles between the bonds are changed). As a result of interactions of these oscillations, it is impossible in principle to attribute the absorption band to individual bonds. If we assume that in the ideal case each type of Si-C-bonds corresponds to absorption at a certain frequency or in a narrow frequency interval, it can be concluded from the spectra in Figs. 16–22 that after implantation of carbon into silicon, the contour curve of the IR spectrum covers a large frequency (or wavenumber) range; i.e., the ion implanted layer contains a large number of different types of Si-C-bonds absorbing at different frequencies. Tetrahedral oriented Si-C-bonds with a length of 0.194 nm in crystalline silicon carbide absorb at the frequency corresponding to a wavenumber of 800 cm^{-1} , while the silicon layer amorphized by implantation of carbon ions contains Si-C-bonds with a length larger and smaller than this value and absorb at the frequencies slightly different from 800 cm^{-1} . This may be due to the fact that the stopping particles form a new Si-C-bonds which are not covalent because of variations in their length and in the angles between them. In the implanted amorphous Si-C-layer, one can also expect the presence of shorter double $\text{Si}=\text{C}$ and triple $\text{Si}\equiv\text{C}$ bonds, whose length is much smaller. Among the bonds can be present also the bonds, distances and angles between them (between atoms) are exactly the same as in the crystallite of SiC. For example, Kimura et al. (1981) by electron diffraction observed the crystallites of SiC immediately after implantation. In this case, one can observe non-zero absorption at a frequency of 800 cm^{-1} after implantation.

In addition, in the implanted layer can be expected the presence of long single bonds, free (dangling) bonds and hybridized Si-C-bonds, resonance and other higher order interactions. If the absorption of double $\text{C}=\text{C}$ -bonds ($1620\text{--}1680\text{ cm}^{-1}$) and the triple $\text{C}\equiv\text{C}$ -bonds ($2100\text{--}2200\text{ cm}^{-1}$) is beyond the study of the contour curve of the IR spectrum $500\text{--}1100\text{ cm}^{-1}$, but the vibrations of C-C are in the region $900\text{--}1100\text{ cm}^{-1}$. Nevertheless, the contribution to change the contour of the curve in this range and, in particular, to change the peak area will have a decay of single C-C, double $\text{C}=\text{C}$, $\text{Si}=\text{C}$ or $\text{Si}=\text{Si}$, and triple $\text{C}\equiv\text{C}$, $\text{Si}\equiv\text{C}$ or $\text{Si}\equiv\text{Si}$ bonds, because of the formation after their decay of Si-C-bonds absorbing in this range (Silverstein et al., 1977).

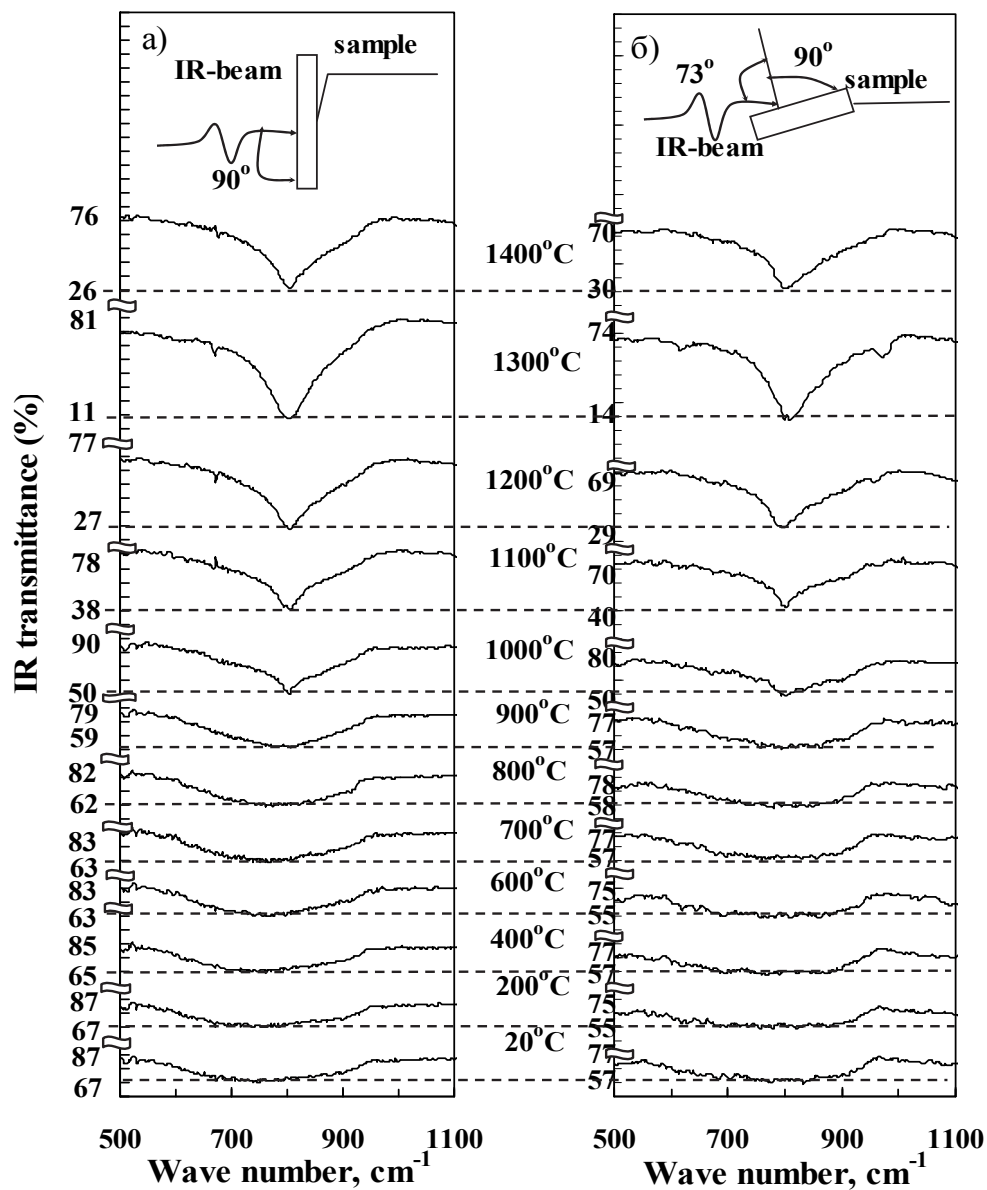


Fig. 17. IR transmission spectra of the $\text{SiC}_{0.95}$ layer recorded (a) under normal incidence of IR radiation on the sample and (b) at an angle of 73° to the normal to the sample surface.

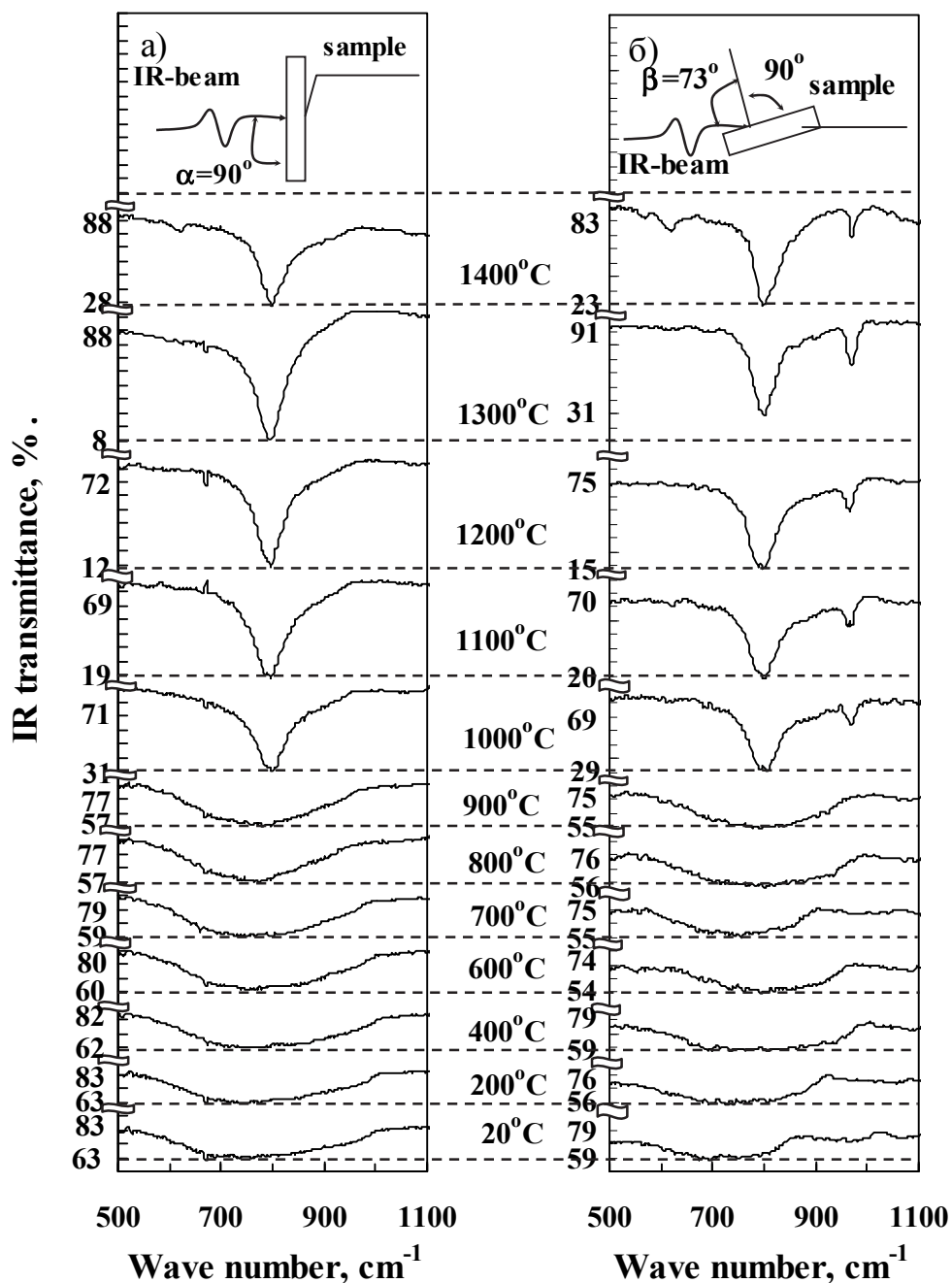


Fig. 18. IR transmission spectra of the $\text{SiC}_{0.7}$ layer recorded (a) under normal incidence of IR radiation on the sample and (b) at an angle of 73° to the normal to the sample surface.

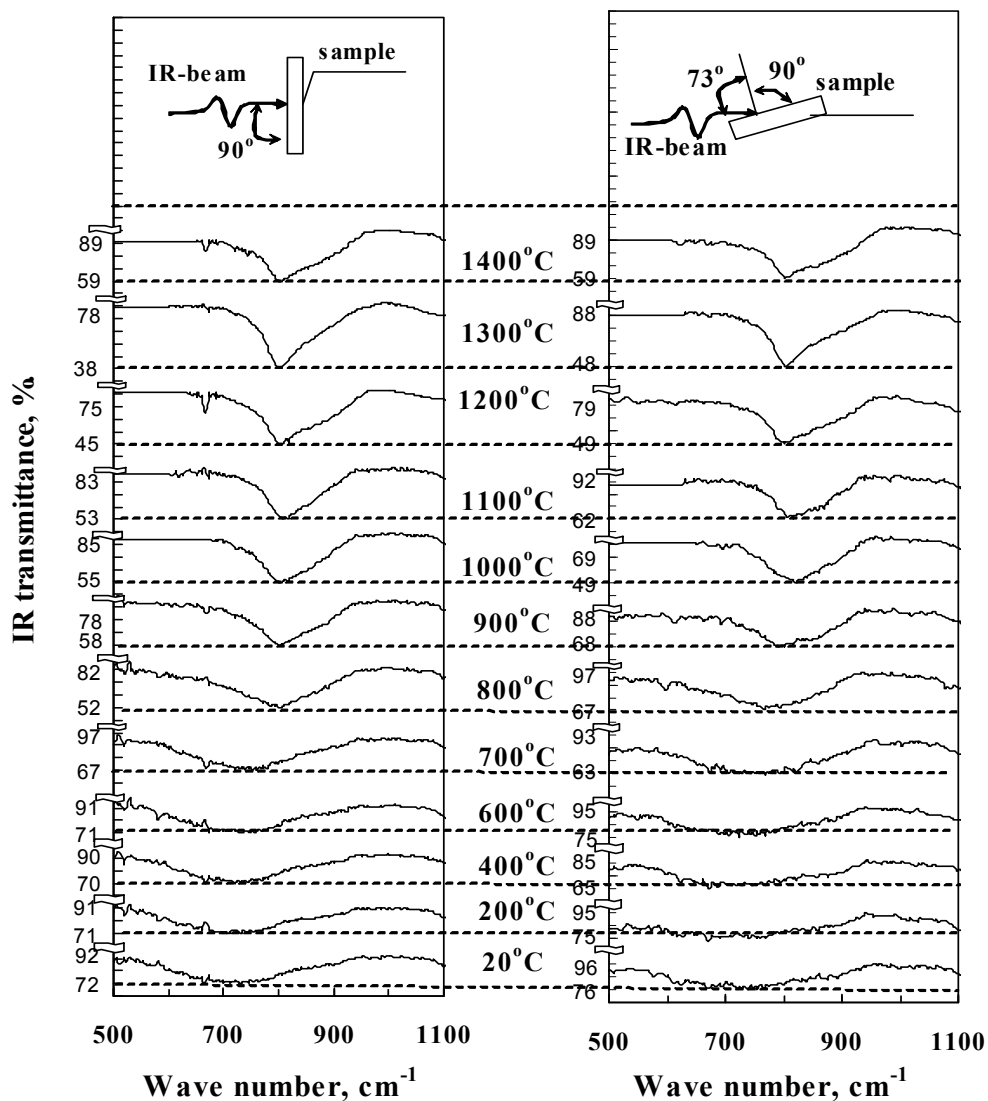


Fig. 19. IR transmission spectra of the $\text{SiC}_{0.4}$ layer recorded (a) under normal incidence of IR radiation on the sample and (b) at an angle of 73° to the normal to the sample surface.

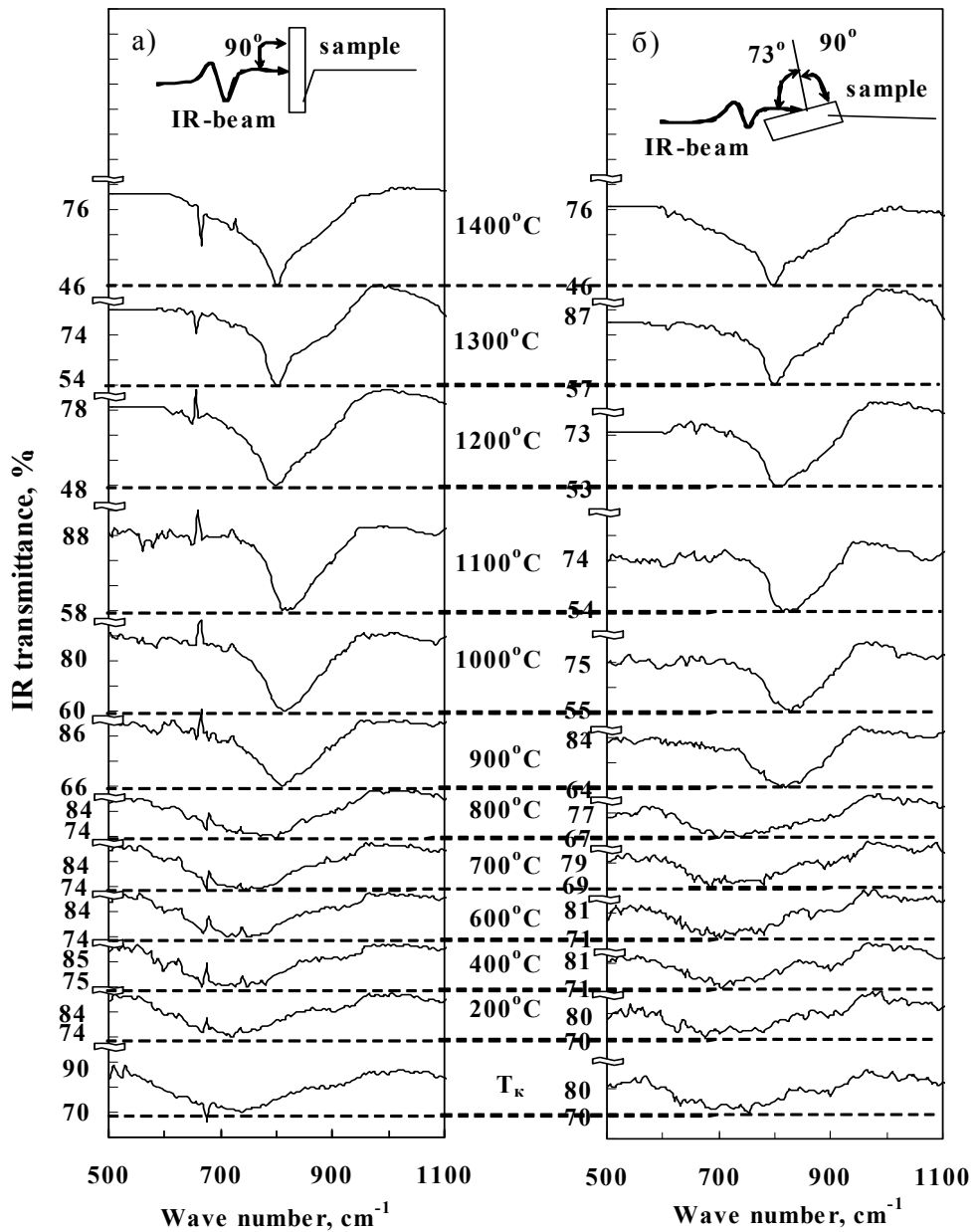


Fig. 20. IR transmission spectra of the $\text{SiC}_{0.12}$ layer recorded (a) under normal incidence of IR radiation on the sample and (b) at an angle of 73° to the normal to the sample surface.

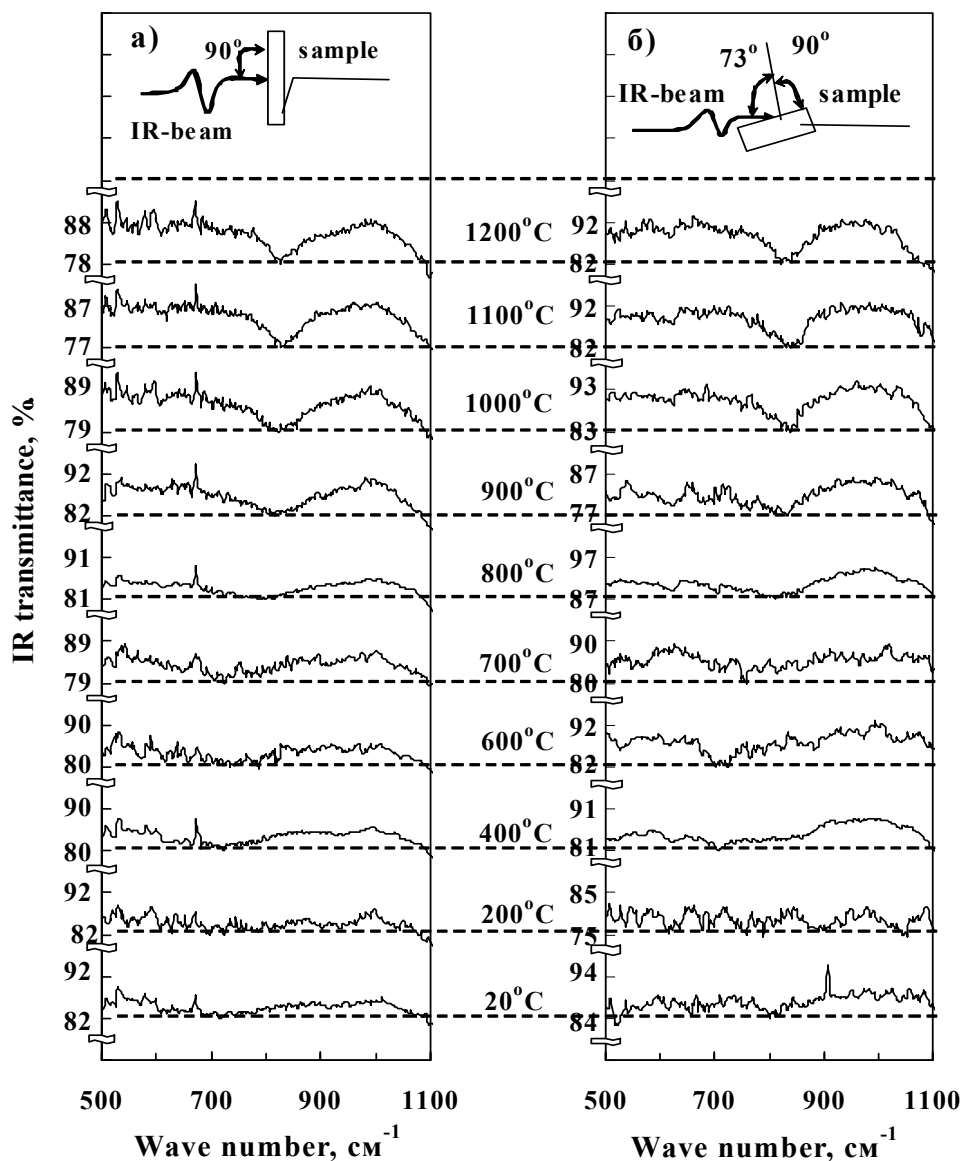


Fig. 21. IR transmission spectra of the $\text{SiC}_{0.03}$ layer recorded (a) under normal incidence of IR radiation on the sample and (b) at an angle of 73° to the normal to the sample surface.

The position of the minimum of the IR transmission peak determines a certain type of bonds, which corresponds to the maximum of absorption at a given temperature. All layers considered here, exhibit after implantation, a transmission peak with the minimum at a frequency of $720\text{--}750\text{ cm}^{-1}$, which is usually typical of amorphous silicon

carbide (Figs. 16-22). For the layers with low carbon concentration $\text{SiC}_{0.4}$, $\text{SiC}_{0.12}$ and $\text{SiC}_{0.03}$, the minimum of IR transmission is shifted in the region $720\text{--}725\text{ cm}^{-1}$ to the left relative position of the minimum peak for the layers with a high concentration of carbon $\text{SiC}_{1.4}$, $\text{SiC}_{0.95}$ and $\text{SiC}_{0.7}$, located in the region $735\text{--}750\text{ cm}^{-1}$ (Fig. 23). This may be due to the prevalence of long weak Si–C-bonds in the layers with low carbon concentration.

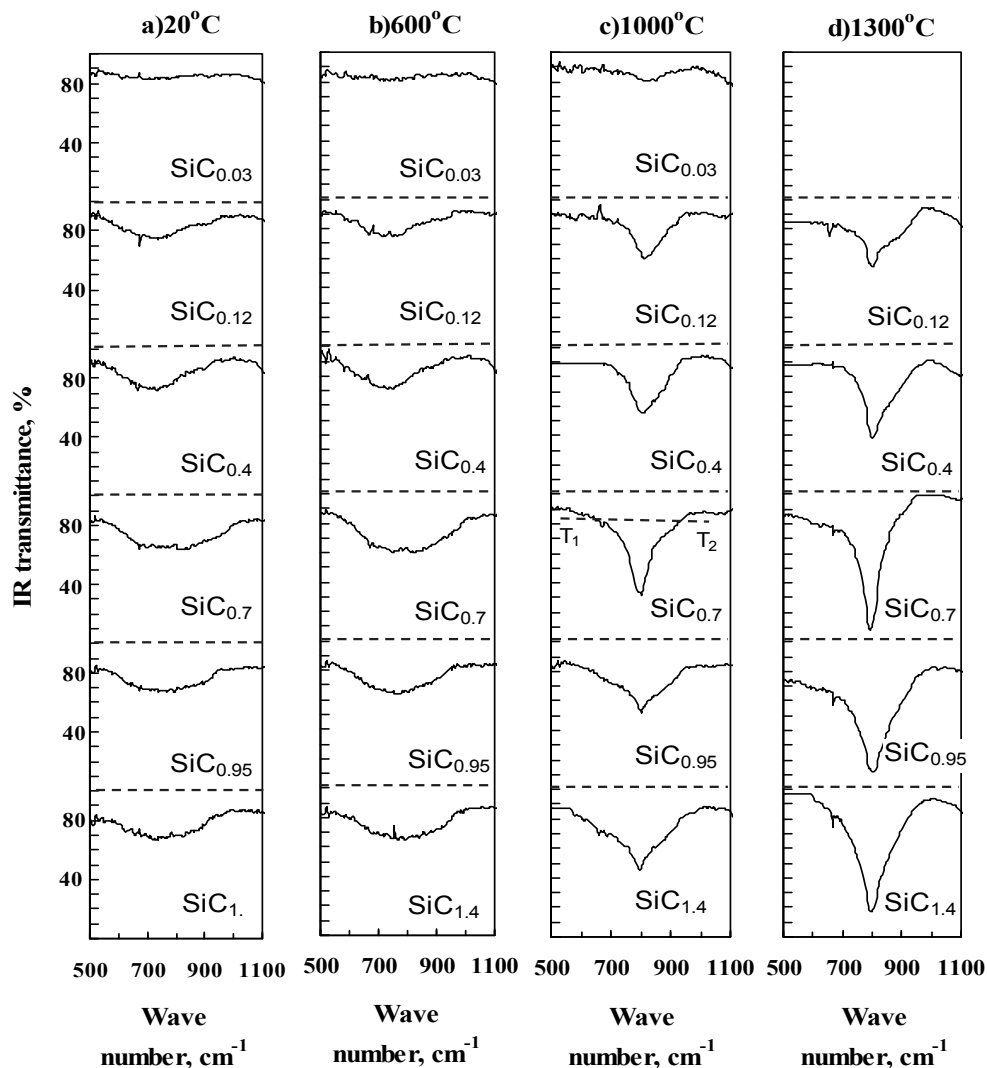


Fig. 22. IR transmission spectra of the $\text{SiC}_{1.4}$, $\text{SiC}_{0.95}$, $\text{SiC}_{0.7}$, $\text{SiC}_{0.4}$, $\text{SiC}_{0.12}$ and $\text{SiC}_{0.03}$ layers recorded after implantation of C^{12} ions ($E = 40, 20, 10, 5$ and 3 keV) into Si (a) and annealing for 30 min at temperatures 600°C (b), 1000°C (c) and 1300°C (d).

As a result of subsequent annealing, the peak is displaced to the right up to 800 cm^{-1} (Fig. 23), indicating the formation of tetrahedral bonds typical of SiC, increases in amplitude and narrows. In the case of incidence of infrared radiation on the sample surface at the Brewster angle (73° from the normal), after annealing at 1000°C the appearance of the LO-phonon peak of SiC at frequency $955\text{--}965\text{ cm}^{-1}$ is observed for the layers with a high concentration of carbon $\text{SiC}_{1.4}$, $\text{SiC}_{0.95}$ and $\text{SiC}_{0.7}$. With increasing of annealing temperature, this peak increases in amplitude synchronously with the peak of TO-phonons of silicon carbide (Figs. 16–18, 23). For layers with low carbon concentration $\text{SiC}_{0.4}$, $\text{SiC}_{0.12}$ and $\text{SiC}_{0.03}$ the LO-phonon peak of SiC was not observed (Fig. 19–21), which may be associated with small crystallite sizes of silicon carbide. At normal incidence of infrared radiation LO-phonon peak was not observed at both high and low concentrations of carbon (Figs. 16–21). Increase of the annealing temperature in the range $1000\text{--}1300^\circ\text{C}$ results in some increase in the wavelength of the amplitude maximum of LO-phonon peak in the case of an excess of carbon for $\text{SiC}_{1.4}$ (Fig. 23, curve 1).

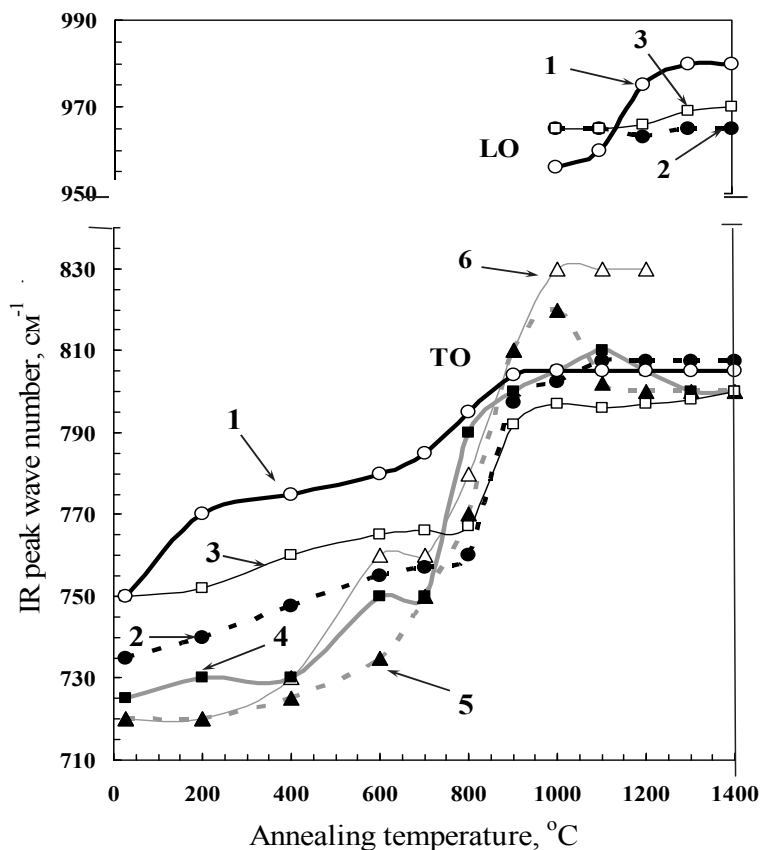


Fig. 23. Wavenumber of the IR transmittance peak for TO- and LO-phonons SiC as a function of the annealing temperature: 1 - $\text{SiC}_{1.4}$, 2 - $\text{SiC}_{0.95}$, 3 - $\text{SiC}_{0.7}$, 4 - $\text{SiC}_{0.4}$, 5 - $\text{SiC}_{0.12}$, 6 - $\text{SiC}_{0.03}$.

In the case of layers with high concentrations of carbon, position of the minimum of IR transmission peak for TO-phonons is smoothly shifted from 750 to 805 cm^{-1} for $\text{SiC}_{1.4}$ with the increase of the annealing temperature in the range of 20–1000°C, from 735 to 807 cm^{-1} for $\text{SiC}_{0.95}$, from 750 to 800 cm^{-1} for $\text{SiC}_{0.7}$, indicating the formation of tetrahedral oriented Si–C-bonds characteristic of SiC (Fig. 23). The minimum of peak most intensively shifts after annealing in the range 800–900°C, which indicates on intensive processes of the layer ordering. Further annealing up to 1400°C does not lead to a noticeable shift of the minimum peak.

In several studies any changes in the IR transmission spectra have also not revealed after annealing at 1000°C (Borders et al., 1971) and 1100°C (Akimchenko et al., 1977b). This was attributed to the completion of the formation of β -SiC. However, as shown in Fig. 23 for $\text{SiC}_{1.4}$, $\text{SiC}_{0.95}$ and $\text{SiC}_{0.7}$ layers, if the curves of the peak position for TO phonons saturates and does not provide additional information in the temperature range 900–1400°C, then the curves for LO-phonon peak position undergo changes at these temperatures, indicating a structural change in ion-implanted layer. It can be assumed that the formation of tetrahedral Si–C-bonds of required length and angle between them is not completed up to 1300°C.

Although the shift of the minimum of the peak to 800 cm^{-1} indicating that tetrahedral Si–C-bonds prevail is observed at 1000°C, X-ray diffraction data show that the formation of SiC crystallites begins at 1000°C for $\text{SiC}_{0.7}$, 1150°C for $\text{SiC}_{0.95}$ and 1200°C for $\text{SiC}_{1.4}$ (Figs. 7 and 8), which means that Si–C-bonds are transformed into tetrahedral oriented bonds in the bulk of crystallites only at these temperatures. The increase in the intensity and number of X-ray lines of SiC upon an increase in the annealing temperature (Fig. 8) indicates an increase in the amount of SiC at the expense of the amorphous phase and perfection of its structure due to annealing of structural defects, respectively. It follows that the location of the minimum of transmission peak at $\sim 800 \text{ cm}^{-1}$ and the predominance of the tetrahedral oriented Si–C-bonds among the optically active bonds at temperatures 900–1000°C is not a sufficient condition for the formation of crystallites of silicon carbide in layers with high carbon content $\text{SiC}_{0.7}$ – $\text{SiC}_{1.4}$. At this temperature, a significant part of C and Si atoms can be incorporated in composition of an optically inactive stable clusters, which does not contribute to the amplitude of the IR transmission peak and are decompose at higher temperatures ($>1150^\circ\text{C}$). This results an increase in the amplitude of the infrared transmission at a frequency of 800 cm^{-1} (Figs. 16, 18 and 22) at these temperatures.

Fig. 24 schematically shows the optically inactive Si–C-clusters, the atoms of which are connected by single, double and triple bonds, lie in one plane. In a flat optically inactive net the free (dangling) bonds to the silicon atoms (atoms №30 and 24) and carbon atoms (№21 and 27) are shown. Free bonds of these and other atoms (№ 4, 11, 12, 15, 17) can connected them with groups of atoms which do not lie on one plane and can form the association of optically active clusters. Since the distance between atoms № 22–4 and №5–22 are equal, the bond can oscillate forming 22–4 and 22–5. One double bond connected three atoms № 5, 6 and 7, i.e. there is the presence of resonance. The presence of two free bonds of the atom № 26 might lead to hybridization, i.e., association. Long single bonds between atoms № 2–3 and 1–18, which decay during low temperature annealing, are shown. Long optically inactive chains, and closed stable clusters of several atoms, connected to each other by double bonds, are also shown in Fig. 24.

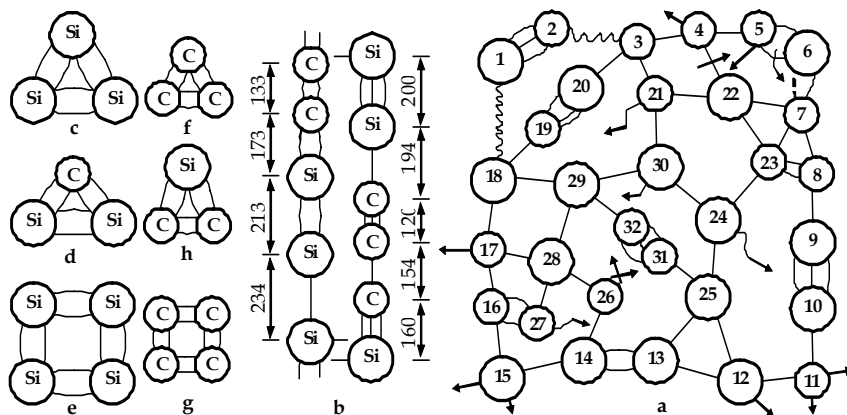


Fig. 24. Possible variants of both the infrared inactive clusters (a-h), chains of them (b) and a flat net of clusters (a) with various types of bonds between the atoms of Si (great circles) and C (small circles). Bond lengths are presented in pm.

It was found that for the layers SiC_x with low carbon concentrations (Fig. 23), the minimum of IR transmission peak for the TO-phonons is shifted to above 800 cm^{-1} as the annealing temperature is increased. In the case of $\text{SiC}_{0.4}$ the position of the peak minimum shifts from 725 to 810 cm^{-1} in the temperature range $20\text{--}1100^\circ\text{C}$ and returns to the 800 cm^{-1} at 1300°C . In the case of $\text{SiC}_{0.12}$ – from 720 to 820 cm^{-1} in the range $20\text{--}1000^\circ\text{C}$ and returns to 800 cm^{-1} at 1200°C . In the case of $\text{SiC}_{0.03}$ – from 720 to 830 cm^{-1} in the range $20\text{--}1000^\circ\text{C}$ and does not change its position during $1100\text{--}1200^\circ\text{C}$. Displacement of the peak minimum into the region above 800 cm^{-1} may be due to the presence of SiC nanocrystals of small size ($\leq 3\text{ nm}$), and an increase in the contribution to the IR absorption amplitude of their surfaces and surfaces of the crystallites Si, containing strong shortened Si–C-bonds. For a layer $\text{SiC}_{0.12}$ and $\text{SiC}_{0.4}$, return of the minimum to 800 cm^{-1} at temperatures of $1100\text{--}1400^\circ\text{C}$ may be caused by incorporation of carbon atoms into the nanocrystals of SiC and the growth of their size up to $3.5\text{--}5\text{ nm}$ and higher.

The observed shift of the peak minimum indicates the following fact: the absorbing at low frequencies energetically unfavorable long single Si–C-bonds decay during annealing at $600\text{--}1000^\circ\text{C}$, and the stronger short or tetrahedral Si–C-bonds absorbing at higher frequencies, are formed. Since the amplitude of IR transmission at 800 cm^{-1} is proportional to the concentration of tetrahedral oriented Si–C-bonds, and the amplitude at a certain frequency is assumed to be proportional to the absorption of Si–C-bonds at this frequency, we measured the IR transmittance amplitude for transverse optical (TO) phonons at wavenumbers of $700, 750, 800, 850$ and 900 cm^{-1} after implantation and annealing at $200\text{--}1400^\circ\text{C}$ (Fig. 25).

It can be seen from Figs. 25a–c that in the temperature range $20\text{--}1300^\circ\text{C}$, the amplitude of the peak at 800 cm^{-1} increases from 15 to 62% for the $\text{SiC}_{1.4}$ layer, from 14 to 68% for the $\text{SiC}_{0.95}$ layer, and from 18 to 87% for the $\text{SiC}_{0.7}$ layer. In the interval $20\text{--}900^\circ\text{C}$, the amplitude varies insignificantly. The maximal number of tetrahedral Si–C-bonds at 1300°C is observed in the $\text{SiC}_{0.7}$ layer. For these layers with high carbon concentration, the amplitudes of almost all frequencies (except 900 cm^{-1}) increase at 400°C , which can be due to ordering of the layer

and the formation of optically active Si-C-bonds. A certain increase in the amplitude at 800 cm^{-1} indicates the formation of tetrahedral Si-C-bonds at low temperatures.

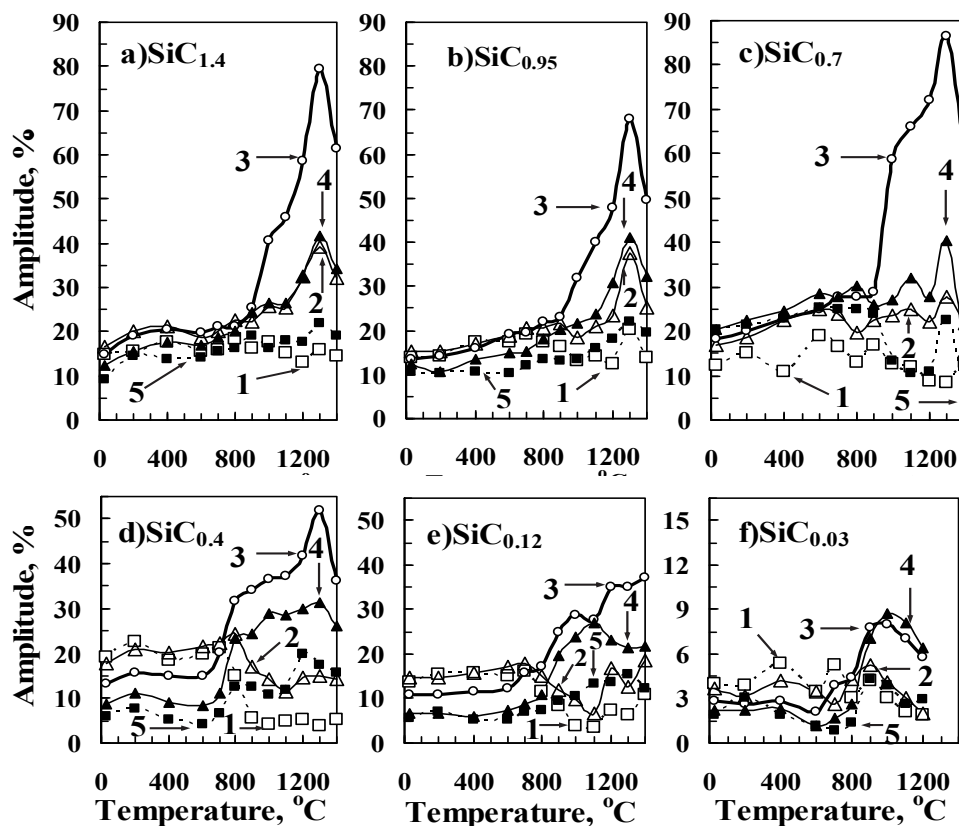


Fig. 25. Effect of the annealing temperature on the IR transmittance amplitude at wavenumbers of (1-□) 700 cm^{-1} , (2-Δ) 750 cm^{-1} , (3-○) 800 cm^{-1} , (4-▲) 850 cm^{-1} , and (5-■) 900 cm^{-1} under normal incidence of IR radiation on the sample surface: a) $\text{SiC}_{1.4}$; b) $\text{SiC}_{0.95}$; c) $\text{SiC}_{0.7}$; d) $\text{SiC}_{0.4}$; e) $\text{SiC}_{0.12}$; f) $\text{SiC}_{0.03}$.

The amplitudes at 800 cm^{-1} and close frequencies of 750 and 850 cm^{-1} considerably increase after annealing at temperatures in the interval 900–1300°C. This means that in $\text{SiC}_{1.4}$, $\text{SiC}_{0.95}$ and $\text{SiC}_{0.7}$ layers with a high carbon concentration, intense formation of tetrahedral Si-C bonds begins at 900–1000°C and continues up to 1300°C. This can be due to breakdown of carbon and silicon clusters (chains and flat nets) as well as single Si-C-bonds during annealing. The most pronounced decay of long single Si-C-bonds absorbing at a frequency of 700 cm^{-1} (Fig. 25a-c, curve 1) occurs during annealing at 800–1200°C. Annealing of $\text{SiC}_{1.4}$, $\text{SiC}_{0.95}$ and $\text{SiC}_{0.7}$ layers at 1400°C resulted in a decrease in the amplitudes in the entire frequency range 700–900 cm^{-1} , which is apparently due to decomposition of SiC as a result of carbon desorption from the layer. It can be seen from Fig. 25 that the dependences of IR transmission amplitudes on the annealing temperature for different wavenumbers for $\text{SiC}_{1.4}$, $\text{SiC}_{0.95}$ and $\text{SiC}_{0.7}$ layers with a

high carbon concentration are almost analogous, but differ considerably from the dependences for SiC_{0.4}, SiC_{0.12} and SiC_{0.03} layers with a low carbon concentration. This indicates the same nature of carbon and carbon-silicon clusters in SiC_{1.4}, SiC_{0.95} and SiC_{0.7} layers.

For SiC_{0.4}, SiC_{0.12} and SiC_{0.03} layers with a low carbon concentration, measurements of the IR transmission amplitude show (Figure 25, d-f) that in the temperature range 20–1300°C, the amplitude at 800 cm⁻¹ increases from 13 to 52% for the SiC_{0.4} layer, from 11 to 37% for the SiC_{0.12} layer, and from 2.8 to 8% for the SiC_{0.03} layer. At temperatures 20–600°C, in these layers dominate the long and weak Si–C-bonds, which absorb at frequencies of 700 and 750 cm⁻¹ (Fig. 25d-f, curves 1 and 2) and decay at low temperatures. A noticeable increase in the amplitudes is observed at frequencies of 800 and 850 cm⁻¹ in the temperature range 700–1000°C, which indicates an increase in the number of tetrahedral and nearly to tetrahedral short Si–C-bonds. A distinguishing feature for SiC_{0.4}, SiC_{0.12} and SiC_{0.03} layers with a low carbon concentration is an intense increase in the number of tetrahedral bonds at low temperatures (700°C), which is due to a low concentration of stable carbon clusters (chains, flat nets, etc.) disintegrating at higher temperatures, because low content of carbon atoms. Consequently, in the range of 800–900°C by the number of tetrahedral Si–C-bonds and the amplitude at 800 cm⁻¹ (35%) the SiC_{0.4} layers exceed all the above considered layers SiC_{1.4}, SiC_{0.95}, SiC_{0.7}, SiC_{0.12} and SiC_{0.03}.

For SiC_{0.4} and SiC_{0.12} layers in the temperature range 700–1100°C, the increase in the amplitudes at frequencies of 800, 850, and 900 cm⁻¹ is accompanied by a decrease in the amplitudes at 700 and 750 cm⁻¹, indicating an increase in the number of tetrahedral and strong short Si–C-bonds due to disintegration of long weak bonds that prevailed after implantation. Intensive formation of Si–C-bonds with the tetrahedral orientation, which absorb at a frequency of 800 cm⁻¹ (Fig 25d and e, curves 3) at 1200°C is due to disintegration of strong optically inactive clusters of C and Si atoms. The SiC_{0.4} layer with a higher carbon concentration differs from the SiC_{0.12} layer because it contains stronger clusters disintegrating at 1300°C, which is manifested in a sharp increase in the amplitude at this temperature. As in the case of SiC_{1.4}, SiC_{0.95} and SiC_{0.7} layers with a high carbon concentration, the decrease in the amplitudes for SiC_{0.4} at 1400°C is due to disintegration of SiC crystallites and desorption of carbon from the layer (Fig. 25d, curves 2–5).

Increase in the number of tetrahedral bonds in the layer SiC_{0.03} in the temperature range 800–900°C occurs simultaneously with some increase in amplitude for all frequencies, i.e. not due to the decay of optically active bonds. For this layer with very low carbon concentration is difficult to assume the presence of a noticeable amount of stable carbon and carbon-silicon clusters. We can assume that a significant increase of tetrahedral bonds can occur by reducing the number of dangling bonds of carbon atoms.

We assume that the total area of the SiC-peak of IR transmission is the area of region between the curve of the IR spectrum and the baseline $|T_1T_2|$ (Fig. 16a), and it is equal to the total absorption of infrared radiation at all frequencies and is roughly proportional to the number of all types of absorbing Si–C-bonds (Wong et al., 1998; Chen et al., 1999). Peak area was determined from the spectra of IR transmission (Figs. 16–21), based on the approximation:

$$A = \frac{1}{2}(T_1 + T_2)(\nu_2 - \nu_1) - \int \tau(\nu) d\nu \approx \frac{1}{2}(T_1 + T_2)(\nu_2 - \nu_1) - \sum \tau(\nu) \delta\nu, \quad (2)$$

where A – total absorption (or transmission) in relative units in the frequency range $\nu_1 < \nu < \nu_2$, $\tau(\nu)$ – transmission at frequency ν , T_1 and T_2 – the values of IR transmission at frequencies ν_1 and ν_2 , respectively, $\delta\nu$ – step of measurements, equal to 2.5 or 5 cm^{-1} .

Fig. 26 shows the peak area of IR transmission for TO phonons as a function of the annealing temperature and the concentration of carbon for layers $\text{SiC}_{1.4}$, $\text{SiC}_{0.95}$, $\text{SiC}_{0.7}$, $\text{SiC}_{0.4}$, $\text{SiC}_{0.12}$ and $\text{SiC}_{0.03}$. It is seen that in the range of 27–1200°C the number of optically active Si–C-bonds is highest in the layer $\text{SiC}_{0.7}$. A smaller number of Si–C-bonds in the SiC_x layers if $x < 0.7$ is caused by lower carbon content, and if $x > 0.7$ – due to the high concentration of stable clusters, decomposing at higher temperatures. Therefore, at 1300°C number of optical active Si–C-bonds is the highest in layer $\text{SiC}_{1.4}$.

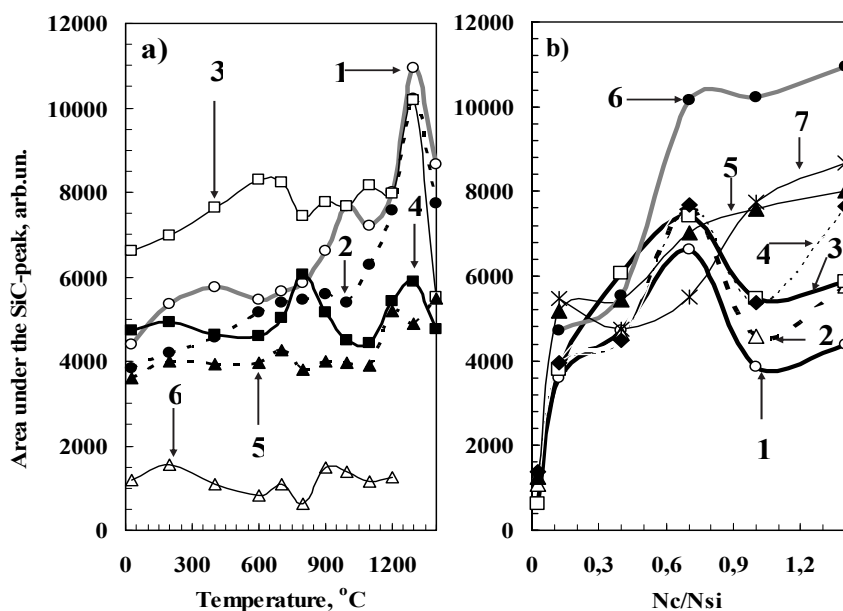


Fig. 26. Effect of the annealing temperature and concentration of carbon on the area under the IR transmittance SiC-peak for TO phonons under normal incidence of IR radiation on the sample surface: a) $\text{SiC}_{1.4}$ (1), $\text{SiC}_{0.95}$ (2), $\text{SiC}_{0.7}$ (3), $\text{SiC}_{0.4}$ (4), $\text{SiC}_{0.12}$ (5) и $\text{SiC}_{0.03}$ (6); b) 27 °C (1), 400°C (2), 800°C (3), 1000°C (4), 1200°C (5), 1300°C (6), 1400°C (7).

For layers $\text{SiC}_{1.4}$, $\text{SiC}_{0.95}$ and $\text{SiC}_{0.7}$ with high carbon concentration, the peak area of IR transmission immediately after implantation has the lowest value (Fig. 26a). In the temperature range 20–1400°C, the value of the peak area for $\text{SiC}_{1.4}$ is changed in the range of values within 4380–10950 arb. units, for $\text{SiC}_{0.95}$ – within 3850–10220 units, for $\text{SiC}_{0.7}$ – within 6620–10170 units, and tends to increase with annealing temperature, indicating a significant amount of carbon atoms do not bound with silicon in the layers immediately after implantation: $\sim [1 - (4380/10950) \times 100/1.4] \approx 70\%$ for $\text{SiC}_{1.4}$, $\sim [1 - (3850/10220)] \times 100\% \approx 62\%$ for $\text{SiC}_{0.95}$, $\sim [1 - (6620/10170)] \times 100\% \approx 35\%$ for $\text{SiC}_{0.7}$. These estimates can be valid if we assuming that after annealing at 1300°C all clusters broke up and all carbon atoms formed optically active Si–C-bonds in the layer (except the excess atoms in $\text{SiC}_{1.4}$). In the case of a

partial decay of the clusters at 1300°C, the estimations of the proportion of carbon atoms included in the optically inactive clusters suggest even higher values. In general, the assertions do not contradict the data (Chen et al., 2003; Wong et al., 1998; Chen et al., 1999), where the growths of area of Si–C-peak after annealing, were shown. We evaluated the linearity of the dependence of the area and number of optically active Si–C-bonds on the carbon concentration, basing on data of the peak area (Table 4).

T, °C	A, arb. un.					
	SiC _{0.03}	SiC _{0.12}	SiC _{0.4}	SiC _{0.7}	SiC _{0.95}	SiC _{1.4}
20°C	1709	3588	4719	6622	3848	4384
200°C	1840	3990	4929	6966	4198	5347
400°C	1464	3921	4638	7647	4571	5757
600°C	1672	3979	4595	8296	5152	5442
700°C	1963	4248	5035	8227	5394	5665
800°C	1127	3795	6061	7428	5458	5864
900°C	1924	4004	5150	7772	5571	6619
1000°C	2708	3958	4499	7674	5386	7664
1100°C	2069	3910	4437	8158	6296	7190
1200°C	2428	5181	5428	7980	7570	8011
1300°C	0	4886	5805	10169	10221	10953
1400°C		5473	4749	5510	7741	8670

Table 4. Area, A, under the IR transmittance SiC-peak for TO phonons obtained from the IR spectra for SiC_x layers after implantation and annealing

In the layer SiC_{0.03} the number of optically active Si–C-bonds after annealing should be roughly proportional to the quantity of carbon atoms due to the low concentration of carbon and stable carbon or carbon-silicon clusters as well. We take the maximum value of the area of Si–C-peak for the SiC_{0.03} layer at 1000°C as equal to 1. If the proportionality is linear, an increase in the concentration of carbon in SiC_x layer on n_1 times ($n_1 = (N_C/N_{Si})/0.03 = x/0.03$) should increase the peak area on n_2 times ($n_2 = A_x(T)/A_{0.03}(1000^\circ\text{C})$), and $n_1 = n_2$, if not come saturation in the amplitude of the transmission, and the carbon atoms are not included in the optically inactive clusters. Since the saturation amplitude of the IR transmission is not reached (Fig. 25) and $n_2 < n_1$, so a values $100\% \times n_2/n_1$ show the portion of carbon atoms forming optically active Si–C-bonds in the SiC_x layer. As it turned out, at 1300°C in the layer SiC_{1.4} only 9% of the C atoms form the optically active Si–C-bonds, in SiC_{0.95} – 12%, in SiC_{0.7} and SiC_{0.4} – 16%, in SiC_{0.12} – 45%, while the other carbon atoms remain in the composition of strong clusters. The total number of SiC (optically active Si–C-bonds) in the SiC_x layers after annealing at 1300°C increases with the fractional degree of carbon concentration $(x/0.03)^y$, where $y \sim 0.37 \pm 0.09$ (Table 5).

In (Wong et al., 1998) at a fixed energy the total number of formed SiC increases with the fractional degree of doses, namely, D^y with y defined as 0.41. In this paper, SiC layers were synthesized using the ion source MEVVA implantation in p-Si of carbon ions with energies in the range 30–60 keV and doses ranged within $(0.3\text{--}1.6) \times 10^{18} \text{ cm}^{-2}$. In this case, the infrared absorption spectra of SiC layers were decomposed into two or three components, one of which belonged to the amorphous SiC, while the other two to β -SiC.

Really, as seen in Table 5, the increase of carbon concentration x in the layer $\text{SiC}_{0.12}$ in 4 times in comparison with $\text{SiC}_{0.03}$ results to a smaller increase in the area of SiC-peak, pointing to the disproportionate increase in the number of optically active Si-C-bonds. At least, the maximum area at 1200°C for a $\text{SiC}_{0.12}$ layer exceeds the maximum area for $\text{SiC}_{0.03}$ layer only in 1.91 times. Further increase in the concentration of carbon x in the SiC_x layers in 13, 23, 32, 47 times leads to an increase in the number of optically active Si-C-bonds in several times less than expected – no more than 4.04 times even for high temperature annealing.

Both the peak areas and the number of bonds do not increase linearly with the increase of concentration and it is not caused by saturation of amplitude values. As in the case of $N_C/N_{\text{Si}} = 0.12$, the increase of concentration in 13.3 times at $N_C/N_{\text{Si}} = 0.4$, has led to an increase in the amplitude of only 9 times, and an area of 2.1 times (5805 un.) at 1300°C (Tables 4 and 5), although the amplitude of the IR transmittance at the minimum of the peak is far from saturation (52%). This confirms that the determining factor is the presence of strong clusters, in the structure of which is included the majority of the carbon atoms. That is at 1300°C in the $\text{SiC}_{0.4}$ layer only $n_1/n_2 = 2.1/13.33 = 16\%$ of the carbon atoms form an optically active Si-C-bonds, and in the $\text{SiC}_{0.12}$ layer – 45%. Then, in the optically inactive stable clusters are included the rest 84% and 55% of carbon atoms (Table 5), respectively, resulting in no increase in peak area proportionally to the concentration of carbon. Since there is a predominance of the tetrahedral oriented bonds among the optically active Si-C-bonds, the amount of tetrahedral Si-C-bonds is sufficient for the appearance of SiC crystallites in the layers, which is observed on the X-ray diffraction pattern.

SiC_x	$\text{SiC}_{0.03}$		$\text{SiC}_{0.12}$		$\text{SiC}_{0.4}$		$\text{SiC}_{0.7}$		$\text{SiC}_{0.95}$		$\text{SiC}_{1.4}$	
$n_1=x/0.03$	1.0		4.0		13.3		23.3		31.7		46.7	
$T, ^\circ\text{C}$	$\frac{A_x}{A_{0.03}}$	Si-C	$\frac{A_x}{A_{0.03}}$	Si-C	$\frac{A_x}{A_{0.03}}$	Si-C	$\frac{A_x}{A_{0.03}}$	Si-C	$\frac{A_x}{A_{0.03}}$	Si-C	$\frac{A_x}{A_{0.03}}$	Si-C
	$A_{0.03}$	%	$A_{0.03}$	%	$A_{0.03}$	%	$A_{0.03}$	%	$A_{0.03}$	%	$A_{0.03}$	%
20	0.63	63	1.3	33	1.7	13	2.4	10	1.4	4	1.6	3
200	0.68	68	1.5	37	1.8	14	2.6	11	1.6	5	2.0	4
400	0.54	54	1.4	36	1.7	13	2.8	12	1.7	5	2.1	5
600	0.62	62	1.5	37	1.7	13	3.1	13	1.9	6	2.0	4
700	0.72	72	1.6	39	1.9	14	3.0	13	2.0	6	2.1	4
800	0.42	42	1.4	35	2.2	17	2.7	12	2.0	6	2.2	5
900	0.71	71	1.5	37	1.9	14	2.9	12	2.1	6	2.4	5
1000	1.00	100	1.5	37	1.7	12	2.8	12	2.0	6	2.8	6
1100	0.76	76	1.4	36	1.6	12	3.0	13	2.3	7	2.7	6
1200	0.90	90	1.9	48	2.0	15	2.9	13	2.8	9	3.0	6
1300		90	1.8	45	2.1	16	3.8	16	3.8	12	4.0	9
$\gamma(1300^\circ\text{C})$			0.40		0.28		0.42		0.38		0.36	

Table 5. Relative values of area ($n_2 = A_x(T)/A_{0.03}(1000^\circ\text{C})$) of IR transmission SiC-peak and the proportion of carbon atoms ($100\% \times n_2/n_1$) which forms an optically active Si-C-bonds in the SiC_x layers.

Evaluation results may be debatable, since the literature contains different points of view concerning inclusion of carbon into SiC. Akimchenko et al. (1977a) after implantation of Si ($E = 40 \text{ keV}$, $D = 3.7 \times 10^{17} \text{ cm}^{-2}$) in diamond and annealing at temperatures of 500–1200°C assumed that almost 100% of implanted carbon atoms included in the SiC. This conclusion was made from accordance of calculated layer thickness (80 nm) with ones found from the absorption near 810 cm^{-1} (70 nm). A comparison with the magnitude of the SiC thickness (8–10 nm) obtained by X-ray diffraction, allowed to conclude that 10–15% of atoms of the disordered SiC united into β -SiC crystallites, which contribute to the X-ray reflection, and the rest remains in the amorphous state. Kimura et al. (1982) basing on data from the optical density of the infrared transmission spectra have established that all implanted carbon are included in β -SiC after annealing at 900–1200°C, if the concentration of implanted carbon is less or equal to the stoichiometric composition of SiC at the peak of the distribution. In the case of higher doses, the excess carbon atoms form clusters and are not included into β -SiC, even after annealing at 1200°C. The activation energy required for inclusion of carbon atoms in the β -SiC, increases with increasing of implantation doses, since more energy is required for the decomposition of carbon clusters. Durupt et al. (1980) showed that if the annealing temperature below 900°C, the formation of SiC is less pronounced in the case of high dose, and annealing at higher temperature removes the differences.

On the other hand, Borders et al. (1971) from the infrared absorption and Rutherford backscattering data found that about half of carbon atoms implanted into the silicon ($E = 200 \text{ keV}$, $D = \sim 10^{17} \text{ cm}^{-2}$) included in micro-SiC. According to our estimates, the concentration of carbon atoms in the layer was lower than 10% ($x < 0.1$). Kimura et al. (1981) from the analysis of infrared spectra revealed that after implantation ($E = 100 \text{ keV}$) and annealing at 900°C about 40–50% of carbon atoms united with Si atoms to form β -SiC, and this value monotonically increased to 70–80% with increasing of annealing temperature up to 1200°C. The number of carbon atoms included in the β -SiC was affected by dose of carbon ions. Calcagno et al. (1996) showed that the optical band gap and the intensity of the infrared signal after annealing at 1000°C increased linearly with carbon concentration, reaching a maximum at the stoichiometric composition of SiC. At higher carbon concentrations intensity of the infrared signal undergoes saturation, and the band gap decreases from 2.2 to 1.8 eV. By Raman spectroscopy is shown that this is due to the formation of clusters of graphite. Simon et al. (1996) after the high-temperature (700°C) implantation of carbon ions into Si ($E = 50 \text{ keV}$, $D = 10^{18}$ and $2 \times 10^{18} \text{ cm}^{-2}$) show that the carbon excess precipitates out, forming carbon clusters. It is assumed that the stresses and defects, formed after the first stage of implantation, form traps, which attract the following carbon atoms. Liangdeng et al. (2008) after implantation of C ions ($E = 80 \text{ keV}$, $D = 2.7 \times 10^{17} \text{ ион/см}^2$) in the Raman spectra observed double band with center in 1380 and 1590 cm^{-1} corresponding to the range of graphitized amorphous carbon. The authors suggest that since solid solubility of carbon in a-Si at a temperature close to the melting point of Si, is about 10^{17} /cm^3 , and almost disappears at room temperature, the carbon has a tendency to form precipitates. Bayazitov et al. (2003) after implantation of carbon ions ($E = 40 \text{ keV}$, $D = 5 \times 10^{17} \text{ cm}^{-2}$) in silicon and pulsed ion beam annealing ($W = 1.0 \text{ J/cm}^2$, $\text{C}^+(\sim 80\%)$ and $\text{H}^+(\sim 20\%)$) have formed a β -SiC layer with an average size of grain about 100 nm. Increasing the energy density per pulse up to 1.5 J/cm^2 leads also to appearance of graphite grains of sizes about 100 nm, as well as visually observed darkening of the sample. When exposed by radiation of ruby laser ($\lambda = 0.69 \text{ }\mu\text{m}$, $\tau = 50 \text{ nsec}$, $W = 0.5\text{--}2 \text{ J/cm}^2$) also formed the graphite grains, beginning from $W = 0.5 \text{ J/cm}^2$.

Tetelbaum et al. (2009) by implantation in SiO₂ film of Si ions ($E = 100$ keV, $D = 7 \times 10^{16}$ cm⁻²) provided the concentration of excess silicon at the peak of the ion distribution about 10 at.%. Then the same number of carbon atoms was implanted. The obtained data of the white photoluminescence with bands at ~400, ~500 and ~625 nm, attributed to nanoinclusion of phases of SiC, C, nanoclusters and small nanocrystals Si, respectively (the arguments supported by references to the results of Perez-Rodriguez et al. (2003) and Fan et al. (2006)). Similarly, Zhao et al. (1998) received a peak at 350 nm, and a shifting by the annealing the blue peak at 410–440, 470, 490 nm. The existence of inclusions phases of carbon and silicon carbide in the films of SiO₂ in (Tetelbaum et al., 2009) was confirmed by X-ray photoelectron spectroscopy by the presence of the C–C (with energy ~285 eV) and Si–C (with energy ~283 eV). Comparing the amplitudes I_{RFS} one can conclude that a number of C–C is comparable to the number of Si–C-bonds, and a luminescence at 500 nm (carbon clusters) is considerably greater than the luminescence at 400 nm (silicon carbide). Belov et al. (2010) used higher doses of carbon ions ($E = 40$ keV): 6×10^{16} cm⁻², 9×10^{16} cm⁻² and 1.2×10^{17} cm⁻², in which the concentration of carbon (by our estimation) do not exceed 25% at the maximum of the carbon distribution. The authors believe that the luminescent centers, illuminated at wavelengths below 700 nm, represent the nanoclusters and nanocrystals of (Si:C), and amorphous clusters of diamond-like and graphitized carbon. In this case, with increasing of carbon doses the intensity of photoluminescence from Si nanocrystals (>700 nm) varies little, and concluded that a significant portion of the implanting carbon is included into the carbon clusters. The high content of graphitized clusters in the films also discussed in (Shimizu-Iwayama et al., 1994). All these data suggest that a significant or most of the carbon atoms are composed of carbon clusters, although the concentration of carbon atoms in a layer of "SiO₂ + Si + C" was around 9 at.%. In our opinion, this confirms our high estimates of carbon content in the optically inactive C- and C–Si-clusters, made basing the analysis of IR spectra. Analysis of the behavior of the curves in Fig. 26 may be interesting from the point of studying the influence of decay of clusters and Si–C-bonds on the formation of tetrahedral oriented Si–C-bonds. Basing on the analysis one can suggest possible mechanisms of formation of silicon carbide grains in the layer and put forward a number of hypotheses. For example, the growth curves of SiC-peak area for the SiC_{1.4}, SiC_{0.95} and SiC_{0.7} layers with a high carbon concentration have the maxima of values, which may be related with the formation and breaking of bonds and clusters in the implanted layer. Intensive growth of area in the range 1100–1300°C caused by the decay of stable optically inactive clusters (Table 5) and an increase in the number of all types of Si–C-bonds absorbing at all frequencies of considered range, in particular, the tetrahedral oriented bonds (800 cm⁻¹). However, the growth of these bonds (curves 3 in Figure 25) is not always accompanied by an increase in area under the IR transmittance peak.

Variation of the peak area for the SiC_{1.4} layer (Fig. 26) has peaks at 400, 1000 and 1300°C. The growth of the peak area in the range of 20–800°C for SiC_{1.4}, SiC_{0.95} and SiC_{0.7} layers with high carbon concentrations is caused by a weak ordering of the amorphous layer and the formation of optically active Si–C-bonds, including the tetrahedral oriented bonds (Fig. 25a). Significant growth of area in the range 800–1000°C is resulted by an increase of the absorption in the range 800 ± 50 cm⁻¹, i.e. by an intensive formation of the tetrahedral and near tetrahedral Si–C-bonds due to the decay of such optically inactive clusters as flat nets and chains (Fig. 24). Decrease of Si–C-peak area (Fig. 26, curves 1 and 3) in ranges of 400–600°C or 600–800°C caused by decay of long single bonds absorbing near 700 or 750 cm⁻¹.

¹ (Fig. 25a, curves 1 and 2). Decrease in area at 1400°C is associated with a decrease in amplitude at all considered frequencies, especially at 800 cm⁻¹, indicating that the decay of a large number of tetrahedral Si-C-bonds and desorption of ~ 15% of carbon atoms are taken place.

As shown in Fig. 26 (curve 3), the number of optically active Si-C-bonds in the temperature range 20–1200°C is the highest for the layer SiC_{0.7}. In the temperature range 20–1300°C, the amplitude at 800 cm⁻¹ increases in 4.4 times from 20 to 87%, while the area of SiC-peak grow only in $3.76/2.45 = 1.54$ times.. It follows that growth in the number of tetrahedral bonds is taken place not only due to the decay of optically inactive Si-C-clusters, but as a result of decay of long single Si-C-bonds as well, which absorb at a frequency of 700 cm⁻¹ (Fig. 25c, curve 1), with their transformation into a tetrahedral (curve 3) and close to tetrahedral (curve 4) bonds, which absorb near 800 and 850 cm⁻¹. Most intensively this process occurs near the surface of SiC crystallites (Fig.12b) in the range 900–1300°C showing the mechanism of the formation of SiC crystallites.

The temperature dependence of both the amplitude of the IR transmission at different wave numbers and the area of SiC-peak for the SiC_{1.4}, SiC_{0.95} and SiC_{0.7} layers has a similar character, which, as it was mentioned above, indicates the common nature of carbon and carbon-silicon clusters in these layers with a high concentration of carbon. Analysis of the behavior of the curves in Fig. 26 (curves 4, 5 and 6) shows that the curves of the area changes of the peak for the SiC-layers with low carbon concentration SiC_{0.4}, SiC_{0.12} and SiC_{0.03} also have the maxima and minima of magnitude, which can be associated with the formation and breaking of bonds and clusters. These layers are characterized by an higher proportion (%) of carbon atoms forming an optically active Si-C-bonds (Table 5), although the total number is low in comparison with SiC_{1.4}, SiC_{0.95} and SiC_{0.7} layers (Fig. 26).

The value of the area for the SiC_{0.4} layer in the temperature range 20–1400°C has not a continuous upward trend. Maximum of area at 800°C is due to the formation of tetrahedral and close to tetrahedral bonds, absorbing near 800 and 850 cm⁻¹ (Fig. 25d, curves 3 and 4), respectively. The formation of tetrahedral bonds (800 cm⁻¹) at temperatures of 900–1100°C (Fig. 25d, curve 3) is accompanied by decreasing of peak area due to its narrowing resulting from the decay of long single Si-C-bonds, which absorbed near 700 and 750 cm⁻¹ and prevailed at temperatures below 800°C. The formation of Si and SiC crystallites in the layer is taken place almost simultaneously, which suggests intense movement of C and Si atoms and the increase in the number of dangling bonds. The increase in area in the range 1200–1300°C (Fig. 26) is caused by growth of tetrahedral (Fig. 25, curve 3) and close to tetrahedral (Fig. 25, curves 2 and 4) Si-C-bonds due to decay of optically inactive clusters.

For layers SiC_{0.12} and SiC_{0.03} with carbon concentration much lower than stoichiometric for SiC, the absence of significant growth of area in the temperature range 200–1100°C is revealed due to the small amount of optically inactive unstable carbon flat nets and chains, the decay of which could cause an intensive formation of absorbing bonds. Nevertheless, a significant increase in amplitude at 800 cm⁻¹ is observed due to the formation of tetrahedral bonds. Increase in the area after annealing at 900–1000°C for the SiC_{0.03} layer together with growth of the amplitudes of all types of optically active Si-C-bonds may be caused by the formation of silicon crystallites, which accompanied by the displacement of carbon atoms and a reduction in the number of dangling bonds of carbon atoms. For layers SiC_{0.12} and SiC_{0.4} the significant growth of area at temperatures 1200–1300°C caused by an increase in the number of all types of optically active bonds due to decay of stable carbon clusters.

The half-width of the Si-C-peak of IR transmission were measured (Fig. 27). Narrowing of the peak occurs due to intensive formation of tetrahedral oriented Si-C-bonds, absorbing at 800 cm^{-1} , and decay of bonds, which absorb at frequencies far from the value of 800 cm^{-1} . Since the tetrahedral bonds correspond to the crystalline phase of silicon carbide, so the narrowing of the SiC-peak of the IR spectrum is related with the processes of the implanted layer ordering. For a layer $\text{SiC}_{1.4}$ a sharp narrowing of the peak from 300 to 110 cm^{-1} is taken place in the range $800\text{--}1200^\circ\text{C}$, and then the half-width does not change significantly. The most intensively this process occurs in the range $900\text{--}1000^\circ\text{C}$. On X-ray diffraction patterns (Fig. 7), the appearance of lines of polycrystalline β -SiC was observed after annealing at 1200°C and above. This implies that the appearance of SiC crystallites in the layer is recorded when the formation of tetrahedral bonds (peak narrowing) is substantially complete (110 cm^{-1}). Assumptions about the relationship between the size of SiC crystallites and half-width of the peak were also expressed in (Wong et al., 1998; Chen et al., 1999). For the $\text{SiC}_{0.7}$ layer in range $900\text{--}1000^\circ\text{C}$, a sharp narrowing of the peak from 280 to 85 cm^{-1} is taken place and occurred more intensive up to 67 cm^{-1} at 1200°C than for layers with a higher carbon concentration $\text{SiC}_{0.95}$ (115 cm^{-1} , 1200°C) and $\text{SiC}_{1.4}$ (108 cm^{-1} , 1300°C), indicating a much lower concentration of strong clusters in the layer $\text{SiC}_{0.7}$.

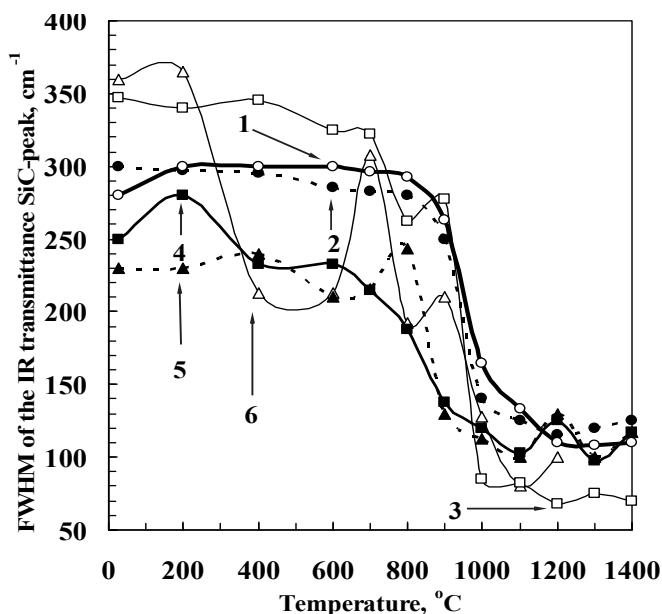


Fig. 27. Effect of the annealing temperature on the FWHM of the IR transmittance SiC-peak for TO phonons under normal incidence of IR radiation on the sample surface: 1 – $\text{SiC}_{1.4}$, 2 – $\text{SiC}_{0.95}$, 3 – $\text{SiC}_{0.7}$, 4 – $\text{SiC}_{0.4}$, 5 – $\text{SiC}_{0.12}$, 6 – $\text{SiC}_{0.03}$.

For a layer $\text{SiC}_{0.12}$, a sharp narrowing of the peak from 240 to 100 cm^{-1} (Fig. 27, curve 5) in the range $800\text{--}1100^\circ\text{C}$ is shown, and then is not substantially reduced, demonstrating the formation of polycrystalline SiC phase at this temperature. In general, for the $\text{SiC}_{0.4}$, $\text{SiC}_{0.12}$ and $\text{SiC}_{0.03}$ layers with low carbon concentration a sharp narrowing of the peak occurs at

temperatures of about 100°C lower than for the layers SiC_{1.4}, SiC_{0.95} and SiC_{0.7} due to a lower concentration of strong clusters.

Thus, we have shown a negative effect of stable carbon and carbon-silicon clusters on the crystallization of SiC in the layers. Heat treatment up to 1200°C does not lead to complete disintegration of the clusters and the release of C and Si atoms to form SiC. In this regard, identification of alternative ways of processing the films to break down clusters and form a more qualitative structure of the SiC films is important. As shown in section 3.3, the characteristics of glow discharge hydrogen plasma and treatment (27.12 MHz, 12.5 W, 6.5 Pa, 100°C, 5 min) were sufficient to decay the tetrahedral Si-Si and Si-C-bonds and can be used for the destruction of stable carbon and carbon-silicon clusters. For IR analysis, the sample with the SiC_{0.95} film was cut into two parts and one of these samples was treated by hydrogen plasma. Fig. 28 shows the IR transmittance spectra of these SiC_{0.95} layers, untreated by plasma (a) and treated by hydrogen plasma (b) after annealing at 900°C for 30 minutes.

Peak maxima occur at 790 cm⁻¹, indicating the prevalence of tetrahedral oriented Si-C-bonds characteristic of crystalline SiC. Measurements of the half-widths of the spectra in Fig. 28a, b give the magnitudes 148 and 78 cm⁻¹ for pre-untreated and treated by hydrogen plasma SiC_{0.95} layer, respectively. If the value of 148 cm⁻¹ is characteristic for the temperature range 900–1000°C (Fig. 27, curve 2), but the value of 78 cm⁻¹, in principle, was unattainable for the SiC_{0.95} layer without pre-treatment by plasma throughout the temperature range 200–1400°C. Thus, we can conclude that annealing at 900°C of SiC_{0.95} layers, treated by hydrogen plasma with power of 12.5 watts only, has led to the formation of β-SiC crystalline layer, which superior in structure quality the untreated by plasma layer subjected to isochronous annealing in the range 200–1400°C. Obviously, the observed effects of plasma-induced crystallization is a consequence of the decay of clusters in the pre-treatment by glow discharge hydrogen plasma.

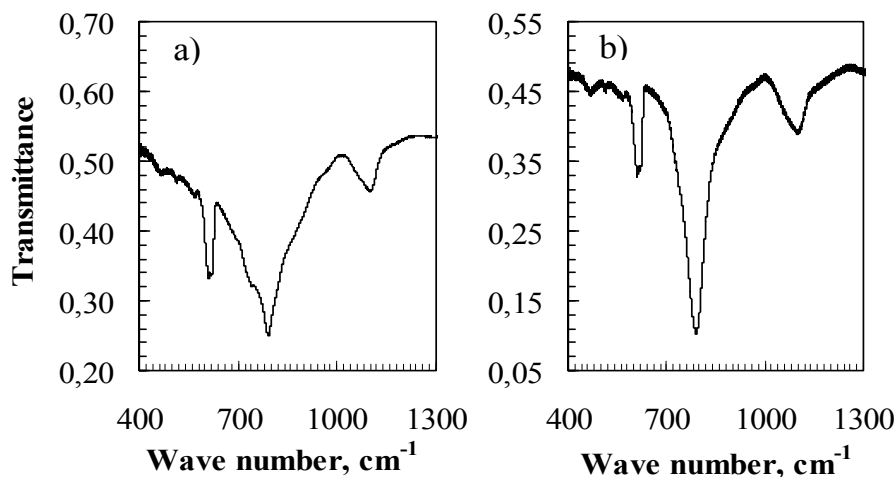


Fig. 28. IR transmission spectra for SiC_{0.95} layer after annealing at the temperature 900°C for 30 min (a) and after processing by glow discharge hydrogen plasma for 5 min and annealing at the temperature 900°C for 30 min (b).

3.5 Investigations by atomic force microscopy

AFM studies of the surface microstructure of the surface of the $\text{SiC}_{0.95}$ layer of area $500 \times 500 \text{ nm}^2$, and $1 \times 1 \text{ }\mu\text{m}^2$ show (Fig. 29a), that after implantation, the surface of the layer looks flat with fluctuations in the height ranged within 6 nm. The areas above the average line of the surface have bright light colors and the areas below the same have dark colors, from which begins the account of height. Annealing at 800°C (Fig. 29b) leads to the deformation of the surface and to an appearance of furrows indicating an intensive translations of atoms. After annealing at 1400°C the surface consists of grains with sizes of 30–50 nm. The variations in height ranged within 66 nm. Comparison of grain sizes with X-ray data on the average crystallite sizes of SiC (3–10 nm) shows that the grains are composed of crystallites of SiC.

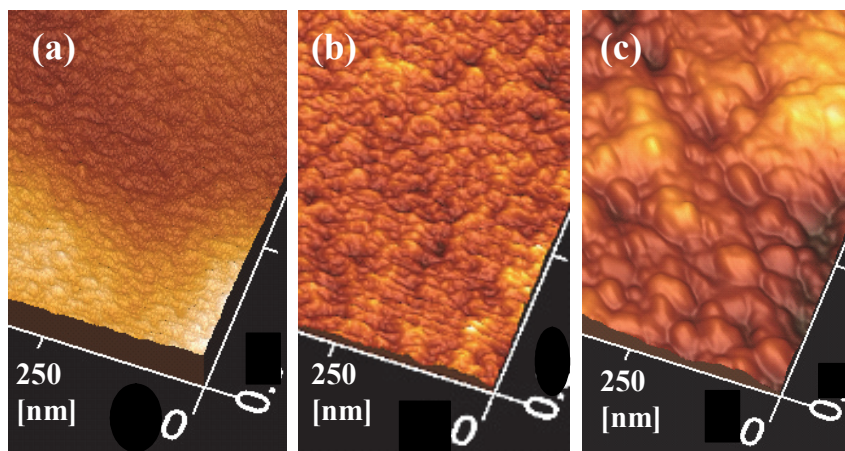


Fig. 29. AFM images from the surface of thin ($\sim 130 \text{ nm}$) $\text{SiC}_{0.95}$ film (a) after multiple implantation and annealing at (b) 800°C and (c) 1400°C .

In general, we can see that after implantation the surfaces of $\text{SiC}_{1.4}$, $\text{SiC}_{0.95}$, $\text{SiC}_{0.7}$, $\text{SiC}_{0.4}$ and $\text{SiC}_{0.12}$ layers looks smooth with the fluctuations of the height in range of 2–6 nm (Fig. 30). At temperatures of 800 – 1400°C the surface of these layers are deformed with the formation of grains with sizes of ~ 30 – 100 nm . For example, after implantation the smooth surface of $\text{SiC}_{1.4}$ layer looks broken with fluctuations of the height in range of 2 nm. Annealing at 1400°C leads to a clear fragmentation of grains on the surface. It is seen that the grains with sizes of $\sim 100 \text{ nm}$ are composed of subgrains, which probably represent the SiC crystallites with an average size of 10 nm. The surface of $\text{SiC}_{0.7}$ layer, after annealing at 1250°C for 30 minutes, consists of granules of a size of 50–100 nm and flat areas.

Amorphous after implantation, the surface structure of the $\text{SiC}_{0.4}$ layer is also transformed after annealing at 1200°C for 30 minutes and forms a granular structure consisting of spherical grains of Si and SiC with sizes of ~ 50 – 100 nm , which suggests an intensive movements of atoms in this layer at high temperature due to the lower content of stable clusters in the film. The surface of the $\text{SiC}_{0.12}$ layer after annealing at 1400°C consists of grains with sizes of 50 nm. The smooth surface of $\text{SiC}_{0.03}$ layer is recrystallized at 1250°C and contains evenly distributed inclusions of SiC in the form of point protrusions with a diameter of 20 nm (Fig. 30).

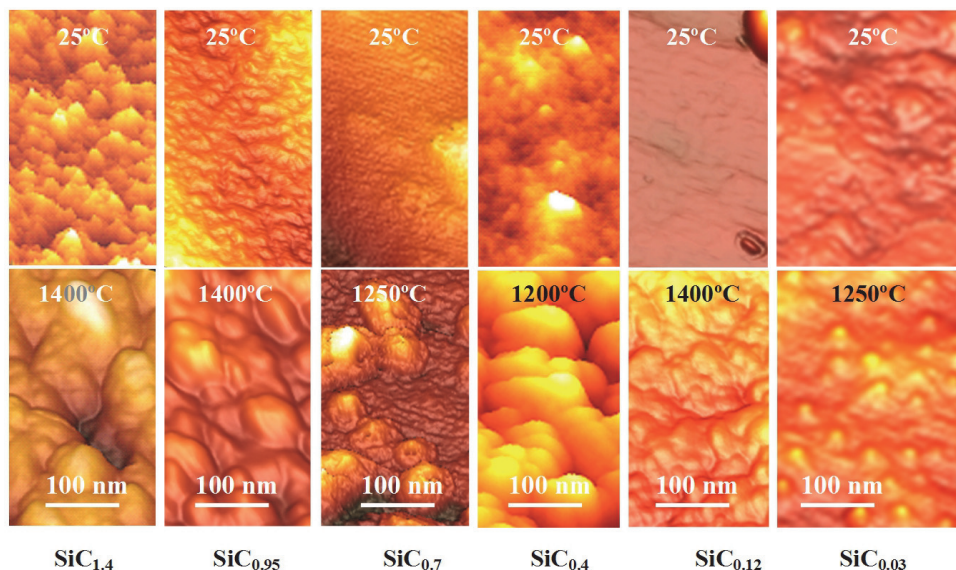


Fig. 30. Atomic force microscopy of the surface of SiC_x layers with various carbon concentration before and after high temperature annealing

In Fig. 31 the AFM data on changes in surface topography of the annealed at 1400°C $\text{SiC}_{1.4}$ layer before (Fig. 31a) and after (Fig. 31b and c) processing by glow discharge hydrogen plasma (27.12 MHz, 12.5 W, 6.5 Pa, 100°C, 5 min) in two various areas with sizes of $1 \times 1 \mu\text{m}^2$, are presented. The more increased fragments are also shown. Processing by hydrogen plasma does not lead to complete destruction of the granular structure (Fig. 31b), although in some areas granular structure significantly damaged (Fig. 31c), which correlates with the X-ray data (Fig. 7).

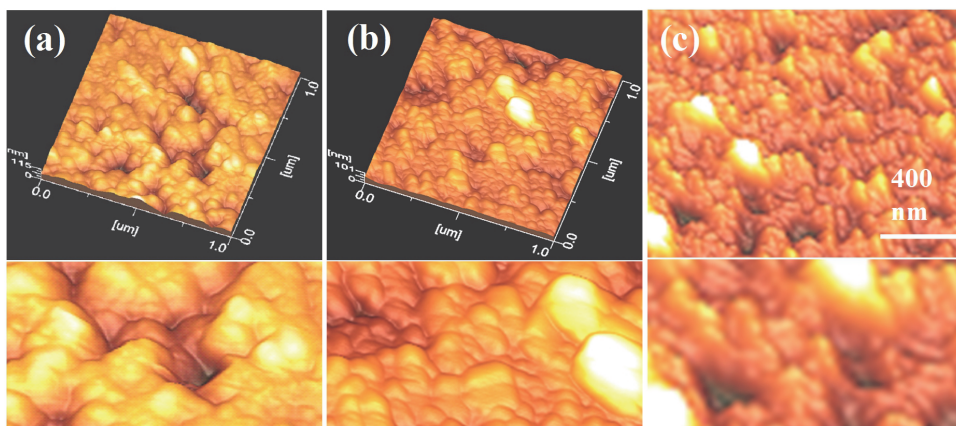


Fig. 31. Atomic force microscopy of $\text{SiC}_{1.4}$ layers after annealing at the temperature of 1400°C (a) and subsequent processing by glow discharge hydrogen plasma for 5 min (b, c).

Fig. 32a, b shows the surface areas of the untreated by hydrogen plasma $\text{SiC}_{0.95}$ film after annealing at 900°C , which have a granular structure and consist of grains with sizes within $\sim 50\text{--}250$ nm. On the enlarged fragments one can also see the flat areas which can be associated with the amorphous component. Surface after treatment by glow discharge hydrogen plasma for 5 min and annealing at 900°C has a more developed granular structure (Fig. 32c, d) and consist of grains with sizes within $\sim 150\text{--}400$ nm. These results correlate with the IR spectroscopy data (Fig. 28).

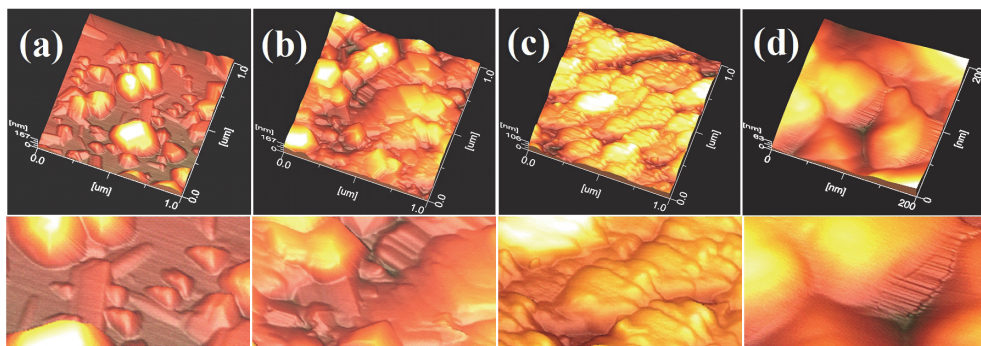


Fig. 32. Atomic force microscopy of $\text{SiC}_{0.95}$ layer: (a, b) after synthesis and annealing at the temperature of 900°C for 30 min; (c, d) after synthesis, processing by glow discharge hydrogen plasma for 5 min and annealing at 900°C for 30 min.

4. Conclusion

1. For SiC_x layers, formed by multiple ion implantation in Si of $^{12}\text{C}^+$ ions with energies 40, 20, 10, 5 and 3 keV, the regularities of influence of the decay of clusters and optically active bonds on the formation of tetrahedral oriented Si–C-bonds, characteristic of crystalline silicon carbide, were revealed. Formation of these bonds in the $\text{SiC}_{1.4}$, $\text{SiC}_{0.95}$ and $\text{SiC}_{0.7}$ layers with a high carbon concentration occurs mainly as a result of the decay of optically inactive Si–C-clusters in the temperature range $900\text{--}1300^\circ\text{C}$; in $\text{SiC}_{0.12}$ and $\text{SiC}_{0.4}$ layers – as a result of the decay of clusters in the range of $1200\text{--}1300^\circ\text{C}$ and of optically active long single Si–C-bonds in the range of $700\text{--}1200^\circ\text{C}$; in $\text{SiC}_{0.03}$ layers – by reducing the number of dangling bonds of carbon atoms in the range $900\text{--}1000^\circ\text{C}$.
2. The values of carbon concentration in silicon and the temperature ranges which are optimal for the formation of SiC, are revealed. After annealing at 1200°C of homogeneous SiC_x layers, largest sizes of spherical, needle- and plate-type SiC grains up to 400 nm and the largest number of tetrahedral oriented Si–C-bonds are observed for the $\text{SiC}_{0.7}$ layer, which is due to a low carbon content in the $\text{SiC}_{0.03}$, $\text{SiC}_{0.12}$ and $\text{SiC}_{0.4}$ layers, and a high concentration of strong clusters in the $\text{SiC}_{0.95}$ and $\text{SiC}_{1.4}$ layers. In the range of $800\text{--}900^\circ\text{C}$ the most number of tetrahedral Si–C-bonds is characteristic for $\text{SiC}_{0.4}$ layers.
3. A structural model of $\text{SiC}_{0.12}$ layer, which shows the changes in phase composition, phase volume and average crystallite size of SiC and Si in the temperature range $20\text{--}1250^\circ\text{C}$, is proposed. After annealing at 1200°C , about 50% of its volume, free from

- Si-C-clusters, is consisted of Si crystallites with average size ~ 25 nm, 25% of the volume – β -SiC crystallite with size of ~ 5 nm and 25% – the c-Si recrystallized near the transition “film – substrate”.
4. The regularities of changes in the surface structure of the SiC_x layers ($x = 0.03\text{--}1.4$) with the increase of temperature are revealed. At temperatures of $800\text{--}1400^\circ\text{C}$ the surface layers are deformed with the formation of grains with sizes of $\sim 30\text{--}100$ nm, consisting of crystallites, and the recrystallized at 1250°C smooth surface of $\text{SiC}_{0.03}$ layer contains evenly distributed Si:C inclusions in the form of point protrusions with a diameter of ~ 20 nm.
 5. Size effects were revealed, which manifested in the influence of the crystallite sizes of silicon carbide on its optical properties. The differences of the $\text{SiC}_{0.03}$, $\text{SiC}_{0.12}$ and $\text{SiC}_{0.4}$ layers with low carbon concentration from the $\text{SiC}_{1.4}$, $\text{SiC}_{0.95}$ and $\text{SiC}_{0.7}$ layers with high carbon concentration are manifested in the absence of LO-phonon peak of SiC in the IR transmission spectra and in a shift at 1000°C of minimum SiC-peak for TO phonons in the region of wave numbers higher than 800 cm^{-1} characteristic for the tetrahedral bonds of crystalline SiC, which is caused by small sizes of SiC crystallites (≤ 3 nm) and by an increase of contribution in the IR absorption of their surfaces, and the surfaces of Si crystallites containing strong short Si-C-bonds as well.
 6. The estimations of the proportion of carbon atoms that form clusters in the SiC_x layers are evaluated. At 1300°C in the $\text{SiC}_{1.4}$ layer only $\sim 9\%$ of C atoms form the optically active Si-C-bonds, in $\text{SiC}_{0.95}$ – 12% , in $\text{SiC}_{0.7}$ and $\text{SiC}_{0.4}$ – 16% , in $\text{SiC}_{0.12}$ – 45% , while the remaining carbon atoms are included in composition of stable clusters. The total number N of formed Si-C-bonds in SiC_x layers was growing with a fractional power of carbon concentration x : $N = a \cdot (n_1)^y$, where $y \approx 0.37 \pm 0.09$, $n_1 = x/0.03$, $a = \text{const}$.
 7. It was shown that processing by hydrogen glow discharge plasma (27.12 MHz , 12.5 W , 6.5 Pa , 100°C , 5 min) of polycrystalline $\text{SiC}_{1.4}$ layer leads to partial disintegration of β -SiC crystallites in layer and complete decay of Si crystallites in the transition layer “film–substrate” (“SiC–Si”). Processing by plasma and annealing at 900°C of $\text{SiC}_{0.95}$ layer has led to the formation of β -SiC crystalline layer, which superior in structure quality the untreated by plasma layer subjected to isochronous annealing in the range $200\text{--}1400^\circ\text{C}$. Phenomenon of plasma-induced crystallization is a consequence of the decay of clusters during pre-treatment by glow discharge hydrogen plasma.

5. Acknowledgement

The authors are very grateful to Mukhamedshina D.M. for processing the samples by glow discharge hydrogen plasma and Mit' K.A. for AFM measurements.

6. References

- Akimchenko, I.P., Kisseleva, K.V., Krasnopevtsev, V.V., Milyutin, Yu.V., Touryanski, A.G., Vavilov, V.S. (1977). The structure of silicon carbide synthesized in diamond and silicon by ion implantation. *Radiation Effects*, Vol. 33., pp.75–80.
- Akimchenko, I.P., Kazdaev, H.P., Krasopevtsev, V.V. (1977). IK-pogloshenie β -SiC, sintezirovannogo pri ionnoi implantacii C v Si. *Fizika i Tekhnika Poluprovodnikov*, T.11, vyp. 10., pp.1964–1966 (in Russian).

- Akimchenko, I.P., Kazdaev, H.R., Kamenskikh, I.A., Krasnopevtsev, V.V. (1979). Opticheskie i fotoelektricheskie svoistva struktury SiC-Si, poluchennoi pri implantacii ionov ugleroda v kremnii. Fizika i Tekhnika Poluprovodnikov, T.13, vyp.2., pp. 375-378 (in Russian).
- Akimchenko, I.P., Kisseleva, K.V., Krasnopevtsev, V.V., Touryanski, A.G., Vavilov, V.S. (1980). Structure and optical properties of silicon implanted by high doses of 70 and 310 keV carbon ions. Radiation Effects, Vol. 48., pp.7-12.
- Aleksandrov, P.A., Baranova, E.K., Demakov, K.D., Komarov, F.F., Novikov, A.P., Shiryaev, S.Y. (1986). Sintez monokristallicheskogo karbida kremniya s pomoshyu odnoshagovoi tehniki vysokointensivnogo ionnogo legirovaniya. Fizika i Tekhnika Poluprovodnikov, T.20, v.1, pp. 149-152 (in Russian).
- Baranova, E.K., Demakov, K.D., Starinin, K.B., Strelcov, L.N., Haibullin, I.B. (1971). Issledovanie monokristallicheskih plenok SiC, poluchennykh pri bombardirovke ionami C⁺ monokristallov Si. Doklady AN SSSR, vol. 200, pp. 869-870 (in Russian).
- Bayazitov, R.M., Haibullin, I.B., Batalov, R.I., Nurutdinov, R.M. (2003a). Formation of cubic silicon carbide layers on silicon under the action of continuous and pulsed carbon ion beams. Technical Physics, Vol. 48, iss. 6, pp. 742-744.
- Bayazitov, R.M., Haibullin, I.B., Batalov, R.I., Nurutdinov, R.M., Antonova, L.Kh., Aksenov, V.P., Mikhailova, G.N. (2003b) Structure and photoluminescent properties of SiC layers on Si, synthesized by pulsed ion-beam treatment. Nucl. Instrum. and Meth. in Phys. Res. B., V. 206, pp. 984-988.
- Belov, A.I., A.N. Mihailov, D.E. Nikolichev, A.V. Boryakov, A.P. Sidorin, A.P. Grachev, A.V. Ershov, D.I. Tetelbaum (2010). Formation and "white" photoluminescence of nanoclusters in SiO_x films implanted with carbon ions. Semiconductors. Vol. 44, iss. 11, pp. 1450-1456.
- Burenkov, A.F., Komarov, M.A., Temkin, M.M. (1985). In: Prostranstvennye raspredeleniya energii, vydelennoi v kaskade atomnykh stolknovenii v tverdykh telakh, Energoizdat., 245 c. (in Russian).
- Borders, J.A., Picraux, S.T. and Beezhold, W. (1971). Formation of SiC in silicon by ion implantation. Appl.Phys.Lett., Vol. 18, iss. 11., pp.509-511.
- Calcagno, L., Compagnini, G., Foti, G., Grimaldi, M.G., Musumeci, P. (1996). Carbon clustering in Si_{1-x}C_x formed by ion implantation. Nucl.Instrum. and Meth. in Phys.Res., B 120, pp.121 - 124.
- Chen, D., Cheung, W.Y., Wong, S.P (1999). Ion beam induced crystallization effect and growth kinetics of buried SiC layers formed by carbon implantation into silicon. Nucl. Instrum. and Meth. in Phys.Res., B148, pp. 589-593.
- Chen D., Wong, S.P., Yang Sh., Mo D. (2003). Composition, structure and optical properties of SiC buried layer formed by high dose carbon implantation into Si using metal vapor vacuum arc ion source. Thin Solid Films, Vol. 426, pp.1-7.
- Durupt, P., Canut, B., Gauthier, J.P., Roger, J.A. and Pivot, J (1980). RBS, infrared and diffraction compared analysis of SiC synthesis in C implanted silicon. Mater. Res. Bull, 15, pp. 1557-1565.
- Edelman, F.L., Kuznetsov, O.N., Lezheiko, L.V. and Lubopytova, E.V. (1976). Formation of SiC and Si₃N₄ in silicon by ion implantation. Radiation Effects, 29, pp. 13-15.
- Fan, J.Y., Wu, X.L., Chu, P.K. (2006). Low-dimensional SiC nanostructures: Fabrication, luminescence, and electrical properties. Prog.Mater.Sci., Vol. 51., pp. 983-1031.

- Fissel, A., Kaizer, U., Schroter, B., Richter, W., Bechstedt, A. (2001). MBE growth and properties of SiC multi-quantum well structures. *Applied Surface Science*, 184, iss. 1, pp. 37–42.
- Fissel, A., Kaizer, U., Pfennighaus, K., Schroter, B., Richter, W. (1996). Growth of 6H-SiC on 6H-SiC(0001) by migration enhanced epitaxy controlled to an atomic level using surface superstructures. *Applied Physics Letters*, 68, pp. 1204–1206.
- Fissel, A., Schroter, B., Kaiser, U., Richter, W. (2000). Advances in the molecular-beam epitaxial growth of artificially layered heteropolytypic structures of SiC. *Appl. Phys. Lett.*, Vol. 77., pp. 2418–2420.
- Frangis, N., Stoemenos, J., Van Landuyt, J., Nejim, F., Hemment, P.L.F. (1997). The formation of 3C-SiC in crystalline Si by carbon implantation at 950°C and annealing – a structural study. *Journal of Crystal Growth*, 181, pp.218–228.
- George, V.C., Das, A., Roy, M., Dua, A.K., Raj, P., Zahn, D.R.T. (2002). Bias enhanced deposition of highly oriented β -SiC thin films using low pressure hot filament chemical vapour deposition technique. *Thin Solid Films*, Vol. 419, pp. 114–117.
- Gerasimenko, N.N., Kuznetsov, O.N., Lezheyko, L.V., Lyubopytova, E.V., Smirnov, L.S., Edelman, F.L. (1974). Nekotorye svoistva plenok SiC, poluchennykh ionnym vnedreniem v strukture Al-SiC-Si. *Mikroelektronika*, T.3., Vyp.5, pp. 467–468 (in Russian).
- Gibbons, J.F., Johnson, W.S. and Mylroic, S.W. (1975). *Projected Range Statistics*. Part 1. 93 p. 2nd ed. Dowden, Stroudsburg, PA.
- Gonzalez-Varona, O., Perez-Rodriguez, A., Garrido, B., Bonafos, C., Lopez, M., Morante, J.R., Montserrat, J., Rodriguez, R. (2000). Ion beam synthesis of semiconductor nanoparticles for Si based optoelectronic devices. *Nucl. Instrum. Methods Phys. Res.*, B, V. 161–163, pp. 904–908.
- Kantor, Z., Fogarassy, E., Grob, A., Grob, J.J., Muller, D., Prevot, B., Stuck, R. (1997). Evolution of implanted carbon in silicon upon pulsed excimer laser annealing: epitaxial Si_{1-y}C_y alloy formation and SiC precipitation. *Appl. Surf. Sci.*, 109/110, pp. 305–311.
- Kerdiles, S., Rizk, R., Gourbilleau, F., Perez-Rodriguez, A., Garrido, B., Gonzalez-Varona, O., Morante, J.R. (2000). Low temperature direct growth of nanocrystalline silicon carbide films. *Mater.Sci.Eng.*, B, Vol.69, pp. 530–535.
- Khohlov, A.F., Pavlov, D.A., Mashin, A.I., Mordvinova, Y.A. (1987). Izvalentnoe legirovanie amorphnogo kremniya uglerodom. *Fizika I tehnika poluprovodnikov*, T.21, vyp.3, pp. 531–535 (in Russian).
- Kimura, T., Kagiya, Sh. and Yugo, Sh. (1984). Auger electron spectroscopy analysis of SiC layers form by carbon ion implantation into silicon. *Thin Solid Films*, Vol. 122, pp.165–172.
- Kimura, T., Kagiya, Sh. and Yugo, Sh. (1982). Characteristics of the synthesis of β -SiC by the implantation of carbon ions into silicon. *Thin Solid Films*, Vol. 94, pp.191–198.
- Kimura, T., Kagiya, Sh. and Yugo, Sh. (1981). Structure and annealing properties of silicon carbide thin layers formed by ion implantation of carbon ions in silicon. *Thin Solid Films*, 81, pp.319–327.
- Lebedev, A.A., Mosina, G.N., Nikitina, I.P., Savkina, N.S., Sorokin, L.M., Tregubova, A.C. (2001). Investigation of the structure of (p)3C-SiC-(n)6H-SiC. *Tech. Phys. Lett.*, Vol. 27, P. 1052–1054.

- Lebedev, A.A., Strel'chuk, A.M., Savkina, N.S., Bogdanova, E.V., Tregubova, A.S., Kuznetsov, A.N., Sorokin, L.M. (2002a). Investigation of the p-3C-SiC/n⁺-6H-SiC heterostructures with modulated doping. *Tech. Phys. Lett.*, Vol. 28, iss. 12, p. 1011-1014.
- Lebedev, A.A., Strel'chuk, A.M., Davydov, D.V., Savkina, N.S., Kuznetsov, A.N., Sorokin, L.M. (2002b). Electrical characteristics of (p)3C-SiC-(n)6H-SiC heterojunctions. *Tech. Phys. Lett.*, Vol. 28, iss.9, pp. 792-794.
- Lebedev, A.A., Nelson, D.K., Razbirin, B.S., Saidashev, I. I., Kuznetsov, A.N., Cherenkov, A. E. (2005) Study of the properties of two-dimensional electron gas in p-3C-SiC/n⁺-6H-SiC heterostructures at low temperatures. *Semiconductors*, Vol. 39, iss.10, P. 1194-1996.
- Liangdeng, Y., Intarasiri, S., Kamwanna, T., Singkarat, S. (2008). Ion beam synthesis and modification of silicon carbide. In book "Ion beam applications in surface and bulk modification of insulators". - IAEA, Austria, Vienna, IAEA-TECDOC-1607. - P.63-92.
- Liao, F., Girshick, S.L., Mook, W.M., Gerberich, W.W., Zachariah, M.R. (2005). Superhard nanocrystalline silicon carbide films. *Appl. Phys. Lett.*, Vol. 86, pp. 171913-171915.
- Lindner, J.K.N. (2003). High-dose carbon implantations into silicon: fundamental studies for new technological tricks. *Appl. Phys. A.*, Vol. 77, pp. 27-38.
- Lindner, J.K.N., Volz, K., Preckwinkel, U., Gotz, B., Frohnwieser, A. Stritzker, B., Rauschenbach, B. (1996). Formation of buried epitaxial silicon carbide layers in silicon by ion beam synthesis. *Materials Chemistry and Physics*, 46 (2-3), pp.147-155.
- Mandal, S., Seal, A., Dalui, S.K., Dey, A.K., Ghatak, S. and Mukhopadhyay, A.K. (2001). Mechanical characteristics of microwave sintered silicon carbide. *Bull. Mater. Sci.*, V. 24, № 2, pp. 121-124.
- Martin, P., Daudin, B., Dupuy, M., Ermolieff, A., Olivier, M., Papon, A.M. and Rolland, G. (1990). High temperature ion beam synthesis of cubic SiC. *J. Appl. Phys.*, 67 (6), pp.2908-2912.
- Nishino, S., Jacob, C., Okui, Y. (2002). Lateral over-growth of 3C-SiC on patterned Si(111) substrates. *Journal of Crystal Growth*, 237-239, pp. 1250-1253.
- Pajagopalan, T., Wang, X., Lanthouh, B., Ramkumar, C. (2003). Low temperature deposition of nanocrystalline silicon carbide films by plasma enhanced chemical vapor deposition and their structural and optical characterization. *J. Appl. Phys.*, Vol.94, iss.3., pp. 5252-5260.
- Perez-Rodriguez, A., Gonzalez-Varona, O., Garrido, B., Pellegrino, P., Morante, J.R., Bonafos, C., Carrada, M., Claverie, A. (2003). White luminescence from Si⁺ and C⁺ ion-implanted SiO₂ films. *J. Appl. Phys.*, V. 94., 1., pp. 254-262.
- Preckwinkel U., Lindner, J.K.N., Stritzker B., Rauschenbach B. (1996). Structure and strain measurements on SiC formed by carbon ion implantation. *Nucl. Instrum. and Meth. in Phys. Res.*, B 120, pp. 125-128.
- Reeson, M., Stoemenos, J., Hemment, P.L.F. (1990). Mechanism of buried β-SiC formation by implanted carbon in silicon. *Thin Solid Films*, Vol. 191, pp. 147-164.
- Rothmund, W., Fritzsche, C.R. (1974). Optical absorption and electrical conductivity of SiC films produced by ion implantation *J. Electrochem. Soc.: Solid-state science and technology*, Vol. 121, №4., pp. 586-588.

- Savkina, N.S., Lebedev, A.A., Davydov, D.V., Strelchuk, A.M., Tregubova, A.S., Raynaud, C., Chante, J.P., Locatelli, M.L., Planson, D., Nilan, J., Godignon, P., Campos, F.J., Nestres, N., Pascual, J., Brezeanu, G., Batila, M. (2000). Low-doped 6H-SiC n-type epilayers grown by sublimation epitaxy. *Materials Science and Engineering*, B77, pp. 50–54.
- Semenov, A.V., Puzikov, V.M., Dobrotvorskaya, M.V., Fedorov, A.G., Lopin, A.V. (2008). Nanocrystalline SiC films prepared by direct deposition of carbon and silicon ions. *Thin Solid Films*, Vol. 516, iss.10., pp. 2899–2903.
- Semenov, A.V., Puzikov, V.M., Golubova, E.P., Baumer, V.N., Dobrotvorskaya, M.V. (2009). Low-temperature production of silicon carbide films of different polytypes. *Semiconductors*, Vol. 43, iss. 5, pp. 685–689.
- Semenov, A.V. Lopin, A.V, Puzikov, V.M., Baumer, V.N., Dmitruk, I.N. (2010). Fabrication of heterostructures based on layered nanocrystalline silicon carbide polytypes. *Semiconductors*, Vol. 44, iss. 6, pp. 816–823.
- Serre, C., Romano-Rodríguez, A., Pérez-Rodríguez, A., Morante, J. R., Fonseca, L., Acero, M.C., Kögler, R. and Skorupa, W. (1999). β -SiC on SiO₂ formed by ion implantation and bonding for micromechanics applications. *Sensors and Actuators A: Physical*, 74, 1–3, pp. 169–173.
- Shimizu-Iwayama, T., Nakao, S., Saitoh, K. (1994). Visible photoluminescence in Si⁺-implanted thermal oxide films on crystalline Si. *Appl. Phys. Lett.*, Vol.65(14), pp.1814–1816.
- Silverstein, R., Bassler, G., Morril, T. (1988). *Spektrometriceskaya identifikaciya organicheskikh soedinenii*. M: Mir, 590 s. (in Russian).
- Simon, L., Faure, J., Mesli, A., Heiser, T., Grob, J.J., Balladore, J.L. (1996). XTEM and IR absorption analysis of silicon carbide prepared by high temperature carbon implantation in silicon. *Nucl.Instrum. and Meth. in Phys.Res.*, B 112, pp. 330–333.
- Singh, S.K., Mohanty, B.C. and Basu, S. (2002). Synthesis of SiC from rice husk in a plasma reactor. *Bull.Mater.Sci.*, V. 25, № 6, pp. 561–563.
- Spillman, H., Wilmott, P.R. (2000). Growth of SiN_x and SiC_x thin films by pulsed reactive crossed-beam laser ablation. *Applied Physics. A. - Materials Science & Processing*, Vol. 70., Iss. 3., pp. 323–327.
- Srikanth, K., Chu, M., Ashok, S., Nguyen, N., Vedam, K. (1988). High-dose carbon ion implantation studies in silicon. *Thin Solid Films*, 163, pp.323–329.
- Sun, Y., Miyasato, T.J.(1988). Characterization of cubic SiC films grown on thermally oxidized Si substrate. *J. Appl. Phys.*, Vol. 84., pp. 2602–2611.
- Tetelbaum, D.I., Mikhaylov, A.N., Belov, A.I., Vasiliev, V.K., Kovalev, A.I., Wainshtein, D.L., Golan, Y., Oshero, A. (2009). Luminescence and structure of nanosized inclusions formed in SiO₂ layers under double implantation of silicon and carbon ions. *Journal of Surface Investigation. X-ray, Synchrotron and Neutron Techniques*, Vol. 3, № 5, pp. 702–708.
- Theodossiu, E., Baumann, H. and Bethge, K. (1999). Formation of SiC surface layer by ion implantation. *J. Appl. Phys.*, 86., pp. 4703–4705.
- Wong, S.P., Chen, D., Ho, L.C., Yan, H., Kwok, R.W.M. (1998). Infrared absorption spectroscopy study of phase formation in SiC layers synthesized by carbon implantation into silicon with a metal vapor vacuum arc ion source. *Nucl. Instrum. and Meth. in Phys.Res.*, B140, pp.70–74.

- Yan, H., Wang, B., Song, X.M., Tan, L.W., Zhang, S.J., Chen, G.H., Wong, S.P., Kwok, R.W.M., Leo, W.M.L. (2000). Study on SiC layers synthesized with carbon ion beam at low substrate temperature. *Diamond and related materials*, Vol. 9, pp. 1795–1798.
- Zhao, J., Mao, D.S., Lin, Z.X., Jiang, B.Y., Yu, Y.H., Liu, X.H., Wang, H.Z. and Yang, G.Q. (1998). Intense short wavelength photoluminescence from thermal SiO₂ films co-implanted with Si and C ions. *Appl. Phys. Lett.*, V. 73, №13, pp. 1838–1840.

SiC as Base of Composite Materials for Thermal Management

J.M. Molina

*Instituto Universitario de Materiales de Alicante, Universidad de Alicante
Departamento de Química Inorgánica, Universidad de Alicante
Spain*

1. Introduction

Some of the high-end applications in energy-related topics such as electronics, aeronautics and research in elementary particles have reached their technological limits because of the impossibility of finding materials capable of removing the excessive heat generated in running their equipments and, at the same time, maintaining their dimensional stability in environments often extremely aggressive, namely, wide temperature range of use (218-423K), corrosive environments (>98% humidity), fast heating-cooling cycles or interaction with accelerated particles. The growing needs for thermal control are a consequence of the unlimited increasing power consumption in the operation of their equipments. These applications, that exclude the use of monolithic materials given their required unique combination of properties, force the use of composite materials that exhibit high heat transport and, at the same time, do maintain their dimensional stability under operational conditions. Despite the significant progress in the development of composite materials for these applications in recent years, nowadays there is a need to find new materials capable of withstanding the extreme conditions that are impingingly demanded for the new heat sinks. Power electronics and optoelectronics demand thermal conductivities (TC) above 350 W/mK and 450 W/mK respectively; aeronautics is less demanding (>250 W/mK). The coefficients of thermal expansion (CTE) should be matched to those of the architectures on which they are mounted to prevent failures by thermo-mechanical fatigue (it is required 3-6 ppm/K for optoelectronics and less than 12 ppm/K for power electronics, both in the 293-500K range, and 10-14 ppm/K in the range 233-344 K for aeronautics). In applications such as collimators in particle accelerators, apart from a great resistance to radiation damage, materials with more than 300 W/mK of TC and approximately 10-12 ppm/K of CTE are needed. All applications require isotropic materials with a flexural strength of >120 MPa and the lowest possible density, especially those for aeronautics.

SiC-based metal matrix composite materials have shown, up to now, a perfect combination of properties such that to cover the increasing demanding of the energy-related industries. Among them, Al/SiC has become a leader material and nowadays is considered the state-of-the-art in thermal management. This material, in which SiC is present as particulate, cannot meet the future requirements for heat dissipation and dimensional control given its limited thermal conductivity (about 180 W/mK) and relatively high coefficient of thermal

expansion (around 10 ppm/K). For this reason, during the last years research has been directed to develop new and alternative materials that can replace the traditional Al/SiC and allow the emergence and growth of new and more efficient equipments. Several solutions have been proposed, most of them based on the use of different finely divided reinforcement materials embedded in a metallic matrix. The use of metals as matrix seems to be a question with no discussion, since metal consolidates the preform, is thermally stable (something important for some applications), is lighter than many ceramics and at the same time allows in most cases an easier machining process. Moreover, the global properties of the material can be widely varied by playing with the metallurgical state of the metallic matrix. Al, Ag and Cu and their corresponding alloys with interfacial active elements have proven to be appropriate matrices for composites conceived and designed for the above mentioned applications. Nowadays, among the different options considered as reinforcements in composites for electronics we find that SiC is still leadering the choice. Different combinations of SiC with other reinforcements (such as alumina or diamond) or the use of mixtures of SiC particles of different sizes (bimodal or multimodal distributions of particles) have proven to be essential to match the extreme requirements of electronics. A very recent composite material, developed and patented at the University of Alicante, is based on the use of mixtures of graphite flakes and SiC particles (or alternatively other reinforcements) in order to make a preform in which flakes tend to form layered structures. The SiC particles act as a separator between layers of flakes and on the other hand allow reduce the thermal expansion coefficient in the transversal direction which otherwise would be inadmissibly high. One clear competitor for the SiC-based composites is the family of those fabricated with diamond particles. Even though their thermal properties are very attractive they pose important problems related to obtain pieces with complicated geometries, as diamond is very difficult or even impossible to be machined. Within this scenario the new research on composites based on machinable reinforcements seems to be the only industrially attractive option for many applications.

Most of these composites are fabricated by pressure infiltration of the metal into the preform, assisted either by gas or by mechanical means (squeeze casting). The selection of proper materials quality as well as of optimal fabrication conditions is completely essential to meet the target properties.

The present chapter presents different SiC-based composite materials which have been evolving over time aiming to be useful for thermal management. It also analyzes the different aspects of the fabrication that affect the thermal properties of these composites.

2. Fabrication procedures of composites for thermal management

The limitations of metallic materials that had traditionally been used as heat sinks in the electronic industry very soon attracted the attention of other alternative systems. The composite materials made out of metals as matrix and ceramics as reinforcement became immediately potential candidates for a wide variety of applications in electronic packaging (Clyne, 2000a). The following Ashby's map allow us to think about the different possibilities of metal-ceramic combinations for the aforementioned applications.

Among ceramics, SiC is one with relatively high thermal conductivity (500 W/mK for monocrystals, 250-350 for polycrystals) and a coefficient of thermal expansion (around 4.7 ppm/K) very close to that of silicon (2.5-3.6 ppm/K). Its low price, especially for the non-most pure forms of SiC, makes this ceramic to have a very high performance/price ratio. For

the sake of comparison we shall mention that very pure SiC particles can be as costly as three times the price of those of normal grades (less than 99.8% purity). Their thermal conductivity is somehow higher but nevertheless not sufficient to justify their use in comparison to other less expensive ceramics (like diamond). Diamond, in its turn, has a very high thermal conductivity but the performance/price ratio is still its limiting factor. However, seemingly this ceramic represents a good choice for the coming future in the electronics industry given that their price has followed a continuously decreasing tendency during the last ten years.

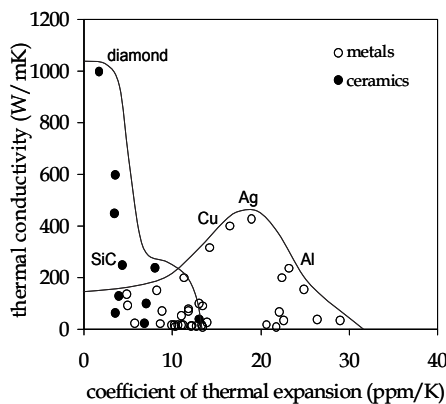


Fig. 1. Ashby's map of thermal conductivity and coefficient of thermal expansion for different metallic and ceramic materials

On the side of metals, aluminium turns out to be one of the most attractive. Although its thermal properties are not excellent, is a light metal and has a low melting point. Its combination with SiC in proper amounts may generate composite materials with the desired properties for thermal management. Given that the thermal conductivities of both SiC and Al are very similar, the expected value of this property for their composites is rather in the same range. The most accounting effect on composites is the thermal expansion coefficient, which can be varied over a wide range by playing with the volume fraction of Al and SiC phases. In fact, in view of the Ashby's map, it becomes apparent that high volume fractions of SiC are necessary if the coefficient of thermal expansion needs to be considerably reduced. It is this last condition what limits in practice the number of fabrication procedures that can be chosen in order to manufacture composites for heat sinking.

As a general rule, only those processing techniques that allow obtain a high volume fraction of reinforcement are useful. In this sense, infiltration of the molten metal into packed preforms has been recognized as the most appropriate procedure. Since most ceramics are not wetted by molten metals, infiltration typically requires be pressure-assisted. The way in which the molten metal is forced into the open space of the ceramic preform determines the two main infiltration techniques, namely gas-pressure infiltration and squeeze casting (or mechanically-assisted infiltration). Alternatively, the powder-metallurgy technique has also been used for those systems where the configuration of the preform is such that intrusion techniques become difficult or where the preform might suffer of dimensional damage when high pressures are required.

2.1 Gas-pressure assisted infiltration

In general, pressure does not exceed 15MPa and this allows fabricate pieces with complex shapes without taking the risk of a considerable deformation of the preform. The method is highly versatile because, with a simple modification of the main mould, pieces of different geometries can be fabricated. Final machining is sometimes needed although, if moulds are properly designed in such a way that the demoulding process turns out not to be difficult, neat-shape fabrication is feasible. The main drawback of this technique stems from the limited rate of metal penetration into the preforms, resulting difficult the manufacture of large pieces. This restriction is a consequence of the technology characteristics; in particular of the low pressures applied and the wettability-reactivity characteristics of the system at hand.

2.2 Mechanically-assisted infiltration

The metal is forced to penetrate into the ceramic preform at very high pressures (in the range 50-100 MPa) by means of a piston mechanically driven. This method is called “squeeze casting” and its application into the fabrication of MMC’s is very extended, although it is not free of drawbacks related with the high pressures used. This may cause deformations in the preforms that alter the global shape and the relative presence of metal and ceramic phases. The solution to this problem not always seems to be found by diminishing the working pressure because infiltration rate or metal-ceramic reaction are for some systems important issues to be considered. The necessity of huge installations, occasionally very expensive, is another drawback of squeeze casting. Its main advantage is that the high working pressures effectively ensure infiltration and the final composite materials can be free of remaining porosity.

2.3 Powder-metallurgy

Although powder metallurgy has become an excellent technique for the manufacturing of relatively complicate shaped metallic pieces, in the field of composite materials is not an extensively used fabrication method. This technique allows obtaining high volume fractions of reinforcement (75%) and moreover offers a perfect control of reactivity between metal and ceramic phases. However, a clear drawback is the difficulty encountered for the control of porosity in the material, which seems a phase that inherently appears when using this technique. The control of the oxygen content (as metallic oxides existing concomitantly in the metallic powder) seems also to limit the possible massive use of this technique in the industrial fabrication of composite materials.

Recently, another technique derived from the already mentioned powder-metallurgy has become a matter of interest. This technique is called “spark-plasma” and it consists of heating the metallic or graphitic mould, as well as the powder compact in case of conductive samples, by means of an electrical current that flows through it. This technique allows a fast processing of the materials but, nevertheless, it suffers from the same disadvantages of the classical powder-metallurgy route.

3. Measurement and estimation of thermal properties in composites for thermal management

3.1 Property needs in materials for electronics

As already explained, there are several requirements for those materials considered for electronics. An ideal heat sink must extract the heat generated in excess in a given running

equipment but at the same time has to be thermally stable in order to maintain the dimensionality of the architecture on which they are mounted. This already points out that the main properties that are essential for those materials are two: thermal conductivity and thermal expansion coefficient. While the former needs to be as high as possible the later is restricted to a certain range, typically between the limits of 3 and 14 ppm/K. Although these two properties are limiting, other characteristics of the materials (i.e. density, cost) may also take a significant importance for certain applications. In the present context only the two main properties are reviewed.

3.2 Measurement of thermal properties

Thermal conductivity is measured by mainly two means. The simplest one consists of comparing the thermal conduction of the sample with a reference material by connecting the sections of both and establishing a thermal gradient. It is called the comparative stationary method and provides accurate and relatively fast measurements. Another more sophisticated method is based on the use of a laser flash, which measures the heat propagation in non-stationary conditions caused by the flash of a laser impacting the surface of the material.

The coefficient of thermal expansion is typically accessed through the use of a thermo-mechanical analyser, which subjects the sample to a thermal cycling over a certain range of temperature. The dimensions of the sample are followed in one, two or alternatively three axis. In fact, what is measured is the dimension change with the increase in temperature (units of ppm/K).

3.3 Estimation (modelling) of thermal properties

3.3.1 Coefficient of thermal expansion

A very simple and tentative model for the estimation of this property in composite materials consists of averaging over the volume fraction of the corresponding phases:

$$\alpha = \alpha_r V_r + \alpha_m (1 - V_r) \quad (1)$$

where the subscripts m and r denote matrix and reinforcement, respectively. This simple approach is called the linear rule of mixtures and offers a back-of-the-envelope calculation of what the coefficient of thermal expansion must approximately be.

More sophisticated treatments are all based on thermoelasticity theory (Clyne, 2000b). Schapery's model gives upper (+) and lower (-) bounds on the CTE. The specific expression for the former is:

$$\alpha^{(+)} = \alpha_r + (\alpha_m - \alpha_r) \frac{K'_m (K'_r - K_c^{(-)})}{K_c^{(-)} (K'_r - K'_m)} \quad (2)$$

where K' refers to bulk modulus; $K_c^{(-)}$ is Hashin and Shtrickman's lower bound to the bulk modulus of the composite, namely,

$$K_c^{(-)} = K'_m + \frac{V_r}{\frac{1}{K'_r - K'_m} + \frac{V_m}{K'_m + \frac{4}{3}\mu_m}} \quad (3)$$

where μ_m is the shear modulus of the matrix. The upper bound to the bulk modulus is obtained by interchanging the subscripts m and r everywhere in Eq. (3) which, when inserted in Eq. (2), gives the lower bound on the CTE.

3.3.2 Thermal conductivity

The thermal conductivity of composite materials containing thermally conductive inclusions has been extensively studied. One of the simplest analytical models that assume a non-idealized interface between matrix and reinforcement is that derived by Hasselman and Johnson for spherical particles in a pore-free infinite matrix (Clyne, 2000b):

$$K_c = \frac{K_m \left[2K_m + K_r^{eff} + 2V_r (K_r^{eff} - K_m) \right]}{2K_m + K_r^{eff} - V_r (K_r^{eff} - K_m)} \quad (4)$$

where K is the thermal conductivity, K^{eff} is the effective thermal conductivity, V is the volume fraction, and the subscripts c , m and r refer to composite, matrix and reinforcement, respectively. This model has been proved to give accurate predictions when particles and matrix exhibit a low ratio of conductivities, which is the case for SiC particles and pure Al or many Al-based alloys. The effective thermal conductivity of particles K_r^{eff} is defined as:

$$K_r^{eff} = \frac{K_r^{in}}{1 + \frac{2K_r^{in}}{D \cdot h}} \quad (5)$$

where K_r^{in} stands for the intrinsic thermal conductivity of the particles, and D and h are the average particle diameter and the interfacial thermal conductance, respectively.

The differential effective medium (DEM) scheme has been applied with success to model and interpret transport properties in different composite materials (Clyne, 2000b; Molina et al., 2008a; Molina et al., 2008b; Molina et al., 2009; Tavangar et al., 2007; Weber et al., 2010). Its predictive capacity is in many cases considerably superior to other available models in literature (see for example (Tavangar et al., 2007)). The leading integral equation of the DEM approach for the thermal conductivity of a multi-phase composite material is:

$$\int_{K_m}^{K_c} \frac{dK}{K \sum_i f_i \frac{-(K - K_{r_i}^{eff})}{(K - K_{r_i}^{eff}) \cdot P - K}} = -\ln(1 - V_r) \quad (6)$$

where K_c is the thermal conductivity of the composite material, f_i is the fraction of the i inclusion in the total amount of inclusions of the composite (hence, $\sum_i f_i = 1$) and P is the polarization factor of the inclusion. $K_{r_i}^{eff}$ is the effective thermal conductivity of the i inclusion, which is related to its intrinsic thermal conductivity, K_r^{in} , the matrix/inclusion interface thermal conductance h , and the diameter D of the inclusion by Eq. (5).

In general, the integral on the left hand side of Eq. (6) has no analytical solution and has to be solved numerically by means of appropriate mathematical software.

4. SiC-based composite materials for thermal management applications

4.1 SiC reinforcements

Nowadays it is easy to find many suppliers of silicon carbide in different forms (i.e. particles, fibers, sheets, rods, tubes) with a relatively huge variety of dimensions. The market of these products is related to abrasive or refractory applications. When speaking about fabrication of composite materials, different sources of silicon carbide, all finely divided (like particles or fibers), are mainly searched (Clyne, 2000a). Among all these forms of silicon carbide being used as reinforcements for composite fabrication, particles of different purity grades and shapes have been mostly used. The commonest particles are angular in shape (Fig. 2), although some have being processed with perfect spherical geometry. Though spherical shapes are always interesting for modelling purposes its use has been restricted due to its prohibitive price. SiC particles are mainly fabricated in two grades, differentiated by its colour: green powder for purities higher than 99% and black powder for purities in the range 98%-99%.

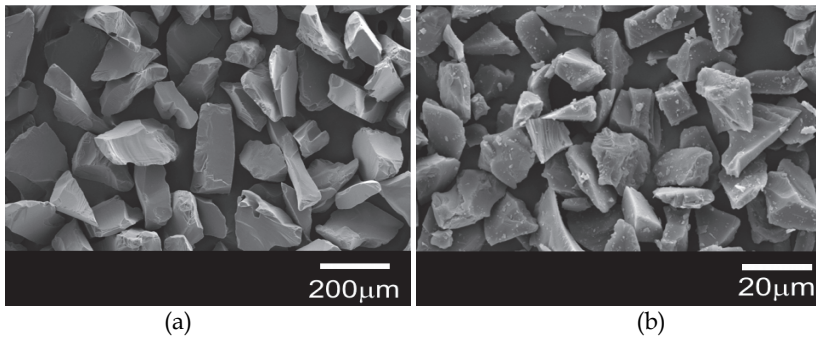


Fig. 2. Scanning electron microscopy images of commercial particles of SiC of two different average size diameters: (a) 170 μm (corresponding to 100 mesh; SiC100) and (b) 17 μm (corresponding to 500 mesh; SiC500)

An important parameter of particulate systems is the relation between their average diameter and specific surface area, measured by means of a laser diffraction technique and gas adsorption, respectively. The importance of this correlation will be shown later on in next sections.

Mathematically, these two intrinsic properties are related as follows:

$$D = \frac{6\lambda}{\rho \cdot S_r} \quad (7)$$

where D is the average particle diameter, ρ is the density of SiC (with a nominal value of 3210 kg/m³), S_r is the specific surface area (m²/kg) and λ is a geometrical factor introduced to account deviations from sphericity, surface roughness and particle size distribution. λ typically takes values greater than unity for angular particles prepared by milling of SiC blocks and turns out to be especially important for the modelling of different properties.

4.2 Metal matrix composites with reinforcement of mono or multimodal distribution of SiC particles

For years, the only materials able to mitigate the increasing demanding of heat removal in energy-related industrial applications have been composite materials made out of a proper combination of a metal and SiC particles.

Al/SiC composites have been extensively studied. Less studied materials are those with other metals such as copper or silver. We find only few references to those materials that point out their possible use in thermal management. Their potential as heat-dissipating materials is very high given the intrinsic properties of their constitutive elements. However, several problems arise when manufacturing these materials by liquid state processing routes. Estimates based on standard composite models indicate that the Cu/SiC system containing 50-60 vol.% SiC should yield materials with very good thermal properties: around 275 W/mK of thermal conductivity and 7-9 ppm/K of thermal expansion coefficient. Nevertheless, studies carried out on this system have demonstrated that those thermal properties are not achieved, mainly due to the detrimental reactivity at the metal-ceramic interface, which conducts to a solid solution of Si into the Cu matrix. An attempt to overcome the problem by protecting the SiC by an oxide layer has been demonstrated to be helpful but still not sufficient to attain the required properties (Narciso et al., 2006).

On its hand, the Ag/SiC system presents a problem of reactivity as well (Narciso et al., 1997, as cited in Molina et al., 2010). Ag dissolves a large amount of oxygen that can react with the SiC particles. The gas evolved in the reaction considerably reduces the metal/ceramic contact area and, hence, affects dramatically the thermal properties of the composite. The solution of oxidizing the SiC particles seems to improve, as in the case of Cu/SiC, the final properties of the material. However, for both systems, Cu/SiC and Ag/SiC, seemingly the only way to achieve the expected thermal properties by liquid state routes is to reduce the contact time between SiC particles and molten metal (details of the importance of the processing route will be given in following sections).

Given that in the Al/SiC system the problems related with reactivity are less accused, admissibly high thermal properties can be easily obtained. We will briefly summarize here two main kinds of materials obtainable when only SiC is used as reinforcement: composites based on a monomodal distribution of SiC particles and those based on bimodal distributions.

4.2.1 Al/SiC with monomodal distribution of particles

The traditional heat sinks in electronics, based on metallic combinations, promptly found a serious competitor in the Al/SiC family. These materials experimented a great impact on the industries and still nowadays represent the state-of-the-art in thermal management.

One of the most complete data collections on thermal properties of Al/SiC composites with monomodal distribution of particles can be accessed through (Arpon et al., 2003a; Arpon et al., 2003b; Molina et al., 2003a). The materials were fabricated by gas-pressure assisted infiltration of compacted SiC particles with molten Al at 750°C. Metallographic studies give evidence of the proper distribution of particles in the metal and the absence of particle breaking, given the special care taken during the packing procedure (Fig. 3).

The thermal properties achieved by those composites have been reviewed in the following table (Table 1). It is clearly seen that the dependence of the thermal properties on the material characteristics is different for thermal conductivity and for the coefficient of thermal expansion. While the former depends strongly on the volume fraction and average size of the SiC particles, the latter is only dependent on the volume fraction of SiC.

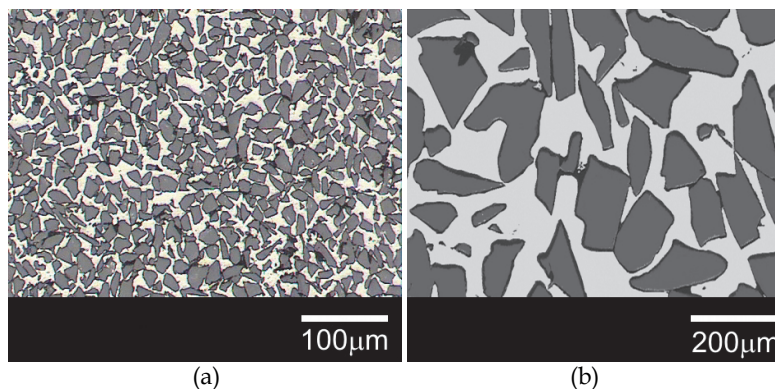


Fig. 3. Optical micrographs of cross sections of different samples of Al/SiC composites containing SiC particles of different average size diameters: (a) 17 μm (corresponding to 500 mesh; SiC500) and (b) 170 μm (corresponding to 100 mesh; SiC100)

SiC particles	V_r	D (μm)	TC (W/mK)	CTE (ppm/K)
SiC100	0.58	167	221	12.7
SiC180	0.58	86	209	13.2
SiC240	0.6	57	203	12.5
SiC320	0.59	37	204	12.9
SiC400	0.58	23	194	13.1
SiC500	0.55	17	193	13.4
SiC800	0.53	9	154	14.9

Table 1. Main characteristics of Al/SiC composites with monomodal distribution of particles; V_r is the particle volume fraction, D is the average size determined by laser diffraction, TC is the thermal conductivity (W/mK) and CTE refers to the thermal expansion coefficient

Modelling thermal conductivity in these composites is relatively simple. The two model schemes here reviewed are both applicable with similar results given that, as already explained, the phase contrast for aluminium and SiC is close to 1. In this sense, the plot in Fig. 4a might be obtained from Eq. (4) or Eq. (6) with almost indistinguishable results.

If now we speculate about how thermal conductivity can be improved in these composites, we may think that the thermal conductivity of the SiC filler cannot be increased (for a given quality purity) and that the interface thermal conductance between Al and SiC is indeed of the order 10^8 W/m²K (in agreement with other experimental works and calculated data with the acoustic mismatch model (Molina et al., 2009)). The largest potential comes from the metal, in improving the matrix conductivity to the value of pure aluminium (273 W/mK). In the experiments presented here, gas pressure infiltration was used to fabricate the composites. Seemingly, there was some chemical interaction between the metal and the quartz crucible during the time metal was molten prior to infiltration. The result of this

reaction was that metal was alloyed with Si and the matrix conductivity diminished down to a value as low as 185 W/mK (Molina et al., 2008b).

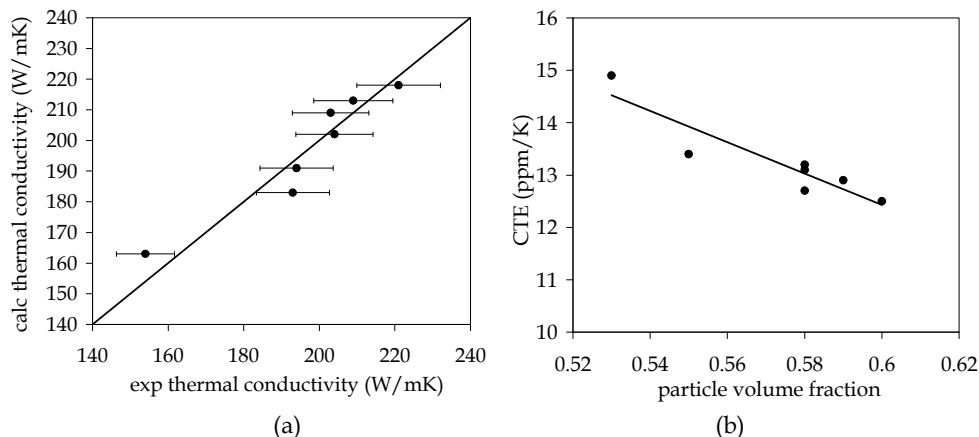


Fig. 4. Experimental results for Al/SiC composites containing SiC particles of different average size diameters: (a) thermal conductivity compared with predicted values obtained with the DEM scheme (the values taken for modelling are: $K_m = 185$ W/mK, $K_r^{in} = 253$ W/mK and $h = 7.5 \cdot 10^7$ W/m² K); and (b) coefficient of thermal expansion (α) versus volume fraction of reinforcement (the line corresponds to a fitting with equation $\alpha = -29.88V_r + 30.36$)

The coefficient of thermal expansion of the different composites versus the SiC volume content is shown in Fig. 4b. All composite materials showed a low value of thermal expansion, increasingly lower when the SiC content is increased. The linear relation encountered for this property with the SiC volume fraction reinforces the conclusion that CTE is only dependent on the volume fraction of the different phases present, in qualitative agreement with most analysis of this property (Arpon et al., 2003a; Molina et al., 2003a), no matter the size, shape or size distribution of the particles.

4.2.2 Al/SiC with bimodal distribution of particles

For certain high-demanding electronic applications Al/SiC composites based on a monomodal distribution of SiC particles were unable to properly operate as admissible heat sinks. For those applications where the heat generated was in excess and/or the material had to accomplish with very restricted thermal expansion, new methods for increasing the volume fraction of SiC particles in the metal were developed.

It has been established that the minimum volume fraction needed for these composites is about 0.6. The logical reasoning to achieve high volume fractions of particles consists of mixing and packing particles of largely different sizes (size ratio >10). During the past few years diverse groups have been working in the ceramic particle packing of multimodal mixtures (Molina et al., 2002).

A very simple and intuitive model for the prediction of particle packing was presented and validated in (Molina et al., 2002) and the main features can be summarized as follows. When

a bimodal mixture is considered (two different particle sizes), the following model with two limits mathematically separated can be applied:

a. Fine particle end

$$V_r = \frac{1}{X_{cp} + \frac{1 - X_{cp}}{V_{sp}}} \quad (8)$$

b. Coarse particle end

$$V_r = \frac{V_{cp}}{X_{cp}} \quad (9)$$

where V_r is the total volume fraction; V_{cp} and V_{sp} are the volume fractions in compacts of only coarse and small particles, respectively; and X_{cp} is the fraction of coarse particles in the powder mixture.

Other mathematical schemes, like that proposed by Yu and Standish (Yu & Standish, 1987, as cited in Molina et al., 2002), make use of experimental information through an empirical parameter with adjustable value. Fig. 5 shows experimental results of packing obtained with mixtures of two largely different sizes of SiC (17 μm and 170 μm). Fig. 5 puts in clear evidence that the particle volume fraction of the compacts made from bimodal mixtures can be tailored by simply controlling the relative amount of large and small particles. Moreover, the experimental results for the particle volume fraction are rationalized using the simple model (Eq. (8) and Eq. (9)) that assumes that small particles can be easily accommodated in the free space left by large particles. Therefore, the local compactness of fine particles is nearly constant for coarse particle percentages up to that for which the maximum global compactness is reached.

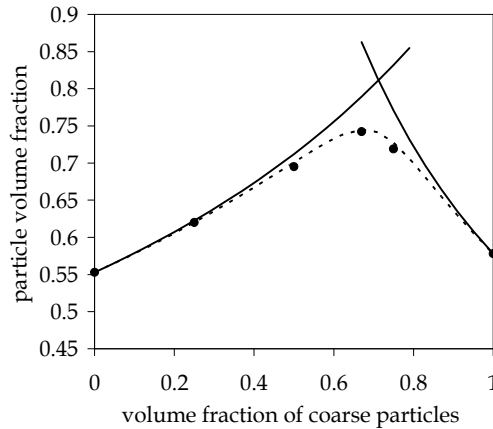


Fig. 5. Volume fraction of particles attained in packed preforms of a bimodal mixture of SiC formed by angular particles of 17 μm and 170 μm . The continuous lines correspond to the two branches of the simple geometrical model described by Eq. (8) and Eq. (9); the broken line refers to a semiempirical scheme proposed by (Yu & Standish, 1987, as cited in Molina et al., 2002).

For gas-pressure Al-infiltrated bimodal preforms, optical microscopy revealed that, up to a 60% of coarse particles, the SiC particles appear homogeneously distributed in the Al matrix, being the coarse particles embedded in a bed of small particles (Fig. 6a). For higher percentages of coarse particles, the spaces between the touching large particles were somewhat irregularly filled with the small particles (Fig. 6b).

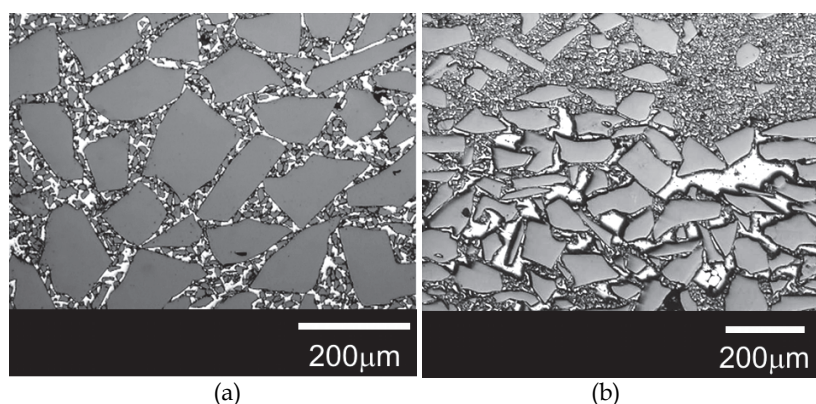


Fig. 6. Optical micrographs of cross sections of different samples of Al/SiC composites containing a mixture of SiC particles of two largely different sizes (17 μm and 170 μm) in different proportions: (a) 67% coarse particles + 33% small particles; and (b) 75% coarse particles + 25% small particles, showing inhomogeneous filling

The main thermal properties of composite materials obtained by gas pressure infiltration of ceramic preforms containing a bimodal mixture of SiC particles (170 μm + 17 μm) with pure Al are gathered in Table 2.

% of coarse particles	V_r	TC (W/mK)	CTE (ppm/K)
25	0.62	215	10.8
50	0.69	220	9.0
67	0.74	228	7.8
75	0.72	225	8.4

Table 2. Main characteristics of Al/SiC composites with bimodal distribution of particles (SiC100/SiC500); V_r is the particle volume fraction, TC is the thermal conductivity (W/mK) and CTE refers to the coefficient of thermal expansion (ppm/K)

The experimental results of thermal conductivity for these composites are plotted in Fig. 7 versus the percentage of coarse particles. The results follow a trend similar to that of particle volume fraction (see Fig. 5) illustrating the close relationship between the two magnitudes. The figure shows as well the predictions offered by the DEM model, Eq. (6), for three different series of inputs (Molina et al., 2008b).

The best results are obtained when the model takes into account that, instead of inserting in Eq. (5) the average particle diameter D measured by laser diffraction, the characteristic length scale of the finely divided powder might be better represented by a calculated value of D obtained from the specific surface area of the particles (Eq. (7)) (Molina et al., 2005). When considering bimodal mixtures, a proper length scale characteristic of the particle reinforcement might be obtained by averaging the ratio λ/S with the volume fraction for each present particle, as follows:

$$D = \frac{6}{\rho} \left[\frac{\lambda_{cp}}{S_{cp}} V'_{cp} + \frac{\lambda_{sp}}{S_{sp}} V'_{sp} \right] \quad (10)$$

V' is the volume fraction of a given particle size in the mixture; the subscripts cp and sp refer to coarse and small particles, respectively. Based on experimental measurements the values of λ deduced for the two particle types here considered are: $\lambda_{cp}=6.8$ and $\lambda_{sp}=2.7$; the values used for the specific surface area are: $S_{cp}=91 \text{ m}^2/\text{kg}$ and $S_{sp}=338 \text{ m}^2/\text{kg}$.

Fig. 8a reports results for the coefficient of thermal expansion versus particle volume fraction for all Al/SiC composites presented in Table 1 and Table 2 containing either a single particle size or bimodal particle distributions. As shown in the figure the whole set of data can be satisfactorily accounted for by means of a linear fitting. As already pointed out in the former section, this indicates that what matters, as long as the CTE is concerned, is the global particle volume fraction, neither the particle size and shape nor the particle size distribution (Arpon et al., 2003a).

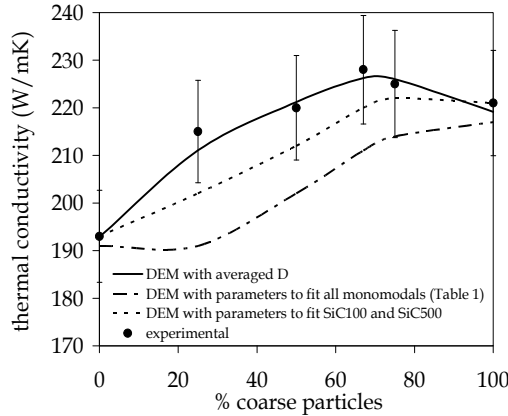


Fig. 7. Thermal conductivity of Al/SiC composites obtained by gas pressure infiltration of aluminium into preforms of bimodal SiC mixtures (SiC100/SiC500) versus the percentage of coarse particles. Dots correspond to experimental results; the dashed lines are different calculations within the DEM scheme. The values taken for modelling are: $K_m = 185 \text{ W/mK}$, $K_r^{in} = 253 \text{ W/mK}$ and $h = 7.5 \cdot 10^7 \text{ W/m}^2 \text{ K}$

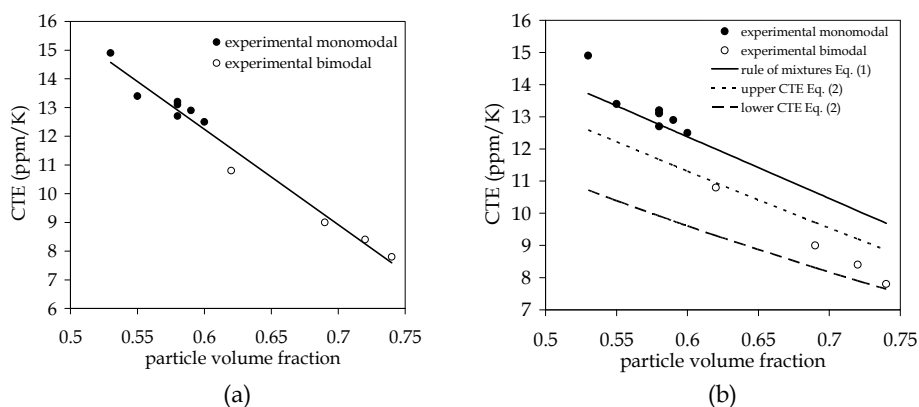


Fig. 8. Thermal expansion coefficient in the range 50-300°C versus particle volume fraction for Al/SiC composites having either a single particle size (full circles) or bimodal particle distributions (empty circles): (a) fitting by a straight line of equation $\alpha = -33.20V_r + 32.16$; (b) theoretical results predicted by different models

Different theoretical results for the coefficient of thermal expansion have been depicted in Fig. 8b for composites containing mono- and bimodal distributions of SiC particles. The present discrepancies between experimental results and predictions can be qualitatively understood by noting that those two models have been developed using thermoelasticity theory. In this sense, experimental results of CTE obtained at lower temperatures might be closer to the predictive values, given that plastic deformation becomes greater at higher temperatures. These results, in consequence, illustrate the failure of the thermoelasticity framework upon which most theories are based.

4.3 Metal matrix composites with a hybrid mixture of reinforcement (SiC+ceramic)

4.3.1 Metal/SiC-diamond composites

Being diamond a very interesting ceramic due to its superior thermal properties its use as particulate in metal matrix composites for thermal management applications has been largely evaluated. Many have been the composites fabricated with excellent thermal properties. However, these composites have no lack of some disadvantages: the price of diamond particles makes the material cost too high and machinability is very difficult or even impossible. In an attempt to overcome some of these problems and at the same time combine the unique properties of diamond and SiC together, a new material containing both types of ceramics was presented in (Molina et al., 2008a). The proposal consists of using as reinforcement a mixture of diamond and SiC particles of similar size. The preform is afterwards consolidated with Al by gas pressure infiltration. The aim of using this particular mixture of ceramics is to achieve a decrease in the material costs maintaining the thermal conductivity at a certain high value. In Fig. 9a it is shown the predicted property of thermal conductivity for three different combinations of SiC and diamond particles. As clearly shown, there is no big advantage in using a mixture of SiC100 (170 μm) and diamond-500 (16 μm) in respect to the use of monomodal SiC100 (170 μm) particles. Even when only the most conducting diamond phase is present, the thermal conductivity of the composite is still

very low, given that interface resistance becomes very important for the small particle size here considered (16 μm). A different situation is found when mixtures of diamond-100 (170 μm) and SiC500 (16 μm) are considered, for which the maximum thermal conductivity is about 550 W/mK (that corresponds to a monomodal diamond particle distribution of 170 μm of average diameter). Fig. 9a also includes the calculation for a system in which SiC and diamond particles have the same average diameter (170 μm).

In (Molina et al., 2008a) powder mixtures containing 20, 40, 50, 60, 70, 80 and 90 vol.% of diamond (of about 200 μm of average diameter) were prepared by dry mixing with SiC (of same average size). Given the similarity in shape and size of the diamond and the SiC particles, the relative density of the preforms was in the range of 58 ± 1 vol.% for all samples.

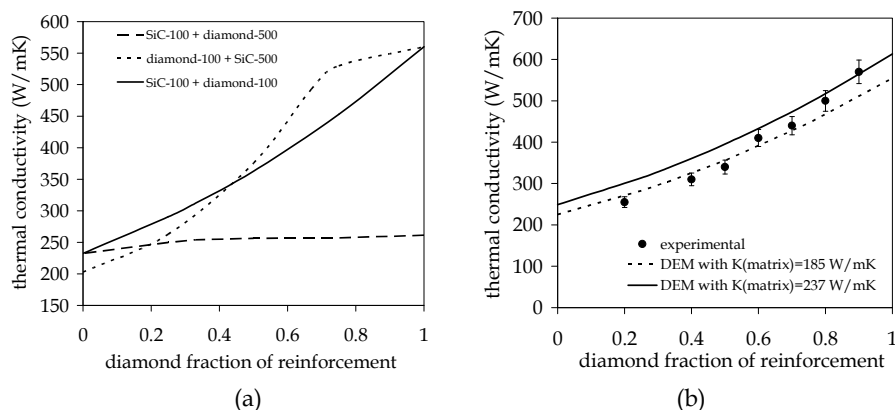


Fig. 9. Thermal conductivity of aluminium-matrix composites containing different mixtures of diamond and SiC particles: (a) calculated values with the DEM scheme for three sets of mixtures; (b) experimental and calculated values with the DEM scheme for mixtures of powders of similar size (200 μm) for two intrinsic values of matrix thermal conductivity

	SiC	Diamond
Intrinsic thermal conductivity (W/mK)	259	1450
Interface thermal conductance with pure aluminium (W/m ² K)	1.05×10^8	5×10^7

Table 3. Parameters used in the calculations of Fig. 9 for the intrinsic thermal conductivity and interface thermal conductance with pure aluminium for SiC and diamond

The thermal conductivity of these composites was characterised and the results are gathered in Fig. 9b, along with the prediction obtained with the generalized differential effective medium scheme. The composites fabricated with this combination of ceramics exhibit high thermal conductivities for the whole range of ceramic proportions. Modelling in Fig. 9 has been developed within the parameters collected in Table 3.

Fig. 9b shows two predictive lines corresponding to different inputs for the intrinsic thermal conductivity of the metal. While for the SiC-rich mixture content end a thermal conductivity of the matrix of 185 is needed to fit experimental data, this value increases to the thermal conductivity of pure aluminium (237 W/mK) for those mixtures with predominant presence

of diamond particles. The reason behind this is that the thermal conductivity of the nominally pure aluminium matrix is influenced by take-up of some silicon from the silicon carbide. It was shown in (Molina et al., 2008b) that the intrinsic value of the thermal conductivity of pure aluminium in composites fabricated via gas-pressure infiltration might be as low as 185 W/mK, because of the presence of silicon in solid solution in combination with precipitated silicon phase in the matrix. Reactivity of liquid aluminium and SiC in the “as-received” condition seems unavoidable in gas-pressure infiltration, since the time elapsed during pressurization of the chamber and posterior solidification is of the order of some minutes, depending on the special characteristics of the equipment at hand. Decreasing as much as possible the infiltration temperature seems then to be a successful way to avoid metal-ceramic reactivity in SiC-based systems.

4.3.2 Metal/SiC-graphite flakes composites

A very recent family of composite materials has been developed and patented at the University of Alicante (Narciso et al., 2007; Prieto et al., 2008). The invention is concerned with a composite material with high thermal performance and low cost which has a layered structure achieved by proper combination of different components. The components of the material are three: 1) a phase mainly formed by graphite flakes (phase A); 2) a second phase (phase B) involving particles or fibers of a material which can act as a phase separator of phase A (phase B is a ceramic material preferably selected from the group of SiC, BN, AlN, TiB₂, diamond and carbon fibers); and finally, 3) a third phase (phase C) formed by a metallic alloy. The three present phases must have good thermal properties, although their main function is different for each one: phase A (graphite flakes) is the principal responsible of the properties of the final material, phase B acts as a separator of the layers of phase A and phase C has to consolidate the preform.

The resultant layered structure of these composites is mainly due to the fact that graphite flakes naturally tend to lie on top of each other, especially when a given pressure is applied. It is in fact due to this tendency to get densely packed that, when only flakes are present, they almost leave no space between them and infiltration becomes an almost unfeasible task. The presence of another ceramic (phase B), like SiC particles, allows molten metal infiltration by keeping the graphite flakes separated. The feasibility of the fabrication procedure of these composites was demonstrated in (Prieto et al., 2008).

A representative illustration of the microstructures of these composites is given in Fig. 10.

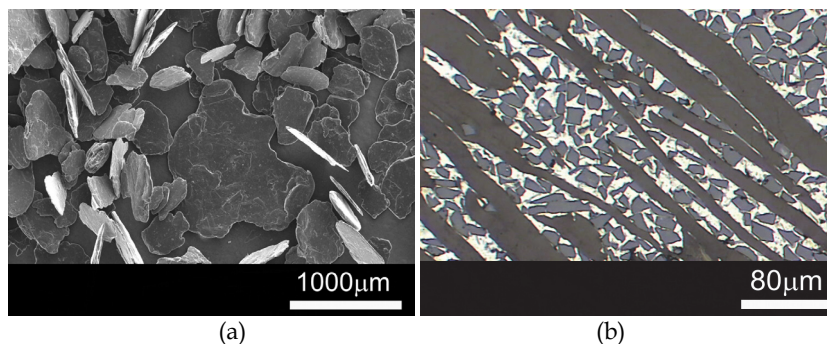


Fig. 10. Micrographs of: (a) graphite flakes and (b) composite material obtained by infiltration with Al-12%Si of preforms obtained by mixing graphite flakes (60%) with SiC particles (40%)

Table 4 shows the most significant results of the thermal properties for some of these materials. These composites recently developed present exceptionally high values of thermal conductivity. The thermal properties are clearly anisotropic, given the fact mentioned before that graphite flakes are oriented in a plane, for which they exhibit the maximum thermal conductivity and the lowest CTE (xy-plane in Table 4).

Reinforcement	Metal	V_r	CT (W/mK)	CTE (ppm/K)
60% graphite flakes + 40% SiC	Al-12%Si	0.88	xy: 368 z: 65	z: 11 xy: 7.0
63% graphite flakes + 37% SiC	Ag-3%Si	0.88	xy: 360 z: 64	z: 11 xy: 8.0

Table 4. Thermal properties of metal/SiC-graphite flakes composites. xy refers to the graphene planes, while the direction perpendicular to it is denoted by z

Although the properties presented in Table 4 are very good, the authors of the patent (Narciso et al., 2007) have already encountered even more promising values when special conditions of infiltration are used. The thermal properties of these composites are currently being evaluated by means of different modelling schemes, conveniently adapted to account for both the anisotropic microstructure of the materials at the mesoscale and the anisotropy in the intrinsic thermal properties of the graphite flakes. Modelling on this system arouses special interest since it is a very cheap and machinable material which has attracted the interest for many applications and represents a clear alternative candidate for heat sinking.

5. Selection of processing conditions for fabrication of SiC-based composite materials for thermal management

The thermal properties of composite materials are mainly determined by the intrinsic properties of their constituents and the characteristics of the matrix-reinforcement interface. Aside an appropriate selection of the constituents it is essential to control the processing conditions during fabrication of the material in order to generate a proper interface able to effectively transfer the heat across the different constituent phases. During fabrication of a composite material by infiltration or squeeze casting some of these processing conditions concern:

- Ceramic particulate (average diameter, size distribution, shape, packed volume fraction)
- Liquid metal (surface tension, viscosity)
- Liquid-solid interface (wettability, reactivity)
- Experimental variables (maximum applied pressure, pressurization rate, temperature, infiltration atmosphere)

Next sections will focus on different aspects in regard to the most important parameters that mainly determine the thermal properties of SiC-based composite materials: wettability-reactivity at the liquid-solid interface, maximum applied pressure and pressurization rate.

5.1 Threshold pressure for infiltration

An outstanding technologically relevant parameter in composite materials processing is the threshold (P_0), or minimum, pressure to achieve the entrance of the molten metal into the porous preform. Being essential for materials validation, its measurement is, however, not simple. One of the methods to get the threshold pressure of a given system is to infiltrate a

preform at various applied pressures and measure, for a fixed time, the infiltrated height for each pressure (Garcia-Cordovilla et al., 1999, Molina et al., 2004; Molina et al, 2008; Piñero et al, 2008). Data are then analysed by means of Darcy's law:

$$h^2 = \frac{2k \cdot t}{\mu \cdot (1 - V_r)} (P - P_0) \quad (11)$$

where k is the permeability of the porous solid, t is the infiltration time and μ the viscosity of the liquid metal. P_0 can be easily derived from plots of h^2 vs P .

Threshold pressure and contact angle are intimately correlated by means of the so-called capillary law:

$$P_0 = 6\lambda \cdot \gamma_{lv} \cdot \cos\theta \frac{V_r}{(1 - V_r) \cdot D} = \gamma_{lv} \cdot \Sigma \cdot \cos\theta \quad (12)$$

being θ the contact angle and γ_{lv} the surface tension of the molten metal at the infiltration temperature. The value of P_0 is clearly dependent on the wetting characteristics of the system and, hence, may be strongly affected by the reactive phenomena occurring at the interface between metal and substrate while the infiltration front moves over the substrate surface. The study of this parameter becomes especially interesting for those systems where infiltration front movement and reaction cannot be decoupled in time. A remarkable fact that has to be taken in consideration is that if infiltration occurs too rapidly, reaction could be prevented and the system may behave as non-reactive. A conclusive study regarding these points was presented in (Molina et al., 2007b; Tian et al., 2005), which discusses results for infiltration of pure Al and Al-12wt%Si into compacts of as-received and thermally oxidized SiC particles. The main results of this study are summarized in Fig. 11a.

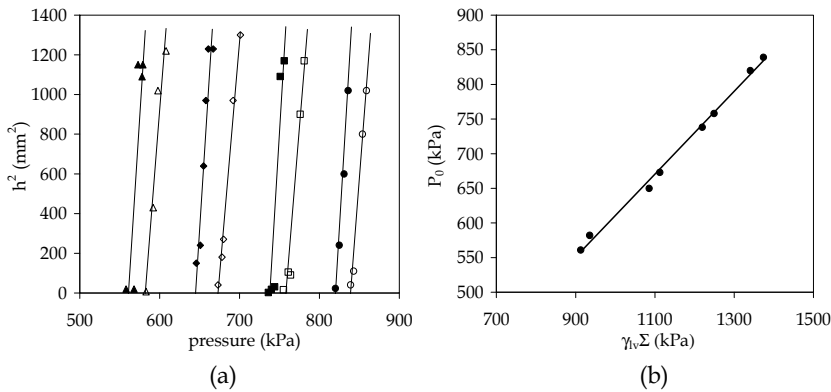


Fig. 11. (a) Plots of the square of the infiltrated height h^2 as a function of applied pressure P for gas pressure infiltration at 700°C of Al and Al-12%Si in preforms of SiC particles in the as-received and oxidized conditions: Al/SiC500 (○), Al-12%Si/SiC500 (●), Al/SiC500ox (□), Al-12%Si/SiC500ox (■), Al/SiC400 (◇), Al-12%Si/SiC400 (◆), Al/SiC400ox (△) and Al-12%Si/SiCox (▲). The straight lines are linear fittings of experimental data; (b) Threshold pressure P_0 versus $\gamma_{lv}\Sigma$ for the different systems in (a). The line corresponds to a fitting with equation $P_0 = 0.603 \gamma_{lv}\Sigma + 32.9$ kPa

The most important conclusion is that the contact angle derived from a fitting of the experimental data (Fig. 11b) by means of Eq. (12) is the same for all cases studied. The infiltration behaviour of the different systems, governed by a unique contact angle, indicates that the metal/particle interface is in both cases the same. Instead of being a metal/SiC contact, there exists an interlayer of silica between both. The very thin silica layer that covers naturally the SiC particles seems to be thick enough to partly remain after reaction with the metal during infiltration at these low temperatures and relatively rapid infiltration kinetics. Another system with remarkable interest is Ag/SiC (Garcia-Cordovilla et al., 1999; Molina et al., 2003b). Silver is a metal with high capacity for dissolution of oxygen in the molten state. This oxygen can rapidly oxidize the SiC particles. This was observed to affect directly the threshold pressure of the system by increasing its value. The apparent contact angle derived from the data was 168°. The authors suggested that the gas evolved during the oxidation of SiC reduced the contact area and, in consequence, wetting.

5.2 Drainage curves for gas-pressure infiltration

Determination of threshold pressures is often not sufficient to fully characterize wetting in infiltration processing. Intrinsic capillary parameters, characteristic of dynamic wetting of a discrete reinforcement, are not, per se, equal to those derived in near-static conditions (i.e. sessile drop measurements). Furthermore, preforms are invaded over a range of pressures that is governed by the complex internal geometry of open pores within the preform (Rodriguez-Guerrero et al., 2008). A more thorough characterization of wetting is obtained by the so-called drainage curves. These are plots of the metallic saturation (fraction of non-wetting fluid in the porous medium) versus the pressure difference between the fluid and the atmosphere in the pores. These drainage curves contain all information related to wetting of the porous preform by the non-wetting liquid. With the assumption that irreversibility effects (e.g. Haines jumps) and other inertial losses can be neglected, the work of immersion (W_i) can be calculated as the work necessary to fully infiltrate the preform (W) divided by the total preform/infiltrant interface created per unit volume of reinforcement:

$$W_i = \frac{W}{A_v \cdot V_r} = \frac{(1 - V_r) \cdot \int P dS}{A_v \cdot V_r} \quad (13)$$

where P , S and V_r are saturation, applied pressure and volume fraction of reinforcement, respectively; A_v is the particle specific surface area per unit volume of preform. The contact angle can be easily derived by making use of the following relationship:

$$W_i = \gamma_{lv} \cdot \cos \theta \quad (14)$$

Recently, a new technique was proposed for the direct measurement of capillary forces during the infiltration process of high-temperature melting non-wetting liquids into ceramic preforms. In essence, the equipment is a high-temperature analogue of mercury porosimetry. The device can track dynamically the volume of metal that is displaced during pressurization and hence allows obtaining in a single experiment the entire drainage curve characterizing capillarity in high-temperature infiltration of particles by molten metal (Bahraini et al., 2005; Bahraini et al., 2008; Molina et al., 2007a; Molina et al., 2008d). The technique was validated in an study of wetting of silicon carbide by pure aluminium and by aluminium-silicon eutectic alloy using drainage curves obtained during gas pressure infiltration at 750°C.

With relatively fast pressurization rates the drainage curves for a metal/SiC system that can be obtained are shown in Fig. 12 for SiC320 particles of about $37\ \mu\text{m}$ of average diameter. The shape of the curves is determined by the shape of particles in the preform. Any change of (i) the work of immersion, (ii) the particle volume fraction and/or (iii) the particle size (which is accounted for by A_v parameter) will cause a predictable shift over the pressure axis. The values of contact angle derived from the drainage curves for different sizes of SiC particles with Al and Al-12%Si are in the range $110\text{--}113^\circ$. These values are fully consistent with measurements with the sessile drop method for the wetting of oxide-covered SiC by molten aluminium free of a surface layer of oxide. In these infiltration experiments the triple line is forced to move at a motion rate which is well above the “natural” rate dictated by reaction kinetics in the sessile drop method. Hence, infiltration and reaction processes are decoupled in time and the SiC surface is covered before reaction can take place at the interface. Nevertheless, when pressurization rate is decreased, the interfacial reaction can take place concomitantly with the motion of the triple line and both phenomena may interact to provoke different behaviours in drainage curves. Fig. 13 shows drainage curves for the infiltration of SiC particles with molten Al and Al-Si eutectic at a reduced pressurization rate of 0.05MPa/s together with the curves obtained for the same systems at 0.13MPa/s .

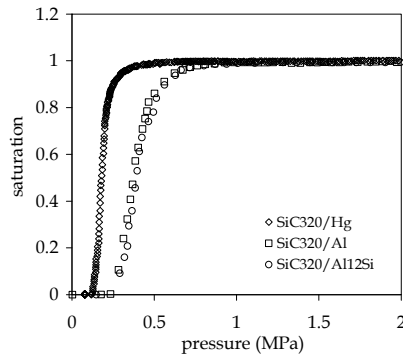


Fig. 12. Drainage curves of SiC320 infiltrated with Hg, Al and Al-12%Si at 750°C

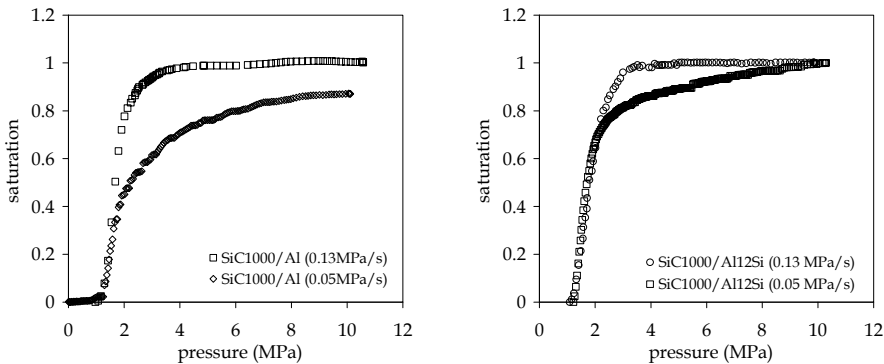


Fig. 13. Drainage curves at 750°C of (a) SiC1000/Al and (b) SiC1000/Al-12%Si, measured at the two pressurization rates of 0.13 and 0.05MPa/s

The curves of Fig. 13 show that interfacial reactions, which have proven in sessile-drop experiments to aid wetting, under forced pressure-driven infiltration can hinder infiltration of SiC preforms by aluminium-based melts. These effects can be due to the fact that chemical interactions can cause morphological changes at the solid/liquid interface. As a corollary, rapid pressure infiltration is preferable in processing metal matrix composites featuring interfacial reactivity.

5.3 Gas pressure infiltration vs squeeze casting

It is interesting to compare the resulting materials processed by two different liquid-state routes, namely gas-pressure infiltration and squeeze casting, which make use of different pressures and pressurization rates (this having a direct implication on the contact time between molten metal and particles before metal is solidified).

In (Weber et al., 2010) it is presented a complete study of comparison of the different properties encountered for Al/SiC composites processed by these two fabrication techniques. In this work, bimodal powder mixtures of green quality SiC powders with average sizes of 170 μm and 17 μm , respectively, were used. A set of samples was processed by squeeze casting while other two sets were prepared by gas pressure-assisted infiltration at two largely different infiltration kinetics. Fig. 14a resumes the thermal conductivities for both series of composites together with modelling predictions using the DEM scheme.

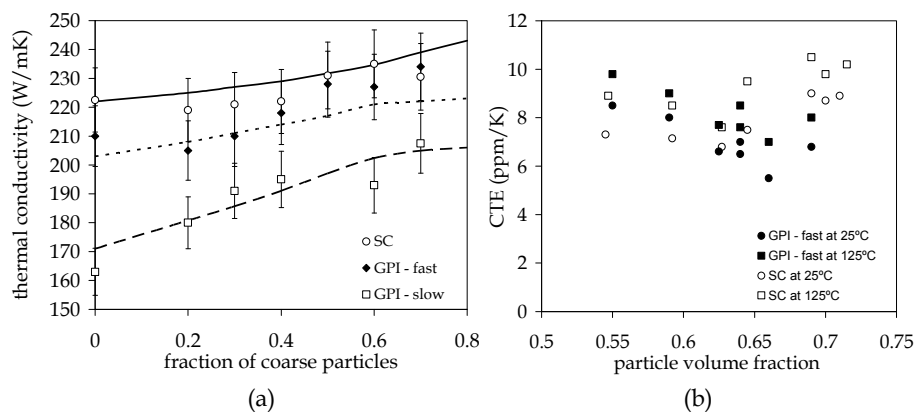


Fig. 14. (a) Thermal conductivity of the Al/SiC composites produced by infiltration of aluminium into preforms of mono- and bimodal SiC mixtures (SiC100/SiC500) versus the fraction of coarse particles. SC refers to squeeze casting and GPI refers to gas pressure infiltration. The lines correspond to calculations with the DEM scheme; (b) Coefficient of thermal expansion for the Al/SiC composites in (a) for temperatures of 25°C and 125°C

For the squeeze cast samples, thermal conductivity was in between 225 and 235 W/mK with a slight tendency to increase with the amount of large particles. For the samples prepared by fast GPI, the thermal conductivity increased from around 200 W/mK for the composite containing only small particles with increasing fraction of large particles up to 230 W/mK. For the slow GPI samples, values increased from 160 to 205 W/mK with increasing fraction of large particles. For the modelling of thermal conductivity, different matrix conductivities have been taken into account. While for SC samples the matrix conductivity is that of pure

aluminium (237 W/mK) due to the lack of time to react with the reinforcement, for the GPI samples values of 190 W/mK and 170 W/mK for GPI fast and GPI slow, respectively, have been used. Interestingly enough, the interface thermal conductance varies as well its value with the contact time corresponding to each processing technique. For SC and fast GPI the interface thermal conductance is found to be 1.4×10^8 W/m²K. For the slow GPI this parameter has a value which is about the half, most probably due to the abundant reaction product (Al_4C_3) at the interface (Weber et al., 2010).

The results of the CTE measurements are collected in Fig. 14b. The physical CTEs (measured in a range of $\pm 5^\circ\text{C}$ around the indicated temperature) are given for the SC and the fast GPI samples only, yet for two temperatures of technical interest, i.e., 25°C and 125°C . The CTE decreases in general with increasing SiC volume fraction and is typically 1–1.5 ppm/K higher at 125°C than at ambient temperature.

5.4 Effect of porosity

In a non-wetting system like Al/SiC infiltration of the metal into the open channels of the preform does not take place at a single, well-defined pressure but, as already seen, it rather takes place progressively with the applied pressure when this pressure exceeds a certain threshold (threshold pressure). In order to obtain a hundred percent filling of the porous space of the preform by the metal an infinitely large pressure, impossible to obtain in laboratory, would be needed. For a given infiltration pressure, therefore, defects at the contact area of particles will exist and porosity will hence be unavoidable.

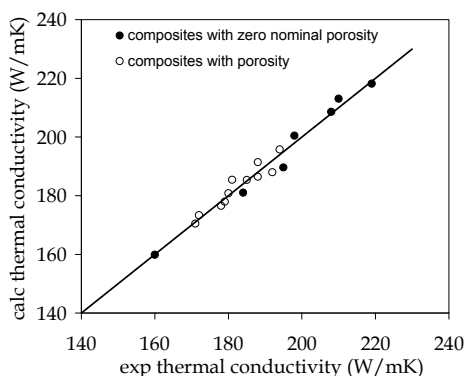


Fig. 15. Plot of the thermal conductivity calculated with the two-step Hasselman-Johnson model versus that determined experimentally. The line represents the identity function. DEM scheme offers identical results

Porosity does affect the two main properties which are important in materials for thermal management and, hence, may limit its use for this application. Depending on the nature of both, metal and reinforcement, voids in the material may increase or decrease the coefficient of thermal expansion of the composite material, being this effect very dependent on the geometry of the pores. On the other hand, the presence of porosity does decrease strongly the thermal conductivity of any material, being monolithic or composite. The voids, present in the metallic phase, can be treated as inclusions of zero conductivity in the metal. In a

recent paper (Molina et al., 2009) it has been demonstrated that a simple application of the Hasselman-Johnson model in a two-step procedure (which accounts for the presence of two types of inclusions, reinforcement particles and voids, and the metallic matrix) offers a good approximation of the experimental results of thermal conductivity obtained for Al-12%Si/SiC composite materials. Alternatively, the DEM model may be used as in (Molina et al., 2008a; Molina et al., 2008b) for accounting for the two types of inclusions (SiC particles and pores) at the time. Results of both models are equivalent since the phase contrast in the Al/SiC (or Al-Si/SiC) system is too low. It has been recently demonstrated (Tavangar et al., 2007) that the Hasselman-Johnson scheme increasingly offers inconsistent predictions for the thermal conductivity of composites as the effective phase contrast - ratio between effective thermal conductivity of reinforcement and matrix thermal conductivity - exceeds roughly four.

6. Conclusion

Several composite materials containing SiC as reinforcement, either single or combined with other ceramics, have been presented as serious candidates to cover the specific demand of heat dissipation for thermal management applications. Aside from the metal/SiC composites with monomodal distribution of SiC particles, which nowadays define the state of the art in materials for electronics, those derived from combinations of SiC with either SiC of another largely different size (bimodal mixtures) or other ceramics (hybrid mixtures with diamond or graphite flakes) present high values of thermal conductivity and coefficients of thermal expansion extremely low such as to represent the future generation of heat sinks for electronics. The use of these composites is mainly determined by the specific requirements for every application, taking into account not only the thermal properties but also density, isotropy or ease of machinability (when complex shapes are needed). The spectrum covered by the SiC-based composites aims to offer specific solutions for the different problems of heat dissipation encountered in the energy-related industries such as electronics or aeronautics.

This contribution emphasizes the fact that the choice of a proper fabrication processing is as important as a good selection of the constituents of the composite material. Being aluminium a very used metal for the fabrication of SiC-based composites, processing by liquid state routes must take into account the high reactivity between Al and SiC at the temperature of molten aluminium. In these sense, squeeze casting, which operates allowing very short contact times between metal and reinforcement, offers composites with the highest values of thermal conductivity. Several specific conditions should be taken into account in gas pressure infiltration to give appropriate materials with acceptable thermal properties. In any case, porosity has to be avoided because dramatically decreases the thermal conductivity of the materials. For this purpose, a certain minimum pressure that ensures complete saturation is needed along with a certain pressurization rate in order to force that infiltration and reactivity can be decoupled in time, since interfacial reaction can hinder infiltration.

7. Acknowledgement

The author acknowledges all those who have actively participated to the research presented in this contribution. Special thanks are given to M. Bahraini, L. Weber and A. Mortensen,

from the École Polytechnique Fédérale de Lausanne (Switzerland). R. Arpón, R.A. Saravanan, C. García-Cordovilla, R. Prieto, J. Narciso and E. Louis, from the University of Alicante (Spain), are also gratefully acknowledged. J.M. Molina wants also to express his gratitude to the “Ministerio de Ciencia e Innovación” for a “Ramón y Cajal” contract.

8. References

- Arpon, R.; Molina, J.M.; Saravanan, R.A.; Garcia-Cordovilla, C.; Louis, E. & Narciso, J. (2003). Thermal expansion behaviour of aluminium/SiC composites with bimodal particle distributions. *Acta Materialia*, Vol.51, (January 2003), pp. 3145-3156, ISSN 1359-6454
- Arpon, R.; Molina, J.M.; Saravanan, R.A.; Garcia-Cordovilla, C.; Louis, E. & Narciso, J. (2003). Thermal expansion coefficient and thermal hysteresis of Al/SiC composites with bimodal particle distributions. *Materials Science Forum*, Vols.426-432, (July 2003), pp. 2187-2192, ISSN 0255-5476
- Bahraini, M.; Molina, J.M.; Kida, M.; Weber, L.; Narciso, J. & Mortensen, A. (2005). Measuring and tailoring capillary forces Turing liquid metal infiltration. *Current Opinion in Solid State & Materials Science*, Vol.9, pp. 196-201, ISSN 1359-0286
- Bahraini, M.; Molina, J.M.; Weber, L. & Mortensen, A. (2008). Direct measurement of drainage curves in infiltration of SiC particle preforms. *Materials Science & Engineering A*, Vol.495, (January 2008), pp. 203-207, ISSN 0921-5093
- Clyne, T.W (2000). An introductory overview of MMC systems, types and developments, In: *Comprehensive Composite Materials*, A. Kelly & C. Zweben (Eds.), 1-26, Elsevier Science, ISBN 0-080437214 (Volume 3), Oxford UK, United Kingdom
- Clyne, T.W (2000). Thermal and electrical conduction in MMCs, In: *Comprehensive Composite Materials*, A. Kelly & C. Zweben (Eds.), 447-468, Elsevier Science, ISBN 0-080437214 (Volume 3), Oxford UK, United Kingdom
- Garcia-Cordovilla, C.; Louis, E. & Narciso, J. (1999). Pressure infiltration of packed ceramic particulates by liquid metals. *Acta Materialia*, Vol.47, No.18 (August 1999), pp. 4461-4479, ISSN 1359-6454
- Molina, J.M.; Saravanan, R.A.; Arpon, R.; Narciso, J.; Garcia-Cordovilla, C. & Louis, E. (2002). Pressure infiltration of liquid aluminium into packed SiC particulares with a bimodal size distribution. *Acta Materialia*, Vol.50, No.2, (September 2001), pp. 247-257, ISSN 1359-6454
- Molina, J.M.; Arpon, A.; Saravanan, R.A.; Garcia-Cordovilla, C.; Louis, E. & Narciso, J. (2003). Thermal expansion coefficient and wear performance of aluminium/SiC composites with bimodal particle distributions. *Materials Science and Technology*, Vol.19, (July 2002), pp. 491-496, ISSN 0861-9786
- Molina, J.M.; Garcia-Cordovilla, C.; Louis, E. & Narciso, J. (2003). Pressure infiltration of silver into compacts of oxidized SiC. *Materials Science Forum*, Vols.426-432, (July 2003), pp. 2181-2186, ISSN 0255-5476
- Molina, J.M.; Arpon, R.; Saravanan, R.A.; Garcia-Cordovilla, C.; Louis, E. & Narciso, J. (2004). Threshold pressure for infiltration and particle specific surface area of particle compacts with bimodal size distributions. *Scripta Materialia*, Vol.51, (June 2004), pp. 623-627, ISSN 1359-6462
- Molina, J.M.; Piñero, E.; Narciso, J.; Garcia-Cordovilla, C. & Louis, E. (2005). Liquid metal infiltration into compacts of ceramic particles with bimodal size distributions. *Current Opinion in Solid State & Materials Science*, Vol.9, pp. 202-210, ISSN 1359-0286

- Molina, J.M.; Rodriguez-Guerrero, A.; Bahraini, M.; Weber, L.; Narciso, F.; Rodriguez-Reinoso, F.; Louis, E. & Mortensen, A. (2007). Infiltration of graphite preforms with Al-Si eutectic alloy and mercury. *Scripta Materialia*, Vol.56, (January 2007), pp. 991-994, ISSN 1359-6462
- Molina, J.M.; Tian, J.T.; Garcia-Cordovilla, C.; Louis, E. & Narciso, F. (2007). Wettability in pressure infiltration of SiC and oxidized SiC particle compacts by molten Al and Al-12wt%Si alloy. *Journal of Materials Research*, Vol.22, No.8, (April 2007), pp. 2273-2278, ISSN 0884-2914
- Molina, J.M.; Rhême, M.; Carron, J. & Weber, L. (2008). Thermal conductivity of aluminium matrix composites reinforced with mixtures of diamond and SiC particles. *Scripta Materialia*, Vol.58, (October 2007), pp. 393-396, ISSN 1359-6462
- Molina, J.M.; Narciso, J.; Weber, L.; Mortensen, A. & Louis, E. (2008). Thermal conductivity of Al-SiC composites with monomodal and bimodal particle distributions. *Materials Science & Engineering A*, Vol.480, (July 2007), pp. 483-488, ISSN 0921-5093
- Molina, J.M.; Prieto, R.; Duarte, M.; Narciso, J. & Louis, E. (2008). On the estimation of threshold pressures in infiltration of liquid metals into particle preforms. *Scripta Materialia*, Vol.59, (March 2008), pp. 243-246, ISSN 1359-6462
- Molina, J.M.; Bahraini, M.; Weber, L. & Mortensen, A. (2008). Direct measurement of drainage curves in infiltration of SiC particle preforms: influence of interfacial reactivity. *Journal of Materials Science*, Vol.43, No.15 (April 2008), pp. 5061-5067, ISSN 0022-2461
- Molina, J.M.; Prieto, R.; Narciso, J. & Louis, E. (2009). The effect of porosity on the thermal conductivity of Al-12wt%Si/SiC composites. *Scripta Materialia*, Vol.60, (December 2008), pp. 582-585, ISSN 1359-6462
- Molina, J.M.; Narciso, J. & Louis, E. (2010). On the triple line in infiltration of liquid metals into porous preforms. *Scripta Materialia*, Vol.62, (March 2010), pp. 961-965, ISSN 1359-6462
- Narciso, J.; Weber, L.; Molina, J.M.; Mortensen, A. & Louis, E. (2006). Reactivity and thermal behaviour of Cu-Si/SiC composites: effects of SiC oxidation. *Materials Science and Technology*, Vol.22, No.12, (February 2006), pp. 1464-1468, ISSN 0861-9786
- Narciso, J.; Prieto, R.; Molina, J.M. & Louis, E. (2007). Production of composite materials with high thermal conductivity. Spanish patent (P002700804 2007), European Application Patent (EP2130932-A1 2009), US Application Patent (US 20100143690-A1 2010)
- Piñero, E.; Molina, J.M.; Narciso, J. & Louis, E. (2008). Liquid metal infiltration into particle compacts chemically and morphologically heterogeneous. *Materials Science & Engineering A*, Vol.495, (November 2007), pp. 288-291, ISSN 0921-5093
- Prieto, R.; Molina, J.M.; Narciso, J. & Louis, E. (2008). Fabrication and properties of graphite flakes/metal composites for thermal management applications. *Scripta Materialia*, Vol.59, (February 2008), pp. 11-14, ISSN 1359-6462
- Rodriguez-Guerrero, A.; Molina, J.M.; Rodriguez-Reinoso, F.; Narciso, J. & Louis, E. (2008). Pore filling in graphite particle compacts infiltrated with Al-12wt%Si and Al-12wt%Si-1wt%Cu alloys. *Materials Science & Engineering A*, Vol.495, (January 2008), pp. 276-281, ISSN 0921-5093

- Tavangar, R.; Molina, J.M. & Weber, L. (2007). Assessing predictive schemes for thermal conductivity against diamond-reinforced silver matrix composites at intermediate phase contrast. *Scripta Materialia*, Vol.56, (November 2006), pp. 357-360, ISSN 1359-6462
- Tian, J.T.; Molina, J.M.; Narciso, J.; Garcia-Cordovilla, C. & Louis, E. (2005). Pressure infiltration of Al and Al-12wt%Si alloy into compacts of SiC and oxidized SiC particles. *Journal of Materials Science*, Vol.40, (October 2004), pp. 2537-2540, ISSN 0022-2461
- Weber, L.; Sinicco, G. & Molina, J.M. (2010). Influence of processing route on electrical and thermal conductivity of Al/SiC composites with bimodal particle distribution. *Journal of Materials Science*, Vol.45, No.8 (November 2009), pp. 2203-2209, ISSN 0022-2461

Bulk Growth and Characterization of SiC Single Crystal

Lina Ning and Xiaobo Hu
JiaXing University & Shandong University
China

1. Introduction

Sublimation method was used to grow bulk SiC by J.A. Lely for the first time in 1955 (Lely, 1955). It was improved then by Tairov and Tsvetkov and became the most mature method for bulk SiC growth. In this chapter, we will introduce the growth of hexagonal SiC. Although the bulk growth method is well known and used widely, there are still plenty of details which are different and unique for different groups.

The growth of 4H-SiC is not as stable as that of 6H-SiC. That is to say the growth of 4H-SiC needs a harsh growth conditions. In order to grow high quality 4H polytype, the polytype transition of 4H-SiC single crystals had been studied.

Although single crystals of SiC are commercially available, owing to the specific structures of SiC, there are still some structural defects, such as micropipes, mis-orientations, dislocations, stacking faults, basal plane dislocations, particle inclusions, precipitates and so on, which hinder its applications. So in this chapter we also introduce the recent progress in research of structural defects in 6H-SiC single crystals. Three kinds of typical structural defects in 6H-SiC single crystals were investigated. First, we describe the strain field of a micropipe by the theory of screw dislocation. Stress birefringence images from micropipes with different Burgers vectors have been simulated. The results are compared with polarized optical microscopic observations. Second, elementary screw dislocations were observed by back-reflection synchrotron radiation topography (BRSRT). Based on the reflection geometry, the image of an elementary screw dislocation was simulated. Elementary screw dislocation is a pure screw dislocation with Burger vector lc . Finally, Basal plane bending was detected by high resolution X-ray diffractometry (HRXRD) and transmission synchrotron white-beam x-ray topography (SWBXT).

The observation and investigation of the structural defects helped us to understand their formation mechanisms. This makes it possible for us to further decrease or eventually eliminate them.

2. Bulk growth

All the samples were grown by the sublimation method in our group. The crystal growth procedure has been described in detail elsewhere (Hu et al., 2006). The growth of 6H and 4H polytypes are mainly the same, except for temperature range, growth pressure, seed polarity and also growth process.

2.1 Growth of 4H-SiC

During the sublimation growth process of 4H-SiC, other foreign polytypes nucleated easily since the stacking energies for different SiC polytypes are nearly same. Most of the researchers believed that, it is the growth temperature, the polarity and mis-orientation of the seed that influence the stability of polytypic structure during the growth. Schulze (Norbert et al., 1999) and Straubinger (Straubinger et al., 2001) used different polarity seeds to grow 4H-SiC and found that a stable 4H polytype could be obtained by using the seed with 4H C-face. Further research found that the off-axis C-face seeds with misorientation axis towards the $\langle 11\text{-}20 \rangle$ direction are better (Rost et al., 2006) for 4H-SiC growth than other seeds. The defects density decreased with the increase of seed mis-orientation from C-face.

2.2 Polytype transition of 4H-SiC

In this chapter, 4H C-face seeds with an 8° mis-orientation towards $[11\text{-}20]$ were used to grow 4H-SiC. In order to make out the relationship between the polytype of the as-grown crystal and the surface morphology, the morphology of as-grown surface and polytype transition of 4H-SiC single crystals had been studied by optical microscopy and Raman spectroscopy.

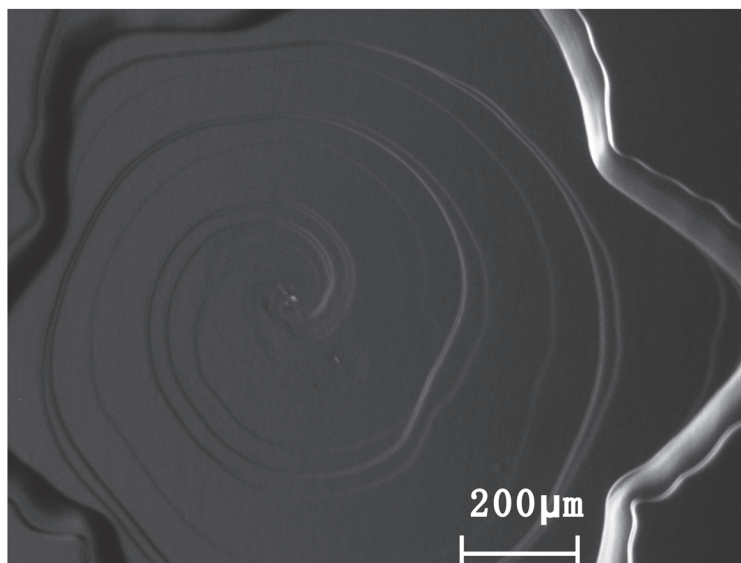


Fig. 1. The morphology of the facet of 4H-SiC

There are two growth mechanisms. Fig. 1 is the morphology of the facet of 4H-SiC. In this region, screw dislocation mechanism controls the growth process. Fig. 2 is the morphology of the area out of the facet. In this region, rough surface growth mechanism dominates. In Fig. 2, there are also two different morphologies. In area A, the growth steps are very fine. In area B, the surface is smooth. There is a slit between the two areas, which is not a scratch caused by machining or annealing after growth. Normally the slit is along the $\langle 11\text{-}20 \rangle$ direction and extends several or dozens of milli-meters on the as-grown surface.

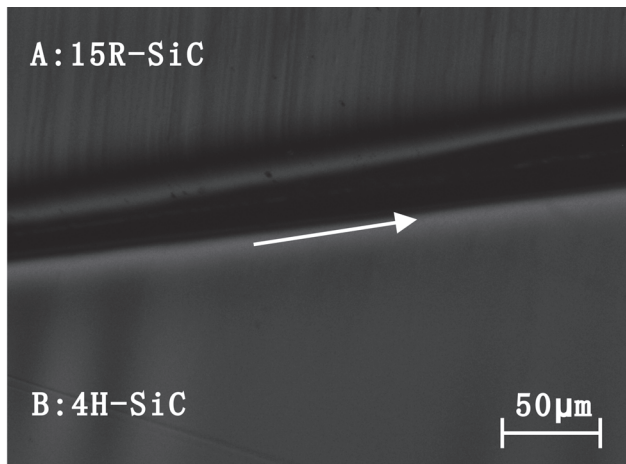


Fig. 2. Micrograph of the as-grown surface showing the existence of 4H-SiC, 15R-SiC at two sides of the slit

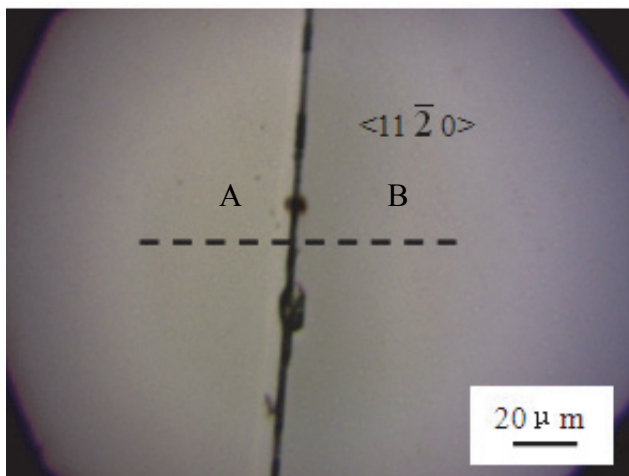


Fig. 3. Schematic diagram of one-dimensional Raman scanning route across the slit

In order to identify the polytype structures in the two areas with different morphologies, Raman spectroscopy were used. One-dimensional Raman scanning was done cross the slit in a range of 100 μm, as shown in Fig. 3. The dashed line represents the scanning path, and the real line is the actual position of slit which is along the $\langle 11\bar{2}0 \rangle$ direction.

The intensity ratio of folded transverse acoustic (FTA) mode of 15R-SiC (Raman shift at 172.3 cm⁻¹) (Wang et al., 2004) and 4H-SiC (Raman shift at 204.99 cm⁻¹) (Wang et al., 2004) was introduced. In Fig. 4, the horizontal coordinate is along the dashed line in Fig. 3, and the longitudinal coordinate is the intensity ratio. According to the intensity ratio, the scanning scope can be divided into three regions. In region A, the intensity ratio is much greater than

one, so it is mainly 15R-SiC whose Raman spectrum is shown in Fig. 5a. In region B, the intensity ratio is much lower than one, so it is mainly 4H-SiC whose Raman spectrum is shown in Fig. 5b. Between the two regions, i.e. near the slit, the intensity ratio drops suddenly. Two points, C and D at a distance of $4\mu\text{m}$, were chosen as reference points in this region. The corresponding Raman spectra are shown in Fig. 5c and d.

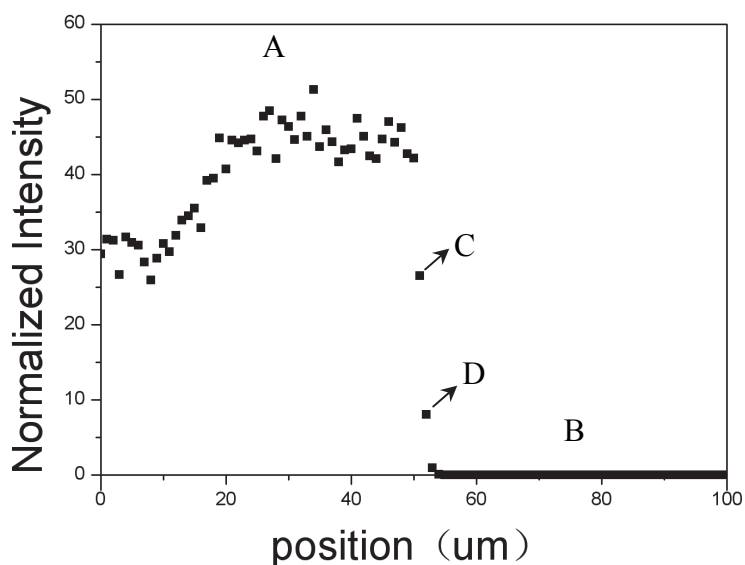


Fig. 4. The intensity ratio of FTA mode along the dashed line in Fig. 3.

From Fig. 5c and 5d, 15R and 4H polytypes appear at the same time. The characteristic peak of 15R-SiC dominates at point C. Both the characteristic peaks of 15R and 4H-SiC are weak and the intensity of the background signal is strong at point D. That is to say, the phonon state density is irregular in this area. In other words, the Si-C di-atom stacking near slit is not completely disorder but contains short range order of 4H and 15R-SiC.

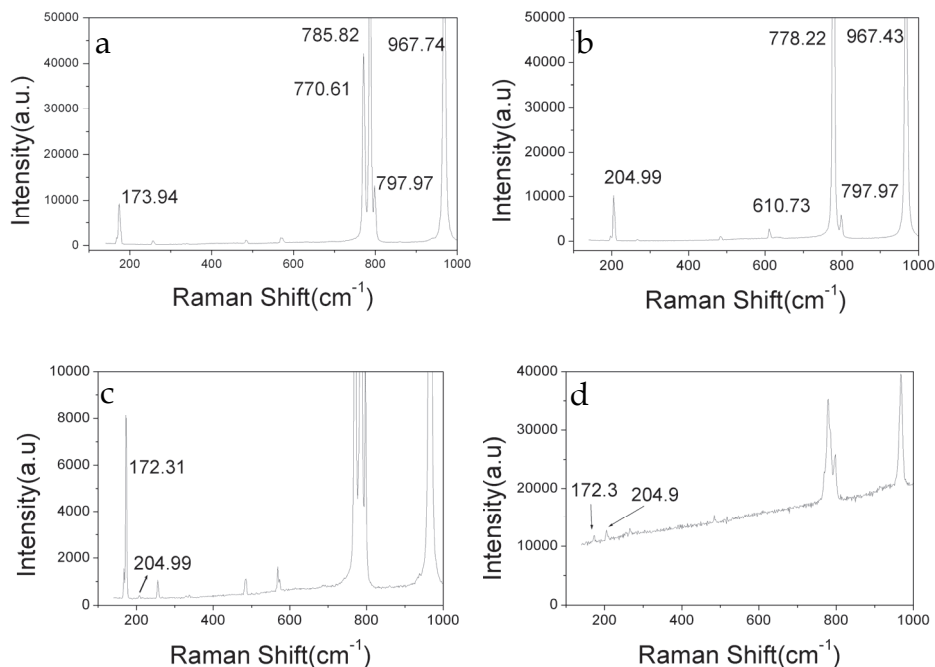


Fig. 5. The Raman spectra at different points of one-dimensional Raman scanning, (a) region A, 15R-SiC; (b) region B, 4H-SiC; (c) point C 15R- and 4H-SiC; (d) point D 4H- and 15R-SiC.

2.3 Summary

In summary, the polytype transition is a process in which the stacking structure changes from long range order to short range order and then back to long range regular. The transition region in our observation is in a range of about 2-3 μ m. The slit is just the sign of the polytype transition.

3. Characterizations

There are some structure defects in SiC single crystals which hinder its applications. For example, the micropipes increase leakage current and reduce the breakdown voltage of SiC devices (Neudeck & Powell, 1994; Wahab et al., 2000). All the samples used in this section were 6H-SiC wafers grown by sublimation method.

3.1 Micropipes

Hollow tubes called micropipes, which generally run along the *c* axis, are often found in sublimation grown SiC crystals. There has been much debate regarding the nature of micropipes and several models have been proposed to illuminate the formation mechanism of micropipes. One is based on Frank's theory, which interpreted the formation of micropipes as the stress relaxation of screw dislocations with large Burgers vectors (Frank, 1951). The diameter of micropipes depends on the Burgers vectors of screw dislocations:

$$D = \mu \mathbf{b}^2 / 4\pi\gamma \quad (1)$$

Where *D* is the core diameter, μ the shear module, \mathbf{b} the Burgers vector and γ the surface energy. The longer the Burgers vector, the larger is the diameter of the micropipes. The other model suggests that deposition or voids on the growth surface cause the generation of micropipes (Giocondi et al., 1997; Liu et al., 2005). It has been proposed that the large steps interact with unit screw dislocations and the heterogeneous phase to form the micropipe.

3.1.1 Experimental observations

Fig. 6a and 6c show the stress birefringence images of two typical micropipes with different diameters respectively. They look like butterflies with four bright wings, and have a dark core in the center. The wings' length varies with the diameter of micropipe. The wings' brightness was also not uniform from the center to the outside. The longer the distance from the center, the weaker is the brightness of the wings. Fig. 6b and 6d exhibit the bright field images of the two micropipes respectively. The open cores were visible distinctly in the centers of micropipes especially for the one with large diameter. When we rotated the sample, the birefringence pattern rotated simultaneously (as shown in Fig. 7).

3.1.2 Theoretical explanations

In this chapter we describe the strain field of a micropipe by the theory of screw dislocation. According to Frank's theory, micropipes are dislocations with large Burgers vectors. Therefore the strain field caused by the micropipes could be described by dislocation theory and stress birefringence image from a micropipe could be simulated. The existence of micropipes changes the crystal from uniaxial to biaxial crystal in the neighbour area of a micropipe. So the interference intensity near a micropipe should be written as follows:

$$I = \begin{cases} (A / r^2) \sin^2(2\theta - 2\alpha) & \text{when } r > r_0 \\ 0 & \text{when } r < r_0 \end{cases} \quad (2)$$

where r_0 is the diameter of the micropipe, α is the angle between $\langle 2\text{-}1\text{-}10 \rangle$ direction and polarizer, *A* is constant which can be expressed as:

$$A = \frac{I_0 \cdot \mu^2 \cdot b^2 \cdot n^6 \cdot \pi_{44}^2 \cdot \Delta l^2 \cdot \cos^2 2\beta}{64\lambda^2} \quad (3)$$

When $r > r_0$, the contour equation of the intensity curve can be obtained

$$r^2 = \frac{I_0}{I} f^2 \sin^2(2\theta - 2\alpha) \mu m^2 \quad (4)$$

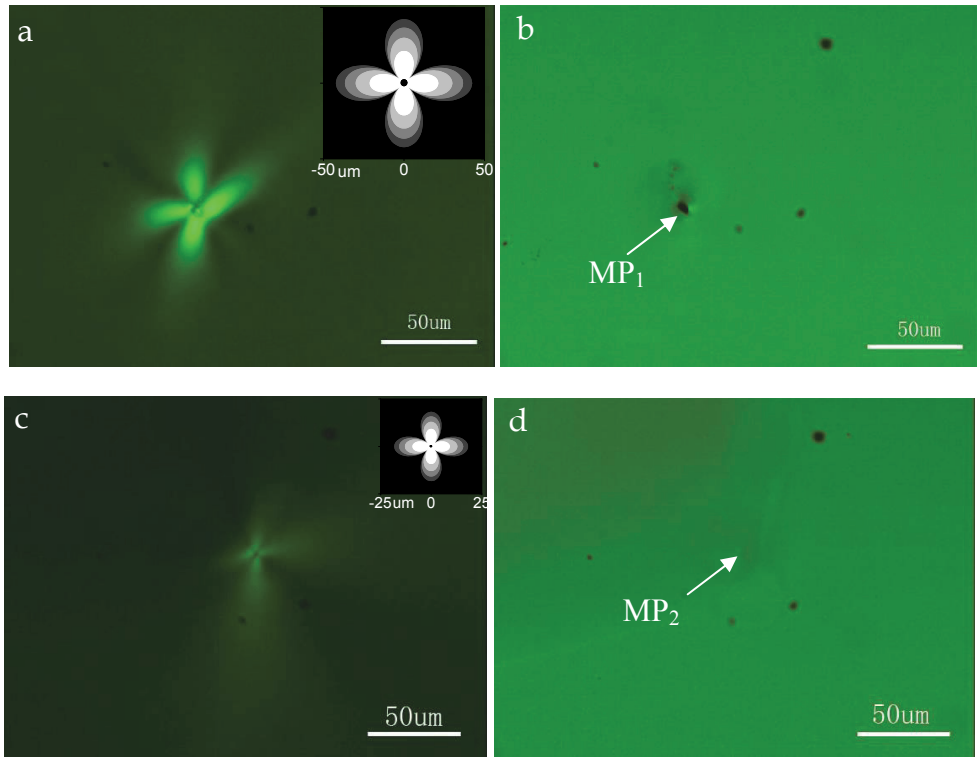


Fig. 6. Microscopic images of two micropipes (MP_1 and MP_2). (a) A unique interference pattern observed by a polarizing optical microscope for MP_1 . (b) A bright-field optical microscopic image for MP_1 . (c) A unique interference pattern observed by a polarizing optical microscope for MP_2 . (d) A bright-field optical microscopic image for MP_2 . Images (a) and (b) are the same micropipe with a larger Burgers vector; images (c) and (d) are the same micropipe with a smaller Burgers vector. The insets in the upper right of (a) and (c) give the simulation of MP_1 and MP_2 , respectively. The black spots that appear in the four images are foreign particles on the lens.

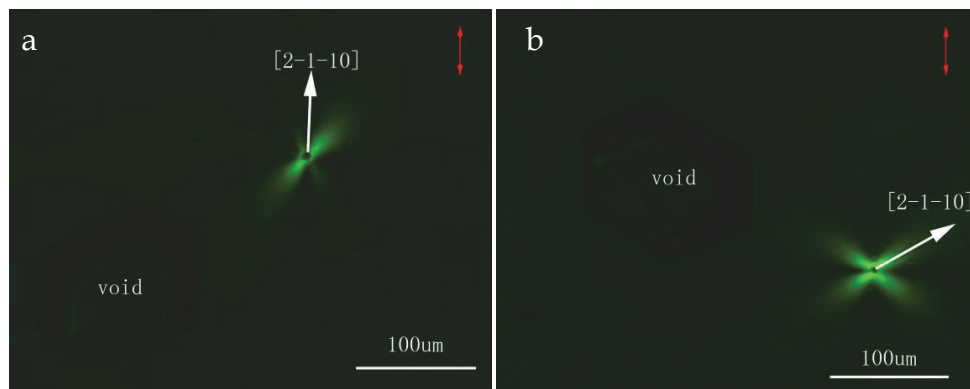


Fig. 7. Microscopic images of micropipe observed by a polarizing optical microscope with different α . The red and white arrows represent the directions of the polarizer and the $\langle 2-1-10 \rangle$ direction, respectively. (a) $\alpha = 0$. (b) $\alpha = \pi/4$.

From Eq. 4, we can get interference intensity contours with different I_0/I , as shown in Fig. 6. The smaller the intensity of incident beam, the longer is the birefringence pattern's radius.

In Fig. 6 the diameters of MP₁ and MP₂ are about 4.0μm and 0.66μm. According to Eq. 1 and Eq. 4, the lengths of the brightest wings (in case of $I=I_0$) for the two micropipes could be calculated (Table 1). The observed and calculated values for these wings are nearly the same with two different micropipes. The insets in the upper rights of Fig. 6a and 6c give the simulation of MP₁ and MP₂ respectively. The simulation images are indeed a butterfly with four wings having a gradual changed intensity and a black core as same as the recorded images. However the four wings are not symmetrical in Fig. 6a. This may be caused by the off-orientation of the sample. The core of MP₁ is not circular in Fig. 6b, which can not happen in on-axis sample for the consideration of energy. This indicates the off-axis of the sample surface.

From Eq. 4, it is known that the birefringence images rotated with different α . For example, if we rotate the sample for $\pi/4$ ($\alpha = \pi/4$), the equal interference intensity contours rotated for $\pi/4$. This result fit well with the experimental results shown in Fig. 7, where the red and white arrows represent the directions of the polarizer and $\langle 2-1-10 \rangle$ direction respectively. A void is taken as a reference point in Fig. 7. In Fig. 7a, $\langle 2-1-10 \rangle$ direction is parallel to the polarizer, the bright wings make an angle of $\pi/4$ with $\langle 2-1-10 \rangle$ direction. In Fig. 7b, $\langle 2-1-10 \rangle$ direction make an angle of $\pi/4$ with the polarizer, the bright wings make an angle of zero with $\langle 2-1-10 \rangle$ direction. We can conclude that the calculated rotation property also agreed with the experimental results.

MP	Observed core diameter (D)	length of the brightest wing (r)	
		Observed	Calculated
MP1	4.00μm	22.2μm	21μm
MP2	0.66μm	8.3μm	9μm

Table 1. The observed and calculated wing lengths of MP₁ and MP₂ in case of $I=I_0$

3.1.3 Evolution of micropipes during growth

Fig. 8 shows the microscopic images for the same area but in different growth stages of the same crystal. The micropipes' distribution proves that Fig. 8a and 8b, 8c and 8d are the same areas in different growth stages respectively. The diameter of the micropipe is increasing with the crystal growth which can be proved by the size of bright wings in the birefringence images. It means that the stress can be released through micropipes during crystal growth.

According to statistic of the densities of micropipe along crystal growth, the micropipe density decreased with growth process for almost all samples, except one. That is to say, in case of optimizing growth conditions, micropipe density can be decreased and crystal quality can be improved.

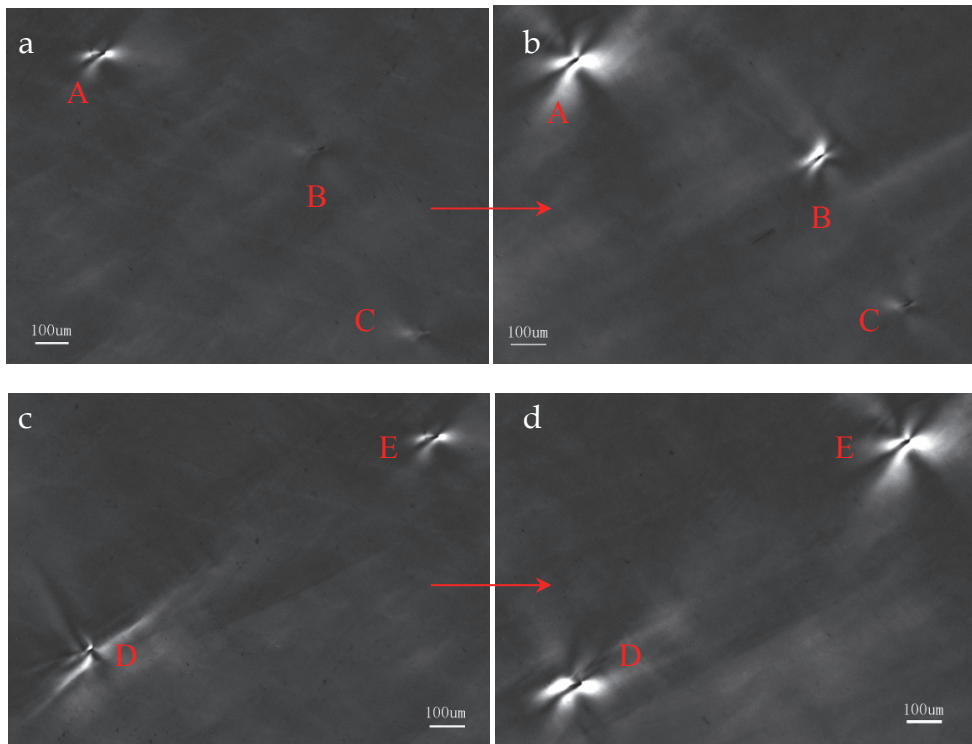


Fig. 8. Development of micropipes along growth direction, the red arrows represent the growth direction. Figure a and b belong to a same area; Fig. c and d belong to another same area.

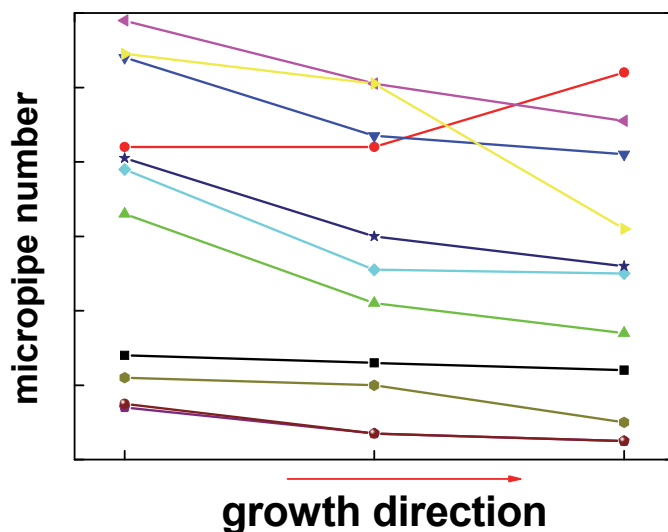


Fig. 9. Micropipes distribution along growth direction

3.1.4 Summary

In summary, the birefringence images of micropipes in 6H-SiC single crystals were observed by a polarization optical microscope. Based on the Frank's theory, the micropipes were treated as screw dislocations with huge Burgers vectors. Due to the strain caused by a micropipe, the SiC crystal in the neighbour area around a micropipe transferred from uniaxial into biaxial crystal. In the meanwhile, the refractive index ellipsoid was described by three principal refractive indexes and birefringence occurred. Based on above consideration, the birefringence images of micropipes with different Burgers vectors were simulated. The results agreed well with the observations. It confirms indirectly the Frank's theory that a micropipe is actually the super-screw dislocation with huge Burgers vector. With crystal growth, the micropipe density has a tendency of decrease and the diameter of micropipes can be enlarged for the stress release.

3.2 Elementary screw dislocations

Although the elementary screw dislocations did not seriously deteriorate the performance of device as micropipes, they prevent the realization of high-efficiency, reliable electronic devices (Lendenmann, 2001; Malhan et al., 2003; Neudeck et al., 1998).

In order to assess the density of elementary screw dislocation, back-reflection synchrotron radiation topograph of (0001) wafer was taken. In experimental setup, symmetric diffraction geometry with 00030 reflection was used. The angle between incident beam and sample surface was 83° . In this case, the selected X-ray wavelength is 0.1nm. The distance between sample and film was 20cm. The illumination area is 1mm x 1mm.

Fig. 10 shows the back-reflection synchrotron radiation topograph of SiC (0001) wafer with 00030 reflection. From the topograph, many white dots with the same diameters of 26-28 μm can be observed. As the simulation results in following paragraphs, these white dots correspond to elementary screw dislocations. Therefore, the density of elementary screw dislocation in this wafer was measured to be $1.56 \times 10^4 / \text{cm}^2$.

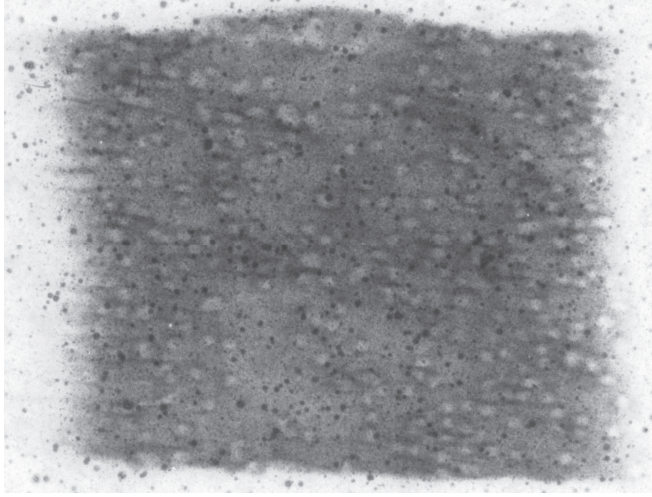


Fig. 10. Back-reflection synchrotron radiation topograph of SiC wafer with 00030 reflection

The image of elementary screw dislocation can be simulated by ray-tracing method (Huang et al., 1999). As well known, for a screw dislocation along z axis, its displacement field can be described as

$$u_z = (b / 2\pi) \tan^{-1}(y / x) \quad (5)$$

Here b is the Burgers vector of screw dislocation. y and x are the coordinate position of arbitrary point in distorted area. From Eq. 5, the position-dependent orientation of the (0001) reflection plane can be expressed by the following equation.

$$\begin{aligned} n_x(x, y, z) &= by / r(b^2 + 4\pi^2 r^2)^{1/2} \\ n_y(x, y, z) &= -bx / r(b^2 + 4\pi^2 r^2)^{1/2} \\ n_z(x, y, z) &= 2\pi r / (b^2 + 4\pi^2 r^2)^{1/2} \end{aligned} \quad (6)$$

Where $r = (x^2 + y^2)^{1/2}$. For the numerical simulation of the screw dislocation, the distorted lattice was divided into a set of small cubes of constant. All the cubes were assumed to have the same integrated diffraction density I_0 . The recording plane was also divided into a set of squares of constant area. Then the intensities from all the cubes were projected to the corresponding squares according to the traces of the diffracted beams. The sum of intensities each square received after the projection represents the local contrast level. Eventually, all the calculated intensity can be plotted as a gray-scale topograph to give the simulation of the screw dislocation image.

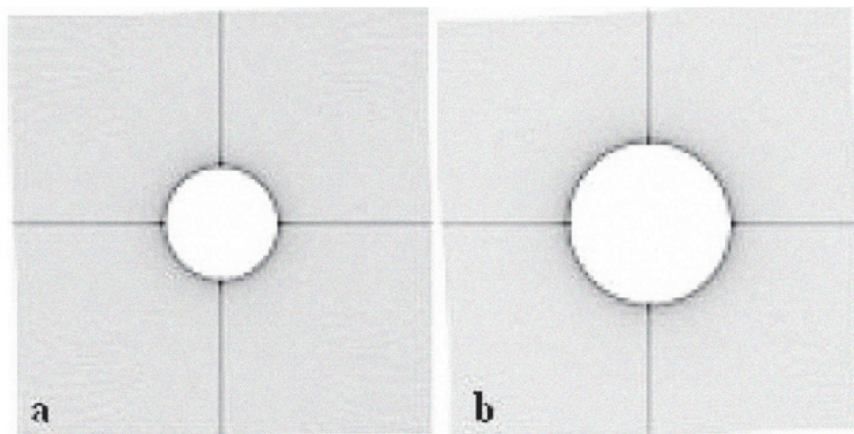


Fig. 11. The simulation images of screw dislocations with different Burgers vectors. (a). Elementary screw dislocation with Burgers vector $1c$; (b). Screw dislocation with Burgers vector $2c$. The image area is $100\mu\text{m} \times 100\mu\text{m}$.

Fig. 11a and 11b show the simulation images of an elementary screw dislocation with Burgers vector $1c$ and a screw dislocation with Burgers vector $2c$ respectively. From the simulation images, the white dot diameter corresponding to an elementary screw dislocation with Burgers vector $1c$ was measured to be $28\mu\text{m}$. It is in well agreement with synchrotron observation. As for the screw dislocation with Burgers vector $2c$, the corresponding white dot diameter from simulation was measured to be $39\mu\text{m}$. Obviously, almost all the white dots in Fig. 10 correspond to elementary screw dislocations.

3.3 Basal plane bending

Recently, basal plane bending of SiC single crystals has attracted much attention (Lee et al., 2008; Seitz et al., 2006). In the case of basal plane bending, the normal orientation of the basal plane varies with the position from point to point. Basal plane bending causes serious lattice deformation and leads to the formation of low-angle boundaries. It was found that the degree of basal plane curvature in the facet region was less serious than that in the periphery region (Seitz et al., 2006). Therefore only the central part of a substrate can meet the requirements of device applications in the case of basal plane bending. For evaluating the crystal quality, $\langle 0001 \rangle$ orientated 6H-SiC samples were tested by HRXRD and SWBXT. The HRXRD was conducted by XPERT-PRO diffractometer. The incident beam was adjusted by the beam conditioner of four Ge(022) collimated crystals so that the X-ray beam on the sample was accurately the Cu-K α_1 ($\lambda=1.54056\text{\AA}$) radiation. The symmetrical diffraction geometry has been used in the measurement. The slits for the incident beam and detector are $0.5\text{mm} \times 4\text{mm}$ and two degree respectively. The tube voltage and tube current are 40kV and 40mA respectively.

Several samples were investigated by transmission synchrotron topography performed at the 4W1A beam line of Beijing Synchrotron Radiation Laboratory. In our experiment, the electron energy of storage ring was 2.2GeV and the beam current was 80-100mA. Transmission synchrotron topographs were taken by transmission Laue geometry. The

samples were orientated with the (0001) surface perpendicular to the incident beam and the topographs were recorded by Fuji film.

3.3.1 Experimental results-HRXRD

Fig. 12 shows the plot of the relative ω_{006} rocking curve peak position as a function of the beam position across the diameters of a 2 inch wafer. The three groups of data in Fig. 12 were got from three different diameters of the same wafer. In case of precisely orientated crystal without any basal plane bending, ω is equal to Bragg angle. But the HRXRD test here is not the case. When the incident beam is located on the left of the center, the ω is larger than Bragg angle and the deviation of ω from Bragg angle is proportional to the distance between detected point and the center of the wafer. The farther the distance of the detected point from the center, the larger the deviation of surface from the basal plane. When the incident beam is located on the right of the center, the result is reversal, i.e. the ω is smaller than Bragg angle. The HRXRD experimental result implies that the (0001) basal plane in the sample is a concave face rather than a planar.

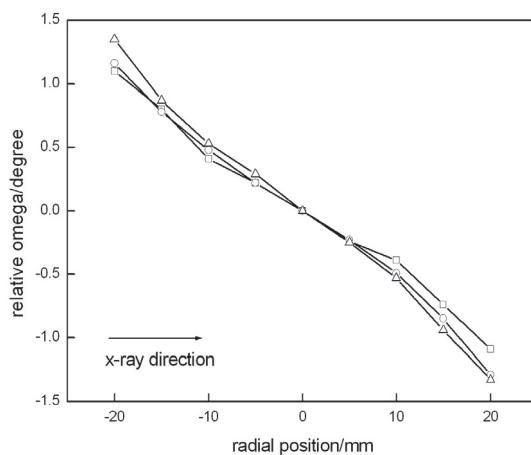


Fig. 12. Relative omega ($\Delta\omega_{006}$) peak position as a function of the beam position across the diameter of a 2 inch 6H-SiC wafer. The three lines were got from three different diameters on the same wafer.

3.3.2 Experimental results-SWBXT

The shape of the diffraction spots should be the same as that of footprint of X-ray source for a highly perfect crystal. In case of any lattice deformation, the diffraction spots for different reflections assume different shapes. Fig. 13 shows two transmission synchrotron topographs from two different samples. From this figure, it could be seen that the two samples have different distortion cases and each diffraction spot has its own shape in the two topographs. In Fig. 13a, all the diffraction spots are shrunk along the diffraction vector direction. In contrast, it seems that all the diffraction spots are stretched along the same line in Fig. 13b. No doubt, the two samples exist obviously structural imperfection. But is basal plane bending which causes the distortion of the diffraction spots?

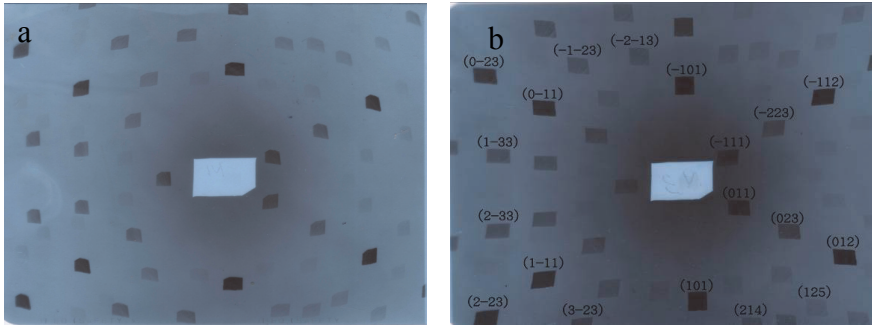


Fig. 13. Synchrotron white-beam transmission images for two different samples under the same experimental conditions.

3.3.3 Theory and simulation results for SWBXT

In order to explore the relationship between the distortion of the diffraction spots and lattice imperfection, the shapes of Laue spots have been simulated based on the (0001) Si face concave sphere model.

We establish two Cartesian systems X, Y, Z at sample (X and Y are parallel to the vertical and the horizontal base line respectively, Z is opposite to the incident X-ray direction, as shown in Fig. 14), which stands for the spatial system and X', Y', Z' (X', Y' and Z' are parallel to $\langle 10-10 \rangle$, $\langle -12-10 \rangle$ and $\langle 0001 \rangle$ direction respectively), which stands for the crystallophysical system. The unit vectors for X, Y, Z and X', Y', Z' systems are $\vec{i}, \vec{j}, \vec{k}$ and $\vec{i}', \vec{j}', \vec{k}'$ respectively.

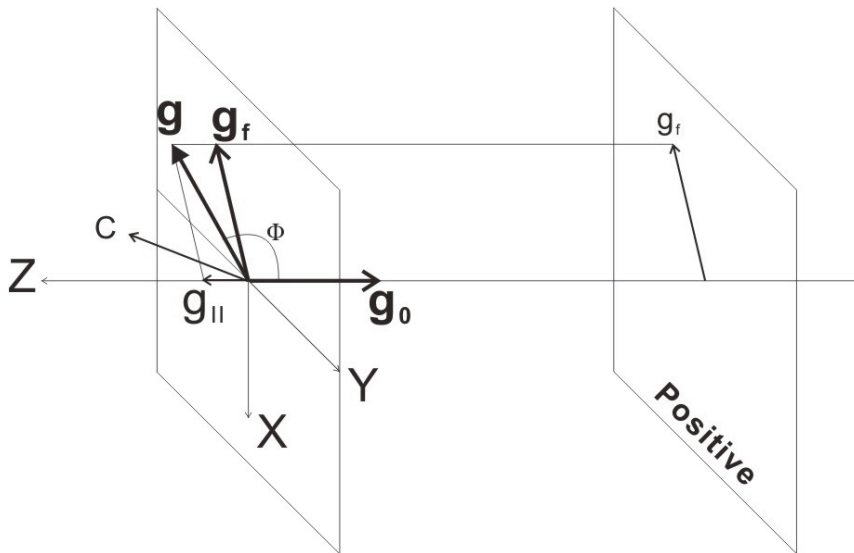


Fig. 14. Diffraction geometry of synchrotron white-beam topography in transmission mode. Where \mathbf{g}_0 is the incident unit vector; \mathbf{g} is the diffraction vector; Φ is the angel between \mathbf{g} and \mathbf{g}_0 .

If the sample surface is exactly the (0001) plane, the two Cartesian systems coincide. Otherwise there will be a rotation for X', Y', Z' system using X, Y, Z system as reference coordinate. Based on the HRXRD measurement, it is believed that the (0001) plane after bending is a concave sphere with a radius of R and only the center of the 2 inch wafer is exactly the (0001) plane. Here the center of 2 inch wafer is taken as the origin of the X, Y, Z system. Therefore the position of the spherical center is located at $(0, 0, R)$. The c axis for an arbitrary $(x, y, 0)$ point on the sample surface deviates from the $\langle 0001 \rangle$ direction in case of basal plane bending. In other words, the Z' directional vector at $(x, y, 0)$ could be described as $(\cos\alpha, \cos\beta, \cos\gamma)$ in X, Y, Z coordinate system, where

$$\cos\alpha = \frac{-x}{\sqrt{x^2 + y^2 + R^2}}, \quad \cos\beta = \frac{-y}{\sqrt{x^2 + y^2 + R^2}}, \quad \cos\gamma = \frac{R}{\sqrt{x^2 + y^2 + R^2}} \quad (7)$$

The directional vector from $(0, 0, 0)$ to $(x, y, 0)$ point could be written as $(\cos\delta, \sin\delta, 0)$, where

$$\cos\delta = \frac{x}{\sqrt{x^2 + y^2}}, \quad \sin\delta = \frac{y}{\sqrt{x^2 + y^2}} \quad (8)$$

In case of basal plane bending, for an arbitrary point $(x, y, 0)$ on sample surface, a new system X', Y', Z' is established. Such system is unique and has exclusiveness. The new system X', Y', Z' is got from the rotation of X, Y, Z system around a defined axis in XY plane whose directional vector is $(\sin\delta, -\cos\delta, 0)$. So the base vector transformation relationship between the two systems can be derived:

$$\begin{pmatrix} i' \\ j' \\ k' \end{pmatrix} = \begin{pmatrix} \cos^2\delta \cos\gamma + \sin^2\delta & \cos\delta \sin\delta \cos\gamma - \cos\delta \sin\delta & \cos\delta \sin\gamma \\ \cos\delta \sin\delta \cos\gamma - \cos\delta \sin\delta & \cos^2\delta + \sin^2\delta \cos\gamma & \sin\delta \sin\gamma \\ -\cos\delta \sin\gamma & -\sin\delta \sin\gamma & \cos\gamma \end{pmatrix} \begin{pmatrix} i \\ j \\ k \end{pmatrix} \quad (9)$$

In one setup of our experiment, the X-ray is perpendicular to the sample surface and parallel to $\langle 000-1 \rangle$ at central point of sample, i.e. the positive plane of (0001) is facing to the incident beam. Here we define the Laue image of (0001) wafer in such setup as positive image. Similarly the Laue image of (0001) wafer is defined as negative image when the (000-1) C-face is facing to the incident beam. So the incident unit vector \mathbf{g}_0 in positive image and the diffraction vector \mathbf{g} for hkl reflection can be expressed as:

$$\mathbf{g}_0 = -\vec{k} \quad (10)$$

$$\mathbf{g} = h\mathbf{a}^* + k\mathbf{b}^* + l\mathbf{c}^* \quad (11)$$

where \mathbf{a}^* , \mathbf{b}^* and \mathbf{c}^* are reciprocal space base vectors. In X', Y', Z' system, they can be expressed as follows:

$$\mathbf{a}^* = \frac{2}{\sqrt{3}a} \vec{i}', \mathbf{b}^* = \frac{1}{\sqrt{3}a} \vec{i}' + \frac{1}{a} \vec{j}', \mathbf{c}^* = \frac{1}{c} \vec{k}' \quad (12)$$

In case of basal plane bending, the crystallophysical system, X' , Y' , Z' , varies with sample position continuously. For analysis convenience, the diffraction vector \mathbf{g} could be divided into two parts, projection of \mathbf{g} on XY plane, i.e. \mathbf{g}_f and projection of \mathbf{g} on \mathbf{g}_0 direction. The following formula can be got in X, Y, Z system:

$$\begin{aligned} \mathbf{g}_f = & \left\{ \left(\frac{2h}{\sqrt{3}a} + \frac{k}{\sqrt{3}a} \right) (\cos^2 \delta \cos \gamma + \sin^2 \delta) + \frac{k}{a} (\sin \delta \cos \delta \cos \gamma - \right. \\ & \left. - \sin \delta \cos \delta) - \frac{l}{c} \cos \delta \sin \gamma \right\} \vec{i} + \left\{ \left(\frac{2h}{\sqrt{3}a} + \frac{k}{\sqrt{3}a} \right) (\sin \delta \cos \delta \cos \gamma - \right. \\ & \left. - \sin \delta \cos \delta) + \frac{k}{a} (\cos^2 \delta + \sin^2 \delta \cos \gamma) - \frac{l}{c} \sin \delta \sin \gamma \right\} \vec{j} \end{aligned} \quad (13)$$

If the angle between \mathbf{g} and \mathbf{g}_0 is Φ , the diffraction angle θ can be written as follow according to their relationship in Fig. 14:

$$\sin \theta = -\cos \Phi = -\frac{B}{\sqrt{A}} \quad (14)$$

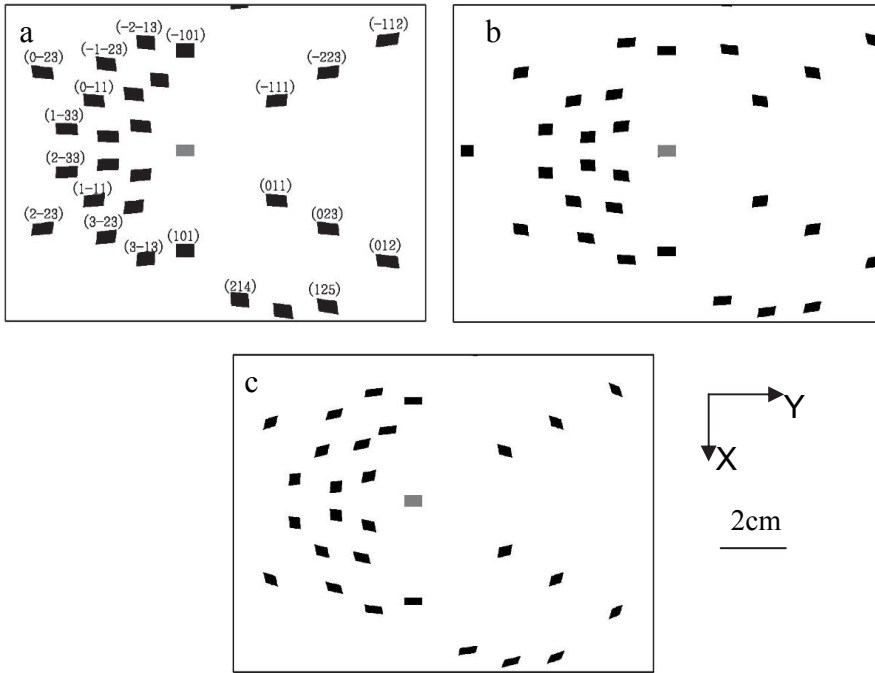


Fig. 15. The simulation results with conditions are as follows: light spot is $4\text{mm} \times 6\text{mm}$ (the gray rectangle), $D=10\text{cm}$, $a=0.3078\text{nm}$, $c=1.5117\text{nm}$, $x_0 \in [-2, 2]$, $y_0 \in [-3, 3]$. (a) concave plane, $R=100\text{cm}$. (b) convex plane, $R=100\text{cm}$. (c) convex plane, $R=60\text{cm}$.

where

$$\begin{cases} A = \left(\frac{2h}{\sqrt{3}a} + \frac{k}{\sqrt{3}a}\right)^2 + \left(\frac{k}{a}\right)^2 + \left(\frac{l}{c}\right)^2 \\ B = -\left(\frac{2h}{\sqrt{3}a} + \frac{k}{\sqrt{3}a}\right)\cos\delta\sin\gamma - \frac{k}{a}\sin\delta\sin\gamma - \frac{l}{c}\cos\gamma \end{cases} \quad (15)$$

So the distance between the diffraction spots with the center spot on the positive image for hkl reflection, d , can be expressed as follow:

$$d = D \cdot \tan 2\theta = D \cdot \frac{-2B\sqrt{A-B^2}}{A-2B^2} \quad (16)$$

where D is the distance between the sample and the film.

According to Eq. 13 and Eq. 16, the exact position of the diffraction spots on the positive image for hkl reflection can be determined. Moreover, for an arbitrary $(x, y, 0)$ point on sample surface, its accurate positions for different reflections could be calculated.

According to the descriptions above, for an arbitrary reflection, the corresponding diffraction spot shape could be simulated. It was found that the shapes of diffraction spots depended on the diffraction vector, the basal plane bending radius and incident beam direction. In simulation, a $4\text{mm} \times 6\text{mm}$ illumination area was given and the positions for 20 points along the periphery of illumination area with 1mm interval were calculated for different reflections. Finally from one to its neighbor point was connected for each reflection and a series of Laue spots with distortion shapes were obtained. The simulation results are shown in Fig. 15a when a concave surface of (0001) wafer faces to the X-ray. The shapes for five typical areas of a (0001) wafer were simulated, i.e. center region O and four different quadrant regions A, B, C and D. It was found that the diffraction spots' distortion did not show remarkably difference for the five different areas.

The simulations for (000-1) convex face, i.e. negative image were shown in Fig. 15b and 15c. The two images correspond to different curvature radiuses. It was found that the distortions of the Laue spots became more serious with a smaller curvature radius.

In SWBXT experiment, the area of footprint of X-ray area was $4\text{mm} \times 6\text{mm}$ and the sample holder had a small rotation around X axis. The simulation ignored the holder rotation and diffraction intensity variations of different reflections. The above ignorance has no effect on distortion tendency of the Laue spots.

Sample 1 and 2 were etched, for the purpose of knowing their polarity (Si face or C face). From the etching results, it was known that the illuminated lattice plane for sample 1 and 2 are (000-1) and (0001) respectively. According to HRXRD results, (0001) plane is concave and (000-1) plane is convex. Therefore the illuminated lattice plane for sample 1 and 2 are convex and concave respectively.

Comparing the simulation results with the experimental observations, we can see obviously that Fig. 15b and Fig. 15a are nearly the same as Fig. 13a and Fig. 13b respectively. The main diffraction spots have the same distortion trend, which are shrunk and stretched along the diffraction directions respectively. When a convex lattice plane faces to x-ray source, its function is similar to a convex lens which make the X-ray focus and diffraction spots smaller. Similarly, the concave lattice face is like a concave lens, which make the X-ray defocus and diffraction spots larger.

3.3.4 Discussions

The HRXRD and SWBXT simulation results can confirm that basal plane bending exist in SiC single crystals. In SiC crystal growth experiments with different conditions, we found that the basal plane bending was caused mainly by the thermal mismatch between seed and holder which deteriorated the wafer's quality, i.e. increasing the density of low angle grain boundaries. Recently, the basal plane bending was eliminated by improving the seed attachment technique.

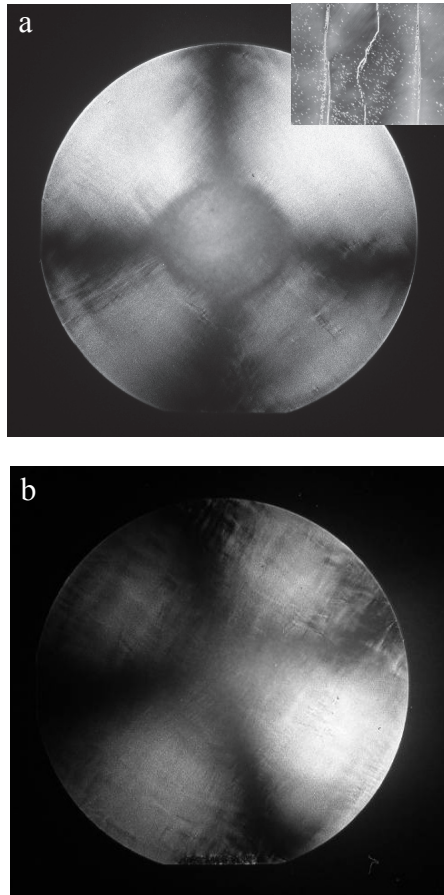


Fig. 16. Stress images for different wafers. The vertical directions $\langle 10\text{-}10 \rangle$. (a) wafer with bending (The insert is a microscopic image of low angle grain boundaries after etching). (b) wafer without bending.

Fig. 16 are two stress images for two wafers grown with different conditions. The vertical direction is $\langle 10\text{-}10 \rangle$. Fig. 16a stands for a wafer with basal plane bending. It can be seen obviously that there is a boundary between the center area (the facet) and the outside region. And a mass of low angle grain boundaries assembled along the $\langle 10\text{-}10 \rangle$ directions. The existence of grain boundaries deteriorated the crystal quality and reduced its usable

area. The insert of Fig. 16a is a microscopic image for $\langle 10\text{-}10 \rangle$ direction after etching. The white lines are low angle grain boundaries after etching. Fig. 16b stands for a wafer without basal plane bending. The boundary between the facet and the outside region disappeared. And the assembly of low angle grain boundaries along $\langle 10\text{-}10 \rangle$ direction disappeared too. The stress for the whole wafer became more uniform. That is to say, the large number of grain boundaries along $\langle 10\text{-}10 \rangle$ direction could be caused by basal plane bending.

4. Conclusion

In this chapter, polytype transition mechanism during 4H-SiC growth, the nature of micropipe and the existence of basal plane bending has been proposed. Elementary screw dislocations were also detected by back-reflection synchrotron radiation topography. All the results obtained above helped us to optimize the growth condition and then improve the crystal quality.

5. Acknowledgment

This work was supported by National Basic Research Program of China under grant No. 2009CB930503 and No. 2011CB301904, Natural Science Foundation of China under grant No. 51021062 and 50802053.

6. References

- Lee, J. W. ; Skowronski, M. ; Sanchez, E. K. & Chung, G. (2008). Origin of basal plane bending in hexagonal silicon carbide single crystals, *Journal of Crystal Growth*, Vol. 310, No. 18, pp. 4126-4131, ISSN 0022-0248.
- Lely, J.A. (1955). Darstellung von einkristallen von silicium carbid und beherrschung von art und menge der eingebauten verunreinigungen, (in German). *Ber. Deut. Keram. Ges.*, Vol. 32, pp. 229-236.
- Seitz, C. ; Herro, Z. G. ; Epelbaum, B. M. ; Hock, R. & Magerl, A. (2006). Lattice-plane curvature and small-angle grain boundaries in SiC bulk crystals, *Journal of Applied Crystallography*, Vol. 39, pp. 17-23, ISSN 0021-8898.
- Hu, X. B. ; Xu, X. G. ; Li, X. X. ; Jiang, S. Z. ; Li, J. ; Wang, L. ; Wang, J. Y. & Jiang, M. H. (2006). Stacking faults in SiC crystal grown by spontaneous nucleation sublimation method, *Journal of Crystal Growth*, Vol. 292, pp. 192-196, ISSN 0022-0248.
- Schulze, N. ; Barrett, D. L. ; Pensl, G. ; Rohmfeld, S. & Hundhausen, M. (1999). Near thermal Equilibrium Growth of SiC by Physical Vapor Transport, *Materials Science and Engineering B*, Vol. 61-62, pp. 44-47, ISSN 0921-5107.
- Straubinger, T. L. ; Bickermann, M. ; Hofmann, D. ; Weingartner, R. ; Wellmann, P.J. & Winnacker, A. (2001). Stability Criteria for 4H-SiC Bulk Growth, *Materials Science Forum*, Vol. 353-356, pp. 25-28, ISSN 0255-5476.
- Rost, H. ; Schmidbauer, M. ; Siche, D. & Fornari, R. (2006). Polarity- and Orientation-related Defect Distribution in 4H-SiC Single Crystals, *Journal of Crystal Growth*, Vol. 290, No. 1, pp. 137-143, ISSN 0022-0248.
- Wang, L. ; Hu, X. B. ; Dong, J. ; Li, J. ; Jiang, S. Z. ; Li, X. X. ; Xu, X. G. ; Wang, J. Y. & Jiang, M. H. (2004). (in Chinese). Polytypes Identification of SiC Crystal by Micro-Raman Spectroscopy, *Journal of Functional Materials*, Vol. 35, pp. 3400-3404, ISSN 1001-9731.

- Wahab, Q. ; Ellison, A. ; Henry, A. ; Janzen, E. ; Hallin, C. ; Persio, J. D. & Martinez, R. (2000). Influence of epitaxial growth and substrate-induced defects on the breakdown of 4H-SiC Schottky diodes, *Applied Physics Letters*, Vol. 76, No. 19, pp. 2725-2727, ISSN 1077-3118.
- Neudeck, P. G. & Powell, J. A. (1994). Performance limiting micropipe defects in silicon carbide wafers, *IEEE Electron Device Letters*, Vol. 15, No. 2, pp. 63-65, ISSN 0741-3106.
- Frank, F. C. (1951). Capillary equilibria of dislocated crystals, *Acta Crystallographica*, Vol. 4, No. 6, pp. 497-501.
- Liu, J. L. ; Gao, J. Q. ; Cheng, J. K. ; Yang, J. F. & Qiao, G. J. (2005). Model for micropipe formation in 6H-SiC single crystal by sublimation method, *Material Letters*, Vol. 59, pp. 2374-2377, ISSN 0167-577X.
- Giocondi, J. ; Rohrer, G. S. ; Skowronski, M. ; Balakrishna, V. ; Augustine, G. ; Hobgood, H. M. & Hopkins, R. H. (1997). An atomic force microscopy study of super-dislocation/micropipe complexes on the 6H-SiC(0001) growth surface, *Journal of Crystal Growth*, Vol. 181, pp. 351-362, ISSN 0022-0248.
- Neudeck, P. G. ; Huang, W. & Dudley, M. (1998). Breakdown degradation associated with elementary screw dislocations in 4H-SiC p+n junction rectifiers, *Solid-State Electron*, Vol. 42, No. 12, pp. 2157-2164, ISSN 0038-1101.
- Lendenmann, H. ; Dahlquist, F. ; Johansson, N. ; Soderholm, R. ; Nilsson, P.A. ; Bergman, J. P. & Skytt, P. (2001). Long term operation of 4.5kV PiN and 2.5kV JBS diodes, *Material Science Forum*, Vol.. 353-356, pp. 727-730, ISSN 0255-5476.
- Malhan, R.K. ; Nakamura, H. ; Onda, S. ; Nakamura, D. & Hara, K. (2003). Impact of SiC structural defects on the degradation phenomenon of bipolar SiC devices, *Material Science Forum*, Vol. 433-436, pp.917-920, ISSN 0255-5476.
- Huang, X.R. ; Dudley, M. ; Vetter, W. M. ; Huang, W. ; Si, W. & Carter Jr, C.H. (1999) Superscrew dislocation contrast on synchrotron white-beam topographs: an accurate description of the direct dislocation image, *Journal of Applied Crystallography*, Vol. 32, pp. 516-524, ISSN 0021-8898.

SiC, from Amorphous to Nanosized Materials, the Exemple of SiC Fibres Issued of Polymer Precursors

Philippe Colomban

*LADIR, CNRS – Université Pierre-et-Marie-Curie
France*

1. Introduction

Silicon carbide materials are interesting because of their high thermal stability, high thermal conductivity, extreme hardness and good electrical properties. Some of these properties are directly related to the SiC structure that alternates the Si and C atom layers. SiC have applications as single crystal wafer (wide-gap semiconductor for high power device), as air, spacecraft and nuclear plant thermostructural composites because it is possible to prepare the materials in various forms (fibre, matrix and composite) from organic liquid or vapour precursors. Thus it is possible to adjust the crystallinity, from the amorphous to the crystalline state, including intermediate nanocrystalline state. The later state guaranties the optimal mechanical properties. Non-destructive Raman microspectrometry intrinsically probes the matter at the subnanoscale and offers a "bottom-up" approach that is especially efficient for the analysis of ill-crystallised and nanostructured materials. The great advantage of Raman spectroscopy is first to make possible the recording of series of spectrum by automatic mapping. However, because the Raman intensity depends on the polarisability tensor derivative, the scattered intensity – and the sensitivity – varies order of magnitude with the nature of the chemical bond. Comparison with transmission electron microscopy (TEM) is in general required to discriminate if the phonon coherence length is determined by the domain or the grain size. Both techniques are efficient to identify the different polytypes as well as the nature and degree of the disorder.

2. About the chemistry

The properties of the materials are determined by their chemical bonds and the arrangement of the latter. The uniqueness of silicon carbide properties arises from the nature of the bond. Si-C bond as Si-O and Si-N ones are among the strongest chemical bonds in the matter (Bond dissociation energy > 350 KJ/mole). Consequently, this gives a very good chemical and thermal stability as well very high melting temperature, high mechanical properties and hardness. Silicon atoms form with C, N and O atoms the same tetrahedral coordination that allows very intimate mixture (oxycarbides, oxynitrides, etc.). Furthermore, a hydrogen atom can establish a bond with these oxygen, nitrogen and carbon atoms. This offers a large versatility of preparation routes, including polymerisation process. Consequently, because

silicon and carbon atoms form easily X-C and X-H bonds, a large variety of liquid or gaseous hybrid/organic precursors are available (Mc Diarmid, 1961; Fritz et al., 1965; Corriu & Lanneau, 1970; Lucke et al., 1997) and the control of their reactivity, viscosity/diffusivity dilution, etc. gives rise to a variety of preparation routes leading to monoliths, films, fibres, composites, crystal,..., from the amorphous state to the single crystal, including nanomaterials (Gough & Kern, 1967; Parlier & Colomban, 1996; Naslain, 2004).

The mix of atomic orbital led to an intermediate electric behaviour between that of carbon (a semi-metal) and silica (an insulator), the electronic gap is intermediate (2-3 eV) and the material is a semiconductor. Since the diffusion coefficient of oxygen atom in silica is very low (due to the very covalent character of the Si-O bond), the oxidation is blocked in a very large temperature range (except in water-rich atmosphere when volatile species are formed) that gives a good stability to $\text{Si}(\text{X})_n$ compounds in air. The latter properties are searched for thermomechanical applications: the nanosized state combines the advantage of amorphous (homogeneity, lack of interface/phases) and crystalline (high density of bonds per volume unit) phases. Very high thermal conductivity contributes well to the unique properties of silicon carbide. Since nothing is perfect, the building of the SiC with a single type of bond makes that orientation disorder is possible and gives rise to two types of Si-C bilayer stacking. Their combination leads to series of structures: the polytypes and it is difficult to prepare materials without coexistence of the different phases. This behaviour is observed for all structures which are built up by corner-sharing tetrahedron. They can be regarded as consisting of stacked bi-layers.

The availability of volatile/liquid silanes led to the preparation of SiC materials in various forms (McDiarmid, 1961; Fritz et al., 1965; Gough & Kern, 1967; Learn & Khan, 1970; Corriu & Lanneau, 1970; Kumar & Litt, 1988; Schmidt et al., 1991): films/coatings (Rynders et al., 1991), fibres (a SiC coating is deposited on a carbon fibre core (Hurwitz et al., 1991; Tanaka et al., 1995; idem, 1996; Popovska et al., 1997), monoliths and fibre-reinforced composites (Yajima et al., 1980; Tanaka & Kurachi, 1988; Bouillon et al., 1991 a & b; Monthieux et al., 1990; idem, 1991; Delplancke et al., 1991; Lee & Yano, 2004). The growth rate was slow and for the preparation of thick monoliths or composites weeks are required with sometimes an intermediate machining of the parts in order to avoid the closure of the porosity that occurs at the sample surface, avoiding the completion of the core densification. This technology was used to prepare important parts of civil and military launch vehicles, missiles as well as aircraft engines (Parlier & Colomban, 1996; Mouchon & Colomban, 1996; Naslain, 2004) and extended to the preparation of other Si-based materials such as nitrides (Durham et al., 1991).

In the 80s Japanese groups developed liquids with appropriate viscosity (polycarbosilanes: PCS) as precursors for SiC fibre (Okamura et al., 1985). The difficulty concerned the production of a form of polycarbosilane which would have the "good" viscosity to be spun and then converted in small-diameter ceramic filaments. The small diameter ($\sim 10 \mu\text{m}$) is required to permit the bending of the fibre during the weaving process and hence to prepare a variety of textile fabrics: satin, taffeta, etc. (Mouchon & Colomban, 1995; idem, 1996). It was found that very high molecular weight was not necessarily best and polymers with molecular weights of around 1500 were used for commercial production. Then the progress allowed preparing more complex compositions (Si/TiC, etc. (Stewart et al., 1991; Hasegawa et al., 1991; Burns et al., 1992; Hurwitz et al. 1993)) under more complex states (Tanaka et al., 1988; Langguth, 1995). The viscosity was adapted for an easy infiltration of the precursor

in the porous performs (Greil, 1995; Parlier & Colomban, 1996; Lucke et al., 1997; Greil, 2000) and the technology was extended to multicomponent oxide precursors with the development of sol-gel routes (Colomban, 1989; Colomban & Wey, 1997; Colomban, 2005). A big problem was the achievement of the right stoichiometry: silicon excess was very detrimental because of the relatively low temperature melting of silicon; on the other hand, carbon excess, not detrimental from the thermomechanical point of view, led to a great reactivity to air and to high electrical conductivity (Chauvet et al., 1992a; idem, 1992b; Mouchon & Colomban, 1996). However, the polymer precursors are linear macromolecules (1D) but SiC synthesis requires a 3D crosslinking. This was first achieved by Si-O-Si bridges but the oxygen atoms react with carbon excess at ~1200-1300°C (Karlin & Colomban, 1997; idem, 1998). The use of gamma irradiation for the crosslinking allows approaching better the stoichiometry and the thermal stability of SiC materials issued from polymeric precursor was increased (Ischikawa et al., 1991; Yang et al., 1991; Torecki et al., 1991; idem, 1992; Ischikawa, 1995; Ischikawa et al., 1998). Residual hydrogen atoms evolve above 1000°C whereas the free carbon created by the destruction of the methyl groups reacted with the Si-O group with the evolution of CO gas and forming new Si-C bonds above 1300°C, enhancing the crystallisation process.

Alternative route was developed by US Sacks' group (Torecki et al., 1992; Sacks et al., 1998): they used high-molecular-weight PCS. The infusible PCS was prepared by pressure pyrolysis of polydimethylsilane and the fibres formed by the dry spinning of concentrated PCS-based polymer solutions which were then pyrolysed in an inert atmosphere at 1000 to 1200°C.

The room temperature ultimate tensile strength ranges between 2.5 and 3.5 GPa as a function of the fibre grade with Young's modulus ranging between ~200 and 400 GPa, very close to the best properties achieved for bulk ceramics, films or crystals : ~430 GPa (Biswas et al., 2001; Dirras et al., 2004; Chung & Han, 2008). The axial room temperature thermal conductivity ranges between ~2-3 (oxygen rich, amorphous SiC) up to 50-60 W/mK for crystalline nearly stoichiometric SiC (Simon & Bunsell, 1984). The electrical conductivity from ~0.01 to 10 S.cm⁻¹ is highly related to the carbon content (Chauvet et al., 1992 a & b; Mouchon & Colomban, 1996). The reduction of the oxygen content in the fibres made by irradiating PCS produced fibres ~35% stiffer than the first generation fibres. The 1400°C creep rates are slightly improved (Sha et al., 2004). Actually the thermal stability in air remains poor for the first and 2nd generation SiC fibres, ca. ~1100°C. The third generation stoichiometric fibres exhibit properties much closer to those of bulk SiC but the thermal stability in air remains much lower than that of oxide fibers (Mouchon & Colomban, 1995; Colomban, 1997; Baxter et al., 2000, Ruggles-Wrenn & Kutsal, 2010; Ruggles-Wrenn & Whiting, 2011).

3. Polytypes

Polytypes are observed in a variety of covalent compounds where rotation along the covalent bond does not require a lot of energy. This often gives rise to more or less lamellar compounds with stacking faults along one direction: carbides (Feldmann et al., 1968; Salvador & Sherman, 1991; Choyke & Pensl, 1997), sulfides (CdS, ZnS, TiS₂, ... (Kaflawi et al., 1969; Schneide & Kirby, 1972; Tronc et al., 1975; Moret & Huber, 1976; Lincot et al., 1997; Agrosi et al., 2009; Alvarez-Garcia et al., 2009; Chi et al., 2011), nitrides (Komatsu et al., 2010) but also some oxides (e.g. BaTiO₃ perovskites (Wu et al., 2006; idem, 2009)) and even diamond (Fayette et al., 1995; Bhargava et al., 1995).

As sketched in **Figure 1**, SiC structures consist of alternate layers of Si and C atoms forming a bi-layer. These bi-layers are stacked together to form face-centre cubic unit-cell (cubic stacking = ABC-ABC-ABC-, the so-called zinc-blende type cell, to be abbreviated c-SiC) or closed-packed hexagonal system (hexagonal stacking = AB-AB-AB-, the so-called wurzite cell, to be abbreviated h-SiC). Two consecutive layers form a bilayer which is named “h” (h for hexagonal) if it is deduced from the one below by a simple translation. If not, when an additional 180° rotation (around the Si-C bond linking the bilayers) is necessary to get the superposition, the bilayer is named “k” (for “kubic”). The “k” stacking is the reference of β -SiC cubic symmetry, only. The infinite combination of h/c stacking sequences led to hundreds of different polytypes (Feldman et al., 1968; Choyke & Pensl, 1997).

Very similar structures are known for many compounds. Formation of polytypes arises because the energy required to change from one type to the other is very low. Consequently, different structures can be formed during the synthesis, simultaneously, especially for layer materials (CdS, SiC, TiS_2 , MoS_2 , BN, AlN, talc, micas, illites, perovskites, see references above) including MBE superlattices (Yano et al., 1995). Polytypes structure consists of close packed planes stacked in a sequence which corresponds neither to the face-centered cubic system nor the close-packed hexagonal system but to complex sequences associating both cubic and hexagonal stackings, ones such as = -ABABCABAB-, or -ABCAABAB A-, or -ABABCABBA-, etc.).

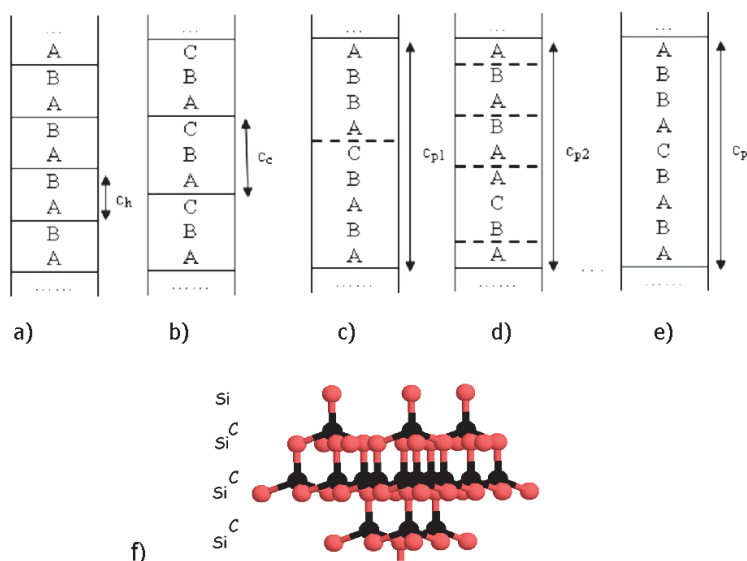


Fig. 1. Schematic diagrams of the (a) hexagonal, (b) cubic, (c,d) polytypes modifications and of the stacking fault disorder (e). SiC structures alternate layers of Si and C atoms to form a SiC bi-layer, AB or AC (e).

4. From amorphous to crystalline materials

The precursor route led to a rather progressive transformation of a more or less 1D organised framework to a 3D amorphous one and subsequent thermal treatments control

the crystallization. The first problem to solve (Table 1) was the way to establish the bridge between the polymeric $(\text{Si-C})_n$ chains: i) the first route (NLMTM Nippon Carbon fibre (Ishikawa, 1995)) is the thermal oxidation (Si-O-Si bridge) at relatively low temperature ($\sim 200^\circ\text{C}$), the resulting SiO_2 content decreases from ~ 25 to ~ 10 wt% with improvements), ii) the second one is the electronic irradiation that allows forming Si-C bridges but leads to a carbon excess (C/Si ~ 1.4 in Hi-NicalonTM Nippon Carbon fibre (Berger et al.; 1995; idem, 1999); alternatively the grafting of Ti or Zr alkoxide (Ti or Zr addition) leads to rather similar material but the fibres could be made with smaller diameter (UBE Industries TyrannoTM LOX-M, ZE and TE grade fibres (Berger et al., 1997; idem, 1999); iii) the optimization of the organic precursor and associated thermal treatments gives stoichiometric SiC fibre (SA3TM Ube Industries, SylramicTM Dow Corning Corp. Fibres and Hi-NicalonTM Type S (Lipowitz et al., 1995; Ishikawa et al., 1998; Berger et al., 1999; Bunsell & Piant, 2006). The high temperature of the manufacture process leads to much larger grain sizes.

Generation	1 st	2 nd	3 rd			
Producer	Nippon Carbon	Nippon Carbon	Ube Industries	Ube Industries	Dow Corning Corp.	Nippon Carbon
Grade	NLM Nicalon	Hi-Nicalon	ZE,TE	SA3	SYLRAMIC	Hi-S
Reticulation	Si-O bond	Electron irradiation	Electron irradiation	Si-O bond	Si-O bond	Electron irradiation
Grain size / nm	<2	5-10	5-10	<50	<50	<50
Si/C stoichiometry	1.3	<1.3	<1.3	~ 1	~ 1	~ 1
Diameter / μm (+/- 3)	15	12	11	7.5	10	12

Table 1. Small diameter SiC fibre generations.

The first generations fibre microstructures consist of an amorphous ternary phase made of SiO_xC_y tetrahedra (Porte & Sartre, 1989) with $x+y = 4$, with ~ 1.4 - 1.7 nm SiC crystallites and $\sim 5\%$ of randomly oriented free carbon aggregates, 1 nm in size (NicalonTM 200 grade, $x = 1.15$). Carbon (002) lattice fringe images showed small stacks of two fringes of around 0.7 nm in size suggesting that the basic structural unit (BSU) was a face-to-face association of aromatic rings, called dicoronenes, in which the hydrogen-to-carbon atomic ratio is 0.5. Accordingly, a porosity level of 2% was present (Le Coustumer et al., 1995 a & b). Other studies proposed that the intergranular phase should be written as $\text{SiO}_x\text{C}_{1-x/2}$, which suggests that the composition varies continuously from SiC to SiO_2 as the oxygen traces varied (Bodet et al., 1995). The removal of oxygen from the cross-linking process resulted in a stoichiometry closer to Si/C = 1 and an increase in size of the β -SiC grains which were in the range of 5 to 10 nm in commercial fibres. The TEM images show well ordered SiC

surrounded by highly disorderd/amorphous SiC interphase and free carbon grains (Monthieux et al., 1990; idem, 1991; Havel, 2004; Havel et al., 2007).

5. How to identify the polytypes, the stacking disorder and the relative proportion of each polytypes?

The challenge for the nanotechnologies, which is to achieve perfect control on nanoscale related properties, requires correlating the production conditions to the resulting nanostructure.

Transmission electron microscopy (darkfield and high resolution images, electronic diffraction, etc. (see e.g. Mirguet et al., 2009; Sciau et al., 2009)) is the most efficient technique to determine the grain size, the defaults (disorder, superstructures, amorphous interface, voids, etc.) but the technique is destructive, time-consuming and may modify the sample structure. Moreover the representativity of the samples is always poor.

Raman spectrometry is a very interesting technique to study nanomaterials since it investigates the matter at a sub-nanometer scale, i.e. the scale of the chemical bonds. The automatic mapping (best spatial resolution ~ 0.5 to $1 \mu\text{m}^2$ as a function of objective aperture and laser wavelength) allows a very representative view of the sample surface. Each Raman peak corresponds to a specific vibration (bending, stretching, librational, rotational and lattice modes) of a given chemical bond, and provides information (even on heterogeneous materials, e.g. composites) such as the phase nature and symmetry, distribution, residual stress,... (Colomban, 2002; Gouadec & Colomban, 2007). Since the Raman scattering efficiency depends on the polarisability of the electronic cloud, it can be very sensitive to light elements involved in covalent bonds (C, H, N, B, O, ...), which is a valuable advantage, when compared to X-ray/electron-based techniques (EDS, micro-probe,...). In the case of coloured materials if the exciting laser energy is close to that of absorbing electronic levels, resonance Raman scattering occurs and the technique becomes a surface analysis in the range of ~ 20 to 100 nm in-depth penetration (also depending on the wavelength, (Gouadec & Colomban, 2007)). Then, the selection of a given wavelength allows probing specific layers. The main advantages compared to infrared spectrometry are that the laser in a Raman equipment can be focused down to ~ 0.5 - $1 \mu\text{m}^2$, allowing for imaging specific areas (Gouadec et al, 2001; Colomban, 2003; idem, 2005) and that Raman peaks are narrower than IR bands (Gouadec & Colomban, 2007 and references herein).

Fig. 2a shows the representative electronic diffraction pattern ($[2-1-10]$ axis) of a SA3TM fibre thermally treated at 1600°C in inert atmosphere. Most of the Bragg spots correspond to 6H SiC (hexagonal $P6_3mc$ space group), i.e. to the most simple polytype (Fig. 1). The diffuse scattering along the horizontal axis ($[01-11]$), arises from the stacking disorder of the SiC bilayer units. On the contrary, the disorder signature is weaker on the X-ray diffraction pattern (small polytype peak at $d = 0.266 \text{ pm}$, **Fig. 2b**). However Bragg diffraction highlights the most crystalline part and sweeps the information on low crystalline (e.g. carbon) second phases. Fig. 3 shows the corresponding Raman spectra. For 1st and even 2nd generation fibres the Raman spectrum is dominated by the carbon doublet that overlaps the SiC Raman fingerprint. Specific thermal and chemical treatments are necessary to eliminate most of the carbon second phases and thus to have access to the Raman signal of the SiC phases (Havel & Colomban, 2005).

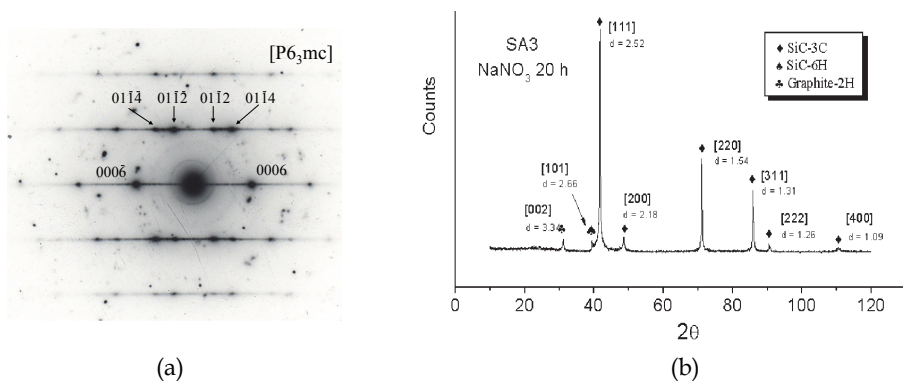


Fig. 2. a) Representative electron diffraction pattern recorded on SA3™ (Ube Industries Ltd, see Table 1) fibre thermally treated at 1600°C under inert atmosphere (Courtesy, L. Mazerolles); b) X-ray diffraction pattern recorded on powdered SA3™ fibre (the immersion in molten NaNO₃ do not modify the pattern, (Havel & Colombari, 2005)).

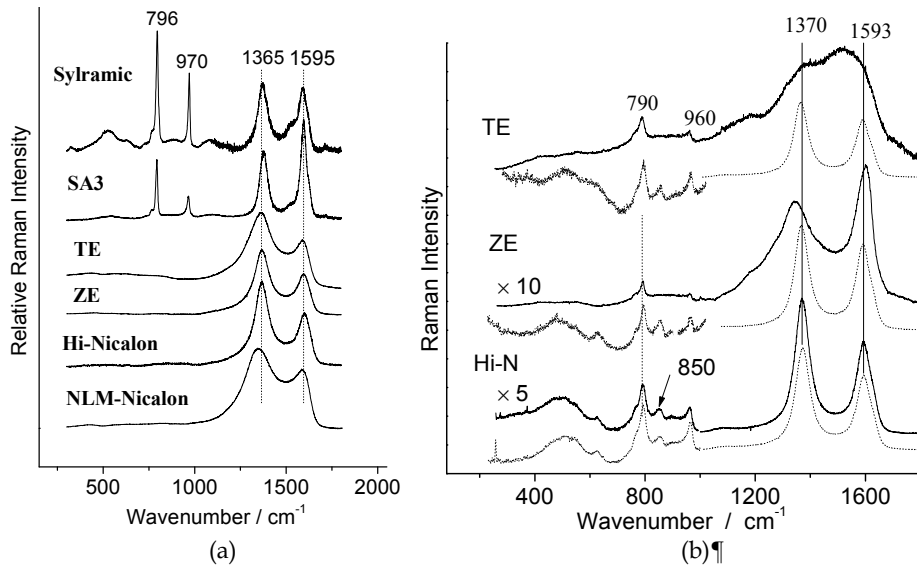


Fig. 3. Representative spectra of the as-produced fibres (a) and after different thermal/chemical treatments in order to highlight the SiC fingerprint (b).

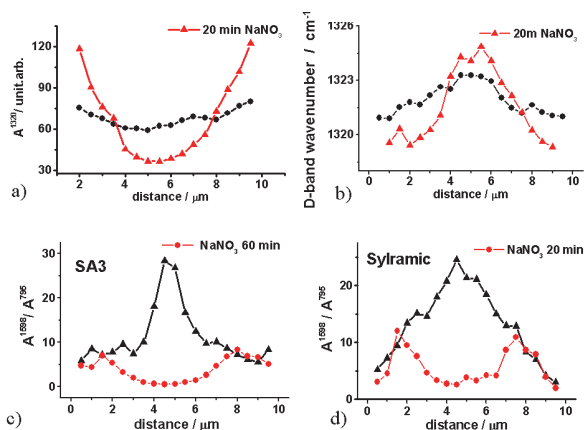


Fig. 4. Variations of a) the $\sim 1320 \text{ cm}^{-1}$ Raman peak area (A^{1320}) and b) its wavenumber shift across the diameter of a NLM™ fibre polished section, as-received (dot) and after a chemical attack (triangle) eliminating the carbon phase; a comparison of the variation of the "carbon rate" (Raman peaks surfaces ratio $A^{1598} / A^{795}(\text{C/SiC})$) along the diameter of SA3™ (c) and Sylramic™ fibres section (d) ($\lambda = 632 \text{ nm}$, $P = 0.5 \text{ mW}$, $t = 60 \text{ s}$).

Raman peaks attribution of the disordered carbons present in SiC fibres has been previously discussed (Karlin & Colombar, 1997; idem, 1998; Gouadec et al., 1998). Pure diamond (sp^3 C-C bonds) and graphite (in plane sp^2 C=C bond) have sharp stretching mode peaks at 1331 and 1581 cm^{-1} respectively. The two main bands of amorphous carbons are then assigned to diamond-like (D band for diamond and disorder) and graphite-like (G band for graphite) entities. Because diamond Raman scattering cross-section is much lower than that of graphite ($\sim 10^{-2}$), a weak $\text{C}_{\text{sp}^3}\text{-C}_{\text{sp}^3}$ stretching mode is expected. Actually, given the small size of carbon moieties and the strong light absorption of black carbons the contribution of the chemical bonds located near their surface will be enlarged (resonance Raman, the Raman wavenumbers shift with used laser wavelength, see in (Gouadec & Colombar, 2007)). The D band corresponds to vibration modes involving $\text{C}_{\text{sp}^3}\text{-C}_{\text{sp}^2}/\text{sp}^3$ bonds also called $\text{sp}^{2/3}$. This band presents a strong resonant character, evidenced by a high dependence of the intensity and position on wavelength. Additional components below 1300 cm^{-1} arise from hydrogenated carbons and those intermediate between D and G bands have been assigned to oxidised and special carbon phases (Karlin & Colombar, 1997; idem, 1998; Colombar et al., 2002). The wavenumber of the sp^3 carbon bond (D peak) measures the aromaticity degree (aromaticity is a function of the "strength and extension size" of the π electronic clouds and thus also function of the crystal order) and hence is directly related to the electric properties of the material (Mouchon & Colombar, 1996). This value depends directly on the thermal treatment temperature history and hence is also related to the mechanical properties, see details in (Gouadec & Colombar, 2001; Colombar, 2003).

The plot of the carbon fingerprint parameters recorded across the fibre section diameter (on fracture) shows the very anisotropic carbon distribution (Fig. 4). Chemical treatments eliminate the carbon in the analysed SiC volume and hence allow a better study of the SiC phases (Havel & Colombar, 2005).

The Raman spectrum of well crystallised SiC phases is observed between 600 and 1000 cm^{-1} (Feldman et al., 1968; Nakashima et al., 1986; idem, 1987; idem, 2000; Nakashima & Hangyo, 1991; Nakashima & Harima, 1997; Okimura et al., 1987; Tomita et al., 2000; Hundhausen et al., 2008). The main Raman peaks centred at 795 and 966 cm^{-1} correspond to the transverse (TO) and longitudinal (LO) optic modes respectively of the (polar) cubic 3C phase, also called β SiC. Any other definite stacking sequence is called α -SiC and displays either hexagonal or rhombohedral lattice symmetry. Polytypes in the α -SiC structure induce the formation of satellite peaks around 766 cm^{-1} and of additional features between the TO and LO modes (Figs 5 & 6). However, the TO mode is twice degenerated; while TO_1 is centred at 796 cm^{-1} , TO_2 is a function of the “h” layers concentration in the structure. A linear variation of 0.296 $\text{cm}^{-1}/\%$ has been demonstrated (Salvador & Sherman, 1991; Feldman et al., 1968).

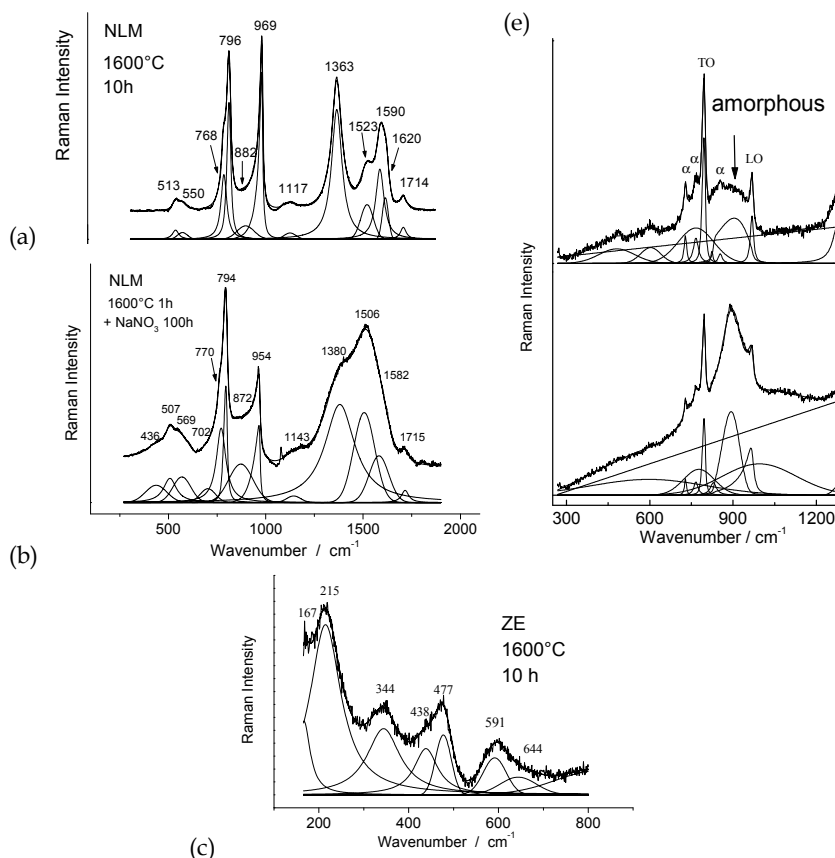


Fig. 5. Representative Raman spectra recorded for NLMTM Nicalon fibres thermally and chemically treated (a,b). Detail on the disorder-activated acoustic modes observed for ZETM fibre (c) and for very amorphous SiC zone are shown.

The main effect of the disorder is the break of the symmetry rules that excludes the Raman activity of the vibrational, optical and acoustical, modes (phonons) of the whole Brillouin

zone: only zone centre modes give rise to a Raman activity. Because the wavenumber of these modes shift with wavevector value, they give broad asymmetric bands. Fig. 6 illustrates the apparition of satellite peaks because the step-by-step Brillouin Zone folding associated to the formation of polytypes. On the contrary, stacking disorder lead to a projection of the vibrational density of state on the vertical energy axis and broad asymmetric bands are observed.

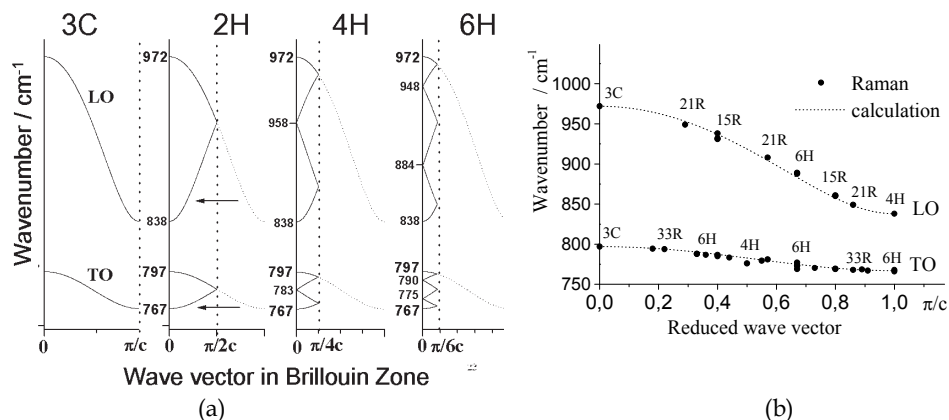


Fig. 6. a) Sketch of the folding of the original phonon Brillouin zone in the stretching LO/TO mode region along the stacking axis of the reference cubic symmetry by factor 2 (2H polytype), 4 (4H) and 6 (6H). b) Satellite peak wavenumbers for series of polytypes (after Nakashima & Harima, 1997).

The comparison of the Figures 2a (Diffraction & diffuse scattering) and 2b (Raman scattering) points out the very different sensitivity of these two methods. Fig. 4 compares the Raman spectra of the different generation SiC fibres, with carbon excess ranging from ~20 wt% (1st generation) to less than 1 wt% (3rd generation). A small wavenumber shift may be associated to the change of the exciting wavelength. Another important point is that for coloured materials, the interaction between laser light and matter must be very strong and hence the light absorption. This may have detrimental effect (local heating – and thermal induced wavenumber shift – (Colomban, 2002), oxidation and phase transition (Gouadec et al., 2001) in the lack of attention but this also controls the penetration depth of the laser light: the penetration can be limited to a few (tenths of) nanometers (Gouadec & Colomban, 2007).

Figs 5 to 9 give examples of the variety of Raman signatures observed on SiC materials issued of the organic precursor routes.

The narrow peaks pattern of crystalline polytypes is obvious and assignments are univocal with the comprehensive work of Nakashima (Nakashima et al., 1986; idem, 1987; Nakashima & Harima, 1997), see Fig. 6. The most stringent new features are the very broad bands observed at ~730 and 870 cm⁻¹ and the structured pattern below 600 cm⁻¹. The first feature corresponds to the amorphous silicon carbide and the second one to the acoustic modes rendered active because of the very poor crystallinity of the fibre.

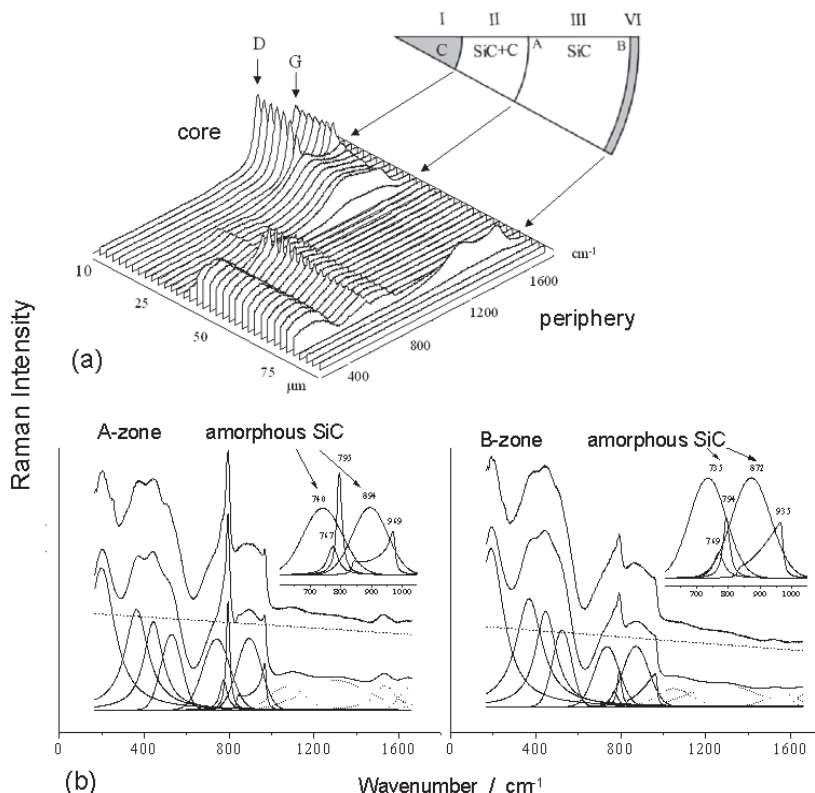


Fig. 7. a) Raman spectra recorded every 2 μm along a line from the centre of a SCS-6 Textron™ fibre ($L = 532\text{nm}$, 1mW , 120s/spectrum); b) representative spectra of the pure SiC (III) zone; the different components have been fitted with Gaussian or Lorentzian lines: the broad 740 and 894 cm^{-1} bands correspond to amorphous SiC, the 767 cm^{-1} band to 6H-SiC and the 795 cm^{-1} band to 3C-SiC polytypes.

The apparition of disordered activated acoustic phonon in the Raman spectrum is not surprising in compounds with large stacking disorder (Chi et al., 2011). Additional multiphonon features are not excluded. However, many Raman studies of such materials have been made using exciting laser line leading to a resonance spectrum, simpler, in which the contribution of the disordered activated modes is low or even not detected.

Very similar features are observed for SiC materials prepared by Chemical Vapour Infiltration. The Raman spectra of the SiC coating deposited on a small diameter ($\sim 7\mu\text{m}$) carbon fibre core to obtain the SCS-6 Textron™ fibre, a $\sim 120\mu\text{m}$ thick fibre used to reinforce metal matrix consist in features where the acoustic phonon intensity becomes stronger than the optical ones. Furthermore the latter group is dominated by the broad bands of the amorphous SiC.

Because of the different laser line absorption, Rayleigh confocal imaging allows to have very interesting image of the heterogeneous material (Colomban & Havel, 2002; Colomban, 2003; Havel & Colomban, 2003; idem, 2004; idem, 2005; idem, 2006). Fig. 8 shows representative spectra recorded on the deposit obtained around the fibres of a textile perform. In order to

optimise the thermomechanical properties of the composite a first coating of the SiC fibre with BN has been made. The spectra show the 3C (narrow peak at 799 and 968 cm^{-1}), 6H (786 cm^{-1}), 8H or 15R (768 cm^{-1}) as well the broad and strong contribution of amorphous SiC (optical modes at 750 & 900 cm^{-1} and acoustic modes at 450 cm^{-1} with shoulder at 380 and 530 cm^{-1}). Traces of carbon (1350-1595 cm^{-1} doublet) are also observed. We assign the broad Gaussian peaks at $\sim 700 \text{ cm}^{-1}$ and $\sim 882 \text{ cm}^{-1}$ to the amorphous SiC. Indeed, the position of the band at ca 882 cm^{-1} is exactly between the two optical modes at a wavenumber of $(796+969) / 2 = 882.5 \text{ cm}^{-1}$. Dkaki et al. (Dkaki et al., 2001) already assigned the band at ca. 740 cm^{-1} to the amorphous SiC phase.

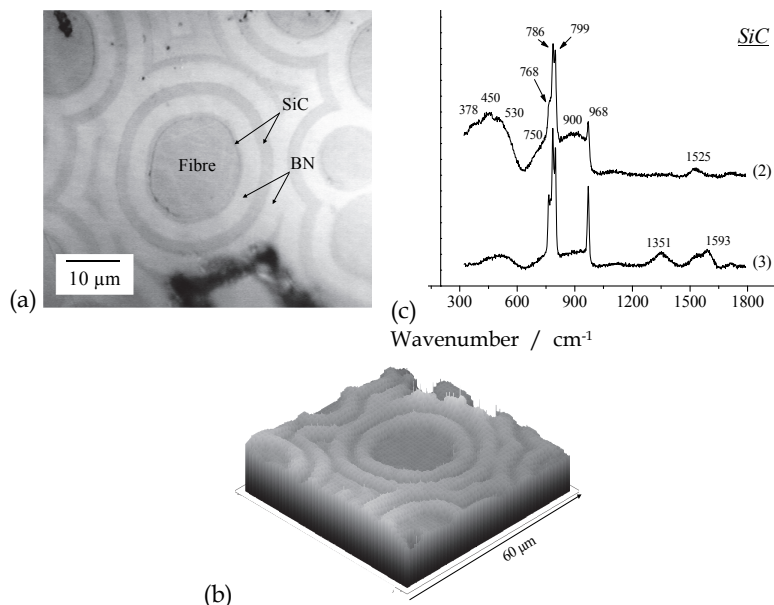


Fig. 8. Optical photomicrograph (a) and Rayleigh image (b) of a SiC (BN coated) fibre reinforced-SiC matrix composite. Examples of SiC spectra are given in c). Polytypes are evidenced by 786 (4H) and 768 (6H) cm^{-1} TO modes. The fingerprints of 3C (799 cm^{-1}) and amorphous (900 cm^{-1} broad band) SiC are also present.

When classically used, a Raman spectrometer is built to avoid the elastic (Rayleigh) scattering which is much more intense ($\times 10^6$) than the inelastic one (Raman) and masks it. However, the Rayleigh signal contains useful information (volume of interaction and dielectric constant) that can be recorded in only few seconds, giving rise to topological and/or chemical maps (a high resolution Raman image requires tenths of hours!). The combination of Rayleigh image and Raman scattering is very interesting to study indentation figures (Colomban & Havel, 2002). Rayleigh scattering gives image of the topology mixed with information on the chemical composition through the variation of the optical index. Fig. 9 presents the Rayleigh image of the Vickers indented zone of the mixed SiC+C region (zone II) of a SCS-6 polished section (see Fig. 7). The automatic XY mapping has been performed with an objective with an Z axis extension of the focus volume sufficiently large to be bigger than the indentation depth. Thus, a 3D view is obtained. The

up-deformation of the fibre matter close to the edges resulting from the pyramidal shape of the Vickers indenter is obvious. The residual stress is calculated using the experimental relationship previously established under pressure (Salvador & Sherman, 1991; Olego et al., 1982). The amorphization is obvious at the center of the indented area with the relative increase of the intensity of the 760-923 cm^{-1} doublet and the decrease of the TO/LO doublet; note, the up-shift of the TO mode from 796 to 807 cm^{-1} . Similar information can be extracted from the D carbon band using the relationship established by Gouadec & Colombari, 2001.

Peak	Out of the indented area		At the tip position	
	$\bar{\nu}$ (cm^{-1})	P (GPa)	$\bar{\nu}$ (cm^{-1})	P (GPa)
TO	796 ± 2	0	807 ± 6	3 ± 2
LO	969 ± 2	0	969 ± 4	3 ± 2
D	1351 ± 3	0	1369 ± 4	3 ± 1

Table 2. Comparison between the TO/LO peak wavenumbers measured at the tip and out of the 50 g Vickers indented area on SCS-6 TextronTM fibre, mixed SiC-C zone II (see Fig. 7a).

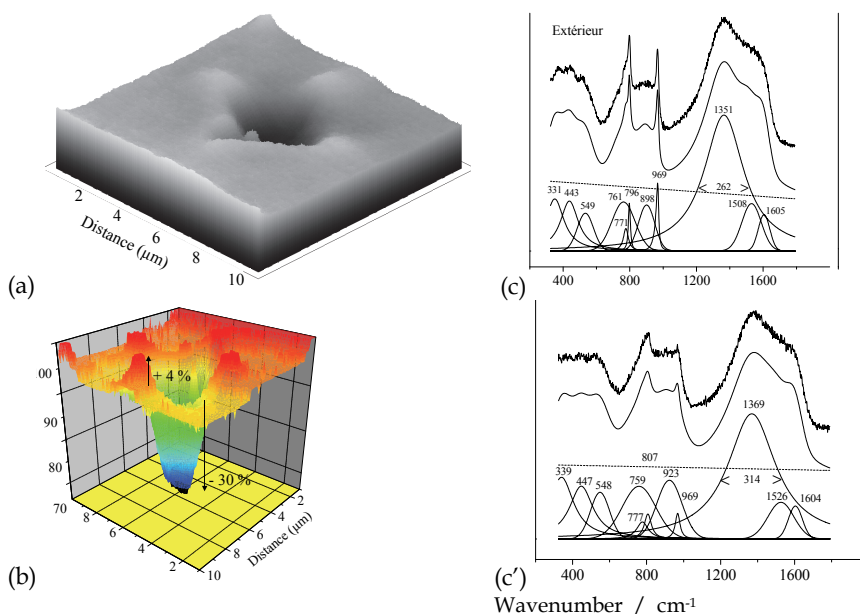


Fig. 9. (a,b) Rayleigh images of the Vickers indented area on the mixed SiC+C II region of a SCS-6 TextronTM fibre (100x100 spectra, 3s/Spectrum, 10^{-6} mW, $\lambda = 532$ nm); c,c') representative spectra (step: $0.1\mu\text{m}$) recorded at the core (c') and the periphery (c) of the indented area; the fitting of the different component allows calculating the residual hydrostatic pressure (see Table 2).

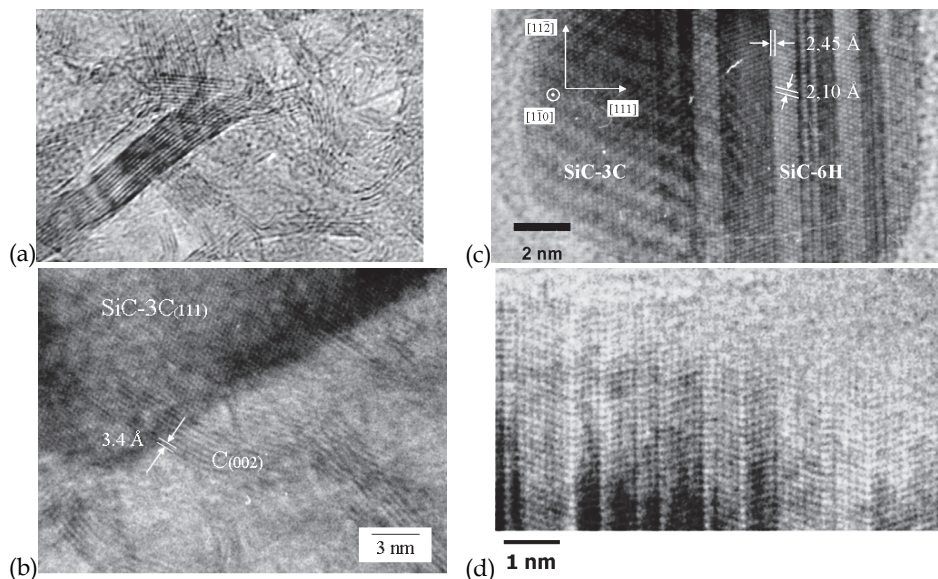


Fig. 10. TEM photomicrographs showing the carbon slabs in 1600°C thermally treated SA3 fibre (a,b) and the extension of the polytypes in thermally treated NLM 202™ (c) and SA3™ (d) fibres. The progressive transition between crystalline layers and amorphous zone is shown in (d) (Courtesy, L. Mazerolles).

6. Microstructure and defects

Fig. 10 shows representative high resolution Transmission Electron Microscopy (TEM) images recorded on thermally treated NLM 202 Nicalon™ and SA3™ fibres (Table 1). Structural studies of SiC nanocrystals were carried out on fragments of fibres deposited on a copper grid after crushing in an agate mortar (Havel, 2004; Havel et al., 2007). In SA3™ fibre the carbon phase appears to be well organized, graphitic, according to the narrow doublet of the Raman spectra (Fig. 3a). The interplane spacing is 0.33 pm. The stacking sequence of SiC bilayers is clear in Fig. 10c & d, because the contrast jump relative to the Bragg peak shifts. The domain sizes along the stacking direction might reach 3-4 nm. Figure 10c shows a typical HRTEM image of a nanocrystal with a size of 15 nm along its longest axis consisting of two regions corresponding to the α and β phases. The stacking faults, which are clearly seen on the micrograph, show no periodicity along the c axis of the hexagonal structure. Stacking faults can be considered as a perturbation of the β -SiC 3C stacking sequence so that the α phase can be seen as a sequence of β -SiC domains of various sizes ranging from 0.2 to 5 nm. The progressive transition between crystalline domains explains the variety of Raman fingerprint. There is a good agreement between Raman and TEM data.

7. Quantitative extraction of the (micro)structural information present in the Raman spectrum

For the decomposition of the SiC Raman peaks we used the spatial correlation model (SCM), which was established by Richter et al. (Richter et al., 1981), and by Nemanich et al.

(Nemanich et al., 1981) and then popularised Parayantal and Pollack (Parayantal & Pollack, 1984). A comprehensive description for non-specialist has been given in our previous work (Gouadec & Colombar, 2007). It can be briefly explained as follows. In "large" crystals, phonons propagate "to infinity" and because of the momentum selection rule the first order Raman spectrum only consists of "q=0" phonon modes, i.e. the centre of the Brillouin Zone (Fig. 6). However, since crystalline perfection is destroyed by impurities or lattice disorder, including at the surface where atoms environment is singular, the phonon function of polycrystals is spatially confined. This results in an exploration of the wavevectors space and subsequent wavenumber shifts and band broadening. Another effect is the possible activation of "symmetry forbidden" modes. This is linked to the Brillouin zone folding as illustrated in Fig. 6. In the 6H polytype structure, the zone is folded three times at the Γ centre point and the reduced wave vectors that can be observed are at $q = 0, 0.33, 0.67$ and 1 (Feldman et al., 1968; Nakashima et al., 1987; Nakashima & Harima, 1997). The Raman line broadening can be described by the (linear) dependence of its half width upon the inverse grain size, as reported previously for many nanocrystalline materials including CeO_2 (Kosacki et al., 2002), BN (Nemanich et al., 1981), Si (Richter et al., 1981), etc.

In equation (1), the SCM describes the crystalline quality by introducing a parameter L_0 , the coherence length, which is the average extension of the material homogeneity region. Noting q the wave vector expressed in units of π/a (a being the lattice unit-cell parameter) and Γ_0 the half width of Raman peaks for the ordered reference structure, the intensity $I(\bar{\nu})$ at the wavenumber $\bar{\nu}$ is then given by equation (2). (Richter et al., 1981; Nemanich et al., 1981; Gouadec & Colombar, 2007).

The exponential function represents a Gaussian spatial correlation and $\bar{\nu}(q)$ is the mode dispersion function, which can be deduced from neutron scattering measurements or from calculations often based on a rigid-model structure (Parayanthal & Pollak, 1984; Weber et al., 1993; Kosacki et al., 2002).

$$I(\bar{\nu}) = I_0 \times \int_{q=0}^{q=1} e^{-\frac{k_{ZZ}^2 \times (q-q_0)^2 \times L_0^2}{16 \times \pi^2}} \times \frac{dq}{[\bar{\nu} - \bar{\nu}(q)]^2 + \left(\frac{\Gamma_0}{2}\right)^2} \quad (1)$$

While the one dimensional disorder (in the stacking direction) leads to the polytypes formation, a complete disorder induces the total folding of the Brillouin zone and the apparition of a very broad Raman signal (density of state spectrum, e.g. Fig. 9c). The phonon confinement is observed for small grains in a well crystallized state.

The dispersion curve can be modelled with the Eq. 2-4 (Parayanthal & Pollak, 1984). Our 6H reference corresponds to coefficients A and B of respectively 3.18×10^5 and 1.38×10^{10} for TO and 4.72×10^5 and 8.52×10^{10} for LO modes (Havel & Colombar, 2004).

$$\bar{\nu}(q) = \sqrt{A + \sqrt{A^2 - B \times (1 - \cos(\pi q))}} \quad 0 \leq q \leq 1 \quad (2)$$

with

$$A = \frac{1}{2} \times \bar{\nu}_{(q=0)}^{-2} \quad (3)$$

and

$$B = \frac{1}{2} \times \bar{v}_{(q=1)}^{-2} \times \left(\bar{v}_{(q=0)}^{-2} - \bar{v}_{(q=1)}^{-2} \right) \quad (4)$$

The SCM has been used to determine the size and structure of SiC nanocrystals extracted from annealed SiC fibre. The Raman spectra of the NLM fibres annealed 1h and 10h are shown in Fig 5. The SiC Raman signature, is composed of the 2 optical TO and LO modes. A satellite at 768 cm⁻¹ indicates the presence of the 6H-SiC polytype (Fig. 6). The most interesting parameter in this SiC signature is the strong asymmetry of the LO peak at ~ 969 cm⁻¹ (see also Fig. 7). The TO peak is much less asymmetric and centred at 796 cm⁻¹. The elementary peaks obtained from the decomposition of the experimental spectrum are shown in Fig. 5 and the adjustment parameters (position, q_0 and L_0) are summarized in Table 3. Note that the accuracy on the calculated reduced wavevector, q_0 , is increased for the LO mode because its dispersion curve explores a wider wavenumber range (838-972 cm⁻¹) than the TO mode (767-797 cm⁻¹).

Peak	Parameter	1h	10h	1h + corroded
TO	\bar{V} (cm ⁻¹)	796.8	795.6	794.2 ± 2
	q_0	0.22 ± 0.02	0.26 ± 0.01	0.30 ± 0.01
	L_0 (nm)	5.6 ± 1.5	6.5 ± 1.2	5.6 ± 0.6
LO	\bar{V} (cm ⁻¹)	961.7	969.5	954.5
	q_0	0.18 ± 0.03	0.00 ± 0.07	0.26 ± 0.01
	L_0 (nm)	2.9 ± 0.4	3.8 ± 0.9	5.2 ± 0.5

Table 3. Peak fitting parameters of the TO and LO peaks of SiC calculated from the Raman spectra of the NLM fibres annealed 1h and 10h at 1600°C and annealed 1h then corroded 100h in NaNO₃ (Havel & Colombar, 2005).

For the fibre annealed for 1h, the L_0 parameters of both TO and LO peaks show a confinement dimension in the range of 2.5 to 7 nm, in good agreement with the TEM image. After 10h annealing, the TO and LO peaks become sharper and more intense, indicating an increase in the size of the nanocrystals. This is confirmed by the L_0 parameter, which gives a confinement dimension slightly higher, between 3 and 8 nm, according to the polytype domain size (Fig. 10).

8. Raman imaging

Raman imaging is very powerful, especially for heterogeneous materials but its rise is limited because of a lack of real control on the x, y, z spatial resolution (changing the diameter of confocal hole allows however some possibility) and of the huge recording time required (the spectrometer has often to be used during night time). However, a precise study of the laser shape, can improve the control on the resolution and since the CCD detectors are more and more sensitive, Raman images will now require more reasonable acquisition time (hours!). Note, that once the image is recorded, the set of spectra (also called hyperspectrum) has to be

analysed, which is much more time-consuming than the acquisition itself. This is why automatic decomposition software must be developed (Havel et al., 2004; Gouadec et al., 2011).

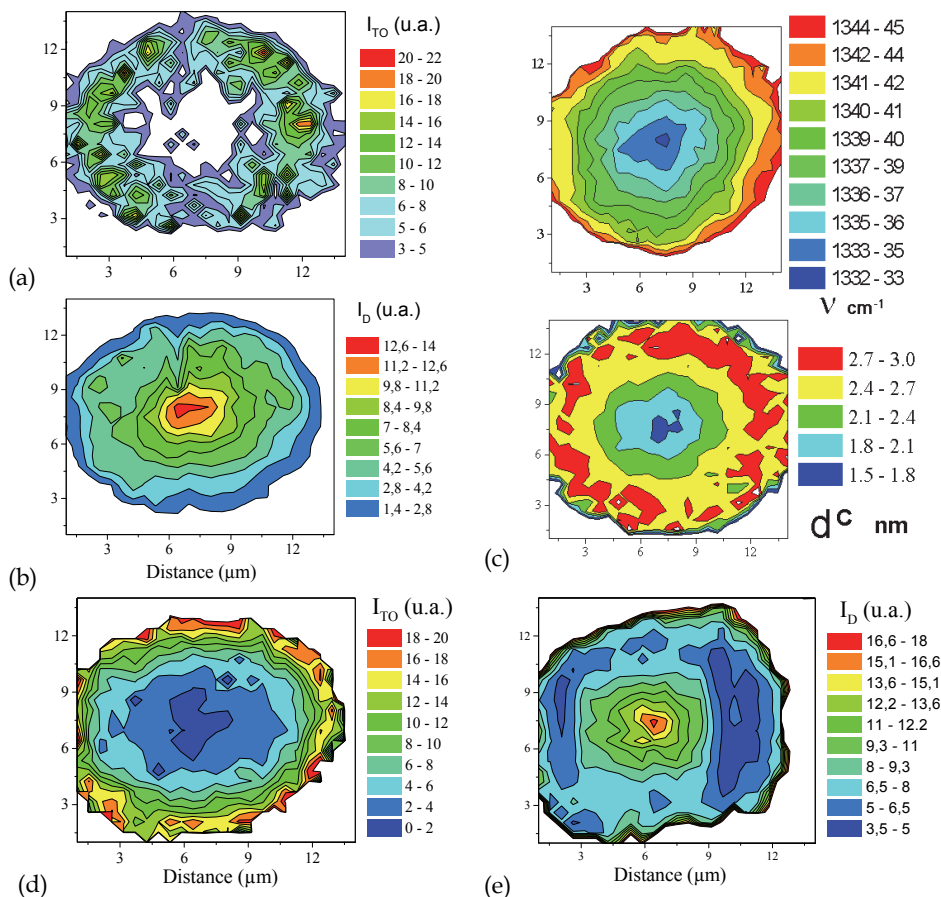


Fig. 11. Raman maps of the TO SiC (a) and D C stretching mode intensity (b) and D C wavenumber (c-top) recorded on the section of a SA3™ fibre (30x30 spectra, 0.5μm step, x100 objective, $\lambda = 632$ nm). The c-bottom image is a calculation, see text. Evolution of the TO and D band intensity after a thermal treatment at 1600°C is shown in d) and e).

Because of their interesting thermal and mechanical properties, SiC composites (SiC fibres + SiC matrix) find numerous applications in the aerospace industry and new ones are expected in fusion ITER plant (Roubin et al., 2005). However, their expensive cost has to be balanced with a long lifetime, which is not yet achieved. To increase their lifetime, we first have to understand their behaviour under chemical and mechanical stresses, and thus, to characterize their nanostructure. In this section, we focus on the SiC fibres, which are analysed across their section. Indeed, this approach allows observing the chemical variations that may exist between the fibre's core and surface. Fig. 11 shows Raman maps

of the Tyranno SA3™ (Ube Industry) fibre polished sections: a full spectrum is recorded each 0.5 μm (the hyperspectrum) and after computation, Raman parameters are extracted and mapped. Figures 11a & b consider the intensity variation of the TO SiC and D carbon peaks (see also Fig. 4); this later line is assigned to the vibrations of peculiar carbon moieties, which are thought to be located at the edges of the sp^2 carbon grains (Fig. 10a). Fig. 11c (top) shows the wavenumber shift of the later D band. In this particular case, the wavenumber shift represents the aromaticity of the carbon species. It has been reported that this parameter also depends on the residual strain as is shown in equation 5 (Gouadec & Colomban, 2001).

$$\Delta\bar{\nu}_D = 10 \text{ cm}^{-1} / \text{GPa} \quad (5)$$

The radial anisotropy results from the fibre preparation process: the fibre is heated from outside and the departure of the H and C excess takes place at the fibre surface. Consequently, because of the thermodynamic rules, the temperature of the fibre surface is higher than that of the core, that keep C and H excess. After thermal treatment at 1600°C a better homogeneity is achieved. Obviously, the specific microstructures of the different fibre grades can be analysed using a “simpler” and faster diameter line-scan (Fig. 4).

The first maps (Figs 10a, b & c-top), representing the distribution of a simple Raman parameter, may be of limited physical interest. However, it can be translated (through models) to a property' map (Colomban, 2003). The resulting image as exemplified in (Fig. 11c-bottom) gives the distribution of physical parameters; we call it a “Smart image”.

For instance, the size of short-range ordered vibrational units in carbon moieties can be deduced from the Raman parameters. It is based on the ratio of the intensity, I , of the two main carbon Raman peaks (I_D/I_G), as first proposed by Tiunstra & Koenig, 1970.

$$I_D / I_G = C_1 / S_g \quad (6)$$

with the grain size S_g in nm and the constant $C = 44$ for 5145.5 nm laser excitation; this formula works well for relatively large grains (>2 nm). A new model (7) takes into account the Raman efficiency, d , of the D^{1340} with respect to that of G^{1600} , as well as R , the ratio of atoms on the surface of each grain with respect to the bulk, e_t the surface thickness and L_g , the coherent length (\sim the grain size of Tuinstra and Koenig model). Assuming a spherical shape of all grains the following equation can be proposed (Colomban et al., 2001).

$$d \times R \approx d \times \left[\left(1 - \frac{2 \times e_t}{L_g} \right)^{-3} - 1 \right] \quad (7)$$

This model has been used to calculate the carbon grains size distribution in SA3™ fibre's cross sections. We observe that the intensity ratio is much higher in the core than near the surface and the carbon grain size appears approximately 2-3 times smaller on the fibre's core than on its periphery because the thermal gradient during the process.

The Raman data can be translated through equation 5 to a map of the maximum tolerable strain (Colomban, 2003). The resulting image (Fig. 12) clearly evidences that the fibre's mechanical properties are better (~ 3.5 GPa) in the core than near the surface (~ 2 GPa).

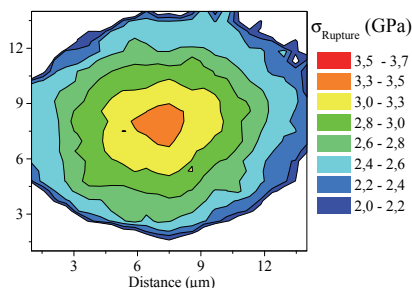


Fig. 11. Raman map of calculated ultimate tensile strength of the SiC zones in a SA3™ fibre section.

“Smart Raman images” in this section bring a lot of interesting information. First, there is a huge difference between the fibre’s core and surface with a radial gradient of physical properties as function of the fibre’ producer and additional treatments. Second, the maximum tolerable strain is observed in the fibre’s core, where the carbon species are the smallest (~ 1.5 nm). The core/skin differences are due to the elaboration process (spinning, sintering steps, etc.).

9. Acknowledgments

The author thanks Drs Havel, Karlin, Gouadec, Mazerolles and Parlier for their very valuable contributions to the study of SiC materials.

10. References

- Agrosi, G., Tempesta, G., Capitani, G.C., Scandale, E. & Siche, D. (2009). Multi-analytical study of syntactic coalescence of polytypes in a 6H-SiC sample, *J. Crystal Growth*, 311, 4784-4790.
- Alvarez-Garcia, J., Barcones, B., Perez-Rodriguez, A., Romano-Rodriguez, A., Morante, J.R., Janotti, A., Wei, S.-H. & Scheer, R., (2005). Vibrational and crystalline properties of polymorphic CuInC₂ (C= Se,S), *Phys. Rev. B*, 71, 054303.
- Aoki, M., Miyazaki, M. & Nishiguchi, T. (2009). TEM Observation of the polytype transformation of Bulk SiC Ingot, in *Silicon Carbide and Related Materials 2007*, Parts 1 & 2, *Mater. Sci. Forum*, 600-603, 365-368.
- Baxter D., Bellosi, A. & Monteverde, F. (2000). Oxidation and burner rig corrosion of liquid phase sintered SiC, *J. Eur. Ceram. Soc.*, 20, 367-382.
- Berger, M.-H., Hochet, N. & Bunsell, A.R. (1995) Microstructure and thermomechanical stability of low-oxygen Nicalon fibers, *J. Microsc.-Oxford*, 177[3], 230-241.
- Berger, M.-H., Hochet, N. & Bunsell, A.R. (1997). Microstructure evolution of the latest generation of small-diameter SiC-based fibers tested at high temperature, *J. Microsc.-Oxford* 185 (Part 2), 243-258.
- Berger, M.-H., Hochet, N. & Bunsell A.R. (1999). Properties and microstructure of small-diameter SiC-based fibers ch. 6, pp 231-290 in *Fine Ceramic Fibers*, Ed. A.R. Bunsell & M.-H. Berger, Marcel-Dekker Inc., New-York.
- Bhargava, S., Bist, H.D. & Sahli, S., (1995). Diamond polytypes in the chemical vapor deposited diamond films, *Appl. Phys. Lett.*, 67, 1706-1708.

- Biswas, K., Rixecker, G., Wiedmann, I., Schweizer, M., Upadhyayaya, G.S. & Aldinger, F. (2001). Liquid phase sintering and microstructure-property relationships of silicon carbide ceramics with oxynitride additives, *Mater. Chem. Phys.*, 67, 180-191.
- Bodet, R., Bourrat, X., Lamon, J. & Naslain R. (1995). Tensile creep-behaviour of a silicon carbide-based fiber with low-oxygen content, *J. Mater. Sci.*, 30[3], 661-677.
- Bouillon, E., Langlais, F., Pailler, R., Naslain, R., Cruege, F., Huong, P.V., Sarthou, J.C., Delpech, A., Laffon, C., Lagarde, P. Monthieux, M. & Oberlin, A. (1991a). Conversion mechanisms of a polycarbosilane precursor into an SiC-based ceramic material, *J. Mater. Sci.*, 26, 1333-1345.
- Bouillon, E., Mocaer, D., Villeneuve, J.F., Pailler, R., Naslain, R., Monthieux, M. Oberlin, A., Guimon, C. & Pfister G. (1991b). Composition microstructure property relationships in ceramic monofilaments resulting from the pyrolysis of a polycarbosilane precursor at 800 to 1400°C, *J. Mater. Sci.*, 26, 1517-1530.
- Bunsell, A.R. & Piant, A., (2006). A review of the development of three generations of small diameter silicon carbide fibers, *J. Mater. Sci.*, 41, 823-839.
- Burns, G.T., Taylor, R.B., Xu, Y.R., Zangvil, A. & Zank G.A. (1992). High-temperature chemistry of the conversion of siloxanes to silicon carbides, *Chem. Mater.*, 4[6], 1313-1323.
- Chauvet, O., Stoto, T. & Zupirolli, L. (1992a). Hopping conduction in a nanometer-crystalline system- a SiC fibre, *Phys. Rev. B* 46[13], 8139-8146.
- Chauvet, O., Zupirolli, L. & Solomon L. (1992b). Electronic properties of disordered SiC materials, *Mater. Sci. Engn. B.-Solid State Mater. Adv. Techn.* 11[1-4], 303-306.
- Chen, J., Lien, S.C., Shin, Y.C., Feng Z.C., Kuan, C.H., Zhao, J.H. & Lu, W.J., (2009). Occurrence of polytype transformation during nitrogen doping of SiC bulk wafer, in *Silicon Carbide and Related Materials 2007, Parts 1 & 2*, *Mater. Sci. Forum*, 600-603, 39-42.
- Chi, T.T.K., Gouadec, G., Colomban, Ph., Wang, G., Mazerolles, L., Thanh, D.X. & Liem, N.Q. (2011). Off Resonance Raman Spectroscopy of Wurtzite CdS Ground to the nanoscale: Discrimination between structural and size-related effects, *J. Raman Spectrosc.*, 42, 1007-1015. doi:10.1002/jrs.2793.
- Chollon, G., Czerniak, M., Pailler, R., Bourrat, X., Naslain, R., Pillot, J.P. & Cannet, R. (1997). A model SiC-based fibre with low oxygen content prepared from polysilane precursor, *J. Mater. Sci.*, 32[4], 893-911.
- Choyke, W.J. & Pensl, G. (1997), Physical properties of SiC, *MRS Bull.*, 22[3], 25-29.
- Chung, G.-S. & Han, K.-B. (2008). H₂ carrier gas dependence of Young' modulus and hardness of chemical vapour deposited polycrystalline 3C-SiC thin films, *Microelectr. J.*, 39, 1413-14515.
- Colomban, Ph. (1989). Gel Technology in Ceramics, Glass-Ceramics and Ceramic-Ceramic Composites, *Ceramics Inter.*, 15, 23-50.
- Colomban, Ph., (1997). The corrosion of ceramic-matrix composites, *Mater. Sci. Forum*, 251-254, 833-844.
- Colomban, Ph., (2002). Analysis of Stress and Strain in Ceramic, Polymer and Metal Matrix Composites by Raman Spectroscopy, *Adv. Engn. Mater.* 4[8], 535-542.
- Colomban, Ph., Gouadec, G., & Mazerolles, L. (2001). Alkaline corrosion of SiC and Carbon Fibers surface. A Raman and electron microscopy study, *Proc. 103th Ann. Amer. Cer. Soc. Conf. Engn., Ceramic. Trans.* 128, 157-168.
- Colomban, Ph., Gouadec, G. & Mazerolles, L. (2002). Raman analysis of materials corrosion: the example of SiC fibers, *Mater. Corr.*, 53, 306-315.

- Colomban, Ph. & Havel, M. (2002). Raman Imaging of Stress-induced Phase Transformation in Transparent ZnSe Ceramics and Sapphire Single Crystal, *J. Raman Spectrosc.*, 33[10], 789-795.
- Colomban, Ph. (2003). Raman analyses and "smart" imaging of nanophases and nanosized materials, *Spectroscopy Europe*, 15[6], 8-15.
- Colomban Ph. & Wey, M. (1997). Sol-gel control of the matrix net-shape sintering in 3D reinforced ceramic matrix composites, *J. Eur. Ceramic Soc.*, 17 [12], 1475-1483.
- Colomban, Ph. (2005). Nano/micro-structure and Property Control of Single and Multiphase Materials, ch 12, 303-339, in *Chemical Processing of Ceramics, Second Edition*, Komarneni S. & Lee B. Eds, CRC Press, Boca Raton, FL, USA.
- Corriu, R. & Lanneau, L. (1970). Application des propriétés réductrices des organomagnésiens à la preparation de nouveaux organosilanes asymétriques, *Tetrahedron Lett.*, 2, 165-168.
- Delplancke, M.P., Powers, J.M., Vandentop, G.J. & Somorjai, G.A. (1991). Preparation of $\text{Si}_x\text{C}_y\text{H}_z$ films from methylsilane by plasma enhanced chemical vapor deposition, *Thin Solid Films*, 202[2], 289-298.
- Devaty, R.P. & Choyke, W.J., (1997). Optical characterization of silicon carbide polytypes, *phys. Stat. Sol. (a)-Appl. Res.*, 162, 5-38.
- Dkaki, M., Calcagno, L., Makthari, A.M. & Raineri V. (2001). Infrared spectroscopy and transmission electronic microscopy of polycrystalline silicon carbide, *Mater. Sci. Semicond. Process.*, 4[1-3], 201-204.
- Dirras, G.F., Djemia, P., Roussigné & Y., Jackson, K.M. (2004). Investigating the elastic properties of β -SiC films, *Mater. Sci. Engn. A*, 387-389, 302-306.
- Durham, S.J.P., Shanker, K. & Drew, R.A.L. (1991). Carbothermal synthesis of silicon-nitride. Effect of reaction conditions, *J. Am. Ceram. Soc.*, 74, 31-37.
- Fayette, L., Mermoux, M., Marcus, B., Brunet, F., Germi, P., Pernet, M., Abello, L., Lucazeau, G. & Garden, J. (1995). Analysis of the fine structure of the Raman line and of X-ray reflection profiles for textured CVD diamond films, *Diamond & Related Mater.*, 4[11], 1243-1250.
- Feldman, D.W., Parker, J.H., Choyke, W.J. & Patrick, L. (1968). Phonon dispersion curves by Raman scattering in SiC polytypes 3C, 4H, 6H, 15R and 21R, *Phys. Rev.*, 173[3], 787-797.
- Fritz, G., Grobe, J. & Kummer, D. (1965). Carbosilanes, *Adv. Inorg. Chem.*, 7, 349-418.
- Gouadec, G. & Colomban, Ph. (2001). Non-destructive mechanical characterization of SiC fibers by Raman spectroscopy, *J. Eur. Ceram. Soc.*, 21, 1249-1259.
- Gouadec, G., Karlin, S. & Colomban, Ph. (1998). Raman extensometry study of NLM202 and Hi-Nicalon® SiC fibres, *Composites Part B*, 29[3], 251-261.
- Gouadec, G., Colomban, Ph. & Bansal, N.P. (2001). Raman study of Hi-Nicalon-fiber-reinforced celsian composites: I, distribution and nanostructure of different phases, *J. Am. Ceram. Soc.*, 84, 1129-1135.
- Gouadec, G. & Colomban, Ph. (2007). Raman study of Nanomaterials : How spectra related to disorder, particle size and mechanical properties, *Progr. Cryst. Growth & Charact. Mater.*, 53[1], 1-56.
- Gouadec, G., Bellot-Gurlet, L., Baron, D. & Colomban, Ph. (2011). Raman mapping for the investigation of nanophased materials, ch. 4 in *Raman Imaging*, Zoubir A. Ed., Springer, in press.
- Gough, J.R.C. & Kern, D. (1967). Studies on the coating of fuel particles for the "dragon" reactor experiment, *J. Nuclear Energy*, 21[8], 623-624.

- Greil, P. (1995). Active-Filled-Controlled Pyrolysis of Pre ceramic Precursors, *J. Am. Ceram. Soc.*, 78[4], 835-848.
- Greil, P. (2000). Polymer derived engineering ceramics, *Adv. Engn. Mater.* 2[6], 339-348.
- Hasegawa, Y., Feng, C.X., Song, Y.C., Song, Y.C. & Tan, Z.L. (1991). Ceramic fibers from polymer precursors containing Si-O-Ti bonds - 2 Synthesis of various types of ceramic fibers, *J. Mater. Sci.*, 26[13], 3657-3664.
- Havel, M. (2004) *Imageries Raman et Rayleigh de nanophases. Nouveaux outils pour l'étude de la corrosion de matériaux hétérogènes. Application aux fibres et composites céramiques*, Thesis, Université Paris 6, Paris.
<http://www.ladir.cnrs.fr/pages/theses/TheseHavel.pdf>
- Havel, M. & Colombar, Ph. (2003). Skin/bulk nanostructure and corrosion of SiC based fibres. A surface Rayleigh and Raman study, *J. Raman Spectrosc.*, 34[10], 786-794.
- Havel, M. & Colombar, Ph. (2004). Rayleigh and Raman images of the bulk/surface nanostructure of SiC based fibres, *Composites Part B*, 35, 139-147.
- Havel, M. & Colombar, Ph. (2005). Raman and Rayleigh mapping of corrosion and mechanical aging in SiC fibres, *Comp. Sci. Techn.*, 65, 353-358.
- Havel, M. & Colombar, Ph. (2006). Smart Raman and Rayleigh Spectroscopy for the Analysis of Nanomaterials, *Microscopy and Analysis*, 20[3], 11-14.
- Havel, M., Baron, D. & Colombar, Ph. (2004). "Smart" Raman/Rayleigh imaging of nanosized SiC materials using the spatial correlation model, *J. Mater. Sci.*, 39, 6183-6190.
- Havel, M., Baron, D., Mazerolles, L. & Colombar, Ph. (2007). Phonon Confinement in SiC Nanocrystals: Comparison of the Size Determination using Transmission Electron Microscopy and Raman Spectroscopy, *Appl. Spectrosc.*, 61, 855-859.
- Hundhausen, M., Püsche, R., Röhl, J. & Ley, L. (2008). Characterization of defects in silicon carbide by Raman Spectroscopy, *phys. stat. sol. (b)*, 245, 1356-1368.
- Hurwitz, F.I., Farmer, S.C., Terepka, F.M. & Leonhardt T.A. (1991). Silsesquioxane-derived ceramic fibers, *J. Mater. Sci.*, 26[5], 1247-1252.
- Hurwitz, F.I., Heimann, P., Farmer, S.C. & Hembree, D.M. (1993). Characterization of the pyrolytic conversion of Polysilsesquioxanes to Silicon Oxycarbides, *J. Mater. Sci.*, 28[24], 6622-6630.
- Ischikawa, T. (1995). Recent development of the SiC fiber Nicalon and its composites including properties of the SiC fiber Hi-Nicalon for ultra high temperature, *Comp. Sci. & Techn.* 51[2], 135-144.
- Ischikawa, T., Kohtoku, Y., Kumagawa, K., Yamamura, T. & Nagasawa, T. (1998). High-strength alkali-resistant sintered SiC fibre stable to 2000°C, *Nature*, 391[6669], 773-775.
- Ischikawa, T., Yamamura, T. & Okamura, K. (1991). The oxidation resistance of Si-Ti-Co fiber produced from cross-linked organometallic polymer, *Nippon Kagaku Kaishi*, 10, 1278-1283.
- Kiflawi, I., Mardix, S. & Kalman, Z.H. (1969). Zinc sulphide needles containing new polytypes, *Acta Crystallogr. Sect. B -Structural Crystallogr. & Cryst. Chem. B*, 25 2413.
- Karlin, S. & Colombar, Ph. (1997). Raman study of the chemical and thermal degradation of as received and sol-gel embedded Nicalon and Hi-Nicalon SiC fibres used in ceramic matrix composites, *J. Raman Spectrosc.*, 28, 219-228
- Karlin, S. & Colombar, Ph. (1998). Micro Raman study of SiC fibre-oxide matrix reaction, *Composites Part B*, 29B, 41-50.

- Komatsu, S., Kobayashi, K., Sato, Y., Hirano, D., Nakamura, T., Nagata, T., Chikyo, T., Watanabe, T., Takizawa, T., Nakamura, K. & Hashimoto, T. (2010). Photoinduced phase transformation in Boron Nitride: new polytypic forms of sp(3) bonded (6H- and 30H-)BN, *J. Phys. Chem. C*, 114[31], 13176-13186.
- Kosacki, I., Suzuki, T., Petrovsky, V., Anderson, H.U. & Colomban, Ph. (2002). Raman scattering and lattice defects in nanocrystalline CeO₂ thin films, *Solid State Ionics*, 149, 99-105
- Kosacki, I., Petrovsky, V., Anderson, H.U. & Colomban, Ph. (2002). Spectroscopy of nanocrystalline ceria and zirconia thin films, *J. Am. Ceram. Soc.*, 85[11], 2646-2650.
- Kumar, K. & Litt, M.H. (1988). A new silane polymer as a precursor to SiC, *J. Polymer Sci. Part C Polymer Lett.*, 26, 25-32.
- Kumagawa, K., Yamaoka, H., Shibuya, M. & Yamamura, T. (1998). Fabrication and mechanical properties of new improved Si-C-(O) Tyranno fiber, *Ceram. Engn. Sci. Proc.*, 19[3], 65-72.
- Langguth, K. (1995). Preparation of macro-porous SiC-Al₂O₃ composites with polysilanes and polycarbosilanes, *Ceram. Int.*, 21, 237-242.
- Learn, A.J. & Khan, I.H. (1970). Growth morphology and crystallographic orientation of β -SiC films formed by chemical conversion, *Thin Solid Films*, 5, 145-155.
- Le Coustumer, P., Monthieux, M. & Oberlin, A. (1995a). Further studies of the stability of PCS-based ceramic fibers at high temperature. 1 Oxidation behaviour, *Brit. Ceram. Trans.* 94[5], 177-184 .
- Le Coustumer, P., Monthieux, M. & Oberlin, A. (1995b). Further studies of the stability of PCS-based ceramic fibers at high temperature. 2 Effect of all carbon environment, *Brit. Ceram. Trans.*, 94[5], 185-190 .
- Lee, J.-S. & Yano, T. (2004). Fabrication of short-fiber-reinforced SiC composites by polycarbosilane infiltration, *J. Eur. Ceram. Soc.*, 24, 25-31.
- Lincot, D., Mokili, B., Froment, M., Cortes, R., Bernard, M.-C., Witz, C. & Lafait, J. (1997). Phase transition and related phenomena in chemically deposited polycrystalline Cadmium Sulfide thin film, *J. Phys. Chem. B*, 101, 2174-2181.
- Lipowitz J., Rabe J.A., Ngyuen, K.T., Orr, L.D. & Androl, R.R. (1995). Structure & properties of polymer-derived stoichiometric fiber, *Ceram. Eng. Sci. Proc.*, 16[5], 55-63.
- Lipowitz J., Rabe J.A., Zangvil A. & Xu, Y. (1997). Structure & properties of SYLRAMIC™ Silicon carbide fiber - A polycrystalline, stoichiometric β SiC composition, *Ceram. Eng. Sci. Proc.*, 18[3], 147-157.
- Lucke, J., Hacker, J., Suttor, D. & Ziegler, G. (1997). Synthesis and characterization of silazane-based polymers as precursors for ceramic matrix composites, *Appl. Organometallic Chem.*, 11[2], 181-194.
- Marinova, M., Zoulis, G., Robert T., Mercier, F., Mantzari, A., Galben, I., Kim-Hak, O., Lorenzzi, J., Julliaguet, S., Chaussende, D., Ferro, G., Camassel, J. & Polychroniadis, E.K. (2009). Defect-induced polytype transformations in LPE grown SiC epilayers on (111) 3C-SiC seeds grown by VLS on 6H-SiC, *Physica B-Condensed Matter.*, 404[23-24], 4727-4730.
- Martin, H.P., Muller, E., Irmer, G. & Babonneau, F. (1997). Crystallisation behaviour and polytype transformation of polymer-derived silicon carbide, *J. Eur. Ceram. Soc.*, 17[5], 659-666
- MacDiarmid, A.G. (1961). Silanes and their derivatives, *Adv. Inorg. Chem.* 3, 207-256.
- Mirguet, C., Roucau, C. & Sciau, P. (2009). Transmission electron microscopy a powerful means to investigate the glazed coating of ancient ceramics, *J. Nano Research*, 8, 141-146.

- Monthieux, M. , Oberlin, A. & Bouillon, E. (1990). Relationship between microtexture and electrical properties during heat treatment of SiC fiber precursor, *Composite Sci. & Techn.*, 37, 21-35.
- Monthieux, M. Cojean, M. Delverdier, O., Le Coustumer P. & Madigou, V. (1991). Characterization of ceramic composites and of their constituents – Precursors, Fibers and Interphases, *Microsc. Microanalysis Microstructures*, 2[1], 47-57.
- Moret, R. & Huber, M. (1976). Structure of new polytypes of Titanium Sulfide. *Acta Crystallogr. Section B-Structure Sci.*, 32, 1302-1303.
- Mouchon, E. & Colombari, Ph. (1996). Microwave absorbent: preparation, mechanical properties and r.f.-microwave conductivity of SiC (and/or mullite) fibre reinforced Nasicon matrix composites, *J. Mater. Sci.*, 31, 324-334.
- Mouchon, E. & Colombari, Ph. (1995). Oxide ceramic matrix-oxide fibers woven fabric composites exhibiting dissipative fracture behavior, *Composites* 26, 175-182
- Nakashima, S., Nakakura, Y. & Inoue, Z. (1987). Structural identification of SiC polytypes by Raman scattering: 27R and 33R polytypes, *J. Phys. Soc. Jpn*, 56[1], 359-364.
- Nakashima, S. & Hangyo, M. (1991). Raman intensity profiles and the stacking structure in SiC polytypes, *Solid. State Comm.*, 80, 21-24.
- Nakashima, S. & Harima, H. (1997). Raman investigation of SiC polytypes, *phys. stat. sol. (a) Appl. Res.*, 162, 39-64.
- Nakashima, S., Katahama, H., Nakakura, Y. & Mitsuishi, A. (1986). Relative Raman intensities of the folded modes in SiC polytypes, *Phys. Rev. B*, 33[8], 5721-5729.
- Nakashima, S., Wada, A. & Inoue, Z. (1987). Raman scattering from anisotropic phonon modes in SiC polytypes, *J. Phys. Soc. Jpn*, 56, 3375-3380.
- Nakashima, S., Nakatake, Y., Harima, H., Katsuno, M. & Ohtani, N. (2000). Detection of stacking fault in 6H-SiC by Raman scattering, *Appl. Phys. Lett.*, 77[22], 3612-3614.
- Narisawa, M., Okabe, Y. Okamura, K., Taki, T. & Kamiyama, T. (2000). Silicon-29 solid state MAS NMR investigation of silicon carbide powder prepared with a precursor method, *J. Ceram. Soc. Jpn*, 108[12], 1110-1114.
- Naslain, R. (2004). Design, preparation and properties of non-oxide CMCs for application in engines and nuclear reactors: an overview, *Comp. Sci. Techn. Engr.* 64[2], 155-170.
- Naslain, R.R., Pailler, R., Bourrat, X., Bertrand, S., Heurtevent, F., Dupel, P. & Lamouroux, F. (2001). Synthesis of highly tailored Ceramic matrix Composites by pressure pulsed CVD, *Solid State Ionics*, 141, 541-548.
- Nemanich, R.J., Solin, S.A. & Martin, R.M. (1981). Light-scattering study of boron-nitride microcrystals, *Phys. Rev. B* 23[12], 6348-6356.
- Okamura, K., Matsuzawa, T. & Hasegawa, Y. (1985). Gamma-ray irradiation curing on polycarbosilane fibers as the precursor of SiC fibers, *J. Mater. Sci.*, 4, 55-57.
- Okimura, H., Sakuma, E., Lee, J.H., Mulkaida, H., Misawa, S. Endo, K. & Yoshida, S. (1987). Raman scattering of SiC: application to the identification of heteroepitaxy of SiC polytypes, *J. Appl. Phys.* 61[3], 1134-1136.
- Ono, K. & Kurachi, Y. (1991). Kinetic Studies on beta SiC formation from homogeneous precursors, *J. Mater. Sci.*, 26, 388-392.
- Parayanthal, P. & Pollak, F.H. (1984). Raman scattering in alloy semiconductors – Spatial correlation model, *Phys. Rev. Lett.* 52[20], 1822-1825.
- Parlier, M. & Colombari, Ph. (1996). Composites à matrice céramique pour applications thermostructurales, *La Recherche Aérospatiale*, 5/6, 457-469.
- Popovska, N., Emig, G., Edie, D.D. & Rhee, B.S. (1997). Chemical vapor deposition of silicon carbide on carbon fibers with round and nonround cross-section, *High Temp. & Mater. Sci.*, 37[1], 1-11.

- Porte, L. & Sartre, A. (1989). Evidence for a silicon oxycarbide phase in the Nicalon silicon carbide fibre, *J. Mater. Sci.*, 24, 271-275.
- Richter, H, Wang, Z.P. & Ley, L. (1981). The one-phonon Raman spectrum in microcrystalline silicon, *Solid State Comm.*, 39(5), 625-629.
- Rohmfeld, S., Hundhausen, M. & Ley, L. (1998). Raman scattering in polycrystalline 3C-SiC: Influence of stacking faults, *Phys. Rev. B*, 58, 9858-9862.
- Roubin, P., Martin, C., Arnas, C., Laffon, C., Parent, P., Colomban, Ph., Pegourié, B. & Brosset, C. (2005). Raman spectroscopy and X-ray diffraction studies of some deposited carbon layers in Tore Supra, *J. Nuclear Mater.*, 337-339, 990-994.
- Ruggles-Wrenn, M.B. & Whiting, B.A. (2011). Cyclic creep and recovery behaviour of Nextel™ 720 alumina ceramic composite at 1200°C, *Mater. Sci. Eng. A*, 528[3], 1848-1856.
- Ruggles-Wrenn, M.B. & Kutsal, T. (2010). Effect of steam environment on the creep behaviour of Nextel™ 720 idem alumina-mullite ceramic composite at elevated temperature, *Composite Part A- Appl. Sci. & Manuf.*, 41[12], 1807-1816.
- Rynders, S.W., Scheeline, A. & Bohn, P.W. (1991). Structure evolution in a SiC-H film prepared from tetramethylsilane, *J. Appl. Phys.*, 69, 2951-2960.
- Sacks, M.D. (1998). Effect of composition and heat treatment conditions on the tensile strength and creep resistance of SiC-based fibers, *J. Eur. Ceram. Soc.*, 19[13-14], 2305-2315.
- Salvador, G. & Sherman, W.F. (1991), Pressure dependence of the Raman spectrum in 6H-silicon carbide, *J. Mol. Struct.*, 247, 373-384.
- Sasaki, Y. Nishina, Y., Sato, M. & Okamura, K. (1987). Raman study of SiC fibers made from PCS, *J. Mater. Sci.*, 22, 443-448.
- Schmidt, W.R., Interrante, L.V., Doremus, R.H., Trout, T.K., Marchetti, P.S. & Maciel, G.E. (1991). Pyrolysis Chemistry of an Organometallic precursor to Silicon Carbide, *Chem. Mater.*, 3, 257-267.
- Schneide, J. & Kirby, R.D. (1972). Raman scattering of ZnS polytypes, *Phys. Rev. B*, 6[4], 1290-1296.
- Sciau, Ph., Salles, Ph., Roucau, C., Mehta, A. & Benassayag, G. (2009). Applications of focused ion beam for preparation of specimens of ancient ceramics for electron microscopy and Synchrotron X-ray studies, *Micron*, 40[5-6], 597-604.
- Sha, J.J., Nozawa, T., Park, J.S., Katoh, Y. & Kohyama, A. (2004). Effect of heat treatment on the tensile strength and creep resistance of advanced SiC fibers, *J. Nuclear Mater.*, 329-333, 592-596.
- Simon, G. & Bunsell, A.R. (1984). Mechanical and structural characterization of the Nicalon silicon-carbide fiber, *J. Mater. Sci.*, 19[11], 3649-3657.
- Song, Y. Feng, C. Tan, Z. & Lu, Y. (1990). Structure and properties of polytitanocarbosilane as the precursor of SiC-TiC fiber, *J. Mater. Sci. Lett.*, 9[11], 1237-1243.
- Stewart, R.M., Dando, N.R., Seyferth, D. & Perrota, A.J., (1991). Characterization of Hydridomethyl-polysilazane - A precursor to SiC/SiN ceramics, *Abtr. Paper Am. Chem. Soc.*, 202, 340-POLY.
- Tanaka, H. & Kurachi, Y. (1988). Synthesis of beta-SiC powder from organic precursor and its sinterability, *Ceram. Int.*, 14, 109-115.
- Tanaka, A., Onari, S. & Arai, T. (1993). Low-frequency Raman scattering from CdS microcrystals embedded in a germanium dioxide glass matrix, *Phys. Rev. B* 47[3], 1237-1243.

- Tanaka, T., Tamari, N., Kondoh, I. & Iwasa, M. (1995). Fabrication and evaluation of 3-dimensional Tyranno fiber-reinforced SiC composites by repeated infiltration of polycarbosilane, *J. Ceram. Soc. Jpn*, 103, 1-5.
- Tanaka, T. Tamari, N. Kondoh, I. & Iwasa M., (1996). Fabrication and mechanical properties of 3-dimensional Tyranno fiber reinforced SiC composites by repeated infiltration of polycarbosilane, *J. Ceram. Soc. Jpn*, 104, 454-457.
- Tuinstra, F.T., Koenig, J.I. (1970). Raman spectrum of Graphite, *J. Chem. Phys.*, 53, 1126-1130.
- Tomita, T., Saito, S., Baba, M., Hundhausen, M., Suemoto, T. & Nakashima, S. (2000). Selective resonance effect of the folded longitudinal phonon modes in the Raman spectra of SiC, *Phys. Rev. B*, 62, 12896-12901.
- Toreki, W., Batich, C.D. & Choi, G.J. (1991). High molecular weight polycarbosilane as a precursor to oxygen free SiC fibers, *Abstr. Paper Am. Chem. Soc.*, 202, 360-POLY
- Toreki, W.M., Batich, C.D., Sacks, M.D., Saleem, M., Choi, G.J. & Morrone, A.A. (1992). Polymer-derived silicon-carbide fibres with low-oxygen content and improved thermomechanical stability, *Comp. Sci. Techn. Eng.*, 1351[2], 145-159.
- Tronc, E., Moret, R. & Legendre, J.J. & Huber, M. (1975). Refinement of polytypes structure 12R Ti₈S₁₂. *Acta Crystallogr. Section B-Structure Sci.*, 31, 2800-2804.
- Yajima, S., Okamura, K., Tanaka, J. & Hayase, T. (1980). Synthesis of aluminium composite reinforced with continuous SiC Fiber obtained from the precursor fiber of an organo-silicon precursor polymer, *J. Mater. Sci.*, 15, 2130-2131.
- Yang, Y.M., Liu, X.W., Tan, Z.L., Yang, S.J., Lu, Y. & Feng, C.X. (1991). Synthesis of SiC fiber with low oxygen content and high tensile strength using a polyblend precursor, *J. Mater. Sci.*, 26[19], 5167-5170.
- Yano, M., Utatsu, T., Iwai, Y. & Inoue, F. (1995). A Raman scattering study on the interface sharpness of INAS/ALSB/GASB/ALSB polytypes superlattices grown by molecular-beam epitaxy. *J. Cryst. Growth*, 150 [1-4], 868-873.
- Weber, W.H., Hass, K.C. & McBride, J.R. (1993). Raman study of CeO₂ - 2nd order scattering, lattice dynamics and particle size effects, *Phys. Rev. B*, 48[1], 178-185.
- Wu, Y.-C., Wang, S.-F. & Lu, H.-Y. (2006). Stacking Faults and Stacking Fault Energy of Hexagonal Barium Titanate, *J. Am. Ceram. Soc.*, 89, 3778-3787.
- Wu, Y.-C., Wang, S.-F. & Chen, S.-H. (2009). Microstructural Investigation of Ba(Ti_(1-x)Mn_x)O₃ Ceramics with 6H- and 12R-polytypes, *J. Am. Ceram. Soc.*, 92, 2099-2108.

Micropipe Reactions in Bulk SiC Growth

M. Yu. Gutkin,^{1,2,3} T. S. Argunova,^{4,6} V. G. Kohn,⁵
A. G. Sheinerman¹ and J. H. Je⁶

¹*Institute of Problems of Mechanical Engineering, RAS, St. Petersburg*

²*Department of Physics of Materials Strength and Plasticity, St. Petersburg State
Polytechnical University, St. Petersburg*

³*Department of Theory of Elasticity, St. Petersburg State University,
St. Petersburg*

⁴*Ioffe Physical-Technical Institute, RAS, St. Petersburg*

⁵*National Research Center 'Kurchatov Institute', Moscow*

⁶*X-ray Imaging Center, Department of Materials Science and Engineering, Pohang
University of Science and Technology, Pohang*

^{1,2,3,4,5}*Russia*

⁶*Republic of Korea*

1. Introduction

Structural defects in silicon carbide (SiC) single crystals such as dislocations, micropipes, inclusions, etc., have been investigated by different methods, including x-ray diffraction topography (Huang et al., 1999), visible light and scanning electron microscopies (SEM) (Epelbaum & Hofmann, 2001; Kamata et al., 2000), AFM and TEM (Yakimova et al., 2005). In particular, defects were imaged in polarized light (Ma, 2006) or made visible in electron beam-induced current and electroluminescence images (Wang et al., 2005). Their morphology has been classified and examined well enough. However, the correlation between structure and morphology still remains an important issue, in which a direct correspondence is complicated by transformation behaviors of structural defects. For example, micropipes — superscrew dislocations with hollow cores (Frank, 1951; Huang et al., 1999) — can dissociate into full-core dislocations (Epelbaum & Hofmann, 2001; Kamata et al., 2000; Yakimova et al., 2005) and react with each other (Gutkin et al., 2009a; Ma, 2006) or with foreign polytype inclusions (Gutkin et al., 2006; Ohtani et al., 2006).

Recent developments have stimulated the progress in defect studies. The push was the production of high-quality crystals (Müller et al., 2006; Nakamura et al., 2004). For example, 4H-SiC with micropipe densities as low as 0.7 cm^{-2} is commercially available; and the growth of the epitaxial layers with a dislocation density $< 10 \text{ cm}^{-2}$ has been demonstrated (Müller et al., 2006). Such low defect densities are very suitable for x-ray imaging techniques, whose development is pulled by the advent of synchrotron radiation (SR) sources. The combination of synchrotron x-ray topography and optical microscopy succeeded in shedding light on the elucidation of the origin and transformation of dislocations and stacking faults (Tsuchida et al., 2007). The highly coherent beams allowed to analyze dislocation types and structures (Nakamura et al., 2007; Wierzchowski et al., 2007), the Burgers vectors senses and

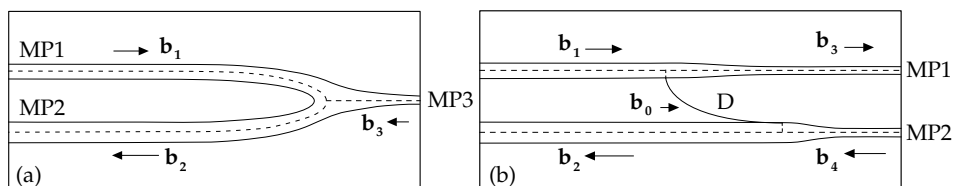


Fig. 1. Sketch of the contact (a) and contact-free (b) reactions between micropipes MP1 and MP2 in a longitudinal section of growing SiC crystal. (a) The micropipes contain superscrew dislocations with opposite Burgers vectors \mathbf{b}_1 and \mathbf{b}_2 . The micropipes meet each other and react, forming a new micropipe MP3 that contains a superscrew dislocation with the sum Burgers vector $\mathbf{b}_3 = \mathbf{b}_1 + \mathbf{b}_2$. (b) The micropipes contain superscrew dislocations with opposite Burgers vectors \mathbf{b}_1 and \mathbf{b}_2 . Micropipe MP1 emits a half-loop of full-core dislocation D with Burgers vector \mathbf{b}_0 . As a result, the Burgers vector of MP1 changes from \mathbf{b}_1 to $\mathbf{b}_3 = \mathbf{b}_1 - \mathbf{b}_0$, and the radius of MP1 decreases. Dislocation D glides from MP1 to MP2; the frontal (top) segment of D is absorbed by MP2. Micropipe MP2 changes its Burgers vector from \mathbf{b}_2 to $\mathbf{b}_4 = \mathbf{b}_2 + \mathbf{b}_0$, and, as a consequence, also decreases its radius.

magnitudes (Chen et al., 2008; Nakamura et al., 2008), and the propagation and distribution of threading dislocations (Kamata et al., 2009) in detail.

A decisive advantage of third generation SR sources is the availability of phase contrast imaging which has a strong potential for studying hollow defects in SiC. To image objects with relatively small cross sections, such as micropipes, high temporal coherence is not necessary; and the spatial coherence required is directly yielded by SR source. In this work, we briefly survey the results of white beam phase contrast imaging to investigate the reactions of micropipes in SiC. We also give a short review of their experimental characterization, theoretical modeling, and computer simulation. The improvement of the crystal quality enabled us to develop our research from the collective effects in dense groups of micropipes to remote interactions between distant micropipes. The morphology of individual micropipe, which was not resolvable by diffraction topography, has been examined by phase-contrast imaging. The computer simulation of phase contrast images allowed us to determine the cross-section sizes of micropipes (Kohn et al., 2007).

In our experimental studies, different transformations and reactions between micropipes in SiC crystals have been documented: ramification of a dislocated micropipe into two smaller ones (Gutkin et al., 2002); bundling and merging that led to the generation of new micropipes or annihilation of initial ones (Gutkin et al., 2003a;b); and interaction of micropipes with foreign polytype inclusions (Gutkin et al., 2006) followed by agglomeration and coalescence of micropipes into pores (Gutkin et al., 2009b).

Theoretical analyses of micropipes interactions show that micropipe split happens if the splitting dislocation overcomes the pipe attraction zone and the crystal surface attraction zone; bundling and twisting of dislocation dipoles arise when two micropipes are under strong stress fields from dense groups of other micropipes; micropipes are attracted by foreign polytype inclusion stress fields, initiating the nucleation and growth of pore on the inclusion. When micropipes come in contact with each other [Fig. 1(a)], strong interactions occur. Such interactions are expected to become less probable for low micropipe densities. In the meanwhile, remote elastic interactions between dislocations were detected and known to govern the propagation of elementary screw dislocations (Nakamura et al., 2008). In our study we experimentally measured the variation in cross-sections of two neighboring micropipes and revealed that they reduced their diameters (approximately by half) one after another

	Spectrum	Effective size, μm	Divergence, μrad	Source-sample
Source	6–40 keV	160(H) \times 60(V)	5(H) \times 2(V)	34 m
	Sensitivity	Matrix size, px	View field, (H)	CCD-sample
Detector	14 bit	1600(H) \times 1200(V)	4 mm–280 μm	5 cm–1 m

Table 1. Source and detector attributes for x-ray imaging

during the crystal growth (Gutkin et al., 2008). This ‘contact-free’ reaction between two micropipes, MP1 and MP2, as illustrated in Fig. 1(b), is different with a ‘contact’ reaction [Fig. 1(a)]. Here MP1 and MP2 contain opposite-sign superscrew dislocations with Burgers vectors \mathbf{b}_1 and \mathbf{b}_2 , respectively.

In the ‘contact’ reaction, the elastic attraction of the two opposite dislocations induces the gradual shift of the two micropipes to each other during the crystal growth, resulting in the formation of a new micropipe MP3 containing a new superscrew dislocation with the sum Burgers vector $\mathbf{b}_3 = \mathbf{b}_1 + \mathbf{b}_2$, $b_3 < (b_1, b_2)$, where b_i is the Burgers vector magnitude, $i = 1, 2, 3$. As the micropipe radius is in the quadratic dependence on its Burgers vector magnitude (Frank, 1951), the profit of this reaction is evident: instead of two micropipes we get only one with a much smaller radius. In the special case of $b_3 = b_0$, where b_0 is the Burgers vector magnitude of the elemental full-core dislocation, micropipe MP3 is normally healed.

In case of a contact-free interaction micropipe MP1 emits a full-core dislocation half-loop D, which expands by gliding, reaches the surface of micropipe MP2 and reacts with its dislocation. The corresponding dislocation reactions are described by equations: $\mathbf{b}_1 - \mathbf{b}_0 = \mathbf{b}_3$ and $\mathbf{b}_2 + \mathbf{b}_0 = \mathbf{b}_4$, where \mathbf{b}_3 and \mathbf{b}_4 are the Burgers vectors of micropipes MP1 and MP2, respectively. This reaction explains the radii reduction of both micropipes by the emission of the full-core dislocation in MP1 and its absorption in MP2. Strong reduction in the radii can lead to their gradual healing.

Reaction between micropipes is always a positive process in view of their elimination during the crystal growth. Therefore, one should better understand the mechanisms of reactions and the factors stimulating such reactions. In our studies, micropipes are assumed to be screw dislocations with hollow cores (Huang et al., 1999), as made certain by combining phase contrast and bragg-diffraction imaging.

2. Samples and techniques

SiC crystals were grown by the sublimation sandwich method. In this technique Si-C vapor species brought from the source (polycrystalline SiC powder) are sublimated on the seed (a crystalline SiC wafer). The source and the seed are separated by a small distance and put into the growth container with an axial temperature gradient. To improve the quality of SiC crystals, a tantalum container was used (Vodakov et al., 1997). The container was filled with Ar (the Ar pressure: 80 mbar). The growth temperature was 2180° C, and the growth rate was 0.5 mm \times h⁻¹. Polytype inclusions were studied by using n-type crystals N-doped, with a donor concentration 2×10^{18} cm⁻³. They contained B to a concentration $(1-2) \times 10^{17}$ cm⁻³. Besides, doping of SiC by Al to a concentration of approximately $(2-7) \times 10^{17}$ cm⁻³ occurred because of the presence of Al in the polycrystalline SiC source. The samples were on-axis wafers cut perpendicular to the [0001] growth direction and axial-cut slices along the growth direction obtained from 4H and 6H boules. The wafers were polished from the both sides down to ≈ 0.4 mm thick.

X-ray imaging experiments were performed on the 7B2 X-ray Microscopy beamline at the Pohang Light Source (PLS) in Pohang, Korea. The source was the 7B2 bending magnet port of the PLS storage ring. Unmonochromatized ('white') beam was propagated through polished beryllium window of 2 mm thick and then through a specimen with no optical elements in between. Passing through a CdWO_4 scintillator crystal of 200 μm thick, the X-ray beam was converted to visible lights, which were then reflected from a mirror (a polished silicon wafer) and directed to a detector with a charge coupled device (CCD) matrix. The source and the detector attributes are listed in table 1. Prior to recording, the visible light image was magnified by a lens system with the magnification $1 \times -50 \times$. Under a low magnification [for example, by using 1500 μm (H) view field] the overall defect density and distribution were visualized. The $\approx 300 \mu\text{m}$ (H) view field provided a very useful enlargement for the examination of micropipes. Optical micrographs were taken on a Zeiss universal microscope equipped with a CCD. Scanning electron microscopy was done on a JEOL JSM-6330F FESEM operating at 12 kV. Photoluminescence (PL) images of polytype inclusions were taken with the PL microscope in visible as well as ultraviolet lights under the magnifications of $50 \times -200 \times$.

3. Contact-free reactions between micropipes

3.1 Model

Let us turn back to Fig. 1(b) sketching the contact-free reaction between two micropipes. Direct experimental justifications of this mechanism has not been provided up to now. However, using computer simulation of phase contrast images (Kohn et al., 2007), we have demonstrated the correlated reduction in the radii of two remote micropipes in SiC (Gutkin et al., 2008). As shown below, this effect indirectly supports our model.

The first stage of the contact-free reaction is the split of a dislocation from a micropipe at the crystal growth front. Recently the possibility of such a split event has been analyzed within a three-dimensional model (Gutkin & Sheinerman, 2004). Here we consider a simplified two-dimensional model of a contact-free reaction between two parallel micropipes. Fig. 2 shows micropipes with circular cross sections of the radii r_1 and r_2 that contain screw dislocations with the Burgers vectors \mathbf{b}_1 and \mathbf{b}_2 , respectively. The distance between the micropipe axes is denoted as d . Let the first micropipe emits a screw full-core dislocation with the Burgers vector \mathbf{b}_0 [Fig. 2(a)]. We also assume that a shear stress $\tau^0 = \tau_{yz}^0$ associated with thermal stresses appearing during the growth of SiC acts in the region between the examined micropipes and far from their surfaces. To analyze the possibility of the emission, we can use the corresponding variation ΔW on the total energy of the system. It is calculated (per unit dislocation length) using the previous results (Gutkin & Sheinerman, 2002; Gutkin et al., 2009c) for the stresses and energies of dislocations lying in an isotropic medium with two cylindrical voids. However, in the case of interest, when $d \gg r_1, r_2$, it is sufficient to separately consider the effects of the two voids on the shear stress as well as on the image force exerted by the micropipe surfaces on the emitted dislocation and the forces of dislocation interaction. In this approximation, the thermal shear stress τ_{yz} acting on the emitted dislocation in between the micropipes, taken with account for the stress concentration near their surfaces, is $\tau_{yz} = \tau^0 [1 + r_1^2/x^2 + r_2^2/(d-x)^2]$, where x is the coordinate of the emitted dislocation. The second and third terms in brackets reflect the effects of the first and second void (Thölen, 1970), respectively, in the limiting case $d \gg r_1, r_2$ when the mutual influence of the voids is negligible. The total elastic force acting on the emitted dislocation (per its unit length) follows

as

$$F(d \gg r_1, r_2) \approx b_0 \tau_{yz} \quad (1)$$

$$+ \frac{Gb_0}{2\pi} \left\{ \frac{b_1 - b_0}{x} - \frac{b_2}{d - x} + \frac{b_0}{x} - \frac{b_0 x}{x^2 - r_1^2} - \frac{b_0}{d - x} + \frac{b_0(d - x)}{(d - x)^2 - r_2^2} \right\},$$

where G is the shear modulus. In brackets of formula (1), the first and second terms correspond to the interactions of the emitted dislocation with dislocations within micropipes MP1 and MP2, respectively; the third-fourth and fifth-sixth terms correspond to the image force (Gutkin & Sheinerman, 2002; Pirouz, 1998) exerted by the surface of MP1 and MP2, respectively.

The energy ΔW associated with dislocation emission is given by $\Delta W = \int_{r_1}^{x-b_0} F(x)dx + W_c$, where $W_c \approx Gb_0^2/(4\pi)$ is the dislocation core energy (Hirth & Lothe, 1982). Substitution of (1) to the latter relation for ΔW yields:

$$\Delta W = b_0 \tau^0 \left(x - \frac{r_1^2}{x} + \frac{r_2^2}{d - x} - \frac{r_2^2}{d - r_1} \right) \quad (2)$$

$$+ \frac{Gb_0^2}{4\pi} \left\{ 1 + \ln \frac{(x^2 - r_1^2)[(d - x)^2 - r_2^2]}{b_0 r_1 (d - x)^2} + \frac{2b_1}{b_0} \ln \frac{r_1}{x} + \frac{2b_2}{b_0} \ln \frac{d}{d - x} \right\}.$$

In the following calculations, we will use the Frank relation (Frank, 1951) $r_i = Gb_i^2/(\pi\gamma)$ between the Burgers vectors magnitudes b_i and micropipe radii r_i , where γ is the surface energy. Numerical evaluation of ΔW for the case of growing 4H-SiC crystal with $G = 165$ GPa, $\gamma/G = 1.4 \cdot 10^{-3}$ nm (Si et al., 1997) and equilibrium micropipes [for which the Frank relation (Frank, 1951) is valid] shows that ΔW depends primarily on the Burgers vectors of micropipe dislocations and on the level of thermal shear stress τ_0 [Fig. 2(b,c)].

Let us first consider the case when $\tau^0 = 0$ [Fig. 2(b)]. As is seen, the dislocation exchange is most energetically favorable if the Burgers vectors \mathbf{b}_1 and \mathbf{b}_2 are opposite in sign. At the same time, to move from one micropipe to the other, the emitted dislocation must overcome an energetic barrier. If the Burgers vectors of the two micropipes are of the same sign, the emitted dislocation must overcome two energetic barriers on its way from one micropipe to the other. In this case, the possibility for the dislocation exchange between these micropipes is governed by the difference of the Burgers vector magnitudes. If $(b_1 - b_2) < 3b_0$, then we have: $\Delta W > 0$, and the dislocation exchange is impossible. If $(b_1 - b_2 \geq 3b_0)$, then the dislocation reaction can occur if the emitted dislocation is able to overcome the two energetic barriers. The presence of two energetic barriers results in the appearance of an equilibrium position for the emitted dislocation, situated in between the micropipes.

Figure 2(c) shows the case where micropipes initially have the same Burgers vectors, equal in magnitude to $7b_0$, and the dislocation emission occurs under the action of a thermal shear stress τ^0 . One can see that the stress τ^0 reduces the energetic barriers for the dislocation exchange. In the range of stress values from 10 to 100 MPa, which are characteristic for bulk SiC growth (Ma et al., 2003; Müller et al., 2000), the first barrier decreases weakly while the second one strongly. The first barrier has the height of about $1.5Gb_0^2/\pi$ per unit dislocation length, which for a 4H-SiC crystal with $G = 165$ GPa and $b_0 = 1$ nm gives $\approx 0.48Gb_0^2l \approx 125$ eV per unit distance $l \approx 0.252$ nm (Dudley et al., 2003) between basal atomic planes. This value is obviously very high that is not surprising due to the model of an infinite medium considered within the classical theory of linear elasticity. Moreover, in reality, the dislocation

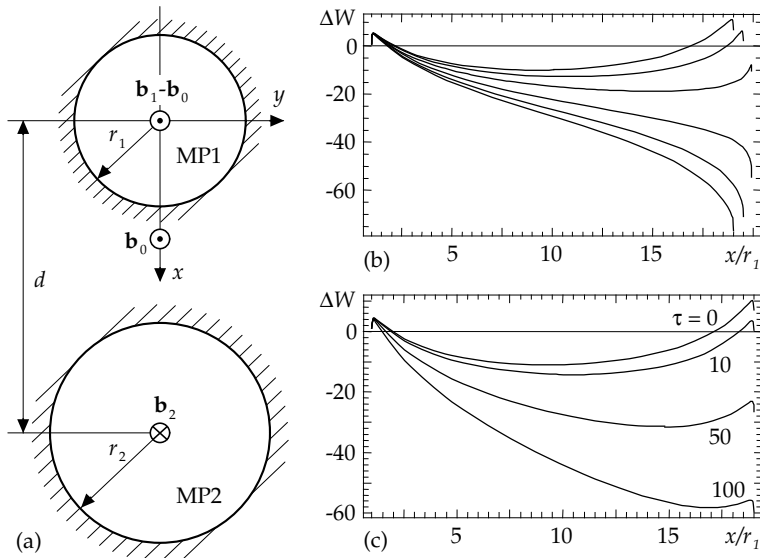


Fig. 2. A model of contact-free reaction between two micropipes realized through screw dislocation exchange. Micropipe MP1 emits a dislocation with the Burgers vector \mathbf{b}_0 , which moves to micropipe MP2 and is absorbed by it (a). Dependences of the energy ΔW associated with the emission of a dislocation by a micropipe near a second micropipe on the normalized dislocation coordinate x/r_1 for $d/r_1 = 20$ and $b_1/b_0 = 7$. (b) $\tau^0 = 0$ and $b_2/b_0 = -7, -5, -2, 2, 5, 7$ (from bottom to top). (c) $b_2/b_0 = 7$ and $\tau^0 = 0, 10, 50$, and 100 MPa. The energy ΔW is given in units of $Gb_0^2/4\pi$, the stress values are given at the curves in MPa.

emission is expected to occur within a rather thin subsurface layer under the growth front where the conditions can be very far from equilibrium due to high temperature and surface effects. The height of the second barrier is approximately five times higher at $\tau^0 = 0$ but it falls down to $\approx 0.16Gb_0^2l$ at $\tau^0 = 100$ MPa. The equilibrium position of the emitted dislocation increases from $\approx 9r_1$ at $\tau^0 = 0$ to $\approx 17r_1$ at $\tau^0 = 100$ MPa. One can conclude that thermal shear stress greatly promotes dislocation transfer and makes it possible even in the case of micropipes having large Burgers vectors of the same sign.

3.2 Correlated reduction in micropipe cross sections in SiC growth

To observe micropipe cross-sections at different distances from the surface of a grown crystal, we prepared a special sample, which was axial-cut slice along the growth direction (0001) obtained from 4H-SiC boule. So micropipes located almost parallel to the growth axis were nearly parallel to the surface. Micropipes grouped along the boundaries of foreign polytype inclusions (6H and 12R) which appeared at ≈ 1 cm distance from the seed/boule interface. Below the inclusions over the area of 1 cm^2 micropipes were undetectable. The sample (rotated to have a horizontal position of the micropipe axis for better edge enhancement in a more coherent vertical direction) was sequentially placed at different distances from the detector. We obtained nine images for the distances from 5 to 45 cm starting with the first image registered at 5 cm from the sample. Three micropipes forming a group were examined: two in contact and the third lying remotely. The variation in cross-section sizes along the axes of MP1 and MP2 from the group are shown in Fig. 3(a), while phase contrast image of the

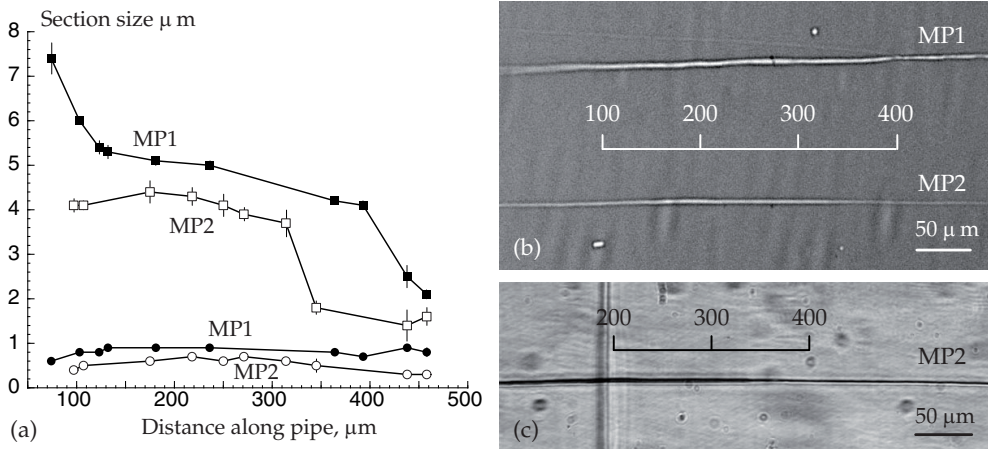


Fig. 3. (a) Variation in cross-section sizes along the axes of MP1 and MP2 from the group of micropipes (squares – transverse and circles – longitudinal diameters, respectively); (b) phase contrast image of the group (the growth direction is from left to right); (c) optical micrograph in transmission light of MP2 lying remotely from two micropipes in contact.

group and the optical micrograph of the remote micropipe MP2 are demonstrated in (b) and (c), respectively.

For all sample-to-detector distances and for different points along the axis of micropipes, the intensity profiles normal to the axis were measured. To determine the characteristic sizes of the micropipe cross sections in different points along the micropipe axis, we applied a computer simulation (Kohn et al., 2007) of the measured intensity profiles, assuming that these sections can have variations in longitudinal (along the beam) and transverse (across the beam) sizes. For every micropipe cross section under investigation, the computer program calculated many profiles for various possible section sizes on the base of Kirchhoff propagation (Kohn et al., 2007) to find the profile, which gives the best fit to the experimental profile registered for this section. The coincidence allowed us to determine both the longitudinal and transverse sizes of the section. We found that the micropipes had elliptical cross sections extended in transverse direction. The transverse and longitudinal diameters of micropipes MP1 and MP2 are presented in Fig. 3(a) versus the distance along the pipe axes increasing in the growth direction. It is seen that, with growth, the transverse size of MP1 reduces from 7.4 to 2.1 μm . At the same time, the transverse size of the MP2 reduces from 4.1 to 1.6 μm . In contrast, the longitudinal diameters remain almost the same and of the order of 0.8 μm for the MP1 and 0.5 μm for the MP2. In the correlated decrease of MP1 and MP2 cross section sizes in Fig. 3(b) several features are apparent. A remarkable decrease of the MP1 cross section size occurs in the distance interval from 74 to 132 μm while the transverse diameter of MP2 drastically decreases later in the distance interval from 314 to 345 μm . In addition, a rapid decrease of the transverse diameter of MP1 happens in the distance interval from 393 to 458 μm when the transverse diameter of MP2 remains almost invariable.

We explain the changes in the cross sections of the two neighboring micropipes by the contact-free reaction between them. Experimental data in Fig. 3(a,b) tend to confirm the reaction schematically shown in Fig. 1(b). Most likely, during the rapid decrease of its cross section area MP1 emits a full-core dislocation moving towards MP2 and finally absorbed by it.

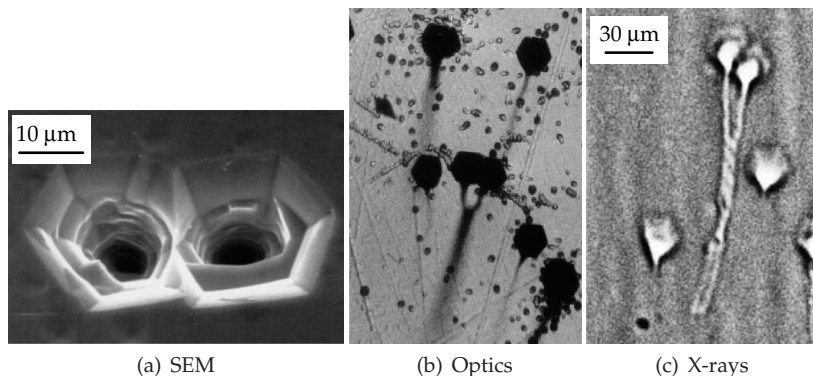


Fig. 4. (a) SEM image of a ramified micropipe; (b) transmission light microscopy image of the same micropipe; (c) SR phase-contrast image of another ramified configuration.

For a new possible mechanism of the contact-free reactions between micropipes, our calculations have demonstrated that, depending on the signs of the micropipe Burgers vectors (prior to dislocation exchange between micropipes), the moving dislocation must overcome one or two energetic barriers. In the case where the initial micropipe Burgers vectors are of the same sign, the dislocation exchange can happen only if the difference between the micropipe Burgers vector magnitudes is large enough (not less than three magnitudes of the elementary Burgers vector). The energetic barrier(s) that the dislocation has to surmount on its way from one micropipe to the other can supposedly be overcome under the growth front where the conditions can be very far from equilibrium due to high temperature and surface effects. Correlated reduction in micropipe cross-sections indirectly supports our suggestion that micropipes can interact each other without a direct contact, by the proposed mechanism.

4. Elastic interaction and split of micropipes

4.1 Ramification of micropipes

Three imaging techniques: SEM, optical microscopy, and x-ray phase contrast imaging were applied to study the split of micropipes. The SiC samples were on-axis wafers cut perpendicular to the [0001] growth direction, and the ends of screw dislocations with Burgers vector aligned along the [0001] axis were visible on the etched (0001) surface. A typical SEM image of a ramified dislocation with a hollow core is shown in Fig. 4(a), and Fig. 4(b) is a transmission light image of the same configuration. However, SEM is insensitive and light microscopy is limitedly suited for the detection of micropipes in the wafer interior. By using the phase contrast imaging [Fig. 4(c)] ramified micropipes were clearly detected in the bulk, and the numbers of single and ramified ones within each view field were calculated. It appeared that the density of nearby single dislocations as well as the presence of dislocation boundaries did not influence the number of ramified micropipes. Their distribution over the wafer area was almost homogeneous with an average density of two per each view field, the latter being $0.6 \times 0.4 \text{ mm}^2$.

Let us determine when a dislocated micropipe is favorable to split into a pair of parallel micropipes with smaller radii and Burgers vectors. For the sake of simplicity, we focus on the case when the angle between ramifying segments of the micropipe "tree" is small enough to allow one to model these segments as a pair of parallel micropipes extending through the entire crystal.

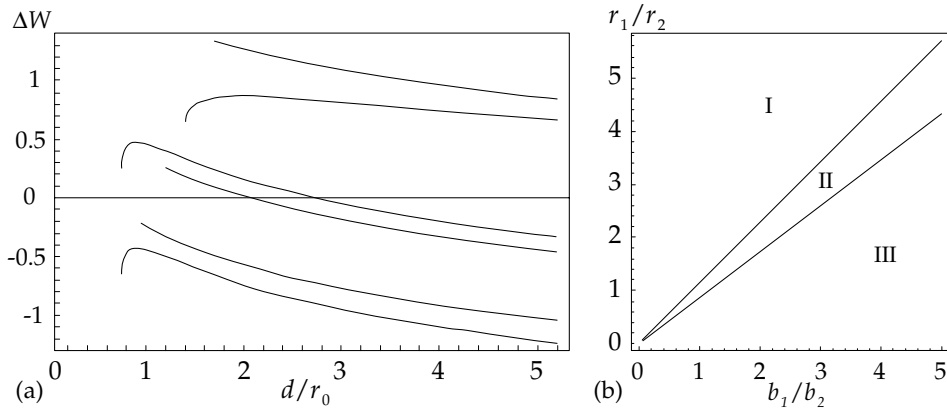


Fig. 5. (a) The dependences of ΔW [in units of $Gb_0^2/(4\pi)$] on the normalized distance d/r_0 between the micropipe axes, for the following values of parameters: $(\tilde{r}_1 = 0.05, \tilde{r}_2 = \tilde{b}_1 = 0.5, \kappa = 3)$, $(\tilde{r}_1 = 0.3, \tilde{r}_2 = 0.45, \tilde{b}_1 = 0.4, \kappa = 3)$, $(\tilde{r}_1 = \tilde{r}_2 = \tilde{b}_1 = 0.5, \kappa = 1)$, $(\tilde{r}_1 = 0.05, \tilde{r}_2 = \tilde{b}_1 = 0.5, \kappa = 1)$, $(\tilde{r}_1 = 0.3, \tilde{r}_2 = \tilde{b}_1 = 0.8, \kappa = 3)$, and $(\tilde{r}_1 = 0.6, \tilde{r}_2 = 0.9, \tilde{b}_1 = 0.4, \kappa = 3)$, from bottom to top. (b) The system state diagram in the coordinate space $(b_1/b_2, r_1/r_2)$. The curves separate parameter regions I and III, where both attraction area and unstable equilibrium position exist for two micropipes, from parameter region II, where the micropipes repulse at any distance.

The crystal is modeled as an isotropic medium with the shear modulus G and specific surface energy γ . Let the radius and the Burgers vector of the micropipe prior to the split be r_0 and $\mathbf{b}_0 = b_0 \mathbf{e}_z$ while the radii and the Burgers vectors of two micropipes generated due to the split be r_1, r_2 and $\mathbf{b}_1 = b_1 \mathbf{e}_z, \mathbf{b}_2 = b_2 \mathbf{e}_z$, respectively. The distance between the micropipe axes is denoted by d while that between the micropipe free surfaces is designated by h ($h = d - r_1 - r_2$). We suppose that the micropipe ramification is possible if the energy of two growing ramifying micropipe segments (per their unit length) is smaller than the energy of the original micropipe (per its unit length). Also, we assume that the micropipe ramification requires the repulsion of the ramifying segments. To find the conditions for the split we have calculated the energy change due to the split of a micropipe into two contacting ones and the interaction force between two parallel micropipes (Gutkin et al., 2002). The energy ΔW resulting from the micropipe split is shown in Fig. 5(a). It is presented in units of $Gb_0^2/(4\pi)$ in dependence on the normalized distance d/r_0 between the micropipe axes for different values of the parameters $\tilde{r}_1 = r_1/r_0, \tilde{r}_2 = r_2/r_0, \tilde{b}_1 = b_1/b_0$, and $\kappa = 8\pi^2\gamma r_0/(Gb_0^2)$. As is seen in Fig. 5(a), ΔW either monotonously decreases with d or has a maximum. In the first case, the micropipes formed due to the split repulse at any distance. If the curve ΔW has a maximum, the micropipes repulse at any distance greater than some critical distance d_c and attract each other at distances smaller than d_c . In this case, the micropipes separation requires overcoming an energetic barrier.

It is important to note that the reverse process of the micropipe merging may follow the micropipe split. Indeed, the split may be possible only on account of the reduction in the total micropipe surface area. If the micropipes formed due to the split stay in contact, they are energetically favored to coalesce and produce a single micropipe with a radius close enough to the equilibrium one. In this case, the split and following coalescence of the micropipes results only in a decrease in the micropipe radius, that is, in its partial overgrowth. We suppose that the merging of the micropipe segments generated after the split does not occur if these

segments repulse as soon as they have been formed. As is shown above [see Fig. 5(a)], the micropipes may either repulse at any distance or repulse at distances d greater than the critical distance d_c and attract each other at $d < d_c$. The ramification of the micropipe segments (not followed by their coalescence) is possible if they repulse at any distance or the critical distance d_c [and the corresponding energy barrier $W(d = d_c) - W(d = r_1 + r_2 + a)$ that the micropipes have to overcome to go outside of the attraction area] is small enough.

Now let us determine the parameter region where the ramifying micropipe segments (modeled as a pair of parallel micropipes) repulse at any distance. This parameter region is shown in Fig. 5(b) that depicts the system state diagram in the coordinate space $(b_1/b_2, r_1/r_2)$. The upper and lower curves separate regions I and III, where the micropipes attract each other at short distances while they repel each other at long distances, and the corresponding critical distance $h_c = d_c - r_1 - r_2$ between the micropipe free surfaces exists, from region II, where the micropipes repulse at any distance. As is seen, an attraction area may exist for two same-sign micropipes if b_1/b_2 and r_1/r_2 differ by more than 15%–25%.

The parameter region where the micropipe ramification does not require overcoming an energetic barrier is given by the intersection of the corresponding parameter regions shown in Fig. 5(a, b). Such a ramification is possible if the micropipes are of the same sign, the radius of the original micropipe exceeds the equilibrium one, the total micropipe surface area reduces due to the ramification, and the radii of the ramifying micropipes are approximately in the same ratio as the magnitudes of their dislocation Burgers vectors.

4.2 Merging and twisting of micropipes

Many morphologies of twisted and coalesced micropipes have been observed experimentally in SiC crystals by means of x-ray phase contrast imaging. The examples of twisted configurations are shown in Figs. 6(a) and 7(a). To explain these phenomena, we have

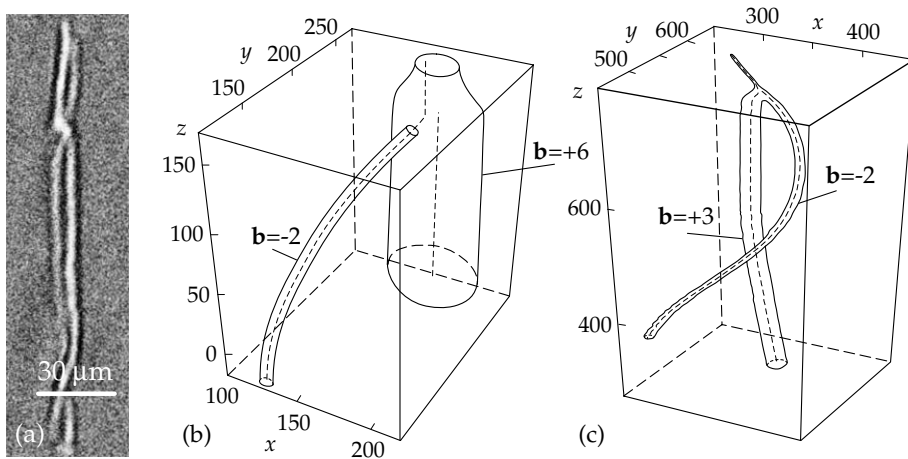


Fig. 6. SR phase-contrast image of micropipe twisting (a); coalescence of micropipes with different magnitudes of Burgers vectors results in the generation of a new micropipe segment (b, c). The coalescing micropipes come to each other along the shortest way (b) or twist (c). The Burgers vectors are shown in units of c , which is the lattice parameter in the growth direction. The coordinates x and y are given in units of $Gc^2/(8\pi^2\gamma)$. The length of micropipes (along the z axes) is in arbitrary units that depend on the growth rate.

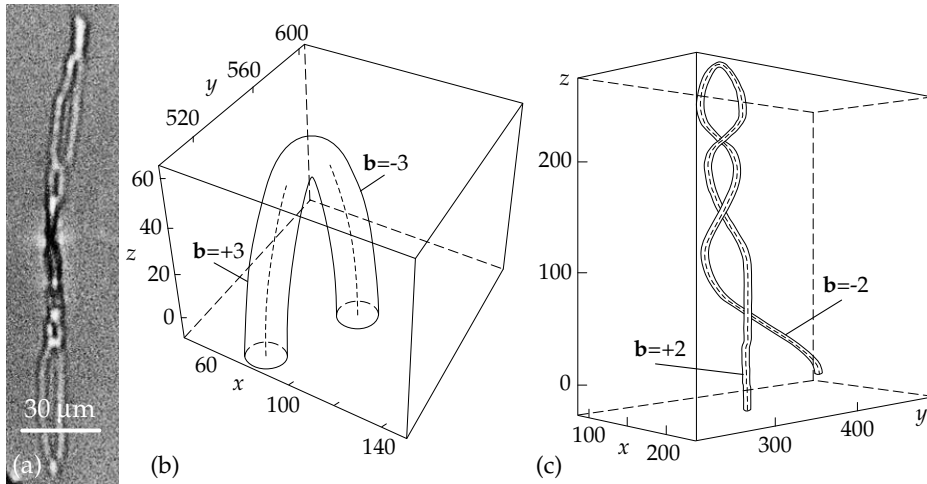


Fig. 7. SR phase-contrast image of semi-loops resulting from macropipes twisting (a); coalescence of micropipes with equal magnitudes of Burgers vectors results in the annihilation of the subsurface micropipe segments (b, c). The coalescing micropipes come to each other along the shortest way (b) or twist (c). For the units see the caption to Fig. 6.

performed a computer simulation of micropipe evolution (Gutkin et al., 2003a;b). For computer modeling, a simple computer code has been elaborated to simulate 2D dynamics of pipes within Newton's approach. We considered the lateral motion of subsurface micropipe segments. The equations of the motion of subsurface micropipe segments had the form:

$$m_k \mathbf{a}_k = \frac{Gb_k}{2\pi} \sum_{i \neq k} b_i \left(\sqrt{h^2/r_{ik}^2 + 1} - 1 \right) \mathbf{e}_{ik} - 4\gamma R_k \mathbf{e}_k, \quad (3)$$

where k denotes the number of a specified micropipes, i denotes the numbers of other micropipes, \mathbf{a}_k is the micropipe segment acceleration, m_k is its effective mass, R_k is its radius, G is the shear modulus, b_k is the projection of the micropipe dislocation Burgers vector onto the direction of the dislocation line, h is the height of subsurface micropipe segments, γ is the specific surface energy, r_{ik} is the distance between the i th and k th micropipes, \mathbf{e}_{ik} is the unit vector directed from the i th to the k th micropipe, and \mathbf{e}_k is the unit vector whose direction coincides with the direction of the lateral micropipe motion. The first term on the right-hand side of formula (3) describes the total force of the interaction of the k -th micropipe with other micropipes, while the second term specifies the force of surface tension related to the steps appearing on micropipe cylindrical surfaces during lateral displacements of micropipe segments.

As a result of the simulation, various reactions between the subsurface micropipe segments were observed. It has been shown that the reaction of micropipe coalescence gives rise to the generation of new micropipes with smaller diameters and Burgers vectors or annihilation of initial micropipes (see Figs. 6,7), which leads to diminishing their average density. Using the results of 2D simulation, we reconstructed some typical defect configurations in a 3D space. They may be subdivided into planar and twisted micropipe configurations. The planar configurations arise when the interacting pair of micropipes has incomparable diameters or is located far (at the distance of more than about 5 average micropipe diameters) from other

micropipes. The twisted configurations like double spirals form if the interacting micropipes have comparable diameters and are located within dense groups of other micropipes.

5. Role of micropipes in the formation of pores at foreign polytype boundaries

5.1 Interaction of micropipes with polytype inclusions

SR phase contrast imaging, optical and scanning electron microscopies, and color photoluminescence have been used to study the interaction of micropipes with foreign polytype inclusions in 4H-SiC bulk crystals. The boules had been grown on carbon-terminated faces of the 6H-SiC seeds by the sublimation sandwich method in Ar atmosphere and in the presence of Sn vapor. The Sn vapor promotes the transformation of the polytype of the substrate into 4H-SiC (Vodakov et al., 1997). Several wafers were cut from 4H-SiC boules. One wafer, 0.4 mm thick and misoriented 8° away from the basal plane, was further cut into 0.5 mm wide bars. X-ray experiment was performed in two regimes: (1) via the translation of the wafer to map micropipe distributions over the area and (2) via the rotation of the bar samples to reveal the spatial orientations of macro- and micropores. In the latter case, the rotation axis was perpendicular to the beam and parallel to the long edges of the bar. The rotation interval was 180° with a 2° step. The images were recorded in a step by step sequence.

Figure 8(a) shows SEM image of a typical pore located at the boundary of a foreign polytype inclusion. The pore uncovers a slit on a molten KOH treated surface. Figure 8(b) displays the illumination of the inclusion itself excited by an ultraviolet light at room temperature. When the inclusion is located close to the wafer surface, its polytype can be easily identified by the color of PL. In low N doped samples at room temperature, 6H polytype inclusions have yellow PLs (Saparin et al., 1997). A sketch of the inclusion, pore, and micropipes is shown in Fig. 8(c).

For the purposes of the model, it is important to find a way by which micropipes accumulate at the inclusions. Figure 9 shows several representative phase-contrast images registered while rotating the sample in the SR beam. The sample had the shape of a bar. In the image, a relatively thick micropipe [indicated as MP1 on Fig. 9(b)] follows the growth direction, while the much thinner (and therefore much more mobile) MP2 inclines towards the inclusion boundary. On the other hand, the thick MP3 also bends towards the inclusion, and its surface becomes steplike. MP4 revolves about MP5, which follows the growth direction. The inset in (c) displays twisted micropipes turning to another inclusion of 6H-SiC in the same crystal.

Earlier, the reactions of micropipes — twisting and bundling — were discussed in terms of the stress fields from the other surrounding micropipes. (Gutkin et al., 2003a;b). However, in this study, stress fields seem to result from the inclusions. The remarkable deviation from the growth direction, the transformation of shape, and the reactions of micropipes prove that they are strongly influenced by the inclusions. Attracted by the inclusions, micropipes collect into

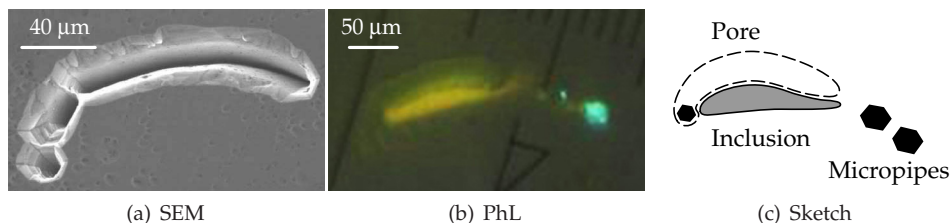


Fig. 8. (a) SEM image of the pore. (b) PL image of the inclusion. (c) Sketch of the inclusion, the pore, and the micropipes.

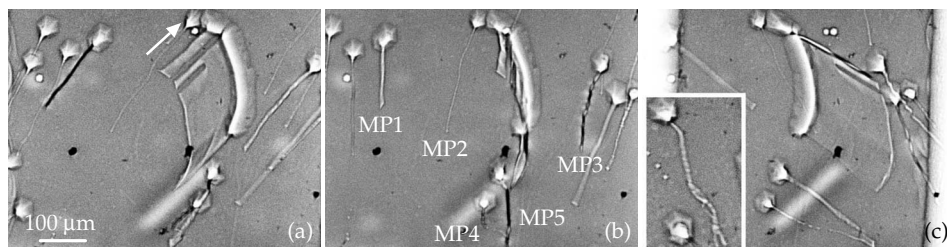


Fig. 9. Representative phase contrast images among the sequences of the images registered while rotating the sample, (a)–(c) show the same region as Fig. 8, the inset in (c) displays the image of twisted micropipe recorded at another place in the same sample, and the growth direction is indicated in (a) by an arrow. The elongated white spot is a defect of the scintillator.

bundles at the inclusion boundaries. This phenomenon was observed throughout this crystal and other similar crystals. The gathering of micropipes is followed by the reduction of their density in the neighboring regions.

The observations were interpreted based on the following model (Gutkin et al., 2006). At the boundaries of the other polytypes inclusions the lattice mismatch should exist that gives rise to essential elastic deformation, whose orientational constituent relaxes with the formation of micropipes. At the sites of micropipe accumulation, micropipes elastically interact, which leads to the merge of several micropipes with the generation of cavities along the inclusion boundaries. As a result, the misfit stresses completely relax. Due to the action of image forces, the free surfaces of the cavities thus formed attract new micropipes and, absorbing them, propagate along the inclusion boundaries.

5.2 Pore growth by micropipe absorption at foreign polytype boundaries

In the previous section we outlined the results of the elastic interaction of micropipes with polytype inclusions. In this section the processes of micropipe accumulation and their coalescence into a pore is discussed. The pores generated in this way may grow at the expense of absorbed micropipes.

We have observed that pores of different sizes and shapes are always present at the boundaries of foreign polytype inclusions in SiC samples under study. Figure 10 illustrates the representative morphology of a typical pore in a 4H-SiC wafer. Comparison of the phase-contrast image [Fig. 10(a)] with the PL image [Fig. 10(b)] clearly shows that pores are located along the inclusion boundaries as sketched in Fig. 10(c). The slit pore (1) surrounds one of the inclusion edges, while tubular pores (2)–(5) are located at the inclusion corners. Pore shape reflects a stage in its development. The pore nucleation is initiated as a tube form by initial accumulation of some micropipes near the inclusion boundary. In the process of sequential attraction and absorption of new micropipes, the pore shape changes and step by step transforms into a slit, which can then propagate along the inclusion boundary.

Images of another wafer cut of the same 4H-SiC boule are shown in Fig. 11. The SEM image [(Fig. 11(a)] represents etch pits of not only pores, but also micropipes, which appear as faceted pits on the top of the tubes. We see that pores are produced by agglomeration of micropipes. The PL dark green image displayed in the inset to (a) represents a 21R-SiC inclusion in the 4H-SiC wafer. [At room temperature, n-type 6H and 4H polytypes containing N and B show yellow and light green PL, respectively, while Al activated luminescence for rhombohedral 21R polytype taken at 77 K is dark green (Saparin et al., 1997).] The marked pores are located at

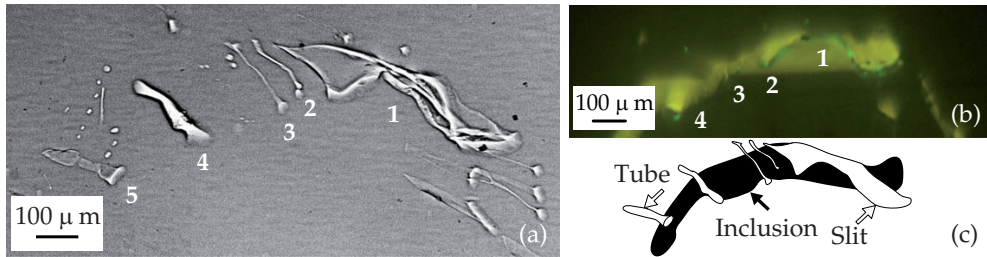


Fig. 10. Pores and micropipes at the boundary of 6H-SiC inclusion in 4H-SiC wafer. (a) SR phase-contrast image. (b) PL image. (c) The sketch outlines the inclusion and the pores as indicated by the black and white arrows, respectively. The number 1 points to a slit pore and the numbers 2–5 to tubular pores.

the edge of the left (concave) inclusion as defined in Fig. 11(c). The pores spread over the inclusion boundary and propagate deeply inside the wafer. The phase-contrast image [Fig. 4(b)] also reveals that the pores are produced through the coalescence of micropipes. The observed micropipes remarkably deviate from the growth direction, which we attribute to the interaction of micropipes with the polytype inclusion.

Mapping with a lower magnification revealed a significant reduction in micropipe density nearby to the pores, which can be explained by the absorption of micropipes by the pores.

The following scenario for pore growth is suggested, as is illustrated by the sketch in Fig. 12. At the beginning, a few neighboring micropipes are attracted to an inclusion with no pore to accommodate the orientation mismatch between the inclusion and the matrix crystalline lattices [Fig. 12(a)] (Gutkin et al., 2006; 2009b). This orientation mismatch is described mathematically through the components of the inclusion plastic distortions (Gutkin et al., 2006). In the case of two nonvanishing plastic distortion components, micropipes are attracted to a corner of the inclusion [Figs. 12(a) and 12(b)], where they have an equilibrium position (Gutkin et al., 2006; 2009b). Let the first micropipe occupy its equilibrium position at this corner [Fig. 12(b)]. Then another micropipe, containing a dislocation of the same sign as the first micropipe, is attracted by the inclusion to the same equilibrium position. If the inclusion is "powerful" enough (that is the plastic distortions are large), the attraction force exerted by

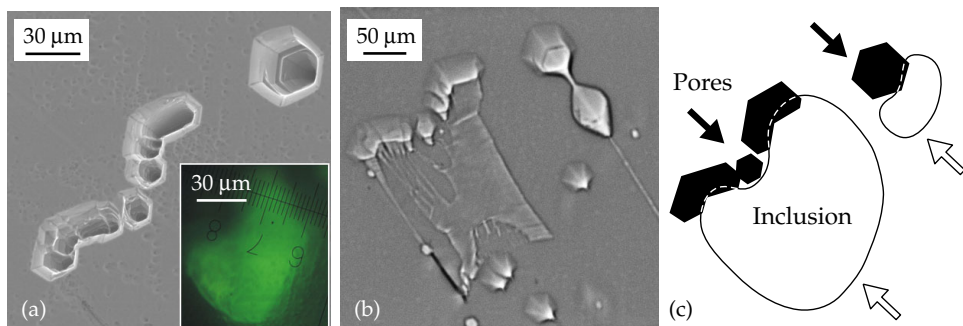


Fig. 11. Agglomeration of micropipes into the pores at the boundary of a 21R-SiC inclusion in the 4H-SiC wafer. (a) SEM image of the pore. Inset shows PL image of the 21R-SiC inclusion. (b) SR phase-contrast image reveals merging of micropipes into slit pores in the wafer interior. (c) Sketch of the inclusion and the pores.

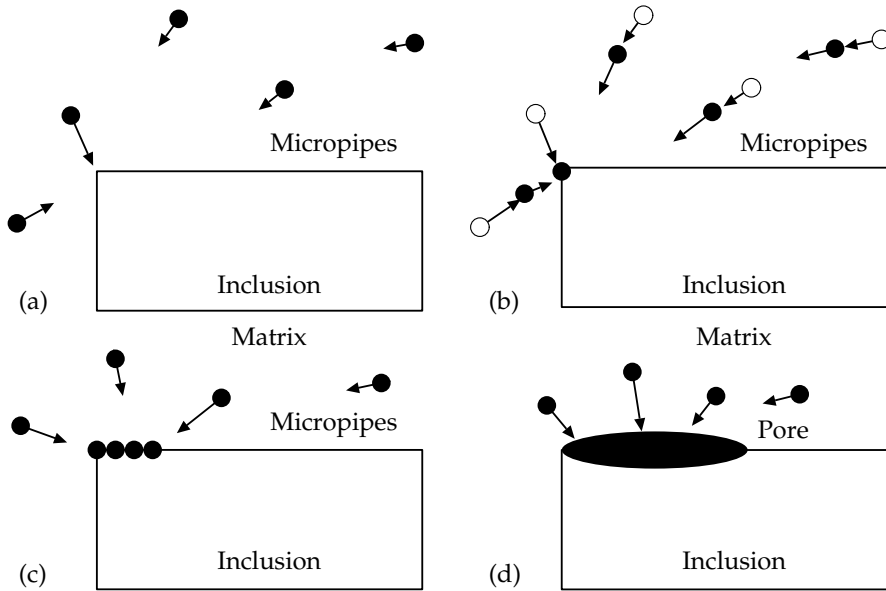


Fig. 12. Scheme of nucleation and extension of a pore at the inclusion/matrix interface through agglomeration of micropipes. (a) Micropipes are attracted to their equilibrium positions at a corner of the inclusion. (b) The first micropipe occupies its equilibrium position at the corner; the others come closer to it. (c) Some micropipes are agglomerated at the corner and form a pore; the others are attracted both to the corner and to the free surface of the pore. (d) The pore propagates along the inclusion/matrix interface by absorption of close micropipes.

the inclusion and the free surface of the first micropipe is stronger than the repulsion force between micropipe dislocations, and so the second micropipe merges with the first one. Some of such micropipes, which have been attracted to this corner [Fig. 12(c)], agglomerate and form a pore. After the pore has been formed, some other micropipes move to the same equilibrium position at the inclusion boundary and are absorbed by the pore [Fig. 12(d)], resulting in the pore growth and the change of the dislocation charge accumulated at the boundary. This process continues until the pore occupies the entire inclusion facet or until the pore size becomes so large that the inclusion stops to attract new micropipes.

To analyze the conditions at which pore growth along a foreign polytype inclusion at the expense of micropipes absorbed is favored, we suggest a two-dimensional (2D) model of the inclusion, pore and micropipes. Within the model, the inclusion is infinitely long and has a rectangular cross-section (Fig. 13). The long inclusion axis (z -axis) is oriented along the crystal growth direction while the inclusion cross-section occupies the region ($x_1 < x < x_2$, $y_1 < y < 0$). The mismatch of the matrix and the inclusion crystal lattices is characterized by the inclusion plastic distortions β_{xz} and β_{yz} (Gutkin et al., 2006). The inclusion/matrix interface contains an elliptic pore, and mobile micropipes lie nearby. The pore is assumed to grow at the expense of micropipes absorbed (Fig. 12). For definiteness, we suppose that the pore is symmetric with respect to the upper inclusion facet $y=0$. The pore semiaxes are denoted as p and q , and the pore surface is defined by the equation $x^2/p^2 + y^2/q^2 = 1$.

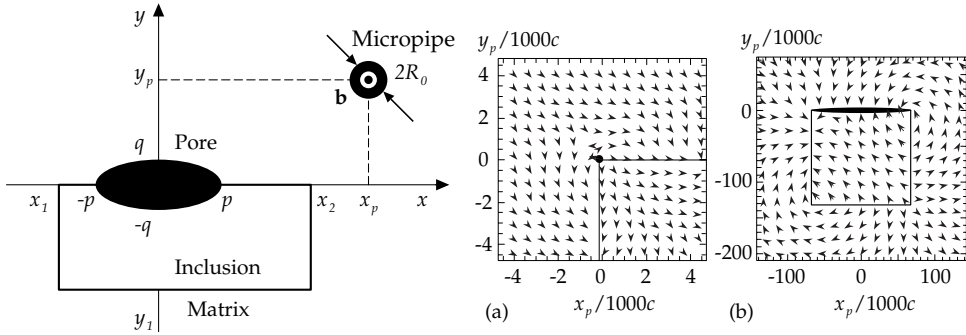


Fig. 13. Elliptic pore at the inclusion boundary and a mobile micropipe nearby.

Fig. 14. Vector fields of the force F exerted by a 4H-SiC inclusion (containing a pore on its boundary) in a 6H-SiC matrix on a mobile micropipe with the magnitude $4c$ of the dislocation Burgers vector. (a) The inclusion plastic distortion components are equal and very small, $\beta_{xz} = \beta_{yz} = 5 \times 10^{-4}$, and the inclusion contains only one micropipe at the corner. (b) The inclusion plastic distortion components are equal and very large, $\beta_{xz} = \beta_{yz} = 0.05$, and the inclusion contains a dislocated elliptic pore which is produced by the coalescence of 306 micropipes and occupies the whole inclusion facet. The arrows show the force directions, and their length is proportional to the force magnitude.

For simplicity, in the following analysis we presume that all micropipes attracted to the inclusion boundary have the same Burgers vectors \mathbf{b} and the same radii R_0 (Fig. 13). The micropipe radius R_0 is supposed to be related to its Burgers vector magnitude b by the Frank relation (Frank, 1951) $R_0 = Gb^2/(8\pi^2\gamma)$, where G is the shear modulus and γ is the specific surface energy. Also, the pore is assumed to grow in such a way that one of its semi-axes q is constant and equal to the micropipe radius R_0 ($q = R_0$), while the other semi-axis p increases. The volume of the elliptic pore is supposed to be equal to the total volume of the micropipes that merge to form the pore. The free volume conservation equation $\pi p q = N \pi R_0^2$ (where N is the number of micropipes agglomerated into the pore) along with the relation $q = R_0$ gives the following expression for the larger pore semi-axis p : $p = N R_0$.

To analyze the conditions for pore growth, we have calculated the force $\mathbf{F} = F_x \mathbf{e}_x + F_y \mathbf{e}_y$ exerted on a micropipe by the inclusion containing the pore. To do so, we have neglected the short-range effect of the micropipe free surface and considered the micropipe as a screw dislocation with the Burgers vector \mathbf{b} and coordinates (x_p, y_p) (Fig. 13). The inclusion stress field has been calculated by integrating the stresses of virtual screw dislocations distributed over inclusion facets, with the density determined by the value of the corresponding component of inclusion plastic distortion. To account for the influence of the elliptic pore, we have used the solution for a screw dislocation near an elliptic pore (Zhang & Li, 1991) in the calculation of the stress field of an individual virtual dislocation. The same solution was used to separately account for micropipe attraction to the free surface of the elliptic pore. The calculation scheme used to cast the quantities F_x and F_y is described in (Gutkin et al., 2009b). As an example, in the following analysis, we consider a 4H-SiC inclusion in the 6H-SiC matrix. We assume that the inclusion has the square cross-section with the facet dimension of $200 \mu\text{m}$ and put $\gamma/G = 1.4 \times 10^{-3} \text{ nm}$ (Si et al., 1997). The magnitude of the micropipe dislocation Burgers vector is chosen to take the values of $4c$, where $c \approx 1 \text{ nm}$ is the 4H-SiC lattice parameter (Goldberg et al., 2001).

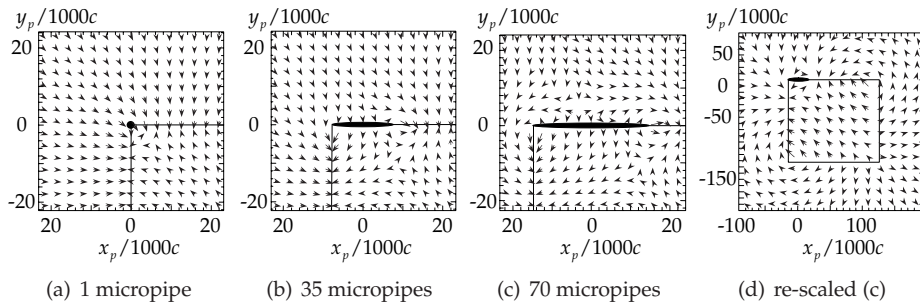


Fig. 15. Vector fields of the force F exerted by a $4H$ -SiC inclusion (containing a pore on its boundary) in a $6H$ -SiC matrix on a mobile micropipe with the magnitude $4c$ of the dislocation Burgers vector, for $\beta_{xz} = \beta_{yz} = 5 \times 10^{-3}$. (a) One micropipe lies at the inclusion corner, and another one is attracted to the same place. (b) 35 micropipes merge into the pore, which still attracts new micropipes. (c) 70 micropipes merge into the pore, and the latter starts to repulse new micropipes. (d) Figure (c) in a smaller scale. The arrows show the force directions, and their length is proportional to the force magnitude.

Consider pore growth in the case of equal plastic distortions $\beta_{xz} = \beta_{yz} = \beta$. Figures 14(a) and 14(b) show the final pore configurations when β is very small and very large, respectively. If β is very small (here we take $\beta = 5 \times 10^{-4}$), only one micropipe is attracted to its equilibrium position at the inclusion corner [Fig. 14(a)]. The following micropipes attracted to the inclusion boundary will come to new equilibrium positions at the inclusion boundary far away from the corner. As a result, micropipes do not merge into a larger pore. In contrast, if β is very large (here $\beta = 0.05$), the following micropipes come first to the corner and further to the growing pore. In this case, the pore can occupy the whole inclusion facet, which is illustrated in Fig. 14(b).

The process of pore growth in the intermediate case (here $\beta = 5 \times 10^{-3}$) is shown step by step in Fig. 15. Initially, the first micropipe is attracted to its equilibrium position at the inclusion corner [Fig. 15(a)]. Then new micropipes are attracted to the same equilibrium position and merge, thereby forming a pore. When the pore is not too large, the value of inclusion plastic distortion is sufficient for the pore to attract new micropipes. This case is illustrated in Fig. 15(b), which shows the force vector field (acting on micropipes) around the pore that has absorbed 35 micropipes. However, the situation drastically changes when the pore size becomes large enough [Fig. 15(c)]. Although in this situation a micropipe attraction region still exists near the pore surface, the force on the micropipe is repulsive at some distance from the pore, and the micropipe cannot approach the pore. Under the action of the force field, the micropipe has to round the pore and come to a new equilibrium position at the inclusion boundary far from the pore. The presence of a new equilibrium position for new micropipes is clearly seen in Fig. 15(d), which represents Fig. 15(c) in a smaller scale.

Thus, the analysis of the forces exerted on micropipes by the inclusion and elliptic pore has shown that the pore attracts micropipes until their number reaches a critical value. After that, the micropipes absorbed by the pore produce a repulsion zone for new micropipes, and pore growth stops. The critical pore size is determined by the values of inclusion plastic distortions. At their small values, isolated micropipes form at the inclusion/matrix interface; at medium values micropipes coalesce to form a pore of a certain size; at large values the pore occupies the whole inclusion boundary.

6. Summary

We have briefly reviewed our recent experimental and theoretical studies of collective behavior of micropipes during the bulk SiC growth. The micropipes grow up with the propagation of the crystal growth front and come into reactions with each other as well as with other structural imperfections like foreign polytype inclusions and pores. The reactions between micropipes are either contact-free or contact. A contact-free reaction occurs when one micropipe emits a full-core dislocation, while another micropipe accepts it. We have theoretically described the conditions necessary for such a reaction and provided its indirect experimental evidence. As to contact reactions, we have experimentally documented different transformations and reactions between micropipes in SiC crystal, such as ramification of a dislocated micropipe into two smaller ones, bundling and merging that led to the generation of new micropipes or annihilation of initial ones, interaction of micropipes with foreign polytype inclusions followed by agglomeration and coalescence of micropipes into pores. Theoretical analyses of each configuration have shown that micropipe split happens if the splitting dislocation overcomes the pipe attraction zone and the crystal surface attraction zone. Bundles and twisted dislocation dipoles arise when two micropipes are under strong influence of the stress fields from dense groups of other micropipes. Foreign polytype inclusions attract micropipes due to the action of inclusion stress fields. The micropipe absorption by a pore that has been nucleated at the boundary of inclusion depends on the inclusion distortion. The pore growth stops when the pore absorbs a critical amount of micropipes or occupies the whole inclusion boundary. The general issue is that any kind of the above reactions is quite desired because they always lead to micropipe healing and/or cleaning the corresponding crystal areas from micropipes. Moreover, the contact-free reactions can be treated as a mechanism of thermal stress relaxation, while the micropipe interaction with foreign polytype inclusions and accumulation on their boundaries is a mechanism of misfit stress accommodation.

7. Acknowledgements

This work was supported by the Creative Research Initiatives (Functional X-ray Imaging) of MEST/NRF of Korea. Support of the Russian Foundation of Basic Research (Grant No 10-02-00047-a) is also acknowledged.

8. References

- Chen, Y. ; Dudley, M.; Sanchez, E. K.; Macmillan, M. F. (2008). Simulation of grazing-incidence synchrotron white beam X-ray topographic images of micropipes in 4H-SiC and determination of their dislocation senses. *J. Electron. Mater.*, Vol. 37, No. 5, 713–720, ISSN: 0361-5235.
- Dudley, M.; Huang, X.-R.; Vetter, W. M. (2003) Contribution of x-ray topography and high-resolution diffraction to the study of defects in SiC. *J. Phys. D: Appl. Phys.*, Vol. 36, No. 10A, A30–36, ISSN 0022-3727.
- Epelbaum, B. M. & Hofmann, D. (2001). On the mechanisms of micropipe and macrodefect transformation in SiC during liquid phase treatment . *J. Cryst. Growth*, Vol. 225, 1–5, ISSN: 0022-0248.
- Frank, F. C. (1951). Capillary equilibria of dislocated crystals. *Acta Crystallogr.*, Vol. 4, 497–501, ISSN: 0108-7673.
- Goldberg, A.; Levinstein, M. E.; Rumyantsev, S. L. (2001). In: *Properties of Advanced Semiconductor Materials GaN, AlN, InN, BN, SiC, SiGe*, Levinstein, M. E.; Rumyantsev, S. L.; Shur, M. S. (Eds.), 93, Wiley, New York.

- Gutkin, M. Yu.; Sheinerman, A. G.; Argunova, T. S.; Je, J.-H.; Kang, H.-S.; Hwu, Y.; Tsai, W.-L. (2002). Ramification of micropipes in SiC crystals. *J. Appl. Phys.*, Vol. 92, No. 2, 889–894, ISSN 0021-8979.
- Gutkin, M. Yu. & Sheinerman, A. G. (2002). Elastic Interaction of Micropipes in Crystals. *Physica Status Solidi B*, Vol. 231, No. 2, 356–372, ISSN: 1521-3951.
- Gutkin, M. Yu.; Sheinerman, A. G.; Argunova, T. S.; Mokhov, E. N.; Je, J.-H.; Hwu, Y.; Tsai, W.-L.; Margaritondo, G. (2003). Micropipe evolution in silicon carbide. *Appl. Phys. Lett.*, Vol. 83, No. 11, 2157–2159, ISSN 0003-6951.
- Gutkin, M. Yu.; Sheinerman, A. G.; Argunova, T. S.; Mokhov, E. N.; Je, J.-H.; Hwu, Y.; Tsai, W.-L.; Margaritondo, G. (2003). Synchrotron radiographic study and computer simulation of reactions between micropipes in silicon carbide. *J. Appl. Phys.*, Vol. 94, No. 11, 7076–7082, ISSN 0021-8979.
- Gutkin, M. Yu. & Sheinerman, A. G. (2004). Split and sealing of dislocated pipes at the front of a growing crystal. *Physica Status Solidi B*, Vol. 241, No. 8, 1810–1826, ISSN: 1521-3951.
- Gutkin, M. Yu.; Sheinerman, A. G.; Argunova, T. S.; Yi, J.-M.; Kim, M.-U.; Je, J.-H.; Nagalyuk, S. S.; Mokhov, E. N.; Margaritondo, G.; Hwu, Y. (2006). Interaction of micropipes with foreign polytype inclusions in SiC. *J. Appl. Phys.*, Vol. 100, 093518 (10 pp.), ISSN 0021-8979.
- Gutkin, M. Yu.; Sheinerman, A. G.; Smirnov, M. A.; Kohn, V. G.; Argunova, T. S.; Je, J.-H.; Jung, J.-W. (2008). Correlated reduction in micropipe cross sections in SiC growth. *Appl. Phys. Lett.*, Vol. 93, 151905 (3 pp.), ISSN 0003-6951.
- Gutkin, M. Yu.; Sheinerman, A. G.; Argunova, T. S. (2009). Micropipes in silicon carbide crystals. *Phys. Stat. Sol. C*, Vol. 6, No. 8, 1942–1947, ISSN: 1610-1642.
- Gutkin, M. Yu.; Sheinerman, A. G.; Smirnov, M. A.; Argunova, T. S.; Je, J.-H.; Nagalyuk, S. S.; Mokhov, E. N. (2009). Micropipe absorption mechanism of pore growth at foreign polytype boundaries in SiC crystals. *J. Appl. Phys.*, Vol. 106, 123515 (7 pp.), ISSN 0021-8979.
- Gutkin, M. Yu.; Sheinerman, A. G.; Smirnov, M. A. (2009). Elastic behavior of screw dislocations in porous solids. *Mech. Mater.*, Vol. 41, No. 8, 905–918, ISSN: 0167-6636.
- Hirth, J. P. & Lothe, J. (1982). *Theory of Dislocations*, Wiley, New York.
- Huang, X. R.; Dudley, M.; Vetter, W. M.; Huang, W.; Wang, S. (1999). Direct evidence of micropipe-related pure superscrew dislocations in SiC. *Appl. Phys. Lett.*, Vol. 74, No. 3; 353–355, ISSN 0003-6951.
- Kamata, I.; Tsuchida, H.; Jikimoto, T.; Izumi, K. (2000). Structural transformations of screw dislocations via thick 4H-SiC epitaxial overgrowth. *Jpn. J. Appl. Phys.*, Vol. 39, No. 12A, 6496–6500, ISSN 0021-4922.
- Kamata, I.; Nagano, M.; Tsuchida, H.; Chen, Y.; Dudley, M. (2009). Investigation of character and spatial distribution of threading edge dislocations in 4H-SiC epilayers by high-resolution topography. *J. Cryst. Growth*, Vol. 311, 1416–1422, ISSN: 0022-0248.
- Kohn, V. G.; Argunova, T. S.; Je, J.-H. (2007). Study of micropipe structure in SiC by x-ray phase contrast imaging. *Appl. Phys. Lett.*, Vol. 91, 171901 (3 pp.), ISSN 0003-6951.
- Ma, R.-H.; Zhang, H.; Dudley, M.; Prasad, V. (2003). Thermal system design and dislocation reduction for growth of wide band gap crystals: application to SiC growth. *J. Cryst. Growth*, Vol. 258, No. 3–4, 318–330. ISSN: 0022-0248.
- Ma, X. (2006). Superscrew dislocations in silicon carbide: Dissociation, aggregation, and formation. *J. Appl. Phys.*, Vol. 99, 063513 (6 pp.), ISSN 0021-8979.
- Müller, St. G.; Glass, R. C.; Hobgood, H. McD.; Tsvetkov, V. F.; Brady, M.; Henshall, D.; Jenny, J. R.; Malta, D.; Carter Jr., C. H. (2000). The status of SiC bulk growth from an industrial point of view. *J. Cryst. Growth*, Vol. 211, No. 1–4, 325–332, ISSN: 0022-0248.

- Müller, St. G.; Brady, M. F.; Burk, A. A.; Hobgood, H. McD; Jenny, J. R.; Leonard, R. T.; Malta, D. P.; Powell, A. R.; Sumakeris, J. J.; Tsvetkov, V. F.; Carter Jr., C. H. (2006). Large area SiC substrates and epitaxial layers for high power semiconductor devices - An industrial perspective. *Superlattices Microst.*, Vol. 40, 195–200, ISSN: 0749-6036.
- Nakamura, D.; Gunjishima, I.; Yamaguchi, S.; Ito, T.; Okamoto, A.; Kondo, H.; Onda, S.; Takatori K. (2004). Ultrahigh-quality silicon carbide single crystals. *Let. Nature*, Vol. 430, 1009–1012, ISSN: 0028-0836.
- Nakamura, D.; Yamaguchi, S.; Gunjishima, I.; Hirose, Y.; Kimoto T. (2007). Topographic study of dislocation structure in hexagonal SiC single crystals with low dislocation density. *J. Cryst. Growth*, Vol. 304, 57–63, ISSN: 0022-0248.
- Nakamura, D.; Yamaguchi, S.; Hirose, Y.; Tani, T.; Takatori, K.; Kajiwara, K.; Kimoto T. (2008). Direct determination of Burgers vector sense and magnitude of elementary dislocations by synchrotron white x-ray topography. *J. Appl. Phys.*, Vol. 103, 013510 (7 pp.), ISSN 0021-8979.
- Ohtani, N.; Katsuno, M.; Tsuge, H.; Fujimoto, T.; Nakabayashi, M.; Yashiro, H.; Sawamura, M.; Aigo, T.; Hoshino T. (2006). Propagation behavior of threading dislocations during physical vapor transport growth of silicon carbide (SiC) single crystals. *J. Cryst. Growth*, Vol. 286, 55–60, ISSN: 0022-0248.
- Pirouz, P. (1998). On micropipes and nanopipes in SiC and GaN. *Philos. Mag. A*, Vol. 78, No. 3, 727–736, ISSN: 1478-6435.
- Saparin, G. V.; Obyden, S. K.; Ivannikov, P. V.; Shishkin, E. B.; Mokhov, E. N.; Roenkov, A. D.; Hofmann, D. H. (1997). Three-Dimensional Studies of SiC Polytype Transformations. *Scanning*, Vol. 19, 269–274, ISSN: 1932-8745.
- Si, W.; Dudley, M.; Glass, R.; Tsvetkov, V.; Carter Jr., C. (1997). Hollow-core screw dislocations in 6H-SiC single crystals: A test of Frank's theory. *J. Electron. Mater.*, Vol. 26, No. 3, 128–133, ISSN: 0361-5235.
- Thölén, A. R. (1970). The stress field of a pile-up of screw dislocations at a cylindrical inclusion. *Acta Metall.*, Vol. 18, No. 4, 445–455, ISSN: 1359-6454
- Tsuchida, H.; Kamata, I.; Nagano M. (2007). Investigation of defect formation in 4H-SiC epitaxial growth by X-ray topography and defect selective etching. *J. Cryst. Growth*, Vol. 306, 254–261, ISSN: 0022-0248.
- Vodakov, Yu. A.; Roenkov, A. D.; Ramm, M. G.; Mokhov, E. N.; Makarov, Yu. N. (1997). Use of Ta-container for sublimation growth and doping of SiC bulk crystals and epitaxial layers. *Phys. Status Solidi B*, Vol. 202, 177–200, ISSN: 1521-3951.
- Wang, Y.; Ali, G. N.; Mikhov, M. K.; Vaidyanathan, V.; Skromme, B. J.; Raghothamachar, B.; Dudley, M. (2005). Correlation between morphological defects, electron beam-induced current imaging, and the electrical properties of 4H-SiC Schottky diodes. *J. Appl. Phys.*, Vol. 97, 013540 (10 pp.), ISSN 0021-8979.
- Wierzchowski, W.; Wieteska, K.; Balcer, T.; Malinowska, A.; Graeff, W.; Hofman, W. (2007). Observation of individual dislocations in 6H and 4H-SiC by means of back-reflection methods of X-ray diffraction topography. *Cryst. Res. Technol.*, Vol. 42, No. 12, 1359–1363, ISSN: 0232-1300.
- Yakimova, R.; Vouroutzis, N.; Syväjärvi, M.; Stoemenos, J. (2005). Morphological features related to micropipe closing in 4H-SiC. *J. Appl. Phys.*, Vol. 98, 034905 (6 pp.), ISSN 0021-8979.
- Zhang, T.-Y. & Li, J. C. M. (1991). Image forces and shielding effects of a screw dislocation near a finite-length crack. *Mater. Sci. and Eng. A*, Vol. 142, No. 1, 35–39, ISSN: 0921-5093.

Thermal Oxidation of Silicon Carbide (SiC) – Experimentally Observed Facts

Sanjeev Kumar Gupta and Jamil Akhtar

*Central Electronics Engineering Research Institute (CEERI)/ Council of Scientific and Industrial Research (CSIR)
India*

1. Introduction

The thin thermally grown SiO_2 plays a unique role in device fabrication of Si-VLSI Technology. The well established growth mechanisms and continuous research to grow high quality SiO_2 on Si substrate has to lead the development of planner-Technology and permits the fabrication of well defined diffused or ion-implanted junctions of precisely controllable dimensions. Among the all wide bandgap semiconductors, Silicon Carbide (SiC) is the only compound semiconductor which can be thermally oxidized in the form of SiO_2 , similar to the silicon growth mechanism. This means that the devices which can be easily fabricated on Si substrate (Power MOSFET, IGBT, MOS controlled thyristor etc.) can also be fabricated on SiC substrate. Moreover, a good knowledge of SiO_2/Si interface has been established and has to lead great progress in Silicon-Technology that can be directly applied to development of SiC-Technology.

Similar to the Silicon-Technology, high quality thin SiO_2 is most demanded gate oxide from the SiC based semiconductor industries to reduce the cost and process steps in device fabrication. Various oxidation processes has been adopted such as dry oxidation [1], wet oxidation [2], chemical vapour deposition (CVD) [3], and pyrogenic oxidation [4-6] in order to achieve the most suitable process to realize the SiC-based MOS structures. To develop the basic growth mechanism of SiO_2 on SiC surfaces apart from the Si growth mechanisms, worldwide numbers of researchers are intensively working on the above specified problems. Since SiC is a compound material of Si and C atoms, that is why the role of C atoms during the thermal growth of SiO_2 has been observed to be very crucial. Several studies [7-9] confirm the presence of C species in the thermally grown oxide, which directly affect the interface as well as dielectric properties of metal-oxide-semiconductor structures [10]. For this reason, rigorous studies on electrical behavior of thermally grown SiO_2 on SiC play a fundamental role in the understanding and control of electrical characteristics of SiC-based devices. It has been reported that the growth rate of SiC polytypes is much lower than that of Si [11-13]. The rate of reaction on the surface of SiC is much slower than that of Si under the same oxidation conditions. In case of SiC, another unique phenomenon has been observed that the oxidation of SiC is a face terminated oxidation, means the both polar faces (Si and C face) have different oxidation rates [14-15]. These oxidation rates are also depend on the crystal orientation of SiC and polytypes i.e. Silicon carbide shows an anisotropic oxidation nature.

2. Specification of used 4H-SiC substrate

The availability of the right kind of material has put a restriction for the fabrication of semiconductor devices. There are limited sources where single crystalline SiC substrate is available. At present, the most known firm is M/s CREE Research Inc USA, which is known worldwide for the supply of basic SiC substrates in 2" or larger diameter sizes. In this reported work n-type 4H-SiC material was the obvious selection with maximum possible epitaxy layer (50 μm) on Si-face with lowest possible doping. Accordingly, CREE Research Inc. USA supplied the following structure on a 2" diameter wafer. Figure 1 (a) shows the schematic details of used 4H-SiC substrate and (b) shows the 2" wafer hold by tweezers showing optical transparency by looking at carrier holder through the wafer.

3. Kinetics of thermal oxidation

3.1 Thermal oxidation setup

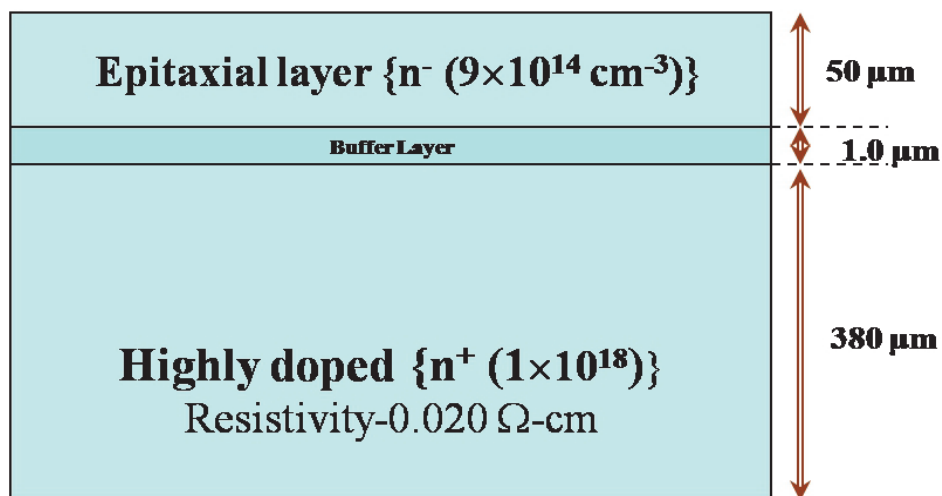
Thermal oxidation is the proficient process in VLSI technology which is generally carried out in oxidation furnace (or diffusion furnace, since oxidation is basically based on the diffusion mechanism of oxidizing agent) that provides the sufficient heat needed to elevate the oxidizing ambient temperature. The furnace which was used for thermal growth of SiO_2 on 4H-SiC is typically consisted of:

1. a fool proof cabinet
2. a heating assembly
3. a fused quartz horizontal process tubes where the wafers undergo oxidation
4. a digital temperature controller and measurement system
5. a system of gas flow meter for monitoring involved gases into and out of the process tubes and
6. a loading station used for loading (or unloading) wafers into (or from) the process tubes as shown in figure 2.

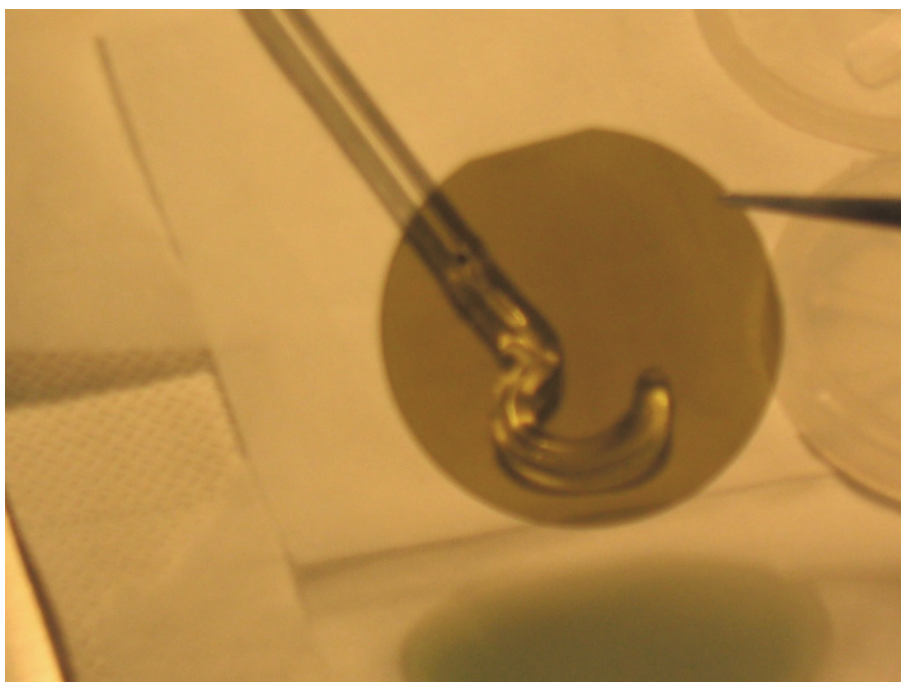
The heating assembly usually consists of several heating coils that control the temperature around the furnace quartz tube. There are three different zones in the quartz tube i.e. left, right and center. The temperature of both end zones (left and right) was fixed at $400^\circ\text{C} \pm 50^\circ\text{C}$ throughout the process. For the ramp up and ramp down of furnace temperature, there are three digital control systems for all three zones. The furnace consists of two different gas pipe lines, one is for N_2 gas and other is for dry/wet O_2 gas. To control the gas flow, there are MATHESON'S gas flow controllers. A quartz bubbler has been used to generate the steam using highly pure DI-water. There is a temperature controller called heating mental to control the temperature of bubbler. Wet oxygen as well as dry oxygen or dry nitrogen has been passed through a quartz nozzle to the quartz furnace tube.

3.2 Sample preparation

The cleaning procedure, which is generally used in Si-Technology, has been adopted for this work. All chemicals used in wet-chemical procedure were MOS grade. The wafers were treated for all three major chemical cleaning procedures i.e. Degreasing, RCA and Piranha. Degreasing has three conjugative cleaning steps. First, the wafers were dipped in 1, 1, 1-Trichloroethane (TCE) and boiled for ten minutes to remove the grease on the surface of wafers. Second, the wafers were dipped in acetone and boiled for ten minutes, to remove



(a)



(b)

Fig. 1. (a) Schematic details of 4H-SiC substrate which was used and (b) A 2" diameter 4H-SiC wafer hold by tweezers showing optical transparency by looking at carrier holder through the wafer

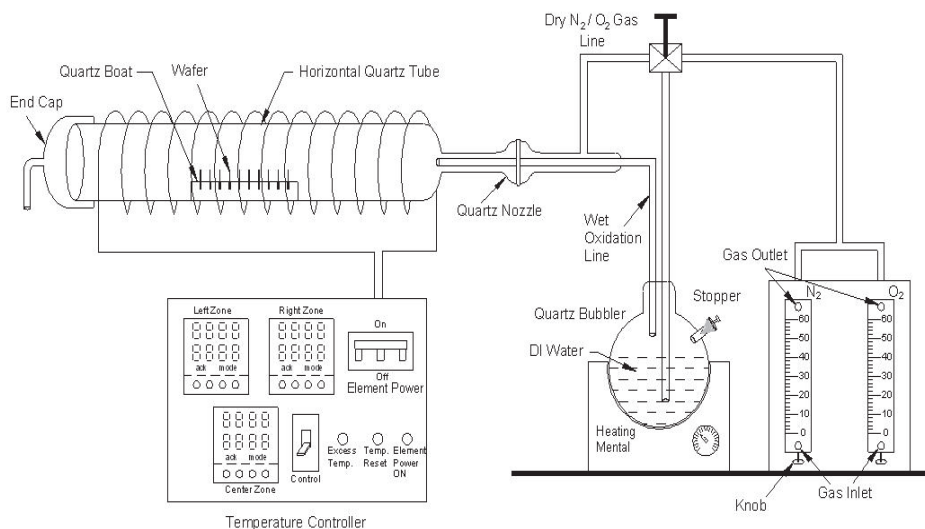


Fig. 2. Schematic diagram of horizontal oxidation furnace

light metal ions. Third, the wafers were dipped in methanol and boiled for ten minutes. Then the wafers were rinsed in de-ionized (DI) water. Subsequently, the standard Radio Corporation of America (RCA) cleaning procedure was followed. This process consisted of two stages, which is termed as standard cleaning-1 (SC-1) and SC-2. In SC-1, the wafers were dipped in high pH alkaline mixture (NH₄OH, H₂O₂ and DI-water) in the ratio of (1:1:5) at some temperature for 10 minutes. There are three main purpose of SC-1: (1) to remove the organic substances on the 4H-SiC wafer surface due to wet oxidation effect, (2) to expose the surface so that any trace metals can be desorbed, and (3) to enable hydrous oxide film to form and dissolve continuously. After SC-1, the wafers were thoroughly ringed in DI-water and then dipped in 10% hydrofluoric (HF) acid for one minute to etch off any remaining SiO₂ (native oxide). The SC-2 consisted of a mixture of (HCl, H₂O₂ and DI-water) in the ratio of (1:1:6). The wafers were dipped in the mixture for 10 minutes at some temperature followed by thoroughly ringed in DI-water and native oxide removal using 10% HF solution. The SC-2 cleaning process could able to dissolve alkali ions, water insoluble hydro oxide compounds and any dual trace metals that was unable to disrobe by SC-1. The last cleaning treatment is known as Piranha cleaning. The piranha solution consisted of a mixture of (H₂SO₄ and H₂O₂) in the ratio of (7:1). Then wafers are dipped in this solution for 15 minutes to remove any heavy metal resident on the wafer surface. Finally, the wafers were thoroughly rinsed in DI- water which, is followed by 10% HF dip.

3.3 Oxidation methodology

Thermal oxidation process was divided into six groups of different temperature range starting from 1050°C to 1150°C for different oxidation time i.e. 30, 60, 90, 120, 150 and 180 minutes. The both oxidizing ambient (steam and dry) had been tried to analyze the exact behavior of thermal oxidation on both faces of 4H-SiC. The wafers were placed in quartz glassware known as boats, which are supported by fused silica paddles inside the process tube of the center zone. A boat can contain many wafers. The oxidizing agent comes with the contact of wafers

and diffusion take place at the surface of substrate. This diffusion mechanism is resulted into a vast variation in oxidation rate. In the experiment of wet oxidation the temperature of quartz bubbler (filled with DI water) is always kept at constant 85°C. 0.4 LPM (liter per minutes) flow of wet molecular oxygen has been maintained in the helical path through out the process tube. While in the experiment of dry oxidation, a continuous flow of constant dry oxygen is maintained throughout the process. The samples of each group were loaded and unloaded at 800°C in the 1.9 LPM flow of nitrogen for different time as described above, the ramp up and ramp down temperature of furnace 5°C/min as shown in figure 3.

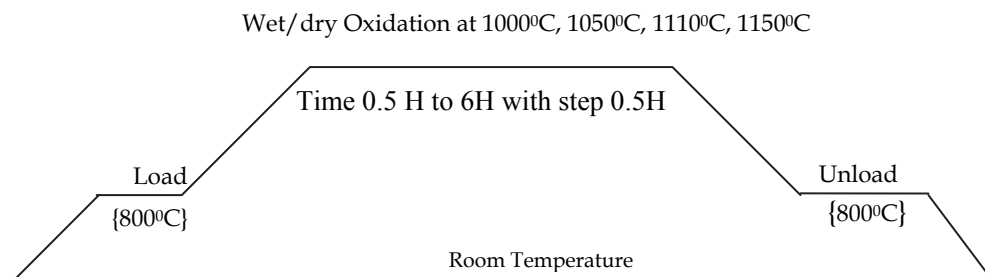


Fig. 3. Process flow of wet thermal oxidation

3.4 Determination of oxide thickness

The thickness of thermally grown oxide on both terminating faces was experimentally captured by ellipsometry technique followed by DAKTEK surface profiler verification.

3.4.1 Basic principle of ellipsometry

In ellipsometry technique a polarized coherent beam of light is reflected off the oxide surface at some angle. In this experiment, He-Ne Laser (6328 Å), was used as a source. The monochromatic light passes through a polarizing prism, which results in linearly polarized light. The polarization of light is changed by the reflection so it is now elliptically polarized. The reflected polarized light is then passed through another prism which is rotating about the axis of the light and finally onto a photodetector. This light is now reflected off of the sample which we wish to study. The reflected light intensity is measured as a function of polarization angle. By comparing the incident and reflected intensity and the change in the polarization angle, the film thickness was estimated. The output of the photodetector is displayed on a computer monitor. The principle of operation of an ellipsometer is illustrated by the schematic drawing of the ellipsometer shown in the figure 4 below.

3.4.2 Basic principle of surface profiler

The profiler has sharply, pointed, conical diamond with a rounded tip stylus, resting lightly on the surface, is traversed slowly across it, and the up and down movement of the stylus relative to a suitable datum are magnified and recorded on a base representing the distance traversed, a graph representing the cross-section will be obtained. Figure 5 shows the schematic diagram of surface profiler. Figure 6 (a) shows a sharp step on the oxidized surface which has been realized by photolithography. Figure 6 (b) shows the experimentally measured thickness of test sample.

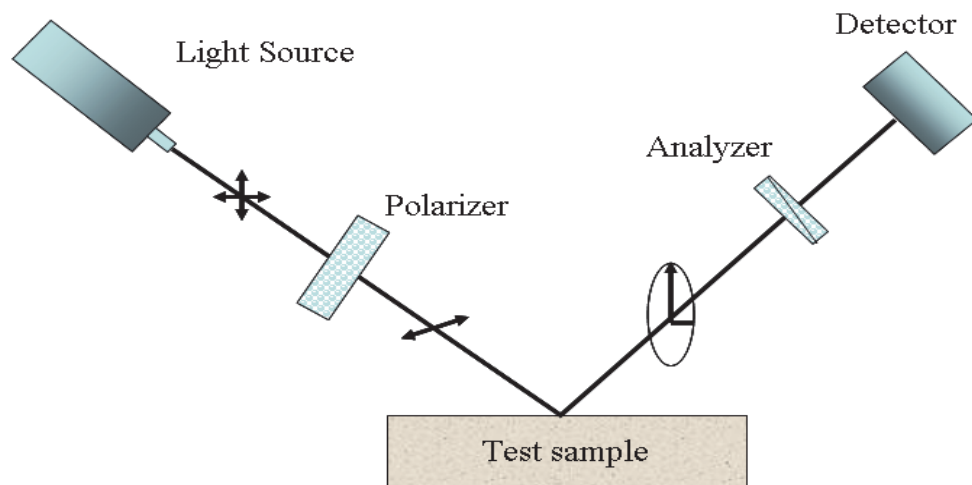


Fig. 4. Schematic drawing of an ellipsometer

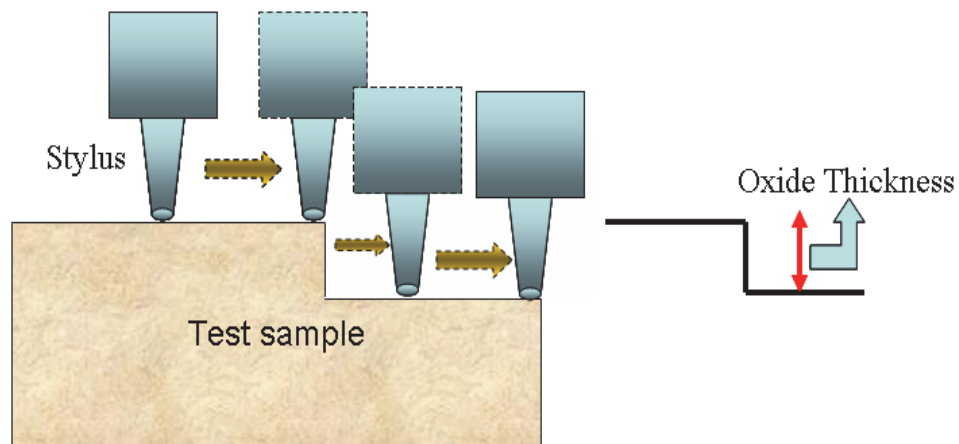


Fig. 5. Schematic drawing of surface profiler

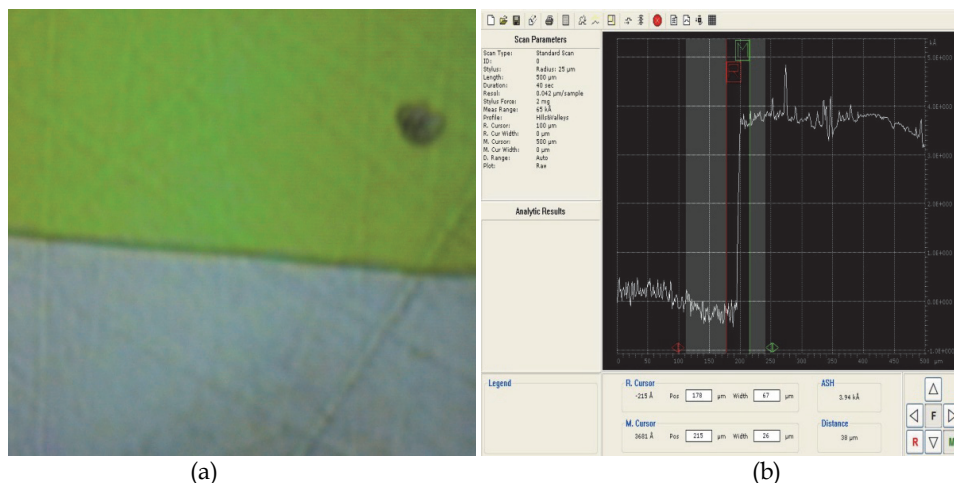
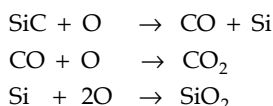


Fig. 6. (a) Oxide step on 4H-SiC (b) Oxide thickness measurements using surface profiler

The measured oxide thickness was plotted as a function of oxidation time, which is shown in figure 7 and 8. The measured thickness was verified by surface profiler also.

4. Basic growth mechanism of 4H-SiC

The thermal oxidation growth mechanism of SiC is described by same rules as Si, which is well explained by Deal and Grove [16] with some modifications. Finally, the growth rate equation (linear-parabolic) is the same as explained for Si-oxidation. During thermal oxidation of silicon carbide most of the excess carbon is believed to be removed from the interface through the formation of CO₂, which diffuses through the oxide and is thereafter released from the sample surface. However, some of the carbon can remain within the oxide and form carbon clusters or graphitic regions. Such regions near the SiO₂/SiC are expected to be electrically active and could be responsible for the interface states [17]. The process of SiC thermal oxidation can be divided into three steps. First, the oxidation of the SiC surface occurs through the interaction of an oxygen atom into the chemical bond of a SiC molecule. This oxygen insertion creates a Si-O-C species, which then splits into a CO molecule and a Si atom with a dangling bond. These CO molecules diffuse through the oxide of the oxide surface and react with an oxygen atom, creating CO₂. Second, the Si atom reacts with oxygen atoms, which are at the SiC surface in the initial oxidation or diffuses through the oxide to the oxide SiC interface, forming SiO₂. These three processes can be summarized by the following reactions:



Contrary to the relatively simple oxidation of Si, there are five major steps in the thermal oxidation of SiC.

1. transport of molecular oxygen gas to the oxide surface
2. in-diffusion of oxygen through the oxide film
3. reactions with SiC at the oxide/SiC interface

4. Out-diffusion of product gases (e.g., CO_2) through the oxide film and
5. removals of product gases away from the oxide surface.

The last two steps are not involved in the oxidation of Si. The oxidation of SiC is about one order of magnitude slower than that of Si under the same conditions. The first and last steps are rapid and are not rate-controlling steps. But among the remaining steps, the rate-controlling step is still uncertain as discussed in several articles [12]. It has been reported in various research papers that the thermal growth kinetics of SiC is governed by linear parabolic law of Deal and Grove, as derived for Silicon [12] [18-20].

$$X_0^2 + AX_0 = B(t + \tau) \quad (1)$$

Where, X denotes the oxide thickness and t is oxidation time. The quantity τ corresponds to a shift in the time coordinate that correct for the presence of the initial layer of oxide thickness and A and B are constants. The above equation is a quadratic equation. The solution of equation can be written as

$$\frac{X_0}{A/2} = \left(1 + \frac{t + \tau}{A^2/4B} \right)^{1/2} - 1 \quad (2)$$

In order to observe the experiment more precise, four numbers of samples were oxidized at same temperature for same oxidation time. All obtained values of thickness are statistically plotted as the function of oxidation time, which is shown in figure 7 (Si-face) and Figure 8 (C-face).

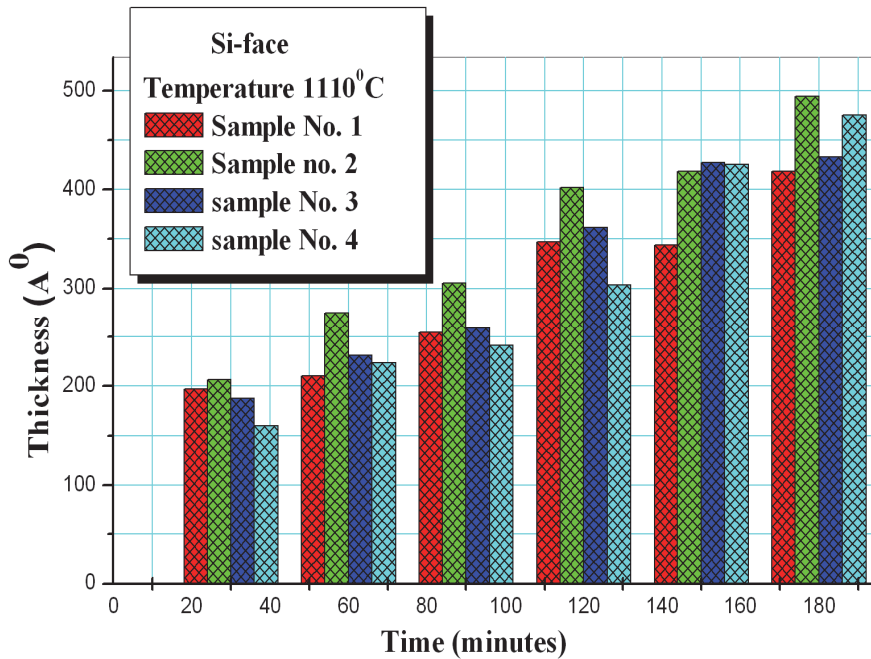


Fig. 7. Growth of thermal oxide on Si-face

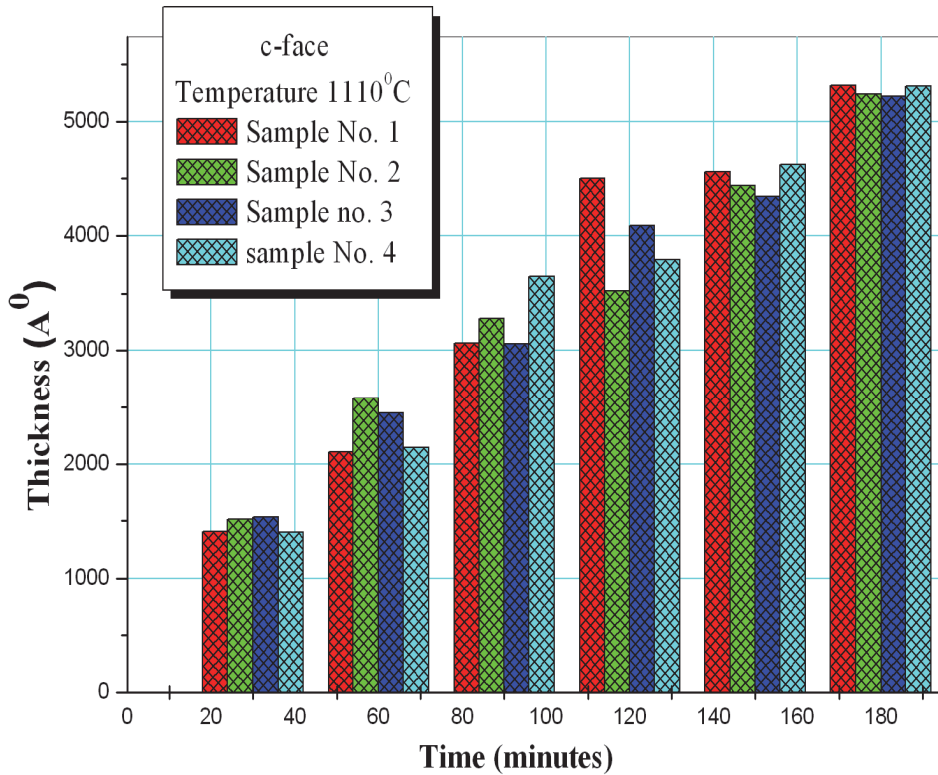


Fig. 8. Growth of thermal oxide on C-face

There are two limiting case of equation 2

1. For long oxidation time i.e. thick oxidation Equation 2 becomes

$$X_0^2 = Bt \quad (3)$$

This relation is called parabolic law and B is called parabolic rate constant. This limiting case is diffusion controlled case because diffusion flux becomes small in comparison to the substrate surface reaction flux. Here the rate of oxidation is limited by the availability of oxidant at the Si rich interface as well as C rich interface, which is controlled by the diffusion process.

2. For short oxidation time i.e. thin oxide equation 2 can be written as

$$X_0 = \frac{B}{A}(t + \tau) \quad (4)$$

This relation is called linear law and the quantity B/A is called the linear rate constant because in this case enough oxidant is transported across the oxide layer, and the oxidation rate is controlled by concentration of oxidant at the surface [21].

Wet thermal oxidation of the C-face of 4H-SiC is systematically slower than that of Si for identical conditions of temperature, pressure and time. Since the oxidation rate has been

shown to depend only feebly on the polytypes for the Si-face and not at all for the C-face. It is realistic to believe that although there may be small quantitative differences between the oxidation processes of different polytypes along the perpendicular directions to the bilayer stacking units. The main processes involved in oxidation are diffusion, interface reaction rates and so on, should be largely analogous, and so it is practical to discuss oxidations mechanisms without paying special attention to the polytypes. Figure 9 shows the quantitative oxide thickness up to 6 hours after analyzing the growth dynamic as explained above at 1110°C. A number of oxidation experiments have been repeated in order to verify the previously obtained results. Wet and dry thermal oxidations have been performed separately at the different temperature. Figure 10 (a, b, c and d) shows the experimentally measured thermal oxide thickness at the different temperature as explained above by the method of wet and dry oxidation on Si as well as C-face. In both cases (dry and wet), a face terminated behavior has been observed means C-face always oxidized faster than that of Si-face under same oxidation condition. This discrepancy in growth rate is termed as growth rate multiplication factor (GRMF), means how much oxidation on C-face is faster than that of Si-face. A very simple equation has been formulated by just dividing the oxide thickness on C-face to oxide thickness on Si-face (equation 5).

$$GRMF = \frac{X_0|_{C-face}}{X_0|_{Si-face}} \quad (5)$$

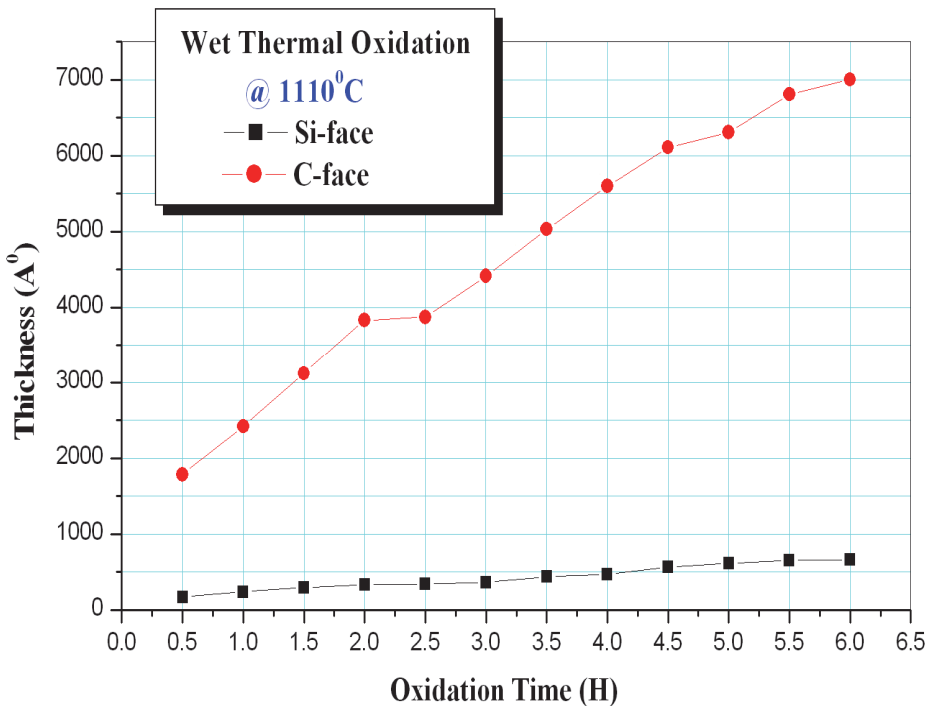


Fig. 9. Experimental growth of wet thermal oxide on both terminating face

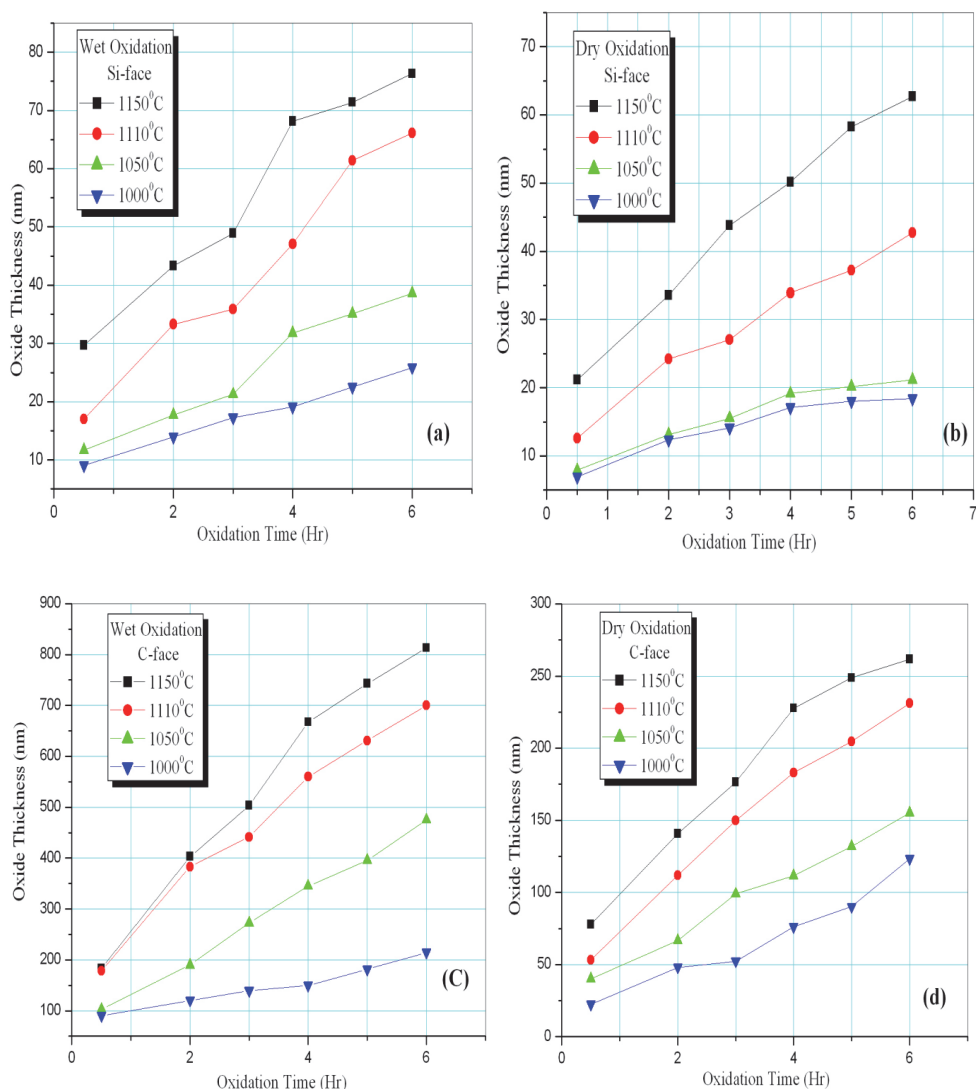


Fig. 10. (a) Plots of oxide growth profile on Si-face by wet oxidation, (b) by dry oxidation, (c) wet oxidation on C-face and (d) dry oxidation on C-face

The growth rate multiplication factor (GRMF) on both terminating faces has been calculated as a function of oxidizing ambient (dry and wet). It was observed that in case of dry oxidation GRMF is found in the range of 4-6, means in case of dry oxidation C-face oxidize 4 to 6 times faster than that of Si-face. In the similar way for wet oxidation this GRMF is found in the range of 8-12, means in case of wet oxidation C-face oxidize 8 to 12 times faster than that of Si-face. Figure 11 shows the experimentally measured GRMF in both oxidizing ambient.

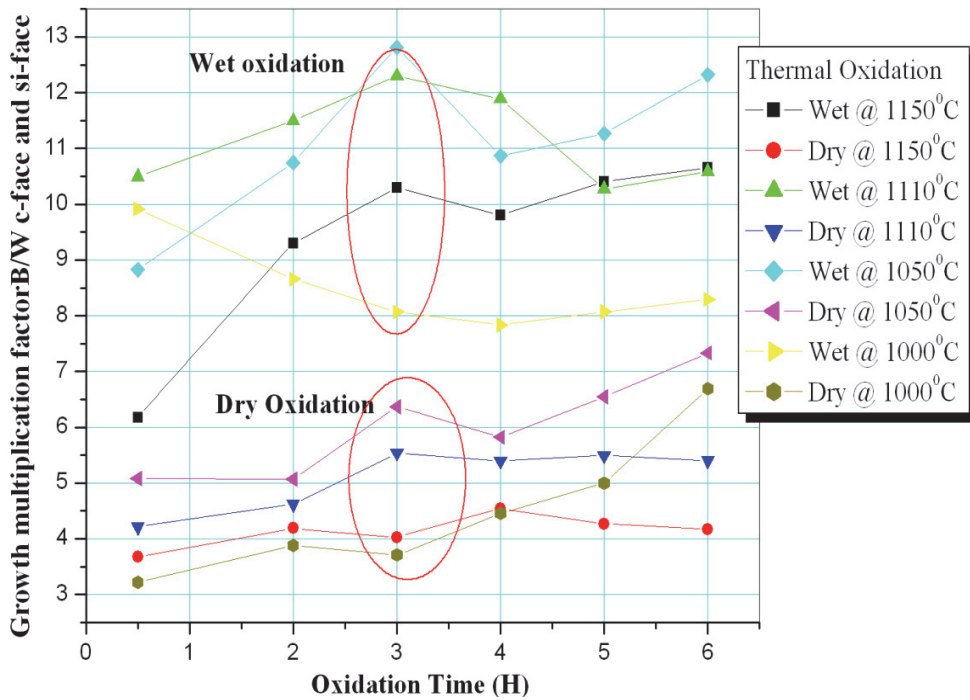


Fig. 11. Determination of growth rate multiplication factor between both terminating faces by the method of wet and dry oxidation process

5. Determination of average growth rates

We have applied the Deal and Grove oxidation model to the relations between oxide thickness X and oxidation time t . The quantitative values of the linear parameters B/A and parabolic parameter B in the Deal-Grove equation has been used by fitting to the calculated curve to the observed values in the entire thickness range. The fits are in general good at all of the oxidation temperatures. However, to observe the growth rate behavior for both terminating faces, the grown oxide is divided by its oxidation time. We have derived the oxidation rates dX_0/dt as a function of oxide thickness for dry as well as wet oxidation on both terminating faces. Since we are calculating the growth rate of all samples after each successive experiment that's why we are calling it average growth rate.

$$\left. \frac{dX_0}{dt} \right|_{\text{sample1}} \Rightarrow \text{Average} \left. \frac{dX_0}{dt} \right|_{\text{sample1}} \quad (6)$$

Figure 12 (a, b, c and d) shows the values of dX_0/dt as a function of oxide thickness (grown by the method of wet oxidation) at various oxidation temperatures. We have successfully obtained the values of the oxidation rate even in the thin oxide thickness range of less than 10 nm by these experiments. Figure 13 (a, b, c and d) shows the values of dX_0/dt as a function of oxide thickness (grown by the method of wet oxidation) at various oxidation

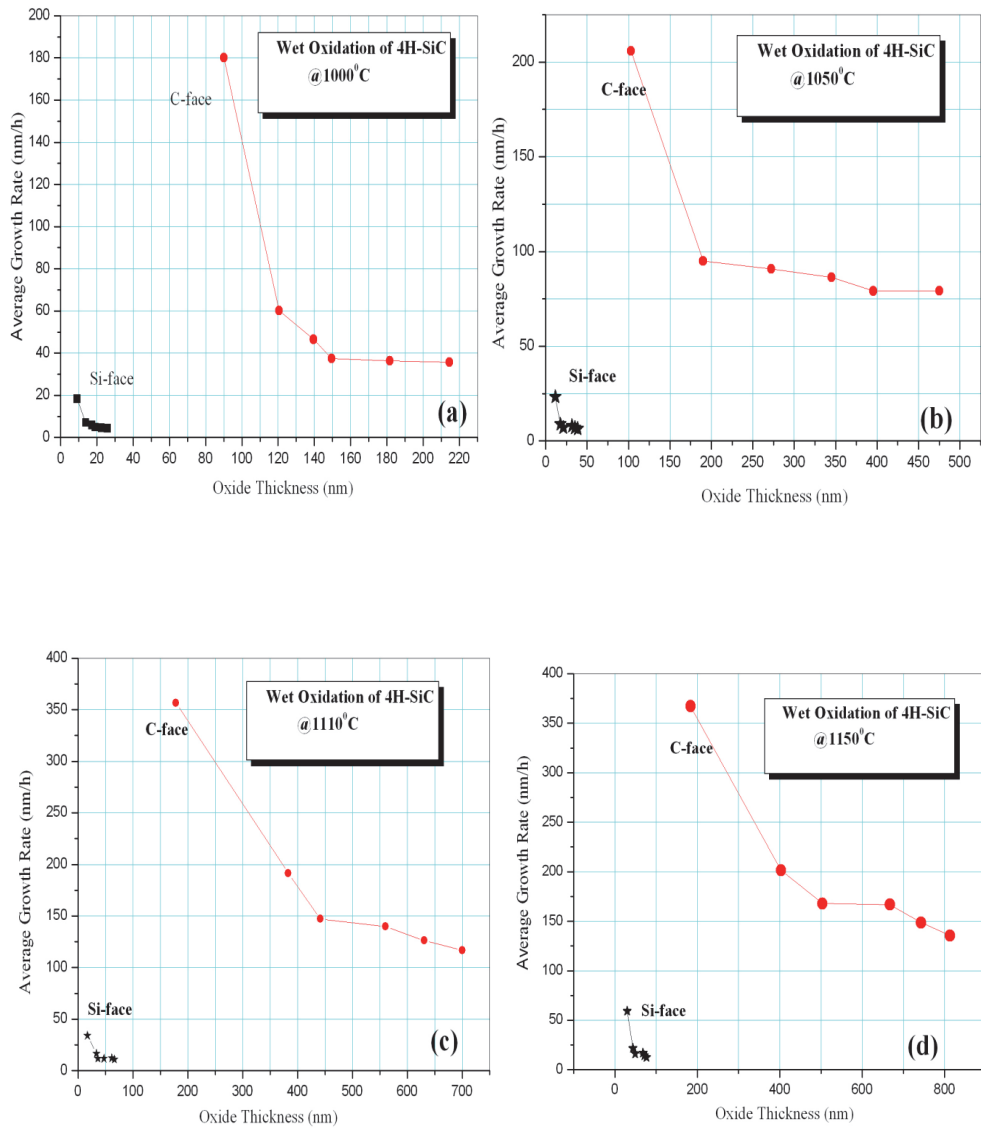


Fig. 12. (a) Plots of face terminated wet oxidation growth rate at 1000°C, (b) at 1050°C, (c) at 1110°C and (d) at 1150°C

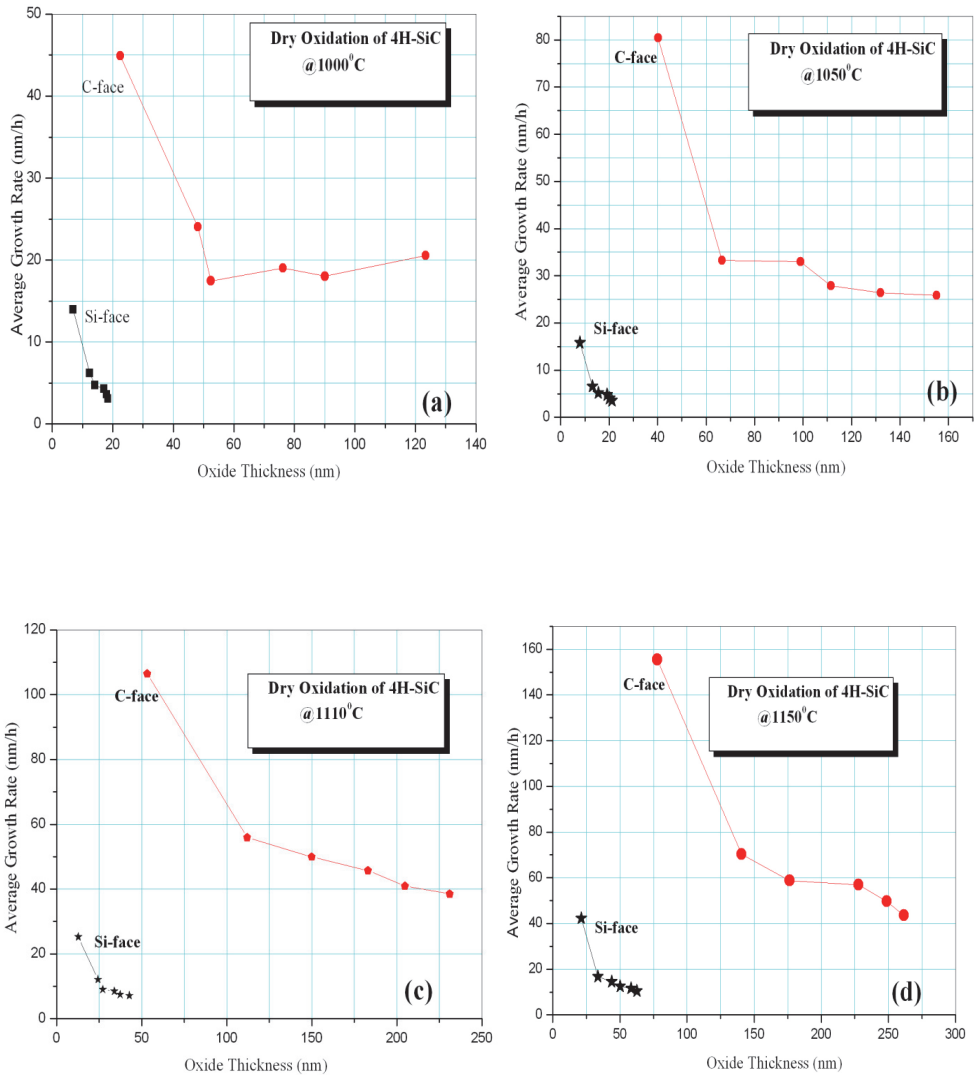


Fig. 13. (a) Plots of face terminated dry oxidation growth rate at 1000°C, (b) at 1050°C, (c) at 1110°C and (d) at 1150°C

temperatures. Initial oxide growth rate of 19, 24, 35, 67 nm/h (on Si-face) while 180, 220, 357, 374 nm/h (on C-face) have been calculated at 1000°C, 1050°C, 1110°C and 1150°C respectively. Similarly, thermal oxide growth for dry oxidation has been found to be 12, 17, 25, 42 nm/h (on Si-face) while 44.5, 81, 113, 157 nm/h (on C-face) have been calculated at 1000°C, 1050°C, 1110°C and 1150°C respectively. However, in the smaller thickness range, the values of dX_0/dt are not constant but increases with decreasing oxide thickness, i.e., the oxide growth rate enhancement occur at any temperature in this study in both case (Si-face and C-face). It is evident from the above data that the nature of growth rate is parabolic for all cases and initial average growth rate for wet oxidation is faster than that for dry oxidation. C-face is having the higher growth rate than that of Si-face at each oxidation temperature in both oxidations ambient. Figure 14 show the face terminated growth rate, revealing that the average growth rates of dry and wet oxide on Si-face is slower than that of C-face.

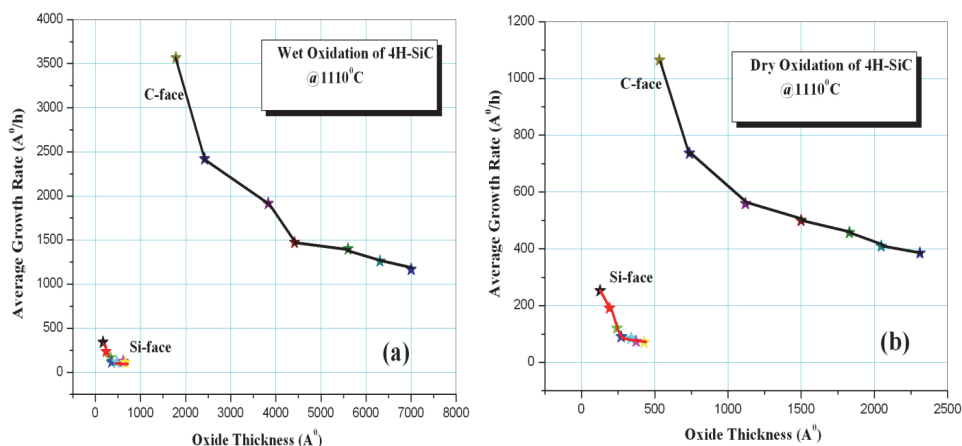


Fig. 14. Plots of oxidizing ambient terminated growth rate in wet oxidation and (b) in dry oxidation

6. Determination of rate constants

Thermal oxide growth rate constants have been determined by fitting the experimentally measured curve to the measurement made by Deal and Grove (as explained above) of oxide thickness as a function of oxidation time at various oxidation temperatures. In this experiment dry and wet thermal oxidation has been performed (as explained in section 2.3) at 1000°C, 1050°C, 1110°C and 1150°C for different oxidation time. In each individual experiment, the value of τ has been fixed to zero for all temperature range. A plot of oxide thickness (X_0) versus t/X_0 from equation 1 should yield a straight line with intercept $-A$ and slope B . Figure 15 (a) and Figure 15 (b) shows the X_0 versus t/X_0 plots of wet oxidation on Si-face (figure a) and C-face (figure b) of 4H-SiC. It has been observed that the absolute value of A increasing with decreasing oxidation temperature. At the same condition, the slope of the plots increases with increasing temperature. Measured values of these constants from the figure 15 are listed in table 1.

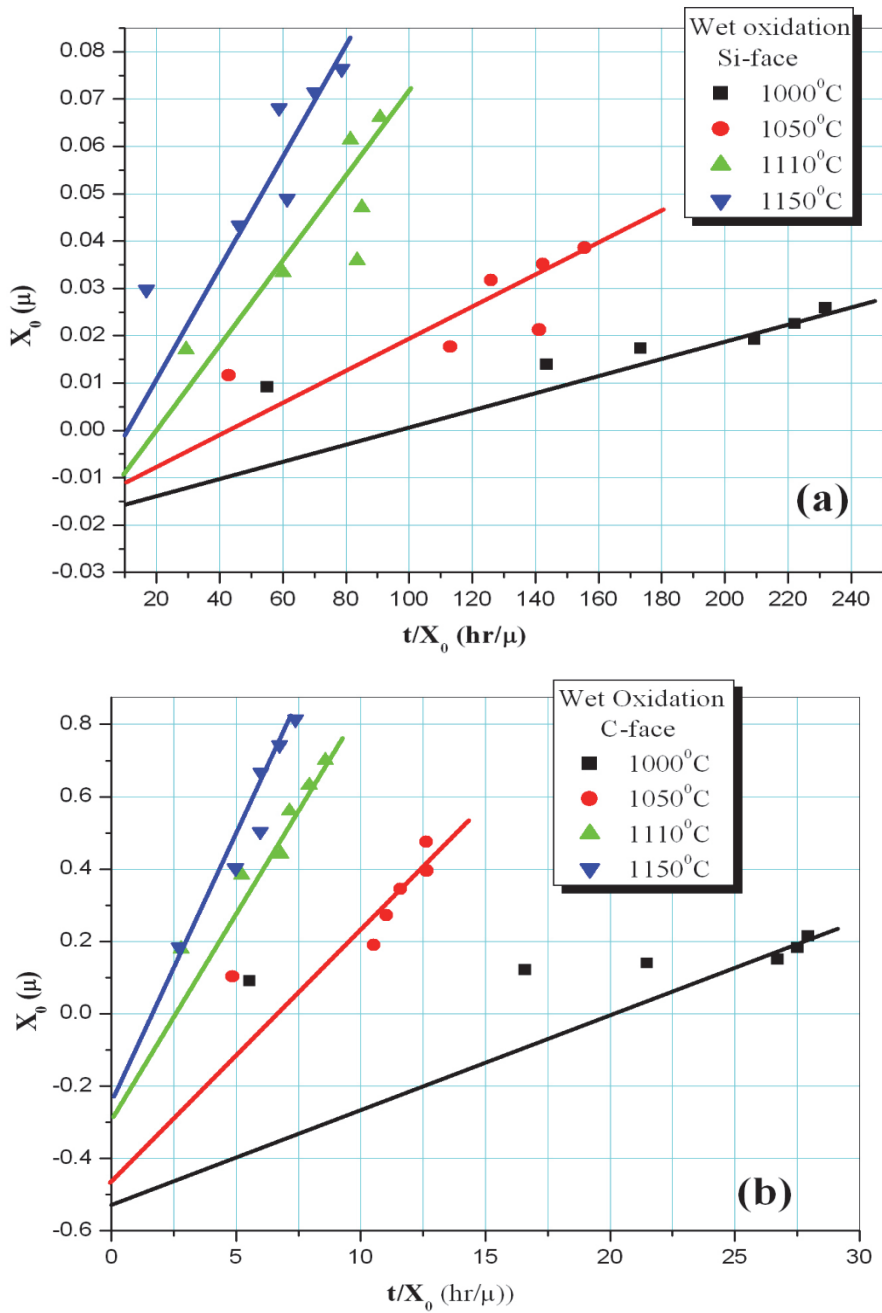


Fig. 15. (a) Experimentally measured curve of X_0 versus t/X_0 for wet oxidation on Si-face and (b) on C-face

Figure 16 (a) and 2.16 (b) are the again X_0 and t/X_0 for face terminated (Si-face and C-Face) oxidation in dry ambient at different oxidation time. The plots are straight line again (as shown in figure 16) with intercept $-A$ and slope B . The measured linear as well as parabolic rates constant are listed in table 2.

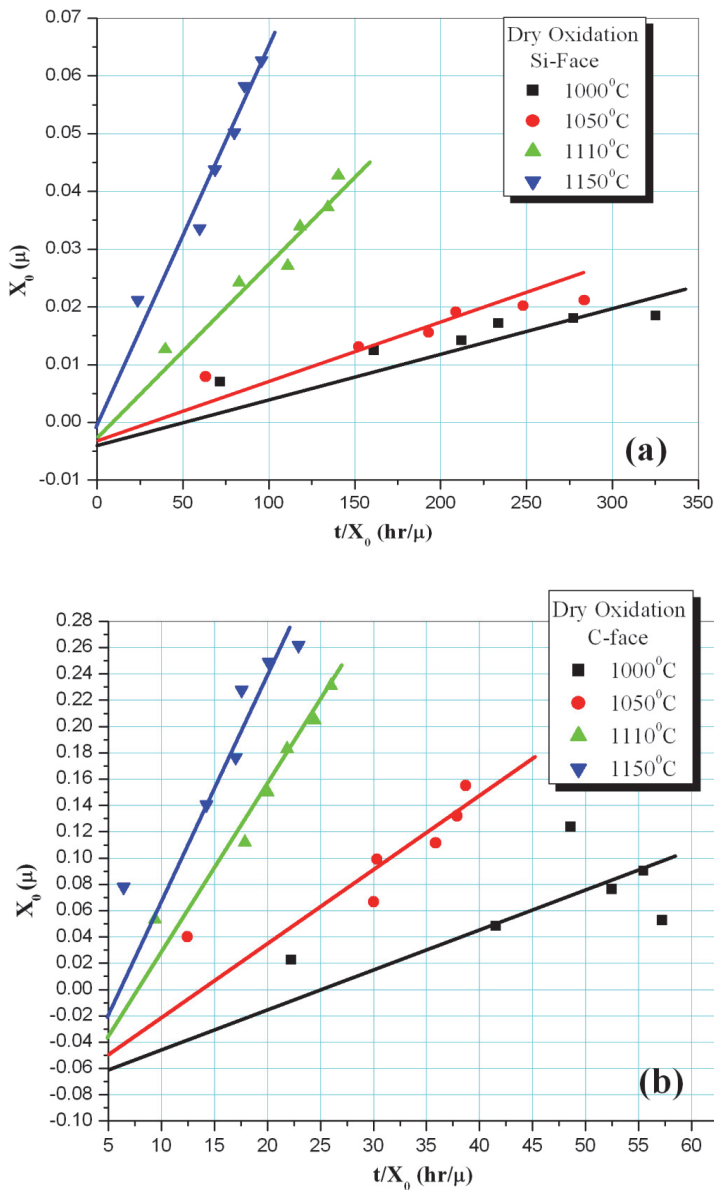


Fig. 16. (a) Experimentally measured curve of X_0 versus t/X_0 for dry oxidation on Si-face and (b) on C-face

Temperature (°C)	1000	1050	1110	1050
Si-face (Dry oxidation)	0.0000748	0.0001035	0.0003021	0.0006130
C-face (Dry oxidation)	0.00309	0.00568	0.01251	0.01711
Si-face (Wet oxidation)	0.000158	0.00033088	0.0008830	0.00120
C-face (Wet oxidation)	0.02571	0.06825	0.11303	0.14207

Table 1. Experimentally measured Parabolic Rate Constant (B)

Temperature (°C)	1000	1050	1110	1050
Si-face (Dry oxidation)	0.01533	0.02728	0.14081	0.58161
C-face (Dry oxidation)	0.05072	0.11643	0.34992	0.93078
Si-face (Wet oxidation)	0.01022	0.02916	0.10441	0.88499
C-face (Wet oxidation)	0.04887	0.14882	0.40398	0.61975

Table 2. Experimentally measured Linear Rate Constant (B/A)

7. Determination of activation energy

The rate of any reaction depends on the temperature at which it is run. As the temperature increases, the molecules move faster, and therefore, they collide more frequently to each other. As a result of these collisions, the molecules also carried more kinetic energy. Thus, the proportion of collisions that can overcome the activation energy for the reaction increases with temperature. The only way to explain the relationship between temperature and the rate of a reaction is to assume that the rate constant depends on the temperature at which the reaction is run. In 1889, Swedish scientist Svante Arrhenius showed that the relationship between temperature and the rate constant of a reaction. Arrhenius's research was a follow up of the theories of reaction rate by Serbian physicist Nebojsa Lekovic. Activation energy may also be defined as the minimum energy required to start a chemical reaction. The activation energy of a reaction is usually denoted by E_a and given in units of kilojoules per mole or in eV.

$$K = Ze^{-\frac{E_a}{RT}} \quad (7)$$

Where, K is the rate constant for the reaction, Z is a proportionality constant that varies from one reaction to another, E_a is the activation energy for the reaction, R is the ideal gas constant in joules per mole kelvin, and T is the temperature in kelvin.

The Arrhenius equation can be used to determine the activation energy for a reaction. Taking the natural logarithm of both sides of the equation we get

$$\ln(K) = \ln(Z) - \frac{E_a}{RT} \quad (8)$$

This equation is then to fit as the equation for a straight line.

$$Y = mX + C \quad (9)$$

$$\ln(K) = -\frac{E_a}{R} \left(\frac{1}{T} \right) + \ln(Z) \quad (10)$$

According to this equation, a plot of $\ln(K)$ versus $1/T$ should give a straight line with a slope of $-E_a/R$, from which the value of activation energy can easily be determined.

Figure 17 (a) and (b) shows the straight line tendency of linear rate constant (B/A) with $1/T$. Using above equation activation energy has been calculated on both faces of 4H-SiC for wet oxidation as well as dry oxidation and are listed in table 3. Similarly, using parabolic rate constant the rate constants are plotted with $1/T$ (figure 18 (a) and (b)) and the activation energy on both terminating faces has been calculated and presented in table 3.

The linear rate constants B/A show the apparent activation energy of 2.81 eV (dry oxidation on Si-face), 2.274 eV (dry oxidation on C-face), 2.677 eV (wet oxidation on Si-face) and 2.131 eV (wet Oxidation C-face). Similarly parabolic rate constant B show the apparent activation energy of 2.86 eV (dry oxidation on Si-face), 2.0261 eV (dry oxidation on C-face), 2.505 eV (wet oxidation on Si-face) and 1.539 eV (wet Oxidation C-face). It has been found that the activation energy of C-face in both oxidations ambient is always less than that of Si-face, which clearly indicates a face terminated mechanism. Hence different oxidation rates on both faces of 4H-SiC, may be attributed to different activation energies found at both faces.

Activation energy (E_a)	Si-face (Dry oxidation)	C-face (Dry oxidation)	Si-face (Wet oxidation)	C-face (Wet oxidation)
From linear rate constant (B/A)	2.81 eV	2.274 eV	2.677eV	2.131 eV
From parabolic rate constant (B)	2.86 eV	2.0261 eV	2.505 eV	1.539 eV

Table 3. Experimentally measured value of Activation Energy (E_a) in linear region and parabolic region

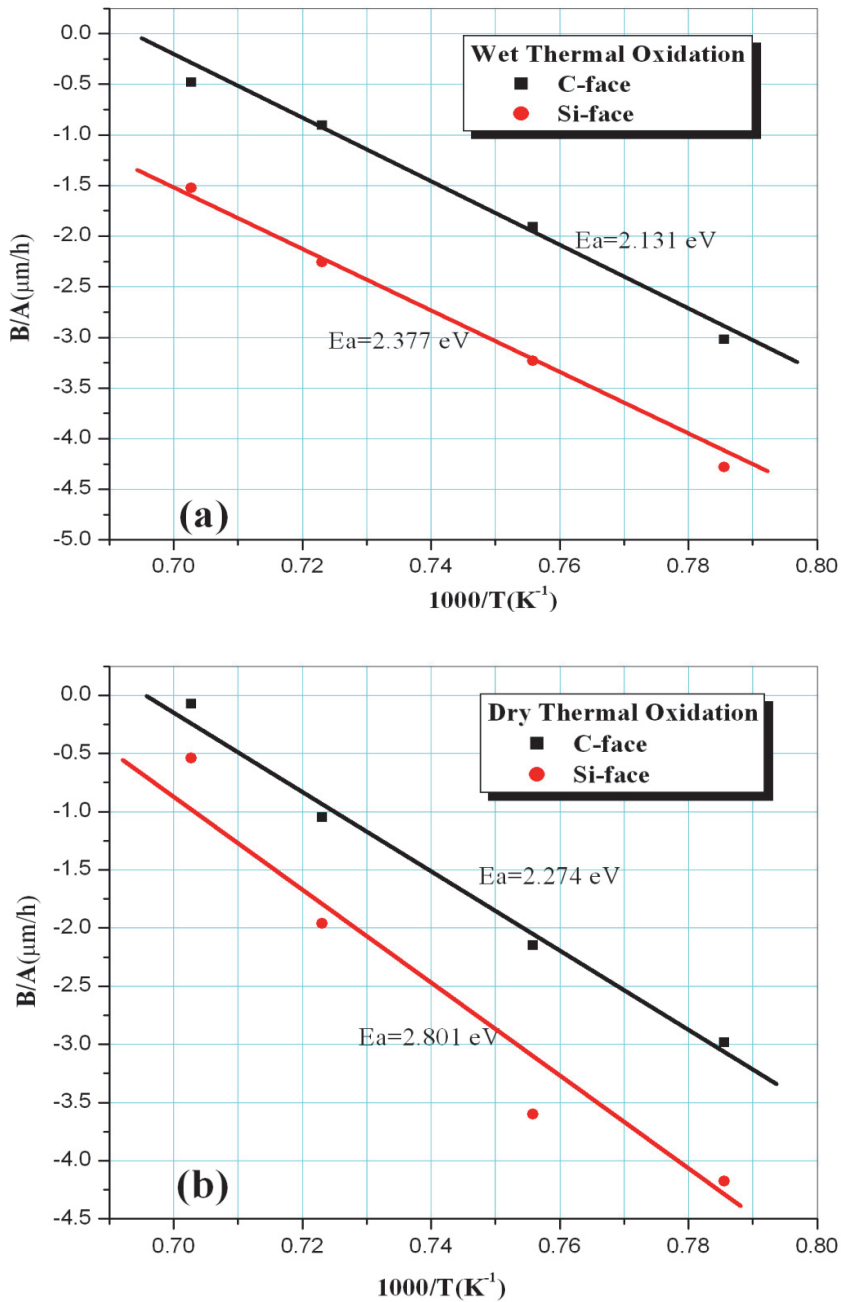


Fig. 17. (a) Linear rate constant (B/A) as a function of $1/T$ for oxidation in wet ambient and (b) in dry ambient. Calculated activation energy is shown in their respective plots

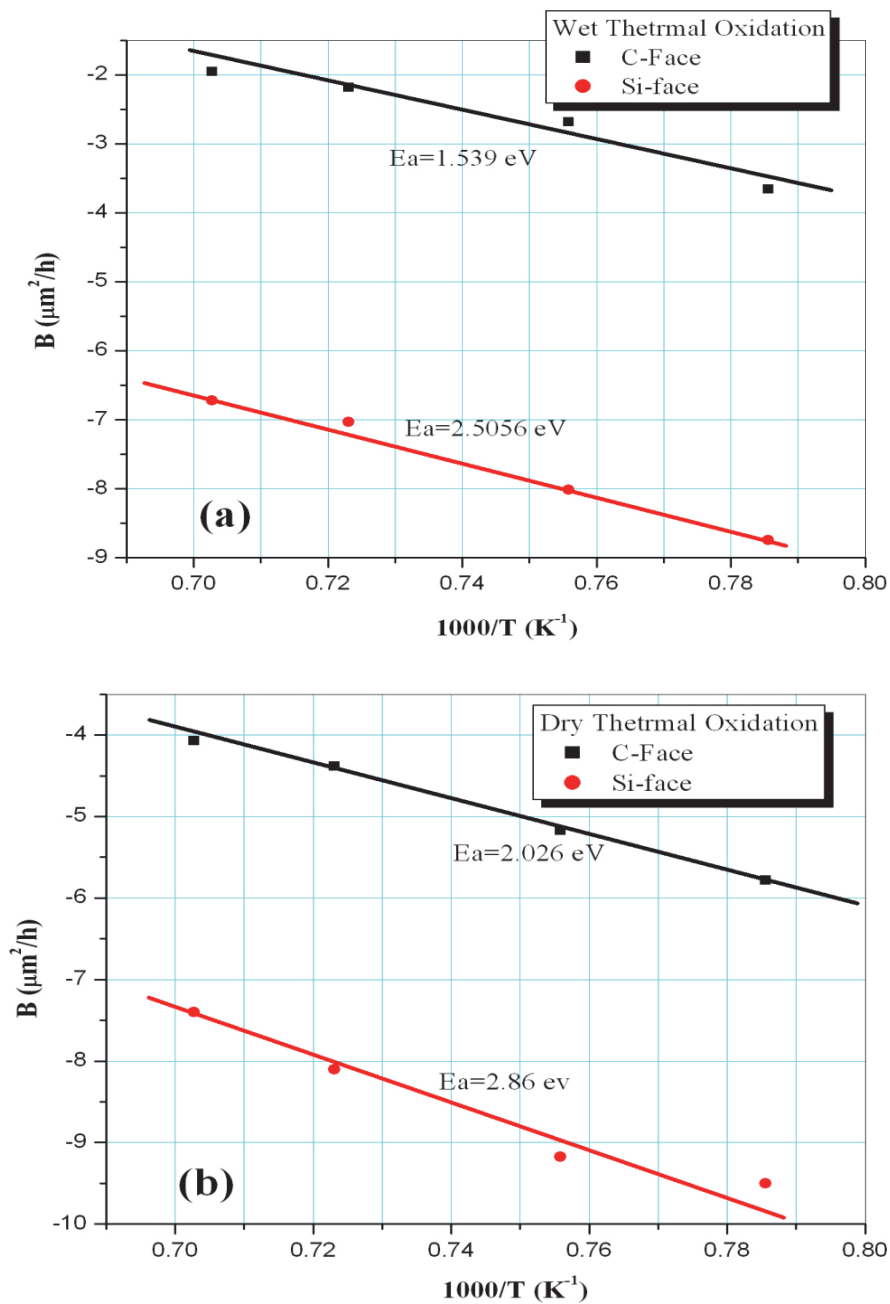


Fig. 18. (a) Parabolic rate constant (B) as a function of $1/T$ for oxidation in wet ambient and (b) in dry ambient. Calculated activation energy is shown in their respective plots

8. Conclusions

This chapter presents a systematically experimental study of the thermal oxide mechanism on 4H-SiC. On the basis of experimental results obtained, the following conclusions have been drawn.

- Thermal oxidation is a process that incorporates the interaction of molecular oxygen with oxidizing species, which are present on the substrate surface. The different mechanisms, through which oxygen is incorporated in the bulk and interface oxide regions during thermal oxidation of 4H-SiC, is namely the reaction with the SiC substrate and consumption of carbon clusters at both terminating faces.
- A face terminated oxidation behavior has been observed which indicates that the oxidation growth rate on C-face is faster than that of Si-face.
- In the thermal oxidation process of 4H-SiC, Si-face remains silicon rich face and C-face remains carbon rich face. This known observation indicates towards discrete nature of oxidation mechanism.
- The growth rate multiplication factor (GRMF) has been calculated for both oxidizing ambient (dry and wet). It has been concluded that in case of dry oxidation GRMF is found in the range of 4-6, means in case of dry oxidation C-face oxidize 4 to 6 times faster than that of Si-face. Similarly, for wet oxidation this GRMF is found in the range of 8-12, means in case of wet oxidation C-face oxidize 8 to 12 times faster than that of Si-face.
- It has been observed that the nature of growth rate is parabolic for all cases and initial average growth rate for wet oxidation is always faster than that of dry oxidation.
- It has been observed that the absolute value of rate constant (A) increases with decreasing oxidation temperature. At the same condition, the slope of the plots increases with increasing temperature means the value of rate constant B, increases with increasing temperature.
- The activation energy at both faces of 4H-SiC has been calculated using Arrhenius plots. It has been found that the activation energy of C-face for both oxidations ambient is always less than that of Si-face, which clearly indicates a face terminated mechanism.

9. References

- [1] I. Vickridge, J. Ganem, Y. Hoshino and I. Trimaille, "Growth of SiO₂ on SiC by dry thermal oxidation: mechanisms", J. Phys. D: Appl. Phys. Vol. 40, pp. 6254-6263, 2007.
- [2] Hiroshi Yano, Fumito Katafuchi, Tsunenobu Kimoto, and Hiroyuki Matsunami, "Effects of Wet Oxidation/ Anneal on Interface Properties of Thermally Oxidized SiO₂ /SiC MOS System and MOSFET's", IEEE Trans. Electron Devices, Vol. 46, No. 3, pp. 504-510, 1999.
- [3] K. Kamimura, D. Kobayashi, S. Okada, T. Mizuguchi, E. Ryu, R. Hayashibe, F. Nagaume and Y. Onuma, " Preparation and characterization of SiO₂/6H-SiC metal-insulator-semiconductor structure using TEOS as source materials", Appl. Surf. Sci., Vol. 184, Issue 1-4, pp. 346-349, 2001.

- [4] P. T. Lai, J. P. Xu, H. P. Wu, C. L. Chen, "Interface properties and reliability of SiO₂ grown on 6H-SiC in dry O₂ plus trichloroethylene", *Microelectron. Reliab.* Vol. 44, Issue 4, pp. 577-580, 2004.
- [5] M. Meakawa, A. Kawasuso, Z. Q. Chen, M. Yoshikawa, R. Suzuki, T. Ohdaria, "Structural defect in SiO₂/SiC interface probed by a slow positron beam", *Appl. Surf. Sci.* Vol. 244, Issue 1-4, pp. 322-325, 2005.
- [6] C. Zetterling, M. Ostling, C. I. Harris, P. C. Wood, S. S. Wong, "UV-ozone precleaning and forming gas annealing applied to wet thermal oxidation of p-type silicon carbide", *Mater. Sci. Semicond. Process.*, Vol. 2, Issue 1, pp. 23-27, 1998.
- [7] Eckhard Pippel and Jörg Woltersdorf, Halldor O. Oafsson and Einar O. Sveinbjornsson, "Interfaces between 4H-SiC and SiO₂: Microstructure, nanochemistry, and near-interface traps", *J. Appl. Phys.*, Vol. 97, p. 034302, 2005.
- [8] Mark Schürmann, Stefan Dreiner, Ulf Berges, and Carsten Westphal, "Investigation of carbon contaminations in SiO₂ films on 4H-SiC (0001)", *J. Appl. Phys.*, Vol. 100, p. 113510, 2006.
- [9] X. D. Chen, S. Dhar, T. Isaacs-Smith, J. R. Williams, L. C. Feldman, and P. M. Mooney, "Electron capture and emission properties of interface states in thermally oxidized and NO-annealed SiO₂/4H-SiC", *J. Appl. Phys.*, Vol. 103, p. 033701, 2008.
- [10] V. R. Vathulya, D. N. Wang and M. H. White, "On the correlation between the carbon content and the electrical quality of thermally grown oxide on p-type 6H-Silicon Carbide", *Appl. Phys. Lett.*, Vol. 73, pp. 2161-2163, 1998.
- [11] I.C. Vickridge, J. J. Ganem, G. Battisig, and E. Szilagy, "Oxygen isotropic tracing study of the dry thermal oxidation of 6H-SiC", *Nucl. Instrum. Methods Phys. Res.*, Vol. 161B, pp. 462-466, 2000.
- [12] Y. Song, S. Dhar, L.C. Feldman, G. Chung, and J.R. Williams, "Modified deal and grove model for the thermal oxidation of silicon carbide", *J. Appl. Phys.*, Vol. 95, pp. 4953-4957, 2004.
- [13] J. M. Knaup, P. Deak, T. Frauenheim, A. Gali, Z. Hajnal, and W.J. Choyke, "Theoretical study of the mechanism of dry oxidation of 4H-SiC", *Physical Review B* Vol. 71, pp. 235321-235328, 2005.
- [14] M. Schuermann, S. Dreiner, U. Berges and C. Westphal, "Structure of the interface between ultra thin SiO₂ film and 4H-SiC (0001)", *Physical Review B* Vol. 74, pp. 035309-035313, 2006.
- [15] P. Fiorenza and V. Raineri, "Reliability of thermally oxidized SiO₂/4H-SiC by conductive atomic force microscopy", *J. Appl. Phys.*, Vol 88, pp. 212112-212115, 2006.
- [16] B.E. Deal and A.S. Grove, "General relationship of the thermal oxidation of silicon", *J. Appl. Phys.*, Vol. 36, p. 3770, 1965.
- [17] Eckhard Pippel and Woltersdorf, "Interface between 4H-SiC and SiO₂: microstructure, nanochemistry and interface traps", *J. Appl. Phys.*, Vol. 97, p. 034302, 2005.
- [18] D. Schmeiber, D. R. Batchelor, R. P. Mikolo, O. Halfmann and A. L-Spez, "Oxide growth on SiC (0001) surfaces", *Appl. Surf. Sci.* Vol 184, Issue 1-4, pp. 340-345, 2001.
- [19] M. T. Htun Aung, J. Szmids and M. Bakowski, "The study of thermal oxidation on SiC surface", *J Wide Bandgap Material*, Vol. 9. No. 4, pp. 313-318, 2002.

- [20] R. Kosugi, K. Fukuda and K Arai, "Thermal oxidation of (0001) 4H-SiC at high temperature in ozone-admixed oxygen gas ambient", Appl. Phys. Lett. Vol. 83, p. 884, 2003.
- [21] E. H. Nicollian and J. R. Brews, MOS (Metal Oxide Semiconductor) Physics and Technology, John Wiley and sons, New York, p. 673, 1981.

Creation of Ordered Layers on Semiconductor Surfaces: An *ab Initio* Molecular Dynamics Study of the SiC(001)- 3×2 and SiC(100)- $c(2\times 2)$ Surfaces

Yanli Zhang and Mark E. Tuckerman
Department of Chemistry, New York University
USA

1. Introduction

The chemistry of hybrid structures composed of organic molecules and semiconductor surfaces is opening up exciting new areas of development in molecular electronics, nanoscale sensing devices, and surface lithography (Filler & Bent, 2002; Kachian et al., 2010; Kruse & Wolkow, 2002). Covalent attachment of organic molecules to a semiconducting surface can yield active devices, such as molecular switches (Filler & Bent, 2003; Flatt et al., 2005; Guisinger, Basu, Greene, Baluch & Hersam, 2004; Guisinger, Greene, Basu, Baluch & Hersam, 2004; He et al., 2006; Rakshit et al., 2004) and sensors (Cattaruzza et al., 2006) or passivating insulating layers. Moreover, it is assumed that the reactions can be controlled by “engineering” specific modifications to organic molecules, suggesting possible new lithographic techniques.

One of the goals of controlling the surface chemistry is the creation of ordered nanostructures on semiconducting surfaces. Indeed, there has been some success in obtaining locally ordered structures on the hydrogen terminated Si(100) surface (Basu et al., 2006; Hossain et al., 2005b; Kirczenow et al., 2005; Lopinski et al., 2000; Pitters et al., 2006). These methods require a dangling Si bond without a hydrogen to initialize the self-replicating reaction. Another popular approach eliminates the initialization step by exploiting the reactivity between surface dimers on certain reconstructed surfaces with the π bonds in many organic molecules. The challenge with this approach lies in designing the surface and/or the molecule so as to eliminate all but one desired reaction channel. Charge asymmetries, such as occur on the Si(100)- 2×1 surface, lead to a violation of the usual Woodward-Hoffman selection rules, which govern many purely organic reactions, allowing a variety of possible [4+2] and [2+2] surface adducts.

Silicon-carbide (SiC) is often the material of choice for electronic and sensor applications under extreme conditions (Capano & Trew, 1997; Mélinon et al., 2007; Starke, 2004) or subject to biocompatibility constraints (Stutzmann et al., 2006). SiC has a variety of reconstructions that could possibly serve as candidates for creating ordered organic/semiconductor interfaces. However, the choice of the reconstruction is crucial. Multiple reactive sites, such as occur on some of the SiC surfaces, will lead to a broad distribution of adducts.

The exploration of hybrid organic-semiconductor materials and the reactions associated with them is an area in which theoretical and computational tools can play an important role. Indeed, modern theoretical methods combined with high-performance computing,

have advanced to a level such that the thermodynamics and reaction mechanisms can be routinely studied. These studies can aid in the interpretation of experimental results and can leverage theoretical mechanisms to predict the outcomes of new experiments. This chapter will focus on a description of one set of such techniques, namely, those based on density functional theory and first-principles or *ab initio* molecular dynamics (Car & Parrinello, 1985; Marx & Hutter, 2000; 2009; Tuckerman, 2002). As these methods employ an explicit representation of the electronic structure, electron localization techniques can be used to follow local electronic rearrangements during a reaction and, therefore, generate a clear picture of the reaction mechanism. In addition, statistical mechanical tools can be employed to obtain thermodynamic properties of the reaction products, including relative free energies and populations of the various products. Following a detailed description of the computational approaches, we will present two applications of conjugated dienes reacting with different choices of SiC surfaces (Hayes & Tuckerman, 2008). We will investigate how the surface structure influences the thermodynamics of the reaction products and how these thermodynamic properties can be used to guide the choice of the surface in order to control the product distribution and associated free energies.

2. Computational methods

Because the problem of covalently attaching an organic molecule to a semiconductor surface requires the formation of chemical bonds, a theoretical treatment of this problem must be able to describe this bond formation process, which generally requires an *ab initio* approach in which the electronic structure is accounted for explicitly. Assuming the validity of the Born-Oppenheimer approximation, the goal of any *ab initio* approach is to approximate the ground-state solution of the electronic Schrödinger equation $\hat{H}_{\text{elec}}(\mathbf{R})|\Psi_0(\mathbf{R})\rangle = E_0(\mathbf{R})|\Psi_0(\mathbf{R})\rangle$, where \hat{H}_{elec} is the electronic Hamiltonian, and \mathbf{R} denotes a classical configuration of the chemical nuclei in the system. Ultimately, in order to predict reaction mechanisms and thermodynamics, one needs to use the approximate solution of the Schrödinger equation to propagate the nuclei dynamically using Newton's laws of motion. This is the essence of the method known as *ab initio* molecular dynamics (AIMD) (Car & Parrinello, 1985; Marx & Hutter, 2000; 2009; Tuckerman, 2002). Unless otherwise stated, all of the calculations to be presented in this chapter were carried out using the implementation of plane-wave based AIMD implemented in the PINY_MD package (Tuckerman et al., 2000).

In this section, we will briefly review density functional theory (DFT) as the electronic structure method of choice for the studies to be described in this chapter. DFT represents an optimal compromise between accuracy and computational efficiency. This is an important consideration, as a typical AIMD calculation requires that the electronic structure problem be solved tens to hundreds of thousands of times in order to generate one or more trajectories of sufficient length to extract dynamic and thermodynamic properties. We will then describe the AIMD approach, including several technical considerations such as basis sets, boundary conditions, and electron localization schemes.

2.1 Density functional theory

As noted above, we seek approximate solutions to the electronic Schrödinger equation. To this end, we begin by considering a system of N nuclei at positions $\mathbf{R}_1, \dots, \mathbf{R}_N \equiv \mathbf{R}$ and M electrons with coordinate labels $\mathbf{r}_1, \dots, \mathbf{r}_M$ and spin states s_1, \dots, s_M . The fixed nuclear positions

allow us to define the electronic Hamiltonian (in atomic units) as

$$\hat{H}_{\text{elec}}(\mathbf{R}) = -\frac{1}{2} \sum_{i=1}^M \nabla_i^2 + \sum_{i>j} \frac{1}{|\mathbf{r}_i - \mathbf{r}_j|} - \sum_{I=1}^N \sum_{i=1}^M \frac{Z_I}{|\mathbf{R}_I - \mathbf{r}_i|} \quad (1)$$

where Z_I is the charge on the I th nucleus. The time-independent electronic Schrödinger equation or electronic eigenvalue problem

$$\left[-\frac{1}{2} \sum_{i=1}^M \nabla_i^2 + \sum_{i>j} \frac{1}{|\mathbf{r}_i - \mathbf{r}_j|} - \sum_{I=1}^N \sum_{i=1}^M \frac{Z_I}{|\mathbf{R}_I - \mathbf{r}_i|} \right] \Psi(\mathbf{x}_1, \dots, \mathbf{x}_M, \mathbf{R}) = E(\mathbf{R}) \Psi(\mathbf{x}_1, \dots, \mathbf{x}_M, \mathbf{R}) \quad (2)$$

which assumes the validity of the Born-Oppenheimer approximation, could, in principle, yield all of the electronic energy levels and eigenfunctions at the given nuclear configuration \mathbf{R} . Here $\mathbf{x}_i = \mathbf{r}_i, s_i$ is a combination of coordinate and spin variables. Unfortunately, for large condensed-phase problems of the type to be considered here, an exact solution of the electronic eigenvalue problem is computationally intractable.

The Kohn-Sham (KS) (Kohn & Sham, 1965) formulation of density functional theory (DFT) (Hohenberg & Kohn, 1964) replaces the fully interacting electronic system described by Eq. (2) by an equivalent non-interacting system that is required to yield the same *ground-state* energy and wave function as the original interacting system. As the name implies, the central quantity in DFT is the ground-state density $n_0(\mathbf{r})$ generated from the ground-state wave function Ψ_0 via

$$n_0(\mathbf{r}) = M \sum_{s_1=-1/2}^{1/2} \cdots \sum_{s_M=-1/2}^{1/2} \int d\mathbf{r}_2 \cdots d\mathbf{r}_M |\Psi_0(\mathbf{r}, s_1, \dots, s_M)|^2 \quad (3)$$

where, for notational convenience, the dependence on \mathbf{R} is left off. The central theorem of DFT is the Hohenberg-Kohn theorem, which states that there exists an exact energy $E[n]$ that is a functional of electronic densities $n(\mathbf{r})$ such that when $E[n]$ is minimized with respect to $n(\mathbf{r})$ subject to the constraint that $\int d\mathbf{r} n(\mathbf{r}) = M$ (each $n(\mathbf{r})$ must yield the correct number of electrons), the true ground-state density $n_0(\mathbf{r})$ is obtained. The true ground-state energy is then given by $E_0 = E[n_0]$. The KS noninteracting system is constructed in terms of a set of mutually orthogonal single-particle orbitals $\psi_i(\mathbf{r})$ in terms of which the density $n(\mathbf{r})$ is given by

$$n(\mathbf{r}) = \sum_{i=1}^{N_s} f_i |\psi_i(\mathbf{r})|^2 \quad (4)$$

where f_i are the occupation numbers of a set of N_s such orbitals, where $\sum_i f_i = M$. In closed-shell systems, the orbitals are all doubly occupied so that $N_s = M/2$, and $f_i = 2$. In open-shell systems, we treat all of the electrons in double and singly occupied orbitals explicitly and take $N_s = M$. When virtual or unoccupied orbitals are needed, we can take $N_s > M/2$ or $N_s > M$ for closed and open-shell systems, respectively, and take $f_i = 0$ for the virtual orbitals.

In KS theory, the energy functional is taken to be

$$\mathcal{E}[\{\psi\}] = -\frac{1}{2} \sum_{i=1}^{N_s} f_i \langle \psi_i | \nabla^2 | \psi_i \rangle + \frac{1}{2} \int d\mathbf{r} d\mathbf{r}' \frac{n(\mathbf{r})n(\mathbf{r}')}{|\mathbf{r} - \mathbf{r}'|} + E_{\text{xc}}[n] + \int d\mathbf{r} n(\mathbf{r}) V_{\text{ext}}(\mathbf{r}, \mathbf{R}) \quad (5)$$

The first term in the functional represents the noninteracting quantum kinetic energy of the electrons, the second term is the direct Coulomb interaction between two charge distributions, the third term is the exchange-correlation energy, whose exact form is unknown, and the fourth represents the “external” Coulomb potential on the electrons due to the fixed nuclei, $V_{\text{ext}}(\mathbf{r}, \mathbf{R}) = -\sum_I Z_I / |\mathbf{r} - \mathbf{R}_I|$. Minimization of Eq. (5) with respect to the orbitals subject to the orthogonality constraint leads to a set of coupled self-consistent field equations of the form

$$\left[-\frac{1}{2} \nabla^2 + V_{\text{KS}}(\mathbf{r}) \right] \psi_i(\mathbf{r}) = \sum_j \lambda_{ij} \psi_j(\mathbf{r}) \quad (6)$$

where the KS potential $V_{\text{KS}}(\mathbf{r})$ is given by

$$V_{\text{KS}}(\mathbf{r}) = \int d\mathbf{r}' \frac{n(\mathbf{r}')}{|\mathbf{r} - \mathbf{r}'|} + \frac{\delta E_{\text{xc}}}{\delta n(\mathbf{r})} + V_{\text{ext}}(\mathbf{r}, \mathbf{R}) \quad (7)$$

and λ_{ij} is a set of Lagrange multipliers used to enforce the orthogonality constraint $\langle \psi_i | \psi_j \rangle = \delta_{ij}$. If we introduce a unitary transformation U that diagonalizes the matrix λ_{ij} into Eq. (6), then we obtain the Kohn-Sham equations in the form

$$\left[-\frac{1}{2} \nabla^2 + V_{\text{KS}}(\mathbf{r}) \right] \phi_i(\mathbf{r}) = \varepsilon_i \phi_i(\mathbf{r}) \quad (8)$$

where $\phi_i(\mathbf{r}) = \sum_j U_{ij} \psi_j(\mathbf{r})$ are the KS orbitals and ε_i are the KS energy levels, i.e., the eigenvalues of the matrix λ_{ij} . If the exact exchange-correlation functional were known, the KS theory would be exact. However, because $E_{\text{xc}}[n]$ is unknown, approximations must be introduced for this term in practice. The accuracy of DFT results depends critically on the quality of the approximation. One of the most widely used forms for $E_{\text{xc}}[n]$ is known as the generalized-gradient approximation (GGA), where in $E_{\text{xc}}[n]$ is approximated as a local functional of the form

$$E_{\text{xc}}[n] \approx \int d\mathbf{r} f_{\text{GGA}}(n(\mathbf{r}), |\nabla n(\mathbf{r})|) \quad (9)$$

where the form of the function f_{GGA} determines the specific GGA approximation. Commonly used GGA functionals are the Becke-Lee-Yang-Parr (BLYP) (1988; 1988) and Perdew-Burke-Ernzerhof (PBE) (1996) functionals.

2.2 Ab initio molecular dynamics

Solution of the KS equations yields the electronic structure at a set of fixed nuclear positions $\mathbf{R}_1, \dots, \mathbf{R}_N \equiv \mathbf{R}$. Thus, in order to follow the progress of a chemical reaction, we need an approach that allows us to propagate the nuclei in time. If we assume the nuclei can be treated as classical point particles, then we seek the nuclear positions $\mathbf{R}_1(t), \dots, \mathbf{R}_N(t)$ as functions of time, which are given by Newton's second law

$$M_I \ddot{\mathbf{R}}_I = \mathbf{F}_I \quad (10)$$

where M_I and \mathbf{F}_I are the mass and total force on the I th nucleus. If the exact ground-state wave function $\Psi_0(\mathbf{R})$ were known, then the forces would be given by the Hellman-Feynman theorem

$$\mathbf{F}_I = -\langle \Psi_0(\mathbf{R}) | \nabla_I \hat{H}_{\text{elec}}(\mathbf{R}) | \Psi_0(\mathbf{R}) \rangle - \nabla_I U_{\text{NN}}(\mathbf{R}) \quad (11)$$

where we have introduced the nuclear-nuclear Coulomb repulsion

$$U_{\text{NN}}(\mathbf{R}) = \sum_{I>J} \frac{Z_I Z_J}{|\mathbf{R}_I - \mathbf{R}_J|} \quad (12)$$

Within the framework of KS DFT, the force expression becomes

$$\mathbf{F}_I = - \int d\mathbf{r} n_0(\mathbf{r}) \nabla_I V_{\text{ext}}(\mathbf{r}, \mathbf{R}) - \nabla_I U_{\text{NN}}(\mathbf{R}) \quad (13)$$

The equations of motion, Eq. (10), are integrated numerically for a set of discrete times $t = 0, \Delta t, 2\Delta t, \dots, \mathcal{N}\Delta t$ subject to a set of initial coordinates $\mathbf{R}_1(0), \dots, \mathbf{R}_N(0)$ and velocities $\dot{\mathbf{R}}_1(0), \dots, \dot{\mathbf{R}}_N(0)$ using a solver such as the velocity Verlet algorithm:

$$\begin{aligned} \mathbf{R}_I(\Delta t) &= \mathbf{R}_I(0) + \Delta t \dot{\mathbf{R}}_I(0) + \frac{\Delta t^2}{2M_I} \mathbf{F}_I(0) \\ \dot{\mathbf{R}}_I(\Delta t) &= \dot{\mathbf{R}}_I(0) + \frac{\Delta t}{2M_I} [\mathbf{F}_I(0) + \mathbf{F}_I(\Delta t)] \end{aligned} \quad (14)$$

where $\mathbf{F}_I(0)$ and $\mathbf{F}_I(\Delta t)$ are the forces at $t = 0$ and $t = \Delta t$, respectively. Iteration of Eq. (14) yields a full trajectory of \mathcal{N} steps. Eqs. (13) and (14) suggest an algorithm for generating the finite-temperature dynamics of a system using forces generated from electronic structure calculations performed “on the fly” as the simulation proceeds: Starting with the initial nuclear configuration, one minimizes the KS energy functional to obtain the ground-state density, and Eq. (13) is used to obtain the initial forces. These forces are then used to propagate the nuclear positions to the next time step using the first of Eqs. (14). At this new nuclear configuration, the KS functional is minimized again to obtain the new ground-state density and forces using Eq. (13), and these forces are used to propagate the velocities to time $t = \Delta t$. These forces can also be used again to propagate the positions to time $t = 2\Delta t$. The procedure is iterated until a full trajectory is generated. This approach is known as “Born-Oppenheimer” dynamics because it employs, at each step, an electronic configuration that is fully quenched to the ground-state Born-Oppenheimer surface.

An alternative to Born-Oppenheimer dynamics is the Car-Parrinello (CP) method (Car & Parrinello, 1985; Marx & Hutter, 2000; Tuckerman, 2002). In this approach, an initially minimized electronic configuration is subsequently “propagated” from one nuclear configuration to the next using a fictitious Newtonian dynamics for the orbitals. In this “dynamics”, the orbitals are given a small amount of thermal kinetic energy and are made “light” compared to the nuclei. Under these conditions, the orbitals actually generate a potential of mean force surface that is very close to the true Born-Oppenheimer surface. The equations of motion of the CP method are

$$\begin{aligned} M_I \ddot{\mathbf{R}}_I &= -\nabla_I [\mathcal{E}[\{\psi\}, \mathbf{R}] + U_{\text{NN}}(\mathbf{R})] \\ \mu |\ddot{\psi}_i\rangle &= -\frac{\partial}{\partial \langle \psi_i |} \mathcal{E}[\{\psi\}, \mathbf{R}] + \sum_j \lambda_{ij} |\psi_j\rangle \end{aligned} \quad (15)$$

where μ is a mass-like parameter for the orbitals (which actually has units of energy \times time²), and λ_{ij} is the Lagrange multiplier matrix that enforces the orthogonality of the orbitals as a holonomic constraint on the fictitious orbital dynamics. Choosing μ small ensures that the

orbital dynamics is adiabatically decoupled from the true nuclear dynamics, thereby allowing the orbitals to generate the aforementioned potential of mean force surface. For a detailed analysis of the CP dynamics, see Marx et al. (1999); Tuckerman (2002). As an illustration of the CP dynamics, Fig. 1 of Tuckerman & Parrinello (1994) shows the temperature profile for a short CPAIMD simulation of bulk silicon together with the kinetic energy profile from the fictitious orbital dynamics. The figure demonstrates that the orbital dynamics is essentially a “slave” to the nuclear dynamics, which shows that the electronic configuration closely follows that dynamics of the nuclei in the spirit of the Born-Oppenheimer approximation.

2.3 Plane wave basis sets and surface boundary conditions

In AIMD calculations, the most commonly employed boundary conditions are periodic boundary conditions, in which the system is replicated infinitely in all three spatial directions. This is clearly a natural choice for solids and is particularly convenient for liquids. In an infinite periodic system, the KS orbitals become Bloch functions of the form

$$\psi_{i\mathbf{k}}(\mathbf{r}) = e^{i\mathbf{k}\cdot\mathbf{r}} u_{i\mathbf{k}}(\mathbf{r}) \quad (16)$$

where \mathbf{k} is a vector in the first Brioullin zone and $u_{i\mathbf{k}}(\mathbf{r})$ is a periodic function. A natural basis set for expanding a periodic function is the Fourier or plane wave basis set, in which $u_{i\mathbf{k}}(\mathbf{r})$ is expanded according to

$$u_{i\mathbf{k}}(\mathbf{r}) = \frac{1}{\sqrt{V}} \sum_{\mathbf{g}} c_{i,\mathbf{g}}^{\mathbf{k}} e^{i\mathbf{g}\cdot\mathbf{r}} \quad (17)$$

where V is the volume of the cell, $\mathbf{g} = 2\pi\mathbf{h}^{-1}\hat{\mathbf{g}}$ is a reciprocal lattice vector, \mathbf{h} is the cell matrix, whose columns are the cell vectors ($V = \det(\mathbf{h})$), $\hat{\mathbf{g}}$ is a vector of integers, and $\{c_{i,\mathbf{g}}^{\mathbf{k}}\}$ are the expansion coefficients. An advantage of plane waves is that the sums needed to go back and forth between reciprocal space and real space can be performed efficiently using fast Fourier transforms (FFTs). In general, the properties of a periodic system are only correctly described if a sufficient number of \mathbf{k} -vectors are sampled from the Brioullin zone. However, for the applications we will consider, we are able to choose sufficiently large system sizes that we can restrict our \mathbf{k} -point sampling to the single point, $\mathbf{k} = (0,0,0)$, known as the Γ -point. At the Γ -point, the plane wave expansion reduces to

$$\psi_i(\mathbf{r}) = \frac{1}{\sqrt{V}} \sum_{\mathbf{g}} c_{i,\mathbf{g}} e^{i\mathbf{g}\cdot\mathbf{r}} \quad (18)$$

At the Γ -point, the orbitals can always be chosen to be real functions. Therefore, the plane-wave expansion coefficients satisfy the property that $c_{i,\mathbf{g}}^* = c_{i,-\mathbf{g}}$, which requires keeping only half of the full set of plane-wave expansion coefficients. In actual applications, plane waves up to a given cutoff $|\mathbf{g}|^2/2 < E_{\text{cut}}$ are retained. Similarly, the density $n(\mathbf{r})$ given by Eq. (4) can also be expanded in a plane wave basis:

$$n(\mathbf{r}) = \frac{1}{V} \sum_{\mathbf{g}} n_{\mathbf{g}} e^{i\mathbf{g}\cdot\mathbf{r}} \quad (19)$$

However, since $n(\mathbf{r})$ is obtained as a square of the KS orbitals, the cutoff needed for this expansion is $4E_{\text{cut}}$ for consistency with the orbital expansion.

At first glance, it might seem that plane waves are ill-suited to treat surfaces because of their two-dimensional periodicity. However, in a series of papers (Minary et al., 2004; 2002;

Tuckerman & Martyna, 1999), Martyna, Tuckerman, and coworkers showed that clusters (systems with no periodicity), wires (systems with one periodic dimension), and surfaces (systems with two periodic dimensions) could all be treated using a plane-wave basis within a single unified formalism. Let $n(\mathbf{r})$ be a particle density with a Fourier expansion given by Eq. (19), and let $\phi(\mathbf{r} - \mathbf{r}')$ denote an interaction potential. In a fully periodic system, the energy of a system described by $n(\mathbf{r})$ and $\phi(\mathbf{r} - \mathbf{r}')$ is given by

$$E = \frac{1}{2} \int d\mathbf{r} d\mathbf{r}' n(\mathbf{r}) \phi(\mathbf{r} - \mathbf{r}') n(\mathbf{r}') = \frac{1}{2V} \sum_{\mathbf{g}} |n_{\mathbf{g}}|^2 \tilde{\phi}_{-\mathbf{g}} \quad (20)$$

where $\tilde{\phi}_{\mathbf{g}}$ is the Fourier transform of the potential. For systems with fewer than three periodic dimensions, the idea is to replace Eq. (20) with its first-image approximation

$$E \approx E^{(1)} \equiv \frac{1}{2V} \sum_{\mathbf{g}} |n_{\mathbf{g}}|^2 \tilde{\phi}_{-\mathbf{g}} \quad (21)$$

where $\tilde{\phi}_{\mathbf{g}}$ denotes a Fourier expansion coefficient of the potential in the non-periodic dimensions and a Fourier transform along the periodic dimensions. For clusters, $\tilde{\phi}_{\mathbf{g}}$ is given by

$$\tilde{\phi}_{\mathbf{g}} = \int_{-L_z/2}^{L_z/2} dz \int_{-L_y/2}^{L_y/2} dy \int_{-L_x/2}^{L_x/2} dx \phi(\mathbf{r}) e^{-i\mathbf{g} \cdot \mathbf{r}} \quad (22)$$

for wires, it becomes

$$\tilde{\phi}_{\mathbf{g}} = \int_{-L_z/2}^{L_z/2} dz \int_{-L_y/2}^{L_y/2} dy \int_{-\infty}^{\infty} dx \phi(\mathbf{r}) e^{-i\mathbf{g} \cdot \mathbf{r}} \quad (23)$$

and for surfaces, we obtain

$$\tilde{\phi}_{\mathbf{g}} = \int_{-L_z/2}^{L_z/2} dz \int_{-\infty}^{\infty} dy \int_{-\infty}^{\infty} dx \phi(\mathbf{r}) e^{-i\mathbf{g} \cdot \mathbf{r}} \quad (24)$$

The error in the first-image approximation drops off as a function of the volume, area, or length in the non-periodic directions, as analyzed in Minnary et al. (2004; 2002); Tuckerman & Martyna (1999).

In order to have an expression that is easily computed within the plane wave description, consider two functions $\phi^{\text{long}}(\mathbf{r})$ and $\phi^{\text{short}}(\mathbf{r})$, which are assumed to be the long and short range contributions to the total potential, i.e.

$$\phi(\mathbf{r}) = \phi^{\text{long}}(\mathbf{r}) + \phi^{\text{short}}(\mathbf{r})$$

$$\tilde{\phi}(\mathbf{g}) = \tilde{\phi}^{\text{long}}(\mathbf{g}) + \tilde{\phi}^{\text{short}}(\mathbf{g}). \quad (25)$$

We require that $\phi^{\text{short}}(\mathbf{r})$ vanish exponentially quickly at large distances from the center of the parallelepiped and that $\phi^{\text{long}}(\mathbf{r})$ contain the long range dependence of the full potential, $\phi(\mathbf{r})$.

With these two requirements, it is possible to write

$$\begin{aligned}
 \tilde{\phi}^{\text{short}}(\mathbf{g}) &= \int_{D(V)} d\mathbf{r} e^{-i\mathbf{g}\cdot\mathbf{r}} \phi^{\text{short}}(\mathbf{r}) \\
 &= \int_{\text{all space}} d\mathbf{r} e^{-i\mathbf{g}\cdot\mathbf{r}} \phi^{\text{short}}(\mathbf{r}) + \epsilon(\mathbf{g}) \\
 &= \tilde{\phi}^{\text{short}}(\mathbf{g}) + \epsilon(\mathbf{g})
 \end{aligned} \tag{26}$$

with exponentially small error, $\epsilon(\mathbf{g})$, provided the range of $\phi^{\text{short}}(\mathbf{r})$ is small compared size of the parallelepiped. In order to ensure that Eq. (26) is satisfied, a convergence parameter, α , is introduced which can be used to adjust the range of $\phi^{\text{short}}(\mathbf{r})$ such that $\epsilon(\mathbf{g}) \sim 0$ and the error, $\epsilon(\mathbf{g})$, will be neglected in the following.

The function, $\tilde{\phi}^{\text{short}}(\mathbf{g})$, is the Fourier transform of $\phi^{\text{short}}(\mathbf{r})$. Therefore,

$$\begin{aligned}
 \tilde{\phi}(\mathbf{g}) &= \tilde{\phi}^{\text{long}}(\mathbf{g}) + \tilde{\phi}^{\text{short}}(\mathbf{g}) \\
 &= \tilde{\phi}^{\text{long}}(\mathbf{g}) - \tilde{\phi}^{\text{long}}(\mathbf{g}) + \tilde{\phi}^{\text{short}}(\mathbf{g}) + \tilde{\phi}^{\text{long}}(\mathbf{g}) \\
 &= \hat{\phi}^{\text{screen}}(\mathbf{g}) + \tilde{\phi}(\mathbf{g})
 \end{aligned} \tag{27}$$

where $\tilde{\phi}(\mathbf{g}) = \tilde{\phi}^{\text{short}}(\mathbf{g}) + \tilde{\phi}^{\text{long}}(\mathbf{g})$ is the Fourier transform of the full potential, $\phi(\mathbf{r}) = \phi^{\text{short}}(\mathbf{r}) + \phi^{\text{long}}(\mathbf{r})$ and

$$\hat{\phi}^{\text{screen}}(\mathbf{g}) = \tilde{\phi}^{\text{long}}(\mathbf{g}) - \tilde{\phi}^{\text{long}}(\mathbf{g}). \tag{28}$$

Thus, Eq. (28) becomes leads to

$$\langle \phi \rangle = \frac{1}{2V} \sum_{\mathbf{g}} |\tilde{n}(\mathbf{g})|^2 [\tilde{\phi}(-\mathbf{g}) + \hat{\phi}^{\text{screen}}(-\mathbf{g})] \tag{29}$$

The new function appearing in the average potential energy, Eq. (29), is the difference between the Fourier series and Fourier transform form of the long range part of the potential energy and will be referred to as the screening function because it is constructed to “screen” the interaction of the system with an infinite array of periodic images. The specific case of the Coulomb potential, $\phi(\mathbf{r}) = 1/r$, can be separated into short and long range components via

$$\frac{1}{r} = \frac{\text{erf}(\alpha r)}{r} + \frac{\text{erfc}(\alpha r)}{r} \tag{30}$$

where the first term is long range. The parameter α determines the specific ranges of these terms. The screening function for the cluster case is easily computed by introducing an FFT grid and performing the integration numerically (Tuckerman & Martyna, 1999). For the wire (Minary et al., 2002) and surface (Minary et al., 2004) cases, analytical expressions can be

worked out. In particular, for surfaces, the screening function is

$$\begin{aligned} \bar{\phi}^{\text{screen}}(\mathbf{g}) = & -\frac{4\pi}{g^2} \left\{ \cos\left(\frac{g_c L_c}{2}\right) \right. \\ & \times \left[\exp\left(-\frac{g_s L_c}{2}\right) - \frac{1}{2} \exp\left(-\frac{g_s L_c}{2}\right) \operatorname{erfc}\left(\frac{\alpha^2 L_c - g_s}{2\alpha}\right) \right. \\ & \quad \left. - \frac{1}{2} \exp\left(\frac{g_s L_c}{2}\right) \operatorname{erfc}\left(\frac{\alpha^2 L_c + g_s}{2\alpha}\right) \right] \\ & \left. + \exp\left(-\frac{g^2}{4\alpha^2}\right) \operatorname{Re}\left[\operatorname{erfc}\left(\frac{\alpha^2 L_c + i g_c}{2\alpha}\right)\right] \right\} \end{aligned} \quad (31)$$

When a plane wave basis set is employed, the external energy is made somewhat complicated by the fact that very large basis sets are needed to treat the rapid spatial fluctuations of core electrons. Therefore, core electrons are often replaced by atomic pseudopotentials or augmented plane wave techniques. Here, we shall discuss the former. In the atomic pseudopotential scheme, the nucleus plus the core electrons are treated in a frozen core type approximation as an “ion” carrying only the valence charge. In order to make this approximation, the valence orbitals, which, in principle must be orthogonal to the core orbitals, must see a different pseudopotential for each angular momentum component in the core, which means that the pseudopotential must generally be nonlocal. In order to see this, we consider a potential operator of the form

$$\hat{V}_{\text{pseud}} = \sum_{l=0}^{\infty} \sum_{m=-l}^l v_l(r) |lm\rangle \langle lm| \quad (32)$$

where r is the distance from the ion, and $|lm\rangle \langle lm|$ is a projection operator onto each angular momentum component. In order to truncate the infinite sum over l in Eq. (32), we assume that for some $\bar{l} \geq \bar{l}$, $v_l(r) = v_{\bar{l}}(r)$ and add and subtract the function $v_{\bar{l}}(r)$ in Eq. (32):

$$\begin{aligned} \hat{V}_{\text{pseud}} &= \sum_{l=0}^{\infty} \sum_{m=-l}^l (v_l(r) - v_{\bar{l}}(r)) |lm\rangle \langle lm| + v_{\bar{l}}(r) \sum_{l=0}^{\infty} \sum_{m=-l}^l |lm\rangle \langle lm| \\ &= \sum_{l=0}^{\infty} \sum_{m=-l}^l (v_l(r) - v_{\bar{l}}(r)) |lm\rangle \langle lm| + v_{\bar{l}}(r) \\ &\approx \sum_{l=0}^{\bar{l}-1} \sum_{m=-l}^l \Delta v_l(r) |lm\rangle \langle lm| + v_{\bar{l}}(r) \end{aligned} \quad (33)$$

where the second line follows from the fact that the sum of the projection operators is unity, $\Delta v_l(r) = v_l(r) - v_{\bar{l}}(r)$, and the sum in the third line is truncated before $\Delta v_l(r) = 0$. The complete pseudopotential operator is

$$\hat{V}_{\text{pseud}}(r; \mathbf{R}_1, \dots, \mathbf{R}_N) = \sum_{I=1}^N \left[v_{\text{loc}}(|\mathbf{r} - \mathbf{R}_I|) + \sum_{l=0}^{\bar{l}-1} \Delta v_l(|\mathbf{r} - \mathbf{R}_I|) |lm\rangle \langle lm| \right] \quad (34)$$

where $v_{\text{loc}}(r) \equiv v_I(r)$ is known as the local part of the pseudopotential (having no projection operator attached to it). Now, the external energy, being derived from the ground-state expectation value of a one-body operator, is given by

$$\varepsilon_{\text{ext}} = \sum_i f_i \langle \psi_i | \hat{V}_{\text{pseud}} | \psi_i \rangle \quad (35)$$

The first (local) term gives simply a local energy of the form

$$\varepsilon_{\text{loc}} = \sum_{I=1}^N \int d\mathbf{r} n(\mathbf{r}) v_{\text{loc}}(|\mathbf{r} - \mathbf{R}_I|) \quad (36)$$

which can be evaluated in reciprocal space as

$$\varepsilon_{\text{loc}} = \frac{1}{\Omega} \sum_{I=1}^N \sum_{\mathbf{g}} n_{\mathbf{g}}^* \tilde{v}_{\text{loc}}(\mathbf{g}) e^{-i\mathbf{g} \cdot \mathbf{R}_I} \quad (37)$$

where $\tilde{v}_{\text{loc}}(\mathbf{g})$ is the Fourier transform of the local potential. Note that at $\mathbf{g} = (0,0,0)$, only the nonsingular part of $\tilde{v}_{\text{loc}}(\mathbf{g})$ contributes. In the evaluation of the local term, it is often convenient to add and subtract a long-range term of the form $Z_I \text{erf}(\alpha_I r)/r$, where $\text{erf}(x)$ is the error function, each ion in order to obtain the nonsingular part explicitly and a residual short-range function $\tilde{v}_{\text{loc}}(|\mathbf{r} - \mathbf{R}_I|) = v_{\text{loc}}(|\mathbf{r} - \mathbf{R}_I|) - Z_I \text{erf}(\alpha_I |\mathbf{r} - \mathbf{R}_I|)/|\mathbf{r} - \mathbf{R}_I|$ for each ionic core.

2.4 Electron localization methods

An important feature of the KS energy functional is the fact that the total energy $E[\{\psi\}, \mathbf{R}]$ is invariant with respect to a unitary transformation within space of occupied orbitals. That is, if we introduce a new set of orbitals $\psi'_i(\mathbf{r})$ related to the $\psi_i(\mathbf{r})$ by

$$\psi'_i(\mathbf{r}) = \sum_{j=1}^{N_s} U_{ij} \psi_j(\mathbf{r}) \quad (38)$$

where U_{ij} is a $N_s \times N_s$ unitary matrix, the energy $E[\{\psi'\}, \mathbf{R}] = E[\{\psi\}, \mathbf{R}]$. We say that the energy is invariant with respect to the group $\text{SU}(N_s)$, i.e., the group of all $N_s \times N_s$ unitary matrices with unit determinant. This invariance is a type of gauge invariance, specifically that in the occupied orbital subspace. The fictitious orbital dynamics of the AIMD scheme as written in Eqs. (15) does not preserve any particular unitary representation or gauge of the orbitals but allows the orbitals to mix arbitrarily according to Eq. (38). This mixing happens intrinsically as part of the dynamics rather than by explicit application of the unitary transformation.

Although this arbitrariness has no effect on the nuclear dynamics, it is often desirable for the orbitals to be in a particular unitary representation. For example, we might wish to have the true Kohn-Sham orbitals at each step in an AIMD simulation in order to calculate the Kohn-Sham eigenvalues and generate the corresponding density of states from a histogram of these eigenvalues. This would require choosing U_{ij} to be the unitary transformation that diagonalizes the matrix of Lagrange multipliers in Eq. (6). Another important representation is that in which the orbitals are maximally localized in real space. In this representation, the orbitals are closest to the classic “textbook” molecular orbital picture.

In order to obtain the unitary transformation U_{ij} that generates maximally localized orbitals, we seek a functional that measures the total spatial spread of the orbitals. One possibility for this functional is simply to use the variance of the position operator $\hat{\mathbf{r}}$ with respect to each orbital and sum these variances:

$$\Omega[\{\psi\}] = \sum_{i=1}^{N_s} \left[\langle \psi_i | \hat{\mathbf{r}}^2 | \psi_i \rangle - \langle \psi_i | \hat{\mathbf{r}} | \psi_i \rangle^2 \right] \quad (39)$$

The procedure for obtaining the maximally localized orbitals is to introduce the transformation in Eq. (38) into Eq. (39) and then to minimize the spread functional with respect to U_{ij} :

$$\frac{\partial}{\partial U_{ij}} \Omega[\{\psi'\}] = 0 \quad (40)$$

The minimization must be carried out subject to the constraint the U_{ij} be an element of $SU(N_s)$. This constraint condition can be eliminated if we choose U to have the form $U = \exp(iA)$, where A is an $N_s \times N_s$ Hermitian matrix, and performing the minimization of Ω with respect to A .

A little reflection reveals that the spread functional in Eq. (39) is actually not suitable for periodic systems. The reason for this is that the position operator $\hat{\mathbf{r}}$ lacks the translational invariance of the underlying periodic supercell. A generalization of the spread functional that does not suffer from this deficiency is (Berghold et al., 2000; Resta & Sorella, 1999)

$$\Omega[\{\psi\}] = \frac{1}{(2\pi)^2} \sum_{i=1}^{N_s} \sum_I \omega_I f(|z_{I,ii}|^2) + \mathcal{O}((\sigma/L)^2) \quad (41)$$

where σ and L denote the typical spatial extent of a localized orbital and box length, respectively, and

$$z_{I,ii} = \int d\mathbf{r} \psi_i^*(\mathbf{r}) e^{i\mathbf{G}_I \cdot \mathbf{r}} \psi_j(\mathbf{r}) \equiv \langle \psi_i | \hat{O}^I | \psi_j \rangle \quad (42)$$

Here $G_I = 2\pi(\mathbf{h}^{-1})^T \hat{\mathbf{g}}_I$, where $\hat{\mathbf{g}}_I = (l_I, m_I, n_I)$ is the I th Miller index and ω_I is a weight having dimensions of $(\text{length})^2$. The function $f(|z|^2)$ is often taken to be $1 - |z|^2$, although several choices are possible. The orbitals that result from minimizing Eq. (41) are known as *Wannier orbitals* $|w_i\rangle$. If $z_{I,ii}$ is evaluated with respect to these orbitals, then the orbital centers, known as *Wannier centers*, can be computed according to

$$w_\alpha = - \sum_\beta \frac{h_{\alpha\beta}}{2\pi} \text{Im} \ln z_{\beta,ii} \quad (43)$$

Wannier orbitals and their centers are useful in analyzing chemically reactive systems and will be employed in the present surface chemistry studies.

Like the KS energy, the fictitious CP dynamics is invariant with respect to gauge transformations of the form given in Eq. (38). They are not, however, invariant under time-dependent unitary transformations of the form

$$\psi'_i(\mathbf{r}, t) = \sum_{j=1}^{N_s} U_{ij}(t) \psi_j(\mathbf{r}, t) \quad (44)$$

and consequently, the orbital gauge changes at each step of an AIMD simulation. If, however, we impose the requirement of invariance under Eq. (44) on the CP dynamics, then not only would we obtain a gauge-invariant version of the AIMD algorithm, but we could also then fix a particular orbital gauge and have this gauge be preserved under the CP evolution. Using techniques for gauge field theory, it is possible to devise such a AIMD algorithm (Thomas et al., 2004). Introducing orbital momenta $|\pi_i\rangle$ conjugate to the orbital degrees of freedom, the gauge-invariant AIMD equations of motion have the basic structure

$$\begin{aligned}
 M_I \ddot{\mathbf{R}}_I &= -\nabla_I [\mathcal{E}[\{\psi\}, \mathbf{R}] + U_{\text{NN}}(\mathbf{R})] \\
 |\dot{\psi}_i\rangle &= |\pi_i\rangle + \sum_j B_{ij}(t) |\psi_j\rangle \\
 |\dot{\pi}_i\rangle &= -\frac{1}{\mu} \frac{\partial}{\partial \langle \psi_i |} \mathcal{E}[\{\psi\}, \mathbf{R}] + \sum_j \lambda_{ij} |\psi_j\rangle + \sum_j B_{ij}(t) |\pi_j\rangle
 \end{aligned} \tag{45}$$

where

$$B_{ij}(t) = \sum_k U_{ki} \frac{d}{dt} U_{kj} \tag{46}$$

Here, the terms involving the matrix $B_{ij}(t)$ are gauge-fixing terms that preserve a desired orbital gauge. If we choose the unitary transformation $U_{ij}(t)$ to be the matrix that satisfies Eq. (40), then Eqs. (45) will propagate maximally localized orbitals (Iftimie et al., 2004). As was shown in Iftimie et al. (2004); Thomas et al. (2004), it is possible to evaluate the gauge-fixing terms in a way that does not require explicit minimization of the spread functional (Sharma et al., 2003). In this way, if the orbitals are initially localized, they remain localized throughout the trajectory.

While the Wannier orbitals and Wannier centers are useful concepts, it is also useful to have a measure of electron localization that does not depend on a specific orbital representation, as the latter does have some arbitrariness associated with it. An alternative measure of electron localization that involves only the electron density $n(\mathbf{r})$ and the so-called kinetic energy density

$$\tau(\mathbf{r}) = \sum_{i=1}^{N_s} |f_i \nabla \psi_i(\mathbf{r})|^2 \tag{47}$$

was introduced by Becke and Edgecombe (1990). Defining the ratio $\chi(\mathbf{r}) = D(\mathbf{r})/D_0(\mathbf{r})$, where

$$\begin{aligned}
 D(\mathbf{r}) &= \tau(\mathbf{r}) - \frac{1}{4} \frac{|\nabla n(\mathbf{r})|^2}{n(\mathbf{r})} \\
 D_0(\mathbf{r}) &= \frac{3}{4} (6\pi^2)^{2/3} n^{5/3}(\mathbf{r})
 \end{aligned} \tag{48}$$

the function $f(\mathbf{r}) = 1/(1 + \chi^2(\mathbf{r}))$ can be shown to lie in the interval $f(\mathbf{r}) \in [0, 1]$, where $f(\mathbf{r}) = 1$ corresponds to perfect localization, and $f(\mathbf{r}) = 1/2$ corresponds to a gas-like localization. The function $f(\mathbf{r})$ is known as the *electron localization function* or ELF. In the studies to be presented below, we will make use both of the ELF and the Wannier orbitals and centers to quantify electron localization.

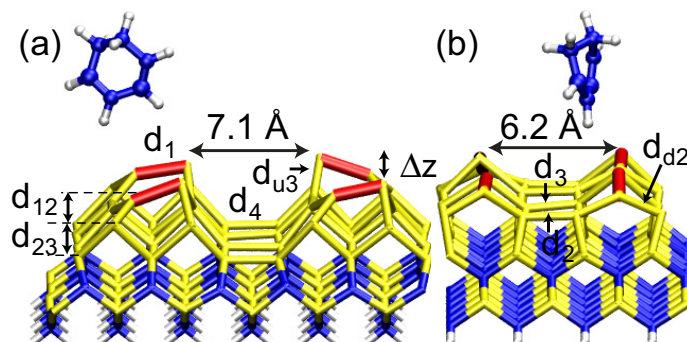


Fig. 1. View of 1,3-CHD + 3C-SiC(001)-3 \times 2 system (a) along dimer rows and (b) between dimers in a row. Si, C, H, and the top Si surface dimers are represented by yellow, blue, white, and red, respectively. The dimers are spaced farther apart by $\sim 60\%$ along a dimer row and $\sim 20\%$ across dimer rows relative to Si(100)-2 \times 1.

3. Reactions on the 3C-SiC(001)-3 \times 2 surface

Silicon-carbide (SiC) and its associated reactions with a conjugated diene is an interesting surface to study and to compare to the pure silicon surface. In previous work (Hayes & Tuckerman, 2007; Minary & Tuckerman, 2004; 2005), we have shown that when a conjugated diene reacts with the Si(100)-2 \times 1 surface, a relatively broad distribution of products results, in agreement with experiment (Teague & Boland, 2003; 2004), because the surface dimers are relatively closely spaced. Because of this, creating ordered organic layers on this surface using conjugated dienes seems unlikely unless some method can be found to enhance the population of one of the adducts, rendering the remaining adducts negligible. SiC exhibits a number of complicated surface reconstructions depending on the surface orientation and growth conditions. Some of these reconstructions offer the intriguing possibility of restricting the product distribution due to the fact that carbon-carbon or silicon-silicon dimer spacings are considerably larger.

SiC is often the material of choice for electronic and sensor applications under extreme conditions (Capano & Trew, 1997; Mélinon et al., 2007; Starke, 2004) or subject to biocompatibility constraints (Stutzmann et al., 2006). Although most reconstructions are still being debated both experimentally and theoretically (Pollmann & Krüger, 2004; Soukiassian & Enriquez, 2004), there is widespread agreement on the structure of the 3C-SiC(001)-3 \times 2 surface (D'angelo et al., 2003; Tejeda et al., 2004)(see Fig. 1), which will be studied in this section. SiC(001) shares the same zinc blend structure as pure Si(001), but with alternating layers of Si and C. The top three layers are Si, the bottom in bulk-like positions and the top decomposed into an open 2/3 + 1/3 adlayer structure. Si atoms in the bottom two-thirds layers are 4-fold coordinated dimers while those Si atoms in the top one-third are asymmetric tilted dimers with dangling bonds. Given the Si-rich surface environment and presence of asymmetric surface dimers, one might expect much of the same Si-based chemistry to occur with two significant differences: (1) altered reactivity due to the surface strain (the SiC lattice constant is $\sim 20\%$ smaller than Si) and (2) suppression of interdimer adducts due to the larger dimer spacing compared to Si ($\sim 60\%$ along a dimer row, $\sim 20\%$ across dimer rows). Previous theoretical studies used either static (0 K) DFT calculations of hydrogen (Chang et al., 2005; Di Felice et al., 2005; Peng et al., 2007a; 2005; 2007b), a carbon

nanotube (de Brito Mota & de Castilho, 2006), or ethylene/acetylene (Wieferink et al., 2006; 2007) adsorbed on SiC(001)- 3×2 or employed molecular dynamics of water (Cicero et al., 2004) or small molecules of the $\text{CH}_3\text{-X}$ family (Cicero & Catellani, 2005) on the less thermodynamically stable SiC(001)- 2×1 surface. Here, we consider cycloaddition reactions on the SiC- 3×2 surface that include dynamic and thermal effects. A primary goal for considering this surface is to determine whether 3C-SiC(001)- 3×2 is a promising candidate for creating ordered semiconducting-organic interfaces via cycloaddition reactions.

In the study Hayes and Tuckerman (2008), the KS orbitals were expanded in a plane-wave basis set up to a kinetic energy cut-off of 40 Ry. As in the 1,3-CHD studies described above, exchange and correlation are treated with the spin restricted form of the PBE functional (Perdew et al., 1996), and core electrons were replaced by Troullier-Martins pseudopotentials (Troullier & Martins, 1991) with S, P, and D treated as local for H, C, and Si, respectively. The resulting SiC theoretical lattice constant, 4.39 Å, agrees well with the experimental value of 4.36 Å (Tejeda et al., 2004). The full system is shown in Fig. 1. The 3×2 unit cell is doubled in both directions to include four surface dimers to allow the possibility of all interdimer adducts. Again, the resulting large surface area, (18.6 Å \times 12.4 Å), allows the Γ -point approximation to be used in lieu of explicit k-point sampling. Two bulk layers of Si and C, terminated by H on the bottom surface, provide a reconstructed ($1/3 + 2/3$) Si surface in reasonable agreement with experiment (see below). The final system has 182 atoms [24 atoms/layer \times (1 Si adlayer + 4 atomic layers) + 2×24 terminating H]. The simulation cell employed lengths of 18.6 Å and 12.4 Å along the periodic directions and 31.2 Å along the nonperiodic z direction.

Both the CHD and SiC(001) surface were equilibrated separately under NVT conditions using Nosé-Hoover chain thermostats (Martyna et al., 1992) at 300 K with a timestep of 0.1 fs for 1 ps and 3 ps, respectively. When the equilibrated CHD was allowed to react with the equilibrated surface, the time step was reduced to 0.05 fs in order to ensure adiabaticity. The CHD was placed 3 Å above the surface, as defined by the lowest point on the CHD and the highest point on the surface. Each of twelve trajectories was initiated from the same CHD and SiC structures but with the CHD placed at a different orientations and/or locations over the surface. The subsequent initialization procedure was identical to the CHD-Si(100) system: First the system was annealed from 0 K to 300 K in the NVE ensemble. Following this, it was equilibrated with Nosé-Hoover chain thermostats for 1 ps at 300K under NVT conditions, keeping the center of mass of the CHD fixed. Finally, the CHD center of mass constraint was removed and the system was allowed to evolve under the NVE ensemble until an adduct formed or 20 ps elapsed.

The reactions that occur on this surface all take place on or in the vicinity of a single surface Si-Si dimer. However, as Fig. 2 shows, there is not one but rather four adducts that are observed to form. Adduct labels from the Si + CHD study are used for consistency. As postulated, the widely spaced dimers successfully suppressed the interdimer adducts that formed on the Si(100)- 2×1 surface (Hayes & Tuckerman, 2007). From the twelve trajectories, three formed the [4+2] Diels-Alder type intradimer adduct (A), one produced the [2+2] intradimer adduct (D), five exhibited hydrogen abstraction (H), and one resulted in a novel [4+2] subdimer adduct between Si in d_1 and d_2 (G) (see Fig. 1). The remaining trajectories only formed 1 C-Si bond within 20 ps. Although the statistics are limited, these results suggest that H abstraction is favorable, consistent with the high reactivity of atomic H observed in experimental studies on this system (Amy & Chabal, 2003; Derycke et al., 2003). What is somewhat more troublesome, from the point of view of creating well-ordered

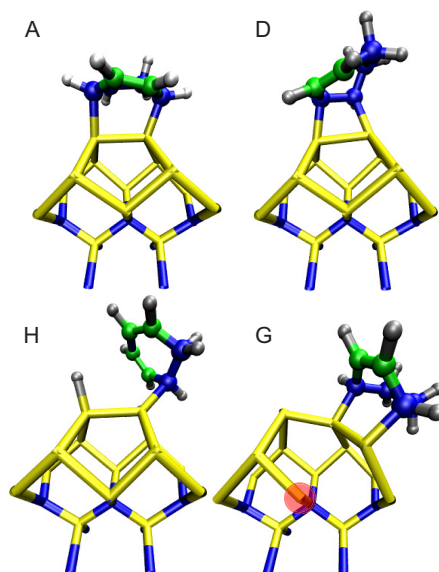


Fig. 2. Snapshots of the four adducts which formed on the SiC surface: (A) [4+2] intradimer adduct, (D) [2+2] intradimer adduct, (H) hydrogen abstraction, and (G) [4+2] subsurface dimer adduct. Si, C, and H are represented by yellow, blue, and silver, respectively. The remaining C=C bond(s) is highlighted in green. The larger spacing between dimers suppresses interdimer adducts. However, adduct (G) destroys the surface, rendering this system inappropriate for applications requiring well-defined organic-semiconducting interfaces.

organic-semiconducting interfaces is the presence of the subdimer adduct G. All the surface bonds directly connected to the adduct slightly expand to 2.42-2.47 Å, with the exception of one bond to a Si in the third layer, (highlighted in red in Fig. 2G) which disappears entirely. The energetic gain of the additional strong C-Si bond outweighs the loss of a strained Si-Si bond. The end effect is the destruction of the perfect surface and the creation of an unsaturated Si in the bulk. One adduct is noticeably missing: the [2+2] subdimer adduct. At several points during the simulation this adduct was poised to form but quickly left the vicinity. Most likely, the strain caused by the four-member ring combined with the two energetically less stable unsaturated Si prevented this adduct from forming, even though the [2+2] intradimer and [4+2] subdimer adducts are stable.

In Fig. 3, we show the carbon-carbon and CHD-Si distances as functions of time for the different adducts observed. This figure reveals that the mechanism of the reactions proceeds in a manner very similar to that of CHD and 1,3-butadiene on the Si(100)-2×1 surface: It is an asymmetric, nonconcerted mechanism that involves a carbocation intermediate. What differs from Si(100) is the time elapsed before the first bond forms and the intermediate lifetime. On the Si(100)-2×1 surface the CHD always found an available "down" Si to form the first bond within less than 10 ps or 40 Å of wandering over the surface. On the SiC(001)-3×2 surface the exploration process sometimes required up to 20 ps and over 100 Å. While the exact numbers are only qualitative, the trend is significant. The Si(100) dimers are more tilted on average, and hence expected to be slightly more reactive. However, the dominant contribution is

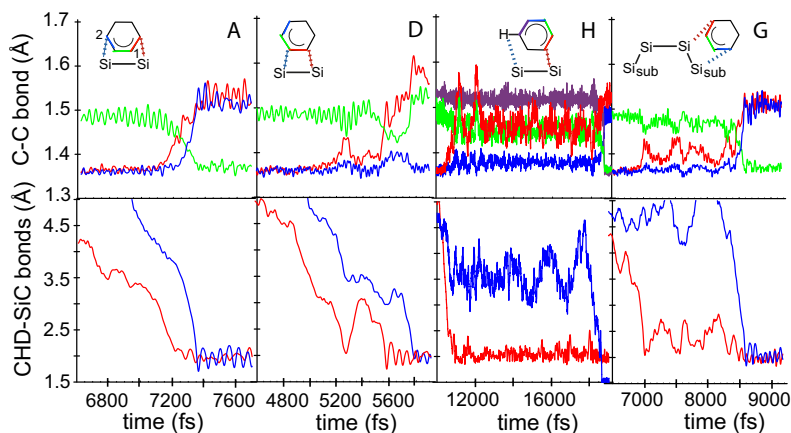


Fig. 3. Relevant bond lengths (Å) vs time (fs) during product formation for four representative adducts. The top row displays the C-C bonds lengths (moving average over 25 fs) while the bottom row plots the first and second CHD - SiC surface bond. The color-coded inset identifies the bond being plotted for each adduct type. Change in the C-C bond length closely correlates with surface-adduct bond formation. Intermediate lifetimes over all trajectories range from 0.05 - 18⁺ ps.

likely the density of tilted dimers: Si has 0.033 dimers/Å², but SiC only has 0.017 dimers/Å². Regardless of whether dimer flipping occurs, it is simply more difficult to find a dimer on the SiC surface.

An important consideration in cycloaddition reactions such as those studied here is the possibility of their occurring through a radical mechanism. Multi-reference self consistent field cluster calculations of the SiC(001)-2x1 surface suggest that the topmost dimer exhibits significant diradical character (Tamura & Gordon, 2003), and since DFT is a single-reference method, multi-reference contributions are generally not included. However, cluster methods may bias the results by unphysically truncating the system instead of treating the full periodicity. For instance, cluster methods predict that Si(100)-2x1 dimers are symmetric (Olson & Gordon, 2006), contrary to experimental evidence (Mizuno et al., 2004; Over et al., 1997), while periodic DFT correctly captures the dimer tilt (Hayes & Tuckerman, 2007). In order to estimate the importance of diradical mechanisms and surface crossing, a series of single point energy calculations at regular intervals during four representative trajectories are plotted in Fig. 4. Three electronic configurations are considered: singlet spin restricted (SR) where the up and down spin are identical (black down triangles), singlet spin unrestricted (SU) where the up and down spin can vary spatially (red up triangles), and triplet SU (green squares). In all cases, the triplet configuration is unfavorable. However, at two places in the transition state (Adduct A in Fig. 4a at 3000 fs and Adduct G in Fig. 4d at 8500 fs) the single SU is slightly favored. Thus, multi-reference methods, which can account for surface crossing, may yield alternative reaction mechanisms.

4. Reactions on the SiC(100)-2x2 surface

There is considerable interest in the growth of molecular lines or wires on semiconductor surfaces. Such structures allow molecular scale devices to be constructed using

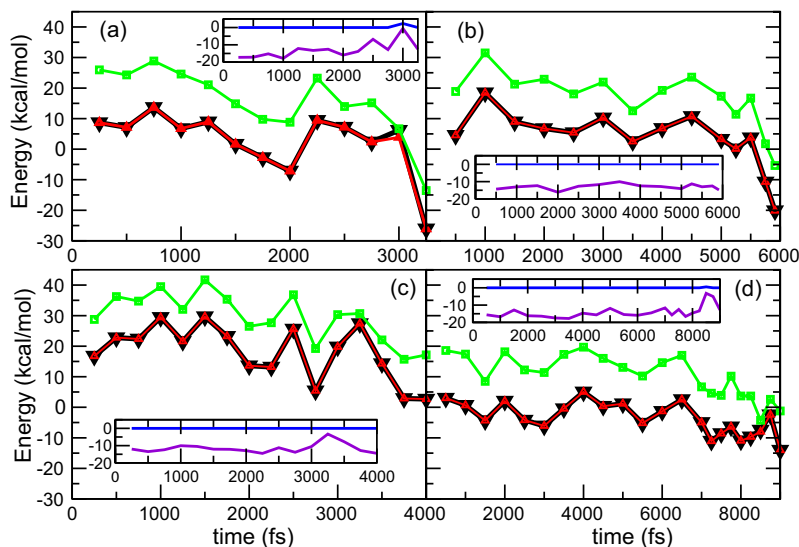


Fig. 4. Spin restricted (black down triangles), singlet spin-unrestricted (red up triangles), and triplet unrestricted (green squares) energies at regular intervals during a representative (a) [4+2] intradimer adduct [A], (b) [2+2] intradimer adduct [D], (c) H-abstraction, and (d) [4+2] subdimer trajectory. Energies are relative to the value at $t=0$ in (a). The insets show the difference between the spin restricted and unrestricted singlet energies (blue line) and spin restricted and triplet unrestricted energies (purple). The triplet configuration is always highest in energy. In (a) at 3000 fs and (d) at 8500 fs the singlet transition state configuration is favorable by 2.3 and 0.5 kcal/mol, respectively. Thus, a radical mechanism may also occur in this system.

semiconductors such as H-terminated Si(111) and Si(100) or Si(100)-2 \times 1 as the preferred substrates. Various molecules can be grown into lines on the H-terminated surfaces (McNab & Polanyi, 2006), and on the Si(100)-2 \times 1 surface, styrene and derivatives such as 2,4-dimethylstyrene or longer chain alkenes can be used to grow wires along the dimer rows (DiLabio et al., 2007; 2004; Hossain et al., 2005a;c; 2007a;b; 2008; Zikovskiy et al., 2007). More recently, allylic mercaptan and acetophenone have been shown to grow across dimer rows on the H:Si(100)-2 \times 1 surface (Ferguson et al., 2009; 2010; Hossain et al., 2005c; 2008; 2009). Other semiconductor surface can be considered for such applications, however, these have not received as much attention. An intriguing possible alternate in the silicon-carbide family is the SiC(100)-2 \times 2 surface.

The SiC(100)-2 \times 2 surface exhibits the crucial difference from the SiC(100)-3 \times 2 in that it is characterized by C \equiv C triple bonds, which bridge Si-Si single bonds. These triple bonds are well separated and reactive, suggesting the possibility of restricting the product distribution for the addition of conjugated dienes on this surface. Fig. 5 shows a snapshot of this surface. Previous *ab initio* calculations suggest that these dimers react favorably with 1,4-cyclohexadiene (Bermudez, 2003). Here, we present new results on the free energy profile at 300 K for the reaction of this surface with 1,3-cyclohexadiene.

In general, reaction mechanisms and thermodynamic barriers for the cycloaddition reactions studied here can be analyzed by computing a free energy profile for one of the product states,

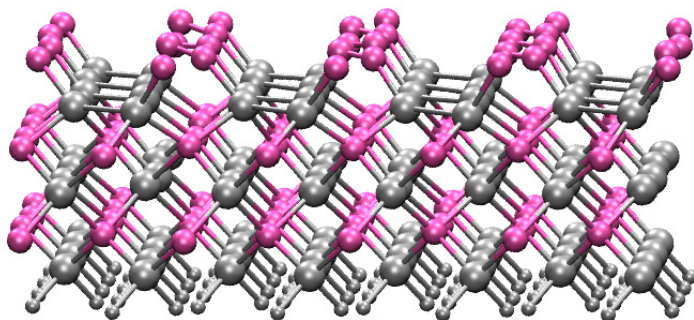


Fig. 5. Snapshot of the SiC-2×2 surface. Pink and grey spheres represent carbon and silicon atoms, respectively.

which we take to be the Diels-Alder-type [4+2] intradimer product. In the present case, the expect some of the barriers to product formation to be sufficiently high that specialized free energy sampling techniques are needed. Here, we employ the so-called blue moon ensemble approach (Carter et al., 1989; Sprik & Ciccotti, 1998) combined with thermodynamic integration. In order to define such a free energy profile, we first need to specify a reaction coordinate capable of following the progress of the reaction. For this purpose, we choose a coordinate ξ of the form

$$\xi = \frac{1}{2} \left| \left(\mathbf{r}_{C_a^s} + \mathbf{r}_{C_b^s} \right) - \left(\mathbf{r}_{C_1^m} + \mathbf{r}_{C_4^m} \right) \right| \quad (49)$$

where C_1^m and C_4^m are the carbons in the 1 and 4 positions in the organic molecule, and C_a^s and C_b^s are the two surface carbon atoms with which covalent bonds will form with C_1^m and C_4^m . Over the course of the reactions considered, ξ decreases from approximately 4 Å to a value less than 1.5 Å. In the aforementioned blue moon ensemble approach (Carter et al., 1989; Sprik & Ciccotti, 1998), the coordinate ξ is constrained at a set of equally spaced points between the two endpoints. At each constrained value, an AIMD simulation is performed over which we compute a conditional average $\langle \partial H / \partial \xi \rangle_{\text{cond}}$, where H is the nuclear Hamiltonian. Finally, the full free energy profile is reconstructed via thermodynamic integration:

$$\Delta G(\xi) = \int_{\xi_0}^{\xi} d\xi' \left\langle \frac{\partial H}{\partial \xi'} \right\rangle_{\text{cond}} \quad (50)$$

An example of such a free energy profile for the [4+2] cycloaddition reaction of 1,3-butadiene with a single silicon surface dimer on the Si(100)-2×1 surface is shown in Fig. 6 (Minary & Tuckerman, 2004). We show this profile as an example in order that direct comparison can be made between reactions on this surface and those on the SiC(100)2×2 surface. The profile in Fig. 6 shows an initial barrier at $\xi = 3.2$ Å of approximately 23 kcal/mol. As ξ decreases, a shallow minimum/plateau is seen at $\xi = 2.75$ Å, and such a minimum indicates a stable intermediate. This intermediate was identified as a carbocation in which one of the C-Si bonds had formed prior to the second bond formation (Hayes & Tuckerman, 2007; Minary & Tuckerman, 2004; 2005). This stable intermediate was interpreted as clear evidence that the reaction proceeds via an asymmetric, non-concerted mechanism.

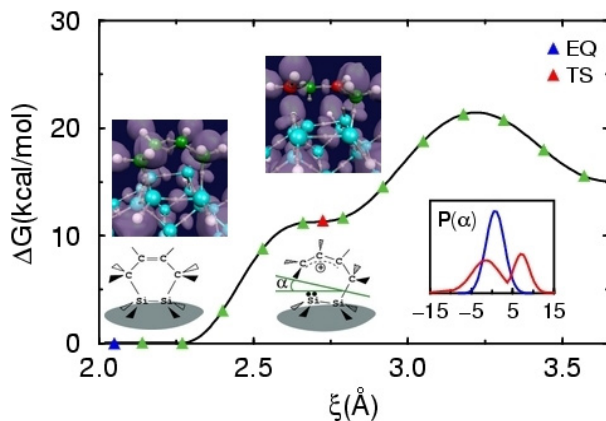


Fig. 6. Free energy along the reaction pathway leading to a Diels–Alder [4+2] adduct. Blue and red triangles indicate the product (EQ) and intermediate states (IS), respectively. Inset shows the buckling angle (α) distribution of the Si dimer for both the IS (red) and the EQ configurations (blue). The snapshots include configurations representing the IS and EQ geometries. Blue, green, and white spheres denote Si, C, and H atoms, respectively, and gray spheres indicate the location of Wannier centers. Red spheres locate positively charged atoms. The purple surface is a 0.95 electron localization function (ELF) isosurface.

In the present study of 1,3-cyclohexadiene with the SiC(100)-2 \times 2 surface, the KS orbitals were expanded in a plane-wave basis set up to a kinetic energy cut-off of 60 Ry. As in the 1,3-CHD studies described above, exchange and correlation are treated with the spin restricted form of the PBE functional (Perdew et al., 1996), and core electrons were replaced by Troullier-Martins pseudopotentials (Troullier & Martins, 1991) with S, P, and D treated as local for H, C, and Si, respectively. The periodic slab contains 128 atoms arranged in 6 layers (including a bottom passivating hydrogen layer). Proper treatment of surface boundary conditions allowed for a simulation cell with dimensions $L_x = 17.56 \text{ \AA}$, $L_y = 8.78 \text{ \AA}$, and $L_z = 31 \text{ \AA}$ along the nonperiodic dimension. The surface contains 8 C \equiv C dimers. This setup is capable of reproducing the experimentally observed dimer buckling (Derycke et al., 2000) that static *ab initio* calculations using cluster models are unable to describe (Bermudez, 2003). In Fig. 7, we show the free energy profile for the [4+2] cycloaddition reaction of 1,3-cyclohexadiene with one of the C \equiv C surface dimers. The free energy profile is calculated by dividing the ξ interval $\xi \in [1.59, 3.69]$ into 15 equally spaced intervals, and each constrained simulation was equilibrated for 1.0 ps followed by 3.0 ps of averaging using a time step of 0.025 fs. All calculations are carried out in the NVT ensemble at 300 K using Nosé-Hoover chain thermostats (Martyna et al., 1992). In contrast to the free energy profile of Fig. 6, the profile in Fig. 7 shows no evidence of a stable intermediate. Rather, apart from an initial barrier of approximately 8 kcal/mol, the free energy is strictly downhill. The reaction is thermodynamically favored by approximately 48 kcal/mol. The suggestion from Fig. 7 is that the reaction is symmetric and concerted in contrast to the reactions on the other surfaces we have considered thus far. Fig. 7 shows snapshots of the molecule and the surface atoms

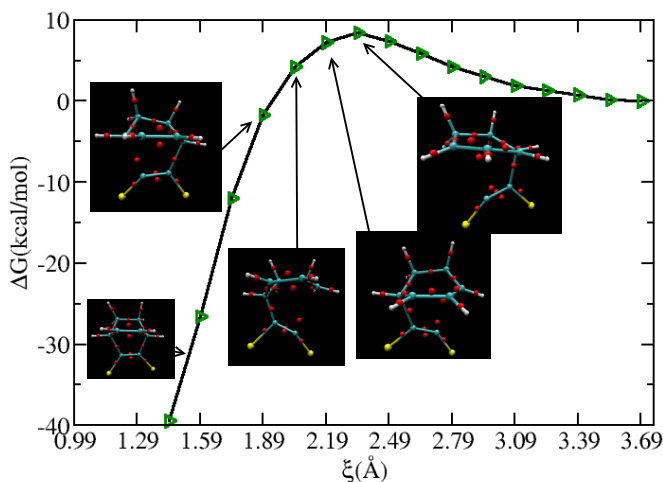


Fig. 7. Free energy profile for the formation of the [4+2] Diels-Alder-like adduct between 1,3-cyclohexadiene a $\text{C}\equiv\text{C}$ dimer on the $\text{SiC-}2\times 2$ surface. Blue, white and yellow spheres represent C, H, and Si, respectively. Red spheres are the centers of maximally localized Wannier functions.

with which it interacts at various points along the free energy profile. In these snapshots, red spheres represent the centers of maximally localized Wannier functions. These provide a visual picture of where new covalent bonds are forming as the reaction coordinate ξ is decreased. By following these, we clearly see that one CC bond forms before the other, demonstrating the asymmetry of the reaction, which is a result of the buckling of the surface dimers. The buckling gives rise to a charge asymmetry in the $\text{C}\equiv\text{C}$ surface dimer, and as a result, the first step in the reaction is a nucleophilic attack of one of the $\text{C}=\text{C}$ bonds in the cyclohexadiene on the positively charged carbon in the surface dimer, this carbon being the lower of the two. Once this first CC bond forms, the second CC bond follows after a change of approximately 0.3 \AA in the reaction coordinate with no stable intermediate along the way toward the final [4+2] cycloaddition product. In addition, the Wannier centers show the conversion of the triple bond on the surface to a double bond in the final product state. Further evidence for the concerted asymmetric nature of the reaction is provided in Fig. 8, which shows the average carbon-carbon lengths computed over the constrained trajectories at each point of the free energy profile. It can be seen by the fact that one CC bond forms before the other that there is a slight tendency for an asymmetric reaction, despite its being concerted.

In order to demonstrate that the [4+2] Diels-Alder type cycloaddition product is highly favored over other reaction products on this surface, we show one additional example of a free energy profile, specifically, that for the formation of a [2+2] cycloaddition reaction with a single surface $\text{C}\equiv\text{C}$ dimer. This profile is shown in Fig. 9. In contrast to the [4+2] Diels-Alder type adduct, the barrier to formation of this adduct is roughly 27 kcal/mol (compared to 8 kcal/mol for the Diels-Alder product). Thus, although the [2+2] reaction

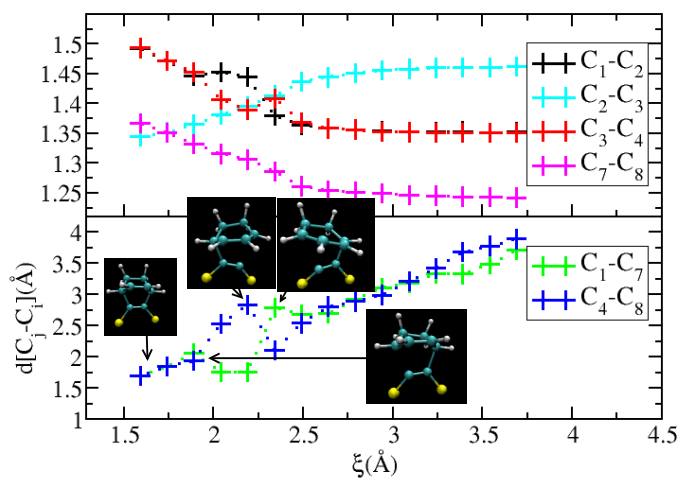


Fig. 8. Average carbon-carbon bond lengths obtained from each constrained simulation.

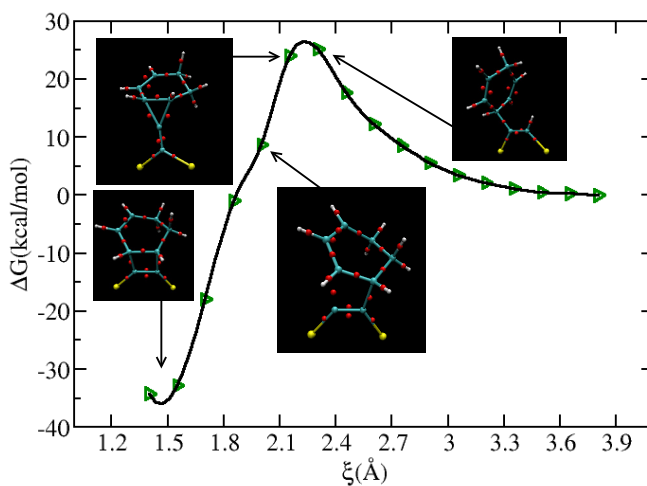


Fig. 9. Free energy profile for the formation of the [2+2] adduct between 1,3-cyclohexadiene and a $C\equiv C$ dimer on the SiC-2 \times 2 surface. Blue, white and yellow spheres represent C, H, and Si, respectively. Red spheres are the centers of maximally localized Wannier functions.

is thermodynamically favorable, this barrier is sufficiently high that we would expect this particular reaction channel to be highly suppressed compared to one with a 19 kcal/mol lower barrier. The free energy profile, together with the snapshots taken along the reaction path, also suggests that this reaction occurs via an asymmetric, concerted mechanism, as was found for the [4+2] Diels-Alder type product.

Although we have not shown them here, we have computed free energy profiles for a variety of other adducts, including interdimer and sublayer adducts, and in all cases, free energy barriers exceeding 20 kcal/mol (or 40 kcal/mol in the case of the sublayer adduct) were obtained. These results strongly suggest that the product distribution this surface would, for all intents and purposes, be restricted to the single [4+2] Diels-Alder type product, implying that this surface might be a candidate for creating an ordered organic/semiconductor interface.

5. References

- Amy, F. & Chabal, Y. J. (2003). Interaction of H, O₂, and H₂O with 3C-SiC surfaces, *J. Chem. Phys.* 119: 6201–6209.
- Basu, R., Kinser, C. R., Tovar, J. D. & Hersam, M. C. (2006). Bromine functionalized molecular adlayers on hydrogen passivated silicon surfaces, *Chem. Phys.* 326: 144–150.
- Becke, A. D. (1988). Density-functional exchange-energy approximation with correct asymptotic behavior, *Phys. Rev. A* 38: 3098–3100.
- Becke, A. D. & Edgecombe, K. E. (1990). A simple measure of electron localization in atomic and molecular systems, *J. Chem. Phys.* 92: 5397.
- Berghold, G., Mundy, C. J., Romero, A. H., Hutter, J. & Parrinello, M. (2000). General and efficient algorithms for obtaining maximally localized wannier functions, *Phys. Rev. B* 61: 10040–10048.
- Bermudez, V. M. (2003). Computational study of cycloaddition reactions on the SiC(100)-c(2x2) surface, *Surf. Sci.* 540(2–3): 255–264.
- Capano, R. J. & Trew, R. J. (1997). Silicon carbide electronic devices and materials, *MRS Bulletin* 22: 19.
- Car, R. & Parrinello, M. (1985). Unified approach for molecular dynamics and density-functional theory, *Phys. Rev. Lett.* 55: 2471–2474.
- Carter, E. A., Ciccotti, G., Hynes, J. T. & Kapral, R. (1989). Constrained reaction coordinate dynamics for the simulation of rare events, *Chem. Phys. Lett.* 156: 472.
- Cattaruzza, F., Cricenti, A., Flamini, A., Girasole, M., Longo, G., Prosperi, T., Andreano, G., Cellai, L. & Chirivino, E. (2006). Controlled loading of oligodeoxyribonucleotide monolayers onto unoxidized crystalline silicon; fluorescence-based determination of the surface coverage and of the hybridization efficiency; parallel imaging of the process by atomic force microscopy, *Nucl. Acids Res.* 34: e32.
- Chang, H., Wu, J., Gu, B.-L., Liu, F. & Duan, W. (2005). Physical origin of hydrogen-adsorption-induced metallization of the SiC surface: *n*-type doping via formation of hydrogen bridge bond, *Phys. Rev. Lett.* 95: 196803.
- Cicero, G. & Catellani, A. (2005). Towards sic surface functionalization: An *ab initio* study, *J. Chem. Phys.* 122: 214716.
- Cicero, G., Catellani, A. & Galli, G. (2004). Atomic control of water interaction with biocompatible surfaces: The case of SiC(001), *Phys. Rev. Lett.* 93(1): 016102.
- D'angelo, M., Enriquez, H., Aristov, V. Y., Soukiassian, P., Renaud, G., Barbier, A., Noblet, M., Chiang, S. & Semond, F. (2003). Atomic structure determination of the

- Si-rich β -SiC(001)- 3×2 surface by grazing-incidence x-ray diffraction: A stress-driven reconstruction, *Phys. Rev. B* 68: 165321.
- de Brito Mota, F. & de Castilho, C. M. C. (2006). Carbon nanotube adsorbed on a hydrogenated Si-rich β -SiC(100)(3×2) surface: First principles pseudopotential calculations, *Phys. Rev. B* 74: 165408.
- Derycke, V., Soukiassian, P. G., Amy, F., Chabal, Y., D'Angelo, M. D., Enriquez, H. B. & Silly, M. G. (2003). Nanochemistry at the atomic scale revealed in hydrogen-induced semiconductor surface metallization, *Nat. Mater.* 2: 253–254.
- Derycke, V., Soukiassian, P., Mayne, A. & Dujardin, G. (2000). Scanning tunneling microscopy investigation of the C-terminated β -SiC(100) c(2×2) surface reconstruction: Dimer orientation, defects, and antiphase boundaries, *Surf. Sci.* 446: L101–L107.
- Di Felice, R., Bertoni, C. M., Pignedoli, C. A. & Catellani, A. (2005). Hydrogen-Induced Surface Metallization of β -SiC(001)-(3×2) Revisited by Density Functional Theory Calculations, *Phys. Rev. Lett.* 94: 116103.
- DiLabio, G. A., Dogel, S. A., Anagaw, A., Pitters, J. L. & Wolkow, R. A. (2007). Theoretical and spectroscopic study of the reaction of diethylhydroxylamine on silicon(100)- 2×1 , *Phys. Chem. Chem. Phys.* 9: 1629.
- DiLabio, G. A., Piva, P. G., Kruse, P. & Wolkow, R. A. (2004). Dispersion interactions enable the self-directed growth of linear alkane nanostructures covalently bound to silicon, *J. Am. Chem. Soc.* 126: 16048.
- Ferguson, G. A., Than, C. T. L. & Raghavachari, K. (2009). Line growth on the h/si(100)- 2×1 surface: Density functional study of allylic mercaptan reaction mechanisms, *J. Phys. Chem. C* 113: 11817.
- Ferguson, G. A., Than, C. T. L. & Raghavachari, K. (2010). Extending molecular lines on the si(100)- 2×1 surface: A theoretical study of the effect of allylic mercaptan adsorbates on radical chain reactions, *J. Phys. Chem. C* 1: 679.
- Filler, M. A. & Bent, S. F. (2002). The surface as molecular reagent: Organic chemistry at the semiconductor interface, *Prog. Surf. Sci.* 73: 1–56.
- Filler, M. A. & Bent, S. F. (2003). The surface as molecular reagent: organic chemistry at the semiconductor interface, *Prog. Surf. Sci.* 73: 1–56.
- Flatt, A., Chen, B. & Tour, J. (2005). Fabrication of carbon nanotube-molecule-silicon junctions, *J. Am. Chem. Soc.* 127: 8918.
- Guisinger, N., Basu, R., Greene, M., Baluch, A. & Hersam, M. (2004). Observed suppression of room temperature negative differential resistance in organic monolayers on si(100), *Nanotechnology* 15: S452.
- Guisinger, N., Greene, M., Basu, R., Baluch, A. & Hersam, M. (2004). Room temperature negative differential resistance through individual organic molecules on silicon surfaces, *Nano. Lett.* 4: 55.
- Hayes, R. L. & Tuckerman, M. E. (2007). Role of surface dimer dynamics in the creating ordered organic-semiconductor interfaces, *J. Am. Chem. Soc.* 129: 12172–12180.
- Hayes, R. L. & Tuckerman, M. E. (2008). Kinetic effects on the cycloaddition of 1,3-cyclohexadiene to the 3c-sic(001)- 3×2 surface studied via ab initio molecular dynamics, *J. Phys. Chem. C* 112: 5880–5887.
- He, J., Chen, B., Flatt, A., Stephenson, J., Condell, D. & Tour, J. (2006). Metal-free silicon-molecule-nanotube testbed and memory device, *Nature Materials* 5: 63.
- Hohenberg, P. & Kohn, W. (1964). Inhomogeneous electron gas, *Phys. Rev. B* 136: 864–871.

- Hossain, M. Z., Kato, H. S. & Kawai, M. (2005a). Controlled fabrication of 1d molecular lines across the dimer rows on the si(100)-(2x1)-h surface through the radical chain reaction, *J. Am. Chem. Soc.* 127: 15030.
- Hossain, M. Z., Kato, H. S. & Kawai, M. (2005b). Controlled fabrication of 1d molecular lines across the dimer rows on the si(100)-2x1-h surface through the radical chain reaction, *J. Am. Chem. Soc.* 127: 15030–15031.
- Hossain, M. Z., Kato, H. S. & Kawai, M. (2005c). Fabrication of interconnected 1d molecular lines along and across the dimer rows on the si(100)-(2 x 1)-h surface through the radical chain reaction, *J. Phys. Chem. B* 109: 23129.
- Hossain, M. Z., Kato, H. S. & Kawai, M. (2007a). Competing forward and reversed chain reactions in one-dimensional molecular line growth on the si(100)-(2 x 1)-h surface, *J. Am. Chem. Soc.* 129: 3328.
- Hossain, M. Z., Kato, H. S. & Kawai, M. (2007b). Selective chain reaction of acetone leading to the successive growth of mutually perpendicular molecular lines on the si(100)-(2x1)-h surface, *J. Am. Chem. Soc.* 129: 12304.
- Hossain, M. Z., Kato, H. S. & Kawai, M. (2008). Self-directed chain reaction by small ketones with the dangling bond site on the si(100)-(2 x 1)-h surface: Acetophenone, a unique example, *J. Am. Chem. Soc.* 130: 11518.
- Hossain, M. Z., Kato, H. S. & Kawai, M. (2009). Valence states of one-dimensional molecular assembly formed by ketone molecules on the si(100)-(2 x 1)-h surface, *J. Phys. Chem. C* 113: 10751.
- Iftimie, R., Thomas, J. W. & Tuckerman, M. E. (2004). On-the-fly localization of electronic orbitals in car-parrinello molecular dynamics, *J. Chem. Phys.* 120: 2169.
- Kachian, J. S., Wong, K. T. & Bent, S. F. (2010). Periodic trends in organic functionalization of group iv semiconductor surfaces, *Acc. Chem. Res.* 43: 346–355.
- Kirczenow, G., Piva, P. G. & Wolkow, R. A. (2005). Linear chains of styrene and methylstyrene molecules and their heterojunctions on silicon: Theory and experiment, *Phys. Rev. B* 72: 245306.
- Kohn, W. & Sham, L. J. (1965). Self-consistent equations including exchange and correlation effects, *Phys. Rev. A* 140: 1133–1138.
- Kruse, P. & Wolkow, R. A. (2002). Gentle lithography with benzene on si(100), *Appl. Phys. Lett.* 81: 4422.
- Lee, C., Yang, W. & Parr, R. G. (1988). Development of the colle-salvetti correlation-exchange formula into a functional of the electron density, *Phys. Rev. B* 37: 785–789.
- Lopinski, G. P., Wayner, D. D. M. & Wolkow, R. A. (2000). Self directed growth of molecular nanostructures on silicon, *Nature* 406: 48–51.
- Martyna, G. J., Klein, M. L. & Tuckerman, M. E. (1992). Nose-Hoover Chains - the canonical ensemble via continuous dynamics, *J. Chem. Phys.* 97: 2635–2643.
- Marx, D. & Hutter, J. (2000). *Modern Methods and Algorithms of Quantum Chemistry*, NIC, FZ Juelich, chapter Ab Initio Molecular Dynamics: Theory and Implementations, pp. 301–449.
- Marx, D. & Hutter, J. (2009). *Ab Initio Molecular Dynamics*, Cambridge University Press, Cambridge.
- Marx, D., Tuckerman, M. & Martyna, G. (1999). Quantum dynamics via adiabatic ab initio centroid molecular dynamics, *Comp. Phys. Comm.* 118: 166–184.
- McNab, I. R. & Polanyi, J. C. (2006). Molecules on h-terminated si(111), *Chem. Rev.* 106: 4321.

- Mélinon, P., Masenelli, B., Tournus, F. & Perez, A. (2007). Playing with carbon and silicon at the nanoscale, *Nat. Mater.* 6: 479–490.
- Minary, P., Morrone, J. A., Yarne, D. A., Tuckerman, M. E. & Martyna, G. J. (2004). Long range interactions on wires: A reciprocal space based formalism, *J. Chem. Phys.* 121: 11949–11956.
- Minary, P. & Tuckerman, M. E. (2004). Reaction pathway of the [4+2] diels-alder adduct formation on si(100)-2x1, *J. Am. Chem. Soc.* 126: 13920–13921.
- Minary, P. & Tuckerman, M. E. (2005). Reaction mechanism of cis-1,3-butadiene addition to the si(100)-2x1 surface, *J. Am. Chem. Soc.* 127: 1110–1111.
- Minary, P., Tuckerman, M. E., Pihakari, K. A. & Martyna, G. J. (2002). A new reciprocal space based treatment of long range interactions on surfaces, *J. Chem. Phys.* 116: 5351–5362.
- Mizuno, S., Shirasawa, T., Shiraishi, Y. & Tochihara, H. (2004). Structure determination of Si(100)-c(4x2) surfaces at 80 K and electron beam effect below 40 K studied by low-energy electron diffraction, *Phys. Rev. B* 69: 241306.
- Olson, R. M. & Gordon, M. S. (2006). The structure of the Si₉H₁₂ cluster: A coupled cluster and multi-reference perturbation theory study, *J. Chem. Phys.* 124: 081105.
- Over, H., Wasserfall, J., Ranke, W., Ambiatello, C., Sawitzki, R., Wolf, D. & Moritz, W. (1997). Surface atomic geometry of Si(001)-(2x1): A low-energy electron-diffraction structure analysis, *Phys. Rev. B* 55: 4731–4736.
- Peng, X., Krüger, P. & Pollmann (2007a). Hydrogenated sic(001)-(3x2) surface: Semiconducting and metallic structures, *Phys. Rev. B* 76: 125303.
- Peng, X., Krüger, P. & Pollmann, J. (2005). Metallization of the 3C-SiC(001)-(3x2) surface induced by hydrogen adsorption: A first-principles investigation, *Phys. Rev. B* 72: 245320.
- Peng, X., Krüger, P. & Pollmann, J. (2007b). Why thermal h₂ molecules adsorb on sic(001)-c(4x2) and not on sic(001)-(3x2) at room temperature, *Phys. Rev. B* 75: 073409.
- Perdew, J. P., Burke, K. & Ernzerhof, M. (1996). Generalized gradient approximation made simple, *Phys. Rev. Lett.* 77: 3865–3868.
- Pitters, J. L., Dogel, I., DiLabio, G. A. & Wolkow, R. A. (2006). Linear nanostructure formation of aldehydes by self-directed growth on hydrogen-terminated silicon(100), *J. Phys. Chem. B* 110: 2159–2163.
- Pollmann, J. & Krüger, P. (2004). Reconstruction models of cubic SiC surfaces, *J. Phys.-Condens. Mat.* 16: S1659–S1703.
- Rakshit, T., Liang, G., Ghosh, A. & Datta, S. (2004). Silicon-based molecular electronics, *Nano lett.* 4: 1803.
- Resta, R. & Sorella, S. (1999). Electron localization in the insulating state, *Phys. Rev. Lett.* 82: 370–373.
- Sharma, M., Wu, Y. D. & Car, R. (2003). Ab initio molecular dynamics with maximally localized wannier functions, *Intl. J. Quant. Chem.* 95: 821.
- Soukiassian, P. G. & Enriquez, H. B. (2004). Atomic scale control and understanding of cubic silicon carbide surface reconstructions, nanostructures and nanochemistry, *J. Phys.-Condens. Mat.* 16: S1611–S1658.
- Sprik, M. & Ciccotti, G. (1998). Free energy from constrained molecular dynamics, *J. Chem. Phys.* 109: 7737.
- Starke, U. (2004). *Silicon Carbide: Fundamental Questions and Applications to current device technology*, Springer-Verlag, Berlin, Germany.

- Stutzmann, M., Garrido, J. A., Eickhoff, M. & Brandt, M. S. (2006). Direct biofunctionalization of semiconductors: A survey, *Phys. Stat. Sol. A* 203(14): 3424–3437.
- Tamura, H. & Gordon, M. S. (2003). Multiconfigurational self-consistent field study of the silicon carbide (001) surface, *J. Chem. Phys.* 119: 10318–10324.
- Teague, L. C. & Boland, J. J. (2003). Stm study of multiple bonding configurations and mechanism of 1,3-cyclohexadiene attachment on si(100)-2x1, *J. Phys. Chem. B* 107: 3820–3823.
- Teague, L. C. & Boland, J. J. (2004). Kinetically controlled reaction of 1,3-cyclohexadiene on si(100), *Thin Solid Films* 464-465: 1–4.
- Tejeda, A., Dunham, D., García de Abajo, F. J., Denlinger, J. D., Rotenberg, E., Michel, E. G. & Soukiassian, P. (2004). Photoelectron diffraction study of the si-rich 3c-sic(001)-(3x2) structure, *Phys. Rev. B* 70: 045317.
- Thomas, J. W., Iftimie, R. & Tuckerman, M. E. (2004). Field theoretic approach to dynamical orbital localization in ab initio molecular dynamics, *Phys. Rev. B* 69: 125105.
- Troullier, N. & Martins, J. L. (1991). Efficient pseudopotentials for plane-wave calculations, *Phys. Rev. B* 43: 1993–2006.
- Tuckerman, M. E. (2002). *Ab initio* molecular dynamics: Basic concepts, current trends and novel applications, *J. Phys.-Condens. Mat.* 14: R1297–R1355.
- Tuckerman, M. E. & Martyna, G. J. (1999). A reciprocal space based method for treating long range interactions in ab initio and force-field-based calculations in clusters, *J. Chem. Phys.* 110: 2810–2821.
- Tuckerman, M. E. & Parrinello, M. (1994). Integrating the car-parrinello equations .1. basic integration techniques unified approach for molecular dynamics and density-functional theory, *J. Chem. Phys.* 101: 1302–1315.
- Tuckerman, M. E., Yarne, D. A., Samuelson, S. O., Hughes, A. L. & Martyna, G. J. (2000). Exploiting multiple levels of parallelism in molecular dynamics based calculations via modern techniques and software paradigms on distributed memory computers, *Comput. Phys. Commun.* 128: 333–376.
- Wieferink, J., Krüger, P. & Pollmann, J. (2006). Improved hybrid algorithm with Gaussian basis sets and plane waves: First-principles calculations of ethylene adsorption on β -SiC(001)-(3 \times 2), *Phys. Rev. B* 74: 205311.
- Wieferink, J., Krüger, P. & Pollmann, J. (2007). First-principles study of acetylene adsorption on β -SiC(001)-(3 \times 2), *Phys. Rev. B* 75: 153305.
- Zikovsky, J., Dogel, S. A., Haider, A. B., DiLabio, G. A. & Wolkow, R. A. (2007). Self-directed growth of contiguous perpendicular molecular lines on h-si(100) surfaces, *J. Phys. Chem. A* 111: 12257.

Optical Properties and Applications of Silicon Carbide in Astrophysics

Karly M. Pitman¹, Angela K. Speck²,
Anne M. Hofmeister³ and Adrian B. Corman³

¹*Planetary Science Institute*

²*Dept. of Physics & Astronomy, University of Missouri-Columbia*

³*Dept. of Earth & Planetary Sciences, Washington University in St. Louis
USA*

1. Introduction

Optical properties, namely, spectra and optical functions, of silicon carbide (SiC) have been of great interest to astrophysicists since SiC was first theoretically posited to exist as dust, i.e., submicron-sized solid state particles, in carbon-rich circumstellar regions (Gilman, 1969; Friedemann, 1969). The prediction that SiC in space should re-emit absorbed radiation as a spectral feature in the $\lambda = 10\text{--}13\ \mu\text{m}$ wavelength region (Gilra, 1971, 1972) was confirmed by a broad emission feature at $\lambda \sim 11.4\ \mu\text{m}$ in the spectra of several carbon-rich stars (Hackwell, 1972; Treffers & Cohen, 1974). Many carbon-rich, evolved stars exhibit the $\lambda \sim 11\ \mu\text{m}$ feature in emission, and SiC is now believed to be a significant constituent around them (Speck, 1998; Speck et al., 2009 and references therein).

1.1 Role of SiC in stellar environments

Detection of SiC in space provides much information on circumstellar environments because the chemical composition and structure of dust in space is correlated with, e.g., the pressure, temperature, and ratios of available elements in gas around stars. The mere presence of SiC implies that the carbon-to-oxygen (C/O) must be high. Different polytypes of SiC identify the temperature and gas pressure within the dust forming region around a star. The significance of SiC in stars is tied intimately to stellar evolution, as dust grains participate in feedback relationships between stars and their circumstellar envelopes that affect mass-loss rates, i.e., stellar lifetimes. Meteoritic SiC grains exhibit signatures of s-process enrichment, one of the main attributes of the evolutionary track of carbon-rich stars.

1.1.1 S-process isotopic signatures in SiC

Elements more massive than helium have been formed in stars. All elements $> {}^{56}\text{Fe}$ are generated by neutron capture because there is no Coulomb barrier for adding a neutral particle. In the s-process (slow neutron capture), neutrons are added to atomic nuclei slowly as compared to the rate of beta decay (cf. Burbidge, et al. 1957, a.k.a., B²FH; Cameron 1957). The precise isotopes of heavy elements depend on the rate of neutron capture, which, in turn, is strongly dependent on the properties of the stellar sources. Thus, it is possible to

uniquely identify different masses or types of stars as the sources of isotopically non-solar dust grains. SiC was the first meteoritic dust grain to be discovered that, on the basis of its isotopic composition, obviously formed before and survived the formation of the solar system (Bernatowicz et al., 1987). Further studies of the precise isotopic compositions of these meteoritic “presolar” grains have identified their stellar sources. For SiC, 99% of the presolar grains are characterized by high abundances of s-process elements, indicative of formation around certain classes of evolved, intermediate mass stars (described below).

1.1.2 Space environments containing SiC

Figure 1 illustrates the varied space environments in which SiC has been detected. To understand the nature of SiC in these environments and how SiC originally formed in the universe, Figure 2 and the following text describe how these categories of stars evolve.

1.1.2.1 Asymptotic Giant Branch (AGB) stars

Figure 2 illustrates the evolution of low-to-intermediate-mass stars (LIMS; 0.8-8 times the mass of the Sun, $M_{\odot} = 1.98892 \times 10^{30}$ kg). In the late stages of evolution, LIMS follow a path up the Asymptotic Giant Branch (AGB; Iben & Renzini, 1983). During the AGB phase, stars are very luminous ($\sim 10^3$ – $10^4 L_{\odot}$, where $L_{\odot} = 3.839 \times 10^{33}$ erg/s) and large ($\sim 300 R_{\odot}$, where $R_{\odot} = 6.995 \times 10^8$ m) but have relatively low surface temperature (~ 3000 K). AGB stars pulsate due to dynamical instabilities, leading to intensive mass loss and the formation of circumstellar shells of gas and dust. The carbon-to-oxygen ratio (C/O) controls the chemistry around the star: whichever element is less abundant will be entirely locked into CO molecules, leaving the more abundant element to control dust formation. Therefore, AGB stars can be either oxygen-rich or carbon-rich. Approximately 1/3 of AGB stars are C-rich (i.e., $C/O > 1$). Whereas C-stars are expected to have circumstellar shells dominated by amorphous or graphitic carbon, SiC is also expected to form; its IR spectrum provides a diagnostic tool not available from the carbonaceous grains. Therefore, SiC has been of greatest interest to astrophysicists seeking to understand the evolution of dust shells and infrared features of C-stars (Baron et al., 1987; Chan & Kwok, 1990; Goebel et al., 1995; Speck et al., 1997; Sloan et al., 1998; Speck et al., 2005, 2006; Thompson et al., 2006). For Galactic sources, the majority of C-stars should first condense TiC, then C, then SiC, as supported by meteoritic evidence (e.g., Bernatowicz et al., 2005). As C-stars evolve, mass loss is expected to increase. Consequently, their circumstellar shells become progressively more optically thick, and eventually the central star is obscured. Volk et al. (1992, 2000) christened such stars “extreme carbon stars” (e.g., Fig. 1a). Extreme carbon stars are expected to represent that small subset of C-rich AGB stars just prior to leaving the AGB. Because that phase is short-lived, the number of extreme C-stars is intrinsically small and few of these objects have been found in space (~ 30 known in the Galaxy: Volk et al., 1992, versus $\sim 30,000$ known visible C-stars: Skrutskie et al., 2001).

1.1.2.2 Post-AGB stars

Once the AGB phase ends, mass loss virtually stops, and the circumstellar shell begins to drift away from the star. At the same time, the central star begins to shrink and heat up from $T = 3000$ K until it is hot enough to ionize the surrounding gas, at which point the object becomes a planetary nebula (PN; e.g., Fig. 1c). The short-lived post-AGB phase, as the star evolves toward the PN phase, is also known as the proto- or pre-planetary nebula (PPN) phase (e.g., Fig. 1b). As the detached dust shell drifts away from the central star, the dust cools, causing a PPN to have cool infrared colors. Meanwhile, the optical depth of the dust shell decreases,

allowing the central star to be seen and making such objects optically bright. The effect of decreasing optical depth and cooling dust temperatures changes the appearance of the circumstellar envelope, revealing features that were hidden during the AGB phase.



Fig. 1. Astronomical objects in which SiC has been detected. Left to right: (a) Hubble Space Telescope image of the extreme carbon star AFGL 3068. Source: Maunon & Huggins (2006); <http://www.planetastronomy.com> (b) The Egg Nebula, illustrating polarization through a thick vertical dust belt in the center of a pre- or proto-planetary nebula. Source: NASA and The Hubble Heritage Team (STScI/AURA); W. Sparks (STScI), R. Sahai (JPL); <http://heritage.stsci.edu> (c) IC 418, the Spirograph Nebula, is one of only a handful of galactic planetary nebulae that actually show SiC emission. Source: NASA and The Hubble Heritage Team (STScI/AURA); R. Sahai (JPL), A. Hajian (USNO); <http://hubblesite.org>

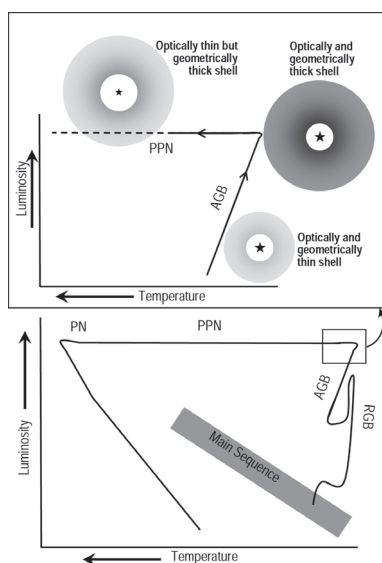


Fig. 2. Schematic diagram of the evolution of low-to-intermediate-mass stars. Bottom: A $1M_{\odot}$ star begins its life on the main sequence, converting H into He in its core; when H is depleted, it exits to the Red Giant Branch (RGB), then the Asymptotic Giant Branch (AGB), where SiC formation occurs. Intense mass loss depletes the remaining H in the star's outer envelope in a few $\times 10^4$ years (Volk et al., 2000) and terminates the AGB phase. Stars may then become proto-planetary nebulae (PPN), or later planetary nebulae (PN).

Infrared (IR) spectroscopy is used to probe the nature of SiC dust grains in space because dust particles of a given size, shape, temperature, structure, and composition have their own signature IR spectrum. Dust grains absorb high energy photons from stars and re-emit in the IR, in accordance with the specific (low) temperatures of any given grain. Therefore, to account for the energy budget in astronomical environments, astrophysicists are also interested in how SiC dust grains absorb and scatter UV-vis photons, which requires knowledge of SiC optical functions. Lines of evidence or constraints that astrophysicists use to aid studies of SiC dust in space include evidence from meteoritic studies, comparisons between the positions and shapes of spectral features for astronomical objects and laboratory analogue materials, spatial distributions of materials, and theoretical models for dust formation.

2. Silicon carbide in meteorites

SiC particles were the first presolar dust grains found in meteorites (Bernatowicz et al., 1987) and remain the best studied (e.g. Clayton & Nittler, 2004; Bernatowicz et al., 2006; Hoppe, 2009). Presolar grains are ancient refractory dust with the isotopic makeup of stars that exist as individual particles or clusters found in the matrix, or fine-grained crystalline mass, of a meteorite. Ages of meteoritic SiC grains are discussed by Ott (2010). Figure 3 describes the family of meteorite classes that contain presolar SiC grains. The most studied meteorites that contain presolar SiC are carbonaceous chondrites (e.g., the class CM2 Murchison and Murray meteorites, classes CI1 = Orgueil, CV3 = Allende) which are considered to be the most primitive or least processed solid materials in the Solar System. Presolar SiC is also found in other stony meteorite types as well: enstatite chondrites (e.g., EH4 = Indarch, EH3 = Qingzhen) and ordinary chondrites (e.g., H/L 3.6 = Tieschitz, LL 3.1 = Bishunpur, Krymka, LL 3.5 = Chainpur, L/LL 3.4 = Inman; LL 3.0 = Semarkona). Investigations via scanning and transmission electron microscopy have revealed the physical morphology of presolar SiC grains (Figure 4). Whereas presolar grains are rare (Clayton & Nittler, 2004) and very small (typically less than 1 μm in size: Amari et al., 1994), presolar SiC grains are more abundant than other presolar compositions (up to 30 ppm in the Murchison meteorite: Ott & Merchel, 2000) and, at 1.5 nm to 26 μm in size, many are large enough to be probed for their isotopic composition (Yin et al., 2006; Speck et al. 2009, and references therein).

As discussed in the introduction, SiC presolar grains are identified by their anomalous isotopic compositions. In fact, their isotopic compositions have not only identified their likely cosmic sources, but also have provided key tests of hypotheses for nucleosynthesis (element creation) and generate the data needed to refine those hypotheses. Whereas ~1% of presolar SiC probably emanates from stellar environments such as novae and supernovae, the vast majority have isotopic compositions consistent with formation around AGB stars. Because the s-process is the dominant method of forming heavy elements in AGB stars, the SiC grains that form within AGB stellar envelopes are excellent tracers of unadulterated s-process isotopes. Studies of these presolar grains are used to determine s-process timescales, stellar temperature and masses, and neutron exposure rates of stellar nuclei.

Compared to solar isotopes, presolar SiC grains exhibit anomalous isotopic compositions for their major components C and Si, as well as trace elements: N, Mg, Ca, Ti, Sr, Zr, Mo, Ba, Nd, Sm, Dy, and the noble gases (Hoppe & Ott, 1997). Based on such isotopic analyses, six types of presolar SiC have been established according to their Si, $^{12}\text{C}/^{13}\text{C}$, $^{14}\text{N}/^{15}\text{N}$, and $^{26}\text{Al}/^{27}\text{Al}$ ratios (e.g., table 2, Ott, 2010 and references therein): “mainstream” SiC, versus

types A, B, X, Y, and Z. The “mainstream” SiC population, constituting ~ 87-94% of known presolar SiC grains, is believed to have originated around C-rich AGB stars. Compared to “mainstream” SiC, A and B SiC grains have low $^{12}\text{C}/^{13}\text{C}$ but a similar Si profile; they are thought to derive from a particular class of C-star. Y and Z SiC grains are typically small as compared to other presolar SiC grains, are easily distinguished from the “mainstream” class by their Si content, and come from either low mass, low metallicity AGB stars that undergo different types of processing or possibly novae. Type X SiC grains are the most rare (~1% of presolar SiC), are generally collections of many < 100 nm-sized rather than individual grains, and have been posited to derive from ejecta of core-collapse (Type II) supernovae.

Laboratory studies of presolar meteoritic SiC grains have utilized and developed many innovative techniques (see review by Hoppe, 2009). Initial works relied on ion microprobe and secondary ion mass spectrometry (SIMS) techniques to determine isotopic compositions for light and intermediate mass elements in individual presolar SiC grains, including C, N, Si, Ca, Ti, Mg, Al, O, V, Fe, Sr, Y, Zr, Nb, Ba, Ce, Nd, B (Amari et al., 1992, 1995, 1996, 1997a, 1997b; Hoppe et al. 1994a, 1994b, 1996, 2000, 2001). Post 2001, efforts to drive down the diameter of the primary ion beam and thus be able to probe presolar grains smaller than 0.5 μm resulted in a series of studies using the Cameca NanoSIMS 50 ion microprobe (Besmehn & Hoppe, 2002; Hoppe & Besmehn, 2002; Gyngard, 2009). Time-of-flight secondary ion mass spectrometry (TOF-SIMS) has been applied to submicron presolar SiC grains in an effort to sputter less sample (Henkel et al., 2007), and atomic probe tomography (field ion microscope + TOF mass spectrometer) has also been tested on presolar and synthetic SiC grains to significantly improve upon the spatial resolution of NanoSIMS (Heck et al., 2010). Resonance ion mass spectrometry (RIMS) studies have further quantified the isotopic compositions of heavy elements such as Zr, Mo, and Ba in presolar SiC grains (e.g., Nicolussi et al., 1997, 1998; Savina et al., 2003; Barzyk, 2007). Laser heating experiments by Nichols et al. (1992) and later work by Heck (2005) have yielded the isotopic compositions of He and Ne in presolar SiC. Combinations of SIMS, RIMS, gas mass spectrometry, and other experimental methods (e.g., SEM, TEM, Auger spectroscopy) are currently being employed in analyses of presolar SiC grains (cf. Stroud et al., 2004).

A subset of studies on the isotopic compositions of presolar SiC grains investigates the effect of grain sizes on concentrations of s-process elements. Prombo et al. (1993) found a correlation between grain size and the concentration of s-process elements in the presolar SiC grains taken from the Murchison meteorites. Presolar SiC grains from the Indarch meteorite yielded similar results (Jennings et al., 2002). In both cases, the smaller grains have higher relative abundances of s-process elements.

In addition to the isotopic studies of presolar SiC, crystallographic studies have shown that nearly all are of the β -polytype (cubic crystal structure) and the 6H- α -polytype is never found. In the Murray C2 carbonaceous chondritic meteorite in which presolar SiC was first unequivocally detected, cubic and {111}-twinned cubic were the most common structural forms (Bernatowicz et al. 1987, 1988a, 1988b). Daulton et al. (2002, 2003) itemize the amount of 3C β -SiC (80%), 2H α -SiC (3%), and intergrowths of these two forms (17%) present in presolar SiC grains. This is significant in astrophysics because which polytype of SiC forms in space strongly depends on the temperature and gas pressure within the dust-forming region. 2H and 3C are the polytypes that form at the lowest temperature where SiC condenses; which of 2H or 3C SiC forms depends on many factors, such as Si/C ratio.

For further reviews of SiC and cosmic dust in meteorites, see also Anders & Zinner (1993), Hoppe & Ott (1997), Hoppe & Zinner (2000), Hoppe (2009), Ott (2010), and Henning (2010).

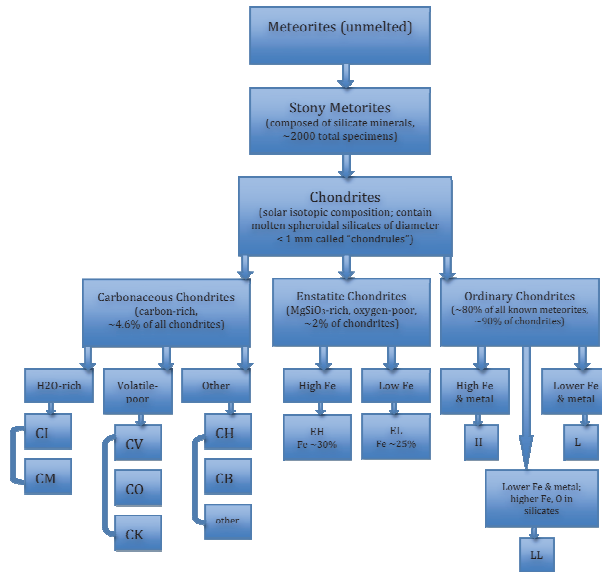


Fig. 3. Meteorite classification formalism, adapted from The Natural History Museum, London (<http://www.nhm.ac.uk>). Presolar SiC grains are dominantly found in the carbonaceous chondrite classes CM, CI, and CV, but occur over a range of subclasses. The numbers (e.g., the "2" in "CM2") represent the petrologic grade of the meteorite (Van Schmus & Wood, 1967); "1" or "2" refers to the degree of hydration or aqueous alteration, whereas for a value of 3 or greater, higher numbers imply successively higher degrees of thermal metamorphism.

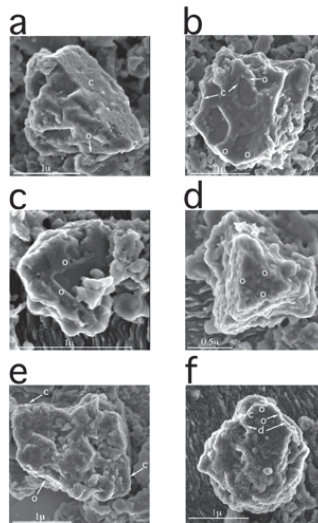


Fig. 4. Microscopy images of pristine presolar SiC grains, courtesy of T. Bernatowicz. Scale bar = 1 μm for all images except panel (d) = 0.5 μm.

3. Laboratory astrophysics of silicon carbide

For SiC, the major spectral features result from cation-anion charge transfer and/or electronic band gap transitions in the visible-UV, as well as from lattice vibrations in the IR. Vibrational motions involving a change in the dipole moment are IR active. The nearest-neighbor interaction between Si and C produces a strong band in the IR, regardless of polytype. The stacking disorder that exists for SiC lowers crystal symmetry, resulting in vibrational transitions that increase in number with polytype complexity. For all polytypes of SiC, the transverse optic mode (TO) is present at $\sim 12.5 \mu\text{m}$ and the longitudinal optic mode (LO) is seen at $\sim 10.3 \mu\text{m}$ (Nakashima & Harima, 1997). Electronic transitions occur throughout the visible-UV and are strongest at $\sim 0.111 \mu\text{m}$ (Philipp & Taft, 1960). Laboratory astrophysics studies focus on low energy or IR wavelength SiC spectral features (at $\lambda \sim 11 \mu\text{m}$, $21 \mu\text{m}$) to identify cosmic SiC in space, and also quantify the optical depth of and chemical impurities or defects in cosmic SiC via the general spectral behavior of the UV.

3.1 Spectroscopic studies: Ultraviolet and infrared

Past laboratory spectral studies utilized by astrophysicists are published across multiple disciplines. Although UV measurements for other sample types, e.g., extinction of light from SiC smoke particles (Stephens, 1980), have also been used in astrophysics, this paragraph reviews the state of single-crystal SiC spectroscopic studies in the UV and gives examples of UV SiC spectra in Figures 5 and 6. The polytypes that matter most to astrophysicists are 3C, 2H, and 4H, on the basis of the meteoritic record; data on other forms (e.g., 8H, 15R, 21R) have not been considered. Because the 6H form of α -SiC is available commercially with large faces perpendicular to c axis, for which unpolarized measurements provide data on $E \perp c$, there is a wealth of laboratory spectra on 6H in this orientation. The first α -SiC laboratory reflectance data (e.g., Philipp, 1958; Wheeler, 1966) were gathered at resolutions lower by at least a factor of two than can be attained with modern instrumentation. In the ultraviolet, modern commercial instruments exist and are inexpensive for wavelengths down to $0.192 \mu\text{m}$ (or, for a factor of $\times 10$ more in cost, down to $0.164 \mu\text{m}$, the “vacuum UV”). However, spectral data for SiC used by astrophysicists does not extend much past 200 nm , as summarized in Figure 5. Early works on UV SiC spectroscopy studied in the astrophysics literature include Choyke & Patrick (1957), Philipp (1958), and Philipp & Taft (1960). Choyke & Patrick (1957) measured transmission (converted to absorption coefficient in cm^{-1}) for one α -SiC plate, whereas Philipp (1958) measured absorption for yellow 3C and colorless 6H SiC single crystal samples of varying thicknesses. In both studies, samples were not well characterized in terms of SiC impurities, stacking faults, and defects, which are highly important in the UV-vis. Philipp & Taft (1960) presented reflectance spectra from ~ 0.11 to $0.62 \mu\text{m}$ for hexagonal SiC. Because reliable reflectivity standards were not available at that time, uncertainties in absolute R were large (i.e., $> 5\%$). Hofmeister et al. (2009) published new data on the visible to soft UV range (1.11 - $0.303 \mu\text{m}$) for α - and β -SiC single crystals with emphasis on impurities. In that study, absorbance spectra were provided for 6H and 3C SiC ($E \parallel c$ and $E \perp c$) as electronic tables for $\lambda = 2.5$ - $16.36 \mu\text{m}$; figure 7 of that work provides absorbance spectra shortward of $2.5 \mu\text{m}$. Additional laboratory UV absorption spectra (e.g., Choyke & Patrick 1968, 1969) and reflectivity spectra, including experimentally measured and calculated data (Wheeler, 1966; Belle et al., 1967; Lubinsky et al., 1975; Rehn et al., 1976; Gavrilenko, 1995; Logothetidis & Petalas, 1996; Adolph et al., 1997; Gavrilenko & Bechstedt,

1997; Theodorou et al., 1999; Ismail & Abu-Safia, 2002; Xie et al., 2003; Lindquist et al., 2004) that extend into the vacuum UV are available in the semiconductor literature. In particular, the effect of SiC polytype on reflectivity was discussed by Lambrecht et al. (1993, 1994, 1997); we note that the reflectivity values from Lambrecht et al. (1997) are too low by 20%, caused by calibrating against a low value of real index of refraction ($n=2.65$) at $\sim 0.31 \mu\text{m}$ (e.g., Petalas et al., 1998). The spectroscopic ellipsometry study by Petalas et al. (1998) provides reflectivity in agreement with Philipp & Taft (1960) and Wheeler (1966). The reflectivity data by Wheeler (1966) have been used extensively in comparison in the physics and materials literature but show structure on the spectral peaks that may not be real since those features were not observed subsequently; thus, those data are not shown explicitly in Figure 5. For further discussion, see the review by Devaty & Choyke (1997).

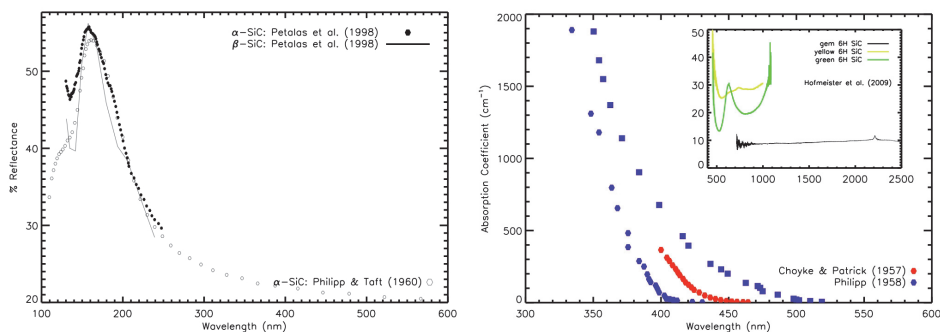


Fig. 5. UV-visible reflectance spectra and absorption coefficients. $1 \text{ nm} = 10^{-3} \mu\text{m}$. Panel (a): Open symbols: Philipp & Taft (1960), solid symbols and line: Petalias et al. (1998). Panel (b): Squares = 3C SiC, hexagons = 6H SiC. Inset: gem 6H SiC = synthetic moissanite.

In the infrared, many laboratory studies of SiC are available in astrophysics, some of which should be compared to semiconductor-relevant data with care. Spitzer et al. (1959a) obtained reflectivity data from a thin ($0.06 \mu\text{m}$) film of β -SiC that was vapor-deposited on a Si surface. Spitzer et al. (1959b) provided laboratory data for both polarizations of 6H single-crystals. Another widely cited source in astrophysics is the α -SiC E \perp c data shown in figure 9.6 of Bohren & Huffman (1983); that work did not provide experimental details, such as which polytype of α -SiC was used. Mutschke et al. (1999) presented averages of spectral parameters from many experimental studies of SiC from the 1960's to 1990's to obtain TO frequency positions, LO frequency positions or oscillator strengths, and full width at half maximum values for SiC. Other published works on SiC from astrophysics (e.g., Friedemann et al., 1981; Borghesi et al., 1985; Orofino et al., 1991; Papoular et al., 1998; Mutschke et al., 1999; Andersen et al., 1999, and references therein) are predominantly laboratory absorbance studies of powder samples, embedded in a (usually KBr) matrix. Strong differences in the spectra and optical properties obtained from powders (cf. Huffman, 1988; Mutschke et al., 1999) can be attributed to variations in clustering of grains, dilution, mean and distributions of grain size and shape. Laser pyrolysis has also been used to produce SiC particles most closely resembling those found in stellar environments (cf. Willacy & Cherchneff, 1998; Mutschke et al., 1999). Because the laser pyrolysis SiC samples are not of the order of several mm in diameter (cf. Hofmeister et al., 2003), those

measurements should not be used for determining bulk optical functions. A wavelength shift (the KBr matrix correction, cf. Friedemann et al., 1981) has been applied to some laboratory spectra of sub- μm SiC grains dispersed in single-crystal matrices. Studies of thin films and isolated nanoparticles of β -SiC have shown that this wavelength shift is unnecessary when measurements are made carefully (Speck et al., 1999; Clément et al., 2003). Past astrophysical studies were also divided on whether the crystal structure of SiC can be determined from IR spectra (in favor: Borghesi et al., 1985; Speck et al., 1999; opposed: Spitzer et al., 1959a, 1959b; Papoular et al., 1998; Andersen et al., 1999; Mutschke et al., 1999). Pitman et al. (2008) showed that spectroscopic differences exist between α -SiC $E \parallel c$, versus β -SiC or α -SiC ($E \perp c$). Pitman et al. (2008) provided electronic mid- and far-IR room temperature reflectance spectra of thin film 6H SiC (two orientations, several varieties) and semiconductor grade purity 3C SiC.

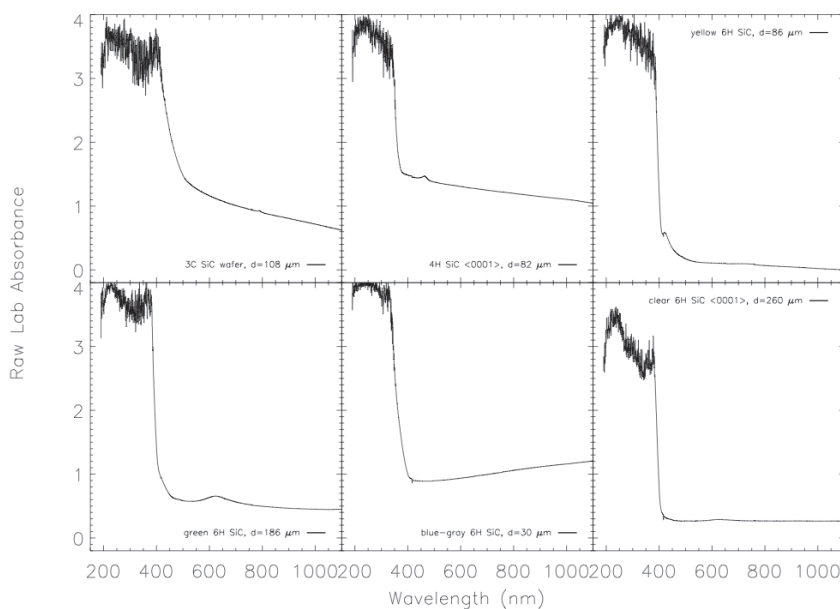


Fig. 6. Comparing the effects of color impurities and polytype of SiC in the UV-vis. $1 \text{ nm} = 10^{-3} \mu\text{m}$. d = thickness of sample. Vertical axis given in common log absorbance.

The two SiC spectral features of greatest interest to astrophysicists are at 11 and $21 \mu\text{m}$. The utility of the $11 \mu\text{m}$ feature (shown in Figure 7) will be discussed in Section 4. Among the C-rich post-AGB stars (PPNe), approximately half exhibit a feature in their infrared spectra at $21 \mu\text{m}$. This enigmatic feature has been widely discussed since its discovery (Kwok et al., 1989) and has been attributed to both transient molecular and long-lived solid-state species, but most of these species have been discarded. The most promising carrier is SiC (Speck & Hofmeister, 2004), on the basis of lab spectroscopy (Figure 8). The peak positions and profile shapes of the $21 \mu\text{m}$ band are remarkably constant, both in space (Volk et al., 1999) and in laboratory SiC spectra (Table 1). Kimura et al. (2005a, 2005b) produced nano-diamond

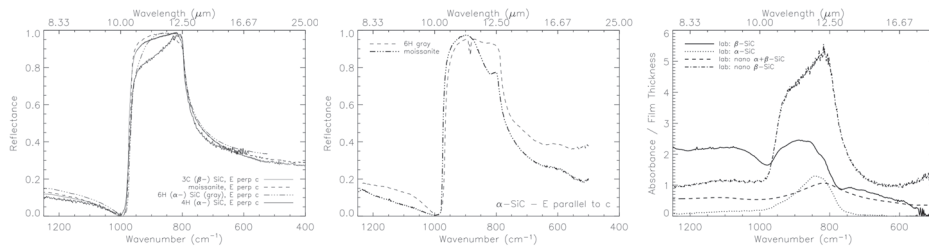


Fig. 7. $\lambda \sim 11 \mu\text{m}$ feature in SiC. Panels (a, b): Mid- and mid+far-IR specular reflectivity spectra of bulk SiC, for different orientations. Panel (c): Laboratory (common log) absorbance, divided by thin film thickness for bulk versus nanocrystalline β -SiC, α -SiC, and a mixture of the two. Data from this work, K. M. Pitman et al., A&A, vol. 483, pp. 661-672, 2008, reproduced with permission © ESO.

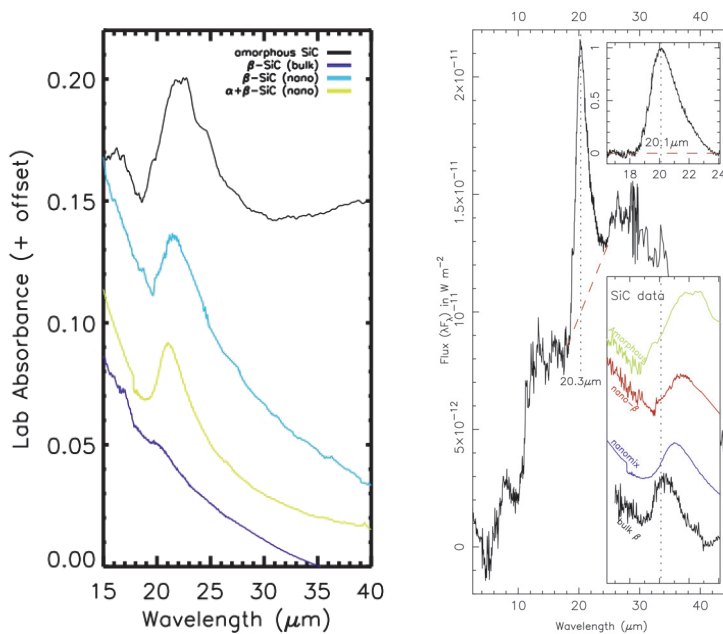


Fig. 8. The $\lambda \sim 21 \mu\text{m}$ feature in the SiC laboratory spectra is prominent in nanocrystalline and amorphous SiC, present but not as strong in bulk SiC. Laboratory IR absorbance spectra of SiC shown in bulk, nanocrystalline, amorphous, blends of α - and β -SiC. Some data from Speck & Hofmeister (2004); new β -SiC nanocrystalline data included longward of $20 \mu\text{m}$. At $19.8 \mu\text{m}$, a “S-shaped” beamsplitter artifact or spectral spike occurs. The amorphous SiC sample was polycard (i.e., this spectrum has a different baseline than the other 3 spectra, most noticeable at $\lambda > 21 \mu\text{m}$). The amorphous SiC spectrum was offset by -0.19 in vertical axis; the other spectra were not offset. Instrumental noise was smoothed for amorphous SiC at $\lambda < 20 \mu\text{m}$ and again for nanocrystalline β -SiC spectra at $\lambda > 27 \mu\text{m}$. The steep rise to short λ occurs because this feature is a shoulder on the main band near $11 \mu\text{m}$.

	Position (cm ⁻¹)	Height	Width
Amorphous SiC	450.172	0.1340	102.16
Nanocrystalline β -SiC	463.52	0.09291	34.3971
	424.75	0.07975	58.4357
Nanocrystalline α + β SiC	472.69	0.1274	60.794
	433.09	0.03869	74.790

Table 1. Peak parameters of $\lambda \sim 21 \mu\text{m}$ feature in SiC. Values reported in frequency (cm⁻¹ = $10^4/\lambda(\mu\text{m})$). Amorphous SiC spectrum was best fitted with a single Gaussian peak and multi-point baseline correction. Peaks in the IR actually tend to be Lorentzian in shape; the 21 μm feature in the nanocrystalline spectra were fitted with two Lorentzian peaks (for the TO and LO modes) and a two-point linear baseline correction.

samples with Si replacing C from 10 to 50% by various methods; its IR spectrum exhibits bands at 9.5 and 21 μm , and the relative strength of the 21 μm band increases with C content. On this basis, Kimura et al. (2005a, 2005b) concluded that the 21 μm band in IR spectra of SiC samples also results from excess C. Jiang et al. (2005) calculated IR spectra of astronomical dust for various sub- μm grain sizes and a range of peak strengths for the 21 μm band at $T \sim 70 \text{ K}$. That work concluded that the 21 μm feature was too weak to be SiC unless very high concentrations of impurity were observed. However, relative peak intensities are affected by factors not explored in that study. The intensity of emission at 21 μm would be enhanced relative to that at 11 μm by either lower temperature or larger (non-uniform) grain sizes. A more serious objection to the assignment is that the astronomy environment could possess Si-rich nano-diamond. Quantifying the strengths of the 21 μm SiC feature in both structures and low temperature measurements is needed to differentiate between these possibilities.

3.2 Optical functions of SiC

Optical functions or “optical constants” are the real and imaginary parts of the complex index of refraction $m = n + ik$ that vary as a function of wavelength, temperature, and dust species (composition, structure). $n(\lambda)$ is the real index of refraction where the crystal is not strongly absorbing, and $k(\lambda) = A/4\pi v$ represents the extinction or gradual loss of intensity due to absorption of photons as an electromagnetic wave interacts with matter. As discussed in the introduction, there is a substantial market for the optical functions of SiC within the astrophysics community. In the IR, the optical functions of SiC used in 20th century astronomical studies derive primarily from three studies: Bohren & Huffman (1983), Pégourié (1988), and Laor & Draine (1993). These data were for α -SiC, often in a single polarization, whereas SiC dust surrounding astronomical objects is β -SiC, and included a wavelength shift to “correct” for the KBr matrix. Pitman et al. (2008) derived and provided electronic tables of SiC optical functions out to $\lambda \sim 2000 \mu\text{m}$ for 6H (α -)SiC in both polarizations as well as 3C (β -)SiC; Hofmeister et al. (2009) extended these data shortward into the UV. For all spectral regions, the latter papers showed that 3C SiC and the $E \perp c$ polarization of 6H SiC have almost identical optical functions that can be substituted for each other in modeling astronomical environments. This result agreed with previous work

by Mutschke et al. (1999). However, optical functions for the $E \parallel c$ orientation of 6H SiC can differ slightly (peaks shifted to lower frequency). Figure 9 presents optical functions for 4H SiC, with comparison to the other polytypes from Pitman et al. (2008), and optical functions comparing colored versus colorless samples of SiC from Hofmeister et al. (2009). In the UV, n and k were also calculated for 6H SiC at $\sim 0.25\text{--}1.24\ \mu\text{m}$ by Obarich (1971) and Ninomiya & Adachi (1994); works presented above also included calculated dielectric functions for other polytypes, from which one may further obtain n and k in the UV.

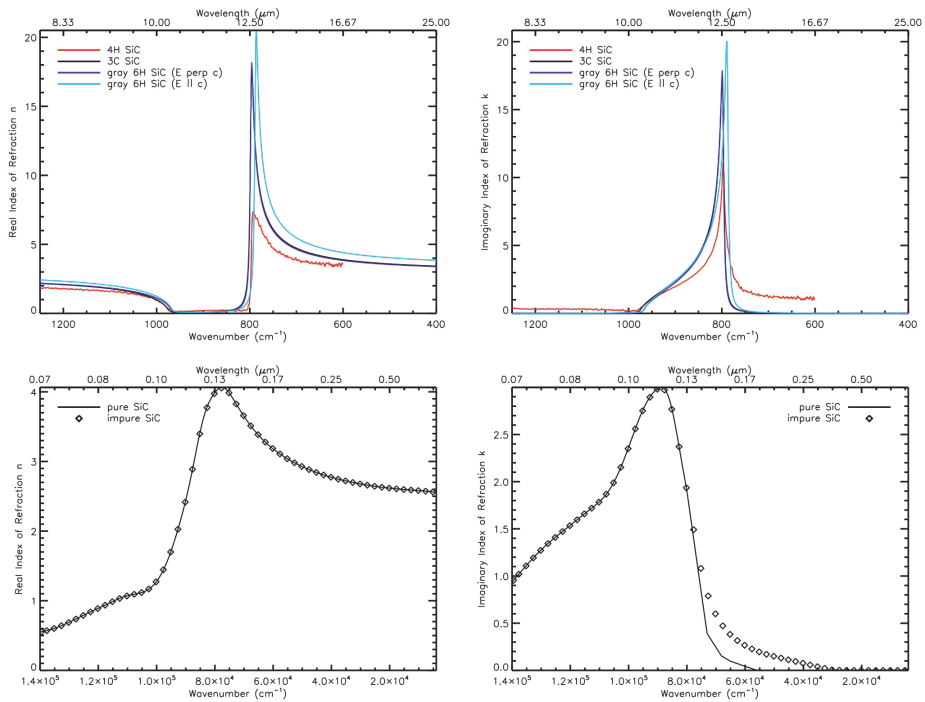


Fig. 9. UV-vis optical functions derived from experimental specular reflectance data via Lorentz-Lorenz classical dispersion analysis, showing the effect of polytype (top panels; 3C and 6H from Pitman et al. 2008, 4H from this work) and of impurities (bottom panels: Hofmeister et al. 2009, applicable to 3C or 6H $E \perp c$). Left: real index of refraction n . Right: imaginary index of refraction k . With the exception of 6H SiC $E \parallel c$ orientation, the optical functions for SiC are generally similar, regardless of polytype. As compared to 99.8% pure (colorless) SiC samples, the effect of impurities in colored SiC samples manifests in k .

4. Application #1: Observational astronomy

In this section, we outline the ways in which astrophysicists compare laboratory spectra and optical functions of SiC to determine the nature and evolution of SiC dust grains around classes of astronomical objects and environments, e.g., C-rich AGB stars (i.e., carbon stars).

4.1 Matching spectral features

The first step in identifying the nature of dust grains in space is to match the positions and widths of astronomically observed spectral features with those seen in laboratory spectra. To do this we must consider what actually contributes to the spectrum when we look at a dusty star. The spectrum, F_λ , is made of contributions to the light from the star (which is essentially a blackbody, or perfect light absorber at all wavelengths) and the circumstellar material. In the infrared, the circumstellar material is dominated by the dust, the emission from which is determined by the species, i.e., composition, crystal structure, size, and shape of the grains. The spectrum can be represented by Eq. 1,

$$F_\lambda = \sum_{i=1, j=1}^{n, m} w_j \times Q_j \times B_i \quad (1)$$

where $B_\lambda(T)$ is the Planck function for a black body of temperature T , so that B_i represents a single dust grain at a single temperature (of which there are n in total). Each Q_j represents the extinction efficiency (or rate at which a dust particle absorbs, scatters, or extinguishes light divided by the incident power per unit area) for a single grain type as defined by its size, shape, composition and crystal structure. Each w_j represents the weighting factor for a single grain type (of which there are j in total).

For optically thin environments, where there is little or only single-scattering, the spectrum is dominated by starlight, and one can simply subtract a blackbody continuum relevant to the star (which for carbon stars is ~ 3000 K). However, for very dusty environments, starlight is largely absorbed by the dust and re-emitted in the infrared according to the dust grains' optical functions. Often the system is simplified so that the contributions to the spectrum are dominated by a single dust species and Eq. 1 simplifies to Eq. 2,

$$F_\lambda = w \times Q_\lambda \times B_\lambda(T) \quad (2)$$

In this case one can fit a (blackbody) continuum to the observed spectrum and divide to derive emissivities of the observed spectral features (e.g., Speck et al. 1997).

The circumstellar shells of carbon stars are expected to be dominated by amorphous or graphitic carbon grains (see Speck et al. 2009 and references therein). These dust species do not have diagnostic infrared features, and contribute to the dust continuum emission alone. However, SiC does exhibit a strong infrared feature around $11\mu\text{m}$ as discussed in Section I. The observed $\sim 11\mu\text{m}$ SiC feature has been used extensively to investigate the nature and evolution of dust around carbon stars (Little-Marenin, 1986; Baron et al., 1987; Willems, 1988; Chan & Kwok, 1990; Goebel et al., 1995; Speck et al., 1997; Sloan et al., 1998; Speck et al., 2005; Thompson et al., 2006; Speck et al., 2009), using datasets from both space-based instruments such as the Infrared Astronomical Satellite (IRAS) Low Resolution Spectrometer (LRS: Neugebauer et al., 1984), and the Infrared Space Observatory (ISO: Kessler et al., 1996) Short Wavelength Spectrometer (SWS: de Graauw et al., 1996), as well as instruments in ground-based observatories (e.g., CGS3 on the United Kingdom Infrared Telescope, UKIRT). In fact, the parameters most commonly used to make identifications of SiC dust in space are the strength and peak position of the $\sim 11\mu\text{m}$ feature. From ISO data, there is also a range in shapes and peak positions of the $\sim 11\mu\text{m}$ SiC feature that cannot be simply correlated with the apparent temperature of the

underlying continuum (Thompson et al., 2006). However, there remain several common trends that exist in the observed SiC features:

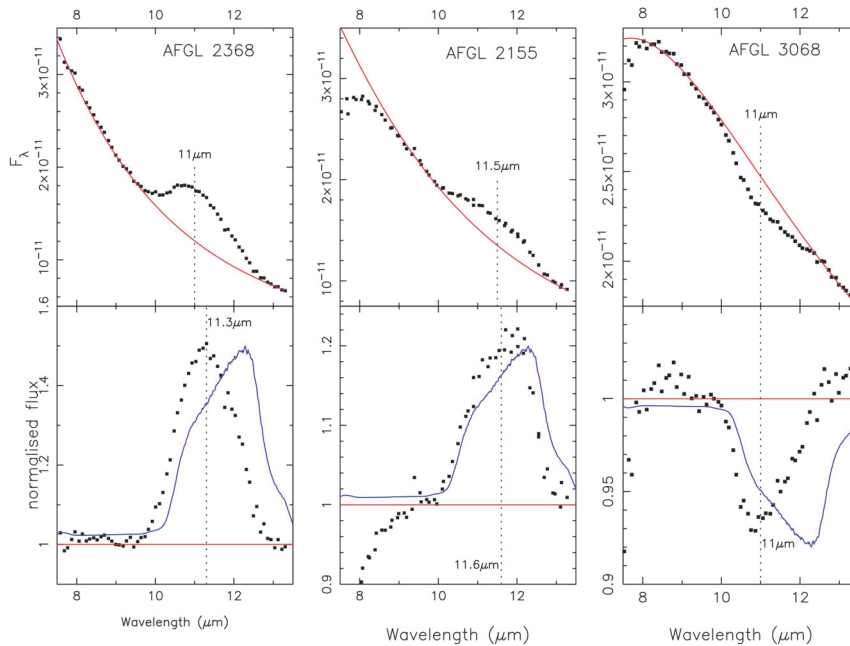


Fig. 10. The 11 μm SiC feature, observed in the spectra of carbon stars. Left hand panels represent stars that have the optically thinnest dust shells; optical depth increases to the right. Top panels: Ground-based observed spectra (black symbols: Speck et al. 1997) with best-fitting blackbody continua (red lines). Bottom panels: Continuum-divided spectra, following Eq. 2, provide the effective Q-values or extinction efficiencies for the dust shells. Blue lines: β -SiC absorbance data of Pitman et al. (2008), converted to absorptivity $A = e^{\text{absorbance}}$, is proportional to Q .

- i. Early in the AGB phase, when the mass-loss rate is low and the shell is optically thin, the $\sim 11 \mu\text{m}$ SiC emission feature is strong, narrow, and sharp.
- ii. As the mass loss increases and the shell becomes optically thicker, the SiC emission feature broadens, flattens, and weakens.
- iii. Once the mass-loss rate is extremely high and the shell is optically thick, the SiC feature appears in absorption.
- iv. Once the AGB phase ends and the thinning dust shell cools, SiC is more rarely observed but may be hidden by other emerging spectral features.

5. Application #2: Radiative transfer modeling

Radiative transfer (RT) modeling uses the optical functions of candidate minerals to model how a given object should look both spectroscopically and in images. Mineral candidates determined by spectral matching can then be input into numerical RT models; examples of

codes used to solve the equation of radiative transfer are DUSTY (Nenkova et al. 2000) and 2-Dust (Ueta & Meixner 2003). The acquisition of new optical functions, for SiC and all materials posited to exist in space, is critical to these numerical efforts. Astrophysicists use RT modeling to determine the effects of grain size and shape distributions, chemical composition and mineralogies, temperature and density distributions on the expected astronomical spectrum, and to place constraints on the relative abundances of different grain types in a dust shell. In this way, astrophysicists can build a list of parameters that describes the circumstellar environment around a star.

In radiative transfer modeling, one simulates SiC dust in space by specifying best estimates for the optical functions, sizes, and shape distributions of the particles. The optical functions mentioned in Section 3 have been tested in a variety of radiative transfer applications. The optical functions of Bohren & Huffman (1983), Pégourié (1988), and Laor & Draine (1993) were used to place limits on the abundance of SiC dust in carbon stars (e.g., Martin & Rogers 1987; Lorenz-Martins & Lefevre 1993, 1994; Lorenz-Martins et al. 2001; Groenewegen 1995; Groenewegen et al. 1998, 2009; Griffin 1990, 1993; Bagnulo et al. 1995, 1997, 1998), Large Magellanic Cloud stars (Speck et al. 2006; Srinivasan et al. 2010), and (proto-)planetary nebulae (Clube & Gledhill 2004; Hoare 1990; Jiang et al. 2005). Those optical functions have also been used in studies of dust formation (e.g., Kozasa et al. 1996), hydrodynamics of circumstellar shells (e.g., Windsteig et al. 1997; Steffen et al. 1997), and mean opacities (Ferguson et al. 2005; Alexander & Ferguson 1994). In their radiative transfer models of dust around C-stars, Groenewegen et al. (2009) offered a comparison of the performance of the optical functions of Pitman et al. (2008), shown in Figure 3.5, against α -SiC from Pégourié (1988), and β -SiC from Borghesi et al. (1985) in matching observed 11 μ m features in astronomical spectra. Ladjal et al. (2010) concluded that the Pitman et al. (2008) modeled the shape and peak position of the 11 μ m feature well in evolved stars. The intrinsic shape for SiC grains in circumstellar environments is not known but distributions of complex, nonspherical shapes (Continuous Distribution of Ellipsoids, CDE, Bohren & Huffman 1983; Distribution of Hollow Spheres, Min et al. 2003; aggregates, Andersen et al. 2006, and references therein) are the best estimate at present. Most of these produce a feature at $\lambda \sim 11 \mu$ m that is broad as compared to laboratory SiC spectra, but matches astronomically observed spectra. There is no clear consensus on what the grain size distribution for SiC grains in space should be (see review by Speck et al. 2009). SiC dust is generally found in circumstellar, not interstellar, dust, which limits the assumptions on size. Strictly speaking, the SiC optical functions of Pégourié (1988) and Laor & Draine (1993) should be used with the corresponding grain size distribution of the ground and sedimented SiC sample measured in the lab (\propto diameter^{-2.1}, with an average grain diameter = 0.04 μ m). Bulk n and k datasets (e.g., Pitman et al. 2008; Hofmeister et al. 2009) can be used with any grain size distribution.

Once optical functions, sizes, and shape distributions have been selected for the SiC particles, astrophysicists are free to test the influence of percent SiC dust content on an astronomical spectrum. Figure 11 gives examples of synthetic spectra of SiC-bearing dust shells of varying optical thicknesses around a $T=3000$ K star using the radiative transfer code DUSTY. Simply changing the optical functions and/or shape distribution results in substantial differences in the modeled astronomical spectrum, and thus interpretations of the self-absorption and emission in the circumstellar dust shell.

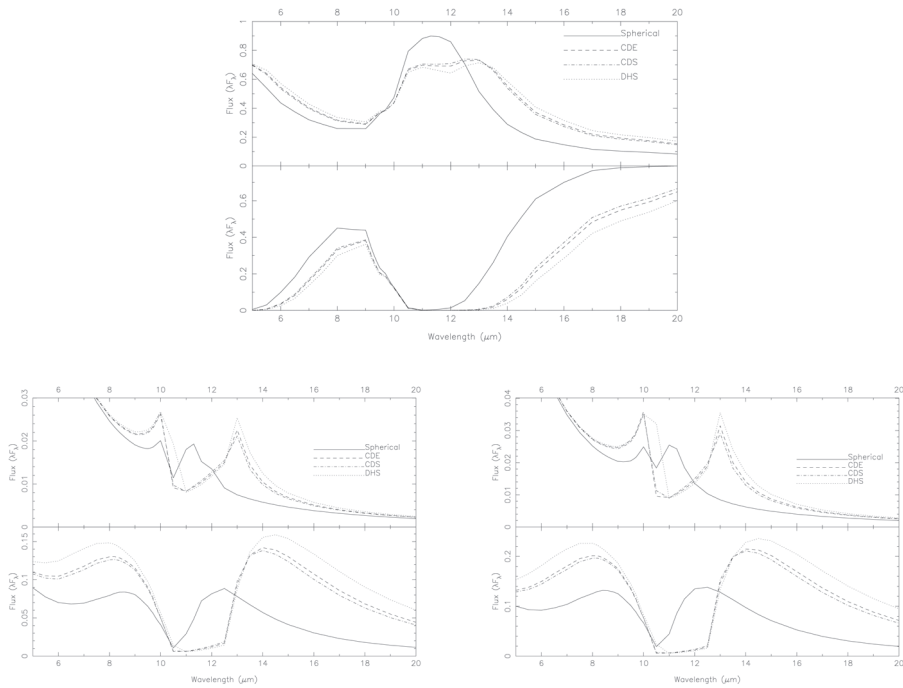


Fig. 12. Synthetic spectra of stellar light flux generated with DUSTY code. Top panel: Pégourié (1988) α -SiC optical functions. Bottom panel: Pitman et al. (2008) SiC optical functions. Left hand versus right hand columns compare α -SiC (weighted average of $1/3 E_{||c}$, $2/3 E_{\perp c}$) versus β -SiC. Line styles compare different shape distributions (spherical, CDE, CDS = continuous distribution of ellipsoids; spheroids, DHS = distribution of hollow spheres). See Corman (2010) and Corman et al. (2011) for more examples.

6. Conclusion

Since the 1960s, laboratory and theoretical astrophysics investigations of SiC grains have culminated in several important findings:

1. $\sim 99\%$ of meteoritic SiC grains were formed around carbon-rich Asymptotic Giant Branch stars, and that of these, $> 95\%$ originate around low-mass ($< 3M_{\odot}$) carbon stars;
2. Nearly all SiC grains in space are crystalline, with $> 80\%$ of these occurring as the cubic 3C polytype, and the rest comprising the lower temperature 2H polytype or 3C/2H combinations;
3. The grain size distribution of SiC in space includes both very small and very large grains (1.5 nm - 26 μm), with most grains in the 0.1-1 μm range. Single-crystal SiC grains can exceed 20 μm in size. The sizes of individual SiC crystals are correlated with s-process element concentration.
4. There is no consensus on the shape of SiC particles in space. SEM and TEM imagery of presolar SiC grains provides a guide. In numerical radiative transfer model calculations,

distributions of complex, nonspherical shapes (continuous distributions of ellipsoids or hollow spheres; fractal aggregates) are assumed.

5. Complimentary spectroscopic measurements of synthetic SiC made by the semiconductor and astrophysics communities have provided consistent values for optical functions, once different methodologies have been accounted for. Laboratory astrophysics studies of SiC focus on general UV spectral behavior and two specific IR spectral features (at $\lambda \sim 11 \mu\text{m}$, $21 \mu\text{m}$) that can be matched to astronomical spectra. The effects of orientation, polytype, and impurities in SiC are all important to astronomical studies.
6. Variations in optical functions with impurities and structure, as well as assumptions on size and shape distributions, strongly affects the amount of light scattering and absorption inferred in space.

Optical properties of SiC warrant future study. Vacuum UV data from the semiconductor literature need to be better integrated into the astrophysics literature. Laboratory studies on SiC have considered the effect of varying temperature from early on (e.g., Choyke & Patrick 1957). However, most data were collected only at room temperature. Temperature-dependent spectra and optical functions are necessary, especially low-temperature measurements. Chemical vapor-deposited SiC samples are available from the semiconductor industry for β -SiC. For future work, other forms of β -SiC would be better for determining optical functions, e.g., single crystals for the non-absorbing near-IR to visible region. Further measurements of solid solutions of SiC and C, with focus on impurities likely to be incorporated in astrophysical environments rather than doped crystals, should be pursued in the UV. Although IR spectra of 2H SiC can be constructed from available data (e.g., Lambrecht et al. 1997) because folded modes are not present, 2H SiC also warrants direct measurement for its importance in space.

7. Acknowledgment

Authors' laboratory and theoretical work shown in this chapter was kindly supported by the National Science Foundation under grants NSF-AST-1009544, NASA APRA04-000-0041, NSF-AST-0607341, and NSF-AST-0607418. Credit: K. M. Pitman et al., *A&A*, vol. 483, pp. 661-672, 2008, reproduced with permission © ESO. Data from Speck & Hofmeister (2004) and Hofmeister et al. (2009) reproduced with permission from the AAS. Figure 2.2 was kindly provided by T. Bernatowicz. The authors thank Jonas Goldsand for his assistance on laboratory sample preparation and data collection. This is PSI Contribution No. 506.

8. References

- Adolph, B., Tenelsen, K., Gavrilenko, V. I., & Bechstedt, F. (1997). Optical and loss spectra of SiC polytypes from ab initio calculations, *Phys. Rev. B*, Vol. 55, pp. 1422-1429
- Alexander, D. R., & Ferguson, J. W. (1994). Low-temperature Rosseland opacities, *Astrophys. J.*, Vol. 437, No. 2, pp. 879-891
- Amari, S., Lewis, R. S., & Anders, E. (1994). Interstellar grains in meteorites. I - Isolation of SiC, graphite, and diamond, size distributions of SiC and graphite. II - SiC and its noble gases, *Geochim. Cosmochim. Ac.*, Vol. 58, p. 459.
- Amari, S., Hoppe, P., Zinner, E., & Lewis, R. S. (1992). Interstellar SiC with unusual isotopic compositions - Grains from a supernova?, *Astrophys. J. Lett.*, Vol. 394, pp. L43-L46.

- Amari, S., Hoppe, P., Zinner, E., & Lewis, R. S. (1995). Trace-element concentrations in single circumstellar silicon carbide grains from the Murchison meteorite, *Meteoritics*, Vol. 30, No. 6, p. 679
- Amari, S., Zinner, E., & Lewis, R. S. (1996) CA and TI Isotopic Compositions of Size-Separated SiC Fractions from the Murchison Meteorite, *Lunar Planet. Sci.*, Vol. 27, page 23
- Amari, S., Nittler, L. R., Zinner, E., & Lewis, R. S. (1997a). Presolar SiC Grains of Type A+B, *Meteorit. Planet. Sci.*, Vol. 32, p. A6
- Amari, S., Nittler, L. R., Zinner, E., & Lewis, R. S. (1997b). Continued search for rare types of presolar SiC - Grains X and Y, *Lunar Planet. Sci.*, Vol. 28, p. 33.
- Anders, E., & Zinner, E. (1993). Invited Review - Interstellar grains in primitive meteorites: Diamond, silicon carbide, and graphite, *Meteoritics*, Vol. 28, pp. 490-514
- Andersen, A. C., Loidl, R., & Höfner, S. (1999). Optical properties of carbon grains: Influence on dynamical models of AGB stars, *Astron. Astrophys.*, Vol. 349, pp. 243-252
- Andersen, A. C., Mutschke, H., Posch, Th., Min, M., & Tamanai, A. (2006). Infrared extinction by homogeneous particle aggregates of SiC, FeO and SiO₂: Comparison of different theoretical approaches, *J. Quant. Spectrosc. Rad. Trans.*, Vol. 100, No. 1-3, pp. 4-15
- Bagnulo, S., Doyle, J. G., & Griffin, I. P. (1995). A study of the size and composition of dust grains in the circumstellar envelope of IRC +10 216, *Astron. Astrophys.*, Vol. 301, p. 501
- Bagnulo, S., Doyle, J. G., & Andretta, V. (1998). Observations and modelling of spectral energy distributions of carbon stars with optically thin envelopes, *Mon. Not. R. Astron. Soc.*, Vol. 296, pp. 545-563
- Bagnulo, S., Skinner, C. J., Doyle, J. G., & Camphens, M. (1997). Carbon stars with detached dust shells: the circumstellar envelope of UU Aurigae, *Astron. Astrophys.*, Vol. 321, pp. 605-617
- Baron, Y., Papoular, R., Jourdain de Muizon, M., & Pégourié, B. (1987). An analysis of the emission features of the IRAS low-resolution spectra of carbon stars, *Astron. Astrophys.*, Vol. 186, p. 271
- Barzyk, J. G. (2007). Multielement isotopic analysis of presolar silicon carbide, Ph.D. thesis (Proquest, AAT 3252254), The University of Chicago, Illinois, USA, 102 pages
- Belle, M. L., Prokofeva, N. K., & Reifman, M. B. (1967). *Soviet Phys. - Semicond.*, Vol. 1, p. 315
- Bernatowicz, T. J., Croat, T. K., & Daulton, T. L. (2006). Origin and Evolution of Carbonaceous Presolar Grains in Stellar Environments, In: *Meteorites and the Early Solar System II*, eds. D. S. Lauretta & H. Y. McSween, Jr. (Tucson: University of Arizona Press), 109
- Bernatowicz, T., Fraundorf, G., Ming, T., Anders, E., Wopenka, B., Zinner, E., & Fraundorf, P. (1987). Evidence for interstellar SiC in the Murray carbonaceous meteorite, *Nature*, Vol. 330, No. 24, p. 728-730
- Bernatowicz, T., Fraundorf, G., Fraundorf, P., & Tang, M. (1988a). TEM Observations of Interstellar Silicon Carbide from the Murray and Murchison Carbonaceous Meteorites, *51st Meeting of the Meteoritical Society*, July 18-22, 1988, Fayetteville, Arkansas, No. 665, p.1

- Bernatowicz, T., Fraundorf, G., Fraundorf, P., & Ming, T. (1988b). TEM Observations of Interstellar Silicon Carbide from the Murray and Murchison Carbonaceous Meteorites, *Meteoritics*, Vol. 23, p. 257
- Bernatowicz, T. J., Akande, O. W., Croat, T. K., & Cowsik, R. (2005). Constraints on Grain Formation around Carbon Stars from Laboratory Studies of Presolar Graphite, *Astrophys. J.*, Vol. 631, p. 988
- Besmehn, A., & Hoppe, P. (2002). NanoSIMS Study of an Unusual Silicon Carbide X Grain from the Murchison Meteorite, *Meteorit. Planet. Sci.*, Vol. 37, Supplement, p. A17
- Blöcker, T., & Schönberner, D. (1991). New pre-white dwarf evolutionary tracks, In: *White Dwarfs*, NATO Advanced Science Institutes (ASI) Series C, Vol. 336, eds. G. Vauclair, E. Sion, p. 1, Kluwer, Dordrecht
- Bohren, C. F., & Huffman, D. R. (1983). *Absorption and Scattering of Light by Small Particles*, John Wiley & Sons Inc., ISBN 0-471-29340-7, New York, 530 pp.
- Borghesi, A., Bussoletti, E., Colangeli, L., & de Blasi, C. 1985, Laboratory study of SiC submicron particles at IR wavelengths - A comparative analysis, *Astron. Astrophys.*, Vol. 153, No. 1, pp. 1-8
- B²FH = Burbidge, E. M., Burbidge, G. R., Fowler, W. A., & Hoyle, F. (1957). Synthesis of the Elements in Stars, *Rev. Mod. Phys.*, Vol. 29, p. 547
- Cameron, A. G. W. (1957). Nuclear Reactions in Stars and Nucleogenesis, *Publ. Astron. Soc. Pac.*, Vol. 69, p. 201
- Chan, S. J., & Kwok, S. (1990). Evolution of infrared carbon stars, *Astron. Astrophys.*, Vol. 237, p. 354
- Choyke, W. J., & Patrick, L. (1957). Absorption of Light in Alpha SiC near the Band Edge, *Phys. Rev.*, Vol. 105, p. 1721
- Choyke, W. J., & Patrick, L. (1968). Higher Absorption Edges in 6H SiC, *Phys. Rev.*, Vol. 172, No. 3, pp. 769-772
- Choyke, W. J., & Patrick, L. (1969). Higher Absorption Edges in Cubic SiC, *Phys. Rev.*, Vol. 187, No. 3, pp. 1041-1043
- Clayton, D. D., & Nittler, L. R. (2004). Astrophysics with Presolar Stardust, *Annu. Rev. Astron. Astr.*, Vol. 42, p. 39
- Clément, D., Mutschke, H., Klein, R., & Henning, Th. (2003). New Laboratory Spectra of Isolated β -SiC Nanoparticles: Comparison with Spectra Taken by the Infrared Space Observatory, *Astrophys. J.*, Vol. 594, No. 1, pp. 642-650
- Clube, K. L., & Gledhill, T. M. (2004). Mid-infrared imaging and modelling of the dust shell around post-AGB star HD 187885 (IRAS 19500-1709), *Mon. Not. R. Astron. Soc.*, Vol. 355, No. 3, pp. L17-L21
- Corman, A. B. (2010). Carbon Stars and Silicon Carbide, PhD thesis, University of Missouri-Columbia, USA
- Corman, A. B., Hofmeister, A. M., Speck, A. K., & Pitman, K. M. (2011). Optical Constants of Silicon Carbide. III. Shape Effects on Small Silicon Carbide Grains, *Astrophys. J.*, in preparation
- Daulton, T. L., Bernatowicz, T. J., Lewis, R. S., Messenger, S., Stadermann, F. J., & Amari, S. (2002). Polytype Distribution in Circumstellar Silicon Carbide, *Science*, Vol. 296, No. 5574, pp. 1852-1855
- Daulton, T. L., Bernatowicz, T. J., Lewis, R. S., Messenger, S., Stadermann, F. J., & Amari, S. (2003). Polytype distribution of circumstellar silicon carbide - microstructural

- characterization by transmission electron microscopy, *Geochim. Cosmochim. Ac.*, Vol. 67, No. 24, pp. 4743-4767
- de Graauw, T., et al. (1996). Observing with the ISO Short-Wavelength Spectrometer, *Astron. Astrophys.*, Vol. 315, pp. L49-L54
- Devaty, R. P., & Choyke, W. J. (1997). Optical Characterization of Silicon Carbide Polytypes, *Phys. Status Solidi (A), Applied Research*, Vol. 162, No. 1, pp. 5-38
- Ferguson, J. W., Alexander, D. R., Allard, F., Barman, T., Bodnarik, J. G., Hauschildt, P. H., Heffner-Wong, A., & Tamanai, A. (2005). Low-Temperature Opacities, *Astrophys. J.*, Vol. 623, No. 1, pp. 585-596
- Friedemann, C. (1969). Evolution of silicon carbide particles in the atmospheres of carbon stars, *Physica*, Vol. 41, p. 139
- Friedemann, C., Gürtler, J., Schmidt, R., & Dorschner, J. (1981). The 11.5 micrometer emission from carbon stars - Comparison with IR spectra of submicrometer-sized silicon carbide grains, *Astrophys. Space Sci.*, Vol. 79, No. 2, pp. 405-417
- Gavrilenko, V. I. (1995). Calculated differential reflectance of the (110) surface of cubic silicon carbide, *Appl. Phys. Lett.*, Vol. 67, pp. 16-18
- Gavrilenko, V. I., & Bechstedt, F. (1997). Optical functions of semiconductors beyond density-functional theory and random-phase approximation, *Phys. Rev. B*, Vol. 55, No. 7, pp. 4343-4352
- Gilman, R. C. (1969). On the Composition of Circumstellar Grains, *Astrophys. J.*, Vol. 155, p. L185
- Gilra, D. P. (1971). Composition of Interstellar Grains, *Nature*, Vol. 229, No. 5282, pp. 237-241
- Gilra, D.P. (1972). Collective Excitations in Small Solid Particles and Astronomical Applications, Ph.D. thesis, University of Wisconsin-Madison, Dissertation Abstracts International, Vol. 33-11, Sect. B, p. 5114
- Goebel, J. H., Cheeseman, P., & Gerbault, F. (1995). The 11 Micron Emissions of Carbon Stars, *Astrophys. J.*, Vol. 449, p. 246
- Griffin, I. P. (1990). A model for the infrared and radio spectral energy distribution of IRC + 10 deg 216, *Mon. Not. R. Astron. Soc.*, Vol. 247, pp. 591-605
- Griffin, I. P. (1993). A model for the circumstellar envelope of WX SER, *Mon. Not. R. Astron. Soc.*, Vol. 260, pp. 831-843
- Groenewegen, M. A. T. (1995). Dust shells around infrared carbon stars, *Astron. Astrophys.*, Vol. 293, pp. 463-478.
- Groenewegen, M. A. T., Whitelock, P. A., Smith, C. H., & Kerschbaum, F. (1998). Dust shells around carbon Mira variables, *Mon. Not. R. Astron. Soc.*, Vol. 293, p. 18
- Groenewegen, M. A. T., Sloan, G. C., Soszyński, I., & Petersen, E. A. (2009). Luminosities and mass-loss rates of SMC and LMC AGB stars and red supergiants, *Astron. Astrophys.*, Vol. 506, No. 3, pp. 1277-1296
- Gyngard, F. (2009). Isotopic studies of presolar silicon carbide and oxide grains as probes of nucleosynthesis and the chemical evolution of the galaxy, Ph.D. thesis (Proquest, AAT 3387342), Washington University in St. Louis, USA, 165 pp.
- Hackwell, J. A. (1972). Long wavelength spectrometry and photometry of M, S and C-stars, *Astron. Astrophys.*, Vol. 21, p. 239
- Heck, P. R. (2005) Helium and neon in presolar silicon carbide grains and in relict chromite grains from fossil meteorites and micrometeorites as tracers of their origin, Ph.D.

- thesis Proquest, AAT C821918), Eidgenoessische Technische Hochschule Zuerich (Switzerland), 155 pp.
- Heck, P. R., Pellin, M. J., Davis, A. M., Martin, I., Renaud, L., Benbalagh, R., Isheim, D., Seidman, D. N., Hiller, J., Stephan, T., Lewis, R. S., Savina, M. R., Mane, A., Elam, J., Stadermann, F. J., Zhao, X., Daulton, T. L., & Amari, S. (2010). Atom-Probe Tomographic Analyses of Presolar Silicon Carbide Grains and Meteoritic Nanodiamonds – First Results on Silicon Carbide, *41st Lunar Planet. Sci. Conf.*, March 1-5, 2010, The Woodlands, Texas, No. 1533, p. 2112
- Henkel, T., Stephan, T., Jessberger, E. K., Hoppe, P., Strebel, R., Amari, S., & Lewis, R. S. (2007). 3-D elemental and isotopic composition of presolar silicon carbides, *Meteorit. Planet. Sci.*, Vol. 42, No. 7, pp. 1121-1134
- Henning, T. (2010). Laboratory Astrophysics of Cosmic Dust Analogues, In: *Lecture Notes in Physics 815 Astromineralogy* (2nd ed.), Th. Henning (ed.), pp. 313-329, Springer-Verlag, ISBN 978-3-642-13258-2, Berlin, Heidelberg
- Hoare, M. G. (1990). The dust content of two carbon-rich planetary nebulae, *Mon. Not. R. Astron. Soc.*, Vol. 244, pp. 193-206
- Hofmeister, A. M., Keppel, E., & Speck, A. K. (2003). Absorption and reflection infrared spectra of MgO and other diatomic compounds, *Mon. Not. R. Astron. Soc.*, Vol. 345, No. 1, pp. 16-38
- Hofmeister, A. M., Pitman, K. M., Goncharov, A. F., & Speck, A. K. (2009) Optical Constants of Silicon Carbide for Astrophysical Applications. II. Extending Optical Functions from Infrared to Ultraviolet Using Single-Crystal Absorption Spectra, *Astrophys. J.*, Vol. 696, No. 2, pp. 1502-1516
- Hoppe, P. (2009). Stardust in Meteorites and IDPs: Current Status, Recent Advances, and Future Prospects, In: *Cosmic Dust - Near and Far*, ASP Conference Series, Vol. 414, ed. Th. Henning, E. Grün, & J. Steinacker, p.148
- Hoppe, P., & Besmehn, A. (2002). Evidence for Extinct Vanadium-49 in Presolar Silicon Carbide Grains from Supernovae, *Astrophys. J.*, Vol. 576, No. 1, pp. L69-L72.
- Hoppe, P., & Ott, U. (1997). Mainstream silicon carbide grains from meteorites, In: *Astrophysical implications of the laboratory study of presolar materials*, AIP Conference Proceedings, Vol. 402, pp. 27-58
- Hoppe, P., & Zinner, E. (2000). Presolar dust grains from meteorites and their stellar sources, *J. Geophys. Res.*, Vol. 105, No. A5, pp. 10371-10386
- Hoppe, P., Amari, S., Zinner, E., Ireland, T., & Lewis, R. S. (1994a). Carbon, nitrogen, magnesium, silicon, and titanium isotopic compositions of single interstellar silicon carbide grains from the Murchison carbonaceous chondrite, *Astrophys. J.*, Vol. 430, No. 2, pp. 870-890
- Hoppe, P., Pungitore, B., Eberhardt, P., Amari, S., & Lewis, R. S. (1994b) Ion imaging of small interstellar grains, *Meteoritics*, Vol. 29, No. 4, pp. 474-475
- Hoppe, P., Strebel, R., Eberhardt, P., Amari, S., & Lewis, R. S. (1996) Small SiC grains and a nitride grain of circumstellar origin from the Murchison meteorite: Implications for stellar evolution and nucleosynthesis, *Geochim. Cosmochim. Ac.*, Vol. 60, No. 5, pp. 883-907
- Hoppe, P., Strebel, R., Eberhardt, P., Amari, S., & Lewis, R. S. (2000) Isotopic properties of silicon carbide X grains from the Murchison meteorite in the size range 0.5-1.5 μm , *Meteorit. Planet. Sci.*, Vol. 35, No. 6, pp. 1157-1176

- Hoppe, P., Lodders, K., Strebel, R., Amari, S., & Lewis, R. S. (2001). Boron in Presolar Silicon Carbide Grains from Supernovae, *Astrophys. J.*, Vol. 551, No. 1, pp. 478-485
- Huffman, D. R. (1988). Methods and Difficulties in Laboratory Studies of Cosmic Dust Analogues, In: *Experiments on Cosmic Dust Analogues*, eds. E. Bussoletti, C. Fusco, & G. Longo, Astrophysics and Space Science Library, Vol. 149, p. 25, Kluwer Academic Publishers, Dordrecht.
- Iben, I., Jr., & Renzini, A. (1983). Asymptotic giant branch evolution and beyond, in: Annual review of Astron. Astrophys.. Vol. 21 (Palo Alto, CA, Annual Reviews, Inc.), pp. 271-342
- Ismail, A. M., & Abu-Safia, H. (2002). Calculated and measured reflectivity of some p-type SiC polytypes, *J. Appl. Phys.*, Vol. 91, No. 7, pp. 4114-4116
- Jennings, C. L., Savina, M. R., Messenger, S., Amari, S., Nichols, R. H., Jr., Pellin, M. J., & Podosek, F. A., (2002). Indarch SiC by TIMS, RIMS, and NanoSIMS, *33rd Lunar Planet. Sci. Conf.*, March 11-15, 2002, Houston, Texas, abstract no. 1833
- Jiang, B. W., Zhang, K., & Li, A. (2005). On Silicon Carbide Grains as the Carrier of the 21 μm Emission Feature in Post-Asymptotic Giant Branch Stars, *Astrophys. J.*, Vol. 630, No. 1, pp. L77-L80
- Kessler, M. F., Steinz, J. A.; Anderegg, M. E.; Clavel, J.; Drechsel, G.; Estaria, P.; Faelker, J.; Riedinger, J. R.; Robson, A.; Taylor, B. G.; Ximénez de Ferrán, S. (1996). The Infrared Space Observatory (ISO) mission, *Astron. Astrophys.*, Vol. 315, No. 2, pp. L27 - L31
- Kimura, Y., Nuth, J. A., III, & Ferguson, F. T. (2005a). Is the 21 Micron Feature Observed in Some Post-AGB Stars Caused by the Interaction between Ti Atoms and Fullerenes? *Astrophys. J.*, Vol. 632, No. 2, pp. L159-L162
- Kimura, Y., Ishikawa, M., Kurumada, M., Tanigaki, T., Suzuki, H., & Kaito, C. (2005b). Crystal structure and growth of carbon-silicon mixture film prepared by ion sputtering, *Journal of Crystal Growth*, Vol. 275, pp. e977-e981
- Kozasa, T., Dorschner, J., Henning, Th., & Stognienko, R. (1996). Formation of SiC grains and the 11.3 μm feature in circumstellar envelopes of carbon stars, *Astron. Astrophys.*, Vol. 307, pp. 551-560
- Kwok, S., Volk, K. M., & Hrivnak, B. J. (1989). A 21 micron emission feature in four proto-planetary nebulae, *Astrophys. J. Lett.*, Vol. 345, pp. L51-L54
- Ladjal, D., Justtanont, K., Groenewegen, M. A. T., Blommaert, J. A. D. L., Waelkens, C., & Barlow, M. J. (2010). 870 μm observations of evolved stars with LABOCA, *Astron. Astrophys.*, Vol. 513, p. A53
- Lambrecht, W. R. L., Segall, B., Suttrop, W., Yoganathan, M., Devaty, R. P., Choyke, W. J., Edmond, J. A., Powell, J. A., & Alouani, M. (1993). Optical reflectivity of 3C and 4H-SiC polytypes: Theory and experiment, *Appl. Phys. Lett.*, Vol. 63, pp. 2747- 2749
- Lambrecht, W. R. L., Segall, B., Yoganathan, M., Suttrop, W., Devaty, R. P., Choyke, W. J., Edmond, J. A., Powell, J. A., & Alouani, M. (1994). Calculated and measured uv reflectivity of SiC polytypes, *Phys. Rev. B*, Vol. 50, pp. 10722-10726
- Lambrecht, W. R. L., Limpijumnon, S., Rashkeev, S. N., & Segall, B. (1997). Electronic Band Structure of SiC Polytypes: A Discussion of Theory and Experiment, *Phys. Status Solidi (B)*, *Applied Research*, Vol. 202, No. 1, pp. 5-33
- Laor, A., & Draine, B. T. (1993). Spectroscopic constraints on the properties of dust in active galactic nuclei, *Astrophys. J.*, Vol. 402, No. 2, pp. 441-468

- Lindquist, O. P. A., Schubert, M., Arwin, H., & Jarrendahl, K. (2004). Infrared to vacuum ultraviolet optical properties of 3C, 4H and 6H silicon carbide measured by spectroscopic ellipsometry, *Thin Solid Films*, Vol. 455–456, pp. 235–238
- Little-Marenin, I. R. (1986). Carbon stars with silicate dust in their circumstellar shells, *Astrophys. J. Lett.*, Vol. 307, pp. L15–L19
- Logothetidis, S., & Petalas, J. (1996). Dielectric function and reflectivity of 3C–silicon carbide and the component perpendicular to the c axis of 6H–silicon carbide in the energy region 1.5–9.5 eV, *J. Appl. Phys.*, Vol. 80, pp. 1768–1772
- Lorenz-Martins, S., & Lefevre, J. (1993). SiC in circumstellar shells around C stars, *Astron. Astrophys.*, Vol. 280, pp. 567–580
- Lorenz-Martins, S., & Lefevre, J. (1994). SiC grains and evolution of carbon stars, *Astron. Astrophys.*, Vol. 291, pp. 831–841
- Lorenz-Martins, S., de Araújo, F. X., Codina Landaberry, S. J., de Almeida, W. G., & de Nader, R. V. (2001). Modeling of C stars with core/mantle grains: Amorphous carbon + SiC, *Astron. Astrophys.*, Vol. 367, pp. 189–198
- Lubinsky, A. R., Ellis, D. E., & Painter, G. S. (1975). Electronic structure and optical properties of 3C–SiC, *Phys. Rev. B*, Vol. 11, p. 1537
- Martin, P. G., & Rogers, C. (1987). Carbon grains in the envelope of IRC +10216, *Astrophys. J.*, Vol. 322, pp. 374–392
- Mauron, N., & Huggins, P. J. (2006). Imaging the circumstellar envelopes of AGB stars, *Astron. Astrophys.*, Vol. 452, pp. 257–268
- Min, M., Hovenier, J. W., & de Koter, A. (2003). Shape effects in scattering and absorption by randomly oriented particles small compared to the wavelength, *Astron. Astrophys.*, Vol. 404, pp. 35–46
- Mutschke, H., Andersen, A. C., Clément, D., Henning, Th., & Peiter, G. (1999). Infrared properties of SiC particles, *Astron. Astrophys.*, Vol. 345, pp. 187–202
- Nakashima, S., & Harima, H. (1997). Raman Investigation of SiC Polytypes, *Physica Status Solidi A – Applied Research*, Vol. 162, p. 39
- Nenkova, M., Ivezić, Z., & Elitzur, M. (2000). *Thermal Emission Spectroscopy and Analysis of Dust, Disks, and Regoliths*, Vol. 196, p. 77
- Neugebauer, G., Soifer, B. T., Beichman, C. A., Aumann, H. H., Chester, T. J., Gautier, T. N., Lonsdale, C. J., Gillett, F. C., Hauser, M. G., & Houck, J. R. (1984). Early results from the Infrared Astronomical Satellite, *Science*, Vol. 224, pp. 14–21
- Nichols, R. H. (1992). The origin of neon-E: Neon-E in single interstellar silicon carbide and graphite grains, Ph.D. thesis, Washington Univ., Seattle, USA
- Nicolussi, G. K., Davis, A. M., Pellin, M. J., Lewis, R. S., Clayton, R. N., & Amari, S. (1997). S-process zirconium in individual presolar silicon carbide grains, *Lunar Planet. Sci.*, Vol. 28, p. 23
- Nicolussi, G. K., Pellin, M. J., Lewis, R. S., Davis, A. M., Amari, S., & Clayton, R. N. (1998). Molybdenum Isotopic Composition of Individual Presolar Silicon Carbide Grains from the Murchison Meteorite, *Geochim. Cosmochim. Ac.*, Vol. 62, pp. 1093–1104
- Ninomiya, S., & Adachi, S. (1994). Optical Constants of 6H SiC Single Crystals, *Jpn. J. Appl. Phys.*, Vol. 33, No. 5A, pp. 2479
- Obarich, V. A. (1971). Optical constants of α -SiC(6H) in the intrinsic absorption region, *J. Appl. Spectrosc.*, Vol. 15, No. 1, pp. 959–961

- Orofino, V., Blanco, A., Mennella, V., Bussoletti, E., Colangeli, L., & Fonti, S. (1991). Experimental extinction properties of granular mixtures of silicon carbide and amorphous carbon, *Astron. Astrophys.*, Vol. 252, No. 1, pp. 315-319
- Ott, U. (2010). The Most Primitive Material in Meteorites, In: *Lecture Notes in Physics 815 Astromineralogy* (2nd ed.), ed. Th. Henning, pp. 277-311, Springer-Verlag, ISBN 978-3-642-13258-2, Berlin, Heidelberg
- Ott, U., & Merchel, S. (2000). Noble Gases and the Not So Unusual Size of Presolar SiC in Murchison, *31st Lunar Planet. Sci. Conf.*, March 13-17, 2000, Houston, Texas, abstract no. 1356
- Papoular, R., Cauchetier, M., Begin, S., & Lecaer, G. (1998). Silicon carbide and the 11.3- μ m feature, *Astron. Astrophys.*, Vol. 329, pp. 1035-1044
- Pégourié, B. (1988). Optical properties of alpha silicon carbide, *Astron. Astrophys.*, Vol. 194, No. 1-2, pp. 335-339
- Petalas, J., Logothetidis, S., Gioti, M., & Janowitz, C. (1998). Optical Properties and Temperature Dependence of the Interband Transitions of 3C- and 6H-SiC in the Energy Region 5 to 10 eV, *Phys. Status Solidi (B)*, Vol. 209, No. 2, pp. 499-521
- Philipp, H. R. (1958). Intrinsic Optical Absorption in Single-Crystal Silicon Carbide, *Phys. Rev.*, Vol. 111, pp. 440
- Philipp, H. R., & Taft, E. A. (1960). Intrinsic Optical Absorption in Single Crystal Silicon Carbide, In: *Silicon Carbide*, ed. J. R. O'Connor & J. Smiltens, pp. 366-370, Pergamon, New York
- Pitman, K. M., Hofmeister, A. M., Corman, A. B., & Speck, A. K. (2008). Optical properties of silicon carbide for astrophysical applications, I. New laboratory infrared reflectance spectra and optical constants, *Astron. Astrophys.*, Vol. 483, pp. 661-672
- Prombo, C. A., Podosek, F. A., Amari, S., & Lewis, R. S. (1993). S-process BA isotopic compositions in presolar SiC from the Murchison meteorite, *Astrophys. J.*, Vol. 410, No. 1, pp. 393-399
- Rehn, V., Stanford, J. L., Jones, V. O., & Choyke, W. J. (1976). *Proc. 13th Internat. Conf. Physics of Semiconductors*, Marves, Rome, 1976, p. 985
- Savina, M. R., Davis, A. M., Tripa, C. E., Pellin, M. J., Clayton, R. N., Lewis, R. S., Amari, S., Gallino, R., & Lugaro, M. (2003) Barium isotopes in individual presolar silicon carbide grains from the Murchison meteorite, *Geochim. Cosmochim. Ac.*, Vol. 67, No. 17, pp. 3201-3214
- Skrutskie, M. F., Reber, T. J., Murphy, N. W., & Weinberg, M. D. (2001). Inferring Milky Way Structure from 2MASS-selected Carbon Stars, *Bulletin of the American Astronomical Society*, Vol. 33, p. 1437
- Sloan, G. C., Little-Marenin, I. R., & Price, S. D. (1998). The carbon-rich dust sequence - Infrared spectral classification of carbon stars, *Astron. J.*, Vol. 115, p. 809
- Speck, A. K. (1998). The Mineralogy of Dust Around Evolved Stars, PhD thesis, University College London
- Speck, A. K., & Hofmeister, A. M. (2004). Processing of Presolar Grains around Post-Asymptotic Giant Branch Stars: Silicon Carbide as the Carrier of the 21 Micron Feature, *Astrophys. J.*, Vol. 600, No. 2, pp. 986-991
- Speck, A. K., Barlow, M. J., & Skinner, C. J. (1997). The nature of the silicon carbide in carbon star outflows, *Mon. Not. R. Astron. Soc.*, Vol. 288, p. 431

- Speck, A. K., Hofmeister, A. M., & Barlow, M. J. (1999). The SiC Problem: Astronomical and Meteoritic Evidence, *Astrophys. J.*, Vol. 513, No. 1, pp. L87-L90
- Speck, A. K., Thompson, G. D., & Hofmeister, A. M. (2005). The Effect of Stellar Evolution on SiC Dust Grain Sizes, *Astrophys. J.*, Vol. 634, pp. 426-435
- Speck, A. K., Cami, J., Markwick-Kemper, C., Leisenring, J., Szczerba, R., Dijkstra, C., Van Dyk, S., & Meixner, M. (2006). The Unusual Spitzer Spectrum of the Carbon Star IRAS 04496-6958: A Different Condensation Sequence in the LMC?, *Astrophys. J.*, Vol. 650, pp. 892-900
- Speck, A. K., Corman, A. B., Wakeman, K., Wheeler, C. H., & Thompson, G. (2009). Silicon Carbide Absorption Features: Dust Formation in the Outflows of Extreme Carbon Stars, *Astrophys. J.*, Vol. 691, pp. 1202-1221
- Spitzer, W. G., Kleinman, D., & Frosch, C. J. (1959a). Infrared Properties of Cubic Silicon Carbide Films, *Phys. Rev.*, Vol. 113, pp. 133-136
- Spitzer, W. G., Kleinman, D., & Walsh, D. (1959b). Infrared Properties of Hexagonal Silicon Carbide, *Phys. Rev.*, Vol. 113, pp. 127-132
- Srinivasan, S., Sargent, B. A., Matsuura, M., Meixner, M., Kemper, F., Tielens, A. G. G. M., Volk, K., Speck, A. K., Woods, P. M., Gordon, K., Marengo, M., & Sloan, G. C. (2010). The mass-loss return from evolved stars to the Large Magellanic Cloud. III. Dust properties for carbon-rich asymptotic giant branch stars, *Astron. Astrophys.*, Vol. 524, p. A49
- Steffen, M., Szczerba, R., Menshchikov, A., & Schoenberner, D. (1997). Hydrodynamical models and synthetic spectra of circumstellar dust shells around AGB stars, *Astron. Astrophys.*, Vol. 126, pp. 39-65
- Stephens, J.R. (1980). Visible and ultraviolet (800-130 nm) extinction of vapor-condensed silicate, carbon, and silicon carbide smokes and the interstellar extinction curve, *Astrophys. J.*, Vol. 237, pp. 450-461
- Stroud, R. M., Nittler, L. R., & Hoppe, P. (2004). Microstructures and Isotopic Compositions of Two SiC X Grains, *Meteorit. Planet. Sci.*, Vol. 39, p. 5039
- Theodorou, G., Tsegas, G., & Kaxiras, E. (1999). Theory of electronic and optical properties of 3C-SiC, *J. Appl. Phys.*, Vol. 85, No. 4, pp. 2179-2184
- Thompson, G. D., Corman, A. B., Speck, A. K., & Dijkstra, C. (2006). Challenging the Carbon Star Dust Condensation Sequence: Anarchist C Stars, *Astrophys. J.*, Vol. 652, p. 1654
- Treffers, R., & Cohen, M. (1974). High-resolution spectra of cool stars in the 10- and 20-micron regions, *Astrophys. J.*, Vol. 188, p. 545
- Ueta, T., & Meixner, M. (2003). 2-DUST: A Dust Radiative Transfer Code for an Axisymmetric System, *Astrophys. J.*, Vol. 586, No. 2, pp. 1338-1355
- Van Schmus, W. R., & Wood, J. A. (1967). A chemical-petrologic classification for the chondritic meteorites, *Geochim. Cosmochim. Ac.*, Vol. 31, pp. 747-765
- Volk, K., Kwok, S., & Langill, P. P. (1992). Candidates for extreme carbon stars, *Astrophys. J.*, Vol. 391, p. 285
- Volk, K., Kwok, S., & Hrivnak, B. J. (1999). High-Resolution Infrared Space Observatory Spectroscopy of the Unidentified 21 Micron Feature, *Astrophys. J.*, Vol. 516, No. 2, pp. L99-L102
- Volk, K., Xiong, G., & Kwok, S. (2000). Infrared Space Observatory Spectroscopy of Extreme Carbon Stars, *Astrophys. J.*, Vol. 530, p. 408

- Wheeler, B. (1966). The ultraviolet reflectivity of α and β SiC, *Solid State Commun.*, Vol. 4, No. 4, pp. 173-175.
- Willacy, K., & Cherchneff, I. (1998). Silicon and sulphur chemistry in the inner wind of IRC+10216, *Astron. Astrophys.*, Vol. 330, p. 676
- Willems, F. J. (1988). IRAS low-resolution spectra of cool carbon stars. II – Stars with thin circumstellar shells. III – Stars with thick circumstellar shells, *Astron. Astrophys.*, Vol. 203, pp. 51-70
- Windsteig, W., Dorfi, E. A., Hoefner, S., Hron, J., & Kerschbaum, F. (1997). Mid- and far-infrared properties of dynamical models of carbon-rich long-period variables, *Astron. Astrophys.*, Vol. 324, pp. 617-623
- Xie, C., Xu, P., Xu, F., Pan, H., & Li, Y. (2003). First-principles studies of the electronic and optical properties of 6H-SiC, *Physica B*, Vol. 336, pp. 284-289
- Yin, Q.-Z., Lee, C.-T. A., & Ott, U. (2006). Signatures of the s-process in presolar silicon carbide grains: Barium through hafnium, *Astrophys. J.*, Vol. 647, pp. 676-684

Introducing Ohmic Contacts into Silicon Carbide Technology

Zhongchang Wang, Susumu Tsukimoto,
Mitsuhiro Saito and Yuichi Ikuhara

*WPI Research Center, Advanced Institute for Materials Research, Tohoku University
2-1-1 Katahira, Aoba-ku,
Japan*

1. Introduction

The promising mechanical and electronic properties of silicon carbide (SiC) are stimulating extensive investigations focused on the applications of its semiconducting and excellent structure properties. As a matter of fact, the interest toward SiC is twofold. On one hand, it is a high-strength composite and high-temperature structural ceramic, demonstrating the ability to function at high-power and caustic circumstances. On the other hand, it is an attractive semiconductor, which has excellent inherent characteristics such as a wide band gap (3.3 eV), high breakdown field (3×10^6 V/cm), more than double the high carrier mobility and electron saturation drift velocity (2.7×10^7 cm/s) of silicon (Morkoc et al., 1994). These intrinsic electronic properties together with the high thermal conductivity (5 W/cm K) and stability make it the most likely of all wide-band-gap semiconductors to succeed the current Si and GaAs as next-generation electronic devices, especially for high-temperature and high-frequency applications. Successful fabrication of SiC-based semiconductor devices includes Schottky barrier diodes, p-i-n diodes, metal-oxide-semiconductor field effect transistors, insulated gate bipolar transistors and so forth. Moreover, current significant improvements in its epitaxial and bulk crystal growth have paved the way for fabricating its electronic devices, which arouses further interest in developing device processing techniques so as to take full advantage of its superior inherent properties.

One of the most critical issues currently limiting its device processing and hence its widespread application is the manufacturing of reliable and low-resistance Ohmic contacts ($< 1 \times 10^{-5}$ Ωcm^2), especially to *p*-type SiC (Perez-Wurfl et al., 2003). The Ohmic contacts are primarily important in SiC devices because a Schottky barrier of high energy is inclined to form at an interface between metal and wide-band-gap semiconductor, which consequently results in low-current driving, slow switching speed, and increased power dissipation. Much of effort expended to date to realize the Ohmic contact has mainly focused on two techniques. One is the high-dose ion-implantation approach, which can increase the carrier density of SiC noticeably and lower its depletion layer width significantly so that increasing tunnelling current is able to flow across barrier region. Although the doping layers with high concentration ($> 10^{20}$ cm^{-3}) were formed, the key problem of this method is the easy formation of lattice defects or amorphization during the ion implantation. These defects are unfortunately very stable and need to be recovered via post-annealing at an extremely high temperature (~ 2000 K), thereby complicating mass production of SiC devices.

The other alternative is to generate an intermediate semiconductor layer with narrower band gap or higher carrier density at the contacts/SiC interface by deposition and annealing technique. To form such layers, many materials have been examined in a trial-and-error designing fashion, including metals, silicides, carbides, nitrides, and graphite. Of all these materials, metallic alloys have been investigated extensively, largely because the fabrication process is simple, standard, and requires no exotic substances. In particular, most of research activities have been focused on TiAl-based alloys, the only currently available materials that yield significantly low contact resistance (Ohmic contact) to the *p*-type SiC. Furthermore, they demonstrate high thermal stability. For example, Tanimoto et al. have developed the TiAl contacts with extremely low specific contact resistance in the range of 10^{-7} to 10^{-6} Ωcm^2 for the *p*-type 4H-SiC with an Al doping concentration of 1.2×10^{19} cm^{-3} (Tanimoto et al., 2002). Although a lot of intriguing results have been obtained regarding the TiAl-based contact systems, the mechanism whereby the Schottky becomes Ohmic after annealing has not been well clarified yet. In other words, the key factors to understanding the formation of origin of Ohmic contact remains controversial. Mohny et al. proposed that a high density of surface pits and spikes underneath the contacts contributes to the formation of Ohmic behaviour based on their observations using the scanning electron microscopy and atomic force microscopy (Mohny et al., 2002). Nakatsuka et al., however, concluded that the Al concentration in the TiAl alloys is fundamental for the contact formation (Nakatsuka et al., 2002). Using the liquid etch and ion milling techniques, John & Capano ruled out these possibilities and claimed that what matters in realizing the Ohmic nature is the carbides, Ti_3SiC_2 and Al_4C_3 , formed between metals and semiconductor (John & Capano, 2004). This, however, differs, to some extent, from the X-ray diffraction (XRD) observations revealing that the compounds formed at the metal/SiC interface are silicides, TiSi_2 , TiSi and Ti_3SiC_2 (Chang et al., 2005). The formation of silicides or carbides on the surface of SiC substrate after annealing may serve as a primary current-transport pathway to lower the high Schottky barrier between the metal and the semiconductors. In addition, Ohyanagi et al. argued that carbon exists at the contacts/SiC interface and might play a crucial role in lowering Schottky barrier (Ohyanagi et al., 2008). These are just a few representative examples illustrating the obvious discrepancies in clarifying the formation mechanism of Ohmic contact. Taking the amount of speculations on the mechanism and the increasing needs for better device design and performance control, understanding the underlying formation origin is timely and relevant.

To develop an understanding of the origin in such a complex system, it is important to focus first on microstructure characterization. Tanimoto et al. examined the microstructure at the interface between TiAl contacts and the SiC using Auger electron spectroscopy and found that carbides containing Ti and Si were formed at interface (Tanimoto et al., 2002). Recently, transmission electron microscopy (TEM) studies by Tsukimoto et al. have provided useful information in this aspect due to possible high-resolution imaging (Tsukimoto et al., 2004). They have found that the majority of compounds generated on the surface of 4H-SiC substrate after annealing consist of a newly formed compound and hence proposed that the new interface is responsible for the lowering of Schottky barrier in the TiAl-based contact system. However, role of the interface in realizing the Ohmic nature remains unclear. It is not even clear how the two materials bond together atomically from these experiments, which is very important because it may strongly affect physical properties of the system. To determine the most stable interface theoretically, one first has to establish feasible models on the basis of distinct terminations and contact sites and then compare them. However, a

direct comparison of the total energies of such models is not physically meaningful since interfaces might have a different number of atoms. On the other hand, the ideal work of adhesion, or adhesion energy, W_{ad} , which is key to predicting mechanical and thermodynamic properties of an interface is physically comparable. Generally, the W_{ad} , which is defined as reversible energy required to separate an interface into two free surfaces, can be expressed by the difference in total energy between the interface and isolated slabs,

$$W_{ad} = (E_1 + E_2 - E_{IF})/A. \quad (1)$$

Here E_1 , E_2 , and E_{IF} are total energies of isolated slab 1, slab 2, and their interface system, respectively, and A is the total interface area. To date, analytic models available for predicting W_{ad} concerning SiC have mostly been restricted to SiC/metal heterojunctions such as SiC/Ni, SiC/Al and SiC/Ti. These models are motivated by the experimental deposition of metals on SiC. However, they neglect the complexity of situation; namely, the compounds (silicides or carbides) can be generated on SiC substrate after annealing and thus the models are only applicable to systems with as-deposited state.

Recent advances in the high-angle annular-dark-field (HAADF) microscopy, the highest resolution, have enabled an atomic-scale imaging of a buried interface (Nellist et al., 2004). However, a direct interpretation of the observed HAADF images is not always straightforward because there might be abrupt structural discontinuity, mixing of several species of elements on individual atomic columns, or missing contrasts of light elements. One possible way out to complement the microscopic data is via atomistic calculation, especially the first-principles calculation. As well known, the atomistic first-principles simulations have long been confirmed to be able to suggest plausible structures, elucidate the reason behind the observed images, and even provide a quantitative insight into how interface governs properties of materials. Consequently, a combination of state-of-the-art microscopy and accurate atomistic modeling is an important advance for determining interface atomic-scale structure and relating it to device properties, revealing, in this way, physics origin of contact issues in SiC electronics.

In addition to determining atomic structure of 4H-SiC/Ti₃SiC₂ interface, the goal of this chapter is to clarify formation mechanism of the TiAl-based Ohmic contacts so as to provide suggestions for further improvement of the contacts. 4H-SiC will hereafter be referred to as SiC. First of all, we fabricated the TiAl-based contacts and measured their electric properties to confirm the formation of Ohmic contact. Next, the metals/SiC interface was analyzed using the XRD to identify reaction products and TEM, high-resolution TEM (HRTEM), and scanning TEM (STEM) to observe microstructures. Based on these observations, we finally performed systematic first-principles calculations, aimed at assisting the understanding of Ohmic contact formation at a quantum mechanical level. The remainder of this chapter is organized as follows: Section 2 presents the experimental procedures, observes the contact microstructure, and determines the orientation relationships between the generated Ti₃SiC₂ and SiC substrate. Section 3 describes the computational method, shows detailed results on bulk and surface calculations, outlines the geometries of the 96 candidate interfaces, and determine the structure, electronic states, local bonding, and nonequilibrium quantum transport of the interface. We provide discussion and concluding remarks in Sec. 4.

2. Experimental characterization

The *p*-type 4H-SiC epitaxial layers (5-μm thick) doped with aluminum ($N_A = 4.5 \times 10^{18} \text{ cm}^{-3}$) which were grown on undoped 4H-SiC wafers by chemical vapor deposition (manufactured

by Cree Research, Inc.) were used as substrates. The 4H-SiC substrates had 8°-off Si-terminated (0001) surfaces inclined toward a $[-2110]$ direction because only 4H-type structure of SiC with polymorph (e.g. 3C, 4H, 6H, 15R etc.) was controllable by lateral growth of the epitaxial layers parallel to (0001)-oriented surface. After chemical cleaning of the substrate surface, a 10 nm-thick sacrificial oxide (SiO_x) layer was grown on the SiC substrate by dry-oxidation at 1423 K for 60 min. The electrode patterns were made by removing the SiO_x layers, where contact metals were deposited by dipping in 5 % diluted hydrofluoric acid solution for 1 min using a photolithography technique. Prior to the deposition of contact materials, the substrates were cleaned by deionized water. Then, Ti and Al stacking layers with high purities were deposited sequentially on the substrate in a high vacuum chamber where the base pressure was below 5×10^{-6} Pa. The thicknesses of the Ti and Al layers investigated in this study are 100 nm and 380 nm, respectively, and these layer thicknesses were chosen to give the average composition of the Ti(20 at%) and Al(80 at%), where the layer thicknesses were measured by a quartz oscillator during deposition. The reasons to choose this average composition was that aluminum rich (more than 75 at%) in TiAl contacts were empirically found to be essential to yield low contact resistance, resulting from formation of the Ti_3SiC_2 compound layers. After depositing, the binary TiAl contact layers were annealed at 1273 K for a storage time of 2 min in an ultra-high vacuum chamber where the vacuum pressure was below 1×10^{-7} Pa.

The surface morphology of the TiAl contact layers on 4H-SiC after annealing was observed using a JEOL JSM-6060 scanning electron microscope (SEM). Microstructural analysis and identification of the Ti_3SiC_2 layers at the contact layers/4H-SiC interfaces after annealing was performed using X-ray diffraction (XRD) and cross-sectional TEM. For XRD analysis, Rigaku RINT-2500 with Cu $K\alpha$ radiation operated at 30 kV and 100 mA was used. In particular, the interfacial structures and an orientation relationship between the contact layers and the 4H-SiC substrates were characterized by cross-sectional high-resolution TEM observations and selected area diffraction pattern (SADP) analysis, respectively, using a JEOL JEM-4000EX electron microscope operated at an accelerating voltage of 400 kV, where the point-to-point resolution of this microscope was approximately 0.17 nm. Z-contrast images were obtained using a spherical aberration (C_s) corrected scanning transmission electron microscope (STEM) (JEOL 2100F), which provides an unprecedented opportunity to investigate atomic-scale structure with a sub-Å electron probe. Thin foil specimens for the TEM and STEM observations were prepared by the standard procedures: cutting, gluing, mechanical grinding, dimple polishing, and argon ion sputter thinning techniques.

2.1 Formation of Ohmic contacts

To verify the formation of Ohmic contact, we measured the electric properties (I - V characteristics) for the TiAl contact systems before and after annealing (Fig. 1). For the system before annealing, its current almost maintains zero despite that the applied bias ranges from -3.0 to 3.0 V, which unambiguously reflects Schottky character of this system. This can be understood by considering that the potential induced by applied bias drops largely at a contact interface between metals and semiconductors, thus hindering the current flow. The annealed system, however, exhibits a typical Ohmic nature, as its I - V curve is nearly linear and the current increases sharply with the rise of applied bias. This drastic change of electric properties suggests that there might be substantial changes in microstructure during annealing.

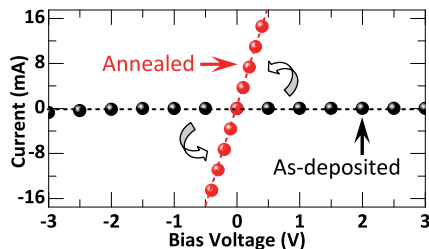


Fig. 1. Current-voltage properties of the TiAl contact system before and after thermal annealing at 1273 K for 2 min.

2.1.1 Formation of Ti_3SiC_2 compound on SiC

To determine the chemical composition of the TiAl contact systems, we performed XRD analyses, as shown in Fig. 2, where textural orientations of the detected matters are shown as well. As expected from the preparation process, one can see in Fig. 2(a) peaks of deposited metals, Ti and Al, and the (0001)-oriented SiC in the system before annealing. It is worthy of mentioning that the detected Ti has a much weaker intensity of diffraction peak than Al, which can be attributed to its lower concentration and smaller grains. On the other hand, the XRD spectrum alters significantly after annealing (Fig. 2(b)), as the original Ti and Al peaks disappear and there emerge new peaks, suggesting that chemical reactions occur.

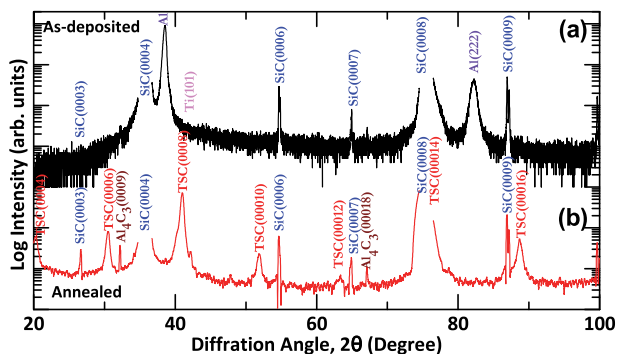


Fig. 2. XRD spectra of (a) as-deposited and (b) annealed TiAl contact systems. The TSC is an abbreviation of Ti_3SiC_2 .

From Fig. 2(b), the reaction products are found to be dominated by ternary Ti_3SiC_2 with a strongly (0001)-oriented texture, as only the (000 l) diffraction peaks are detected. In addition to the Ti_3SiC_2 , binary Al_4C_3 is also present in the annealed specimen. However, its amount is very small because the intensities of its diffraction peaks are comparatively much weaker. The formation of these compounds at elevated temperature is also supported by the Ti-Al-SiC equilibrium phase diagram, which predicts that four phases, SiC, Al_4C_3 , Ti_3SiC_2 , and liquid, can coexist in an equilibrium state when the aforementioned composition of TiAl alloy is adopted. Furthermore, the XRD results agree well with the experimental reports (Johnson and Capano, 2004), but deviate somewhat from those of Nakatsuka et al. (2002) showing that binary Al_3Ti is present as well. This slight difference is mainly because the intensity of Al_3Ti peak is so low that might be overlapped by the strong peaks of SiC and

Ti_3SiC_2 . Finally, the SiC retains (0001)-oriented texture after annealing, thereby facilitating development of hetero-epitaxy between reaction products and substrates.

Figure 3 shows an isothermal section of the pseudo-ternary phase diagram of Al-Ti-SiC system at 1273 K (Viala et al., 1997) based on the experimental measurements of Al-Ti-Si-C quaternary system, where a grey region indicates the existence of binary AlSi-based liquid phases, and thick and fine lines indicates sub-solidus lines and tie-lines, respectively. It is noted that the liquidus line would lie at near the composition region of pure Al, as denoted by a symbol L in Fig. 3. Based on this phase diagram, the liquid phase is predicted to form when the concentration of Al is more than 75 at% in the Ti/Al contacts at 1273 K. In general, both the solutes and solvents have high diffusibility in liquid, the liquid phase has high reactivity to solid (substrate) and hence the reaction products are easily formed at elevated temperatures. Formation of the liquid is believed to play an important role in the TiAl-based contact by rapid thermal anneal process. Here, the effective average composition of the present reaction system, which react Ti-80%Al and SiC, can assume to be at the point a within region (i) in the diagram. In this region, four phases of SiC, Al_4C_3 , Ti_3SiC_2 and liquid with a composition of Al-12%Si (which is a eutectic composition of Al-Si binary alloy) is predicted to maintain constant and coexist in equilibrium. This prediction is consistent with the XRD results obtained from samples annealed at 1273 K for 2 min (Fig. 2(b)), although a small amount of Al_3Ti and Al did not react completely with SiC and remained at this stage. Further annealing of the sample for longer time, for instance, 6 min, renders these unreacted Al_3Ti and Al disappear due to additional reaction to form the carbides (Ti_3SiC_2 and a small amount of Al_4C_3) and to the evaporation of Al-Si liquid phase with a high vapor pressure during annealing in ultra high vacuum. Hence, the average composition of the reaction system seems to shift toward Al-poor area (region (ii), as indicated by an arrow), and reach the point b after annealing. In the region (ii), three phases, SiC, Ti_3SiC_2 and Al-Si liquid with the Si concentrations varied from 12% (at the point c) to 19% (at the point d) are coexistent with their volume being constituted by an array of tie-lines. However, it is not straightforward to control the compounds formed by the rapid thermal annealing process because of occurrence of non-equilibrium phenomena such as evaporation of the liquid phases in this reaction system. This might be the reason why the TiAl-based contacts have been fabricated empirically with no definite designing guidelines.

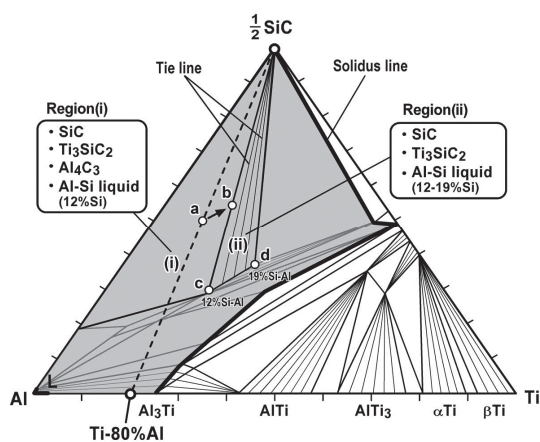


Fig. 3. Isothermal section of a pseudoternary phase diagram of Al-Ti-SiC system at 1273 K.

2.1.2 Growth and microstructure of Ti_3SiC_2 layers on SiC

To characterize the surface morphology of the TiAl contact layer after annealing, the SEM observation was employed. Figure 4 shows a plan-view SEM image from the TiAl contact layer after annealing at 1273 K. The surface is observed to have a uniformly scale-shaped contrast with hexagonal facets, although surface roughness after annealing is aggravated in comparison to that of the sample before annealing. Using a stylus surface profiler, the maximum typical roughness was measured to be about 1 μm . The surface facet planes are found to form parallel to $\langle -2110 \rangle$ directions on the $\text{SiC}(0001)$ substrate surface. The hillocks observed on the surface, which is due to formation of residual Al-based liquid droplet, is, however, absent for the samples annealed at temperatures lower than 1073 K. The surface morphology results from evaporation of the liquid phases with low melting points and high vapor pressures during annealing at high temperatures in ultra high vacuum.

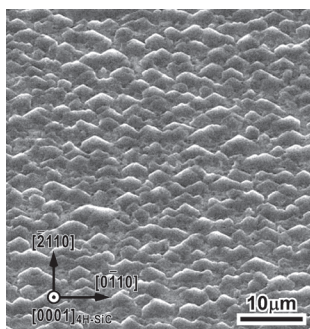


Fig. 4. A plan-view SEM image of the Ti/Al contact layers deposited on SiC after annealing at 1273 K.

Although the XRD can reveal detailed information on chemical composition of reaction products, it provides limited insight into matters concerning how the products distribute and contact the substrate. To observe the microstructure directly, we present in Fig. 5(a) a cross-sectional bright-field TEM image of a representative region in the annealed TiAl contact system. The incident electron beam is along $[0-110]$ direction of the SiC, which is parallel to the tilting axis of the 8° -off $\text{SiC}(0001)$ surface. As seen in this figure, the SiC surface is covered entirely by the plate-shaped Ti_3SiC_2 with thickness ranging from 30 nm to 300 nm. This universal cover means that no any other compounds contact directly the SiC surface, thereby ensuring an exclusive contact of Ti_3SiC_2 to SiC. Consequently, the SiC/ Ti_3SiC_2 interface might play an essential role in the formation of Ohmic contact. In addition, this interface is observed to have a sawtooth-like facet structure and the Ti_3SiC_2 surface inclines by nearly 8° toward the substrate surface, suggesting that the SiC surface affects significantly morphology of formed Ti_3SiC_2 .

To analyze the element species around interface, we further show in Fig. 5(b) the energy-dispersive X-ray spectroscopy (EDS) spectra for the interfacial SiC and Ti_3SiC_2 regions. The substrate is mainly composed of C and Si and the reaction products C, Si, and Ti, in accordance with chemical compositions of the substrate and the main reaction products, respectively. Unexpectedly, no Al peak is identified in either the interfacial SiC or Ti_3SiC_2 area, which seems to contravene the XRD analyses revealing that the Al_4C_3 compound is present in the annealed specimen. This discrepancy is mainly because the amount of Al_4C_3 is so small (Fig. 2(b)) that is hard to be detected by the EDS, or because Al might not distribute near the interface at all but around the Ti_3SiC_2 surface instead. Whatever the reason is, the Al should

not be the key to understanding the formation origin of Ohmic contact. That is, a large amount of Al diffuses into the SiC and introduces a heavily *p*-doped SiC, which result in narrower depletion area and thus more tunneling. As a matter of fact, this has also been suggested by analyzing interfacial chemical composition and local states, which shows that no additional Al segregates to interface, suggestive of a clean contact of Ti_3SiC_2 to SiC (Gao et al., 2007).

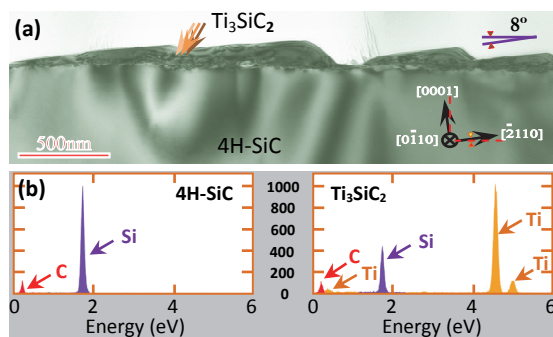


Fig. 5. (a) Cross-sectional bright-field TEM image of the annealed TiAl contact system showing exclusive reaction product of Ti_3SiC_2 , and (b) EDS data obtained at the SiC and Ti_3SiC_2 region near to interface. The vertical axis in (b) denotes the counts (i.e., intensity).

Figure 6 shows a selected area diffraction pattern (SADP) at the contacts/SiC interface taken along the same electron-beam direction as in Fig. 5(a). A careful indexing of the pattern confirms again the plate-shaped layers as being ternary Ti_3SiC_2 . The formed Ti_3SiC_2 layers are observed to have epitaxial orientation relationships, $(0001)\text{Ti}_3\text{SiC}_2 // (0001)\text{SiC}$ and $[0-110]\text{Ti}_3\text{SiC}_2 // [0-110]\text{SiC}$ with the SiC substrate, which agrees well with the XRD analyses demonstrating that both materials exhibit the (0001)-oriented textures. These orientation relationships are believed to be beneficial for forming a coherent and well matched interface between SiC and Ti_3SiC_2 , since they both belong to the hexagonal space group with lattice constants of $a = 3.081 \text{ \AA}$ and $c = 10.085 \text{ \AA}$ for the SiC and $a = 3.068 \text{ \AA}$ and $c = 17.669 \text{ \AA}$ for the Ti_3SiC_2 (Harris, 1995).

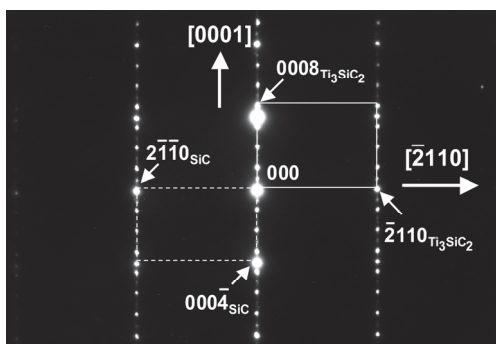


Fig. 6. Selected-area diffraction pattern obtained at the annealed contacts/SiC interface. The arrays of diffraction spots from the SiC and contacts are marked by dashed and solid lines, respectively.

In support of this idea, we present in Fig. 7 a cross-sectional HRTEM image of the SiC/Ti₃SiC₂ interface observed from the [11-20] direction. One can see clearly well arranged (000 \bar{l})-oriented lattice fringes along the direction parallel to the interface in both the Ti₃SiC₂ layer and SiC substrate. The points at which the phase contrast is no longer periodic in either the Ti₃SiC₂ or SiC define the interfacial region. Evidently, the interface is atomically abrupt and coherent without any secondary phase layers, amorphous layers, contaminants, or transition regions, which confirms a clean and direct contact of the Ti₃SiC₂ with SiC on atomic scale. The interface has (0001)-oriented terraces and ledges, as marked by letters T_i (i = 1, 2, 3, 4) and L_j (j = 1, 2, 3) in Fig. 7, respectively. The morphology of the terraces is observed to be atomically flat and abrupt as well. On the other hand, the ledge heights are found to be defined well as $n \times$ (a half unit cell height of 4H-SiC: 0.5 nm), where n represents the integer, e.g., $n = 11$ for L₁, $n = 2$ for L₂, and $n = 1$ for L₃. This unique interface morphology is caused by the chemical reaction of TiAl and SiC, and anisotropic lateral growth of the epitaxial Ti₃SiC₂ layers along the directions parallel to SiC(0001), as indicated by arrows in Fig. 7. In addition, no misfit dislocations are clearly visible at interface in present HRTEM micrograph and further examination of other interfacial regions demonstrates that the density of misfit dislocations is extremely low in this system. This can be explained from the small lattice mismatch between the two materials (less than 0.5%). Unfortunately, it remains unclear from this figure how the two materials atomically bond together at interface, which is very important because the bonding nature is well known to be able to affect the physical properties of interfacial systems significantly.

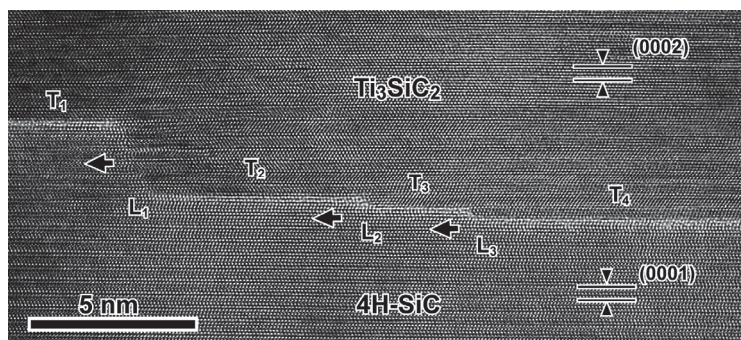


Fig. 7. A cross-sectional HRTEM micrograph of the interface between the Ti₃SiC₂ layer and the 4H-SiC substrate, which is taken along the SiC [-2110] zone axis.

2.1.3 Interface atomic-scale structures

Figure 8 shows a typical HAADF image of the SiC/Ti₃SiC₂ interface. A simple looking at this figure confirms a clean and atomically sharp contact between the two materials, which means a successful growth of the epitaxially Ti₃SiC₂ on SiC. Brighter spots in the image represent atomic columns of Ti, while the comparatively darker ones are Si, since the intensity of an atomic column in the STEM, to good approximation, is directly proportional to the square of atomic number (Z) (Pennycook & Boatner, 1988). Not surprisingly, due to small atomic number of C, its columns are not scattered strongly enough to be visualized, thereby making the image incomplete. Further complementing of this image so as to relate the atomic structure to property requires the first-principles calculations.

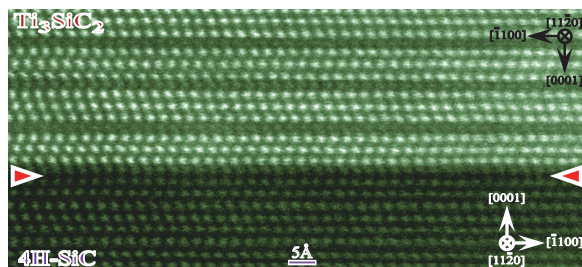


Fig. 8. A typical HAADF-STEM image of the SiC/ Ti_3SiC_2 interface in the annealed TiAl contact system observed from the $[11\bar{2}0]$ direction. The position of interface is indicated by two arrows

To see the interface atomic-scale structure clearer, we magnify the cross-sectional HAADF image of the SiC/ Ti_3SiC_2 interface in Fig. 9(a) and further filter it to reduce noise (Fig. 9(b)). The interface location is indicated by a horizontal line, which is determined based on the arrangement of atomic columns in bulk SiC and Ti_3SiC_2 . The Si-terminated Ti_3SiC_2 is observed intuitively to make a direct contact with the Si-terminated SiC substrate with the interfacial Si atoms of Ti_3SiC_2 sitting above hollow sites of the interfacial Si plane of SiC. However, as we will see in the upcoming simulations, this interpretation is premature in that it neglects a possibility, namely, the unseen C might be trapped at interface. Another interesting feature in this figure is that no Al columns are detected surrounding interface, which eliminates the possibility of additional *p*-doping via Al diffusion into the top few SiC layers. Since there are also no pits, spikes, or dislocations which might act as pathways for current transport, we conclude that the clean and coherent SiC/ Ti_3SiC_2 interface should be critical for the Ohmic contact formation. The ensuing question is how this interface lowers the Schottky barrier, which is rather difficult to investigate by experiment alone but can be suggested by calculations.

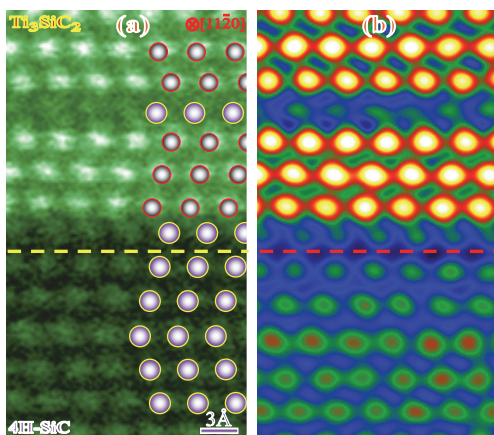


Fig. 9. A(a) Magnified HAADF image of the SiC/ Ti_3SiC_2 interface. An overlay is shown as well for easy reference. The bigger balls denote Si and the smaller ones Ti. (b) The same image as in (a) but has been low-pass filtered to reduce the noise.

3. Atomistic modelling of the functional interface

Calculations of electronic structure and total energy were carried out using the Vienna *ab initio* simulation package (VASP) within the framework of density- functional theory (DFT) (Kresse & Hafner, 1993). The projector augmented wave (PAW) method was used for electron-ion interactions and the generalized gradient approximation (GGA) of Perdew and co-worker (PW91) was employed to describe the exchange-correlation functional. The single-particle Kohn-Sham wave function was expanded using the plane waves with different cutoff energies depending on calculated systems of either bulk or slab. Sampling of irreducible wedge of Brillion zone was performed with a regular Monkhorst-Pack grid of special k points, and electronic occupancies were determined according to a Methfessel-Paxton scheme with an energy smearing of 0.2 eV. All atoms were fully relaxed using the conjugate gradient (CG) algorithm until the magnitude of the Hellmann-Feynman force on each atom was converged to less than 0.05 eV/Å, yielding optimized structures.

The electron transport properties of the above systems were explored with the fully self-consistent nonequilibrium Green's function method implemented in Atomistix ToolKit (ATK) code. This method has been applied to many systems successfully. The local density approximation (LDA) and the Troullier-Martins nonlocal pseudopotential were adopted, and the valence electrons were expanded in a numerical atomic-orbital basis set of single zeta plus polarization (SZP). Trial calculations exhibit similar results by using double zeta plus polarization (DZP) basis sets for all atoms, thereby validating the use of SZP. Only Γ -point was employed in the k -point sampling in the surface Brillouin zone. A cutoff of 100 Ry for solving Poissons equation and various integrals is utilized to present charge density and a rather large k -point value, 200, is chosen for accurately describing electronic structure along transport direction.

3.1 Bulk and surface calculations

3.1.1 Bulk properties

We first assess accuracy of the computational methods by performing a series of bulk calculations. It is known that the 4H-SiC, one of the most common SiC polymorphs, belongs to hexagonal $P6_3mc$ space group with $a = 3.081\text{\AA}$ and $c = 10.085\text{\AA}$. A unit cell of SiC consists of four Si-C bilayers with a total of 8 atoms. The Ti_3SiC_2 also has a hexagonal crystal structure but within the $P6_3mmc$ space group ($a = 3.068\text{\AA}$ and $c = 17.669\text{\AA}$). The atomic positions of Ti correspond to the $2a$, Si to the $2b$, and C to the $4f$ Wyckoff sites of the space group and the phase is composed of a layered structure with a double Ti-C block, each made up of two edge-sharing CTi6 octahedra. Note that the Ti atoms of Ti_3SiC_2 occupy two types of structurally nonequivalent positions: one (Ti1, two per unit cell) has C atoms as nearest neighbors, while the other (Ti2, four per unit cell) has Si atoms (see Fig. 13(a)). The optimum lattice constants of bulk 4H-SiC calculated using the above parameters are $a = 3.095\text{\AA}$ and $c = 10.131\text{\AA}$, 100.5% of the experimental value, while those of bulk Ti_3SiC_2 are $a = 3.076\text{\AA}$ and $c = 17.713\text{\AA}$, 100.25% of the experimental one (Harris, 1995).

Figure 10(a) shows calculated band structure of 4H-SiC along the high-symmetry lines. The top of occupied valence band (VB) is located at Γ point and the bottom of conduction band (CB) is at M point, causing the SiC to be an indirect gap semiconductor. The calculated energy band gap is 2.25 eV, which is smaller than the experimental value of 3.26 eV, but close to the calculated value of 2.18 eV (Käckell et al., 1994) and 2.43 eV (Ching et al., 2006). Deviation from the experimental value is attributed to the well-known drawback of the DFT

which tends to underestimate band gap. The band gap in Fig. 10(a) can also be seen from the total DOS shown in Fig. 11(a). Besides this gap around the Fermi level (E_F), there is also a gap of more than 1 eV located at about -10 eV below the E_F , dividing the entire VB into two parts. The lower part of the VB originates mainly from the bonding between the s states of the Si and C, while the upper one is dominated by p orbitals of Si and C in a form of sp^3 hybridization. The CB part, however, shows a continuum state throughout the whole region, which is reflected from interweaving lines above E_F (Fig. 10(a)).

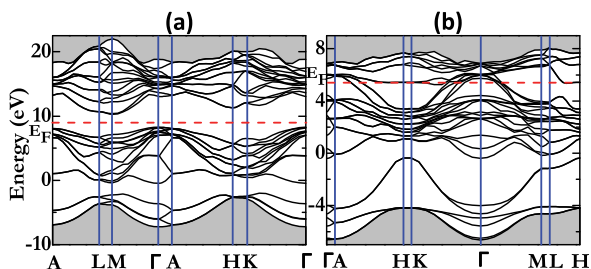


Fig. 10. Energy band structure of (a) 4H-SiC and (b) Ti_3SiC_2 along the major symmetric directions. The dotted lines in red denote the Fermi level (E_F).

In contrast, Ti_3SiC_2 exhibits clearly a metallic nature with bands crossing the E_F , as shown in Fig. 10(b), thereby resulting in a peak in the total DOS at E_F in Fig. 11(b). It is worth noting that the presence of the band at E_F is caused by the energetic overlap of Ti d states with the gap levels of SiC (Fig. 11(b)), not an artifact due to the DFT underestimation of band gap. This metallic character is in agreement with reported experimental results and other theoretical studies. From Fig. 10(b), one can see that the VB of Ti_3SiC_2 is also separated into two parts at approximately 5.7 eV below E_F , the lower part of which is composed of metalloid states having a typical s symmetry while the upper part of which consists of complex bands. It is also clear from Fig. 11(b) that these complicated states just below E_F are dominated by strongly hybridized bonding states containing mainly p orbitals of both Si and C and d orbitals of Ti. The contribution to the CB, however, comes predominantly from antibonding d states of Ti, as shown in the PDOS of Ti in Fig. 11(b). The magnitude of DOS at E_F is equal to 3.5 states/eV per unit cell, originating considerably from Ti d states together with a slight contribution from Si p states

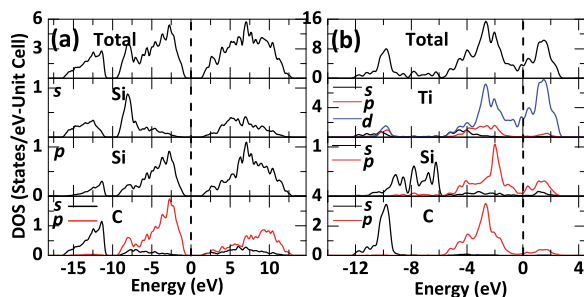


Fig. 11. Calculated total and partial densities of states (PDOS) for (a) 4H-SiC and (b) Ti_3SiC_2 . The Fermi level is set to zero and marked by a vertical dash line. The PDOS of Ti encompasses those of two types of nonequivalent Ti positions, Ti1 and Ti2.

3.1.2 Surface properties

To simulate a bulklike interface, it is essential to ensure that the two sides of the interface slabs used in calculations are thick enough to exhibit a bulklike interior because properties of a thin film may differ significantly from those of the bulk. To determine the minimum layer necessary for a bulklike slab, we first performed calculations on the convergence of surface energy with respect to slab thickness and then considered an additional series of surface relaxations as a function of slab layers. The surface energy of Ti_3SiC_2 , σ_T , under pressure P and temperature T can be expressed as follows:

$$\sigma_T = \frac{1}{2A}(E_{\text{slab}}^{\text{total}} - N_{\text{Ti}}\mu_{\text{Ti}} - N_{\text{Si}}\mu_{\text{Si}} - N_{\text{C}}\mu_{\text{C}} - PV - TS) \quad (2)$$

where, $E_{\text{slab}}^{\text{total}}$ denotes total energy of a relaxed and isolated slab, and μ_X , N_X , A represent chemical potential of X ($X = \text{Ti}, \text{Si}, \text{C}$), number of X atoms in the slab, and surface area, respectively. For Eq. (2), the TS term can be deleted at 0 K and meanwhile, the PV term is negligible for low pressure because we are considering a condensed matter system. Further, chemical potential of condensed phase of Ti_3SiC_2 , $\mu_{\text{Ti}_3\text{SiC}_2}$, can be given by a sum of three terms representing chemical potential of each species within the crystal:

$$\mu_{\text{Ti}_3\text{SiC}_2} = 3\mu_{\text{Ti}} + \mu_{\text{Si}} + 2\mu_{\text{C}}. \quad (3)$$

Since the total chemical potential of surface system, $\mu_{\text{Ti}_3\text{SiC}_2}$, is in equilibrium with that of its bulk, $E_{\text{Ti}_3\text{SiC}_2}^{\text{bulk}}$, we thus have

$$\mu_{\text{Ti}_3\text{SiC}_2} = E_{\text{Ti}_3\text{SiC}_2}^{\text{bulk}}. \quad (4)$$

Replacing Eq. (4) with Eqs. (2) and (3), one can eliminate the $\mu_{\text{Ti}_3\text{SiC}_2}$ and μ_{C} variables in the surface energy of Ti_3SiC_2 , σ_T , and obtain

$$\sigma_T = \frac{1}{2A}[E_{\text{slab}}^{\text{total}} - \frac{1}{2}N_{\text{C}}E_{\text{Ti}_3\text{SiC}_2}^{\text{bulk}} - \mu_{\text{Ti}}(N_{\text{Ti}} - \frac{3}{2}N_{\text{C}}) - \mu_{\text{Si}}(N_{\text{Si}} - \frac{1}{2}N_{\text{C}})]. \quad (5)$$

When the chemical potentials of the Ti and Si equal total energies of the hexagonal close-packed bulk Ti, $E_{\text{Ti}}^{\text{bulk}}$, and fcc bulk Si, $E_{\text{Si}}^{\text{bulk}}$, respectively, the Eq. (5) can be redefined as

$$\sigma_T^0 = \frac{1}{2A}[E_{\text{slab}}^{\text{total}} - \frac{1}{2}N_{\text{C}}E_{\text{Ti}_3\text{SiC}_2}^{\text{bulk}} - E_{\text{Ti}}^{\text{bulk}}(N_{\text{Ti}} - \frac{3}{2}N_{\text{C}}) - E_{\text{Si}}^{\text{bulk}}(N_{\text{Si}} - \frac{1}{2}N_{\text{C}})]. \quad (6)$$

Similarly, the surface energy of the SiC, σ_{S}^0 , can be given by the following equation under the condition that chemical potential of Si is equal to its bulk total energy.

$$\sigma_{\text{S}}^0 = \frac{1}{2A}[E_{\text{slab}}^{\text{total}} - N_{\text{C}}E_{\text{SiC}}^{\text{bulk}} - E_{\text{Si}}^{\text{bulk}}(N_{\text{Si}} - N_{\text{C}})] \quad (7)$$

Experimentally, the SiC(0001) plane was observed to be a favorable substrate surface that allows epitaxial growth of Ti_3SiC_2 with also a (0001)-oriented face. Four types of SiC terminations within the (0001) surface have been investigated, as shown in Fig. 12(b)-(e). In view of the unequal atom species at two sides of a stoichiometric slab, a non-stoichiometric

slab with identical surface layer must be used to extract surface energy of a particular termination. Initial convergence tests show that 10 Å of vacuum, $8 \times 8 \times 1$ irreducible k points and a cut-off energy of 400 eV ensure total-energy convergence to less than 1 meV/atom. All of the atoms were fully relaxed until magnitude of force on every atom is smaller than 0.05 eV/Å. With these parameters, we first calculated surface energies of Si-terminated SiC with slabs varying from 5 to 17 layers using Eq. (7) and found that a 9-layer slab is enough to exhibit good convergence of surface energy. Next, we examined relaxation of the SiC(0001) surface slabs so as to ensure that they are reasonably converged with respect to slab layers. The SiC(0001) surface shows a low degree of interlayer relaxations with maximum of less than 3% of the bulk spacing for 9 or more layers thick.

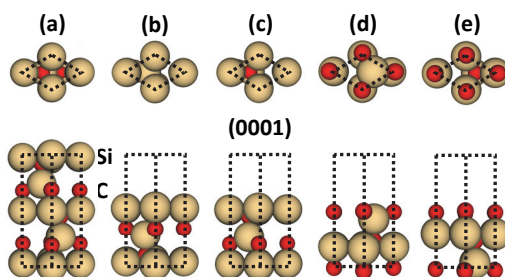


Fig. 12. Schematic plot of 4H-SiC: (a) bulk, (b) Si1, (c) Si2, (d) C1, and (e) C2 terminations. The upper part shows the top view, while the lower one shows the side view. Only the top five of nine symmetric layers are presented for each termination.

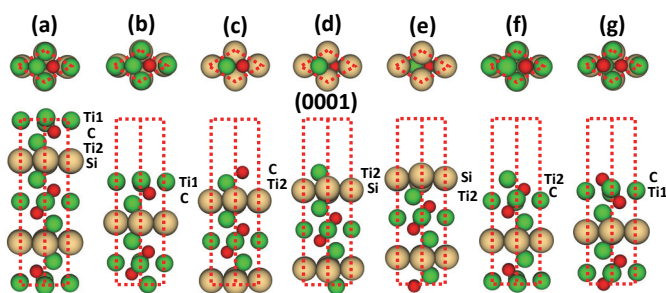


Fig. 13. Top (upper part) and side (lower part) view of Ti_3SiC_2 : (a) bulk, (b) Ti1(C), (c) C(Ti2), (d) Ti2(Si), (e) Si(Ti2), (f) Ti2(C), and (g) C(Ti1) termination. Only the top nine layers of each symmetric slab are presented for each termination.

The $\text{Ti}_3\text{SiC}_2(0001)$ surface can be terminated with C, Si, any of two types of Ti (Ti1 and Ti2), or their combinations, yielding a total of six possible surface geometries. Figure 13(b)-(g) shows the six terminations: Ti1(C), C(Ti2), Ti2(Si), Si(Ti2), Ti2(C), and C(Ti1), where the letter in the brackets denotes sub-surface atom. The surface energies of Ti1(C) termination calculated using Eq. (6) is found to converge well to 0.84 J/m² by a 13-layer-thick slab. Further, interlayer relaxations also show a good convergence for slabs having 13 layers or more. Contrast to the small relaxation presented in the SiC(0001), here there is a larger interlayer relaxation, especially for the first layer, which attenuates rapidly within two

surface layers. Lastly, we also calculated the surface energies of the remaining terminations in Fig. 13(c)-(g) to be 4.10, 0.64, 1.12, 1.56 and 5.60 J/m², respectively. In summary, we have calculated the bulk and surface properties for SiC and Ti₃SiC₂ and shown that these values are consistent with existing experimental and theoretical data, thereby offering not only detailed information but also a verification of applicability of the method and model for further interface investigation.

3.1.3 Interface construction and calculation process

A total of 96 possible candidate interface models have been considered within the above orientation relations, including four SiC terminations (Fig. 12(b)-(e)), six Ti₃SiC₂ terminations (Figs. 13(b)-(g)), and four different stacking sequences for each combination of SiC and Ti₃SiC₂ terminations. In the four stacking sequences, the interfacial Ti (C or Si) of Ti₃SiC₂ are located (i) on top (OT) of the surface atoms of SiC, (ii) at the center of the rhombic (RC) unit cell, (iii) above second-layer (SL) atoms of SiC, and (iv) above hollow sites (HS) of SiC, as shown in Fig. 14. These stacking sequences are of high symmetry and thus more likely to correspond to total-energy extrema. According to the surface calculations, our interface models are composed of a nine-layer symmetric SiC(0001) slab (bottom of Figs. 12(b)-(e)) connected to a symmetric Ti₃SiC₂(0001) slab (top of Fig. 13(b)-(g)) of at least 13 atomic layers. A 10 Å area of vacuum was added so as to minimize the coupling perpendicular to the interface. To form coherent interfaces, in-plane lattice constants of the Ti₃SiC₂ slab are expanded by 0.63% to match those of the harder SiC slab, while out-of-plane ones are fixed to their GGA optimized bulk values. Two steps were adopted to estimate W_{ad} . First, total energies were calculated for various separations as two slabs were brought increasingly closer from a large initial separation. As a consequence, the total energy is found to behave like a parabola, passing through a minimum at the equilibrium separation. The unrelaxed W_{ad} was obtained by computing the energy difference between the interface at equilibrium separation and the unrelaxed isolated slabs. Next, full relaxation of each isolated slab and interface slab was allowed, which yielded an estimate of relaxed W_{ad} .

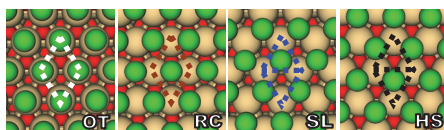


Fig. 14. Schematic plots of four different stacking sequences. Only the Ti layer of Ti₃SiC₂ proximal to the interface is presented for clarity. The smallest red spheres, intermediate green spheres, and largest golden spheres represent C, Ti, and Si atoms, respectively. The dotted parallelogram outlines the SiC rhombic unit cell projected along the [0001] direction.

3.1.4 Determination of interface atomic structure

To clarify the mechanism theoretically, we first determined atomic structure of SiC/Ti₃SiC₂ interface via complementing the acquired HAADF image (Fig. 9). In light of bulk structures of 4H-SiC and Ti₃SiC₂, the aforementioned orientation relations, and the relative stacking order of Ti and Si, the observed image in Fig. 9 can be intuitively fitted by two models among all the 96 candidates: SiSi and SiCSi model (Fig. 15). In the SiSi model, the interfacial Si atoms of Ti₃SiC₂ sit above the hollow sites of interfacial Si plane of SiC, where the optimal distance between interfacial Si-Si planes (denoted as d_1 in Fig. 15(a)) and that between

interfacial Si-Si atoms projected onto paper plane (denoted as $d2$ in Fig. 15(a)) are calculated to be 2.13 and 2.53 Å (Table I), respectively. These distances, however, deviate severely from their average experimental values, 2.5 and 2.8 Å, which are obtained by characterizing quantitatively the HAADF image (Fig. 9(a)). In addition, an examination of interface stability by calculating the W_{ad} indicates that the SiSi model is not favored at all (1.62 J/m²). It is even less stable than the model with interfacial Si of Ti₃SiC₂ resting straight atop the interfacial Si of SiC (2.58 J/m²), which contravenes again the observed image. Why does the less preferred interface predicted by our simulations emerge in experiments? It is worth noting that many other regions have been examined using the STEM but no other possibility is observed.

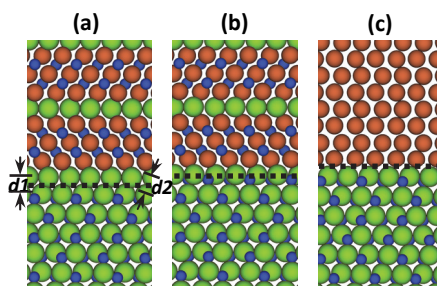


Fig. 15. Relaxed SiC(0001)/Ti₃SiC₂(0001) interface models (a) without interfacial C atoms (SiSi) and (b) with interfacial C atoms (SiCSi). (c) Optimized SiC(0001)/Ti(0001) interface model. The distance between interfacial Si-Si layers (Si-Ti layers for (c)) is represented by $d1$ and that between interfacial Si-Si atoms (Si-Ti atoms for (c)) projected onto the paper plane by $d2$. The interfaces are represented by dotted lines.

Could these pronounced discrepancies between results of experiment and calculation be ascribed to computational inaccuracies? Since the calculation parameters described above are verified to be sufficient to ensure a total energy precision of better than 1 meV/atom, one might be concerned that another numerical inaccuracy arises from size effect of the used slabs. However, we found this inaccuracy to be within 0.1 J/m² via enlarging the slabs along the interface, so that it does not affect our simulated W_{ad} . In addition, convergence tests show that the used slab thickness yields surface energy convergence to smaller than 0.02 J/m². Furthermore, the used GGA functional was tested to evaluate bulk lattice constants and distances between atoms within an error of less than 0.5%. Finally, there is a small lattice mismatch of 0.63% at interface, which can be damped out by structural optimization. Moreover, Wang et al. have reported that a lattice mismatch as large as 3.9% at an interface varies the W_{ad} only by less than 5% (Wang et al., 2002). Therefore, it seems that the discrepancies should not simply be attributed to the computational error.

To resolve these paradoxes, we noticed that a possibility might be ignored, that is, the unseen C might be trapped at interface, altering the local environment there. To test this hypothesis, the other SiCSi model was established by introducing C into the interfacial layer from the consideration of crystal extension and stacking sequences. The calculated W_{ad} of this SiCSi model is listed in Table I, where the interface is strengthened substantially after the incorporation of C. Investigation into its fully optimized atomic configuration (Fig. 15(b)) reveals that the incorporation of C does not induce significant interface reconstruction. Namely, the two Si layers proximal to the interface maintain the stacking

seen in Fig. 15(a), thus matching the HAADF image geometrically. Quantitatively, the $d1$ and $d2$ distances are now 2.53 Å and 2.81 Å (see Table I), respectively, very close to the obtained experimental values. Therefore, the introduction of interfacial C monolayer resolves the inconsistencies between simulations and experiments. Finally, we superimpose the calculation-inferred atomic structure of SiCSi interface (Fig. 15(b)) onto the HAADF image (Fig. 9(a)) and find that they match very well.

	SiSi	SiCSi	SiTi
W_{ad} (J/m ²)	1.62	6.81	2.06
$d1$ (Å)	2.13	2.31	2.36
$d2$ (Å)	2.53	2.81	2.97
SBH (eV)	1.05	0.60	1.10

Table 1. Relaxed W_{ad} (J/m²), optimal interfacial distances $d1$ and $d2$ (Å), and calculated p -type Schottky barrier heights (SBH) (eV) for the SiC/Ti₃SiC₂ interfaces without (SiSi) and with interfacial C (SiCSi), and for the SiC/Ti interface (SiTi). Refer to Fig. 15 for their schematic configurations

3.1.5 Schottky barrier height

To further examine whether the determined interface has a less Schottky character, we calculated p -type Schottky barrier height (SBH), an important quantity in analyzing electric properties of a metal/semiconductor contact interface. The p -type SBH is calculated from the difference between the E_F of interface supercell and the valence-band top of bulk SiC region. It should be noted that due to the well-known problem of discontinuity in the exchange-correlation potential across heterointerface, an exact quantitative estimation of SBH is unlikely. However, the qualitative comparisons between the calculated SBHs for different interface configurations should be reliable. The p -type SBHs for the SiC/Ti₃SiC₂ interfaces with and without interfacial C are listed in Table I, where the SBH for the SiTi interface (Fig. 15(c)) is listed as well for comparison. From this Table, one can see that the SiCSi interface shows the lowest SBH, meaning that it is of the least Schottky nature.

3.1.6 Electronic structure and chemical bonding

To shed light on origin of decrease in SBH and junction strengthening in the SiCSi interface, several analytic approaches were applied to characterize in detail interfacial electronic states and bonding nature. First, we calculated planar-averaged charge density and its difference along the interface normal. The density difference is evaluated by subtracting the sum of charge density of isolated SiC and Ti₃SiC₂ slabs from the total interface charge density. As seen in Fig. 16(a), after introducing the C, an interfacial Si-C pair is generated in the SiCSi case in a way similar to the pair in bulk SiC. As a result of the formation of the pair, there is a dramatic accumulation of charge within the interfacial region, in contrast to what is seen in either the SiSi or SiTi interface (Fig. 16(a)). This indicates that the covalent bonding is strengthened for the SiCSi. Evidently, the large degree of charge accumulation at interface is at the expense of depletion of charge in the sub-interfacial layers between Si and Ti, suggestive of weakened bonding between them. This is a short-range effect, however, since the charge density returns to its bulk value by the second layer. From Fig. 16(b), we note that the planar-averaged density difference for the SiCSi most prominently deviates from zero around the interface, reflecting the most significant charge transfer between SiC and Ti₃SiC₂ slabs. In addition, charge is

observed to be depleted noticeably in both the sub-interfacial SiC and Ti_3SiC_2 region for the SiCSi, suggesting that the atoms second nearest to the interface contribute to the interfacial bonding. These missing charges, to a large extent, make their way onto the more electronegative C ions, indicative of formation of ionic bonding.

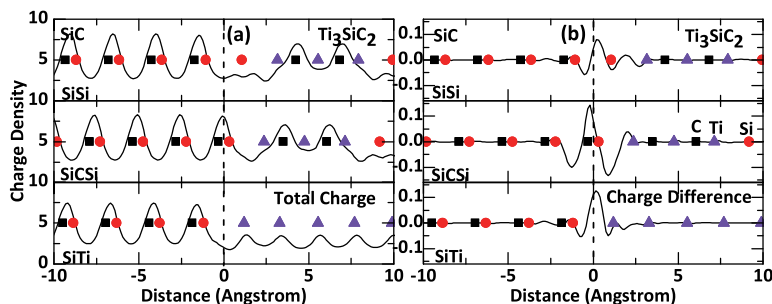


Fig. 16. Planar-averaged (a) total charge density and (b) charge-density difference for the relaxed SiSi, SiCSi, and SiTi interfaces along [0001] direction. The solid rectangles, circles, and triangles give the locations of C, Si, and Ti atoms, respectively. The interface position is set to zero and indicated by a vertical line

Figure 17 presents DOS projected on selected atomic layers of the SiCSi interface in order to gain insight into electronic states. Overall PDOS shape of interfacial Si of Ti_3SiC_2 resembles to some extent that of a Si layer deeper in SiC but deviates remarkably from that of a Si layer deeper in Ti_3SiC_2 (7th layer), which can be reflected from the formation of Si-C pair. Moreover, this suggests that the substrate has a fundamental effect on the interface electronically. A key feature in this figure is that a strong interaction is observed between the sub-interfacial Ti *d* and Si *p* states below E_F , which continues well into the SiC surface, inducing noticeable gap states in the interfacial C at E_F . This means that the interfacial C layer, the first monolayer on the substrate, is metallized, indicative of possible electric conductivity. In fact, the gap states can extend as far as they can into deeper layers of SiC, as there appear weak but visible peaks at E_F in the PDOSs of the 2nd and 3rd layers of SiC. Consequently, a local weak metallicity might occur in top few layers of the semiconductor surface, which could enable current flow through the SiC. Apart from the peaks in SiC, all of the Ti_3SiC_2 layers exhibit notable peaks at E_F , which can be attributed to the large degree of overlap between Ti *d* and C (Si) *p* states. Finally, we note significant hybridization between the interfacial C *sp* and Si *sp* states, suggestive of covalent bonding at interface.

To identify the bonding type directly, we further show contour plots of charge densities (Fig. 18) and their differences (Fig. 19) along the (11-20) plane for the optimized SiSi, SiCSi and SiTi interfaces. From Fig. 18, we notice first that the bonding interaction between the interfacial Si and C for the SiCSi interface is remarkably similar to the Si-C interaction deeper into SiC: the majority of charge is localized on C with humps directed towards their adjacent Si. We thus conclude that the interfacial bonding for the SiCSi is of mixed covalent-ionic nature. The interfacial bonds for the SiSi interface, however, exhibit covalent character with a small amount of charge accumulated within the interfacial region (Fig. 18(a)), in consistence with our analyses on planar-averaged density-difference (Fig. 16). As for the SiTi, the charge distribution of interfacial Ti is almost identical to that of Ti away from interface, having a character of weakly but broadly distributed charge density. This indicates that the interfacial bonds for the SiTi take on weakly metallic nature, yet maintain a small degree of covalency. The covalency can be

further confirmed from the density-difference plot (Fig. 19(c)) displaying charge accumulation along the interfacial Si-Ti bonds. The amount of charge accumulated on the Si-Ti bonds is larger than that on the interfacial Si-Si bonds of SiSi (Fig. 19(a)) but far less significant than that on the interfacial Si-C bonds of SiCSi (Fig. 19(b)). This heaviest charge accumulation along the interfacial Si-C bonds, together with the mixed covalent-ionic character at the SiCSi interface, explains the largest W_{ad} associated with the SiCSi interface (Table I). Finally, we note from both figures that charge variations due to the interface are screened rapidly with distance from interface, suggesting that the interface effect is confined to within a short range, in agreement with the previous analyses on PDOS and planar-averaged charge.

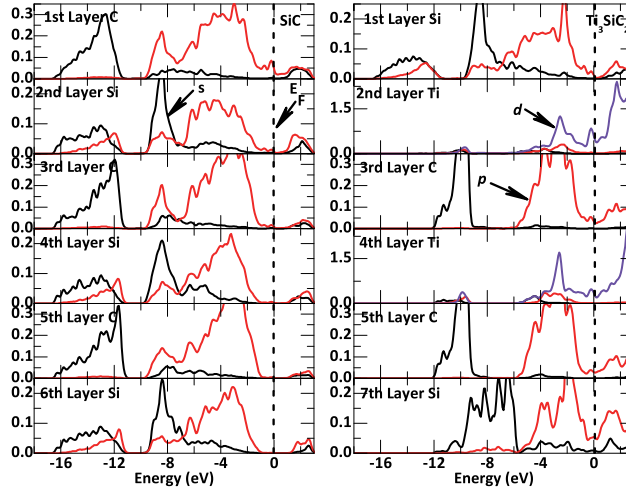


Fig. 17. PDOS (states/eV atom) projected on the atomic layers close to the relaxed SiCSi interface. The left panel shows PDOSs of SiC layers and the right one those of Ti_3SiC_2 layers. The first layer is the atomic layer proximal to interface. The E_F is set to zero.

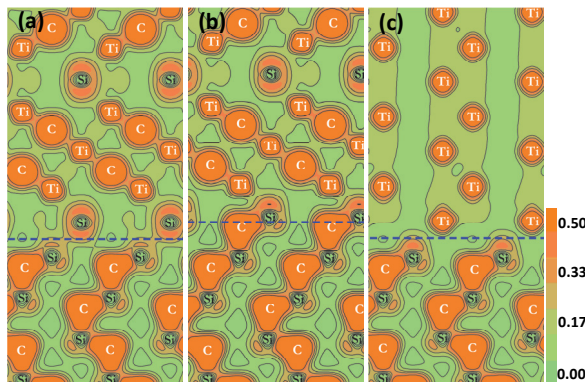


Fig. 18. Contour plots of charge densities for (a) SiSi, (b) SiCSi, and (c) SiTi interfaces taken along the (11-20) plane. The interface is represented by a horizontal line and the atoms that intersect the contour plane are labeled.

To further explain the decrease in SBH for the SiCSi, we plotted the variation of electrostatic potential along the interface normal in Fig. 20, where potential changes for the SiSi and SiTi interfaces are shown as well. As a result of the large interface dipole generated by the considerable charge transfer (Fig. 16(b)) and the partial ionicity (Fig. 18(b)), the electrostatic potential of interfacial Si in the SiCSi is lowered significantly relative to its adjacent SiC region (Fig. 20(b)), which consequently enables the reduction of SBH. This is contrary to the SiSi (Fig. 20(a)) and SiTi (Fig. 20(c)) cases, as their electrostatic potentials are high at interface. These high potentials indicate that electrons might be transferred from the SiC surface to the interface, resulting in electron depletion on substrate surface. Moreover, we note in Fig. 20 that electrostatic potential for Si atoms is always lower than that for the Ti or C atoms, which explains the lower electron density of Si shown in the charge-distribution plot (Fig. 18).

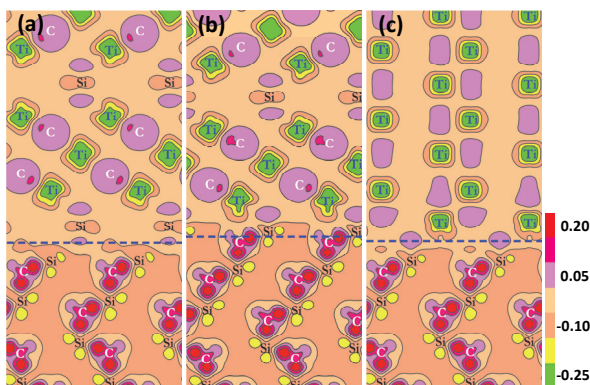


Fig. 19. Contour plots of charge-density differences for (a) SiSi, (b) SiCSi, and (c) SiTi interfaces taken along the (11-20) plane. The difference of charge density presents redistribution of charge in the interface relative to its isolated system.

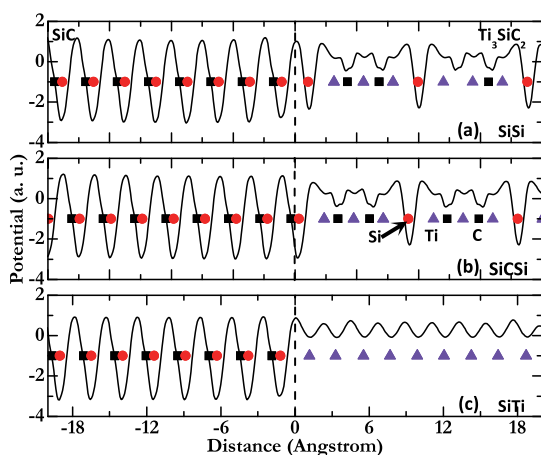


Fig. 20. Electrostatic potential as a function of distance from interface along the [0001] direction for (a) SiSi, (b) SiCSi, and (c) SiTi interfaces. Interface position is set to zero.

3.1.7 Electron density near fermi level

Although the charge-distribution analysis can reveal valuable information on interfacial bonding, it provides restrained insight into how electrons distribute around E_F , which matters because density around E_F directly determines the current transmission. Figure 21 illustrates an electron-density isosurface and its slice along the (11-20) plane for the optimized SiCSi interface around E_F . From Fig. 21(a), one can see that charges surrounding interfacial Si are connected and broadly distributed in a sheet-like fashion, which suggests a possible electrical conductivity through this region. In addition, there also appear heavily accumulated electrons within the interfacial area, which are connected along the interface and extended as far as several atomic layers into the SiC. These characters can also be confirmed from the slice plot in Fig. 21(b), meaning that current might flow over the top few atomic layers of semiconductor, thereby causing Ohmic property. As expected, the electron density at E_F is extremely high for the Ti_3SiC_2 (i.e., sea of electrons) but becomes nil for the SiC layers away from interface (Fig. 21(b)), which can be understood from their intrinsic metallic and semiconducting nature.

3.1.8 Quantum electron transport property

To examine electrical conductivity and gain insight into how the interface influences current transport, we devised a two-probe system, $\text{Ti}/\text{Ti}_3\text{SiC}_2/\text{SiC}/\text{Ti}_3\text{SiC}_2/\text{Ti}$, and investigated nonequilibrium quantum transport properties. Figure 22(a) schematically shows a model of the sandwich transport system, which can be divided into a left semi-infinite electrode, a scattering region, and a right semi-infinite electrode. The scattering region consists of hexagonal SiC and Ti_3SiC_2 layers and the periodic boundary conditions are imposed along the directions parallel to the interface. The SiC/ Ti_3SiC_2 interface could be either the SiSi or SiCSi, whereas other interfaces are maintained identical for the sandwich systems. In this sense, the difference between the two systems can be mainly attributed to their differing SiC/ Ti_3SiC_2 interfaces. Furthermore, we also calculated the $\text{Ti}/\text{SiC}/\text{Ti}$ system, wherein the SiTi model shown in Fig. 15(c) was taken as the SiC/Ti interface.

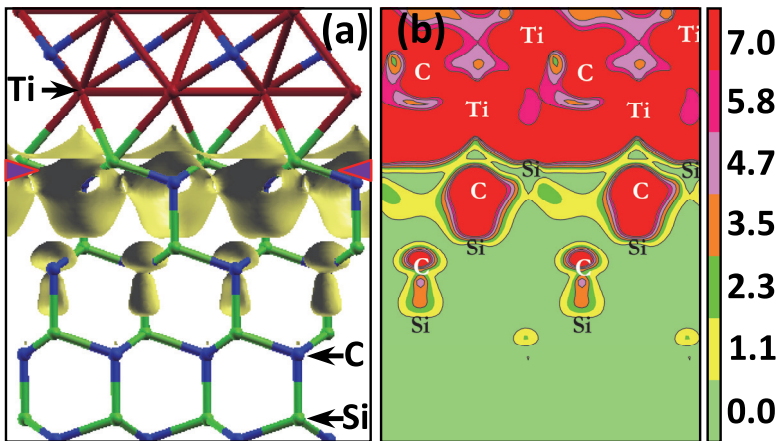


Fig. 21. Isosurface and (b) electron density plot along the (11-20) plane in the energy window ($E_F - 0.5 \text{ eV}$, E_F) for the SiCSi interface. The interface is marked by two arrows.

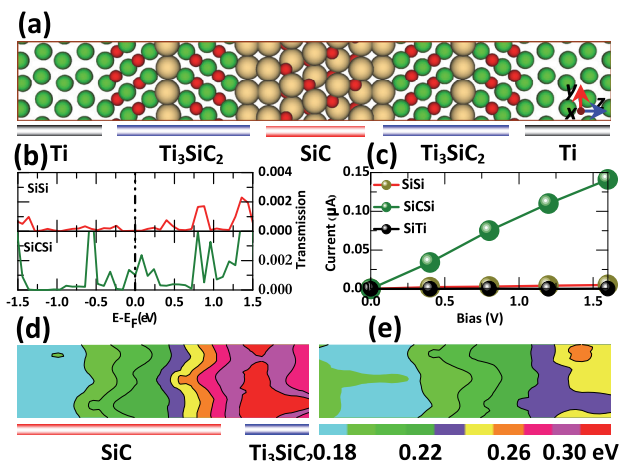


Fig. 22. Schematic plot of a two-probe Ti/Ti₃SiC₂/SiC/Ti₃SiC₂/Ti transport system. The system has infinite extent in the (x, y) directions and extends to $\pm \infty$ in the z direction. (b) Transmission spectra under 0 V and (c) I - V curves for the two relaxed systems including the SiSi and SiCSi interfaces. The I - V curve for the system including the SiTi interface is also shown for comparison. Difference in effective potential along the (11-20) plane under an applied bias voltage of 0.4 V for (d) SiSi and (e) SiCSi cases

Figure 22(b) shows transmission spectra for the relaxed SiSi, SiCSi, and SiTi systems, where one can see that the spectra differ from one another suggesting variations in electronic structures with interface geometries. The most interesting feature is the presence of transmission peaks at E_F for the SiCSi, which is attributable to the electrons distributed around the interface at E_F . Further calculations on electrical properties (e.g., I - V curve) for the three systems reveal that the current in the SiCSi case increases much faster than either the SiSi or SiTi case as the applied bias voltage increases (Fig. 22(b)), which can be explained by its lowest SBH (Table I). Finally, in comparing the general trend of the calculated I - V with that of the experimental curve (Fig. 1), we find that they agree qualitatively: both the annealed specimen and the SiCSi model clearly show Ohmic behavior, thereby validating the application of the SiCSi model to describe the Ohmic contacts in the TiAl-based system. Finally, we examined how applied bias voltages vary from the interface to the SiC region. Figure 22(d) and (e) illustrate the difference in effective potential along the (11-20) plane between the bias voltage of 0.4 V and the one of 0.0 V for the two relaxed systems including SiSi and SiCSi. One can see that the voltage drops less intensively from interface to SiC in the SiCSi case, suggestive of a less Schottky nature.

4. Discussion and conclusion

The current understanding of formation origin of Ohmic contact, which is based mainly on experimental studies of property measurement and structure characterization, can be summarized in three main points: (1) the deposited Al (80 at%) might diffuse in part into the SiC and dope heavily the semiconductor because Al is well-known to act as a p -type dopant for SiC, (2) the high density of pits, spikes, or dislocations may be generated underneath the contacts after annealing so that current can transport primarily through these defects due to

the possible enhancement of electric field at these features and semiconductor doping at these locations, (3) formation of intermediate semiconductor layer between the deposited metals and semiconductor, which consists of silicides or carbides, could divide the high barrier height into lower ones, thus reducing the effective barrier height.

The findings presented first demonstrate that no Al is clearly segregated around the interfacial region, in particular at the top few layers of SiC, which rules out the possibility of additional Al doping. Though a small amount of residual Al is found to be present, mostly in a form of Al_4C_3 compound, it may locate on the surface of annealed contacts rather than in the layer directly contacted to the SiC, thus playing a negligible role in Ohmic contact formation. The majority of deposited Al is evaporated during annealing because of its low melting point and high equilibrium vapor pressure. The dominant role played by Al in the TiAl system is to assist the formation of liquid alloy so as to facilitate chemical reaction. Furthermore, careful characterization of the interfacial region reveals that the substrate and the generated compound are epitaxially oriented and well matched at interface with no clear evidence of high density of defects. This suggests that the morphology might not be the key to understanding the contact formation. In support of this speculation, it has been observed previously that Ti Ohmic contacts can be possibly generated without any pitting and that pit-free Ohmic contacts can be fabricated.

One remaining theory is the alloy-assisted Ohmic contact formation. This alloy is determined to be ternary Ti_3SiC_2 , which has also been corroborated by other experiments. Since the bulk Ti_3SiC_2 has already been found to be of metallic nature both in experiment and theory, the contact between Ti_3SiC_2 and its covered metals should show Ohmic character and thus the SiC/ Ti_3SiC_2 interface should play a significant role in Ohmic contact formation. This idea is supported by the fact that the determined interface has a lowered SBH due to the large dipole shift at interface induced by the partial ionicity and the considerable charge transfer. In addition, the interfacial states, as indicated by the electron distribution at E_F , are also viewed as a contributing factor in reducing the SBH. These states might be further enhanced by the possible presence of point defects at interface, although these structural defects have not been detected by the TEM study.

The calculations predict that an atomic layer of carbon emerges as the first monolayer of Ohmic contacts, which eventually affects interface electronic structure. Such trapped carbon was previously studied in both other interfacial systems theoretically by DFT and the TiNi Ohmic contacts on 4H-SiC experimentally by Auger electron spectroscopy (Ohyanagi et al., 2008). It was proposed that the carbon could be segregated to interfacial area, strengthening interface substantially and reducing Schottky barrier dramatically. Further, it was reported that the Ohmic contact can be realized by depositing carbon films only onto the SiC substrate, indicative of the determinative role of carbon in the Ohmic contact formation (Lu et al., 2003). The important role played by carbon can be traced to the two interfacial Si layers, which provide possible sites for carbon segregation due to the strong Si-C interaction. Finally, recent observation shows that atomic-scale Ti_3SiC_2 -like bilayer can be embedded in the SiC interior, forming an atomically ordered multilayer that exhibits an unexpected electronic state with the point Fermi surface. The valence charge is found to be confined largely within the bilayer in a spatially connected way, which serves as a possible conducting channel to enhance the current flow over the semiconductor.

Several experimental methods can be used to probe the Ohmic character of Ti_3SiC_2 contacts on SiC discussed in this chapter. For example, based on the results regarding morphology of grown layers, epitaxial Ti_3SiC_2 layers can be deposited directly onto the SiC substrate by

means of sputtering, molecular beam epitaxy (MBE), or pulsed-laser deposition (PLD). In particular, the crucial effect of interfacial carbon can be possibly examined using the MBE and PLD techniques, which allow a layer-by-layer deposition of crystalline thin films. If the outcome of such investigations is positive for Ohmic contact formation, direct deposition of epitaxial Ti_3SiC_2 thin films rather than the metals would be a potential processing technique for easier realization of ordered structure and better control of Ohmic property.

To summarize, we have determined in this chapter atomic-scale structure of Ohmic contacts on SiC and related it to electronic structure and electric property, aimed at understanding the formation mechanism of Ohmic contact in TiAl-based system. The combined HAADF-DFT study represents an important advance in relating structures to device properties at an atomic scale and is not limited to the contacts in SiC electronics. Our results show that the main product generated by chemical reaction can be epitaxial and have atomic bonds to the substrate. The contact interface, which could trap an atomic layer of carbon, enables lowered Schottky barrier due to the large interfacial dipole shift associated with the considerable charge transfer. These findings are relevant for technological improvement of contacts in SiC devices, and this chapter presents an important step towards addressing the current contact issues in wide-band-gap electronics.

5. Acknowledgment

We thank S. Watanabe (Univ. of Tokyo) for allowing our use of computational resources. The present study was supported in part by a Grant-in-Aid for Scientific Research on Priority Area, "Atomic Scale Modification (474)" from the Ministry of Education, Culture, Sports, Science, and Technology of Japan. Z. W acknowledges financial supports from the Grant-in-Aid for Young Scientists (B) (Grant No. 22760500), the IKETANI Science and Technology Foundation (Grant No. 0221047-A), and the IZUMI Science and Technology Foundation. S. T. thanks the supports from Nippon Sheet Glass Foundation and the MURATA Science Foundation. The calculations were carried out on a parallel SR11000 supercomputer at the Institute for Solid State Physics, Univ. of Tokyo.

6. References

- Chang, S. C.; Wang, S. J.; Uang, K. M. & Liou, B. W. (2005). Investigation of Au/Ti/Al Ohmic Contact to N-type 4H-SiC, *Solid State Electronics*, Vol.49, No.12, (December 2005), pp. 1937-1941, ISSN 0038-1101
- Ching, W. Y.; Xu, Y. N.; Rulis, P. & Ouyang, L. Z. (2006). The Electronic Structure and Spectroscopic Properties of 3C, 2H, 4H, 6H, 15R and 21R Polymorphs of SiC, *Materials Science and Engineering A*, Vol.422, No.1-2, (April 2006), pp. 147-156, ISSN 0921-5093
- Gao, M.; Tsukimoto, S.; Goss, S. H.; Tumakha, S. P.; Onishi, T.; Murakami, M. & Brillson, L. J. (2007). Role of Interface Layers and Localized States in TiAl-Based Ohmic Contacts to p-Type 4H-SiC, *Journal of Electronic Materials*, Vol.36, No.4, (April 2007), pp. 277-284, ISSN 0361-5235
- Harries, G. L. (1995). *Silicon Carbide*, INSPEC, ISBN 0-85296-870-1, London, United Kingdom

- Johnson, B. J. & Capano, M. A. (2004). Mechanism of Ohmic Behavior of Al/Ti Contacts to p-type 4H-SiC After Annealing, *Journal of Applied physics*, Vol.95, No.10, (May 2004), pp. 5616-5620, ISSN 0021-8979
- Käckell, P.; Wenzien, B. & Bechstedt, F. (1994). Electronic Properties of Cubic and Hexagonal SiC Polytypes from ab initio Calculations, *Physical Review B*, Vol.50, No.15, (October 1994), pp. 10761-10768, ISSN 1098-0121
- Kresse, G. & Hafner, J. (1993). Ab initio Molecular Dynamics for Liquid Metals, *Physical Review B*, Vol.47, No.1, (January 1993), pp. 558-561, ISSN 1098-0121
- Lu, W.; Mitchel, W. C.; Thornton, C. A.; Collins, W. E.; Landis, G. R. & Smith, S. R. (2003), Ohmic Contact Behavior of Carbon Films on SiC, *Journal of The Electrochemical Society*, Vol.153, No.3, (January 2003), pp. G177-G182, ISSN 0013-4651
- Mohney, S. E.; Hull, B. A.; Lin, J. Y. & Crofton, J. (2002). Morphological study of the Al-Ti Ohmic Contact to p-type SiC, *Solid State Electronics*, Vol.46, No.5, (May 2002), pp. 689-693, ISSN 0038-1101
- Morkoc, H.; Strite, S.; Gao, G. B.; Lin, M. E.; Sverdlov, B. & Burns, M. (1994). Large-band-gap SiC, III-V Nitride, and II-VI ZnSe-based Semiconductor Device Technologies, *Journal of Applied physics*, Vol.76, No.3, (August 1994), pp. 1363-1398, ISSN 0021-8979
- Nakatsuka, O.; Takei, T.; Koide, Y. & Murakami, M. (2002). Low Resistance TiAl Ohmic Contacts with Multi-Layered Structure for p-Type 4H-SiC, *Materials Transactions*, Vol.43, No.7, (July 2002), pp. 1684-1688, ISSN 1345-9678
- Nellist, P. D.; Chisholm, M. F.; Dellby, N.; Krivanek, O. L.; Murfitt, M. F.; Szilagyi, Z. S.; Lupini, A. R.; Borisevich, A.; Sides, Jr. W. H. & Pennycook, S. J. (2004). Direct Sub-Angstrom Imaging of a Crystal Lattice, *Science*, Vol.305, No.5691, (September 2004), pp. 1741, ISSN 0036-8075
- Ohyanagi, T.; Onose, Y. & Watanabe, A. (2008). Ti/Ni Bilayer Ohmic Contact on 4H-SiC, *Journal of Vacuum Science and Technology B*, Vol.26, No.4, (August 2008), pp. 1395-1362, ISSN 1071-1023
- Pennycook, S. J. & Boatner L. A. (1988). Chemically Sensitive Structure-Imaging with a Scanning Transmission Electron Microscope, *Nature*, Vol.336, No.6199, (December 1988), pp. 565-567, ISSN 0028-0836
- Perez-Wurfl, I.; Krutsinger, R.; Torvik, J. T. & Van Zeghbroeck, B. (2003). 4H-SiC Bipolar Junction Transistor with High Current and Power Density, *Solid State Electronics*, Vol.47, No.2, (February 2003), pp. 229-231, ISSN 0038-1101
- Tanimoto, S.; Kiritani, N.; Hoshi, M. & Okushi, H. (2002). Ohmic Contact Structure and Fabrication Process Applicable to Practical SiC Devices, *Materials Science Forum*, Vol.389-393, No.2, (January 2002), pp. 879-884, ISSN 0255-5476
- Tsukimoto, S.; Nitta, K.; Sakai, T.; Moriyama, M. & Murakami, M. (2004). Correlation Between the Electrical Properties and the Interfacial Microstructures of TiAl-Based Ohmic Contacts to p-type 4H-SiC, *Journal of Electronic Materials*, Vol.33, No.5, (May 2004), pp. 460-466, ISSN 0361-5235
- Viala, J. C.; Peillon, N.; Bosselet, F. & Bouix, J. (1997). Phase Equilibria at 1000°C in the Al-C-Si-Ti Quaternary system: an Experimental Approach, *Materials Science and Engineering A*, Vol.229, No.1-2, (June 1997), pp. 95-113, ISSN 0921-5093

Wang, X. G.; Smith, J. R. & Evans, A. (2002), Fundamental Influence of C on Adhesion of the $\text{Al}_2\text{O}_3/\text{Al}$ Interface, *Physical Review Letters*, Vol.89, No.28, (December 2002), pp. 286102-1-4, ISSN 0031-9007

SiC-Based Composites Sintered with High Pressure Method

Piotr Klimczyk

Institute of Advanced Manufacturing Technology

Poland

1. Introduction

Silicon carbide-based materials usually have high hardness (2500 – 2800 HV) and thus have superior wear resistance. Nevertheless, the tribological performance of SiC is determined by many factors, such as the grain size of mated materials or the reactions in the presence of oxygen and humidity in the surrounding atmosphere. For example, in unlubricated sliding, wear resistance of SiC ceramics can be greater in air than in inert atmosphere owing to thin soft oxide films reducing friction and local surface pressure. (Gahr et al., 2001; Guicciardi et al., 2007). The friction and wear properties of SiC materials (both in dry and lubricating conditions) have been studied extensively because they are used in applications like bearings, cylinder liners and mechanical seals (Murthy et al., 2004).

Silicon carbide-based ceramics have high melting point (~2500 °C), high thermal conductivity (43 – 145 W/m·K – depending on a temperature and phase composition), low thermal expansion (~ $4.5 \times 10^{-6} \text{K}^{-1}$), and high temperature capability. Silicon carbide is a semiconductor which can be doped n-type by nitrogen or phosphorus and p-type by aluminium, boron, gallium or beryllium. Due to the combination of its thermal and electrical properties, SiC is applied in a resistance heating, flame igniters and electronic components. Relatively pure SiC has also an excellent corrosion resistance in the presence of hot acids and bases (Richerson, 2004).

Silicon carbide powder compacts are difficult to densify without additives because of the covalent nature of the Si-C bonds and the associated low self-diffusion coefficient. Therefore, Reaction Sintering (RS) in the presence of liquid silicon as well as Hot Isostatic Pressing (HIP) are frequently used to obtain a high quality, full dense SiC ceramics. Typical room temperature flexural strength of SiC-based materials is about 350-550 MPa. High-strength RS-SiC (over 1000 MPa in a 3-point bending test) was developed by controlling the residual Si size under 100 nm. (Magnani et al., 2000; Suyama et al., 2003). Silicon carbide ceramics have the ability to increase in strength with increase of temperature. It was reported that flexural strength of some kind of commercial SiC ceramic increase is from 413 MPa at the room temperature to around 580 MPa at 1800 °C (Richerson, 2004). For hot-pressed silicon carbide with addition of 0.15-1.0 wt% Al_2O_3 , the high-temperature strength has been improved from 200 MPa to 700 MPa by decreasing the grain boundary concentration of both Al and O at 1500 °C (Kinoshita et al., 1997).

A favorable combination of properties makes SiC materials suitable for many engineering applications, including parts of machines and devices exposed to the abrasion, the high temperature, the corrosive environment, etc. A major disadvantage of SiC ceramic materials is their low fracture toughness, which usually does not exceed about $3.5 \text{ MPa}\cdot\text{m}^{1/2}$ (Lee et al., 2007; Suyama et al., 2003). Low values of K_{Ic} coefficient exclude these materials from numerous applications with dynamic loads, e.g. in machining processes.

There are various ways to improve the fracture toughness of ceramic materials. One of them involves obtaining a composite material by the introduction of the additional phases in the form of nano-, micro- or sub-micro-sized particles to the base material. Some papers indicate that nanosized structures have great potential to essentially improve the mechanical performance of ceramic materials even at high temperatures (Awaji et al., 2002; Derby, 1998; Kim et al., 2006; Niihara et al., 1999). Depending on the type of introduced particles, composites can take advantage of different strengthening mechanisms, such as the crack deflection, crack bridging, crack branching, crack bowing, crack pinning, microcracking, thermal residual stress toughening, transformation toughening and synergism toughening. For example, metallic particles are capable of plastic deformation, thus absorption of energy and bridging of a growing crack, resulting in increased strengthening (Fig. 1a) (Yeomans, 2008). On the other hand, hard ceramic particles, like borides or nitrides, can introduce a favorable stress state which can cause a toughening effect by crack deflection and crack bifurcation (Fig. 1b) (Xu, 2005). An addition of metal borides such as ZrB_2 , TaB_2 , NbB_2 or TiB_2 , promote densification of SiC powder as well as improve hardness and other mechanical properties of the material as a whole (Tanaka et al., 2003).

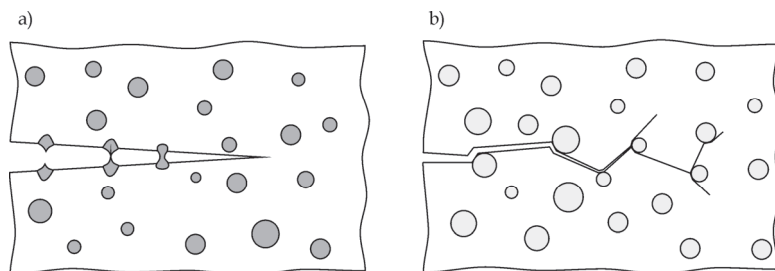


Fig. 1. Example of strengthening mechanisms which can occur in ceramic matrix composites with dispersed “soft” metallic or/and “hard” ceramic particles: a) crack bridging, b) crack deflection and crack bifurcation

The wide group of materials containing the silicon carbide are $\text{SiC}/\text{Si}_3\text{N}_4$ composites. In such materials predominant phase is silicon nitride, while SiC content does not usually exceed 30 vol.%. Silicon nitride has a lower hardness but a higher fracture toughness than silicon carbide. If SiC particles are uniformly dispersed in the Si_3N_4 ceramics, high strength can be obtained from room temperature to elevated temperature. It was reported that the strength of 1000 MPa at 1400°C is obtained in nano-composites having ultra-fine SiC particles added into the Si_3N_4 matrix. This improvement was mainly attributed to the suppression of a grain boundary sliding by intergranular SiC particles bonded directly with the Si_3N_4 grain in the atomic scale without any impurity phases (Hirano & Niihara, 1995; Yamada & Kamiya, 1999). $\text{SiC}/\text{Si}_3\text{N}_4$ composites have an ability to crack healing under high temperature and applied stress, to exhibit a significantly higher creep resistance and fracture

toughness compared to the monolithic materials. (Ando et al., 2002; Lojanová et al., 2010; Sajgalík et al., 2000; Takahashi et al., 2010).

The combination of the fair fracture toughness with high hardness, wear resistance and mechanical strength at elevated temperatures makes SiC/Si₃N₄ ceramics a promising material for cutting tools (Eblagon et al., 2007). Despite many studies on materials based on silicon carbide and silicon nitride, there is a lack of knowledge about the SiC/Si₃N₄ composites where the predominant phase is SiC. In the presented work, the materials contained from 0 to 100% of silicon carbide were investigated.

2. Description of experiment

The purpose of the presented experiment was to study the influence of High Pressure - High Temperature (HPHT) sintering on the phase composition, microstructure and selected properties of SiC/Si₃N₄ composites as well as to study the effect of the addition of third-phase particles selected from metals (Ti) or ceramics (TiB₂, cBN - cubic Boron Nitride) to the SiC - Si₃N₄ system. The main goal was to improve fracture toughness and wear resistance of the investigated materials.

The composites were manufactured and tested in two stages. The first stage consisted in sintering of materials having, in its initial composition, only SiC and/or Si₃N₄ powder(s). Samples sintered from nano-, sub-micro- and micropowders with various silicon carbide to silicon nitride ratios were investigated at this stage.

At the second stage the best SiC/Si₃N₄ composite manufactured at the first stage was subjected to modification, consisting of:

- use of various types of SiC and Si₃N₄ powders,
- addition of metallic phase in the form of Ti particles,
- addition of boride (TiB₂) phase,
- addition of superhard (cBN) phase.

All materials were sintered with the HPHT method. The parameters of sintering: time and temperature were chosen individually for each composition. The obtained samples were subjected to a series of studies, which included: phase composition and crystallite size analysis by X-ray diffraction, measurements of density by hydrostatic method and Young's modulus by the ultrasonic method, measurement of hardness and fracture toughness using Vickers indentation as well as studies of tribological properties using the Ball-On-Disk method.

2.1 HPHT method of sintering

Pressure is a versatile tool in solid state physics, materials engineering and geological sciences. Under the influence of high pressure and temperature there are a lot of changes in physical, chemical and structural properties of materials (Eremets, 1996). It gives a possibility to generate of new, non-existent in nature phases, or phases which occur only in inaccessible places, such as the earth core (Manghnani et al., 1980). The use of pressure as a parameter in the study of materials was pioneered principally by Professor P. W. Bridgman, who for forty years investigated most of the elements and many other materials using diverse techniques (Bridgman, 1964). There are many design solutions to ensure High Pressure - High Temperature (HPHT) conditions for obtaining and examination of materials. Depending on the design assumptions, it is possible to achieve very high pressures, up to several hundred gigapascals, as in the case of Diamond Anvils Cell (DAC).

Such devices, due to their small size, are intended solely for laboratory investigations (XRD in-situ study, neutron diffraction etc.) (Piermarini, 2008). For the purposes of industrial and semi-industrial production of materials the most frequently the “Belt” or “Bridgman” type of equipment is used (Eremets, 1996; Hall, 1960; Khvostantsev et al., 2004). These apparatuses provide a relatively large working volume, the optimum pressure distribution and the possibility of achieving high temperatures.

In the toroidal type of Bridgman apparatus the quasi-hydrostatic compression of the material is achieved as a result of plastic deformation of the so called “gasket” (Fig. 2).

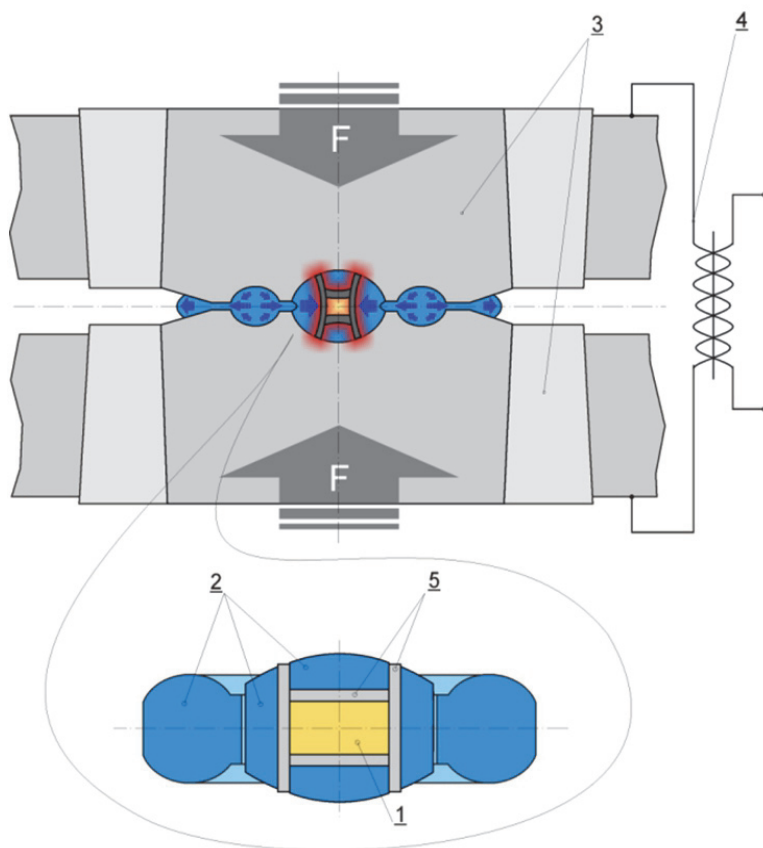


Fig. 2. Sintering process in a Bridgman-type HPHT system. Quasi-hydrostatic compression of the preliminary consolidated powders (sample - 1) is achieved as a result of plastic deformation of the gasket material (2) between anvils (3); electrical heating is provided by a high-power transformer (4) and graphite resistive heater (5)

Gaskets are made of special kinds of metamorphic rocks such as pyrophyllite, “lithographic stone” or catlinite (Filonenko & Zibrov, 2001; Prikhna, 2008). The toroidal chamber, depending on its volume (usually from 0.3 to 1 cm³), can generate pressures up to 12 GPa and temperature up to ~2500 °C. The presented system is used often for production of

synthetic diamonds and for sintering of wide range of superhard composites based on polycrystalline diamond (PCD) or polycrystalline cubic boron nitride (PcBN). Under the influence of a simultaneous action of pressure and temperature the sintering process occurs much faster than in the case of free sintering. A typical duration of sintering process with HPHT method is about 0.5 – 2 minutes (Fig. 3) while the free sintering requires several hours. Short duration of the process contributes to the grain growth limitation, which is essential in the case of sintering of nanopowders. The materials obtained with HPHT method are characterized by almost a 100% level of densification, isotropy of properties and sometimes by a completely different phase composition in relation to the same free-sintered materials, due to the different thermodynamic conditions of the manufacturing process.

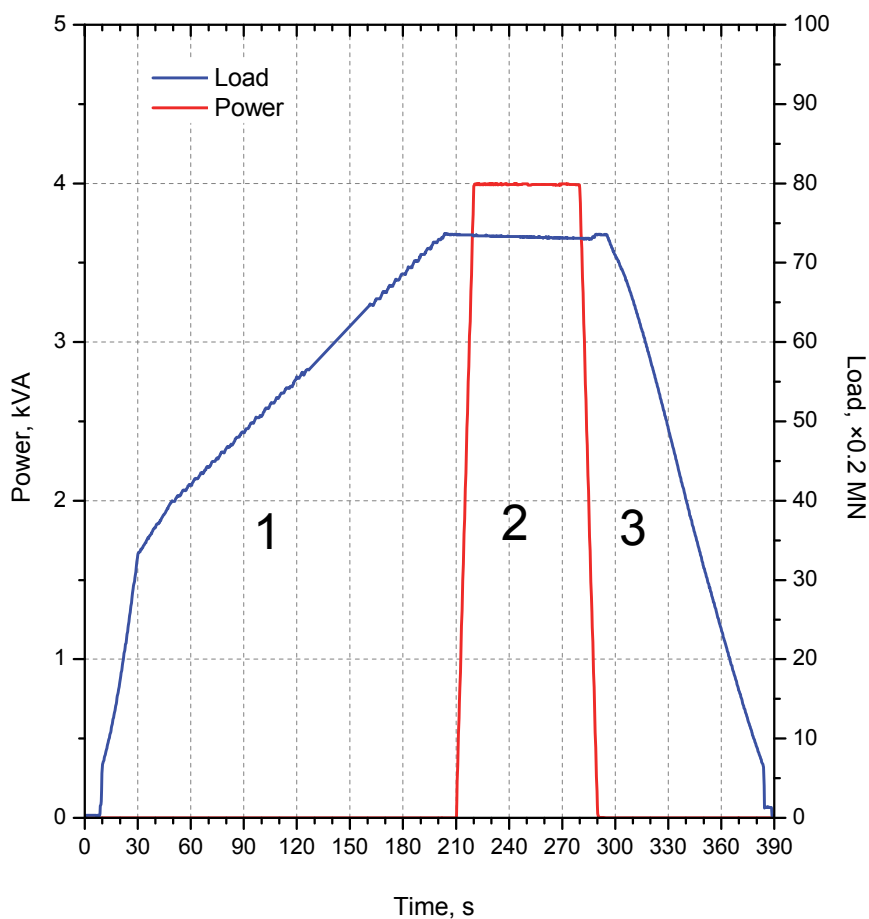


Fig. 3. Three stages of an example process of HPHT sintering: 1 - loading, 2 - sintering, 3 - unloading

2.2 Samples preparation

Powders used for the preparation of mixtures for sintering of SiC/Si₃N₄ materials are listed in Table 1.

Powder	Category	Particle size [μm]	Manufacturer	Description
SiC	nano	<5 nm	France	beta
SiC	sub-micro	0.1 – 1	Goodfellow, UK	alpha
SiC	micro	1.2	AGH, Poland	
Si ₃ N ₄	nano	<20nm	Goodfellow, UK	amorphous
Si ₃ N ₄	sub-micro	0.1 – 0.8	Goodfellow, UK	alpha
Si ₃ N ₄	sub-micro	0.6	H.C. Starck, Germany	alpha>90%, M11-grade
Si ₃ N ₄	micro	1 – 5	AEE, USA	alpha>85%
TiH ₂	micro	<44	Fluka, Switzerland	
TiB ₂	micro	2.5 – 3.5	H.C. Starck, Germany	F-grade
cBN	nano	0 – 0.1	Element6, South Africa	Micron+ABN, M0.10-grade
cBN	micro	3 – 6	Element6, South Africa	Micron+ABN, M36-grade

Table 1. Powders used for preparation of mixtures for sintering of SiC/Si₃N₄ materials

The following mixtures were prepared by mixing the appropriate powders (Table. 1) in an isopropanol environment using the Fritsch Pulverisette 6 planetary mill.

nano-SiC/Si₃N₄ materials

100 % SiC(nano)

100 % Si₃N₄(nano)

50 SiC(nano)/50 Si₃N₄(nano) – vol. %

sub-micro-SiC/Si₃N₄ materials

95 SiC(sub-micro)/5 Si₃N₄(sub-micro, Starck) – vol. %

70 SiC(sub-micro)/30 Si₃N₄(sub-micro, Starck) – vol. %

50 SiC(sub-micro)/50 Si₃N₄(sub-micro, Starck) – vol. %

100 % Si₃N₄(sub-micro, Starck)

micro-SiC/Si₃N₄ materials

70 SiC(micro)/30 Si₃N₄(micro) – vol. %

100 % Si₃N₄(micro)

70SiC/30Si₃N₄ composite (modification by using various SiC and Si₃N₄ powders)

70 SiC(sub-micro)/30 Si₃N₄(sub-micro, Starck) – vol. %

70 SiC(sub-micro)/30 Si₃N₄(sub-micro, Goodfellow) – vol. %

70 SiC(micro)/30 Si₃N₄(micro) – vol. %

70 SiC(sub-micro)/30 Si₃N₄(micro) – vol. %

70SiC/30Si₃N₄ composite + Ti (modification by addition of the third, metallic phase)

70 SiC(sub-micro)/30 Si₃N₄(sub-micro, Starck) + 8 vol. % Ti - from TiH₂(micro)

70SiC/30Si₃N₄ composite + TiB₂ (modification by addition of the third, boride phase)

70 SiC(sub-micro)/30 Si₃N₄(sub-micro, Starck) + 8 vol. % TiB₂(micro)

70 SiC(sub-micro)/30 Si₃N₄(sub-micro, Starck) + 30 vol. % TiB₂(micro)

70SiC/30Si₃N₄ composite + cBN (modification by addition of the third, nitride phase)70 SiC(sub-micro)/30 Si₃N₄ (sub-micro, Starck) + 8 vol.% cBN(micro)70 SiC(sub-micro)/30 Si₃N₄ (sub-micro, Goodfellow) + 8 vol.% cBN(nano)70 SiC(sub-micro)/30 Si₃N₄ (sub-micro, Starck) + 30 vol.% cBN(micro)

After drying, the mixtures were preliminarily compressed into a disc of r 15 mm diameter and 5 mm height under pressure of ~ 200 MPa. The green bodies with the addition of TiH₂ were additionally annealed in a vacuum at a temperature of 800 °C for 1h in order to remove the hydrogen and obtain pure metallic titanium. The materials were obtained at high pressure (6 GPa) in the wide range of temperatures (430 – 2150 °C depending of composition) using a Bridgman-type toroidal apparatus (Fig. 2). The sintering temperatures were established experimentally for each material to obtain crack-free samples with the highest values of density and mechanical properties. The duration of the sintering process was 40s for nanopowders and 60 s for the others.

The sintered compacts were subsequently ground to remove remains of graphite after the technological process of sintering and to obtain the required quality and surface parallelism for Young's modulus determination. The samples provided for microscopic investigations and for mechanical tests were additionally polished using diamond slurries.

2.3 Investigation methods

Densities of the sintered samples were measured by the hydrostatic method. The uncertainty of the measurements was below 0.02 g/cm³, which gave a relative error value of below 0.5 % (excluding measurements of small pieces of broken samples, where the error was up to 0.1 g/cm³, due to their insufficient volume and mass).

Young's modulus of the samples obtained by HPHT sintering was measured by means of transmission velocity of ultrasonic waves through the sample, using a Panametrics Epoch III ultrasonic flaw detector. Calculations were carried out according to (Eq. 1):

$$E = \rho \cdot C_T^2 \frac{3C_L^2 - 4C_T^2}{C_L^2 - C_T^2} \quad (1)$$

where: E - Young's modulus, C_L - velocity of the longitudinal wave, C_T - velocity of the transversal wave, ρ - density of the material.

The velocities of transverse and longitudinal waves were determined as a ratio of sample thickness and relevant transition time. The accuracy of calculated Young's modulus (Eq. 1) was estimated to be below 2 %.

Hardness of sintered samples was determined by the Vickers method using a digital Vickers Hardness Tester (FUTURE-TECH FV-700). Five hardness measurements, with indentation loads of 2.94, 9.81 and 98.1 N, were carried out for each sample. Standard deviations of HV values were relatively high but usually no more than 5 % of the average values.

Indentation fracture toughness was calculated from the length of cracks which developed in a Vickers indentation test (with indentation load - 98.1 N) using Niihara's equation (Eq. 2):

$$\frac{K_{Ic} \phi}{H \sqrt{a}} \left(\frac{H}{E \phi} \right)^{\frac{2}{5}} = 0.129 \cdot \left(\frac{c}{a} \right)^{\frac{3}{2}} \quad (2)$$

where: K_{Ic} - critical stress intensity factor, φ - constrain factor, H - Vickers hardness, E - Young's modulus, a - half of indent diagonal, c - length of crack.

Microstructural observations were carried out on the densified materials using a JEOL JXA-50A Scanning electron Microscope equipped with back scattering electron (BSE) imaging.

In the Ball-On-Disc tests, the coefficient of friction and the specific wear rate of the sintered samples in contact with Si_3N_4 ball were determined using a CETR UMT-2MT (USA) universal mechanical tester. In the Ball-On-Disc method, sliding contact is brought about by pushing a ball specimen onto a rotating disc specimen under a constant load (Fig. 4). The loading mechanism applied a controlled load F_n to the ball holder and the friction force was measured continuously during the test using an extensometer. For each test, a new ball was used or the ball was rotated so that a new surface was in contact with the disc. The ball and disc samples were washed in ethyl alcohol and dried.

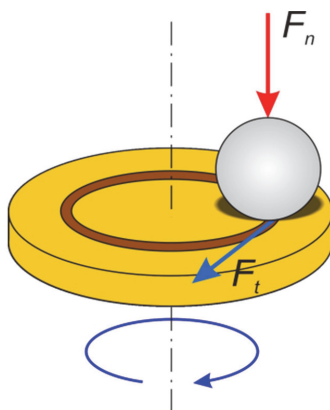


Fig. 4. Material pair for the Ball-On-Disc method: 1 - Si_3N_4 ball; 2 - sample (disc)

The size of the disc-shaped samples was ~ 13.5 in diameter and ~ 3.8 mm in height with the surfaces flatness and parallelism within 0.02 mm. The roughness of the tested surface was not more than $0.1 \mu\text{m } R_a$. The following test conditions were established: ball diameter - 2 mm, applied load - 4 N, sliding speed - 0.1 m/s, diameter of the sliding circle - $2 \div 5$ mm, sliding distance - 100 m, calculated duration of the test - 1000 s. The tests were carried out without lubricant at room temperature. Each test was repeated at least three times. Coefficient of friction was calculated from (Eq. 3):

$$\mu = \frac{F_f}{F_n} \quad (3)$$

where: μ - coefficient of friction, F_f - measured friction force, F_n - applied normal force.

After completing the test, according to ISO 20808:2004 E standard, the cross-sectional profile of the wear track at four places at intervals of 90° was measured using a contact stylus profilometer PRO500 (CETR, USA). Then the average cross-sectional area of the wear track was calculated. The volume of material removed was calculated as a product of cross-sectional area of the wear track and their circumference. Specific wear rate was calculated from (Eq. 4):

$$W_s = \frac{V}{F_n \cdot L} \quad (4)$$

where: W_s - specific wear rate, V - volume of removed material, L - sliding distance.

3. Materials sintered from nano-, sub-micro-, and micro-SiC/Si₃N₄ powders

A macroscopic view, phase composition and crystallite size of materials sintered from nanopowders under the pressure of 6 GPa at temperatures ranging from 430 to 1880 °C in the period of time 40s are shown in Table 2.

Initial powders	β-SiC powder, 4.1 nm	Si ₃ N ₄ amorphous powder, < 20 nm	Composite: 50 SiC/50 Si ₃ N ₄ - vol. %
Temperature of sintering	Sintered material: appearance, phase composition, crystallite size		
430°C	-	 amorphous Si ₃ N ₄	-
650°C	 β-SiC (4.1 nm)	 amorphous Si ₃ N ₄	 β-SiC (4.5 nm) + amorphous Si ₃ N ₄
890°C	 β-SiC (4.1 nm)	 amorphous Si ₃ N ₄	 β-SiC (11.1 nm) + amorphous Si ₃ N ₄
1170°C	 β-SiC (4.4 nm)	 orthorhombic Si _{1.8} Al _{0.2} O _{1.2} N _{1.8} (77)	 β-SiC (8.0 nm) + orthorhombic Si _{1.8} Al _{0.2} O _{1.2} N _{1.8} (20.0 nm)

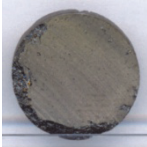


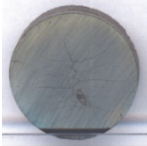

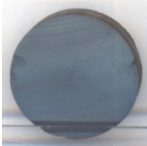
Initial powders	β -SiC powder, 4.1 nm	Si_3N_4 amorphous powder, < 20 nm	Composite: 50 SiC/50 Si_3N_4 - vol. %
Temperature of sintering	Sintered material: appearance, phase composition, crystallite size		
1450°C	 β -SiC (10.6 nm)	 β - Si_3N_4 (77.4 nm)	 β -SiC (10.2 nm) + orthorhombic $\text{Si}_{1.8}\text{Al}_{0.2}\text{O}_{1.2}\text{N}_{1.8}$ (31.0 nm)
1880°C	 β -SiC (110 nm)	 β - Si_3N_4 (143 nm)	 β -SiC (51.8 nm) + β - Si_3N_4 (86.9 nm)

Table 2. A macroscopic view, phase composition and crystallite size of SiC/ Si_3N_4 materials sintered from nanopowders under the pressure of 6 GPa at temperatures ranging from 430 to 1880 °C in the period of time 40s

The initial crystallite size of sintered SiC nanopowder was about 4.1 nm and did not change until the sintering temperature of 1170 °C. At the sintering temperature of 1450°C crystallites reached an average size of 10.6 nm while at the maximum applied temperature (1880 °C) their size was 110 nm. This material showed no phase transformation. The sinters obtained at 1880 °C as well as the initial powder have the cubic structure of β -SiC phase. Sintered Si_3N_4 powder remained amorphous until the temperature of 890 °C. At the temperature of 1170 °C a new phase crystallized. The X-ray diffraction pattern of this phase corresponds to the o'-sialon with orthorhombic structure and $\text{Si}_{1.8}\text{Al}_{0.2}\text{O}_{1.2}\text{N}_{1.8}$ stoichiometry. As evidenced by the chemical formula, this compound has a low content of aluminum with reference to silicon while the quantities of nitrogen and oxygen are comparable. It can be assumed that o'-sialon is a transition phase between the amorphous silicon nitride and a completely crystalline β - Si_3N_4 phase. O'-sialon was formed probably due to embedding a certain amount of oxygen and impurities adsorbed on the surface of powder to an atomic lattice of crystallizing silicon nitride. The crystallite size of this phase was estimated to around be 77 nm. The samples obtained at temperatures of 1450 and 1880 °C contain only β - Si_3N_4 phase with the crystallite size 77.4 and 143 nm respectively.

50 SiC/50 Si_3N_4 - vol. % nanocomposite was sintered at the same temperatures as silicon carbide powder without additions. The phase composition of sintered composites did not differ qualitatively from the sum of their components sintered separately. There was no formation of new phases in the reaction between silicon carbide and silicon nitride. Sintering of composites, especially at higher temperatures, leads to lower grain growth than it is in single-phase powders sintered separately. This indicates a favorable effect of inhibiting grain growth in the composite.

The comparison of physical-mechanical properties of nano-, sub-micro- and micro-SiC/Si₃N₄ materials sintered at different temperatures is presented in Fig. 5 and Table 3. Generally, nanocomposites are characterized by the lowest physical-mechanical properties of the three granulometric types of the investigated materials. Densities and Young's modulus values of the best nanostructured samples do not exceed 2.55 g/cm³ and 135 GPa respectively. In most cases, nanostructured SiC/Si₃N₄ samples are characterized by a lot of cracks (see Table 2). Cracking of such ceramics occurs as a result of the presence in their structure of residual micro- and macro-stresses which overcome the strength of the produced material. The fine powder is characterized by a very large specific surface and high gas content in the sample due to the absorption process of the material particles. During heating, as a result of the increase in temperature, the volume of gases increases, which causes cracking or even permanent fragmentation of the sample. In order to prevent the cracking phenomena in the samples, various conditions of the sintering process were tested. Depending on composition, materials characterized by the highest level of densification and the best mechanical properties were obtained at different temperatures: 890 °C for pure Si₃N₄ and 1880 °C for 50 Si₃N₄/50 SiC – vol.% composite. Unfortunately, some of these samples had cracks as well. Different kinds of internal cracks, delamination and other defects of microstructure occurred in most of the nanostructured samples. These defects cause a scattering of caustic waves propagated through the material and, in consequence, the impossibility of Young's modulus measurements using ultrasonic probes (marked as **nm in Table 3). Composites without cracks were obtained only from micro- and sub-micro-structured powders. Only for these composites hardness and fracture toughness were measured.

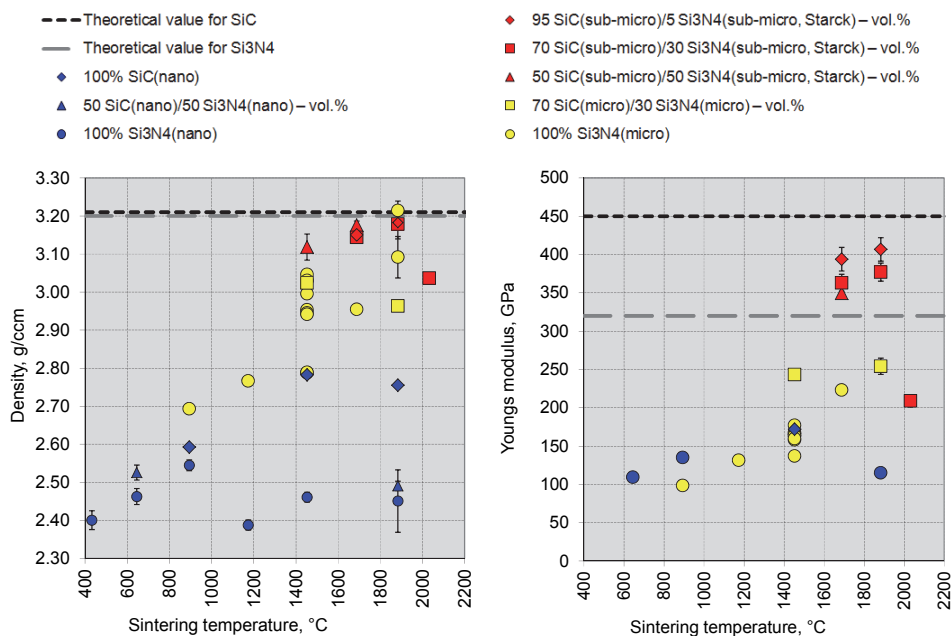


Fig. 5. Density and Young modulus of nano-, sub-micro-, and micro-SiC/Si₃N₄ materials sintered at different temperatures

Sample composition	Sintering temp. range	*Sintering temp. optimal for (properties) / description	Density	Youngs modulus	Poisson's ratio	Hardness			Fracture toughness
vol. %	°C	°C	g/ccm % of theoretic	GPa % of theoretic	-	HV _{0.3}	HV ₁	HV ₁₀	MPa m ^{1/2}
nanomaterials (initial powders: β -SiC<5nm, amorphous Si ₃ N ₄ <20nm) sintered at 6GPa for 40s									
100 SiC(nano)	650-1880	1450 /cracks	2.78 87	172 38	0.24	-	-	-	-
50 SiC(nano) / 50 Si ₃ N ₄ (nano)	650-1880	1880 /small chipping	2.49 78	**nm -	**nm	-	-	-	-
100 Si ₃ N ₄ (nano)	430-1880	890	2.54 80	135 42	0.24	-	-	-	-
sub-micro-structured materials (powders: α -SiC 0.1-1 μ m, α -Si ₃ N ₄ 0.6 μ m) sintered at 6GPa for 60s									
95 SiC(sub-micro) / 5 Si ₃ N ₄ (sub-micro, Starck)	1690-2150	1880 /cracks	3.18 99	407 92	0.17	-	-	-	-
70 SiC(sub-micro) / 30Si ₃ N ₄ (sub-micro, Starck)	1690-2030	*1690 (K _{IC})	3.14 98	363 87	0.19	2810	2630	2240	5.6
		*1880 (ρ , E, HV)	3.18 99	377 90	0.19	3130	2970	2400	4.9
50 SiC(sub-micro) / 50Si ₃ N ₄ (sub-micro, Starck)	1450-1880	1690	3.18 99	349 91	0.21	2700	2560	2140	5
100Si ₃ N ₄ (sub-micro, Starck)	1170-1690	/cracs	- -	- -	-	-	-	-	-
micro-structured materials (initial powders: SiC 1.2 μ m, α -Si ₃ N ₄ 1-5 μ m,) sintered at 6GPa for 60s									
70 SiC(micro) / 30 Si ₃ N ₄ (micro)	1450-1880	1450 /small cracks	3.02 94	243 58	0.16	-	1880	1510	4.6
100 Si ₃ N ₄ (micro)	890-1880	*1450 (ρ)	3.03 95	167 52	0.2	-	1250	1060	4.8
		*1690 (E) /small chipping	2.95 92	223 70	0.22	-	-	-	-

Table 3. Physical-mechanical properties of selected nano-, sub-micro- and micro-SiC/Si₃N₄ materials sintered at optimal temperatures; *optimum temperature for selected properties, e.g. 1690 (K_{IC}) - the best fracture toughness; **nm - non measurable with ultrasonic method

	Si ₃ N ₄ based ceramics				SiC based ceramics			Sub-micro-70SiC/30Si ₃ N ₄ composites (this work)	
	StarCeram N 7000 H.C. Starck	StarCeram N 8000 H.C. Starck	EKatherm Ceradyne	Ceralloy 147-A Ceradyne	StarCeram S H.C. Starck	Hexoloy SA Saint Gobain	Ceralloy 146-S5 Ceradyne		
Density, g/ccm	>3.22	>3.23	>3.24	3.18	3.10	3.10	3.20	3.14	3.18
Young's modulus, GPa	290	310	310	310	395	410	430	363	377
Vickers hardness, HV	1500	1520	1450 (300g)	1650 (300g)	2500	2800 (100g Konopp)	2600 (300g)	2812 (300g)	3132 (300g)
Fracture toughness, MPa m ^{1/2}	6.7	6.0	7.0	4.5	3.0	4.6	4.3	5.6	4.9

Table 4. Comparison of commercial advanced SiC/Si₃N₄-based ceramics¹ with sub-micro-structured 70 SiC/30 Si₃N₄ – vol.% composites obtained by HPHT sintering

The composites obtained from submicron powders are characterized by the best properties. Density and Young's modulus of the best 70 SiC/30 Si₃N₄ – vol.% compacts sintered at 1880 °C were 3.18 g/cm³ and 377 GPa respectively (over 99% and 90% of the theoretical values). This material is also characterized by the highest hardness (HV1 ~3000) and relatively good fracture toughness (4.9 MPa m^{1/2}). The same material sintered at a lower temperature (1690 °C) has slightly lower values of density (3.14 g/cm³), Young's modulus (363 GPa) and hardness (HV1 2626) but higher fracture toughness (5.6 MPa m^{1/2}) - Table 3. HPHT sintered sub-micro-70 SiC/30 Si₃N₄ – vol.% composites have a better combination of mechanical properties than comparable commercial materials (Table 4).

The composites obtained from the micro-sized powders have their properties intermediate between the nano- and sub-micro-structured materials. Even though the best micro-SiC/Si₃N₄ samples are crack free and have fairly good density (>94% of theoretical values) and indentation fracture toughness (4.6 – 4.8 MPa m^{1/2}), their Young's modulus and hardness are much lower than for the sub-micro-structured samples. The insufficient mechanical properties of microstructured Si₃N₄-SiC materials can be attributed not only to grain size but also to specific properties of the initial powder resulting from their production method (e.g. shape of the grains, impurities, oxidation etc.). The choice of suitable initial powders for the given method of sintering is the critical factor in achieving good quality of ceramics.

¹ Data from: H.C. Starck Ceramics GmbH& Co. KG, Ceradyne Inc. and Saint – Gobain Advanced Ceramics – commercial data sheets)

For all the investigated samples, independently of their grain size, a strong influence of indentation load on hardness values can be observed. Increasing the indentation load causes a decrease in hardness values (Table 3).

4. Modifications of 70 SiC/30 Si₃N₄ composite

Density and Young's modulus of various 70 SiC/30 Si₃N₄ – vol.% composites sintered at different temperatures with and without additions of Ti, TiB₂ and cBN phases are presented in Figs 6-11 and in Table 5.

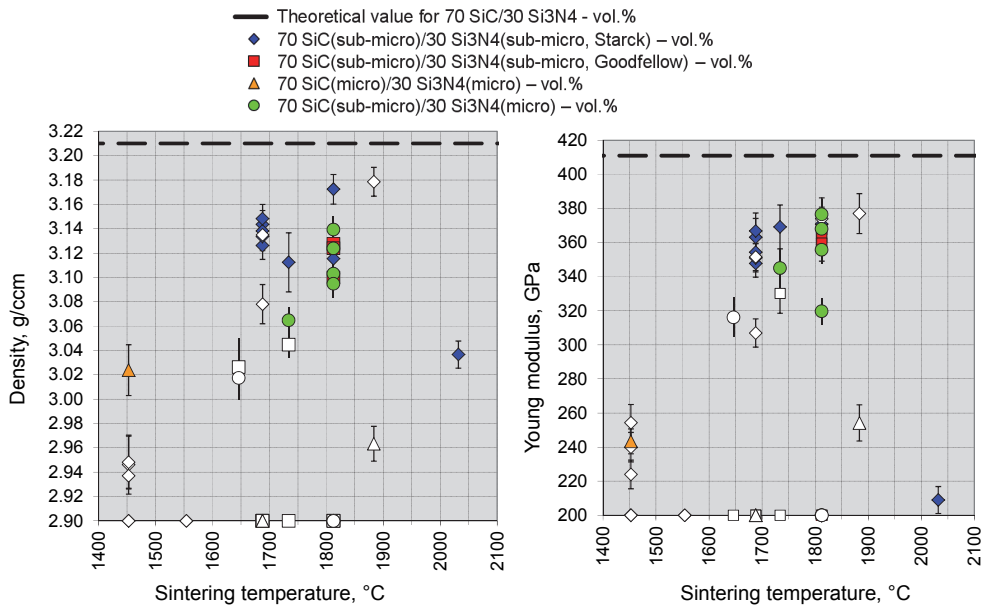


Fig. 6. Density and Young's modulus of various kinds of 70 SiC/30 Si₃N₄ – vol.% composites sintered at different temperatures. Colored symbols – samples without cracks; white symbols – samples with cracks; white symbols placed on temperature axis – broken samples

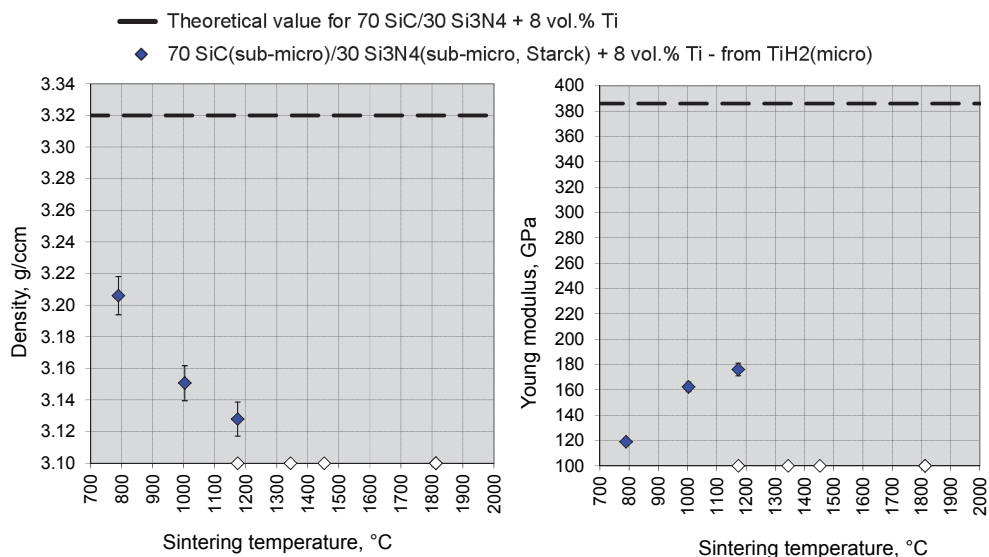


Fig. 7. Density and Young's modulus of 70 SiC/30 Si₃N₄ + 8 vol.% Ti composites sintered at different temperatures. Dark symbols – samples without cracks; white symbols – samples with cracks; white symbols placed on temperature axis – broken samples

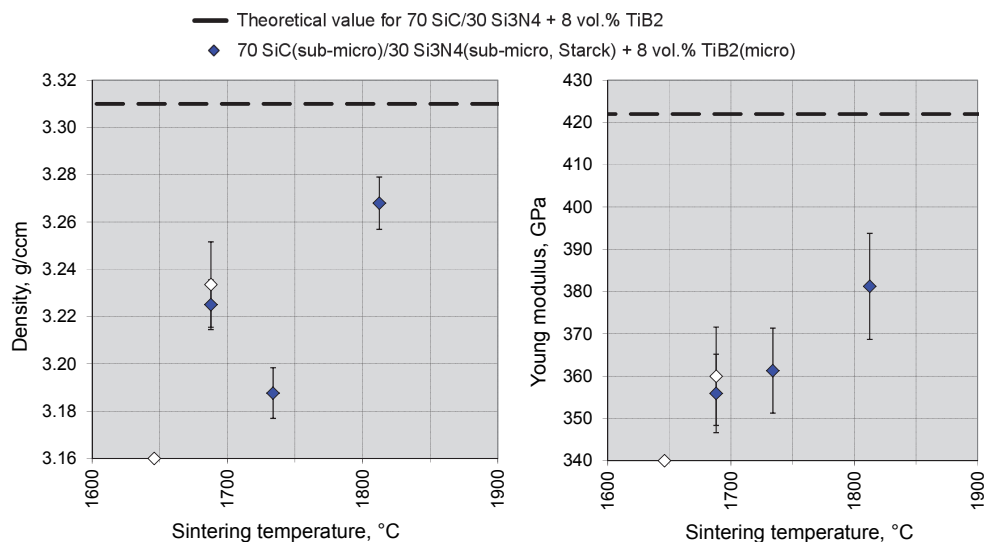


Fig. 8. Density and Young's modulus of 70 SiC/30 Si₃N₄ + 8 vol.% TiB₂ composites sintered at different temperatures. Dark symbols – samples without cracks; white symbols – samples with cracks; white symbols placed on temperature axis – broken samples

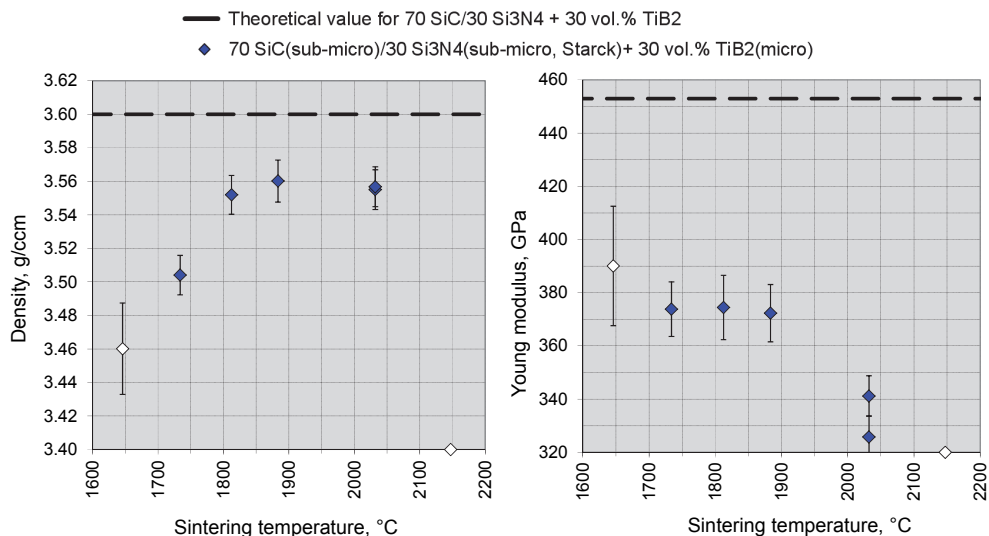


Fig. 9. Density and Young's modulus of 70 SiC/30 Si₃N₄ + 30 vol.% TiB₂ composites sintered at different temperatures. Dark symbols – samples without cracks; white symbols – samples with cracks; white symbols placed on temperature axis – broken samples

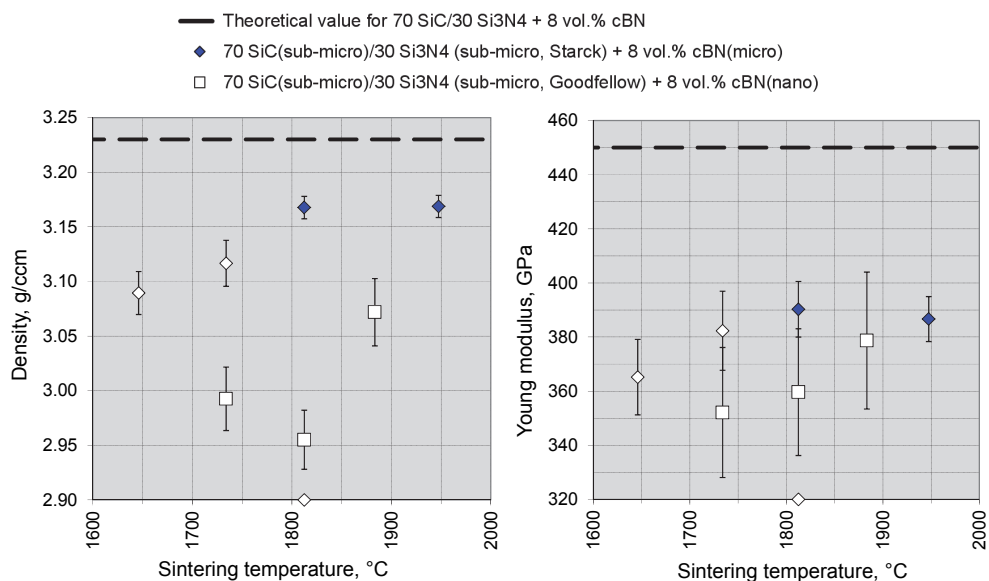


Fig. 10. Density and Young's modulus of 70 SiC/30 Si₃N₄ + 8 vol.% cBN composites sintered at different temperatures. Dark symbols – samples without cracks; white symbols – samples with cracks; white symbols placed on temperature axis – broken samples

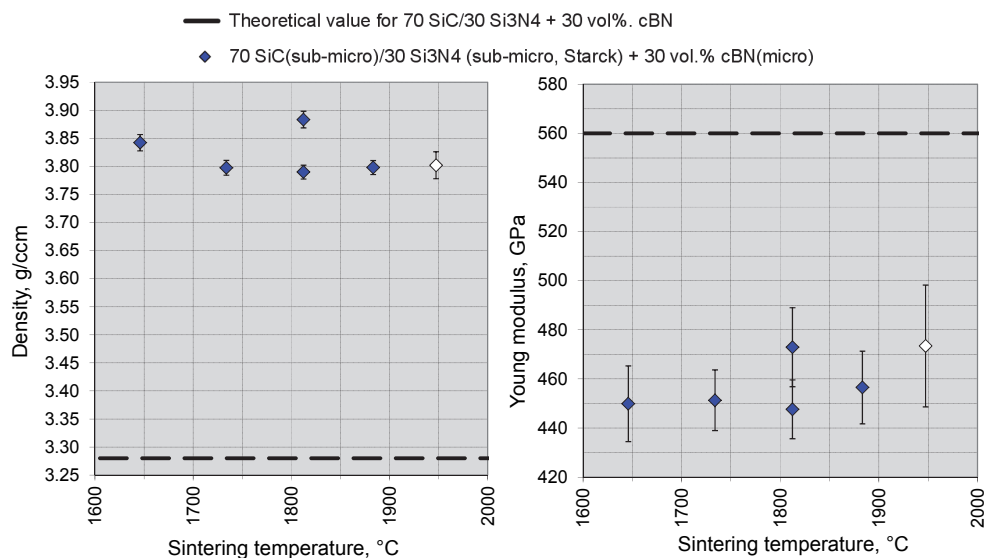


Fig. 11. Density and Young's modulus of 70 SiC/30 Si₃N₄ + 30 vol.% cBN composites sintered at different temperatures. Dark symbols – samples without cracks; white symbols – samples with cracks

Among the composites sintered without additional phases, the highest degree of densification and best mechanical properties were demonstrated by composite obtained from submicron powders 70 SiC(sub-micro)/30 Si₃N₄(sub-micro, Starck) – vol%. (Fig. 6 and Table 5). This composite was selected for modification by the addition of the third phase particles.

The modification of the 70 SiC/30 Si₃N₄ composite by the addition of Ti was not successful. The samples with the addition of 8 vol.% Ti introduced in the form of TiH₂, sintered at low temperatures, were characterized by a very low Young's modulus, whilst all the samples sintered at temperatures above ~1200 °C were cracked. A decrease in density was observed with increasing sintering temperature, whilst Young's modulus showed an upward trend (Fig. 7).

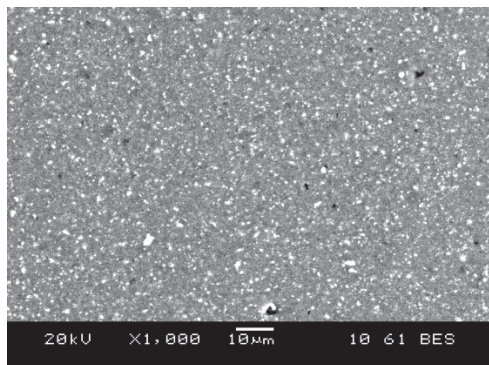
The composites with the addition of TiB₂ were characterized by a high degree of densification, a high Young's modulus and improved K_{IC} as compared to the unmodified composite. No improvement in hardness was observed (Table 5). In the case of 70 SiC/30 Si₃N₄ material with the addition of 8 vol.% TiB₂, there is some increase in density and Young's modulus with increasing temperature (Fig. 8). Composite with the addition of 30 vol.% TiB₂, shows an increase in density with sintering temperature up to a maximum value, and then its stabilization. A further increase of the sintering temperature results in cracking of the samples (Fig. 9).

The composites modified by the addition of 8 vol.% cBN micropowder have better properties than the composites with TiB₂ but a tendency to cracking of this material is noticeable. The use of nano-cBN particles as a modifier causes the deterioration of the properties and cracking of samples (Fig. 10). The composites modified by the addition of 30 vol.% cBN micropowder, showed the best mechanical properties (Fig. 11 and Table 5).

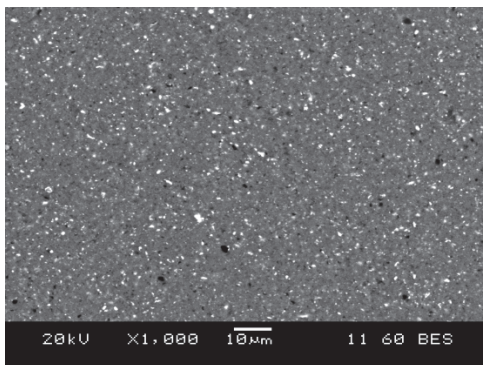
Sample composition	Sintering temp. range	Sintering temp. optimal for (properties) / description	Density	Youngs modulus	Poisson's ratio	Hardness		Fracture toughness
vol. %	°C	°C	g / cm % of theoretic	GPa % of theoretic	GPa	HV ₁	HV ₁₀	MPa m ^{1/2}
70SiC/30Si ₃ N ₄ composite								
70 SiC(sub-micro)/ 30 Si ₃ N ₄ (sub-micro, Starck)	1450-2030	*1880 (ρ, E, HV)	3.18 99	377 92	0.19	2970	2400	4.9
		*1690 (K _{Ic})	3.14 98	363 87	0.19	2630	2240	5.6
70 SiC(sub-micro)/ 30 Si ₃ N ₄ (sub-micro, oodfellow)	1650-1810	1810 /cracks	3.13 97	368 89	0.20	2772	2268	5.7
70 SiC(micro)/ 30 Si ₃ N ₄ (micro)	1450-1880	1450 /small cracks	3.02 94	243 58	0.16	1880	1510	4.6
70 SiC(sub-micro)/ 30 Si ₃ N ₄ (micro)	1650-1810	*1810 (ρ, E, HV)	3.10 97	368 90	0.20	2748	2392	5.6
		*1730 (K _{Ic}) /small cracks	3.06 95	345 84	0.20	2576	2278	6.0
70SiC/30Si ₃ N ₄ composite + Ti								
70 SiC(sub-micro)/ 30 Si ₃ N ₄ (sub-micro, Starck) + 8 Ti - from TiH ₂ (micro)	790-1810	*790 (ρ)	3.21 97	119 31	0.13	-	-	-
		*1170 (E)	3.13 94	176 46	0.10	-	-	-
70SiC/30Si ₃ N ₄ composite + TiB ₂								
70 SiC(sub-micro)/ 30 Si ₃ N ₄ (sub-micro, Starck) + 8 TiB ₂ (micro)	1650-1810	*1810 (ρ, E)	3.27 99	381 90	0.20	2488	2364	4.2
		*1690 (K _{Ic})	3.23 97	356 84	0.18	2526	2324	6.1
70 SiC(sub-micro)/ 30 Si ₃ N ₄ (sub-micro, Starck) + 30 TiB ₂ (micro)	1650-2150	*1810 (ρ, HV)	3.55 99	374 83	0.17	2564	2318	5.8
		*1730 (K _{Ic})	3.50 97	374 83	0.17	2390	2260	6.4
70SiC/30Si ₃ N ₄ composite + cBN								
70 SiC(sub-micro)/ 30 Si ₃ N ₄ (sub-micro, Starck) + 8cBN(micro)	1650-1950	1950 /cracks	3.17 98	387 86	0.19	2850	2408	6.4
70 SiC(sub-micro)/ 30 Si ₃ N ₄ (sub-micro, Goodfellow) + 8cBN(nano)	1730-1880	1880 /cracks	3.07 95	379 84	0.17	-	-	-
70 SiC(sub-micro)/ 30 Si ₃ N ₄ (sub-micro, Starck) + 30cBN(micro)	1650-1950	*1810 (ρ, E) /cracks	3.88 118	473 84	0.18	3038	2612	7.4
		*1880 (HV, K _{Ic})	3.80 116	457 82	0.18	3190	2790	7.5

Table 5. Physical-mechanical properties of the best samples selected from different modifications of 70 SiC/30 Si₃N₄ composites; *optimum temperature for selected properties, e.g. 1690 (K_{Ic}) - the best value of fracture toughness

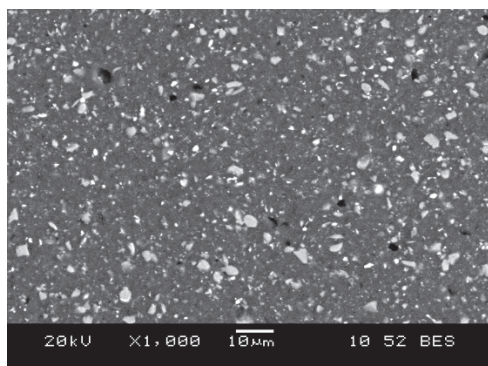
SEM microstructures of 70 SiC/30 Si₃N₄ with and without the addition of TiB₂ and cBN are presented in Fig. 12. The microstructures of the investigated samples are compact and dense, with the ingredients uniformly distributed in the volume of the composite. This demonstrates successful blending, using a planetary mill; EDS analysis, however, showed a



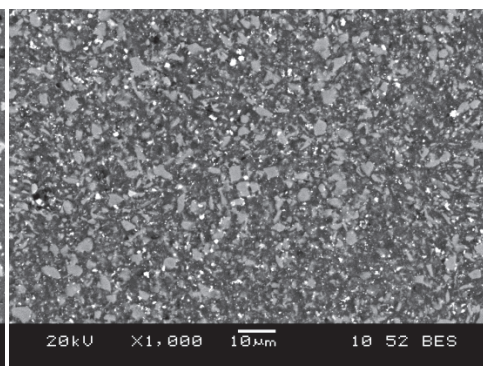
70 SiC(sub-micro)/30 Si₃N₄(sub-micro, Starck) - vol.%



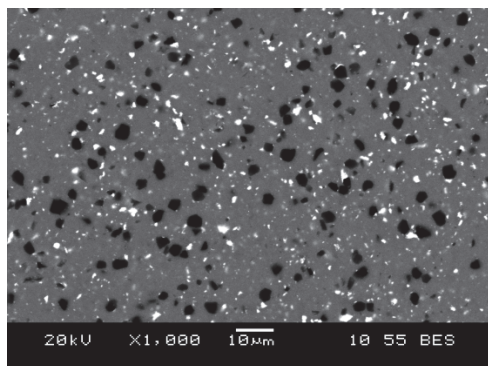
70 SiC(micro)/30 Si₃N₄(micro) - vol.%



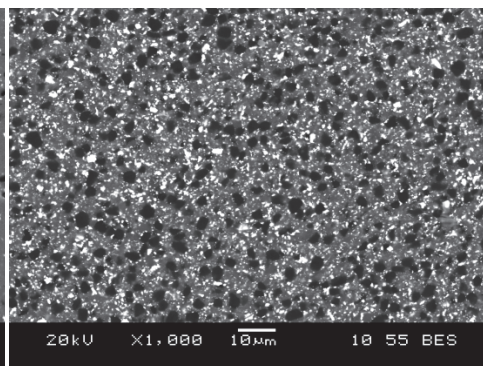
70 SiC(sub-micro)/30 Si₃N₄(sub-micro, Starck) + 8 vol.% TiB₂(micro)



70 SiC(sub-micro)/30 Si₃N₄(sub-micro, Starck) + 30 vol.% TiB₂(micro)



70 SiC(sub-micro)/30 Si₃N₄(sub-micro, Starck) + 8 vol.% cBN(micro)



70 SiC(sub-micro)/30 Si₃N₄(sub-micro, Starck) + 30 vol.% cBN(micro)

Fig. 12. SEM microstructures of selected 70 SiC/30 Si₃N₄ composites with and without the addition of TiB₂ and cBN

high content of tungsten carbide and zirconium dioxide from the vessel and grinding media used to prepare the mixtures (white areas visible in the microstructures - Fig. 12). The highest quantity of WC was admixed to composite containing 30% of cBN super-abrasive powder. WC has density of 15.7 g/cm^3 . It explains too high value (118%) of relative density of 70 SiC/30 Si₃N₄ + 30vol.% cBN composite.

An example of a crack which developed in a Vickers indentation test in the composite modified by addition 30% of cBN is presented in Fig. 13. In this material the mixed mode of crack propagation can be observed. Some parts of fracture are of an intra-crystalline character (indicated as **1** in Fig. 13) while some are inter-crystalline (indicated as **2** in Fig. 13). In both cases the change of direction of crack propagation is visible. A similar effect can be observed in the composites modified by the TiB₂ phase. This indicates that the crack deflection mechanism influences on toughening of composites modified by ceramic particles.

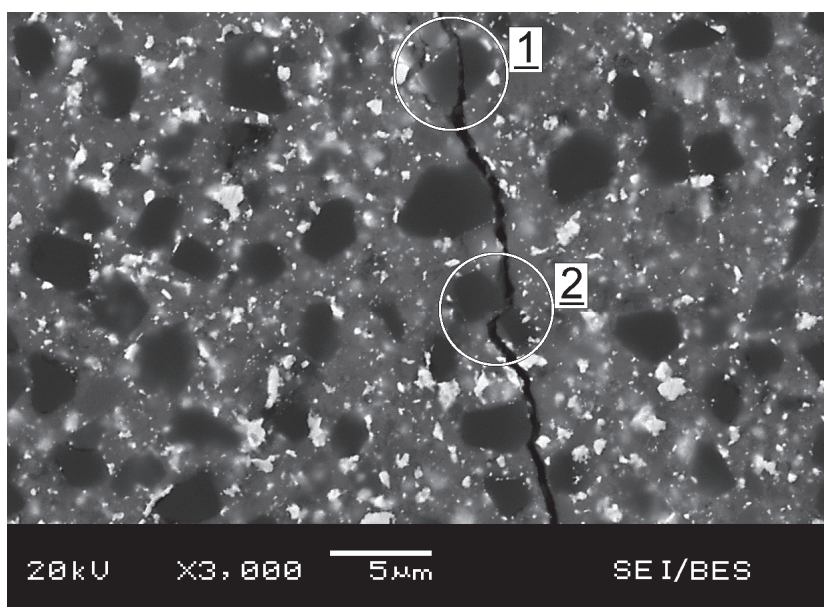


Fig. 13. SEM microstructure of 70 SiC/30 Si₃N₄ composite modified by addition of 30 vol.% cBN phase (the darkest areas). Mixed mode of crack propagation visible: 1) crack propagates through the cBN grains, 2) crack propagates around the cBN grains

High-quality composites, characterized by the homogeneous microstructure, without cracks (formed during the third stage of HPHT sintering process - cooling and releasing of the pressure) and high values of Young's modulus, hardness and fracture toughness were subjected to the tribological tests. The above criteria were fulfilled for following materials:

70 SiC(sub-micro)/30 Si₃N₄(sub-micro, Starck) - vol.%,

70 SiC(sub-micro)/30 Si₃N₄(micro) - vol.%,

70 SiC(sub-micro)/30 Si₃N₄(sub-micro, Starck) + 8 vol.% TiB₂(micro),

70 SiC(sub-micro)/30 Si₃N₄(sub-micro, Starck) + 30 vol.% TiB₂(micro),

70 SiC(sub-micro)/30 Si₃N₄ (sub-micro, Starck) + 30 vol.% cBN(micro).

Additionally, for comparison, the commercial Si_3N_4 based cutting tool material (ISCAR, IS9-grade) was also tested. The mean curves of friction coefficient for investigated materials in a sliding contact with the Si_3N_4 ball are presented in Fig. 14. A comparison of the specific wear rate determined by the wear tracks measurement is presented in Fig. 15.

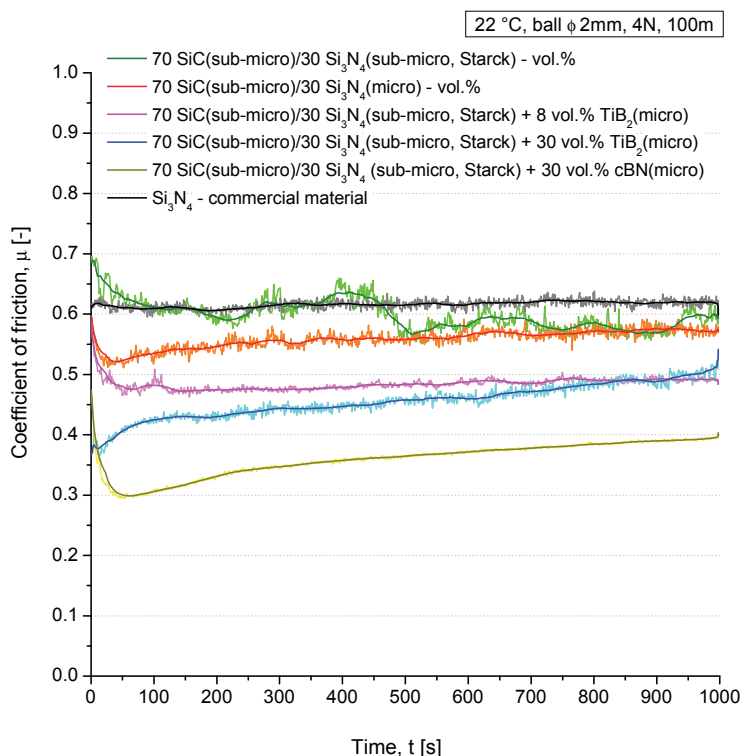


Fig. 14. Coefficient of friction of selected 70 SiC/30 Si_3N_4 – vol.% composites with and without the addition of TiB_2 and cBN

70 SiC/30 Si_3N_4 composites, sintered without additional phases, as well as the commercial material had the highest coefficients of friction. Average values of the friction coefficient for 70 SiC(sub-micro)/30 Si_3N_4 (sub-micro, Starck), 70 SiC(sub-micro)/30 Si_3N_4 (micro) composites and for commercial Si_3N_4 based cutting tool material were 0.60, 0.56 and 0.62 respectively. The composites modified by the addition of a TiB_2 phase were characterized by intermediate values of the friction coefficient. Average values of the friction coefficient for 70 SiC(sub-micro)/30 Si_3N_4 (sub-micro, Starck) + 8 vol.% TiB_2 (micro) and 70 SiC(sub-micro)/30 Si_3N_4 (sub-micro, Starck) + 30 vol.% TiB_2 (micro) materials were 0.48 and 0.46 respectively. The composite with the addition of 30% cBN was characterized by the lowest average coefficient of friction, at only 0.36. High coefficients of friction generate thermal stress, which is detrimental to the wear behavior of materials. Hard ceramic bodies – possessing high fracture toughness and low coefficients of friction – used in mechanical

systems that involve high loads, velocities and temperatures, will reduce costs and be less harmful to the environment.

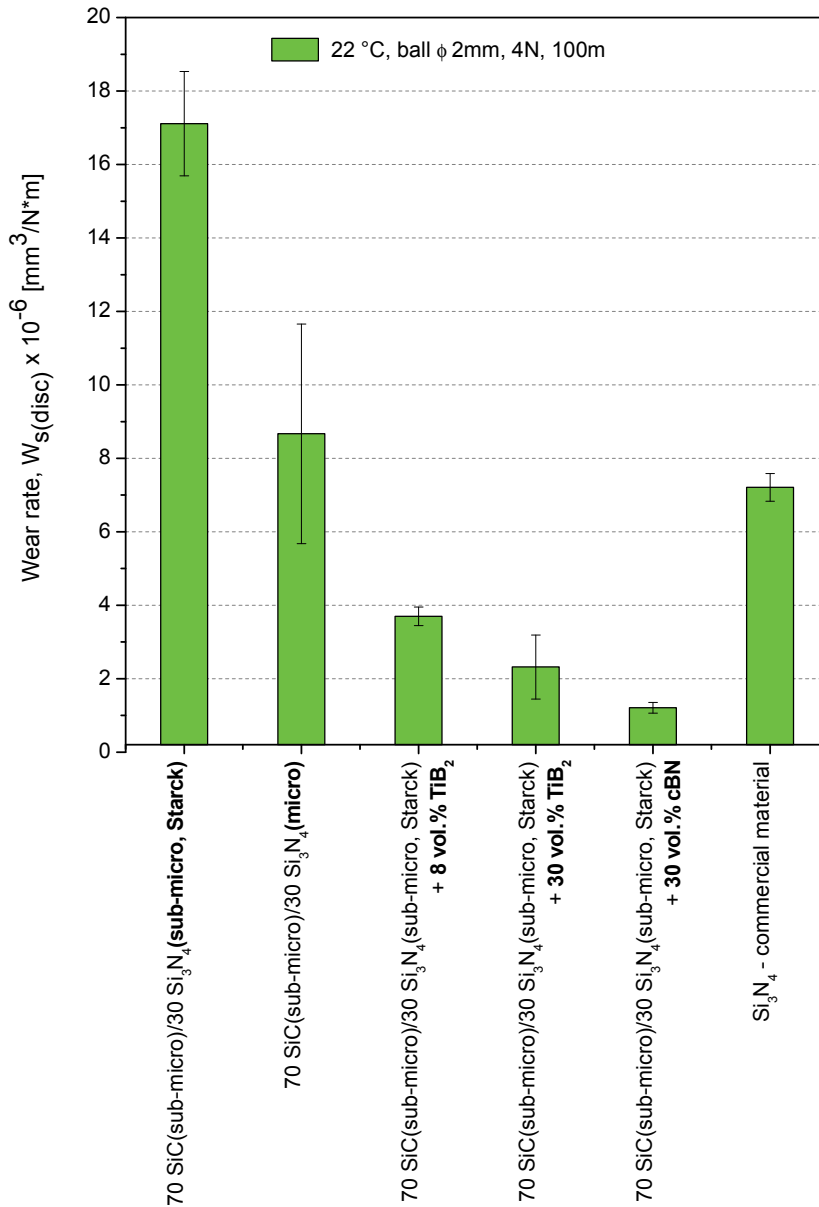


Fig. 15. Wear rate of selected 70 SiC/30 Si₃N₄ - vol.% composites with and without the addition of TiB₂ and cBN

Specific wear rates of investigated materials, in most cases, show a similar trend to the trends exhibited by their coefficients of friction. Only 70 SiC/30 Si₃N₄ composites without addition of third phase and commercial material show some deviations from this trend. 70 SiC(sub-micro)/30 Si₃N₄(sub-micro, Starck) composite is the least wear resistant. Their specific wear rate reached value of $17.1 \times 10^{-6} \text{ mm}^3/\text{N}\cdot\text{m}$. Subsequently 70 SiC(sub-micro)/30 Si₃N₄(micro) and commercial material are classified. Their specific wear rates are 8.7×10^{-6} and $7.2 \times 10^{-6} \text{ mm}^3/\text{N}\cdot\text{m}$ respectively. Significantly better are composites modified by addition of TiB₂ particles. The specific wear rate of 70 SiC(sub-micro)/30 Si₃N₄(sub-micro, Starck) + 8 vol.% TiB₂(micro) and 70 SiC(sub-micro)/30 Si₃N₄(sub-micro, Starck) + 30 vol.% TiB₂(micro) samples equal 3.7×10^{-6} and $2.3 \times 10^{-6} \text{ mm}^3/\text{N}\cdot\text{m}$ respectively. The highest wear resistant is exhibited by 70 SiC(sub-micro)/30 Si₃N₄ (sub-micro, Starck) + 30 vol.% cBN(micro) composite with its specific wear rate value equals only $1.2 \times 10^{-6} \text{ mm}^3/\text{N}\cdot\text{m}$.

5. Conclusions

The performed research proves that the HPHT sintering is a method of the future for compacting SiC/Si₃N₄ nanopowders, due to the short time of the process amounting to 40 seconds that permits the grain growth limitations. The obtained compacts were characterized by the crystallites sizes of 4 to 143 nm, depending on the sintering parameters. SiC and SiC/Si₃N₄ samples sintered from nanopowders are characterized by the presence of cracks. Cracking of such ceramics occurs as a result of residual micro- and macro-stresses in their structure which overcome the strength of the produced material. The fine powder is characterized by a very large specific surface and high gas content in the sample due to the absorption process of the material particles. During heating, as a result of the increase in temperature, the volume of gases increases, which causes cracking or even permanent fragmentation of the sample. The research regarding the mechanical properties of SiC/Si₃N₄ composites indicates that materials obtained from submicron powders display the best properties. Density and Young's modulus of the best 70 SiC/30 Si₃N₄ - vol.% compacts, sintered at 1880 °C, were 3.18 g/cm³ (over 99% the theoretical values) and 377 GPa respectively. This material is also characterized by the highest hardness (HV1 ~3000) and relatively good fracture toughness (4.9 MPa·m^{1/2}). The same material sintered at a lower temperature (1690 °C) has slightly lower values of density (3.14 g/cm³), Young's modulus (363 GPa) and hardness (HV1 2626) but higher fracture toughness (5.6 MPa·m^{1/2}). HPHT sintered sub-micro-70 SiC/30 Si₃N₄ - vol.% composites have a better combination of mechanical properties than comparable commercial materials.

The research concerning modification of sub-micro-70 SiC/30 Si₃N₄ - vol.% composites proves that the addition of the third phase in the form of TiB₂ or cBN particles contribute to their further improvement. Composites modified by the addition of 30vol.% cBN micropowder are characterized by the best combination of Young's modulus, hardness, fracture toughness, coefficient of friction and the specific wear rate. Such properties predispose 70 SiC/30 Si₃N₄ + 30vol.% cBN composites to various advanced engineering applications including their use for wear parts and cutting tools.

6. Acknowledgments

This study was carried out within the framework of the project funded by the Polish Ministry of Science and Higher Education (Project number: DPN/N111/BIALORUS/2009).

The author would like to thank Prof. M. Bućko from AGH University of Science and Technology in Krakow for XRD analysis. The author would also like to thank his colleagues from The Institute of Advanced Manufacturing Technology in Krakow for Vickers's indentation tests and for SEM studies. Finally, the author would like to thank his supervisor Prof. L. Jaworska for her optimism and valuable advice throughout this research.

7. References

- Ando, K.; Houjyou, K.; Chu, M.C.; Takeshita, S.; Takahashi, K.; Sakamoto, S. & Sato, S. (August 2002). Crack-healing behavior of $\text{Si}_3\text{N}_4/\text{SiC}$ ceramics under stress and fatigue strength at the temperature of healing (1000 °C). *Journal of the European Ceramic Society*, Vol. 22, No. 8, pp. 1339 - 1346, ISSN 0955-2219
- Awaji, H.; Choi, S. & Yagi, E. (July 2002). Mechanisms of toughening and strengthening in ceramic-based nanocomposites. *Mechanics of Materials*, Vol. 34, No. 7, pp. 411 - 422, ISSN 0167-6636
- Bridgman, P.W. (1964). *Collected Experimental Papers*, Harvard University Press, ISBN 0674137507, Cambridge, Massachusetts, USA
- Derby, B. (October 1998). Ceramic nanocomposites: mechanical properties. *Current Opinion in Solid State and Materials Science*, Vol. 3, No. 5, pp. 490-495, ISSN 1359-0286
- Eblagon, F.; Ehrle, B.; Graule, T. & Kuebler, J. (2007). Development of silicon nitride/silicon carbide composites for wood-cutting tools. *Journal of the European Ceramic Society*, Vol. 27, No. 1, pp. 419 - 428, ISSN 0955-2219
- Eremets, M.I. (1996). *High pressure Experimental Methods*, Oxford University Press, ISBN 0-19-856269-1, New York, USA
- Filonenko, V.P. & Zibrov, I.P. (September 2001). High-Pressure Phase Transitions of M_2O_5 (M = V, Nb, Ta) and Thermal Stability of New Polymorphs. *Inorganic Materials*, Vol. 37, No. 9, pp. 953-959, ISSN 0020-1685
- Gahr, K.Z.; Blattner, R.; Hwang, D. & Pöhlmann, K. (October 2001). Micro- and macro-tribological properties of SiC ceramics in sliding contact. *Wear*, Vol. 250, No. 1-12, pp. 299 - 310, ISSN 0043-1648
- Guicciardi, S.; Sciti, D.; Melandri, C. & Pezzotti, G. (February 2007). Dry sliding wear behavior of nano-sized SiC pins against SiC and Si_3N_4 discs. *Wear*, Vol. 262, No. 5-6, pp. 529 - 535, ISSN 0043-1648
- Hall, H.T. (February 1960). Ultra-High-Pressure, High-Temperature Apparatus: the "Belt". *Review of Scientific Instruments*, Vol. 31, No. 2, pp. 125-131, ISSN 0034-6748
- Hirano, T. & Niihara, K. (March 1995). Microstructure and mechanical properties of $\text{Si}_3\text{N}_4/\text{SiC}$ composites. *Materials Letters*, Vol. 22, No. 5-6, pp. 249 - 254, ISSN 0167-577X
- Khvostantsev, L.G.; Slesarev, V.N. & Brazhkin, V.V. (2004). Toroid type high-pressure device: history and prospects. *High Pressure Research*, Vol. 24, No. 3, pp. 371-383, ISSN
- Kim, Y.; Lee, Y. & Mitomo, M. (August 2006). Sinterability of Nano-Sized Silicon Carbide Powders. *Journal of the Ceramic Society of Japan*, Vol. 114, No. 1332, pp. 681-685, ISSN 0914-5400
- Kinoshita, T.; Munekawa, S. & Tanaka, S.I. (February 1997). Effect of grain boundary segregation on high-temperature strength of hot-pressed silicon carbide. *Acta Materialia*, Vol. 45, No. 2, pp. 801 - 809, ISSN 1359-6454

- Lee, S.M.; Kim, T.W.; Lim, H.J.; Kim, C.; Kim, Y.W. & Lee, K.S. (May 2007). Mechanical Properties and Contact Damages of Nanostructured Silicon Carbide Ceramics. *Journal of the Ceramic Society of Japan*, Vol. 115, No. 1341, pp. 304-309, ISSN 0914-5400
- Lojanová, S.; Tatarko, P.; Chlup, Z.; Hnatko, M.; Dusza, J.; Lencés, Z. & Sajgalík, P. (July 2010). Rare-earth element doped $\text{Si}_3\text{N}_4/\text{SiC}$ micro/nano-composites--RT and HT mechanical properties. *Journal of the European Ceramic Society*, Vol. 30, No. 9, pp. 1931 - 1944, ISSN 0955-2219
- Magnani, G.; Minocari, G. & Pilotti, L. (June 2000). Flexural strength and toughness of liquid phase sintered silicon carbide. *Ceramics International*, Vol. 26, No. 5, pp. 495 - 500, ISSN 0272-8842
- Manghnani, M.; Ming, L. & Jamieson, J. (November 1980). Prospects of using synchrotron radiation facilities with diamond-anvil cells: High-pressure research applications in geophysics. *Nuclear Instruments and Methods*, Vol. 177, No. 1, pp. 219 - 226, ISSN 0029-554X
- Murthy, V.S.R.; Kobayashi, H.; Tamari, N.; Tsurekawa, S.; Watanabe, T. & Kato, K. (July 2004). Effect of doping elements on the friction and wear properties of SiC in unlubricated sliding condition. *Wear*, Vol. 257, No. 1-2, pp. 89 - 96, ISSN 0043-1648
- Niihara, K.; Kusunose, T.; Kohsaka, S.; Sekino, T. & Choa, Y.H. (1999). Multi-Functional Ceramic Composites through Nanocomposite Technology. *Key Engineering Materials*, Vol. 161-163, No. , pp. 527-534, ISSN 1013-9826
- Piermarini, G.J. (2008). Diamond Anvil Cell Techniques, In: *Static Compression of Energetic Materials*, S.M. Peiris & G.J. Piermarini, (Eds.), 1-74, Springer, ISBN 978-3-540-68146-5, Berlin Heidelberg, Germany
- Prikhna, A. (February 2008). High-pressure apparatuses in production of synthetic diamonds (Review). *Journal of Superhard Materials*, Vol. 30, No. 1, pp. 1-15, ISSN 1063-4576
- Richerson, D.W. (2004). Advanced ceramic materials, In: *Handbook of advanced materials*, J.K. Wessel, (Ed.), 65-88, John Wiley & Sons, Inc., ISBN 0-471-45475-3, Hoboken, New Jersey, USA
- Sajgalík, P.; Hnatko, M.; Lofaj, F.; Hvizdos, P.; Dusza, J.; Warbichler, P.; Hofer, F.; Riedel, R.; Lecomte, E. & Hoffmann, M.J. (April 2000). SiC/ Si_3N_4 nano/micro-composite -- processing, RT and HT mechanical properties. *Journal of the European Ceramic Society*, Vol. 20, No. 4, pp. 453 - 462, ISSN 0955-2219
- Suyama, S.; Kameda, T. & Itoh, Y. (March-July 2003). Development of high-strength reaction-sintered silicon carbide. *Diamond and Related Materials*, Vol. 12, No. 3-7, pp. 1201 - 1204, ISSN 0925-9635
- Takahashi, K.; Jung, Y.; Nagoshi, Y. & Ando, K. (June 2010). Crack-healing behavior of $\text{Si}_3\text{N}_4/\text{SiC}$ composite under stress and low oxygen pressure. *Materials Science and Engineering: A*, Vol. 527, No. 15, pp. 3343 - 3348, ISSN 0921-5093
- Tanaka, H.; Hirotsaki, N. & Nishimura, T. (December 2003). Sintering of Silicon Carbide Powder Containing Metal Boride. *Journal of the Ceramic Society of Japan*, Vol. 111, No. 1300, pp. 878-882, ISSN 0914-5400
- Xu, C. (2005). Effects of particle size and matrix grain size and volume fraction of particles on the toughening of ceramic composite by thermal residual stress. *Ceramics International*, Vol. 31, No. 4, pp. 537 - 542, ISSN 0272-8842

- Yamada, K. & Kamiya, N. (March 1999). High temperature mechanical properties of Si_3N_4 - MoSi_2 and Si_3N_4 - SiC composites with network structures of second phases. *Materials Science and Engineering A*, Vol. 261, No. 1-2, pp. 270 - 277, ISSN 0921-5093
- Yeomans, J. (2008). Ductile particle ceramic matrix composites--Scientific curiosities or engineering materials?. *Journal of the European Ceramic Society*, Vol. 28, No. 7, pp. 1543-1550, ISSN 0955-2219

Part 2

Silicon Carbide: Electronic Devices and Applications

SiC Devices on Different Polytypes: Prospects and Challenges

Moumita Mukherjee

*Centre for Millimeter-Wave Semiconductor Devices and Systems (CMSDS), Institute of
Radio Physics and Electronics, University of Calcutta, West Bengal,
India*

1. Introduction

Imaging, broadband communication and high-resolution spectroscopic applications in the mid- and far-infrared regions have underscored the importance of developing reliable solid-state sources operating in the frequency range from 0.3 Terahertz to 10.0 Terahertz (1000 to 30 μm wavelength). Recent studies suggest that Terahertz (THz) interactions can enable a variety of new applications on the wide range of solids, liquids, gases, including polymers and biological materials such as proteins and tissues. Compared to microwave and MM-wave, far-infrared or THz frequency range has significant reduction in the antenna sizes and greater communication bandwidth. Commercial applications comprise thermal imaging, remote chemical sensing, molecular spectroscopy, medical diagnosis and surveillance. Military applications comprise night vision, rifle sight enhancement, missile tracking, space based surveillance and target recognition. Despite the technical advantages, the major challenge today in THz technology is the development of a portable high-power THz source. During the past few years, significant efforts were devoted to search of reliable semiconductor sources at the THz regime.

Recently, several solid-state physics research group, the world over, are focusing their research attention in developing semiconductor devices those can generate THz oscillations. A promising concept for THz sources utilizing plasma waves in a gated 2D electron gas (2DEG) was proposed in the early 90-ties. Thereafter, recent experimental observations and theoretical studies have revealed that resonant detection and coherent emission of THz radiation can be effectively induced by excitation of plasma oscillations in the electron channel of Field Effect Transistors (FET). Another promising THz source is the Quantum Cascade Laser (QCL). QCL were first demonstrated in 1994 based on a series of coupled quantum wells constructed using MBE. Although in the mid-infrared region ($5 < \lambda < 10 \mu\text{m}$) these devices have been in development for more than ten years, it is only recently that the first THz laser has been reported at 4.4 THz. These lasers are made from 1,500 alternating layers of GaAs and AlGaAs and have produced 2.0 mW of peak power (20.0 nW average power). Advances in output power and operating wavelength continue at a rapid pace. Low Temperature Grown (LTG) GaAs photo-mixer can provide up to around $2 \mu\text{W}$ of output power at the frequency of 1.0 THz and their operation frequency can be as high as 5 THz. Of the several available terahertz source technologies, those based on the difference frequency technique are very promising, as they can produce a relatively high power terahertz beam

over the frequency from 100 GHz to 3.5 THz, which is tunable. Recently THz output power level exceeding 10 mW (occasionally 100 mW) at the frequency of around 1.0 THz has been demonstrated with a special type of electro-optically tunable compact terahertz source.

It is clear from the brief review that the commercially available recent THz sources are complex and bulky. It will be more useful if THz frequency oscillation can be generated from a small sized single solid state source. Among all the two terminal solid state sources, IMPATT diodes have already been established as the most efficient semiconductor sources that can generate highest MM-wave power. Conventional Si and GaAs based IMPATT diodes were found to be reliable but they are limited by power and operating frequencies due to the limitation imposed by their inherent material parameters. WBG semiconductor such as Silicon Carbide (SiC) has received remarkable attention during the last decade as a promising device material for high-temperature, high-frequency and high- power device applications due to its high thermal conductivity, high saturation velocity of charge carriers and high critical field for breakdown. SiC exhibits higher value of thermal conductivity (3-10 times), critical electric field (5-10 times) and saturated carrier velocity (~ 2 times) compared to the conventional semiconductor materials such as Si and GaAs. For a better comparison of the possible high-power, high-frequency performances of these materials, some commonly knew FOMs (Figure of Merit). Taking *Keyes'* and *Johnson's* FOM for Si as unity, the *Keyes'* and *Johnson's* FOM for GaAs are 0.45 and 7.1, respectively, while those for SiC are 5.1 and 278. From the FOMs for high-frequency and high-temperature operation, SiC appears to be superior to both Si and GaAs.

SiC crystallizes in numerous polytypes. The three most common polytypes are the cubic phase, 3C and the hexagonal phases, 4H, and 6H-SiC. The cubic structure, referred to as β -SiC, is expected to have the highest saturation drift velocity. However, the energy bandgap of the 3C phase is significantly smaller than either the 4H or 6H phases, implying a lower breakdown voltage. In addition to this, β -SiC is difficult to grow in a mono-crystalline form due to its meta-stability resulting in a solid-state transformation into an alpha (α)-structure. Due to difficulty in the growth of β -SiC, most of the efforts for producing bulk mono-crystalline growth have concentrated on the more easily prepared α -polytypes, referred to as 4H-SiC and 6H-SiC. Thus due to the availability and quality of reproducible single-crystal wafers in these polytypes, 4H- and 6H-SiC-based electronic devices presently exhibit the most promise. The energy band gap of >3.0 eV in hexagonal (4H and 6H) SiC enables the devices based on such materials, to support peak internal electric field (E_c) about ten times higher than Si and GaAs. Higher E_c increases the breakdown voltage, an essential criterion for generation of high output power in a device. Higher E_c also permits incorporation of higher doping level in the depletion layer of the device, which in turn, reduces the width of the active region. Thus the device layers can be made very thin. The transit times of carriers become very small in a thin layered semiconductor if the carrier drift velocities are high. The intrinsic material parameters of hexagonal SiC are thus favorable for the realization of high-power devices.

2. History of IMPATT devices

A device possesses negative resistance when the A.C. current lags the voltage by a phase angle between 90° and 270° . The negative resistance in an avalanche diode occurs as a result of 180° phase difference between the A.C. current and voltage in a p-n junction reverse-biased to avalanche breakdown. The phase difference is produced by the time delay

inherent in the build-up of the avalanche current, coupled with the phase delay developed as the carriers traverse the depletion layer. The word IMPATT stands for “impact ionization avalanche transit time”. IMPATT diodes employ impact-ionization and transit-time properties of semiconductor structures to produce negative resistance at microwaves and millimeter waves frequencies. The negative resistance arises from two delays which cause the current to lag behind the voltage. One is the ‘avalanche delay’ caused by finite buildup time of the avalanche current; the other is the ‘transit-time delay’ caused by the finite time required by the carriers to cross the “drift” region. When these two delays add up to half-cycle time, the diode electronic resistance is negative at the corresponding frequency. IMPATT devices have emerged as most powerful solid-state devices for generation of high CW and pulsed power at millimeter wave frequencies. These devices also provide high oscillator output power with high DC to RF conversion efficiency in Silicon Monolithic Millimeter Wave Integrated Circuits (SIMMWIC).

In a practical mm-wave IMPATT oscillator the diode is embedded in a circuit which is resonant at a frequency within the negative-resistance band of the device. The oscillation is initiated by random noise fluctuations, which grows in a negative-resistance medium at the resonant frequency of the circuit. In practice the device has to be mounted either in a coaxial line or in a section of wave-guide or in a micro strip circuit.

In 1954, Schokley first studied the microwave negative resistance from the transit time delay of an electron bunch in a forward biased p-n junction diode. Afterwards, in 1958, W. T. Read showed that the finite delay between an applied RF voltage and the external current is due to the generation of carriers in a reverse biased p+n i n+ diode under avalanche breakdown and the subsequent drift of carriers through the depletion layer. This would lead to a negative resistance of the device at microwave frequencies. In 1965, Johnston et al experimentally observed microwave oscillation from a simple p+nn+ device. At the same time Lee et al also reported oscillation at microwave frequency from a Read diode. Small signal analysis of avalanche diodes of general doping profiles was carried out by T. Misawa, who showed that the negative resistance occurs in any reverse biased p-n junction diode of arbitrary doping profile.

In 1968 Lee et al first reported resonant-cap mounted IMPATT oscillator together with a simplified equivalent circuit. Their report showed CW power of 100 mW at 50 GHz with an overall efficiency of 2 percent. In the same year Misawa [9] reported millimeter-wave oscillation from silicon avalanche diode with abrupt junction mounted in a resonant-cap waveguide circuit. His report shows a CW output power in the range of 23 to 150 mW for the 50 to 84 GHz frequency range with a maximum efficiency of 3 percent. In 1970, Misawa and Kenyon reported mechanical tuning characteristics of resonant-cap IMPATT oscillators at millimeter-wave frequencies. Since then, fast advances in semiconductor technology, rapid advances have been made towards further development of various IMPATT diode structures as well as IMPATT based oscillators and amplifiers to meet the to-days high power requirement in higher frequency band. In recent years lot of interest has been created regarding IMPATT diodes and oscillators based on SiC as a semiconducting material. Considerable advancement regarding device physics, device fabrication and the optimum circuit design for IMPATT oscillator and amplifiers has pushed the frequency range to mm and sub mm regions which has resulted in the emergence of IMPATTs the most powerful solid state devices for generation of microwave and mm wave power.

To understand the operation and performance of IMPATT devices and oscillators knowledge of the basic IMPATT phenomena is required and briefly discussed in the following section. To build an IMPATT oscillator the device has to be mounted in a suitable microwave/mm-wave circuits. The performance of the oscillator strongly depends not only on the device but also on the circuit in which the device is embedded. The various microwave/mm-wave circuits that are being widely used to construct IMPATT oscillators have been reviewed briefly.

A brief review of the fundamental physical processes involved in IMPATT action followed by a review of the various IMPATT structures and oscillators will be presented in this section. The factors, which determine the avalanche delay and the transit time delay for high frequency operation of IMPATT will also be briefly discussed.

2.1 High field properties of charge carriers in IMPATT devices

The different scattering interactions between the charge carriers and the lattice lead to the emission of both acoustic and optical phonons which give rise to the saturation of carrier's drift velocity in semiconductors which is one of the fundamental physical phenomenon involved in IMPATT action.

Drift velocity of charge carriers has been observed to be linear upto the electric field 10^4 V.m⁻¹ and it reaches a scattering limited value independent of the electric field when the field is very high ($>10^6$ V.m⁻¹). At low values of electric field (E), which the principal scattering phenomenon is acoustic phonon, the drift velocity (v_d) of charge carriers in semiconductor varies as :

$$v_d = \mu_o E \quad (1)$$

Where μ_o is the low field mobility and can be expressed as,

$$\mu_o = \frac{q \langle v^2 \tau_o \rangle}{m^* \langle v^2 \rangle} \quad (2)$$

Where q is the charge of the electron, m^* is the effective mass of the carrier, τ_o is the relaxation time and v is the carrier velocity. The brackets in the above expression indicate Maxwellian average.

In the low field region (Ohmic region), the rate of energy through acoustic phonon collision is small and the scattering is isotropic. Assuming energy distribution to be Maxwellian at lattice temperature T and a constant mean free path, the low field mobility is given by,

$$\mu_o = \frac{4ql_a}{3(2\pi m^* KT)^{0.5}} \quad (3)$$

Where l_a is the mean free path for acoustic phonon collision and K is the Boltzman constant. At high electric field ($>10^6$ V.m⁻¹) high-energy electrons (hot electrons) interact more strongly with lattice and there is a departure from the linear dependence of drift velocity with the electric field. The thermal equilibrium is lost because the rate of energy gained from the field is more than the amount lost to the crystal lattice through low energy acoustic phonon collision. At this high field, emission of optical phonons is a dominant phenomenon, which are quanta of high frequency thermal vibrations of the lattice in which

two face centered cubic sub lattices of the crystal vibrate in the opposite directions. Excitation of the optical phonons are possible when the electrons gain a minimum energy equal to optical phonon energy or Ramam energy $\varepsilon_{op} = (\frac{h}{2\pi})\omega_o$, where ω_o is the angular frequency for optical mode of vibration and h is the Planck's constant. The values of ε_{op} for GaAs and Silicon are obtained from neutron scattering experiments [18-21] and are of the order of 0.035 eV and 0.063 eV respectively. At a high field ($>10^7$ V.m⁻¹), the average carrier kinetic energy exceeds the optical phonon energy ε_{op} and thereby a transfer of energy to the lattice via optical phonon is created and reaches a scattering limited average drift velocity independent of the electric field and is given by,

$$v_d = \left[\frac{8\varepsilon_{op} \tanh(\varepsilon_{op} 2KT)}{3\pi m^*} \right]^{0.5} \quad (4)$$

Drift velocity of carriers in Si at different field has been accurately determined by a number of workers using the time of flight technique and the space charge resistance technique [23-26]. The time of flight technique provides direct measurement of the drift velocity of both majority and minority carriers accurately. In 1967, Duh and Moll measured the carrier drift velocity in Si at high electric field ($> 10^7$ V.m⁻¹) and it shows that a slow increase of v_d in the field range $(2.6 - 4.35) \times 10^7$ V.m⁻¹. At a high field (2×10^7 V.m⁻¹) impact ionization becomes an important scattering mechanism in addition to optical phonon scattering. At such high electric fields the energy gained by the electrons from the electric field is lost mostly in ionizing collisions that results an electron-hole (e-h) pair. According to Roy and Ghosh, at the ionizing fields the drift velocity $v(E)$ is expressed by

$$v(E) = \frac{v_s}{\left[\left(1 + \frac{l_{op}}{l_i}\right) \left(1 + \frac{\varepsilon_i}{l_i q E}\right) \right]^{0.5}} \quad (5)$$

Where l_{op} and l_i is the mean free path for optical phonon collision and ionizing collision respectively, v_s is the saturated drift velocity, ε_i is the threshold energy for ionizing collision, q is the charge of electron and E is the electric field. This theoretical investigation shows that the drift velocity for electrons in Si passes through a maximum before attaining saturation.

Danda and Nicolet give an expression which fits well with the experimental results for Si for field dependence of carrier drift velocity in the following form:

$$v(E) = v_s \left[1 - \exp\left(-\frac{\mu_o E}{v_s}\right) \right] \quad (6)$$

Where $v(E)$ is the carrier drift velocity at field E . The values of low field mobility (μ_o) of carriers can be obtained from the slopes of v - E curves at low field.

2.2 Impact ionization

At very high electric field ($> 10^7$ V.m⁻¹) electrons (minority carriers) gain energy at a faster rate than they can lose through the emission of optical phonon in a reverse biased p-n junction. As

a result, it collides with bound electron in the valence band and excites them into the conduction band, creating an e-h pair and the phenomenon is termed as **impact ionization**. Important parameters for impact ionization are the **ionization threshold energy** E_t (i.e. minimum energy required to cause an ionizing collision) and the **ionization rate** α (i.e. average number of ionizing collisions by the carrier in traversing unit distance in the direction of electric field). From energy conservation principle, E_t should be equal to the band gap energy (E_g). The values of E_g for Si and GaAs at room temperature are 1.10eV and 1.43eV respectively. If both energy and momentum conservation are taken into account, the threshold energy E_t should be equal to $1.5E_g$ for parabolic band structure having the same effective masses for the carrier. If the electron energy exceeds E_t , emission of optical phonons or ionizing collision may produce an e-h pair. The probability of either types of collision depends on the mean free path for optical collision (l_{op}) and on the mean free path for ionizing collision (l_i). The relative probability of second collision being an ionizing collision is $l_{op} l_i$. The ionization rate (α) is a function of l_{op} , l_i , E_t and E_g . In 1954, Wolff first assumed that the probability of ionizing collision is much greater than the optical phonon collision and is valid at high electric field. However, Shockley derive an expression at low field, such that electrons acquire ionization threshold energy E_t and then produces an ionizing collision in the first attempt without suffering a single optical phonon collision which is given by,

$$\alpha = \frac{qE}{r\epsilon_{op}} \exp\left(-\frac{E_t}{qEl_r}\right) \quad (7)$$

The most important theoretical study of field-dependence of ionization rate was carried out by G. A. Baraff, by solving Boltzman transport collision equation in terms of a space and energy dependent collision density, considering the acoustic phonon, optical phonon and ionizing collision. The values of ionization rate ' α ' can be obtained from universal Baraffs plot for any semiconductor for which the parameters l_{op} , E_t and ϵ_{op} are known.

2.3 Avalanche breakdown

Under typical doping profile and reverse bias condition of a p-n junction diode, the total voltage drop occurs across a very thin space charge depletion region. Thermally generated electrons and holes (minority carriers) in the p and n regions diffusing towards the n and p edges of the depletion layer results a small reverse saturation current in the reverse bias condition. A single minority carrier experiences there a very high electric field and creates e-h pair by impact ionization. These generated electron and hole produces additional e-h pair as they further drift toward n and p sides.

If a single electron yield N number of e-h pairs while drifting across the avalanche region of length x_a then,

$$N = \int_0^{x_a} \alpha(E) dx \quad (8)$$

Equal ionization rates for electrons and holes generate N^2 number of e-h pairs and the process continues and this is known as avalanche multiplication. Therefore, the total current after avalanche multiplication becomes,

$$J = J_s(1 + N + N^2 + \dots) = \frac{J_s}{1 - N} = MJ_s \quad (9)$$

Where J_s is the initial reverse saturation current and M is called the multiplication factor. The current multiplication factors M_n and M_p for electrons and holes are given by J/J_{ns} and J/J_{ps} respectively. A small amount of reverse saturation current (J_{ns} , J_{ps}) multiplied by very high multiplication factor grows to a very high current and this phenomenon is known as avalanche breakdown. At breakdown M and J tends to infinity and then,

$$N = \int_0^{x_g} \alpha(E) dx = 1 \quad (10)$$

Considering the carrier multiplication process initiated by both electrons and holes at the two edges of the depletion layer and unequal ionization rates of charge carriers, Lee et al derived the generalised breakdown condition of the p-n junction. In Fig. 1(a), J_{ps} and J_{ns} are the saturation currents for holes and electrons entering the depletion layer of a reverse biased p-n junction at $x = -x_1$ and $x = x_2$ respectively. The increase of electron and hole current at x is equal to the charges generated per second in distance δx may be written as,

$$\delta J_n = -\delta J_p = \alpha_n J_n \delta x + \alpha_p J_p \delta x \quad (11)$$

Therefore the continuity equations for electrons and holes can be written as,

$$\frac{\partial J_n}{\partial x} = \alpha_n J_n + \alpha_p J_p \quad (12)$$

$$\frac{\partial J_p}{\partial x} = -\alpha_n J_n - \alpha_p J_p \quad (13)$$

Since the diffusion current is very small compared to the drift current, then the hole drift current $J_p = qp v_p$ and the electron drift current $J_n = qn v_n$, where v_p and v_n are the saturated drift velocities for holes and electrons, n and p are the carrier density for electrons and holes. Thus the total drift current density $J = (J_n + J_p)$ is independent of x .

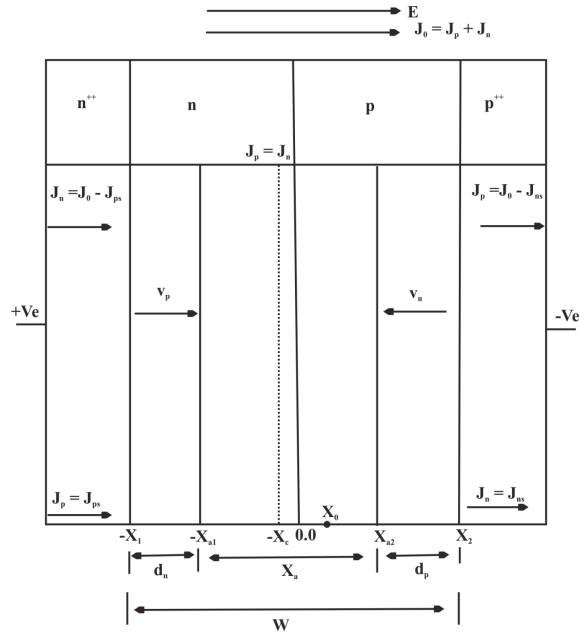
Eliminating J_p from equation (11) one obtains,

$$\frac{\partial J_n}{\partial x} = -(\alpha_n - \alpha_p) J_n = \alpha_n J \quad (14)$$

Using the boundary conditions $J_n(x=0) = J_{ns}$ and $J_n(x=W) = J - J_{ps}$ and using the

integrating factor $\exp\{-\int_0^x (\alpha_n - \alpha_p) dx\}$ the above equation reduces to

$$\begin{aligned} J_s - J_{ps} + J_{ps} \exp\left\{-\int_0^W (\alpha_n - \alpha_p) dx\right\} &= J \left[1 - \int_0^W \alpha_n \exp\left\{-\int_0^x (\alpha_n - \alpha_p) dx'\right\} dx\right] \\ 1 - k + k \exp\left\{-\int_0^W (\alpha_n - \alpha_p) dx\right\} &= M \left[1 - \int_0^W \alpha_n \exp\left\{-\int_0^x (\alpha_n - \alpha_p) dx'\right\} dx\right] \end{aligned} \quad (15)$$



X_0 = position of field maximum (E_0), X_c = position of avalanche centre ($J_p = J_n$),
 W = total active layer width, d_{np} = drift layer width for electrons and holes,
 X_a = avalanche layer width, J_a = total current density

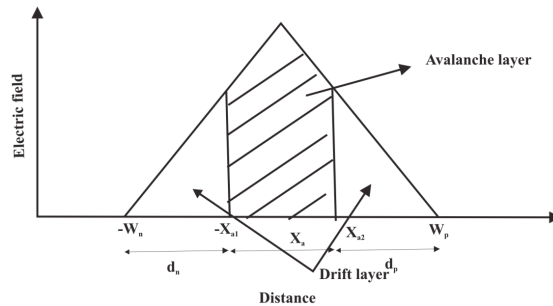
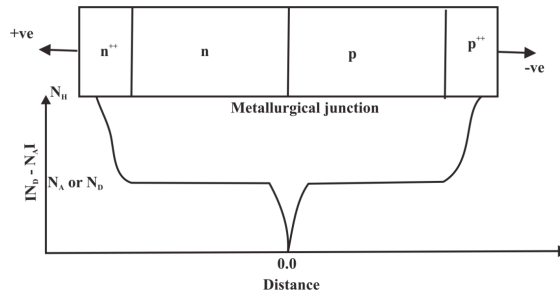


Fig. 1. (a) Avalanche multiplication; (b) carrier current profile and (c) Electric field profile in the depletion region of a reverse biased p-n junction.

Where $k = \frac{J_{ps}}{J_s}$, $M = \frac{J}{J_s}$, and $J_n = J_{ns} + J_{ps}$

Where M is the multiplication factor and J_s is the total reverse saturation current. Thus

$$M = [1 - k + k \exp\{-\int_0^W (\alpha_n - \alpha_p) dx\}] / [1 - \int_0^W \alpha_n \exp\{-\int_0^x (\alpha_n - \alpha_p) dx'\} dx]$$

$$\frac{1}{M} = \frac{1}{\xi} [1 - \int_0^W \alpha_n \exp\{-\int_0^x (\alpha_n - \alpha_p) dx'\} dx] \quad (2.4.8)$$

Where $\xi = 1 - k + k \exp\{-\int_0^W (\alpha_n - \alpha_p) dx\}$

In a similar way using the boundary condition, $J_p(x=0) = J - J_{ns}$ and $J_p(x=W) = J_{ps}$ we get,

$$\frac{1}{M} = \frac{\exp\{-\int_0^W (\alpha_n - \alpha_p) dx\}}{\xi} [1 - \int_0^W \alpha_p \exp\{\int_0^x (\alpha_n - \alpha_p) dx'\} dx] \quad (16)$$

Multiplying equation (15) by (1-k) and equation (16) by k and adding one obtain,

$$1 - \frac{1}{M} = \frac{1-k}{\xi} \int_0^W \alpha_n \exp\{-\int_0^x (\alpha_n - \alpha_p) dx'\} dx +$$

$$\frac{k}{\xi} \exp\{-\int_0^W (\alpha_n - \alpha_p) dx\} \cdot \int_0^W \alpha_p \exp\{\int_0^x (\alpha_n - \alpha_p) dx'\} dx \quad (17)$$

Now, M may be written as,

$$2M = (1-k)M_n + kM_p \text{ where } M_n = \frac{J}{J_{ns}} \text{ and } M_p = \frac{J}{J_{ps}}$$

When avalanche breakdown occurs i.e. M tends to infinity for a mixture of electron and hole injection, one obtain,

$$\frac{1-k}{\xi} \int_0^W \alpha_n \exp\{-\int_0^x (\alpha_n - \alpha_p) dx'\} dx +$$

$$\frac{k}{\xi} \exp\{\int_0^W (\alpha_n - \alpha_p) dx\} \cdot \int_0^W \alpha_p \exp\{-\int_0^x (\alpha_n - \alpha_p) dx'\} dx = 1 \quad (18)$$

In case of pure electron or hole injection i.e. in which multiplication is initiated purely by electrons ($k=0, J_{ps}=0$) or purely by holes ($k=0, J_{ns}=0$), the breakdown condition reduces to

$$1 - \frac{1}{M_n} = \int_0^W \alpha_n \exp\left\{-\int_0^x (\alpha_n - \alpha_p) dx'\right\} dx = 1 \quad (2.4.12a)$$

$$1 - \frac{1}{M_p} = \int_0^W \alpha_p \exp\left\{\int_0^x (\alpha_n - \alpha_p) dx'\right\} dx = 1 \quad (19)$$

For $\alpha_n = \alpha_p$, the above equation reduces to $N = \int_0^{x_i} \alpha(E) dx = 1$.

Therefore, the above equation governs the avalanche breakdown, the static and dynamic properties of IMPATT diodes. The enhancement of mobile space charge density modify the electric field profile, breakdown voltage and the depletion layer width, because the ionization rates get modified at various points in the space charge layer.

2.4 Basic IMPATT phenomena

The operation of an IMPATT device is based on two basic physical mechanisms: one is the **avalanche multiplication** caused by **impact ionization** [4] and the other is the **finite transit time** required by the charge carriers to **cross the depletion layer** with saturated drift velocity. The avalanche process turns out to be an inductive process causing a phase delay between the applied r.f. voltage and the generated r.f. current. The transit-time process adds an extra phase delay. Thus the device exhibits a high-frequency negative resistance when the combined phase delay due to the avalanche process and the finite transit time of the drifting carriers lie between 90° and 270° .

The IMPATT phenomena were studied by Read and Misawa by considering two different devices models. Read considered an $n^+p\text{-}i\text{-}p^+$ diode structure and assumed that the spatial extent of avalanche zone is negligibly small. But Misawa in his $p\text{-}i\text{-}n$ avalanche diode structure assumed an extended avalanche zone. However, in practical IMPATT structure like SDR, DDR etc, the avalanche zone is neither too thin like Read diode nor too wide like Misawa diode but it is intermediate between the two having finite avalanche zone width. In section 2.5.1 mechanisms of IMPATT mode of operation has been discussed with reference to (a) Read and (b) Misawa diodes and in the next section and a brief overview of various practical IMPATT diode structures will be presented.

Several authors including Read and Misawa have carried out analysis of microwave/mm-wave properties for different IMPATT structures and have found that the active diode impedance when the device generates microwave/mm-wave can be represented by a high frequency negative resistance in series with a capacitance. The magnitude of the negative resistance being much smaller than the capacitive impedance, the device is mainly capacitive.

2.5 Mechanism of IMPATT mode of operation in (i) read diode and (ii) misawa diode

2.5.1 Read diode

A schematic diagram of Read diode structure $n^+p\text{-}i\text{-}p^+$ along with its doping profile and electric field distribution at reverse biased to avalanche breakdown is shown in Fig. 2. In the Read structure the superscript plus sign denotes very high doping and the i or v refers to

intrinsic material. The device consists essentially of two regions; One is the narrow p-region at which avalanche multiplication occurs. This region is also called the **high field region or the avalanche region**. The other is the i (or v) region through which the generated holes must drift while moving towards the p⁺ contact. This region is also called the **intrinsic region or the drift region**. When the reverse biased voltage is well above the punch through or breakdown voltage, the space between the n⁺p junction and the i-p⁺ junction happens to be the space-charge region. Carriers (holes) moving in the high field near the n⁺-p junction acquire energy to knock valance electrons into the conduction band, thus producing hole-electron pairs. The rate of pair production, or avalanche multiplication, is a sensitive nonlinear function of the field. By proper doping, the field can be given a relatively sharp peak so that avalanche multiplication is confined to a very narrow region at the n⁺-p junction. The electrons move in to the n⁺- region and the holes drift through the space charge region to the p⁺- region with a constant velocity v_d (called the saturated drift velocity). The transit time of a hole across the drift region (i.e. i-region of length L) is given by $\tau = L / v_d$.

The phenomenon of negative resistance in Read diode can be understood with reference to Fig. 3. In actual practice, to form oscillator, the diode is mounted in a microwave/mm-wave resonant circuit. An a.c. voltage can be maintained at a given frequency in the circuit thus the total voltage across the diode is the sum of the d.c. and a.c. voltages, mathematically: $V_T(t) = V_{DC} + V_D \sin \omega t$, and the form of this total diode voltage is shown in Fig. 3(a). This total voltage causes breakdown at the n⁺-p junction during the positive half cycle of the a.c. voltage when V_T is above the breakdown value, and the carrier current (i.e. the hole current in this case) $I_0(t)$ generated at the n⁺ p junction by the avalanche multiplication grows exponentially with time while the voltage is above the critical (i.e. breakdown) value. During the negative half cycle, when V_T is below the breakdown voltage for the diode, the current $I_0(t)$ decays exponentially to a small steady state value. The carrier current $I_0(t)$ is the current at the junction only and is in the form of a pulse of very short duration as shown in Fig. 3(b). Therefore, the carrier current $I_0(t)$ reaches its maximum in the middle of the a.c. voltage or lags by 90° behind the said a.c. voltage. The direction of the electric field is such that the generated holes are injected into the space-charge region towards the negative terminal. An equal number of generated electrons move to the left, back into the n⁺- contact to maintain space charge neutrality. As the injected holes traverse the drift space, they induce a current $I_e(t)$ in the external circuit which is approximately a square wave as shown in fig.3(c). The current $I_e(t)$ flows in the external circuit for a time τ during which the holes are moving across the space-charge region. Thus, on the average, the external current $I_e(t)$ due to the moving holes is delayed by $\tau/2$ or 90° relative to the pulsed carrier current $I_0(t)$ generated at the n⁺-p junction. Because the carrier current $I_0(t)$ is already delayed by 90° relative to the a.c. voltage, the external current $I_e(t)$ is then delayed by as a total of 180° relative to the applied a.c. voltage. In general, a device exhibits negative resistance at its terminals when the a.c. current flowing through it lags the a.c. voltage by a phase angle which lies between 90° and 270°.

2.5.2 Misawa diode

The device structure, doping profile and electric field distribution of Misawa diode i.e. a p-i-n diode reverse biased to avalanche breakdown is shown in Fig. 4 (a-c). Misawa assumed an

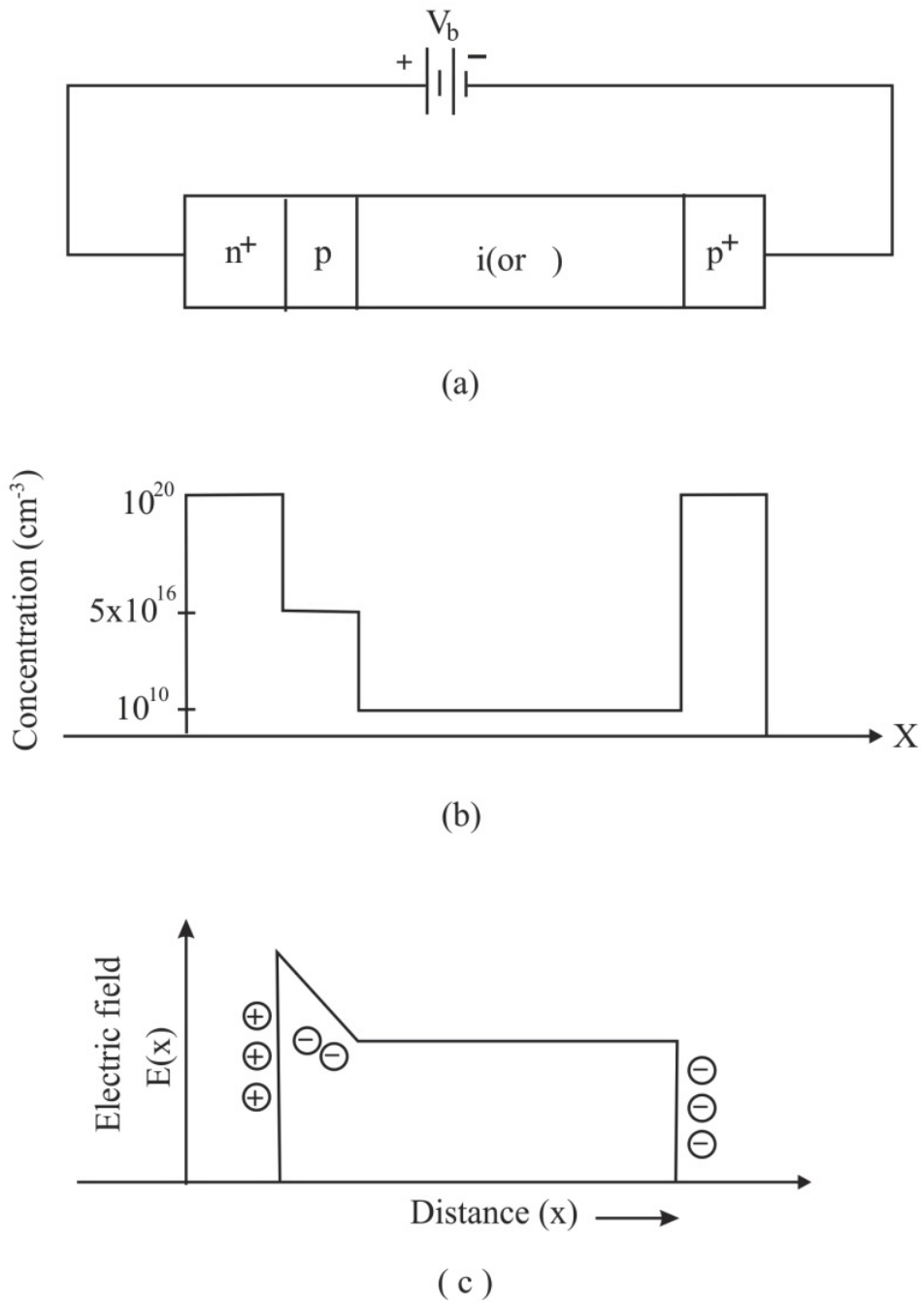
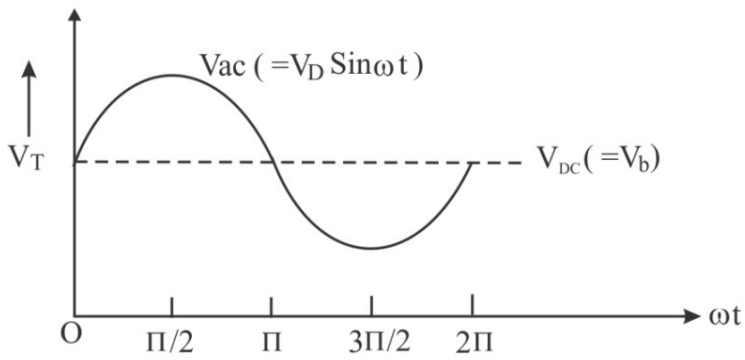
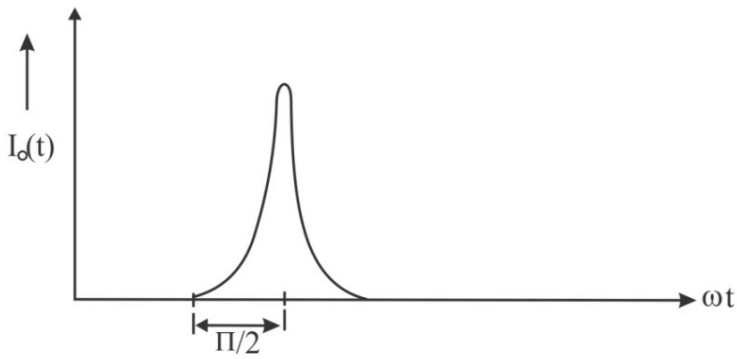


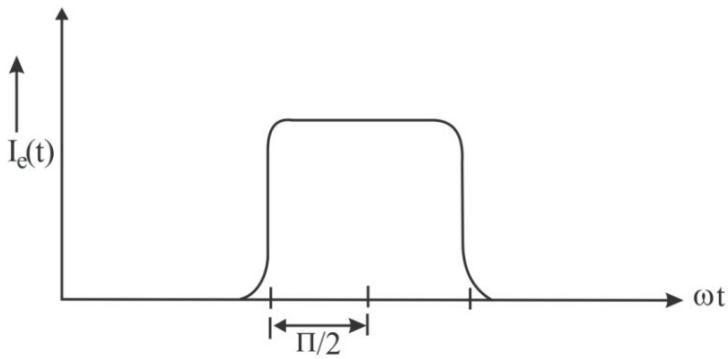
Fig. 2. (a) Read (n^+p-i-p^+) structure (b) Doping profile and (c) Electric field distribution.



(a)



(b)



(c)

Fig. 3. Voltage and currents in Read diode, (a) Total diode voltage, (b) Carrier current generated at n^+ -p junction by avalanche multiplication and (c) Current induced in the external circuit.

uniform avalanching i.e. the field remains high enough for avalanche multiplication of charge carriers to take place throughout the active region (i.e. i-region). The origin of negative resistance can be understood as follows. The electrons and holes enter the i-region from the p- and n- regions respectively Fig. 4 (a) and they move with saturated velocities and generates holes and electrons simultaneously in this region. Now let us consider a fluctuation in the electron density (\tilde{n}_0) in the i-region which will be moving towards the x-direction with saturated drift velocity being carried by the electrons moving is the same direction Fig. 4(d). The electric field wave (\tilde{E}) caused by this perturbation in the electron density lags the electron density wave by 90° . Now the generation rate of electron-hole pairs is larger both when the electric field is stronger and when there are more carriers. Therefore, in this case of an electron density perturbation the generation rate peaks somewhere between the place where the field is strongest and the place where the density is largest. This means that the generation rate (G) leads the electron density wave by less than 90° . It is to be noted that since the d.c. field is in negative x-direction, the field becomes strongest at its negative peak. The increased generation rate gives rise to an excess electron density ($\Delta\tilde{n}$) which lags the rate by 90° . Thus the resultant electron density (\tilde{n}) gives a current (\tilde{j}_n) which lags the field by more than 90° . The current due to hole density wave also lags the field by more than 90° . The situation is shown in Fig. 4 (e). Thus the current generated in the device lags the field by more than 90° and hence the device exhibits negative resistance property.

2.6 Practical IMPATT diode

The Read and Misawa diodes that have been discussed are idealized IMPATT structures. But practical IMPATT diodes which have been fabricated and are in wide use are intermediate between the two in the sense that the avalanche zone is well defined having a finite width neither too thin nor too wide. The charge is injected from a well defined avalanche zone into the drift zone approximately 90° behind the r.f. voltage and then the injected charge travels with saturated drift velocity in the drift region. The practical Single Drift Region (SDR) and Double Drift Region (DDR) IMPATT which are now commonly used belong to this category. Diodes have been fabricated from various semiconductor materials i.e. Germanium, Silicon, Gallium Arsenide, Indium Phosphide and recently from Silicon Carbide.

2.7 Impedance properties and equivalent circuit of IMPATT diode

A knowledge of the nature of device impedance is quite important to understand the mechanism of microwave/mm-waves generation by IMPATT diodes. Also an insight into the impedance properties of the device helps one to choose the microwave/mm-wave circuit necessary to construct oscillators with these devices. Several authors including Read, Gilden and Hines have analyzed the small-signal impedance properties of Read type IMPATT diode. Misawa has calculated the small signal impedance of the p-i-n avalanche diode both analytically and numerically. Gummel and Scharfetter extended the small signal analysis of Gilden and Hines and obtained small-signal admittance plots for a more realistic Read structure. Also Scharfetter and Gummel carried out large-signal numerical solution for Si Read diode and obtained the diode admittance as a function of frequency and r.f. voltage amplitude.

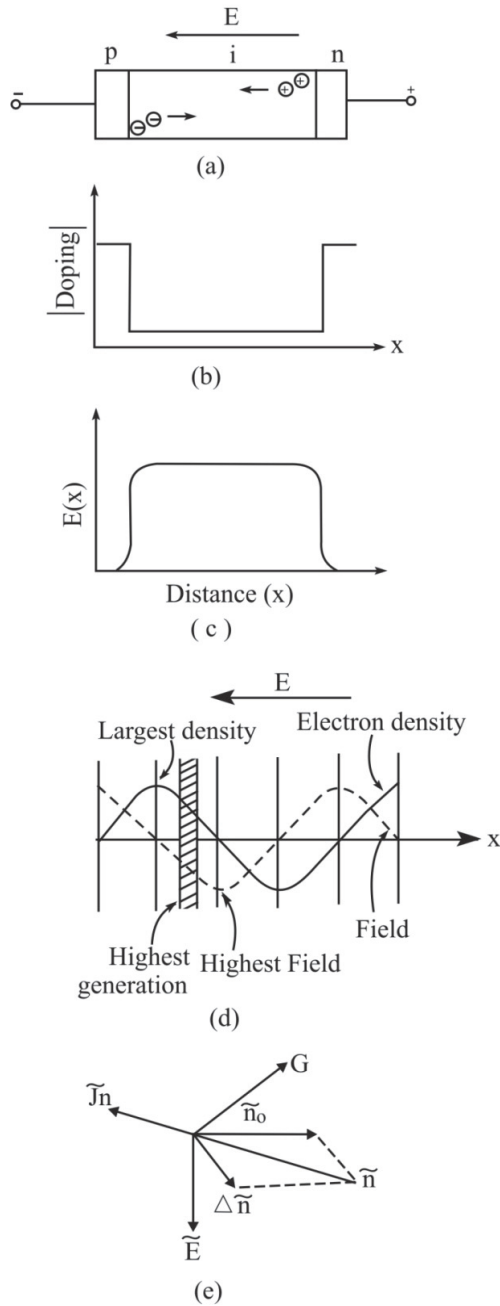


Fig. 4. (a) Misawa diode (p-i-n) structure, (b) Doping profile (c) Electric Field distribution (d) Electric field and generated electron density wave and (e) Phase diagram (current and field)

Gilden and Hines derived an expression for the diode terminal impedance in a Read type structure by assuming a thin avalanche zone where space charge and signal delay is negligible and a wide drift zone where no carriers are formed but where space-charge and transit time effects are significant. Denoting Z_a as avalanche zone impedance, Z_d as drift zone impedance and R_s as the passive resistance of the inactive zone, Gilden and Hines obtained the following expression for the terminal impedance

$$Z = R_s + Z_a + Z_d = R_s + \frac{1}{j\omega C_a} \left(1 - \frac{\omega_a^2}{\omega^2}\right)^{-1} + \frac{1}{\omega C_d} \left\{ \left(1 - \frac{\omega^2}{\omega_a^2}\right)^{-1} \left(\frac{1 - \cos\theta}{\theta}\right) \right\} + \frac{1}{j\omega C_d} \left\{ 1 - \left(1 - \frac{\omega^2}{\omega_a^2}\right)^{-1} \left(\frac{\sin\theta}{\theta}\right) \right\} \quad (20)$$

where ,

$$C_a = \frac{\epsilon A}{l_a}, \text{ avalanche zone capacitance}$$

$$C_d = \frac{\epsilon A}{l_d}, \text{ drift zone capacitance}$$

$$\theta = \frac{\omega l_d}{v_d}, \text{ transit angle in the drift zone}$$

$$\omega_a^2 = \frac{2\alpha' v_d J_0}{\epsilon}, \text{ avalanche resonance frequency}$$

with $\alpha' = \frac{d(\alpha)}{dE}$, the derivative of ionization rate w.r.t. electronic field E , J_0 is the d.c.

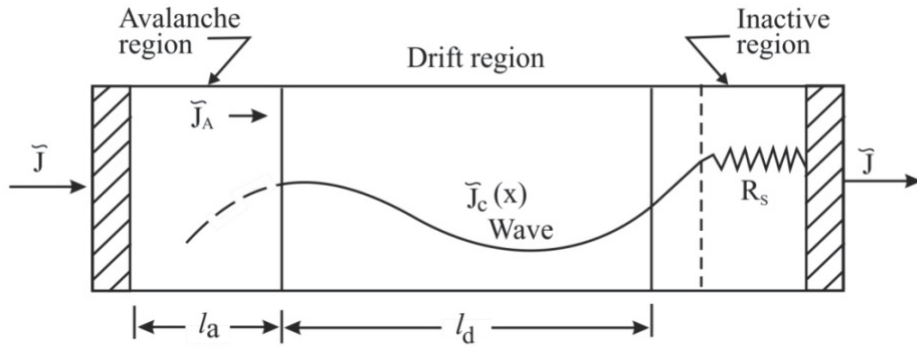
current density. l_a and l_d the avalanche zone and drift zone lengths, v_d is the saturated drift velocity, A is the cross - sectional area, and ϵ is the permittivity.

It can be observed from equation (20) that the avalanche zone is represented by an antiresonant circuit as shown in Fig. 5. The drift zone consists of a resistive and a reactive part. The resistive part (i.e. the real part of Z_d) is negative for all frequencies above ω_a (except for nulls at $\theta = 2\pi \times \text{integer}$) and below this frequency it is positive. It is important to note that the avalanche zone does not contribute to the device negative resistance. For small transit angles i.e. for $\theta < \pi/4$, equation (20) reduces to :-

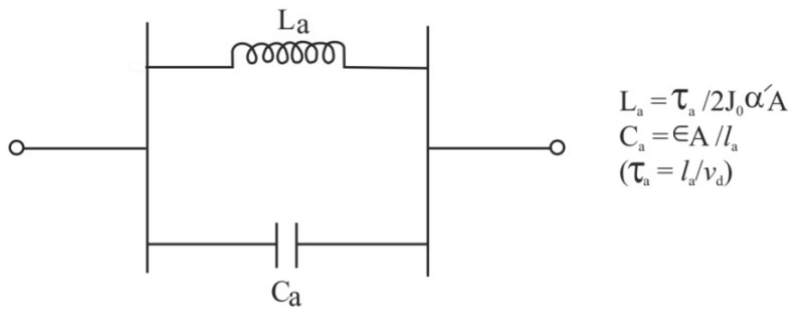
$$Z = R_s + \frac{l_d}{v_d \epsilon A} \left(1 - \frac{\omega^2}{\omega_a^2}\right)^{-1} + \frac{1}{j\omega C} \left(1 - \frac{\omega^2}{\omega_a^2}\right)^{-1} \quad (21)$$

$$\text{Where, } C = \frac{\epsilon A}{l_a + l_d}.$$

A typical plot of equation (21) is shown in Fig.6. It is observed that the diode reactance, X , changes from inductive to capacitive at the avalanche resonance frequency and also the resistive part, R , changes sign at the same frequency and become negative above ω_a . Thus the device possesses negative resistance for all frequencies above ω_a and there the device reactance is capacitive.



(a)



(b)

Fig. 5. (a) Model of Read diode with avalanche region, drift region and inactive region. (b) Equivalent circuit of the avalanche region.

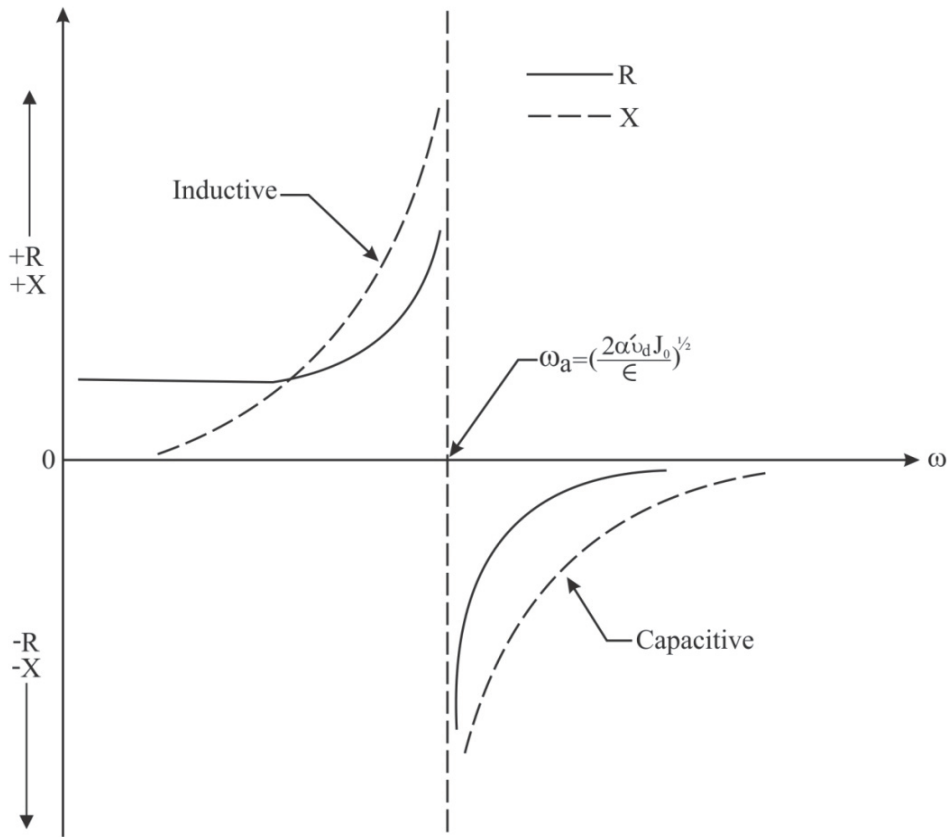


Fig. 6. Typical Impedance variation with frequency for a Read diode.

Gummel and Scharfetter extended the small-signal analysis of Gilden and Hines to include diode in which the avalanche region is not necessarily narrow. They obtained small signal admittance plots for a Read diode and for more realistic diode structures in which the avalanche region occupies an appreciable fraction of the total depletion region. They found that the optimum performance is achieved when the avalanche region is one third of the drift region. Scharfetter and Gummel have developed large-signal numerical analysis for Read diodes with a realistic doping profile including the effect of microwave circuit in which the diode is placed.

The results of investigation on impedance properties of IMPATT diode by various workers can be summed up to obtain an idea of the r.f. equivalent circuit for the IMPATT diode chip. In general, the diode equivalent circuit will consist of a negative resistance $-R_D$ in series with a capacitive impedance X_D (or alternatively by a negative conductance $-G_D$ in parallel with a capacitive susceptance B_D). The r.f. equivalent circuit of IMPATT diode chip is shown in Fig. 7 (a). Some important observation regarding the nature and values of R_D and X_D is worth mentioning. First, the magnitude of R_D is usually much smaller than X_D . Consequently, the magnitude of the chip impedance is approximately equal to X_D . Secondly, for most cases of

interest, X_D can be approximated with sufficient accuracy by the reactance of the junction (chip) capacitance at the breakdown voltage. Thirdly, the values of the negative resistance are generally small compared with the usual transmission line impedances. Further, it may be mentioned that the magnitude of negative resistance of IMPATT diode varies with signal level and that it increases with increasing signal level.

The properties of IMPATT diode chip have so far been discussed, but the chip by itself is difficult to handle and it is prone to mechanical damage and environmental contamination. So, it is necessary to provide the diode chip with a robust, hermetically sealed package. The package also provides the necessary heat- sink arrangements for dissipating the heat from the diode chip to the ambient .A common type of commercially available S4 package has been shown in Fig.2.6.3.(b) and also equivalent circuit of the packaged IMPATT diode having packaged parasitics . To a good approximation, the package can be described by two reactive elements a series inductance, L_p and a shunt capacitance C_p .The exact values of L_p and C_p varies from one package style to another.

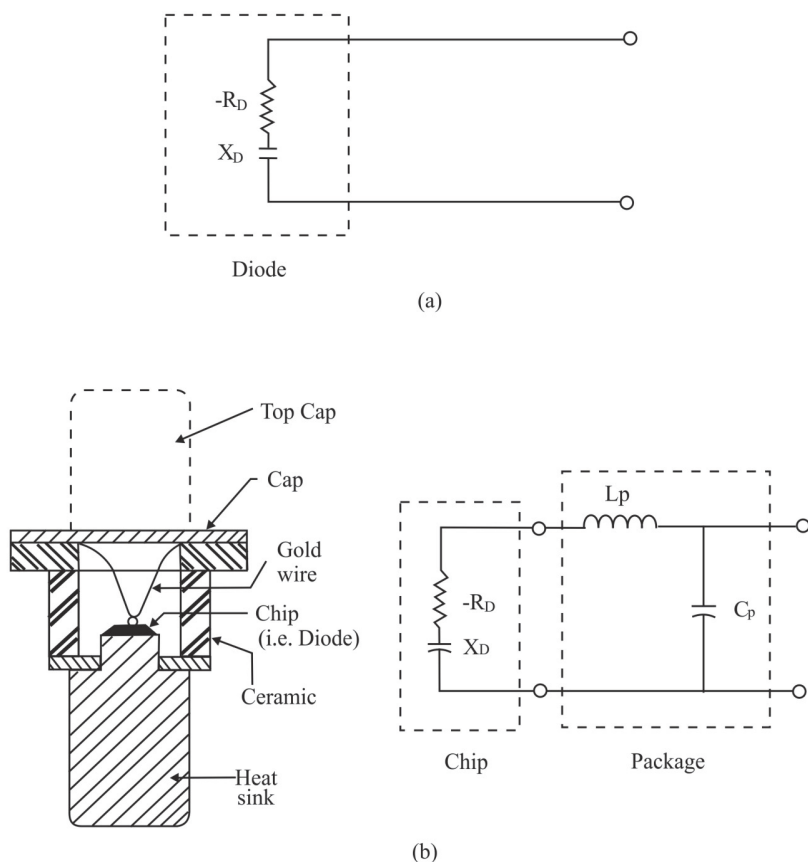


Fig. 7. (a) IMPATT diode chip r.f. equivalent circuit and (b) Cross-section of the chip in S4 package with equivalent circuit of the packaged IMPATT diode.

3. Simulation experiment

Different polytypes of SiC are shown in Figure 8. At first, SiC diodes are designed and optimized through a generalized double iterative simulation technique used for the analysis of IMPATT action [1]. The fundamental device equations, i.e. the one-dimensional *Poisson's* equation and the combined current continuity equations under steady-state conditions, have been numerically solved subject to appropriate boundary conditions, through an accurate and generalized double iterative computer algorithm, described elsewhere. Iteration over the value and location of field maximum are carried out until the boundary conditions of $E(x)$ and $P(x) = [J_p(x) - J_n(x)]/J_0$ are satisfied at both the edges of diode active layer. The DC solution gives the electric field $E(x)$ profile, normalized current density $P(x)$ profile, the maximum electric field (E_m), drift voltage drop (V_D), breakdown voltage (V_B) and avalanche zone width (x_a). The breakdown voltage (V_B) is calculated by integrating the spatial field profile over the total depletion layer width. The boundary conditions for current density profiles are fixed by assuming a high multiplication factor ($M_{n,p}$) $\sim 10^6$, since it is well known that, avalanche breakdown occurs in the diode junction when the electric field is large enough such that the charge multiplication factors (M_n, M_p) become infinite. The edges of the depletion layer are also determined accurately from the DC analysis.

The small-signal analysis of the IMPATT diode provides insight into the high-frequency performance of the diode. The range of frequencies exhibiting negative conductance of the diode can easily be computed by *Gummel-Blue* method [2]. From the DC field and current profiles, the spatially dependent ionization rates that appear in the *Gummel-Blue* equations are evaluated and fed as input data for the small-signal analysis. The edges of the depletion layer of the diode, which are fixed by the DC analysis, are taken as the starting and end points for the small-signal analysis. The spatial variation of high-frequency negative resistivity and reactivity in the depletion layer of the diode are obtained under small-signal conditions by solving two second order differential equations in $R(x, \omega)$ and $X(x, \omega)$. $R(x, \omega)$ and $X(x, \omega)$ are the real and imaginary part of diode impedance $Z(x, \omega)$, such that, $Z(x, \omega) = R(x, \omega) + j X(x, \omega)$. The total integrated diode negative resistance (Z_R) and reactance (Z_x) at a particular frequency (ω) and current density J_0 , are computed from numerical integration of the $R(x)$ and $X(x)$ profiles over the active space-charge layer.

At resonance, the reactance of the resonant cavity is mainly capacitive in nature. When the magnitude of negative conductance of the diode $|-G|$ is equal to the load conductance G_L , the condition of resonance is satisfied and as a result, power is absorbed in G_L and at the same time oscillation starts to build up in the circuit. *Adlerstein et al.* developed a method for determining R_s from the threshold condition of IMPATT oscillation [3]. In the present method, the author has determined the value of series resistance (R_s) from the admittance characteristics using a realistic analysis of *Gummel-Blue* [2] and *Adlerstein et al* [3]. The author has considered the effect of R_s in the realistic analysis of output power from the THz diodes. The basic mechanism of optical control of IMPATT diode is discussed earlier. In summary, the leakage current entering the depletion region of the reversed biased p-n junction of an un-illuminated IMPATT diode is only due to thermally generated electron-hole pairs and it is so small that the multiplication factors ($M_{n,p}$) become very high. When optical radiation of suitable wavelength (photon energy $hc/\lambda > E_g$) is incident on the active layer of the device, the leakage current increases significantly due to photo-generation of charge carriers. The enhancement of the leakage current under optical illumination of the devices is manifested as the lowering of $M_{n,p}$. The photo-sensitivity of IMPATTs are studied under two

illumination configuration: (a) Top Mounted and (b) Flip chip. The corresponding diagrams are shown in Figure 9.

In order to assess the role of leakage currents in controlling the dynamic properties of IMPATT oscillators at THz frequencies, simulation experiments are carried out on the effect of electron current multiplication factor, M_n , (keeping hole current multiplication factor M_p very high $\sim 10^6$) and M_p (keeping M_n very high $\sim 10^6$) on (i) the small-signal admittance characteristics, (ii) the negative resistivity profiles, (iii) quality factor at peak frequencies (Q_p), (iv) device negative resistance at peak frequencies ($-Z_{RP}$) and (v) maximum power output of DDR SiC IMPATTs.

4. Observations from simulation experiment

DC simulation program is used to obtain the $E(x)$ and $P(x)$ profiles of flat profile SiC IMPATT diodes which are designed and optimized for operation at 0.3 THz regime. The optimized design parameters and corresponding bias current densities for each diode are shown in Table 1. In figures 10(a-c), plots of $E(x)$ and $P(x)$ profiles of DDR SiC based un-illuminated and illuminated (TM and FC configuration) IMPATTs are presented. It is interesting to note that there are small changes in the electric field profile due to the lowering of M_n , corresponding to TM illumination configuration, while the variation is comparatively much prominent due to the lowering of M_p , corresponding to FC illumination configuration. Analysis of $P(x)$ profiles, as shown in figure 10(a-c), reveals that avalanche centre, at which $J_P = J_n$, moves towards the metallurgical junction from n-side with the lowering of both M_n and M_p . Similar to $E(x)$ profiles, $P(x)$ profiles of SiC based DDRs are also much sensitive to hole leakage current. Table 2 shows that the 4H-SiC IMPATT breaks down at 135.0 V, which is atleast 22.7% higher than its 6H-SiC and 3C-SiC counterpart. The variation of breakdown voltage (VB) of the designed SiC based IMPATTs, with the enhancement of photo-leakage current is shown in Figure 11. It is clear that compare to TM illumination configuration, in case of FC illumination

configuration the diode breakdown voltages decreases more. Moreover, the breakdown voltage of the illuminated hexagonal SiC based devices reduces much than its illuminated cubic SiC counterpart.

DDR diode type	Doping conc. (n region) (10^{23} m^{-3})	Doping conc. (p region) (10^{23} m^{-3})	Width of the n region (nm)	Width of the p region (nm)	Current density (10^9 A m^{-2})
4H-SiC	6.5	6.5	250.0	250.0	3.4
6H-SiC	8.0	8.0	250.0	250.0	3.5
3C-SiC	8.0	8.0	250.0	250.0	3.7

Table 1. Design Parameters of SiC IMPATT Diodes at 0.3THz Frequency

4H-SiC based diode is found to be more efficient (14%) than 6H-SiC and 3C-SiC based diodes, under almost similar operating condition. Moreover the negative conductance of the 4H-SiC IMPATT is found to be $\sim 55.0\%$ and 7.0% higher than 6H-SiC and 3C-SiC based IMPATT. The higher value of diode breakdown voltage and negative conductance in 4H-SiC based diode increases the RF power level. It is clear from the table 2, that 4H-SiC based

IMPATT is capable of delivering a RF power density of $36.45 \times 10^{10} \text{ Wm}^{-2}$, which is ~ 2.5 times and 1.6 times higher than 6H-SiC and 3C-SiC based IMPATTs, respectively. Furthermore, the device negative resistance ($-Z_{RP}$) at peak frequencies of the 4H-SiC based device is atleast 45% higher than its counterparts. The higher value of negative resistance is an essential criterion for getting sustained oscillation from the THz devices. The quality factor of 4H-SiC based device is found to be best among all the designed diodes.

Diode parameters	4H-SiC DDR	6H-SiC DDR	3C-SiC DDR
Peak electric field (E_m) (10^8 V m^{-1})	4.25	3.8	5.65
Breakdown voltage (V_B) (V)	135.0	109.0	110.0
Efficiency (η) (%)	14.0	12.0	12.5
Peak frequency (f_p) (THz)	0.325	0.35	0.353
Peak negative conductance ($-G_p$) (10^6 S m^{-2})	162.0	102.0	152.0
Device quality factor ($-Q_p$)	1.26	2.45	1.79
Device negative resistance at peak frequency ($-Z_{RP}$) ($10^{-9} \Omega \text{m}^2$)	2.35	1.30	1.60
RF output power density (P_{RF}) (10^{10} Wm^{-2})	36.45	15.15	22.99

Table 2. DC and high-frequency properties of SiC IMPATT Diodes at around 0.3 THz Frequency

The values of RS for all the three designed diodes are estimated from Adlerstein's approach, as mentioned in earlier section and the results are shown in Table 3. It is depicted that among all the designed diodes, the magnitude of parasitic positive series resistance is least in case of 4H-SiC based devices. Moreover, Table 3 also shows that the ratios of negative resistance : positive series resistance in 4H-SiC, 6H-SiC and 3C-SiC based diodes are 3.3: 2.21: 2.96. The much higher value of negative resistance than its positive series resistance in 4H-SiC based device indicates that IMPATT diode based on 4H-SiC material system will be an potential candidate for generating THz power. The effects of RS on the admittance characteristics of the devices are shown in Figure 12. Figure 12 indicates that parasitic series resistance degrades the admittance characteristics of the designed SiC based DDRs. The degradation of admittance characteristics due to the presence of RS is more serious in 6H-SiC based IMPATT.

Thus the present study definitely establishes that the prospects of 4H-SiC based IMPATT as a high power, efficient THz source is far better than its 6H-SiC and 3C-SiC counterparts.

The effects of optical illumination on the THz behavior of the designed diodes are shown in Table 4. The computed values of $-GP$, $-ZRP$, PRF , f_p and $-QP$ for different electron and hole current multiplication factors are shown in Table 4. Admittance plots of all the SiC DDR IMPATTs under optical illumination are shown in Figure 13. It is evident from the Figure as well as from Table 4 that the values of $|-GP|$ at the optimum frequencies decrease with the lowering of M_n and M_p . At the same time, the frequency ranges over which the devices exhibit negative conductance, shift towards higher frequencies with the

lowering of Mn and Mp. The simulated results for the illuminated 4H-SiC IMPATT diode (Table 4) indicate that the values of $|-GP|$ and PRF decrease nearly by the same percentage ($\sim 3.8.0\%$) as Mn decreases from 106 to 25, keeping the value of MP constant at 106. On the other hand, for a similar variation of Mp from 106 to 10 (keeping the value of Mn constant at 106), reduces the values of $|-GP|$ and PRF by $\sim 35.0\%$. Similar trend is reflected in Figure 13. In the case of 6H-SiC and 3C-SiC IMPATT diodes, as the value of Mn decreases from 106 to 25 (corresponding to TM illumination configuration), $|-GP|$ and PRF decrease by 5.2% and 2% , respectively (Table 4). Similarly for the FC illumination configuration of 6H-SiC and 3C-SiC IMPATTs, the decrease of MP from 106 to 25, causes a reduction in the values of $|-GP|$ and PRF by 18.2% and 21.6% , respectively.

Diode type	Negative conductance (-G) (10^6 Sm^{-2})	Susceptance (B) (10^6 Sm^{-2})	Estimated load conductance (g) (10^6 Sm^{-2})	Negative resistance ($-Z_R$) ($10^{-9} \Omega \text{ m}^2$)	Series Resistance (R_s) ($10^{-9} \Omega \text{ m}^2$)
4H-SiC	153.0	150.0	130.0	3.34	1.02
6H-SiC	95.0	152.0	63.7	2.95	1.33
3C-SiC	150.0	153.0	125.0	3.26	1.1

Table 3. Series resistance of the designed diodes at THz regime (frequency = 0.3 THz)

It is evident from Table 4, that in the case of 4H-SiC based TM diode, a lowering of Mn from 106 to 25 causes the diode negative resistance ($-Z_{Rp}$) to decrease by 3.0% , while there is a corresponding lowering of $-Z_{Rp}$ by 51.0% in case of FC diode. Similarly for TM 6H-SiC and 3C-SiC diodes, the value of $-Z_{Rp}$ reduces by 20.0% and 10.0% , respectively, as Mn decreases from 106 to 25 (Table 4), whereas, for a similar variation of MP, $|-Z_{Rp}|$ reduces by 40.0% and 25.0% , respectively in 6H-SiC and 3C-SiC based diodes. The device quality factors are also found to degrade with the lowering of Mn and MP, in case of all the SiC based diodes.

It is further evident from figure 13 that in α -SiC and β -SiC based DDR devices a lowering of Mp causes larger upward shift in frequency than corresponding lowering of Mn. The optimum frequency of oscillation (fP) shifts upwards by 15.0 GHz and 45.0 GHz respectively for TM and FC IMPATTs based on 4H-SiC. On the other hand, in case of 6H-SiC and 3C-SiC based TM IMPATTs, fP shifts upward by 1.0 GHz and 2.0 GHz , respectively. Whereas under FC illumination configuration, the values of fP shifts upward by 3.0 GHz and 7.0 GHz respectively for 6H-SiC and 3C-SiC based diodes.

Thus the studies reveal that, effects of photo-illumination on the frequency up shift as well as on the modulation of the THz behavior of the SiC devices are found to be more pronounced in FC illumination configuration than that for TM illumination configuration under similar operating condition. These results show an identical trend as observed previously for MM-wave SiC devices [4].

DDR diode type	M_n	M_p	f_p (THz)	$-G_p$ (10^8 $S m^{-2}$)	$-Z_{Rp}$ (10^{-9} Ωm^2)	P_{RF} (10^{10} $W m^{-2}$)	$-Q_p$
4H-SiC (unilluminated)	10^6	10^6	0.325	162.0	2.35	36.90	1.26
4H-SiC (TM)	50	10^6	0.33	158.0	2.30	35.99	1.32
4H-SiC (TM)	25	„	0.34	156.0	2.29	35.54	1.34
4H-SiC (FC)	10^6	50	0.35	135.0	1.48	30.75	2.0
4H-SiC (FC)	10^6	25	0.37	120.0	1.15	27.33	2.50
6H-SiC (unilluminated)	10^6	10^6	0.35	101.0	1.30	14.99	2.58
6H-SiC (TM)	50	10^6	0.353	99.0	1.12	14.70	2.84
6H-SiC (TM)	25	„	0.36	96.0	1.03	14.25	2.91
6H-SiC (FC)	10^6	50	0.362	90.0	0.84	13.36	3.50
6H-SiC (FC)	10^6	25	0.38	85.4	0.76	12.68	3.80
3C-SiC (unilluminated)	10^6	10^6	0.353	152.0	1.60	22.99	1.80
3C-SiC (TM)	50	10^6	0.353	150.0	1.50	22.68	1.90
3C-SiC (TM)	25	„	0.355	149.0	1.44	22.53	1.94
3C-SiC (FC)	10^6	50	0.356	138.6	1.44	20.96	2.0
3C-SiC (FC)	10^6	25	0.360	125.0	1.20	18.91	2.32

Table 4. Optical illumination effects on SiC IMPATTs in the THz regime (frequency = 0.3 THz).

To study the microscopic properties of the devices the authors has computed the spatial distribution of negative resistivity ($R(x)$) in the depletion layer of the device, which would give an insight into the region of depletion layer that contribute to THz power. The computed $R(x)$ profiles at the respective optimum frequencies f_p of the DDRs are shown in figure 14. The computed $R(x)$ profiles in each case is characterized by two negative resistivity peaks (R_{max}) in the middle of each drift layer along with a central negative resistivity minimum (R_{min}) located near the metallurgical junction. Furthermore, the magnitude of negative resistivity peaks produced by holes in the hole drift layer ($R_{max,p}$) is appreciably higher compared with the peak produced by electrons in the electron drift layer ($R_{max,n}$). This may be due to the fact that in SiC, hole is more ionizing carrier than electrons [5]. The study also reveals that under normal operating conditions of the DDRs, the values of R_{min} is appreciable, which indicates that the central avalanche zone of all the DDR SiC IMPATTs contributes appreciably to the THz power although to a lesser extent than the corresponding drift zone. Some qualitative estimate of the THz-power contributed by the avalanche region of the devices can be obtained from the contribution of the small-signal negative resistance ($-Z_R$) from the avalanche zone, which is the area of the $R(x)$ profile bounded by avalanche zone. The dependence of magnitudes of the negative resistivity peaks in the two drift layers of 4H-SiC, 6H-SiC and 3C-SiC diodes can be explained by considering the relative magnitudes of the ionization rates of electrons and holes in the avalanche zone. It is observed that in case of all the diodes, under optical illumination, the magnitudes of the peaks of the negative resistivity profiles decrease and

their locations shift towards the $nn++$ and $pp++$ edges of the drift layer with the decrease of M_n or M_p . The depression of the peaks and the shift of the $R(x)$ profiles are less pronounced in TM diode structure (Figure 14) while the same are more pronounced in FC diode structure (Figure 14). The optical illumination studies on the three types of SiC DDRs thus reveals that 4H-SiC based IMPATT is comparatively more photo- sensitive than its counterparts.

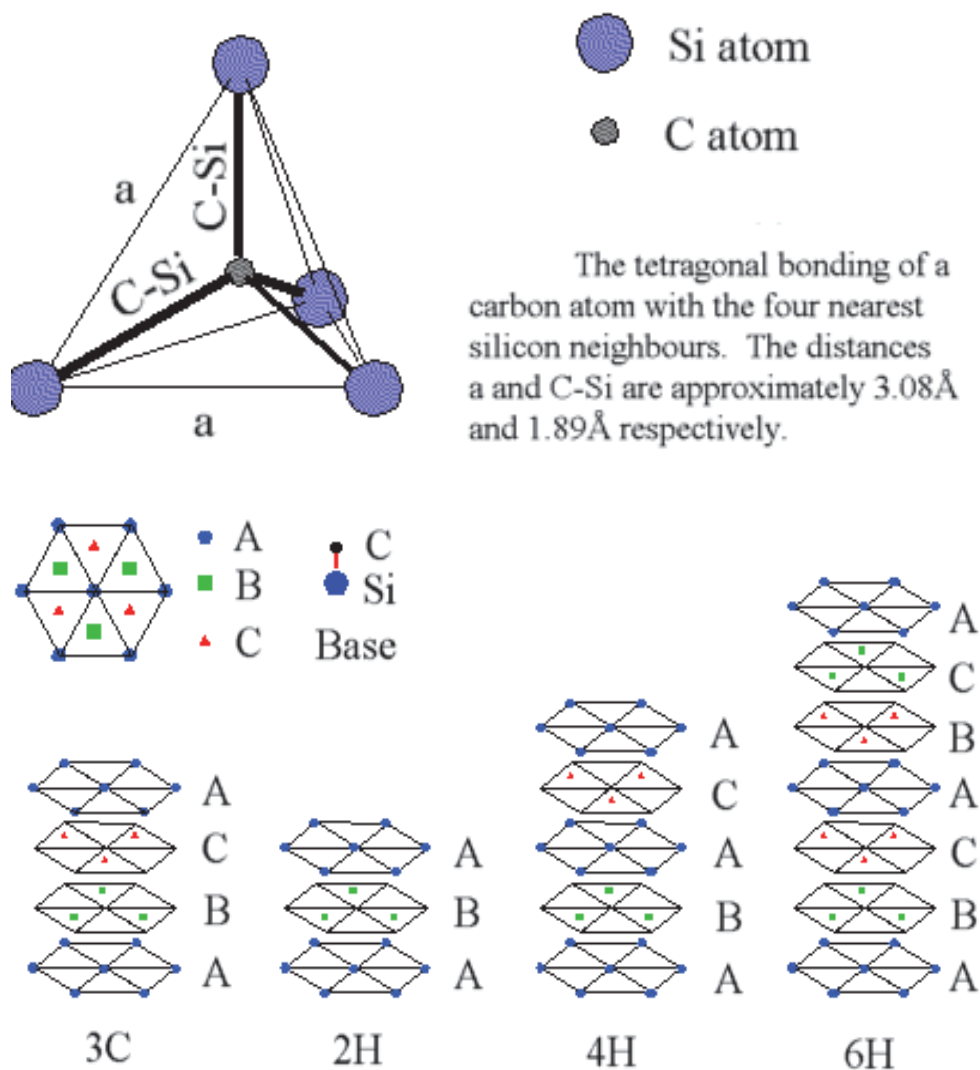


Fig. 8. The stacking sequence of double layers of the three most common SiC polytypes

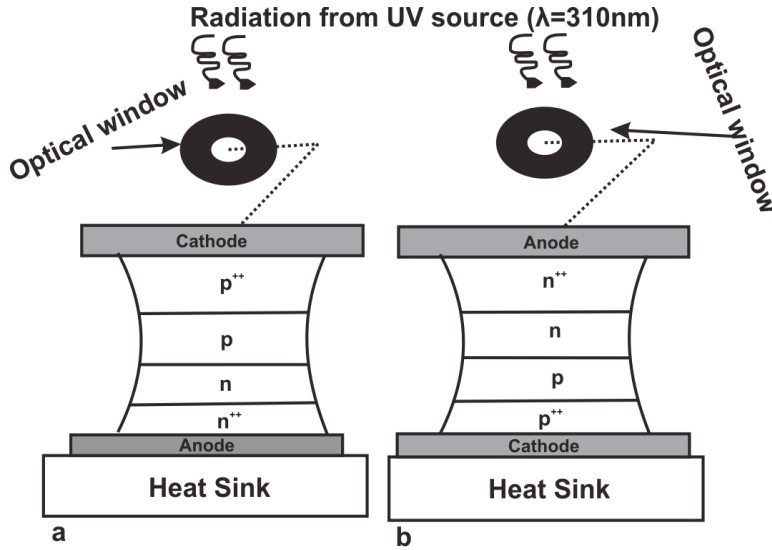


Fig. 9. (a) Top-Mounted IMPATT and (b) Flip-Chip IMPATT

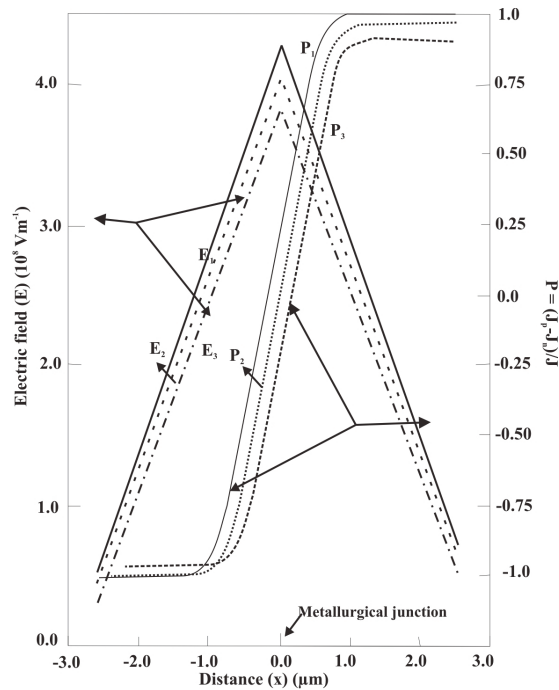


Fig. 10. (a) Electric field and normalised current density profiles of 4H-SiC IMPATT at THz region. E_1 and P_1 are un-illuminated diodes and $E_{2,3}$ and $P_{2,3}$ are illuminated TM (2) and FC (3) diodes.

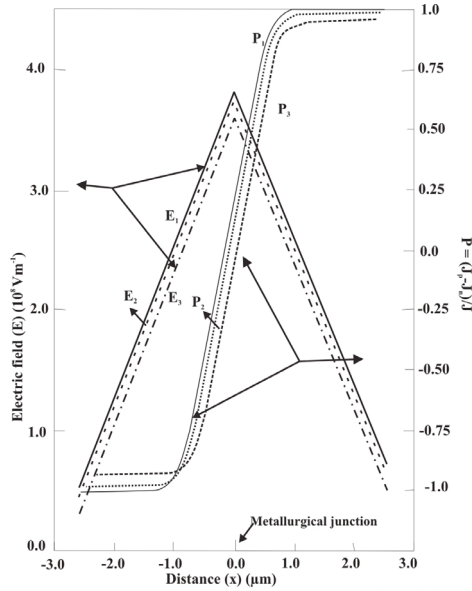


Fig. 10. (b) Electric field and normalised current density profiles of 6H-SiC IMPATT at THz region. E1 and P1 are un-illuminated diodes and E2,3 and P2,3 are illuminated TM (2) and FC (3) diodes.

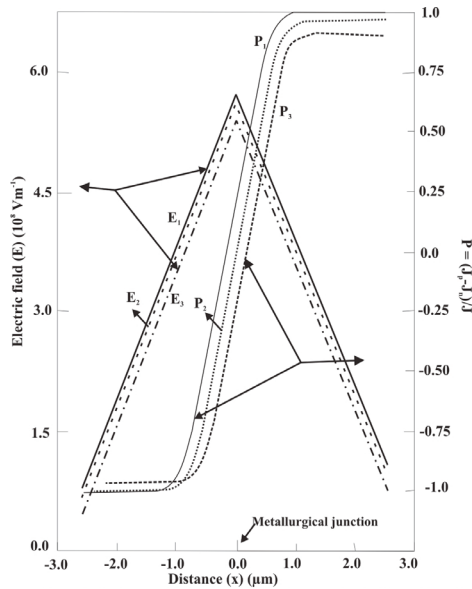


Fig. 10. (c) Electric field and normalised current density profiles of 3C-SiC IMPATT at THz region. E1 and P1 are un-illuminated diodes and E2,3 and P2,3 are illuminated TM (2) and FC (3) diodes.

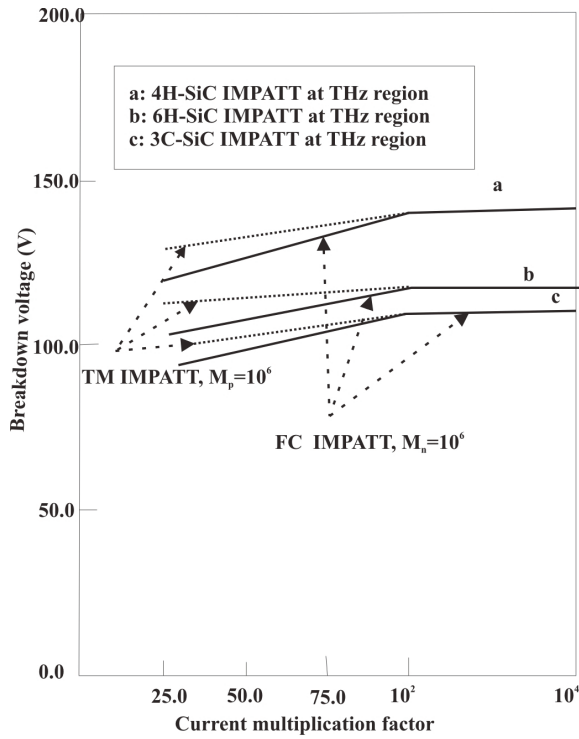


Fig. 11. Plots of breakdown voltage as a function of electron and hole current multiplication factors of SiC THz IMPATTs.

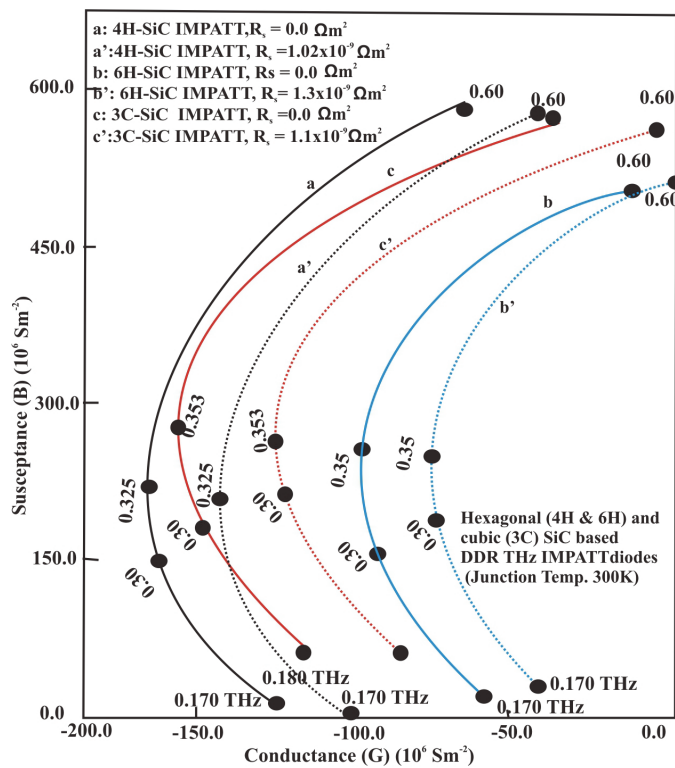


Fig. 12. Admittance plots of SiC DDR IMPATTs in the Terahertz region, dotted lines are incorporating the series resistance effects.

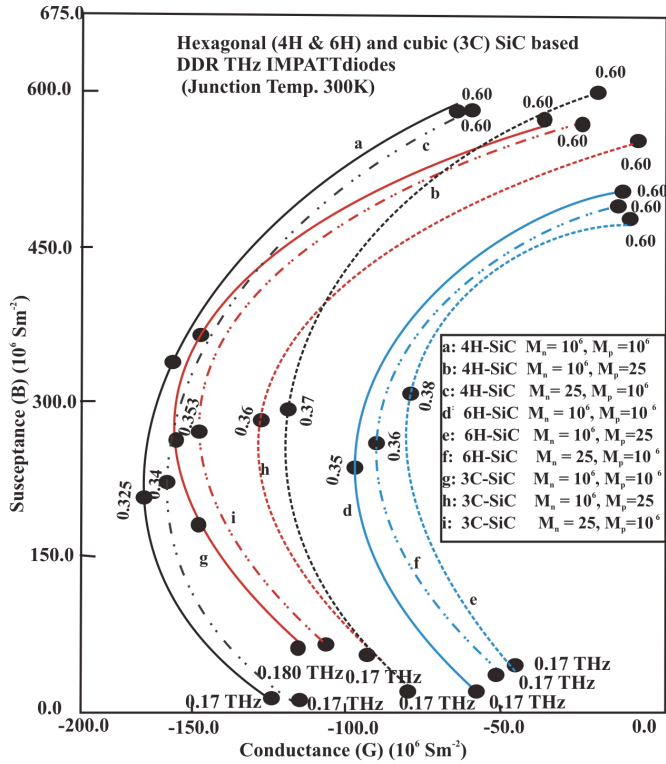


Fig. 13. Effect of photo-illumination on FC and TM illumination configuration of SiC (3C, 4H and 6H type) based terahertz DDR IMPATT diodes at room temperature (300K).

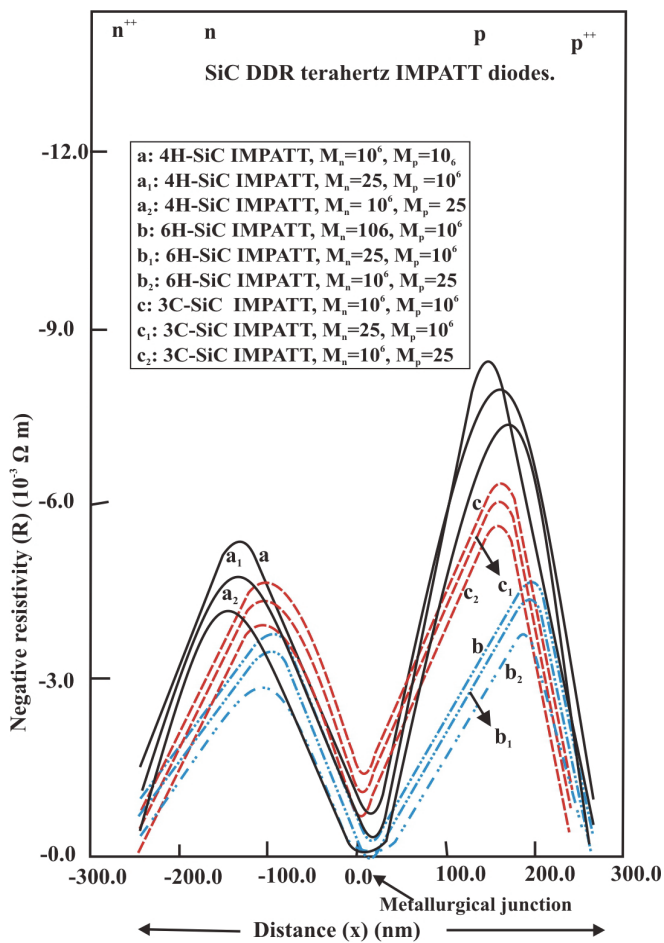


Fig. 14. Effect of radiation on negative resistivity plots of SiC DDR IMPATTs in the Terahertz region.

5. Acknowledgment(s)

The author wish to acknowledge Director, CMSDS, University of Calcutta for providing necessary support to do this work. The author is grateful to (late) Prof. S. K. Roy, Professor and founder Director, CMSDS, University of Calcutta and (late) Prof. Nilratan Mazumder, Professor, West Bengal University of Technology, India for providing their valuable suggestions during this work.

6. References

- [1] Mukherjee, M; Mazumder, N; Roy, S.K; and Goswami, K ; “GaN IMPATT diode: A photosensitive high power Terahertz source”, *Semiconductor Science and Technology*, (2007), vol. 22, pp. 1258-1267.
- [2] Gummel, H. K; Blue, J.L ; ‘A small signal theory of avalanche noise in IMPATT Diodes’, *IEEE Trans. Electron Devices* (1967), vol. 14, p. 569.
- [3] Adlerstein, M. G, Holway, Chu, S. L. “Measurement of series resistance in IMPATT diodes”, *IEEE Trans. Electron Devices*, vol. ED- 30, p. 179,.
- [4] Mukherjee, M; Mazumder, N; Dasgupta, A; “Effect of Charge Bump on Series Resistance and Ka-Band performance of 4H-SiC IMPATT Oscillator”, *Proceedings of “IEEE International symposium on Integrated circuits” (IEEE-ISIC 2007)*, September 26-28, (2007), Nanyang Technological University, and IEEE- Singapore. pp. 61-64
- [5] Electronic Archive: New Semiconductor Materials, Characteristics and Properties (Online) www.ioffe.ru/SVA/NSM/Semicond/SiC.

Recent Developments on Silicon Carbide Thin Films for Piezoresistive Sensors Applications

Mariana Amorim Fraga^{1,2}, Rodrigo Sávio Pessoa^{2,3},
Homero Santiago Maciel² and Marcos Massi²

¹*Institute for Advanced Studies*

²*Plasma and Processes Laboratory, Technological Institute of Aeronautics*

³*IP&D, University of Vale do Paraíba
Brazil*

1. Introduction

The increasing demand for microelectromechanical systems (MEMS) as, for example, piezoresistive sensors with capabilities of operating at high temperatures, mainly for automotive, petrochemical and aerospace applications, has stimulated the research of alternative materials to silicon in the fabrication of these devices. It is known that the high temperature operating limit for silicon-based MEMS sensors is about 150°C (Fraga, 2009).

Silicon carbide (SiC) has shown to be a good alternative to silicon in the development of MEMS sensors for harsh environments due to its excellent electrical characteristics as wide band-gap (3 eV), high breakdown field strength (10 times higher than Si) and low intrinsic carrier concentration which allow stable electronic properties under harsh environments (Cimalla et al., 2007; Wright & Horsfall, 2007; Rajab et al., 2006). In addition, SiC exhibits high elastic modulus at high temperatures which combined with the excellent electronic properties make it very attractive for piezoresistive sensors applications (Kulikovsky et al., 2008).

Silicon carbide can be obtained in bulk or film forms. In recent years, great progress has been made in the field of the growth of SiC bulk. Currently there are 6H-SiC, 4H-SiC and 3C-SiC wafers commercially available. However, these wafers are still very expensive (Hobgood et al., 2004; Camassel & Juillaguet, 2007), so encouraging studies on crystalline and amorphous SiC films deposited on silicon or SOI (Silicon-On-Insulator) substrates using appropriate techniques. The use of SiC films besides being less expensive has another advantage which is the well known processing techniques for silicon micromachining. The challenge is to obtain SiC films with mechanical, electrical and piezoresistive properties as good as the bulk form.

Nowadays, some research groups have studied the synthesis and characterization of SiC films obtained by different techniques namely, plasma enhanced chemical vapour deposition (PECVD), molecular beam epitaxy (MBE), sputtering, among others, aiming MEMS sensors applications (Chaudhuri et al., 2000; Fissel et al., 1995; Rajagopalan et al., 2003; Lattemann et al., 2003).

The purpose of this chapter is to present an overview of the deposition techniques of SiC films, summarizing the deposition conditions that affect the piezoresistive properties of these films, the influence of the temperature on their piezoresistive properties and comparing the performance of piezoresistive sensors based on SiC films with those based in other materials. Moreover, the chapter focus attention is on the development of pressure sensors and accelerometers based on SiC films with suited piezoresistive properties to substitute the silicon in the microfabrication of these sensors so as to extend their endurance under harsh environment.

2. Piezoresistive effect in SiC

2.1 Brief overview

Piezoresistivity is a physical property which has been widely used to convert a mechanical signal into an electrical one, in different device types such as pressure sensors, accelerometers, tactile sensors, strain gauges and flow sensors, among others.

The piezoresistive effect was discovered by Lord Kelvin in 1856. This property is quantified in terms of gauge factor (GF), which is defined as the fractional change in the resistance per unit strain (Window, 1992):

$$GF = \frac{\Delta R}{R} \frac{1}{\varepsilon} \quad (1)$$

where R is the nominal electrical resistance and ε the strain. GF is a dimensionless number that depends on the crystallographic orientation and is related to the elastic or Young's modulus of the material (E) by the following expression,

$$E = \frac{\sigma}{\varepsilon} \quad (2)$$

where σ is the mechanical stress. A positive GF indicates an increase in resistance with stress increases whereas the negative correspond a decrease.

Thus, from eq. (1) and (2), the piezoresistivity can be defined as the fractional change in the resistivity of a material when submitted to a mechanical stress. The change in resistance arises from two effects: the change in the dimension of the resistor and the change in the resistivity of the material itself.

The large piezoresistive effect in silicon and germanium was first observed by Smith in 1954. Since then, it has been noted that the piezoresistive effect in semiconductor materials is highly anisotropic and exhibits a dependence on the dopant type, dopant concentration and crystalline orientation. Furthermore, in 1956 Morin et al. demonstrated the temperature dependence of the piezoresistance of silicon and germanium.

In 1968, Rapatskaya et al. were the first to report the piezoresistive properties of n-type α -SiC (6H-SiC). In the 70's three papers on piezoresistance in SiC were published by Guk: two on the piezoresistive characterization and temperature dependence of the 6H-SiC polytype and one on the piezoresistance of β -SiC (3C-SiC). In 1993, Shor et al. have extended this study on piezoresistive properties of β -SiC discussing the GF and the temperature coefficient of resistance (TCR) of this material for several doping levels. In 1997, Strass et al. investigated the influence of crystal quality on the piezoresistive effect in β -SiC. In 1998, Okojie et al. determined the longitudinal and transverse GF and the TCR of n- and p-type 6H-SiC.

In 2002, Toriyama & Sugiyama performed a theoretical analysis on the piezoresistivity of β -SiC based on electron transfer and the mobility shift mechanism and in 2004 a detailed experimental study on piezoresistive properties of single crystalline, polycrystalline, and nanocrystalline n-type 3C-SiC was reported by Eickhoff et al.

In parallel to these studies on characterization of piezoresistive properties of the SiC polytypes, some SiC sensors have been developed. In the '90s, Okoije et al. developed 6H-SiC pressure sensors for high temperature applications and Ziermann et al. reported a piezoresistive pressure sensor with n-type β -SiC thin-film piezoresistors on Silicon-on-Insulators (SOI) substrate. In 2003, Atwell et al. simulated, fabricated and tested bulk micromachined 6H-SiC piezoresistive accelerometers.

The good performance exhibited by the sensors based on 6H-SiC bulk and on 3C-SiC film have motivated studies on the piezoresistive properties of amorphous SiC (a-SiC) films produced at low temperatures by techniques such as PECVD and magnetron sputtering (Fraga, 2010, 2011a; Fraga et al., 2011b, 2011c).

Table 1 presents the *GF* and *TCR* values of different SiC types and of some other materials commonly used in piezoresistive sensors. As can be observed, the p-type Si has the greater *GF* whereas the a-SiC film the smaller *TCR*.

Material	Form	Dopant	Structure	GF *	TCR (ppm/°C)
p-type Si	bulk	Boron	Crystalline	140	1082
n-type Si	bulk	Phosphorus	Crystalline	-133	1920
Ge	thin film	Boron	Amorphous	10	3100
Polysilicon	thin film	Boron	Polycrystalline	34	100
a-SiC	thin film	Nitrogen	Amorphous	49	36
3C-SiC	thick film	Nitrogen	Crystalline	-31.8	400
6H-SiC	bulk	Nitrogen	Crystalline	15	-240

* GF measured at room temperature

Table 1. Comparison among the properties of some piezoresistive materials reported in literature (Fraga, 2011c; Shor, 1993; Okoije 1998a).

2.2 Physical description

The piezoresistive effect can also be defined as the tensor relationship between applied stress and change in resistivity (Johns, 2005):

$$\frac{\Delta\rho_{ij}}{\rho} = \pi_{ij}\sigma_{kl} \quad (3)$$

where ρ is the resistivity, π is the piezoresistive coefficient and σ is the mechanical stress. In the case of a material with cubic structure, the stress has six components σ_1 , σ_2 , and σ_3 (along the axes of the cube) and σ_4 , σ_5 , and σ_6 (the shear stresses) as shown in Figure 1.

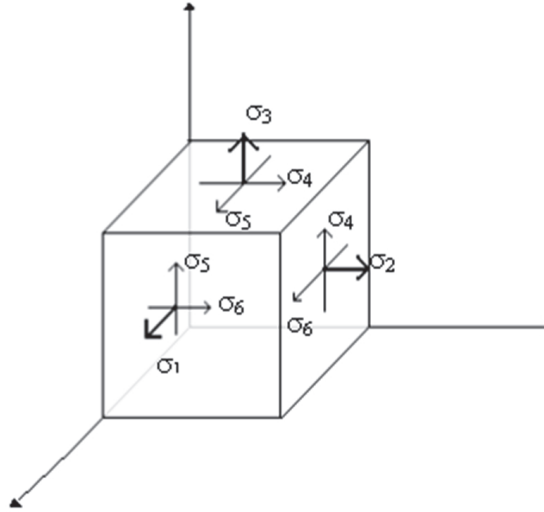


Fig. 1. Schematic illustration of the stress components.

The six stress components and six resistivity components result in a matrix with 36 piezoresistive coefficients. For the cubic crystal structure of materials such as silicon or β -SiC, the matrix simplifies to only three piezoresistive coefficients (π_{11} , π_{12} , and π_{44}) as shown in the following equation (Singh et al., 2002):

$$\begin{bmatrix} \Delta\rho_1 \\ \Delta\rho_2 \\ \Delta\rho_3 \\ \frac{1}{\rho} \Delta\rho_4 \\ \Delta\rho_5 \\ \Delta\rho_6 \end{bmatrix} = \begin{bmatrix} \pi_{11} & \pi_{12} & \pi_{12} & 0 & 0 & 0 \\ \pi_{12} & \pi_{11} & \pi_{12} & 0 & 0 & 0 \\ \pi_{12} & \pi_{12} & \pi_{11} & 0 & 0 & 0 \\ 0 & 0 & 0 & \pi_{44} & 0 & 0 \\ 0 & 0 & 0 & 0 & \pi_{44} & 0 \\ 0 & 0 & 0 & 0 & 0 & \pi_{44} \end{bmatrix} \begin{bmatrix} \sigma_1 \\ \sigma_2 \\ \sigma_3 \\ \sigma_4 \\ \sigma_5 \\ \sigma_6 \end{bmatrix} \quad (4)$$

Although equation (4) models the piezoresistive effect in silicon in the direction of the crystal axes, customarily this effect is measured using only two coefficients: π_l that relates the resistance change due to stress in the longitudinal direction and π_t in the transverse direction. Therefore, the total resistivity change of a material can be simplified considering only changes under longitudinal and transverse stress components,

$$\frac{\Delta\rho}{\rho} = \pi_l \sigma_l + \pi_t \sigma_t \quad (5)$$

The piezoresistive effect can be better understood by the analysis of the behavior of a resistor when submitted to a mechanical stress. It is known that the electrical resistance of an unstressed resistor is given by,

$$R = \rho \frac{L}{A} \quad (6)$$

where L is the length and A the cross-sectional area of the resistor. When the resistor is subjected to a longitudinal stress, the resistivity, cross-sectional area and length will be changed as shown in the equation below:

$$\frac{\Delta R}{R} = \frac{\Delta \rho}{\rho} + \frac{\Delta L}{L} + \frac{\Delta A}{A} \quad (7)$$

This resistor that changes its resistivity with an applied stress is called piezoresistor. As can be observed in equation (7), a fractional resistance change, $\left(\frac{\Delta R}{R}\right)$, can be influenced by two

factors: resistivity change $\left(\frac{\Delta \rho}{\rho}\right)$ and dimensions change $\left(\frac{\Delta L}{L}\right)$, $\left(\frac{\Delta A}{A}\right)$. The dominant factor depends on the material type. In your experiments, Smith observed that for silicon the change in resistivity gives a larger contribution to the resistance changes than the change in dimensions of the resistor (Smith, 1954).

Considering that the components associated with dimension change can be written as a function of the strain, we have:

$$\frac{\Delta L}{L} = \varepsilon_l \quad (8)$$

and

$$\frac{\Delta A}{A} = \frac{\Delta W}{W} + \frac{\Delta H}{H} = 2\varepsilon_t \quad (9)$$

In the above equations the fractional change in length is equal to the longitudinal strain whereas the change in area is the sum of change in width $\left(\frac{\Delta W}{W}\right)$ and height $\left(\frac{\Delta H}{H}\right)$. It is known that $\varepsilon_w = \varepsilon_H = \varepsilon_t$.

Considering also that the longitudinal and transverse strain are related through equation:

$$\varepsilon_t = \nu \varepsilon_l \quad (10)$$

where ν is the Poisson's ratio of the material, thus the equation (7) can be simplified to

$$\frac{\Delta R}{R} = \frac{\Delta \rho}{\rho} + \varepsilon_l(1 + 2\nu) \quad (11)$$

Thus, the gauge factor can be related to resistivity, longitudinal strain and Poisson's ratio by the following equation (Allameh et al., 2006):

$$GF = \frac{1}{\varepsilon_l} \frac{\Delta \rho}{\rho} + (1 + 2\nu) \quad (12)$$

Another important parameter to evaluate the piezoresistive effect is the temperature, whose influence on strain measurement cannot be neglected. When the ambient temperature

changes, the electrical resistance of the resistor changes $\left(\frac{\Delta R}{R}\right)_{\Delta T}$. This influence is measured through temperature coefficient of resistance (TCR) and temperature coefficient of gauge factor ($TCGF$) that describe the parts per million change in resistance (or GF) for every one degree change in temperature. These coefficients can be determined by

$$TCR = \frac{1}{\Delta T} \frac{\Delta R}{R} = \frac{1}{\Delta T} \frac{R_T - R_0}{R_T} \quad (13)$$

$$TCGF = \frac{GF_T - GF_0}{GF_0} \frac{1}{\Delta T} \quad (14)$$

where ΔT is the change in temperature, R_0 and GF_0 are the electrical resistance and the gauge factor measured at room temperature or reference temperature (usually 25°C), respectively; and R_T and GF_T are the electrical resistance and gauge factor measured at an operating temperature.

In a first analysis, the sensitivity of a piezoresistive sensor is evaluated in terms of GF , TCR and $TCGF$, i.e., a sensor with good performance should exhibit high GF and low TCR . For this, there is great interest by the piezoresistive characterization of materials with low TCR . In their study, Shor et al. reported that to reduce the effect of changing in temperature on the performance of a sensor the TCR should be positive and preferably constant, the $TCGF$ negative and $|TCR| > |TCGF|$ (Shor et al., 1993).

In respect to the layout of a piezoresistive sensor, in general the most used configuration for the resistors is the Wheatstone bridge. In this configuration, four resistors are connected in loop as shown in Figure 2 and the output voltage is related to the input voltage according to the following equation:

$$\frac{V_{out}}{V_s} = \frac{V_A - V_B}{V_s} = \frac{R_3}{R_1 + R_3} - \frac{R_4}{R_2 + R_4} \quad (15)$$

where V_s is the supply voltage and V_{out} is the output voltage.

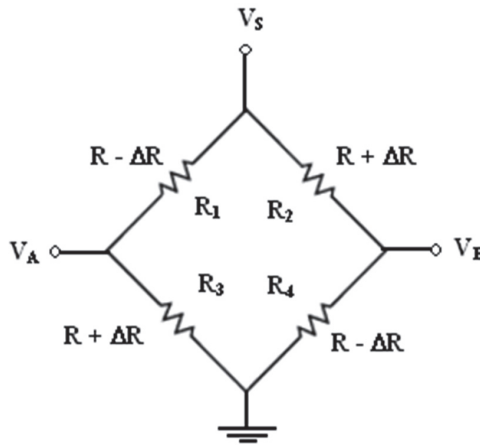


Fig. 2. Wheatstone bridge configuration.

When subjected to a mechanical stress, the electrical resistance of the resistors change leading to a variation of the output voltage, according to the following relationship

$$\frac{\Delta V_{out}}{V_s} = \frac{R_3 + \Delta R_3}{(R_1 + \Delta R_1) + (R_3 + \Delta R_3)} - \frac{R_4 + \Delta R_4}{(R_2 + \Delta R_2) + (R_4 + \Delta R_4)} \quad (16)$$

Whereas the four resistors have the same nominal resistance value ($R_1=R_2=R_3=R_4$) and that under mechanical stress the resistances R_2 and R_3 increases their values in $+\Delta R$, the resistances R_1 and R_4 decreases their values in $-\Delta R$. Therefore, the equation (16) can be simplified to

$$\frac{\Delta V_{out}}{V_s} = \frac{R + \Delta R}{2R} - \frac{(R - \Delta R)}{2R} = \frac{\Delta R}{R} \quad (17)$$

Given this, the sensitivity of a piezoresistive pressure sensor is determined by

$$S = \frac{\Delta R}{R} \frac{1}{\Delta P} = \frac{\Delta V_{out}}{V_s} \frac{1}{\Delta P} \quad (18)$$

where ΔP is change in pressure.

Whereas, for a piezoresistive accelerometer, the sensitivity is defined as the electrical output per unit of applied acceleration:

$$S = \frac{\Delta R}{R} \frac{1}{g} = \frac{\Delta V_{out}}{V_s} \frac{1}{g} \quad (19)$$

where g is the acceleration of gravity.

3. When and why to use SiC films in piezoresistive sensors?

As shown in the previous section, in recent years many researchers have been reported on the piezoresistive characterization of different SiC polytypes aiming the applicability of these materials in sensors. When comparing these studies, it is observed that for a same SiC polytype a dispersion of different values can be obtained for piezoresistive coefficient, GF and TCR (Okoiye, 2002).

It is known that the SiC has about 200 polytypes with different physical properties. This is one of the difficulties in characterizing the piezoresistivity in SiC. Moreover, studies show that maximum value of GF for SiC at room temperature is between 30 at 49 while for the monocrystalline p-type Si is 140 (see Table 1). However, all studies published until now have demonstrated the potential of the 6H-SiC and 3C-SiC polytypes besides a-SiC for the development of piezoresistive sensors for high temperature application. Given this, it is important to evaluate when it is advantageous to use SiC in piezoresistive sensors and whether is better to use SiC in bulk or thin film form.

This analysis should begin with the following question: Why SiC?

Several studies show that the SiC has mechanical and chemical stability at high temperatures. Due to these characteristics the application of SiC sensors is always associated with harsh environments. In these environments, silicon has mechanical and chemical limitations. At temperature greater than 500°C, silicon deforms plastically under small loads

(Pearson et al., 1957). In addition, the silicon does not support prolonged exposure to corrosive media. Another important factor that should be considered is that silicon pressure sensors using p-n junction piezoresistors have exhibited good performance at temperatures up to 175°C and the SOI sensors at temperatures up to 500°C.

Among the semiconductor materials with potential to substitute the silicon in harsh environments, SiC is the most appropriate candidate because its native oxide is SiO₂ which makes SiC directly compatible with the Si technology. This signifies that a sensor based on SiC can be developed following the same steps used in silicon sensors.

On the other hand, the chemical stability that have qualified SiC for harsh environments, makes it difficult to etch the bulk and to integrate any process step with already established Si based processes. Furthermore, the high cost of SiC wafer also difficult the development of “all of SiC” sensors. Faced with these difficulties the use of SiC thin films is quite attractive because the film can be grown on large-area Si substrates and by the ease of using conventional Si bulk micromachining techniques (Fraga et al., 2011a).

The second question is: When to use piezoresistive sensors based on SiC?

As already mentioned in the beginning of this section, at room temperature the monocrystalline silicon has greater *GF* than the SiC, i.e. sensors based on silicon operating on this condition has superior sensitivity. This fact shows that the use of SiC is only justified for specific applications in four main types of harsh environments, namely:

- a. Mechanically aggressive that involve high loads as in oil and gas industry applications which require sensors to operate in pressure ranges up to 35,000 psi and at temperatures up to 200°C (Vandelli, 2008);
- b. Thermally aggressive that involve high temperatures as in combustion control in gas turbine engines, where the operating temperatures are around 600°C (Vandelli, 2008) and in pressure monitoring during deep well drilling and combustion in aeronautical and automobile engines that require sensors to operate at temperatures ranging between 300 and 600°C (Stanescu & Voican, 2007);
- c. Chemically aggressive or corrosive environment as in biomedical and petrochemical applications where chemical attack by fluids is one of the modes of degradation of devices. The SiC sensors are a good choice for these applications because at room temperature, there is no known wet chemical that etches single-crystal SiC (George et al., 2006);
- d. Aerospace environment where sensors should to maintain their functionality under high cumulative doses of radiation. Due to well known chemical inertness of the SiC, sensors based on this material have exhibited great potential for these applications.

4. Brief description of the main techniques to deposit SiC films

Several techniques for obtaining thin films and bulks of SiC have been developed. Some companies that manufacture crystalline silicon wafers also offer SiC bulk wafers up to 4 inches in diameter. However, SiC wafers have an average price fifteen times higher than Si wafers with the same dimensions (Hobgood et al., 2004; Camassel & Juillaguet, 2007). Besides the high cost, another problem of the use of SiC substrates is the difficult micromachining process and high density of defects (Wu et al., 2001). In this context, there is a crescent interest in deposition techniques of SiC films on Si or SOI (Silicon-On-Insulator) substrates. These films can be produced in crystalline and amorphous forms.

Crystalline SiC (c-SiC) thin films can be produced by techniques that use temperatures higher than 1000°C as chemical vapour deposition (CVD) (Chaudhuri et al., 2000), molecular beam epitaxy (MBE) (Fissel et al., 1995) and electron cyclotron resonance (ECR) (Mandracci et al., 2001). However, it is known that this high substrate temperature required for growing crystalline SiC onto Si substrate can degrade the quality of the SiC/Si interface leading to many defects in the grown films, which often prevents the film processing in conjunction with other microfabrication processes involved in a MEMS device fabrication. Conversely, there are attractive processes for the synthesis of thin films at low temperature as those based on plasma assisted techniques, such as plasma chemical vapour deposition (PECVD) and plasma sputtering, which operate at temperatures below 600°C (Rajagopalan et al., 2003; Lattemann et al., 2003). But SiC films obtained at low temperature processes are amorphous (a-SiC) or nano-crystallines (nc-SiC) and, thus, can exhibit properties somewhat different from those observed in crystalline films (Foti, 2001). Because of this, a process usually used to improve the crystallinity of the a-SiC films is the annealing (Rajab et al., 2006).

Among the techniques used to deposit SiC films, in this chapter only four of them will be described: CVD, PECVD, magnetron sputtering and co-sputtering. These techniques were chosen because have been used with success in the deposition of undoped and doped SiC films for MEMS sensors application. A common point among them is the ease to perform the “in situ” doping by the addition of dopant gas (N_2 , PH_3 or B_2H_6) during the film deposition.

4.1 Chemical deposition processes: CVD and PECVD techniques

One of the most popular (laboratory) thin film deposition techniques nowadays are those based on chemical deposition processes such as chemical vapor deposition (CVD) and plasma enhanced chemical vapor deposition (PECVD) (Grill, 1994; Ohring, 2002; Bogaerts et al., 2002).

CVD or thermal CVD is the process of gas phase heating (by a hot filament, for example (Gracio et al., 2010)) in order for causing the decomposition of the gas, generating radical species that by diffusion can reach and be deposited on a suitably placed substrate. It differs from physical vapor deposition (PVD), which relies on material transfer from condensed-phase evaporant or sputter target sources (see section 4.2.). A reaction chamber is used for this process, into which the reactant gases are introduced to decompose and react with the substrate to form the film. Figure 3a illustrates a schematic of the reactor and its main components. Basically, a typical CVD system consists of the following parts: 1) sources and feed lines of gases; 2) mass flow controllers for metering the gas inlet; 3) a reaction chamber for decomposition of precursor gases; 4) a system for heating up the gas phase and wafer on which the film is to be deposited; and 5) temperature sensors.

Concerning the gas chemistry of CVD process for SiC film production, usually silane (SiH_4) and light hydrocarbons gases are used, such as propane or ethylene, diluted in hydrogen as a carrier gas (Chowdhury et al., 2011). Moreover, the main CVD reactor types used are atmospheric pressure CVD (APCVD) and low-pressure CVD (LPCVD).

As a modification to the CVD system, PECVD arose when plasma is used to perform the decomposition of the reactive gas source. By chemical reactions in the plasma (mainly electron impact ionization and dissociation), different kinds of ions and radicals are formed which diffuse toward the substrate where chemical surface reactions are promoted leading

to film growth. The major advantage compared to simple CVD is that PECVD can operate at much lower temperatures. Indeed, the electron temperature of 2–5 eV in PECVD is sufficient for dissociation, whereas in CVD the gas and surface reactions occur by thermal activation. Hence, some coatings, which are difficult to form by CVD due to melting problems, can be deposited more easily with PECVD (Bogaerts et al., 2002; Peng et al., 2011). Among the kinds of plasma sources that have been used for this application stand out the radiofrequency (rf) discharges (Bogaerts et al., 2002), pulsed discharges (Zhao et al., 2010) and microwave discharges (Gracio et al., 2010).

Basically, in PECVD the substrate is mounted on one of the electrodes in the same reactor where the species are created (see Figure 3b). Here, we focused the rf discharge because it is the configuration more used in research and industry. The rf PECVD reactor essentially consists of two electrodes of different areas, where the substrate is placed on the smaller electrode, to which the power is capacitively coupled. The rf power creates a plasma between the electrodes. Due to the higher mobility of the electrons than the ions, a sheath is created next to the electrodes containing an excess of ions. Hence, the sheath has a positive space charge, and the plasma creates a positive voltage with respect to the electrodes. The electrodes therefore acquire a dc self-bias equal to their peak rf voltage (self-bias electrode). The ratio of the dc self-bias voltages is inversely proportional to the ratio of the squared electrode areas, i.e., $V_1/V_2 = (A_1/A_2)^2$ (Lieberman & Lichtenberg, 2005).

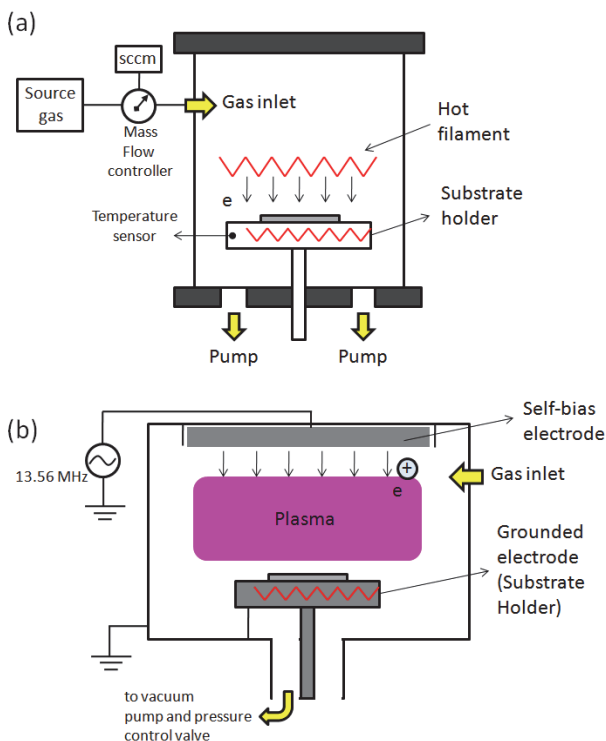


Fig. 3. Schematic diagram of CVD (a) and PECVD (b) systems.

Therefore, the smaller electrode acquires a larger bias voltage and becomes negative with respect to the larger electrode. The negative sheath voltage accelerates the positive ions towards the substrate which is mounted on this smaller electrode, allowing the substrate to become bombarded by energetic ions facilitating reactions with substrate surface.

In order to maximize the ion to neutral ratio of the plasma, the plasma must be operated at the lowest possible pressure. Nevertheless, the ions are only about 10 percent of the film-forming flux even at pressures as low as 50 mTorr. Lower pressures cannot be used as the plasma will no longer strike. A second disadvantage of this source is the energy spread in the ion energy distribution, prohibiting a controlled deposition. This energy spread is due to inelastic collisions as the ions are accelerated towards the substrate. The effect of this energy spread is to lower the mean ion energy to about 0.4 of the sheath voltage. Still, another disadvantage of the rf PECVD source is that it is not possible to have independent control over the ion energy and the ion current, as they both vary with the rf power. On the other hand, PECVD allows the deposition of uniform films over large areas, and PECVD systems can be easily scaled up (Neyts, 2006).

The most used precursor gases to deposit SiC films by PECVD are SiH_4 , as the silicon source, and methane (CH_4), as carbon source. Finally, Figure 4 illustrates the deposition mechanism of chemical vapor deposition technique (Grill, 1994). Basically the mechanism occurs by the following steps: (i) a predefined mix of reactant gases and diluents inert gases are introduced at a specified flow rate into the reaction chamber; (ii) a heat source is applied in order to dissociate the reactant gases; (iii) the resulting radical species diffuse to the substrate; (iv) the reactants get adsorbed on the surface of the substrate; (v) the reactants undergo chemical reactions with the substrate to form the film; and (vi) the gaseous by-products of the reactions are desorbed and evacuated from the reaction chamber.

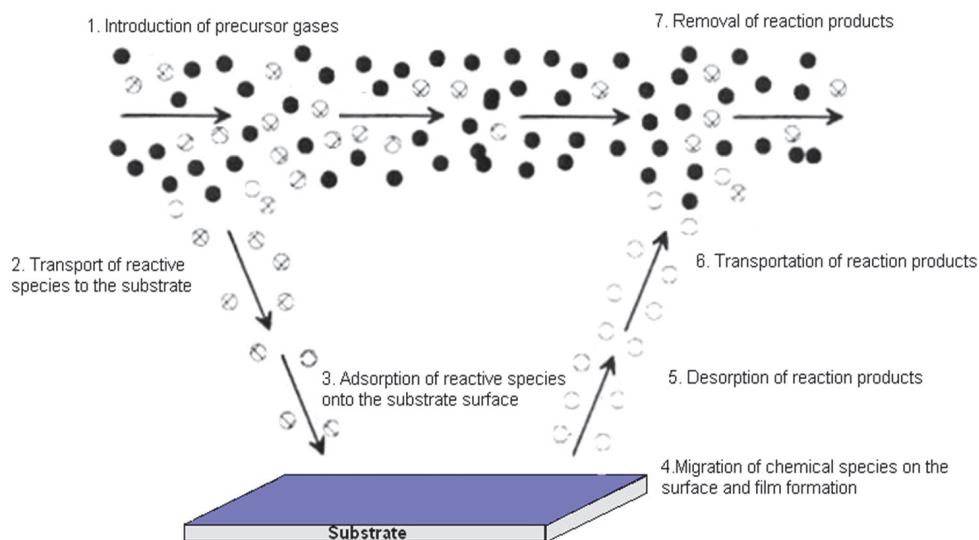


Fig. 4. Chemical vapor deposition mechanism. Adapted from (Doi, 2006).

4.2 Physical deposition processes: Magnetron sputtering and co-sputtering techniques

The physical deposition process comprise the physical sputtering and reactive sputtering techniques. Basically, these techniques differ when a neutral gas (physical sputtering) is added together with a reactive gas (reactive sputtering). In physical sputtering, ions (and atoms) from the plasma bombard the target, and release atoms (or molecules) of the target material. Argon ions at 500–1000 V are usually used. The sputtered atoms diffuse through the plasma and arrive at the substrate, where they can be deposited (Bogaerts et. al., 2002). In reactive sputtering, use is made of a molecular gas (for example, N_2 or O_2). Beside the positive ions from the plasma that sputter bombard the target, the dissociation products from the reactive gas will also react with the target. Hence, the film deposited at the substrate will be a combination of sputtered target material and the reactive gas (Bogaerts et al., 2002; Berg, 2005; Lieberman & Lichtenberg, 2005). The sputter deposition process is schematically presented in Figure 5.

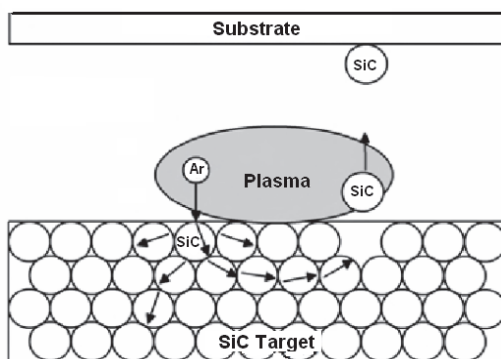


Fig. 5. Schematic of sputtering process.

Basically the steps of sputtering process are the following: (i) the neutral gas is ionized by an external power supply, producing a glow discharge or plasma; (ii) a source (the cathode, also called the target) is bombarded in high vacuum by gas ions due to the potential drop acceleration in the cathode sheath; (iii) atoms from the target are ejected by momentum transfer and diffuse through the vacuum chamber; (iv) atoms are deposited on the substrate to be coated and form a thin film.

Because sputter yields are of order unity for almost all target materials, a very wide variety of pure metals, alloys, and insulators can be deposited. Physical sputtering, especially of elemental targets, is a well understood process enabling sputtering systems for various applications to be relatively easily designed. Reasonable deposition rates with excellent film uniformity, good surface smoothness, and adhesion can be achieved over large areas (Lieberman & Lichtenberg, 2005).

Typically, the sputtering process can be accomplished using a planar configuration of electrodes and a dc power supply, where one electrode is biased negatively (cathode) and suffer the sputtering process. However, the sputtering yield is directly dependent on the gas pressure (best sputtering rates are in the range of mTorr) a fact that compromises the efficiency of planar geometry for this application: it is great for pressures above 100 mTorr. To solve this problem, it was developed the magnetron discharge where the plasma is magnetically enhanced by placing magnets behind the cathode target, i.e., a crossed electric and magnetic field configuration is

created. Figure 6 shows a schematic drawing of a conventional dc magnetron sputtering discharge. The trapping of the secondary electrons results in a higher probability of electron impact ionization and hence higher plasma density, increasing the sputtering flux and allowing operation at lower pressures, bellows 10 mTorr. Furthermore, the discharge voltage can be lowered into the range of 300-700 V. The main problem with the magnetron sputtering configuration is that the sputtering is confined to a small area of the target cathode governed by the magnetic field. The discharge appears in the form a high-density annulus of width w and radius R , as seen in Figure 6. Sputtering occurs in the corresponding track of the target. This area, known as the race track, is created by the uneven ion density.

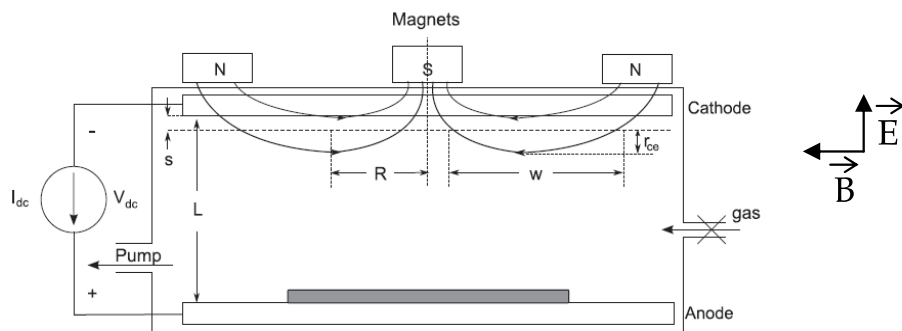


Fig. 6. Schematic drawing of a conventional dc magnetron sputtering discharge. Adapted from (Bogaerts et al., 2002).

Deposition of SiC films by the Magnetron Sputtering technique is performed generally using a SiC target in Ar atmosphere or a silicon target with precursor gases Ar plus CH₄ (Stamate et al., 2008). The dual magnetron (or co-sputtering) method also has been used to deposit SiC films. In this technique, the films are produced by co-sputtering of carbon and silicon targets (see Figure 7) with Ar as precursor gas (Kikuchi et al., 2002; Kerdiles et al., 2002). The co-sputtering technique offers as main advantage to obtaining of SiC films with different electrical, structural and mechanical properties by the variation of C/Si ratio in the film deposited (Kikuchi et al., 2002). Using this technique, it is possible to obtain a range of SiC film compositions by applied different power on each target (Medeiros et al., 2011).

5. Requirements of SiC films for piezoresistive sensors application

In order to develop piezoresistive sensors with high performance based on SiC films is necessary to optimize the properties of the SiC thin-film piezoresistors to maximize their sensitivity with the minimum temperature-dependent resistance variation (Luchinin & Korlyakov, 2009).

The first step for this optimization is the choice of the technique to deposit SiC films onto an insulator on Si substrates. Silicon dioxide (SiO_2) is the most used insulator material for this purpose, but some studies have showed silicon nitride (Si_3N_4) or aluminum nitride (AlN) as alternative materials. In general, good results have been achieved with the SiO_2 , although this material has a coefficient of thermal expansion (CTE) significantly lower than the SiC, giving rise to thermal stresses at the SiC/ SiO_2 interface. Many studies have shown CVD, PECVD and sputtering as appropriate techniques to deposit SiC films on SiO_2/Si (Zanola, 2004).

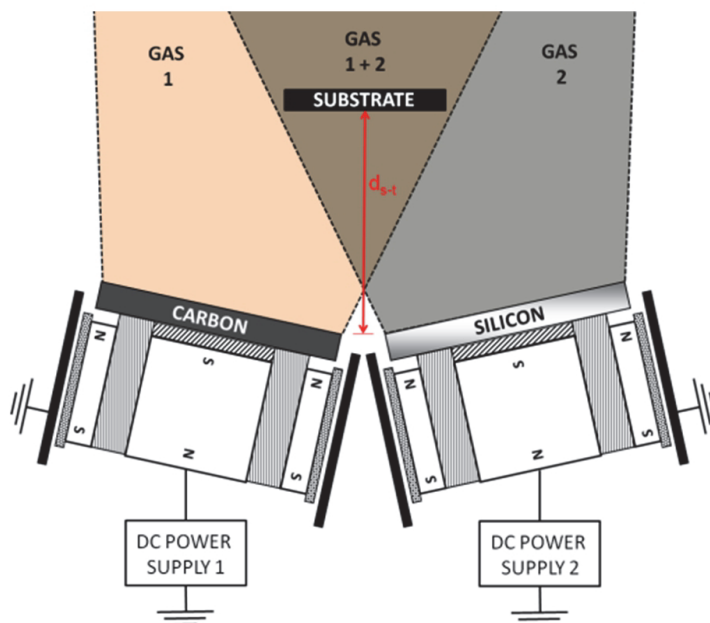


Fig. 7. Schematic diagram of magnetron co-sputtering deposition technique.

After the film deposition, the residual stress must be investigated. SiC films obtained by CVD have low residual stress due to high temperatures involved in this process. However, films obtained by PECVD and sputtering exhibit a significant tensile or compressive residual stress that is dependent on various deposition parameters. To reduce this stress post-deposition thermal annealing is usually performed (Zorman, 2006).

The following step is used to determine the chemical, physical and structural properties of the as-deposited SiC film. For piezoresistive sensor applications, it is fundamental the knowledge of the orientation, elastic modulus, doping concentration and resistivity of the film. After determining these properties, the piezoresistive characterization of the film is started. First, a test structure must be developed. Generally, this structure consists of a SiC thin-film piezoresistor fabricated by photolithography, lift-off and etching processes as illustrated in Figure 8.

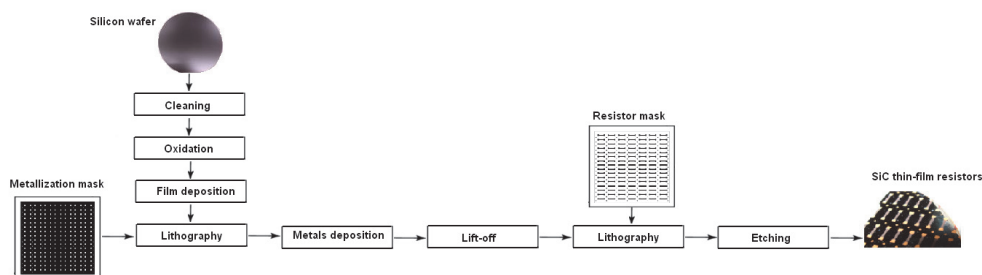


Fig. 8. Schematic flow diagram of the SiC thin-film resistor fabrication process.

The most used technique to determine the value of GF of a piezoresistor is the cantilever deflection method. In this method, the piezoresistor is glued near to the clamped end of a cantilever beam and on the free end of the beam different loads are applied. The value of GF is obtained by monitoring the resistance change when the resistor is subjected to different applied stress. Once determined the GF , the TCR and the $TCGF$ are determined to evaluate the influence of the temperature (see details on topic 2).

Table 2 summarizes the main requirements that SiC film should present to be successfully used in the development of piezoresistive sensors. As can be seen, the resistivity of the SiC thin film should be low (preferably of the order of $\text{m}\Omega\cdot\text{cm}$) because its thickness in general less than $1.0\ \mu\text{m}$. As the depth of the SiC thin-film piezoresistor is equals the thickness film, it is necessary a low resistivity film to form low electrical resistance piezoresistors.

Electrical and Mechanical Characteristics	Requirement
Elastic modulus	The greater
Residual stress	The lower
Resistivity	The lower
GF	The greater
TCR	The lower
$TCGF$	The lower

Table 2. Main requirements of SiC films for piezoresistive sensor applications.

6. Examples of piezoresistive sensors based on SiC films

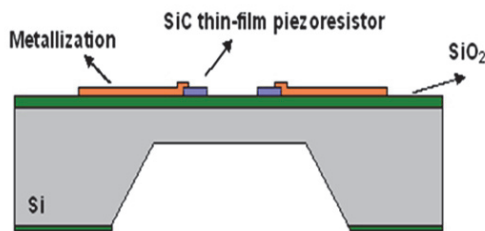
Among the many silicon-based microsensors, piezoresistive pressure sensors are one of the widely used products of microelectromechanical system (MEMS) technology. This type of sensor has dominated the market in recent decades due to characteristics such as high sensitivity, high linearity, and an easy-to-retrieve signal through bridge circuit. The main applications of Si-based piezoresistive pressure sensors are in the biomedical, industrial and automotive fields. However, these sensors have a drawback that is the influence of the temperature on their performance. For some applications, this temperature effect can be compensated by an external circuit, which adds substantial cost to the sensor.

Given this, many studies have been performed aiming to reduce the temperature effects on the performance of the sensor through the use of piezoresistive sensing elements formed by wide bandgap semiconductor thin film as the SiC. The goal is to develop sensors as small as possible and enable to operate at high temperatures. For this, besides making the piezoresistors based on material with suitable properties for high temperature applications should also be used stable electrical contacts with excellent environmental stability. It is known that the metallization type also influences the performance of the devices at harsh environments. Studies show that for SiC sensors the best high-temperature contacts are metal as Au, Ni, Ti and W and binary compounds such as TiSi_2 and W_2Si_5 (Cocuzza, 2003).

A typical SiC thin-film based piezoresistive pressure sensor consists of SiC thin-film piezoresistors, configured in Wheatstone bridge, on a diaphragm. The monocrystalline silicon is the material most used to form the diaphragm due its mechanical properties which make it an excellent material for elastic structural members of a sensor. In addition, the Si diaphragms can be easily fabricated by KOH anisotropic etching from the backside of a (100) silicon wafer using

the SiO_2 or Si_3N_4 film as etch mask. It is also necessary to grow SiO_2 or Si_3N_4 on the front side of the wafer to perform the electrical insulation of the SiC thin-film piezoresistors from the substrate. Generally, the SiC thin-film piezoresistors are produced by RIE (reactive ion etching). Figure 9 illustrates two piezoresistive pressure sensors based on SiC films: one with six PECVD a-SiC thin-film piezoresistors, configured in Wheatstone bridge, on a SiO_2/Si square diaphragm with Ti/Au metallization (Fraga et al., 2011b) and the other with phosphorus-doped APCVD polycrystalline 3C-SiC piezoresistors on $\text{Si}_3\text{N}_4/\text{3C-SiC}$ diaphragm with Ni metallization (Wu et al., 2006).

(a) SiC thin-film piezoresistors on SiO_2/Si diaphragm



(b) SiC thin-film piezoresistors on $\text{Si}_3\text{N}_4/\text{SiC}$ diaphragm

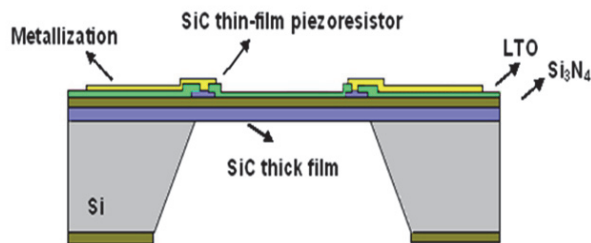


Fig. 9. Schematic illustration of piezoresistive pressure sensors based on SiC films.

Another sensor type that has been developed based on SiC is the accelerometer. However, for now, the studies are still focused on piezoresistive accelerometers based on 6H-SiC bulk substrate (Atwell et al., 2003) or on SiC thin-film capacitive accelerometers (Rajaraman et al., 2011).

This occurs because the capacitive accelerometer is usually more sensitive than piezoresistive one and furthermore can be used in a wide range of temperature. On the other hand, the capacitive accelerometers have elevated cost and necessity of signal conditioning circuit (Koberstein, 2005). The motivation to develop piezoresistive accelerometers on 6H-SiC bulk is the possibility of obtaining superior performance at high temperature in comparison with capacitive accelerometer.

As mentioned earlier, the cost of the 6H-SiC is also elevated which has stimulated the researches on SiC thin-film piezoresistive accelerometer. The simplest model for this accelerometer is illustrated in Figure 10. This accelerometer consists of a SiC thin-film piezoresistor (or four piezoresistors configured in Wheatstone bridge) on a silicon cantilever beam which has a rigid silicon proof mass attached at its free end. The basic principle of this type of sensor is that the acceleration moves the proof mass so deflecting the cantilever which works as a spring. The mass shift produces a variation of the internal stress of the spring that can be sensed by the piezoresistor. The value of the acceleration can be inferred by the measurement of the magnitude of the stress. The main problem of this accelerometer is that all its structure is built on silicon which can limit the performance at harsh environments.

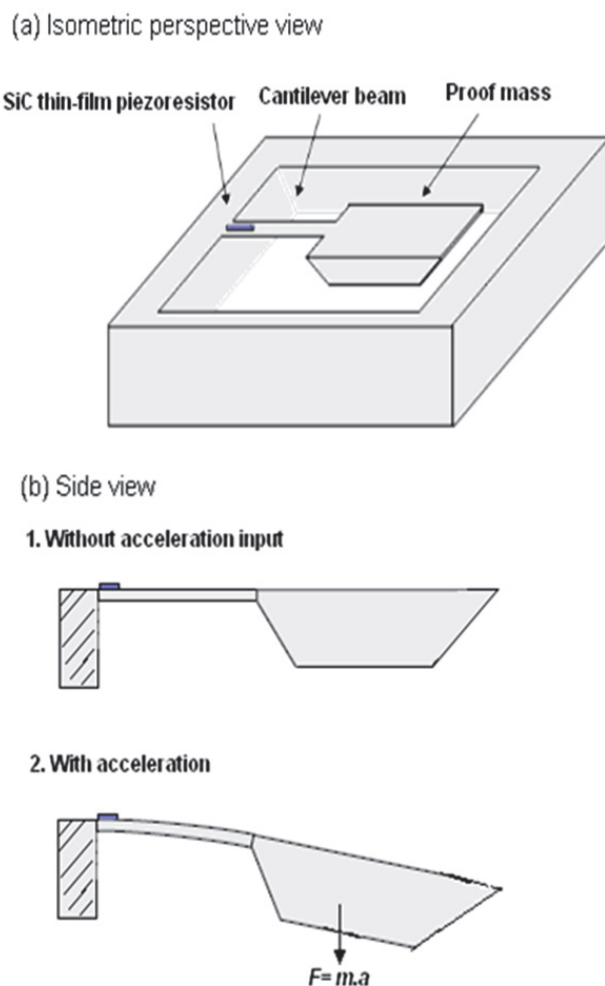


Fig. 10. Schematic illustration of a SiC thin-film based piezoresistive accelerometer.

7. Summary

It is notable that in recent years significant advances have been made in the SiC thin film technology for piezoresistive sensors application. These advances include improvement of deposition techniques to optimize the electrical, mechanical and piezoresistive properties of crystalline and amorphous SiC films which have enabled the development of sensors appropriate for harsh environments with costs lower than those based on SiC bulk.

This chapter reviewed the concepts of piezoresistivity, presented a brief survey on the studies of piezoresistive properties of SiC films, described the main techniques that are being used to deposit SiC films for MEMS sensor applications, discussed when and why to use SiC and what are the requirements that SiC films must attain to be applied successfully in piezoresistive sensors. Furthermore, it was shown examples of SiC film based pressure sensors and accelerometers.

8. Acknowledgments

The authors acknowledge the financial support of Brazilian agencies: program PNPd-CAPES (process number 02765/09-8), CNPq (process number 152912/2010-0) and AEB. We also would like to thank the institutions that have provided their infrastructure for the experiments: Plasma and Processes Laboratory of the Technological Institute of Aeronautics, Microfabrication Laboratory of the Brazilian Synchrotron Light Laboratory (LMF-LNLS), Institute for Advanced Studies (IEAv), Center of Semiconductor Components (CCS-UNICAMP), Faculty of Technology of São Paulo (FATEC-SP) and Associate Laboratory of Sensors (LAS-INPE).

9. References

- Allameh, S. M.; Soboyejo, W.O.; Srivatsan, T.S. (2006) *Silicon-Based Microelectromechanical Systems (Si-MEMS)*, In: *Advanced Structural Materials: Properties, Design Optimization, and Applications*, pp.63-94.
- Atwell, A.R.; Okojie, R.S.; Kornegay, K.T.; Roberson, S.L.; Beliveau, A. (2003) *Sensors and Actuators A: Physical*, Vol.104, pp.11-18.
- Berg, S.; Nyberg, T. (2005) *Thin Solid Films*, Vol.476, pp.215-230.
- Bogaerts A.; Neyts E.; Gijbels R.; Mullen J. (2003) *Spectrochimica Acta Part B*, Vol.57, pp.609-658.
- Camassel, J.; Juillaguet, S. (2007) *J. Phys. D: Appl. Phys.*, Vol.40, pp.6264-6277.
- Chaudhuri, J.; Ignatiev, K.; Edgar, J.H.; Xie, Z.Y.; Gao, Y.; Rek, Z. (2000) *Mater. Sci. Eng. B*, Vol.76, pp.217-224.
- Chowdhury, I.; Chandrasekhar, M.V.S.; Klein, P.B.; Caldwell, J.D.; Sudarshan, T. (2011) *Journal of Crystal Growth*, Vol.316, pp.60-66.
- Cimalla, V.; Pezoldt, J.; Ambacher, O. (2007) *J. Phys. D: Appl. Phys.*, Vol.40, pp.6386-6434.
- Cocuzza, M. (2003) *Development of silicon and silicon carbide-based micro-electromechanical systems*, PhD thesis, Polytechnic of Turin.
- Doi, I. (2006) *Técnicas de deposição: CVD, notas de aula da disciplina IE726 – Processos de Filmes Finos*, Universidade Estadual de Campinas.
- Eickhoff, M.; Möller, M.; Kroetz, G.; Stutzmann, M. (2004) *J. Appl. Phys.*, Vol.96, pp. 2872-2877.
- Fissel, A.; Kaiser, U.; Ducke, E.; Schroter, B.; Richter, W. (1995) *J. Cryst. Growth*, Vol.154, pp.72-80.

- Foti, G. (2001) *Applied Surface Science* Vol.184, pp.20-26.
- Fraga, M.A. (2009) *Desenvolvimento de sensores piezoresistivos de SiC visando aplicação em sistemas aeroespaciais*, PhD thesis, Instituto Tecnológico de Aeronáutica.
- Fraga, M.A.; Furlan H.; Massi, M.; Oliveira I.C. (2010a) *Microsyst Technol.*, Vol. 16, pp.925-930.
- Fraga, M.A. (2011a) *Materials Science Forum*, Vol. 679-680, pp.217-220.
- Fraga, M.A.; Furlan, H.; Massi, M.; Oliveira, I.C.; Mateus, C.F.R.; Rasia, L.A. ; (2011b) *Microsyst. Technol.*, In press.
- Fraga, M.A.; Furlan H.; Pessoa, R.S. (2011c) *Comparison among performance of strain sensors based on different semiconductor thin films*, *Proceedings of the SPIE Microtechnologies - Smart Sensors, Actuators and MEMS Conference*, Prague, April 2011.
- George T.; Son K.A.; Powers R.A.; Del Castillo L.Y.; Okojie R. (2006) *Harsh environment microtechnologies for NASA and terrestrial applications*, *Proceedings of IEEE sensors*, Irvine, November 2005.
- Gracio, J. J.; Fan, Q. H.; Madaleno, J. C. (2010) *J. Phys. D: Appl. Phys.*, Vol.43, 374017 (22pp).
- Grill, A. (1994) *Cold Plasmas in Materials Fabrication: From Fundamentals to Applications*, IEEE Press, 257p.
- Guk, G. N.; Usol'tseva, N.Y.; Shadrin, V.S.; Mundus-Tabakaev, A.F. (1974a) *Sov. Phys. Solid State*, Vol.8, pp. 406-407 as cited in (Okoiye, 2002).
- Guk, G.N.; Lyubimskii, V.M.; Gofman, E.P.; Zinovév, V.B; Chalyi, E.A. (1974b) *Sov. Phys. Solid State*, pp.104-105.
- Guk, G. N. ; Usol'tseva, N.Y. ; Shadrin, V.S. ;Prokop'eva, N.P (1976) *Sov. Phys. Solid State*, Vol. 10, pp.83-84 as cited in (Shor et al., 1993).
- Hobgood, H. McD.; Brady, M. F.; Calus, M. R.; Jenny, J. R.; Leonard, R. T.; Malta, D. P.; Müller, S. G.; Powell, A. R.; Tsvetkov, V. F.; Glass, R. C.; Carter, C. H. (2004) *Mater. Sci. Forum*, Vol.457-460, pp.3-8.
- Johns, G.K. (2005) *Journal of Applied Engineering Mathematics*, Vol. 2, pp. 1-5.
- Kerdiles, S.; Rizk, R.; Gourbilleau, F.; Perez-Rodriguez, A.; Garrido, B.; Gonzalez-Varona, O.; Morante, J.R. (2002) *Materials Science and Engineering B*, Vol.69-70, pp.530-535.
- Kikuchi, N; Kusano, E.; Tanaka, T.; Kinbara, A.; Nanto, H. (2002) *Surface and Coatings Technology*, Vol.149, pp.76-81.
- Koberstein, L. (2005) *Modelagem de um acelerômetro de estado sólido*, Master dissertation in Electrical Engineering, University of São Paulo.
- Kulikovsky V. ; Vorlíček, V.; Boháč, P.; Stranyánek, M.; Čtvrtlík, R.; Kurdyumov, A. ; Jastrabík, L. (2008) *Surface & Coatings Technology*, Vol.202, pp.1738-1745.
- Lattemann, M.; Nold, E.; Ulrich, S.; Leiste, H.; Holleck, H. (2003) *Surface and Coatings Technology*, Vol.174-175, pp.365-369.
- Lieberman, M.A.; Lichtenberg, A.J. (2005) *Principles of Plasma Discharges and Materials Processing*, 2nd edn, New York: Wiley.
- Luchinin, V.V.; Korlyakov, A.V. (2009), *Materials and elements of constructions for extreme micro- and nanoengineering*, *Proceedings of the EUROCON*, pp.1242-1245.
- Mandracci, P.; Chiodoni, A.; Cicero, G.; Ferrero, S.; Giorgis, F.; Pirri, C.F.; Barucca, G.; Musumeci, P.; Reitano, R. (2001) *Applied Surface Science* Vol.184, pp.43-49.
- Medeiros, H. S.; Pessoa, R.S.; Sagás, J.C.; Santos, L.V.; Fraga, M.A.; Maciel, H.S.; Sobrinho, A. S. S.; Massi, M. (2010) *Effect of Concentration of Carbon and Silicon in the SiC Thin Film Deposition by Dual Magnetron Sputtering System*, In : IX SBPMat, Ouro Preto-MG, Brazil.
- Morin, F. J.; Geballe, T. H.; Herring, C. (1956) *Physical Review*, Vol.10, No.2, pp.525-539.
- Neyts, E. (2006) *Mathematical Simulation of the Deposition of Diamond-like carbon (DLC) Films*, PhD thesis, Universiteit Antwerpen.

- Okojie, R.S.; Ned, A.A.; Kurtz, A.D.; Carr, W.N. (1996) α (6H)-SiC pressure sensors for high temperature applications, Micro Electro Mechanical Systems (MEMS '96) Proceedings, pp.146-149.
- Okojie, R.S.; Ned, A.A.; Kurtz, A.D.; Carr, W.N. (1998a) *IEEE Trans. Elec. Dev.*, Vol. 45, pp.785-790.
- Okojie, R.S.; Ned, A.A.; Kurtz, A.D. (1998b) *Sensors and Actuators A: Physical*, Vol.66, pp.200-204.
- Okojie, R.S. (2002) *Fabrication and characterization of single-crystal silicon carbide MEMS*. In: *MEMS Handbook*, Mohamed Gad-el-Hak, pp.20.1-20.31, CRC Press.
- Ohring, M. (2002) *Material Science of Thin Films: Deposition & Structure*, San Diego, CA : Academic Press, 2^o edition, 794 p.
- Pearson, G.L.; Read Jr., W.T.; Feldman, W.L. (1957) *Acta Metallurgica*, Vol. 5, pp.181-191.
- Peng, X.; Matthews, A.; Xue, S. (2011) *J. Mater. Sci.*, Vol.46, pp.1-37.
- Rajab, S.M.; Oliveira, I.C.; Massi, M.; Maciel, H.S.; dos Santos Filho, S.G.; Mansano, R.D. (2006) *Thin Solid Films*, Vol.515, pp.170-175.
- Rajagopalan, T.; Wang, X.; Lahlouh, B.; Ramkumar, C.; Dutta, P.; Gangopadhyay, S. (2003) *Journal of Applied Physics*, Vol.94(8), pp.5252-5260.
- Rajaraman, V.; Pakula, L.S.; Yang, H.; French, P.J.; P. M. Sarro (2011) *Int J Adv Eng Sci Appl Math*, Vol. 2, pp. 28-34
- Rapatskaya, I.V.; Rudashevskii, G.E.; Kasaganova, M.G.; Islitsin, M.I.; Reifman, M.B.; E.F. Fedotova, E.F. (1968) *Sov. Phys. Solid State*, Vol. 9, pp. 2833-2835 as cited in Okojie, 2002.
- Singh, R.; Ngo, L.L.; Seng H.S.; Mok, F.N.C. (2002) *A Silicon piezoresistive pressure sensor, Proceedings of the First IEEE International Workshop on Electronic Design, Test and Applications*, pp.181-184.
- Shor, J.S.; Goldstein, D.; Kurtz, A.D. (1993) *IEEE Trans. Elec. Dev.*, Vol. 40, pp.1093-1099.
- Smith, C.S. (1954) *Physics Review*, Vol. 94, pp. 42-49.
- Stamate, M.D.; Lazar, I.; Lazar, G. (2008) *Journal of Non-Crystalline Solids*, Vol.354, pp.61-64.
- Stanescu, C.D.; Voican, C. (2007) *Accelerated Stress Testing of SiC Pressure Transduce*, In: *Proceedings of Fascicle of Management and Technological Engineering*, Vol. VI, pp.779-784.
- Strass, J.; Eickhoff, M.; Kroetz, G. (1997) *The influence of crystal quality on the piezoresistive effect of β -SiC between RT and 450°C measured by using microstructures*, In: *International Conference on Solid State Sensors and Actuators*, Vol. 2, pp.1439-1442.
- Toriyama, T.; Sugiyama S. (2002) *Appl. Phys. Lett.*, Vol. 81, pp.2797-2799.
- Vandelli, N. (2008) *SiC MEMS Pressure Sensors for Harsh Environment Applications*, MicroNano News, pp.10-12.
- Window, A.L. (1992) *Strain Gauge Technology*, Springer, London.
- Wright, N. G.; Horsfall, A. B. (2007) *J. Phys. D: Appl. Phys.*, Vol. 40, pp.6345-6354.
- Wu, C.H.; Stefanescu, H.; Zorman, C. A.; Mehregany, M. (2001) *Fabrication and Testing of Single Crystalline 3C-SiC piezoresistive Pressure Sensors*, In: *Euroensors XV*.
- Wu C.H.; Zorman C.A.; Mehregany M. (2006) *IEEE Sensors Journal*, Vol.6, pp. 316-324.
- Zanola, P.; Bontempi, E.; Ricciardi, C.; Barucca, G.; Depero, L.E. (2004) *Materials Science and Engineering B*, Vol.114-115, pp. 279-283.
- Zhao, D.; Mourey, D.A.; Jackson, T.N. (2010) *Journal of Electronic Materials*, Vol. 39, No. 5, pp. 554-558.
- Ziermann, R.; von Berg, J.; Reichert, W.; Obermeier, E.; Eickhoff, M.; Krotz, G. (1997) *A high temperature pressure sensor with β -SiC piezoresistors on SOI substrates*, *International Conference on Solid State Sensors and Actuators*, Chicago, June 1997.
- Zorman, C.A.; Fu, X.; Mehregany M. (2006) *Deposition techniques for SiC MEMS* In: *Silicon Carbide Micro Electromechanical Systems*, pp. 18-45.

Opto-Electronic Study of SiC Polytypes: Simulation with Semi-Empirical Tight-Binding Approach

Amel Laref¹ and Slimane Laref²

¹*Department of Physics and Astronomy, King Saud University,
Riyadh 11451, Saudi Arabia*

and Department of physics, National Taiwan University, Taipei 106

²*Université de Lyon, CNRS, Ecole Normale Supérieure de Lyon, Institut de Chimie de
Lyon, Laboratoire de Chimie, Lyon*

¹*Taiwan*

²*France*

1. Introduction

The recent growing scientific and technological interest on silicon carbide (SiC) arises from its peculiar physical properties, i.e., its mechanical, and chemical stability. Moreover, SiC is considered to be a promising material for electronic and optical devices. Microelectronic devices made of SiC can be used in high-power, high-speed, high temperature, high-frequency, and even hard-radiation application (1)-(4). The strong bonding between Si and C atoms in SiC makes this material very resistant to high temperature and radiation damage. In view of this extraordinary application potential a thorough knowledge of the structural and electronic properties of SiC is a matter of both ionic interest and technological importance. In addition to its traditional use as an abrasive (carborundum) there is currently much interest in materials made from SiC fibres, which compare well with their carbon fibre counterparts. Over a two hundred chemically stable semiconducting polytypes of SiC exist, they have a high bulk modulus and generally wide band gap. From such difference in stacking order it is possible to get almost 200 different crystal structures (1)-(10) of which the two extremes are the pure cubic polytype (with zinc blende structure) and the pure hexagonal one (with wurtzite structure). SiC is the most prominent of a family of close packed materials which exhibit a one dimensional polymorphism called polytypism. In addition, numerous hexagonal and rhombohedral structures (11)-(19) of SiC have been identified in addition to the common cubic form. In fact, SiC is one of the few compounds which form many stable and long-range ordered modifications, so-called polytypes (11)-(17). Previously, SiC has been subject to many theoretical studies. With this respect, a variety of structural, electronic and optical properties in SiC have been investigated by many theoretical groups (12)-(15) and the results can be related to the experimental works (7)-(10). In the last years, first-principle calculations have been applied to determine the ground-state properties of cubic and hexagonal polytypes of SiC (19)-(53). Based on previous theoretical works, the high-pressure behavior (18)-(33), and the effect of atomic relaxation on structural properties

were also investigated (14)–(18). Some attempts towards the explanation of the existence of a large number of metastable SiC polytypes have been also undertaken (14)–(37). The electronic band structures of some SiC polytypes have been calculated by several groups (14)–(47). Further studies went deep into the optical properties of SiC polytypes (14)–(33). The optical and spectroscopic properties of SiC polymorphs have also been investigated by many groups both experimentally (7)–(14) and theoretically (19)–(25). Due to the problem of sample availability, most measurements were on 6H-SiC and 3C-SiC (54)–(57). Very recently, some measurements on 4H-SiC have also been reported (58)–(61). There are considerable variations in the measured optical properties mainly because the photon energy is limited to less than 6.6 eV using the popular ellipsometry technique. The use of vacuum-ultraviolet (VUV) spectroscopy can extend the energy range significantly and so far has only been carried out on 6H-SiC (57). Recent advances in crystal growth of SiC have allowed the study of the optical properties of different polytypes (54)–(60). In addition, tight-binding (TB) method has proven to be very useful for the study of both semiconductors and metallic systems, especially in systems which are too large to be studying via ab-initio techniques. This method is about 2 or 3 orders of magnitude faster than the ab initio formulations, and at the same time it describes with suitable accuracy the electronic structure of the systems. The computational efficiency of the TB method derives from the fact that the Hamiltonian can be parametrized. Furthermore, the electronic structure information can be easily extracted from the TB hamiltonian, which, in addition, also contains the effects of angular forces in a natural way. In order to use a more realistic method, we present a TB model with sp^3s^* basis, representing exact curvatures of lowest conduction bands. The TB approach is standard and widely used for the electronic properties of a wide variety of materials. In the present contribution we overview our most recent results on the electronic structures and optical properties of SiC polytypes (62). Hence, the SiC polytypes can be considered as natural superlattices, in which the successive layers consist of Hexagonal SiC material of possibly different width. Our TB model can treat SiC polytypes as superlattices consisting hexagonal bulk-like blocks. We have investigated to which extent it is acceptable approximation for existing polytypes when various of nH-SiC crystal are used to present polytype superlattices. Indeed, this is an accurate approximation by building blocks consist of n-layers of nH-SiC. By representing in general the polytypes as superlattices, we have applied our recent TB model (62) that can treat the dimensions of the superlattice. Within this model we take for each sublayer linear combination of atomic orbitals of hexagonal SiC which are subsequently matched at the interfaces to similar combinations in the adjacent sublayers by using the boundary conditions. Polytypic superlattices, in comparison with heterostructure superlattices, have two important additional features, namely (i) the polytypes are perfectly lattice-matched superlattices and (ii) the polytypes have an energy band offset between adjacent layers equal to zero by definition. We can obtain with our TB model the band structures and particularly the energy band gaps of SiC polytypes and their wave functions. Our recent TB model (62) is very efficient when extended it to investigate the electronic properties of wurtzite (wz) superlattices in (0001) direction.

This chapter is organized as follows: Section 1 provides a review for the large band-gap SiC based semiconductor device technology. In the next section we present the different polytism of SiC. A fundamental concept of the TB theory for SiC polytypes is described in section 3. Our recent TB model is specifically applied to study the electronic and optical properties of SiC polytypes and it can be applied to nH-SiC wurtzite superlattices. The present approach is also suited for all wurtzite semiconductor superlattices and large complex unit cells which

can be treated where the transferability of the hopping parameters is required. Section 4 deals with some of our recent results of the electronic and optical properties of SiC polytypes. To reach these, we analyzed this statement in terms of optoelectronic properties of SiC polytypes. Finally in section 5 we summarize and conclude.

2. A review of the large band-gap SiC based semiconductor device technology

The recent surge of activity in wide band-gap semiconductors has arisen from the need for electronic devices capable of operation at high power levels, and high-radiation resistance, and separately, a need for optical materials, especially emitters, which are active in the blue and ultraviolet (UV) wavelengths (63)-(69). In this aspect, there has been renewed interest in SiC as one of the wide band gap compounds with great potential for the next generation of electronic devices operating at high temperature (61)-(68). This compound has been also used primarily in light-emitting diodes. SiC's intrinsic material properties as well as its existence in various polytypes have led to a revival of technological interest. Crystal growth of SiC polytypes has recently shown considerable progress, the expectation now being that the manufacturing of different electronic devices becomes feasible. The wide band-gap semiconductor SiC, with its excellent thermal conductivity, large breakdown fields, and resistance to chemical attack, will be the material of choice for these applications. Realized prototype power devices of SiC, like rectifier diodes, and junction field-effect transistors, show indeed encouraging performance results under extreme conditions (54)-(66). In the optical device arena, the ever increasing need for higher density optical storage and full color display technologies are driving researchers to develop wide band-gap semiconductor emitting technologies which are capable of shorter wavelength operation. Since the different energy gap values of SiC all happen to lie in the visible range of the spectrum, SiC is an interesting optical device material. Indeed, blue light emitting diodes were the first electronic SiC devices which found a good sale. Some SiC polytypes are in addition most promising as photodetective material sensitive to ultraviolet radiation. SiC is a good candidate for a short wave length diode laser. Prototype transistors have been fabricated from SiC, and the microwave and high temperature performance of SiC transistors have been studied. Devices like field effect transistors, bipolar storage capacitors, and ultraviolet detectors have been fabricated (57)-(64). SiC has a relatively high atomic bonding energy which is responsible for its mechanical strength and chemical stability at high temperatures. This material can without major difficulty, be crystallized in several polytypes, primarily due to similar geometric structures and atomic bonds (1)-(11). The different stacking of C-Si bilayers remarkably influences the properties of SiC. The most pronounced example concerns their electronic structure. Hence, a controlled epitaxial growth of different polytypes on each other would lead to high-quality heterostructures of chemical identical material with a locally adjustable band gap (7)-(14). Meanwhile, growth of heterocrystalline structures seems to be possible (4), but exhibits problems with the reproducibility and the crystal quality. Another possibility to create a combination of two polytypes is a solid-solid phase transition, which transforms one polytype into another one (6)-(8). However, polytypism also gives some advantages for constructing electronic devices, for example homo-material heterostructures. Quantum wells can be made by embedding a SiC polytype in another polytype with a wider gap (55)-(60). Among the SiC polytypes, 6H is most easily prepared and best studied, while the 3C and 4H polytypes are attracting more attention for their superior electronic properties. The very simple structure 2H is, in fact, very rarely produced by the employed growth techniques. Already, commercial applications have been done but most of the developments in industry

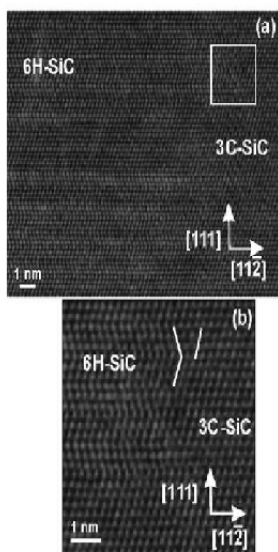


Fig. 1. (a) HRTEM image, displaying that the 3C/6H-SiC polytypic transformation takes place by three bilayers thin lamellae twinned along the (111) planes and bounded along the (11 $\bar{2}$) planes. Image (b) presents a magnification of the area marked by the square in (a) (56).

and research laboratories focus on two hexagonal polytypes : the 6H and 4H-SiC varieties. The polytypism of SiC makes it non-trivial to grow single phase material, but it also offers some potential advantages if crystal growth methods can be developed sufficiently to capitalize on the possibility of polytype homo/heterojunctions (see figure 1).

2.1 Polytypism in SiC

SiC is a wide band gap semiconductor that can be synthesized in a variety of polytypes: polytypism, can be considered as a one dimensional variant of polymorphism (1)-(8). Indeed, while the term polymorphism generally refers to the possibility of an element or compound to crystallize in different structures, polytypes only differ for the stacking sequence of atomic layers along one crystalline direction. We include SiC in the group of polytypes because of its simplicity and the fact that its hexagonality is 100%. All various SiC-polytypes have the same stoichiometry and the same bonding configuration between next nearest neighbors. More than 200 polytypes of SiC exhibiting a wide range of properties have been reported (1). There are a lot of more complex polytypes in which the bonding arrangement (cubic vs. hexagonal) are repeated periodically. Due to that periodic repetition the SiC-polytypes are also called to be natural superlattices. However, only few of those polytypes are commonly found and those are relatively simple compared to the rest. The bandgaps differ widely among the polytypes ranging from 2.3 eV for 3C-SiC to 2.9 eV in 6H SiC to 3.3 eV for 2H SiC. In general, the greater the wurtzite component, the larger the bandgap.

A shorthand has been developed to catalogue the literally infinite number of possible polytype crystal structure. In this notation the number of layers in the stacking direction, before the sequence is repeated, is combined with the letter representing the Bravais lattice type: cubic

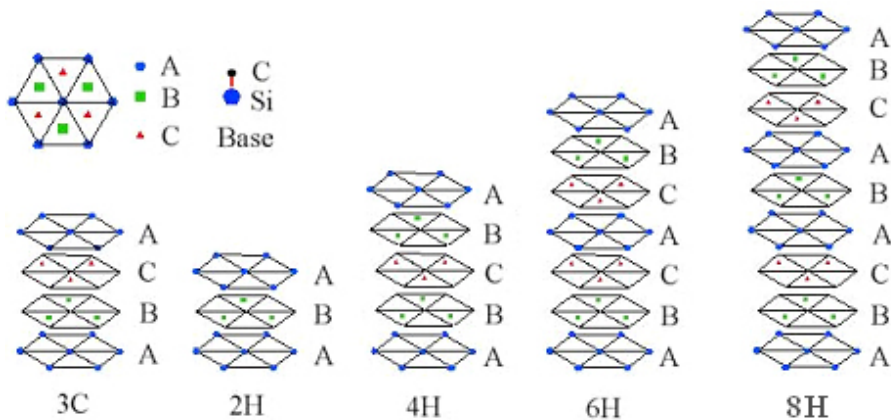


Fig. 2. Three-dimensional perspective views of the primitive hexagonal unit cells of the 3C-(zinc-blende), 2H-(wurtzite), 4H-, 6H-, and 8H-SiC polytypes. The stacking sequences ABC (3C), AB (2H), ABCB (4H), ABCACB (6H) and ABCAB ACB (8H) are also indicated.

(C) or hexagonal (H). With reference to figure 2, if the first Si-C layer is labelled A, the next layer that can be placed according to a closed packed structure will be placed either on B or C. The different polytypes are constructed by permutations of these three positions. In figure 2 the stacking sequence is shown for the most common polytypes, 3C, 2H, 4H, 6H, and 8H, which are very interesting for their technological applications. Three-dimensional perspective views of the primitive hexagonal unit cells of the 2H-, 3C-, 4H-, 6H-, and 8H-SiC polytypes. In the case of SiC, the basic units are tetrahedrons with a C(Si) atom at the center, surrounded by four Si(C) atoms covalently bonded: these units are periodically repeated in closed-packed hexagonal layers, whose stacking sequence gives rise to the different polytypes. Though being different in the long range order, the several polytypes show a similar local chemical environment for both the carbon and silicon species; in particular each Si(C) atom is situated above the center of a triangle of C(Si) atoms and underneath a C(Si) atom belonging to the next layer in a tetrahedral coordination. The SiC-polytypes consist of double silicon-carbon layers which are stacked on top of each other in the c-axis direction. A local arrangement of three consecutive double layers is called hexagonal, if it is like the arrangement of double layers in wurzite. It is called cubic, if the stacking arrangement is the same as for the zinc-blende structure. The basic structural elements is the SiC bilayer composed of one Si [0001] plane and the adjacent C[0001] plane. The SiC polytypes are differentiated by the stacking sequence of the tetrahedrally bonded SiC bilayers, such that the individual bond lengths and local atomic environments are nearly identical, while the overall symmetry of the crystal is determined by the stacking periodicity. Each SiC bilayer, while maintaining the tetrahedral bonding scheme of the crystal, can be situated in one of three possible positions with respect to the lattice. These are each arbitrarily assigned the notation A, B, or C. Depending on the stacking order, the bonding between Si and C atoms in adjacent bilayer planes is either of a zincblende (cubic) or wurtzite (hexagonal) nature. Zincblende bonds are rotated 60° with respect to nearest neighbors while hexagonal bonds are mirror images (Figure 2). Each type of bond provides a slightly altered atomic environment making some lattice sites inequivalent in polytypes with mixed bonding schemes and reducing the overall symmetry. These effects are important when considering the substitutional incorporation and electronic transport properties of

SiC. If the stacking is ABCABC..., the purely cubic, i.e., a zinc-blende structure consisting of two interpenetrating face-centered (fcc) cubic lattices. Zincblende structure commonly abbreviated as 3C SiC (or β -SiC) is realized (Figure 2). 3C SiC is the only possible cubic polytype. The stacking direction of the basal planes perpendicular to the planes is in fact [111] direction of the cubic unit cell of 3C-SiC as indicated in the figure. The family of hexagonal polytypes is collectively referred to as alpha SiC. The purely wurtzite ABAB... stacking sequence is denoted as 2H SiC reflecting its two bilayer stacking periodicity and hexagonal symmetry. All of the other polytypes are mixtures of the fundamental zincblende and wurtzite bonds. Some common hexagonal polytypes with more complex stacking sequences are 4H-, 6H- and 8H- SiC (Figure 2). Since the SiC polytypes are mixtures of cubic and hexagonal stackings, a quantity defined as the hexagonality H representing the fraction of hexagonal stackings out of all the stackings (cubic + hexagonal) in a polytype is used frequently to describe how much the polytype is cubic-like or hexagonal-like in structural sense [5]. As it is obvious from the definition, the hexagonality of 2H-SiC is 100 % and that of 3C-SiC is 0 %. It is naturally expected that a polytype with a smaller H should be closer to 3C, i.e., more cubic-like than one with a larger H in other material properties as well as in structure, and this is generally true for most of the polytypes. 4H-, 8H-SiC are composed equally of cubic and hexagonal bonds, while 6H-SiC is two-thirds cubic. Despite the cubic elements, each has overall hexagonal symmetry. All these polytypes have higher periodicity (more Si-C bilayers) along the c-axis than 2H-SiC and they are in general called α -SiC together with 2H-SiC. 4H- and 6H-SiC are the most common polytypes, and single crystal wafers of these polytypes are currently available and hence all recent research for making commercial devices out of SiC are focused on these polytypes.

3. Empirical tight-binding model for hexagonal and n-hexagonal systems: General formalism of the tight-binding model for (0001) wurtzite:

The tight-binding approximation for band structure calculations uses atomic energy parameters and the expansion of the electron wave functions in terms of a linear combination of atomic orbitals (LCAO). In the LCAO method, the basic problem is to find the Hamiltonian matrix elements between the various basis states, as in the original paper of Slater and Koster (70); the matrix elements can be written for the basis functions sp^3 considering various possible interactions. In our recent calculations, a standard semi-empirical sp^3s^* tight-binding method (71) has been employed and the matrix elements are parametrized in order to reproduce the principal features to know the band structures.

The general form of the Hamiltonian is (72).

$$H(k) = \sum_{bb',l} \sum_{\alpha\beta} e^{ik \cdot R_{bb'}^l} E_{\alpha\beta}^{bb'} \left(R_{bb'}^l \right) \quad (1)$$

where l labels the sublayers, b and b' refer to the atomic basis within a sublayer, and α and β are atomiclike orbitals. Given the $E_{\alpha\beta}^{bb'}$'s (bulk band structure) and the $R_{bb'}^l$'s (SL geometry), we can construct the Hamiltonian matrix and diagonalize it directly for the eigensolutions. In our recent study, we have performed a TB method with an sp^3s^* basis set (71). We used the nearest-neighbor TB parameters with a basis of five orbitals (s , p_x , p_y , p_z , and s^*) per atom. We have derived a TB Hamiltonian pH ($p = 2, 4, 6, 8, \dots$) for different polytypes of SiC from the wz TB model. The label pH ($p = 2, 4, 6, 8, \dots$) is the hexagonality for different polytypes. Consider a TB Hamiltonian of two different alternating wz crystals labelled "ca" in (0001)

direction, where c and a are labelled cation and anion atoms. The pH ($p = 2, 4, 6, 8, \dots$) contains $2(2n)$ atoms in a unit cell at R_i with five orbitals each; $|\alpha j\rangle$, where α denotes the s , $x(=p_x)$, $y(=p_y)$, $z(=p_z)$ and s^* (=excited s) orbitals, and j represents the site index in a unit cell which runs from 1 through $2(2n)$.

For each wave vector \mathbf{k} in the Brillouin zone (BZ), the Bloch functions can be constructed by the linear combination of atomic orbitals $|\xi, \mathbf{r}_\alpha, \mathbf{R}_l\rangle$:

$$|\xi, \mathbf{r}_\alpha, \mathbf{k}\rangle = \frac{1}{\sqrt{N}} \sum_l e^{i\mathbf{k} \cdot \mathbf{R}_l + i\mathbf{k} \cdot \mathbf{r}_\alpha} |\xi, \mathbf{r}_\alpha, \mathbf{R}_l\rangle \quad (2)$$

Here ξ is a quantum number that runs over the basis orbitals s , s^* , p_x , p_y , and p_z on the different types of sites α in a unit cell. The N wave vectors \mathbf{k} lie in the first BZ with the origin of the l th unit cell at \mathbf{R}_l , and \mathbf{r}_α represents the positions of the atoms in this unit cell.

The electronic eigen-states of the pH ($p = 2, 4, 6, 8, \dots$) are expanded as:

$$\begin{aligned} |k, \lambda\rangle &= \sum_{\xi, \alpha} \langle \xi, \mathbf{r}_\alpha, \mathbf{k} | k, \lambda \rangle |\xi, \mathbf{r}_\alpha, \mathbf{k}\rangle \\ &= \sum_{\xi, \alpha} C_{\xi\alpha}(\mathbf{k}, \lambda) |\xi, \mathbf{r}_\alpha, \mathbf{k}\rangle \end{aligned} \quad (3)$$

λ denotes the band index and $C_{\xi\alpha}(\mathbf{k}, \lambda)$ is the eigen-wavefunction, which can be obtained by solving the Schrödinger equation.

$$\sum_{\xi, \alpha'} [\langle \xi, \mathbf{r}_\alpha, \mathbf{k} | H | \xi', \mathbf{r}_{\alpha'}, \mathbf{k} \rangle - E_\lambda(\mathbf{k}) \delta_{\xi\xi'} \delta_{\alpha\alpha'}] \langle \xi, \mathbf{r}_\alpha, \mathbf{k} | k, \lambda \rangle = 0 \quad (4)$$

Therefore, we obtain the Hamiltonian matrix for pH ($p = 2, 4, 6, 8, \dots$).

$$H = \begin{matrix} & \begin{matrix} 1 & 2 & 3 & \dots & n-1 & n & 1 & 2 & 3 & \dots & n \end{matrix} \\ \begin{matrix} 1 \\ 2 \\ 3 \\ 4 \\ \vdots \\ n-1 \\ n \\ 1 \\ 2 \\ \vdots \\ n-1 \\ n \end{matrix} & \left[\begin{array}{cccccccccccc} Ha & Hac & & & & & & & & & H_0^{+ca} \\ & Hc & H_{0ac} & & & & & & & & \\ & & Ha & & & & & & & & \\ & & & Hc & & & & & & & \\ & & & & \ddots & & & & & & \\ & & & & & \ddots & & & & & \\ & & & & & & Ha & & & & \\ & & & & & & & Hc & H_{0ac} & & \\ & & & & & & & Ha & Hac & & \\ & & & & & & & & Hc & H_{0ac} & \\ & & & & & & & & & \ddots & \\ & & & & & & & & & & Ha & Hac \\ & & & & & & & & & & & Hc \end{array} \right] \end{matrix} \quad (5)$$

Here, the blocks $H_{c(a)}$, H_{ac} , and H_{0ac} denote intra-material interactions for pH ($p = 2, 4, 6, 8, \dots$), and every element represents a 5×5 matrix. The blocks H_{ca} and H_{0ca} are expressed as:

$$H_{ac} = \begin{bmatrix} a & ac \\ ac^+ & c \end{bmatrix}, \quad H_{0ac} = \begin{bmatrix} aa & ac \\ ca & cc \end{bmatrix} \quad (6)$$

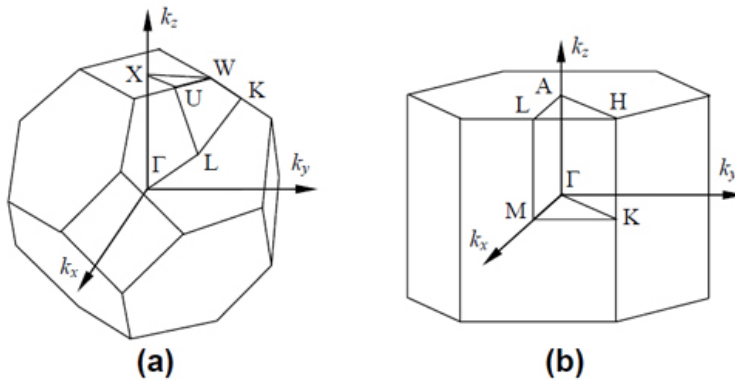


Fig. 3. Brillouin zones of (a) cubic (b) hexagonal structures.

The diagonal elements $H(j = a, \text{ and } c)$ correspond to intra-site energies, and the others contain the nearest atomic interactions in the same layer (H_{ij}) or between two neighbor layers (H_{0ij}) perpendicular to the (0001) direction. The terms a and c are regarded as the anion and cation atoms of the SiC semiconductor. The intra-material elements in the Hamiltonian can be formed uniquely by using the corresponding bulk parameters. Our TB parameters (62) give the correct indirect and direct gap in comparison with Ref.(73) and are checked for their transferability to all considered structures by calculating the optoelectronic properties of different polytypes of SiC. This method reduces the size of the Hamiltonian matrix considerably compared with methods based on plane-wave basis and allows us to treat localized states. Our TB Hamiltonian can be generalized to the wz based SL's in (0001) direction with two different compounds and is efficient when extended it to investigate the electronic properties of wz SL's. Then, we present some of our recent results which we have obtained by our TB model for electronic and optical properties of SiC polytypes.

4. Electronic and optical properties of polytypic SiC

We start this section with some of our recent results for SiC polytypes in order to illustrate the electronic and optical properties of this system. With a TB scheme, the detailed calculations of electronic structure and optical properties of different polytypes of SiC are presented.

4.1 Electronic band structures of 3C-, 2H-, 4H-, 6H-, and 8H-SiC:

A very important aspect of the polytypism of SiC is the change in energy band structure, and how it does appear in the different polytypes. Having established the geometric structure for the polytypes, the electronic band structure was calculated along the symmetry directions (62). Figure 3 shows the BZs of cubic, and hexagonal polytypes with high symmetry points marked. The labeling of the symmetry points and the three symmetry lines out from the Γ point in the relevant hexagonal Bzs are shown in Figure 3.

The corresponding band structure of 3C-SiC is shown in figure 4. The conduction band minimum (CBM) for 3C-SiC is lying at the X point and the number of CBMs equals to three (2). The resulting TB band structures of SiC polytypes (2H, 4H, 6H, and 8H) are also represented in Figure 4 versus high-symmetry lines A-L-M- Γ -A-H-K- Γ . For all polytypes the gap is systematically identified as an indirect one. The valence band maximum is located for

all polytypes at the centre of the BZ. The valence band maximum (VBM) is found to be at the center of the BZ at Γ point for all polytypes. The zero energy is used for all polytypes. In the case of 2H-SiC, the CBM is at the K point with two equivalent CBMs (73), (74), (75), (77), while 4H-SiC has its CBM at the M point giving three equivalent CBMs (22), (25),(76), (78),(79) [Figure 4]. For 6H-SiC, the theoretical calculations predict the conduction band supplying the global CBM to be very flat along the ML line and the CBM resides at some place on the line, resulting in six equivalent CBMs (22), (25), (78),(79). This has been confirmed experimentally from the Raman scattering measurement by Colwell et al. (80). However, the exact location of the CBM and the detailed shape of conduction band affecting the determination of effective electron mass are not yet well-established, either experimentally or theoretically. There are similarities between the band structures of the hexagonal polytypes, both in the valence and the conduction bands, especially between 4H, 6H and 8H-SiC structures. A significant difference between 2H and the other three hexagonal polytypes is that in 2H-SiC the two lowest conduction bands have an intersection along MK line and that the lowest band at K point has a one-dimensional representation (in the single group representation). Both in 4H, 6H and 8H-SiC the two lowest conduction bands at K point are degenerate. The intersection in 2H-SiC makes it possible for the second lowest band at the M point to provide a global conduction band minimum at the K point with C_{3v} symmetry whereas the minimum for 4H-SiC is at M (C_{2v}) and for 6H-, and 8H-SiC along the ML line (also C_{2v} symmetry), 44 % out from M towards L. The variation in band energy gaps is coming from the different locations of CBMs. This is related with the stacking and period of each polytype. Interestingly, it is predicted theoretically that the offsets of VBMs among different polytypes are quite small, at most 0.10-0.13 eV for the case of 2H and 3C (11),(14). In other words, the VBMs of all polytypes are similarly located in energy. This means that the considerable variation of band gap for different polytypes is mainly due to the difference of CBM location.

Another interesting point to note in the conduction band structures of SiC polytypes is the location of second CBM. According to the calculation done by Persson et al. (26),(38), the second CBM of 3C-SiC is at the same symmetry point (X) as the first one with 2.92 eV higher in energy and this was confirmed experimentally from optical absorption measurements with slightly larger energy difference (3.1 eV) between the two minima (13). Persson et al. calculations also show that the three hexagonal polytypes (2H, 4H, 6H) have their second CBMs located at the M point and the energy difference between the first and second CBMs is 0.60 eV for 2H, 0.122 eV for 4H, and 1.16 eV for 6H respectively. The energy position of the second CBM in 4H-SiC has been probed experimentally by BEEM (56)-(58) and optical phonon spectra measurements (59)-(63), with measured energy that ranges 0.10-0.14 eV above the first CBM. The band gaps of several common polytypes of SiC have been measured carefully by Choyke et al. from the optical absorption or luminescence spectra of the polytypes (27). The measured band gaps range widely from 2.390 eV for 3C-SiC to 3.330 eV for 2H-SiC and lot of work has been done to understand all details of the corresponding variations. Those for 4H- and 6H-SiC which are in between the two extreme cases in structure are measured to be 3.265 eV and 3.023 eV respectively. So, from fig.4, it is clear that the valence and the conduction bands are well described. Moreover, our results are in good agreement with the experimental results (74). All energies are with reference to the top of the valence band. The results show that SiC is an indirect gap semiconductor. In addition, the calculated energy gaps of SiC are in good agreement with the other results (73), (74), (75), (77).

Values of lowest indirect forbidden gaps (E_g) are listed in Table 1 in comparison with the available data in the literature and experimental results. Our TB model provides good results

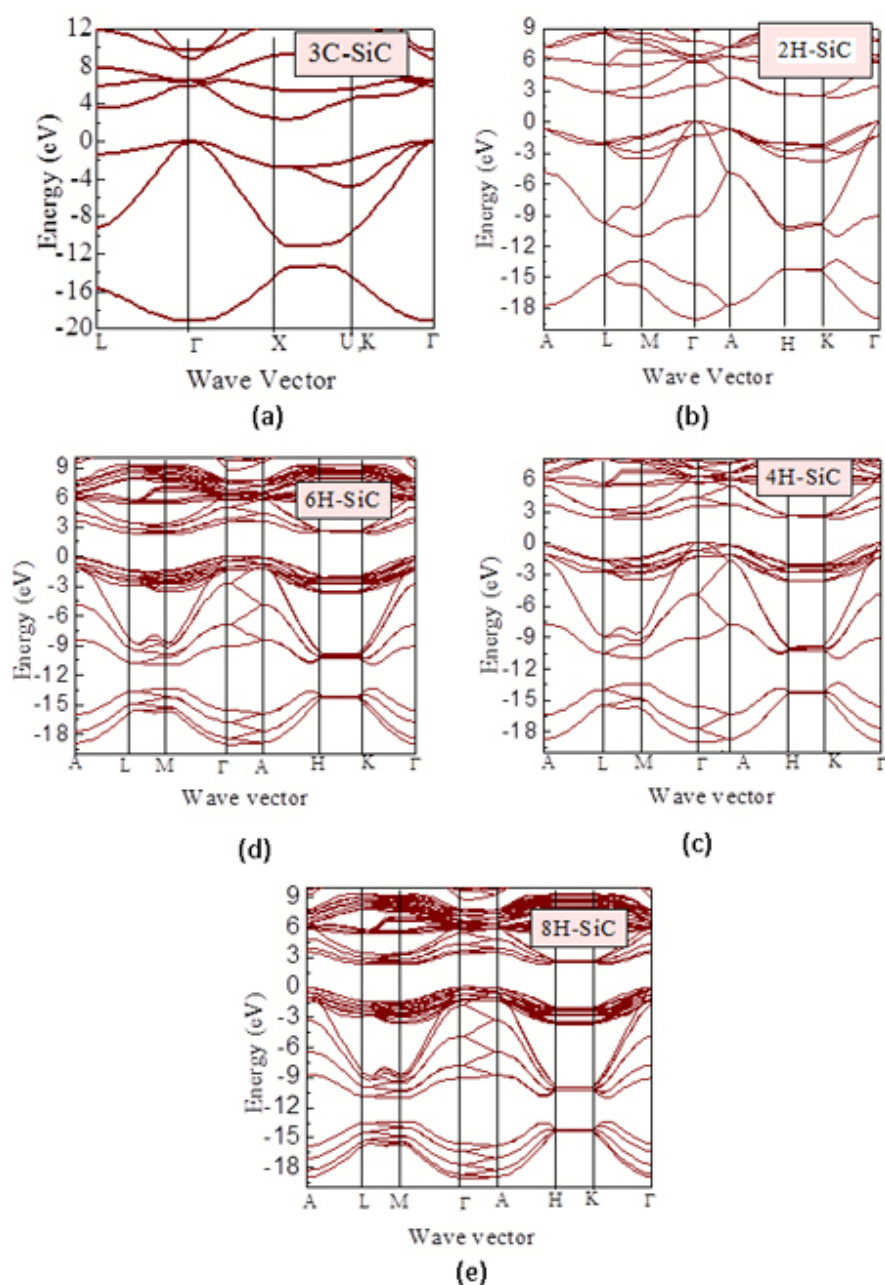


Fig. 4. Band structures for 3C-, 2H-, 4H-, 6H-, and 8H-SiC calculated by our sp^3s^* TB model (62).

	This work	Experiment	GW	LDA+U	GGA/LDA	EPM	ETB	NTB
3C	2.389	2.39 ^c	2.38 ^b	2.52 ^d	1.5 ^e , 1.27 ^f	2.30 ^g	2.47 ^h	1.33 ⁱ
2H	3.33	3.30 ^a	3.31 ^b	3.33 ^d	2.10 ^f			
4H	3.20	3.19 ^a	3.18 ^b	3.16 ^d	2.57 ^e , 2.18 ^f	3.20 ^g		
6H	2.86	2.85 ^a	2.84 ^b	2.90 ^d	2.28 ^e , 1.96 ^f	2.99 ^g		
8H	2.86	2.86 ^a	2.84 ^b					

Table 1. Values of indirect gap of SiC polytypes (62).

^a Experimental data (75)

^b GW calculations (73)

^c Experimental data(74)

^d LMTO calculations (78)

^e GGA calculations (79)

^f LDA calculations (25)

^g EPM calculations (22)

^h ETB values (76)

ⁱ NTB values (77)

which agree with other calculations (22), (25), (73), (75), (76), (77), (78),(79) and experimental data (74). The general findings that all considered polytypes are indirect semiconductors are not surprising, including that the conduction-band minimum is located at X point in the zinc-blende structure or at M in the hexagonal BZ of 2H. Diamond and silicon show a similar behavior, there the conduction-band minima are situated on the Γ X line near X [110]. The X point in the fcc BZ represents the position of the minimum in the zinc-blende 3C-SiC. Two of these X points are folded onto M points of the hexagonal BZ of the corresponding 2H structure. The exact positions depend on the details of the calculations, the ratio c/a of the hexagonal lattice constants, as well as the atomic positions within the hexagonal unit cells. Moreover, the upper valence band has the lowest energy in X, so that the repulsive interaction between the lowest conduction band and the highest valence band should be small. In the wurtzite structure, the situation is changed. First of all, the zinc-blende X is folded onto 2/3LM in the hexagonal BZ of 2H. This point has a lower symmetry and the bonding and antibonding combinations of the C 2s orbital and a Si 3p orbital, of which the state mainly consists, can interact with more closer lying states. The minimum at K point, that has a similar orbital character as the states at the zinc blende W point, gives rise to the lowest empty band. The energetical distance of the valence and conduction bands in K point is remarkably reduced. The resulting stronger interaction pushes the conduction-band minimum away from the valence bands. States on the LM line near M point form the lowest conduction-band minimum. Surely, the minimum in the wurtzite structure 2H-SiC is located at the **k** point in the center of the BZ edge parallel to the c axis similarly to hexagonal diamond (79). We find the conduction band minima at M point for 4H and, respectively, at about 0.63LM for 6H and 8H. This result is somewhat surprising since the fcc X point should map onto 1/3LM for 4H and M for 6H and 8H. That means that the simplifying folding argument is not exactly valid going from one polytype to another one. The actual arrangement of atoms and bonds in the unit cells gives rise to changes in the band positions and dispersion. The exact minimum position is particularly sensitive to the details of the atomic structure since the lowest conduction band between L and M is rather flat. This flatness increases with the lowering of the LM distance in k space. Increasing the period of the superstructure along the optical axis (line Γ -A in the BZ) causes band folding, which can be seen for the Γ -A and K-H

directions for the SiC polytypes shown in Figure 4. The overall features of the band structures agree well with previous calculations. Differences concern the magnitudes of the various band gaps, where the effect is related to the variations in the position of the conduction-band minima. An interesting problem concerns the preparation of heterostructures on the base of chemically identical, but structural inequivalent semiconductors, more strictly speaking of different polytypes. The key parameters of such structures are the band offsets at the interface.

4.2 Effective masses of 3C-, 2H-, 4H-, 6H-, and 8H-SiC

The effective electron masses for the different polytypes have been calculated and measured experimentally by different scientific groups (19), (22), (26), (81), (82), (83). The values vary depending on the experimental techniques or model used, especially for the hexagonal polytypes. Results for the lowest conduction band minima in K , M points, or at the LM line near M point are calculated (62). For electrons we give the full inverse effective-mass tensor along the principal axis determined by the c axis of the structure and the position of the minimum in k space. We consider the longitudinal masses $m_{||}$ parallel to the connection line between the minimum position and more strictly speaking parallel $M\Gamma(4H)$, $KT(2H)$ and $(LM)\Gamma(6H, 8H)$. The two transverse masses $m_{\perp 1}$, $m_{\perp 2}$ are distinguished according to the anisotropy of the system. m_{\perp} denotes the transverse mass parallel to the c axis. In the calculation of $m_{\perp 1}$ we use the direction ML . For the estimation of the second transverse mass $m_{\perp 2}$ of the hexagonal polytypes we replace the correct direction by the line MK in an approximate manner.

Our previously calculated values of the electron effective masses in three principal directions with the tight-binding method (62) are presented in table 2 in comparison with other theoretical and experimental data. All values of the electron effective masses agree with experimental values, when available, and for 3C-, 2H-, and 4H-SiC, our results agree with the majority of earlier calculations (22). We report in the same table our values of m^* for 8H-SiC. There is no available experimental data for comparison. No clear trend with the hexagonality or the extent of the unit cell can be derived from table 2 for the electron masses. This is not astonishing since the conduction band minima appear at different k points in the BZ. Only in 4H case one observes the minimum at the same point M . A remarkable anisotropy of the electron effective mass tensor is found for 6H and 4H. In space directions (nearly) parallel to $M\Gamma$ and $L\Gamma$ heavy electrons appear whereas the mass for the electron motion in the plane perpendicular to c axis but parallel to the edge MK of the hexagonal BZ is small. This is a consequence of the flatness of the lowest conduction bands in the most space directions. The electron-mass anisotropy in the 2H polytypes at M or K is much smaller. The findings for the conduction band masses have consequences for the electron mobility, since this property is proportional to the inverse mass. We expect that at least for the mostly available 6H- and 4H-SiC polytype, the current directions should be carefully selected. Otherwise, too small electron mobilities result. 2H-SiC have more parabolic behavior around their minima, whereas in 4H- and 6H-SiC the interaction between the two close-lying bands at the M point will affect the parabolicity, especially for the flat curvatures in the c direction. The best agreement between theory and experiment seems to be for the 2H-SiC pure hexagonal polytype and the 3C-SiC cubic polytype. For the 8H-SiC polytype there are not yet any experimental results for the effective electron masses. Also there is only one experimental report for the longitude effective mass of 6H-SiC. For the hole effective masses there are few theoretical reports of the polytypes and even fewer are the experimental values. The effective electron masses of 3C- and 4H-SiC have been measured experimentally and

Mass	3C	2H	4H	6H	8H
m_{\parallel}	0.69	0.40	0.60	0.65	0.67
	0.667 ^c	0.42 ^a	0.58 ^a	0.68 ^a	
	0.70 ^b	0.43 ^f	0.53 ^b	0.44 ^b	
	0.449 ^d		0.58 ^e	0.77 ^e	
	0.68 ^f		0.57 ^f	0.75 ^f	
$m_{\perp 1}$	0.25	0.24	0.36	1.19	1.38
	0.247 ^c	0.22 ^a	0.33 ^a	1.25 ^a	
	0.24 ^b	0.26 ^f	0.31 ^e	1.14 ^b	
	0.23 ^f		0.31 ^f	1.42 ^e	
				1.83 ^f	
$m_{\perp 2}$	0.25	0.40	0.21	0.10	0.15
	0.247 ^c	0.42 ^a	0.29 ^a	0.13 ^a	
	0.24 ^b	0.43 ^f	0.19 ^b	0.43 ^e	
	0.23 ^f		0.28 ^e	0.24 ^f	
			0.28 ^f		

Table 2. Effective masses of electrons in the conduction-band-minima. All values in units of the free-electron mass m_0 (62).

^a Experimental values (81).

^b EPM calculations (22).

^c Experimental values (82).

^d LMTO (GW) (83).

^e LMTO (19).

^f FPLAPW (26).

reported by several groups, and they agree quite well with the theoretically calculated values (19), (26), (83). For 6H-SiC, only the longitudinal effective mass along the c-axis has been measured (82), but due to the peculiar band shape along the direction there is still a large inconsistency between the measured value and the calculated ones, even among the values calculated theoretically by different groups (19), (26), (83). However, only the hole effective masses of 4H-SiC have been measured experimentally and reported by Son et al. (81).

4.3 Total density of states of 3C-, 2H-, 4H-, 6H-, and 8H-SiC

We have applied the tetrahedron technique directly from the eigenvalues and the angular momentum character of each state. This is done by dividing up the Brillouin zone into 48 tetrahedron cube. The total density of states (TDOS) of 3C-SiC, corresponding to the band structure is given in figure 5 (62). The 3C-SiC have valence band density of states qualitatively similar to homopolar semiconductors, except for the gap which opens at X point. This gap is related to different potential for the cation and anion potentials. This "antisymmetric" gap has been proposed as a measure of crystal ionicity. The lowest states contain a low-lying C s-derived band about 17 eV below the VBM. The lowest states of the VB from -17 to -13 eV has primarily s character and is localized on the anion. The large peak at -10 to -7 eV comes primarily from the onset of the second valence band at points X and L. The states of this band is primarily of cation s character, it changes rapidly to anion p-like at the top of valence band. From the Fig 5, it is apparent that there is a significant amount of Si p hybridization all the way up to the VBM. A comparison with the corresponding DOS curve of the experimental

results reveals excellent agreement for energies below 4 eV. The bandwidths and energies are in good agreement with photoemission results (74).

The DOS was determined by the tetrahedron integration over a mesh that was generated by six cuts in the Γ -M direction of the BZ and included 112, 84, 78 and 56 points in the irreducible part of 2H, 4H, 6H and 8H BZ, respectively. In Figure 5 total densities of states of SiC polytypes (62) are shown which can be used for the interpretation of photoemission spectra of SiC. The lowest valence band in 6H SiC between -19.0 and -13.0 eV is dominated by *s*-electrons of C atom. The maximum at 14.85 eV in the total DOS is dominated by the *s*-electron of Si. The upper part of the valence band of 6H SiC is dominated mainly by the *p*-electron of C and Si. The conduction band is mainly dominated by the *s*, and *p*-electrons of Si, whereas *p*-electrons of C are less dominant. There is a noticeable difference of the *p*-state occupation for different polytypes and for different sites in the same polytype. The band width of the valence band agrees with previous works represented in many literatures [(22), (25), (73), (75), (77), (78)], where 18.0 eV were obtained. Our value of the valence band width (≈ 19.0 eV) of 6H SiC is lower than in cubic SiC as expected (25), (73),(78),(79).

In the figure 5, one can see that the valence band, as expected, consists of two subbands. The energy width of these subbands and the total bandwidth are very similar for the four polytypes. In α -SiC polytypes the lower-lying subbands is in the range from about -19.5 to -13 eV and is dominated by the atomic Si 3s+3p states and the localized atomic C 2s states, whereas the higher subband also consists of Si 3p and 2p states. In the higher subband the Si 3s and C 2p states dominate at lower energies and the C 2p states dominate at higher energies. Even if it is not straightforward to compare photoemission spectra with the DOS, the clear peak at about -11.1 eV, arising from the atomic C 2p and Si 3s states, can probably be identified with the experimental value -10.5 eV (74). Also, the total band-width and the width of the higher subband seem to be in agreement with experimental results. The calculated width of the total band (higher subband) is about 8.5 eV for all four polytypes, whereas the experimental results for α -SiC polytypes are about 10.0 eV (74).

Since band structures accurate close to the band gap are desired, it is useful to examine the density of states in this region. As found experimentally (74) and theoretically (25), (73),(78),(79), the major differences between the density of states of the individual SiC polytypes calculated with our TB model band structure is in the conduction bands. The results are compared with results from density-functional theory (DFT) (75). Both results of 2H-, 4H-, 6H-, and 8H-SiC show not only an increasing band gap, but an increase in the steepness of the rise in the density of states at the conduction band edge with increasing hexagonality.

4.4 Optical absorption of 3C-, 2H-, 4H-, 6H-, and 8H-SiC:

Many optical properties, such as the dielectric function, the reflectivity, absorption, etc., are related to the band structure of crystalline solids. Most of them can be derived from the dielectric function which is measured directly and reliably by spectroscopy ellipsometry. It is worth calculating the optical absorption for different polytypes of SiC. Theoretically, the spectra are seen to be dependent on quantities such as density of states and matrix elements coupling the initial to final state. In the case of absorption spectra for bulk semiconductors, the main structures are observed to be correlated with the inter-band critical points. It is very common to assume that the dipole matrix elements involved are constant throughout the Brillouin zone and to compare the spectra directly with joint density of states (48).

We can compute the matrix elements starting from an empirical Hamiltonian even if the full wave functions are not known. The Slater-Koster method is computationally very economical

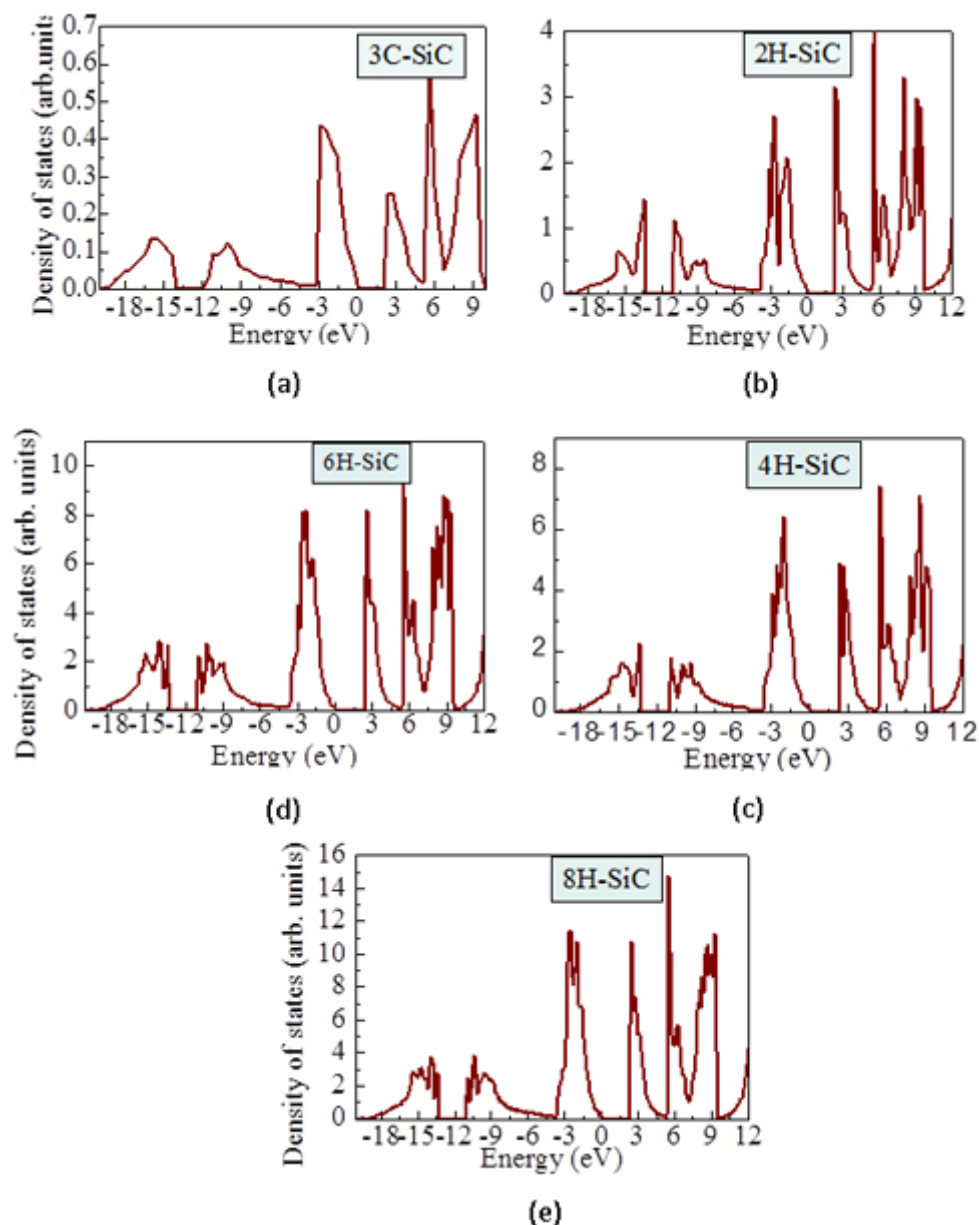


Fig. 5. Density of states for the 3C-, 2H-, 4H-, 6H-, and 8H-SiC polytypes (62).

in obtaining the full-zone band structure of semiconductors, and our procedure for the optical matrix elements requires little additional computation beyond solving the eigenvalue problem for the energies.

4.4.1 Applications of optical matrix elements:

Optical-absorption spectra in semiconductors are normally dominated by transitions from the valence to the conduction bands. Then, it is possible to compute the joint density of states (JDOS) for SiC polytypes that is given by the below formula. The purpose is to see how our TB calculations are extended to optical properties.

$$J(E) = \Omega \sum_{cv} \int_{FBZ} \frac{d^3k}{(2\pi)^3} \delta(E_{cv}(k) - \hbar\omega) \quad (7)$$

where Ω is the real-space unit-cell volume.

where $E_{cv} = E_c(k) - E_v(k)$ for the JDOS per component (48).

We have computed the JDOS for SiC polytypes (62), hence, the interband transitions in Eq.(7) are all of the valence-conduction type. The interest in the JDOS lies in the fact that the momentum matrix elements are assumed constant over the Brillouin zone. The band summations in Eq.(7) involve all states in the valence band and lowest states in the conduction band. The summations in Eq.(7) are over special points in the Brillouin zone. In our calculations, we took 32, 28, 24, 20 special k -points for 2H, 4H, 6H and 8H respectively in the Brillouin zone (21).

4.4.2 Joint density of states of 3C-, 2H-, 4H-, 6H-, and 8H-SiC:

Before discussing the effect of the optical transition matrix elements, we consider the JDOS (see figure 6). In order to get more information on the interband transition, we present our recent calculated joint density of states for SiC polytypes (62). We have determined the transition responsible for the major contributions to these structures. This was done by finding the energy of the desired peak or shoulder on the joint density of states graph and then examining the contribution to joint density of states at that energy from the constituent interband transitions. The fundamental gap is well understood and is attributed to $\Gamma_{15} \rightarrow X_1$ transition in 3C-SiC. We examine a large peak associated to $\Gamma_{15} \rightarrow L_1$ transition which occurs at 3.8 eV. The second major peak in JDOS, comes from the transition $\Gamma_{15} \rightarrow \Gamma_1$ which occurs at 5.2 eV. However, our band structure is satisfactory with respect to these transitions. The principal behavior of the joint density of states is very similar for the various 2H-, 4H-, 6H-, 8H- polytypes considered. The two peaks below the ionic gap exhibit a different behavior with the number n of SiC bilayers in the unit cell. Whereas that at higher energy around 7 eV is rather independent of the polytype, the low-energy peak around 8 eV is broadened with rising number n . We relate this fact to the folding effect parallel to the c axis. It causes an opposite variation of the band curvature along the LM and HK lines in the hexagonal BZ (25), (73), (78). The intensity of the two most pronounced peaks at 3.5 and 2.1 eV in the region of the upper valence bands monotonically follow the hexagonality of the structures (25), (75), (78),(79). Strong contributions to these peaks also arise from the LM line. The most drastic change in the conduction band region occurs near the onset of the density of states. Its steepness over several eV again follows the hexagonality of the polytype. The particular shape of the onset however depends on the number of bilayers and therefore on the folding effect as already has been pointed out by Lee et al. (84). The consequences can be clearly seen in the joint density of states. Their low-energy tails increase with decreasing hexagonality.

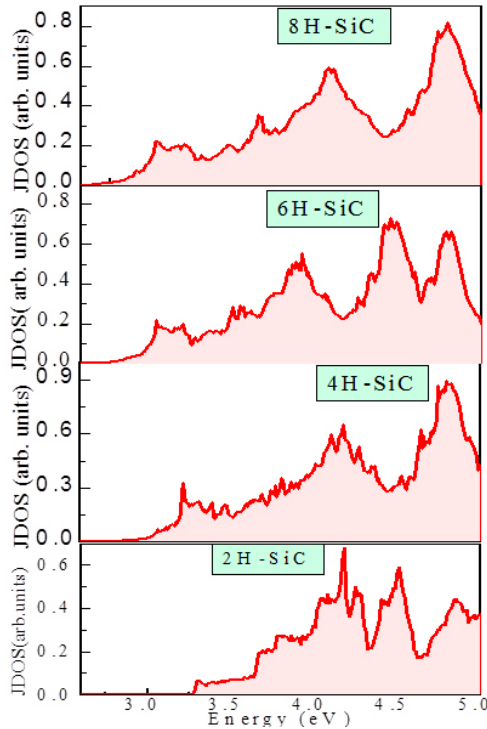


Fig. 6. Joint density of states for the 3C-, 2H-, 4H-, 6H-, and 8H-SiC polytypes (62).

5. Summary and conclusions

This chapter reviewed the general aspects of the optical properties as well as the electronic structures of SiC indirect-band-gap semiconductor polytypes. We presented our recent results of the band structures, the total densities of states, and the optical absorption of different polytypes of SiC using the empirical tight-binding approximation. The set of TB parameters is transferable to all hexagonal 2H-, 4H-, 6H-, and 8H-SiC structures. We illustrated how the tight-binding formalism can be used to accurately compute the electronic states in semiconductor hexagonal polytypes. This approximation is known to yield a sufficiently accurate conduction band and to give its minimum position correctly. To this end we have presented our new developed tight-binding model which carefully reproduces *ab initio* calculations and experimental results of SiC polytypes. It is likely that our TB approach could be applied to SiC polytypes with even larger unit cells than 8H using the variation in band gap with hexagonality in cases where experimental band gaps are undetermined. SiC system exhibits rather interesting features which differ greatly from those other semiconductor compounds with respect to optical properties as well as in electronic structure. We refer to this aspect of superperiodicity that is the possibility of modifying the optical properties of the material. Furthermore, the interband optical matrix elements can be tailored. It has been shown that our recent results indicate that our TB calculations are suitable for describing optical properties in more complex polar semi-conductors. In addition, the optical properties

suggest that the hexagonal SiC polytypes composed of an indirect-band-gap semiconductors offer a great potential for application to optical devices.

6. References

- [1] A. P Verma and P. Krishna, *Polymorphism and Polytypism in Crystals*, (Wiley, New York, 1966).
- [2] W. J. Choyke, in *The Physics and Chemistry of Carbides, Nitrides and Borides*, NATO ASI Ser., Ser. E, Appl. Sci. Vol. **185**, R Freer, Ed. (Kluwer, Dordrecht, 1990), p. 563.
- [3] K. Karch, G. Wellenhofer, P. Pavone, U. Rößler, and D. Strauch, *Structural and Electronic Properties of SiC polytypes*, in *Proceeding of 22nd International Conference On the Physics of Semiconductors*, Vancouver, 1994.
- [4] R. F. Davis, Z. Sitar, B. E. Williams, H. S. Kong, H. J. Kim, J. W. Palmour, J. A. Edmond, J. Ryu, J. T. Glass, and C. H. Carter, Jr. *Mater. Sci. Eng B* **1**, 77 (1988).
- [5] N. W. Jepps and T. F. Page, *Progr. Cryst. Growth Charact.* **7**, 259 (1983).
- [6] *Diamond, SiC and Nitride Wide Bandgap Semiconductors*, edited by C. H. Carter. Jr., et al. (Materials Research Society, Pittsburgh, 1994).
- [7] P. Y. Yu, M. Cardona, *Fundamentals of Semiconductors* – Physics and Material properties, Springer (2005).
- [8] *Silicon Carbide, III-Nitrides and Related Materials*, edited by G. Pensl, H. Morkoç, B. Monemar, and E. Janzén (Trans Tech publications, Switzerland, 1998).
- [9] D. B. Holt, B. G. Yacobi, – Extended Defects in Semiconductors. Electronic Properties, Device Effects and Structures, Cambridge University Press (2007).
- [10] V. I. Gavrilenko, A. V. Postnikov, N. I. Klyui, and V. G. Litovchenko, *Phys. Stat. Sol. B* **162**, 447 (1990).
- [11] M. S. Miao, S. Limpijumnong, and W. R. L. Lambrecht, *Appl. Phys. Lett.* **79**, 4360 (2001).
- [12] Walter R. L. Lambrecht and M. S. Miao, *Phys. Rev. B* **73**, 155312 (2006).
- [13] C. Tivarus, J.P. Pelz, M.K. Hudait, S.A. Ringel, *Appl. Phys. Lett.* **87** 182105 (2005).
- [14] K. J. Russell, Ian Appelbaum, and V. Narayanamurti, *Phys. Rev. B* **71**, 121311(R) (2005).
- [15] W. R. L. Lambrecht, and B. Segall, *Phys. Rev. B* **41**, 2832 (1990).
- [16] K. Karch, G. Wellenhofer, P. Pavone, U. Rößler, and D. Strauch, *Structural and Electronic Properties of SiC polytypes*, in *Proceeding of 22nd International Conference On the Physics of Semiconductors*, Vancouver, 1994.
- [17] J. Bernholc, A. Antonelli, C. Wang, and R. F. Davis, in *Proceedings of the Fifteenth International Conference on Defects in Semiconductors*, Budapest, 1998.
- [18] W. R. L. Lambrecht, B. Segall, M. Methfessel, and M. van Schilfgaarde, *Phys. Rev. B* **44**, 3685 (1991).
- [19] W. R. L. Lambrecht, S. Limpijumnong, S. N. Rashkeev, and B. Segall, *Phys. Stat. Sol. (b)* **202**, 5 (1997).
- [20] W. van Haeringen, P. A. Bobbert, and W. H. Backes, *Phys. Stat. Sol. (b)* **202**, 63 (1997).
- [21] B. Adolph et al., *Phys. Rev. B* **55**, 1422 (1997).
- [22] G. Pennington and N. Goldsman, *Phys. Rev. B* **64**, 45104 (2001).
- [23] A. Bauer, *Phys. Rev. B* **57**, 2647 (1998).
- [24] C. Person, and U. Lindefelt, *J. Appl. Phys.* **82**, 5496 (1997).
- [25] P. Käckell, B. Wenzien, and F. Bechstedt, *Phys. Rev. B* **50**, 10761 (1994).
- [26] C. Persson and U. Lindefelt, *J. Appl. Phys.* **82**, 5496(1997).
- [27] W. J. Choyke, D. R. Hamilton, and Lyle Patrick, *Phys. Rev.* **133**, 1163 (1964).
- [28] Lyle Patrick, D. R. Hamilton, and W. J. Choyke, *Phys. Rev.* **143**, 526 (1994).

- [29] A. O. Konstantinov and H. Bleichner, *Appl. Phys. Lett.* 71, 3700 (1997).
- [30] H. Lendenmann, F. Dahlquist, N. Johansson, R. Sonderholm, P. A. Nilsson, J. P. Bergman, and P. Skytt, *Mater. Sci. Forum* 353-356, 727 (2001).
- [31] R. S. Okojie, M. Zhang, P. Pirouz, S. Tumakha, G. Jessen, and L. J. Brillson, *Appl. Phys. Lett.* 79, 3056 (2001); *Mater. Sci. Forum* 389-393, 451 (2002).
- [32] L. J. Brillson, S. Tumakha, G. Jessen, R. S. Okojie, M. Zhang, and P. Pirouz, *Appl. Phys. Lett.* 81, 2785 (2002).
- [33] H. Iwata, U. Lindefelt, S. Iijberg, and P. R. Briddon, *Mater. Sci. Forum* 389-393, 439 (2002); *J. Appl. Phys.* 93, 1577 (2003).
- [34] P. Pirouz, M. Zhang, J.-L. Dermenet, and H. M. Hobgood, *J. Appl. Phys.* 93, 3279 (2003).
- [35] A. Galeckas, J. Linnros, and P. Pirouz, *Appl. Phys. Lett.* 81, 883 (2002).
- [36] A. T. Blumenau, C. J. Fall, R. Jones, S. Iijberg, T. Frauenheim, and P. R. Briddon, *Phys. Rev. B* 68, 174108 (2003).
- [37] A. T. Blumenau, R. Jones, S. Iijberg, and T. Frauenheim, *Mater. Sci. Forum* 457- 460, 453 (2004).
- [38] P. O. A. Persson, L. Hultman, H. Jacobson, J. P. Bergman, E. Janzifin, J. M. Molina-Aldareguia, W. J. Clegg, and T. Tuomi, *Appl. Phys. Lett.* 80, 4852 (2002).
- [39] H.P. Iwata, U. Lindefelt, S. Iijberg, P.R. Briddon, *Phys. Rev. B*, Vol. 65 (2001).
- [40] H.P. Iwata, U. Lindefelt, S. Iijberg, P.R. Briddon, *J. Phys. Condens. Matter* Vol.14 p. 12733, (2002).
- [41] H.P. Iwata, U. Lindefelt, S. Iijberg, P.R. Briddon, *Physica B*, 340-342 p.165, (2003).
- [42] H.P. Iwata, U. Lindefelt, S. Iijberg, P.R. Briddon, *Microelectronics J.* 34 371 (2003).
- [43] J. Camassel, S. Juillaguet, *J. Phys. D: Appl.Phys.* 40, 6264 (2007)
- [44] A. Chen, P. Srichaikul, *Phys. Stat. Sol. B*202, 81(1997).
- [45] W.Y. Ching et al., *Mater. Sci. And Eng. A* 422, 147-156 (2006).
- [46] A. Galeckas, J. Linnros, B. Breitholtz, H. Bleichner, *J. Appl. Phys.* 90 (2) 980 (2001).
- [47] H. Iwata, U. Lindefelt, S. Oberg, and P. R. Briddon, *Phys. Rev. B* 65, 033203 (2001); *Phys. Rev. B* 68, 245309 (2003).
- [48] T. G. Pedersen, K. Pedersen, and T. B. Kriestensen, *Phys. Rev. B* 63, 20110 (2001).
- [49] D. Vogel, P. Krüger, and J. Pollmann, *Phys. Rev. B* 52, R14316 (1995); *B* 54, 5495 (1996); *B* 55, 12836 (1997).
- [50] G. Litovchenko, *Phys. Stat. Sol. B* 162, 447 (1990).
- [51] G.L. Sun, I.G. Galben-Sandulache, T. Ouisse, J.M. Dedulle, M. Pons, R. Madar, D. Chaussende, *Mat. Sci. For.* 645-648 (2010) pp 63-66.
- [52] Y. Ward, R. J. Young, R. A. Shatwell, *J Mater Sci* 42 (2007), p.5135-5141.
- [53] D. Chaussende, F. Baillet, L. Charpentier, E. Pernot, M. Pons, R. Madar, *J. Electrochem. Soc.* Vol. 150, (2003), p. G653.
- [54] D. Chaussende, F. Mercier, A. Boule, F. Conchon, M. Soueidan, G. Ferro, A. Mantzari, A. Andreadou, E.K. Polychroniadis, C. Balloud, S. Juillaguet, J. Camassel, M. Pons, *J. Cryst. Growth* 310 (2008).
- [55] S. Bai, R. P. Devaty, W. J. Choyke, U. Kaiser, G. Wagner, and M. F. MacMillan, *Appl. Phys. Lett.* 83, 3171 (2003).
- [56] G. Zoulis, J. Sun, M. Beshkova, R. Vasiliauskas, S. Juillaguet, H. Peyre, M. Syvifjirvi, R. Yakimova, J. Camassel, *Mat. Sci. For. Vols.* 645-648 (2010) pp 179-182.
- [57] S. Ha, S. Skowronski, J.J. Sumakeris, M.J. Paisley, M.K. Kas *Phys.Rev. Lett.* Vol. 92, No. 17, 175504 (2004).

- [58] B. J. Skromme, K. Palle, C. D. Poweleit, L. R. Bryant, W. M. Vetter, M. Dudley, K. Moore, and T. Gehoski, *Mater. Sci. Forum* 389-393, 455 (2002); B. J. Skromme, K. C. Palle, M. K. Mikhov, H. Meidia, S. Mahajan, X. R. Huang, W. M. Vetter, M. Dudley, K. Moore, S. Smith, and T. Gehoski, *Mater. Res. Soc. Symp. Proc.* 742, 181 (2003).
- [59] J. Q. Liu, H. J. Chung, T. Kuhr, Q. Li, and M. Skowronski, *Appl. Phys. Lett.* 80, 2111 (2002).
- [60] S. Izumi, H. Tsuchida, T. Tawara, I. Kamata, and K. Izumi, *Mater. Sci. Forum* 483-485, 323 (2005); S. Izumi, H. Tsuchida, I. Kamata, and T. Tawara, *Appl. Phys. Lett.* 86, 202108 (2005).
- [61] H. Fujiwara, T. Kimoto, T. Tojo, and H. Matsunami, *Appl. Phys. Lett.* 87, 051912 (2005).
- [62] A. Laref, S. Laref, *Phys. Stat. Sol. B* 245, N1, 89-100 (2008).
- [63] I.G. Galben-Sandulache, G.L. Sun, J.M. Dedulle, T. Ouisse, R. Madar, M. Pons, D. Chaussende, *Mat. Sci. For.* 645-648 (2010) pp 55-58.
- [64] L. Latu-Romain, D. Chaussende, C. Balloud, S. Juillaguet, L. Rapenne, E. Pernot, J. Camassel, M. Pons, R. Madar, *Mat. Sci. Forum*, vols. 527-529 (2006), pp. 99-102.
- [65] A. A. Lebedev, P. L. Abramov, E. V. Bogdanova, S. P. Lebedev, D. K. Nelson, G. A. Oganessian, A. S. Tregubova, R. Yakimova, *Semicond. Sci. Technol.* 23, 075004 (2008).
- [66] A. A. Lebedev, P. L. Abramov, N. V. Agrinskaya, V. I. Kozub, S. P. Lebedev, G. A. Oganessian, A. S. Tregubova, D. V. Shamshur, and M. O. Skvortsova, *J. Appl. Phys.* 105, 023706 (2009).
- [67] M. Skowronski and S. Ha, *J. Appl. Phys.* 99, 011101 (2006).
- [68] Y. Ward, R. J. Young, R. A. Shatwell, *J Mater Sci* 42 (2007), p.5135-5141.
- [69] T. Quisse, *J. App. Phys.* 75, 2092 (1994).
- [70] J. C. Slater and G.F. Koster, *Phys. Rev* 94, 1498 (1954).
- [71] P. Vogl and H. P. Hjalmarson, and J. D. Dow, *J. Phys. Chem Solids* 44, 365 (1983).
- [72] Y. C. Chang and D. E. Aspnes, *Phys. Rev. B* 41, 12002 (1990).
- [73] B. Wenzien, P. Käckell, F. Bechstedt, and G. Cappellini, *Phys. Rev. B* 52, 10897 (1995).
- [74] R. G. Humphreys, D. Bimberg, W. J. Choyke, *Solid. State. Com.* 39, 163 (1981).
- [75] Landolt-Börnstein, *Numerical and Functional Relationships in Science and Technology*, edited by K. H. Hellwege (Spring-Verlag, Berlin, 1982).
- [76] G.Theodorou, G. Tsegas, and E. Kaxiras, *J. Appl. Phys* 85, 2179 (1999).
- [77] N. Bernstein, H. J. Gotsis, D. A. Papaconstantopoulos, and M. J. Mehl, *Phys. Rev.* B71, 075203 (2005).
- [78] G. Cubiotti, Yu. N. Kucherenko, and V. N. Antonov, *J. Phys. Cond. Mat* 9, 165 (1997).
- [79] J. Kuriplach, M. Sob, G. Brauer, W. Anwand, E.-M. Nicht, P. G. Coleman, and , N. Wagner, *Phys. Rev. B* 59, 1948 (1999).
- [80] P.J. Colwell and M.V. Klein, *Phys. Rev. B* 6, 498 (1972).
- [81] N. T. Son et al., *Appl. Phys. Lett* 66, 107 (1995).
- [82] R. Kaplan, and R. J. Wagner, *Solid State Com.* 55, 67 (1985).
- [83] M. Willatzen, M. Cardona, and N. E. Christensen, *Phys. Rev. B* 51, 13150 (1995).
- [84] K, -H. Lee, C. H. Park, B. -H. Cheong, K. J. Chang, *Solid State Commun.* 92, 869 (1994).

Dielectrics for High Temperature SiC Device Insulation: Review of New Polymeric and Ceramic Materials

Sombel Diaham, Marie-Laure Locatelli and Zarel Valdez-Nava
*University of Toulouse – UPS – INPT – LAPLACE – CNRS
France*

1. Introduction

The keys to successful high power electronic systems are located as much in the ability to build high temperature power devices and to package them with the appropriate materials, as in the aptitude to reduce and control switching and conduction power losses. Particularly, high temperature low loss operation allows an increase in the power rating of these devices. The recent development of wide band gap semiconductor devices should allow improving power electronic systems.

Wide band gap semiconductor materials, especially the most mature silicon carbide (SiC), should allow the electronics operation at high junction temperatures ($>200^{\circ}\text{C}$), high voltages ($>10\text{ kV}$) or in harsh thermal environment, with faster switching and lower power losses active devices than the silicon (Si) counterparts. Such SiC devices impose more severe electrical and thermal stresses to the surrounding insulating materials (polymeric passivation and encapsulation materials and ceramic substrates). Lots of improvements have already been built-up at the die level; however, superior device performance degrees could be reached using higher performance insulation materials.

Among the power device packaging materials for a high temperature operation, typical organic passivation and encapsulation appear nowadays as the most sensitive to the thermal constraints ($T_{\text{max}}=250^{\circ}\text{C}$). Moreover, even if ceramic materials present a high isothermal stability (up to 600°C) they are very sensitive to the large passive or active thermal cycling induced by the power devices or by severe environmental constraints during operation. Therefore, research on high temperature dielectric materials tries to identify new polymeric and ceramic materials electrically, thermally and mechanically suited for the packaging of SiC power devices and to determine their effective limits (properties and durability). In this chapter after a section on the high temperature applicative needs and the new thermal and electrical constraints imposed by SiC devices on the surrounding insulating materials, a complete review of the polymers and ceramics insulating materials which are reported to potentially answer to the packaging issues is carried out through a presentation of their different main physical properties and the sensitive aging parameters in link with microstructure. Among the polymeric materials, BPDA/PDA polyimide (PI), fluorinated parylene (PA-F), polyamide-imide (PAI), and silicone (PDMS) will be studied. On the other hand, mainly aluminium nitride (AlN) and silicon nitride (Si_3N_4) ceramics will be presented.

2. Needs, insulation problematic and constraints

The “high temperature” range and the applicative needs are presented in the first part of this section. Silicon carbide arises today as the solution for above 200 °C operations on the semiconductor point of view. The roles and the types of dielectrics in the current semiconductor devices are described then. Insulating passivation, encapsulation and substrate, involving polymeric or ceramic materials, are the main insulating functions to be satisfied by the device packaging. Besides the high temperature requirement, the specific constraints on these materials and their assembly due to the use of SiC are presented at last.

2.1 Needs for high temperature semiconductor devices

Silicon being the most widely used semiconductor material for active devices active devices, the latter maximal operating junction temperature (T_j) limitation fixes the threshold for the “high temperature” denomination. Hence, operations or environments above 200 °C are qualified as “high temperature”, 200 °C being the highest maximal operating temperature for available silicon devices. For a long time, the list of high temperature electronics markets has been given as follows: deep well logging (300 °C), geothermal research (400 °C), space exploration (500 °C), for which the common points are the high ambient temperature (T_a) of the environment (as indicated into brackets) and their ‘niche’ specificity. The self -heating of semiconductor devices under operation has been identified as a predictable limitation for the silicon based electronics development for a while as well. Today, the trends for higher integration, or more elevated power level, leading to T_j higher than 200 °C, increase the list of the high temperature device markets. In fact, a simple relation between the junction temperature and the power losses (P_d) dissipated through the device can be written as follows:

$$T_j = R_{thja} P_d + T_a \quad (1)$$

where R_{thja} is the thermal path resistance between the device dissipating junction and the system ambient. The wider field of the energy conversion either for industry or transportation applications is concerned nowadays. Indeed, embedded integrated power electronics (with reduced or suppressed cooling requirements, meaning very high R_{thja} values) as well as static converters closer to (or inside) hot engine areas (which may correspond simultaneously to elevated T_a and P_d), are wanted. The aims are mass, volume, and cost savings and higher T_j devices are required.

The recent silicon carbide components emergence (Cooper Jr. & Agarwal, 2002), with promising operating temperatures well above 200 °C (Raynaud, 2010) in the future, represents a perspective of offer which will even encourage new demands. As a consequence, the research for high temperature operating dielectrics suitable for the semiconductor die assembly has become essential for the development of the full systems, as insulating materials are among the key points for its performance and reliability.

2.2 Dielectrics for power device insulation

To realize a discrete (single die) or hybrid (multiple dies) semiconductor device, multiple materials playing different roles are assembled, all of them constituting the device packaging. The semiconductor die itself is not a single material element, as it exhibits different metallized areas (ohmic contact, insulated gate contact, ...), and different dielectric

layers (gate dielectric, primary and secondary passivations, intermetallic insulator, ...). In particular, the secondary passivation is the top final coating layer elaborated at the wafer level state, before sawing the dies. Contrary to the other existing dielectrics which are inorganic (most often SiO_2 and Si_3N_4 , from tens of nm to the order of 1 μm in thickness), the secondary passivation is usually a spin-coated polyimide film (from several μm to few tens of μm thick). Its role is the die protection against premature electrical breakdown, mechanical damages and chemical contamination.

In a multichip semiconductor power device, the die backside contacts require to be insulated from each other and from their common mechanical substrate. Double-side metallized ceramic substrates are mostly used in this case, instead of polymer based substrates suitable for low power and low voltage ratings. Such metallized ceramic substrates allow the electrical interconnection between the dies soldered on them and with the external circuit. Besides their mechanical and insulating functions, the ceramics ensure the thermal interface with the intermediary dissipating baseplate or the cooling system directly. For the die topside electrical connections, several techniques exist today apart from the conventional wire bonding, which have been developed in order to improve the packaging electrical performance, the cooling efficiency, and the '3D' system integration capability. In particular, 'sandwich' structures involve a second metallized insulating substrate (with polyimide (Liu, 1999) or ceramic as dielectric layer) for the chip top electrodes connecting. Either metal posts or bumps (Mermet-Guyennet, 2008) (preliminary brazed on the chip metal pads), or solder bumps (Dieckerhoff, 2006) (preliminary deposited as well), or direct bonding (Bai, 2004), have been used for the attachment between the chip top pads and the ceramic substrate metallization circuit.

Finally, the empty space, existing above the assembly (as in the conventional wire-bonded structures or in the pressure-contacted structures) or present within the gap of the 'sandwich' structures, has to be filled with an insulating material. Its role is to avoid premature electric breakdown and partial discharges, and to protect all the system against humidity and contaminations. This encapsulation function is generally satisfied using silicone gels, which minimize mechanical strains on the assembly. More recently, the use of polymeric underfills, with a thermal expansion coefficient close to the soldered joint ones, is reported for '3D' structures.

2.3 Specific constraints induced by SiC properties

The superior features of silicon carbide compared to silicon ones are recalled in Table 1, in order to introduce their potential impacts on the die surrounding materials conditions under operation. The high temperature ability of this wide energy band gap semiconductor principally arises from its much lower intrinsic carrier density n_i , allowing the translating of the thermal runaway onset (induced by prohibitive leakage currents) above at least 700 °C instead of at maximum 200 °C for silicon, depending on the device blocking voltage ratings. Because no other SiC physical intrinsic mechanism is supposed to limit T_j , the upper T_{jmax} temperature limitation for SiC devices is more likely to be imposed by the high temperature performance and stability of all the die surrounding materials and their related interfaces and by the market need besides. Up to now, several high temperature SiC based circuits and devices have been reported, demonstrating short term operations up to 300 °C or 400 °C ambient temperatures (Mounce, 2006; Funaki, 2007). Connected to the thermal aspect, it should be added that high temperatures, and large thermal cycling magnitudes, mean more

severe thermo-mechanical stresses and fatigue on the device assembly parts, due to their different thermal expansion coefficients. Also, a higher T_a may lead to higher thermal conductivity requirement (for reduced R_{thja}), in order to preserve a sufficient power density level (and its related level of power losses dissipation) for the wanted system operation for a given T_{jmax} (according to relation (1)).

	4H-SiC	Si
E_g @ 300 K (eV)	3.26	1.12
n_i @ 300 K (cm ⁻³)	6x10 ⁻⁸	1.2x10 ¹⁰
n_i @ 473 K (cm ⁻³)	2x10 ³	10 ¹⁴
E_C @ 300 K, for $N_d = 10^{15}$ cm ⁻³ (V/cm)	2.5x10 ⁶	3x10 ⁵
μ_n @ 300 K, for $N_d = 10^{15}$ cm ⁻³ (cm ² /V/s)	850	1,400
v_{sat} @ 300 K (cm/s)	2.2x10 ⁷	10 ⁷
λ_{th} @ 300 K (W/cm/K)	3.8	1

Table 1. Main 4H-SiC and Si semiconductor physical properties.¹

Beyond the high temperature operation ability and related constraints presented above, the high critical electric field E_C is the other SiC specificity inducing major novel stresses to the die surrounding materials, in comparison to the silicon case. Here the insulating dielectrics are more specifically addressed with regard to this aspect. Because the one-order higher E_C property allows faster and higher voltage devices with low conduction losses than the silicon one, SiC components are designed to operate with internal maximal electric fields at blocking state as close as possible to the SiC critical E_C value. As a consequence, even for optimally designed junction termination structures for a given blocking voltage rating, electric field peak values as high as around 3 MV/cm exist near the semiconductor surface, at the device periphery (Locatelli, 2003). Moreover, smaller dimensions of the device are resulting from the higher E_C ability of SiC, including shorter periphery protection extension. Higher average result values of the electrical field as well. The semiconductor surface passivation materials are concerned at first level by such electrical stress enhancement. Besides, the higher the blocking voltage rating, the more the encapsulating material (above the passivation coating) will be impacted too. Today, the record in terms of breakdown voltage for a single SiC component is 19 kV for a SF₆ gas encapsulated diode demonstrator (Sugawara, 2001), and more than 50 kV might be achievable with SiC while 10 kV represent the Si device practical limit.

Last but not least, higher on-state current density, higher switching speed and smaller SiC dies (thanks to a combination of good E_C , electron mobility μ_n , and electron saturation velocity v_{sat} properties), also represent new challenges, especially in terms of connecting materials and highly compact packaging structures. Specific constraints on the insulation elaboration techniques may result so.

¹Among the different SiC polytypes, 4H-SiC is the one used for the commercial power devices production

3. Material choice criteria and main issues

As presented in the previous paragraph, the insulating passivation, encapsulation and substrate are the three main insulating functions to be satisfied by the device packaging, involving organic and ceramic materials. Besides their electrical role, the involved materials may play mechanical, and/or thermal, and/or chemical roles. The aim of this paragraph is to review the main limiting properties or the main influent constraints to be taken into account at high temperature, according to the dielectric nature or its role in the device. Used dielectrics or reported candidates, as materials for high temperature device packaging, are presented at the same time through the proposed result examples. In particular, biphenyltetracarboxylic dianhydride/*p*-phenylene diamine (BPDA/PDA) polyimide (PI), and fluorinated parylene (PA-F) are considered as interesting high temperature insulating surface coating. Limits of polydimethylsiloxane (PDMS) materials, currently used as volumic insulation for encapsulation purpose, are presented as well. The different ceramic/metal couples available for the device assembly insulating substrate are also discussed.

3.1 Thermal stability and degradation of organic materials

Thermal stability is a fundamental parameter for a long-term reliable high temperature operation of polymeric and other organic materials. It appears as the first stage in the material evaluation because it can ensure a stability of the other physical properties. Conventionally, the thermal stability is determined using thermal gravimetric analysis (TGA) either in oxidant or inert atmosphere. This consists in probing the mass loss of a material versus temperature under a controlled heating slope (dynamical TGA, DTGA) or time at a set temperature (isothermal TGA, ITGA). The degradation temperature (T_d) is often defined as the 5%-mass loss onset in DTGA plots. Figure 1 shows a comparison of DTGA measurements of thermo-stable organic materials. According to the material structural chemistry, T_d is more or less elevated. Thus, the thermal stability determined by the means of DTGA in nitrogen reports T_d values of 606 °C, 455 °C, 537 °C, and 456 °C for BPDA/PDA PI, PAI, PA-F and PDMS/silica materials, respectively (Diaham, 2009, 2011a, 2011b).

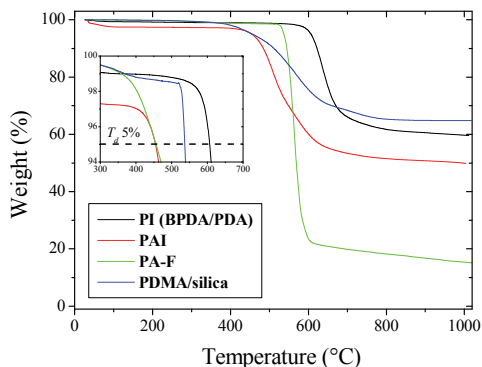


Fig. 1. Comparison of dynamical TGA of thermo-stable organic materials in nitrogen ²

²Heating rate: 10 °C/min

For polymers, the thermal stability is often related to the presence of benzene rings in the monomer structure. In the case of PI materials, it has been shown that the increase in the number of benzene rings contributes to an increase in the degradation temperature (Sroog, 1965). However, the degradation temperature can be also affected by the presence of low thermo-stable bonds in the macromolecular structure. As an example, even if BPDA/PDA and PMDA/ODA (Kapton-type) PI own the same number of benzene rings (i.e. three in the elementary monomer backbone), the absence of the C–O–C ether group in the case of BPDA/PDA PI allows increasing T_d of 60 °C in nitrogen and 110 °C in air in comparison to T_d of PMDA/ODA PI (see Figure 2). Indeed, this is due to the lower thermal stability of the ether bonds inducing earlier degradations than the rest of the structure (Sroog, 1965; Tsukiji, 1990).

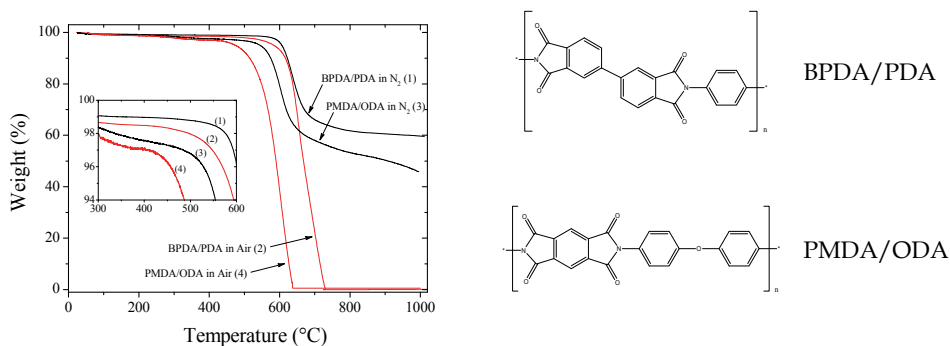


Fig. 2. Dynamical TGA of different structural PI films ²

Although the degradation temperature obtained by DTGA appears as an important parameter for the evaluation of the thermal stability, it is not sufficient to valid that a polymer can endure high temperature during a very long time. In addition, some polymers can exhibit lower T_d values while they display a more stable behavior during time. Therefore, short-term ITGA measurements are recommended in order to identify premature degradation processes. Figure 3 presents ITGA measurements of both BPDA/PDA PI and PA-F films in air. Whereas PA-F films own a lower dynamical T_d value than PI films, they show a better stability under isothermal conditions. Hence, after 5,000 minutes at 350 °C in air atmosphere the weight loss of PA-F is only of 0.5 % compared to 2.4 % for BPDA/PDA PI.

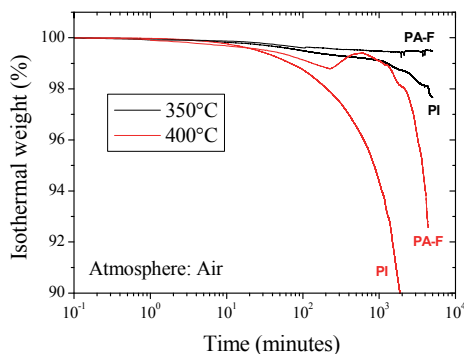


Fig. 3. Comparison of the isothermal TGA of BPDA/PDA PI and PA-F films in air

All these illustrations lead to highlight that the thermal stability is a property difficult to quantify with accuracy. It depends strongly on various structural parameters (materials, ...) and experimental conditions (type of measurements, atmosphere, temperature, ...). However, it appears as an essential information for a first selection of materials for high temperature uses.

3.2 Thermal properties of ceramic materials

In a classical approach for power electronics, the substrates assure the mechanical link and the electrical insulation between the semiconductor die and the rest of the system. For high temperature applications, ceramic materials are a natural choice due to their thermal stability, and high thermal conductivity compared to polymer materials. Ceramic materials on their own present a high isothermal stability (up to 600°C) and seem to be self-sufficient in most cases to insulate electrically appropriately the semiconductor from the environment. However, the presence of an attached metal can be at the origin of several mechanical problems which will be treated in a later section. Furthermore, when high power densities are attained, heat extraction could need to be assisted by high-thermal conductivity ceramics as aluminum nitride, for instance.

The choice of the appropriate insulating ceramic is related to a compromise of electrical properties, thermal characteristics and compatible technologies available to assemble the components. Table 2 presents the characteristics of some of the insulating ceramics that are commercially available to this date. Beryllium oxide (BeO) use is being more and more limited due to toxicity concerns, and is being replaced, when possible, by other ceramic technologies.

	Si ₃ N ₄	AlN	Al ₂ O ₃
Dielectric constant	8-9	8-9	9-10
Loss factor	2x10 ⁻⁴	3x10 ⁻⁴	3x10 ⁻⁴ - 1x10 ⁻³
Resistivity (Ω m)	> 10 ¹²	> 10 ¹²	> 10 ¹²
Dielectric breakdown strength (kV/mm)	10-25	14-35	10-35
Thermal conductivity (W/m K)	40-90	120-180	20-30
Bending strength (MPa)	600-900	250-350	300-380
Young Module (GPa)	200-300	300-320	300-370
Fracture toughness (MPa m ^{1/2})	4-7	2-3	3-5
CTE (mm/m K)	2.7-4.5	4.2-7	7-9
Available substrate technologies for thick film metallization (metal)	AMB (Cu)	DBC (Cu), AMB (Al)	DBC (Cu)

Table 2. Main thermal, mechanical and electrical characteristics of candidate ceramic substrates for SiC device insulation

Despite the availability of ceramic materials of very high thermal conductivity, as BeO or AlN, one must take into account the evolution of this property with temperature. Even in high thermal-conductivity ceramics, the phonon conduction path is disturbed as

temperature increases, so one must expect a decay of this property as temperature increases. Figure 4 shows the temperature dependence of the thermal conductivity of AlN and Al₂O₃ ceramic substrates (Chasserio, 2009). In the case of AlN, this value can decrease abruptly above 100 °C, attaining just over 100 W m⁻¹ K⁻¹ at 300 °C.

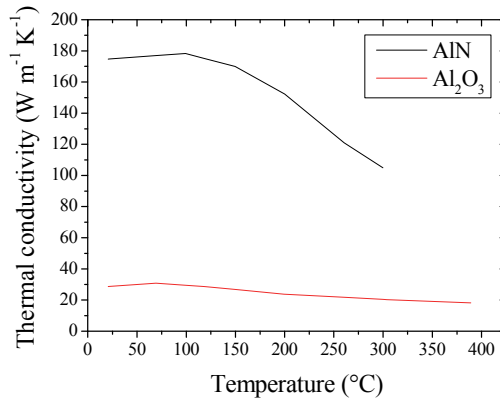


Fig. 4. Temperature dependence of the thermal conductivity for AlN and Al₂O₃ ceramic substrates (values taken from Chasserio, 2009)

3.3 Electrical properties

As the main function of dielectric materials in the environment of the power devices is to separate two different electrical potentials from one to the other, their electrical insulating properties are fundamental and must be accurately known versus temperature. Particularly, in the case of the insulation of high temperature SiC power devices and modules (above 200 °C), the electrical properties of the candidates need to be investigated in the same range.

3.3.1 Dielectric permittivity and loss

The low field dielectric properties are usually defined under the complex dielectric permittivity formalism (ϵ^*), which is made up of the dielectric constant (real part) and the dielectric loss (imaginary part) (see eq. (2)). The ratio between the imaginary part and the real part corresponds to the dielectric loss factor ($\tan \delta$) (see eq. (3)):

$$\epsilon^*(\omega) = \epsilon'(\omega) - j\epsilon''(\omega) \quad (2)$$

$$\tan \delta(\omega) = \frac{\epsilon''(\omega)}{\epsilon'(\omega)} \quad (3)$$

where ϵ' and ϵ'' represent respectively the real and imaginary parts of the complex dielectric permittivity, ω is the angular frequency and $j = \sqrt{-1}$.

The dielectric permittivity and loss result from polarization processes in the material bulk such as the orientation of dipole entities. This phenomenon is strongly dependent on the frequency of study. Moreover, the dipolar mobility being thermally activated, the polarization processes are also strongly temperature-dependent. For good insulating

materials, an acceptable upper limit for the loss factor can be situated around 10^{-2} while it can be as low as 10^{-5} for very performing materials.

Figure 5 shows two examples of the high temperature dependence of the dielectric properties of good insulating dielectrics: (a, c) BPDA/PDA PI films and (b, d) Al_2O_3 ceramic. Typically, at low temperature ($<100^\circ\text{C}$), most of the thermo-stable dielectrics present a non-variant relative permittivity and a loss factor below 10^{-2} . On the contrary, for higher temperatures, it is observed that the magnitude of both ϵ' and $\tan\delta$ exhibits a strong increase all the more important as temperature is high and/or frequency is low. Such magnitudes cannot find explanations in simple dipolar polarization processes (Adamec, 1974). These huge values are mainly associated to interfacial polarization processes (i.e. either due to Maxwell-Wagner-Sillars (MWS) relaxation-type in heterogeneous specimen or electrode polarization) (Kremer & Schönhal, 2003). MWS relaxation and electrode polarization are involved by the drift of mobile charges across the materials towards bulk interfaces (different phases, impurities, ...) or electrodes, respectively. Their occurrence corresponds to the transition where the materials start to become semi-insulating (i.e. $\epsilon' \gg \epsilon_\infty$ and $\tan\delta \gg 10^{-1}$). Consequently, it appears as more judicious to investigate them in terms of electrical conductivity (i.e. property completely controlled by the motion of charges).

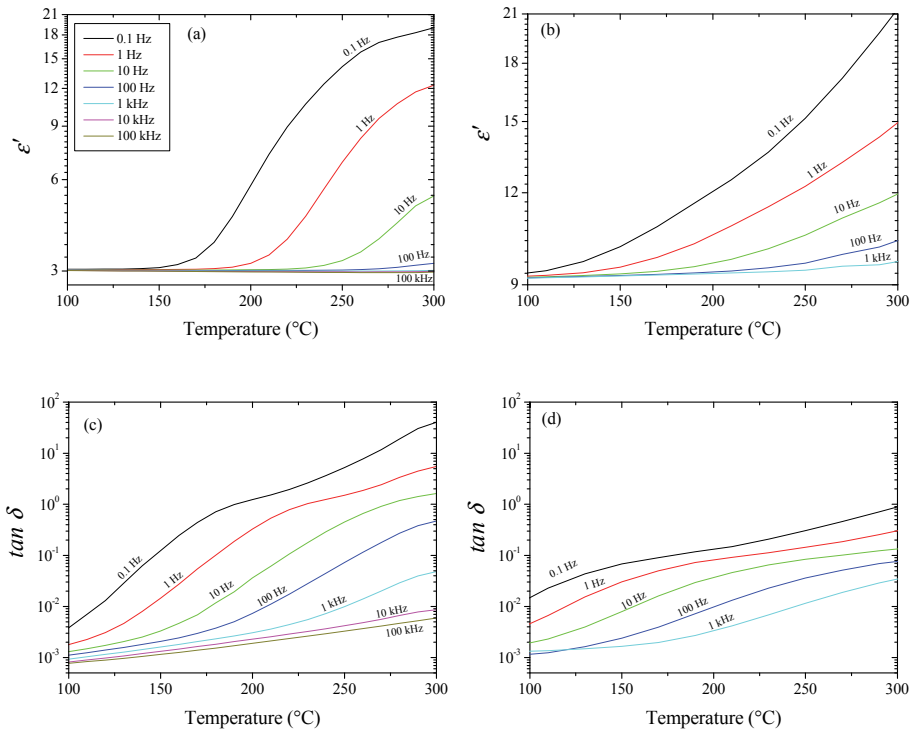


Fig. 5. Dielectric permittivity and loss factor versus temperature for BPDA/PDA PI films (a, c) (from Diahm, 2010a) and alumina ceramic (b, d)

3.3.2 Electrical conductivity

Insulating materials are defined by a volume conductivity largely below $10^{-12} \Omega^{-1} \text{ cm}^{-1}$. The peculiar range of semi-insulating materials corresponds to the conductivity range between that of insulating ones and semiconductors (i.e. from 10^{-12} to $10^{-8} \Omega^{-1} \text{ cm}^{-1}$). When the conduction of mobile charges dominates the dielectric loss, compared to the dipolar processes, it is preferable to represent the loss in the formalism of the alternating conductivity (σ_{AC}) as a function of frequency and temperature using eq. (4) (Kremer & Schönhal, 2003; Jonscher, 1983):

$$\sigma_{AC}(f, T) = 2\pi f \epsilon_0 \epsilon''(f, T) = \sigma_{DC}(T) + A(T) f^s \quad (4)$$

where ϵ_0 is the vacuum permittivity, σ_{DC} is the static volume conductivity, A is a temperature-dependent parameter and s is the exponent of the power law ($0 < s \leq 1$).

In a large frequency range of study, the AC conductivity is made up of a high frequency linear contribution and an independent-frequency region at low frequency characterized by a static conductivity (σ_{DC}) plateau. The DC conductivity is a temperature-dependent property following usually the Arrhenius-like behavior, described by eq. (5). Materials presenting a thermal transition in the investigated temperature range (e.g. glass transition region) follow the non-linear Vogel-Fulcher-Tamman (VFT) behavior given by eq. (6):

$$\sigma_{DC}(T) = \sigma_{\infty} \exp \left[-\frac{E_a}{k_B T} \right] \quad (5)$$

$$\sigma_{DC}(T) = \sigma_{\infty} \exp \left[-\frac{DT_0}{T - T_0} \right] \quad (6)$$

where σ_{∞} is the conductivity at an infinite temperature, E_a is the activation energy, k_B is the Boltzmann's constant, D is the material fragility and T_0 is the Vogel temperature.

DC conductivity is related to the structure and microstructure of the dielectric materials. Moreover, for a given material the dielectric properties are also strongly related to the way used to synthesize and process it. Hence, whereas it is difficult to predict a priori what will be the final DC conductivity from a theoretical point of view, it appears as impossible to estimate before what will be the impact of the material processing on this property. Consequently, it is fundamental to investigate, analyse and understand the origins of such variations of the DC conductivity in close relations with the material physico-chemical properties. Figure 6 presents the main parameters affecting the temperature dependence of the dc conductivity for various thermo-stable polymers. Figure 6a shows the variation of σ_{DC} of 400 °C-cured BPDA/PDA PI films for different thicknesses from 1.5 μm to 20 μm . It is observable an increase in σ_{DC} with increasing thickness. The inset plot, showing the infrared spectra of the PI films, allows relating this evolution to the remaining presence after the material processing of PI precursor (polyamic acid, PAA) residues (Diaham, 2011a). These impurities are a source of ionic species increasing the electrical conduction. Figure 6b shows the temperature dependence of σ_{DC} for two PAI films with different glass transition temperatures (T_g). The increase in T_g for PAI 2 (i.e. 335 °C against 280 °C for PAI 1 obtained by DSC in the inset plot) allows shifting the onset of the σ_{DC} increase towards higher temperature (Diaham, 2009). The glass transition is therefore an important parameter

controlling the charge motion across amorphous dielectrics. For high temperature operation, higher the T_g , wider is the temperature range of use. Figure 6c and 6d present respectively the σ_{DC} temperature dependence of PA-F before and after a 400 °C annealing and as a function of thickness. It is shown that both annealing and material thickness improve the electrical properties (DC conductivity decreases). Inset plots show that the PA-F crystallinity and the crystallite size are increased either with a thermal treatment or increasing thickness. Consequently, when the volume of the crystalline phase is increased the motion of charges within the material becomes more difficult, thus reducing the DC conductivity (Diahm, 2011b).

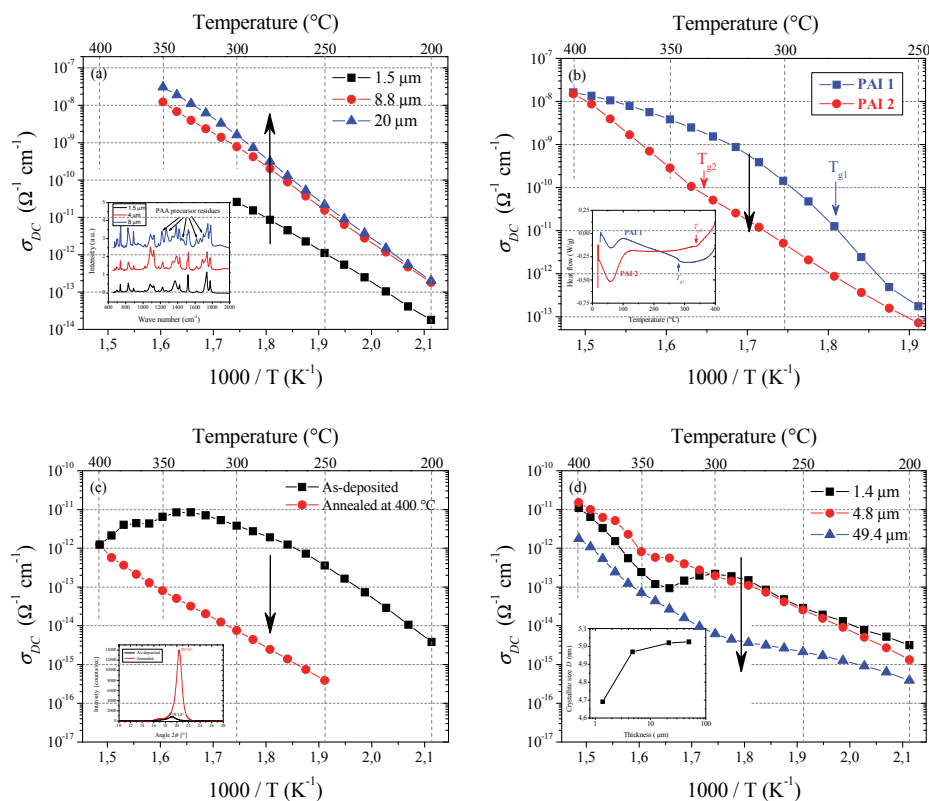


Fig. 6. Main parameters affecting the temperature dependence of the DC conductivity of various polymers: (a) thickness of BPDA/PDA PI films, (b) glass transition temperature in two different PAI films, (c) crystallization temperature for PA-F films, (d) thickness of PA-F films

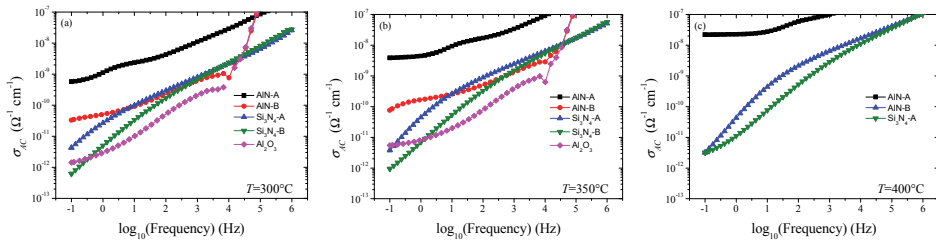


Fig. 7. AC conductivity of various ceramics at (a) 300 °C, (b) 350 °C and (c) 400 °C

In the case of ceramic materials, it is difficult to detect the DC conductivity because of the presence of several interfacial relaxations (from internal or extrinsic origins) at low frequency. Moreover, the pure nature effect of the ceramic on the DC conductivity is difficult to be derived due to the strong additive influence on the synthesized materials. Figure 7 shows the frequency dependence of the AC conductivity of various ceramics at different temperatures. No evidence can be extracted on the substrate nature effect because all the substrates own different sintering processes (temperature, additive types and concentrations, ...). However, these results let expect that most of the ceramics present relatively low DC conductivity less than $10^{-12} \Omega^{-1} \text{ cm}^{-1}$ at 400 °C such as some AlN or Si_3N_4 substrates.

Finally, Figure 8 presents the impact of the sintering process at 1800 °C (i.e. conventional thermal sintering and spark plasma sintering, SPS) on the AC conductivity of AlN ceramics with Y_2O_3 additives. The microstructure, density and the distribution of sintering additives impact the low frequency-dispersion of the dielectric properties. The SPS sintered AlN ceramic has lower AC conductivity values at high temperatures, even if the low-frequency plateau (i.e. DC conductivity) cannot be observed in the investigated frequency range.

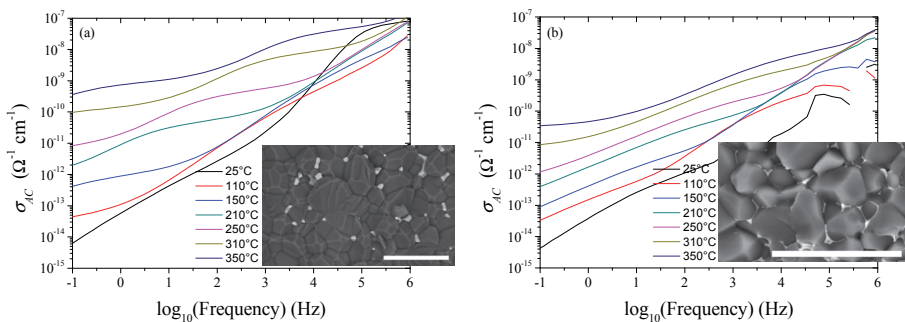


Fig. 8. Sintering process influence on the AC conductivity of 1800 °C-sintered AlN: (a) conventional sintering process and (b) SPS sintering process. Bar length: 10 μm

3.3.3 Dielectric breakdown field

The dielectric strength is the capability of dielectrics to withstand high electric fields without failure. The dielectric breakdown field (E_{BR}) is the upper limit of electric field that dielectrics can support under a voltage supply. Its value strongly depends on the electrode configuration (i.e. plane-plane or needle-plane electrodes). In homogeneous plane-plane electrode configuration, the dielectric breakdown field is given by:

$$E_{BR} = \frac{V_{BR}}{d} \quad (7)$$

where V_{BR} is the breakdown voltage and d is the dielectric thickness.

Experimental breakdown values (EBR) exhibit a dispersion that requires statistical treatment in order to extract a mean value under the specific measurement conditions. Thus, the data are usually analyzed using the Weibull distribution law (Weibull, 1951):

$$F(E_{BR}) = 1 - \exp\left(-\frac{E_{BR} - \gamma}{\alpha}\right)^\beta \quad (8)$$

where $F(E_{BR})$ is the cumulative probability of failure, α is the scale parameter (i.e. the field value for which 63.2% of the samples are failed), β is the shape parameter quantifying the width of the data distribution (i.e. $\beta > 1$ is related to a low scattering of the data) and γ is the threshold parameter (often $\gamma=0$).

Even if the dielectric strength is an intrinsic parameter depending mainly on structural properties, it is the dielectric property the more sensitive to both experimental (electrode configuration, electrode surface, material thickness, voltage waveform, voltage ramp speed, ...) and environmental parameters (temperature, humidity, pressure, ...). If it is an important property to know, this appears as not self-sufficient for dimensioning electronic systems due to the extreme complexity of the electrical and thermal stresses induced by power devices and environmental severe stresses induced by applications. Consequently, the following section only gives the main experimental observable tendencies on the breakdown field of thermo-stable dielectrics. Recently, the influence of several parameters on the dielectric strength has been reported for BPDA/PDA PI and PA-F films (Diahham, 2010b; Khazaka, 2011a).

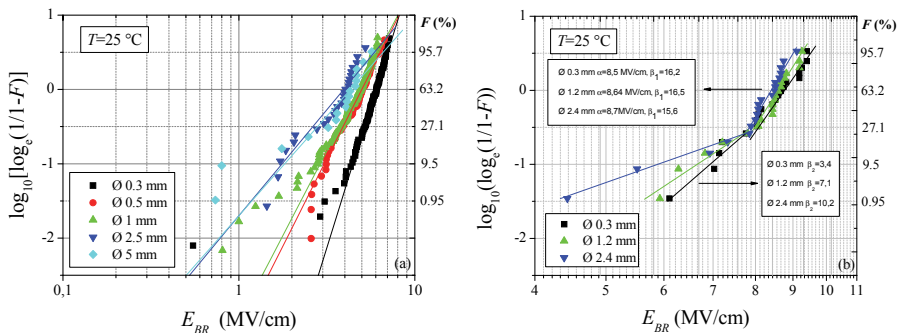


Fig. 9. Electrode diameter influence on the room temperature dielectric strength of BPDA/PDA PI (a) and PA-F (b) films

Figure 9 shows the electrode area influence on the cumulative probability versus E_{BR} at room temperature for BPDA/PDA PI and PA-F films. For PI, it is possible to observe that the cumulative probability curve shifts towards lower breakdown fields with increasing the electrode diameter. The scale parameter α ($F=63.2\%$) decreases also with increasing the electrode diameter. In the same way, the shape parameter β (i.e. the slope of the fitting straight line) decreases with increasing the electrode diameter. These two simultaneous observations typically deal with an increase in the result scattering. They usually are characteristic of an increase in the probability to find defects or impurities in the material bulk leading to the failure of the insulating layer. In the case of PI films, this tendency is associated to the increase in the probability to find polyamic acid and solvent precursor residues in the film. Contrary to PI, PA-F exhibits an area independent dielectric strength behavior at high breakdown field. The fact that PA-F is a by-productless material could explain such a behavior. At low fields, an area dependence appears and is usually related to the presence of surfacic defects (i.e. stacking faults, pinholes, ...). Such studies allow often extrapolating dielectric strength for higher areas which can correspond to more practical cases.

Figure 10 presents the influence of the main other parameters on the dielectric breakdown field of dielectrics. The temperature dependence of the dielectric strength shows a general decrease in α with increasing temperature. For instance, thermo-stable polymers such as PI, PAI and PA-F films illustrate such a tendency (see Figure 10a) (Diaham, 2009, 2010b; Bechara, 2011). The thermal activation of the mobile charge transport and electromechanical constraints are usually brought to light to interpret the origin of the breakdown of polymers. Figure 10b shows the thickness dependence of the dielectric breakdown field of PI and PA-F films. It is usual to observe a general decrease in the breakdown field with increasing thickness for dielectric materials. Here also, this behavior can be explained by an increase in the probability to find defects in the dielectric layer. However, whatever the thickness investigated the dielectric strength remained high above 1 MV/cm.

As seen in the previous section, the processing parameters of ceramics have a great impact on dielectric properties evolution with temperature. When comparing AlN ceramic substrates from two different manufacturers, the differences in the processing conditions (i.e. organic binders, sintering additives, sintering temperature and dwell times) result in subtle differences in the final microstructures and crystallographic phase distributions, that modify considerably the dielectric strength evolution versus temperature (Chasserio, 2009). Figure 10c and 10d present the influence of the ceramic substrate nature and the impact of the sintering process of commercial AlN ceramics on the breakdown field. On one hand, AlN and Si_3N_4 ceramics appear as the materials owning the higher dielectric strength even at high temperature compared to Al_2O_3 and BN ceramics. However, for high temperature insulation applications cautions have to be taken, even in the choice of a same-type of ceramic. Indeed, from one supplier to another, breakdown field values can vary strongly in the high temperature range (see Figure 10d with two different commercial AlN).

3.4 Aging and life time

In power electronics applications, the high operating temperature ($>200\text{ }^\circ\text{C}$) can result from either the ambient environment, the power dissipation, or a combination of both. Thus, after the first stage of initial material characterizations, it is necessary to follow the above properties during aging in harsh environment (temperature during time, thermal cycles, atmospheres, ...) in order to estimate the life time of dielectrics. In this section, the influences of the more usual aging conditions on the main sensitive parameters for each dielectric function in a power device assembly are presented.

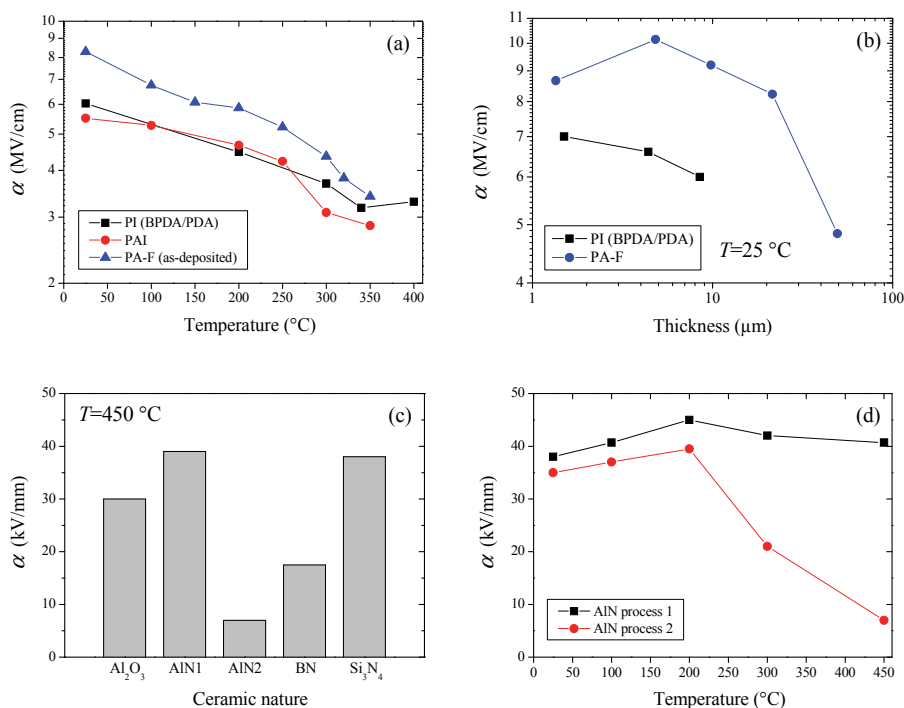


Fig. 10. Main parameters affecting the dielectric strength of various dielectrics: (a) temperature for PI, PAI and PA-F films, (b) thickness for PI and PA-F films at 25°C , (c) temperature and ceramic nature for thick substrates (values taken from Chasserio, 2009), (d) two AlN substrates from different manufacturers (values taken from Chasserio, 2009)

3.4.1 Thermal aging

For organic materials, the thermal aging appears among the more severe aging condition during long term service because temperature can carry out sufficient energy to break the structural bonds constituting the material skeleton. Although approximate models exist to predict accelerated aging under relatively smooth conditions, nowadays nobody can ensure their validity at very high temperatures near the limit of the polymer maximal operating temperature due to the absence of knowledge of the degradation mechanisms. Moreover, despite the importance of such a topic, there is a lack of studies in the literature dealing with long term thermal aging of polymers (Diaham, 2008; Khazaka, 2011b; Wayne Johnson, 2007; Zheng, 2007; Yao, 2010). It is indispensable to perform extremely long aging under such high temperature to validate high temperature reliability. In order to probe thermal-induced degradations, the dielectric breakdown strength is often appreciated because it gives information on the high field properties of dielectrics.

Figure 11 shows the dielectric strength evolution of BPDA/PDA PI films versus time for several aging temperatures in air. The figure compares also the dielectric strength evolution for films coated on different substrates. We can observe first that the life time

depends on exposure temperatures. For instance, while the life time is more than 7,000 hours at 250 °C for PI coatings on stainless steel, it decreases strongly with increasing temperature: around 5,000 hours at 300 °C; 1,000 hours at 340 °C and 400 hours at 360 °C. This result underlines the thermal activation of the degradation. Secondly, the aging of PI coatings depends strongly on their substrate nature. Indeed, when the films are deposited on Si wafers, the life time of the material is strongly increased. For instance, the life time at 300 °C of films deposited on Si is superior than 5,000 hours while the same films deposited on metal substrates (stainless steel) is less than 5,000 hours. This can be interpreted by the difference of the CTE between the PI films and the substrates. In the case of stainless steel substrates (CTE=17 ppm/°C), internal residual mechanical stresses are amounted in the BPDA/PDA PI layer (CTE=3-6 ppm/°C) which lead to premature degradation during thermal aging. The minimization of the CTE mismatch between the Si wafer (CTE=3 ppm/°C) and the BPDA/PDA PI film allows decreasing the mechanical stresses and so increasing the life time of the dielectric material. In the case of coatings on SiC wafers (for the component passivation function), similar results can be expected due to the compatible value of the SiC CTE value (3-5 ppm/°C) with the one of the BPDA/PDA PI.

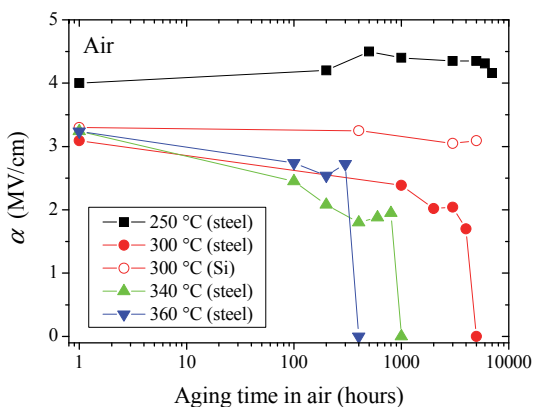


Fig. 11. Dielectric strength versus aging time of BPDA/PDA PI films for different aging temperatures in air. Measured at 250 °C for aging at 250 °C and at 300 °C for higher aging temperatures. Stainless steel or silicon are used as film substrates.

Semicrystalline PA-F films (Parylene HT in commercial form) have been developed for their capability to support very high temperature during very long time even in oxidant atmosphere due to C–F bonds in the monomer structure. This relatively new material is supposedly stable for at least 1,000 hours at 350 °C in air atmosphere and 3 hours at 450 °C (see Figure 12) (Kumar, 2009). Nowadays only one study has been reported on the high temperature electrical properties of PA-F (Diaham, 2011b). This places PA-F among the potential suitable polymers for insulating coating in high temperature electronics applications.

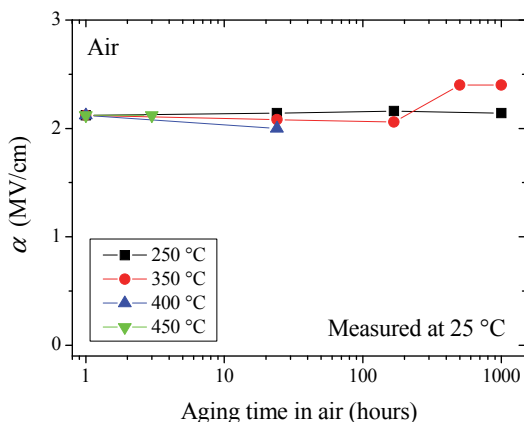


Fig. 12. Dielectric strength versus aging time of PA-F films for different temperatures of aging in air (values taken from Kumar, 2009). Measured at room temperature

Figure 13 shows the room temperature probed dielectric strength of silicone gel and silicone elastomer used for the device encapsulation function during thermal aging at 250 °C in air (Yao, 2010). The breakdown field falls down in the early first stage of aging, whatever the encapsulant materials, showing the difficulty nowadays to identify materials, for this important function of the packaging, able to operate at high temperature with reliability. Comparable results on other silicone-type materials have been reported recently by Zheng (Zheng, 2007). The penury of thick and soft materials appears as the main problem to increase the operating temperature of high voltage power devices above 250 °C, at least without changing radically the architecture of power modules.

3.4.2 Thermal cycling

One of the main problems in power electronic systems, besides the discrete materials performance is their heterogeneous mechanical properties. The thick insulating ceramics are especially under concern, more than the thinner passivation layers or the very soft encapsulating silicone gels classically used in power devices. In a first glance, SiC and the insulating ceramic substrates appear to have a similar CTE, but as stated earlier, metallic conductors that support the assemblies have much larger CTE, often 5 to 10 times larger. This makes the interface of ceramic and metal of the substrate component a susceptible point of failure. Thermal cycling amplifies this effect, as systems are exposed to wide temperature fluctuations over their lifetime.

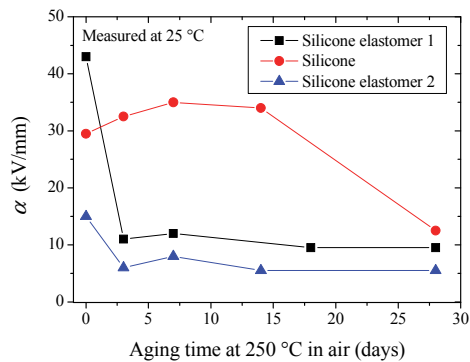


Fig. 13. Dielectric strength versus aging time of silicone and silicone elastomer materials aged at 250 °C in air (values taken from Yao, 2010), measured at room temperature.

In high temperature operating SiC devices, several technologies, such as Al₂O₃ direct-copper-bond (DCB) and AlN DCB are limited in wide temperature cycling (Dupont, 2006a), as the ceramic is fractured by the mechanical stress that is imposed by the copper foil (see Figure 14a).

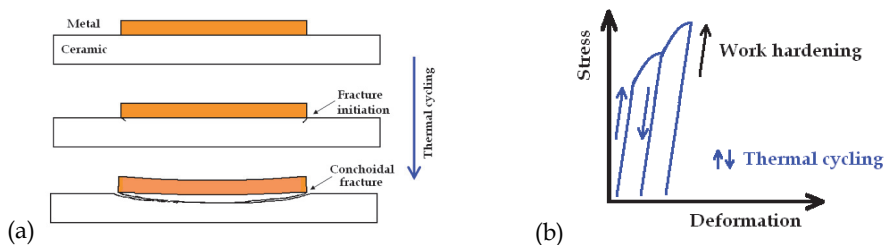


Fig. 14. (a) Failure on DCB substrate due to thermal cycling. Note the fracture across the ceramic material; the conchoidal fracture is initiated close to the copper foil edges. (b) Schema of metal work hardening of DCB ceramic substrate technologies during thermal cycling

The local mechanical stress is incremented by each cycling due to the work hardening of the copper foil, increasing its yield strength (see Figure 14b), this goes on until the maximum acceptable stress is attained at the ceramic, causing its failure (Dupont, 2006b).

For intermediate current levels, it is possible to diminish the metallization thickness to delay failure, or to make dimples applied to the edges of the copper foil (Dupont, 2006a). The availability of new substrate ceramics and available metallization types make possible to increase the reliability in increasing temperature cycling ranges. AlN can be brazed to aluminium, that has a higher CTE when compared to copper, but a lower recrystallization temperature (200-400 °C). This allows for a recrystallization after the work hardening imposed by the thermal cycling, keeping the constraints below the fracture limit of the AlN (Lei, 2009). On the other hand, Si₃N₄ has much higher fracture toughness, allowing it to resist the work hardening of copper across cycling (El Sawy & Fahmy, 1998). Si₃N₄ brazed to copper is claimed to last more than 5,000 cycles, ten times more than DCB technologies (Kyocera, 2009). Alternative approaches involve the use of low CTE metals as Kovar alloys (Lin & Yoon, 2005).

3.4.3 Atmosphere effects

Atmosphere nature acts as an important factor in the degradation of the polymers. In the case of BPDA/PDA PI films, Figure 15 shows the influence of the ambient atmosphere of aging on PI high temperature breakdown voltage. This result shows the increase in the life time when aging is performed into inert atmosphere. Oxygen atoms coming from air atmosphere lead to cut the PI monomer skeleton inducing a thermo-oxidative degradation processes (Khazaka, 2011b). In nitrogen atmosphere, the pure thermal degradation processes start at a further moment or temperature. This highlights the importance of using hermetic cases for power devices or to use oxygen barrier layers to protect PI films against oxygen. The effects of such barriers (e.g. SiO_x , Si_xN_y) have been previously reported elsewhere (Khazaka, 2009).

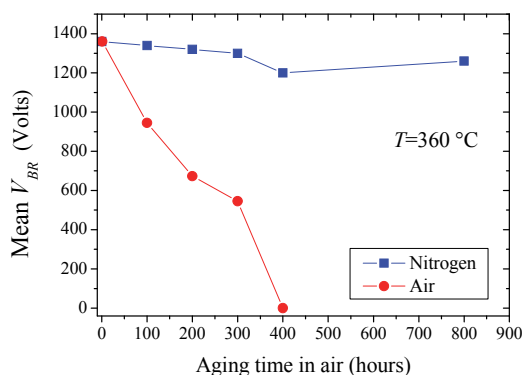


Fig. 15. Influence of the ambient atmosphere on the life time of the mean breakdown voltage of 4 μm -thick BPDA/PDA PI films at 360 °C

On the contrary, the atmosphere nature seems to have low influence in the case of PA-F due to its low permeability to oxygen. This kind of materials could act as a good oxygen barrier coating over other oxygen sensitive polymers to protect them and increase their life time under high temperature conditions.

4. Conclusion

This chapter summarizes recent worldwide research advances regarding reported insulating polymers and ceramics for high temperature power SiC devices and modules. A presentation of their main limiting physical properties regarding high temperature applications, linked to microstructure analyses, is also presented.

Among polymeric materials, BPDA/PDA polyimide (PI) or fluorinated parylene (PA-F) are reported as interesting candidates for high temperature operation due to their highest and longest thermal stability. Moreover, they keep good dielectric properties even above 250 °C and even in oxidative atmosphere. PI film electrical properties are very sensitive to curing process while PA-F ones depend strongly on the crystallinity of the layer. However, even those materials may be not suitable for answering the highest temperature identified needs (above 400 °C) for long-term operation. Other polyamide-imide (PAI) and silicone elastomer (PDMS) materials, widely used up to now as thick insulating in electronic systems, exhibit a long-term operating limit below 250 °C. Today, it remains the issue of the existence of thick

and soft insulating polymeric materials able to withstand high voltage even in the very high temperature range ($>250\text{ }^{\circ}\text{C}$) during thousands of hours in order to answer the insulation of high temperature/high voltage SiC devices. Consequently, future research should concentrate towards this objective.

Regarding ceramics, the high thermal conductivity and the relatively invariant temperature dependence of the dielectric strength of aluminium nitride (AlN) and silicon nitride (Si_3N_4) place them as the more performing ceramic materials to realize metallized substrates for high temperature power electronic modules. However, the choice of their metallization nature and geometrical parameters is of first importance in order to improve the substrate life time. Thus, AlN/Al and $\text{Si}_3\text{N}_4/\text{Cu}$ couples have already shown higher performances than classical DCB technologies, particularly in terms of thermal cycling resistance and could be good alternatives to answer the needs in high temperature and severe cycling substrate applications.

5. Acknowledgment

The authors would like to thank the 'Fondation Nationale de Recherche pour l'Aéronautique et l'Espace' (FNRAE) and the 'Direction Générale des Entreprises' (DGE) for the financial support of this work.

6. References

- Adamec, V. (1974). Polarization Effect in an Epoxy Resin at Elevated Temperatures. *Polymer*, Vol.15, No.8, pp. 496-498
- Bai, J. G.; Calata, J. N. & Lu, G. Q. (2004). Comparative Thermal and Thermo-Mechanical Analysis of Solder-Bump and Direct-Solder Bonded Power Devices Packages having Double Sided Cooling Capability, *Power Electronics Seminar Proceedings* (CPES), pp. 147-153, Virginia Tech, Virginia, USA, April 18-20, 2004
- Bechara, M.; Khazaka, R.; Diahm, S.; & Locatelli, M.-L. (2011). Crystallization Effect on the Dielectric Strength of Fluorinated Parylene at High Temperature. *European Journal of Electrical Engineering*, accepted for publication
- Chasserio, N.; Guillemet-Fritsch, S.; Lebey, T.; & Dagdag, S. (2009). Ceramic Substrates for High-temperature Electronic Integration. *Journal of Electronic Materials*, Vol.38, No.1, pp. 164-174
- Cooper Jr., J. A. & Agarwal, A. (2002). SiC Power Switching Devices - The Second Electronics Revolution, *Proceedings of IEEE*, Vol.90, No.6, p.956, June, 2002.
- Diahm, S.; Locatelli, M.-L. & Lebey, T. (2008). Improvement of Polyimide Electrical Properties during Short-Term of Thermal Aging, *Annual Report Conference on Electrical Insulation and Dielectric Phenomena (CEIDP)*, pp. 79-82, ISBN 978-1-4244-2549-5, Québec City, Canada, October 26-29, 2008
- Diahm, S.; Locatelli, M.-L.; Lebey, T. & Dinculescu, S. (2009). Dielectric and Thermal Properties of Polyamide-imide (PAI) Films, *Annual Report Conference on Electrical Insulation and Dielectric Phenomena (CEIDP)*, pp. 482-485, ISBN 978-1-4244-4559-2, Virginia Beach, Virginia, USA, October 18-21, 2009
- Diahm, S.; Locatelli, M.-L.; Lebey, T. & Dinculescu, S. (2010a). Dielectric Measurements in Large Frequency and Temperature Ranges of an Aromatic Polymer. *The European Physical Journal Applied Physics*, Vol.49, pp. 10401

- Diaham, S.; Zelmat, S.; Locatelli, M.-L.; Dinculescu, S.; Lebey, T. & Decup, M. (2010b). Dielectric Breakdown of Polyimide Films: Area, Thickness and Temperature Dependence. *IEEE Transactions on Dielectrics and Electrical Insulation*, Vol.17, No.1, pp. 18-27
- Diaham, S.; Locatelli, M.-L.; Lebey, T. & Malec, D. (2011a). Thermal Imidization Optimization of Polyimide Thin Films Using Fourier Transform Infrared Spectroscopy and Electrical Measurements. *Thin Solid Films*, Vol.519, No.6, pp. 1851-1856
- Diaham, S.; Bechara, M.; Locatelli, M.-L.; & Tenailleau, C. (2011b). Electrical Conductivity of Parylene F at High Temperature. *Journal of Electronic Materials*, Vol.40, No.3, pp. 295-300
- Dieckerhoff, S.; Guttowski, S. & Reichl, H. (2006). Performance Comparison of Advanced Power Electronic Packages for Automotive Applications, *Automotive Power Electronics*, June 21-22, Paris, France, 2006
- Dupont, L (2006a), *Contribution à l'Etude de la Durée de Vie des Assemblages de Puissance dans des Environnements Haute Température et avec des Cycles Thermiques de Grande Amplitude*, École Normale Supérieure, Cachan, Val-de-Marne, France
- Dupont, L.; Zoubir, K.; Lefebvre, S. & Bontemps, S. (2006b). Effects of metallization thickness of ceramic substrates on the reliability of power assemblies under high temperature cycling. *Microelectronics Reliability*, Vol.46, No.9-11, pp. 1766-1771
- El Sawy, A. & Fahmy, M. (1998), Brazing of Si_3N_4 Ceramic to Copper, *Journal of Materials Processing Technology*, Vol.77, pp. 266-272
- Funaki, T.; Balda, J. C.; Junghans, J.; Kashyap, A. S.; Mantooth, H.A.; Barlow, F.; Kimoto, T. & Hikihara, T. (2007). Power Conversion with SiC Devices at Extremely High Ambient Temperatures, *IEEE Transaction on Power Electronics*, Vol.22, No.4, pp. 1321-1329
- Liu, X.; Calata, J. N.; Wang, J. & Lu, G.Q. (1999). The Packaging of Integrated Power Electronics Modules Using Flip-Chip Technology, *Proceedings of the 17th Annual Power Electronics Seminar of Virginia Tech.*, Virginia, USA, September, pp. 361-367, 1999
- Jonscher, A. K. (1983). *Dielectric Relaxation in Solids*, Chelsea Dielectrics Press, London, U.K.
- Khazaka, R.; Diaham, S.; Locatelli, M.-L. & Despax, B. (2009). Oxidative Thermal Aging Effect on the Electrical Properties of BPDA/PDA Polyimide Films With and Without Oxygen Barrier Layers, *6th International Symposium on Polyimides and Other High Temperature/High Performance Polymers Synthesis, Characterization and Applications*, Melbourne, Florida, USA, November 09-11, 2009
- Khazaka, R.; Bechara, M.; Diaham, S.; & Locatelli, M.-L. (2011a). Parameters Affecting the DC Breakdown Strength of Parylene F Thin Films, *Annual Report Conference on Electrical Insulation and Dielectric Phenomena (CEIDP)*, Cancun, Mexico, October 16-19, 2011
- Khazaka, R.; Diaham, S.; Locatelli, M.-L.; Trupin, C. & Schlegel, B. (2011b). Thermal and Thermo-Oxidative Aging Effects on the Dielectric Properties of Thin Polyimide Films Coated on Metal Substrate, *Annual Report Conference on Electrical Insulation and Dielectric Phenomena (CEIDP)*, Cancun, Mexico, October 16-19, 2011
- Kremer, F. & Schönhals, A. (2003). *Broadband Dielectric Spectroscopy*, Springer-Verlag, Berlin Heidelberg, Germany
- Kumar, R. (2009). Parylene HT: A High Temperature Vapor Phase Polymer for Electronics Applications, *6th International Symposium on Polyimides and Other High*

- Temperature/High Performance Polymers Synthesis, Characterization and Applications*, Melbourne, Florida, USA, November 09-11, 2009
- Kyocera. Kyocera Si₃N₄ AMB Products Kyocera Si₃N₄ AMB Products (AMB ver.6.7). Retrieved March 1, 2009, from http://www.leb.eei.uni-erlangen.de/winterakademie/2008/courses/course3_material.old/lifetimePower/course3_material/lifetimePower/Reliability_6.pdf
- Lei, T. G.; Calata, J. N.; Ngo, K. D. T. & Lu, G. (2009). Effects of Large-Temperature Cycling Range on Direct Bond Aluminum Substrate. *IEEE Transactions on Device and Materials Reliability*, Vol.9, No.4, pp. 563-568
- Lin, Z. & Yoon, R. J. (2005). An AlN-Based High Temperature Package for SiC Devices: Materials and Processing. *Proceedings of the International Symposium on Advanced Packaging Materials: Processes, Properties and Interfaces*, pp. 156-159, 2005
- Locatelli, M. L.; Isoird, K.; Dinculescu, S.; Bley, V.; Lebey, T.; Planson, D.; Dutarde, E. & Mermet-Guyennet, M. (2003). Study of Suitable Dielectric Materials Properties for High Electric Field and High Temperature Power Semiconductor Environment, *European Power Electronics Conference*, Toulouse, France, September 02-04, 2003
- Mermet-Guyennet, M.; Castellazzi, A.; Lasserre, P. & Saiz, J. (2008). 3D Integration of Power Semiconductor Devices Based on Surface Bump Technology, *5th International Conference on Integrated Power Electronic Systems (CIPS)*, Nuremberg, Germany, 2008
- Mounce, S.; McPherson, B.; Schupbach, R. & Lostetter, A. (2006). Ultralightweight, High Efficiency SiC Based Power Electronic Converters for Extreme Environments, *Proceedings of the IEEE Aerospace Conference*, New York, USA, pp. 1-19, 2006
- Raynaud, C.; Tournier, D.; Morel, H. & Planson, D. (2010). Comparison of High Voltage and High Temperature Performances of Wide Bandgap Semiconductors for Vertical Power Devices. *Diamond and Related Materials*, Vol.19, No.1, pp. 1-6
- Sroog, C. E.; Endrey, A. L.; Abramo, S. V.; Berr, C. E.; Edwards, W. M.; & Olivier, K. L. (1965). Aromatic Polypyromellitimides From Aromatic Polyamic Acids. *Journal of Polymer Science Part A: Polymer Chemistry*, Vol.3, pp. 1373-1390
- Sugawara, Y.; Takayama, D.; Asano, K.; Singh, R.; Palmour, J. & Hayashi, T. (2001). 12-19 kV 4H-SiC PiN Diodes with Low Power Losses. *Proceedings of the 13th International Symposium on Power Semiconductor Devices & Ics (IEEE)*, Osaka, Japan, pp. 27-30, 2001
- Tsukiji, M.; Bitoh, W.; & Enomoto, J. (1990). Thermal Degradation and Endurance of Polyimide Films, *Conference Record of the International Symposium on Electrical Insulation (IEEE)*, pp. 88-91, 1990
- Wayne Johnson, R.; Wang, C.; Liu, Y. & Scofield, J. D. (2007). Dielectric Breakdown of Polyimide Films: Area, Thickness and Temperature Dependence. *IEEE Transactions on Electronics Packaging Manufacturing*, Vol.30, No.3, pp. 182-193
- Weibull, W. (1951). A Statistical Distribution of Wide Applicability. *Journal of Applied Mechanics*, Vol.18, pp. 293-297
- Yao, Y.; Chen, Z.; Lu, G.-Q.; Boroyevich, D. & Ngo, K. D. T. (2010). Characterization of Encapsulants for High-Voltage, High-Temperature Power Electronic Packaging, *Electronic Components and Technology Conference (IEEE)*, 2010
- Zheng, Y. & Katsis, D. (2007). Investigation of Silicone-Based Encapsulants for a High Temperature Power Module, *40th International Symposium on Microelectronics (IMAPS)*, San Jose, California, USA, November 11-15, 2007

Application of Silicon Carbide in Abrasive Water Jet Machining

Ahsan Ali Khan and Mohammad Yeakub Ali
*International Islamic University Malaysia
Malaysia*

1. Introduction

Silicon carbide (SiC) is a compound consisting of silicon and carbon. It is also known as carborundum. SiC is used as an abrasive material after it was mass produced in 1893. The credit of mass production of SiC goes to Edward Goodrich Acheson. Now SiC is used not only as an abrasive, but it is also extensively used in making cutting tools, structural material, automotive parts, electrical systems, nuclear fuel parts, jewelries, etc.

AWJM is a well-established non-traditional machining technique used for cutting difficult-to-machine materials. Nowadays, this process is being widely used for machining of hard materials like ceramics, ceramic composites, fiber-reinforced composites and titanium alloys where conventional machining fails to machine economically. The fact is that in AWJM no heat is developed and it has important implications where heat-affected zones are to be avoided. AWJM can cut everything what traditional machining can cut, as well as what traditional machining cannot cut such as too hard material (e.g. carbides), too soft material (e.g. rubber) and brittle material (e.g. glass, ceramics, etc.). The basic cutting tool used in water jet machining is highly pressurized water that is passed through a very small orifice, producing a very powerful tool that can cut almost any material. Depending on the materials, thickness of cut can range up to 25 mm and higher (Kalpakjian & Schmid, 2010). A water jet system consists of three components which are the water preparation system, pressure generation system and the cutting head and motion system.

As far as technology development is concerned, three types of water jet machining have been found and used. The first type is a typical water jet machining which was used in the middle of 18th century. The first attempt was in Russia in 1930s to cut hard rock using the pressurized water jet. The typical water jet machining used only water as the cutting tool which allows only cutting limited materials. The second type is AWJM as the improvement to the original water jet machining technique. Addition of abrasive to water enhances the capability of machining by many times. AWJM is an appropriate and cost effective technique for a number of uses and materials. Third type of AWJM includes cutting of difficult-to-machine materials, milling and 3-D-shaping, turning, piercing, drilling, polishing etc. These operations can be performed just by using plain water jet machining. However, due to special considerations such like the type of material or shape complexity of the part to be produced, the addition of the abrasive material is required.

The use of the AWJM for machining or finishing purposes is based on the principle of erosion of the material upon which the jet is incident. The primary purpose of the abrasive material within the jet stream is to develop enough forces to erode the work material. However, the jet also accelerates the abrasive material to a high speed so that the kinetic energy of the abrasives is high enough to erode the work material. The secondary purpose of the water is to carry away both the abrasive material and the eroded material from the machining zone and clear the work area. AWJM gives a clean cut without any damage of the cut surface.

2. Application of AWJM

Generally, water jets are used for (Momber W. & Kovacevic, R., 1998)

1. industrial cleaning
2. surface preparation
3. paint, enamel and coating stripping
4. concrete hydrodemolition
5. rock fragmentation
6. solid stabilization
7. decontamination
8. demolition
9. metal recycling
10. manufacturing operations

In the area of manufacturing, the water jet-technique is used mainly for material cutting by plain water jets (e.g., plastics, thin metal sheets, textiles, foam, very hard materials like carbides, very soft materials like rubber, etc.). Sometimes burrs are formed due to machining of metals by conventional techniques. Those burrs can be removed by plain water jet machining. Some parts work under dynamic load and fatigue failure is the most common type of failure for those parts. Fatigue strength of those parts can be improves by peening the surface with a high pressure water jet. Fibrous materials like Kevlar cannot be machined by conventional machining techniques because of pullouts of the fibers. But AWJM can be employed to machine those materials without any pullout of fibers. AWJM can also be used for milling 3-D shapes. During abrasive water jet milling the surfaces not to be machined is masked before machining and only the areas to be machined are exposed to the jet head. Turning and grooving can also be performed on a lathe using an abrasive water jet. Piercing, drilling and trepanning are other cutting operations performed by AWJM. Water jet machining is a very common technique used to polish and improve work surface smoothness.

The performance of AWJM depends on some key factors. The hardness of the abrasive is an important factor. Harder the abrasive, faster and more efficient will be the machining process. Machining efficiency of abrasives also depends on their structure. Grain shape is another factor in evaluation of an abrasive material for abrasive water-jet process. Shape of abrasives is characterized by their relative proportions of length, width and thickness. During AWJM machining rate to a large extend depends on the size of the grains. Larger grains have higher kinetic energy and their cutting ability is also higher. But though the material removal rate of smaller grains is smaller, they are used for finishing works. Grain-size distribution and average grain size also play role in the performance of AWJM.

AWJM has many advantages over other machining techniques. They are:

1. Almost all types of materials can be machined by AWJM irrespective of their hardness, softness or brittleness. Almost all types of metals, plastics, fibrous materials, glass, ceramics, rubbers, etc. can be machines by this technique.
2. The surface machined by AWJM is smooth and usually they don't need any subsequent machining operation. Abrasives of very small size should be used to produce a smooth surface.
3. AWJM is performed at room temperature. For that reason there is no problem of heat affected zone like other machining techniques. There is no structural change, no phase transformation, no oxidation or no decarburization of the machined surface.
4. The technique is environment friendly. Abrasives like SiC, garnet, alumina, silica sand, olivine together with water are environmental friendly. They don't emit any toxic vapor or unpleasant odor.
5. A major problem in conventional machining like milling, drilling, etc. is burr forming. But AWJM doesn't produce any burr. Rather the technique is used for deburring.

3. Elements of AWJM

In AWJM abrasives are added to water. The performance of AWJM to a great extend depends on the properties of abrasives. The geometry of cut is a key indicator of AWJM.

3.1 Water abrasive water jet machine

The main element of the abrasive water jet system is the abrasive jet. Water is pressurized up to 400 MPa and expelled through a nozzle to form a high-velocity jet. In AWJM abrasives are added to water using a specially shaped abrasive-jet nozzle from separate feed ports. As the momentum of water is transferred to the abrasives, their velocities increase rapidly. It results a focused, high-velocity stream of abrasives that exits the nozzle and performs the cutting action of the work surface. A schematic diagram of AWJM is presented in Fig.1

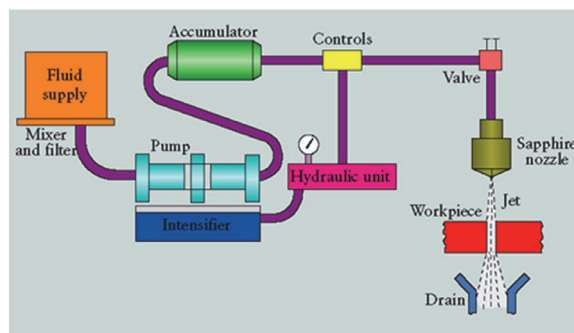


Fig. 1. Abrasive water jet machining (Source: Kalpakjian & Schmid, 2010)

Normal water is filtered and passed to the intensifier. The intensifier acts as an amplifier as it converts the energy from the low-pressure hydraulic fluid into ultra-high pressure water. The hydraulic system provides fluid power to a reciprocating piston in the intensifier center section to amplify the water pressure. Using a control switch and a valve water is pressurized to the nozzle. Abrasive is added to water in the nozzle head (Fig 2) and the

mixture comes out of the nozzle with a very high energy and pressure. In AWJM water is pressurized up to 55,000 pounds per square inch (psi) and then is forced to come out through a small orifice (round or square) at a speed of 2500 feet (762meters) per second, which is about two and half times the speed of sound. As water exits the nozzle at a high speed, the abrasive material is injected into the jet stream or sucked into the stream by a phenomenon known as the 'Venturi' effect. The main purpose of addition of abrasives is to enhance the jet length and improve the cutting ability of the jet. It was found by Chacko et al., 2003 that an addition of polymer to the water jet increases the jet penetration depth. There are two types of AWJM; the slurry and entrainment. The only thing that differentiates them is the way the abrasives are added to the water. In the slurry system, the abrasive is mixed with the water before the water being pressurized. The mix is then pressurized and passed to the end of the nozzle. This method causes extensive wear to the elements or parts of the water jet head due to the friction of the abrasives. In an entrainment system a pipe is connected to the water inlet. When the high-velocity pressurized water passes through the pipe, a vacuum is created causing the abrasive to be sucked into the water stream.

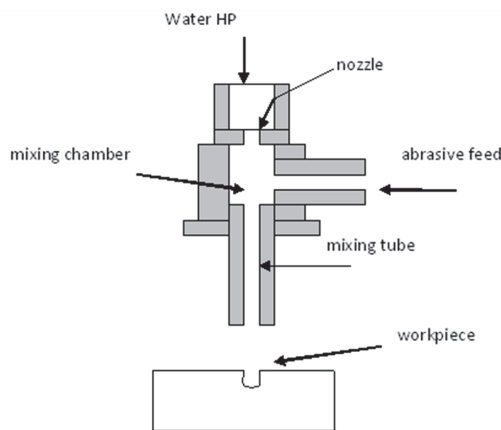


Fig. 2. Abrasive water jet cutting head.

3.2 Abrasives

SiC is known for its very high hardness and abrasion resistance. It is dark gray in color; its hardness and modulus of elasticity are 2,800 knoop (kg/mm^2) and 476 GPa respectively. This material is produced according to specific technology to imitate the natural abrasive. It is heat resistant, and decomposes when heated to about $2,700^\circ\text{C}$. Very pure silicon carbide is white or colorless; crystals of it are used in semiconductors for high-temperature applications. Its small coefficient of expansion, which decreases with increasing temperature, high hardness and sharp crystal edges make it a very good abrasive. It is primarily used for grinding nonferrous materials such as brass, copper, bronze and aluminum. Other applications of SiC include grinding of glass, wood, rubber and plastics. Recently SiC is gaining popularity in as an excellent abrasive for AWJM.

But a survey shows that 90% of the AWJM is done using garnet (Mort, 1995). In industries 80 mesh garnet is a popular abrasive. It is possible to cut slightly faster rate with harder abrasives. However the harder abrasives also cause the mixing tube on the nozzle to wear

rapidly. It is worth mentioning that not all garnets are the same. There are wide variations in purity, hardness, sharpness, etc, that can also affect the cutting speed and operating cost. Garnet is a natural type of abrasive. Garnet has three basic structural components. They are Almandine ($\text{Fe}_3, \text{Al}_2(\text{SiO}_4)_3$), Pyrope ($\text{Mg}_3\text{Al}_2(\text{SiO}_4)_3$) and Spessartite ($\text{Mn}_3\text{Al}_2(\text{SiO}_4)_3$). Garnet also contains impurities like SiO_2 , Al_2O_3 , FeO , MnO , MgO , and CaO . The hardness of garnet abrasive particles of Almandine, Pyrope and Spessartite are 7-7.5 Mohs, 7.5 Mohs and 7-7.5 Mohs respectively. Aluminum Oxide (Al_2O_3) is another popular abrasive used in AWJM. It is also known as alumina. Its melting point is about $2,000^\circ\text{C}$ and specific gravity is about 4.0. It is insoluble in water and organic liquids and slightly soluble in strong acids and alkalis. Alumina is available in two crystalline forms. Alpha alumina is composed of colorless hexagonal crystals. Gamma alumina is composed of minute colorless cubic crystals with specific gravity about 3.6 that are transformed to the alpha form at high temperatures. Alumina powder is formed by crushing crystalline Alumina. It is white when pure. Alumina is extremely tough and is wedge shaped. It is used for high-speed penetration in tough materials without excessive shedding or fracturing of the grains. It is mainly used for grinding high tensile strength materials like carbon steels, alloy steels, tough bronze and hard woods. Other abrasives used in AWJM are olivine, slag, silica sand, etc.

3.3 Geometry of cut

The surface of cut is not vertical. It is characterized by a taper. Based on the width of cut at the top and the bottom it is calculated as follows:

$$T_R = (b - a) / 2$$

For a divergent (V-shaped) slot b is larger than a as shown in Fig. 3.

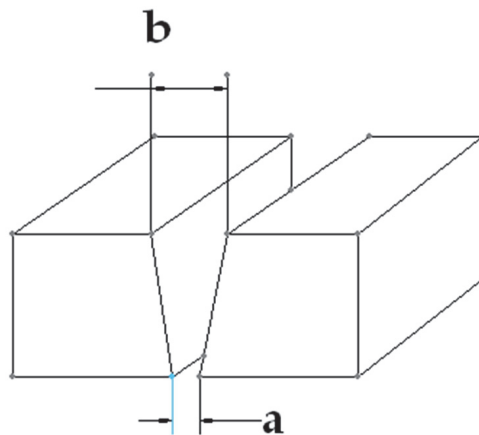


Fig. 3. Usual geometry cut

Hochheng & Chang, 1994 and Momber et al., 1996 investigated the top width of cut during AWJM of ceramics using magnesite and bauxite abrasives and found that the top width of cut decreases with the work feed. But the top width of cut increases with increase in pressure and SOD. However, the slot may be of different shapes as shown in Fig. 4.

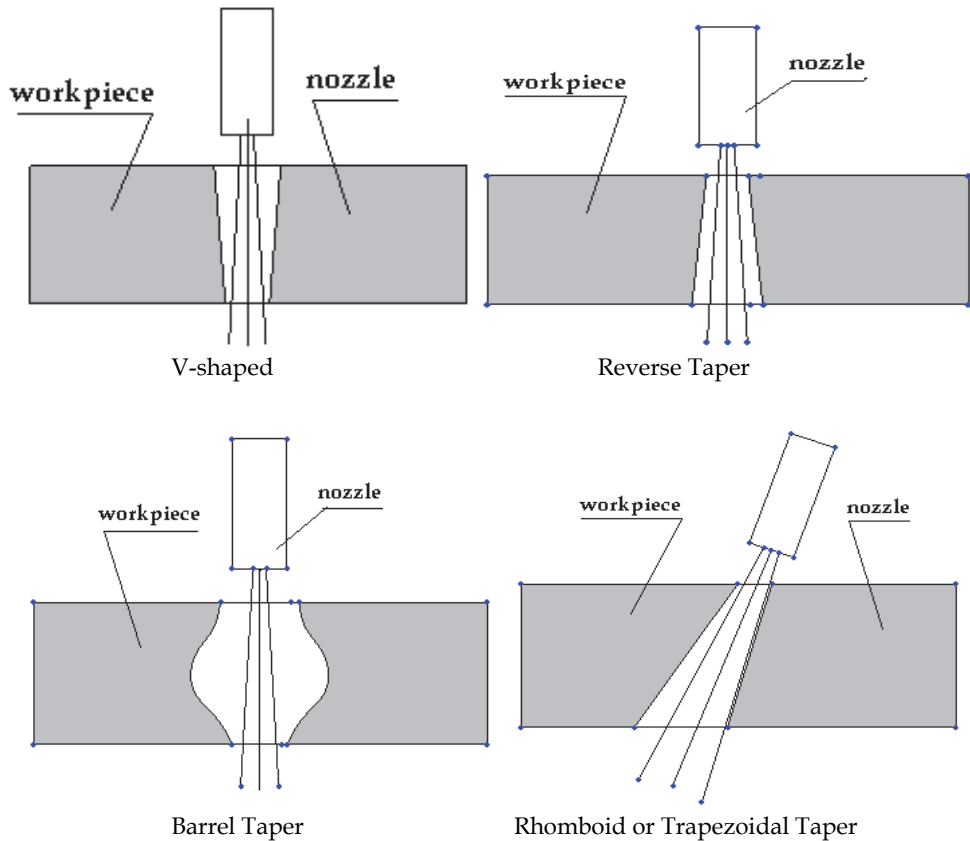


Fig. 4. Different shapes of the taper produced

V shaped taper is produced a result of the jet spending more time over an area to erode the top of the material more than the bottom. Also, "splash back" as the abrasives are bounced back from the material will tend to erode the sides. This is the most common type of taper. Reverse taper tends to happen during AWJM of soft materials where the material is rapidly eroded or when work feed rate is very slowly. Because as the jet stream expands farther away from the nozzle, it removes more material from the bottom than from the top. Barrel taper is produced where the middle is wider than the top or the bottom. Barrel taper is usually produced during machining of very thick materials. Rhomboid taper is actually normal V-shaped taper that has been tilted. It is produced when the nozzle is not perpendicular to the work surface.

Along the vertical surface the quality of the surface is not uniform. It can be divided into three zones (Fig. 5). At the top there is a small initial damaged zone height h_{IDZ} . After that zone there is a smoother zone of height h_{SC} . At the bottom of the surface there is a wavy surface of height h_{RC} .

A typical waviness of the cut slot is shown in Fig. 6. Because the cutting tool is basically a beam of water, it acts as a "floppy tool". The jet lags between where it first enters the material and where it exits. Bottom of the jet lags behind the cutting head.

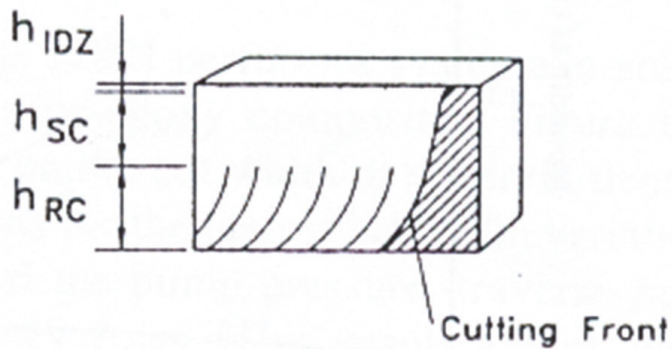


Fig. 5. Surface cut by AWJM (Source: Momber & Kovacevic, 1998)

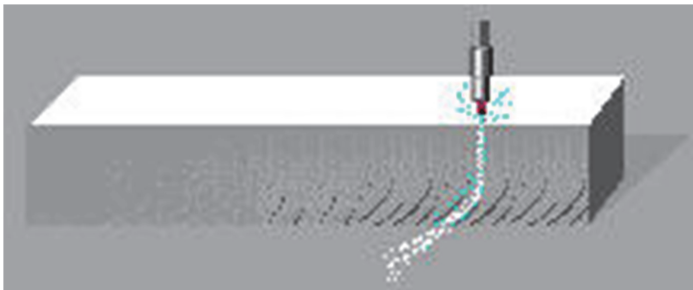


Fig. 6. Waviness of the cut surface (Source: Waterjet machining tolerances, 2011, <http://waterjets.org>)

4. Machining of carbides by SiC

4.1 Influence of jet pressure on work surface roughness

Experiments were conducted to investigate the influence of pressure on surface roughness. During the experiments the jet pressure were varied from 35 kbar to 50 kbar. Work feed rate, abrasive flow rate and depth of cut were kept constant at 1.36 mm/min, 135 g/min and 3.18 mm respectively. The results show that increasing in pressure will decrease the roughness of work materials. In short surface finish becomes smoother and better. It is presented in Fig. 7. From Fig. 8 is evident that surface roughness drastically increases at a higher depth from the top surface. Fig. 9 shows the deterioration of surface smoothness along the depth of the cut surface.

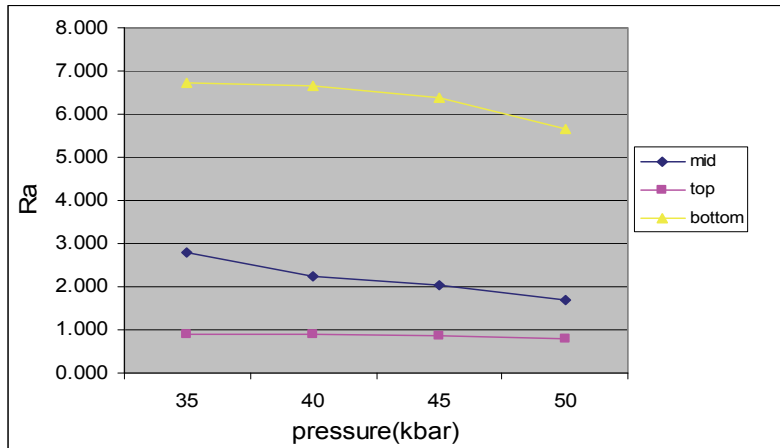


Fig. 7. Effect of pressure on surface roughness

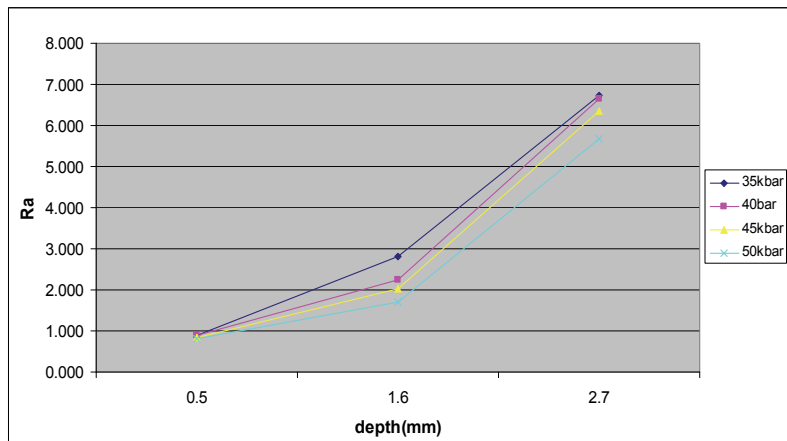
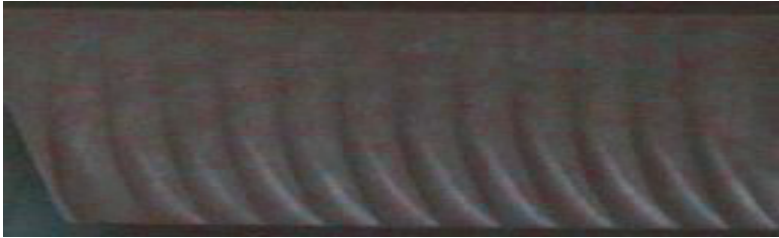


Fig. 8. Surface roughness at different depths from the top surface of carbide



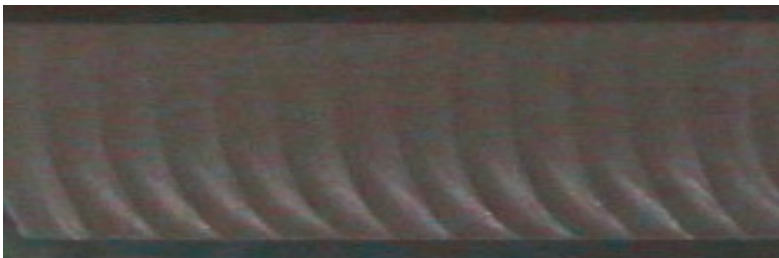
Pressure: 35kbar



Pressure: 40kbar



Pressure: 45kbar



Pressure: 50kbar

Fig. 9. Surfaces of the machined insert carbide tools at constant flow rate (135g/min)

4.2 Influence of abrasive flow rate on surface roughness

This section presents the results of the experiments conducted to investigate the influence of abrasive flow rate on surface finish. In these experiments abrasive flow rate was varied from 135 g/min to 175 g/min. Work feed rate and jet pressure were kept constant at 1.36 mm/min and 45 kbar respectively. It can be observed from Fig. 10 that abrasive flow rate play a vital role in water jet cutting. Surface roughness values are presented at the top, middle and at the bottom of the cut surface. The surface roughness decreases due to larger amount per minute of abrasives used. Means the surface of the cutting profile becomes smoother with higher flow rate. In Fig. 11 surface roughness at different depths from the top surface of carbide is presented. Increasing the flow rate will reduce surface roughness. Surfaces cut at different abrasive flow rate are presented in Fig. 12.

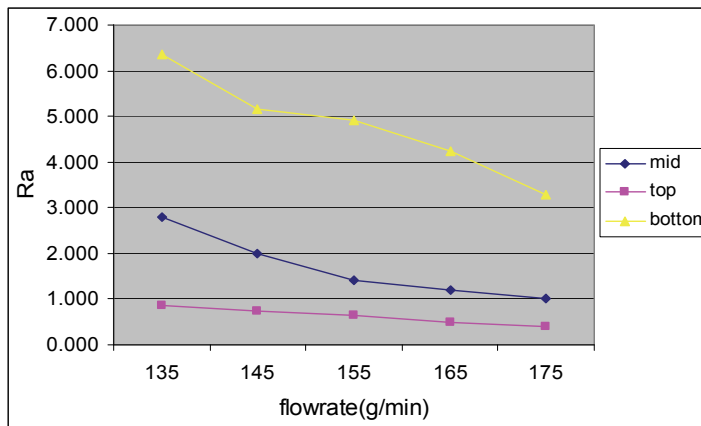


Fig. 10. Effect of abrasive mass flow rate on surface roughness during machining carbide.

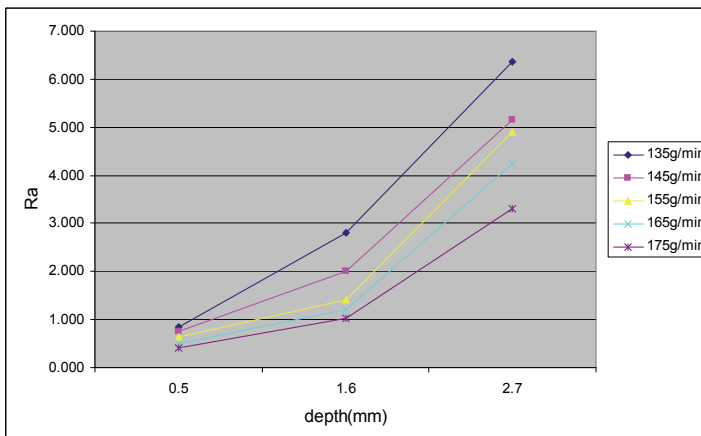


Fig. 11. Surface roughness at different depths from the top surface of carbide



Abrasive mass flow rate: 135 g/min



Abrasive mass flow rate: 145 g/min



Abrasive mass flow rate: 155 g/min



Abrasive mass flow rate: 165 g/min



Abrasive mass flow rate: 175 g/min

Fig. 12. Photographs of the machined carbides by varying the flow rate

5. Contamination

In AWJM material removal occurs through erosion and results from the interaction between an abrasive water jet and the work-piece materials. However, there are certain drawbacks in this technology. One of them is the contamination of the surfaces generated during the machining process by fractured abrasives. This contamination may generate serious problems with the further treatment of these surfaces, such as grinding, welding and/or coating. Other surface properties such as fatigue resistance will also influence negatively by surface contaminants.

Although particle embedment is a shortcoming of this technology, it can be minimized by controlling the machining parameters. However, it was reported that if the nozzle is oscillated during AWJM, then contamination reduces to a great extent (Chen et al., 2002 and Siores et al., 2006). The present study presents the influence of machining parameters on surface contamination of mild steel. Some investigations performed for the blasting of steel surfaces by air-driven solid particles found that the higher the blasting angle, the higher the contamination. Other than that, there is also a study to reduce the contamination by using the oscillation nozzle. The major aim of the present study is to investigate abrasive contamination on the surface of the mild steel during the AWJM. Furthermore, the parameters of the AWJM which are the feed rate, flow rate of the abrasive and the pressure were varied during the AWJ cutting process in order to study their level of contaminations with the changes of parameters. Then a quantitative microstructure analysis using Digital Camera Microscope was performed to investigate abrasive contamination at the cutting surfaces. In this microscope the number of embedded SiC abrasives can be counted when the image of the surface is captured. To investigate the contamination of the surfaces by abrasives, 16 experiments were conducted with variables shown in the Table 1.

No.	Pressure (kpsi)	Flowrate (g/s)	Feedrate (mm/min)
1	25	5	10
2	25	10	20
3	25	15	30
4	25	20	40
5	30	5	20
6	30	10	10
7	30	15	40
8	30	20	30
9	35	5	30
10	35	10	40
11	35	15	10
12	35	20	20
13	40	5	40
14	40	10	30
15	40	15	20
16	40	20	10

Table 1. Experimental variables

For the analysis of the abrasive contamination, three zones with different depths namely Zone A, Zone B and Zone C have been analyzed. The zones of measuring abrasive contamination are shown in Fig. 13.

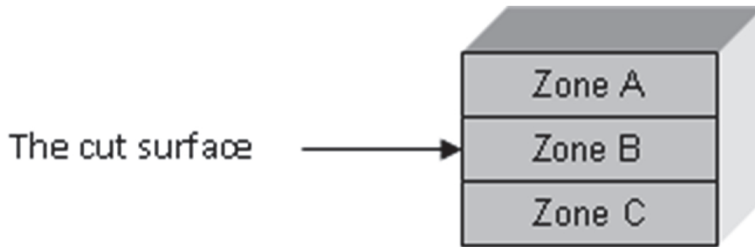
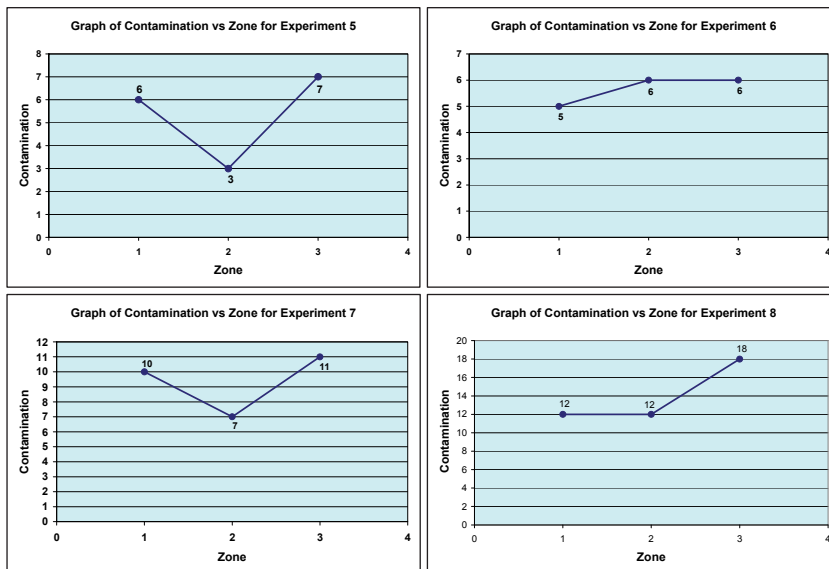


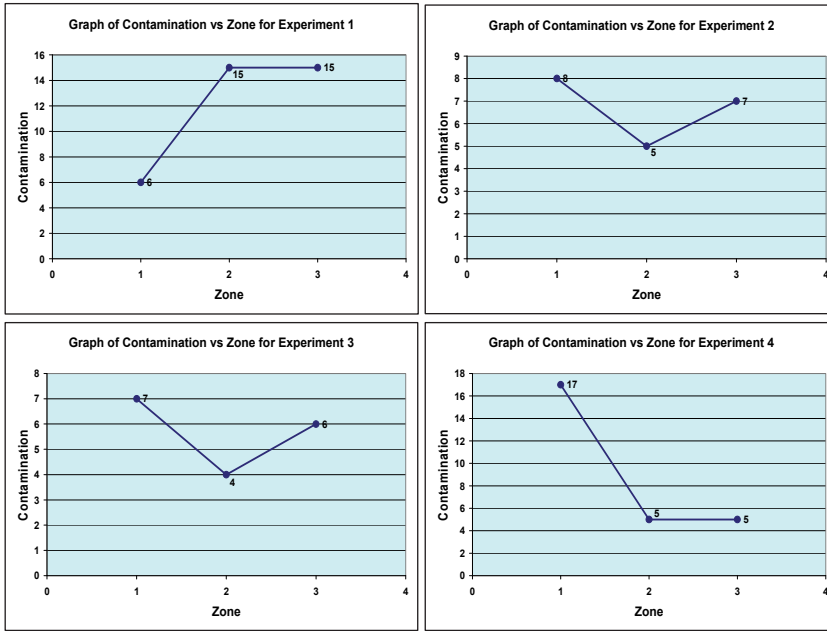
Fig. 13. Measured zone of contamination

The relationship of the abrasive flow rate with abrasive contaminations at zones A, B and C are presented in Fig.14. In this figure zone 1, zone 2 and zone 3 stand for zones A, B and C respectively. In Fig. 14 Contamination has been presented for four different levels of pressures: 25 kpsi, 30 kpsi, 35kpsi and 40 kpsi with the changes of flow rate and feed rate. From these graphs it can be observed that the pattern of the graph is basically same for these sixteen samples. Most of the graphs show that the minimum amount of abrasive contamination is at Zone B. It is also observed that in most of the cases the maximum contamination is at zone C. As the abrasives move down they lose their kinetic energy and due to friction with the work surface they are embedded to it. This is also supported by the work of (Keyurkumar, 2004).

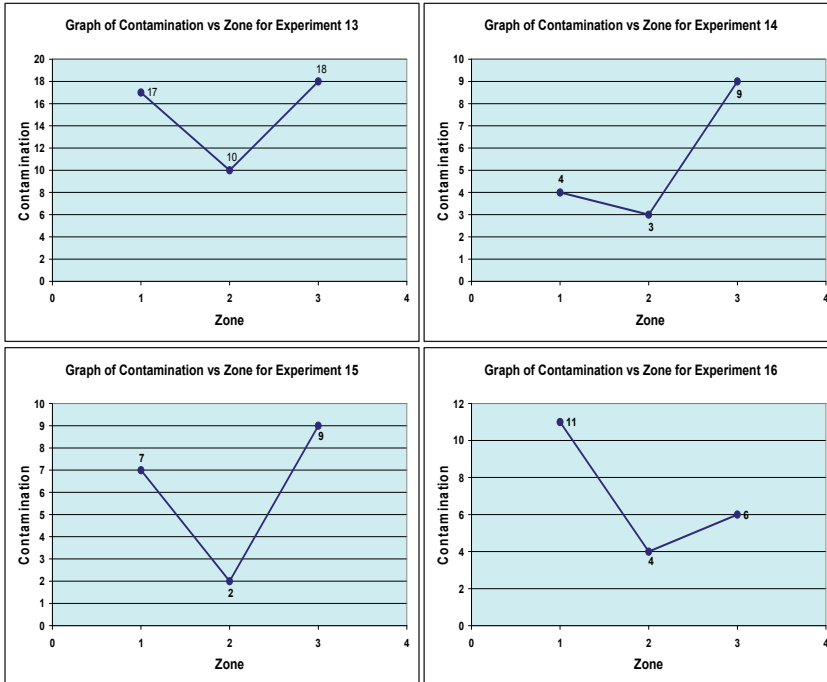
Embedding of abrasives on the cut surface for a few experiments are shown Table 2.



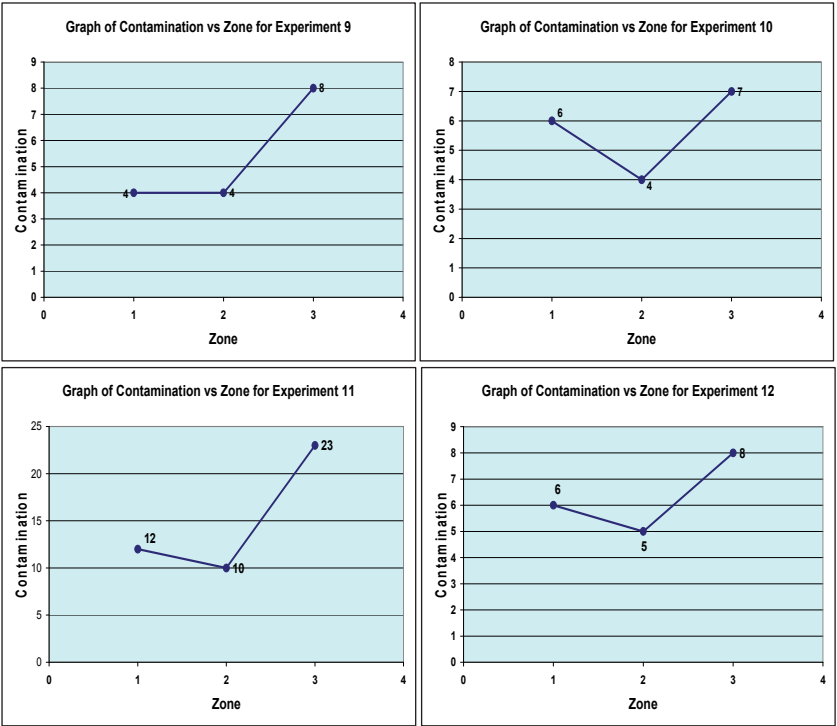
(a) Pressure 25 kpsi



(b) Pressure 30 psi






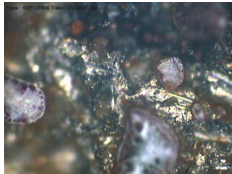

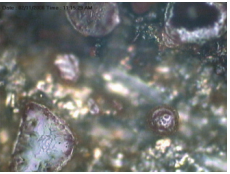
(c) Pressure 35 kpsi

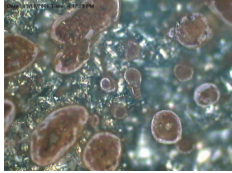
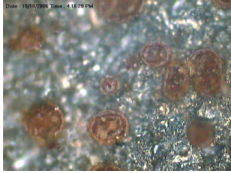
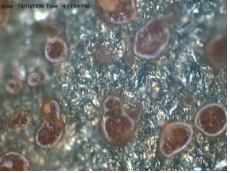


(d) Pressure 40 psi

Fig. 14. Contamination at different zones and at different pressures.

Experiment 5	Zone A	Zone B	Zone C
Pressure : 30 kpsi Flow rate : 5 g/s Feed rate : 20mm/min			
Contaminations	6	3	7

Experiment 6	Zone A	Zone B	Zone C
Pressure : 30 kpsi Flow rate : 10 g/s Feed rate : 10 mm/min			
Contamination	5	6	6

Experiment 13	Zone A	Zone B	Zone C
Pressure : 40 kpsi Flow rate : 5 g/s Feed rate : 40 mm/min			
Contamination	17	10	18

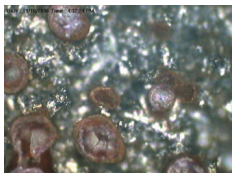

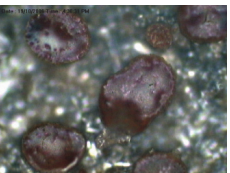
Experiment 16	Zone A	Zone B	Zone C
Pressure : 40 kpsi Flow rate : 20 g/s Feed rate : 10 mm/min			
Contamination	11	4	6

Table 2. Embedding of the abrasives

5.1 Comparison of SiC with other abrasives in AWJM

In order to compare the capability of SiC with other abrasives, glass was taken as the work material. The main properties of glass are: hardness- 600 knoops, density- 2200 kg/m³, tensile strength- 70 MN/m² and specific heat capacity- 750 J/kg °C. Three types of abrasives used in the present study were garnet, Al₂O₃ and SiC. Their hardness is 1350 knoops, 2100 knoops and 2500 knoops respectively. Experiments were conducted on a water jet machine WJ 4080. The machine was equipped with a controller type 2100 CNC Control. The nozzle used for the abrasive water jet was made of carbide with the orifice diameter of 0.1 mm. The jet was perpendicular to the work surface. The abrasive water jet in cutting process is shown in Fig. 15. After the cutting process the top width and the bottom width of the slot was measured using an optical microscope Mitutiyo Hismet II.



Fig. 15. Experimental set-up

5.2 Effect of different cutting parameters on taper of cut

Taper of cut was calculated according to the mathematical expression; $T_R = (b - a)/2$, where T_R , b and a are taper of cut, top width of cut and the bottom width of the cut respectively. Experimental investigations showed that during AWJM with different abrasives, the width of cut at the top of the slot was always greater than that at the bottom of the slots. It was explained by Wang et al., 1999 that as the abrasive particles move down the jet, they lose their kinetic energy and the relative strength zone of the jet is narrowed down. As a result, the width of cut at the bottom of the slot is smaller than that at the top. Influence of standoff distance (SOD) of the jet from the target material on the taper of cut during AWJM with different types of abrasives is illustrated in Fig. 16. It can be observed that the garnet abrasives produced the largest taper of cut followed by Al₂O₃ and SiC abrasives. Among the three types of abrasives used, SiC is the hardest material and consequently it retains its cutting ability as it moves down. Therefore, the difference between the widths at the top and bottom of the slot is small and consequently, the taper angle is also smaller. On the other hand, garnet abrasives lose their sharpness and as a result the bottom width becomes much narrower than the top width. Fig. 16 also shows that for all kinds of abrasives, the taper of cut increases with SOD. This is due to the divergence shape of the jet. As SOD is increased, the jet focus area also increases resulting increase in the width of cut.

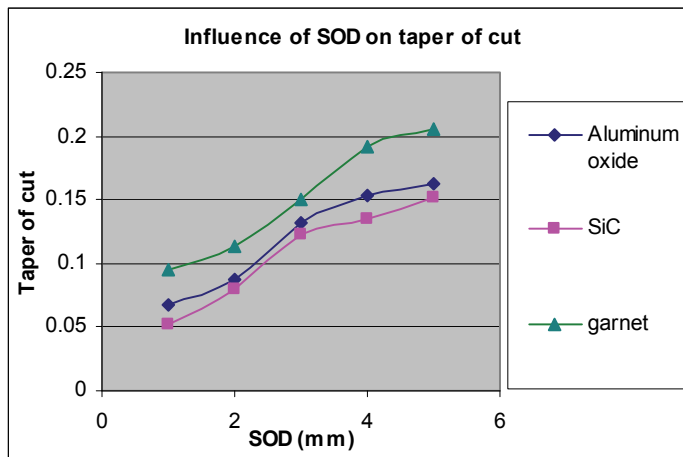


Fig. 16. Influence of SOD on taper of cut

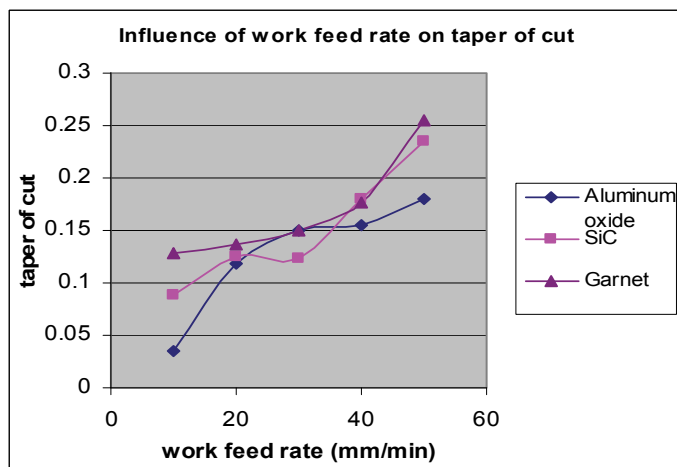


Fig. 17. Influence of feed rate on taper of cut

Fig. 17 shows the relationship between work feed rate and taper of cut during AWJM using different abrasive materials. For all types of abrasives the taper of cut shows an increasing trend with increase in work feed rate. With increase in work feed rate the machining zone is exposed to the jet for a shorter time. Cutting process is less effective at the jet exit that results an increase in taper of cut. Conner & Hashish, 2003 also found similar effect of feed rate on taper of cut during AWJM of aerospace materials using garnet abrasives. Garnet abrasives demonstrate a high taper of cut followed by SiC and Al_2O_3 .

Influence of pressure on taper of cut is illustrated in Fig. 18. Taper of cut decreases with increase in jet pressure for all the types of abrasives used. At a higher pressure the abrasives have higher energy and they retain their cutting ability as they move down from the jet

entrance to the jet exit. As a result, taper of cut reduces with increase in jet pressure. Louis et al., 2003 indicates some other positive aspects of using higher pressure. He found that the depth of penetration of the jet increases and cutting efficiency improves with increase in pressure. On the other hand, abrasive flow rate can be reduced if the jet pressure is increased. However, taper of cut is smaller for SiC abrasives followed by Al_2O_3 and garnet. SiC abrasives being harder than Al_2O_3 and garnet abrasives retain their sharp edges both at the entrance and the exit of the jet and produce the smallest width of cut. On the other hand, garnet abrasives being comparatively softer lose the sharpness of their cutting edges when they are near the jet exit.

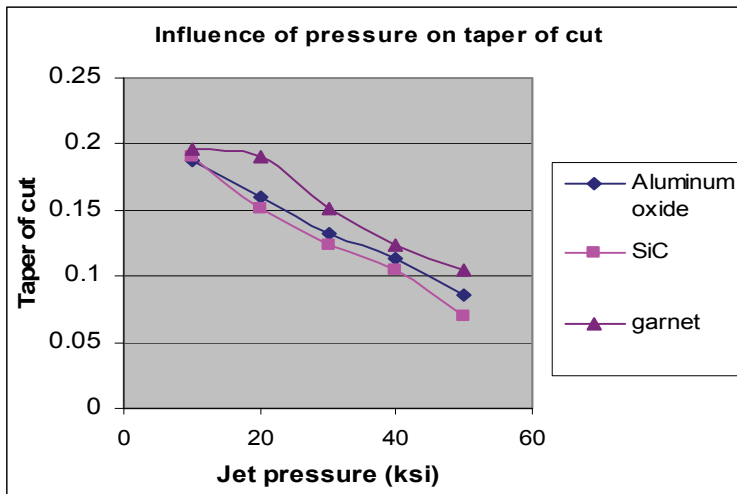


Fig. 18. Effect of pressure on taper of cut

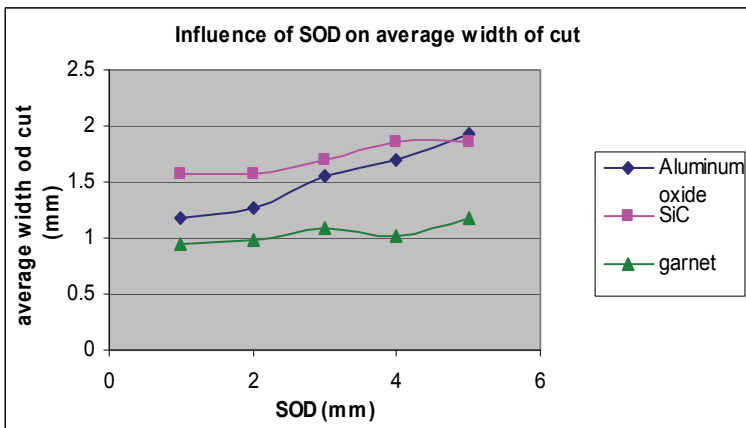


Fig. 19. Effect of SOD on taper of cut

5.3 Effect of different parameters on average width of cut

It has been established that though the abrasive water jet is a divergent one, the effective cutting zone of the jet is convergent, since the abrasives at the outer zone of the jet lose their kinetic energy. As a result, the width of cut at the jet entrance is always greater than the same at the jet exit. In Fig. 19 to Fig. 21 the average value of the widths of the jet entrance and jet exit has been taken as the width of cut. From Fig. 19 it is obvious that the average width of cut increases with increase in SOD which is due to the divergence shape of the jet. It was found that SiC produced the widest slot followed by Al_2O_3 and garnet. This is by virtue of higher hardness of SiC that enables more effective material removal.

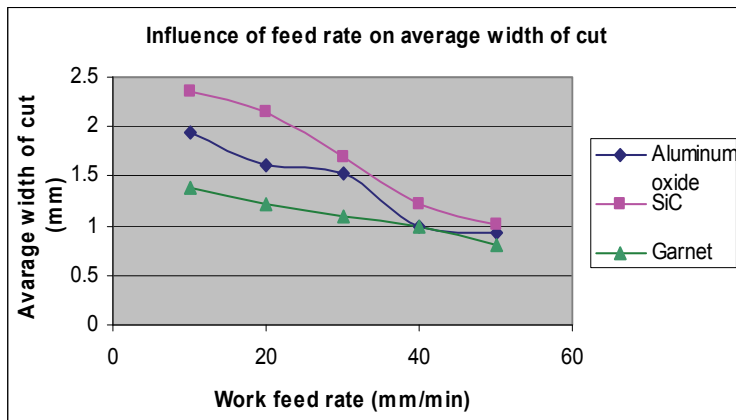


Fig. 20. Effect of feed on width of cut

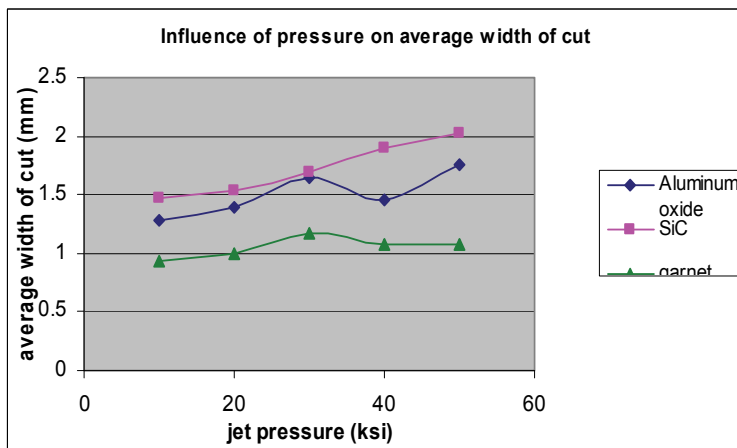


Fig. 21. Effect of pressure on width of cut

Influence of work feed rate on the average width of cut is illustrated in Fig. 20. Average width of cut decreases with increase in work feed rate since with the increase in feed rate the

work is exposed to the jet for a shorter period. The effect of pressure on average width of cut during AWJM is shown in Fig. 21. A higher pressure produces a jet of higher energy with capability of more effective cutting. From Fig. 19, Fig. 20 and Fig. 21 it was observed that in all the cases the average width of cut produced by SiC was higher than those produced by Al_2O_3 and garnet abrasives. It can be concluded that hardness is a key property of abrasive materials.

6. Conclusions

From the above discussions it can be concluded that during AWJM of carbides using SiC abrasives, machined surface roughness reduces if the jet pressure is increased. Surface smoothness deteriorates from the top of cut towards the exit of cut. The roughness of cut surface reduces with increase in abrasive flow rate since more abrasives are available per unit area of cut. The lower most zone of the cut surface is the most contaminated zone followed by the top most zone and the middle zone. Taper of cut increases with increase in SOD. Garnet abrasives produce a larger taper of cut followed by Al_2O_3 and SiC. This is due to higher hardness of SiC compared to Al_2O_3 and garnet. Taper of cut also increases with increase in work feed rate. But taper of cut reduces with increase in pressure. A higher pressure increases the kinetic energy of the abrasives and the divergence of the jet is reduced that causes a decrease in taper of cut. An increase in SOD increases the focus area of the jet and increases the average width of cut. But increase in feed rate reduces the average width of cut since the surface to be cut is exposed to the jet for a shorter time. A higher jet pressure increases the kinetic energy of the abrasive particles and enhances their cutting ability. As a result, increase in pressure causes increase in the average width of cut. SiC is harder than Al_2O_3 and garnet. As a result, its cutting ability is also higher than that of Al_2O_3 and garnet. Therefore, the average width of cut produced by SiC is higher than those produced by Al_2O_3 and garnet.

7. Acknowledgement

The authors of this work are indebted to the Research Management Center, International Islamic University Malaysia (IIUM) for its continuous help during the research work. The author is also grateful to Momber W. & Kovacevic, R. (1998), since some information has been taken from their book.

8. References

- Chen F., Patel K., Siores E. & Momber A. (2002). Minimizing particle contamination at abrasive water jet machined surfaces by a nozzle oscillation technique. *International Journal of Machine Tools & Manufacture*, Vol. 42, pp. 1385-1390, ISSN 0890-6955
- Chacko, V.; Gupta, A. & Summers, A. (2003). Comparative performance study of polyacrylamide and xanthum polymer in abrasive slurry jet, *Proceedings of American Water Jet Conference*, Houston, Texas, USA [3]
- Hocheng, H. & Chang, R. (1994). Material removal analysis in abrasive water jet cutting of ceramic plates. *Journal of Materials Processing Technology*, Vol. 40, pp. 287-304, ISSN 0924-0136

- Conner, I & Hashish, M. (2003). Abrasive water jet machining of aerospace structural sheet and thin plate materials. *Proceedings of American water Jet Conference*, Houston, Texas, USA
- Kalpakjian, S. & Schmid, R. (2010). *Manufacturing Engineering and Technology*, Pentice Hall, ISBN 978-981-06-8144-9, Singapore
- Keyurkumar, P. (2004). Quantitative Evaluation of Abrasive Contamination In Ductile Material During Abrasive Water Jet Machining And Minimizing With A Nozzle Head Oscillation Technique. *International Journal of Machine Tools & Manufacture*, Vol. 44, pp. 1125-1132, ISSN 0890-6955
- Louis, H.; Mohamed, M. & Pude, F. (2003). Cutting mechanism and cutting efficiency for water pressures above 600 MPa. *Proceedings of American Water Jet Conference*, Houston, Texas, USA
- Momber, W.; Eusch, I & Kovacevic, R. (1996). Machining refractory ceramics with abrasive water jet. *Journal of Materials Science*, Vol. 31, pp. 6485-6493, ISSN 0022-2461
- Momber W. & Kovacevic, R. (1998). *Principles of Abrasive Water Jet Machining*, Springer, ISBN 3540762396, London
- Mort, A. (1995). Results of abrasive water jet market survey, *Proceedings of 8th American Water Jet Conference*, Vol. 1, pp. 259-289, Houston, Texas, USA
- Siores, E.; Chen, L.; Lemma, E. & Wang, J. (2006). Optimizing the AWJ Cutting Process of Ductile Materials Using Nozzle Oscillation Technique, *International Journal of Machine Tools & Manufacture*. Vol.42, pp. 781-789, ISSN 0890-6955
- Wang, J. & Wong, K. (1999). A study of abrasive water jet cutting of metallic coated sheet steel. *International Journal of Machine Tools and Manufacture*, Vol. 39, pp. 855-870, ISSN 0890-6955
- Waterjet machining tolerances, 2011, Available from <http://waterjets.org>

Silicon Carbide Filled Polymer Composite for Erosive Environment Application: A Comparative Analysis of Experimental and FE Simulation Results

Sandhyarani Biswas¹, Amar Patnaik² and Pradeep Kumar²

¹*Department of Mechanical Engineering, National Institute of Technology, Rourkela,*

²*Department of Mechanical Engineering, National Institute of Technology, Hamirpur, India*

1. Introduction

Polymer composites form important class of engineering materials and are commonly used in mechanical components. Because of their high strength-to-weight and stiffness-to-weight ratios, they are extensively used for a wide variety of structural applications as in aerospace, automotive, gear pumps handling industrial fluids, cams, power plants, bushes, bearing cages and chemical industries. Whereas, wear performance in nonlubricated condition is a key factor for the material selection and fabrication procedure (Hutchings, 1992). Glass fiber reinforced polymer composites traditionally show poor wear resistance due to the brittle nature of the fibers. Many researchers have been reported on the effect of fiber, filler and matrix materials so far in the literature regarding economical and functional benefits to both consumers and industrial manufacturers (Budinski, 1997; Chand et al., 2000; Tripathy and Furey, 1993). The addition of hard particulate ceramic fillers not only improves the wear performance of the particulate filled polymer composites but also reduce the cost of the composites. In order to obtain improve wear performances many researchers modified polymers using different fillers (Briscoe et al. 1974; Tanaka 1986; Bahadur et al, 1994; Bahadur and Tabor,1985; Kishore et al. 2000; Wang et al. 2003).

Silicon carbide (SiC) is one such ceramic material that has great potential for overcoming the current inadequacies of abrasive products due to its inherent characteristic of being chemically inert and consequently resistant to improve mechanical and wear resistance material. It has an excellent abrasive nature and has been produced for grinding wheels and other for more than hundred years. Now-a-days the material has been developed into a high quality technical grade ceramic with very good mechanical properties. It is used in abrasives, ceramics, refractories, and other high-performance applications. Silicon carbide is composed of tetrahedra of carbon and silicon atoms with strong bonds in the crystal lattice. This produces a very strong material and not attacked by any acids or alkalis or molten salts up to 800°C (Nordsletten et al. 1996).

To this end, the present research work is undertaken to develop a new class of glass fiber based polymer composite filled with SiC particulate and study the effect of various

operational variables, material parameters and their interactive influences on erosive wear behavior of these composites. A finite element (FE) model (AUTO-DYN) of erosive wear is established for damage assessment and validated by a well designed set of experiments. The eroded surfaces of these composites are analyzed with scanning electron microscopy (SEM), and the erosion wear mechanisms of the composites are investigated.

2. Experimental

2.1 Preparation of composites

In this study, short E-glass fiber with 6mm length (Elastic modulus of 72.5 GPa and density of 2.59 gm/cc) is taken to prepare all the particulate filled (SiC) glass fiber reinforced polyester composites. The unsaturated isophthalic polyester resin (Elastic modulus 3.25GPa and density 1.35gm/cc) is manufactured by Ciba Geigy and locally supplied by Northern Polymers Ltd. New Delhi, India. The composite fabricated in two different parts. One part having different fiber loading with varying the fiber weight fraction from 10wt% to 50wt% at an increment of 10wt% and the second part, SiC filled short glass fiber reinforced polyester resin with three different percentages (0wt%, 10wt% and 20wt% of SiC). The mixture is poured into various moulds conforming to the requirements of various testing conditions and characterization standards. The entrapped air bubbles (if any) are removed carefully with a sliding roller and the mould is closed for curing at a temperature of 30°C for 24 h at a constant pressure of 10 kg/cm².

2.2 Air-jet erosion tester

The solid particle erosion test rig as per ASTM G76 used in the present study consists of an air compressor, a particle feeder, an air particle mixing chamber and accelerating chamber. The equipment was designed to feed erodent particles into a high velocity air stream, which propelled the particles against the specimen surface (Strzepa et al., 1993; Routbort et al., 1981). The erodent particles entrained in a stream of compressed air and accelerated down to a 65mm long brass nozzle with 3mm inside diameter to impact on a specimen mounted on an angle fixture. The velocity of the eroding particles is determined using rotating disc method (Ruff and Ives, 1975). The steady state erosion rate was determined by weighing the sample before and after the end of each test. While the impingement angles ranges from 30° to 90° and the test duration was 20min for each run. The erodent used for this test was river silica sand particle of three different sizes, i.e. 250, 350 and 450µm. The sample was cleaned with a blast of compressed air before each weighing to remove all loosely adhering debris. The mass loss from the target was measured with an analytical balance of ±0.01mg accuracy. The process is repeated every 10 minutes till the erosion rate attains a constant value called steady-state-erosion-rate. Finally, the worn surfaces of some selected samples are examined by scanning electron microscope JEOL JSM-6480LV.

2.3 Finite element model

In the present work, the erosive wear processes are modeled using an explicit dynamic code ANSYS/AUTO-DYN. The eight-node brick hexahedral elements with one integration point are used in the 3D simulation. The mesh is refined to a standard cubic element in order to calculate the erosion rate at the targeted area on the composites. It has been studied in literature that simulating a single particle was not sufficient to get valid results therefore subsequently considered three or more particles were needed to simulate the erosion

process instead of single particle (ElTobgy et al., 2005). In this study, 125 spherical shaped particles were used to ensure the accuracy of the proposed model. All the particles are striking the target area at random locations. There are 10 groups which contain 125 particles aggregately in the proposed model.

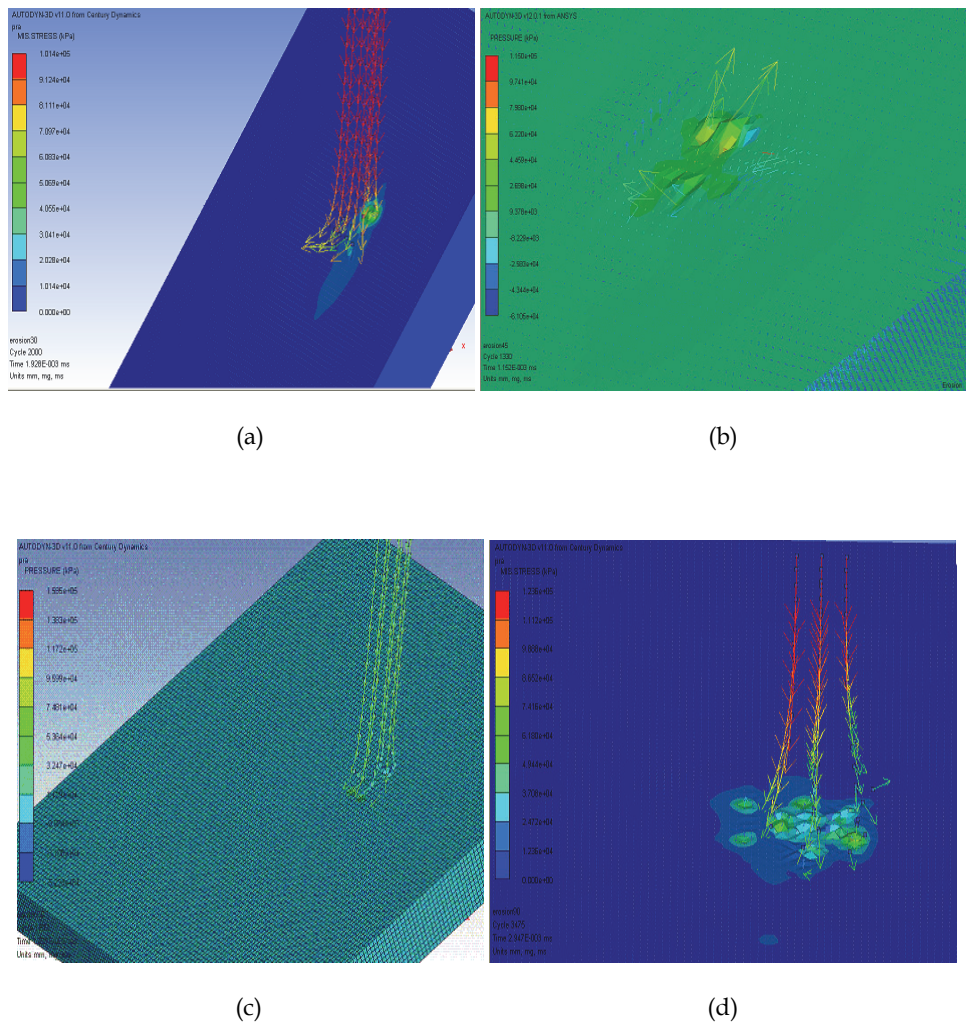


Fig. 1. Schematic diagram of target composite material and nozzle (a: 30° impingement angle, b: 45° impingement angle, c: 60° impingement angle and d: 90° impingement angle)

Each group has 12 particles which would impact the surface simultaneously and followed by another simultaneous particles group, and so on. According to the researchers, the distance between any two particles' centers in the same group is no less than $0.6r$ (r is the radius of the particles) to avoid the damage interaction (Woytowitz and Richman, 1999). The finite element model of the target material and simulated nozzle is shown in Figure 1. For the particles, the rotation degrees of freedom are constrained. Generally, the erosion rate (g/g) was used to characterize the erosion performance of the target materials.

2.4 Taguchi experimental design

Taguchi method is a statistical tool for the purpose of designing experimental procedure and mainly improving product quality. It uses the orthogonal array to set up the experiment for the advantages of less number and optimizes the process parameters by the analysis of signal-to-noise (SN) ratio. Taguchi method has become a powerful analysis tool for improving the experimental results to get high quality at low cost (Peace, 1993; Phadke, 1989). Therefore, a large number of factors are included so that non-significant variables can be identified at earliest opportunity. The impact of five such parameters are studied using $L_{27} (3^{13})$ orthogonal design. The operating conditions under which wear tests are carried out are given in Table 1. In conventional full factorial experiment design, it would require $3^5 = 273$ runs to study five parameters each at three levels whereas, Taguchi's factorial experiment approach reduces it to only 27 runs offering a great advantage in terms of experimental time and cost. The experimental observations are further transformed into signal-to-noise (S/N) ratio. There are several S/N ratios available depending on the type of performance characteristics. The S/N ratio for minimum wear rate can be expressed as "lower is better" characteristic, which is calculated as logarithmic transformation of loss function as shown below (Peace, 1993).

Smaller is the better characteristic:

$$\frac{S}{N} = -10 \log \frac{1}{n} \sum Y^2 \quad (1)$$

where, n the number of observations and y the observed experimental data.

The plan of the experiments is as follows: the first column is assigned to impact velocity (A), the second column to SiC content (B), the fifth column to impingement angle (C), the ninth column to stand-off distance (D) and the tenth column to erodent size (E), the third and fourth column are assigned to $(A \times B)_1$ and $(A \times B)_2$ respectively to estimate interaction between impact velocity (A) and SiC content (B), the sixth and seventh column are assigned to $(B \times C)_1$ and $(B \times C)_2$ respectively to estimate interaction between the SiC content (B) and impingement angle (C), the eighth and eleventh column are assigned to $(A \times C)_1$ and $(A \times C)_2$ respectively to estimate interaction between the impact velocity (A) and impingement angle (C) and the remaining columns are used to estimate experimental errors. The output to be studied is erosion rate (E_r) and the tests are repeated twice corresponding to 54 tests. Furthermore, a statistical analysis of variance (ANOVA) is performed to identify the process parameters that are statistically significant. With the S/N and ANOVA analyses, the optimal combination of the process parameters can be predicted to a useful level of accuracy. Finally, a confirmation experiment is conducted to verify the optimal process parameters obtained from the parameter design.

Control factor	Level			Units
	I	II	III	
A:Impact velocity	43	54	65	m/sec
B: SiC content	0	10	20	%
C:Impingement angle	30	60	90	Degree
D:Stand-off distance	65	75	85	mm
E:Erodent size	250	350	450	μm

Table 1. Levels for various control factors

3. Results and discussion

3.1 Erosive wear of the composites

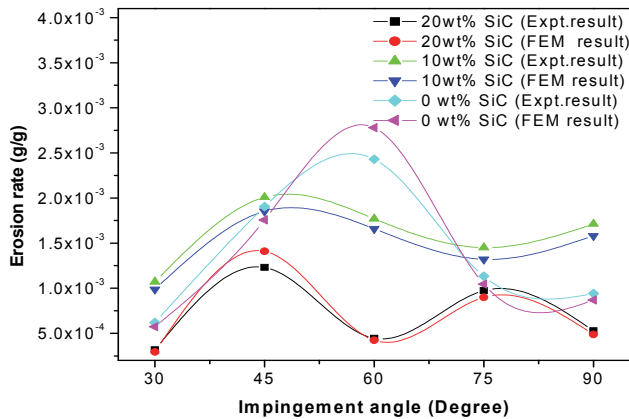
The results have been organized and discussed in two sections. Firstly, the steady state erosion characteristics of the composites are determined for selected level of optimally controlled operating variables and compared the steady state results with the simple finite element simulation results to observe the variations in erosion rate with respective to impingement angle and the next, simulations results have been analyzed under Taguchi's experimental technique.

3.2 Steady state erosion rate

3.2.1 Influence of impingement angle

Solid-particle erosion is a complex wear phenomena influenced by a number of control factors such as impact velocity, angle of impingement, erodent particle size, stand-off-distance, materials properties, erodent particles geometry and environment temperature etc. Among these, impingement angle is the one of the most important parameter and widely studied parameter in the erosion study of materials (Hutchings, 1992; Tsuda et al., 2006). The erosion rate is measured of function of impingement angle, two types of material behavior generally observed in the target material i.e. ductile and brittle nature. The ductile nature of materials is characterized by maximum erosion rate at acute angle (15-30°) and for brittle behavior of materials, the maximum erosion rate is observed at normal impingement angle (90°). But as far as polymer matrix composites are concerned the composite materials show versatile in nature depending upon the fabrication procedure and type of reinforcing material. The reinforced composites show a semi-ductile behavior having the maximum erosion rate in the range of 45-60° (Hutchings, 1992), unlike the above two categories. This classification, however, is not absolute as the erosion of material has a strong dependence on erosion conditions such as the properties of target material.

In the present study of SiC filled glass fiber-polyester composites, the erosion rate increases monotonically with the increase in impingement angle and reaches maximum at 45° impingement angle for particulate filled composites. However, for unfilled composite the maximum erosion rate is found to be at 60° impingement angle. This indicated that all the particulate filled and unfilled composites show semi-ductile erosion behaviour irrespective of filler content. Similarly, the finite element analysis simulated results are in good agreement with the experimental results as observed in Figure 2. As far as erosion resistance is concerned 20wt% SiC filled composites show better erosion resistance among other particulate filled and unfilled composites. Whereas, unfilled composites shows maximum erosion rate as compared with 10wt% and 20wt% SiC filled glass fiber reinforced polyester composites both in experimental and finite element analysis simulated results as shown in Figure 2.

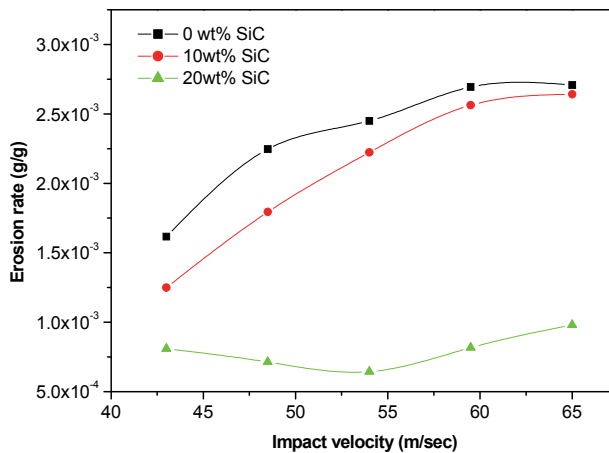


(Impact velocity: 43 m/sec, stand-off distance: 75mm and erodent size: 450 μ m)

Fig. 2. Influence of impingement angle on erosion rates of composites

3.2.2 Influence of impact velocity

Similarly, the variation of erosion rate of unfilled and SiC filled composites with impact velocity is shown in Figure 3. Erosion trials are conducted at five different impact velocities.



(Impingement angle: 60°, stand-off distance: 75mm and erodent size: 450 μ m)

Fig. 3. Influence of impact velocity on erosion rates of composites

It is seen, in the Figure 3 that for all the composite samples, the erosion rates gradually increases with the increase in impact velocity from 43m/sec to 65m/sec respectively. The

increase in erosion rate with increase in impact velocity can be attributed to increased penetration of particles on impact as a result of dissipation of greater amount of particle thermal energy to the target surface. This leads to more surface damage, enhanced sub-critical crack growth etc. and consequently to the reduction in erosion resistance.

3.3 Taguchi analysis and response optimization

The analysis is made using the computational software MINITAB 15. Table 2 shows the experimental design using L_{27} orthogonal array. The overall mean for the S/N ratio of erosion rate is found to be 61.92db for erosion rate is mentioned in the response table.

Expt. No.	Impact Velocity (A)(m/s)	SiC content (B) (%)	Impingement angle (C) (Degree)	Stand-off Distance (D)(mm)	Erodent size (E) (μm)	Erosion rate (Er) (g/g)	S/N Ratio (db)
1	43	0	30	65	250	0.0003303	69.6224
2	43	0	60	75	350	0.0002466	72.1588
3	43	0	90	85	450	0.0001246	78.0908
4	43	10	30	75	350	0.0004458	67.0165
5	43	10	60	85	450	0.0002775	71.1347
6	43	10	90	65	250	0.0023721	52.4974
7	43	20	30	85	450	0.0006133	64.2461
8	43	20	60	65	250	0.0003333	69.5424
9	43	20	90	75	350	0.0006175	64.1873
10	54	0	30	75	450	0.0014625	56.6981
11	54	0	60	85	250	0.0028121	51.0194
12	54	0	90	65	350	0.0027000	51.3727
13	54	10	30	85	250	0.0000917	80.7558
14	54	10	60	65	350	0.0022625	52.9082
15	54	10	90	75	450	0.0027392	51.2476
16	54	20	30	65	350	0.0005450	65.2721
17	54	20	60	75	450	0.0001229	78.2078
18	54	20	90	85	250	0.0007804	62.1535
19	65	0	30	85	350	0.0024783	52.1171
20	65	0	60	65	450	0.0045143	46.9082
21	65	0	90	75	250	0.0031857	49.9359
22	65	10	30	65	450	0.0004354	67.2217
23	65	10	60	75	250	0.0009611	60.3442
24	65	10	90	85	350	0.0004091	67.7625
25	65	20	30	75	250	0.0002840	70.9336
26	65	20	60	85	350	0.0034362	49.2785
27	65	20	90	65	450	0.0035105	49.0927

Table 2. Experimental design using L_{27} orthogonal array

The Effect of control factors on erosion rate is shown in Figure 4. It is observed from response graph that the combination of factors settings are A_1 , B_3 , C_1 , D_3 and E_1 have been found to be the optimum factor level for the erosion rate is concerned on the basis of smaller-the-better characteristics. The corresponding interaction graphs are plotted in the Figures 5a-c.

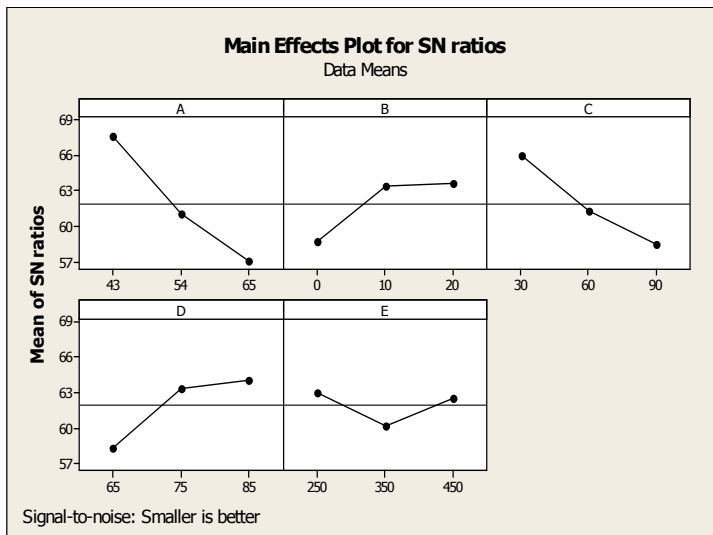


Fig. 4. Effect of control factors on erosion rate

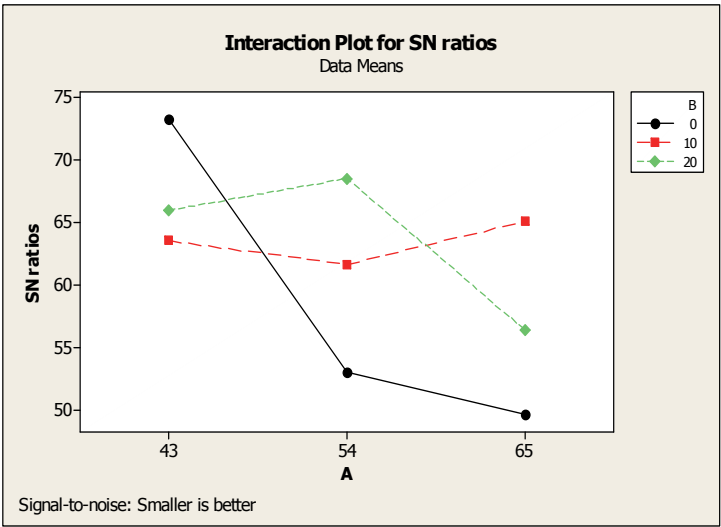


Fig. 5a. Interaction graph between factor A and factor B (A×B) for erosion rate

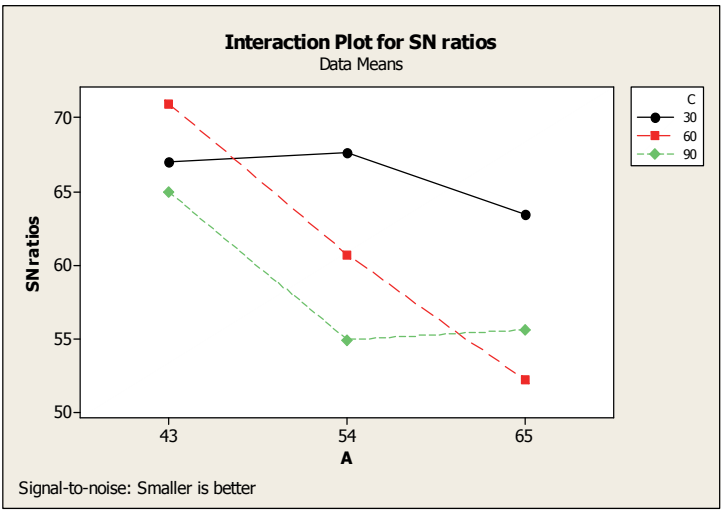


Fig. 5b. Interaction graph between factor A and factor C (A×C) for erosion rate

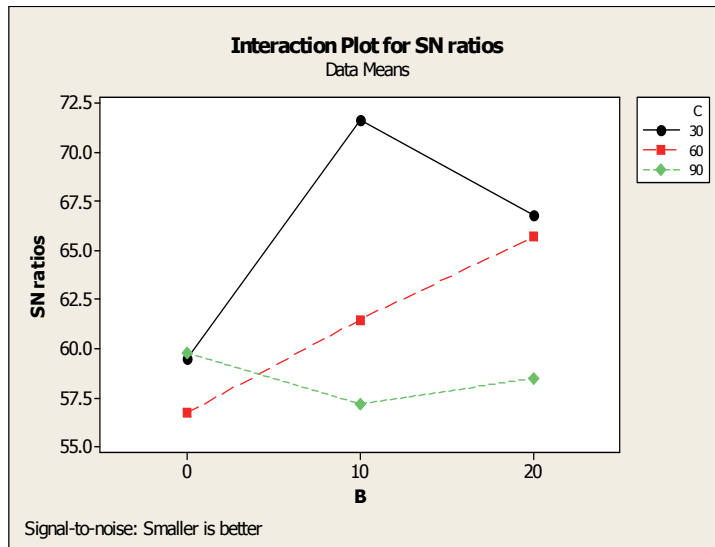
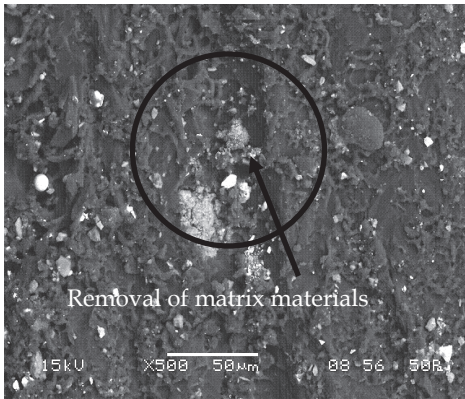


Fig. 5c. Interaction graph between factor B and factor C (B×C) for erosion rate

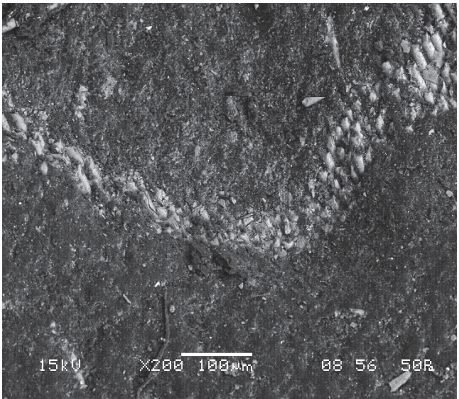
3.4 Surface morphology

The erosion wear mechanisms of SiC filled glass fiber reinforced polyester composites eroded surfaces are observed as per Taguchi experimental design by scanning electron microscopy (SEM). Figure 6a and 6b shows the SEM of eroded composite sample studied at lower impingement angle (see Table 2, Experiment 4). The random distribution of SiC fillers on the composite surface and removable of matrix material on the composite surface are clearly observed from the figures. Figure 6c shows the increase in erosion rate with higher impingement angle (90°) for 10wt% of SiC filled glass-polyester composites (see Table 2, Experiment 6). Figure 6d shows a hole formed after SiC particle was removed from the surface. The inside surface of the hole seemed very smooth and clear which indicated that SiC particles debonded from the matrix surface with the propagation of interfacial cracks due in part to the poor interfacial bond strength (see Table 2, Experiment 11). This is due to the increase in impact velocity from 43m/s to 54m/s and more energy to chip-off the target material.

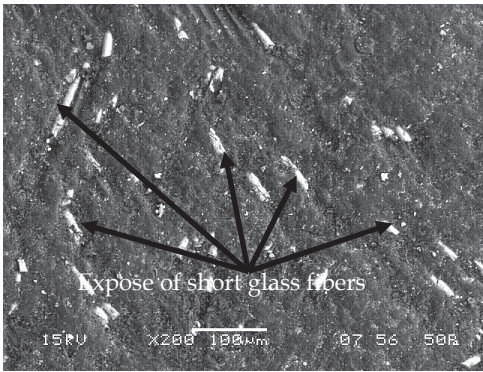
Similarly Figure 6e and 6f show the fibers are protruded above the worn surface due to SiC particles are removed from the upper surface of the composites. However, there is a significant difference between Figures 6e and 6f due to the change in impingement angle and change in impact velocity. Thus, after the removal of the matrix material, there could be a layer of glass fiber and SiC particulates bonded on the matrix material. This indicated the favorable effect of good interfacial bond strength on the wear performance for the composites which helped prolong the lifetime of the SiC particulates to bear erosion and protect the matrix material before it was removed away. It has been reported by few of researchers that the impact on brittle materials at an oblique angle produced radial cracks at an angle to the surface and they can contribute to only matrix material loss (Scattergood et al., 1981; Lawn, 1993). Radial cracks can also contribute to material removal when they drive through a relatively thin wall. In such a case, the material loss will occur without the formation of a lateral crack. Due to the above wear mechanism the larger erodent produce



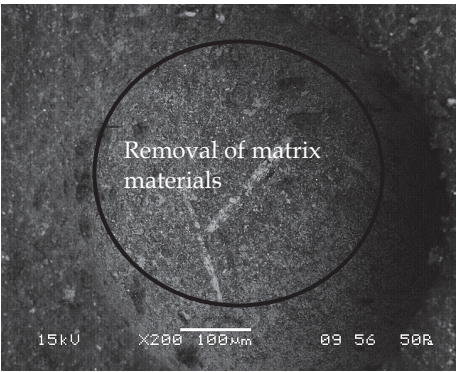
(a)



(b)



(c)



(d)

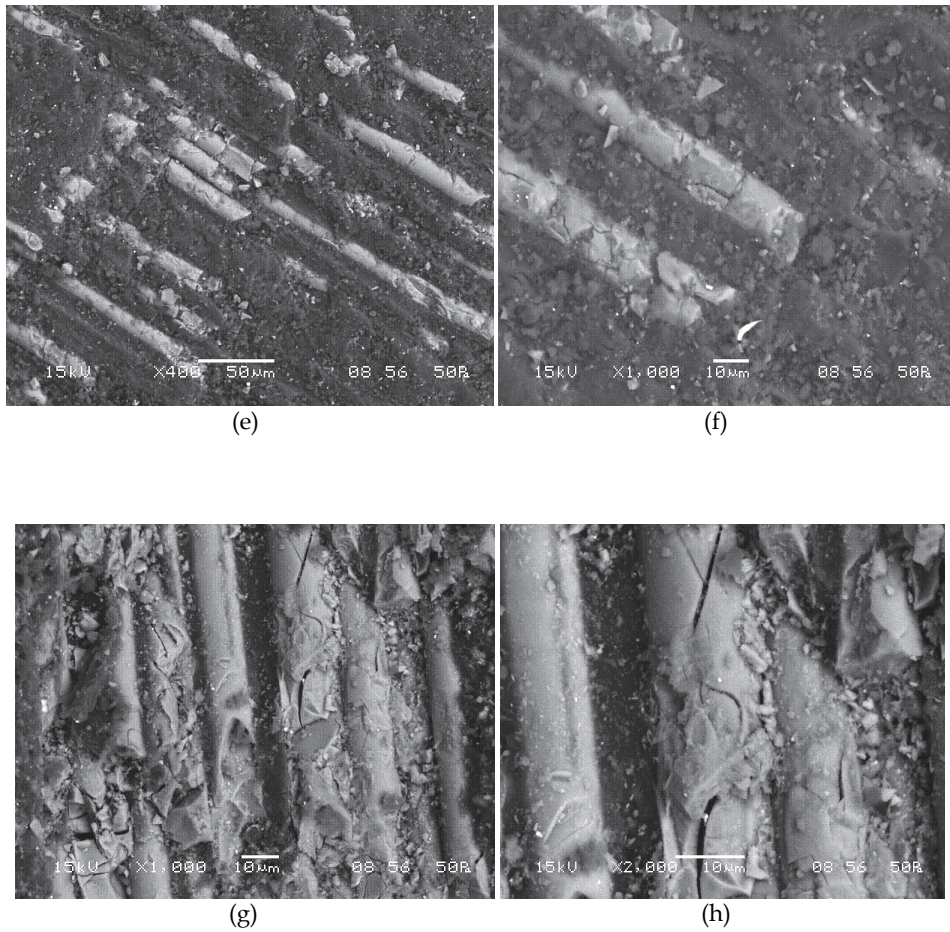


Fig. 6. SEM micrographs of the eroded glass fiber-polyester composites filled with SiC

deeper radial cracks on the eroded surfaces. The tendency for material loss to occur from radial cracking should increase with increase in erodent size (Lee et al., 2005; Milman et al., 1999). However, with the increasing content of the SiC particles in the composites from 10wt% to 20wt%, the wear rate of the composites increased gradually, reached a maximum and then declined gradually. With the further increase in impact velocity from 54m/sec to 65m/sec for 20wt% SiC filled short glass fiber reinforced polyester composites the material removal on the surface is more but the erosion resistance become more as compared with other particulate filled glass-polyester composites as shown in Figure 6g and 6h (see Table 2, Experiment 25). In the present study, the matrix material is removed from the composite surface due to continuous impact of erodent particles with sharp angles and high impact velocity, but the reinforcing glass fibers and SiC particulates are removed slowly then the matrix material. This may be due to the inclusions of high hardness of SiC particles.

3.5 ANOVA and the effects of factors

The results of the experimental trials were investigated using the ANOVA statistical analysis method. Table 3 shows the results of the ANOVA with the erosion rate (E_r) for SiC filled short glass fiber reinforced polyester composites. The objective of ANOVA is to analyze the influence of impact velocity (A), SiC content (B), impingement angle (C), stand-off distance (D) and erodent size (E) on the total variance of the results. This analysis was undertaken for a level of significance of 5% that is for a level of confidence of 95%.

From Table 3, it is concluded that impact velocity ($p = 0.191$), impingement angle ($p = 0.365$), stand-off distance ($p = 0.470$) and SiC content ($p = 0.539$) have great influence on the erosion rate. The interactions of impact velocity and SiC content ($p = 0.283$) has most significant effect on erosion rate but the factor erodent size ($p = 0.828$), interaction between SiC content and impingement angle ($p = 0.717$) and impact velocity and impingement angle ($p = 0.684$) have less significant contribution on erosion rate.

Source	DF	Seq SS	Adj SS	Adj MS	F	P
A	2	510.00	510.00	255.00	2.58	0.191
B	2	143.49	143.49	71.75	0.73	0.539
C	2	258.94	258.94	129.47	1.31	0.365
D	2	181.24	181.24	90.62	0.92	0.470
E	2	39.22	39.22	19.61	0.20	0.828
A×B	4	733.23	733.23	183.31	1.85	0.283
B×C	4	213.85	213.85	53.46	0.54	0.717
A×C	4	237.42	237.42	59.35	0.60	0.684
Error	4	395.79	395.79	98.95		
Total	26	2713.18				

Table 3. ANOVA table for erosion rate

3.6 Confirmation experiment

To determine the optimal conditions and to compare the result with the predicted performance, it is necessary to perform a confirmation experiment. If the generated design fails to meet the predicted requirement, the process must be reiterated using a new system unit and finally the required criteria are satisfied. The confirmation experiment is performed by conducting a new series of test condition in combination of the significant factors and their respective interaction levels on erosion rate as reported in Table 3. The final step is to predict and verify the improvement of the erosion resistance. The predictive value $\bar{\eta}_1$ using the optimal levels of the input parameters can be calculated as:

$$\bar{\eta}_1 = \bar{T} + (\bar{A}_2 - \bar{T}) + (\bar{B}_2 - \bar{T}) + [(\bar{A}_2\bar{B}_2 - \bar{T}) - (\bar{A}_2 - \bar{T}) - (\bar{B}_2 - \bar{T})] + (\bar{C}_3 - \bar{T}) + (\bar{D}_2 - \bar{T}) + (\bar{E}_3 - \bar{T}) \quad (3)$$

$\bar{\eta}_1$: Predicted average

\bar{T} : Overall experimental average

$\bar{A}_2, \bar{B}_2, \bar{C}_3, \bar{D}_2$ and \bar{E}_3 Mean response for factors and interactions at designated levels.

By combining like terms, the equation reduces to

$$\bar{\eta}_1 = \bar{A}_2\bar{B}_2 + \bar{C}_3 + \bar{D}_2 + \bar{E}_3 - 3\bar{T} \quad (4)$$

After solving the above predictive equation the erosion rate is found to be $\bar{\eta}_1 = 57.61$ dB and the experimental result is 56.33 dB. The resulting model seems to be capable of predicting wear rate to a reasonable level of accuracy. An error of 2.22% for the S/N ratio of wear rate is observed. This validates the development of the mathematical model for predicting the measures of performance based on knowledge of the input parameters.

4. Conclusions

1. The present work successfully fabricated SiC filled short glass fiber reinforced polyester composites by simple hand-lay-up techniques and also showed that it was feasible to add SiC particles to the glass-polyester resin composites to improve their erosion resistance.
2. The particle filled composites show good tribological properties as compared with the unfilled glass fiber reinforced polyester composites. The erosion rate for 20wt% SiC filled composites shows superior erosion resistance as compared with the rest of the filled and unfilled composites.
3. The variation of erosion rate with impingement angles, the material loss is dictated mainly more at 60° impingement angles for unfilled composites and for filled composites the maximum erosion resistance show around 45° impingement angle both in experimental and finite element simulated results.
4. On comparison with the experimental results, the FE model (ANSYS/AUTO-DYN) is much closer to the experimental results. The major advantages of simulated results are during experimental study it is very difficult to analysis the flow direction and particularly at low impingement angle most of the erodent particles are sliding on the target composite materials instead of reback of erodent particles from the composite surface. However, finite element simulated model can be easily implemented to measure the residual stress and the depth of penetration which is difficult to determine by experimental method.

5. In eroded samples observed in SEM shows mostly two types of wear mechanisms i.e. micro-cutting and micro-ploughing actions. As far as SiC filled glass polyester composite is concerned the matrix material is removed at faster rate from the composite surface due to continuous impact of erodent particles with sharp angles and high impact velocity, but the reinforcing glass fibers and SiC particulates are removed slowly then the matrix material. This may be due to the inclusions of high hardness of SiC particles.

5. Acknowledgement

The authors are grateful to the financial supports of the research project Ref. No. SR/FTP/ETA-49/08 by Department of Science and Technology, India.

6. References

- Bahadur, S. & Tabor, D. (1985). Role of fillers in friction and wear behaviour of HDPE In: *Polymer wear and its control*, Volume 287-268 (L.H. Lee (ed.) ACM symposium series, Washington DC.
- Bahadur, S.; Fu, Q.; & Gong, D. (1994). The effect of reinforcement and the synergism between CuS and carbon fiber on the wear of nylon, *Wear*, Vol. 178, pp. 123-130.
- Briscoe, B. J.; Pogonion, A. K.; & Tabor, D. (1974). The friction and wear of high Density polyethylene; the action of lead oxide and copper oxide fillers, *Wear*, Vol.27, pp. 19-34.
- Budinski, K.G. (1997). Resistance of particle abrasion to selected plastics, *Wear*, Vol. 203-204, pp. 303-309.
- Chand, N.; Naik, A.M.; & Neogi, S. (2000). Three-body abrasive wear of short glass fiber polyester composite, *Wear*, Vol. 242, pp.38-46.
- ElTobgy, M. S.; Ng, E. & Elbestawi, M. A. (2005). Finite Element Modeling of Erosive Wear, *International Journal of Machine Tools and Manufacture*, Vol. 45, pp. 1337-1346.
- Hutchings, I. M. (1992). Ductile brittle transitions and wear maps for the erosion and abrasion of brittle materials, *Journal of Physics D: Applied Physics*, Vol. 25, pp. A212-A221.
- Kishore.; Sampathkumaran, P.; Seetharamu, S.; Vynatheya, S.; Murali, A.; Kumar, R. K. (2000). SEM observations of the effect of velocity and load on the slide wear characteristics glass-fabric-epoxy composites with different fillers, *Wear*, Vol. 237, pp. 20-27.
- Lawn, B. (1993). *Fracture in Brittle Solids*, 2nd ed., Cambridge University Press, Cambridge, UK.
- Lee, S. H.; Lee, Y. I.; Kim, Y.W.; Xie, R. J.; Mitomo, M. & Zhan, G. D. (2005). Mechanical Properties of Hot-Forged Silicon Carbide Ceramics, *Scripta Materialia*, Vol. 52, pp. 153-156.
- Milman, Y.V.; Chugunova, S. I.; Goncharova, I. V.; Chudoba, T.; Lojkowski, W. & Gooch, W. (1999). Temperature Dependence of Hardness in Silicon-Carbide Ceramics with Different Porosity, *International Journal of Refractory Metals and Hard Materials*, Vol. 17, No. 5, pp. 361-368.
- Nordsletten, L.; Hogasen, A.; Konttinen, Y.; Santavirta, S.; Aspenberg, P.; Aasen, A. (1996). Human monocytes stimulation by particles of hydroxyapatite, silicon carbide, and

- diamond: in vitro studies of new prosthesis coatings. *Biomaterials*, Vol. 17, pp.1521-1527.
- Patnaik, A.; Biswas, S.; Kaundal, R.; Satapathy A. (2011). Damage Assessment of Short Glass Fiber Reinforced Polyester Composites: A comparative Study, *Composites*, In Tech open access publisher, ISBN 978-953-307-1100-7.
- Peace, G. S. (1993). *Taguchi methods: A hand-on approach*. Reading, MA: Addison-Wesley.
- Phadke, M. S. (1989). *Quality engineering using robust design*. Englewood Cliffs, NJ: Prentice-Hall.
- Routbort, J. L.; Gulden, M. E. & Marshall, E. (1981). Particle Size Distribution Effects on the Solid Particle Erosion of Brittle Materials, *Wear*, Vol. 71, pp. 363-373.
- Ruff, A.W.; Ives, L.K. (1975). Measurement of solid particle velocity in erosive wear, *Wear*, Vol. 35, pp. 195-199.
- Scattergood, R. O.; Routbort, J. L. & Turner, A. P. L. (1981). Velocity and Size Dependence of the Erosion Rates in Silicon, *Wear*, Vol. 67, pp. 227-232.
- Strzepa, P.; Zamirowski, E. J.; Kupperman, J. B.; Goretta, K. C. & Routbort, J. L. (1993). Indentation, Erosion and Strength Degradation of Silicon-Alloyed Pyrolytic Carbon, *Journal of Materials Science*, Vol. 28, pp. 5917-5921.
- Tanaka, K., (1986). Effect of various fillers on the friction and wear of PTFE-based composites, In: *Friction and Wear of Polymer composites*, Vol. 205, pp. 137-174, (Friedrich K editor), Elsevier, Amsterdam.
- Tripathy, B. S.; Furey, M.J.; (1993). Tribological behaviour of unidirectional graphite-epoxy and carbon-PEEK composites. *Wear*, Vol. 162-164, pp. 385-391.
- Tsuda, K.; Kubouchi, M.; Sakai, T.; Saputra, A. H. & Mitomo, N. (2006). General Method for Predicting the Sand Erosion Rate of GFRP, *Wear*, Vol. 260, pp. 1045-1052.
- Wang, J.; Gu, M.; Songhao, Ge. S. (2003). The role of the influence of MoS₂ on the tribological properties of carbon fiber reinforced Nylon 1010 composites, *Wear*, Vol. 255, pp. 774-779.
- Woytowitz, P. J. & Richman, R. H. (1999). Modeling of Damage from Multiple Impacts by Spherical Particles, *Wear*, Vol. 233-235, pp. 120-133.

Comparative Assessment of Si Schottky Diode Family in DC-DC Converter

Nor Zaihar Yahaya
Universiti Teknologi Petronas
Malaysia

1. Introduction

Semiconductors are important as they can serve as switching agents. Unlike semiconductor that work in linear mode such as in power amplifiers and linear regulators, large amount of energy is lost in the power circuit before the processed energy reaches the output. This applies for power conversion from source to load which requires high efficiency. Power will be dissipated in the form of heat once the system has low efficiency (Batarseh, 2004). A Silicon Schottky, (SiS) is a common diode used in power electronics circuits, whereas Silicon Carbide Schottky, (SiCS) is a diode that overall could perform the same operation but at a higher efficiency rate, for example in terms of switching losses.

An ideal semiconductor device would perform within these criteria; possessing large breakdown voltage, low voltage drop during on-state, high switching speed and low power loss. To increase the performance of a semiconductor device, doping process will be experienced by the device, where the characteristic of the device will be altered by adding some impurity atoms to the pure semiconductor material. The material will then be recognized as extrinsic material of *n*-type and *p*-type. A predetermined number of impurity atoms will be added into the silicon or germanium based semiconductor. For silicon, the *n*-type is created by introducing impurity elements with five valence electrons (*pentavalent*), such as antimony, arsenic and phosphorus. The *n*-type semiconductor will have electrons as majority carriers due to one extra free electron to move within the newly formed *n*-type material. On the other hand, *p*-type material is formed by doping the silicon crystal with impurity atoms having three valence electrons such as boron, gallium and indium. A *p*-type semiconductor will have holes as majority carriers due to insufficient number of electrons to complete the covalent bonds.

A forward bias or “on” condition is established once the positive potential is applied to the *p*-type material and the negative potential to the *n*-type material. The application of forward-bias potential will “pressure” electrons in the *n*-type materials and holes in the *p*-type material to recombine with the ions near the boundary and reduce the width of depletion region. If an external potential of volts is applied across the *p*-*n* junction such that the positive terminal is connected to the *n*-type material and the negative terminal is connected to the *p*-type material, the number of uncovered positive ions in the depletion region of the *n*-type material will increase because there are large number of free electrons drawn to the

positive potential of the applied voltage. The number of uncovered negative ions will also increase in the p-type material. Thus, the net effect is a widening of the depletion region and the diode is reverse-biased (Boylestad & Nashelsky, 1999).

2. Silicon Schottky (SiS) diodes

The Schottky diode or Schottky Barrier diode is a semiconductor device that is widely used as a mixer or detector diode. It is also used in power applications as a rectifier, because of its low forward voltage drop leading to lower level of power loss (Malvino, 1980).

Schottky diode is a unipolar device, where the current transport is mainly due to majority carriers. It does not rely on holes or electrons when they enter the opposite type of region as in the case of a conventional diode and therefore it gives better speed. This diode also has low turn-on voltage and high frequency capability with low capacitance (Mohammed et al., 2005).

2.1 Silicon Carbide (SiC) material

Silicon Carbide, (SiC) is a type of wide-bandgap semiconductor having advantages of fast recovery times. SiC diode is seen to have no change (or lesser) on switching loss when temperature increases, whereas SiS diode's behaviour changes in temperature (Ozpincci & Tolbert, 2003). This device has the potential to operate more efficiently by producing less heat and able to work at high temperature compared to Silicon, (Si) diodes. The cause of increasing temperature is the increase in electron's thermal energy which causes reduction of barrier height in the SiS diodes. Therefore, the power losses in SiS diode is due to the increase in its peak reverse recovery current (Chinthavali et al., 2004).

The SiC diode also comes in small size and lighter weight compared to normal schottky diode. It has a bandgap energy at most three times higher and due to this, it also gives better electrical breakdown strength about 10 times higher. This means that electronic devices in SiC can operate at a voltage of 5 to 20 times higher and with current density about 200 to 400 times higher (Wide Bandgap Semiconductor Devices, 2006).

The normal schottky diode has small forward voltage and the reverse breakdown voltage cannot be made too high (currently, approx. 100 to 200 volts). It is normally used for general rectification such as the rectification of power supplies for low voltage and high current application or for high frequency rectification with small reverse recovery time.

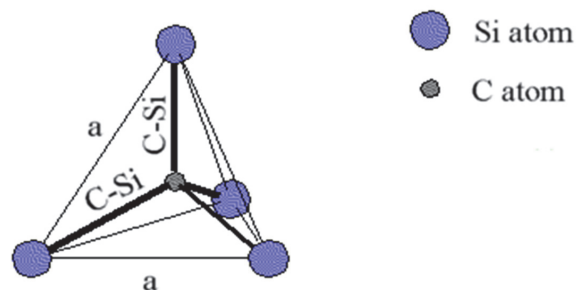


Fig. 1. The tetragonal bonding of a carbon atom with the four nearest silicon neighbours (IFM, 2006).

From Fig. 1, the four Si atoms make a covalent bonding with a single Carbon, (C) atom in order to form a SiC. The C atom is located in the middle of the structure, and the distances between all atoms which marked C-Si are the same. The position of C and Si in periodic table is shown in Fig. 2.

5 B Boron 2.34	6 C Carbon 2.62	7 N Nitrogen 1.251
13 Al Aluminum 2.70	14 Si Silicon 2.33	15 P Phosphorus 1.82
31 Ga Gallium 5.91	32 Ge Germanium 5.32	33 As Arsenic 5.72

Fig. 2. Position of Carbon and Silicon in Periodic Table

The SiC possesses an increased tolerance to radiation damage, making it a preferred material for defense and aerospace applications. Due to high tolerance of temperature in SiC material (up to 650°C) (Silicon Carbide Electronics, 2006), it is used in various industries, such as aircraft, automotive, communications, power and spacecraft.

In terms of schottky's perspective, SiCS diode has higher critical field and higher barrier height than SiS diode. These two advantages give result in a reduced on-resistance and lower leakage current (Kearney et al., 1990). It has been demonstrated that the SiC material has the potential to improve power FET performance (Balaga, 1989).

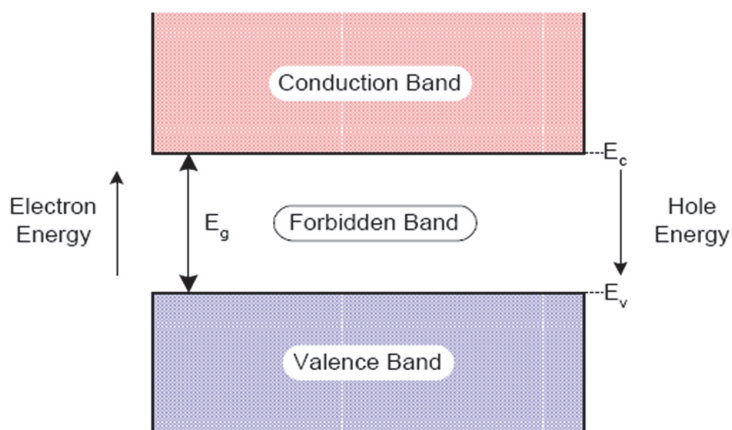


Fig. 3. Energy band diagram of a semiconductor (Ozpincci & Tolbert, 2003)

The characteristic of SiC diode being a wide bandgap semiconductor results in more energy to excite the electron from its covalent bonding during turn-off compared to SiS diode. As shown in Fig. 3, the energy level is measured from the distance between the conduction band and the valence band of the semiconductor that is $E_g = E_c - E_v$. An insulator would have a larger bandgap that it would take a lot of energy for the electrons to move from the

valence band to the conduction band whereas a conductor would have no forbidden band. The wider the bandgap of a semiconductor is, the more thermal energy is needed to excite the electrons to the valence band. Therefore a wide bandgap semiconductor could operate at higher temperature without affecting its electrical property.

3. Diode characteristics

The static property of a diode includes the I-V and reverse characteristics. The SiS diode would have a lower voltage drop than the SiCS diode. During turn-on, there is a high level injection of carrier for SiS diode that leads to a smaller amount of voltage to forward bias the diode. Due to smaller band-gap in SiS diode compared to SiCS, a higher voltage is required to forward bias the SiCS diode (Yahaya & Chew, 2004). However, SiCS can handle large reverse voltage before having an overshoot of leakage current compared to SiS diode. The study also looks at the dynamic characteristics for both SiS and SiCS diode in terms of forward voltage drop, reverse recovery time and reverse recovery current which is given in Table 1 (Pierobon et al., 2002).

Characteristics	SiC Schottky (SDP 04S60)	Si Schottky (SB30-03F)
Reverse Recovery Time	Does not change much in change of temperature	Temperature dependent
Reverse Recovery Current	Negligible	Temperature dependent
Switching Losses	Low	High
Voltage (V) and Current (I) Rating	600V/4A	30V/3A

Table 1. Dynamic Characteristics Comparison

From Table 1, the dynamic characteristic of SiCS diode shows that the reverse recovery time is independent on temperature, in addition to having negligible reverse recovery current and low switching losses. On the other hand, SiS diode shows an increase in reverse recovery time, t_{rr} and reverse recovery current, I_{RR} as temperature increases as well as high switching losses.

3.1 Reverse recovery

Reverse recovery is one measurable quantity that can be used to indicate the performance and hence the efficiency of the device. The reverse recovery in a diode occurs when a device conducts in forward bias long enough to establish steady state due to the presence of minority charge carriers. These charges must be removed prior to blocking in reverse direction (Ahmed, 1999).

Fig. 4 shows the characteristic of reverse recovery exhibited by a diode. The diode current conducts in reverse direction due to free carriers in the diode. The t_a is the time which is based on the charge stored in the depletion region of the junction. It is seen that the charges are removed faster in abrupt recovery as shown in Fig. 4 (b) compared to soft recovery, Fig. 4 (a).

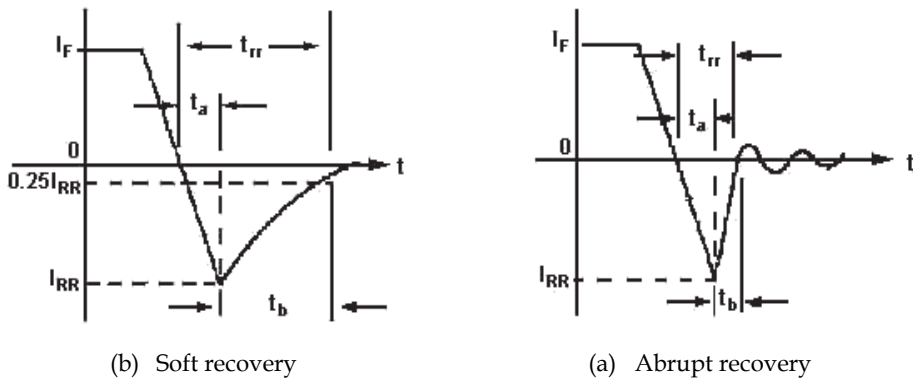


Fig. 4. Diode reverse recovery

The t_{rr} is obtained by adding t_a and t_b . Whilst reverse recovery current is the rate of fall current multiplied with the time taken due to stored charge. The I_{RR} is directly proportional to di/dt . The formula for I_{RR} is given by Eq. (1) (Power Electronic Circuits, 2006).

$$I_{RR} = \sqrt{2 \times Q_{RR} di/dt} \quad (1)$$

It can be seen that if the rate of fall current is high, the I_{RR} will also be high.

4. Methodology

A chopper circuit, better known as a dc-to-dc converter is used to obtain variable dc voltage from a constant voltage dc source. The SiS and SiCS diodes are characterized using this circuit. The diodes under test (D1_SiC and D2_Si) represent each of the diodes used in the simulation.

Major components used in the simulation are:

M1 and M2: IRF520 – 9.2A/100V MOSFET

DUT (D1_SiC): SDP06S60/INF – 6A/600V SiCS diode

(D2_Si): SB30-03F – 3A/30V SiS diode

$R_{load} = 55 \Omega$

$I_{load} = 500 \mu H$

The values of R_{g1} and R_{g2} used in the simulation are 21Ω , with temperature at $27^\circ C$ and V_{cc} is 25 V.

The circuit shown in Fig. 5 is constructed by arranging the load resistor and load inductor in series whereas the diode under test is in parallel to the loads. The pulse voltage (V_{pulse}) is in series with the gate of MOSFET and a limiting resistor, R_{g1} is placed in between the gate and V_{pulse} .

The DC source current from V_{cc} will provide current during turn-on of the switch (MOSFET). The turn-on and turn-off of the switch will be determined by V_{pulse} . V_{gg1} will provide pulse signal to the MOSFET (M1) and the signal will appear at V_{gs} . The pulse signal will then forward bias the gate-source junction of the MOSFET, using current that passes through R_{g1} , or known as I_g and eventually the voltage. As a result, the MOSFET is turned on. The drain current will increase slowly until the pulse signal drops to zero. The current

will stop flowing once I_g drops below the threshold value of the MOSFET. Since there is no current flowing through drain, the MOSFET is turned off.

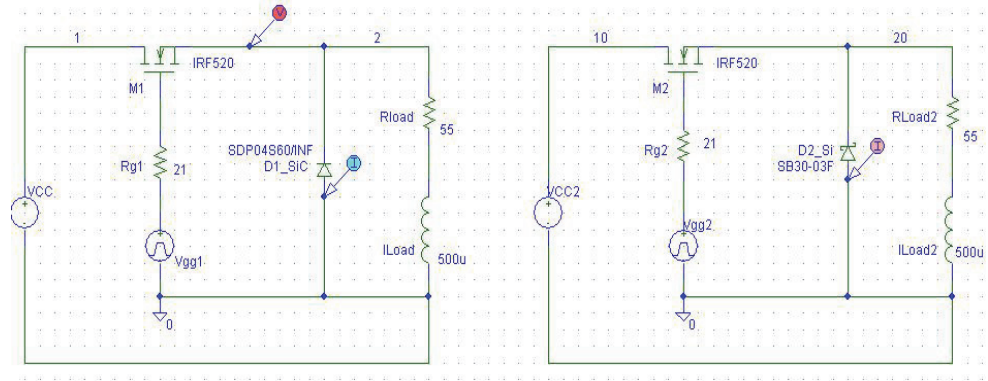


Fig. 5. Inductive Load Chopper Circuit

In the loop containing $D1_SiC$, R_{load} and I_{load} , during turn-on of MOSFET, $D1_SiC$ will be turned off due to no current flowing through $D1_SiC$. The DC current from the DC source will flow through the resistor, R_{load} , inductor, I_{load} , drain of the MOSFET and then to the gate at the source of the MOSFET. When the current flows through I_{load} , it charges up the inductor.

$D1_SiC$ is turned on once MOSFET is turned off. This occurs when current stored in the I_{load} (inductor) starts to flow and goes through $D1_SiC$. $D1_SiC$ will then be in forward biased until MOSFET is turned on again by V_{gg1} (V_{pulse}) signal. Just a few moment before $D1_SiC$ is turned off, the current will be forced to flow in reverse direction. This is when reverse recovery current appears, which is the interest of this work.

The cycle of the signal will repeat again by charging and discharging I_{load} in inductor to turn on and off of the MOSFET and $D1_SiC$. The PSpice settings are shown in Fig. 6.

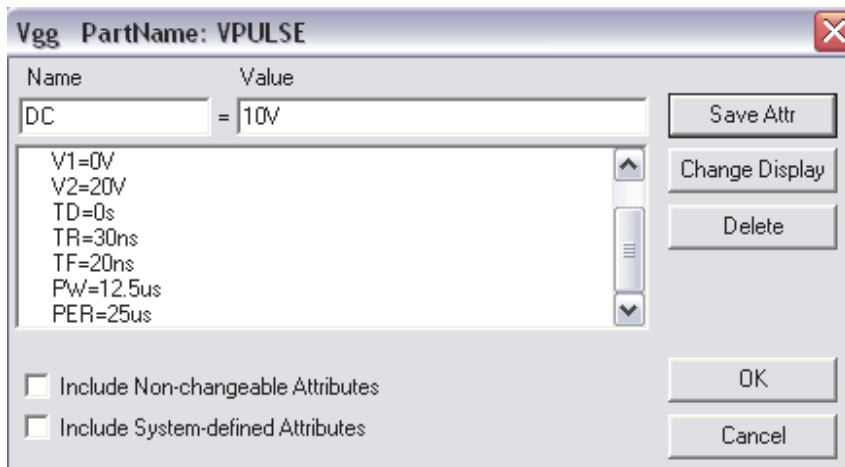


Fig. 6. V_{pulse} Setting

Fig. 6 shows the V_{pulse} setting used in this work. The DC voltage provided by the V_{pulse} is set to 20 V and the same applies to V2. V1 is set to be 0 V. V1 and V2 are for maximum and minimum voltage of the pulse respectively. The rise and fall time of the pulse are both configured to be 30 ns and 20 ns. The frequency of the pulse is 40 kHz with 0.5 duty ratio. Therefore, the period (PER) is 25 μs and the pulse width (PW), 12.5 μs , representing the 0.5 duty ratio.

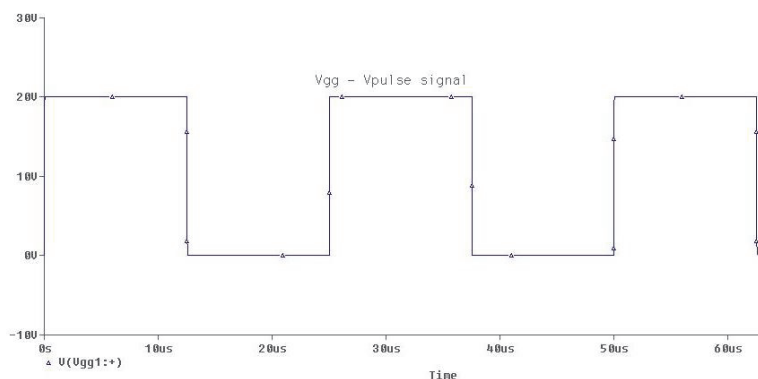


Fig. 7. V_{gg1} (V_{pulse}) Signal

Fig. 7 shows the signal waveform from the V_{pulse} . The signal is the same for both circuits since the parameters used in both circuits are identical. Here, V_{pulse} for SiCS diode circuit is shown to represent V_{pulse} for both circuits. The correct signal shows square wave with pulse period of 25 μs and the maximum voltage is at 20 V whereas the minimum is 0 V. For the duty ratio of 0.5, half period is seen at 12.5 μs .

4.1 Finding V_{gs} and V_{ds}

In order to find the voltage across gate (g) and source (s) of the MOSFET, voltage-differential marker is used. The marker will be placed at the gate and source according to polarity and current flow. The illustration is shown in Fig. 8.

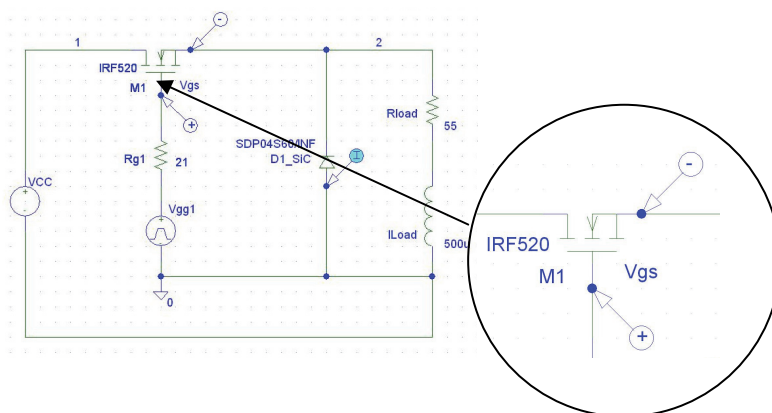


Fig. 8. Finding V_{gs} of Silicon Schottky and Silicon Carbide Schottky diode using voltage differential probe.

Again, similar method is applied to measure V_{ds} . The voltage differential marker is placed at the drain and source of the MOSFET as shown in Fig. 9.

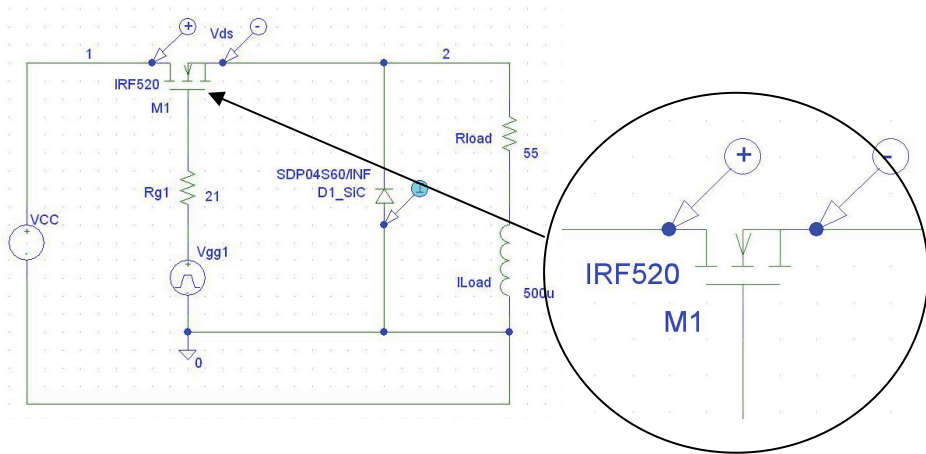


Fig. 9. Finding V_{ds} of Silicon Schottky and Silicon Carbide Schottky diode using voltage differential probe.

The simulation is carried out one at a time starting with finding the voltage across gate and source, and then followed by finding the voltage across the drain and source. Any overshoots or ringing will be noticed and the results are measured.

4.2 Finding reverse recovery current

The next process in the simulation is to capture the reverse recovery current produced by SiCS and SiS diode. The current marker is now placed at the node terminal of the diode and then the circuit is simulated.

Fig. 10 shows the location where current marker/probe is placed on the circuit in order to measure SiCS and SiS currents.

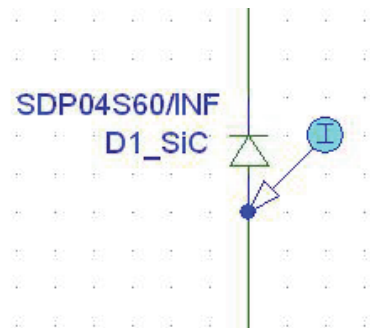


Fig. 10. Current probe placed on the diode under test (DUT)

A diode current will be displayed and by using the 'zooming' tool, the reverse recovery currents of both diodes are measured and analyzed.

4.3 Finding diode turn-off power loss and MOSFET turn-on power loss

The PSpice software is already equipped with a function in calculating power loss. The conventional way is by using the equation $P = IV$, but by using PSpice, the power loss can be measured straightforward. The power loss function is within the 'add trace' function for example $W(M1)$ and $W(M2)$.

4.4 Finding the effect of varying frequency to the reverse recovery loss in the diode

The frequency of the inductive load chopper circuit used in this project is obtained from the V_{pulse} . Therefore, in order to vary the frequency, the period (PER) within the V_{pulse} setting will be adjusted according to formula $f=1/T$, where in this case T is the period (PER). It is also noted that after the period has been changed, the PW (pulse width) is changed to configure 0.5 duty ratio setting.

5. Results and discussion

The overshoot gate and drain voltages of MOSFET during turn-on in both circuits are measured based on SiCS and SiS diodes as well as the load current. In addition, the respective turn-off reverse recovery overshoot current is also determined to observe the influence of carbide material property in the diode.

5.1 Results of V_{gs} and V_{ds}

Fig. 11 shows the voltage waveform of V_{gs} for SiCS and SiS diode. There is voltage overshoot seen during the turn-on of the MOSFET and in Fig. 12, the overshoot portion (circle) is enlarged.

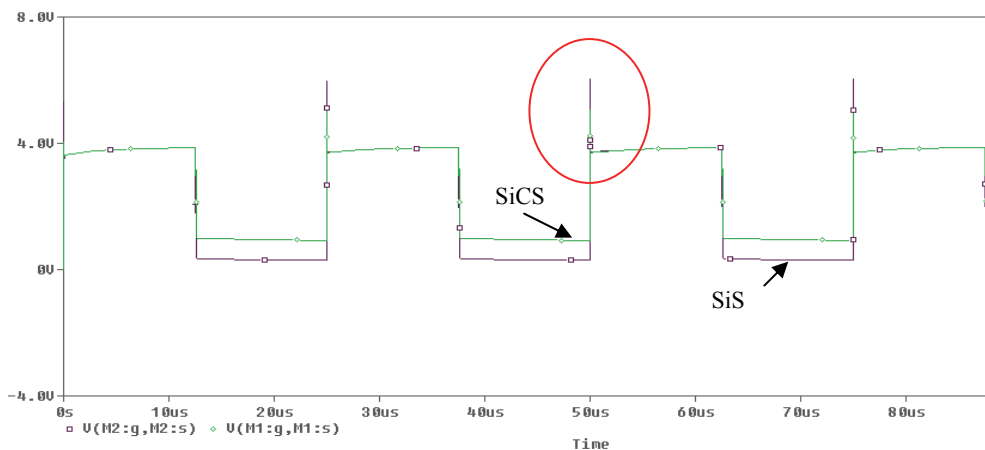


Fig. 11. V_{gs} of switch M1 and M2 applied at SiC Schottky Diode and Si Schottky Diode Circuit respectively.

As seen in Fig. 12, the overshoot voltage of MOSFET using SiS diode is higher than using SiCS diode with 6.0217 V, compared to MOSFET with SiCS of only 5.0484 V.

From this result, MOSFET turn-on power loss is also smaller in SiCS diode circuit compared to SiS circuit, due to low voltage ringing during turn-on, which will be later discussed in this chapter.

Fig. 13 shows the voltage across drain and source of the MOSFET for both circuits using SiCS and SiS diode. On the other hand, Fig. 14 shows the overshoot during turn-on as referred to the circle shown in Fig. 11.

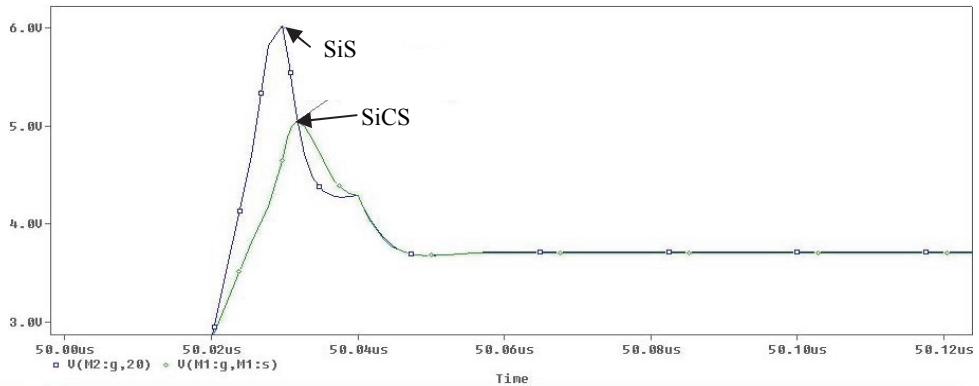


Fig. 12. V_{gs} overshoot of M1 (SiCS circuit) and M2 (SiS circuit)

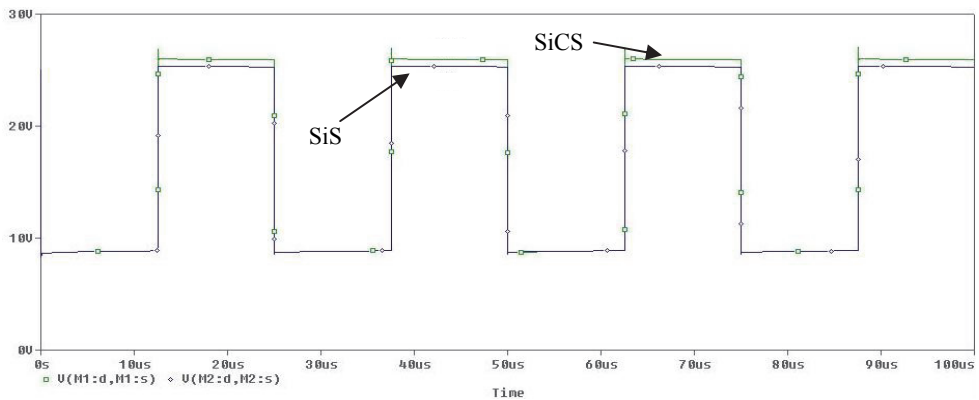


Fig. 13. V_{ds} of switch M1 and M2 applied at SiC Schottky Diode and Si Schottky Diode Circuit respectively

From Fig. 14, it is noticed that the MOSFET's V_{ds} overshoot is visible in SiCS diode circuit having value of 26.956 V. Whilst for SiS diode circuit, no overshoot is recorded at V_{ds} . However, the peak V_{ds} value is 25.277 V for SiS better than SiCS. This is the drawback found in the findings.

Fig. 15 indicates the load resistor's current, I_{Rload} for both circuits. From the figure, the maximum value of I_{Rload} in SiCS diode circuit is 230.766 mA, with a minimum of 45.078 mA. As for I_{Rload} in SiS diode circuit, the maximum is 232.897 mA and minimum of 54.207mA. The values obtained from Fig. 15 above will be used to calculate load output power of the circuits.

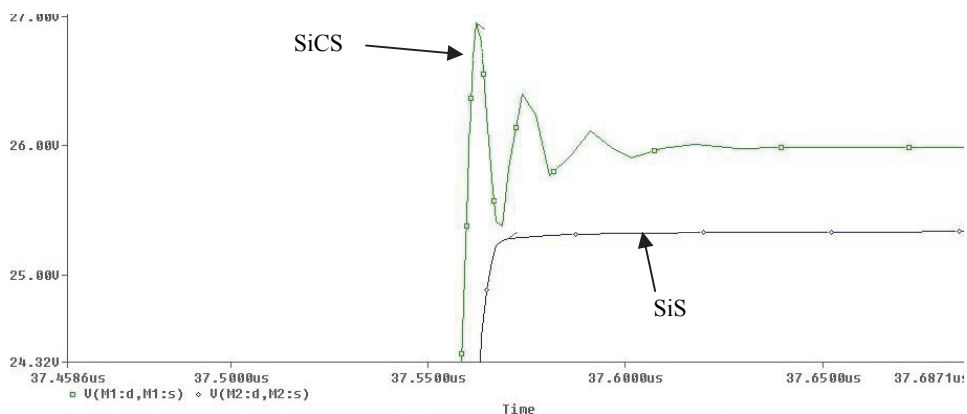


Fig. 14. V_{ds} overshoot of forward switch M1 (SiC circuit) and M2 (Si circuit)

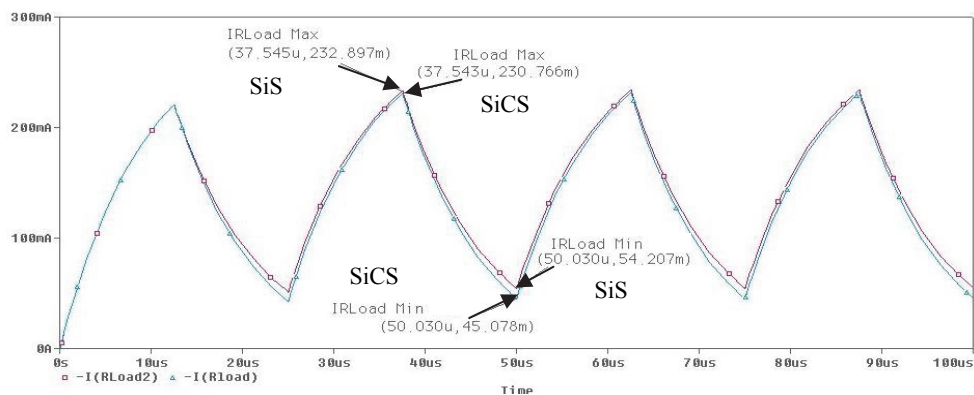


Fig. 15. I_{Rload} for Silicon Carbide Schottky and Silicon Schottky Circuit

The load power for the circuits are obtained from calculation:

a. Silicon Carbide Schottky diode circuit:

$$\begin{aligned} I_{Rload,avg} &= (I_{Rload,max} - I_{Rload,min}) / 2 \\ &= (230.766 \text{ mA} - 45.078 \text{ mA}) / 2 \\ &= 92.844 \text{ mA} \end{aligned}$$

With R_{load} value of 55Ω , the output power (P_{out}) is obtained:

$$\begin{aligned} P_{out} &= I_{Rload,avg}^2 \times R_{Rload,load} \\ &= (92.844 \text{ mA})^2 \times 55 \Omega \\ &= 474.100 \text{ mW} \end{aligned}$$

b. Silicon Schottky diode circuit:

$$\begin{aligned} I_{Rload,avg} &= (I_{Rload,max} - I_{Rload,min}) / 2 \\ &= (232.297 \text{ mA} - 54.207 \text{ mA}) / 2 \\ &= 89.045 \text{ mA} \end{aligned}$$

With R_{load} value of 55Ω , the output power (P_{out}) is obtained:

$$\begin{aligned} P_{out} &= I_{Rload,avg}^2 \times R_{Rload,load} \\ &= (89.045 \text{ mA})^2 \times 55 \Omega \\ &= 436.096 \text{ mW} \end{aligned}$$

From the calculation, the output power, P_{out} generated by SiCS diode circuit is 474.100 mW and 436.096 mW for SiS diode circuit. The P_{out} of SiCS diode is higher by 8.016 %. This is because SiCS diode provides higher output current, thus higher efficiency.

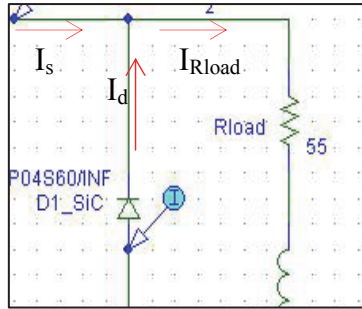


Fig. 16. Source current, I_s , Current across diode, I_d and load current, I_{Rload}

Fig. 16 shows the flow of current to the load. This explanation is referred to current divider for diode current, $I_d = I_s - I_{Rload}$. The I_{Rload} of SiCS diode is obviously lower than SiS due to lower I_{Rload} . Therefore, the SiS diode is proven to have larger power loss.

The carbide element in SiCS diode helps in increasing the output current and hence the output power of the circuit. This is due to the fact that SiC has lower reverse recovery current, I_{RR} thus lower power losses at the diode during turn-off.

5.2 Results of reverse recovery current

From Fig. 17, it can be seen that there are negative overshoot during turn-off of the diode having I_{RR} below 0A. In this simulation, the transient setting is set to be 100 μ s.

Fig. 18 shows a significant difference of I_{RR} overshoot between SiCS diode and SiS diode. It is observed that the I_{RR} of SiS diode is -1.0245 A, whereas -91.015 mA for SiS diode. The

advantage of carbide is that the leakage current from anode to cathode is lower due to the fact that SiC structure of metal-semiconductor barrier is two times higher than Si and its smaller intrinsic carrier concentration (Scheick et al., 2004), (Libby et al., 2006). The I_{RR} in SiCS diode is also smaller than SiS as SiC has no stored charges where a majority carrier device could operate without high-level minority carrier injection. Therefore, during the turn-off of the SiCS diode, most of the stored charges are removed (Bhatnagar & Baliga, 1993). The low switching losses of SiCS diode is due to high breakdown field of SiCS which results in reduced blocking layer thickness, in conjunction to the reduced charges (Chintivali et al., 2005).

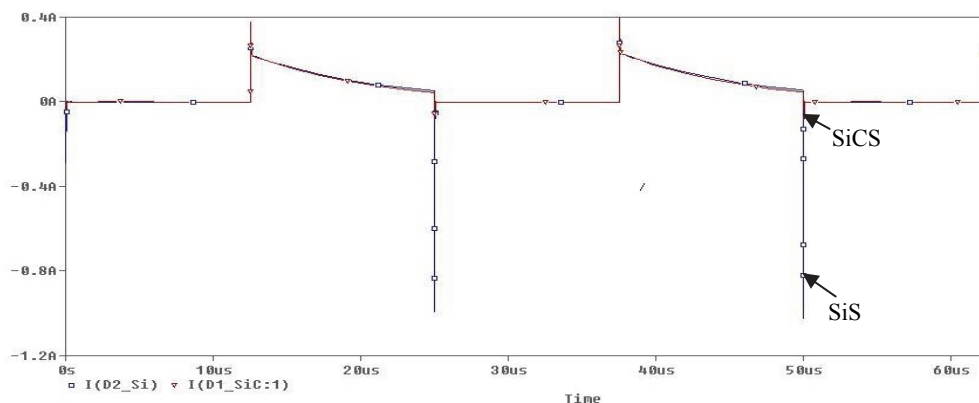


Fig. 17. Diode Current, I_d at Silicon Schottky and Silicon Carbide Schottky Diode

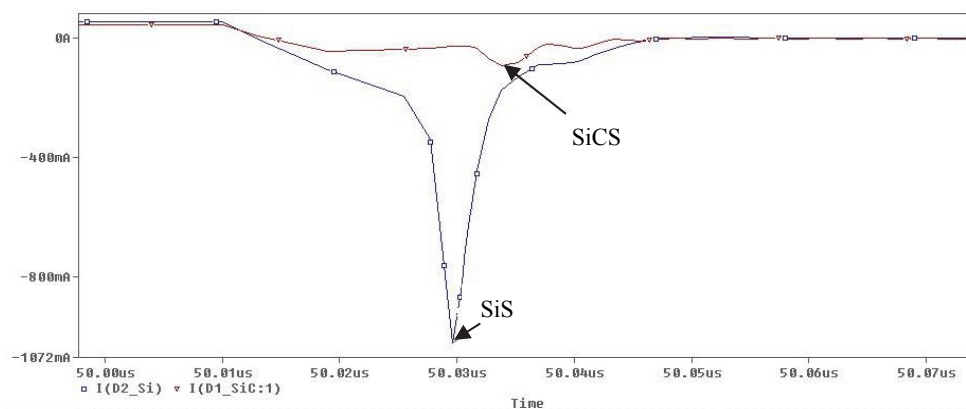


Fig. 18. Reverse Recovery Current of Silicon Schottky and Silicon Carbide Schottky Diode

From Fig. 19, it can be seen that SiS diode has a turn-off loss of 3.0704 W larger than SiCS diode, 818.590 mW. With higher I_{RR} , more power loss will be dissipated because more power is required for the diode to be fully turned off due to a larger stored charge.

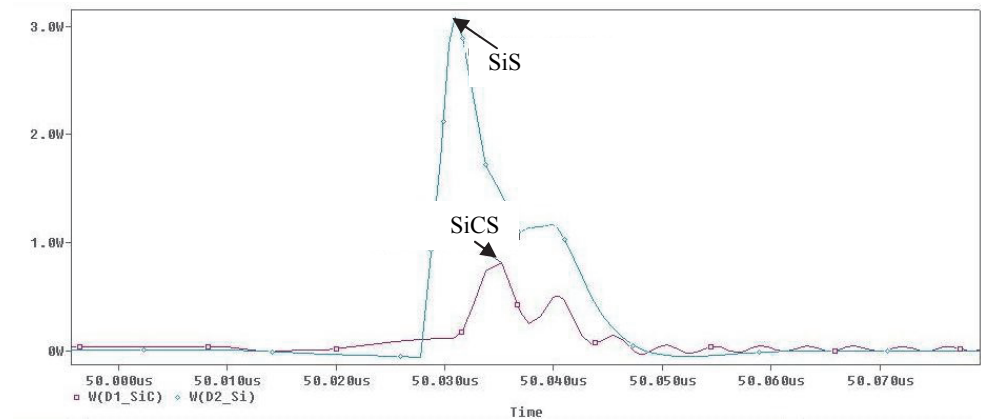


Fig. 19. Turn Off Loss of Silicon Schottky and Silicon Carbide Schottky Diode

Fig. 20 shows that MOSFET turn-on power loss in SiS diode circuit (20.619 W) is higher than in SiCS diode (790.777 mW). The higher power loss of MOSFET SiS diode indicates higher power loss produced by the diode during turn-off. The carbide material in SiCS diode is the main factor why such lower power loss is generated. From the results for V_{gs} of the MOSFET, it can be seen that lower current spike is observed in SiCS diode circuit during turn-on. With lower voltage ringing effect in SiCS diode, lower power loss will be produced by the MOSFET. It is found that, carbide material in SiCS diode has eventually given some influence in improving the circuit's performance.

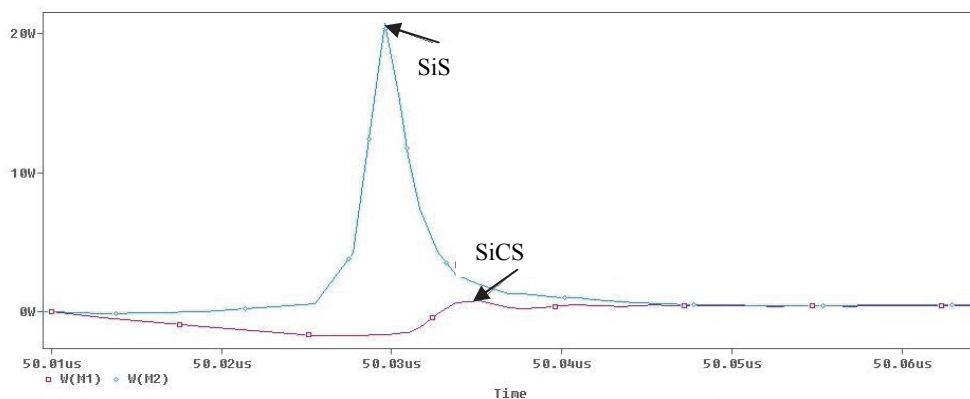


Fig. 20. MOSFET turn-On Power Loss during DUT turn-Off

Characteristics	Si Schottky Diode	SiC Schottky Diode	Percentage Improvement (%)
Output Power, P_{out}	436.096mW	474.100mW	8.016%
Peak Reverse Recovery Current, I_{rr}	-1.0245A	-91.015mA	91.12%
DUT Turn-Off Loss	3.0704W	818.59mW	73.34%
MOSFET Turn-On Loss	20.619W	790.777mW	96.16%

Table 2. Simulation Results

From Table 2, SiS diode has higher peak I_{RR} of -1.0245 A compared to SiCS diode, -91.015mA. As for turn-off loss of both diodes, it also shows that SiS diode generates more losses. This is also applied to MOSFET power loss during turn-on where there shows an improvement of 96.16 % when SiCS diode is used.

5.3 The effect of varying frequency to the reverse recovery loss of the diode under test (DUT)

From Fig. 21, it is obvious that SiCS diode circuit does not experience much difference in frequency variation. As for SiS diode, it shows an increase in power loss. However, it is also noted that once frequency is higher than 50 kHz, the power loss in SiS diode is maintained at around 3.6 W to 3.7 W. Nevertheless, SiCS diode has shown the ability in operating at higher switching frequency with minimal power loss.

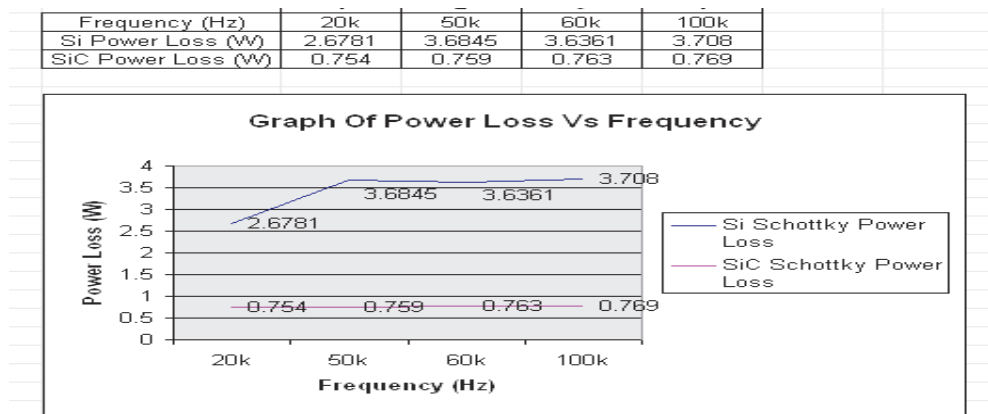


Fig. 21. Graph of Power Loss vs Frequency of Silicon Schottky and Silicon Carbide Schottky Diode

6. Conclusion

This work is about the comparative study of silicon schottky and silicon carbide schottky diode using PSpice simulation. An inductive load chopper circuit is used in the simulation and the outputs in terms of reverse recovery, turn-off power losses of both diodes and turn-on losses of the MOSFET are analyzed. It is proven that silicon schottky diode has produced

higher reverse recovery current than silicon carbide schottky diode. Therefore, lesser power losses are generated in silicon carbide schottky diode with 91.12 % improvement. The results also confirmed that the ringing at the switch (MOSFET) has been reduced by 16.16 %. Eventually, the carbide element has helped in achieving higher output power by 8 %. The turn-off losses in diodes have also been reduced by 73.34 % using silicon carbide schottky diode as well as the MOSFET turn-on power losses which is reduced by 96.16 % mainly due to the reduction in reverse recovery current.

7. Acknowledgment

The authors wish to thank Universiti Teknologi PETRONAS for providing financial support to publish this work.

8. References

- [1] Ahmed, A. (1999) *Power Electronics for Technology*, Purdue University-Calumet, Prentice Hall.
- [2] Baliga, B. J. (1989) Power semiconductor device figure of merit for high-frequency applications, *IEEE Electron Device Letters*, Vol. 10, Iss. 10, pp. 455-457.
- [3] Batarseh, I. (2004), *Power Electronic Circuits*, University of Central Florida: John Wiley & Sons, Inc.
- [4] Bhatnagar, M. & Baliga, B. J. (1993) Comparison of 6H-SiC, 3C-SiC, and Si for power devices, *IEEE Transactions on Electronics Devices*, Vol. 40, Iss. 3, pp. 645-655.
- [5] Boylestad, R. L. & Nashelsky, L. (1999) *Electronic Devices and Circuit Theory*, 7th Edition, Prentice Hall International, Inc.
- [6] Chintivali, M. S.; Ozpineci, B. & Tolbert, L. M. (2005) High-temperature and high-frequency performance evaluation of 4H-SiC unipolar power devices, *Applied Power Electronics Conference and Exposition 2005, Twentieth Annual IEEE*, Vol. 1, pp. 322-328.
- [7] Chinthavali, M. S.; Ozpineci, B. & Tolbert, L. M. (2004) Temperature-dependent characterization of SiC power electronic devices, *IEEE Power Electronics in Transportation*, pp. 43-47.
- [8] IFM, Materials Science Division Linköpings Universitet, Crystal Structure of Silicon Carbide (2006)
<http://www.ifm.liu.se/matephys/AAnew/research/sicpart/kordina2.htm>.
- [9] Kearney, M. J.; Kelly, M. J.; Condie, A. & Dale, I. (1990) Temperature Dependent Barrier Heights In Bulk Unipolar Diodes Leading To Improved Temperature Stable Performance, *IEEE Electronic Letters*, Vol. 26, Iss. 10, pp. 671 – 672.
- [10] Libby, R. L.; Ise, T. & Sison, L. (2006) Switching Characteristics of SiC Schottky Diodes in a Buck DC-DC Converter, *Proc. Electronic and Communications Engineering Conf*, <http://www.dilnet.upd.edu.ph/~irc/pubs/local/libby-switching.pdf>.
- [11] Malvino, A. P. (1980) *Transistor Circuit Approximation*, 3rd Edition, McGraw-Hill, Inc.
http://www.eng.uwi.tt/depts/elec/staff/rdefour/ee33d/s2_rrchar.html
- [12] Mohammed, F.; Bain, M.F.; Ruddell, F.H.; Linton, D.; Gamble, H.S. & Fusco, V.F., (2005) A Novel Silicon Schottky Diode for NLTL Applications, *Electron Devices, IEEE Transactions*, Vol. 52, Iss. 7, pp. 1384 – 1391.
- [13] National Aeronautics and Space Administration, Silicon Carbide Electronics (2006)

- <http://www.grc.nasa.gov/WWW/SiC/index.html>.
- [14] Ozpincci, B. & Tolbert, L. M. (2003) Characterization of SiC Schottky Diodes at Different Temperatures, *IEEE Power Electronics Letters*, Vol. 1, No. 2, pp. 54-57.
 - [15] Ozpincci, B. & Tolbert, L. M. (2003) Comparison of Wide-Bandgap Semiconductors For Power Electronics Applications, Oak Ridge National Laboratory, Tennessee.
 - [16] Pierobon, R.; Buso, S.; Citron, M.; Meneghesso, G.; Spiazzi, G. & Zanon, E. (2002) Characterization of SiC Diodes for Power Applications, *IEEE Power Electronics Specialists Conference*, Vol. 4, pp. 1673 – 1678.
 - [17] Power Electronic Circuits (2006) University of West Indies.
http://www.eng.uwi.tt/depts/elec/staff/rdefour/ee33d/s1_dvice.html.
 - [18] Purdue University Nanoscale Center, Wide Bandgap Semiconductor Devices (2006)
<http://www.nanodevices.ecn.purdue.edu/widebandgap.html>.
 - [19] Scheick, L.; Selva, L. & Becker, H. (2004) Displacement Damage-induced Catastrophic Second Breakdown in Silicon Carbide Schottky Power Diodes, *Nuclear Science IEEE Transactions*, Vol. 51, Iss. 6, pp. 3193- 3200.
 - [20] Yahaya, N. Z. & Chew, K. K. (2004) Comparative Study of The Switching Energy Losses Between Si PiN and SiC Schottky Diode, *National Power & Energy Conference*, pp. 216-229.

Compilation on Synthesis, Characterization and Properties of Silicon and Boron Carbonitride Films

P. Hoffmann¹, N. Fainer², M. Kosinova², O. Baake¹ and W. Ensinger¹

¹*Technische Universität Darmstadt, Materials Science*

²*Nikolaev Institute of Inorganic Chemistry, SB RAS*

¹*Germany*

²*Russia*

1. Introduction

During the last years the interest in silicon and boron carbonitrides developed remarkably. This interest is mainly based on the extraordinary properties, expected from theoretical considerations. In this time significant improvements were made in the synthesis of silicon carbonitride SiC_xN_y and boron carbonitride BC_xN_y films by both physical and chemical methods.

In the Si-C-N and B-C-N ternary systems a set of phases is situated, namely diamond, SiC, $\beta\text{-Si}_3\text{N}_4$, c-BN, B_4C , and $\beta\text{-C}_3\text{N}_4$, which have important practical applications. SiC_xN_y has drawn considerable interest due to its excellent new properties in comparison with the Si_3N_4 and SiC binary phases. The silicon carbonitride coatings are of importance because they can potentially be used in wear and corrosion protection, high-temperature oxidation resistance, as a good moisture barrier for high-temperature industrial as well as strategic applications. Their properties are low electrical conductivity, high hardness, a low friction coefficient, high photosensitivity in the UV region, and good field emission characteristics. All these characteristics have led to a rapid increase in research activities on the synthesis of SiC_xN_y compounds. In addition to these properties, low density and good thermal shock resistance are very important requirements for future aerospace and automobile parts applications to enhance the performance of the components. SiC_xN_y is also an important material in micro- and nano-electronics and sensor technologies due to its excellent mechanical and electrical properties. The material possesses good optical transmittance properties. This is very useful for membrane applications, where the support of such films is required (Fainer et al., 2007, 2008; Mishra, 2009; Wrobel, et al., 2007, 2010; Kroke et al., 2000).

The structural similarity between the allotropic forms of carbon and boron nitride (hexagonal BN and graphite, cubic BN and diamond), and the fact that B-N pairs are isoelectronic to C-C pairs, was the basis for predictions of the existence of ternary BC_xN_y compounds with notable properties (Samsonov et al., 1962; Liu et al., 1989; Lambrecht & Segall, 1993; Zhang et al., 2004). This prediction has stimulated intensive research in the last 40 years towards the synthesis of ternary boron carbonitride. BC_xN_y compounds are interesting in both the cubic (c-BCN) and hexagonal (h-BCN) structure. On the one hand, the

synthesis of c-BCN is aimed at the production of super-hard materials since properties between those of cubic boron nitride (c-BN) and diamond would be obtained (Kulisch, 2000; Solozhenko et al., 2001). On the other hand, h-BCN has potential applications in microelectronics (Kawaguchi, 1997), since it is expected to behave as semiconductor of varying band gap depending on the composition and atomic arrangement (Liu et al., 1989), or in the production of nanotubes (Yap, 2009).

2. Methods of synthesis

Considerable efforts in the synthesis of SiC_xN_y and BC_xN_y films have been made by a large variety of deposition methods (both physical and chemical techniques).

2.1 Physical Vapour Deposition (PVD)

2.1.1 Silicon carbonitrides

2.1.1.1 Laser based methods

CSi_xN_y thin films were grown on Si(100) substrates by pulsed laser deposition (PLD) assisted by a radio frequency (RF) nitrogen plasma source (Thäringen et al., 1999). Up to about 30 at% nitrogen and up to 20 at% silicon were found in the hard amorphous thin films (23 GPa).

SiC_xN_y films were grown on silicon substrates using the pulsed laser deposition (PLD) technique (Soto et al., 1998; Boughaba et al., 2002). A silicon carbide (SiC) target was ablated by the beam of a KrF excimer laser in a nitrogen (N_2) background gas. Smooth, amorphous films were obtained for all the processing parameters. The highest values of hardness and Young's modulus values were obtained in the low-pressure regime, in the range of 27–42 GPa and 206–305 GPa, respectively.

SiC_xN_y thin films have been deposited by ablation a sintered silicon carbide target in a controlled N_2 atmosphere (Trusso et al., 2002). The N_2 content was found to be dependent on the N_2 partial pressure and did not exceed 7.5%. A slight increase of sp^3 hybridized carbon bonds has been observed. The optical band gap E_g values were found to increase up to 2.4 eV starting from a value of 1.6 eV for a non-nitrogenated sample.

2.1.1.2 Radio frequency reactive sputtering

Nanocrystalline SiC_xN_y thin films were prepared by reactive co-sputtering of graphite and silicon on Si(111) substrates (Cao et al., 2001). The films grown with pure nitrogen gas are exclusively amorphous. Nanocrystallites of 400–490 nm in size were observed by atomic force microscopy (AFM) in films deposited with a mixture of N_2 +Ar.

Amorphous silicon carbide nitride thin films were synthesized on single crystal Si substrates by RF reactive sputtered silicon nitride target in a CH_4 and Ar atmosphere (Peng et al., 2001). The refractive index decreased with increasing target voltage.

SiCN films were deposited by RF reactive sputtering and annealed at 750°C in nitrogen atmosphere (Du et al., 2007). The as-deposited film did not show photoluminescence (PL), whereas strong PL peaks appeared at 358 nm, 451 nm, and 468 nm after annealing.

The a- SiC_xN_y thin films were deposited by reactive sputtering from SiC target and N_2 /Ar mixtures (Tomasella et al., 2008). For more than vol.30 % of nitrogen in the gas mixture, a N-saturated Si-C-N film was formed. All the structural variations led to an increase of the optical band gap from 1.75 to 2.35 eV.

SiCN films were deposited on Si(100) substrates by RF sputtering methods using SiC targets and N₂ as reactant gas (Chen et al., 2009). A high substrate temperature is not favorable for the N₂ incorporation into the SiCN films. The stoichiometry of these SiCN films was given as Si_{32.14}C_{39.10}N_{28.76}, which is close to SiCN. The film grown at room temperature showed a light structure.

2.1.1.3 Radio frequency magnetron sputtering

Amorphous SiC_xN_y films were prepared by RF magnetron reactive sputtering using sintered SiC targets and a mixture of Ar and N₂ (99.999%) (Xiao et al., 2000; Li et al., 2009). The results revealed the formation of complex networks among the three elements Si, C and N, and the existence of different chemical bonds in the SiC_xN_y films such as C-N, C=N, C≡N, Si-C and Si-N. The stoichiometry of the as-deposited films was found to be close to SiCN (Si_{36.9}C_{30.4}N_{32.7}).

Nanostructured and amorphous SiC_xN_y films have been deposited by magnetron sputtering of SiC under reactive gas environment at 700-1000°C (Lin et al., 2002). Gas mixtures containing CH₄ and N₂ with various ratios were used for deposition. As the CH₄/N₂ ratio was increased, the SiC_xN_y films changed from mirror-like smooth films to column-like and ridge-like C-rich SiC_xN_y nanostructures. The chemical composition of these films varied from Si₃₁C₃₅N₂₅O₉ up to Si₅C₈₉N₃O₃.

SiCN films have been produced by means of reactive magnetron sputtering of a Si target in an Ar/N₂/C₂H₂ atmosphere (Hoche et al, 2008). Depending on their position in the Si-C-N phase diagram, the hardness of the films varies over a broad range, with maximum values at about 30 GPa, while Young's modulus remains in a narrow range around 200 GPa.

The nano-composite SiCN thin films on silicon, glass and steel have been produced by magnetron sputtering at different substrate temperatures ranging from 100°C to 500°C at 400 W RF power from SiC targets in Ar/N₂ atmosphere (Mishra et al, 2008; Mishra, 2009). The nanocomposite SiCN films were found to have nanocrystals of 2-15 nm of the β-C₃N₄ phase distributed in an amorphous matrix. The microhardness values of the films were found to vary between 25-47 GPa and was dependent on deposition and substrate temperatures.

SiCN films were deposited on n-type Si(100) and glass substrates by RF reactive magnetron sputtering of a polycrystalline silicon target under mixed reactive gases of C₂H₂ and N₂ (Peng et al., 2010). The SiCN films deposited at room temperature are amorphous, and the C, Si and O compositions in the films are sensitive to the RF power, except N.

2.1.1.4 Reactive DC magnetron sputtering

Si-C-N films were deposited on p-type Si(100) substrates by DC magnetron co-sputtering of silicon and carbon in nitrogen-argon mixtures using a single sputter target with variable Si/C area ratios (Vlcek et al, 2002). The substrate temperature was adjusted at T_s=600°C by an ohmic heater and the RF-induced negative substrate bias voltage, U_b was 500V. With a rising Ar concentration in the gas mixture, the Si content in the films rapidly increases (from 19 to 34 at.% for a 40 at.% Si fraction in the erosion target area), while the C content decreases (from 34 to 19 at.%) at an almost constant N concentration (39-43 at.%). As a result, the N-Si and Si-N bonds dominate over the respective N-C and Si-O bonds, preferred in a pure N₂ discharge, and the film hardness increases up to 40 GPa.

2.1.1.5 Ion Beam Sputtering Assisted Deposition (IBAD)

SiCN films have been successfully synthesized at a temperature below 100°C from an adenine ($C_5N_5H_5$)-silicon-mixed target sputtered by an Ar ion beam (Wu et al., 1999). The chemical composition of these films varied from $Si_{24}C_{60}N_{13}O_3$ up to $Si_{32}C_{34}N_{19}O_{15}$. Only amorphous films for Si-rich SiCN were obtained, while the films with low Si incorporation and deposited at high Ar ion beam voltage contained nanocrystallites.

High-dose nitrogen ion implantation into SiC is a possible way to produce a-SiC_xN_y (Ishimaru et al., 2003; Suvorova et al., 2009). SiC crystal target was implanted by nitrogen ions at ambient temperature up to a fluence of $5 \times 10^{17} \text{ N}^+/\text{cm}^2$, followed by thermal annealing at 1500°C for 30 min. a-SiC_xN_y possesses an intermediate bond length between Si–C and Si–N.

2.1.1.6 Dual Ion Beam Sputtering (DIBS)

SiCN films were deposited by dual ion beam sputtering (DIBS) of a SiC target in mixed Ar/N₂ atmosphere at 100°C (Zhou et al., 2010). The results showed that the variations of surface roughness and hardness for the SiCN films with the assisting ion beam energy were in the range of 7–27 nm and 23–29 GPa, respectively.

2.1.1.7 Combined High Power Pulse Magnetron Sputtering (HPPMS) - DC sputtering

Amorphous SiCN coatings were synthesized by conventional DC and RF magnetron sputtering as well as with a combined sputtering process using one target in the DC mode and one target in the HPPMS mode (Hoche et al, 2010). The SiCN's Young's modulus of approximately 210 GPa makes SiCN coatings promising for the deposition onto steel. Structural differences can originate from the different carbon sources. By using acetylene a distinct amount of carbon ions can be achieved in the plasma.

2.1.1.8 An arc enhanced magnetic sputtering hybrid system

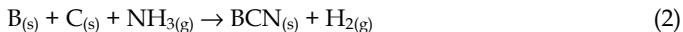
SiCN hard films have been synthesized on stainless steel substrates by an arc enhanced magnetic sputtering hybrid system using a Si target and graphite target in gases mixed of Ar and N₂ (Ma et al., 2008). The microstructure of the SiCN films with a high silicon content are nanocomposites in which nano-sized crystalline C₃N₄ hard particles are embedded in the amorphous SiCN matrix. The hardness of the SiCN films is found to increase with increasing silicon contents, and the maximum hardness is 35 GPa. The SiCN hard films show a low friction coefficient of 0.2.

2.1.1.9 Microwave Electron Cyclotron Resonance (ECR) plasma enhanced unbalance magnetron sputtering

SiCN thin films were prepared by microwave ECR plasma enhanced unbalanced magnetron sputtering (Gao et al., 2007). The Si–C–N bonds increased from 17.14% to 23.56% while the graphite target voltage changed from 450V to 650V. The optical gap value progressively decreases from 2.65 to 1.95 eV as the carbon content changes from 19.7 at.% to 26.4 at.%. The maximum hardness of the thin films reaches 25 GPa.

2.1.2 Boron carbonitrides

The goal to synthesize boron carbonitride with the participation of the gas phase and to examine its structure and properties was put forward by Kosolapova et al. (Kosolapova et al., 1971). The product corresponding to BCN composition, as indicated by chemical analysis, was obtained by nitrogenization of a mixture of amorphous boron and carbon black in nitrogen or ammonia within the temperature range 2073–2273K.



The BCN obtained according to reactions (1) and (2) was characterized by a somewhat larger unit cell parameter (0.6845 nm) than that of hexagonal boron nitride (0.6661 nm) or graphite (0.6708 nm). As the authors reported, the BCN powder was oxidized at 1073 K. This result indicates that this material did not contain carbon or boron carbide, because the interaction of these compounds with oxygen starts already at a temperature of 773 and 873 K, respectively.

2.1.2.1 Laser based methods

Using a disk combining together two semidisks, one of h-BN and one of graphite, as target, Perrone et al. deposited at room temperature polycrystalline films: a mixture of c-BCN and h-BCN by PLD in vacuum and amorphous h-BN in nitrogen gas ambient (Perrone, 1998; Dinescu, 1998). The targets used by Teodorescu et al. for film deposition were both a half C and half BN disk and a $\frac{3}{4}$ h-BN and $\frac{1}{4}$ C disk (Teodorescu et al., 1999). The influence of substrate temperature on composition and crystallinity of BCN films has been investigated. Films deposited on heated substrates are amorphous, while films produced at room temperature are polycrystalline. Wada et al. deposited BCN films from a hot-pressure BCN target consisting of graphite and h-BN powder in an 1:1 ratio (Wada et al., 2000). Later the same group (Yap et al., 2001) demonstrated that BCN films with the composition of BC_2N can be obtained by RF plasma-assisted pulsed laser deposition (PLD) at 800°C on Si substrate, but these films were carbon doped BN compounds (BN:C). Furthermore, hybridized BCN films can be deposited on Ni substrate under similar synthesis conditions. Another laser-based technique was pulsed laser ablation of a sintered B_4C target in the environment of a nitrogen plasma generated from ECR microwave discharge in nitrogen gas, with growing films being simultaneously bombarded by the low-energy nitrogen plasma stream (Ling, 2002; Pan, 2003). The prepared films are composed of boron, carbon, and nitrogen with an average atomic B/C/N ratio of 3:1:3.8. It was found that the assistance of the ECR nitrogen plasma facilitated nitrogen incorporation and film formation. Nitrogen ion beam generated by a Kaufman ion gun was applied to assist reactive PLD of BCN thin films from sintered B_4C (Ying, 2007). It is demonstrated that with nitrogen ion beam assistance, BCN films with nitrogen content of more than 30 at.% can be synthesized. The bonding characteristics and crystalline structure of the films were also found to be influenced by the substrate temperature. With increasing substrate temperature to 600°C, the BCN films exhibit nanocrystalline nature. Recently, amorphous BCN films were produced by laser ablation of B_4C target in nitrogen atmosphere (Yang, 2010).

2.1.2.2 Radio frequency reactive sputtering

Ternary boron carbonitride thin films were prepared by RF reactive sputtering method from a hexagonal h-BN target in an Ar-CH_4 atmosphere. The films with different C contents were obtained by varying the CH_4 partial pressure. The films deposited under the optimum conditions exhibit a structure of polycrystalline BC_2N (Yue et al., 2000).

2.1.2.3 Radio frequency magnetron sputtering

BCN films of diverse compositions have been deposited by magnetron sputtering, mainly from h-BN and graphite targets (Ulrich et al., 1998, 1999; Zhou et al., 2000; Lei et al., 2001; Yokomichi et al., 2002; Liu et al., 2005, 2006) or B_4C target (Louza et al., 2000; Martinez et al., 2001; Bengy et

al., 2009; Nakao et al., 2010) or B and graphite targets (Byon et al., 2004; Kim et al., 2004; Zhuang et al., 2009). In most cases the films were amorphous. It has been concluded that various intermediate compounds were obtained under different experimental conditions. Ulrich et al. (Ulrich et al., 1998, 1999) still obtained BCN films with C and BN phase separation. Liu et al. (Liu et al., 2005, 2006) also obtained the films of atomic-level BCN compounds from h-BN and graphite targets under various experimental conditions. In addition to the synthesis of microscopic ternary BCN films, the correlation between the chemical composition of films and the choice of targets has also been discussed. Lousa et al. (Lousa et al., 2000) found that the atomic ratio of B/C in the films kept almost constant as 4:1, similar to that of the target (B_4C).

2.1.2.4 Reactive DC magnetron sputtering

Reactive DC magnetron sputtering technique has been investigated to grow BC_xN_y films. Thin films were synthesized by pulsed DC magnetron sputtering from BN + C (Martinez et al., 2002) or B_4C (Johansson et al., 1996; Freire et al., 2001; Reigada et al., 2001; Chen et al., 2006) or B_4C + C (Xu et al., 2006a, 2006b) targets in Ar/ N_2 atmosphere. Effects of target power, target pulse frequency, substrate bias and pulse frequency on surface roughness were studied. Linss et al. used a set of targets with different B/C ratios (B, B_4C , BC, BC_4 , C) (Linss et al., 2004a, 2004b). Real ternary phases, presenting BCN bonds, were only found at low nitrogen contents; in boron-rich films. At higher nitrogen contents, the FTIR and XPS spectra were dominated by BN, CC/CN and $C\equiv N$ bonds, suggesting a phase separation into BN and C/ CN_x phases.

2.1.2.5 Ion Beam Assisted Deposition (IBAD)

During the last 10 years ion beam assisted deposition is used for boron carbonitride film deposition. The films were deposited by evaporating B_4C or B targets to produce BCN films. The assistance was performed with ions from the precursor gas nitrogen. IBAD has permitted to cover a wide range of compositions as a function of deposition parameters. Albella's group (Gago et al., 2000, 2001, 2002a, 2002b, 2002c) also reported that the c-BCN coatings had been synthesized successfully through evaporating B_4C target and the simultaneous bombardment of the ions from the mixture gas $Ar+N_2+CH_4$. Subsequently, they paid much attention to studying the chemical composition and bonding of the BCN coatings (Caretti et al., 2003, 2004, 2007, 2010). The structure of the BC_xN compounds grown by IBAD has shown to be quite sensitive to the C concentration (Caretti et al., 2010), as expected for compounds with supposedly different mechanical and electronic properties. The structure varies from a hexagonal laminar phase when $x < 1$ to a fully amorphous compound for $x \geq 4$. For $x = 1$, the compound consists of curved hexagonal planes in the form of a fullerene-like structure, being an intermediate structure in the process of amorphization due to C incorporation (Caretti et al., 2007, 2010).

Boron carbonitride (BCN) coatings were deposited on Si(100) wafers and Si_3N_4 disks by using IBAD from a boron carbide target. The BCN coatings were synthesized by the reaction between boron and carbon vapor as well as nitrogen ion simultaneously. The influence of deposition parameters such as ion acceleration voltage, ion acceleration current density and deposition ratio on the surface roughness and mechanical properties of the BCN coatings was investigated (Fei Zhou et al., 2006a, 2006b, 2006c).

2.1.2.6 Cathodic arc plasma deposition

Tsai et al. demonstrated that boron carbon nitride (BCN) thin films were deposited on Si (100) substrates by reactive cathodic arc evaporation from graphite and B_4C composite

targets. Ar+N₂ gases were added to the deposition atmosphere under pressure of 0.1–0.3 Pa. The deposition parameters included the substrate bias, the flow rate and ratio of the reactive gases have been varied. The analytical results (FEGSEM, HRTEM and XRD, see section 4) showed that the films revealed an amorphous cauliflower-like columnar structure (Tsai, 2007).

2.1.2.7 Ion beam implantation

BCN hybrid thin films were grown from ion beam plasma of borazine (B₃N₃H₆) on highly oriented pyrolytic graphite substrate at room temperature, 600°C, and 850°C. The substrate temperature and ion fluence were shown to have significant effects on the coordination and elemental binding states in BCN hybrid films (Uddin et al., 2005a, 2005b, 2006)

2.1.2.8 Electron-cyclotron-wave-resonance PACVD

Nanocrystalline BCN thin films were prepared on n-type Si(100) wafers using the electron-cyclotron-wave-resonance plasma-assisted chemical vapor deposition, whereby the energy for precursor ions was adjusted between 70 and 180 eV. ECR plasma of nitrogen was asymmetrically RF biased to sputter the high-purity h-BN/graphite target (Cao, 2003).

2.2 Chemical Vapor Deposition (CVD)

Chemical vapor deposition (CVD) is one of the potential growing techniques of SiC_xN_y and BC_xN_y films.

2.2.1 Silicon carbonitrides

2.2.1.1 Thermal CVD

The Si-C-N deposits were obtained by CVD using the mixture of gaseous compounds such as SiCl₄, NH₃, H₂, and C₃H₈ at very high temperatures from 1100 up to 1600°C (Hirai et al., 1981). The obtained amorphous deposits were mixtures of amorphous a-Si₃N₄, SiC and pyrolytic C (up to 10 wt. %). The deposits surface had a pebble-like structure.

The SiC_xN_y coatings were obtained by CVD at 1000–1200 °C using TMS-NH₃-H₂ (Beneddouch et al., 1997). It was found that SiC_xN_y films are not simply a mixture of the phases SiC and Si₃N₄, and have a more complex relationship between the three elements, corresponding to the existence of Si(C_{4-n}N_n) units.

Cubic crystalline Si_{1-x-y}C_xN_y films have been grown using various carbon sources by rapid-thermal CVD (Ting et al., 2002). The heat source was an ultraviolet halogen lamp with high-energy density. A mixture of carbon source, NH₃, and SiH₄ diluted in hydrogen was used as the source gas and introduced to the furnace. The different carbon sources are SiH₃CH₃, C₂H₄, and C₃H₈. The substrate's temperature was raised quickly from room temperature to 1000°C with a temperature raising rate in the range of 300–700°C/min. The Si_{1-x-y}C_xN_y films grown with C₃H₈ gas possesses the most desirable characteristics for electronic devices and other applications.

a-SiCN:H films were successfully obtained through an in-house developed vapor-transport CVD technique in a N₂ atmosphere (Awad et al, 2009). Polydimethylsilane (PDMS) was used as a precursor for both silicon and carbon, while NH₃ was mixed with argon to ensure the in-situ nitrogenation of the films. The increase of the N fraction in the a-SiCN:H films resulted in an increase of the average surface roughness from 4 to 12 nm. The a-SiCN:H films were found to be sensitive to their N content.

2.2.1.2 Hot-wire CVD method (HWCVD)

$\text{Si}_x\text{N}_y\text{C}_z\text{:H}$ films were produced by HWCVD, plasma assisted HWCVD (PA-HWCVD) and plasma enhanced (PECVD) using a gas mixture of SiH_4 , C_2H_4 and NH_3 without hydrogen dilution (Ferreira et al., 2006). For the HWCVD process the filament temperature was kept at 1900°C while for the PECVD component an RF power of 130W was applied. HWCVD films have higher carbon incorporation. PA-HWCVD films are N rich. PECVD films contain C and N bonded preferentially in the hydroxyl groups and the main achieved bonds are those related to C-H, C-N and Si- CH_x -Si.

a-SiCN:H thin films were deposited by HWCVD using SiH_4 , CH_4 , NH_3 and H_2 as precursors (Swain et al., 2008). Increasing the H_2 flow rate in the precursor gas more carbon is introduced into the a-SiCN:H network resulting in a decrease of the silicon content in the films from 41 at.% to 28.8 at.% and sp^2 carbon cluster increases when the H_2 flow rate is increased from 0 to 20 sccm.

2.2.1.3 Plasma Enhanced CVD (PECVD)

SiOCH and SiNCH films were deposited using TMS, mixed with O_2 or N_2 . (Latrasse et al, 2009). Plasmas of O_2/TMS and N_2/TMS gas mixtures can be sustained between 5 and 25 Pa.

SiCN cone arrays were synthesized on Si wafers using a microwave plasma CVD reactor with gas mixtures of CH_4 , SiH_4 , Ar, H_2 and N_2 as precursors (Cheng et al., 2006). The typical process temperature was 900°C . The SiCN cones have nanometer-sized tips and their roots vary from nanometers to micrometers. Field emission characteristic of SiCN cone arrays shows a low turn-on field with relatively high current density.

The amorphous SiCN films were grown on the Si(100) and fused silica substrates by microwave CVD using a mixture of SiH_4 , NH_3 , CH_4 and H_2 gases in various proportions (Chen et al., 2005). The stronger affinity of silicon to bond with nitrogen than to bond with carbon results in the complete absence of Si-C bonds in a-SiCN thin films.

SiCN coatings deposited on a Si substrate are produced by PECVD using methyltrichlorosilane (MTCS), N_2 , and H_2 as starting materials (Ivashchenko et al, 2007). The coatings are nanostructured and represent $\beta\text{-C}_3\text{N}_4$ crystallites embedded into the amorphous a-SiCN matrix with a hardness of 25 GPa and an Young's modulus of above 200 GPa). SiCN thin films deposited by PACVD using TMS and NH_3 have been investigated in order to determine their corrosion protective ability (Loir et al, 2007).

SiCN films were synthesized on Si wafer by microwave plasma CVD (MWCVD) with CH_4 (99.9%), high-purity N_2 (99.999%) as precursors, and additional Si column as sources (Cheng et al, 2004). When no hydrogen was introduced, the well-faceted crystals can be achieved at modest N_2 flow rate. A higher temperature results in second nucleation on previous crystals, larger crystalline size, and perfect crystalline facet.

Large and well faceted hexagonal crystallites in SiCN films can grow on Si and Ti substrates under higher nitrogen gas flow in the gaseous mixture of CH_4 and H_2 in the normal process of diamond deposition using a microwave plasma chemical vapor deposition (MP-CVD) (Fu et al., 2001).

2.2.2 Boron carbonitrides

The processes of CVD, considered in the present review, can be divided into three groups: 1) use of boron trichloride, 2) use of boron hydride, and 3) use of complex boron-nitrogen

compounds, as initial substances for obtaining boron carbonitride films. The first attempt of CVD production of boron carbonitride was reported by Badyan and co-authors (Badyan et al., 1972a) in which they used the CVD process with BCl_3 , CCl_4 , N_2 , and H_2 as starting materials:



At the synthesis temperature 2223K, they obtained solid solution with the $(\text{BN})_x\text{C}_{1-2x}$ composition, which was confirmed by X-ray diffraction (XRD) data. The authors assumed that the obtained material is a solution with substitution at the atomic level, as a result of substitution of a pair of carbon atoms in the hexagonal graphite lattice by nitrogen and boron atoms. Experimentally determined density of the material was $2.26 \pm 0.02 \text{ g/cm}^3$, which is close to the density of graphite (2.26 g/cm^3) and h-BN (2.27 g/cm^3). At a temperature above 2273 K, the obtained compound decomposed yielding boron carbide B_4C , graphite and nitrogen. Unfortunately, these works contain only a few data on the chemical and phase composition of the obtained compounds.

The BCN material was more thoroughly characterized for the first time by Kaner et al. (Kaner et al., 1987). In this paper, boron carbonitride with graphite-like structure was synthesized in the heated gas mixture:



In order to prevent the formation of h-BN, the authors recommend at first to mix BCl_3 and C_2H_2 (they do not react at low temperature), and then add ammonia into the hot region of the reactor. Chemical composition of the products obtained at 673 and 973 K was $\text{B}_{0.485}\text{C}_{0.03}\text{N}_{0.485}$ and $\text{B}_{0.35}\text{C}_{0.30}\text{N}_{0.35}$, respectively. The X-ray photoelectron analysis demonstrated that this material is not a simple mixture of boron nitride and graphite. The B1s and N1s spectra indicate that boron is bound both to carbon and to nitrogen atoms, while nitrogen atoms are bound both to carbon and to boron. These compounds exhibited semiconductor properties at room temperature. Transmission electron microscopy (TEM) showed that the film is a uniform material with grain size of about 10 nm.

Further investigations of the synthesis of boron carbonitride, involving the initial mixture of boron trichloride and methyl cyanide

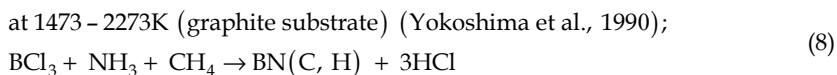
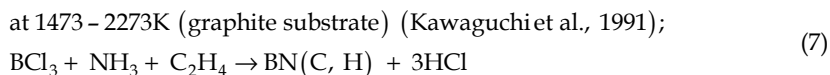
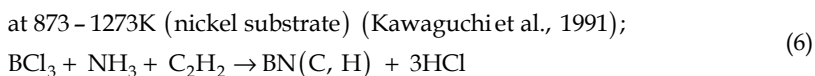


at temperature above 1173 K resulted in obtaining the stoichiometric compound BC_2N with lattice parameters $a=2.5\text{\AA}$ and $c=3.4\text{\AA}$ (Kouvetakis et al., 1989).

The synthesis of boron carbonitride by CVD from the gaseous mixture of boron trichloride, ammonia and acetylene at 973-1323 K resulted in obtaining BCN solid solution (Saugnas et al., 1992). Both amorphous and polycrystalline films were obtained; their composition was $\text{C}_5\text{B}_2\text{N}$. The material was stable to heating up to 1973K.

Nevertheless, by the 90-ies the chemical and phase composition, and properties of the compounds of this ternary system remained poorly investigated.

The h-BN films containing small amount of carbon and hydrogen as impurities were synthesized by means of CVD. The formula ascribed to this compound was $\text{BN}(\text{C,H})$. The synthesis of the films was performed using different initial gas mixtures within different temperature ranges:



In all these cases, BCl_3 and hydrocarbons (C_2H_2 , C_2H_4 or CH_4) were mixed beforehand to avoid the formation of boron nitride; ammonia was admitted directly into the reaction region near the substrate. The X-ray diffraction patterns of the BN(C,H) film synthesized according to reaction (6) were recorded by means of powder diffraction (Kawaguchi et al., 1991); the patterns contain a very broad (001) reflex and several reflexes the positions of which are close to the positions of peaks in t-BN. Additionally, the films synthesized according to reactions (7) and (8) exhibited diffraction patterns with only one diffraction reflex (001), the position of which is close to the positions of reflexes in h-BN, t-BN or graphite. The (100) and (101) reflexes are very weak and broadened. This result indicates that the BN(C,H) films obtained by means of CVD at high temperature possess the structure similar to that of t-BN. A similar ternary compound $\text{BC}_{0.43}\text{N}_{0.29}$ with turbostratic structure was synthesized on graphite at $T=1650\text{K}$ from a mixture of boron trichloride, methane, ammonia, and hydrogen at reduced pressure (Bessmann et al., 1990).

Amorphous boron-carbon-nitrogen (a-BCN) films have been fabricated by hot-wire CVD using BCl_3 , C_2H_2 and N_2 or NH_3 (Yokomichi et al., 2004).

The N concentration of the films synthesized by using a N_2 was below several at.%, and Cl atoms were incorporated to 3–5 at.%. The N concentration increased and the Cl concentration decreased by using NH_3 gas. In the case of NH_3 gas, the N concentration was nearly equal to the B concentration in most cases. The nearly identical concentrations in N and B resulted from high chemical reactivity between the BCl_3 and NH_3 gases, and the decrease in Cl concentration resulted from the removal as HCl due to NH_3 gas. These results indicate that the combination of BCl_3 and NH_3 is suitable for fabrication of a-BCN films by the CVD method.

BCN films were deposited by PECVD from a mixture of $\text{BCl}_3+\text{C}_2\text{H}_4+\text{N}_2+\text{H}_2+\text{Ar}$ in an industrial-scale DC plasma CVD plant (Kurapov et al., 2003, 2005). It was shown that the power density at the substrate has a large effect on the structure evolution of the BCN thin films. The authors suggest that with increasing power density the structure of the deposited films changed from an orientation where the c-axis is parallel to the substrate surface to a more randomly oriented structure.

During the last 10 years a group from Osaka University, Japan, studies intensively the PECVD synthesis from $\text{BCl}_3+\text{CH}_4+\text{N}_2+\text{H}_2$ mixtures and the properties of BC_xN_y films. The BC_xN_y films produced at 650°C were polycrystalline (Aoki et al., 2007, 2008a, 2008b, 2009a, 2009b, 2009c, 2009d; Etou, et al., 2002; Kimura, et al., 2005, 2009; Mazumder et al., 2009; Nesládek et al., 2001; Okada et al., 2006; Shimada et al., 2006; Sugino & Hieda, 2000; Sugino et al., 2000, 2001, 2002, 2008, 2010; Sugiyama et al., 2003, 2002; Tai et al., 2003; Umeda et al., 2004; Watanabe et al., 2008; Yuki et al., 2004; Zhang et al., 2005).

Amorphous BCN:H films were first prepared by Montasser et al. in 1984 by means of RF and microwave plasma-stimulated CVD using the initial gas mixture composed of diborane, ethane (or methane) and nitrogen (or argon) (Montasser et al., 1984, 1985, 1990). The synthesis of transparent stable films of hydrogenated boron carbonitride $B_xC_yN_z:H$ is described on substrates made of NaCl, Si and glass (at room temperature). Film deposition rate was 2-12 nm/min, refractive index 1.3-1.6. Correlation between micro-hardness and chemical composition of the film was established; in turn, it depends on synthesis conditions: total pressure in the reactor, concentration ratio of the initial compounds $B_2H_6:CH_4$ (or C_2H_6), and plasma discharge power. The $B_xC_yN_z:H$ films exhibited very complicated IR spectra; the authors have specially stressed that it is impossible to make conclusions concerning types of chemical bonds in the material basing only on the IR spectroscopic data.

Amorphous $BC_xN_y:H$ films were prepared in a capacitively coupled RF-PECVD reactor at deposition temperatures $<200^\circ\text{C}$ starting from $B_2H_6+CH_4+N_2+H_2$ gas mixture (Dekempeneer et al., 1996, 1997). Films were deposited on Si, steel and glass substrates. By varying the partial pressure of the gases, the composition was varied in a wide area of the B-N-C triangle. The same initial gas mixture was used by Polo et al. (Polo et al., 1998, 1999). It was found that the films had a less ordered structure.

Both amorphous and polycrystalline coatings were deposited by microwave low pressure CVD (LPCVD) using a mixture of $B_2H_6+CH_4+NH_3+H_2$ at substrate temperature in the range $800-1350^\circ\text{C}$. (Stanishevsky, 2010). Amorphous coatings were usually formed at lower substrate temperatures and were non-homogeneous across the coating thickness. Polycrystalline coatings were generally represented by both diamond and boron nitride phases. In one case, a polycrystalline coating with the composition of B_2CN_4 was fabricated. The turbostratic structure of BC_xN_y with various compositions was synthesized by bias-assisted hot-filament CVD (HFCVD) (Yu et al., 1999a, 1999b; Wang, 1999) within the temperature range 873-1273 K from $B_2H_6+CH_4+N_2+H_2$ mixture. Investigation of the films by means of XPS demonstrated that the three atoms B, C, N are chemically bound. Boron carbonitride is the main phase in all the deposited samples, though in some cases (at high temperature) this phase was co-deposited with boron carbide. The growth rate of BCN films decreased substantially with increased temperature. Chemical composition and morphology of the layers were also dependent on deposition temperature. The turbostratic BC_xN_y films were also grown by HFCVD from mixture of $B_2H_6+CH_4+NH_3+H_2$ (Xie et al., 1998).

Laser-assisted CVD was used for preparation of single-phase BC_xN_y layers at low temperature in a gas atmosphere containing $B_2H_6+CH_4+NH_3$, where the starting composition ratio could be varied in a large range. Layers exhibited turbostratic structure. Some planar structure, containing especially CB_2N groups, were suggested for the "unit cell" of CBN solid solutions (Morjan et al., 1999).

BCN films were deposited from mixture $B_2H_6+CH_4+N_2+H_2$ with electron beam excited plasma-chemical vapor deposition (EBEP-CVD) (Hasegawa et al., 2002, 2003). By controlling the flow rate ratios of the process gases, films with composition expressed as B_xC_yN , where $x=0.9-4.7$ and $y=0.5-6.0$ were obtained.

3. Syntheses of layers by single-source precursors

3.1 Silicon carbonitrides

The review highlights of the synthesis, processing and properties of non-oxide silicon-based bulk ceramics materials derived from silazanes and polysilazanes (Kroke et al., 2000).

At the present time, the alternative way of synthesis of silicon carbonitride films is through the use of low-toxicity siliconorganic compounds of various compositions and structures used as single source-precursors containing all the necessary elements Si, C, and N in one molecule. These compounds are of special interest because the molecular structure of the initial organosilicon compound affects the chemical and phase compositions plus the microstructure of deposited silicon carbonitride films.

3.1.1 Hexamethyldisilazane (HMDSN)

SiCN films were deposited by HWCVD method using HMDSN which is an organic liquid material (Izumi et al, 2006; Limmanee et al, 2008). It is found that the composition ratio of SiCN can be controlled by changing the flow rate of NH_3 . SiCN films can be deposited at the substrate temperature of 100°C . The dielectric constant can be controlled from 2.9 to 7 by changing the flow rate of NH_3 . The best efficiency of 13.75% for polycrystalline silicon solar cells using a-SiCN:H films was achieved at the temperature of 750°C .

SiCN films were obtained at a substrate temperature of 250°C by HWCVD using HMDSN (Nakayamada et.al, 2008). No SiCN film thickness was changed at all for 1 week in 10wt.% H_2SO_4 . A high corrosion resistance was confirmed.

SiCN nanopowders with different chemical compositions and characteristics can be prepared by CO_2 laser pyrolysis of organosilicon precursors (HMDSN or TMDSN, see section 3.1.9) or their mixture with silane (Dez et.al, 2002). A correlation is established between the synthesis conditions of powders and their chemical composition, morphology, structure and thermal stability.

a-SiCN thin films were deposited at $250\text{--}500^\circ\text{C}$ using a microwave plasma assisted CVD process fed with a mixture of CH_4 , N_2 , Ar and hexamethyldisilazane (Bulou et al., 2010). The increase of the CH_4 rate results in less organic, films of higher density and in an increase of the refractive index. The CH_4 addition to the gaseous mixture leads to a value of the Si/N ratio of films very close to stoichiometric Si_3N_4 .

Si:C:N:H thin films were deposited by PECVD using HMDSN as monomer and Ar as carrier gas (Vassallo et al., 2006). The films become more amorphous and inorganic at increasing RF plasma power. The wettability of the film has been studied and related to the chemical composition and to the morphology of the deposited layers.

SiC_xN_y films were synthesized with the composition varying in a wide range from those similar to silicon carbide to those similar to silicon nitride. HMDS was used by PECVD as single-source precursor in the mixtures with helium, nitrogen or ammonia in the wide range of temperatures from 100 up to 800°C and RF plasma powers from 15 up to 70 W (Fainer et.al., 1999, 2000, 2001a, 2001b, 2003, 2004, 2008).

3.1.2 Ethylsilazane

Thin films of amorphous Si-C-N were grown on Si(100) substrates by the pyrolysis of ethylsilazane in mixtures with H_2 in the temperature range of 873-1073K. (Bae et al., 1992). It was shown that the refraction index of these films varied from 1.81 to 2.09, elastic recoil detection decreased from 21 to 8% in the range of temperatures from 873K to 1073K. The chemical composition of the films was determined to be $\text{Si}_{43}\text{C}_7\text{N}_{48}\text{O}_2$.

3.1.3 Polysilazane

Non-stoichiometric X-ray-amorphous $\text{Si}_{3+x}\text{N}_4\text{C}_{x+y}$ was deposited during pyrolysis of polysilazane at 1440°C . (Schonfelder, 1993). The heating up to 1650°C results in formation of a mixture of the nanocomposites $\text{Si}_3\text{N}_4/\text{SiC}$ or $\text{Si}_3\text{N}_4/\text{SiC}/\text{C}$.

3.1.4 Bis(dimethylamino)dimethylsilane (BDMADMS)

SiCN thin films for membrane application were deposited by PECVD from bis(dimethylamino)dimethylsilane (BDMADMS) (Kafrouni et al., 2010). Single gas permeation tests have been carried out and a helium permeability of about 10^{-7} mol m⁻² s⁻¹ Pa⁻¹ was obtained with an ideal selectivity of helium/nitrogen of about 20. Moreover these PECVD membranes also seem to be stable at higher temperature in air (up to 500°C).

a-Si:C:N:H films were produced by RPCVD from dimethylaminodimethylsilane (Blaszczyk-Lezak et al., 2005, 2006). The films deposited at different substrate temperatures (30–400°C). Strong adhesion to a substrate, high hardness ($H=28\text{--}35\text{ GPa}$), low friction coefficient ($\mu=0.04$, against stainless steel), and strong resistance to wear (predicted from high “plasticity index” values $H/E^*=0.10\text{--}0.12$) were found for these films suggest that these materials are promising coatings for improving tribological properties of engineering materials for advanced technology.

Siliconnitride-like films were deposited at low temperatures using RF inductively coupled plasma fed with bis(dimethylamino)-dimethylsilane (BDMADMS) and argon (Ar) (Mundo et al., 2005). The results indicate that at high power input and low monomer-to-Ar ratio, low carbon and high nitrogen content films can be obtained, stable and with a refractive index of 1.87.

3.1.5 Bis(dimethylamino)methylsilane (BDMAMS)

The RPCVD with bis(dimethylamino)methylsilane precursor was used for the synthesis of Si:C:N films (Blaszczyk-Lezak et al., 2007). The increase of T_s enhances crosslinking in the film via the formation of nitridic Si-N and carbidic Si-C bonds. On the basis of the structural data a hypothetical crosslinking reaction has been proposed, contributing to silicon carbonitride network formation.

3.1.6 Tris(dimethylamino)silane (TrDMAS)

Amorphous SiCN films were fabricated by RPCVD using H₂ and TrDMAS, (Me₂N)₃SiH, as a novel single-source precursor, being a carrier of Si-N and C-N units (Wrobel et al., 2010). The Arrhenius plot of the temperature dependence of the film density implies that for $T_s > 200^\circ\text{C}$ a thermally enhanced crosslinking process predominates, and the density reaches a high value of $\rho \approx 3.0$ g cm⁻³ at $T_s = 350^\circ\text{C}$. SiCN films are morphologically homogeneous materials exhibiting very low surface roughness $R_{rms} = 0.3$ nm. The photoluminescence of SiCN films is sensitive to the contribution of the Si-CH₂-N links.

3.1.7 Bis(trimethylsilyl)carbodiimide (BTSC)

Amorphous SiCN coatings were prepared on steel substrates by RF-PECVD from BTSC (Zhou et al., 2006; Probst et al., 2005; Stelzner et al., 2005). The results of the studies show that the coatings obtained on the RF-powered electrode (cathode) were black, thick (>20 μm) and hard (21–29 GPa), while those grown on the grounded electrode (anode) were yellow, thin (<4 μm) and soft (~ 5 GPa). The surfaces of all coatings were very smooth with a maximum rms roughness between 2 nm and 5 nm for an area of $5\mu\text{m} \times 5\mu\text{m}$. Wear tests at 600°C showed that the coatings possess an excellent high-temperature stability.

3.1.8 Dimethyl(2,2-dimethylhydrazino)silane (DMDMHS) and dimethyl-bis-dimethylhydrazino silane (DM-bis-DMHSN)

SiCN films were synthesised by RPECVD using a novel single-source precursors dimethyl(2,2-dimethylhydrazino) silane $(\text{CH}_3)_2\text{HSiNHN}(\text{CH}_3)_2$ (DMDMHS) and dimethyl-bis-dimethylhydrazino silane $(\text{CH}_3)_2\text{Si}[\text{NHN}(\text{CH}_3)_2]_2$ (DM-bis-DMHSN), which are silyl derivatives of 1,1-dimethylhydrazine (Smirnova et al., 2003). The films were found to be predominantly amorphous with a number of crystallites embedded in an unstructured matrix. The crystalline phase can be indexed as a tetragonal cell with lattice parameters $a=9.6 \text{ \AA}$ and $c=6.4 \text{ \AA}$. This novel material has an optical band gap varying within the energy range from 2.0 to 4.7 eV.

3.1.9 Tetramethyldisilazane (TMDSN)

Si:C:N films were produced by RPCVD from mixture of a 1,1,3,3-tetramethyldisilazane precursor with H_2 (Błaszczyk-Lezak et al., 2006a, 2006b; Wrobel et al., 2007). An increase in T_s leads to the elimination of the organic groups and subsequent crosslinking via the formation of Si-C and Si-N networks. In view of the relatively high hardness (16 GPa) and a low friction coefficient μ value (0.02-0.05 against stainless steel) found for the a-Si:C:N film deposited at $T_s=400^\circ\text{C}$, this material may be useful as a tribological coating for metals.

3.1.10 Hexamethylcyclotrisilazane (HMCTS)

Silicon nitride films were obtained in glow-discharge plasma from HMCTS in a mixture with nitrogen gas or ammonia at low temperatures (below 150°C) (Voronkov et al., 1981). Chemical composition was analyzed with IR-spectroscopy and demonstrated that in the films obtained at such conditions are present Si-N, C-C, Si-H (or $\text{Si-C}\equiv\text{N}$) and N-H bonds.

The silicon nitride films synthesized from HMCTS with a set of additional gases such as NH_3 , H_2 , and N_2 by PECVD at temperatures ($150\text{--}400^\circ\text{C}$) and plasma power of 5-50 W (Brooks & Hess, 1987, 1988). The films obtained from a gas mixture (HMCTS + NH_3) and characterized by lesser than 4 at. % carbon and hydrogen content of about 25 at. % are close to the chemical composition of silicon nitride films. The Si-N bonds are dominant. The films obtained from the mixture (HMCTS + H_2), contain significant amount of carbon (30-40 at. %) and 21 at. % of hydrogen. These films contain both Si-N and Si-C bonds.

SiCN films were obtained by RPECVD using HMCTS in a mixture with helium or nitrogen in the range of temperatures of $100\text{--}750^\circ\text{C}$ and plasma powers of 15-50W (Fainer et al, 2009a, 2009b). The low temperature $\text{Si}_x\text{N}_y\text{O}_z\text{:H}$ films are compounds with chemical bonds among the main elements Si, N, and C together with impurity elements such as hydrogen and oxygen. The empirical formula of the high-temperature films is represented by Si_xN_y . The absence of hydrogen in these films leads to good thermal stability and microhardness. These films exhibit an excellent transparency with a transmittance of ~92-95% in the spectral range $\lambda=380\text{--}2500 \text{ nm}$.

3.1.11 N-bromhexamethyldisilazane

SiCN films were produced from the new volatile organosilicon compound N-bromhexamethyldisilazane (Smirnova et al, 2008). An increase in the refractive index from 1.5 to 2.2 and a decrease in the optical band gap width from 4.5 to 2.1 eV is observed as the chemical composition of the films changes in the temperature interval of 470-870K.

3.2 Boron carbonitrides

During the recent years, special attention was paid to the introduction of volatile compounds – single-source precursors – containing all the necessary atoms (boron, carbon, and nitrogen) for the synthesis of boron carbonitrides. The use of complex organoelemental volatile compounds should be considered as an essential step forward. Since these compounds are incombustible and rather stable toward reactions in the natural atmosphere, their application in technology is preferable over chemically active boron trichloride and diborane. These substances have a well-defined ratio of B:C:N due to their stoichiometry, and they can be evaporated and easily handled due to their chemical and physical properties. With these compounds, one can obtain layers of different composition using different gaseous additives (ammonia, nitrogen, hydrogen).

In CVD processes, molecular precursors such as dimethylamine borane $(\text{CH}_3)_2\text{HN}\cdot\text{BH}_3$ (DMAB), trimethylamine borane $(\text{CH}_3)_3\text{N}\cdot\text{BH}_3$ (TMAB), triethylamine borane $(\text{C}_2\text{H}_5)_3\text{N}\cdot\text{BH}_3$ (TEAB), N,N',N'' -trimethylborazine $(\text{CH}_3)_3\text{N}_3\text{B}_3\text{H}_3$, N,N',N'' -triethylborazine $(\text{C}_2\text{H}_5)_3\text{N}_3\text{B}_3\text{H}_3$, tris-(dimethylamino)borane $\text{B}(\text{N}(\text{CH}_3)_2)_3$, (N-pyrrolidino)diethylborane $\text{C}_8\text{H}_{18}\text{BN}$, pyridine borane $\text{C}_5\text{H}_5\text{NBH}_3$, and triazaborabicyclohexane $\text{BN}_3\text{H}_2(\text{CH}_2)_6$ have been used as boron, carbon, and nitrogen sources.

3.2.1 Trimethylamine borane (TMAB)

Kosinova et al. pioneered the use of trimethylamine borane complex $(\text{CH}_3)_3\text{N}\cdot\text{BH}_3$ in both RF PECVD (40.68 MHz) and LPCVD processes for BCN film deposition (Kosinova et al., 2001, 2003a, 2003b; Fainer et al., 2001). Boron carbonitride films were grown by PECVD using TMAB and its mixtures with ammonia, hydrogen, or helium. The effects of the starting-mixture composition and substrate temperature on the chemical composition of the deposits were studied. The results indicate that the initial composition of the gas mixture, the nature of the activation gas, and substrate temperature play a key role in determining the deposition kinetics and the physicochemical properties of the deposits. Depending on these process parameters, one can obtain h-BN, h-BN + B_4C , or h- BC_xN_y films.

h-BCN films with a thickness of $\approx 4 \mu\text{m}$ were synthesized on Si(100) substrate by RF (13.56 MHz, 1kW) and microwave (2.45 GHz) PECVD using mixture of TMAB and H_2 as precursors (Mannan et al., 2007). The temperature of deposition was 300 and 600°C for RF PECVD, and 840-850°C for MF PECVD processes. The films were amorphous with an inhomogeneous microstructure confirmed by XRD and FEG-SEM. XPS and FTIR suggested that the films were consisted of a variety of bonds between B, C and N atoms such as B-N, B-C and C-N. Oxygen was inevitably incorporated as a contaminant (13-15 at.%). The effects of the deposition conditions, including microwave power and carrier gas, on the film properties was studied by Kida (Kida, 2009). The deposition time varied between 0.5 h and 2 h with microwave powers of 200, 300, and 400W (2.45 GHz). Substrate temperatures depended on the microwave power applied and ranged between 700 and 900°C. N_2 and a gas mixture of CH_4 (10vol.%) and H_2 (90vol.%) were used as carrier gases. The films deposited were found to have fibrous nanostructures consisting of nanosized fibers. For the films deposited under N_2 flow, boron and nitrogen contents of the films increased as the microwave power increased, leading to the formation of B-N and C-N bonds, as confirmed by FTIR. Moreover, deposition at higher microwave power reduced the oxygen content in the films. However, for films deposited under CH_4+H_2 flow, B-O bond formation dominated ($\text{B}_{30}\text{C}_{15}\text{N}_4\text{O}_{51}$), owing to the high reactivity of boron with oxygen in the absence of N_2 .

3.2.2 Dimethylamine borane (DMAB)

Boron nitride films were obtained by means of PECVD of DMAB+(CH₃)₂NH·BH₃ - in mixture with ammonia (Schmolla et al., 1983; Bath et al., 1989, 1991, 1994) or nitrogen (Baehr et al., 1997; Boudiombou et al., 1997; Abdellaoui et al., 1997).

Amorphous and poor crystalline phases in the B-C-N system were obtained by plasma chemical decomposition of DMAB in mixture with hydrogen and argon (Loeffler et al., 1997).

3.2.3 Triethylamine-borane (TEAB)

In the study of Levy et al., films consisting of B-N-C-H have been synthesized by LPCVD using the liquid precursor TEAB = (C₂H₅)₃N·BH₃ complex both with and without ammonia (Levy et al., 1995). In the absence of NH₃, the growth rate dependency on temperature follows an Arrhenius behaviour with an apparent activation energy of 11 kcal/mole. The addition of NH₃ has the effect of lowering the deposition temperature to 300°C and doubling the apparent activation energy. The deposits were found to be in all cases amorphous. A significant increase in carbon concentration was observed above 650°C due to the break up of the amine molecule. The addition of NH₃ was used to reduce the carbon content in the films. The same result of the ammonia effect was also obtained by Kosinova et al. (Kosinova et al., 1999, 2001). The BCN films were deposited on Si(100), GaAs(100) and fused silica substrates using TEAB with and without ammonia by both LPCVD and RF-PECVD (40.68 MHz) methods.

With TEAB in the direct current glow discharge plasma process (GD-PECVD) the highest carbon concentrations (48–73 at.%) in BCN films are obtained without using an additional carbon source (Thamm et al., 2005). Elastic recoil detection analysis (ERDA) measurements yield information on the layer composition regarding the concentrations of the elements boron, carbon, nitrogen, and hydrogen. The hydrogen content in the produced BCN layers strongly depends on the substrate temperature and increases up to 35 at.%. Depth profiles show a homogeneous distribution of the elements B, C, N, and H over the entire layer thickness.

The paper of Mannan et al. presents the chemical bonding states and the local structures of oriented hexagonal BCN films with the grain size of around 100 nm synthesized by microwave PECVD (MW-PECVD) using mixture TEAB and CH₄+H₂ as the carrier gas (Mannan et al., 2008). The deposition was performed at different microwave power settings of 200–500W at working pressure of 5.0 Torr. The substrate temperature was measured to be 750 and 850°C, respectively. It was estimated a particle size of around 100–150 nm. The crystallinity was not good as the hexagonal structures appeared in a short-range order which could not be detected by XRD.

3.2.4 Tris-(dimethylamino)borane (TDMAB)

Homogeneous carbon boronitride coatings were produced with cold-wall CVD varying the temperature of the deposition substrate from 800°C up to 1400°C using tris-(dimethylamino) borane B[N(CH₃)₂]₃ as a single-source molecular precursor. The deposition temperature has an influence on the growth rate as well as on the coating composition (C: 35–75at%; B: 12–40at%; N: 7–24at%). Below 700°C substrate temperature no deposition can be observed. At temperatures between 700°C and 800°C the layers grow very slowly and they are oriented parallel to the substrate's surface. If temperatures are raised to 900°C the layer already seems to be under stress as it cracks into small pieces during cooling to room temperature. Higher

substrate temperatures lead to the formation of hemispheres (approximately 10 μm in diameter) on the surface, thus increasing the roughness of the BCN layers (Gammer et al., 2002).

BCN-layers were deposited in a hot-filament supported reactor using TDMAB (Weissenbacher et al., 2002, 2006). These experiments were strongly influenced by the stability of the Ta-filament. At filament temperatures of 1500°C layer deposition on the surface of the filament takes place, at temperatures higher than 2000°C liquid phase formation led to filament breakdown in many cases. The morphology of the deposited BCN layers on hard metal substrates (WC-Co) depends on the deposition conditions and films contain high amounts of tantalum (BCN-Ta layers).

Methyl-BCN films were deposited by plasma-assisted CVD (PACVD) using mixture of TDMAB and N_2 at 350°C (Aoki et al., 2010a, 2010b).

Hexagonal boron carbonitride hybrid films - sp^2 -BCN phase with h-BN-like configuration - have been synthesized on Si(100) and on highly oriented pyrolytic graphite, respectively, by RF-PACVD using TDMAB (Mannan et al., 2009a, 2009b, 2010). The deposition was performed at different RF powers of 400–800W, at the working pressure of 2×10^{-1} Torr and temperature 650–750°C.

The influence of the B/C/N containing single-source precursors pyridine-borane (PB) and triazaborabicyclodecane (TBBID) on the chemical composition of boron carbonitride thin films was investigated in (Hegemann et al., 1997, 1999). The films are deposited via a PACVD process, activated by 13.56 MHz radio frequency (RF). N_2 , Ar and He serve as carrier gases. It becomes evident, that from a certain bias voltage, the self-bias in capacitively RF electrical discharges mainly influences the chemical composition of the BCN films independent of the kind of the used precursor. Films that were either deposited in He using a low power density or in N_2 using a high power density showed comparable properties. Analysis of these films showed their chemical composition to be BC_4N .

3.2.5 (N-pyrrolidino)-diethylborate (PEB)

BCN films were deposited on polycarbonate and silicon wafer by means of different RF PACVD (inductively coupled and capacitively coupled RF PACVD), by use of liquid organic compound (N-pyrrolidino)diethylborane ($\text{C}_8\text{H}_{18}\text{BN}$) as precursors. Deposition was carried out on at 95–120°C. A mixture of argon, hydrogen, and nitrogen was used as process gas. The layer shows a columnar structure. The composition of BCN films deposited ranged between $\text{BC}_{7.3}\text{N}_{0.8}$ and $\text{BC}_{0.9}\text{N}_{0.6}$ (Wöhle et al., 1999; Ahn et al., 2003).

3.2.6 Borazine derivatives

Amorphous semiconductor BCN films were produced by means of pyrolysis of borazine derivatives (tris(1,3,2-benzodiazaborolo)borazine) at 1073 K (Maya, 1988a, 1988b; Maya, & Harris, 1990). Quartz, titanium and silicon were used as substrates. Chemical analysis showed that the synthesized material had the composition $\text{BC}_{5.2}\text{N}_{1.8}\text{H}_{1.9}\text{O}_{0.45}$. The density of the coating was 2.05 – 2.09 g/cm³.

3.2.6.1 Trimethylborazine

Mixtures of N,N',N'' -trimethylborazine = $(\text{CH}_3)_3\text{N}_3\text{B}_3\text{H}_3$ (TMB) (the B:C:N ratio 1:1:1) and argon have been used to deposit BCN:H films by means of ECR PECVD processes at 100–150°C (Weber et al., 1992, 1993). Amorphous BCN layers were deposited on a polycarbonate substrate by RF PACVD at low temperature (95–120°C) using a mixture of TMB and H_2 , N_2 , or Ar (Wöhle et al., 1999). The composition of the layers varied in a wide range. The boron

content of the films ranged from 3at% to 42at%, the carbon content from 16at.% to 80at.%, and oxygen content from 2at.% to 10 at.%. BCN films with hexagonal turbostratic graphite like structure were deposited by both isothermal chemical vapour deposition (ITCVD) under atmospheric pressure and PECVD from gaseous mixtures of trimethylborazine, toluene and ammonia at 950°C (Stockel, 2002, 2003). Parallels between ITCVD and PECVD films emerged in the case of chemical composition and the correlation between carbon content and hardness values. Considerable differences exist with regard to the microstructure, especially the texture of the films. Moreover in ITCVD films the carbon is preferentially incorporated between the BN basal planes, whereas in PECVD films it is incorporated preferentially in between the BN basal planes as well. BCN coatings were deposited on polycarbonate by means of a capacitively or inductively coupled RF-PACVD (capacitive coupled plasma (CCP) vs. inductively coupled plasma (ICP)) using the elemental-organic compound trimethylborazine as precursor. The influence of the plasma parameters on the properties of films has been discussed (Ahn et al., 2003).

BCN:H films on silicon substrates were deposited with two different PECVD techniques (Thamm et al., 2005, 2007). A microwave plasma with RF-bias enhancement (MW-PECVD) and a direct current glow discharge plasma system (GD-PECVD) was used with TMB and benzene as an additional carbon source. Argon and nitrogen were used as plasma gases. Substrate temperature, substrate bias and gas composition were varied. The hydrogen content in the produced BCN layers strongly depends on the substrate temperature and increases up to 35at.%. Depth profiles show a homogeneous distribution of the elements B, C, N, and H over the entire layer thickness. Impurities such as oxygen or argon are detected in only small quantities (below 0.5at.%) and the concentration does not increase towards the surface. The hydrogen content mostly depends on the substrate temperature during the coating process. If the layers are deposited on 50°C substrate temperature (MW-PECVD) the hydrogen content increases up to 35at.%. If the temperature is increased up to 800°C, only 8at.% hydrogen are detected, independently of the plasma gas. The variation of the MW plasma power and RF-bias have no significant effects on the layer composition. Multicomponent films were grown by PECVD from N-trimethylborazine–nitrogen mixtures at temperatures from 373 to 973 K and varied RF power. According to XPS and IR spectroscopy results, the major component of the films is boron nitride. The films grown at temperatures below 673 K contain hydrogen. The higher temperature films contain carbon (Sulyaeva et al., 2007, 2009, 2010).

3.2.6.2 Triethylborazine (TEB) and Tripropylborazine (TPB)

Thermolysis of N-triethylborazine = $(C_2H_5)_3N_3B_3H_3$ (TEB) and N-triethylborazine = $(C_3H_7)_3N_3B_3H_3$ (TPB) at 500°C produces homogeneous, amorphous boron carbonitride phases, whose compositions are dependent upon the borazine substituent, and whose structures are similar to that of icosahedral boron carbide B_4C (Brydson et al., 2002). The deposition of BCN-layers by decomposing TEB was performed in a hot-filament CVD apparatus and for the gas activation a carburized Ta wire was used. Untreated, etched and diamond coated WC–Co hardmetal inserts were used as substrates. Substrate temperature was 890°C. The deposition parameters filament temperature (1800–2200°C), precursor flow rate and gas atmosphere were varied. The layer growth rates increased with the precursor flow rate and showed less influence of the substrate material. Layer morphology was of the pyrolytic type. When the layers became thick they tended to eliminate from the substrate. Due to the atomic hydrogen produced at the filament the deposition rate decreased in case

of hydrogen atmosphere compared to the experiments in argon atmosphere. This can be explained by etching reactions of the atomic hydrogen. Due to the etching reactions of the atomic hydrogen the IR-spectra also look different. Nevertheless, it was not possible to identify a cubic phase from the IR or XRD measurements (Weissenbacher et al., 2003).

4. Physical and chemical characterization

Mainly for judging the synthesis success, the products have to be characterized for physical and chemical properties. The analytical procedures are quite different, belonging to the interest of the scientists. One part is interested in the physical parameters, e.g., as mechanical (e.g., dimension, hardness, roughness), optical (e.g., reflectivity, absorption coefficient), thermal (e.g., conductivity), and electrical and electronic (e.g., resistivity, conductivity, band gap) properties. An other part examines the chemical properties, e.g., the elemental composition, the phase state (e.g., crystallinity, amorphous state), the character of chemical bonds (e.g., participation of the elements, single/double/triple, energy, distances, ionic/covalent/metal/van der Waals), and the chemical reactivity (e.g., inertness). Obviously, there is a relation between the physical and the chemical parameters.

The first citation of a carbonitride, to our knowledge, was given by a Soviet group (Dubovik & Struk, 1965). They referred to papers, published earlier (Samsonov et al., 1962; Chelepenkov et al., 1964). These scientists synthesized the product by nitriding of boron carbide and were interested in an excellent thermal resistance. The test of the material as crucibles at 1600-2000°C was successful, but a fundamental characterization was not performed. This situation changed a little later, when the elemental composition and structure of carbonitrides of different productions were determined (Kosolapova et al., 1971). Such information was derived from X-ray and electron diffraction measurements. Later on, nearly all papers dealing with the synthesis of silicon or boron carbonitrides contain a voluminous chapter with physical and/or chemical characterization of the products.

The description of the methods is partly taken from text books, lecture notes, application notes of manufacturers of analytical instruments, from the internet encyclopaedia Wikipedia, and from other not-authorized sources in the internet.

4.1 Ellipsometry

Ellipsometry is an optical method in material science and surface physics (Fujiwara, 2007; Tompkins, 2006). It permits to determine the real and the imaginary part of the complex dielectrical refractory index and of the thickness of thin layers, as well. It can be used for various materials, as organic and inorganic substances (metals, semiconductors, insulators). Ellipsometry is working in a wide range: UV, visible part, and far in the IR (THz range) light. By means of this method the change of the polarization state at reflection or transmission is determined. This change is given by the relation of the reflection coefficients vertical r_s and parallel r_p to the incidence plane of the polarized light. In nearly all cases a model analysis is carried out, in which the optical constants are described by a model dielectric function. In all former papers of the authors the absorption coefficient, refractory index, and the thickness of the silicon and boron carbonitride layers are determined by ellipsometry (Fainer et al., 1997; Kosinova et al., 1999; Hoffmann et al., 2007; Baake et al., 2010).

4.2 Indentation

The hardness of the synthesized products is determined by usual methods, described in text books. The so called Mohs' hardness (mainly for minerals) is divided in a graduation

scale of 10 parts. These parts are defined by the materials which scratch the surface of a sample. The indentation, and mainly the nano-indentation is a local (positional) high-resolution method for the characterization of thin solid samples. The method is based on the measurement of force and path during an elastic/plastic contact of a hard tester (indenter) with the sample. The advantages of this procedure are: Extremely high-resolution lateral and in the depth, no optical measurement at indentation is necessary, simultaneous determination of the hardness and of the Young's modulus, generation and measurement of defined scratches. In most cases, a diamond tip is pressed into the sample with increasing force. Then the force is decreased to zero. First, an elastic deformation is observed, followed by a plastic deformation at higher force. Only the elastic deformation is traced back during the unloading. Several methods are given to evaluate the data. In most cases, the contact stiffness is determined at the beginning of the unloading (Bauer-Marschallinger et al., 2007).

4.3 Scanning electron microscopy (SEM)

In this type of an electron microscope the sample is scanned by a high-energy beam of electrons. Utilizable information are mainly derived from signals of secondary electrons (SE), of back-scattered electrons (BSE), and of characteristic X-rays. The secondary electrons can produce very high-resolved images of the sample surface, showing details less than 5 nm in size. Because the intensity of the BSE signal is strongly related to the atomic number (Z) of the specimen, BSE images provide information about the lateral distribution of different elements. In case of relaxation of the excited atoms in the sample, characteristic X-rays are emitted. These are used to determine the elemental composition and to measure the abundance of the elements in the sample. The information depth is related to the primary electron energy (0.5 keV – 40 keV), to the mean atomic number and the density of the sample, and to the energy of the emitted X-rays (Moseley's law gives the relation between energy and atomic number). The electrons typically are thermoionically emitted from a tungsten (W) or a lanthanum hexaboride (LaB₆) cathode. For conventional imaging in SEM, the specimen must be electrically conductive. Nonconductive specimens, e.g. ceramics, tend to charge and, therefore, have to be coated by an ultrathin conducting layer (e.g., gold, carbon). Back scattered electron imaging, quantitative X-ray analysis, and X-ray mapping of materials (e.g., metals, ceramics, geological) require that the surfaces have to be ground and polished to an ultra smooth surface. Special high resolution coating techniques are used for high magnification imaging of inorganic thin films. As an example, SEM images of carbonitride layers are given in Fig. 1.

The most common imaging mode collects the low-energy (< 50 eV) secondary electrons (SE), which originate from a thin (few nanometers) surface layer of the sample. These electrons are biased to about + 2 kV and detected by scintillator-photomultiplier systems. The high-energetic back-scattered or reflected electrons are usually measured by detectors of the scintillation or semiconductor types. The X-rays are detected by wavelength-WDXRS) or energy-dispersive (EDXRS) systems. Expended systems contain several WDXRS detectors (arranged vertically and horizontally) and one EDXRS detector – so called electron micro probe analyzer (EMPA). More detailed information is given in the text books and in special papers. As introduction the monography of Goldstein et al. is suggested (Goldstein et al., 1981).

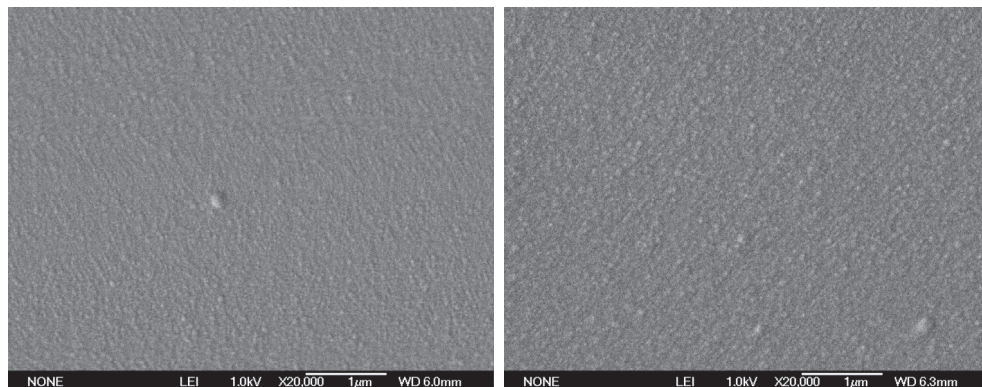


Fig. 1. Typical SEM images of surfaces of PECVD SiC_xN_y film (left) and BC_xN_y (right).

4.4 Atomic Force Microscopy (AFM)

The atomic force microscopy (AFM) or scanning force microscopy (SFM) provides a three-dimensional profile of the sample surface (in comparison to SEM, which works two-dimensional). It is of very high-resolution on the order of fractions of a nanometer. The AFM consists of a cantilever with a sharp tip (silicon or silicon nitride) to scan the sample surface. When the probe is brought to the proximity of the specimen mechanical contact force, van der Waals forces, capillary forces, chemical bonding, electrostatic and magnetic forces, Casimir forces, and/or solvation forces influence the deflection of the cantilever. The deflection is, typically, measured by a laser spot reflected from the top of the cantilever. In best cases, individual surface atoms can be identified. The advantages of AFM are in comparison to SEM: The receiving of a three-dimensional image, the sample viewing without any treatments (coatings), working perfectly in ambient air, giving true atomic resolution in ultra-high vacuum (and in liquid environment). The disadvantages are: Single scan image size in the micrometer range (height: 10-20 µm, scanning area: 150×150 µm²), and a limitation in the scanning speed (Giessibl, 2003; Sugimoto et al., 2007).

4.5 X-ray (XRD), electron, and neutron diffraction

The diffraction methods are used to determine the arrangement of atoms within a crystal. That directly means that the method is not suitable for amorphous materials. Beneath the structure and phases, a quantitative determination of the elemental composition can be derived. Therefore, X-ray diffraction was first used for the characterization of carbonitrides (Kosolapova et al., 1971). X-ray crystallography is called the chief method for characterizing the atomic structure of new materials.

A regular array of scatterers (crystal) produces a regular array of spherical waves. In most directions these waves cancel one another out through destructive interference, they add constructively in a few specific directions, determined by Bragg's law (8)

$$2d \cdot \sin \Theta = n \cdot \lambda, \quad (8)$$

where d = spacing between diffraction planes, Θ =incident angle, n =any integer, and λ =wavelength of the beam. That is successful because the wavelength λ is typically of the

same order of magnitude as the spacing d between planes of the crystal ($1\text{--}100\text{ \AA}$). The initial studies revealed the typical radii of atoms, and confirmed many theoretical models of chemical bonding, such as the tetrahedral bonding of carbon in the diamond structure (Bragg & Bragg, 1913). In material sciences, many complicated systems (e.g., fullerenes) were analyzed using single-crystal methods. The Cambridge Structural Database contains over 500,000 structures; over 99 % of them were determined by X-ray diffraction.

In laboratories X-ray diffraction devices contain X-ray tubes (X-ray generators) as sources. Electrons are thermally emitted from a metal and extracted through a strong electric potential (e.g., 50 kV) and directed to a metal plate (mostly Cu). Thereby, bremsstrahlung and some characteristic lines are emitted. Usually, the X-ray tube has a stationary anode (2 kW). For application of an intensive beam a rotating anode (14 kW) is used. The brightest and most useful X-ray source is a synchrotron. These systems allow a better resolution, and they make it convenient to tune the wavelength (energy) of the radiation. An XRD diffraction diagram recorded at a synchrotron beam is given in Fig. 2.

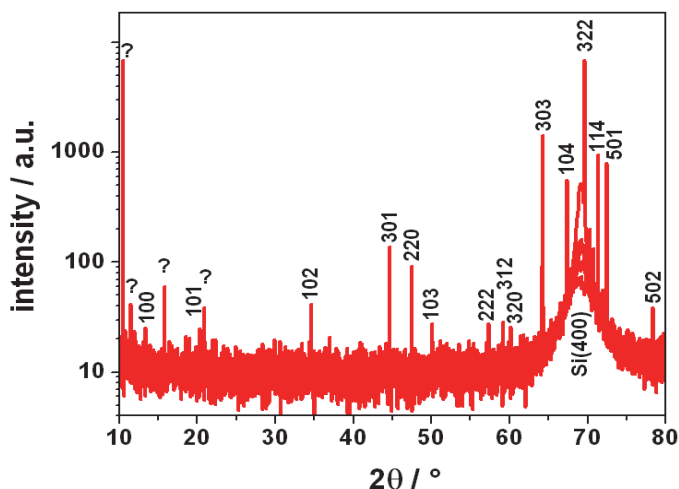


Fig. 2. The typical XRD-SR pattern of nanocomposite SiC_xN_y film shows that the peaks' position is close to standard $\alpha\text{-Si}_3\text{N}_4$ phase. There are some unknown peaks at small diffraction angles indicated by "?", which do not correspond to peaks positions of other known phases of the Si-C-N system.

The intensities of the reflections are recorded by photographic film, area detector or by a charge-coupled device (CCD) image sensor. To collect the total information, the crystal must be rotated step-by-step through 180° ($\Theta/2\Theta$ -geometry). As an additional method grazing incidence XRD is used.

Electrons interact with positively charged atomic nuclei and with the surrounding electrons, whereas X-rays interact with valence electrons only, and neutrons scatter by atomic nuclei. Whereas X-rays interact relatively weakly with the electrons, for some applications electron beams are used to examine relatively thin crystals ($> 100\text{ nm}$). The strong interaction of charged electrons with matter by Coulomb forces (about 1000 times stronger than for X-rays) allows determination of the atomic structure of extremely small volumes. The field of application of electron diffraction ranges from bio molecules over organic thin films to the

complex structures of (nanocrystalline) intermetallic compounds and zeolites. Electron diffraction is used in solid state physics and chemistry in devices as transmission electron microscopy (TEM, see 4.13) or scanning electron microscopy (SEM, see 4.3).

For structural determination of light elements neutron diffraction is the favoured method (Ibberson & David, 2002). For application of monochromatic, intense beams nuclear reactors and spallation neutron sources are used. Neutrons being uncharged scatter much more readily from the atomic nuclei than from the electrons. As mentioned, neutron scattering is very useful for observing the positions of light elements, especially hydrogen, which is essentially invisible in the X-ray diffraction. The samples are mostly exposed as powders and their sizes are relatively large.

4.6 X-ray Reflectometry (XRR)

X-ray reflectometry is a highly accurate method for the determination of layer thickness (Als-Nielsen, 2001). The reflectance of the sample is measured as a function of the grazing incidence angle of X-rays. Due to interference effects of the radiation from each layer, oscillations are observed in the reflectance curve. The oscillation period is mainly determined by the layer thickness, the oscillation amplitude depends on the densities and on the surface roughness. The reflectance curve can be fitted according to the Fresnel equations. XRR can provide information on the thickness, roughness and density of thin films on a substrate. Using synchrotron radiation layers can be distinguished with similar optical constants.

4.7 Nuclear Magnetic Resonance spectroscopy (NMR)

Nuclear magnetic resonance is one of the most important methods for the determination of the molecular structure of mostly organic and organometallic, rarely of inorganic compounds (Keeler 2005). All stable isotopes that contain an odd number of protons and/or neutrons have an intrinsic magnetic moment. The most commonly studied nuclei are ^1H , ^{13}C , ^{19}F , and ^{31}P . The liquid or solid sample is placed between very narrow positioned poles of a huge magnet. The magnet produces a field of extremely high stability and homogeneity. This field is varied by a so called sweep coil. In the measurements the applied magnetic field is reduced (absorbed) by induction effects, yielding an "effective field strength". This effect is also called "shielding" and varies with the electron distribution of atoms. The change of a resonance line due to binding effects is called the chemical shift. The spectra are recorded in relation to the proton signal of tetramethylsilane = $\text{Si}(\text{CH}_3)_4$ (TMS). An example of NMR being used in the determination of a structure is that of buckminsterfullerene (C_{60}). As this structure contains no hydrogen, ^{13}C NMR has to be used (longer acquisition time since ^{13}C is not the common isotope of carbon). However, the spectrum was obtained and was found to exhibit a single peak, confirming the unusual structure of C_{60} (Taylor et al., 1990).

4.8 Infrared Spectroscopy (IR)

The infrared spectroscopy deals with the electromagnetic spectrum of the near- (14000-4000 cm^{-1} ; 0.8-2.5 μm ; to excite overtone or harmonic vibrations), mid- (4000-400 cm^{-1} ; 2.5-25 μm ; to study fundamental vibrations and associated rotational-vibrational structures) and far-infrared (400-10 cm^{-1} ; 25-1000 μm ; used for rotational spectroscopy) regions; this light has a longer wavelength (lower frequency) than visible light. IR spectroscopy has been applied successfully for characterization in organic and inorganic compounds. Also it was successfully utilized in the field of semiconductor microelectronics (Lau 1999). Molecules absorb specific frequencies

that are characteristic of their structures; these absorptions are at resonant frequencies. A molecule to be "IR active" must be associated with changes in the permanent dipole. Molecules with the number N atoms have many vibrational modes: linear have $3N-5$ and nonlinear molecules have $3N-6$ vibrational degrees of freedom (e.g., H_2O has 3 degrees or modes). Stretching, bending, rocking, wagging and twisting vibrations were distinguished. Gaseous samples are measured in cells with a long path length of 5-10 cm. Liquid samples are placed between two plates of salt (e.g., NaCl, KBr, CaF). Solid samples are crushed with e.g. Nujol (oily agent) and smeared as a thin film onto salt plates. Sometimes microtomy cuts can be used. The techniques' arrangement consists of a light source (e.g., Nernst glower, Globar = SiC rod, mercury vapour lamp), a monochromator (former: Prisms, today: Gratings) or interferometer (mainly for FTIR technique), the sample position, and the detection arrangement (thermocouple, Golay detector, PbS cell, PbSe cell, or other semiconductors). Thus absorption spectra will be recorded as function of the frequency. Today the Fourier-transform-technique is used mostly. It permits to analyze a large amount of data when the total spectrum is recorded simultaneously (Fellgett's advantage or multiplex advantage). By this way both speed and signal-to-noise ratio are improved (White 1990). Fig. 3 exhibits the FTIR spectrum of a carbonitride sample.

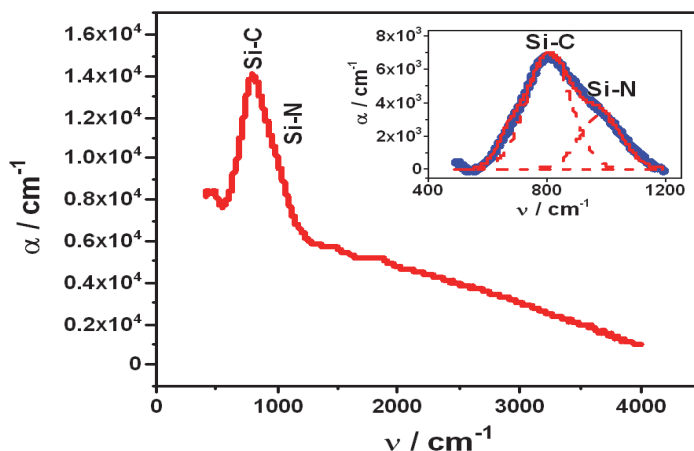


Fig. 3. FTIR spectra of PECVD SiC_xN_y film grown at 973 K: total view and deconvolution of the main adsorption band into components.

4.9 Raman spectroscopy

Raman spectroscopy permits like IR spectroscopy to study vibrational and rotational modes of molecules (Gardiner, 1989). Whereas IR spectroscopy is mostly working in the absorption mode, the Raman scatter spectra are recorded in 90° geometry. Therefore both methods are complementary. Raman spectroscopy relies on inelastic (Raman) scattering of monochromatic (laser) light in the visible, near IR and near UV range, resulting in the energy of the laser photons being shifted down (Stokes lines) and up (Anti-Stokes lines). The light from the sample is collected with a lens, sent through a monochromator (holographic gratings, multiple dispersion stages, Czerny-Turner arrangements), and directed to a detector (photomultiplier, CCD camera).

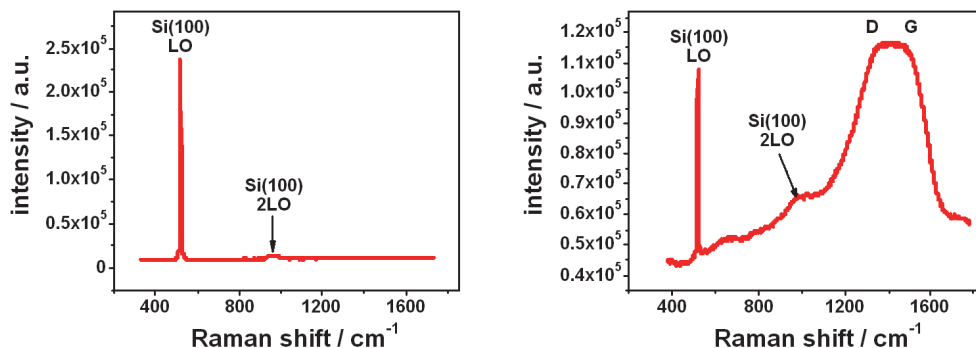


Fig. 4. Typical Raman spectra of PECVD SiC_xN_y film grown at 373-673 K (left) and 873-973 K (right).

The Raman spectra provide a fingerprint by which the molecule can be identified. In solid state physics Raman spectroscopy characterizes materials and finds the crystallographic orientation of a sample. Raman spectra of carbonitride samples are shown in Fig. 4. In nanotechnology, a Raman microscope can be used to analyze nanowires to better understand the composition of the structures. Variations of Raman spectroscopy have been developed. The usual purpose is to enhance the sensitivity (e.g., surface-enhanced Raman), to improve the spatial resolution (Raman microscopy), or to acquire very specific information (resonance Raman) (Lombardi & Birke, 2008).

4.10 Wavelength and/or energy dispersive X-ray spectroscopy (WDX/EDX)

For excitation of atoms to emit X-rays, radiation of higher energy is required. For X-ray fluorescence (XRF) the emission of X-ray tubes, of radionuclides, or of synchrotron radiation is applied (Beckhoff et al. (Eds.), 2006; Van Grieken & Markowicz (Eds.), 2002). For the excitation of X-rays in SEM (see 4.3) electrons are used. The principle structure of a XRF device to determine the elemental composition is quite simple: source – sample – detector. The main properties of XRF systems are: simple element identification by Moseley's law; to be applied for non-destructive analysis of solid samples (compact or powders); simple conditions for the elemental region $20 < Z < 92$; for light elements vacuum conditions, windowless detectors and special sources are needed; the detection limit is in the range 10^{-4} - 10^{-7} g/g is related to the device, the source, the detector, the element, and the composition of the sample. The information depth depends on the incident energy, the composition of the sample, and the energy of the excited X-radiation – it varies from the μm -range to some cm-range. For a quantitative determination, calibration procedures using standard materials of a composition similar to the unknown sample or an evaluation using fundamental parameters are used. The principle of XRF is the excitation of electrons to a higher energy level (their relaxation leads to the emission of X-rays). These X-rays are divided in K-, L-, and M series, depending on the ground level of the electrons. Various cathodes (e.g., Cr, Pd, W) of the tubes or various radionuclides (^{55}Fe , ^{109}Cd , ^{241}Am) are used for a high efficient excitation. The incident X-ray beam usually is directed in an angle of 45° on the sample. The very intensive synchrotron radiation has various advantages: Continuous spectrum from about 1 eV up to many 10 keV, and tunable for optimal excitation (resonance), highly collimated beam. Semiconductor diodes are applied for energy-dispersive detection (EDX). An EDX spectrum of the light elements in a

silicon carbonitride sample is given in Fig. 5. In that case the spectra are recorded simultaneously. For wavelength-dispersive (WDX) detection a system with a diffraction monocrystal (or monolayer), collimators, and a combined proportional/scintillation counter are used. In that case the spectra are recorded sequentially. This system exhibits a better energetic resolution. For a quantitative analysis, calibration measurements are inserted in the procedure using reference materials with a composition similar to the sample to be analyzed. In all cases a validation is necessary: Either by measurement of well-known standard reference materials (SRM) or by comparison with the result of an independent analytical method.

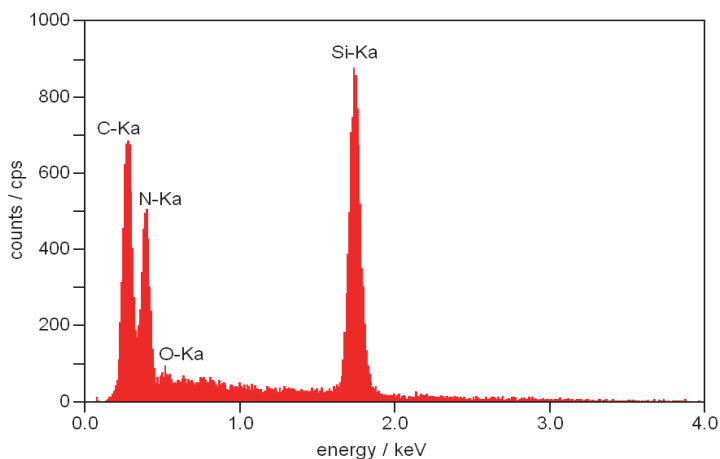


Fig. 5. EDS spectrum of PECVD SiC_xN_y grown at 973 K using a (HMDS+He+ NH_3) mixture.

A special arrangement is used in the so called “total-reflection XRF (TXRF)”. The incident beam is directed onto a flat (polished) sample at an angle of $1\text{--}2^\circ$. In case of total reflection the penetration depth is in the nm-range. Therefore, this method can be used for surface analysis. As sample carrier quartz, plexiglass, glassy carbon, or boron nitride are applied. The absolute lower limit of detection (LLD) varies between 5 and 100 pg, that corresponds to a relative LLD of about 0.1–2 ng/g. The field of application is very broad: microsamples (droplets, particles), surface analysis, thin films from high vacuum techniques, semiconductor handling, evaporation and sputter procedures, and laser mirror production (Hein et al., 1992). A powerful technique can be build up by arranging a TXRF unit at a synchrotron beam line (Beckhoff et al., 2007).

4.11 Near-edge X-ray Absorption Fine Structure spectroscopy (NEXAFS)

NEXAFS, also known as “X-ray Absorption Near Edge Structure” (XANES), is an absorption spectroscopy method. Electrons from the core level are excited by photons to partially filled and empty states and the consequent emission of photoelectrons is measured (Hemraj-Benny et al., 2006). The resulting core hole is filled either via an Auger process or by capture of an electron from another shell followed by emission of a fluorescent photon. The absorption intensity is detected as a function of the exciting photons’ energy. NEXAFS measurements can detect specific bonds in molecules as well as the angular dependence of the specific orbitals involved (Stöhr 1992). The fluorescent photons originate from the the top 200 nm of the film, whereas the Auger electrons arise from the top 10 nm.

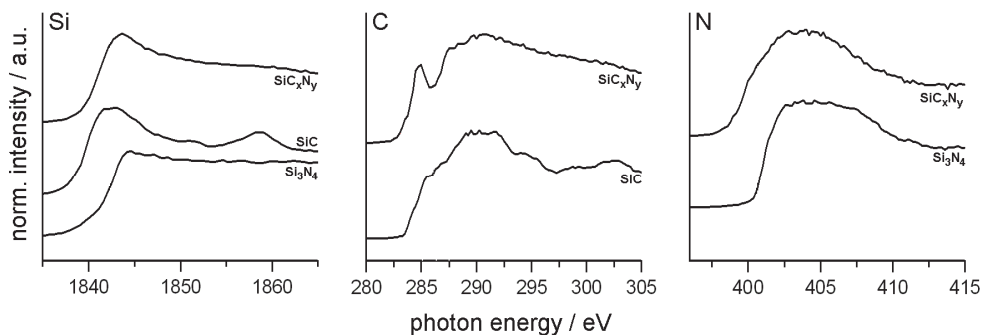


Fig. 6a. NEXAFS spectra of Si_3N_4 , SiC , and SiC_xN_y .

In a total-reflection geometry (see Figs. 6a,b) at the sample, the information depth using photon detection decreases to about 5 nm (Baake et al., 2010). As an example, detailed spectral resonances at the carbon K-edge yield information about the bonding environment of this atom, such as functionalized species and chemisorbed impurities. The lower π^* resonance can provide insights into bond hybridization, while the σ^* resonance is a measure of the intramolecular bond length. Since the light from the synchrotron source used is linearly polarized, the intensity of the π^* and σ^* transitions will be sensitive to the orientation of these orbitals (Hemraj-Benny et al., 2006).

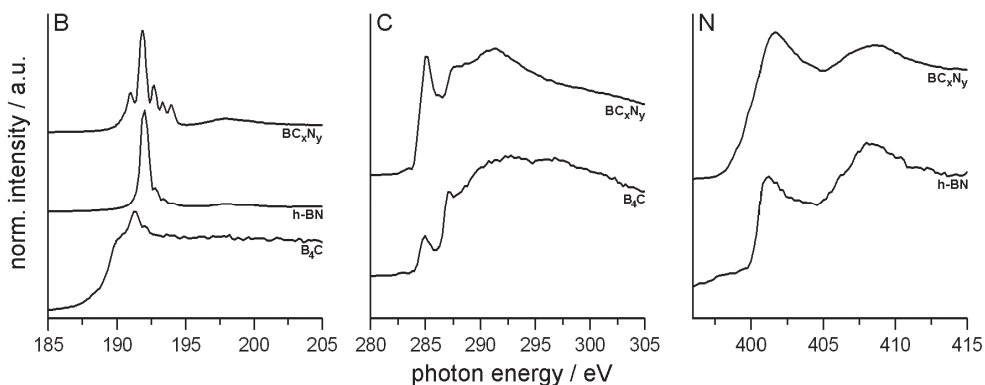


Fig. 6b. NEXAFS spectra of BN , B_4C , and BC_xN_y .

The great power of NEXAFS derives from its elemental specificity. Additionally, NEXAFS can be used to determine: presence of defects and amorphous content in carbon nanotubes, varying degrees of bond hybridization in mixed sp^2/sp^3 -bonded carbon materials, degree of vertical alignment in nanotube samples, nature of oxygen-containing functional groups on nanotube surfaces (Hemraj-Benny et al., 2006). Applying grazing-incidence XRF-NEXAFS it will be possible to build up a profile of chemical bonding in multilayered samples (Pagels et al., 2010).

4.12 X-ray Photoelectron Spectroscopy (XPS)

X-ray photoelectron spectroscopy (XPS) is a technique that measures the elemental composition, empirical formula, chemical state and the electronic state of the elements in the

sample (Briggs & Seah 1990). The spectra are obtained by irradiation of a sample with a monochromatic X-ray beam while simultaneously measuring the kinetic energy and number of electrons that escape from a surface layer of 1 to 10 nm. XPS is a surface analysis technique. It is also known as “Electron Spectroscopy for Chemical Analysis (ESCA)”. XPS detects all elements except hydrogen and helium.

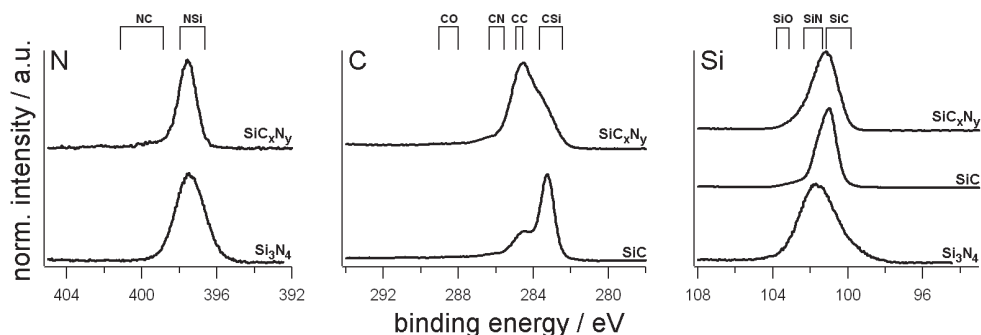


Fig. 7a. XPS spectra of Si_3N_4 , SiC , and SiC_xN_y .

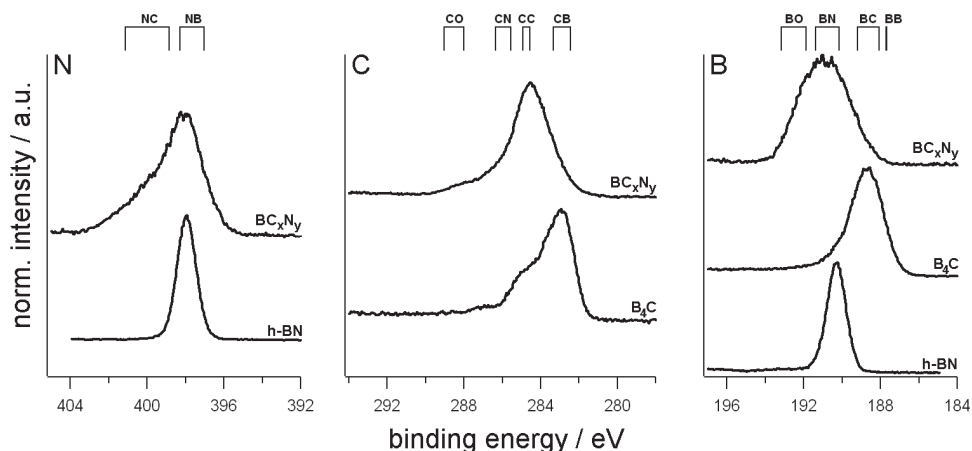


Fig. 7b. XPS spectra of BN , B_4C , and BC_xN_y .

A typical spectrum is a plot of the intensity of the electrons detected versus their binding energy of (see Fig.7a,b for several silicon and boron compounds). The peaks in such a spectrum correspond to the electron configuration of the compounds in the sample. The number of detected electrons in a characteristic peak is directly related to the amount of the element in the area irradiated. To generate atomic percentage values the signal intensity must be corrected by the “relative sensitivity factor (RSF)”.

Monochromatic Al K_α X-rays with an energy of 1486.7 eV are used for excitation. As electron analyzer a “Concentric Hemispherical Analyzer (CHA)” is applied with a channeltron.

Under optimum conditions, the quantitative accuracy of the atomic percent values is 90-95% for major peaks and 60-80% of the true value for weaker signals (10-20% of the strongest signal). The binding energy will be determined via the equation (9)

$$h \cdot \nu = E_{\text{kin}} + E_{\text{B}}^{\text{V}}(k), \quad (9)$$

where $h \cdot \nu$ = irradiation energy, E_{kin} =energy of the emitting electron, and $E_{\text{B}}^{\text{V}}(k)$ =binding energy. The determination of the different binding energies of an element in a sample is the most important power of XPS. It is stated by the “chemical shift” in comparison to a pure substance. For fixing the energy resolution over the total measuring region the electrons are limited to a constant velocity before their entrance into the analyzer (“pass energy”).

4.13 Transmission Electron Microscopy (TEM)

In transmission electron microscopy (TEM) an electron beam is transmitted through an ultra thin sample. An image is formed from the interaction (e.g., absorption, diffraction) of the electrons with the specimen. The electrons are guided through an expanded electron optical column. The imaging device is a fluorescent screen, a photographic film, or a CCD camera (Fultz & Howe, 2007; Rose, 2008). The analytical power of a TEM is described by the resolution properties: By reduction of spherical aberrations a magnification of 50 million times (resolution: $0.5 \text{ \AA} = 50 \text{ pm}$) is reached. The ability to determine the position of atoms has made the high-resolution TEM (HRTEM) an indispensable tool for nanotechnology research, including heterogeneous catalysis and the development of semiconductor devices for electronics and photonics (O’Keefe & Allard, 2004). High quality samples will have a thickness of only a few tens of nanometers. Preparation of TEM specimen is specific to the material under analysis. Some of the methods for preparing such samples are: Tissue sectioning by a microtome, sample staining, mechanical milling, chemical etching, and ion etching (sputtering). Recently, focussed ion beams (FIB) have been used for sample preparation (Baram & Kaplan, 2008).

For measurement of the fine structure of absorption edges to determine chemical differences in nano structures, electron energy loss spectroscopy (EELS) can be used. This method is a supplement to NEXAFS and XPS (mainly for nano sized samples).

4.14 Secondary Ion Mass Spectrometry (SIMS)

The advantages of secondary ion mass spectrometry (SIMS) can shortly be described as: Detection limit in the range of parts per million (ppm) or below, all elements can be measured (H-U), full isotopic analysis, atomic and molecular detection, rapid data acquisition, and three dimensional imaging capability (depth profiling) (Goldsmith et al., 1999). SIMS is based on the impact of primary ions (0.5-20 keV) on the sample surface, resulting in the sputtering of positive and negative secondary ions (atomic and molecular), electrons, and neutral species. SIMS instruments are build up by a primary ion source (e.g., O^- , O_2^+ , Cs^+), a sample manipulation system, a secondary ion extraction system, magnetic and electric fields mass spectrometer (double focussing) (also quadrupole and time of flight devices are applied), and several kinds of detectors (Faraday cup, electron multiplier, microchannel plate). As an example, a SIMS profile is given in Fig. 8 of a layered sample with the substrate Si(100) and a BCN layer on a Cu layer.

As positive ions are only a small fraction of the total sputtered material, a method called “secondary neutrals mass spectrometry (SNMS)” is in use. The transformation of raw spectral or image intensities into meaningful concentrations is still challenging.

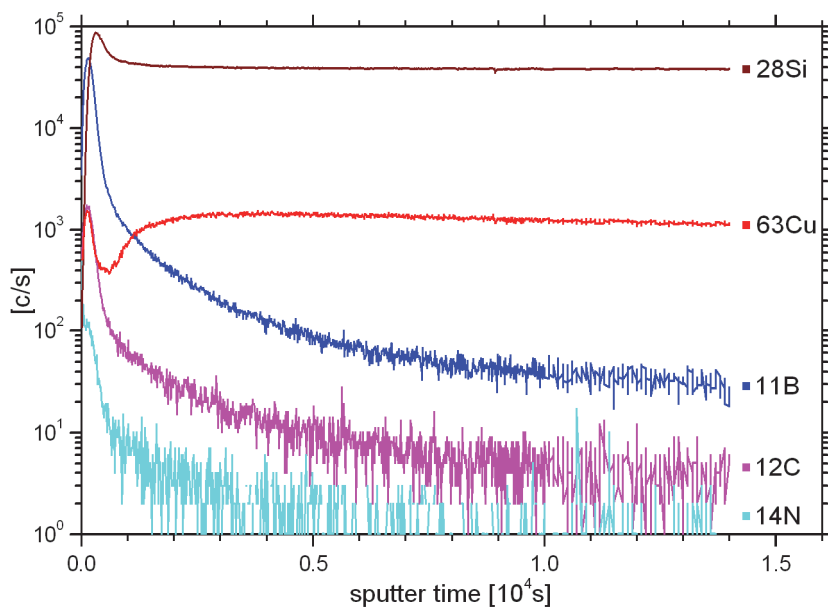


Fig. 8. SIMS profile of a layered system BCN/Cu/Si.

4.15 Rutherford back scattering (RBS)

Rutherford back scattering (RBS) is a method applied in material science for the determination of the composition, the structure and of the depth profile in a sample (Oura et al., 2003). A beam of high energy (1-3 MeV) ions is directed on a sample. The ions partly backscattered at nuclei (the scattering at electrons leads to some extent to a decrease of the resolution) are detected. The energy of these backscattered ions is a function of the mass of the atoms (and of the scatter angle), at which the collision take place. An RBS instrument consists of an ion source (linear particle accelerator or an alpha particle source) and an energy sensitive detector (silicon surface barrier detector). In practice, the compositional depth profile can be determined from an intensity-energy measurement. The elements are characterized by the peak position in the spectrum and the depth can be derived from the width and shifted position of these peaks. Crystal structures (channeling) and surface information can also be evaluated from the spectra.

4.16 Elastic Recoil Detection Analysis (ERDA)

Elastic recoil detection analysis is a nuclear technique in materials science to obtain elemental concentration depth profiles in thin films. An energetic ion beam is directed at the sample to be depth profiled. As in RBS an elastic nuclear interaction with the atoms of the sample is observed. The energy of the incident ions (some MeV) is enough to recoil the atoms which are detected with a suitable detector. The advantage in ERDA is that all atoms of the sample can be recoiled if a heavy incident beam is used. For example, a 200 MeV Au beam is used with an ionization detector. In the right recoil angle the scattered incident beam ions do not reach the detector. ERDA is often used with a relatively low energy ^4He beam (2 MeV) for depth profiling of hydrogen.

5. Properties of carbonitride compounds

5.1 Silicon carbonitride compounds

Currently, strict conditions of modern technologies and aggressive working environment dictate higher requirements for construction materials quality. Two approaches are implemented to create new advanced materials: Synthesize radically new materials, or improve existing ones.

In the last twenty years, researchers from different countries are studying the possibility to synthesize a new class of multifunctional materials based on the ternary compound silicon carbonitride SiCN. Varying the elemental composition of silicon carbonitrides, that is, synthesis of any set of compounds, corresponding to the ternary phase diagram of Si-C-N from silicon and carbon nitrides to silicon carbide, diamond, and their mixtures, can obtain new materials with desired physical and chemical properties in a wide range.

It is assumed that these materials may possess the unique properties combining the best ones of the compounds mentioned, such as high mechanical strength and hardness, high thermal resistance, and chemical inertness. Silicon carbide SiC is studied as a promising high-temperature semiconductor material. It is known that silicon nitride Si₃N₄ is one of the key materials of modern electronics and a basic component of the ceramic composites. In recent years, there have been active attempts to synthesize carbon nitride C₃N₄ as a material having higher hardness than the one of diamond.

According to the literature, in those years several researchers have attempted to obtain silicon nitride films, not only with the use of ammonolysis of monosilane widely applied at that time, but also to develop many alternative ways of synthesis, in particular, with the use of organosilicon compounds. In the beginning of the 80-ies of the last century scientists from the Irkutsk Institute of Chemistry, specialized in synthesis of organosilicon compounds, used them as single-source precursors to obtain silicon nitride films. Hence, silicon nitride films were obtained in glow-discharge plasma from HMCTS in mixtures with N₂ or NH₃ at low temperatures (below 150°C) (Voronkov et al., 1981). There Si-N, C-C, Si-H (or Si-C≡N) and N-H chemical bonds were determined in the films obtained at such conditions. Later silicon nitride films were deposited by PECVD using a mixture of HMCTS and a wider set of additional gases such as NH₃, H₂, and N₂, and higher temperatures up to 400°C and plasma power (5-50 W) (Brooks & Hess, 1987, 1988). The set of characterization methods has been expanded. We can assume that so called silicon nitride films in reality consist of silicon carbonitride, whereas the films obtained from the mixture HMCTS+H₂ have significant amounts of carbon (30-40at.%) and 21at.% of hydrogen and contain both Si-N and Si-C bonds.

Later on, the films were obtained by plasma enhanced chemical decomposition using HMCTS in the mixture with helium or nitrogen in the temperature range of 100-750°C and plasma powers of 15-50 W (Fainer et al., 2009a, 2009b). Physical and chemical as well as functional properties of these films were studied by FTIR, Raman spectroscopy, XPS, EDXRS, XRD using synchrotron radiation, SEM, AFM, nanoindentation, ellipsometry, spectrophotometry, and electrophysical methods. The evaluation of the results obtained by spectroscopic methods showed that the low temperature SiC_xN_y films are compounds in which chemical bonding are present among Si, N, and C and with impurity elements, such as hydrogen and oxygen. Thus, a formula SiC_xN_yO_z:H is more correct. Electrophysical and mechanical characteristics, and other physicochemical properties have allowed new consideration of these SiC_xN_yO_z:H films as perspective interlayer dielectric films in

microelectronics devices of novel generation. The empirical formula of the high-temperature films is represented as SiC_xN_y . It was established that the films are nanocomposite materials consisting of an amorphous part and nanocrystals with a size of 1-60 nm having lattice parameters close to those of the standard phase $\alpha\text{-Si}_3\text{N}_4$. According to the Raman spectroscopic data, the films synthesized at a high temperature (up to 1023K) contain an insignificant number of graphite nanocrystals. The films synthesized from the mixture of HMCTS and helium or nitrogen exhibit an excellent transparency with a transmittance of 92–95% in the spectral range $\lambda=380\text{--}2500\text{ nm}$.

Thus, the increase number of research techniques and improving their accuracy revealed that the films obtained from one and the same single-source precursor HMCTS are silicon carbonitrides. SiC_xN_y films are nanocomposite materials consisted of an amorphous part and distributed nanocrystals having lattice parameters close to those of the standard phase $\alpha\text{-Si}_3\text{N}_4$. The films grown at above 973K contain inclusions of free graphite nanocrystals with a size of about 1 nm.

The compilation of publications, especially the earlier ones shows that among the authors involved in the synthesis of silicon carbonitride, no assumptions exist about what is meant by the term “carbonitride”. Typically, the researchers saw it as a material having in its structure the elements of Si, C, and N. In this case, it may be a mixture of individual compounds as Si_3N_4 , C, and SiC, and/or ternary SiC_xN_y compounds of variable composition.

What is silicon carbonitride, what its possible structure, let us consider some examples. In one of the first publications Si-C-N deposits were obtained by CVD using mixtures of gaseous compounds such as SiCl_4 , NH_3 , H_2 , and C_3H_8 and very high temperatures from 1100 up to 1600°C (Hirai & Goto, 1981). The obtained amorphous deposits were mixtures of amorphous $\alpha\text{-Si}_3\text{N}_4$, SiC, and pyrolytic C (up to 10 weight %). The deposits surface had a pebble-like structure.

Thin films of amorphous silicon nitride and silicon carbonitride were grown on Si(100) substrates by pyrolysis of ethylsilazane $[\text{CH}_2\text{CH}_3\text{SiH}_2\text{NH}]$ in mixtures with ammonia or hydrogen in the temperature range of 873-1073K (Bae et al., 1992). The films were studied by AES, RBS, and nuclear reaction analysis. It was shown, that the refraction index varied from 1.81 to 2.09. The hydrogen content was determined by ERDA to decrease from 21 to $8\pm 1\%$ in silicon carbonitride with increasing deposition temperature (873-1073K). According to AES the chemical composition of the films was determined as $\text{Si}_{43}\text{C}_7\text{N}_{48}\text{O}_2$. The silicon carbonitride films contained the bonds Si-C-N and Si-H.

Non-stoichiometric X-ray-amorphous $\text{Si}_{3+x}\text{N}_4\text{C}_{x+y}$ was deposited during pyrolysis of polysilazane at 1440°C (Schonfelder et al., 1993). The heating up to 1650°C results in formation of a mixture of nanocomposites $\text{Si}_3\text{N}_4/\text{SiC}$ or $\text{Si}_3\text{N}_4/\text{SiC}/\text{C}$.

SiC_xN_y coatings were obtained by CVD at 1000–1200°C using $\text{TMS-NH}_3\text{-H}_2$ (Beneddouché et al., 1997). These coatings were analyzed by XPS, Raman spectrometry, FTIR, TEM/EELS and ^{29}Si magic-angle spinning NMR (^{29}Si MAS-NMR). The main bonds are Si-C, Si-N, and C-C in these films. It was demonstrated that silicon carbonitride coatings obtained at high temperatures are nonhydrogenated. To clarify the chemical environment of silicon atoms by carbon and nitrogen atoms the $\text{SiKL}_{2,3}\text{L}_{2,3}$ line shapes were analyzed. It was shown that these peaks are decomposed into components corresponding to an intermediate position between the tetrahedra $\text{Si}(\text{C})_4$ and $\text{Si}(\text{N})_4$, i.e., silicon carbonitride films are not simply a mixture of phases of SiC and Si_3N_4 , and have a more complex relationship between the three elements, corresponding to the existence of $\text{Si}(\text{C}_{4-n}\text{N}_n)$ units. Mixed coordination shells

around silicon have been confirmed by TEM/EELS analyses. Also links were observed between the three elements: Silicon, nitrogen and carbon, which was confirmed by FTIR, and NMR.

Remote microwave hydrogen plasma CVD (RP-CVD) was used with BDMAHMS as precursor for the synthesis of silicon carbonitride (Si:C:N) films (Błaszczak-Lezak et al., 2007). The Si:C:N films were characterized by XPS and FTIR, as well as by AFM. The increase of T_s enhances crosslinking in the film via the formation of nitridic Si-N and carbidic Si-C bonds. On the basis of the structural data a hypothetical crosslinking reaction contributing to silicon carbonitride network formation have been proposed.

Si:C:N films were produced by RPCVD from a 1,1,3,3-TMDSN precursor and at a substrate temperature in the range of 30–400°C (Wrobel et al., 2007). The effects of the substrate temperature on the rate and yield of the RP-CVD process and chemical structure (examined by FTIR) of the resulting films were investigated. The Si:C:N film properties were characterized in terms of density, hardness (2.5–16 GPa), Young's modulus (43–187 GPa), and friction coefficient (0.02–0.05). With the IR structural data, reasonable structure–property relationships were determined.

Physical, optical, and mechanical properties were investigated of amorphous hydrogenated silicon carbonitride (a-Si:C:N:H) films produced by the remote PECVD from (dimethylamino)dimethylsilane in relation to their chemical composition and structure (Błaszczak-Lezak et al., 2006). The films deposited at different substrate temperatures (30–400°C) were characterized in terms of their density (1.95–2.27 g/cm³), refractive index (1.8–2.07), adhesion to a substrate, hardness (24–35 GPa), Young's modulus (150–198 GPa), friction coefficient (0.036–0.084), and resistance to wear predicted from the "plasticity index" values $H/E^0 = 0.10$ –0.12. The correlations between the film compositional parameters, expressed by the atomic concentration ratios N/Si and C/Si, as well as structural parameters described by the relative integrated intensities of the absorption IR bands from the Si-N, Si-C, and C-N bonds, and the XPS Si2p band from the Si-C bonds (controlled by substrate temperature) were investigated. On the basis of the results of these studies, reasonable compositional and structural dependencies of film properties were determined.

In his review Badzian proposed stable and solid phases in the ternary system Si-N-C as silicon carbonitride (Badzian, 2002). Silicon carbonitride films obtained at 1000–1200°C from mixture of tetramethylsilane, ammonia and hydrogen are characterized by a hardness of 38 GPa, that exceeds hardness of both Si₃N₄ and SiC.

Crystalline films of silicon carbonitride were obtained by MW-PECVD using H₂, CH₄, N₂, and SiH₄ mixture (Chen et al., 1998). The ternary compound (CSi)_xN_y exhibits a hexagonal structure and consists of a network wherein Si and C are substitutional elements. While the N content of the compound is in the range 35–40 at.%, the fraction of Si varies and can be as low as 10 at.%. The preliminary lattice parameters a and c are 5.4 and 6.7 Å, respectively. Photoluminescence of silicon carbonitride films has been studied as well. The direct band gap of crystalline (CSi)_xN_y is 3.8 eV at room temperature. The measurements of optical properties have shown that SiCN is a perspective wide-band material with energies suitable for light emitting diodes (LED) in blue and UV spectrum areas.

Si-C-N films were deposited on p-type Si(100) substrates by DC magnetron co-sputtering of silicon and carbon using a single sputter target with variable Si/C area ratios in nitrogen–argon mixtures (Vlcek et al., 2002). As a result, the N-Si and Si-N bonds dominate over the

N-C and Si-O bonds (XPS), preferred in a pure nitrogen discharge, and the film hardness increases up to 40 GPa.

SiCN coatings were deposited on silicon substrates (350°C) by PECVD using mixtures of methyltrichlorosilane (MTCS), nitrogen, and hydrogen (Ivashchenko et al., 2007). The coatings were characterized by AFM, XRD, and FTIR. Their mechanical properties are determined with nanoindentation. The abrasion wear resistance is examined using a ball-on-plane (calowear) test and adhesion to the base was tested using a scratch test. The XRD measurement indicates that the coatings are nanostructured and represent β -C₃N₄ crystallites embedded into an amorphous a-SiCN matrix. The coatings deposited at a higher nitrogen flow rate are amorphous. β -C₃N₄ crystallites embedded into the amorphous a-SiCN matrix promote an increase in hardness (25 GPa) and Young's modulus (above 200 GPa) of SiCN coatings.

Tribological tests have revealed that the friction coefficients of the coatings containing nitrogen are two to three times smaller than those based on SiC and deposited on a silicon substrate. The ball-on-plane tests show that the nanostructured coatings also exhibit the highest abrasive wear resistance. These findings demonstrate that the SiCN films deposited using MTCS show good mechanical and tribological properties and can be used as wear-resistant coatings.

SiCN hard films have been synthesized on stainless steel substrates by an arc enhanced magnetic sputtering hybrid system using a silicon target and graphite target in mixed gases of Ar and N₂ (Ma et al., 2008). The XRD results indicate that basically the SiCN films are amorphous. However, the HRTEM results confirm that the microstructure of the SiCN films with a high silicon content are nanocomposites in which nano-sized crystalline C₃N₄ hard particles are embedded in the amorphous SiCN matrix. The hardness of the SiCN films is found to increase with increasing silicon content, and the maximum hardness is 35 GPa. The SiCN hard films show a surprising low friction coefficient of 0.2 when the silicon content is relatively low.

SiCN films have been produced by means of reactive magnetron sputtering of a silicon target in an argon/nitrogen/acetylene atmosphere (Hoche et al., 2008). The mechanical, chemical, and structural properties have been thoroughly investigated by means of indentation hardness testing, pin on disk wear testing in reciprocating sliding motion, glow discharge optical emission spectroscopy (GDOES), FTIR, Raman spectroscopy, XPS. The main aim of this investigation was to establish the relationship between deposition conditions, resulting mechanical, chemical, structural, and the respective wear properties. Analogous to their position in the Si-C-N phase diagram, the hardness of the films varies over a broad range, with maximum values of around 30 GPa, while Young's modulus remains in a narrow range around 200 GPa. XPS spectra showed the main component to be Si-C, but Si-N and to a minore extent C-C bonds were also detected. Further, IR spectra suggested the presence of the carbodiimide group. Raman spectra show a varying ratio of sp³ to sp² carbon, depending on deposition condition. The hardest films were found along the SiC-Si₃N₄ tie line. In dry sliding their brittleness coupled with a high friction coefficient led to premature coating failure. Carbon rich films have a very low friction coefficient leading to good wear behaviour in dry conditions, but their ability to withstand high Hertzian pressures is reduced. The low friction coefficient of is attributed to more graphitic structures of the free carbon in the films.

To decrease the level of contamination of silicon melts during the Czochralski process the novel protective layer of silicon carbonitride was proposed for the inner surface of quartz

crucibles (Fainer et al., 2008). SiC_xN_y coatings were grown on fused silica substrates from hexamethyldisilazane with helium or ammonia in the temperature interval of 873–1073 K. Change of surface morphology, elemental composition and wetting angles were studied after the interaction of the surface of SiC_xN_y layers with the silicon melt at 1423 K by SEM, EDX and sessile drop measurements. The drop measurements after interaction of liquid Si ($\approx 1450^\circ\text{C}$) with the surface of SiC_4N sample determined a wetting angle of $\approx 90^\circ$ that implying a poor wetting. The lack of etching figures on the SiC_xN_y surface proved, that no chemical reaction starts of Si melt with the SiC_xN_y coating. In case of silicon carbonitride with larger concentration of nitrogen ($\text{Si}_2\text{C}_3\text{N}_2$) wetting angle was obtained as $\approx 60^\circ$ close to that one of Si melt on Si_3N_4 of $\approx 55^\circ$.

Silicon carbonitride (SiC_xN_y) films were grown on silicon substrates using the PLD technique (Boughaba et al., 2002). A SiC target was ablated by the beam of a KrF excimer laser in a N_2 background gas. The morphology, structure, composition, as well as the optical and mechanical properties of the coatings were investigated as functions of the N_2 pressure (1–30 mTorr) and substrate temperature (250 – 650°C). Smooth, amorphous films were obtained for all the processing parameters. The hardness, Young's modulus of the films were found to be a function of the growth regime; the highest values of the hardness and Young's modulus values were obtained in the low-pressure regime, in the range of 27–42 GPa and 206–305 GPa, respectively.

A visible-blind ultraviolet (UV) photodetector (PD) with metal-semiconductor-metal (MSM) structure has been developed on a cubic-crystalline SiCN film (Chang et al., 2003). The cubic-crystalline SiCN film was deposited on Si substrate with rapid thermal CVD (at 1150°C) using SiH_4 , C_3H_8 , NH_3 , and H_2 mixture. The optoelectronic performances of the SiCN-MSMPD have been examined by the measurement of photo and dark currents and the current ratio under various operating temperatures. The current ratio for 254 nm UV light of the detector is about 6.5 at room temperature and 2.3 at 200°C , respectively. The results are better than for the counterpart SiC of 5.4 at room temperature, and less than 2 for above 100°C , thus offering potential applications for low-cost and high-temperature UV detection.

The internal stress, optical gap, and chemical inertness were examined of amorphous silicon-nitride films incorporating carbon prepared by RF magnetron sputtering (Yasui et al., 1989). The carbon composition of the films was less than 15 at.%. The optical band gap was barely affected by the carbon addition. The internal stress was compressive in all films and increased up to $7.3 \times 10^8 \text{ N/cm}^2$ in a-SiN:H films proportional to the nitrogen content, and decreased to less than half in carbon-free films. The buffered HF etch rate increased to greater than $1 \mu\text{m/min}$ in proportion to the nitrogen content in SiN:H films. The etch rate decreased by about one order of magnitude with the addition of carbon.

In several papers thin films of silicon carbonitride are described with compositions varying in the wide range from similar to silicon carbide to similar to silicon nitride. These were synthesized by PECVD using HMDS as single-source precursor in the mixtures with helium, nitrogen or ammonia in the wide range of temperatures from 100 up to 800°C and RF plasma powers from 15 up to 70 W (Fainer et al., 1999, 2000, 2001a, 2001b, 2003, 2004, 2008). The nondestructive method XRD-SR was developed to determine phase composition and crystallinity of the obtained films composed of lightweight elements (Si, N, C) using the facilities of the station "Anomalous Scattering" (International Siberian Center for Synchrotron and Terahertz Radiation, Budker Institute of Nuclear Physics, SB RAS, Novosibirsk, Russia). The application of SR-XRD and high-resolution electron microscopy

with selective area electron diffraction (HRTEM-SAED) yielded to the result that silicon carbonitride films contain nanocrystals close to α -Si₃N₄, distributed in amorphous matrix of the film, i.e. the films are nanocomposite. The spectroscopic results (FTIR, XPS, EDX, AES, Raman) clarified that silicon carbonitride is a ternary compound, in which complex chemical bonds between all three elements – silicon, carbon and nitrogen with impurity of oxygen and inclusion of nanocrystalline graphite – are formed. The formation of mixed Si(C_{4-n}N_n) units could be proposed in the films. Apparently, the formation of nanocrystals With a phase composition close to the standard α -Si₃N₄ and the presence of silicon atoms surrounded by nitrogen and carbon atoms, suggests that some places in the crystal lattice occupied by silicon atoms may be substituted by isovalent carbon atoms. The formation of a substitutional solid solution is in fact possible. The films possess high transparency in the spectral region of 270–3500 nm and a large variation of band gap from 2.0 to 5.3 eV. Hydrogenated silicon oxycarbonitrides are perspective low-k dielectrics in the silicon technology of new generation. Presence of complex chemical bonds between three elements and nanocrystals in the films allowed obtaining films with higher hardness of above 30 GPa as compared with mixture phases such as α -Si₃N₄, SiC or C.

5.2 Boron carbonitride compounds

In the last 20 years the publications dealing with BCN are countless. They are dealing with the production, as described in the paragraphs 2 and 3. Additionally, the methods of characterization of BCN compounds to determine the elemental composition, the crystal structure, the chemical bonding, and several physical properties are abundant. All over the world (e.g., China, France, Germany, Japan, Korea, Spain, Russia, United States, and others) research and commercial materials science institutes were and are engaged in this field. The importance of BCN compounds is shown by the recent edition of a monography (Yap, 2009). Obviously, it is not possible to touch all the activities and to comment them. The selection we have made is therefore somewhat subjective and somewhat accidental.

The first activities on boron carbonitride dealt with high-melting substances, mainly to be applied in space technique. For these specimen neither physical nor chemical characterization is described in the relevant papers (Samsonov et al., 1962; Chepelenkov et al., 1964). Nearly 10 years later, another group (Kosolapova et al., 1971) using XRD measurements characterized the products from elemental composition data as BCN. The structure of this boron carbonitride is based on BN with a somewhat increased period *c* of the crystal lattice. The black powder with a particle (branched) size of the order of 1 μ m showed a density of 2.13 g/cm³ (determined by pycnometry). As secondary constituents or as impurities boron carbide B₄C and graphite C were identified.

In the first (to our knowledge) experimental paper on BCN from the United States (Kaner et al., 1987) another group dealing with BCN is cited (Badzian, 1972). In the paper of Kaner et al. outstanding analytical methods as XRD and XPS were applied for the characterization of the product, not being a mixture of BN+C but a specific new chemical compound B_xC_yN_z with a ratio of boron and nitrogen approximately 1:1 and an increasing fraction of C with increasing temperature at synthesis. This new compound shows a room temperature conductivity $\sigma = 6 \times 10^{-4}$ S/cm (whereas BN is an insulator), a thermal band gap of 0.2 eV, and is intercalated by strong reducing and oxidizing agents.

Referring to the papers of Badyan et al. and Kaner et al. a calculation examination of the BCN compounds was performed by Liu et al. (Liu et al., 1989). The possible atomic

arrangements and the electronic structures of three models of BC_2N were studied. A correlation was found between the structural symmetries and the conducting properties. Two structures were found to have semiconducting gaps and one to be metallic. This behaviour is similar to the relation of graphite to BN. This paper initiated a world wide activity in synthesizing of BC_xN_y by various methods and characterizing the products by an increasing number of analytical methods. Beneath the interest for the chemical structure, the elemental composition, the speciation (chemical bonding), and the relation between chemical situation and physical properties were investigated, up to now.

About 10 years later a review on BCN materials was published (Kawaguchi 1997). The chemical bond energies are given as B-N: 4.00 eV, C-C: 3.71 eV, N-C: 2.83 eV, and N-N: 2.11 eV. Furthermore, the product is described by a possible replacement of nitrogen by carbon in h-BN. The conductivity of BC_2N was found to be variable over several orders of magnitude at room temperature related to the synthesis conditions. The conductivity of BC_3N was 10 times lower than that of carbon plates, and slightly larger than that of BC_2N - the increase at temperatures between 25 and 700°C shows, that BC_3N is stated to be a semiconductor. Additionally, photoluminescence and cathodoluminescence were observed for BN(C,H) films, intercalation chemistry is discussed, and an application of intercalated Li into B/C/N is proposed for Li battery systems. Mainly, for the future it is desirable to receive large-crystalline B/C/N materials, e.g., by a selection of appropriate starting materials for CVD.

In the same year BCN samples were prepared by nitridation of B_4C (Kurmaev et al. 1997). For characterization X-ray emission, XRD, Raman, and TEM-EELS were used. New signals were found (no B_4C , no graphite, no h-BN), which confirmed the structural model in which boron nitride monolayers are in random intercalation with the graphite ones.

BCN films were deposited by RF magnetron sputtering from h-BN and graphite targets in an Ar-N_2 gas mixture (Zhou et al. 2000). A large variety of analytical methods was used: XPS, Auger, FTIR, Raman, XRD, and nanoindentation. B-N, B-C, and C-N bonds were identified. No phase separation between h-BN and graphite was observed. Amorphous BC_2N films with an atomically smooth surface were obtained. As mechanical and tribological parameters were measured: Hardness in the range 10-30 GPa, microfriction coefficient was 0.11 under a load of 1000 μN , and the Young's modulus was within 100-200 GPa.

In the following years a number of papers was published by a Spanish group. Their method of production was the IBAD technique. Therein B_4C was evaporated with concurrent N_2^+ bombardment (Gago et al., 2001a, 2001b, 2002a, 2002b). Various methods were used to identify the character of the products: NEXAFS, FTIR, Raman, HRTEM, and time-of-flight-ERDA. The results can be summarized as follows: c-BCN and h-BCN ($\text{B}_{50}\text{C}_{10}\text{N}_{40}$, solubility of C in h-BN about 15%) were identified, and the transition from amorphous B_xC to h-BN-like structures was observed. As physical parameters a hardness of 35 GPa, a Young's modulus, a friction coefficient of 0.05, and thermal stability were measured.

Fullerene-like B-C-N products were synthesized by dual cathode sputtering (Hellgren et al., 2004). By means of RBS, SEM, HRTEM, and nanoindentation a fullerene-like microstructure was determined and an elastic response was observed.

The incorporation of carbon into the crystal structure of h-BN was stated first by S.C. Ray (Ray et al., 2004) using XRD and NEXAFS examinations.

In these years, a systematic examination of BCN products can be observed from the literature. For chemical bonding determination mainly XPS and NEXAFS (also FTIR) are

used, and the hardness is measured by nanoindentation. Caretti et al. described an experimental reliable change of carbon in BC_xN yielding hexagonal structure (Caretti et al., 2004). They describe a hardness of 17 GPa, a Young's modulus of 170 GPa, and friction and wear experiments. An increase of the carbon flux is followed by an increase of carbon in the product (increase of the sp^3 fraction) that improves the mechanical properties. Morant et al. and Zhou et al. produced samples with a hardness of 33 GPa, determined the roughness, and established excellent friction properties (Morant et al., 2005; Zhou et al., 2006). The chemical properties were determined by XPS with an identification of B-N, B-C, and C-N bonds. The highest value for the hardness of 40 GPa were published in 2005 (Kosinova et al., 2005).

One of first papers dealing with the production of BCN compounds by using a large molecule as precursor is authored by Uddin et al. (Uddin et al., 2005). The product was identified as graphite-like BCN with B-C, B-N, and B-C-N hybrids.

Beneath the usual characterisation of BCN compounds by XPS and FTIR, the chemical behaviour (solubility) in acidic, neutral, and alkaline solutions was examined (Byon et al., 2006). In HCl no anodic dissolution was observed, in NaOH the dissolution depends on the potential and is increasing with increasing pH.

The group from Osaka, Japan, synthesized polycrystalline BCN by PECVD (Tai et al., 2003). Various properties of the films were investigated in the last years: e.g., electrical and optical characteristics (Yuki et al., 2004), influence of UV radiation on dielectric constant (Zhang et al., 2005), adaptation as humidity sensor (Aoki et al., 2007), acid and alkaline wet influence on quality of LSI devices (Watanabe et al., 2008), modification of the tunneling controlled field emission (Sugino et al., 2010).

BCN compounds were synthesized by DC reactive sputtering of B_4C target in a gas mixture of N_2 and Ar (Xu et al., 2006). The composition of the product depends on the N_2/Ar ratio. By nanoindentation the surface morphology and roughness were examined.

A method of BCN production by PECVD with TMB (+benzene) is described by Thamm et al. (Thamm et al., 2007). The main result is: The structure and the mechanical properties are in strong dependence on the substrate temperature.

An amorphous product was synthesized with corrosion protection properties better than B_4C and CN_x (Chen et al. 2006) for commercial application. This is attributed to the smoother morphology of $B_xC_yN_z$ films. The hardness was determined to be 20 ± 3 GPa, and the Young's modulus to 210 ± 30 GPa.

BCN compounds were produced by ball milling of h-BN, graphite and polypropylene (Torres et al., 2007). SEM, XRD, FTIR, and NEXAFS examinations yielded compositions as BCN, BC_2N , BC_4N , $BCNH_2$, a-BCN, and a- BC_4N . The particles are nearly spherical in shape (60 nm), whereas the crystallites have a size of about 1 nm. Tribological studies were performed on a- BC_4N films with a thickness of 2 μm (Caretti et al., 2007). Nanoindentation shows a hardness of 18 GPa and a Young's modulus of 170 GPa, whereas the wear examinations yielded in a constant rate of 2×10^{-7} mm³/Nm and a coefficient of friction of 0.2.

h-BCN was synthesized in a PECVD with triethylamine borane (TEAB) or with tris-(dimethylamine) borane (TDEAB) as single source precursors (Mannan et al., 2008, 2009). The chemical characterization by FTIR, XPS and NEXAFS showed B-N, B-C, C-N, and B-C-N bonds. A h-BCN (or sp^2 -BCN) was produced with a microhardness of 4 GPa (nanoindentation).

Various single source precursors (TMAB, TEAB, TMB) were introduced in a PECVD system. XPS, NEXAFS, and SEM/EDX were used for chemical identification. As results are determined h-BCN with stoichiometric formulas B_2C_3N (produced without NH_3) or B_2CN_3 (produced with NH_3).

Thick (20-70 nm) amorphous $B_xC_yN_z$ films were produced by DMAB ($(CH_3)_2HN:BH_3$) in a CVD procedure (Wu et al., 2010). XPS and SIMS were used for the determination of the elemental composition. The stoichiometry factors varied drastically: $0.46 \leq x \leq 0.68$; $0.07 \leq y \leq 0.43$; $0.01 \leq z \leq 0.26$. The results on thick BCN films are encouraging.

As can be derived from a large number of papers, the synthesized compounds are h-BCN in which carbon is replacing to some extent nitrogen in the hexagonal boron nitride structure. An extended TEM examination enlarge the knowledge in this field (Caretti et al., 2010). For low carbon content the h-BN is preserved in boron carbonitride compounds. By increasing the carbon content towards BCN stoichiometry ($1 < x > 2$) the hexagonal stacking sequence tends into a fullerene-like structure. Increasing the carbon content to the composition BC_4N , the sample exhibit an amorphous structure. Surprisingly, the authors call their compounds "solid solutions", although in various papers the chemical bonds B-C, B-N, and C-N were determined, yielding a defined chemical, completely hybridized compound and not a solution (Caretti et al., 2010).

Only a few papers announced the production of c-BCN (e.g., Gago et al., 2001a). The yield of this material (in IBAD), proposed to be as hard as diamond, was related to the optimization of the deposition temperature, the Ar content in the gas mixture, to the assisting current density, and to the ion energy. Although, the identification of c-BCN is still not proved (Mannan et al., 2011).

6. Acknowledgements

The authors acknowledge the financial support granted by the Deutsche Forschungsgemeinschaft (DFG) for the research projects "nanolayer speciation" (EN 207/22-1) and "chemical and physical characterization of nanolayers" (EN 207/22-2). The authors of the Russian Federation thank RFBR for the grant 07-03-91555-NNIOa and 10-03-91332-NNIOa.

7. References

- Als-Nielsen, J. (2001). *Elements of Modern X-Ray Physics*. Wiley, New York
- Abdellaoui, A., Bath, A., Bouchikhi, B., & Baehr, O. (1997). Structure and optical properties of boron nitride thin films prepared by PECVD. *Mater. Sci. Engin. B*, Vol. B47, No. 3, pp.257-262, ISSN 0921-5107
- Ahn, H., Alberts, L., Kim, Y.-M., Yu J., & Rie, K.T. (2003). BCN coatings at low temperature using PACVD: capacitive vs. inductive plasma coupling. *Surf. Coat. Technol.*, Vol. 169 -170, (June 2003), pp. 251-253, ISSN 0257-8972
- Ahn, H., Klimek, K.S., & Rie K.-T. (2003). BCN coatings by RF PACVD at low temperature. *Surf. Coat. Technol.*, Vol. 174 -175, pp. 1225-1228, ISSN 0257-8972
- Aoki, H., Shima, H., Kimura, C., & Sugino, T. (2007). Characterization of boron carbon nitride film for humidity sensor. *Diamond Related Materials* *Diamond Relat. Mater.*, Vol. 16, No. 4-7, pp. 1300-1303, ISSN 0925-9635

- Aoki, H., Tokuyama, S., Sasada, T., Watanabe, D., Mazumder, M. K., Kimura, C., & Sugino, T. (2008). Dry etching properties of boron carbon nitride (BCN) films using carbon fluoride gas. *Diamond Relat. Mater.*, Vol. 17, No. 7-10, pp.1800-1804, ISSN 0925-9635
- Aoki, H., Watanabe, D., Moriyama, R., Mazumder, M. K., Komatsu, N., Kimura, C., & Sugino, T. (2008). Influence of moisture on BCN (low-K) film for interconnection reliability. *Diamond Relat. Mater.*, Vol. 17, No. 4-5, pp. 628-632, ISSN 0925-9635
- Aoki, H., Hara, M., Masuzumi, T., Mazumder, M. K., Ooi, N., Watanabe, D., Kimura, C., & Sugino, T. (2009). Influence of Cu electroplating solutions on boron carbon nitride (BCN) film. *Appl. Surf. Sci.*, Vol. 255, No. 6, (October 2008), pp. 3719-3722, ISSN 0169-4332
- Aoki, H., Masuzumi, T., Hara, M., Watanabe, D., Kimura, C., & Sugino, T. (2009). Boron carbon nitride film containing hydrogen for 2nm node low-k interconnection, *VLSI Technology, Systems, and Applications (VLSI-TSA) 2009 International Symposium*, Hsinchu, April 2009
- Aoki, H., Masuzumi, T., Watanabe, D., Mazumder, M.K., Sota, H., Kimura, C., & Sugino, T. (2009). Influence of oxygen plasma treatment on boron carbon nitride film composition. *Appl. Surf. Sci.*, Vol. 255, No. 6, October 2008, pp. 3635-3638, ISSN 0169-4332
- Aoki, H., Tokuyama, S., Masuzumi, T., Hara, M., Mazumder, M. K., Watanabe, D., Kimura, C., & Sugino, T. (2009). Synthesis of methyl boron nitride film as low-k insulating film for LSI interconnection. *Diamond Relat. Mater.*, Vol. 18, No. 5-8, pp. 1048-1051, ISSN 0925-9635
- Aoki, H., Hara, M., Masuzumi, T., Ahmed, F., Kimura, C., & Sugino, T. (2010). Dry etching properties of methyl-BCN film with C₄F₈ gas for Cu/low-k interconnection. *Diamond Relat. Mater.*, Vol. 19, No.5-6, (January 2010), pp. 507-509, ISSN 0925-9635
- Aoki, H., Masuzumi, T., Hara, M., Lu, Z., Watanabe, D., Kimura, C., & Sugino, T. (2010). Influence of the methyl group on the dielectric constant of boron carbon nitride films containing it. *Diamond Relat. Mater.*, Vol. 19, No.12, (June 2010), pp. 1437-1440, ISSN 0925-9635
- Awad, Y., El Khakani, M.A., Aktik, C., Mouine, J., Camiré, N., Lessard, M., Scarlete, M., Al-Abadleh, H.A., & Smirani, R. (2009). Structural and mechanical properties of amorphous silicon carbonitride films prepared by vapor-transport chemical vapor deposition. *Surf. Coat. Technol.*, Vol. 204, No.4, (August 2009), pp.539-545, ISSN 0257-8972
- Baake, O., Hoffmann, P.S., Kosinova, M.L., Klein, A., Pollakowski, B., Beckhoff, B., Fainer, N.I., Trunova, V.A., & Ensinger, W. (2010). Analytical characterization of BC_xN_y films generated by LPCVD with triethylamine borane. *Analytical & Bioanalytical Chemistry*, Vol.398, No.2, (June 2010), pp.1077-1084, ISSN 1618-2642
- Badyan, A., Nemiski, T., Appenheimer, S., & Olkusnik, E. (1972). Crystal structure in the system boron - carbon - nitrogen, In: *Himicheskaya soyaz v poluprovodnikah i polumetallah*, pp. 362-366, "Nauka I tehnika", Minsk (in Russian)
- Badzian, A. (2002). Stability of Silicon Carbonitride Phases. *J. Am. Ceram. Soc.*, Vol.85, pp.16-20
- Badzian, A.R., Niemyski, T., Appenheimer, S., & Olkusnik, E. (1972). Graphite-Boron Nitride solid solution by chemical vapor deposition. *Proc. Third Inter.Conf.CVD*. Vol.3, pp.747-753, Salt Lake City, UT, 1972
- Bae, Y. W., Du, H., Gallois, B., Gonsalvest, K. E., & Wilkens, B. J. (1992). Structure and Chemistry of Silicon Nitride and Silicon Carbonitride Thin Films Deposited from

- Ethylsilazane in Ammonia or Hydrogen. *Chem. Mater.*, Vol.4, No.2, pp.478-483, ISSN 0897-4756
- Baehr, O., Theverin, P., Bath, A., Koukab, A., Losson, E., & Lepley, B. (1997). Preparation of boron nitride thin films by microwave plasma enhanced CVD, for semiconductor applications. *Mater. Sci. Engin. B*, Vol.B46, pp.101-104, ISSN 0921-5107
- Baram, M., Kaplan, W.D., (2008). Quantitative HRTEM analysis of FIB prepared specimens. *J. Microscopy*, Vol.232, No.3, pp. 395-405, ISSN 0022-2720
- Bath A., van der Put P.J., Lepley B. (1989). Study of boron nitride gate insulators grown by low temperature plasma enhanced chemical vapor deposition on InP. *Appl. Surf. Sci.*, V.39, pp.135-140, ISSN 0169-4332
- Bath, A., van der Put, P.J., Becht, J.G.M., Schooman, J., & Lepley, B. (1991). Plasma enhanced chemical vapor deposition and characterization of boron nitride gate insulators on InP. *J. Appl. Phys.*, Vol.70, No.8, pp.4366-4370, ISSN 0021-8979
- Bath, A., Baehr, O., Barrada, M., Lepley, B., van der Put, P.J., & Schoonman, J. (1994). Plasma enhanced chemical vapour deposition of boron nitride onto InP. *Thin Solid Films*, Vol.241, pp.278-281, ISSN 0040-6090
- Bauer-Marschallinger, J., Reitingner, B., Pfaff, H. (2007). Nanoindentation und Oberflächenwellen (Laser-ultraschall) zur Charakterisierung dünner Schichten. *Industrielles Symposium Mechatronik*. Linz, Austria
- Beckhoff, B., Kanngießer, B., Langhoff, N., Wedell, R., & Wolff, H. (Eds.), (2006). *Practical X-Ray Fluorescence Analysis*. Springer Verlag, ISBN-10 3-540-28503-9
- Beckhoff, B., Fliegauf, R., Kolbe, M., Müller, M., Weser, J., & Ulm, G., (2007). Reference-Free Total Reflection X-ray Fluorescence Analysis of Semiconductor Surfaces with Synchrotron Radiation. *Analytical Chemistry*, Vol.79, No.20, pp.7873-7382, ISSN 0003-2700
- Beneddouch, A., Berjoan, R., Beche, E., Merle-Mejean, T., Schamm, S., Serin, V., Taillades, G., Pradel, A., & Hillel, R. (1997). Structural characterization of amorphous SiC_xN_y chemical vapor deposited coatings. *J.Appl.Phys.*, Vol.81, No.9, pp.6147-6154, ISSN 0021-8979
- Bengu, E., Genisel, M. F., Gulseren, O. & Ovali, R. (2009). Theoretical and spectroscopic investigations on the structure and bonding in B-C-N thin films. *Thin Solid Films*, Vol. 518, No. 5, pp. 1459-1464, ISSN 0040-6090
- Besmann, T. M. (1990). Chemical Vapor Deposition in the Boron-Carbon-Nitrogen System. *J.Amer. Ceram. Soc.*, Vol.73, Is. 8, April 1990, pp.2498-2501, ISSN 0002-7820
- Blaszczyk-Lezak, I., Wrobel, A. M., Kivitorma, M. P. M., & Vayrynen, I. J. (2005). Silicon Carbonitride Films Produced by Remote Hydrogen Microwave Plasma CVD Using a (Dimethylamino)dimethylsilane Precursor. *Chem. Vap. Deposition*, Vol. 11, No. 1, (January 2005), pp. 44-52, ISSN 0948-1907
- Blaszczyk-Lezak, I., Wrobel, A.M., Aoki, T., Nakanishi, Y., Kucinska, I., & Tracz. A. (2006). Remote nitrogen microwave plasma chemical vapor deposition from a tetramethyldisilazane precursor. 1. Growth mechanism, structure, and surface morphology of silicon carbonitride films. *Thin Solid Films*, Vol. 497, No.1-2, (February 2006), pp. 24-34, ISSN 0040-6090
- Blaszczyk-Lezak, I., Wrobel, A.M., & Bielinski, D.M. (2006). Remote nitrogen microwave plasma chemical vapor deposition from a tetramethyldisilazane precursor. 2. Properties of deposited silicon carbonitride films. *Thin Solid Films*, Vol. 497, No. 1-2, (February 2006), pp. 35-41, ISSN 0040-6090

- Blaszczyk-Lezak, I., Wrobel, A.M., & Bielinski, D.M. (2006). Remote hydrogen microwave plasma chemical vapor deposition of silicon carbonitride films from a (dimethylamino)dimethylsilane precursor: Compositional and structural dependencies of film properties. *Diamond Relat. Mater.*, Vol. 15, No. 10, (October 2006), pp. 1650–1658, ISSN 0925-9635
- Blaszczyk-Lezak, I., Wrobel, A.M., Kivitoroma, M.P.M, Vayrynen, I.J., & Tracz, A. (2007). Silicon carbonitride by remote microwave plasma CVD from organosilicon precursor: Growth mechanism and structure of resulting Si:C:N films. *Appl. Surf. Sci.*, Vol. 253, No. 17, (June 2007), pp. 7211–7218, ISSN 0169-4332
- Boudiombo, J., Baehr, O., Boudrioua, A., Thevenin, P., Loulergue, J.C., & Bath, A. (1997). Modes of propagating light waves in thin films of boron nitride deposited by plasma enhanced chemical vapor deposition. *Mater. Sci. Engin. B*, Vol.B46, pp.96–98, ISSN 0921-5107
- Boughaba, S., Sproule, G.I., McCaffrey, J.P., Islam, M., & Graham, M.J. (2002). Synthesis of amorphous silicon carbonitride films by pulsed laser deposition. *Thin Solid Films*, Vol. 402, pp.99–110, ISSN 0040-6090
- Bragg, W.H., Bragg, W.L., (1913). The structure of the diamond. *Nature*, Vol.91, No.2283, p.557, ISSN 0028-0836.
- Briggs, D.,; Seah, M.P., (1990). *Practical Surface Analysis*. Vol.1, Wiley
- Brooks, T.A., Hess, D.W. (1987). Plasma-enhanced chemical vapor deposition of silicon nitride from 1,1,3,3,5,5 – hexamethylcyclotrisilazane and ammonia. *Thin Solid Films.*, Vol.153, No. 1-3, (March 1987), pp.521–529, ISSN 0040-6090
- Brooks, T.A., Hess, D.W. (1988). Deposition chemistry and structure of plasma-deposited silicon nitride films from 1,1,3,3,5,5 – hexamethylcyclotrisilazane. *J. Appl. Phys.*, Vol.64, No. 2, (January 1988), pp. 841–849, ISSN 0021-8979
- Brydson, R., Daniels, H., Fox, M.A., Greatrex R., & Workman, C. (2002). Synthesis of a new boron carbonitride with a B₄C-like structure from the thermolysis of N-alkylated borazines. *Chem. Commun.*, No.7, (February 2002), pp. 718–719
- Bulou, S., Le Brizoual, L., Miska, P., de Pouques, L., Hugon, R., & Belmahi, M. (2010). a-Si_xN_y thin films deposited by a microwave plasma assisted CVD process using a CH₄/N₂/Ar/HMDSN mixture: methane rate effect. *IOP Conf. Series: Materials Science and Engineering.*, Vol. 12, pp.012002–012005
- Byon, E., Son, M., Hara, N. & Sugimoto, K. (2004). Corrosion behavior of boron-carbon-nitride films grown by magnetron sputtering. *Thin Solid Films*, Vol. 447–448, pp. 197–200, ISSN 0040-6090
- Byon, E.; , Son, M.; , Lee, K.-H.; , Nam, K.-S.; , Hara, N.; , Sugimoto, K., (2006). Electrochemical properties of boron-carbon-nitride films formed by magnetron sputtering. *Electrochim.Acta*, Vol.51, No.13 (August 2005), pp.2662–2668, ISSN: 0013-4686
- Cao, Z. X. (2001). Nanocrystalline silicon carbonitride thin films prepared by plasma beam-assisted deposition. *Thin Solid Films*, Vol. 401, pp.94–101, ISSN 0040-6090
- Cao, Z. X., Oechsner, H. (2003). Optical and mechanical characteristics of nanocrystalline boron carbonitride films synthesized by plasma-assisted physical vapor deposition. *J. Appl. Phys.* Vol. 93, No. 2, (October 2002), pp. 1186–1189
- Caretti, I., Jimenez, I., & Albella J.M. (2003). BCN films with controlled composition obtained by the interaction between molecular beams of B and C with nitrogen ion beams. *Diamond Relat. Mater.*, Vol. 12, pp. 1079–1083, ISSN 0925-9635

- Caretti, I.; Jimenéz, I.; Gago, R.; Cáceres, D.; Abendroth, B.; & Albella, J.M., (2004). Tribological properties of ternary BCN films with controlled composition of bonding structure. *Diamond Relat. Mater.*, Vol.13, No.4-8, pp.1532-1537, ISSN 0925-9635
- Caretti I., Albella J.M., Jiménez I. (2007). Tribological study of amorphous BC₄N coatings. *Diamond Relat. Mater.*, Vol. 16, No.1, (March 2001), pp. 63–73, ISSN 0925-9635
- Caretti, I., Torres, R., Gago, R., Landa-Cánovas, A.R., & Jiménez, I. (2010). Effect of Carbon Incorporation on the Microstructure of BC_xN (x=0.25, 1, and 4) Ternary Solid Solutions Studied by Transmission Electron Microscopy. *Chem. Mater.*, Vol. 22, No.6, (February 2010), pp. 1949–1951, ISSN 0897-4756
- Chang, W.-R., Fang, Y.-K., Ting, Sh.-F., Tsair, Y.-Sh., Chang, Ch.-N., Lin, Ch.-Yu, & Chen, Sh.-F. (2003). The Hetero-Epitaxial SiCN/Si MSM Photodetector for High-Temperature Deep-UV Detecting Applications. *IEEE Electron Device Letters*, Vol. 24, No.9, pp.565-567, ISSN 0741-3106
- Charitidis, C., Panayiotatos, Y., & Logothetidis, S. (2003). A quantitative study of the nano-scratch behavior of boron and carbon nitride films. *Diamond Relat. Mater.*, Vol. 12, No. 3-7, pp. 1088-1092, ISSN 0925-9635
- Chen, C.W., Huang, C.C., Lin, Y.Y., Chen, L.C. & Chen, K.H. (2005). The affinity of Si-N and Si-C bonding in amorphous silicon carbon nitride (a-SiCN) thin film. *Diamond Relat. Mater.*, Vol.14, No.3-7, pp.1126– 1130, ISSN 0925-9635
- Chen, L. C., Chen, C. K., Wei, S. L., Bhusari, D. M., Chen, K. H. & Huang, Y. S. (1998). Crystalline silicon carbon nitride: A wide band gap semiconductor. *Appl. Phys. Lett.*, Vol. 72, No.19, (March 1998), pp.2463-2465, ISSN 0003-6951
- Chen, Y.; Chung, Y.-W.; & Li, S.-Y., (2006). Boron carbide and boron carbonitride thin films as protective coatings in ultra-high density hard disc drives. *Surf. Coat. Technol.*, Vol.200, No.12-13 (February 2005), pp.4072-4077, ISSN 0257-8972
- Chen, Z., Lin, H., Zhou, J., Ma, Z., & Xie, E. (2009). IR studies of SiCN films deposited by RF sputtering method. *J. Alloys and Compounds*, Vol.487, pp. 531–536, ISSN 0925-8388
- Cheng, W., Jiang, J., Zhang, Y., Zhu, H., & Shen, D. (2004). Effect of the deposition conditions on the morphology and bonding structure of SiCN films. *Materials Chemistry and Physics*, Vol. 85, No.2-3, (January 2004), pp.370–376, ISSN 0254-0584
- Cheng, W., Lin F., Shi W., Ma X., Shen D., & Zhang, Y. (2006). Synthesis and field emission property of SiCN cone arrays. *Materials Chemistry and Physics*, Vol.98, (September 2005), pp.500–503, ISSN 0254-0584
- Chepelengkou, Y.V., Em, A.P., Borodulin, P.Y., & Momot, L.B. (1964). Thermal stability of refractory crucibles based on boron nitride. No.6, p.253.
- Dekempeneer, E.H.A., Meneve, J., Kuypers, S., & Smeets, J. (1996). Tribological properties of r.f. PACVD amorphous B-N-C coatings. *Thin Solid Films*, Vol. 281-282, pp. 331-333, ISSN 0040-6090
- Dekempeneer, E., Wagner, V., Gibson, P., Meneve, J., Kuypers, S., van Izendoorn, L., Smeets, J., Geurts, J., & Caudano, R. (1997) Tribology and microstructure of PACVD B-N-C coatings. *Diamond Film & Technol.* Vol.7, No.3, pp. 181-193., ISSN 0917-4540
- Derre, A., Filipozzi, L., Bouyer, F. & Marchand, A. (1994) Parametric study of the chemical vapour deposition of carbon-boron-nitrogen compounds. *J. Mater. Sci.*, Vol. 29, No. 6, pp.1589-1594, ISSN 0022-2461
- Dez, R., Ternergall, F., Reynaud, C., Mayne, M., Armand, X. & Herlin-Boime, N. (2002). Laser synthesis of silicon carbonitride nanopowders; structure and thermal

- stability. *J. European Ceramic Society*, Vol. 22, No.16, (February 2002), pp.2969–2979, ISSN 0955-2219
- Di Mundo, R., d'Agostino, R., Fracassi, F., & Palumbo, F. (2005). A Novel Organosilicon Source for Low Temperature Plasma Deposition of Silicon Nitride-like Thin Films. *Plasma Process. Polym.*, Vol. 2, No. 8 (June, 2005), pp. 612–617, ISSN 1612-8850
- Dinescu, M., Perrone, A., Caricato, A.P., Mirengi, L., Gerardi, C., Ghica, C., & Frunza, L. (1998). Boron carbon nitride films deposited by sequential pulses laser deposition. *Appl. Surf. Sci., Appl. Surf. Sci.*, Vol. 127-129, pp. 692-696, ISSN 0169-4332
- Du, X.-W., Fu, Y., Sun, J., Yao, P., & Cui, L. (2007). Intensive light emission from SiCN films by reactive RF magnetron sputtering. *Materials Chemistry and Physics*. Vol.103, pp.456–460, ISSN 0254-0584
- Dubovik, T.V. & Struk, L.I. (1965). Electric insulation tube of boron carbonitride for protection of metal thermocouples. *Translated from Poroshkovaya Metallurgia*, No.5, pp.107-110
- Etou, Y., Tai, T., Sugiyama, T., & Sugino, T. (2002). Characterization of boron carbon nitride films with a low dielectric constant. *Diamond Relat. Mater*, Vol. 11, No. 3-6, pp. 985-988, ISSN 0925-9635
- Fainer, N.I., Rumyantsev, Yu.M., Kosinova, M.L., Yurjev, G.S., Maximovskii, E.A., & Kuznetsov F.A. (1997). The investigation of properties of silicon nitride films obtained by RPECVD from hexamethyldisilazane. *Appl. Surf. Sci.*, Vol. 113-114, pp. 614-617, ISSN 0169-4332
- Fainer, N.I., Kosinova, M.L., Rumyantsev, Yu.M. & Kuznetsov, F.A. (1999). RPECVD thin silicon carbonitride films using hexamethyldisilazane. *J. Phys. IV*, V. 9, pp.Pr8-769 - Pr8-775, ISSN 1155-4339
- Fainer, N.I., Kosinova, M.L., Yurjev, G.S., Rumyantsev, Yu.M. & Asanov, I.P. (2000). The structure study of thin boron and silicon carbonitride films by diffraction of synchrotron radiation. *NIMA.*, Vol. 448, No. 1-2, (June 2000), pp.294-298, ISSN 0168-9002
- Fainer, N.I., Kosinova, M.L., & Rumyantsev, Y.M. (2001). Thin films of silicon and boron carbonitrides: synthesis, composition and structure research. *Russ. Chem. J.*, Vol. XLV, No. 3., pp. 101-108, ISSN 0373-0247
- Fainer, N.I., Maximovskii, E.A., Kosinova, M.L., & Rumyantsev, Yu.M. (2001). The study of thermal annealing influence on structure and phase composition of silicon carbonitride by diffraction of synchrotron radiation. *Materials Science Forum*, Vol. 378-381, pp.493-498, ISSN 0255-5476
- Fainer, N.I., Maximovskii, E.A., Rumyantsev, Yu.M., Kosinova, M.L. & Kuznetsov, F.A. (2001). Study of structure and phase composition of nanocrystal silicon carbonitride films. *NIMA*. Vol. 470, No. 1, (September 2001), pp.193-197, ISSN 0168-9002
- Fainer, N.I., Rumyantsev, Yu.M., Golubenko, A.N., Kosinova, M.L., & Kuznetsov, F.A. (2003). Synthesis of nanocrystalline silicon carbonitride films by remote plasma enhanced chemical vapor deposition using the mixture of hexamethyldisilazane with helium and ammonia. *J. Cryst. Growth.*, Vol. 248, pp.175-179, ISSN 0022-0248
- Fainer, N.I., Kosinova, M.L., Rumyantsev, Yu.M., & Kuznetsov, F.A. (2004). Physical and chemical properties of silicon carbonitride nanocrystalline films. *J. Struct. Chem.*, Vol. 45, Supplement 1, (January 2004), pp. S65-S70, ISSN 0022-4766
- Fainer, N., Rumyantsev, Y., Kosinova, M., Maximovski, E., Kesler, V. (2007). Low-k dielectrics on base of silicon carbon nitride films. *Surf. Coat. Technol.*, Vol. 201, (April 2007), pp. 9269-9274, ISSN 0257-8972

- Fainer, N.I., Kosinova, M.L., Rumyantsev, Yu.M., Maximovskii, E.A., & Kuznetsov, F.A. (2008). Thin silicon carbonitride films are perspective low-k materials. *Journal of Physics and Chemistry of Solids*, Vol. 69, No. 2-3, (February-March 2008), pp. 661-668, ISSN 0022-3697
- Fainer, N.I., Bakovets, V.V., Kosinova, M.L., Rumayntsev, Yu.M., Maximovski, E.A., & Kuznetsov, F.A. (2008). SiCN coating as the protecting layer of quartz crucibles used for silicon crystallization. *Abstracts of 14-th APAM General Assembly and conference "State of materials research and new trends in material science"*, pp. 84-85, New Delhi, India, November, 2008
- Fainer, N.I., Golubenko, A.N., Rumyantsev, Yu.M., & Maximovskii, E.A. (2009). Use of Hexamethylcyclotrisilazane for Preparation of Transparent Films of Complex Compositions. *Glass Physics and Chemistry*, Vol.35, No.3, (August 2008), pp. 274-283, ISSN 1087-6596
- Fainer, N.I., Rumyantsev, Yu.M., Kesler, V.G., Maximovski, E.A. & Kuznetsov, F.A. (2009). Synthesis and thermal stability of nanocomposite $\text{SiC}_x\text{N}_y\text{:H}$ films from cycle siliconorganic precursor. *ECS Trans.*, Vol. 25, No. 8, pp.921-926, ISSN 1938-5862
- Ferreira, E., Fortunato, I., Vilarinho, P., Viana, A.S., Ramos, A.R., Alves, E., & Martins, R., (2006). Hydrogenated silicon carbon nitride films obtained by HWCVD, PA-HWCVD and PECVD techniques. *Journal of Non-Crystalline Solids*, Vol.352, No.9-20, pp.1361-1366, ISSN 0022-3093
- Filipozzi, L., Derré, A., Conard, J., Piraux, L., & Marchand, A. (1995). Local order and electrical properties of boron carbonitride films. *Carbon*, Vol. 33, IsNo. 12, (August 1995), pp. 1747-1757; ISSN 0008-6223
- Filipozzi, L., Piraux, L., Marchand, A., Derré, A., Adouard, A., & Kinany-Alaoui, M. (1997). Unusual behavior of the magnetoresistance of boron carbonitride films at low temperature. *Journal of Materials Research*, Vol. 12 , IsNo. 07, (December 1996), pp.1711-1721
- Fitzpatrick, P.R., & Ekerdt, J.G., (2008). Film continuity and interface bonding of thin boron carbonitride films on Ge(100) and Si(100). *J. Vac. Sci. Technol.A*, Vol.26, No.6, pp.1397-1401, ISSN 0734-2101
- Freire Jr., F.L., Reigada, D.C., & Prioli, R. (2001). Boron Carbide and Boron-Carbon Nitride Films Deposited by DC-Magnetron Sputtering: Structural Characterization and Nanotribological Properties. *Physica status solidi (a)*, Vol. 187, No. 1, (July 2001), pp 1-12, ISSN 1862-6300
- Fu, Yo., Sun, C. Q, Du, H., & Yan, B. (2001). Crystalline carbonitride forms harder than the hexagonal Si-carbonitride crystallite. *J. Phys. D: Appl. Phys.*, Vol.34, No.9, pp.1430-1435, ISSN 0022-3727
- Fujiwara, H. (2007). *Spectroscopic Ellipsometry: Principles and Applications*. John Wiley & Sons Inc., ISBN 0-470-01608-6
- Fultz, B. & Howe, J. (2007). *Transmission Electron Microscopy and Diffractometry of Materials*. Springer, ISBN 3540738851
- Gago, R., Jimenez, I., & Albella J.M. (2000). Boron[carbon]nitrogen compounds grown by ion beam assisted evaporation. *Thin Solid Films* , Vol. 373, pp. 277-281, ISSN 0040-6090
- Gago, R., Jimenéz, I., Sajavaara, T., Rauhala, E., & Albella, J.M., (2001). X-Ray absorption studies of cubic boron-carbon-nitrogen films grown by ion beam assisted evaporation. *Diamond and Related. Materials*, Vol.10, No.3-7, pp.1165-1169, ISSN 0925-9635

- Gago, R., Jimenez, I., Albella, J.M., & Terminello, L.J., (2001). Identification of ternary boron-carbon-nitrogen hexagonal phases by x-ray absorption spectroscopy. *Appl. Phys. Lett.*, Vol.78, (April 2001), pp.3430-3432, ISSN 0003-6951
- Gago, R., Jimenez, I., Agulló-Rueda, F., Albella, J.M., Czizány, Zs., & Hultman, L. (2002). Transition from amorphous boron carbide to hexagonal boron carbon nitride thin films induced by nitrogen ion assistance. *J. Appl. Phys.*, Vol. 92, No. 9, (August 2002), pp. 5177-5182, ISSN 0021-8979
- Gago, R.; Jimenez, I.; Garcia, I.; Albella, J.M., (2002). Growth and characterisation of boron-carbon-nitrogen coatings obtained by ion beam assisted evaporation. *Vacuum*, Vol.64, No.3-4, pp.199-204, ISSN 0042-207X
- Gago, R., Jimenez, I., Kreissig, U., & Albella, J.M. (2002). X-Ray absorption study of the bonding structure of BCN compounds enriched in carbon by CH₄ ion assistance. *Diamond and Relat.ed Mater.ials*, Vol. 11, pp. 1295-1299, ISSN 0925-9635
- Gammer, K., Kolber, T., Piplits, K., Nowikow, K., Tang, X., Haubner, R., & Hutter, H. (2002). Characterization of carbon-boron nitride-coatings prepared with chemical vapor deposition by auger electron spectroscopy, electron probe microanalysis and secondary ion mass spectrometry. *Thin Solid Films*, Vol. 406, (December 2001), pp. 98-102, ISSN 0040-6090
- Gao, P., Xu, J., Piao, Y., Ding, W., Wang, D., Deng, X., & Dong, C. (2007). Deposition of silicon carbon nitride thin films by microwave ECR plasma enhanced unbalance magnetron sputtering. *Surf. Coat. Technol.*, Vol. 201, No.9-11, pp.5298-5301, ISSN 0257-8972
- Gardiner, D.J. (1989). *Practical Raman spectroscopy*. Springer-Verlag, ISBN 978-0387502540
- Giessibl, F.J. (2003). Advances in atomic force microscopy. *Reviews of Modern Physics.* , Vol.75, No.3, pp.949-983, ISSN: 0034-6861
- Goldsmith, J.G.; ., Lazof, D.B.; ., & Linton, R.W. (1999). *Secondary ion mass spectrometry. Biomedical Applications of Microprobe Analyses*. Academic Press
- Goldstein, G.I.; Newbury, D.E.; Echlin, P.; Joy, D.C.; Fiori, C.; & Lifshin, E. (1981). *Scanning electron microscopy and x-ray microanalysis*. Plenum Press, New York, ISBN 030640768X
- Hasegawa, T., Yamamoto, K. & Kakudate, Y. (2002). Synthesis of B-C-N thin films by electron beam excited plasma CVD. *Diamond and Relat.ed Mater.ials*, Vol. 11, No.3-6, pp. 1290-1294, ISSN 0925-9635
- Hasegawa, T., Yamamoto, K. & Kakudate, Y. (2003). Influence of raw gases on B-C-N films prepared by electron beam excited plasma CVD. *Diamond Relat.ed Mater.ials*, Vol. 12, No.10-11, pp. 1945-1048, ISSN 0925-9635
- Hegemann, D., Riedel, R., Dreblner, W., Oehr, C., Schindler, B., & Brunner H. (1997). Boron Carbonitride Thin Films by PACVD of Single-Source Precursors. *Chem. Vap. Deposition*, Vol. 3, No. 5, pp.257-262, ISSN 1521-3862
- Hegemanna, D., Riedel, R., & Oehr C. (1999). Influence of single-source precursors on PACVD-derived boron carbonitride thin films. *Thin Solid Films*, Vol. 339, (August 1999), pp. 154-159, ISSN 0040-6090
- Hein, M., Hoffmann, P., Lieser, K.H., & Ortner, H., (1992). Application of X-ray fluorescence analysis with total-reflection (TXRF) in material science. *Fresenius J.Anal.Chem.*, Vol.343, No.9-10, pp.760-764, ISSN 0937-0633
- Hellgren, N., Berlind, T., Gueorguiev, G.K., Johansson, M.P., Stafström, S., & Hultman, L. (2004). Fullerene-like B-C-N thin films: a computational and experimental study. *Mater. Sci. Engin. B.*, Vol.113, No.3, (August 2004), pp.242-247, ISSN: 0921-5107

- Hemraj-Benny, T., Banerjee, S., Sambasivan, S., Balasubramanian, M., Fischer, D.A., Eres, G., Puretzky, A.A., Geohegan, D.B., Lowndes, D.H., Han, W., Misevich, J.A., & Wong, S.S. (2006). Near-Edge X-ray Absorption Fine Structure Spectroscopy as a Tool for Investigating Nanomaterials. *Small*, Vol.2, No.1, pp.26-35, online ISSN: 1613-6829
- Hirai, T., & Goto, T. (1981). Preparation of amorphous Si_3N_4 -C plate by chemical vapour deposition. *Journal of Materials Science*, Vol. 16, No.1, pp.17-23, ISSN: 0022-2461
- Hoche, H., Allebrandt, D., Bruns, M., Riedel, R. & Fasel, C. (2008). Relationship of chemical and structural properties with the tribological behavior of sputtered SiCN films. *Surf. Coat. Technol.*, Vol.202, No.22-23, pp.5567-5571, ISSN 0257-8972
- Hoche H., Pusch C., Riedel R., Claudia F. & Klein A. (2010). Properties of SiCN coatings for high temperature applications – Comparison of RF-, DC- and HPPMS-sputtering. *Surf. Coat. Technol.*, Vol.205, Suppl.1, pp.S21-S27, ISSN 0257-8972
- Hoffmann, P.; Baake, O.; Beckhoff, B.; Ensinger, W.; Fainer, N.; Klein, A.; Kosinova, M.; Pollakowski, B.; Trunova, V.; Ulm, G.; Weser, J., (2007). Chemical bonding in carbonitride nanolayers. *Nuclear Instruments and Methods A*, Vol.575, No.1-2, pp.78-84, ISSN: 0168-9002
- Houška, J.; Vlček, J.; Potocký, Š.; Peřina, V., (2007). Influence of substrate bias voltage on structure and properties of hard Si-B-C-N films prepared by reactive magnetron sputtering. *Diamond and Related Materials*, Vol.16, No.1 (March 2006), pp.29-36, ISSN: 0925-9635.
- Ibberson, R.M.; David, W.I.F., (2002). Neutron powder diffraction. In: *Structure determination from powder diffraction data. IUCr monographs on crystallography*, Oxford scientific publications, ISBN 0-19-850091-2
- Ishimaru, M., Naito, M., Hirotsu, Y., & Sickafus, K. E. (2003). Amorphous structures of silicon carbonitride formed by high-dose nitrogen ion implantation into silicon carbide. *Nuclear Instruments and Methods in Physics Research B*, Vol.206, pp.994-998, ISSN 0168-583X
- Ivashchenko, L. A., Ivashchenko, V. I., Porada, O. K., Dub, S. M., Skriskii, P. L., Ushakov, M. V., Karpets, M. V., Stegnii, A. I., & Grishnova L. A. (2007). Hard plasma chemical coatings based on silicon carbon nitride. *Powder Metallurgy and Metal Ceramics*, Vol. 46, No.11-12, pp.543-549, ISSN 1068-1302
- Izumi, A., Oda, K. (2006). Deposition of SiCN films using organic liquid materials by HWCVD method. *Thin Solid Films*, Vol.501, No.1-2, pp.195-197, ISSN 0040-6090
- Jäschke, T.; Jansen, M., (2006). A new borazine-type single source precursor for Si/B/C/N ceramics. *J.Mater.Chem.*, Vol.16, No.27, pp.2792-2799,. ISSN 0959-9428DOI: 10.1039/B601939K
- Johansson, M. P., Ivanov, I., Hultman, L., Münger, E. P., & Schütze, A. (1996). Low-temperature deposition of cubic BN:C films by unbalanced direct current magnetron sputtering of a B4C target. *J. Vac. Sci. Technol. A*, Vol.14, No.6, (August 1996), p.3100-3108, ISSN 0734-2101
- Kafrouni, W., Rouessac, V., Julbe, A., & Durand, J. (2010). Synthesis and characterization of silicon carbonitride films by plasma enhanced chemical vapor deposition (PECVD) using bis(dimethylamino)dimethylsilane (BDMADMS), as membrane for a small molecule gas separation. *Appl. Surf. Sci.*, Vol. 257, No. 4, (December 2010), pp. 1196-1203, ISSN 0169-4332
- Kaner, R. B., Kouvetakis, J., Warble, C. E., Sattler, M. L., and Bartlett, N. (1987). Boron-carbon-nitrogen materials of graphite-like structure. *Materials Research Bulletin*, Vol. 22, IsNo. 3, (March 1987), pp. 399-404, ISSN: 0025-5408

- Kawaguchi, M., Nozaki, K., Kita, Y., & Doi, M. (1991). Photoluminescence characteristics of BN(C,H) prepared by chemical vapour deposition. *J. Mater. Sci.*, Vol.26, No.14, pp.3926-3930, ISSN 0022-2461
- Kawaguchi, M., & Bartlett, N. (1995). Syntheses, Structure, and Intercalation Chemistry of B/C/N Materials Based on the Graphite Network, In: *Fluorine-Carbon and Fluoride-Carbon Materials. Chemistry, Physics, and Applications*, Nakajima, T., pp.187-238, Marcel Dekker, Inc., New York-Basel-Hong Kong.
- Kawaguchi, M., Kawashima, T., Nakajima, T. (1996). Syntheses and Structures of New Graphite-like Materials of Composition BCN(H) and BC₃N(H). *Chem. Mater.*, Vol. 8, No. 6, pp.1197-1201, ISSN 0897-4756
- Kawaguchi, M. (1997). B/C/N Materials Based on the Graphite Network. *Adv.Mater.*, Vol.9, No. 8, pp.615-625, ISSN 1521-4095
- Kawaguchi, M., Sugiyama, A. (1997). Syntheses and characterization of graphite-like material of composition BC₆N₂(H). *Materials Science Research International*, Vol. 3, No.2, (1997) pp. 88-93, ISSN: 1341-1683
- Kawaguchi, M., & Wakukawa, Y. (1999). Synthesis of Graphite-like Material of Composition BC₆N by CVD method at high temperature. *Carbon*, Vol. 37, No. 1, pp.147-163, ISSN: 0008-6223
- Kawaguchi, M., Wakukawa, Y., & Kawano, T. (2001). Preparation and electronic state of graphite-like layered material BC₆N. *Synthetic Metals*, Vol. 125, IsNo. 2, July 2001, pp. 259-263, ISSN: 0379-6779
- Keeler, J.; (2005). *Understanding NMR Spectroscopy*. John Wiley & Sons. ISBN 0470017864
- Kida, T., Shigezumi, K., Mannan, Md. A., Akiyama, M., Baba, Y., & Nagano, M. (2009). Synthesis of boron carbonitride (BCN) films by plasma-enhanced chemical vapor deposition using trimethylamine borane as a molecular precursor. *Vacuum*, Vol. 83, pp. 1143-1146, ISSN 0042-207X
- Kim, D. H., Byon, E., Lee, S., Kim, J.-K. & Ruh, H. (2004). Characterization of ternary boron carbon nitride films synthesized by RF magnetron sputtering. *Thin Solid Films*, Vol. 447-448, pp. 192-196, ISSN 0040-6090
- Kimura, C., Okada, K., Funakawa, Sh., Sakata, Sh., & Sugino, T. (2005). Electron affinity and field emission characteristics of boron carbon nitride film. *Diamond Relat. Mater.*, Vol. 14, No. 3-7, pp. 719-723, ISSN: 0925-9635
- Kimura, C., Sota, H., Aoki, H., & Sugino, T. (2009). Atomic bonds in boron carbon nitride films synthesized by remote plasma-assisted chemical vapor deposition. *Diamond Relat. Mater.*, Vol. 18, No. 2-3, pp. 478-481, ISSN: 0925-9635
- Kosinova, M.L., Fainer, N.I., Rumyantsev, Yu.M., Golubenko, A.N., & Kuznetsov, F.A. (1999). LPCVD boron carbonitride films from triethylamine borane. *J. Phys. IV France.*, Vol. 9, pp. Pr8-915- Pr8-921, ISSN 1155-4339
- Kosinova, M.L., Rumyantsev, Yu.M., Fainer, N.I., Maximovski, E.A., & Kuznetsov, F.A. (2001). The structure study of boron carbonitride films obtained by use of trimethylamine borane complex. *NIMA*, Vol. 470, pp. 253-257, ISSN 0168-9002
- Kosinova, M.L., Fainer, N.I., Sulayeva, V.S., Rumyantsev, Yu.M., Terauchi, M., Shibata, K., Satoh, F., Tanaka, M., & Kuznetsov, F.A. (2001). Structure and composition investigation of RPECVD SiCN and LPCVD BCN films. *J. Phys. IV France.*, Vol. 11, pp. Pr3-987- Pr3-994, ISSN 1155-4339
- Kosinova, M. L., Rumyantsev, Yu. M., Golubenko, A. N., Fainer, N.I., Ayupov, B.M., Dolgovosova, I.P., Kolesov, B.A., Kaichev, V. V., & Kuznetsov, F.A. (2003). Chemical Composition of Boron Carbonitride Films Grown by Plasma-Enhanced

- Chemical Vapor Deposition from Trimethylamineborane. *Inorganic Mater.*, Vol. 39, No. 4, (May 2002), pp. 366–373, ISSN 0020-1685
- Kosinova, M.L., Fainer, N.I., Rumyantsev, Yu.M., Maximovski, E.A., Kuznetsov, F.A., Terauchi, M., Shibata, K., & Satoh, F. (2003). Growth of homogeneous and gradient BC_xN_y films by PECVD using trimethylamino borane complex. *ECS Proc.*, Vol. 2003-08, pp. 708-715, ISSN 1938-5862
- Kosinova, M.L., Fainer, N.I., Sulayeva, V.S., Rumyantsev, Yu.M., Kuznetsov, F.A., Maximovski, E.A., Cao, Z.X., Terauchi, M., Shibata, K., & Satoh, F. (2005). Synthesis, nanoindentation and AFM studies of CVD boron nitride films». *ECS Proc.*, Vol. 2005-09, pp.1082-1087, ISSN 1938-5862
- Kosolapova, T.Ya., Makarenko, G.N., Serebryakova, T.I., Prilutskii, E.V., Khorpyakov, O.T., & Chernysheva, O.I. (1971). Nature of boron carbonitride I. Conditions of preparation of boron carbonitride. *Powder Metallurgy and Metal Ceramics*, Vol. 10, No 1, pp. 22-26, ISSN 1068-1302
- Kouvetakis, J., Sasaki, T., Shen, C., Hagiwara, R., Lerner, M., Krishnan, K. M. & Bartlett, N. (1989). Novel aspects of graphite intercalation by fluorine and fluorides and new B/C, C/N and B/C/N materials based on the graphite network. *Synthetic Metals*, Vol. 34, IsNo. 1-3, pp. 1-7, ISSN: 0379-6779
- Kroke, E., Li, Y.-L., Konetschny, C., Lecomte, E., Fasel, C. , & Riedel, R. (2000). Silazane derived ceramics and related materials. *Mater. Sci. Eng.*, Vol. R26, No.4-6, (January 2000), pp.97-199, ISSN 0927-796X
- Kulisch, W. (2000). Deposition of Diamond-Like Superhard Materials in the B/C/N System. *Phys. stat. sol. (a)*, Vol. 177, No.1, (December 1999), pp. 63-79, ISSN 1862-6300
- Kurapov, D., Neuschütz, D., Cremer, R., Pedersen, T., Wuttig, M., Dietrich, D., Marx, G., & Schneider, J. M. (2002). Synthesis and mechanical properties of BCN coatings deposited by PECVD. *Vacuum*, Vol. 68, IsNo. 4, July 2002, pp.335-339, ISSN: 0042-207X.
- Kurapov, D. and Schneider, J. M. (2005). Structure, Composition, Mechanical, and Tribological Properties of BCN Films Deposited by Plasma Enhanced Chemical Vapor Deposition. *Plasma Chemistry and Plasma Processing*, Vol. 25, No. 6, (aApril 2005), pp.613-623, ISSN: 0272-4324.
- Kurmaev, E.Z.; ., Ezhov, A.V.; ., Shamin, S.N.; ., Cherkashenko, V.M.; ., Andreev, Y.G.; ., & Lundström, T., (1997). X-ray Emission Spectra and Structural Models of BCN Materials. *J.Alloys and Compounds*, Vol.248, No.1-2, pp.86-89, ISSN: 0925-8388
- Lambrecht, W.L., & Segall, B. (1993). Anomalous band-gap behavior and phase stability of c-BN-diamond alloys. *Phys. Rev. B*, Vol. B 47, No. 15, pp. 9289, ISSN 1098-0121
- Latrasse, L., Lacoste, A., Sánchez-López, J.C., Bès, A., Rayar, M. & Pelletier, J. (2009). High deposition rates of uniform films in tetramethylsilane-based plasmas generated by elementary microwave sources in matrix configuration. *Surf. Coat. Technol.*, Vol.203, No.16, (February 2009), pp.2343–2349, ISSN 0257-8972
- Lau, W.S., (1999). *Infrared characterization for microelectronics*. World Scientific. ISBN 9810223528
- Lei, M. K., Li, Q., Zhou, Z. F., Bello, I., Lee, C. S. & Lee, S. T. (2001). Characterization and optical investigation of BCN film deposited by RF magnetron sputtering. *Thin Solid Films*, Vol. 389, No. 1-2, (march March 2001), pp. 194-199, ISSN 0040-6090
- Levy, R.A., Mastromatteo, E., Grow, J.M., Paturi, V., & Kuo, W.P. (1995). Low pressure chemical vapor deposition of B-C-N-H films from triethylamine borane complex. *J. Mater. Res.* Vol. 10, No. 2, (October 1994), pp. 320-327, ISSN 0884-2914

- Li, W.L., Yang, J.L., Zhao, Y. & Fei, W.D. (2009). Effect of assistant RF plasma on structure and properties of SiCN thin films prepared by RF magnetron sputtering of SiC target. *J. Alloys Comp.*, Vol.482, pp.317-319, ISSN 0925-8388
- Limmanee, A., Otsubo, M., Sugiura, T., Sato, T., Miyajima, Sh., Yamada, A., & Konagai, M. (2008). Effect of thermal annealing on the properties of a-SiCN:H films by hot wire chemical vapor deposition using hexamethyldisilazane. *Thin Solid Films*, Vol. 516, No.5, pp.652-655, ISSN 0040-6090
- Lin, H.Y., Chen, Y.C., Lin, C.Y., Tong, Y.P., Hwa, L.G., Chen, K.H., & Chen, L.C. (2002). Field emission of nanostructured amorphous SiCN films deposited by reactive magnetron sputtering of SiC in CH₄/N₂ atmosphere. *Thin Solid Films*, Vol. 416, pp.85-91, ISSN 0040-6090
- Ling, H.,; Wu, J. D.,; Sun, J.,; Shi, W.,; Ying Z. F. & Li, F. M. (2002). Electron cyclotron resonance plasma-assisted pulsed laser deposition of boron carbon nitride films. *Diamond and Related. Materials*, Vol. 11, No. 9 (February 2002), pp. 1623-1628. , ISSN 0925-9635.
- Linss, V., Rodil, S. E., Reinke, P., Garnier, M. G., Oelhafen, P., Kreissig, U. & Richter, F. (2004). Bonding characteristics of DC magnetron sputtered B-C-N thin films investigated by Fourier-transformed infrared spectroscopy and X-ray photoelectron spectroscopy. *Thin Solid Films*, Vol. 467, No. 1-2, (March 2004), pp. 76-87, ISSN 0040-6090
- Linss, V., Barzola-Quiquia, J., Häussler, P. & Richter, F. (2004). Structural properties of d.c. magnetron sputtered B-C-N thin films and correlation to their mechanical properties: a new empirical formula. *Thin Solid Films*, Vol. 467, No. 1-2, (March 2004), pp.66-75, ISSN 0040-6090
- Lippmann, G., (Coord.), (2006-2010). *Progress Summary* 2009. <http://www.google.de/search?client=firefox-a&rls=org.mozilla%3Ad>
- Liu A.Y., Wentzcovitch R.A., & Cohen M.L. (1989). Atomic arrangement and electronic structure of BC₂N. *Phys. Rev. B*, Vol. B 39, No. 3, pp. 1760-1765, ISSN 1098-0121
- Liu, L., Wang, Y., Feng, K., Li, Y., Li, W., Zhao, Ch. & Zhao, Yo. (2006). Preparation of boron carbon nitride thin films by radio frequency magnetron sputtering. *Appl. Surf. Sci.*, Vol. 252, No. 12, (June 2005), pp. 4185-4189, ISSN 0169-4332
- Loeffler, J., Konyashin, I., Bill, J., Uhlig, H., & Aldinger, F. (1997). PACVD nano-crystalline B-C-N thin films obtained by use of an organoboron precursor. *Diamond and Related Materials*, Vol.6, No.5-7, pp.608-611, ISSN 0925-9635
- Loir, A.-S., Pech, D., Steyer, P., Gachon, Y., Herau, C., & Sanchez-Lopez, J. C., (2007). Study of the Si Chemical Bonding and the Semiconductive Behavior of the SiCN Coatings and their Correlation with Anti-Corrosion Properties. *Plasma Process. Polym.*, Vol. 4, pp.173-179, ISSN 1612-8850
- Lombardi, J.R. & Birke, R.L., (2008). An Unified Approach to Surface-Enhanced Raman Spectroscopy. *Journal of Physical Chemistry C*, Vol.112, No.14, pp.5605-5617, ISSN 1932-7447
- Lousa, A., Esteve, J., Muhl, S. & Martínez, E. (2000). BCN thin films near the B₄C composition deposited by radio frequency magnetron sputtering. *Diamond Relat. Mater.*, Vol. 9, No. 3-6, pp. 502-505, ISSN: 0925-9635
- Ma, R., & Bando, Y., (2003). Pyrolytic grown B-C-N and BN nanotubes. *Science & Technology of Advanced Materials*, Vol.4, No.5, pp.403-407, ISSN: 1468-6996
- Ma, S., Xu, B., Wu, G., Wang, Y., Ma, F., Ma, D., Xu, K. & Bell, T. (2008). Microstructure and mechanical properties of SiCN hard films deposited by an arc enhanced magnetic

- sputtering hybrid system. *Surf. Coat. Technol.*, Vol.202, No.22-23, pp.5379-5382, ISSN 0257-8972
- Majoulet, O.; , Alauzun, J.G.; , Gottardo, L.; , Gervais, C.; , Schuster, M.E.; , Bernard, S.; , & Miele, P., (2011). Ordered mesoporous silicoboron carbonitride ceramics from boron-modified polysilazanes: Polymer synthesis, processing and properties. *Microporous and Mesoporous Mater.*, Vol.140, No.1-3, (September 2010), pp.40-50, ISSN: 1387-1811.
- Mannan, Md.A., Nagano, M., Shigezumi, K., Kida, T., Hirao, N., & Baba, Y. (2008). Characterization of Boron Carbonitride (BCN) Thin Films Deposited by Radiofrequency and Microwave Plasma Enhanced Chemical Vapor Deposition. *Amer. J. Appl. Sci.*, Vol. 5, No.6, pp. 736-741, ISSN 1546-9239
- Mannan, Md.A.; , Noguchi, H.; , Kida, T.; , Nagano, M.; , Hirao, M.; , Baba, Y., (2008). Chemical bonding states and local structures of the oriented hexagonal BCN films synthesized by microwave CVD. *Materials Science in Semiconductor Processing*, Vol.11, No.3, (May 2009), pp.100-105, ISSN: 1369-8001
- Mannan, Md.A.; , Nagano, M.; , Kida, T.; , Hirao, N.; , & Baba, Y.; (2009). Characterization of BCN films synthesized by radiofrequency plasma enhanced chemical vapor deposition. *J.Phys.Chem.Solids*, Vol.70, No.1, (August 2008), pp.20-25, ISSN 0022-3697
- Mannan, Md.A., Kida, T., Noguchi, H., Nagano, M., Shimoyama, I., Hirao, N., Baba, Y. (2009). Atomic arrangement, composition and orientation of hexagonal BCN films synthesized by radiofrequency plasma enhanced CVD. *J. Ceram. Soc. Jap.*, Vol.117, No.1364, (January 2009), pp.503-507, ISSN 1882-0743
- Mannan, Md.A., Noguchi, H., Kida T., Nagano, M., Hirao, N., Baba, Y. (2010). Growth and characterization of stoichiometric BCN films on highly oriented pyrolytic graphite by radiofrequency plasma enhanced chemical vapor deposition. *Thin Solid Films*, Vol. 518, No.15, (November 2009), pp. 4163-4169, ISSN 0040-6090
- Mannan, Md.A., Baba, Y., Kida, T., Nagano, M., Shimoyama, I., Hirao, N., & Noguchi, H., (2011). Orientation of B-C-N hybrid films deposited on Ni(111) and polycrystalline Ti substrates explored by X-ray absorption spectroscopy. *Thin Solid Films*, Vol.519, No.6, (September 2010), pp.1780-1786, ISSN: 0040-6090.
- Martínez, E., Lousa, A. & Esteve, J. (2001). Micromechanical and microtribological properties of BCN thin films near the B₄C composition deposited by r.f. magnetron sputtering. *Diamond Relat. Mater*, Vol. 10, No. 9-10, pp. 1892-1896, ISSN: 0925-9635
- Martínez, C., Kyrsta, S., Cremer, R. & Neuschütz, D. (2002). Influence of the composition of BCN films deposited by reactive magnetron sputtering on their properties. *Analytical and Bioanalytical Chemistry*, Vol. 374, No. 4, (July 2002), pp. 709-711, ISSN 1618-2642
- Maya L. (1988). Aminoborane polymers as precursors of C-N-B ceramic materials. *J. Am. Ceram. Soc.*, Vol.71, No. 12, pp.1104-1109
- Maya L. (1988). Semiconducting amorphous film containing carbon, nitrogen and boron. *J. Electrochem. Soc.*, Vol.135, No.5, pp.1278-1281, ISSN: 0013-4651
- Maya, L. & Harris, L.A., (1990). Pyrolytic deposition of carbon films containing nitrogen and/or boron. *J. Am. Ceram. Soc.*, Vol. 73, No.7, (February 1990), pp. 1912-191
- Mazumder, M. K., Aoki, H., Masuzumi, T., Hara, M., Watanabe, D., Kimura, C., Fukagawa, M., Umeda, M., Kusuhashi, M. & Sugino, T. (2009). Properties of boron carbon nitride (BCN) film after plasma ashing *Diamond Relat. Mater*, Vol. 18, No. 2-3, pp. 419-422, ISSN: 0925-9635

- Mishra, S.K., Bhattacharyya, A.S. (2008). Effect of substrate temperature on the adhesion properties of magnetron sputtered nano-composite Si-C-N hard thin films. *Materials Letters*, Vol. 62, No.3, (May 2007), pp.398–402, ISSN: 0167-577X
- Mishra, S. K. (2009). Nano and Nanocomposite Superhard Coatings of Silicon Carbonitride and Titanium Diboride by Magnetron Sputtering. *Int. J. Appl. Ceram. Technol.*, Vol. 6, pp.345–354, ISSN 1546-542X
- Montasser, K., Hattori, S., & Morita, S. (1984). Transparent B-C-N thin films formed by plasma chemical vapour deposition. *Thin Solid Films*, Vol.117, No. 4, pp.311-317, ISSN 0040-6090
- Montasser, K., Hattori, S., & Morita, S. (1985). Characterization of hard transparent B-C-N-H thin films formed by plasma chemical vapor deposition at room temperature. *J. Appl. Phys.*, Vol.58, No.8, pp.3185-3189
- Montasser, R., Morita, S., & Hattori, S. (1991). A promising boron-carbon-nitrogen thin film. *Mat. Sci. Forum...*, Vol.54-55, pp.295-312, ISSN 0255-5476
- Moore, A. W., Strong, S. L., Doll, G. L., Dresselhaus, M. S, Spain, I. L., Bowers, C. W., Issi, J. P. and Piraux, L. (1989) Properties and characterization of codeposited boron nitride and carbon materials. *J. Appl. Phys.*, Vol.65, IsNo. 12, February 1989, pp.5109-5118
- Morant, C.; , Prieto, P.; , Bareño, J.; , Sanz, J.M.; , & Elizalde, E., (2006). Hard BC_xN_y thin films grown by dual ion beam sputtering. *Thin Solid Films*, Vol.515, No1, pp.207-211, ISSN: 0040-6090
- Morjan, I., Conde, O., Oliveira, M., & Vasiliu, F. (1999). Structural characterization of $\text{C}_x\text{B}_y\text{N}_z$ ($x=0.1$ to $x=0.2$) layers obtained by laser-driven synthesis. *Thin Solid Films*, Vol. 340, pp. 95-105, ISSN 0040-6090
- Nakao, S., Sonoda, T., Tsugawa, K., Choi, J. & Kato, T. (2009). Effects of nitrogen gas ratio on composition and microstructure of BCN films prepared by RF magnetron sputtering. *Vacuum*, Vol. 84, No. 5, (June 2009), pp. 642-647, ISSN 0042-207X
- Nakayamada, T., Matsuo, K., Hayashi, Y., Izumi, A. & Kadotani, Y. (2008). Evaluation of corrosion resistance of SiCN films deposited by HWCVD using organic liquid materials. *Thin Solid Films*, Vol. 516, No.5, pp.656–658, ISSN 0040-6090
- Nesládek, M., Vaněček, M., Meykens, K., Haenen, K., Manca, J., De Schepper, L., Pace, E., Pini, A., Verona Rinati, G., Kimura, C., Etou, Y., & Sugino, T. (2001). Study of UV and Subgap Photocurrent Response in Diamond and BCN Thin Films for Detector Applications. *Physica status solidi (a)*, Vol. 185, No. 1, pp. 107–113, ISSN: 1862-6300
- O'Keefe, M.A.; Allard, L.F., (2004). Sub-Ångstrom Electron Microscopy for Sub-Ångstrom Nano-Metrology. *National Nanotechnology Initiative Workshop on Instrumentation and Metrology for Nanotechnology*, Gaithersburg, MD (2004)
- Okada, K., Kimura, C., & Sugino, T. (2006). Surface properties of boron carbon nitride films treated with plasma. *Diamond Relat. Mater.*, Vol. 15, No. 4-8, pp. 1000-1003, ISSN: 0925-9635
- Oura, K.; , Lifshits, V.G.; , Saranin, A.A.; , Zotov, A.V.; , Katayama, M., (2003). *Surface Science: An Introduction*. Springer-Verlag, ISBN 3-540-00545-5
- Pagels, M.; , Reinhardt, F.; , Pollakowski, B.; , Roczen, M.; , Becker, C.; , Lips, K.; , Rech, B.; , Kanngießer, B.; , Beckhoff, B., (2010). GIXRF-NEXAFS investigations on buried ZnO/Si interfaces: A first insight in changes of chemical states due to annealing of the soecimen. *Nucl.Instr.Meth.B*, Vol.268, No.3-4, pp.370-373, ISSN: 0168-583X.

- Pan, W. J.; , Sun, J.; , Ling, H.; , Xu, N.; , Ying Z. F., & Wu, J. D. (2003). Preparation of thin films of carbon-based compounds. *Appl. Surf. Sci.*, Vol. 218, No. 1-4, (April 2003), pp. 298-305. , ISSN 0169-4332
- Peng, X., Song, L., Meng, J., Zhang, Y., & Hu. X., (2001). Preparation of silicon carbide nitride thin films by sputtering of silicon nitride target. *Appl. Surf. Sci.*, Vol.173, pp.313-317, ISSN 0169-4332
- Peng, Y., Zhou, J., Zhang, Z., Zhao, B., & Tan, X. (2010). Influence of radiofrequency power on compositional, structural and optical properties of amorphous silicon carbonitride films. *Appl. Surf. Sci.*, Vol.256, No.7, (September 2009), pp.2189-2192, ISSN 0169-4332
- Perrone, A.; , Caricato, A. P.; , Luches, A.; , Dinescu, M.; , Ghica, C.; , Sandu, V., and & Andrei, A. (1998). Boron carbonitride films deposited by pulsed laser ablation. *Appl. Surf. Sci.*, Vol. 133, No. 4, (February 1998), pp. 239-242. , ISSN 0169-4332
- Polo, M.C., Martínez, E., Esteve, J. & Andújar, J.L. (1998). Preparation of B-C-N thin films by r.f. plasma assisted CVD. *Diamond and Relat.ed Mater.ials*, Vol. 7, No.2-5, pp. 376-379, ISSN 0925-9635
- Polo, M.C., Martínez, E., Esteve, J., & Andújar, J.L. (1999). Micromechanical properties of BN and B-C-N cotings obtained by r.f. plasma-assisted CVD. *Diamond Relat. Mater.*, Vol. 8, No.2-5, pp. 423-427, ISSN 0925-9635
- Popov, C., Saito, K., Ivanov, B., Koga, Y., Fujiwara, Sh. and Shanov, V. (1998) Chemical vapour deposition of BC₂N films and their laser-induced etching with SF₆. *Thin Solid Films*, Vol. 312, IsNo. 1-2, (August 1997), pp. 99-105, ISSN: 0040-6090
- Popov, C., Saito, K., Yamamoto, K., Ouchi, A., Nakamura, T., Ohana, Yo., & Koga, Yo. (1998) Synthesis of nitrogen-rich B-C-N materials from melamine and boron trichloride. *Journal of Materials Science*, Vol. 33, No. 5, pp.1281-1286, ISSN: 0022-2461
- Probst, D., Hoche, H., Zhou, Y., Hauser, R., Stelzner, T., Scheerer, H., Broszeit, E., Berger, C., Riedel, R., Stafast, H., & Koke, E. (2005). Development of PE-CVD Si/C/N:H films for tribological and corrosive complex-load conditions. *Surf. Coat. Technol.*, Vol. 200, No. 1-4, (1 October 2005), pp. 355- 359, ISSN 0257-8972
- Ray, S.C.; , Tsai, H.M.; , Chiou, J.W.; , Jan, J.C.; , Kumar, K.; , Pong, W.F.; , Chien, F.Z.; , Tsai, M.-H.; , Chattopadhyay, S.; , Chen, L.C.; , Chien, S.C.; , Lee, M.T.; , Lin, S.T.; , & Chen, K.H., (2004). X-ray absorption studies of boron-carbon-nitrogen (B_xC_yN_z) ternary alloys. *Diamond Rel.Mater.ials*, Vol.13, No.4-8, pp.1553-1557, ISSN: 0925-9635
- Reigada, D.C. & Freire, F.L. Jr. (2001). Nitrogen incorporation into boron carbide films deposited by dc-magnetron sputtering: film microstructure and tribological properties. *Surface and & Coatings Technology*, Vol. 142-144, (July 2001), pp.889-893, ISSN: 0257-8972
- Rose, H.H.; (2008). Optics of high-performance electron microscopes. *Technology of Advanced Materials*, Vol.9, No.1, (March 2008), pp.014107, ISSN: 1468-6996
- Samsonov, G.V., Semenov, Yu.N., & Borodulin, P.Ya. (1962). Refractory materials on the base of boron nitride.
- Saugnas, F., Teyssandier, F., & Marchand, A. (1992). Characterization of C-B-N solid solutions deposited from a gaseous phase between 900° and 1050°C. *J Am. Ceram. Soc.*, Vol.75, No.1, pp.161-169, ISSN 1551-2916
- Schmolla W., Hartnagel H.L. (1983). Amorphous BN films produced in a double-plasma reactor for semiconductor application. *Solid State Electronics*, Vol.26, No.10, pp.931-939, ISSN 0038-1101

- Schonfelder, H., Aldinger, E., Riedel, R. (1993). Silicon carbonitrides - A novel class of materials, *J. de Physique IV*, Vol. 3, No. C7, pp.1293-1298, ISSN 1155-4339
- Shimada, Y., Chikamatsu, K., Kimura, C., Aoki, H., & Sugino, T. (2006). Effect of plasma treatment on interface property of BCN/GaN structure. *Appl. Surf. Sci.*, Vol. 253, No. 3, pp. 1459-1463, ISSN: 0169-4332
- Smirnova T.P., Badalian, A.M., Yakovkina, L.V., Kaichev, V.V., Bukhtiyarov, V.I., Shmakov, A.N., Asanov, I.P., Rachlin, V.I., & Fomina, A.N. (2003). SiCN alloys obtained by remote plasma chemical vapour deposition from novel precursors. *Thin Solid Films.*, Vol. 429, No. 1-2, (April), pp.144-151, ISSN 0040-6090
- Smirnova, T. P., Badalian, A. M., Borisov, V. O., Bakhturova, L. F., Kaichev, V. V., Podgorbunskaya, T. A., & Rakhlin V. I. (2008). Plasma-Chemical Deposition of SiCN Films from Volatile N-Bromhexamethyldisilazane. *Inorganic Materials.*, Vol. 44, No. 12, (November 2007), pp. 1312-1318, ISSN 0020-1685
- Solozhenko, V.L., Andrault, D., Mezouar, M., & Rubie, D.C. (2001). Synthesis of superhard cubic BC₂N. *Appl. Phys. Lett.*, Vol. 78, No. 10, (November 2000), pp. 1385-1387.
- Soto, G., Samano, E. C., Machorro, R., & Cota, L. (1998). Growth of SiC and SiC_xN_y films by pulsed laser ablation of SiC in Ar and N₂ environments. *J. Vac. Sci. Technol. A*, Vol.16, pp.1311-1315, ISSN 0734-2101
- Stanishevsky, A., Li, H., Badzian, A., Badzian, T., Drawl, W., Khriachtchev, L. & McDaniel, E. (2001). B-C-N coatings prepared by microwave chemical vapor deposition. *Thin Solid Films*, Vol. 398-399, pp. 270-274, ISSN 0040-6090
- Stelzner, Th., Arold, T. M., Falk, F., Stafast, H., Probst, D. & Hoche, H. (2005). Single source precursors for plasma-enhanced CVD of SiCN films, investigated by mass spectrometry. *Surf. Coat. Technol.*, Vol. 200, No. 1-4, (October 2005), pp. 372- 376, ISSN 0257-8972
- Stockel, S., Weise, K., Dietrich, D., Thamm, T., Braun, M., Cremer, R., Neuschütz, D., & G. Marx. (2002). Influence of composition and structure on the mechanical properties of BCN coatings deposited by thermal CVD. *Thin Solid Films.* , Vol. 420 -421, pp. 465-471, ISSN 0040-6090
- Stöckel, S., Weise, K., Thamm, T., Körner, K.-U., Dietrich, D., & Marx · G. (2003). Comparative investigations of structure and properties of BCN coatings deposited by thermal and plasma-enhanced CVD. *Anal. Bioanal. Chem.* Vol. 375, (November 2002), pp. 884-890, ISSN 1618-2642
- Stöhr, J., (1992). *NEXAFS Spectroscopy*. Springer, Berlin
- Sugimoto, Y.; ., Pou, P.; ., Abe, M.; ., Jelinek, P.; ., Perez, R.; ., Morita, S.; ., Custance, O.; (2007). Chemical identification of individual surface atoms by atomic force microscopy. *Nature*, Vol.446, No.7131, pp.64-67.
- Sugino, T. & Hieda, H. (2000). Field emission characteristics of boron carbon nitride films synthesized by plasma-assisted chemical vapor deposition. *Diamond Relat. Mater*, Vol. 9, No. 3-6, pp. 1233-1237, ISSN: 0925-9635
- Sugino, T., Tai, T. & Etou, Y. (2001). Synthesis of boron nitride film with low dielectric constant for its application to silicon ultralarge scale integrated semiconductors. *Diamond Relat. Mater*, Vol. 10, No. 3-7, pp. 1375-1379, ISSN: 0925-9635
- Sugino, T., Etou, Y., Tai, T., & Mori, H. (2002). Dielectric constant of boron carbon nitride films synthesized by plasma-assisted chemical-vapor deposition. *Appl. Phys. Lett.*, Vol. 80, No. 4, (November 2001), p. 649-652
- Sugino, T., Kimura, C. & Aoki, H. (2008). Surface properties and field emission of boron nitride. *Diamond Relat. Mater*, Vol. 17, No. 7-10, pp. 1764-1769, ISSN: 0925-9635

- Sugino, T., Kikuchi, J., Kawai, S., Kimura, C., & Aoki, H. (2010). Improved tunneling controlled field emission of Boron carbon nitride nanofilm. *Diamond Relat. Mater.*, Vol. 19, No. 5-6, pp. 545-547, ISSN: 0925-9635
- Sugiyama, T., Tai, T. & Sugino, T. (2002). Effect of annealing on dielectric constant of boron carbon nitride films synthesized by plasma-assisted chemical vapor deposition. *Appl. Phys. Lett.*, Vol.80, No. 22, April 2002, pp.4214-1 - 4214-4
- Sugiyama, T., Tai, T., Okamoto, A., Yoshitake, M., & Sugino, T. (2003). Influence of the annealing process on properties of Cu/BCN/p-Si structure. *Diamond Relat. Mater.*, Vol. 12, No. 3-7, pp. 1113-1116, ISSN: 0925-9635
- Sulyaeva, V.S., Rumyantsev, Yu.M., Kosinova, M.L., Golubenko, A.N., Fainer, N.I., & Kuznetsov, F.A. (2007). Plasma enhanced chemical vapour deposition of BC_xN_y films prepared from N-trimethylborazine: Modelling, synthesis and characterization. *Surf. Coat. Technol.*, Vol.201, No.22-23, April 2007, pp.9009-9014, ISSN 0257-8972
- Sulyaeva, V.S., Kosinova, M.L., Golubenko, A.N., Rumyantsev, Yu.M., Fainer, N.I., & Kuznetsov, F.A. (2009). PECVD BC_xN_y films from mixtures of N-trimethylborazine with hydrogen and ammonia: modelling, synthesis and characterization. *ECS Transaction*, Vol.25, No. 8, part 1. , pp. 343-348, ISSN 1938-5862
- Sulyaeva, V. S., Kosinova, M. L., Rumyantsev, Yu. M., Golubenko, A. N., Fainer, N. I., Alferova, N. I., Ayupov, B. M., Gevko, P. N., Kesler, V. G., Kolesov, B. A., Maksimovskii, E. A., Myakishev, K. G., Yushina, I. V., & Kuznetsov, F. A. (2010). Properties of BC_xN_y Films Grown by Plasma Enhanced Chemical Vapor Deposition from N-Trimethylborazine-Nitrogen Mixtures. *Inorganic Materials*, Vol. 46, No. 5, pp. 487-494, ISSN 0020-1685
- Suvorova, A. A., Nunney, T., & Suvorov, A. V. (2009). Fabrication of Si-C-N compounds in silicon carbide by ion implantation. *Nuclear Instruments and Methods in Physics Research B*, Vol. 267, No. 8-9, pp. 1294-1298, ISSN 0168-583X
- Swain, B. P., Hwang, N. M. (2008). Study of structural and electronic environments of hydrogenated amorphous silicon carbonitride (a-SiCN:H) films deposited by hot wire chemical vapor deposition. *Appl. Surf. Sci.*, Vol. 254, No.17, (February 2008), pp.5319-5322, ISSN 0169-4332
- Tai, T., Sugiyama, T., & Sugino, T. (2003). Growth and characterization of boron carbon nitride films with low dielectric constant. *Diamond Relat. Mater.*, Vol. 12, No. 3-7, pp. 1117-1121, ISSN: 0925-9635
- Taylor, R.; , Hare, J.P.; , Abdul-Sada, A.K.; , & Kroto, H.W., (1990). Isolation, separation and characterization of the fullerenes C60 and C70: the third form of carbon. *Journal of the Chemical Society, Chemical Communications* Vol.20, pp.1423-1425. , ISSN: 0022-4936.
- Teodorescu, V.S.; , Luches, A.; , Dinu, R.; , Zocco, A.; , Ciobanu, M.F.; , Martino, M.; , Sandu, V. and & Dinescu, M. (1999). Influence of the substrate temperature on BCN films deposited by sequential pulsed laser deposition. *App. Phys. A: Mater. Sci. & Proces.*, Vol. 69, No. 7, pp.S667-S670. , ISSN 0947-8396
- Thamm, T., Körner, K.-U., Bohne, W., Strub, E., Röhrich, J., Stöckel, S., & Marx G. (2005). Characterization of PECVD boron carbonitride layers. *Appl. Surf. Sci., Appl. Surf. Sci.*, Vol. 252, No.1, (March 2005), pp. 223-226, ISSN 0169-4332
- Thamm; T., Wett, D., Bohne, W., Strub, E., Röhrich, J., Szargan, R., Marx, G., & Goedel, W.A. (2007). Investigations on PECVD boron carbonitride layers by means of

- ERDA, XPS and nano-indentation measurements. *Microchim. Acta.*, Vol. 156, No.1-2, (April 2006), pp. 53-56, ISSN: 0026-3672
- Thäringen, T., Lippold, G., Riede, V., Lorenz, M., Koivusaari, K. J., Lorenz, D., Mosch, S., Grau, P., Hesse, R., Streubel, P., & Szargan, R. (1999). Hard amorphous CSixNy thin films deposited by RF nitrogen plasma assisted pulsed laser ablation of mixed graphite/Si3N4-targets. *Thin Solid Films*, Vol. 348, pp.103-113, ISSN 0040-6090
- Ting, S.-F., Fang, Y.-K., Hsien, W.-T., Tsair, Y.-S., Chang, C.-N., Lin, C.-S., Hsieh, M.-C., Chiang, H.-C., & Ho, J.-J. , (2002). Heteroepitaxial Silicon-Carbide Nitride Films with Different Carbon Sources on Silicon Substrates Prepared by Rapid-Thermal Chemical-Vapor Deposition. *Journal of Electronic materials*, Vol. 31, No.12, pp.1341-1346, ISSN 0361-5235
- Tomasella, E., Rebib, F., Dubois, M., Cellier, J., & Jacquet, M. (2008). Structural and optical properties studies of sputtered a-SiCN thin films. *Journal of Physics: Conference Series*, Vol.100, (February 2008), pp.082045. ISSN 1742-6596
- Tompkins, H.G., (2006). *A User's Guide to Ellipsometry*. Dover Publications Inc., Mineola, ISBN 0-486-45028-7
- Torres, R.; , Caretti, I.; , Gago, R.; , Martin, Z.; , Jimenéz, I., (2007). Bonding structure of BCN nanopowders prepared by ball milling. *Diamond Rel. Materials*, Vol.16, No.4-7, pp.1450-1454, ISSN: 0925-9635
- Trusso, S., Barreca, F., & Neri, F. (2002). Bonding configurations and optical band gap for nitrogenated amorphous silicon carbide films prepared by pulsed laser ablation. *J. Appl. Phys.*, Vol. 92, No.5, pp.2485-2489, ISSN 0021-8979
- Tsai, P.-C. (2007). The deposition and characterization of BCN films by cathodic arc plasma evaporation. *Surf. Coat. Technol. Surf. Coat. Technol.*, Vol. 201, (August 2007), pp. 5108-5113, ISSN 0257-8972
- Uddin, Md.N., Shimoyama, I., Baba, Y., Sekiguchi, T., Nath, K.G., & Nagano, M. (2005). B-C-N hybrid synthesis by high-temperature ion implantation. *Appl. Surf. Sci., Appl. Surf. Sci.* Vol.241, (October 2004), pp. 246-249, ISSN 0169-4332
- Uddin, Md.N., Shimoyama, I., Baba, Y., Sekiguchi, T., Nath, K.G. & Nagano, M. (2006). Synthesis and characterization of oriented graphitelike B-C-N hybride. *J. Appl. Phys.*, Vol.99, (February 2006), pp. 084902-1 – 084902-5
- Uddin, Md.N., Shimoyama, I., Baba, Y., Sekiguchi, T., & Nagano, M. (2006). X-ray photoelectron spectroscopic observation on B-C-N hybrids synthesized by ion beam deposition of borazine. *J. Vac. Sci. Technol. A*, Vol.23, No.3, (February 2005), pp. 497-502
- Ulrich, S., Ehrhardt, H., Theel, T., Schwan, J., Westermeyr, S., Scheib, M., Becker, P., Oechsner, H., Dollinger, G. & Bergmaier, A. (1998). Phase separation in magnetron sputtered superhard BCN thin films. *Diamond Relat. Mater*, Vol. 7, No. 6, (October 1997), pp. 839-844, ISSN: 0925-9635
- Ulrich, S., Kratzsch, A., Leiste, H., Scheib, M., Schloßmacher, P., Holleck, H., Binder, J., Schild, D., Westermeyer, S., Becker, P., & Oechsner, H. (1999). Variation of carbon concentration, ion energy, and ion current density of magnetron-sputtered boron carbonitride films. *Surface and Coatings Technology*, Vol. 116-119, pp. 742-750. ISSN: 0257-8972
- Umeda, Sh., Yuki, T., Sugiyama, T., & Sugino, T. (2004). Boron carbon nitride film with low dielectric constant as passivation film for high speed electronic devices. *Diamond Relat. Mater*, Vol. 13, No. 4-8, pp. 1135-1138, ISSN: 0925-9635

- Van Grieken, R.; ., Markowicz, A. (Eds.), (2002). *Handbook of X-ray Spectrometry*. Marcel Dekker, New York
- Vassallo, E., Cremona, A., Ghezzi, F., Dellera, F., Laguardia, L., Ambrosone, G., & Coscia, U. (2006). Structural and optical properties of amorphous hydrogenated silicon carbonitride films produced by PECVD. *Appl. Surf. Sci.*, Vol. 252, No. 22, (8 October 2005), pp. 7993-8000, ISSN 0169-4332
- Vlcek, J., Kormunda, M., Cizek, J., Perina, V., & Zemek, J. (2002). Influence of nitrogen-argon gas mixtures on reactive magnetron sputtering of hard Si-C-N films. *Surface and Coatings Technology*, Vol.160, pp.74-81, ISSN 0257-8972
- Voronkov, M.G., Sulimin, A.D., Yachmenev, V.V., Mirskov, R.G., Kokin, V.N., & Chernova, V.G. (1981). Production of silicon nitride films from hexamethylcyclotrisilazane in high-frequency glow discharge. *Dokl. AN USSR.* , Vol. 259, No.5, pp.1130-1132, ISSN 0002-3264 (in Russian)
- Wada, Y.; Yap, Y. K.; Yoshimura, M.; Mori, Y. & Sasaki, T. (2000). The control of B---N and B---C bonds in BCN films synthesized using pulsed laser deposition. *Diamond and Related Materials*, Vol. 9, No. 3-6, pp. 620-624. , ISSN 0925-9635
- Wang E.G. (1999). A new development in covalently bonded carbon nitride and related materials. *Adv. Mater.*, Vol.11. , No.13, pp.1129-1133, ISSN 1521-4095
- Wang, Z.-C.; ., Kamphowe, T.W.; ., Katz, S.; ., Peng, J.; ., Seifert, H.J.; ., Bill, J.; ., & Aldinger, F., (2000). Effects of polymer thermolysis on composition, structure and high-temperature stability of amorphous silicoboron carbonitride ceramics. *J.Mater.Sc.Letters*, Vol.19, No.19, pp.1701-1704, ISSN: 0261-8028.
- Watanabe, D., Aoki, H., Moriyama, R., Mazumder, M. K., Kimura, C. & Sugino, T. (2008). Characterization of BCN film after wet process for interconnection integration. *Diamond Relat. Mater*, Vol. 17, No. 4-5, pp. 669-672, ISSN: 0925-9635
- Watanabe, M. O., Itoh, S., Mizushima, K., and & Sasaki, T. (1995). Electrical properties of BC₂N thin films prepared by chemical vapor deposition. *J. Appl. Phys.*, Vol.78, No. 4, May 1995, pp.2880-2883
- Watanabe, M. O., Itoh, S., Mizushima, K., and & Sasaki, T. (1996). Bonding characterization of BC₂N thin films. *Appl. Phys. Lett.*, Vol.68, IsNo. 21, (March 1996), pp.2962-2964 (3 pages)
- Watanabe, M.O., Sasaki, T., Itoh, S. and & Mizushima, K. (1996) Structural and electrical characterization of BC₂N thin films. *Thin Solid Films*, Vol. 281-282, pp. 334-336, ISSN: 0040-6090
- Weber, A., Bringmann, U., Klages, C.P., Taube, K., Döllein, G., Meyer, H., & Weidenbach, G. (1992). Plasma deposition of BN, BCN:H and Me-BCN:H films using N-trimethylborazine (Me = Ti, Nb). *J. de Phys. III*, Vol. 2, No.8, (April 1992), pp. 1391-1398
- Weber, A., Bringmann, U., Nikulski, R., & Klages, C.-P. (1993). Growth of cubic boron nitride and boron-carbon-nitrogen coatings using N-trimethylborazine in an electron cyclotron resonance plasma process. *Diamond and Related. Mater.ials*, Vol. 2, No. 2-4, (March 1993), pp. 201-206, ISSN 0925-9635
- Weissenbacher, R., Haubner, R., Aigner, K., & Lux B. (2002). Interactions of Ta-filaments during hot-filament CVD of BCN-layers. *Diamond and Related Materials*, Vol. 11, No.2, (October 2001), pp. 191-197, ISSN 0925-9635
- Weissenbacher, R., Haubner, R. (2003). HF-CVD of B, C, N containing layers on various substrates by the decomposition of Triethylborazine. *Diamond and Related. Mater.ials*, Vol. 12, No.3-7, pp. 884-890, ISSN 0925-9635

- Weissenbacher, R., Haubner, R. (2006). Deposition of B, C, N coatings on WC-Co substrate – Analytical problems indicating c-BN formation. *Int. J. Ref. Met. Hard Mater.*, Vol. 24, No.5, (November 2005), pp.374-379, ISSN 0263-4368
- White, R., (1990). *Chromatography/Fourier transform infrared spectroscopy and its applications*. Marcel Dekker, New York.
<http://books.google.com/books?id=t2VSNnFoO3wC&pg=PA7>
- Wöhle, J., Ahn, H., & Rie, K.-T., (1999). BCN coatings on polymer substrates by plasma CVD at low temperature. *Surf. Coat. Technol. Surf. Coat. Technol.*, Vol. 116-119, pp. 1166-1171, ISSN 0257-8972
- Wrobel, A.M., Blaszczyk-Lezak, I., & Walkiewicz-Pietrzykowska, A. (2007). Silicon Carbonitride Thin-Film Coatings Fabricated by Remote Hydrogen-Nitrogen Microwave Plasma Chemical Vapor Deposition from a Single-Source Precursor: Growth Process, Structure, and Properties of the Coatings. *Journal of Applied Polymer Science.*, Vol. 105, No. 1, (July 2007), pp.122-129, ISSN 0021-8995
- Wrobel, A. M., Blaszczyk-Lezak, I., Uznanski, P., & Glebocki, B. (2010). Silicon Carbonitride (SiCN) Films by Remote Hydrogen Microwave Plasma CVD from Tris(dimethylamino)silane as Novel Single-Source Precursor. *Chem. Vap. Deposition.*, Vol.16, No.7-9 (September 2010), pp. 211-215, ISSN 0948-1907
- Wu, F.; ., Valle, N.; ., Fitzpatrick, R.; ., Ekerdt, J.G.; ., Houssiau, L.; ., Migeon, H.-N., (2011). Elaboration and quantitative investigation of BCN-type films by dynamic SIMS using the MCs_x⁺ mode. *Surf.Interface Anal.*, Vol. 43, No. 1-2, pp. 669-672
- Wu, J.-J., Wu, C.-T., Liao, Y. -C., Lu, T.-R., Chen, L.C., Chen, K.H., Hwa, L.-G., Kuo, C.-T., & Ling, K.-J. (1999). Deposition of silicon carbon nitride films by ion beam sputtering. *Thin Solid Films*, Vol. 355-356, pp. 417-422, ISSN 0040-6090
- Xiao, X.-Ch., Li,Ya-W., Song, Li-X., Peng, X.-F., & Hu, X.-F. (2000). Structural analysis and microstructural observation of SiC_xN_y films by reactive sputtering of SiC in N₂ and Ar. *Appl. Surf. Sci.*, Vol. 156, No. 1-4, (February 2000), pp.155-160, ISSN 0169-4332
- Xie, Z.Y., Edgar, J.H., McCormick, T.L., & Sidorov, M.V. (1998). The effects of the simultaneous addition of diborane and ammonia on the hot-filament-assisted chemical vapor deposition of diamond II. Characterization of diamond and BCN film. *Diamond and Related Materials*, Vol.7, No.9, pp.1357-1363, ISSN 0925-9635
- Xu, S.; Ma, X.; Tang, G., (2006). A Study of Nano-Mechanical Properties and Nano-Scratch Behaviour of Boron Carbonitride Films. *J.Nanoscience and Nanotechnology*, Vol.6, No.5, pp. 1441-1446, ISSN:1533-4880
- Xu, Sh., ., Ma, X., & Su, M. (2006). Investigation of BCN Films Deposited at Various N₂/Ar Flow Ratios by DC Reactive Magnetron Sputtering Plasma Science, *IEEE Transactions on Plasma Science*, Vol. 34, No.4, pp. 1199 - 1203, ISSN 0093-3813.
- Yang, Q.; ., Wang, C.B.; ., Zhang, S.; ., Zhang, D.M.; ., Shen, Q., & Zhang, L.M. (2010). Effect of nitrogen pressure on structure and optical properties of pulsed laser deposited BCN thin films. *Surf. Coat. Technol. Surf. Coat. Technol.*, Vol. 204, No. 11, (November 2009), pp. 1863-1867, ISSN 0257-8972
- Yang, T.-S., Tsai, T.-H., Lee, Ch.-H., Cheng, Ch.-L. , & Wong, M.-Sh. (2001). Deposition of carbon-containing cubic boron nitride films by pulsed-DC magnetron sputtering *Thin Solid Films*, Vol. 398-399, pp. 285-290, ISSN 0040-6090
- Yang, Z.-H.; ., Jia D.-C.; ., Duan, X.-M.; ., Zhou, Y., (2010). Microstructure and thermal stabilities in various atmospheres of SiB_{0.5}C_{1.5}N_{0.5} nano-sized powders fabricated by mechanical alloying technique. *J.Non-Crystalline Solids*, Vol.356, No.6-8, pp.326-333, ISSN: 0022-3093

- Yap, Y. K.; Wada, Y.; Yamaoka, M.; Yoshimura, M.; Mori, Y., & Sasaki, T. (2001). Bond modification of BCN films on Ni substrate. *Diamond and Related Materials*, Vol. 10, No. 3-7, (December 2001), pp. 1137-1141, ISSN 0925-9635
- Yap, Y.K. (Ed.). (2009). *B-C-N Nanotubes and Related Nanostructures*, Springer, ISBN 978-1-4419-0085-2, London, New York.
- Yap, Y.K., Wada, Y., Yamaoka, M., Yoshimura, M., Mori, Y., & Sasaki, T., (2001). Bond modification of BCN films on Ni substrate. *Diamond Related Materials*, Vol.10, No.3-7, pp.1137-1141, ISSN: 0925-9635
- Yasui, K., Fukuda, K., Katoh, H., & Kaneda, Sh. (1989). The influence of carbon addition on the internal stress and chemical inertness of amorphous silicon-nitride films. *Journal of Non-Crystalline Solids*, Vol. 111, No.1-3, pp.173-177, ISSN 0022-3093
- Yasui, H., Hirose, Y., Awazu, K., & Iwaki, M. (2000). The properties of BCN films formed by ion beam assisted deposition. *Colloids and Surfaces B: Biointerfaces*, Vol. 19, pp. 291-295, ISSN
- Ying, Z.F.; Yu, D.; Ling, H.; Xu, N.; Lu, Y.F.; Sun J., & Wu, J.D. (2007). Synthesis of BCN thin films by nitrogen ion beam assisted pulsed laser deposition from a B₄C target. *Diamond Related Materials*, Vol. 16, No. 8 (January 2007), pp. 1579-1585, ISSN: 0925-9635
- Yokomichi, H., Funakawa, T., & Masuda, A. (2002). Preparation of boron-carbon-nitrogen thin films by magnetron sputtering. *Vacuum*, Vol. 66, No. 3-4, pp. 245-249, ISSN 0042-207X
- Yokomichi, H., Futakuchi, T., Yasuoka, M., & Kishimoto, N. (2004). Fabrication of amorphous boron-carbon-nitrogen films by hot-wire CVD. *Journal of Non-Crystalline Solids*, Vol. 338-340, June 2004, pp. 509-512, ISSN 0022-3093
- Yokoshima, S., Goto, T., & Hirai, T. (1990). Dielectric properties of BN-C thick films prepared by chemical vapor deposition. *Proceed. 28th Symposium on the Basic Science of Ceramics*, pp.116-119, Fukuoka, Japan, 1990
- Yu J., & Wang E.G (1999). Turbostratic boron carbonitride film and its field-emitting behavior. *Appl. Phys. Lett.*, Vol.74, No.20, pp.2948-2950, ISSN 0003-6951
- Yu J., Wang E.G., & Xu G. (1999). Synthesis and characterization of B-C-N on molybdenum. *J. Mater. Res.* Vol.14, No.3, Ppp.1137-1141, ISSN 0884-2914
- Yue, J., Cheng, W., Zhang, X., He, D., & Chen, G. (2000). Ternary BCN thin films deposited by reactive sputtering. *Thin Solid Films*, Vol. 375, (November 1999), pp. 247-250, ISSN 0040-6090
- Yuki, T., Umeda, Sh., & Sugino, T. (2004). Electrical and optical characteristics of boron carbon nitride films synthesized by plasma-assisted chemical vapor deposition. *Diamond Related Materials*, Vol. 13, Issues No.4-8, pp. 1130-1134, ISSN 0925-9635
- Zhang, Y., Sun, H., & Chen, C.F. (2004). Superhard Cubic BC₂N Compared to Diamond. *Phys. Rev. Lett.*, Vol. 93, No. 19, pp.195504-1 - 195504-4, ISSN 0031-9007
- Zhang, Zh., Kimura, C., & Sugino, T. (2005). Wavelength-dependent effect of ultraviolet irradiation on dielectric constant of boron carbon nitride films *J. Appl. Phys.*, Vol. 98, No. 3, June 2005, pp. 036105-1 - 036105-4
- Zhou, F., Adachi, K., & Kato, K., (2006). Influence of deposition parameters on surface roughness and mechanical properties of boron carbon nitride coatings synthesized by ion beam assisted deposition. *Thin Solid Films*, Vol.497, No. 1-2, (October 2005), pp.210-217, ISSN: 0040-6090.

- Zhou, F., Adachi, K., & Kato, K. (2006). Comparoson of tribological property of a-C, a-CN_x and BCN coatings sliding against SiC balls in water. *Surf. Coat. Technol.* *Surf. Coat. Technol*, Vol. 200, (March 2005), pp. 4471-4478, ISSN 0257-8972
- Zhou, F., Adachi, K., & Kato, K. (2006). Friction and wear behavior of BCN coatings sliding against ceramic and steel balls in various environments. *Wear*, Vol. 261, (October 2005), pp. 301-310, ISSN 0043-1648
- Zhou, F., Yue, B., Wang, X., Wu, X. & Zhuge L. (2010). Surface roughness, mechanical properties and bonding structure of silicon carbon nitride films grown by dual ion beam sputtering. *J. Alloys Compounds*, Vol.492, No. 1-2, (March 2010), pp.269-276, ISSN 0925-8388
- Zhou, Y., Probst, D., Thissen, A., Kroke, E., Riedel, R., Hauser, R., Hoche, H., Broszeit, E., Kroll, P. & Stafast H. (2006). Hard silicon carbonitride films obtained by RF-plasma-enhanced chemical vapour deposition using the single-source precursor bis(trimethylsilyl)carbodiimide. *J.Europ. Ceram. Soc.*, Vol. 26, No. 8, (4 February 2005), pp.1325-1335, ISSN 0955-2219
- Zhou, Z. F., Bello, I., Lei, M. K., Li, K. Y., Lee, C. S., & Lee, S. T. (2000). Synthesis and characterization of boron carbon nitride films by radio frequency magnetron sputtering. *Surf. Coat. Technol.* *Surf. Coat. Technol*, Vol. 128-129, pp. 334-340, ISSN 0257-8972
- Zhuang, Ch., Zhao, J., Jia, F., Guan, Ch., Wu, Zh., Bai, Y. & Jiang, X. (2009). Tuning bond contents in B-C-N films via temperature and bias voltage within RF magnetron sputtering. *Surf. Coat. Technol.* *Surf. Coat. Technol*, Vol. 204, No 5, (September 2009), pp. 713-717, ISSN 0257-8972